

Monographs in Electrochemistry

Series Editor: F. Scholz

Ángela Molina

Joaquín González

Pulse Voltammetry in Physical Electrochemistry and Electroanalysis

Theory and Applications



Springer

Pulse Voltammetry in Physical Electrochemistry and Electroanalysis

Monographs in Electrochemistry

Series Editor: Fritz Scholz, University of Greifswald, Germany

Surprisingly, a large number of important topics in electrochemistry is not covered by up-to-date monographs and series on the market, some topics are even not covered at all. The series Monographs in Electrochemistry fills this gap by publishing indepth monographs written by experienced and distinguished electrochemists, covering both theory and applications. The focus is set on existing as well as emerging methods for researchers, engineers, and practitioners active in the many and often interdisciplinary fields, where electrochemistry plays a key role. These fields will range – among others – from analytical and environmental sciences to sensors, materials sciences and biochemical research.

More information about this series at <http://www.springer.com/series/7386>

Ángela Molina • Joaquín González

Pulse Voltammetry in Physical Electrochemistry and Electroanalysis

Theory and Applications

 Springer

Ángela Molina
Department of Physical Chemistry
University of Murcia
Murcia
Spain

Joaquín González
Department of Physical Chemistry
University of Murcia
Murcia
Spain

ISSN 1865-1836

Monographs in Electrochemistry

ISBN 978-3-319-21250-0

DOI 10.1007/978-3-319-21251-7

ISSN 1865-1844 (electronic)

ISBN 978-3-319-21251-7 (eBook)

Library of Congress Control Number: 2015955636

Springer Cham Heidelberg New York Dordrecht London

© Springer International Publishing Switzerland 2016

This work is subject to copyright. All rights are reserved by the Publisher, whether the whole or part of the material is concerned, specifically the rights of translation, reprinting, reuse of illustrations, recitation, broadcasting, reproduction on microfilms or in any other physical way, and transmission or information storage and retrieval, electronic adaptation, computer software, or by similar or dissimilar methodology now known or hereafter developed.

The use of general descriptive names, registered names, trademarks, service marks, etc. in this publication does not imply, even in the absence of a specific statement, that such names are exempt from the relevant protective laws and regulations and therefore free for general use.

The publisher, the authors and the editors are safe to assume that the advice and information in this book are believed to be true and accurate at the date of publication. Neither the publisher nor the authors or the editors give a warranty, express or implied, with respect to the material contained herein or for any errors or omissions that may have been made.

Printed on acid-free paper

Springer International Publishing AG Switzerland is part of Springer Science+Business Media (www.springer.com)

Preface of the Editor

Pulse techniques have a long history. Eminent scientists have to be remembered along the pathways of development of modern pulse techniques that are now so frequently used in research and analytical laboratories: Frederick Gardner Cottrell (1877–1948), Mirko Kalousek (1915–1996), Geoffrey Cecil Barker (1915–2000), Robert Allen Osteryoung (1927–2004), to name but a few. Now there are so many different varieties of pulse techniques available that it is difficult to keep an overview and to choose the most appropriate for a certain problem. The authors of this monograph, Ángela Molina and Joaquín González from the Universidad de Murcia, Spain, have undertaken the titanic venture to present a comprehensive and at the same time clearly arranged and systematic survey of pulse techniques. Both authors were best prepared for this task as they have contributed numerous theoretical and experimental studies to this field of electrochemical measuring techniques. The result is the most up-to-date monograph on the theory and application of pulse techniques—a unique book as it has never been written before. I am sure that this monograph will become and remain a first-choice standard work for many years to come.

Greifswald, Germany
March 2015

Fritz Scholz

*Idealization comes first; only then can
description follow*

Acknowledgments

The authors would like to thank the members of the “Electroquímica Teórica y Aplicada” Group of the University of Murcia, especially Professor Carmen Serna and Dr. Eduardo Laborda, and also Professor Fritz Scholz for their help and correction during the preparation of this book.

Contents

1	Some Fundamental Concepts	1
1.1	Introduction	1
1.2	Outer, Surface, and Inner Potentials	2
1.3	Thermodynamics of Electrochemical Processes	4
1.3.1	Interface Between Two Metals in Contact	6
1.4	Electrochemical Potential of the Electron	6
1.5	Nernst's Equation and Standard Electrode Potentials	8
1.5.1	Formal Electrode Potentials	14
1.6	Electrical Double Layer	15
1.6.1	Models for the Electrical Double Layer	21
1.6.2	Specific Adsorption	25
1.7	Kinetics of the Charge Transfer	27
1.7.1	The Butler–Volmer Model	31
1.7.2	The Marcus–Hush Model	33
1.8	Mass Transport	42
1.8.1	Minimization of the Migration Component	49
1.8.2	Temporal Evolution	50
1.8.3	Convection	50
1.8.4	Mass Transport Coefficient	52
1.9	Three-Electrode Systems. Ohmic Drop, Resistance of the Cell, and RC Time Constant	58
1.10	Pulse Versus Step	63
	References	65
2	Single Pulse Voltammetry: Reversible Electrochemical Reactions	67
2.1	Introduction	67
2.1.1	Reversible Electrode Reaction	69
2.2	Planar Electrodes	69
2.2.1	Concentration Profiles	72

2.2.2	Current–Time Curves (Chronoamperometry) and Current–Potential Curves (Voltammetry)	74
2.2.3	Stoichiometric Coefficients Different From the Unity . . .	79
2.3	Ion Transfer Through Liquid Membranes	81
2.3.1	One-Polarized Interface Systems	82
2.3.2	Two-Polarized Interfaces Systems	84
2.3.3	Electron Transfer at the Liquid/Liquid Interface	90
2.4	Dropping Mercury Electrode (DME)	94
2.4.1	dc Polarography	96
2.4.2	Normal Pulse Polarography (NPP)	99
2.5	Spherical Electrodes	101
2.5.1	Unequal Diffusion Coefficients ($D_O \neq D_R$)	103
2.5.2	Equal Diffusion Coefficients ($D_O = D_R$)	108
2.6	Other Electrodes Geometries	111
2.7	Microelectrodes. Steady-State Voltammetry	120
2.8	Rotating Disc Electrode	123
2.9	Thin Layer Voltammetry	126
	References	129
3	Single Pulse Voltammetry: Non-reversible and Complex Electrochemical Reactions	133
3.1	Introduction	134
3.2	Quasi-reversible and Irreversible Electrochemical Reactions . . .	134
3.2.1	Planar Electrodes	135
3.2.2	Dropping Mercury Electrode	152
3.2.3	Spherical Electrodes and Microelectrodes	154
3.2.4	Microdiscs. Steady-State Voltammetry	163
3.2.5	General Expression for the Stationary Current–Potential Response at Microelectrodes	166
3.2.6	Comparison Between Marcus–Hush and Butler–Volmer Kinetics	167
3.3	Multi-electron Electrochemical Reactions	171
3.3.1	Two-Electron Electrochemical Reactions at Planar Electrodes	173
3.3.2	Two-Electron Electrochemical Reactions at Different Electrode Geometries	180
3.3.3	Non-reversible Two-Electron Electrochemical Reactions	183
3.3.4	General Solution for Multi-electron Electrochemical Reactions	185
3.4	First-Order Chemical Reactions Coupled to Charge Transfer Processes	189
3.4.1	Catalytic Mechanism	193
3.4.2	CE Mechanism	196
3.4.3	EC Mechanism	201
3.4.4	Comparison of the Disturbed Regions by Catalytic, CE, and EC Mechanisms	203

3.4.5	Comparison Between the Current–Potential Curves Corresponding to Catalytic, CE, and EC Mechanisms	205
3.4.6	Determination of Kinetic Parameters	207
3.4.7	Spherical Electrodes	210
3.4.8	ECE Mechanism and Other More Complex Reaction Schemes	216
3.4.9	Catalytic Mechanism at Disc Electrodes	218
3.4.10	Reversible Charge Transfers Preceded and Followed by Several Complexation Reactions in Equilibrium (Ladder Mechanism)	220
	References	225
4	Double Pulse Voltammetries	229
4.1	Introduction	229
4.2	Reversible Electrochemical Reactions	233
4.2.1	Application of a Double Potential Pulse to Electrodes and Microelectrodes of Any Geometry	234
4.2.2	Double Pulse Chronoamperometry and Chronocoulometry	239
4.2.3	Reverse Pulse Voltammetry	247
4.2.4	Differential Double Pulse Voltammetry	252
4.2.5	Differential Normal Double Pulse Voltammetry	260
4.2.6	Additive Differential Double Pulse Voltammetry	260
4.3	Nonreversible Electrochemical Reactions	264
4.3.1	Application of a Double Potential Pulse to Planar and Spherical Electrodes	264
4.3.2	Reverse Pulse Voltammetry	266
4.3.3	Differential Double Pulse Voltammetry	270
4.3.4	Additive Double Differential Pulse Voltammetry	274
4.4	Multi-electron Electrochemical Reactions	278
4.4.1	Application of a Double Potential Pulse to Electrodes of Any Geometry	278
4.4.2	Differential Double Pulse Voltammetry	282
4.4.3	Additive Differential Double Pulse Voltammetry	287
4.5	First-Order Chemical Reactions Coupled to Charge Transfer Processes	291
4.5.1	Catalytic Mechanism at Disc, Spherical, and Planar Electrodes	291
4.5.2	CE and EC Mechanisms at Planar Electrodes	301
4.6	Triple Pulse Voltammetries	311
4.6.1	Reverse Differential Pulse Voltammetry	311
4.6.2	Double Differential Triple Pulse Voltammetry	313
	References	314

5	Multipulse and Sweep Voltammetries I	317
5.1	Introduction	317
5.2	Reversible Electrochemical Reactions	321
5.2.1	Application of a Multipulse Sequence to Electrodes and Microelectrodes of Any Geometry	322
5.2.2	Multipulse Chronoamperometry	325
5.2.3	Cyclic Staircase Voltammetry and Cyclic Voltammetry at Electrodes and Microelectrodes of Any Geometry	328
5.3	Non-reversible Electrochemical Reactions	349
5.3.1	Planar Electrodes	349
5.3.2	Reversibility Criteria	352
5.3.3	Other Electrode Geometries: Microelectrodes and Steady-State Voltammetry	354
5.3.4	Marcus–Hush Kinetics	356
5.4	Advantages of Using Microelectrodes	358
5.4.1	Reduction of Ohmic Drop and Capacitive Effects	359
5.4.2	Neglecting Convection	361
5.4.3	Ultrafast Voltammetry	361
5.4.4	Microelectrode Arrays	362
5.4.5	Nanoelectrodes	364
5.5	Ion Transport Through Liquid Membranes	365
5.5.1	One Polarized Interface	365
5.5.2	Two Polarized Interfaces	367
5.5.3	Micro-ITIES and Asymmetrical Diffusion	369
	References	373
6	Multipulse and Sweep Voltammetries II	375
6.1	Introduction	375
6.2	Multi-electron Electrochemical Reactions	376
6.2.1	Application of a Multipulse Sequence to Electrodes and Microelectrodes of Any Geometry	376
6.3	First-Order Chemical Reactions Coupled with the Charge Transfer	390
6.3.1	Catalytic Mechanism	391
6.3.2	CE and EC Mechanisms	401
6.3.3	ECE Mechanism	407
6.3.4	Reversible Charge Transfers Preceded and Followed by Several Complexation Reactions in Equilibrium at Electrodes of Any Geometry (“Ladder” Mechanism)	410
6.4	Surface-Bound Molecules	415
6.4.1	One-Electron Electrochemical Reactions: Statement of the Problem	416
6.4.2	One-Electron Electrochemical Reactions: Cyclic Voltammetry	433

6.4.3	Two-Electron Electrochemical Reactions	440
6.4.4	Electrocatalytic Processes at Modified Electrodes	448
	References	460
7	Differential Multipulse and Square Wave Voltammetries	463
7.1	Introduction	464
7.2	Reversible Electrochemical Reactions at Electrodes and Microelectrodes of Any Geometry	469
7.2.1	Differential Staircase Voltammetry	469
7.2.2	Differential Multipulse Voltammetry	471
7.2.3	Square Wave Voltammetry	474
7.3	Non-reversible Electrochemical Reactions	485
7.3.1	Differential Multipulse Voltammetry	485
7.3.2	Square Wave Voltammetry	489
7.4	Ion Transport Through Liquid Membranes	499
7.4.1	Differential Multipulse Voltammetry	500
7.4.2	Square Wave Voltammetry	500
7.4.3	Micro-ITIES and Asymmetrical Diffusion	503
7.5	Multi-electron Electrochemical Reactions	507
7.5.1	Reversible Electrochemical Reactions	508
7.5.2	Non-reversible Electrochemical Reactions	520
7.6	First-Order Chemical Reactions Coupled to the Charge Transfer Reaction	522
7.6.1	Catalytic Mechanism	523
7.6.2	CE and EC Mechanisms	528
7.6.3	ECE Mechanism	530
7.6.4	Ladder Mechanism	533
7.7	Surface-Bound Molecules	536
7.7.1	One-Electron Electrochemical Reactions	537
7.7.2	Multi-electron Electrochemical Reactions	557
7.7.3	Electrocatalytic Reactions at Modified Electrodes	563
	References	577
	Appendices	581
	About the Authors	661
	About the Editor	663
	Index	665

Chapter 1

Some Fundamental Concepts

Contents

1.1	Introduction	1
1.2	Outer, Surface, and Inner Potentials	2
1.3	Thermodynamics of Electrochemical Processes	4
1.3.1	Interface Between Two Metals in Contact	6
1.4	Electrochemical Potential of the Electron	6
1.5	Nernst's Equation and Standard Electrode Potentials	8
1.5.1	Formal Electrode Potentials	14
1.6	Electrical Double Layer	15
1.6.1	Models for the Electrical Double Layer	21
1.6.2	Specific Adsorption	25
1.7	Kinetics of the Charge Transfer	27
1.7.1	The Butler–Volmer Model	31
1.7.2	The Marcus–Hush Model	33
1.8	Mass Transport	42
1.8.1	Minimization of the Migration Component	49
1.8.2	Temporal Evolution	50
1.8.3	Convection	50
1.8.4	Mass Transport Coefficient	52
1.9	Three-Electrode Systems. Ohmic Drop, Resistance of the Cell, and RC Time Constant	58
1.10	Pulse Versus Step	63
	References	65

1.1 Introduction

The main purpose of this opening chapter is to provide a brief review of different concepts involved in the study of the current–potential response of electrochemical processes. This is necessary for a better understanding of some aspects of the responses of the different electrochemical techniques analyzed in the following chapters.

The electrostatic aspects of electrochemical systems will be introduced first and the electrochemical potential as a key concept is presented (Sects. 1.2–1.4). The electrochemical equilibrium is discussed and Nernst's equation and standard and formal electrode potentials are introduced (Sect. 1.5). The study of electrochemical interfaces under equilibrium ends with the phenomenological and theoretical treatment of the electrical double layer (Sect. 1.6).

The analysis of the kinetics of the charge transfer is presented in Sect. 1.7 for the Butler–Volmer and Marcus–Hush formalisms, and in the latter, the extension to the Marcus–Hush–Chidsey model and a discussion on the adiabatic character of the charge transfer process are also included. The presence of mass transport and its influence on the current–potential response are discussed in Sect. 1.8.

Finally, some practical questions such as the three-electrode setup, the influence of the ohmic drop, the RC time constant, and a short discussion on the nomenclature of the potential perturbations used in this techniques are addressed in Sects. 1.9 and 1.10.

1.2 Outer, Surface, and Inner Potentials

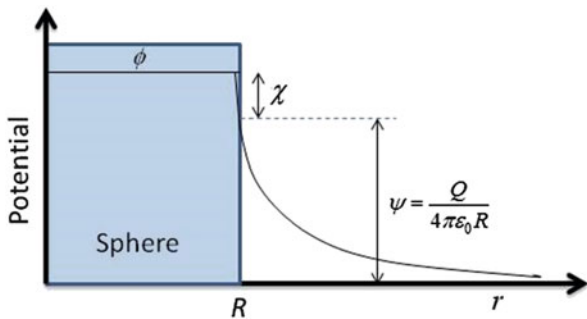
Electrochemistry deals with charged particles that have both electrical and chemical properties. Since electrochemical interfaces are usually referred as electrified interfaces, it is clear that potential differences, charge densities, dipole moments, and electric currents occur at these interfaces. The electrical properties of systems containing charged species are very important for understanding how they behave at interfaces. Therefore, it is important to have a precise definition of the electrostatic potential of a phase [1–6]. Note that what really matters in electrochemical systems is not the value of the potential but its difference at a given interface, although it is illustrative to discuss its main properties.

The potential of a charged species can be divided into different contributions to account for the different arrangements of charges (free charges, oriented dipoles, etc.) that can be found. In order to evaluate these different contributions, a thought experiment can be proposed in which a test charge located at the vacuum at an infinite distance from a given phase is brought inside this phase [3].

The outer or external potential, ψ , of an electrified material phase is defined as the energy required to move this unit test charge from the infinite to a point just outside the phase, with this energy being induced only by the free electrostatic charges, i.e., this potential is purely determined by the charge in the phase and is not influenced by the redistribution of the charge at the surface and the so-called image effects [3, 4, 7]. A distance of about 1 μm fulfills the above requirement and at the same time is not too large to prevent the weakening of the interactions with the charges in the phase. Only the ψ potential and correspondingly $\Delta\psi$ can be experimentally measured [3].

For example, assuming that the phase is an isolated sphere of radius R , the potential experienced by a test positive charge Q is (see Fig. 1.1)

Fig. 1.1 Radial distribution of potential for a metal sphere of radius R carrying a positive charge Q , illustrating the contributions of the outer potential and the surface potential. The inner potential is constant inside the sphere



$$\psi = \frac{Q}{4\pi\epsilon_0(R + r)} \tag{1.1}$$

with ϵ_0 being the vacuum electric permittivity and r the coordinate that defines the movement of the charge.

The surface potential χ of a solid phase is defined as the energy required to move the unit test charge from the infinite toward the anisotropic zone resulting from the surface to the electronic gas which expands beyond the lattice and causes the formation of a dipolar layer although other explanations are possible. During this hypothetical experiment, the charge in the phase turns to zero. Therefore, the potential has nothing to do with the charge of the phase [3, 8].

In the case of a liquid phase, the χ potential is associated with the net preferential orientation of dipoles at the surface. This arrangement is equivalent to a charge separation and a potential difference occurs across the surface dipole layer. The estimation of χ remains unsolved [8].

The inner potential, ϕ , is the sum of the outer and surface potential:

$$\phi = \psi + \chi \tag{1.2}$$

and is related to the energy required to move the unit test charge to a point inside the phase (ϕ is related to the electric field strength E in the interior of the phase by $-\nabla\phi = E$ with ∇ being the gradient operator).

Concerning the potential differences, that corresponding to the outer potentials between two phases α and β is known as the Volta potential difference defined as

$${}^\alpha\Delta^\beta\psi = \psi^\beta - \psi^\alpha \tag{1.3}$$

This is a measurable quantity which is usually called the contact potential difference [4, 6]. The equivalent potential difference for the inner potentials is known as the Galvani potential difference¹,

¹ It may be convenient to regard the Galvani potential difference between two phases in contact as being due to two effects: the orientation of dipoles in the interface between them and the separation of independently mobile charged species across the phase boundary in an analogous way to that discussed for the separation of ϕ into outer and surface potentials [5, 6].

$${}^{\alpha}\Delta^{\beta}\phi = \phi^{\beta} - \phi^{\alpha} \quad (1.4)$$

1.3 Thermodynamics of Electrochemical Processes

The chemical potential of a species “i” in a phase with “m” species is defined as the derivative of the internal energy U of this phase with respect to the number of moles of species “i” (n_i), at constant values of the extensive variables V , S , and the number of moles of the remaining species in the absence of electrical and magnetic fields,

$$\mu_i = \left(\frac{\partial U}{\partial n_i} \right)_{V, S, n_{j \neq i}} \quad (1.5)$$

As the condition of constant entropy is difficult to achieve, it is more convenient to fix other variables.

The variation of internal energy can be written in a general way as

$$dU = -PdV + TdS + \sum_i \mu_i dn_i \quad (1.6)$$

and the Gibbs and Helmholtz energies G and A , respectively, are given by

$$G = U + PV - TS \quad (1.7)$$

$$A = U - TS \quad (1.8)$$

By deriving Eqs. (1.7) and (1.8), and inserting into the result that corresponding to dU (Eq. (1.6)), the expression of the chemical potential given by Eq. (1.5) can be also written as

$$\mu_i = \left(\frac{\partial A}{\partial n_i} \right)_{T, V, n_{j \neq i}} \quad (1.9)$$

$$\mu_i = \left(\frac{\partial G}{\partial n_i} \right)_{T, P, n_{j \neq i}} \quad (1.10)$$

The chemical potential is defined as the change of energy of a phase when an additional mol of particles of species i is introduced at fixed V and S , T and V , or T and P . The most usual definition of the chemical potential is the necessary work to introduce one mole of species i from the infinite to a phase at fixed T and P (i.e., as given in Eq. (1.10)).

μ_i is usually expressed as

$$\mu_i = \mu_i^\ominus + RT \ln a_i \quad (1.11)$$

where μ_i^\ominus is the standard chemical potential independent of the concentration and dependent on temperature and total pressure and a_i is the activity of the component “i” in the phase.

When a chemical change is produced at the equilibrium, it holds

$$\sum_i v_i \mu_i = 0 \quad (1.12)$$

with v_i being the stoichiometric coefficient of species “i” participating in the chemical change which takes positive and negative values for products and reactants, respectively.

In electrochemical systems, some of the participating species are charged and the charge transfer process across an interface is a heterogeneous process. Under these conditions, the Gibbs energy is denoted by \tilde{G} and the following is fulfilled for a given phase of the system:

$$d\tilde{G} = -SdT + VdP + \sum_i \mu_i dn_i + F\phi \sum_i z_i dn_i \quad (1.13)$$

where z_i is the charge of species “i” and ϕ is the inner potential of the phase. On the basis of the previously introduced chemical potential (see Eq. 1.10), the electrochemical potential can be defined as

$$\tilde{\mu}_i = \left(\frac{\partial \tilde{G}}{\partial n_i} \right)_{T, P, n_{j \neq i}} = \mu_i + z_i F \phi \quad (1.14)$$

that is, the necessary work to introduce one mole of charged species i from the infinite to a phase with inner potential ϕ at fixed T and P .

From Eqs. (1.13) and (1.14), at constant P and T , one obtains

$$d\tilde{G} = \sum_i \tilde{\mu}_i dn_i = d\zeta \sum_i v_i \tilde{\mu}_i \quad (1.15)$$

where ζ being the degree of reaction progress. From this equation, the variation of free energy of an electrochemical reaction $\Delta\tilde{G}$ can be defined as

$$\Delta\tilde{G} = \left(\frac{\partial \tilde{G}}{\partial \zeta} \right)_{P, T} = \sum_i v_i \tilde{\mu}_i \quad (1.16)$$

When a chemical change involving charge species is produced in an electrochemical system, under equilibrium conditions the following condition holds:

$$\Delta\tilde{G} = \sum_i v_i \tilde{\mu}_i = 0 \quad (1.17)$$

where $\tilde{\mu}_i$ is the electrochemical potential of species “i” in the corresponding phase. When this species is present in two phases α and β in contact, at the equilibrium, the electrochemical potentials of “i” in both phases are equal, which leads to

$$\mu_i^\alpha + z_i F \phi^\alpha = \mu_i^\beta + z_i F \phi^\beta \quad (1.18)$$

1.3.1 Interface Between Two Metals in Contact

The significance of Eq. (1.18) is that, at the contact between two different phases, for example two different metals, a certain Galvani potential difference exists, which is generated by the difference between the chemical potential of the electrons in each metal. So, for example, if an interface Cu–Fe is considered and the equilibrium is assumed,

$$\tilde{\mu}_{e^-}^{\text{Cu}} = \tilde{\mu}_{e^-}^{\text{Fe}} \quad (1.19)$$

From Eq. (1.14)

$$\mu_{e^-}^{\text{Cu}} - F \phi^{\text{Cu}} = \mu_{e^-}^{\text{Fe}} - F \phi^{\text{Fe}} \quad (1.20)$$

is deduced, which can be written as

$${}^{\text{Cu}}\Delta^{\text{Fe}}\phi = \frac{{}^{\text{Cu}}\Delta^{\text{Fe}}\mu_{e^-}}{F} \quad (1.21)$$

If the contact between two identical metals M and M' is considered, it holds ${}^M\Delta^{M'}\phi = 0$ since $\mu_{e^-}^M = \mu_{e^-}^{M'}$ at equilibrium. Under nonequilibrium conditions, the above does not hold (i.e., $\mu_{e^-}^M \neq \mu_{e^-}^{M'}$) and ${}^M\Delta^{M'}\phi$ is the measured potential difference between the two identical terminals of a suitable voltammeter.

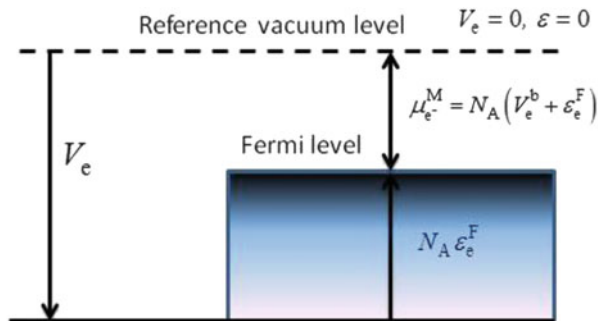
1.4 Electrochemical Potential of the Electron

In the case of electrons from a metal, the electrochemical potential is the work necessary to add one mole of electrons to the metal

$$\tilde{\mu}_{e^-}^M = \mu_{e^-}^M - F \phi^M = \mu_{e^-}^M - F(\chi^M + \psi^M) \quad (1.22)$$

where χ^M and ψ^M are the surface and external potentials of the metal, respectively. $\mu_{e^-}^M$ is the chemical potential of the electrons on the metal defined as the sum of the

Fig. 1.2 Schematic view of the energy diagram for electrons in a non-charged metal



bulk potential energy of the free electrons on the metal resulting from electron–ion and electron–electron interactions V_e^b , which is a negative quantity, and of the kinetic Fermi energy ϵ_e^F (see Fig. 1.2) [5, 9–11]

$$\mu_{e^-}^M = N_A (V_e^b + \epsilon_e^F) \quad (1.23)$$

with N_A being the Avogadro’s number. The surface potential energy V_e^s is related with the surface potential χ^M , $V_e^s = F\chi^M$. The total potential energy V_e is a stabilizing negative energy, $V_e = V_e^b + V_e^s$. The electron work function Φ_e^M given by

$$\Phi_e^M = -(V_e + \epsilon_e^F) \quad (1.24)$$

is the opposite value of the minimum work required to transfer an electron from the Fermi energy level of a metal across a surface to infinity carrying no net charge,

$$\mu_{e^-}^M = -N_A \Phi_e^M + F\chi^M \quad (1.25)$$

Note that

$$-\alpha_{e^-}^M = -(\mu_{e^-}^M - F\chi^M) = N_A \Phi_e^M \quad (1.26)$$

with $\alpha_{e^-}^M$ being the real potential of electrons at the metal, defined as the electrochemical potential of electrons when the metal is not charged (i.e., when $\psi^M = 0$). The work function of different metals, Φ_e^M , is given in Table 1.1

Obviously, different metals would have different chemical potentials and that would account for different Φ_e^M values. In the case of a given metal, Φ_e^M depends on its surface structure at atomic level, since the differences between the work function arise from different dipole layer surfaces.

Table 1.1 Values of the work function for polycrystalline metal surfaces [11, 12]

Metal	Φ_e^M (eV)	Metal	Φ_e^M (eV)	Metal	Φ_e^M (eV)
Ag	4.30	In	3.80	Rh	4.75
Al	4.25	Ir	4.70	Ru	4.60
Au	4.30	La	3.39	Sb	4.08
Ba	2.49	Li	2.38	Sc	3.30
Be	3.92	Mg	3.64	Sm	2.70
Bi	4.40	Mn	3.83	Sn	4.38
Ca	2.80	Mo	4.30	Sr	2.35
Cd	4.10	Na	2.35	Ta	4.12
Ce	3.20	Nb	3.99	Te	4.73
Co	4.41	Nd	3.07	Th	3.41
Cr	4.58	Ni	4.50	Ti	3.95
Cs	1.81	Os	4.70	Tl	4.00
Cu	4.40	Pb	4.00	U	3.74
Fe	4.31	Pd	4.80	V	4.12
Ga	3.96	Pr	2.54	W	4.54
Hf	3.53	Pt	5.32	Zn	4.24
Hg	4.52	Rb	2.16	Zr	3.90
K	2.22	Re	5.00		

1.5 Nernst's Equation and Standard Electrode Potentials

For a chemical reaction in solution



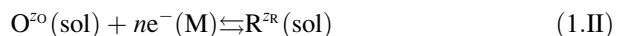
the variation of Gibbs free energy is given by

$$\Delta G = \Delta G^\ominus + RT \ln \left(\frac{a_C^c a_D^d}{a_A^a a_B^b} \right) \quad (1.27)$$

At the equilibrium at constant temperature and pressure $\Delta G = 0$ and

$$K_{\text{eq}} = \exp \left(\frac{-\Delta G^\ominus}{RT} \right) = \left(\frac{a_C^c a_D^d}{a_A^a a_B^b} \right)_{\text{eq}} \quad (1.28)$$

In the case of a redox reaction in a single electrode–solution interface



with

$$n = z_O - z_R \quad (1.29)$$

According to Eq. (1.16), under constant temperature and pressure it holds

$$\Delta\tilde{G} = \tilde{\mu}_R^{\text{sol}} - \tilde{\mu}_O^{\text{sol}} - n\tilde{\mu}_{e^-}^{\text{M}} \quad (1.30)$$

where superscripts “sol” and “M” refer to the solution and metallic phases, respectively. By inserting Eqs. (1.11) and (1.14) into Eq. (1.30), one obtains

$$\begin{aligned} \Delta\tilde{G} = & \mu_R^{\ominus, \text{sol}} + RT \ln a_R^{\text{sol}} + z_R F \phi^{\text{sol}} - \mu_O^{\ominus, \text{sol}} - RT \ln a_O^{\text{sol}} - z_O F \phi^{\text{sol}} \\ & - n(\mu_{e^-}^{\text{M}} - F \phi^{\text{M}}) \end{aligned} \quad (1.31)$$

Equation (1.31) can be rewritten as

$$\Delta\tilde{G} = \Delta G^{\ominus} + RT \ln \left(\frac{a_R^{\text{sol}}}{a_O^{\text{sol}}} \right) + nF(\phi^{\text{M}} - \phi^{\text{sol}}) \quad (1.32)$$

with

$$\Delta G^{\ominus} = \mu_R^{\ominus, \text{sol}} - \mu_O^{\ominus, \text{sol}} - n\mu_{e^-}^{\text{M}} \quad (1.33)$$

which is constant at a given temperature and a pressure of 1 bar. Equation (1.32) illustrates the major characteristic of redox reactions, i.e., the direct relation between the Galvani potential difference between the solution and the electrode and the concentrations of the species in solution.

At the equilibrium $\Delta\tilde{G} = 0$ and [9]

$$\frac{a_R^{\text{sol}}}{a_O^{\text{sol}}} = \exp \left(\frac{-\Delta G^{\ominus} - nF(\phi^{\text{M}} - \phi^{\text{sol}})}{RT} \right) \quad (1.34)$$

A comparison of Eqs. (1.28) and (1.34) indicates that for a redox reaction at the interface electrode–solution under equilibrium the Galvani potential difference at the interface is a function of the activities of species O and R in the solution and it is not possible to fix this potential difference and these activities in an independent way. In contrast, in a chemical equilibrium the concentrations of all reactant species are fixed.

The standard potential E^{\ominus} is the equilibrium potential (that is, the difference of Galvani potentials between the electrode and the solution phase) of an electrode under standard state conditions, i.e., with the relative activities of the different components being equal to the unity at a pressure of 1 bar and a temperature T , and for the reaction Scheme (1.II) it is given by

$$E^{\ominus} = -\frac{\Delta G^{\ominus}}{nF} = (\phi^M - \phi^{\text{sol}})_{a_R=a_O=1} \quad (1.35)$$

By inserting Eq. (1.35) into Eq. (1.34) the well-known Nernst equation is deduced

$$E = \phi^M - \phi^{\text{sol}} = E^{\ominus} - \frac{RT}{nF} \ln \frac{a_R^{\text{sol}}}{a_O^{\text{sol}}} \quad (1.36)$$

The product $nF(\phi^M - \phi^{\text{sol}})$ is the work necessary to transfer n moles of electrons from the bulk of the metal to the bulk of solution.

Unfortunately, it is impossible to measure an absolute value of $(\phi^M - \phi^{\text{sol}})$ in a single electrode–solution interface. To measure this potential difference, it is necessary to build an electrochemical cell with two electrodes. The electrode at which the redox reaction of interest proceeds is called the “working” electrode and the second electrode is needed to close the electrical circuit, and is called a “reference” electrode. The electrode potentials are measured between the working and reference electrodes by using a high impedance voltmeter to guarantee that there is no current flow through the circuit [7, 13].

When the standard hydrogen electrode (SHE) is employed as reference electrode (see Fig. 1.3) with a pressure of 1 bar and activity of protons unity, its standard potential for the reduction of protons in aqueous acidic media is taken as zero, i.e.,

$$\left[E_{\text{H}^+/\text{H}_2}^{\ominus} \right]_{\text{SHE}} = 0 \text{ V} \quad (1.37)$$

In this case the reaction taking place is

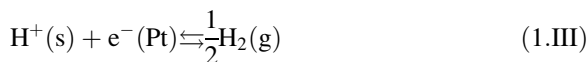
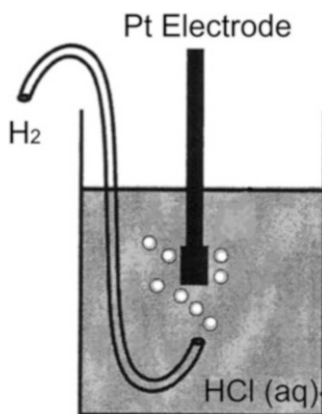


Fig. 1.3 The standard hydrogen electrode



Under equilibrium conditions it is fulfilled

$$-\tilde{\mu}_{\text{H}^+}^{\text{sol}} - \tilde{\mu}_{\text{e}^-}^{\text{Pt}} + \frac{1}{2}\mu_{\text{H}_2}^{\text{g}} = 0 \quad (1.38)$$

By inserting the definition of chemical and electrochemical potentials (Eqs. 1.11 and 1.14) into Eq. (1.38), one obtains

$$F(\phi^{\text{Pt}} - \phi^{\text{sol}}) = \mu_{\text{H}^+}^{\ominus, \text{sol}} - \frac{1}{2}\mu_{\text{H}_2}^{\ominus, \text{g}} + \mu_{\text{e}^-}^{\text{Pt}} + RT \ln \left(a_{\text{H}^+}^{\text{sol}} \left(\frac{p^{\ominus}}{f_{\text{H}_2}} \right)^{1/2} \right) \quad (1.39)$$

with f_{H_2} and p^{\ominus} being the fugacity and the reference pressure of 1 bar. Under standard conditions, the last term in the right-hand side of Eq. (1.39) vanishes and one obtains

$$\left[E_{\text{H}^+/\text{H}_2}^{\ominus} \right]_{\text{SHE}} = \frac{1}{F} \left(\mu_{\text{H}^+}^{\ominus, \text{sol}} - \frac{1}{2}\mu_{\text{H}_2}^{\ominus, \text{g}} + \mu_{\text{e}^-}^{\text{Pt}} \right) = 0 \text{ V} \quad (1.40)$$

In order to determine the standard potentials of other redox couples, electrochemical cells are built in which one of the redox reactions corresponds to the reaction Scheme (1.III). As an example, let us consider the following electrochemical cell (see Fig. 1.4):



The potential difference of the cell is defined as the difference between the Galvani potentials at the right (R) and left (L) terminals named here as the copper wires,

$$E = (\phi^{\text{Cu}^{\text{R}}} - \phi^{\text{Cu}^{\text{L}}}) = (\phi^{\text{Cu}^{\text{R}}} - \phi^{\text{sol}}) - (\phi^{\text{Cu}^{\text{L}}} - \phi^{\text{sol}}) \quad (1.42)$$

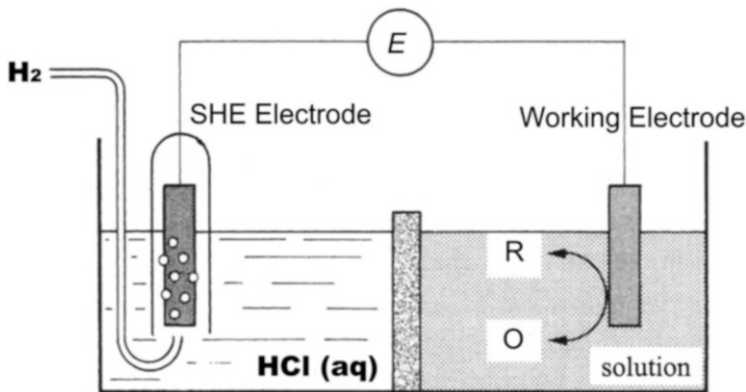


Fig. 1.4 Electrochemical cell for the measure of the electrode potential on the SHE scale

where it has been assumed that both solutions have the same inner potential. Note also that in this case the potential difference has been established between the terminals of the two electrodes and it does not corresponds to the difference in Galvani potentials between the working electrode phase and the solution which contains species O or R. In this particular case, we are interested in the difference $(\phi^{\text{Cu}^{\text{R}}} - \phi^{\text{sol}})$. The following electrochemical equilibria are established:

- At the contacts between pure metals ($\text{M}|\text{Cu}^{\text{R}}$ and $\text{Cu}^{\text{L}}|\text{Pt}$), the electrochemical potential of the electrons in the two phases are equal

$$\left. \begin{aligned} \tilde{\mu}_{\text{e}^-}^{\text{Cu}^{\text{R}}} &= \tilde{\mu}_{\text{e}^-}^{\text{M}} \\ \tilde{\mu}_{\text{e}^-}^{\text{Pt}} &= \tilde{\mu}_{\text{e}^-}^{\text{Cu}^{\text{L}}} \end{aligned} \right\} \quad (1.43)$$

- At the platinum electrode the reaction Scheme (I.III) takes place and Eq. (1.38) holds.
- In the same way, at the working electrode the process $\text{O}^{\text{zO}}(\text{s}) + n\text{e}^-(\text{M}) \rightleftharpoons \text{R}^{\text{zR}}(\text{s})$ occurs and

$$-\tilde{\mu}_{\text{O}}^{\text{sol}} - n\tilde{\mu}_{\text{e}^-}^{\text{M}} + \tilde{\mu}_{\text{R}}^{\text{sol}} = 0 \quad (1.44)$$

By applying the definition of electrochemical potential to conditions (1.38), (1.43), and (1.44) (and taking into account Eq. (1.11)), one obtains

$$\left. \begin{aligned} F(\phi^{\text{Cu}^{\text{R}}} - \phi^{\text{M}}) &= \mu_{\text{e}^-}^{\text{Cu}^{\text{R}}} - \mu_{\text{e}^-}^{\text{M}} \\ F(\phi^{\text{Pt}} - \phi^{\text{Cu}^{\text{L}}}) &= \mu_{\text{e}^-}^{\text{Pt}} - \mu_{\text{e}^-}^{\text{Cu}^{\text{L}}} \\ nF(\phi^{\text{M}} - \phi^{\text{sol}}) &= \mu_{\text{O}}^{\ominus, \text{sol}} - \mu_{\text{R}}^{\ominus, \text{sol}} + n\mu_{\text{e}^-}^{\text{M}} + RT \ln \frac{a_{\text{O}}^{\text{sol}}}{a_{\text{R}}^{\text{sol}}} \\ F(\phi^{\text{sol}} - \phi^{\text{Pt}}) &= -\mu_{\text{H}^+}^{\ominus, \text{sol}} + \frac{1}{2}\mu_{\text{H}_2}^{\ominus, \text{g}} - \mu_{\text{e}^-}^{\text{Pt}} - RT \ln \left(a_{\text{H}^+}^{\text{s}} \left(\frac{p^{\ominus}}{f_{\text{H}_2}} \right)^{1/2} \right) \end{aligned} \right\} \quad (1.45)$$

The total potential difference between the copper wires can be obtained by combining Eq. (1.45),

$$\begin{aligned} nFE &= nF(\phi^{\text{Cu}^{\text{R}}} - \phi^{\text{Cu}^{\text{L}}}) = nF \left[(\phi^{\text{Cu}^{\text{R}}} - \phi^{\text{sol}}) - (\phi^{\text{Cu}^{\text{L}}} - \phi^{\text{sol}}) \right] \\ &= \mu_{\text{O}}^{\ominus, \text{sol}} - \mu_{\text{R}}^{\ominus, \text{sol}} + RT \ln \frac{a_{\text{O}}^{\text{sol}}}{a_{\text{R}}^{\text{sol}}} \\ &\quad - n\mu_{\text{H}^+}^{\ominus, \text{sol}} + \frac{1}{2}n\mu_{\text{H}_2}^{\ominus, \text{g}} - nRT \ln \left(a_{\text{H}^+}^{\text{sol}} \left(\frac{p^{\ominus}}{f_{\text{H}_2}} \right)^{1/2} \right) \end{aligned} \quad (1.46)$$

In the simplest case in which the activities of species O and R are equal to the unity and the SHE reference electrode is considered, the measured potential

Table 1.2 Selected standard potentials in aqueous solution (298 K) [13–15]

Redox reaction	$E_{O,R}^{\ominus}$
$\text{Au}^+ + \text{e}^- \rightleftharpoons \text{Au}$	1.830
$\text{Au}^{3+} + 3\text{e}^- \rightleftharpoons \text{Au}$	1.520
$\text{Cl}_2 + 2\text{e}^- \rightleftharpoons 2\text{Cl}^-$	1.358
$\text{O}_2 + 4\text{H}^+ + 4\text{e}^- \rightleftharpoons 2\text{H}_2\text{O}$	1.229
$\text{Ag}^+ + \text{e}^- \rightleftharpoons \text{Ag}$	0.799
$\text{Fe}^{3+} + \text{e}^- \rightleftharpoons \text{Fe}^{2+}$	0.771
$\text{O}_2 + 2\text{H}^+ + 2\text{e}^- \rightleftharpoons \text{H}_2\text{O}_2$	0.695
$\text{I}_2 + 2\text{e}^- \rightleftharpoons 2\text{I}^-$	0.535
$\text{Cu}^+ + \text{e}^- \rightleftharpoons \text{Cu}$	0.520
$\text{O}_2 + 2\text{H}_2\text{O} + 4\text{e}^- \rightleftharpoons 4\text{OH}^-$	0.401
$\text{Cu}^{2+} + \text{e}^- \rightleftharpoons \text{Cu}^+$	0.159
$\text{H}^+ + \text{e}^- \rightleftharpoons \frac{1}{2}\text{H}_2$	0.000
$\text{Fe}^{3+} + 3\text{e}^- \rightleftharpoons \text{Fe}$	-0.040
$\text{Co}^{2+} + 2\text{e}^- \rightleftharpoons \text{Co}$	-0.277
$\text{Cr}^{3+} + 3\text{e}^- \rightleftharpoons \text{Cr}$	-0.400
$\text{Cd}^{2+} + 2\text{e}^- \rightleftharpoons \text{Cd}$	-0.402
$\text{Fe}^{2+} + 2\text{e}^- \rightleftharpoons \text{Fe}$	-0.440
$\text{Zn}^{2+} + 2\text{e}^- \rightleftharpoons \text{Zn}$	-0.76
$\text{H}_2\text{O} + \text{e}^- \rightleftharpoons \frac{1}{2}\text{H}_2 + \text{OH}^-$	-0.828
$\text{Mn}^{2+} + 2\text{e}^- \rightleftharpoons \text{Mn}$	-1.180
$\text{Al}^{3+} + 3\text{e}^- \rightleftharpoons \text{Al}$	-1.676
$\text{Mg}^{2+} + 2\text{e}^- \rightleftharpoons \text{Mg}$	-2.356
$\text{Na}^+ + \text{e}^- \rightleftharpoons \text{Na}$	-2.714
$\text{K}^+ + \text{e}^- \rightleftharpoons \text{K}$	-2.925
$\text{Li}^+ + \text{e}^- \rightleftharpoons \text{Li}$	-3.045

difference given by Eq. (1.46) is the standard potential E^{\ominus} of the redox couple O/R,

$$E^{\ominus} = \left(\phi^{\text{Cu}^{\text{R}}} - \phi^{\text{sol}} \right)_{a_{\text{R}}=a_{\text{O}}=1} - \left(\phi^{\text{Cu}^{\text{L}}} - \phi^{\text{sol}} \right)_{\text{SHE}} = E_{\text{O,R}}^{\ominus} \text{ vs. SHE} \quad (1.47)$$

If the activities of species O and R are different from the unity, the Nernst's equation is obtained,

$$E = E_{\text{O,R}}^{\ominus} + \frac{RT}{nF} \ln \left(\frac{a_{\text{O}}^{\text{sol}}}{a_{\text{R}}^{\text{sol}}} \right) \quad (1.48)$$

The standard potentials for some redox couples in aqueous solution appear in Table 1.2. More information about formal potentials of a great number of electrochemical systems can be found in [14, 15].

When other reference electrodes are used as, for example, the saturated Calomel electrode (SCE), a constant quantity needs to be added to the right-hand side of Nernst's equation which reflects the difference between the SCE and the SHE electrodes, i.e., in this case the standard potential is

$$E^{\ominus} = \left(\phi^{\text{Cu}^{\text{R}}} - \phi^{\text{sol}} \right)_{a_{\text{R}}=a_{\text{O}}=1} - \left[\left(\phi^{\text{Cu}^{\text{L}}} - \phi^{\text{sol}} \right)_{\text{SCE}} - \left(\phi^{\text{Cu}^{\text{L}}} - \phi^{\text{sol}} \right)_{\text{SHE}} \right] \quad (1.49)$$

The election of the appropriate reference electrode for a given electrochemical system is conditioned by different factors (like the solvent or the temperature). The most important characteristic of a reference electrode is that it should provide a constant and reproducible potential difference when connected to the other semi-cell unit. For a detailed list of different reference electrodes, see [15–17].

1.5.1 Formal Electrode Potentials

It is very rare for the activities of all species involved in an electrode reaction to be constrained to be the unity. In general, the electrode potential is influenced by these activities in the form given by the Nernst's equation (Eq. 1.36). When the reactants or products are in solution, the Nernst's equation can be approximated by replacing the activities by the concentrations, but this can be a very rough approximation in the case of ions. The usual procedure, given that the activity coefficients are almost always unknown, is to incorporate them into the E^{\ominus} term writing, for example

$$E = E^{\ominus} - \frac{RT}{nF} \ln \frac{a_{\text{R}}^{\text{sol}}}{a_{\text{O}}^{\text{sol}}} = E^{\ominus} - \frac{RT}{nF} \ln \frac{\gamma_{\text{R}}}{\gamma_{\text{O}}} - \frac{RT}{nF} \ln \frac{c_{\text{R}}^{\text{sol}}}{c_{\text{O}}^{\text{sol}}} = E_{\text{c}}^{\ominus'} - \frac{RT}{nF} \ln \frac{c_{\text{R}}^{\text{sol}}}{c_{\text{O}}^{\text{sol}}} \quad (1.50)$$

with $E_{\text{c}}^{\ominus'}$ being the formal (or conditional) electrode potential,

$$E_{\text{c}}^{\ominus'} = E^{\ominus} - \frac{RT}{nF} \ln \frac{\gamma_{\text{R}}}{\gamma_{\text{O}}} \quad (1.51)$$

The term “conditional” indicates that its determination is related to specific conditions, which usually deviate from standard conditions. In general, formal potentials may deviate from standard potentials by between a few and hundreds of mV. These deviations are caused not only because of non-unity activity coefficients but also because of the presence of chemical equilibria (see for example [18]).

1.6 Electrical Double Layer

An interface is the region between two phases where the structure and composition is different from that in the bulk of the phases. The thickness of this region extends a few molecular diameters into each phase. When a potential is applied to an interface (i.e., electrode–solution), it presents a resistance to accept current generation (or, vice versa, when a current is applied to the potential change). If the effective resistance is low, the interface is permeable to the charge carriers and is known as “non-polarizable.” In the contrary case, the interface is impermeable to the charge carriers and we are speaking of a “polarizable” interface (the limiting cases of null and infinite resistance correspond to ideally non-polarizable and ideally polarizable interfaces [3, 7, 13]). These behaviors are schematized in Fig. 1.5.

The electrical behavior of a metal–solution interface is similar to that shown by the equivalent circuit in Fig. 1.6 formed by a capacitor and a resistor connected in parallel. If the resistance is small, the potential changes across the capacitor are

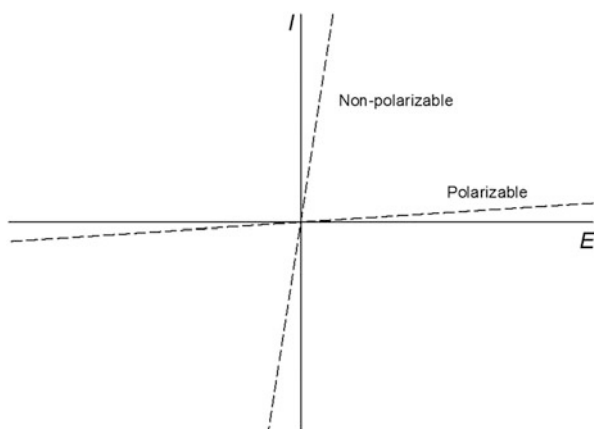


Fig. 1.5 Current–potential plot for polarizable and non-polarizable interphases

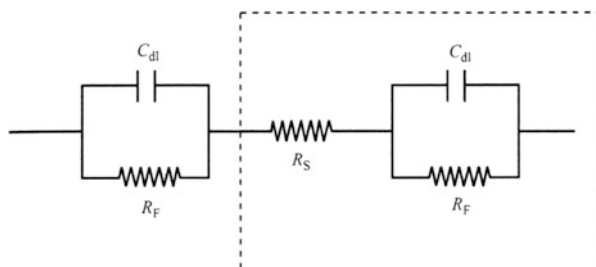


Fig. 1.6 Equivalent circuit for a two-electrode cell. A single interface is usually represented by the elements in the dashed rectangle. C_{dl} , R_F , and R_s denote the double-layer capacitance, the Faradaic resistance, and the solution resistance, respectively

compensated by the charge transfer through the low-resistance whereas the capacitor changes up to applied potential if the resistance is high.

A “non-polarizable” electrode–solution interface is a reversible electrode. Therefore, the potential is determined by the composition of the solution based on the Nernst equation (given by Eq. 1.36). So, for example, for the copper electrode in a solution of CuSO_4 the potential is given by

$$E = E^\ominus + \frac{RT}{2F} \ln a_{\text{Cu}^{2+}}^{\text{sol}} \quad (1.52)$$

with E^\ominus being the standard potential of the couple Cu^{2+}/Cu with respect to the SHE and $a_{\text{Cu}^{2+}}^{\text{sol}}$ the activity of the cupric ions in solution.

In general, an electrical double layer exists whenever two conducting phases meet at an interface that is impermeable to the charge [2, 7, 10].² Here, the electrode–electrolyte interface is considered when it behaves as ideally polarizable, that is, by supposing that the electrode potential is kept in a range in which no, or only negligible, electrochemical reactions occur [2]. This interface can be described as a capacitor so the charge can be accumulated on the metal side using an external voltage source which gives rise to the establishment of equal and opposite charge in the solution side. The properties of the electrical double layer are characterized by the electrostatic equilibrium.

The surface tension σ is a special intensive property of the interface related to an energy per unit area and it depends on the temperature, the composition of the adjacent phases and of the shape of the interface. The surface tension of a liquid is in a direct relation with the magnitude of the intermolecular forces.

The liquid metal mercury–solution interface presents the advantage that it approaches closest to an ideal polarizable interface and, therefore, it adopts the potential difference applied between it and a non-polarizable interface. For this reason, the mercury–solution interface has been extensively selected to carry out measurements of the surface tension dependence on the applied potential. In the case of other metal–solution interfaces, the thermodynamic study is much more complex since the changes in the interfacial area are determined by the increase of the number of surface atoms (plastic deformation) or by the increase of the interatomic lattice spacing (elastic deformation) [2, 4].

The thermodynamic treatment of an interface generally considers a system composed of the interface (γ) and two adjacent homogeneous phases (α and β). The extensive properties of the systems must be ascribed to these three regions, for example, the Gibbs free energy G and the number of moles of a species in the system fulfill

²This double layer may also form in systems as, for example, the interface between two metals of different nature (with different work functions) or between two immiscible electrolytes and even when one of the two phases is an insulator or a semiconductor [7, 10].

$$\begin{aligned} G &= G^\alpha + G^\beta + G^\gamma \\ n_i &= n_i^\alpha + n_i^\beta + n_i^\gamma \end{aligned} \quad (1.53)$$

By assuming that the interface has no volume (Gibbs convention), the following equations can be written:

$$\begin{aligned} dG^\alpha &= -S^\alpha dT + V^\alpha dP + \sum_i \mu_i^\alpha dn_i^\alpha \\ dG^\beta &= -S^\beta dT + V^\beta dP + \sum_i \mu_i^\beta dn_i^\beta \\ dG^\gamma &= -S^\gamma dT + \sigma dA^\gamma + \sum_i \mu_i^\gamma dn_i^\gamma \end{aligned} \quad (1.54)$$

where σdA^γ is the necessary work to increase the interface area, A^γ .

Under constant temperature conditions, Eq. (1.54) for the interface becomes

$$dG^\gamma = \sigma dA^\gamma + \sum_i \mu_i^\gamma dn_i^\gamma \quad (1.55)$$

As the Gibbs energy is a first-order homogenous function of the extensive variables A^γ and n_i^γ , the application of Euler's theorem yields

$$G^\gamma = \sigma A^\gamma + \sum_i \mu_i^\gamma n_i^\gamma \quad (1.56)$$

By differentiation Eq. (1.56) and comparing the result with (1.55), one obtains

$$\sum_i n_i^\gamma d\mu_i^\gamma + A^\gamma d\sigma = 0 \quad (1.57)$$

By solving the surface tension and denoting surface excess of species i , $\Gamma_i = n_i^\gamma/A^\gamma$, the Gibbs's isotherm is obtained:

$$-d\sigma = \sum_i \Gamma_i d\mu_i^\gamma \quad (1.58)$$

This equation will be applied to an electrochemical cell formed by a polarizable and non-polarizable interface in line with the scheme



For the thermodynamic study of the mercury–solution interface, the electrochemical potential will be used in Gibbs's isotherm instead of the chemical potential, due to the presence of charged species. In the metal side of the interface, the components are the electrons in excess and the mercury metal whereas in solution the two ions of the electrolyte and the solvent must be considered in the sum,

$$\begin{aligned}
 -d\sigma &= \sum_i \Gamma_i d\tilde{\mu}_i \\
 &= \Gamma_{\text{Hg}} d\mu_{\text{Hg}} + \Gamma_{e^-} d\tilde{\mu}_{e^-} + \Gamma_{\text{K}^+} d\tilde{\mu}_{\text{K}^+} + \Gamma_{\text{Cl}^-} d\tilde{\mu}_{\text{Cl}^-} + \Gamma_{\text{W}} d\mu_{\text{W}} \quad (1.60)
 \end{aligned}$$

Equation (1.60) is only valid for liquid–liquid interfaces. The term corresponding to electron is related to the charge density in the metal, q^{M}

$$\Gamma_{e^-} d\tilde{\mu}_{e^-} = -F\Gamma_{e^-} d\phi^{\text{Hg}} = q^{\text{M}} d\phi^{\text{Hg}} \quad (1.61)$$

The charge excess in solution, q^{s} , is related with the surface excess of cations and anions in solution,

$$q^{\text{s}} = -q^{\text{M}} = F\Gamma_{\text{K}^+} - F\Gamma_{\text{Cl}^-} \quad (1.62)$$

At the non-polarizable interface the electrochemical equilibrium holds (with the reaction being $2\text{Hg}' + 2\text{Cl}^- \rightleftharpoons \text{Hg}_2\text{Cl}_2 + 2e^-$; see scheme (1.59)). So,

$$\left. \begin{aligned}
 \mu_{\text{Hg}_2\text{Cl}_2} + 2\tilde{\mu}_{e^-}^{\text{Hg}'} &= 2\mu_{\text{Hg}'} + 2\tilde{\mu}_{\text{Cl}^-} \\
 2d\tilde{\mu}_{e^-}^{\text{Hg}'} &= -2Fd\phi^{\text{Hg}'} = 2d\tilde{\mu}_{\text{Cl}^-}
 \end{aligned} \right\} \quad (1.63)$$

The chemical potential of the electrolyte in solution is given by

$$\mu^{\text{KCl}} = \tilde{\mu}_{\text{K}^+} + \tilde{\mu}_{\text{Cl}^-} \quad (1.64)$$

The ionic terms in Eq. (1.60) can be rewritten as

$$\begin{aligned}
 \Gamma_{\text{K}^+} d\tilde{\mu}_{\text{K}^+} + \Gamma_{\text{Cl}^-} d\tilde{\mu}_{\text{Cl}^-} &= \Gamma_{\text{K}^+} d\mu^{\text{KCl}} - \Gamma_{\text{K}^+} d\tilde{\mu}_{\text{Cl}^-} + \Gamma_{\text{Cl}^-} d\tilde{\mu}_{\text{Cl}^-} = \\
 &= \Gamma_{\text{K}^+} d\mu^{\text{KCl}} - \frac{q^{\text{s}}}{F} d\tilde{\mu}_{\text{Cl}^-} = \Gamma_{\text{K}^+} d\mu^{\text{KCl}} + \frac{q^{\text{M}}}{F} d\tilde{\mu}_{\text{Cl}^-} \quad (1.65)
 \end{aligned}$$

Equation (1.60), taking into account (1.61)–(1.65) and that $d\mu_{\text{Hg}} = 0$, becomes

$$-d\sigma = q^{\text{M}} (d\phi^{\text{Hg}} - d\phi^{\text{Hg}'}) + \Gamma_{\text{K}^+} d\mu^{\text{KCl}} + \Gamma_{\text{W}} d\mu_{\text{W}} \quad (1.66)$$

$(d\phi^{\text{Hg}} - d\phi^{\text{Hg}'})$ is the Galvani potential difference between two phases of identical composition and it can be experimentally measured. It will be denoted as E_- because the non-polarizable electrode responds to the activity of the anions in solution.

In line with the Gibbs–Duhem equation,

$$x_{\text{s}} d\mu^{\text{KCl}} + x_{\text{W}} d\mu^{\text{W}} = 0 \quad (1.67)$$

where x_i is the molar fraction of species i (with $i = \text{KCl}$ for the electrolyte and $i = \text{W}$ for the solvent), the last two terms in the right-hand side of Eq. (1.66) can be written as

$$\Gamma_{\text{K}^+} d\mu^{\text{KCl}} + \Gamma_{\text{W}} d\mu_{\text{W}} = \left(\Gamma_{\text{K}^+} - \frac{x_{\text{KCl}}}{x_{\text{W}}} \Gamma_{\text{W}} \right) d\mu^{\text{KCl}} = \Gamma_{\text{K}^+}^{(\text{W})} d\mu^{\text{KCl}} \quad (1.68)$$

where $\Gamma_{\text{K}^+}^{(\text{W})}$ ($= \Gamma_{\text{K}^+} - (x_{\text{KCl}}/x_{\text{W}})\Gamma_{\text{W}}$) is the relative surface excess of ions K^+ [4, 13, 19, 20]. The relative excess is independent of the particular choice of the dividing surface in the Gibbs model for the interface [14]. Only relative excesses can be experimentally measured. The final form of Eq. (1.66) is

$$-d\sigma = q^{\text{M}} dE_{-} + \Gamma_{\text{K}^+}^{(\text{W})} d\mu^{\text{KCl}} \quad (1.69)$$

If the non-polarizable electrode is sensitive to the cation of the electrolyte (consider, for example, the cell $\text{Cu}|\text{Hg}|\text{KCl}(\text{ac.})|\text{K}(\text{Hg})|\text{Cu}'$), a similar result would be obtained

$$-d\sigma = q^{\text{M}} dE_{+} + \Gamma_{\text{Cl}^-}^{(\text{W})} d\mu^{\text{KCl}} \quad (1.70)$$

In general, the result for a 1–1 electrolyte is

$$-d\sigma = q^{\text{M}} dE_{\pm} + \Gamma_{\mp}^{(\text{W})} d\mu^{\text{electrolyte}} \quad (1.71)$$

The election of a reference electrode sensitive to one of the ions of the electrolyte leads to the appearance in Eq. (1.71) of the surface excess of the other. Equation (1.71) is usually named as Lippman's electrocapillary equation.

The surface charge of the metal q^{M} is

$$q^{\text{M}} = - \left(\frac{\partial \sigma}{\partial E_{\pm}} \right)_{\mu^{\text{electrolyte}}} \quad (1.72)$$

In agreement with Eq. (1.72), at the potential of the electrocapillary maximum $q^{\text{M}} = q^{\text{s}} = 0$, i.e., the free net charge on the interface is null. For this reason, this potential is called the zero charge potential (PZC, E_z), and its determination is of great interest in the thermodynamic study of the interface (see Figs. 1.7 and 1.8).

From the surface tension data obtained for different electrolyte concentrations, the relative ionic surface excesses can be determined. Thus, for the cell $\text{Hg}|\text{KCl}(\text{aqueous})|\text{Hg}_2\text{Cl}_2|\text{Hg}'$, from Eq. (1.69), the cation excess is given by

$$\Gamma_{\text{K}^+}^{(\text{W})} = - \left(\frac{\partial \sigma}{\partial \mu^{\text{KCl}}} \right)_{E_{-}} = - \left(\frac{\partial \sigma}{RT \partial \ln a^{\text{KCl}}} \right)_{E_{-}} \quad (1.73)$$

Fig. 1.7 Surface tension of mercury in contact with aqueous solutions of the salt named. $T = 291$ K. Abscissas are measured relative to a “rational” scale in which the potential difference between the mercury and a capillary-inactive electrolyte is arbitrarily set equal to zero at the electrocapillary maximum. Taken from [19] with permission

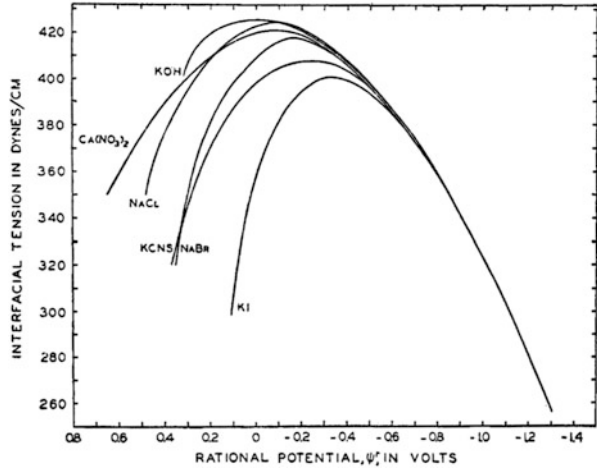
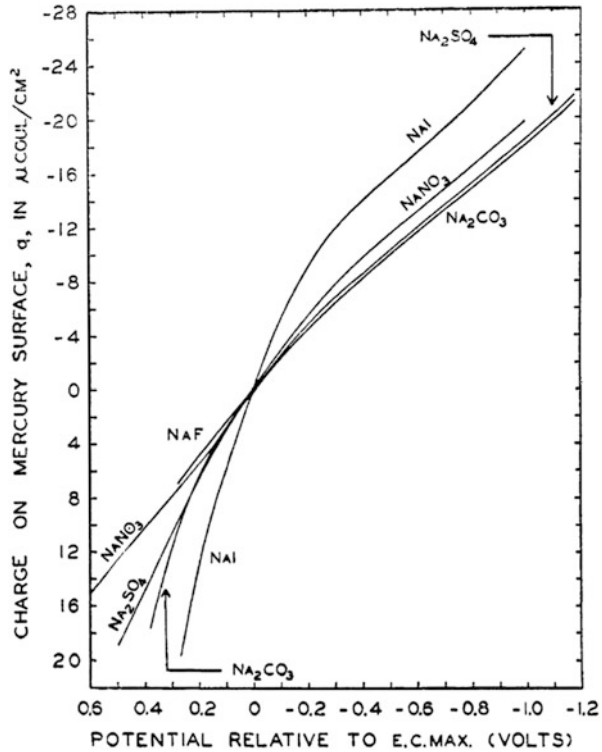


Fig. 1.8 Electronic charge on mercury surface in contact with one-normal solutions (with respect to anion charge) aqueous solutions of the salts named. $T = 298$ K. Taken from [19] with permission



where a^{KCl} is the electrolyte activity. The cationic surface excess is proportional to the cationic density charge in solution which for a 1-1 electrolyte is

$$q_+ = F\Gamma_{\text{K}^+}^{(W)} \tag{1.74}$$

The corresponding anionic charge can be obtained from the electroneutrality condition,

$$q_- = q^s - q_+ = -q^M - q_+ \quad (1.75)$$

which leads to the anionic excess

$$\Gamma_-^{(W)} = -\frac{q_-}{F} \quad (1.76)$$

Other interesting properties are the differential (C_d) and integral (C_i) capacitances, defined as

$$C_d = -\left(\frac{\partial^2 \sigma}{\partial E_{\pm}^2}\right)_{\mu^{\text{electrolyte}}} = \left(\frac{\partial q^M}{\partial E_{\pm}}\right)_{\mu^{\text{electrolyte}}} \quad (1.77)$$

$$C_i = \frac{q^M}{E - E_Z} = \frac{\int_{E_Z}^E C_d dE}{\int_{E_Z}^E dE} \quad (1.78)$$

Except in special cases, the differential capacitance C_d is the most useful magnitude (see Fig. 1.9) since it is that measured with impedance techniques, although the integral capacitance is of interest as average data [13, 19].

Equations (1.72)–(1.78) provide relationships between characteristic parameters of the interface (q^M , q^s , C_d , C_i , and surface concentrations of ionic species) and macroscopic magnitudes such as the surface tension, the applied potential and the bulk concentration of electrolyte. However, they provide no information about the double-layer structure. Next, some theoretical models about the structural and geometrical description of the electrical double layer are discussed briefly.

1.6.1 Models for the Electrical Double Layer

The first double-layer model was developed by Helmholtz more than 100 years ago [4, 13, 19, 21]. This model postulates the double layer as two charged phases, the polarized metal electrode (if the non-electrolytic phase is a metal or electronic conductor) and other parallel layer with the ions of the solution separated by a distance “ d .”³

³ The capacitance of the Helmholtz parallel plate capacitor per surface unit is given by $C_H = \epsilon_r \epsilon_0 / d$, where ϵ_r is the dielectric constant or the relative electric permittivity of the Helmholtz layer and ϵ_0 the electrical permittivity of free space ($\epsilon_0 = 8.854 \times 10^{-12} \text{ C}^2 \text{ J}^{-1} \text{ m}^{-1}$) [3, 4].

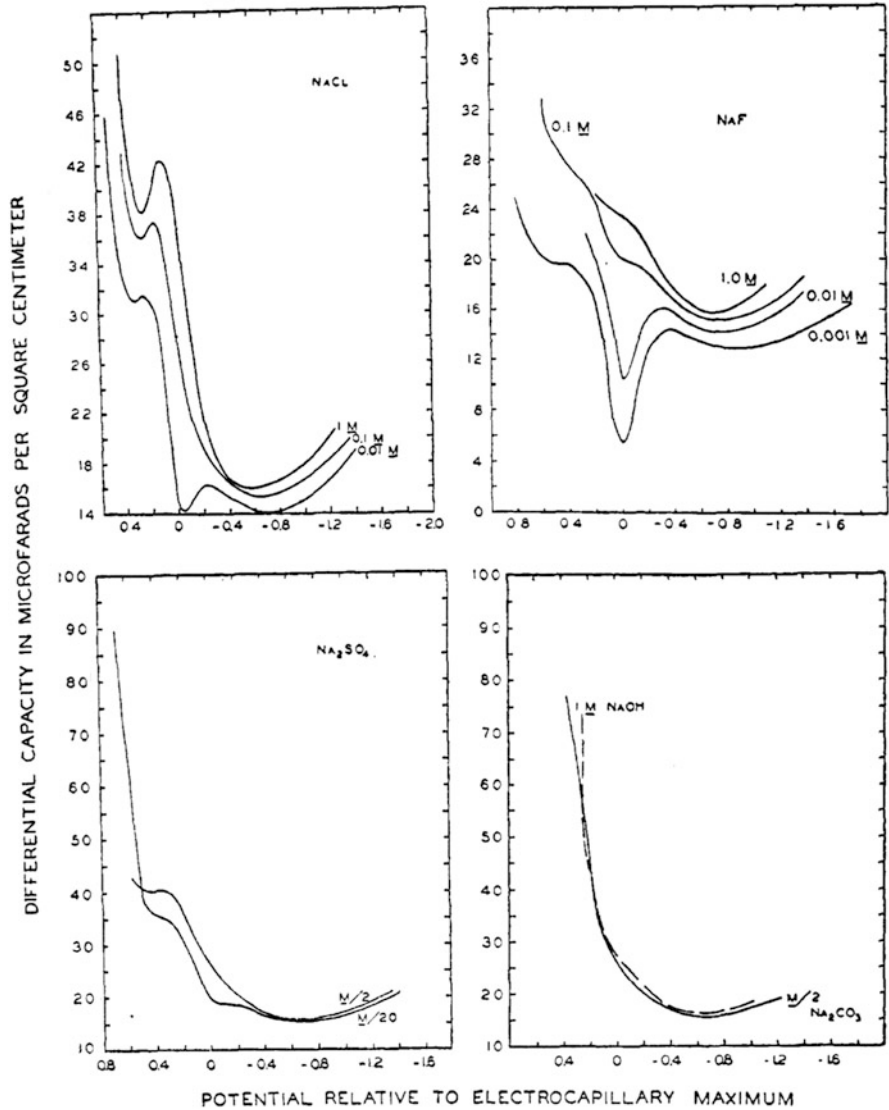


Fig. 1.9 Differential capacitance of the electrical double layer between mercury and aqueous solutions of the salts named. $T = 298$ K. Taken from [18] with permission

However, unlike ordinary capacitors, the experimental observations show that the ratio $q/\Delta\phi$ varies with the potential imposed and, therefore, in contrast to what Helmholtz predicted, asymmetric electrocapillary curves with respect to the surface tension σ edge as in Fig. 1.7 are obtained.

Later, the Gouy–Chapman–Stern model [2, 19, 22–24] describes the interface in the absence of specific adsorption by assuming that the ions can approach the

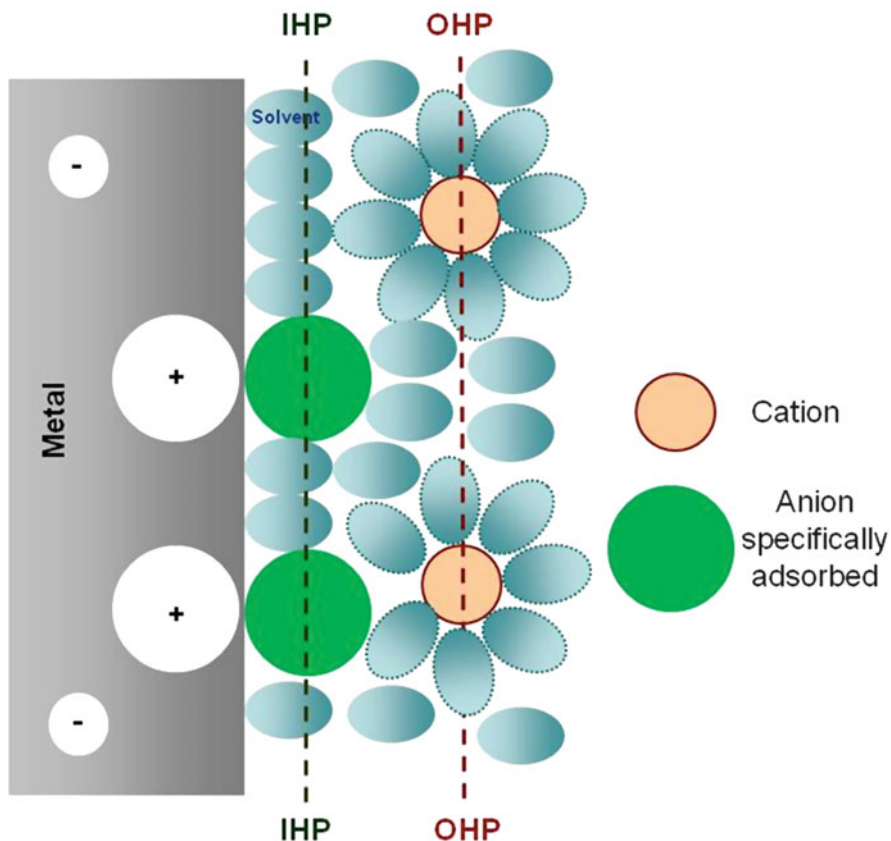


Fig. 1.10 Schematic view of the electrical double layer in agreement with the Gouy–Chapman–Stern–Grahame models. The metallic electrode has a negative net charge and the solvated cations define the inner limit of the diffuse layer at the Helmholtz outer plane (OHP). There are anions adsorbed at the electrode which are located at the inner Helmholtz plane (IHP). The presence of such anions is stabilized by the corresponding “images” at the electrode in such a way that each adsorbed ion establishes the presence of a surface dipole at the interface

electrode surface only up to the Outer Helmholtz Plane (OHP; see Fig. 1.10), from which a diffuse layer is spread into the solution. This layer is in electrostatic and osmotic equilibrium with the ions obeying a Boltzmann’s distribution law (in which the energy terms are purely electrostatic). It is also assumed that the ions of this diffuse layer interact with the electric field as point charges in a continuous dielectric and that the electrical potential depends only on the distance at the OHP, defined as the plane of the closest approach of non-specifically adsorbed ions (see Fig. 1.10). The Gouy–Chapman capacitance per surface unit for a z - z electrolyte is given by

$$C_{G\text{-Ch}} = \frac{\epsilon_r \epsilon_0}{L_D} \cosh\left(\frac{ze_0(\phi^{\text{OHP}} - \phi_z)}{2kT}\right) \quad (1.79)$$

where ϕ^{OHP} is the electrode potential at the OHP, ϕ_z is the potential of zero charge and L_D is the well-known Debye length obtained from the Debye–Hückel theory for electrolyte solutions given by

$$L_D = \left(\frac{\epsilon_r \epsilon_0 kT}{2(ze_0)^2 n_0}\right)^{1/2} \quad (1.80)$$

with n_0 being the number of ions in the bulk of the solution, e_0 the electron charge, and k and T the Boltzmann's constant and the temperature.

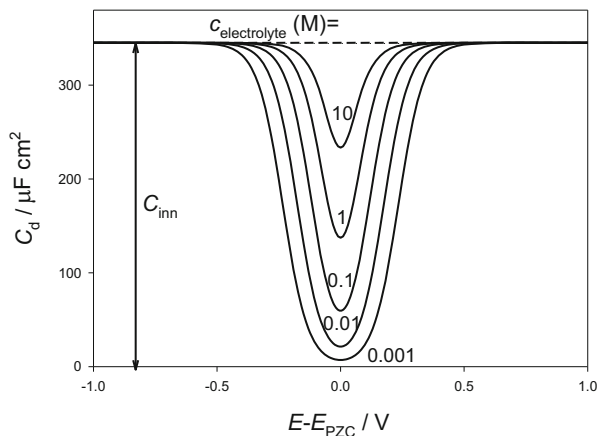
Mathematically, the interface can be described as two capacitors in series:

$$\frac{1}{C_d} = \frac{1}{C_{\text{inn}}} + \frac{1}{C_{G\text{-Ch}}} \quad (1.81)$$

C_{inn} is the capacitance due to the inner layer, which can be experimentally obtained from the plot of $1/C_d$ (with C_d being the capacitance measured at a given charge density) for several electrolyte concentrations versus the calculated $1/C_{G\text{-Ch}}$ at a constant surface charge density (Parsons and Zobel plot) [2]. If this plot is not linear, this is an indication that specific adsorption occurs.

At low electrolyte concentrations ($\leq 10^{-3}$ M solutions), the $C_{G\text{-Ch}}$ term dominates and the inner term can be neglected in Eq. (1.81). Thus, the Gouy–Chapman model agrees well with the experimental values of the double-layer capacitance of non-adsorbing electrolytes. Contrarily, for high electrolyte concentrations the extension of the space charged layer in solution is small and the C_{inn} term becomes dominant (see Fig. 1.11). The inner capacitance C_{inn} depends strongly on the charge density of the metal (showing a maximum at the PZC), and it is extremely sensitive to the nature

Fig. 1.11 Behavior of C_d as a function of the electrolyte concentration for the Stern's model of the electrical double layer, calculated from Eq. (1.81) for a 1:1 electrolyte. $C_{\text{inn}} = 345 \mu\text{F cm}^{-2}$. The concentration of the electrolyte (in M) appears on the curves



of the metal and the solvent. Several models have been proposed to explain this behavior. All of them coincide in that C_{inn} contains contributions from both the metal and the solution at the interface [2, 25]. Thus, the finite size of ions and solvent molecules confers a complex structure to the interface. The decrease of C_{inn} at potentials far from the PZC can be caused by a dielectric saturation leading to a decrease of the dielectric permittivity. On the other hand, the dependence of the surface potential of the metal χ on the charge density causes an increase of the capacitance.

A simple model for the metal called *jellium* has been used to explain this last effect [25]. The model describes the metal as positively charged ions and negative charged electrons. The ionic charge gives rise to a constant positive background charge which drops to zero at the metal surface whereas the electrons are modeled as a quantum-mechanical plasma which interacts with the positive charge and with other external fields. The resulting electronic charge distribution generates a surface dipole moment which leads to a surface potential of the order of several volts. The electric field in the double layer distorts this electronic distribution in the metal and changes the surface potential χ , leading to an increase of the capacitance.

1.6.2 Specific Adsorption

Specific adsorption occurs when the concentration of a species at the interface is greater than one would expect on the basis of electrostatic interactions only [2, 4, 13]. It is usually caused by chemical interactions between the adsorbate and the electrode (chemisorption) although in some cases it is due to weaker interactions such as intermolecular forces (physisorption). The interaction of the adsorbate with the electrode needs to be stronger than that of the solvent. So, adsorption involves, at least, a partial desolvation of the electrode (anions are more likely to be adsorbed than cations). Due to its chemical nature, chemisorption occurs at specific places of the electrode surface.

The amount of adsorbed species is given in terms of the coverage or fraction of the electrode surface covered by the adsorbate, θ . The relationship between the coverage and the concentration in solution of a species under equilibrium conditions is called an “adsorption isotherm.” The ones most employed in electrochemistry are the Langmuir and Frumkin isotherms, deduced from statistical consideration and assuming absence or presence of interactions between the adsorbed molecules in the former and the latter, respectively.

In the discussion of the different models for the structure of double layer developed up to this point, no specific interactions have been considered. However, specific adsorption is a common phenomena in electrochemistry. Since the interactions implied have to be very short range in nature, the chemisorbed species are strongly bound to the electrode surface with the locus of their centers being the inner Helmholtz plane (IHP, see Fig. 1.10), or compact part of the double layer.

Experimental evidence of the presence of specific adsorption can be found from thermodynamic measures both from the values of relative excesses or from the shift of the PZC with the electrolyte concentrations [19]. Currently, this presence can be determined from the combination of electrochemical and spectroscopic methods [4].

Specific adsorption can greatly alter the potential profile in the interfacial region. If we consider the presence of adsorbed ions at the IHP and assume that the solution is concentrated such that the potential drop in the diffuse layer beyond the OHP can be neglected, the total potential difference across the interface could be divided into two components, one from the metal to the IHP and the other from the IHP to the OHP,

$$\phi^M - \phi^{\text{sol}} = (\phi^M - \phi^{\text{IHP}}) + (\phi^{\text{IHP}} - \phi^{\text{OHP}}) \quad (1.82)$$

Each of those potential drops can be written in terms of the corresponding integral capacitance C_i (see Eq. 1.78),

$$\left. \begin{aligned} \phi^M - \phi^{\text{IHP}} &= \frac{q^M}{C_i^{\text{M} \rightarrow \text{IHP}}} \\ \phi^{\text{IHP}} - \phi^{\text{OHP}} &= \frac{q^M + q^{\text{ad}}}{C_i^{\text{IHP} \rightarrow \text{OHP}}} \end{aligned} \right\} \quad (1.83)$$

with q^{ad} being the charge due to the adsorbed ions. By combining Eqs. (1.82) and (1.83), one obtains

$$\phi^M - \phi^{\text{sol}} = \frac{q^M}{C_i^{\text{inn}}} + \frac{q^{\text{ad}}}{C_i^{\text{IHP} \rightarrow \text{OHP}}} \quad (1.84)$$

with C_i^{inn} being the integral capacitance of the inner layer given by

$$\frac{1}{C_i^{\text{inn}}} = \frac{1}{C_i^{\text{M} \rightarrow \text{IHP}}} + \frac{1}{C_i^{\text{IHP} \rightarrow \text{OHP}}} \quad (1.85)$$

The changes in the potential profile of the interfacial region because specific adsorption do indeed affect the electrode kinetics of charge transfer processes, particularly when these have an inner sphere character [13, 26] (see Fig. 1.12). When this influence leads to an improvement of the current response of these processes, the global effect is called “electrocatalysis.”

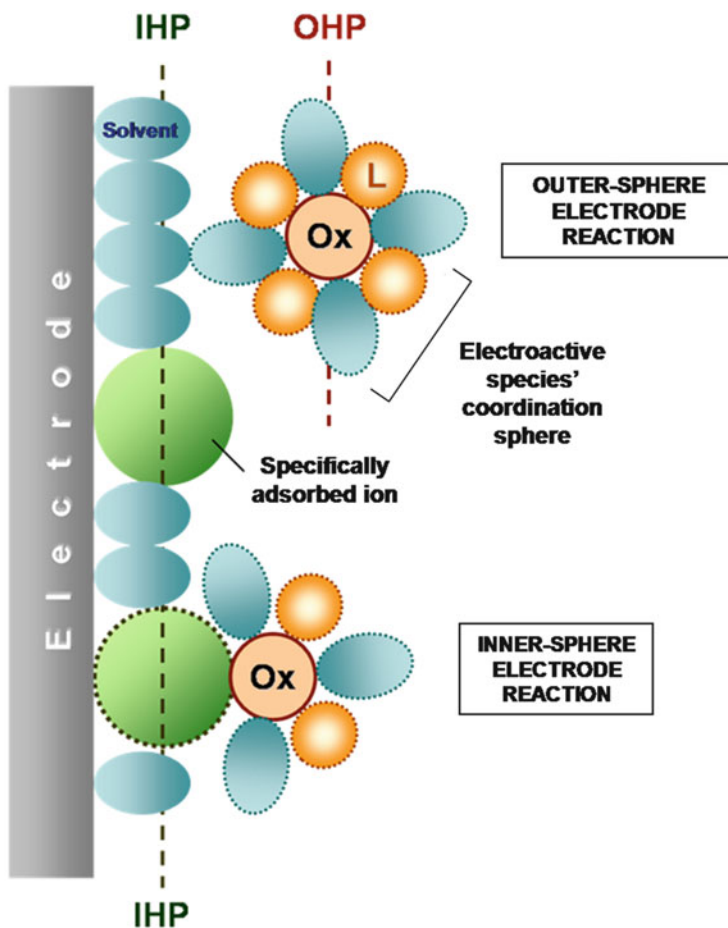


Fig. 1.12 Schematic view of outer-sphere and inner-sphere reactions. IHP and OHP refer to the inner and outer Helmholtz planes, respectively

1.7 Kinetics of the Charge Transfer

Let us consider the kinetics of a one-electron transfer between a metal electrode and a molecule in solution via an outer-sphere mechanism (no strong interaction between the electroactive species and the electrode takes place; see Fig. 1.12) and with no bond breaking or formation:



A distinguishing aspect in electrode kinetics is that the heterogeneous rate constants, k_{red} and k_{ox} , can be controlled externally by the difference between the inner potential in the metal electrode (ϕ^{M}) and in solution (ϕ^{sol}); that is, through the interfacial potential difference $E = \phi^{\text{M}} - \phi^{\text{sol}}$. With the help of an appropriate electrode setup (typically, a three-electrode arrangement and a potentiostat), the E -value can be varied in order to distort the electrochemical equilibrium and favor the electro-oxidation or electro-reduction reactions. Thus, the molar electrochemical Gibbs energy of reaction Scheme (1.IV), as derived from the electrochemical potentials of the reactant and product species, can be written as (see Eqs. 1.32 and 1.33 with $n = 1$)

$$\Delta\tilde{G} = \Delta G^{\ominus} + RT \ln \left(\frac{a_{\text{R}}^{\text{sol}}}{a_{\text{O}}^{\text{sol}}} \right) + F(\phi^{\text{M}} - \phi^{\text{sol}}) \quad (1.86)$$

where superscript “sol” refers to the values of the activities in solution.

Under electrochemical equilibrium conditions ($\Delta\tilde{G} = 0$), the interfacial potential difference is given by the Nernst equation (see Eqs. 1.34 and 1.36):

$$E_{\text{Eq}} = (\phi^{\text{M}} - \phi^{\text{sol}})_{\text{Eq}} = -\frac{\Delta G^{\ominus}}{F} - \frac{RT}{F} \ln \left(\frac{a_{\text{R}}^{\text{sol}}}{a_{\text{O}}^{\text{sol}}} \right) = E^{\ominus} - \frac{RT}{F} \ln \left(\frac{a_{\text{R}}^{\text{sol}}}{a_{\text{O}}^{\text{sol}}} \right) \quad (1.87)$$

where ΔG^{\ominus} is the reaction standard Gibbs energy and E^{\ominus} the standard potential of the redox couple, which contains the nonelectrical terms of the free energy. As stated in Sect. 1.5.1, it is more practical to work in terms of concentrations so Eq. (1.87) can be rewritten as

$$E_{\text{Eq}} = (\phi^{\text{M}} - \phi^{\text{sol}})_{\text{Eq}} = E_{\text{c}}^{\ominus'} - \frac{RT}{F} \ln \left(\frac{c_{\text{R}}^{\text{sol}}}{c_{\text{O}}^{\text{sol}}} \right) \quad (1.88)$$

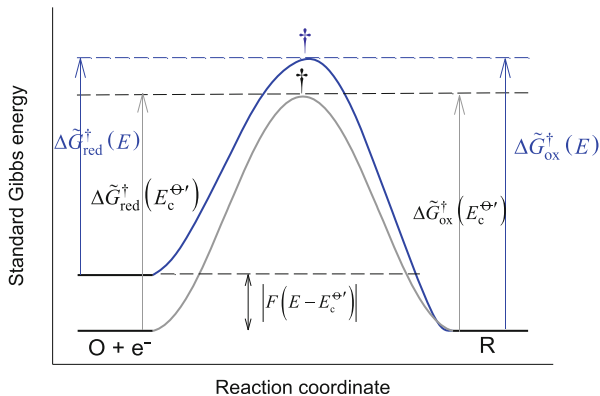
with $E_{\text{c}}^{\ominus'}$ being the formal potential given by Eq. (1.51). It is important to highlight that the values of the interfacial potential at the working electrode (E) as well as the standard and formal redox potentials (E^{\ominus} and $E_{\text{c}}^{\ominus'}$) are relative to the potential of a reference electrode.

Attending to Eq. (1.87), the expression for the reaction Gibbs energy (1.86) can be rewritten as

$$\Delta\tilde{G} = F \left[(\phi^{\text{M}} - \phi^{\text{sol}}) - (\phi^{\text{M}} - \phi^{\text{sol}})_{\text{Eq}} \right] = F(E - E_{\text{Eq}}) \quad (1.89)$$

From the above expression, it is evident that when the applied potential is more negative than E_{Eq} , the interfacial electrochemical equilibrium is broken and the electro-reduction of the oxidized species is thermodynamically favorable.

Fig. 1.13 Influence of the applied potential E on the energy barrier of the heterogeneous electron transfer process: $O + e^- \rightleftharpoons R$. The gray line corresponds to $E = E_c^{\ominus'}$ and the blue line to $E < E_c^{\ominus'}$, where the electrochemical potential of the electron is increased by the amount $F(E - E_c^{\ominus'})$. The energy of the oxidized and reduced species is supposed to be unaffected by the change in E



It is found that heterogeneous electron transfer reactions follow first-order kinetics with respect to the interfacial concentrations of the electroactive species, c_O^s and c_R^s , such that⁴

$$\begin{aligned} v_{\text{red}} &= k_{\text{red}} c_O^s \\ v_{\text{ox}} &= k_{\text{ox}} c_R^s \end{aligned} \quad (1.90)$$

where it is considered that the electron transfer takes place at a fixed distance corresponding to the distance of closest approach to the electrode surface (i.e., the Outer Helmholtz Plane) though electron tunneling is effective in a range of several angstroms [27].

The overall rate of the resulting electro-reduction process, v , is given by

$$v = k_{\text{red}} c_O^s - k_{\text{ox}} c_R^s \quad (1.91)$$

which is directly related to the measured current as follows:

$$\frac{I}{FA} = k_{\text{red}} c_O^s - k_{\text{ox}} c_R^s \quad (1.92)$$

Within a transition-state framework (Fig. 1.13) with the transition state being the same for the reduction “ $O + e^- \rightarrow R$ ” and oxidation “ $R \rightarrow O + e^-$ ” reactions for a given E -value and the barrier being overcome by sufficient thermal activation, the expressions for the rate constants as a function of the activation energies for the

⁴ It will be assumed in this section that the mass transport is much more rapid than the redox kinetics, such that the activities or concentrations of species O and R at the electrode–solution interface can be considered as identical to their bulk values (i.e., $a_i^s = a_i^{\text{sol}}$ and $c_i^s = c_i^{\text{sol}}$ with $i = O, R$). The influence of the mass transport on the current–potential response is treated in Sect. 1.8.

electro-reduction and electro-oxidation reactions ($\Delta\tilde{G}_{\text{red}}^\dagger$ and $\Delta\tilde{G}_{\text{ox}}^\dagger$, respectively) are given by

$$\begin{aligned} k_{\text{red}} &= A_{\text{red}} \exp\left(-\frac{\Delta\tilde{G}_{\text{red}}^\dagger}{RT}\right) \\ k_{\text{ox}} &= A_{\text{ox}} \exp\left(-\frac{\Delta\tilde{G}_{\text{ox}}^\dagger}{RT}\right) \end{aligned} \quad (1.93)$$

with the activation energies being related through the standard reaction Gibbs energy as follows:

$$\Delta\tilde{G}_{\text{red}}^\dagger - \Delta\tilde{G}_{\text{ox}}^\dagger = F(E - E_c^{\Theta'}) \quad (1.94)$$

As discussed below, any proper description of the system needs to consider the continuum of electronic levels in the metal (see Sect. 1.7.2.1). Therefore, one can act on the activation barriers, and hence, on the electrode kinetics, by varying the applied potential difference, E . For example, when the electrode potential is set to a value smaller than the formal potential (see Fig. 1.13), the Gibbs energy of the electrons (and therefore that of the “reactants” $\text{O} + \text{e}^-$) is increased by $\left|F(E - E_c^{\Theta'})\right|$ according to (1.89) under standard conditions. As a result, the energy barrier for the electro-oxidation process is reduced with respect to the barrier for the electro-reduction.

At the equilibrium potential, $E = E_{\text{Eq}}$, the electro-oxidation and electro-reduction rates are equal ($k_{\text{red}}c_{\text{O}}^{\text{s}} = k_{\text{ox}}c_{\text{R}}^{\text{s}}$) such that

$$\frac{k_{\text{red}}(E_{\text{Eq}})}{k_{\text{ox}}(E_{\text{Eq}})} = \frac{c_{\text{R}}^{\text{s}}}{c_{\text{O}}^{\text{s}}} \quad (1.95)$$

Attending to the definitions of the rate constants (1.93), to Eq. (1.94), and to the Nernst relationship (1.88), Eq. (1.95) leads to $A_{\text{red}} = A_{\text{ox}} = A$.

Let us now consider a second particular case where the applied potential corresponds to the formal potential. According to Eq. (1.94), the activation energies are equal when $E = E_c^{\Theta'}$:

$$\Delta\tilde{G}_{\text{red}}^\dagger(E_c^{\Theta'}) = \Delta\tilde{G}_{\text{ox}}^\dagger(E_c^{\Theta'}) = \Delta\tilde{G}^\dagger(E_c^{\Theta'}) \quad (1.96)$$

such that, assuming that the pre-exponential factor is potential independent, the value of the rate constants is also the same:

$$k_{\text{red}}(E_c^{\Theta'}) = k_{\text{ox}}(E_c^{\Theta'}) = A \exp\left(-\frac{\Delta\tilde{G}^\ddagger(E_c^{\Theta'})}{RT}\right) = k^0 \quad (1.97)$$

where k^0 is the standard heterogeneous rate constant corresponding to the rate constant of the reduction/oxidation reactions at the formal potential. The k^0 -value informs about the speed of the electrode reaction: the smaller k^0 , the more sluggish the electron transfer.

Finally, from the definition for k^0 , the expressions for the rate constants (1.93) can be written as

$$\begin{aligned} k_{\text{red}} &= k^0 \exp\left\{-\left(\frac{\Delta\tilde{G}_{\text{red}}^\ddagger(E) - \Delta\tilde{G}^\ddagger(E_c^{\Theta'})}{RT}\right)\right\} \\ k_{\text{ox}} &= k^0 \exp\left\{-\left(\frac{\Delta\tilde{G}_{\text{ox}}^\ddagger(E) - \Delta\tilde{G}^\ddagger(E_c^{\Theta'})}{RT}\right)\right\} \end{aligned} \quad (1.98)$$

Accordingly, the potential dependence of the electrode kinetics is determined by the variation of the activation energy with E , which is established by the “position” of the transition state on the energy profile in Fig. 1.13. This key aspect has been addressed in different ways by the different kinetic models developed. In the following sections, the two main models employed in interfacial electrochemistry will be reviewed.

1.7.1 The Butler–Volmer Model

In the phenomenological Butler–Volmer model (BV) [28, 29], the effect of the applied potential E on the energy of the transition state is assumed to be between that of the oxidized and reduced states, although no molecular description of the activation process is proposed. Accordingly, the activation energies for the reduction and oxidation reactions can be written as:

$$\begin{aligned} \Delta\tilde{G}_{\text{red}}^{\ddagger\text{BV}}(E) &= \Delta\tilde{G}^\ddagger(E_c^{\Theta'}) + \alpha F(E - E_c^{\Theta'}) \\ \Delta\tilde{G}_{\text{ox}}^{\ddagger\text{BV}}(E) &= \Delta\tilde{G}^\ddagger(E_c^{\Theta'}) - \beta F(E - E_c^{\Theta'}) \end{aligned} \quad (1.99)$$

where α and β are the cathodic and anodic transfer coefficients ($0 < \alpha < 1$ and $0 < \beta < 1$), respectively. The α and β values are supposed to be potential independent in the BV formalism and they fulfill that $\alpha + \beta = 1$ (as concluded from Eq. (1.94)). According to Eq. (1.99), the activation energies for the reduction and oxidation

processes in BV are predicted to vary linearly with the applied potential and the magnitude of this variation is parameterized by the transfer coefficients:

$$\alpha = \frac{1}{F} \frac{\partial \Delta \tilde{G}_{\text{red}}^{\dagger \text{BV}}(E)}{\partial E} \quad (1.100)$$

$$\beta = -\frac{1}{F} \frac{\partial \Delta \tilde{G}_{\text{ox}}^{\dagger \text{BV}}(E)}{\partial E}$$

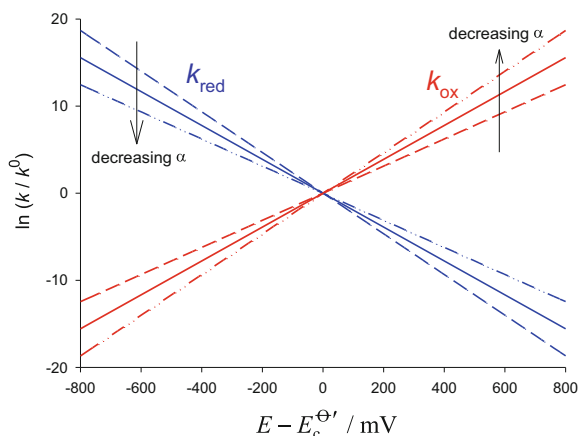
By substitution of the expressions for the activation energies (1.99) in Eq. (1.98), the well-known equations for the BV rate constants are finally obtained:

$$k_{\text{red}}^{\text{BV}} = k^0 \exp \left\{ -\frac{\alpha F (E - E_c^{\ominus'})}{RT} \right\} \quad (1.101)$$

$$k_{\text{ox}}^{\text{BV}} = k^0 \exp \left\{ \frac{(1 - \alpha) F (E - E_c^{\ominus'})}{RT} \right\}$$

Accordingly, the BV model predicts an exponential variation of the electrochemical heterogeneous rate constants with the applied potential. Thus, as shown in Fig. 1.14, the cathodic rate constant increases when the applied potential E is more negative with respect to the formal potential whereas the opposite behavior is predicted for the oxidation rate constant. Note that according to the BV model, the heterogeneous rate constants can be increased (or decreased) unlimitedly by applying larger overpotentials. As discussed below, this is a key difference with respect to the Marcus–Hush model. Figure 1.14 also illustrates that the variation of the rate constants with the applied potential depends on the value of the transfer coefficient which can be defined as

Fig. 1.14 Variation of the reduction and oxidation rate constants with the applied potential according to the Butler–Volmer kinetic model



$$\alpha = -\frac{RT}{F} \frac{\partial \ln\left(\frac{k_{\text{red}}^{\text{BV}}}{k^0}\right)}{\partial E} = 1 - \frac{RT}{F} \frac{\partial \ln\left(\frac{k_{\text{ox}}^{\text{BV}}}{k^0}\right)}{\partial E} \quad (1.102)$$

Thus, the plots $\ln(k_{\text{red}}^{\text{BV}}/k^0)$ vs $(E - E_c^{\Theta'})$ and $\ln(k_{\text{ox}}^{\text{BV}}/k^0)$ vs $(E - E_c^{\Theta'})$ are only symmetrical with respect to $(E - E_c^{\Theta'})$ when $\alpha = 0.5$ so it is fulfilled that $k_{\text{red}}^{\alpha=0.5}(E - E_c^{\Theta'}) = k_{\text{ox}}^{\alpha=0.5}(-(E - E_c^{\Theta'}))$. For $\alpha \neq 0.5$, this relationship does not hold and the abovementioned plots are asymmetric.

The BV model is largely employed in interfacial electrochemistry and it has been satisfactorily applied over the years to describe and classify the kinetics of many redox systems with simple expressions for the rate constants (Eq. 1.101) and in terms of only three parameters (k^0 , α , and $E_c^{\Theta'}$). Nevertheless, BV has some drawbacks. BV is an empirical model and so offers very limited physical insights into the electron transfer event and the nature of the system. This restricts the possibility of making predictions and obtaining molecular information of the system from electrochemical measurements. Moreover, experimental deviations have been reported from the ad infinitum, exponential variations of the rate constants with the overpotential predicted by BV, which are more apparent in the case of surface-confined redox systems [30].

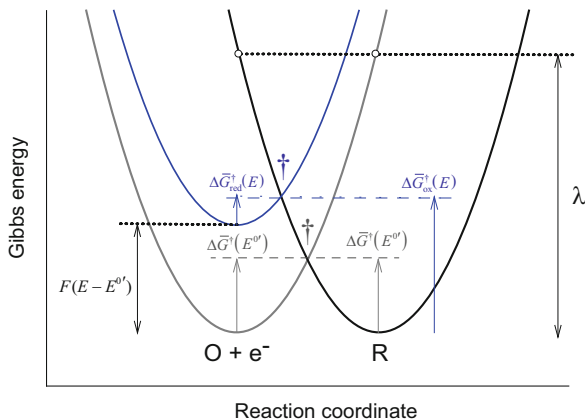
1.7.2 The Marcus–Hush Model

Microscopic models of electron transfer processes aim to provide a connection between the nature of the system and the electron transfer event that is lacking in BV. This enables us to rationalize experimental data in terms of the molecular properties of the system as well as to make predictions. Such approaches include “first-principles” basis for the calculation of the corresponding energy surface and the identification of the fundamental factors behind the activation barrier and the “meaning” of the reaction coordinate.

The Marcus–Hush model [31, 32] tackles the above questions by the harmonic oscillator approximation for the internal energy of the reactant and product states and by applying the Franck–Condon principle and the law of conservation of energy. Figure 1.15 displays the quadratic variation of the Gibbs energy of reactants and products with the reaction coordinate, q , as described in the Marcus theory [31, 33]. This dependence can be identified with the change in the Gibbs free energy because in this model there is no change in the entropy. For the sake of clarity, a single, global reaction coordinate q is considered that combines the vibrational and solvent coordinates (lengths and angles of chemical bonds and orientation of solvent dipole) affected upon the electron transfer, which otherwise lead to a many-dimensional energy surface [34].

The Franck–Condon principle establishes that the atomic nuclei are effectively immobile on the electron tunneling, that is, the nuclear motions can be

Fig. 1.15 Schematic of the energy curves in the Marcus–Hush model with a single, global reaction coordinate q such that the potential energy hyper-surface reduces to two parabolas and the activation energy can be calculated from the intersection point between them. The electronic coupling (Sect. 1.7.2.2) and the continuum of electronic levels in the metal electrode (Sect. 1.7.2.1) are not shown



approximated as “frozen” such that the nuclear configurations do not change. Also, given that the “electronic transition” is radiationless, energy conservation requires that the energies of the initial and final states are the same. From the above two considerations, it is concluded that the electron transfer can only occur at the intersection between the two Gibbs energy curves where the oxidized and reduced states have the same configuration and energy. Accordingly, the activation barrier arises from the need for rearrangement of the structure of the electroactive species and their “surroundings” to the configuration of the transition state where the electron transfer event is possible.

Assuming that the degree of adiabaticity is small enough (i.e., the resonance energy is small), the activation energy for the reaction can be calculated from the intersection of the two parabolas in Fig. 1.15. The difference between the Gibbs energy of the oxidized and reduced systems as a function of the reaction coordinate (q) is given by

$$\begin{aligned} \tilde{G}_{\text{red}}(q) - \tilde{G}_{\text{ox}}(q) &= \\ &= F(E - E_c^{\Theta'}) + \frac{k}{2} \{ (q - q_R)^2 - (q - q_O)^2 \} \end{aligned} \quad (1.103)$$

where q_O and q_R refer to the equilibrium configurations of the oxidized and reduced states, respectively. Also, it has been assumed that the force constants of the harmonic oscillators approximating the behavior of the oxidized and reduced species take the same value k in accordance with the most commonly used, symmetric version of the Marcus theory [30]. Otherwise, different force constants can be included in the theoretical treatment by using of the asymmetric Marcus theory [32, 34].

As discussed above, at the transition state ($q = q_{\ddagger}$) it is fulfilled that $\tilde{G}_{\text{red}}(q_{\ddagger}) = \tilde{G}_{\text{ox}}(q_{\ddagger})$ such that from Eq. (1.103) it can be deduced that

$$q_{\ddagger} = \frac{F(E - E_c^{\Theta'})}{k(q_R - q_O)} + \frac{q_R - q_O}{2} \quad (1.104)$$

and finally the well-known expression for the activation energy within the (symmetric) Marcus–Hush kinetic formalism (MH):

$$\begin{aligned} \Delta \tilde{G}_{\text{red}}^{\ddagger \text{MH}}(E) &= \frac{\lambda}{4} \left(1 + \frac{F(E - E_c^{\Theta'})}{\lambda} \right)^2 \\ \Delta \tilde{G}_{\text{ox}}^{\ddagger \text{MH}}(E) &= \frac{\lambda}{4} \left(1 - \frac{F(E - E_c^{\Theta'})}{\lambda} \right)^2 \end{aligned} \quad (1.105)$$

where $\lambda (= k(q_R - q_O)^2/2)$ is the so-called reorganization energy, which value is the hypothetical energy required to give the reactant (and its environment) the equilibrium nuclear configuration of the product (and its environment), without electron transfer. As can be deduced from Fig. 1.15, the λ -value is related to the curvature of the Gibbs energy curves so larger λ -values mean tighter parabolas. Note that according to (1.105) the MH model predicts a quadratic relationship between the activation energy and the applied potential in contrast with the linear relationship proposed in the BV model (Eq. 1.99). This leads to different variations of the electrochemical rate constants with the applied potential as will be discussed below.

The reorganization energy is a key concept introduced in the MH formalism to understand and predict the electron transfer kinetics given that the λ -value informs about the magnitude of the structural and solvation changes induced by the electron transfer reaction. Two contributions to λ are commonly separated: the inner-sphere reorganization energy (λ_i) associated with changes in the intramolecular vibrations and the outer-sphere reorganization energy (λ_o) that arises from changes in solvation, such that

$$\lambda = \lambda_i + \lambda_o \quad (1.106)$$

The inner component can be estimated from molecular theory by summing over the normal vibrational modes of the species [30, 33, 34]:

$$\lambda_i = \frac{1}{2} \sum_j k_j (q_R - q_O)_j^2 \quad (1.107)$$

where k_j are the force constants for each oscillator.

With respect to the solvation energy, this is usually approximated by modeling the reactants and products as spheres and the solvent as a dielectric continuum (Born theory), which in the case of an interface electron transfer gives rise to the following expression [30, 36]:

$$\lambda_o = \frac{e^2}{8\pi\epsilon_0} \left(\frac{1}{a_0} - \frac{1}{2d} \right) \left(\frac{1}{\epsilon_{op}} - \frac{1}{\epsilon_s} \right) \quad (1.108)$$

where “e” is the elementary charge, ϵ_0 the permittivity of free space, a_0 the radius of the reactant, ϵ_{op} the optical permittivity, ϵ_s the static permittivity, and d the distance from the reactant to the metal surface.

1.7.2.1 The Marcus–Hush–Chidsey Formalism (MHC)

Before considering the expressions for the rate constants, it is convenient to introduce a refinement [37] that has been ignored so far. It has been assumed that the electron transfer only involves the electronic state corresponding to the Fermi level of the electrode. However, the continuum of electronic levels (ϵ) must be considered such that energy levels around the Fermi one can participate and the overall rate of electron transfer is a sum of the rates for each electronic state, weighted by the probability of occupancy/vacancy according to the Fermi–Dirac distribution:

$$k_{\text{red}} = A \int_{-\infty}^{\infty} \frac{\exp\left(-\frac{\Delta\tilde{G}_{\text{red}}^{\dagger}(x)}{RT}\right)}{1 + \exp(-x)} dx$$

$$k_{\text{ox}} = A \int_{-\infty}^{\infty} \frac{\exp\left(-\frac{\Delta\tilde{G}_{\text{ox}}^{\dagger}(x)}{RT}\right)}{1 + \exp(x)} dx \quad (1.109)$$

where the pre-exponential factor A has been approximated to be the same for all the energy levels and $\Delta\tilde{G}_{\text{red/ox}}^{\dagger\text{MH}}(x)$ is the activation energy for each electronic level such that

$$\frac{\Delta\tilde{G}_{\text{red}}^{\dagger\text{MH}}(x)}{RT} = \frac{\Lambda}{4} \left(1 + \frac{\eta + x}{\Lambda} \right)^2$$

$$\frac{\Delta\tilde{G}_{\text{ox}}^{\dagger\text{MH}}(x)}{RT} = \frac{\Lambda}{4} \left(1 - \frac{\eta + x}{\Lambda} \right)^2 \quad (1.110)$$

with $\eta = F(E - E_c^{\Theta'})/RT$, $x = F(\epsilon - E)/RT$, and Λ being the dimensionless reorganization energy: $\Lambda = F\lambda/RT$. By introducing the standard heterogeneous rate constant, k^0 , as the common value of the oxidation and reduction rate constants

at the formal potential the following expressions for the heterogeneous rate constants are finally obtained [30]:

$$\begin{aligned} k_{\text{red}}^{\text{MHC}} &= k^0 \frac{S_{\text{red}}(\eta, \Lambda)}{S_{\text{red}}(0, \Lambda)} = k^0 e^{-\eta/2} \frac{I(\eta, \Lambda)}{I(0, \Lambda)} \\ k_{\text{ox}}^{\text{MHC}} &= k^0 \frac{S_{\text{ox}}(\eta, \Lambda)}{S_{\text{ox}}(0, \Lambda)} = k^0 e^{+\eta/2} \frac{I(\eta, \Lambda)}{I(0, \Lambda)} \end{aligned} \quad (1.111)$$

which depend on Λ and η (Eq. (1.110)). $S_{\text{red/ox}}(\eta, \Lambda)$ and $I(\eta, \Lambda)$ are integrals of the form:

$$\begin{aligned} S_{\text{red/ox}}(\eta, \Lambda) &= \int_{-\infty}^{\infty} \frac{\exp\left[-\frac{\Delta\tilde{G}_{\text{red/ox}}^{\ddagger\text{MH}}(x)}{RT}\right]}{1 + \exp(\mp x)} dx \\ I(\eta, \Lambda) &= \int_{-\infty}^{\infty} \frac{\exp\left[-\frac{(x - \eta)^2}{4\Lambda}\right]}{2 \cosh(x/2)} dx \end{aligned} \quad (1.112)$$

As in BV, the MHC model describes the electrode kinetics as a function of three parameters: the formal potential, the standard heterogeneous rate constant, and the reorganization energy. Nevertheless, important differences can be observed between the two kinetic models with respect to the variation of the rate constants with the applied potential. Whereas in BV rate constants vary exponentially and continuously with $(E - E_c^{\ominus'})$ (Fig. 1.14), MHC predicts a limiting value for the rate constants at large overpotentials (Fig. 1.16a). Thus, at potentials close to the formal potential the $\ln(k_{\text{red/ox}}/k^0)$ vs $(E - E_c^{\ominus'})$ curves obtained in MHC tend to

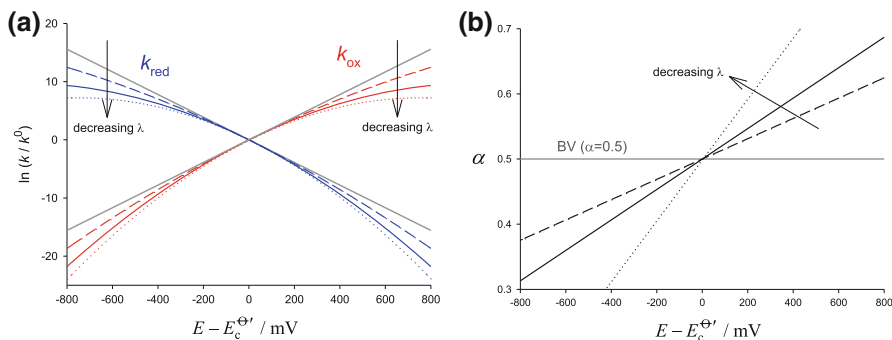


Fig. 1.16 (a) Variation of the reduction and oxidation rate constants with the applied potential according to the Marcus–Hush–Chidsey kinetic model. (b) Variation of the transfer coefficient with the applied potential in the Marcus–Hush–Chidsey model. *Gray solid lines* correspond to the values predicted by the BV model for $\alpha = 0.5$

those in BV for $\alpha = 0.5$ as shown in Fig. 1.16a. As the applied potential becomes more negative, the cathodic rate constant begins to level off and it eventually reaches a *plateau*. An analogous behavior is observed for the anodic rate constant when the applied potential takes very positive values with respect to $E_c^{\ominus'}$. Note that as the reorganization energy is smaller, the “leveling off” takes place at lower overpotentials and the *plateau* value is smaller. Consequently, differences between the predictions of the BV and MHC models are expected to be more apparent at large overpotentials and for systems with small reorganization energies.

Note that the curved $\ln(k_{\text{red/ox}}/k^0)$ vs $(E - E_c^{\ominus'})$ plots imply that the transfer coefficient, defined as $\alpha = -RT(\partial \ln(k_{\text{red}}^{\text{MHC}}/k^0)/\partial E)/F$ (Eq. 1.102), is potential dependent unlike what is assumed in BV. Thus, Fig. 1.16b shows that the MHC model predicts that the transfer coefficient takes the value 0.5 at the formal potential, larger than 0.5 at positive potentials (with respect to $E_c^{\ominus'}$), and smaller than 0.5 at negative potentials. This potential dependence of the transfer coefficient is more significant for small λ -values.

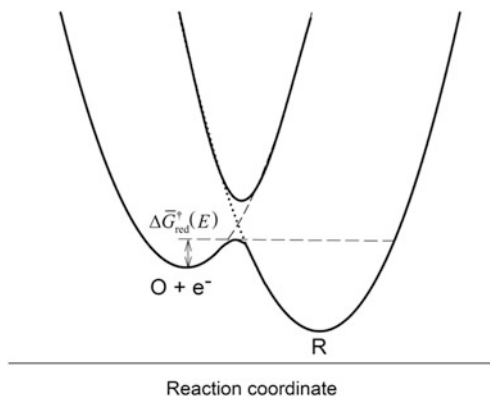
With respect to the effect of the reorganization energy on the rate constants, Fig. 1.16 shows that this is clearly different from that of the BV transfer coefficient. Thus, the λ -value has the same influence on the variation of the cathodic and anodic rate constants with the applied potential. Thus, independently of the value of the reorganization energy, it is fulfilled that $k_{\text{red}}^{\text{MHC}}(E - E_c^{\ominus'}) = k_{\text{ox}}^{\text{MHC}}(-(E - E_c^{\ominus'}))$ [38]. This has important implications with respect to the shape of the voltammetric response predicted by the different models. Thus, the MHC model has been proven, theoretically and experimentally, to be unable to fit the voltammetric response of redox systems that show BV transfer coefficients significantly different from 0.5 [30]. In such cases, as well as in the analysis of surface-confined redox systems, the use of the asymmetric Marcus–Hush theory has been recommended [35] which considers that the force constants for the redox species can be different leading to Gibbs energy curves of different curvatures.

1.7.2.2 Adiabaticity and the Pre-exponential Factor

So far the attention has been on the nuclear reorganization barrier. Nevertheless, other important factors previously “hidden” in the pre-exponential factor (and ultimately in the standard rate constant) have to be considered, namely, the fundamental question of the magnitude of the electronic interaction between electroactive molecules and energy levels in the electrode (i.e., the *degree of adiabaticity*) and its variation with the tunneling medium (electrode–solution interface), the tunneling distance, and the electrode material. Thus, within the transition-state formalism, the rate constant for electron transfer can be expressed as the product of three factors [39–42]:

$$k_{\text{red/ox}} = v_n \kappa_n \kappa_{\text{el}} \quad (1.113)$$

Fig. 1.17 Splitting of the Gibbs energy curves at the intersection region as a result of the electronic interaction between electronic states



ν_n is the effective nuclear vibration frequency that takes the system through the transition state region (the frequency of nuclear-barrier crossing), which depends on intramolecular and/or solvent vibrational modes and, accordingly, it takes values within the range $\nu_n = 10^{12} - 10^{14} \text{ s}^{-1}$ [40, 42]. κ_n refers to the nuclear reorganization discussed in previous sections, which within the MHC formalism can be expressed as:

$$\kappa_n = \int_{-\infty}^{\infty} \frac{\exp\left(-\frac{\Delta\tilde{G}_{\text{red/ox}}^{\ddagger}(x)}{RT}\right)}{1 + \exp(\mp x)} dx \quad (1.114)$$

Finally, κ_{el} is the electronic transmission coefficient that accounts for the probability of electron transfer upon reaching the configuration of the transition state. Note that it has been assumed that the electronic interaction between the redox species and the energy levels in the electrode is independent of the energy of such level x , so the electronic and nuclear factors can be treated separately.

As illustrated in Fig. 1.17, the electronic interaction between the reactant and the electrode surface gives rise to the splitting of the energy curves at the intersection (non-crossing). The extent of the splitting is characterized by the electronic coupling element H_{AB} (see below) and defines the probability of electron transfer when passing over the energy barrier. Thus, when the resonance energy is small (*non-adiabatic reactions*), there is little probability that the system will proceed from the initial to the final state ($\kappa_{\text{el}} \rightarrow 0$), but will predominantly remain in the same diabatic curve and end up at the starting point: reactant. On the other hand, as the electronic interaction is stronger (*adiabatic reactions*), the probability of electron transfer increases and it tends to unity as H_{AB} is larger (see below). Therefore, apart from the reorganization energy-related factors discussed in previous sections, the degree of adiabaticity is a key aspect in understanding and predicting the electrode kinetics so adiabatic processes are faster than the corresponding non-adiabatic ones.

The effect of the reaction adiabaticity on the electronic transmission coefficient can be estimated by making use of an extension of the Landau–Zener formalism [43–47]:

$$\kappa_{\text{el}} = \frac{2 \left[1 - \exp\left(-\frac{v_{\text{el}}}{2v_n}\right) \right]}{2 - \exp\left(-\frac{v_{\text{el}}}{2v_n}\right)} \quad (1.115)$$

where v_{el} is the electron tunneling frequency, which for electrode reactions can be defined as [46]:

$$v_{\text{el}} = \frac{4\pi^2 \rho_M}{h \sqrt{4\pi \frac{\lambda F}{RT}}} H_{\text{AB}}^2 \quad (1.116)$$

with ρ_M being the density of electronic levels in the electrode and h is the Planck constant. The effective average of the electronic coupling element, H_{AB} , decreases exponentially with the electron transfer distance, r :

$$H_{\text{AB}} = H_{0,\text{AB}} \exp\left[-\frac{\beta_r}{2}(r - r_{\text{OHP}})\right] \quad (1.117)$$

where $H_{0,\text{AB}}$ is the electronic coupling element at the distance of closest approach, r_{OHP} , and β_r is the decay constant for electronic coupling that depends on the tunneling medium and takes values of the order of 10^8 cm^{-1} . This reinforces the idea that adiabaticity is a gradual property that can be “varied,” for example, through the distance of closest approach that affects the $H_{0,\text{AB}}$ -value [47, 48]. Therefore, the degree of adiabaticity is ascribed not only to the electrode process itself but also to the characteristics of the electrode | solution interface and the electrode material.

When considering the case of electroactive species in solution, the electron transfer reaction takes place over a range of several angstroms and the heterogeneous rate constant can be written as [46]:

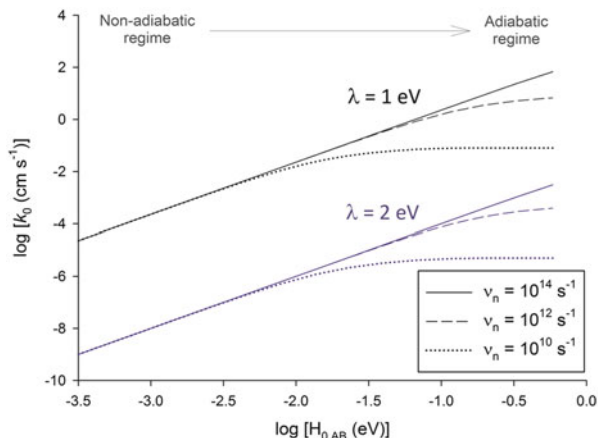
$$k_{\text{red/ox}} = v_n \kappa_n \int_{r_0}^{\infty} \kappa_{\text{el}} dr \quad (1.118)$$

which is well approximated by

$$k_{\text{red/ox}} \approx \frac{v_n \kappa_n}{\beta_r} \ln \left(1 + \frac{4\pi^2 \rho_M H_{0,\text{AB}}^2}{v_n h \sqrt{4\pi \frac{\lambda F}{RT}}} \right) \quad (1.119)$$

Thus, in the non-adiabatic regime it is fulfilled that $\left(4\pi^2 \rho_M H_{0,\text{AB}}^2 / v_n h \sqrt{4\pi \frac{\lambda F}{RT}}\right) \ll 1$ and the rate constant is given by

Fig. 1.18 Variation of the standard heterogeneous rate constant, k^0 , with the electronic coupling element for different ν_n and λ values. The effect of the electronic interaction on the activation energy has been ignored [2, 49]. $\beta_r = 10^8 \text{ cm}^{-1}$, $\rho_M = 0.3 \text{ eV}^{-1}$, $T = 298 \text{ K}$



$$k_{\text{red/ox}}^{\text{non-adia}} \approx \frac{\kappa_n}{\beta_r} \frac{4\pi^2 \rho_M H_{0,AB}^2}{h \sqrt{4\pi \frac{\lambda F}{RT}}} \quad (1.120)$$

whereas in the adiabatic regime, $\left(4\pi^2 \rho_M H_{0,AB}^2 / \nu_n h \sqrt{4\pi \frac{\lambda F}{RT}}\right) \gg 1$, the probability of electron transfer at the transition state tends to unity ($\kappa_{\text{el}} \rightarrow 1$, as inferred from Eq. (1.115)) and the rate constant will become independent of the electronic coupling and the factors that determine it such as the electronic structure of the electrode:

$$k_{\text{red/ox}}^{\text{adia}} \approx \nu_n \kappa_n \quad (1.121)$$

It is interesting to analyze the transition between the non-adiabatic and adiabatic regimes in terms of the standard heterogeneous rate constant, k^0 , given that this is the parameter commonly referred to in kinetic studies. Considering that k^0 is defined as the value of the reduction and oxidation rate constants at the formal potential, its value can be calculated from (1.119) for $\kappa_n = \kappa_n(E = E_c^{\theta'})$.

Figure 1.18 shows the variation of k^0 with the strength of the electronic interaction for typical values of the reorganization energy (λ) and the effective nuclear vibration frequency (ν_n). It has been assumed that the resonance energy is small enough (in comparison with the reorganization energy) for the value of the activation energy not to be significantly smaller than that predicted by the Marcus theory (Sect. 1.7.2). Indeed, this is the case for most outer-sphere reactions.

As predicted by Eq. (1.120), Fig. 1.18 illustrates how the standard rate constant is independent of ν_n in the non-adiabatic regime where it is determined by the strength of the electronic interaction: the stronger the interaction, the faster the electrode reaction. For weakly adiabatic systems, the increase of the rate constant

levels off, tending to a *plateau* in the adiabatic region provided that the lowering of the energy barrier due to the electronic coupling is negligible [2]. Under such a regime, the rate of electron transfer is predicted to be independent of the electronic coupling and limited by the effective nuclear frequency (Eq. 1.121). When the electronic coupling further increases and the decrease of the activation energy is not negligible, this effect is to be included in (1.114) such that the rate constant takes values larger than the limit corresponding to the *plateau* shown in Fig. 1.18 [50].

1.8 Mass Transport

Since electrode reactions tend to make the composition in the nearby solution different from that further away, heterogeneity in the solution almost always exist in electrochemical systems. Mass transport arises as the response of the system to recover the initial homogeneity.

The essential quantity that is considered in the description of mass transport is the flux for species “i” (which is, in fact, a vector) that describes the flow in a given direction in space (moles per area and time units (see Fig. 1.19) [50–52],

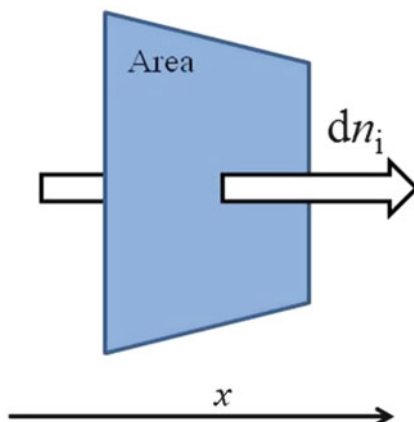
$$J_i = \frac{1}{A} \frac{dn_i}{dt} \quad (1.122)$$

with A being the area that cross species “i.” The flux can be also defined as the product of the local concentration by the velocity of species “i,”

$$J_i = c_i v_i \quad (1.123)$$

In the absence of convection, the change in the flux with the position in the system may be related to the time derivative of the number of moles by applying Gauss’ theorem [4],

Fig. 1.19 Flux of a species “i” in the direction x



$$-\frac{dn_i}{dt} = \oint J_i dA \quad (1.124)$$

where A is the surface area covering a given volume from which species i is flowing out and $-dn_i/dt$ is the rate of loss of this species (in moles per second). The surface integral can be related with the volume integral of the divergence of the flux,

$$\int_V \text{div} J_i dV = \oint J_i dA \quad (1.125)$$

Assuming mass conservation and absence of chemical reactions, it can be written that

$$\frac{dn_i}{dt} = \int_V \frac{\partial c_i}{\partial t} dV \quad (1.126)$$

and by combining Eqs. (1.124)–(1.126)

$$\frac{\partial c_i}{\partial t} = -\text{div} J_i \quad (1.127)$$

This result is called the continuity equation for mass [4, 52]. The cause of the flux is called a “driving force”, which is not used in the Newtonian sense, but instead names any source of perturbation. In the case of mass transport, this cause is typically a gradient (of concentration, electrical potential, or density).

The general equation that relates forces and fluxes is given by Onsager’s theory. For a single force X , it establishes a linear dependence between fluxes and forces that can be written as

$$J_i = L_i X \quad (1.128)$$

with L_i being called as the phenomenological coefficient for the force X .⁵

Equation (1.128) can be expressed in terms of the velocity of species i (see Eq. 1.123), by assuming that this velocity is proportional to the driving force,

$$v_i = u_i X \quad (1.129)$$

with the proportionality constant being named absolute “mobility” (if X is a force per mole, u_i has units of velocity per mole divided by driving force).

By taking into account the relationship between the velocity and the force given by (1.129), Eq. (1.123) can be written as

⁵ If X is a force per mole, the units of L_i are $\text{mol}^2 \text{N}^{-1} \text{m}^{-2} \text{s}^{-1}$ in the I.S.

$$J_i = c_i u_i X \quad (1.130)$$

This general relationship between the flux and the force is known as Teorell's equation [4, 53].

In the absence of convection, a charged species i in an electrolytic solution moves under the influence of a driving force which is, at constant temperature and pressure, the minus gradient of the electrochemical potential, i.e., $X = -\nabla \tilde{\mu}_i$ (see Eqs. (1.11) and (1.14) for the definition of $\tilde{\mu}_i$), with ∇ being the gradient operator which, for a single Cartesian coordinate, is $\nabla = \partial/\partial x$. Since $\tilde{\mu}_i$ has dimensions of energy per mole, where the energy is a force times a length, $\nabla \tilde{\mu}_i$ has dimensions of a force per mole. Note that the gradient of the electrochemical potential includes electric and chemical "forces" acting on an ionic species since

$$X = -\nabla \tilde{\mu}_i = -\nabla \mu_i - z_i F \nabla \phi \quad (1.131)$$

By inserting Eq. (1.131) into Eq. (1.130), the following expression for the flux is obtained:

$$J_i = -c_i u_i \nabla \tilde{\mu}_i = -c_i u_i \nabla \mu_i - c_i u_i z_i F \nabla \phi \quad (1.132)$$

Assuming that, under usual electrochemical conditions, the activity coefficient of species "i" does not vary significantly in the solution, the first term of the right-hand side can be written as (see also Eq. 1.11)

$$c_i u_i \nabla \mu_i = c_i u_i RT \nabla \ln c_i = u_i RT \nabla c_i \quad (1.133)$$

and Eq. (1.132) becomes

$$J_i = -u_i RT \nabla c_i - c_i u_i z_i F \nabla \phi \quad (1.134)$$

In the case of charged species, it is usual to define a charge mobility for the ions, u_i^c , which is related with the absolute mobility by

$$u_i^c = |z_i| F u_i \quad (1.135)$$

The charge mobility has units of velocity divided by electric field, $\text{m}^2 \text{V}^{-1} \text{s}^{-1}$ (see Table 1.3 for values of the mobility of several ions in aqueous solution and [52] for the case of nonaqueous solutions). By inserting Eq. (1.135) into Eq. (1.134), one obtains

$$J_i = -u_i^c \frac{RT}{|z_i| F} \nabla c_i - c_i \frac{z_i}{|z_i|} u_i^c \nabla \phi \quad (1.136)$$

Equations (1.134) or (1.136) are called the Nernst–Planck equation [4, 13, 50, 52]. In the deduction of this equation it has been assumed that the flux of a species i

Table 1.3 Values of the charge mobility of different ions in aqueous solution [4, 14, 51]

Ion	$u_i^c \times 10^9 / \text{m}^2 \text{V}^{-1} \text{s}^{-1}$
Li ⁺	40.1
Na ⁺	51.9
Zn ²⁺	54.7
Mg ²⁺	54.9
F ⁻	57.4
Ca ²⁺	61.6
Si ²⁺	62.5
Ba ²⁺	65.9
K ⁺	76.2
NH ₄ ⁺	76.2
Cl ⁻	79.1
I ⁻	79.6
Cs ⁺	80.0
Rb ⁺	80.6
Br ⁻	80.9
OH ⁻	205.2
H ₃ O ⁺	362.2

is only caused by the corresponding driving force ($\nabla \tilde{\mu}_i$) and, therefore, there is no coupling with other forces.

The expression for the flux given by Eqs. (1.134) and (1.136) clearly shows that it presents two components. The first, originated by a gradient of concentration, is called the diffusive flux (first term in the right-hand side of Eq. (1.136)), and the second, due to a gradient of electric potential, is called migrational flux (second term in the right-hand side of Eq. (1.136)).

The diffusive flux appears as a consequence of a gradient of concentration and is given as (see Eq. 1.136),

$$J_{\text{diffusion},i} = -u_i^c \frac{RT}{|z_i|F} \nabla c_i \quad (1.137)$$

which, taking into account the Nernst–Einstein relationship between the ionic charge mobility and the diffusion coefficient⁶

⁶ Note that, from the relationship between the ionic mobility and the diffusion coefficient given by Eq. (1.138), it is possible to rewrite Eq. (1.132) as $J_i = -\frac{D_i c_i}{RT} \nabla \tilde{\mu}_i$ (see also Eq. (1.135)).

$$u_i^c = \frac{|z_i|F}{RT} D_i \quad (1.138)$$

becomes

$$J_{\text{diffusion},i} = -D_i \nabla c_i \quad (1.139)$$

which is called Fick's first law [52, 55]. The minus sign in this equation indicates that the flux of species i takes place in the opposite direction of the concentration gradient. It is also possible to make an estimation of the size of the ion by imagining it as a small sphere of radius r_{ion} and using the Stokes–Einstein relationship,

$$r_{\text{ion}} = \frac{k_B T}{6\pi\zeta D_i} \quad (1.140)$$

with k_B and ζ being the Boltzmann's constant and the viscosity of the solvent, respectively.

Concerning the migration component of the overall flux, in line with Eq. (1.136), for a $z:z$ electrolyte it is given in terms of charge per area and time as

$$J_{\text{migration},i} = -c_i \frac{z_i}{|z_i|} u_i^c \nabla \phi \quad (1.141)$$

Since the flux can be written as the product of concentration times the velocity (Eq. 1.123), the expression of the migration velocity is (see Eqs. 1.129 and 1.135)

$$v_{\text{migration},i} = -\frac{z_i}{|z_i|} u_i^c \nabla \phi \quad (1.142)$$

The charge mobility of an ion represents the speed that acquires the ion per unit of electric field. The electric migration current corresponding to the ionic movement of a single kind of charge is equal to the flux of charge, i.e., to the rate at which the charge cross any plane normal to the flow (see Eq. 1.141) [56]

$$I_{\text{migration},i} = z_i F A J_{\text{migration},i} = -F A |z_i| c_i u_i^c \nabla \phi \quad (1.143)$$

Equation (1.143) is valid for a single carrier. The total migration current is obtained as

$$I_{\text{migration}} = \sum_{\text{ions}} I_{\text{migration},i} = -F A \nabla \phi \sum_{\text{ions}} |z_i| c_i u_i^c \quad (1.144)$$

The fraction of the total ionic current carried by one particular species is known as the transport number,

$$t_i = \frac{|z_i|c_i u_i^c}{\sum_{\text{ions}} |z_i|c_i u_i^c} = F \frac{|z_i|c_i u_i^c}{\kappa} \quad (1.145)$$

with

$$\kappa = F \sum_{\text{ions}} |z_i|c_i u_i^c \quad (1.146)$$

being the conductivity of the media.

The ionic mobility is related to the molar ionic conductivity of the ion λ_i

$$u_i^c = \frac{\lambda_i}{|z_i|F} \quad (1.147)$$

The molar conductivity of the solution of a z_+z_- electrolyte of concentration c is defined as

$$\Lambda = \frac{\kappa}{c} = F(|z_+|u_+^c + |z_-|u_-^c) = Fz(u_+^c + u_-^c) \quad (1.148)$$

The molar conductivity depends on the concentration in agreement with the Kohlrausch's law,

$$\Lambda = \Lambda^0 - S\sqrt{c} \quad (1.149)$$

with Λ^0 being the molar conductivity at infinite dilution [4] and S a proportionality constant which depends more on the stoichiometry of the electrolyte than on its specific identity. Equation (1.149) is valid for concentrations below 0.05 M.

A theoretical approach for explaining the relationship between S and the characteristics of the electrolyte was provided by Onsager on the basis of the model of ions plus ionic cloud developed in the Debye–Hückel theory, obtaining [4]

$$S = \alpha\Lambda_0 + \beta_0 \quad (1.150)$$

with

$$\alpha = \frac{82.045 \times 10^4}{(\epsilon T)^{3/2}} \quad (1.151)$$

$$\beta_0 = \frac{8.2487}{\zeta \sqrt{\epsilon_r T}} \quad (1.152)$$

Sometimes, the conductivity of the solution may decrease due to the formation of electroneutral ion pairs. Under these conditions, the Fuoss–Onsager equation can be used to calculate the molar conductivity (Λ) of associated electrolytes [57]:

$$\Lambda = \Lambda_0 - S\sqrt{c\theta} + E'c\theta\ln(6E_1c\theta) + Lc\theta - K_a c\theta f_{\pm}^2 \Lambda \quad (1.153)$$

with

$$E' = E_1\Lambda_0 - E_2 \quad (1.154)$$

$$\left. \begin{aligned} E_1 &= \frac{2.942 \times 10^{12}}{(\epsilon_r T)^3} \\ E_2 &= \frac{0.4333 \times 10^8}{\zeta(\epsilon_r T)^2} \end{aligned} \right\} \quad (1.155)$$

$$L = L_1 + L_2(b) \quad (1.156)$$

$$L_1 = 3.202E_1\Lambda_0 - 3.42E_2 + \alpha\beta_0 \quad (1.157)$$

$$L_2(b) = 2E_1\Lambda_0 h(b) + \frac{44E_2}{3b} - 2E'\ln b \quad (1.158)$$

$$h(b) = \frac{2b^2 + 2b - 1}{b^3} \quad (1.159)$$

$$b = \frac{16.7102 \times 10^{-6}}{\epsilon_r T a_0} \quad (1.160)$$

where c is the electrolyte concentration, Λ_0 the molar conductivity at infinite dilution ($c \approx 0$), θ the degree of dissociation, K_a the association constant based on activities, f_{\pm} the mean molar activity coefficient of ions, and a_0 the distance of closest approach. Moreover, ϵ_r and ζ are the relative permittivity and viscosity of the pure solvent and T is the absolute temperature (K).

The results provided by Eq. (1.153) can be improved by using the Fuoss–Hsia equation modified by Fernandez-Prini (for 1:1 electrolytes [58–60]):

$$\Lambda = \Lambda_0 - S\sqrt{c\theta} + Ec\theta\ln(c\theta) + J_1c\theta - J_2(c\theta)^{3/2} - K_a c\theta f_{\pm}^2 \Lambda \quad (1.161)$$

with

$$E = \frac{\kappa^2 a_0^2 b^2}{24c} \Lambda_0 - \frac{\kappa a_0 b \beta_0}{16\sqrt{c}} \quad (1.162)$$

$$J_1 = \delta_1 \Lambda_0 + \delta_2 \quad (1.163)$$

$$J_2 = \delta_3 \Lambda_0 + \delta_4 \quad (1.164)$$

$$\kappa = \frac{50.2901 \times 10^{10} \sqrt{c}}{\sqrt{\epsilon_r T}} \quad (1.165)$$

$$\delta_1 = \left[\frac{(\kappa a_0 b)^2}{24c} \right] \left[1.8147 + 2\ln\left(\frac{\kappa a_0}{\sqrt{c}}\right) + \frac{2(2b^2 + 2b - 1)}{b^3} \right] \quad (1.166)$$

$$\delta_2 = \alpha\beta_0 + \beta_0 \left(\frac{\kappa a_0}{\sqrt{c}} \right) - \beta_0 \left[\frac{\kappa a_0 b}{16\sqrt{c}} \right] \left[1.5337 + \frac{4}{3b} + 2\ln \left(\frac{\kappa a_0}{\sqrt{c}} \right) \right] \quad (1.167)$$

$$\delta_3 = \left[\frac{b^2(\kappa a_0)^3}{24c^{3/2}} \right] \left[0.6094 + \frac{4.4748}{b} + \frac{3.8284}{b^2} \right] \quad (1.168)$$

$$\delta_4 = \frac{\beta_0(\kappa a_0 b)^2}{24c} \left[\frac{2(2b^2 + 2b - 1)}{b^3} - 1.9384 \right] + \alpha\beta_0 \frac{\kappa a_0}{\sqrt{c}} + \frac{\beta_0(\kappa a_0)^2}{c} \quad (1.169)$$

$$- \frac{\beta_0 b(\kappa a_0)^2}{16c} \left[1.5405 + \frac{2.2761}{b} \right] - \left(\frac{\beta_0^2 \kappa a_0 b}{16\Lambda_0 \sqrt{c}} \right) \left(\frac{4}{3b} - 2.2194 \right)$$

1.8.1 Minimization of the Migration Component

The migration contribution to the flux of species “i” can be minimized by the addition of an inert (or supporting) electrolyte in a concentration of two orders of magnitude higher than that of species “i.” These electrolyte supports ions should be electrochemically and chemically inert but increase the ionic strength of the solution. Therefore, they cause a strong decrease of the transport number of species “i.” Indeed (see Eq. 1.145),

$$c_i u_i^c = \frac{\kappa t_i}{|z_i| F} \quad (1.170)$$

and on inserting Eq. (1.170) into Eq. (1.136) and taking into account (1.138), one obtains

$$J_i = - \frac{z_i \kappa t_i}{|z_i|^2 F} \nabla \phi - D_i \nabla c_i \quad (1.171)$$

Under these conditions, the first addend of the right-hand side of Eq. (1.171) is negligible compared to the second, and it can be assumed that $J_{\text{migration},i} \ll J_{\text{diffusion},i}$.

The addition of the inert electrolyte affords other advantages. The most important point is that the conductivity of the solution increases (and thus the ohmic drop decreases through a decrease of the resistance of the cell, R_{cell} ; see Sect. 1.9). Moreover, the diffuse double layer narrows, being formed mainly by the ions of the inert electrolyte (with a sharp potential drop over a very short distance from the electrode surface). This makes the capacitance more reproducible and the Frumkin effects less obtrusive. Activity coefficients of the electroactive species are also less variable (and, therefore, quantities like formal potentials and rate constants), since

the ionic strength of the solution is virtually uniform and constant. Moreover, natural convection becomes less troublesome because the density of a concentrated ionic solution is less affected by small changes in the concentration of electroactive species than in a pure solvent.

It should be taken into account that the effects of the supporting electrolyte can also be adverse, for example, reaction mechanisms can be drastically altered (the ions of the supporting electrolyte may complicate the electroactive species through ionic association processes). However, except in specific cases, the advantages indicated make the addition of supporting electrolyte in excess a standard procedure.

1.8.2 Temporal Evolution

On inserting the expression of the flux given by Eq. (1.136) into the continuity equation for mass given by Eq. (1.127) and taking into account Eq. (1.138), an expression for the temporal evolution of the concentration of species i is obtained:

$$\frac{\partial c_i}{\partial t} = -\text{div}J_i = D_i \nabla^2 c_i + D_i \frac{z_i F}{RT} \nabla \phi \nabla c_i \quad (1.172)$$

For the deduction of this expression, it has been assumed that Poisson's equation holds (i.e., $\nabla^2 \phi = 0$). If the migration contribution can be suppressed (for example, due to the addition of supporting electrolyte), Eq. (1.172) simplifies to Fick's second law:

$$\frac{\partial c_i}{\partial t} = D_i \nabla^2 c_i \quad (1.173)$$

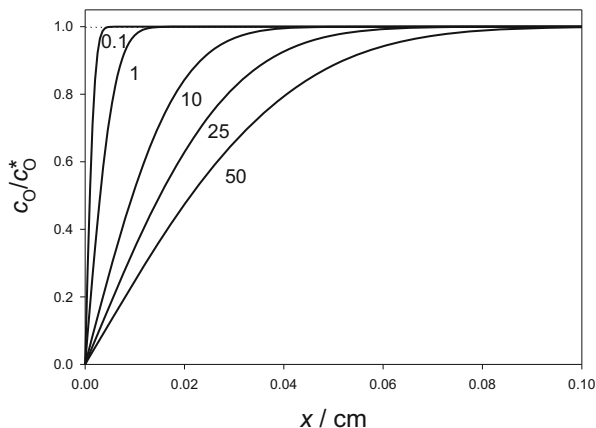
with ∇^2 being the Nabla operator for mass transport by diffusion whose expression for usual electrode geometries is given in Table 2.2.

An example of the concentration profiles of the oxidized species O, calculated for different times and corresponding to the application of a constant potential under linear diffusion conditions, is shown in Fig. 1.20. The electrode reaction at the interface leads to the depletion of species O at the solution region adjacent to the electrode surface. As the time increases, the layer in the solution affected by the diffusive mass transport becomes thicker, which indicates that linear diffusion is unable to restore the initial situation (for a more detailed discussion on concentration profiles and their relation with the current, see Sects. 2.2.1 and 2.2.2).

1.8.3 Convection

There is a third type of mass transport in electrochemical experiments: convection. This can involve the macroscopic or microscopic motion of the solution in which

Fig. 1.20 Concentration profile of the oxidized species resulting from the application of a constant potential with $E \ll E_c^{\theta'}$ under linear diffusion conditions ($\nabla^2 = \partial^2/\partial x^2$) (see Eq. (2.19) in Sect. 2.2). The value of the different times (in seconds) is indicated on the curves. $D_O = 10^{-5} \text{ cm}^2 \text{ s}^{-1}$



the electroactive species are dissolved. Macroscopic motions may arise either because of forced hydrodynamic regimes (such in the case of Dropping Mercury Electrode or the Rotating Disc Electrode) or because of the appearance of density gradients due to strong composition changes generated by the electrochemical reactions [52]. In any case, the expression of the convection flux is

$$J_{\text{convection},i} = c_i v_{\text{convection}} \quad (1.174)$$

where $v_{\text{convection}}$ is related to the motion of the solution. For an incompressible fluid, the expression of the velocity profile is obtained by two differential equations: the continuity equation:

$$\text{div}(v_{\text{convection}}) = 0 \quad (1.175)$$

and the Navier–Stokes equation:

$$\frac{dv_{\text{convection}}}{dt} = -\frac{1}{\rho}(\nabla P - \zeta \nabla^2 v_{\text{convection}} - f) \quad (1.176)$$

where ρ and ζ are the density and viscosity of the fluid, P is the pressure, and f is the force/volume exerted on an element of fluid by gravity [13, 52]. Two different types of flow are considered in hydrodynamic problems. When the flow involves chaotic motion, it is called as turbulent. On the other hand, if the flow occurs as if separate layers of the fluid have steady and characteristic velocities, it is called laminar flow. Under these conditions, the convection flux is proportional to the pressure gradient. Thus, in the case of a fluid moving through a tube with uniform circular cross section of radius R , the convective flux is given by the Poiseuille's equation:

$$J_{\text{convection},i} = c_i v_{\text{convection}} = -c_i \frac{R^2}{8\zeta} \frac{dP}{dx} \quad (1.177)$$

and the velocity profile defined by Eq. (1.177) is typically parabolic [51].

When the three diffusion, migration, and convection fluxes are considered, the temporal evolution of the concentration of a species “i” is given as (see also Eq. 1.175)

$$\frac{\partial c_i}{\partial t} = -\text{div} J_i = D_i \nabla^2 c_i + D_i \frac{z_i F}{RT} \nabla \phi \nabla c_i - v_{\text{convection}} \nabla c_i \quad (1.178)$$

When the migration of species i can be suppressed, Eq. (1.178) becomes

$$\frac{\partial c_i}{\partial t} = D_i \nabla^2 c_i - v_{\text{convection}} \nabla c_i \quad (1.179)$$

which, for electrochemical forced hydrodynamic experiments (with the exception of Dropping Mercury Electrode), is considered only under steady-state conditions (i.e., $\partial c_i / \partial t = 0$). As an example, the stationary solution corresponding to the Rotating Disc Electrode is presented in Sect. 2.8.

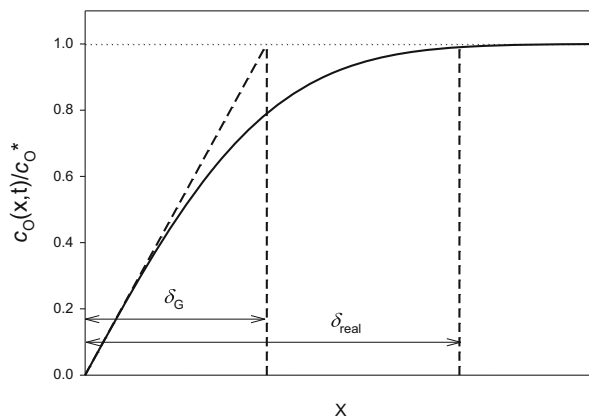
1.8.4 Mass Transport Coefficient

Mass transport gives rise to the appearance of concentration profiles of an electroactive species O like those shown in Fig. 1.20, obtained for the application of a constant potential to a macroelectrode. From this figure it can be seen that there is a region adjacent to the electrode surface where the concentration of species O is different from its bulk value, c_O^* , and, therefore, mass transport takes place. In the following discussion, diffusion will be the only transport mode considered. The thickness of this “diffusion layer,” δ_{real} , can be accurately calculated from the concentration profile as the distance from the electrode surface to a point in solution at which the following condition holds:

$$\frac{c_O(x = \delta_{\text{real}})}{c_O^*} = 1 - \text{error} \quad (1.180)$$

with “error” being the arbitrary tolerance limit considered, for example 0.01. Another widely used concept in this context is the Nernst’s diffusion layer [56, 61], whose thickness δ_{Nernst} is defined as the distance at which the linear concentration profile (obtained from the tangent to the concentration profile curve at the electrode surface; see broken line in Fig. 1.21) takes its bulk value. Given that the term “Nernst” can be misinterpreted in relation to the degree of reversibility of the electrode process, δ_{Nernst} will be referred to hereinafter as the thickness of the

Fig. 1.21 Concentration profile of species O and linear and real diffusion layers (the last with a maximum error of 1 %) obtained by the application of a constant potential with $E \ll E_c^{\theta'}$ to a macroelectrode



“linear diffusion layer,” and it will be denoted by δ_G (with subscript G relative to the electrode geometry).⁷ As can be seen in Fig. 1.21, the thickness of the linear layer is a rough estimation of the real thickness. Anyway, δ_G provides valuable information related to the nature of the electrode process and the diffusion field. Thus, in relation to the geometrical aspects of diffusion, it can be compared to the diameter of a macroelectrode or the maximal diffusion length in an electrochemical cell in order to discuss the validity conditions for the approximation of semi-infinite linear diffusion of electroactive species. Concerning the characteristics of the electrode process, in the case of coupled chemical reactions, the relative thickness of the diffusion and reaction layers is necessary to establish the conditions where steady-state behavior can be reached as well as to quantify the chemical contribution to the electrochemical response [62–65].

In a general way, the measured current I^G when a constant or time variable potential perturbation is applied to a simple charge transfer reaction at an electrode of a given geometry G can be defined from the equivalence between the gradient at the electrode surface and the difference between bulk (c_O^*) and surface (c_O^s) concentrations divided by the diffusion layer thickness, δ_G , of the concentration profile of electroactive species O or R [62],

$$\frac{I^G}{FA_G} = D_O \left(\frac{\partial c_O(q, t)}{\partial q_N} \right)_{q^s} = D_O \frac{\Delta c_O}{\delta_{G,O}} = -D_R \left(\frac{\partial c_R(q, t)}{\partial q_N} \right)_{q^s} = -D_R \frac{\Delta c_R}{\delta_{G,R}} \quad (1.181)$$

⁷Note that the concept of “transport layer” can be extended to other transport modes such as convection. Indeed, in the presence of convection, this concept is associated with the simple idea that the solution can be divided into two parts, a thin layer close to the electrode surface with only diffusion, on the one hand, and the bulk solution where the stirring ensures a perfect mixing, and therefore uniform concentration, on the other [52].

with

$$\left. \begin{aligned} \Delta c_{\text{O}} &= c_{\text{O}}^* - c_{\text{O}}^{\text{s}} \\ \Delta c_{\text{R}} &= c_{\text{R}}^* - c_{\text{R}}^{\text{s}} \end{aligned} \right\} \quad (1.182)$$

q is a set of coordinates on which the concentrations depend, q_{N} is the normal coordinate value at the electrode surface and q^{s} is its value at any electrode surface, D_{O} and D_{R} are the diffusion coefficients of oxidized and reduced species, respectively, and A_{G} is the electrode area.

δ_{G} is, in general, a complex function dependent on the nature of the electrode reaction, the potential, and the time (see Sects. 2.2.2 and 3.2.1.2). However, in the case of a reversible electrochemical process, the surface concentration c_{O}^{s} is only dependent on the applied potential, i.e. $\Delta c_{\text{O}} = \Delta c_{\text{O}}(E)$, and is independent of the electrode geometry and time. Thus, under potentiostatic conditions (see Sect. 2.2.2.2), δ_{G} is independent of the applied potential.

Closely related to the diffusion layer term is the mass transfer coefficient m_i . In a general way, this coefficient is the proportionality constant between the mass transfer flux and the concentration difference between the electrode surface and the bulk of the solution. From the current expression given by Eq. (1.181), one can write

$$\frac{I^{\text{G}}}{FA_{\text{G}}} = m_{\text{O}}\Delta c_{\text{O}} = -m_{\text{R}}\Delta c_{\text{R}} \quad (1.183)$$

where⁸

$$m_i = \frac{D_i}{\delta_{\text{G},i}} \quad i = \text{O}; \text{R} \quad (1.184)$$

The mass transport coefficient is, in general, a complex time and potential-dependent function through the linear diffusion layer thickness, $\delta_{\text{G},i}$. Only under certain conditions does this dependence disappear (as, for example, for nernstian processes under potentiostatic conditions, or at potential values far from $E_c^{\ominus'}$, see below).

Equations (1.183) and (1.184) point to the existence of maximum or limiting currents that can be obtained under mass transport control conditions. These limiting currents correspond to the case of null surface concentrations of the electroactive species, i.e., for $\Delta c_i = c_i^*$,

⁸In some references, it appears the term “resistance to the mass transfer,” $R_{\text{mt},i}$, defined as $R_{\text{mt},i} = 1/m_i$.

$$\left. \begin{aligned} \frac{I_{d,c}^G}{FA_G} &= m_{O,\infty} c_O^* \\ \frac{I_{d,a}^G}{FA_G} &= -m_{R,\infty} c_R^* \end{aligned} \right\} \quad (1.185)$$

where $m_{i,\infty}$ ($i = O, R$) is a potential-independent expression for the mass transport coefficient of species “i” (i.e., corresponding to potentials $E \rightarrow \mp\infty$, with the upper sign corresponding to cathodic limiting currents and the lower to anodic ones). The expressions of $m_{i,\infty}$ for different experimental situations are given in Table 1.4. Note that the only difference between $m_{O,\infty}$ and $m_{R,\infty}$ and also between m_O and m_R is the diffusion coefficient.

For nernstian processes, and under steady-state conditions when $D_O = D_R = D$, the expressions of coefficients fulfill, regardless of the electrode geometry,

$$m_i = m_{i,\infty} = m \quad (1.186)$$

Under reversible conditions and electrode geometries different from the planar one when $D_O \neq D_R$, the mass transport coefficient is a complex function of both diffusion coefficients and, in general, the expressions of m_i and $m_{i,\infty}$ do not coincide. The only case in which $m_i = m_{i,\infty}$ when the diffusion coefficients of species O and R are assumed as different is that corresponding to nernstian processes under planar diffusion (macroelectrodes).

Table 1.4 Mass transport coefficients $m_{i,\infty}$ for different experimental conditions. The values of $m_{i,\infty}$ correspond to the application of a constant potential. The expressions corresponding to the Rotating Disc Electrode (convective mass transport) under stationary conditions and to Dropping Mercury Electrode with the expanding plane model (diffusive–convective mass transport) have also been included

Experimental situation	$m_{i,\infty} = D_i / \delta_{G,i,E \rightarrow \mp\infty}$	Character
Macroelectrode	$\sqrt{\frac{D_i}{\pi t}}$	Transient (Sect. 2.2)
Spherical electrode of radius r_s	$D_i \left(\frac{1}{r_s} + \frac{1}{\sqrt{\pi D_i t}} \right)$	Transient (Sect. 2.5)
Spherical microelectrode of radius r_s	$\frac{D_i}{r_s}$	Stationary (Sect. 2.7)
Disc electrode of radius r_d	$\frac{4 D_i}{\pi r_d} \left(0.7854 + 0.44315 \frac{r_d}{\sqrt{D_i t}} + 0.2146 \exp \left(-0.39115 \frac{r_d}{\sqrt{D_i t}} \right) \right)$	Transient (Sect. 2.7)
Disc microelectrode of radius r_d	$\frac{4 D_i}{\pi r_s}$	Stationary (Sect. 2.7)
Rotating disc electrode of angular velocity ω	$0.62 D_i^{2/3} \omega^{1/2} (\zeta/\rho)^{-1/2}$	Stationary (Sect. 2.8)
Dropping Mercury Electrode with the expanding plane model	$\sqrt{\frac{7}{3}} \sqrt{\frac{D_i}{\pi t}}$	Transient (Sect. 2.4.1)

ζ and ρ are the viscosity and density of the solvent

By solving the expressions of c_{O}^{s} and c_{R}^{s} in Eqs. (1.183) and (1.185) and inserting them into the current–potential relationship given by (1.92), one obtains

$$I^{\text{G}} = \frac{k_{\text{red}}}{m_{\text{O}}} \left(\frac{m_{\text{O}}}{m_{\text{O},\infty}} I_{\text{d,c}}^{\text{G}} - I^{\text{G}} \right) - \frac{k_{\text{ox}}}{m_{\text{R}}} \left(I^{\text{G}} - I_{\text{d,a}}^{\text{G}} \frac{m_{\text{R}}}{m_{\text{R},\infty}} \right) \quad (1.187)$$

where k_{red} and k_{ox} are given by Eq. (1.101) for the Butler–Volmer model and by Eq. (1.111) for the Marcus–Hush–Chidsey one. Since for both models it is fulfilled that $k_{\text{ox}} = e^{\eta} k_{\text{red}}$, Eq. (1.187) can be written as

$$I^{\text{G}} = \frac{k_{\text{red}}}{m_{\text{O}}} \left[\left(\frac{m_{\text{O}}}{m_{\text{O},\infty}} I_{\text{d,c}}^{\text{G}} - I^{\text{G}} \right) - \frac{m_{\text{O}}}{m_{\text{R}}} e^{\eta} \left(I^{\text{G}} - I_{\text{d,a}}^{\text{G}} \frac{m_{\text{R}}}{m_{\text{R},\infty}} \right) \right] \quad (1.188)$$

If a Butler–Volmer formalism is assumed (see Eq. 1.101) for the sake of simplicity, the expression of the current–potential relationship can be rewritten as

$$I^{\text{G}} = \frac{k^0}{m_{\text{O}}} \left[e^{-\alpha\eta} \left(\frac{m_{\text{O}}}{m_{\text{O},\infty}} I_{\text{d,c}}^{\text{G}} - I^{\text{G}} \right) - \frac{m_{\text{O}}}{m_{\text{R}}} e^{(1-\alpha)\eta} \left(I^{\text{G}} - I_{\text{d,a}}^{\text{G}} \frac{m_{\text{R}}}{m_{\text{R},\infty}} \right) \right] \quad (1.189)$$

In agreement with Eq. (1.189), the reversibility degree exhibited by the current–potential response will be determined not only by the value of the rate constants but also by the ratio $R_i = k^0/m_i$ (with k^0 being the heterogeneous rate constant for the charge transfer reaction). Thus, for high values of R_i Eq. (1.189) becomes

$$e^{\eta} = \left(\frac{m_{\text{R}}}{m_{\text{O}}} \right) \frac{\frac{m_{\text{O}}}{m_{\text{O},\infty}} I_{\text{d,c}}^{\text{G}} - I^{\text{G}}}{I^{\text{G}} - I_{\text{d,a}}^{\text{G}} \frac{m_{\text{R}}}{m_{\text{R},\infty}}} \quad (1.190)$$

whereas for low values of R_i the totally irreversible limits of Eq. (1.189) are obtained

$$\begin{aligned} I^{\text{G}} &= \frac{I_{\text{d,c}}^{\text{G}} \frac{m_{\text{O}}}{m_{\text{O},\infty}}}{1 + \frac{k_{\text{red}}}{m_{\text{R}}}} & E \ll E_c^{\ominus'} \\ I^{\text{G}} &= \frac{I_{\text{d,a}}^{\text{G}} \frac{m_{\text{R}}}{m_{\text{R},\infty}}}{1 + \frac{m_{\text{R}}}{k_{\text{ox}}}} & E \gg E_c^{\ominus'} \end{aligned} \quad (1.191)$$

Therefore, the ratio $R_i = k^0/m_i$ allows us to define a “reversibility criteria” for a given current–potential response once the expression of the mass transport coefficient is obtained (see Sects. 3.2.1.4 and 5.3.2). Note that electrochemical reversibility thus considered is not only defined in terms of the intrinsic characteristic of the process (i.e., the particular value of the heterogeneous rate constant and other

kinetic parameters like the charge transfer coefficient or the reorganization energy) but also in terms of extrinsic parameters like the electrode geometry, the nature of the perturbation, and the mass transport modes involved.

By solving the expression of the current in Eq. (1.188), one obtains

$$I^G = \frac{\frac{k_{\text{red}}}{m_{\text{O},\infty}} I_{\text{d,c}}^G + \frac{k_{\text{ox}}}{m_{\text{R},\infty}} I_{\text{d,a}}^G}{1 + \frac{k_{\text{red}}}{m_{\text{O}}} + \frac{k_{\text{ox}}}{m_{\text{R}}}} \quad (1.192)$$

This expression of the current–potential relationship is totally general. For each particular situation, the expressions of the rate constants (through a given kinetic model) and of the limiting currents and mass transport coefficients should be provided to analyze the influence of the different factors that can control the global rate.

The current potential relationship can be written in terms of the inverse of the current. For example, in the case in which $c_{\text{R}}^* = 0$ ($I_{\text{d,a}}^G = 0$), Eqs. (1.181)–(1.184) and (1.192) become

$$\frac{1}{I^G} = \frac{1}{F A_G c_{\text{O}}^* k_{\text{red}}} + \frac{1 + \frac{m_{\text{O}} e^{\eta}}{m_{\text{R}}}}{F A_G c_{\text{O}}^* m_{\text{O}}} \quad (1.193)$$

The first term in the right-hand side of Eq. (1.193) accounts for the pure kinetic resistance of the process (which has been called as “activation” term), whereas the second combines the influence of the potential and of the mass transport through the limiting current (see Eqs. 1.184 and 1.185). The overall behavior of the current–potential response can be seen in Fig. 1.22.

Thus, for the activation zone the current can be approximated by the first term:

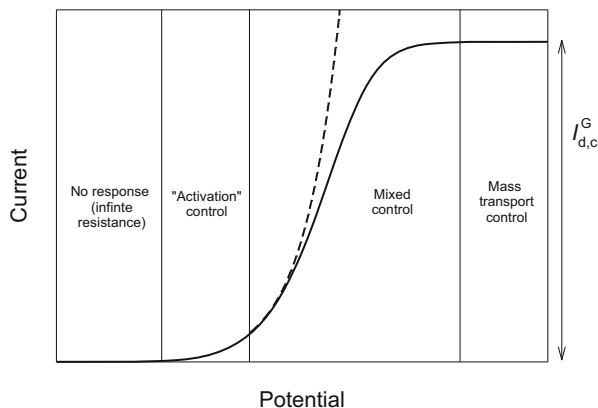
$$I^G \cong F A_G c_{\text{O}}^* k_{\text{red}} \quad (1.194)$$

which indicates that it is the resistance of the redox conversion (through the rate constant k^0) which determines the current at this region. Under these conditions, the depletion of the oxidized species at the electrode surface is negligible and the surface concentration is identical to its bulk value. The relationship between the logarithm of the current and the potential is linear (this is called a “Tafel analysis”) and it allows the determination of the kinetic parameters of the electrode reaction.

For more negative potentials, the current (solid line) deviates from the activation control (given by the dashed line which corresponds to a pure kinetic behavior⁹) and begins to be influenced by the mass transport (second term in Eq. (1.193), which in practice means that $c_{\text{i}}^{\text{s}} \neq c_{\text{i}}^*$), until for certain potentials at which the mass transport controls the overall current ($e^{\eta} \rightarrow 0$ and $k_{\text{red}} \rightarrow \infty$) and under these conditions

⁹ for which the current is given by $I^G = F A_G (k_{\text{red}} c_{\text{O}}^* - k_{\text{ox}} c_{\text{R}}^*)$.

Fig. 1.22 Schematic current–potential response for the reduction of species O calculated from the Butler–Volmer expression (Eqs. 1.92 and 1.101, *dashed line*) and from the general expression which includes mass transport influence (Eq. 1.193, *solid line*)



$$I^G = I_{d,c}^G = FA_G c_O^* m_{O,\infty} = FA_G c_O^* \frac{D_O}{\delta_{G,O,E \rightarrow -\infty}} \quad (1.195)$$

The mass transport limiting current is the maximum current (or rate) that the process can achieve. In order to increase its value, an increase of the electrode area, bulk concentration, or mass transport coefficient is needed. In the last case, this means a decrease of the diffusion layer thickness which can be done, for example, by forced convection.

For a more detailed discussion on the importance of the diffusion layer for different electrochemical techniques, see Sects. 2.2.2, 3.2.1.2, and 5.2.3.3.

1.9 Three-Electrode Systems. Ohmic Drop, Resistance of the Cell, and RC Time Constant

The measured potential difference in an electrochemical cell is the sum of several potential differences. When a current flows through the cell, these potential differences are affected to different degrees with the total change in cell potential being the sum of all these changes. In a cell with two electrodes, denoted as working (W) and reference (R), the change in the overall potential δE is given by

$$\delta E = \sum_{\text{interfaces}} \Delta\phi + IR_{\text{cell}} = {}^W\Delta^{\text{sol}}\phi + {}^{\text{sol}}\Delta^R\phi + IR_{\text{cell}} \quad (1.196)$$

The working electrode–solution interface is that corresponding to the electrode process under study and the reference electrode–solution interface is needed to close the current flow through the cell. The term IR_{cell} denotes the Ohmic drop, with R_{cell} being the resistance of the cell which can be calculated for certain geometries (see below) although, when important enough, it is usually measured and

compensated electronically [51, 65]. In practice, the potential difference should be related directly with the term ${}^W\Delta^{\text{sol}}\phi$.

The usual strategy is to use a second highly non-polarizable electrode (i.e., a Reference electrode) in such a way that the term ${}^{\text{sol}}\Delta^{\text{R}}\phi$ will be negligible compared to that of the working electrode. Under conditions of low ohmic drop, Eq. (1.196) becomes

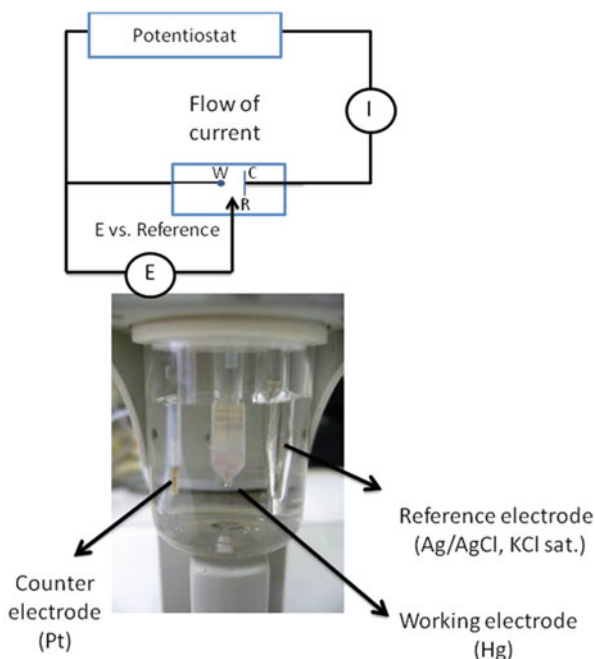
$$\delta E \cong {}^W\Delta^{\text{sol}}\phi \quad (1.197)$$

A better way of measuring changes in potential at the metal–solution interface of the working electrode is to use a three-electrode system in the way shown in Fig. 1.23, in which, together with the working and reference electrodes, a third electrode called a counter electrode is added. In this experimental setup, an external device called a potentiostat–galvanostat is used to pass a constant or time-variable current through the working and counter electrodes or to establish a potential difference (which can be constant or a function of time) between the working and counter electrodes. Note that in this scheme the current flowing between the working and reference electrodes (i.e., the part of the circuit which defines the changes in potential) is essentially zero.¹⁰ Under these conditions, the potential difference at the reference electrode can be considered as constant, irrespective of the current passing through the working and reference electrodes. This allows to ensure that the changes in the potential difference between working and reference are only related to phenomena taking place at the working electrode and, although the difference ${}^W\Delta^{\text{sol}}\phi$ cannot be measured, the changes in this difference can be directly determined. Note that the three-electrode configuration described can be simplified in the case in which the values of the current would be small (for example, in the case of microelectrodes, see Sects. 2.7 and 5.4), since in this case the pass of current through the reference electrode would not alter its non-polarizable condition and therefore the counter electrode could be suppressed. The three-electrode configuration must be modified in the case of the studies of ionic and electronic transfers taking place at membranes or liquid–liquid interfaces (see Sect. 2.3 for more details).

For current to flow across a cell, ions must move through the ionic conductor and to maintain this motion requires an electric field. The field is supplied by a difference of electrical potentials within the ionic conductor between the surface adjacent to the working electrode and the adjacent to the counter electrode. By considering Ohm's law [51]

¹⁰ Although in a three-electrode configuration the potential difference at the third electrode may change greatly, this fact does not affect the measure of the potential difference between the working and reference electrodes. Indeed, the only limitation that affects the counter electrode is that it should be much larger than the working electrode.

Fig. 1.23 Scheme of a three-electrode electrochemical setup and frontal view of a Dropping Mercury Electrode with the three electrodes indicated



$$\frac{I^G}{A_G(x)} = -\kappa \frac{d\phi}{dx} \quad (1.198)$$

the ohmic overpotential, which considers the potential difference between the solution adjacent to the working electrode and at the point where the reference electrode is placed as a consequence of the electric field mentioned above, is given by

$$\Delta\phi_{\text{Ohm}} = \phi_W - \phi_R = \int_R^W d\phi = -\frac{I^G}{\kappa} \int_R^W \frac{dx}{A_G(x)} \quad (1.199)$$

where κ is the electrical conductivity of the ionic conductor. The symbol “ x ” denotes the length coordinate measured from the working electrode in the direction of the current flow and $A_G(x)$ is the area of the equipotential surface at that distance for a given electrode geometry. In order to carry out the integration that appears in Eq. (1.199), it is necessary to specify the geometry of the cell. In the case of simple geometries, this integral is easily determined.

Equation (1.199) can be rewritten as

$$\Delta\phi_{\text{Ohm}} = I^G R_{\text{cell}}^G \quad (1.200)$$

where

Table 1.5 Expressions for the resistance of the cell in different electrode geometries calculated from Eq. (1.201). x is the distance between the working electrode surface and the reference electrode [7, 51, 67]

Electrode geometry	R_{cell}^G/Ω	R_{cell}^G for large $x \gg q_G^*$
Plane electrode (channel cell with constant section, $A(x) = A$)	$\frac{x}{\kappa A}$	$\frac{x}{\kappa A}$
Spherical electrode of radius r_s ($A(r) = 4\pi r_s^2$)	$\frac{1}{4\pi\kappa} \frac{x}{r_s(x+r_s)}$	$\frac{1}{4\pi\kappa} \frac{1}{r_s}$
Cylindrical electrode of radius r_s and length z ($A(r) = 2\pi r_s z$)	$\frac{1}{2\pi\kappa z} \ln\left(1 + \frac{x}{r_s}\right)$	$\frac{1}{2\pi\kappa z} \ln\left(\frac{x}{r_s}\right)$
Small disc electrode of radius r_d	$\frac{1}{4\kappa} \frac{1}{r_d}$	

* q_G is the characteristic dimension of the electrode

$$R_{\text{cell}}^G = -\frac{1}{\kappa} \int_R^W \frac{dx}{A(x)} \quad (1.201)$$

The expressions of R_{cell}^G for different electrode geometries are given in Table 1.5. Note that for the case of spherical and disc electrodes, when $x \gg r_G$ (with r_G being the electrode radius for both geometries), the resistance of the cell becomes constant. In spite of the similarity between the expressions for $R_{\text{cell}}^{\text{spherical}}$ and $R_{\text{cell}}^{\text{disc}}$, an important difference arises in the case of disc electrodes versus spherical or hemispherical ones, and that is that the current density of the latter is uniform through the surface whereas in the case of the disc the current density (i.e., the flux of species) is not homogeneous and, indeed, is very high near the edge of the disc (see Sect. 2.7).

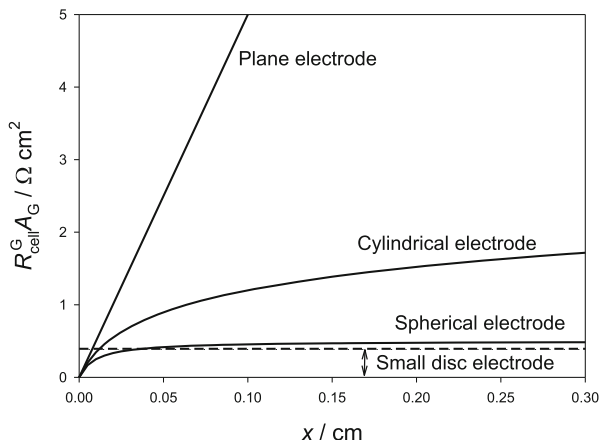
The evolution of $R_{\text{cell}}^G A_G$ versus the distance between the working and reference electrodes has been plotted in Fig. 1.24 for the four geometries presented in Table 1.5. From the curves in this figure, it can be seen that spherical and disc geometries are the best at reducing the value of $R_{\text{cell}}^G A_G$ and, therefore, of the ohmic drop (see Eq. 1.200). This improvement becomes more evident as the electrode size decreases (see Sects. 2.7 and 5.4).

Returning to the three-electrode setup, it could seem that no ohmic drop would affect the measurement of the potential difference between the working and reference electrodes, since there is practically no current flow between both electrodes. However, this is not totally true. The reference electrode is located at a given distance from the working electrode surface, and, as a result of this separation, the potential difference measured contains a part of the ohmic drop in the solution which is called residual ohmic drop, IR_u (with I being the current and R_u the uncompensated resistance). For more details concerning the minimization of the ohmic distortion of the current–potential response, see Sects. 1.8 and 5.4.

It can be assumed, at least approximately, that the current for any electrochemical technique can be expressed as the sum of a pure faradaic current because of the

Fig. 1.24 Cell resistance as a function of the distance between the working and reference electrodes.

$\kappa = 20 \text{ mS cm}^{-1}$. The values of the electrode radius are $r_c = r_s = r_d = 0.01 \text{ cm}$



charge transfer process plus a charging current relative to the process of charge of the double layer (see Sect. 1.6):

$$I = I_{\text{faradaic}} + I_c \quad (1.202)$$

The particular form of the charging current will depend on the potential perturbation. For the application of a potential jump from a rest potential to a constant value E , $\Delta E = E - E_{\text{rest}}$, it is given by [12]:

$$I_c = \frac{\Delta E}{R_u} e^{-\left(\frac{t}{R_u C_d}\right)} \quad (1.203)$$

with C_d being the double-layer differential capacitance. Note that the product $R_u C_d$ has dimension of time and it is usually denoted as the RC time constant of the cell. This time constant establishes a practical limit for carrying out the measurement of the current in order to avoid the influence of the charging current. An illustration of this is seen in Fig. 1.25 in which the faradaic limiting current obtained by the application of a constant potential at a macroelectrode (given by Eq. 2.28), the charging current calculated from Eq. (1.203) for a time constant $R_u C_d = 4 \text{ ms}$, and the sum of the both have been plotted.

As can be seen in this Figure, for times close to zero, the total current is much higher than the pure faradaic current, since at this time the charging current cannot be neglected. From a practical point of view, under these conditions, times above $5R_u C_d$ are required for a measurement of a current without the contribution of the charging component (see the region on the right side of Fig. 1.25). Nevertheless, at long experimental times there is a progressive involvement of convection into the mass transport.

Fig. 1.25 Temporal evolution of the faradaic limiting current obtained by the application of a constant potential at a

macroelectrode $I_{d,c}^{\text{plane}} = FA$

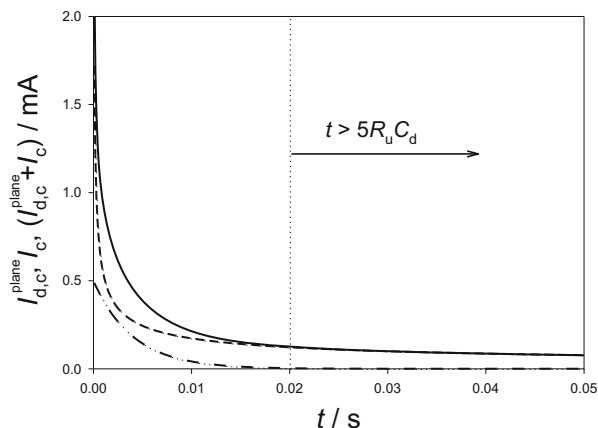
$c_O^* \sqrt{D_O/\pi t}$ (dashed line, Eq. 2.28), the charging current I_c (dashed-dotted line, Eq. 1.203), and the sum of both (solid line).

$A = 0.1 \text{ cm}^2$, $c_O^* = 1 \text{ mM}$,

$D_O = 10^{-5} \text{ cm}^2 \text{ s}^{-1}$,

$R_u = 0.2 \text{ k}\Omega$, $C_d = 20 \text{ }\mu\text{F}$,

$\Delta E = 0.1 \text{ V}$



However, it is important to take into account that the influence of the charging current depends on the potential perturbation (for a more detailed discussion concerning multipulse techniques, see Sect. 5.2.3.4).

1.10 Pulse Versus Step

There has been some controversy in the electrochemical literature concerning the use of the terms “pulse” and “step” in relation to the potential perturbation used in different potential controlled techniques, with no clear distinction between pulses and steps [66]. A brief description of both types of perturbation is provided in this section and a short discussion on the nomenclature is presented.

The term “pulse” has different meanings, but in signal processing it refers to “a rapid, transient change in the amplitude of a signal from a baseline value to a higher or lower value, followed by a rapid return to the baseline value” (see Fig. 1.26a) [68].

In agreement with the above definition, a potential pulse of a given amplitude presents a short duration τ and it returns to its original baseline value, E_{rest} .

A step is defined as a constant perturbation of variable duration (it is not imperative that its duration is short; see Fig. 1.26b).

When a sequence of potential pulses and steps is considered (Fig. 1.26c and d), no restrictions are imposed on the return to a given preestablished value as a baseline in the case of steps (see Fig. 1.26d), whereas for pulses this return takes place after the application of each individual perturbation (Fig. 1.26d).

Once the differences between both types of potential perturbation are clarified, a question arises about the nature of potential-controlled techniques: attending to the nature of the perturbation, are they pulse potential or step potential techniques? If the pulse definition is applied in a strict sense, only Single Pulse Voltammetry is a true pulse technique (see Scheme 2.1), whereas the rest of double and multipotential techniques are indeed multistep techniques (see Sects. 4.1, 5.1 and 7.1).

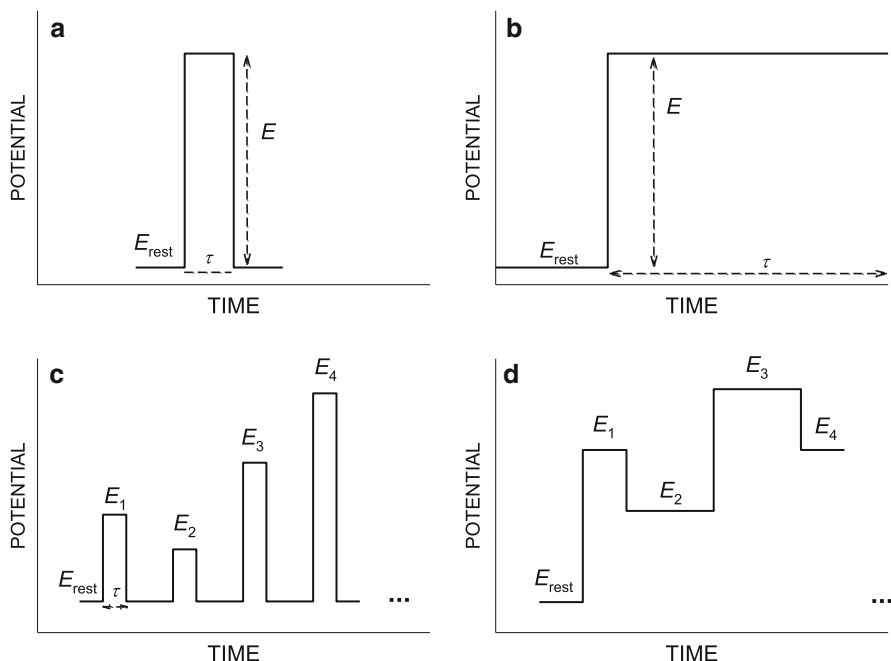


Fig. 1.26 Single potential pulse (a) and step (b) perturbations from a rest value of amplitude E and duration τ . Arbitrary sequence of multiple potential pulses (c) and steps (d)

However, in the electrochemical literature the terms “pulse techniques” and “multipulse techniques” are well established and commonly used to define a set of potential-controlled techniques. In order to maintain this nomenclature, the definition of “pulse” referred to the potential perturbation should be considered as equivalent to that given for a step potential, i.e., without any restriction on the duration of the perturbation and the return to a given resting potential. This will be the criterion followed throughout this book.

There is another characteristic that all these techniques present: the current is sampled at a given moment during the application of any individual potential of the sequence (typically at the end of each applied potential), so the response is a discrete collection of pairs of data (potential–current). Conversely, in the case of techniques like Linear Sweep Voltammetry or Cyclic Voltammetry, the current is recorded continuously (see Sect. 5.1).¹¹

In conclusion, in Pulse and Multipulse techniques the perturbation is given as an arbitrary sequence of constant potentials without any a priori restriction on the duration of each individual potential of the sequence or on the particular waveform employed, and the current is sampled at a pre-fixed time.

¹¹ Under these conditions, the potential perturbation is a continuous function of time.

References

1. Bagotsky VS (2006) Fundamentals of electrochemistry, 2nd edn. Wiley, Hoboken, NJ
2. Schmickler W, Santos E (2010) Interfacial electrochemistry, 2nd edn. Springer, Berlin
3. Bockris JO'M, Reddy AKN, Gamboa-Aldeco M (2000) Modern electrochemistry, vol 2A. Kluwer, New York, NY
4. Fawcett WR (2004) Liquids, solution and interfaces. From classical macroscopic details to modern microscopic details. Oxford University Press, Oxford
5. Trasatti S, Parsons R (1986) Pure Appl Chem 58:437–454
6. Parsons R (1979) In: Whiffen DH (ed) Manual of symbols and terminology for physico-chemical quantities and units (revised). Pergamon, Oxford, Appendix III Electrochemical nomenclature
7. Gileadi E (2011) Physical electrochemistry. Wiley-VCH, Weinheim
8. Bard AJ, Inzelt G, Scholz F (eds) (2012) Electrochemical dictionary, 2nd edn. Springer, Berlin
9. Girault HH (2004) Analytical and physical electrochemistry. Marcel Dekker, New York, NY
10. Bard AJ, Stratmann M, Gileadi E, Urbakh M (eds) (2002) Encyclopedia of electrochemistry, vol 1, Thermodynamics and electrified interfaces. Wiley-VCH, Weinheim
11. Trasatti S (1980) In: Bockris JO'M, Conway BE, Yeager E (eds) Comprehensive treatise of electrochemistry. Plenum, New York, NY
12. Fomenko VS (1981) The emission properties of materials. Naukova Dumka, Kiev
13. Bard AJ, Faulkner LR (2001) Electrochemical methods. Fundamental and applications, 2nd edn. Wiley, New York, NY
14. Zoski CG (ed) (2007) Handbook of electrochemistry. Elsevier, Amsterdam
15. Holze R (2012) Electrochemical thermodynamics and kinetics (Landolt-Börnstein: Numerical Data and Functional Relationships). Springer, Berlin
16. Inzelt G, Lewenstam A, Scholz F (eds) (2013) Handbook of reference electrodes. Springer, Heidelberg
17. Kissinger PT, Heineman WR (1996) Laboratory techniques in electroanalytical chemistry. Dekker, New York, NY
18. Scholz F (ed) (2010) Electroanalytical methods, 2nd edn. Springer, Berlin
19. Grahame DC (1947) Chem Rev 41:441–501
20. Mohilner D (1966) In: Bard AJ (ed) Electroanalytical Chemistry, vol 1. Marcel Dekker, New York, NY
21. von Helmholtz HLF (1879) Ann Phys 7:337
22. Gouy G (1910) J Phys Radium 9:457
23. Chapman DL (1913) Philos Mag 25:475
24. Stern O (1924) Z Elektrochem 30:508
25. Schmickler W (1996) Chem Rev 96:3177–3200
26. Appleby AJ, Zagal JH (2011) J Solid State Electrochem 15:1811–1832
27. Feldberg SW, Sutin N (2006) Chem Phys 324:216–225
28. Butler JAV (1924) Trans Faraday Soc 19:729–733
29. Erdey-Grúz T, Volmer M (1930) Z Phys Chem 150A:203–213
30. Henstridge M, Laborda E, Rees NV, Compton RG (2012) Electrochim Acta 84:12–20
31. Marcus RA (1956) J Chem Phys 24:966–978
32. Hush NS (1958) J Chem Phys 28:962–972
33. Marcus RA (1965) J Chem Phys 43:679
34. Saveánt JM (2006) Elements of molecular and biomolecular electrochemistry: an electrochemical approach to electron transfer chemistry. Wiley, Hoboken, NJ
35. Laborda E, Henstridge M, Batchelor-McAuley C, Compton RG (2013) Chem Soc Rev 42: 4894–4905
36. Marcus RA (1956) J Chem Phys 24:966–978
37. Chidsey CED (1991) Science 251:919–922
38. Oldham KB, Myland JC (2011) J Electroanal Chem 655:65–72

39. Weaver MJ (1992) *Chem Rev* 92:463–480
40. Fawcett WR, Opallo M (1994) *Angew Chem Int Ed* 33:2131–2143
41. Brunschwig BS, Sutin N (1999) *Coord Chem Rev* 187:233–254
42. Sutin N (1982) *Acc Chem Res* 15:275–282
43. Landau L (1932) *Z Sowjetunion* 2:46
44. Zener C (1933) *Proc R Soc Lond A* 140:660–668
45. Zener C (1932) *Proc R Soc Lond A* 137:696–702
46. Feldberg SW (2006) *Chem Phys* 324:216–225
47. Costentin C, Robert M, Savéant JM (2010) *Phys Chem Chem Phys* 12:13061–13069
48. Laborda E, Batchelor-McAuley C, Suwatchara D, Henstridge MC, Compton RG (2013) *J Electroanal Chem* 694:30–36
49. Zhao LB, Mishra AK, Waldeck DH (2013) *J Phys Chem C* 117:20746–20761
50. Bard AJ, Stratmann M, Calvo EJ (2003) *Encyclopedia of electrochemistry*, vol 2, Interfacial kinetics and mass transport. Wiley-VCH, Weinheim
51. Oldham KB, Myland JC, Bond AM (2012) *Electrochemical science and technology. Fundamental and applications*. Wiley, Chichester
52. Yeager E, Bockris JOM, Conway BE, Sarangapani S (eds) (1983) *Comprehensive treatise of electrochemistry*, vol 6, Electrodeics: transport. Plenum Press, New York, NY
53. Tanaka Y (2015) *Ion exchange membranes: fundamentals and applications*, vol 2. Elsevier Science, Amsterdam
54. Izutsu K (2009) *Electrochemistry in non-aqueous solvents*. Wiley, Weinheim
55. Crank J (1980) *The mathematics of diffusion*. Oxford Science, Oxford
56. Ibl N (1981) *Pure Appl Chem* 53:1827–1840
57. Fuoss RM, Onsager L, Skinner JF (1965) *J Phys Chem* 69:2581–2594
58. Fernandez-Prini R (1969) *Trans Faraday Soc* 65:3311–3313
59. Miyoshi K (1973) *Bull Chem Soc Jpn* 46:426–430
60. Yeager HL, Kratochvil B (1975) *Can J Chem* 53:3448–3451
61. Nernst W (1904) *Z Phys Chem* 47:52–55
62. Molina A, Gonzalez J, Martinez-Ortiz F, Compton RG (2010) *J Phys Chem C* 114:4093–4099
63. Molina A, Gonzalez J, Henstridge M, Compton RG (2011) *Electrochim Acta* 56:4589–4594
64. Molina A, Gonzalez J, Laborda E, Compton RG (2013) *Phys Chem Chem Phys* 15:2381–2388
65. Molina A, Laborda E, Gonzalez J, Compton RG (2014) *Phys Chem Chem Phys* 16:7106–7113
66. Bard AJ, Stratmann M, Unwin P (eds) (2003) *Encyclopedia of electrochemistry*, vol 3, Instrumentation and electroanalytical chemistry. Wiley-VCH, Weinheim
67. Newman JS (1966) *J Electrochem Soc* 113:501–502
68. Unknown authors (1996) *National communications system technology and standard division, Telecommunications: Glossary of terms (Federal Standard 1037C)*

Chapter 2

Single Pulse Voltammetry: Reversible Electrochemical Reactions

Contents

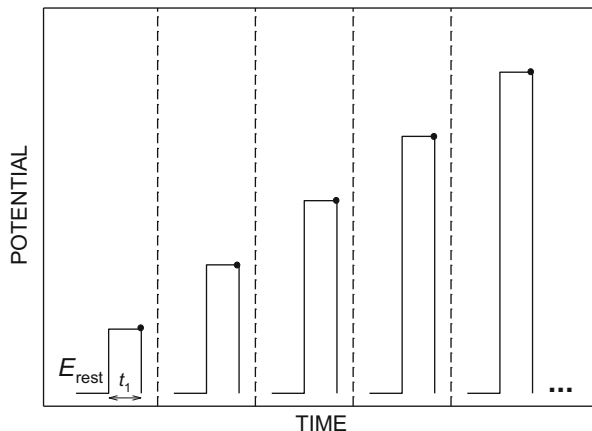
2.1	Introduction	67
2.1.1	Reversible Electrode Reaction	69
2.2	Planar Electrodes	69
2.2.1	Concentration Profiles	72
2.2.2	Current–Time Curves (Chronoamperometry) and Current–Potential Curves (Voltammetry)	74
2.2.3	Stoichiometric Coefficients Different From the Unity	79
2.3	Ion Transfer Through Liquid Membranes	81
2.3.1	One-Polarized Interface Systems	82
2.3.2	Two-Polarized Interfaces Systems	84
2.3.3	Electron Transfer at the Liquid/Liquid Interface	90
2.4	Dropping Mercury Electrode (DME)	94
2.4.1	dc Polarography	96
2.4.2	Normal Pulse Polarography (NPP)	99
2.5	Spherical Electrodes	101
2.5.1	Unequal Diffusion Coefficients ($D_O \neq D_R$)	103
2.5.2	Equal Diffusion Coefficients ($D_O = D_R$)	108
2.6	Other Electrodes Geometries	111
2.7	Microelectrodes. Steady-State Voltammetry	120
2.8	Rotating Disc Electrode	123
2.9	Thin Layer Voltammetry	126
	References	129

2.1 Introduction

In a single potential step voltammetric technique, several constant potentials (of increasing amplitude) are applied with a time length t_1 . When stationary electrodes are used, the time interval between two consecutive potentials must be much greater than t_1 for the initial conditions to be restored (Scheme 2.1). If a Static Mercury Drop Electrode (SMDE) is used, the initial conditions are simply restored by making the drop fall. The measured current at a fixed time value $t = t_1$ is plotted discretely versus the corresponding potential steps [1–3]. The resulting current–potential curve has a sigmoidal shape whose position and slope depend on the

Scheme 2.1 Potential–time waveform for Single Potential Pulse

Voltammetry. E_{rest} is a potential at which no faradaic processes take place at the electrode. *Black dots* indicate the times at which the current is sampled and *vertical dashed lines* correspond to the recovery of the initial equilibrium conditions



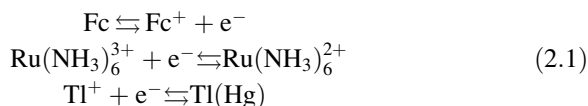
reversibility of the electrode process and the wave height is independent of the electron transfer rate. At each fixed potential value, the current–time variation (which has a typical Cottrellian behavior for reversible processes at planar electrodes when considering diffusive transport only) can be registered. If the length time is in the range 2–200 ms, the electrochemical technique is called Normal Pulse Voltammetry (NPV), originally known as Normal Pulse Polarography (NPP). This technique was introduced by Barker [5–7] and it was originally designed for the Dropping Mercury Electrode (DME), in which the potential pulse is applied at the end of the life of the drop, with the current being dependent on the relation between the pulse time and the drop lifetime. The main reason for measuring the current at the end of short time intervals is to eliminate the capacitive component (see Sect. 1.9) in order to optimize the sensitivity. Today the DME electrode is scarcely used and most electrochemical techniques are used at stationary electrodes

A complete comprehension of Single Pulse electrochemical techniques is fundamental for the study of more complex techniques that will be analyzed in the following chapters. Hence, the concept of “half-wave potential,” for example, will be defined here and then characterized in all electrochemical techniques [1, 3, 8]. Moreover, when very small electrodes are used, a stationary current–potential response is reached. This is independent of the conditions of the system prior to each potential step and even of the way the current–potential was obtained (i.e., by means of a controlled potential technique or a controlled current one) [9, 10]. So, the stationary solutions deduced in this chapter for the current–potential curves for single potential step techniques are applicable to any multipotential step or sweep technique such as Staircase Voltammetry or Cyclic Voltammetry. Moreover, many of the functional dependences shown in this chapter for different diffusion fields are maintained in the following chapters when multipulse techniques are described if the superposition principle can be applied.

2.1.1 Reversible Electrode Reaction

For an electrode reaction to be considered reversible, it is necessary to compare the rate of the charge transfer process and the rate of the mass transport of electroactive species. When the mass transport rate is slower than the charge transfer one, the electrode reaction is controlled by the transport rate and can be considered as electrochemically reversible in that the surface concentration fulfills the Nernst equation when a given potential is applied to the electrode. In Electrochemistry, knowledge of the behavior of reversible electrode processes is very important, since these can be used as a benchmark for more complex systems (see Chap. 5 in [1] and Sect. 1.8.4 for a detailed discussion).

There are many examples of reversible (or nernstian) behavior.¹ For example, the redox conversions of a great number of metallic complexes such as Ferrocene, $\text{Ru}(\text{NH}_3)_6^{3+}$, or metallic cations like Tl^+ (see Eq. (2.1) for the redox reactions in detail²). It is important to highlight that the reversible behavior can also be obtained in many cases by acting on suitable experimental parameters in the particular electrochemical technique used. Under the appropriate experimental conditions, the characterization of these types of processes can be applied to many systems.



2.2 Planar Electrodes

From a practical point of view, a macroelectrode can be considered as an electrode whose characteristic dimension L is much greater than the diffusion layer thickness (i.e., in general $L \gg \sqrt{Dt}$, with D being the diffusion coefficient of the electroactive species). For such an electrode, the geometry becomes irrelevant and it can be considered as an infinite planar electrode for which, if the solution contains a great amount of supporting electrolyte, the mass transport is governed by semi-infinite linear diffusion (i.e., it can be assumed that mass transport occurs only in the dimension x normal to the electrode surface) [11]. For this reason, throughout this book, macroelectrodes will be referred as “planar electrodes.”

We consider an electrochemical reversible reaction



¹ An electrochemical reaction is called “reversible” or nernstian when the Nernst’s equation can be applied to the surface concentrations of electroactive species for any value of the applied potential (see Sect. 1.7).

² The reduction of Tl^+ takes place at a mercury electrode so the metals are amalgamated into the electrode.

The calculation of the concentration profiles of species O and R ($c_O(x, t)$ and $c_R(x, t)$) and of the current when a potential E is applied requires solving of the following diffusion equations:

$$\left. \begin{aligned} \frac{\partial c_O}{\partial t} &= D_O \frac{\partial^2 c_O}{\partial x^2} \\ \frac{\partial c_R}{\partial t} &= D_R \frac{\partial^2 c_R}{\partial x^2} \end{aligned} \right\} \quad (2.2)$$

where D_i is the diffusion coefficient of species i ($= O, R$).

The boundary value problem (bvp) is

$$\left. \begin{aligned} t > 0, \quad x \rightarrow \infty \\ t = 0, \quad x \geq 0 \end{aligned} \right\} \quad c_O = c_O^*, \quad c_R = c_R^* \quad (2.3)$$

with c_O^* and c_R^* being the bulk concentrations of species O and R.

The initial condition ($t = 0$) expresses the homogeneity of the solution at the beginning of the experiment, and the semi-infinite condition ($x \rightarrow \infty$) implies that the potential perturbation is not effective far from the electrode.

When the experiment begins, at the electrode surface ($t > 0, x = 0$) the flux balance implies

$$D_O \left(\frac{\partial c_O}{\partial x} \right)_{x=0} = -D_R \left(\frac{\partial c_R}{\partial x} \right)_{x=0} \quad (2.4)$$

Moreover, if nernstian behavior for the charge transfer reaction is assumed, the following condition holds:

$$c_O^{s,r} = e^\eta c_R^{s,r} \quad (2.5)$$

with

$$\eta = \frac{F}{RT} (E - E_c^{\ominus'}) \quad (2.6)$$

and $c_O^{s,r}$ and $c_R^{s,r}$ are the surface concentrations of species O and R, i.e., the values of the concentration profiles at $x = 0$. Superscript "r" denotes that the electrochemical reaction is reversible. $E_c^{\ominus'}$ is the formal potential of the redox couple O/R (see Sect. 1.5.1).

The current, according to Faraday law and Fick's first law, is given by

$$I^{\text{plane}} = FAD_O \left(\frac{\partial c_O}{\partial x} \right)_{x=0} = -FAD_R \left(\frac{\partial c_R}{\partial x} \right)_{x=0} \quad (2.7)$$

This problem can be easily solved by introducing the new variable,

$$s_i^p = \frac{x}{2\sqrt{D_i t}} \quad i = O, R \quad (2.8)$$

where superscript “p” denotes that the parameter s corresponds to planar diffusion.

By introducing s_i^p parameter into Eq. (2.2), Fick’s second law takes the form:

$$\frac{d^2 c_i}{d(s_i^p)^2} + 2s_i^p \frac{dc_i}{ds_i^p} = 0 \quad i = O, R \quad (2.9)$$

and the boundary value problem (Eqs. 2.3–2.5) becomes

$$s_i^p \rightarrow \infty :$$

$$c_i = c_i^* \quad i = O, R \quad (2.10)$$

$$s_i^p = 0 :$$

$$\sqrt{D_O} \left(\frac{dc_O}{ds_O^p} \right)_{s_O^p=0} = -\sqrt{D_R} \left(\frac{dc_R}{ds_R^p} \right)_{s_R^p=0} \quad (2.11)$$

$$c_O(s_O^p = 0) = e^{\eta} c_R(s_R^p = 0) \quad (2.12)$$

Equation (2.11) refers to the flux conservation and Eq. (2.12) to the establishment of the nernstian equilibrium. Note that under these conditions, the original problem in terms of variables x and t has been transformed into a one-variable problem (s_i^p), that is, c_O and c_R can be expressed only as functions of the variables s_O^p and s_R^p , respectively (which include distance and time variables), because they diffuse with different diffusion coefficients D_O and D_R . This problem can now be solved by making $y_i = dc_i/ds_i^p$, and Eq. (2.9) becomes

$$\frac{dy_i}{ds_i} + 2s_i^p y_i = 0 \quad i = O, R \quad (2.13)$$

whose direct integration leads to

$$y_i = y_i(0)e^{-(s_i^p)^2} \quad (2.14)$$

or,

$$\left(\frac{dc_i}{ds_i^p} \right) = \left(\frac{dc_i}{ds_i^p} \right)_{s_i^p=0} e^{-(s_i^p)^2} \quad (2.15)$$

By integrating (2.15), one obtains

$$c_i(s_i^p) = c_i(s_i^p = 0) + \left(\frac{dc_i}{ds_i^p} \right)_{s_i^p=0} \frac{\sqrt{\pi}}{2} \operatorname{erf}(s_i^p) \quad i = \text{O, R} \quad (2.16)$$

By introducing condition (2.10) in Eq. (2.16), it can be deduced for $s_i^p \rightarrow \infty$ that

$$\left(\frac{dc_i}{ds_i^p} \right)_{s_i^p=0} = \frac{2}{\sqrt{\pi}} (c_i^* - c_i(s_i^p = 0)) \quad (2.17)$$

So, Eq. (2.16) becomes

$$c_i(s_i^p) = c_i(s_i^p = 0) + (c_i^* - c_i(s_i^p = 0)) \operatorname{erf}(s_i^p) \quad (2.18)$$

which can be written more conveniently as

$$\left. \begin{aligned} c_{\text{O}}(x, t) = c_{\text{O}}(s_{\text{O}}^p) = c_{\text{O}}^* + (c_{\text{O}}(s_{\text{O}}^p = 0) - c_{\text{O}}^*) \operatorname{erfc}(s_{\text{O}}^p) \\ c_{\text{R}}(x, t) = c_{\text{R}}(s_{\text{R}}^p) = c_{\text{R}}^* + (c_{\text{R}}(s_{\text{R}}^p = 0) - c_{\text{R}}^*) \operatorname{erfc}(s_{\text{R}}^p) \end{aligned} \right\} \quad (2.19)$$

with $\operatorname{erf}(z)$ being the Error function of “ z ” given by $\operatorname{erf}(z) = 2/\sqrt{\pi} \int_0^z e^{-u^2} du$, and $\operatorname{erfc}(z) = 1 - \operatorname{erf}(z)$.

From Eqs. (2.11), (2.12), and (2.17), the surface concentrations $c_{\text{O}}(s_{\text{O}}^p = 0) = c_{\text{O}}^{s,r}$ and $c_{\text{R}}(s_{\text{R}}^p = 0) = c_{\text{R}}^{s,r}$ are obtained,

$$\left. \begin{aligned} c_{\text{O}}^{s,r} &= \frac{e^\eta (\gamma c_{\text{O}}^* + c_{\text{R}}^*)}{1 + \gamma e^\eta} \\ c_{\text{R}}^{s,r} &= \frac{\gamma c_{\text{O}}^* + c_{\text{R}}^*}{1 + \gamma e^\eta} \end{aligned} \right\} \quad (2.20)$$

with

$$\gamma = \sqrt{\frac{D_{\text{O}}}{D_{\text{R}}}} \quad (2.21)$$

From Eq. (2.20), it is fulfilled that

$$\sqrt{D_{\text{O}}} c_{\text{O}}^{s,r} + \sqrt{D_{\text{R}}} c_{\text{R}}^{s,r} = \sqrt{D_{\text{O}}} c_{\text{O}}^* + \sqrt{D_{\text{R}}} c_{\text{R}}^* \quad (2.22)$$

2.2.1 Concentration Profiles

Equations (2.19) show the concentration profiles for species O and R. The linear concentration profiles of these species correspond to the lines tangent to $c_i(x, t)$ at the electrode surface (i.e., at $x = 0$) and are given by

$$c_i(x, t) = \frac{c_i^* - c_i^{s,r}}{\delta_{p,i}^r} x + c_i^{s,r} \quad i = O, R \quad (2.23)$$

From Eqs. (2.4), (2.8), (2.17), and (2.19),

$$\left(\frac{\partial c_i}{\partial x} \right)_{x=0} = \left(\frac{dc_i}{ds_i^p} \right)_{s_i^p=0} \left(\frac{\partial s_i^p}{\partial x} \right)_{x=0} = \frac{c_i^* - c_i^{s,r}}{\sqrt{\pi D_i t}} \quad i = O, R \quad (2.24)$$

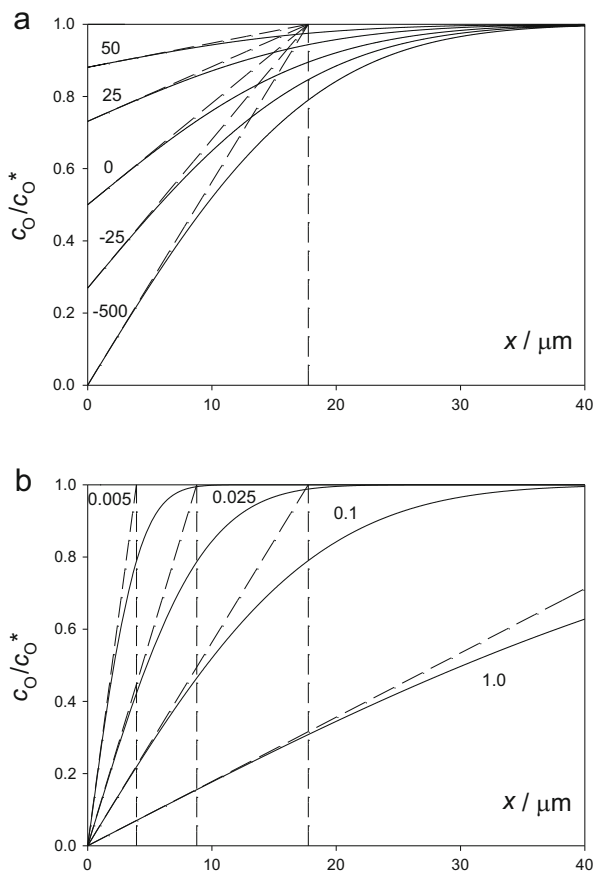
Hence, by comparing Eqs. (2.23) and (2.24) it can be deduced that Nernst diffusion layer for a planar electrode, $\delta_{p,i}^r$, is defined as

$$\delta_{p,i}^r = \sqrt{\pi D_i t} \quad (2.25)$$

In Fig. 2.1, we have plotted the transient accurate concentration profiles for species O, $c_O(x, t)$ (Eq. 2.19), and the linear concentration profiles (Eq. (2.23)) at a

Fig. 2.1 Concentration profiles of species O at a planar electrode calculated from Eq. (2.19) for the application of a potential pulse for different values of $(E - E_c^{\ominus'})$ (in mV) for a fixed time (a), and different values of time (in s) for a fixed potential (b), shown in the curves. *Dashed lines* correspond to their linear concentration profiles.

$t = 0.1$ s (a) and $E - E_c^{\ominus'} = -500$ mV (b).
Reproduced with permission [12]



fixed time and different potential values (Fig. 2.1a), and at a fixed potential and different times (Fig. 2.1b).

From Fig. 2.1a, it can be observed that the Nernst diffusion layer, defined by the abscissa at which the concentration reaches the value c_O^* in the linear concentration profile, is independent of the potential in all the cases in spite of their having been obtained under transient conditions. This is in agreement with Eqs. (2.20) and (2.25), which show that the dependence on the electrode potential is only in the surface concentrations.

Figure 2.1b shows the time dependence of the concentration profiles. It can also be observed that the perturbed region of the solution adjacent to the electrode surface grows with time and the relative difference between the linear diffusion layer and the accurate diffusion layer (determined as the value x for which c_O reaches the 99 % of its bulk value) is greater for shorter times [12].

2.2.2 Current–Time Curves (Chronoamperometry) and Current–Potential Curves (Voltammetry)

By inserting Eq. (2.24) in (2.7), the following expression for the current is obtained:

$$I^{\text{plane}} = FAD_O \frac{(c_O^* - c_O^{s,r})}{\sqrt{\pi D_O t}} = -FAD_R \frac{(c_R^* - c_R^{s,r})}{\sqrt{\pi D_R t}} \quad (2.26)$$

By taking into account Eq. (2.20), the current given by (2.26) becomes

$$I^{\text{plane}} = FA \sqrt{\frac{D_O}{\pi t}} \frac{(c_O^* - c_R^* e^\eta)}{1 + \gamma e^\eta} \quad (2.27)$$

with η given by Eq. (2.6).

Note that the reversible $I(E, t)$ response is expressed as a product of a potential-dependent function $((c_O^* - c_R^* e^\eta)/(1 + \gamma e^\eta))$ and a time-dependent function $(FA \sqrt{D_O}/(\pi t))$. This behavior is characteristic of reversible electrode processes. In the next sections the current–time curves at fixed potential (Chronoamperograms) and current–potential curves at a fixed time (Voltammograms) will be analyzed.

2.2.2.1 Chronoamperometry

Expressions for the cathodic and anodic diffusion-controlled limiting currents, $I_{d,c}^{\text{plane}}$ and $I_{d,a}^{\text{plane}}$, can be easily obtained from Eq. (2.27) by making $e^\eta \rightarrow 0$ and $e^\eta \rightarrow \infty$ (i.e., $E \ll E_c^{\ominus'}$ and $E \gg E_c^{\ominus'}$), respectively. For a simple charge transfer the diffusion-controlled limiting current can also be defined as the current at which the electrode reaction is forced by the applied potential to the point that the surface

concentrations of electroactive reactant species fall to zero and then the current is only limited by the diffusion transport. Hence, $I_{d,c}^{\text{plane}}$ and $I_{d,a}^{\text{plane}}$ can also be obtained by making $c_{\text{O}}^{\text{s,r}} = 0$ and $c_{\text{R}}^{\text{s,r}} = 0$, respectively, in Eq. (2.26),

$$\left. \begin{aligned} I_{d,c}^{\text{plane}} &= FA \sqrt{\frac{D_{\text{O}}}{\pi t}} c_{\text{O}}^* \\ I_{d,a}^{\text{plane}} &= -FA \sqrt{\frac{D_{\text{R}}}{\pi t}} c_{\text{R}}^* \end{aligned} \right\} \quad (2.28)$$

These two equations are known as the Cottrell equations [13]. Equations (2.27) and (2.28) show that the current decays with the square root of time for any value of the applied potential, which only acts as a scale factor, as illustrated in Fig. 2.2. These equations predict very high current at short times, although in practice, the measured current at very short times is influenced both by the intrinsic limitations of the potentiostat and by the cell time constant, with the time needed for the fulfillment of Eqs. (2.27) and (2.28) being higher than $R_{\text{u}}C_{\text{dl}}$ (with R_{u} and C_{dl} being the uncompensated resistance of the cell and the double-layer capacitance; see Sects. 1.6 and 1.9). For sufficiently longer times, deviations from the cottrellian behavior are expected because of the natural convection, that is, the movement of the solution due to density differences, and edge effects, due to nonlinear diffusion at the electrode border.

The measurement of limiting currents is probably the simplest and most widely applicable method for measuring the diffusion coefficients of redox species. In agreement with Cottrell's equation, the value of D_i can be obtained from the plot of

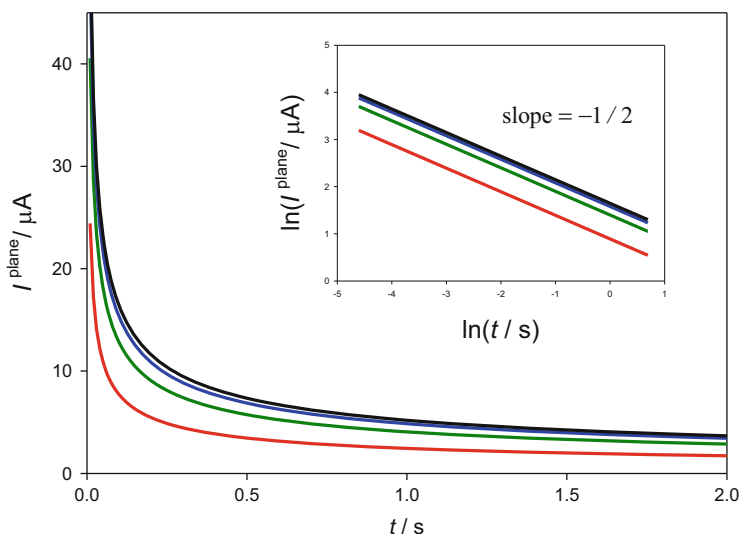


Fig. 2.2 Current–time curves for the application of a constant potential to a planar electrode. $D_{\text{O}} = D_{\text{R}} = 10^{-5} \text{ cm}^2 \text{ s}^{-1}$, $c_{\text{O}}^* = c_{\text{R}}^* = 1 \text{ mM}$, $A = 0.031 \text{ cm}^2$, $T = 298 \text{ K}$. The values of $(E - E_c^{\ominus'})$ in mV are: red, -25 ; green, -50 ; blue, -75 ; black, -100 . The inner figure corresponds to the plot of the logarithm of the current versus the logarithm of time

the logarithm of the limiting current versus the logarithm of time (see inner black curve in Fig. 2.2), by using the relation

$$D_i = \frac{\pi e^{2 \times \text{intercept}}}{(FAC_i^*)^2} \quad (2.29)$$

Additionally, a slope equal to $\frac{1}{2}$ confirms the validity of Eq. (2.28). Note that the Cottrell equation considers planar diffusion as the sole form of mass transport. However, in practice, purely planar diffusion is only achieved with very large or shielding electrodes. Deviations from cottrellian behavior at short times (double-layer current) and long times (convection,³ edge effects⁴) would restrict the applicability of the above equation (see Fig. 2.3).

2.2.2.2 Voltammetry

At a fixed time, the current–potential curve obtained from several potential step experiments has the sigmoidal shape shown in Fig. 2.4. This curve shows some interesting points:

- The potential corresponding to a current $I^{\text{plane}} = (I_{d,c}^{\text{plane}} + I_{d,a}^{\text{plane}})/2$, is called “reversible half-wave potential,” $E_{1/2}^r$, in planar geometry. This parameter can deviate from the formal potential because it is affected by the diffusion coefficients of the electroactive couple and also by the electrode geometry and size (i.e., it is affected by the kinetics of the mass transport); see Fig. 2.21.

To find this point, it is necessary to combine Eqs. (2.26) and (2.28),

$$\left. \begin{aligned} \frac{C_{\text{O}}^{s,r}}{C_{\text{O}}^*} &= 1 - \frac{I^{\text{plane}}}{I_{d,c}^{\text{plane}}} \\ \frac{C_{\text{R}}^{s,r}}{C_{\text{R}}^*} &= 1 - \frac{I^{\text{plane}}}{I_{d,a}^{\text{plane}}} \end{aligned} \right\} \quad (2.30)$$

By inserting Eq. (2.30) in the Nernst condition (Eq. 2.5), one obtains (see also Chap. 7 of [3]),

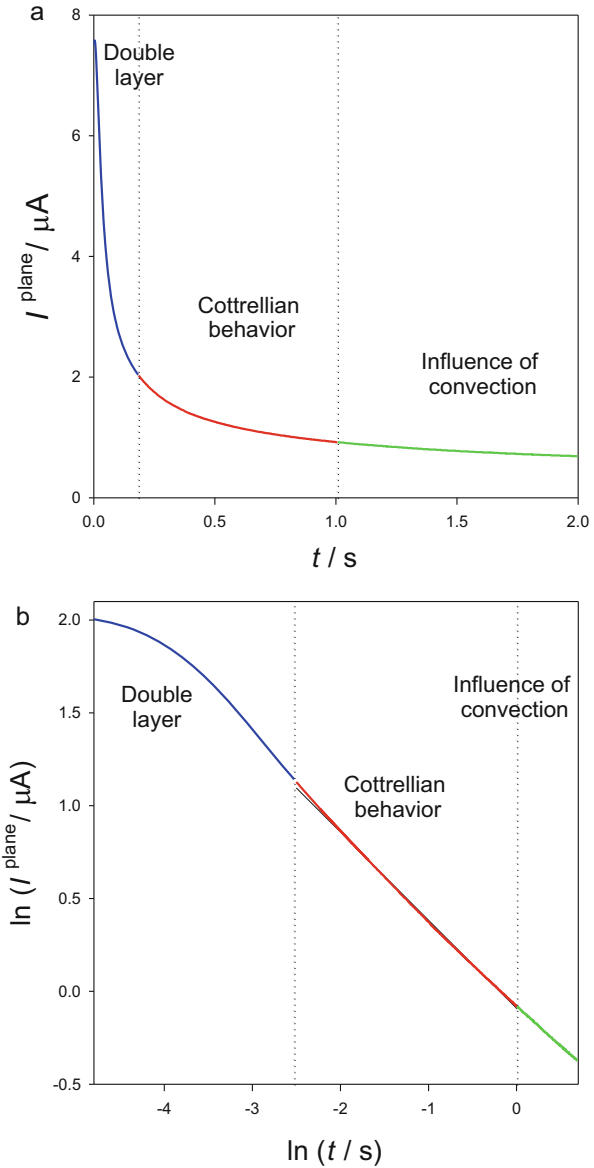
$$E = E_c^{\ominus'} + \frac{RT}{F} \ln \left(\frac{D_{\text{R}}}{D_{\text{O}}} \right)^{1/2} + \frac{RT}{F} \ln \left(\frac{I_{d,c}^{\text{plane}} - I^{\text{plane}}}{I^{\text{plane}} - I_{d,a}^{\text{plane}}} \right) \quad (2.31)$$

$$\text{So, for } I^{\text{plane}} = (I_{d,c}^{\text{plane}} + I_{d,a}^{\text{plane}})/2,$$

³ Natural convection associated to temperature or density gradients or vibrations is present in the usual experiments [14–16].

⁴ Enhancement of the diffusion flux at the edge of an inlaid electrode.

Fig. 2.3 Experimental current–time curve (a) and logarithmic curves (b) for the application of a constant potential to a graphite disc electrode of radius 0.5 mm (planar electrode) for the reduction of $\text{Fe}(\text{CN})_6^{3-}$.
 $c_{\text{Fe}(\text{CN})_6^{3-}}^* = 2 \text{ mM}$,
 $A = 0.0078 \text{ cm}^2$, $T = 298 \text{ K}$,
 $E = -0.1 \text{ V vs. Ag/AgCl}$,
 KCl (saturated) . From the logarithmic analysis in (b) (restricted to the Cottrellian region, i.e., the red line), the following values have been obtained: slope: -0.48 , intercept: -0.475 . The diffusion coefficient of $\text{Fe}(\text{CN})_6^{3-}$ obtained by applying Eq. (2.29) is $1.15 \times 10^{-6} \text{ cm}^2 \text{ s}^{-1}$



$$E = E_{1/2}^r = E_c^{\ominus'} + \frac{RT}{F} \ln \left(\frac{D_R}{D_O} \right)^{1/2} \quad (2.32)$$

- Another important point of the I – E curve is the crossing potential or “equilibrium potential” for which the current takes a null value, $I^{\text{plane}} = 0$ (see Fig. 2.4a). By inserting this condition in Eq. (2.27),

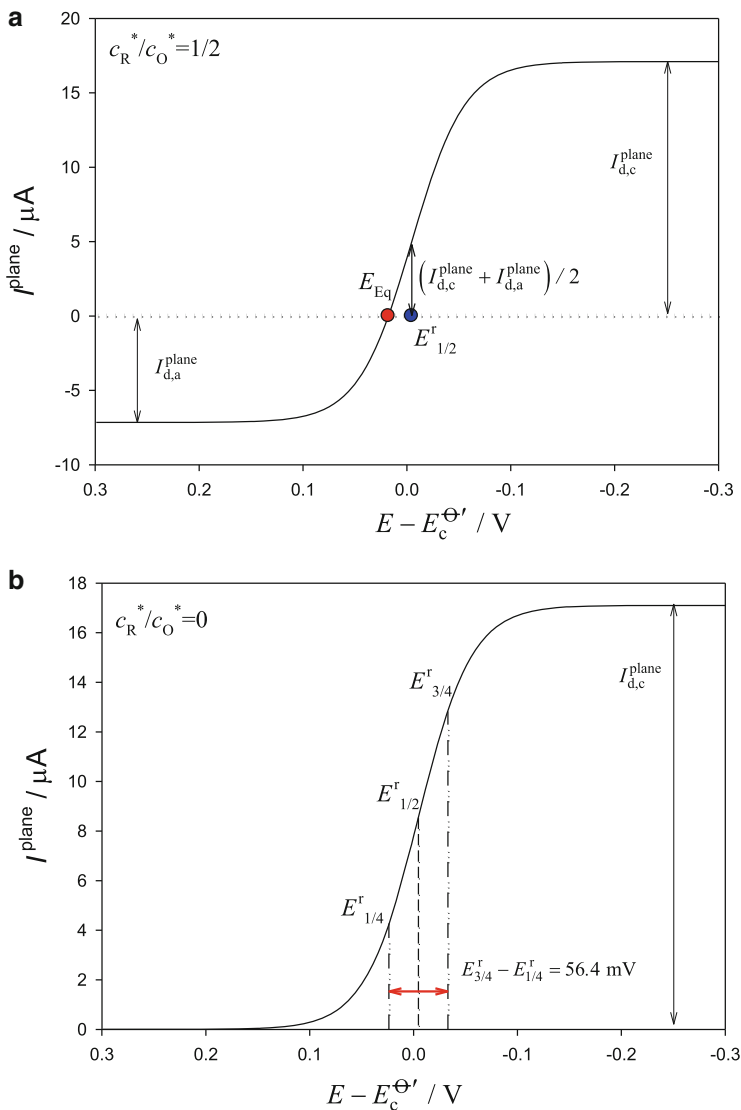


Fig. 2.4 Current–potential curve corresponding to the application of constant potentials to a planar macroelectrode, calculated from Eq. (2.27) with $c_R^*/c_O^* = 0.5$ (a) and 0 (b). $t = 0.1$ s, $A = 0.031$ cm², $D_O = 10^{-5}$ cm² s⁻¹, $\gamma = 1.2$

$$E_{\text{Eq}} = E_c^{\ominus'} + \frac{RT}{F} \ln \left(\frac{c_O^*}{c_R^*} \right) \quad (2.33)$$

Otherwise the I – E – t response (Eqs. 2.26 or 2.27), when only the oxidized species O is initially present in the electrolytic solution, is simplified to

$$I^{\text{plane}} = FA\sqrt{\frac{D_{\text{O}}}{\pi t}} \frac{c_{\text{O}}^*}{1 + \gamma e^{\eta}} = FAD_{\text{O}} \frac{(c_{\text{O}}^* - c_{\text{O}}^{\text{s,r}})}{\sqrt{\pi D_{\text{O}} t}} = FAD_{\text{R}} \frac{c_{\text{R}}^{\text{s,r}}}{\sqrt{\pi D_{\text{R}} t}} \quad (2.34)$$

Under these conditions only a cathodic wave is obtained (see Fig. 2.4b) and Eq. (2.31) takes the simpler form:

$$E = E_{1/2}^{\text{r}} + \frac{RT}{F} \ln \left(\frac{I_{\text{d,c}}^{\text{plane}} - I^{\text{plane}}}{I^{\text{plane}}} \right) \quad (2.35)$$

with the normalized current–potential curve having the following time-independent expression:

$$\frac{I^{\text{plane}}}{I_{\text{d,c}}^{\text{plane}}} = \frac{1}{1 + e^{\frac{F}{RT}(E - E_{1/2}^{\text{r}})}} = \frac{1}{1 + \gamma e^{\eta}} \quad (2.36)$$

This is a consequence of the form of the reversible I – E – t response.

Note that the plot of E vs. $\ln \left(\frac{(I_{\text{d,c}}^{\text{plane}} - I^{\text{plane}})}{(I^{\text{plane}} - I_{\text{d,a}}^{\text{plane}})} \right)$ (or vs. $\ln \left(\frac{(I_{\text{d,c}}^{\text{plane}} - I^{\text{plane}})}{I^{\text{plane}}} \right)$ when R species is not initially present) is linear with a slope 26 mV (if $T = 298$ K) and intercept equal to $E_{1/2}^{\text{r}}$. This slope is characteristic of reversible charge transfer processes. There are other reversibility criteria based on the difference between potentials $E_{3/4}^{\text{r}} - E_{1/4}^{\text{r}}$, corresponding to the currents $I^{\text{plane}} = (3/4)I_{\text{d,c}}^{\text{plane}}$ and $I^{\text{plane}} = (1/4)I_{\text{d,c}}^{\text{plane}}$, with this difference being 56.4 mV (See Chap. 5 of [2]; [17] and Fig. 2.4b).

The analysis of the E vs. $\ln \left(\frac{(I_{\text{d,c}}^{\text{plane}} - I^{\text{plane}})}{(I^{\text{plane}} - I_{\text{d,a}}^{\text{plane}})} \right)$ curve provides not only a reversibility criteria (from the measurement of the slope of the resulting linear plots), but also provides direct evidence that only one electron has been transferred and a direct measurement of the reversible half-wave potential, $E_{1/2}^{\text{r}}$, which is a fundamental parameter of the redox system in a given supporting electrolyte solution. $E_{1/2}^{\text{r}}$ is closely related to the formal potential (Eq. 2.32) and affected by the diffusion coefficients of the oxidized and reduced species. The half-wave potential varies with the size and shape of the electrode used because it depends on the characteristics of mass transport considered (see Fig. 2.21 in Sect. 2.6).

2.2.3 Stoichiometric Coefficients Different From the Unity

A variation of reaction Scheme (2.I) is considered here by assuming other stoichiometries, in line with the reaction scheme [1, 2]:



where n is the number of electrons transferred and v_{O} and v_{R} the stoichiometric coefficients of species O and R, respectively.

The mass transport and the initial conditions are also given by Eqs. (2.2) and (2.3), but the surface conditions are now

$$t > 0, \quad x = 0 :$$

$$\frac{D_{\text{O}}}{v_{\text{O}}} \left(\frac{\partial c_{\text{O}}}{\partial x} \right)_{x=0} = - \frac{D_{\text{R}}}{v_{\text{R}}} \left(\frac{\partial c_{\text{R}}}{\partial x} \right)_{x=0} \quad (2.37)$$

$$(c_{\text{O}}^{s,r})^{v_{\text{O}}} = e^{\eta} (c_{\text{R}}^{s,r})^{v_{\text{R}}} \quad (2.38)$$

where η is given by Eq. (2.6).

As previous sections, by using the variable s_i^{p} (Eq. 2.8), the differential equation system (2.2) and the surface conditions (2.37) and (2.38) become dependent only on s_i^{p} variable:

$$\frac{\sqrt{D_{\text{O}}}}{v_{\text{O}}} \left(\frac{\partial c_{\text{O}}}{\partial s_{\text{O}}^{\text{p}}} \right)_{s_{\text{O}}^{\text{p}}=0} = - \frac{\sqrt{D_{\text{R}}}}{v_{\text{R}}} \left(\frac{\partial c_{\text{R}}}{\partial s_{\text{R}}^{\text{p}}} \right)_{s_{\text{R}}^{\text{p}}=0} \quad (2.39)$$

$$(c_{\text{O}}(s_{\text{O}}^{\text{p}} = 0))^{v_{\text{O}}} = e^{\eta} (c_{\text{R}}(s_{\text{R}}^{\text{p}} = 0))^{v_{\text{R}}} \quad (2.40)$$

Therefore, the surface fluxes and concentration profiles of species i ($i = \text{O}, \text{R}$) are also expressed by Eqs. (2.16)–(2.18). From Eqs. (2.17), (2.39), and (2.40), it is possible to obtain the expression for the relationship between the potential and the surface concentration of species O:

$$E = E_c^{\ominus'} + \frac{RT}{nF} \ln \left(\frac{(c_{\text{O}}^{s,r})^{v_{\text{O}}}}{\left(\frac{v_{\text{R}}}{v_{\text{O}}} \gamma \right)^{v_{\text{R}}} (c_{\text{O}}^* - c_{\text{O}}^{s,r})^{v_{\text{R}}}} \right) \quad (2.41)$$

with γ given by Eq. (2.21).

The expression of the current is

$$I^{\text{plane}} = \frac{FAD_{\text{O}}}{\sqrt{\pi D_{\text{O}}t}} \frac{(c_{\text{O}}^* - c_{\text{O}}^{s,r})}{v_{\text{O}}} \quad (2.42)$$

with the limiting current being

$$I_{\text{d,c}}^{\text{plane}} = \frac{FAD_{\text{O}}}{\sqrt{\pi D_{\text{O}}t}} \frac{c_{\text{O}}^*}{v_{\text{O}}} \quad (2.43)$$

By solving $c_{\text{O}}^{s,r}$ and c_{O}^* in Eqs. (2.42) and (2.43) and inserting them into (2.41), it is obtained

$$E = E_c^{\Theta'} + \frac{RT}{nF} \ln \left(\frac{v_O^{v_O}}{(v_R \gamma)^{v_R}} \left(\frac{\sqrt{\pi t}}{FA\sqrt{D_O}} \right)^{v_O - v_R} \frac{(I_{d,c}^{\text{plane}} - I^{\text{plane}})^{v_O}}{(I_{d,c}^{\text{plane}})^{v_R}} \right) \quad (2.44)$$

Equation (2.44) transforms into (2.31) for the case $v_O = v_R = 1$ (with $I_{d,a} = 0$). The expression of the half-wave potential is obtained by making $I^{\text{plane}} = I_{d,c}^{\text{plane}}/2$ in (2.44),

$$E_{1/2}^r = E_c^{\Theta'} + v_R \frac{RT}{nF} \ln \left(\frac{D_R}{D_O} \right)^{1/2} + \frac{RT}{nF} \ln \left(\frac{(C_O^*)^{v_O - v_R}}{2^{v_O - v_R} \left(\frac{v_R}{v_O} \right)^{v_R}} \right) \quad (2.45)$$

From these expressions of the half-wave potential it can be inferred that, under these conditions, it depends on the bulk concentration of oxidized species and on the particular values of v_O and v_R .

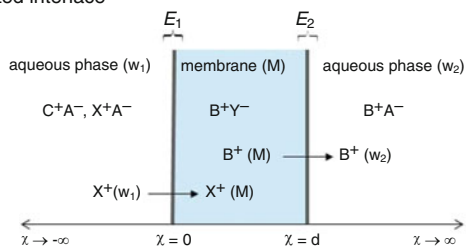
2.3 Ion Transfer Through Liquid Membranes

The study of the ion transfer through artificial liquid membrane systems is important for the elucidation of the ion transfer through biological membranes. In this respect, the Interface between two immiscible electrolyte solutions (ITIES) constitutes a biomimetic medium suitable for studying several fundamental processes, ranging from biocatalysis to cellular respiration of photosynthesis, and many others [18–22]. The first studies of liquid/liquid interfaces (L/L) under the application of an external potential were carried out by Gavach et al. [23], laying the basis for the current electrochemical treatments of ITIES.

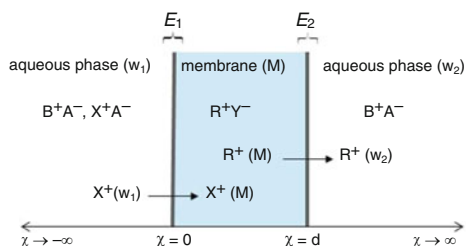
The membrane system considered here is composed of two aqueous solutions w_1 and w_2 , separated by a liquid membrane M, and it involves two aqueous solution/membrane interfaces: w_1/M (outer interface) and M/w_2 (inner interface). If the different ohmic drops (and the potentials caused by mass transfers within w_1 , M, and w_2) can be neglected, the membrane potential, E_M , defined as the potential difference between w_1 and w_2 , is caused by ion transfers taking place at both L/L interfaces. The current associated with the ion transfer across the L/L interfaces is governed by the same mass transport limitations as redox processes on a metal electrode/solution interface. Provided that the ion transport is fast, it can be considered that it is governed by the same diffusion equations, and the electrochemical methodology can be transposed en bloc [18, 24]. With respect to the experimental cell used for electrochemical studies with these systems, it is necessary to consider three sources of resistance, i.e., both the two aqueous and the nonaqueous solutions, with both ITIES sandwiched between them. Therefore, a potentiostat with two reference electrodes is usually used.

Scheme 2.2 A schematic view of the systems with one (a) and two (b) polarized liquid/liquid interfaces: outer (w_1/M) and inner (M/w_2)

a One polarized interface



b Two polarized interfaces



The ion transport through membrane systems can be studied in two forms:

- By using a common ion in the organic membrane and in one of the aqueous phases, such that it can be assumed that the external polarization is only effective at one interface of the membrane, and the current corresponding to a given applied potential is only determined by the transfer of the target ion at one of the interfaces, since the other acts as a reference interface (see Scheme 2.2a).
- In the case of a very hydrophobic supporting electrolyte in the membrane for which it is not possible to have a common ion in the electrolyte of the aqueous phases, a design like that shown in Scheme 2.2b is used. In this situation, both liquid/liquid interfaces in the membrane system are polarized (and the charge transfer reactions are linked to each other through the fulfillment of the electroneutrality of the membrane). These polarization phenomena can be described in terms of the individual electrochemical processes occurring at the two interfaces, which are coupled by virtue of the same intensity of electrical current (in order to maintain the electroneutrality of this system). Moreover, Kihara et al. demonstrated that the useful potential window that this system provides is much wider than that available when only one interface w_1/M is polarized [25–27].

2.3.1 One-Polarized Interface Systems

Many of the systems used for electrochemical studies of ion transfer processes taking place at the ITIES are systems of a single polarized interface. In these kinds of systems, the polarization phenomenon is only effective at the sample solution/

membrane interface, since the potential drop through the other interface is kept constant whatever the nature of this interface (i.e., either liquid/liquid or solid/liquid [28]). In the specific case of a membrane system that separates two aqueous solutions, the non-polarizable interface is achieved by adding a sufficiently high concentration of a common ion in the membrane and inner aqueous solution, by choosing as supporting electrolyte two salts of this common ion with lipophilic and hydrophilic counterions, respectively.

Let us consider the transfer of a cation X^+ between the aqueous phase (w_1) and the organic phase (M),



The distribution of the cation X^+ between both phases in contact leads to the development of a potential drop across the interface,

$$\Delta_M^{w_1} \phi = \phi(w_1) - \phi(M) \quad (2.46)$$

where $\phi(p)$ is the inner potential of the phase p ($= w_1$ or M). This equilibrium potential difference, when X^+ is the only ion that can be transferred, obeys the Nernst equation:

$$\Delta_M^{w_1} \phi = \Delta_M^{w_1} \phi_{X^+}^{\ominus} + \frac{RT}{F} \ln \left(\frac{a_{X^+}^M}{a_{X^+}^{w_1}} \right) = \Delta_M^{w_1} \phi_{X^+}^{\ominus'} + \frac{RT}{F} \ln \left(\frac{c_{X^+}^M}{c_{X^+}^{w_1}} \right) \quad (2.47)$$

with $\Delta_M^{w_1} \phi_{X^+}^{\ominus'}$ being the formal ion transfer potential given by

$$\Delta_M^{w_1} \phi_{X^+}^{\ominus'} = \Delta_M^{w_1} \phi_{X^+}^{\ominus} + \frac{RT}{F} \ln \left(\frac{f_{X^+}^M}{f_{X^+}^{w_1}} \right) \quad (2.48)$$

where R , T , and F have their usual meaning and $a_{X^+}^p$, $f_{X^+}^p$, and $c_{X^+}^p$ are the activity, activity coefficient, and concentration, respectively, of the ion X^+ in the phase p ($= w_1$ or M). $\Delta_M^{w_1} \phi_{X^+}^{\ominus}$ is the standard ion transfer potential, which is related to the standard Gibbs energy of the transfer of X^+ ,

$$\Delta_M^{w_1} \phi_{X^+}^{\ominus} = \frac{\Delta_{w_1}^M G_{X^+}^{\ominus}}{F} \quad (2.49)$$

The standard Gibbs energy of the ion transfer is a direct measurement of lipophilicity, and is related to the standard partition coefficient of the ion in the biphasic system through the following equation:

$$P_{X^+} = \exp \left(- \frac{\Delta_{w_1}^M G_{X^+}^{\ominus}}{RT} \right) \quad (2.50)$$

From the transposition of the theory for NPV to the study of the uptake of a target ion X^+ from an aqueous sample solution to a liquid membrane, the theoretical

equations obtained with the semi-infinite diffusion model can be used to quantify the current response of the ion transfer. The major difference between ionic transfer through and membrane and electronic transfer at a solid electrode is that the boundary condition corresponding to the flux conservation is given by

$$D_{X^+}^{w_1} \left(\frac{\partial c_{X^+}^{w_1}}{\partial x} \right)_{x=0} = D_{X^+}^M \left(\frac{\partial c_{X^+}^M}{\partial x} \right)_{x=0} \quad (2.51)$$

since the concentration of ion X^+ decreases from the aqueous bulk to the membrane surface (i.e., for $-\infty \leq x \leq 0$) and decreases from the membrane surface to the membrane bulk (i.e., for $0 \leq x \leq \infty$). However, as the planar diffusion operator is symmetrical with respect to the x -coordinate, this change does not affect the solution of the differential diffusion equations. So, the equation for the current in NPV of a reversible ion transfer can be written as

$$\left. \begin{aligned} \frac{I}{I_d} &= \frac{\gamma e^\eta}{1 + \gamma e^\eta} \\ E &= E_{1/2}^r + \frac{RT}{F} \ln \left(\frac{I}{I_d - I} \right) \end{aligned} \right\} \quad (2.52)$$

where

$$E_{1/2}^r = \Delta_M^{w_1} \phi_{X^+}^{\ominus'} + \frac{RT}{F} \ln \left(\frac{1}{\gamma} \right) \quad (2.53)$$

$$I_d = FA c_{X^+}^* \sqrt{\frac{D_{X^+}^{w_1}}{\pi t}} \quad (2.54)$$

$$\eta = \frac{F}{RT} \left(E - \Delta_M^{w_1} \phi_{X^+}^{\ominus'} \right) \quad (2.55)$$

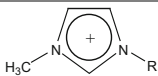
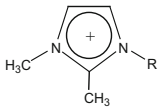
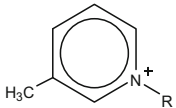
$$\gamma = \left(\frac{D_{X^+}^M}{D_{X^+}^{w_1}} \right)^{1/2} \quad (2.56)$$

with $\Delta_M^{w_1} \phi_{X^+}^{\ominus'}$ being given by Eq. (2.48). From Eq. (2.52), $E_{1/2}^r$ can be easily determined and also the standard ion transfer potential $\Delta_M^{w_1} \phi_{X^+}^{\ominus}$ once the diffusion coefficients are known. Table 2.1 shows the values of $\Delta_M^{w_1} \phi_{X^+}^{\ominus}$ for some ionic liquid cations.

2.3.2 Two-Polarized Interfaces Systems

In these kinds of systems, the polarization phenomenon is effective at the two interfaces involved. Specifically, in membrane systems comprising two ITIES, this

Table 2.1 Standard ion transfer potentials of different *N,N*-alkylimidazolium and 1-butyl-4-methylpyridinium ionic liquid cations [29]

Cation type	R	$\Delta_M^w \phi_{X^+}^-$ (mV)	$\Delta_{w_1}^M G_{X^+}^-$ (kJ/mol)
	C ₄ H ₉	-24.2	-2.33
	C ₆ H ₅	-53.2	-5.13
	C ₆ H ₁₃	-93.2	-8.99
	C ₈ H ₁₇	-162.5	-15.68
	C ₄ H ₉	-35.2	-3.39
	C ₄ H ₉	-51.5	-4.97

behavior is achieved when the membrane contains a hydrophobic supporting electrolyte and the sample aqueous solution (the inner one) contains hydrophilic supporting electrolytes, and there is no common ion between any of the adjacent phases. In this case, the potential drop cannot be controlled individually and the processes taking place at both interfaces are linked to each other by virtue of the same electrical current intensity. Systems of two-polarized interfaces have shown a series of peculiarities that can be advantageous when studying ion transfer processes. Indeed, they provide a potential window about twice that of one-polarized interface systems, the signals of cations and anions with similar standard ion transfer potential values appear widely separated when these systems are used, and the half-wave potential of the ions in these systems is influenced by their concentration.

In Scheme 2.2b interface w_1/M is the outer or working interface, and interface M/w_2 is the inner interface (not a reference interface).

The theoretical characterization of the response of this kind of membrane systems in electrochemical techniques is very interesting for determining thermodynamics and transport parameters of ions.

According to Scheme 2.2b, to solve this problem we must find the following unknown variables.

- At interface w_1/M : The concentration profiles of the target cation at both sides of this interface ($c_{X^+}^{w_1}$ and $c_{X^+}^M$) and the potential drop E_1 .
- At interface M/w_2 : The concentration profiles of the cation R^+ of the supporting electrolyte of the membrane at both sides of this interface ($c_{R^+}^M$ and $c_{R^+}^{w_2}$) and the potential drop E_2 . Note that it has been assumed that R^+ is being transferred at the inner interface, coupled with the transfer of X^+ at the outer one, in order to maintain electroneutrality.

$c_{X^+}^*$ and $c_{R^+}^*$ are the initial concentrations of the target ion in aqueous phase w_1 and of the electrolyte cation R^+ in the membrane, respectively.

Indeed, this is a problem with five unknown variables, the four concentrations above indicated and one of the potential differences at the two interfaces, E_1 or E_2 , since they can be reduced to one potential difference because $E_M = E_1 - E_2$ is known. Four differential equations and the additional condition of equality of the fluxes of the target ion X^+ and the cation R^+ at the outer and inner interfaces, respectively, will be used to obtain the explicit I/E_M curve and the concentration profiles of all the species.

Interface w_1/M or Outer Interface

The differential equations and the boundary value problem (bvp) which can be fulfilled by $c_{X^+}^{w_1}$ and $c_{X^+}^M$ if the thickness of the membrane is greater than the diffusion layer of X^+ into the membrane are:

$$\frac{\partial c_{X^+}^{w_1}}{\partial t} = D_{X^+}^{w_1} \frac{\partial^2 c_{X^+}^{w_1}}{\partial x^2} \quad (2.57)$$

$$\frac{\partial c_{X^+}^M}{\partial t} = D_{X^+}^M \frac{\partial^2 c_{X^+}^M}{\partial x^2} \quad (2.58)$$

in phase w_1 :

$$\left. \begin{array}{l} t = 0, \quad x < 0 \\ t \geq 0, \quad x \rightarrow -\infty \end{array} \right\} c_{X^+}^{w_1} = c_{X^+}^* \quad (2.59)$$

in phase M:

$$\left. \begin{array}{l} t = 0, \quad 0 < x < d \\ t \geq 0, \quad x \rightarrow d \end{array} \right\} c_{X^+}^M = 0 \quad (2.60)$$

$t > 0, \quad x = 0$:

$$c_{X^+}^M = e^{\eta_1} c_{X^+}^{w_1} \quad (2.61)$$

$$D_{X^+}^{w_1} \left(\frac{\partial c_{X^+}^{w_1}}{\partial x} \right)_{x=0} = D_{X^+}^M \left(\frac{\partial c_{X^+}^M}{\partial x} \right)_{x=0} \quad (2.62)$$

with

$$\eta_1 = \frac{F}{RT} \left(E_1 - \Delta_M^{w_1} \phi_{X^+}^\ominus \right) \quad (2.63)$$

and E_1 is unknown.

Interface M/w₂ or Inner Interface

$$\frac{\partial c_{R^+}^{w_2}}{\partial t} = D_{R^+}^{w_2} \frac{\partial^2 c_{R^+}^{w_2}}{\partial x^2} \quad (2.64)$$

$$\frac{\partial c_{R^+}^M}{\partial t} = D_{R^+}^M \frac{\partial^2 c_{R^+}^M}{\partial x^2} + \text{migration term} \quad (2.65)$$

Inside the membrane, the transport of R^+ takes place by diffusion and ionic migration and is described by a very complex differential equation. However, since the current is controlled by the diffusion of the target ion X^+ and since $c_{R^+}^*$ in membrane is high enough, it will be assumed that the R^+ concentration is constant in all the membranes, i.e., in $0 < x < d$. Therefore, Eq. (2.65) can be changed for the following condition:

$$c_{R^+}^M(x, t) = c_{R^+}^* \quad (2.66)$$

in phase M:

$$\left. \begin{array}{l} t = 0, \quad 0 < x < d \\ t \geq 0, \quad x \rightarrow d \end{array} \right\} c_{R^+}^M = c_{R^+}^* \quad (2.67)$$

in phase w₂:

$$\left. \begin{array}{l} t = 0, \quad x \geq d \\ t \geq 0, \quad x \rightarrow \infty \end{array} \right\} c_{R^+}^{w_2} = 0 \quad (2.68)$$

$$t > 0, \quad x = d : c_{R^+}^M = e^{\eta_2} c_{R^+}^{w_2} \quad (2.69)$$

or, according with (2.66):

$$c_{R^+}^* = e^{\eta_2} c_{R^+}^{w_2} \quad (2.70)$$

where

$$\eta_2 = \frac{F}{RT} (E_2 - \Delta_{w_2}^M \phi_{R^+}^{\ominus'}) \quad (2.71)$$

and E_2 is unknown.

The solutions of both problems are simple due to their separate character, with each of them corresponding to the response of reversible charge transfer processes, in such a way that the following is obtained for interface w₁/M:

$$I_1 = FA \sqrt{\frac{D_{X^+}^{w_1}}{\pi t}} (c_{X^+}^* - c_{X^+}^{w_1}(0)) \quad (2.72)$$

and

$$E_1 = \Delta_M^{w_1} \phi_{X^+}^{\ominus'} + \frac{RT}{F} \ln\left(\frac{1}{\gamma_1}\right) + \frac{RT}{F} \ln\left(\frac{I_1}{I_d - I_1}\right) \quad (2.73)$$

with

$$I_d = FA \sqrt{\frac{D_{X^+}^{w_1}}{\pi t}} c_{X^+}^* \quad (2.74)$$

$$\gamma_1 = \sqrt{\frac{D_{X^+}^M}{D_{X^+}^{w_1}}} \quad (2.75)$$

For the interface M/w₂:

$$I_2 = FA \sqrt{\frac{D_{R^+}^{w_2}}{\pi t}} c_{R^+}^{w_2}(d) \quad (2.76)$$

By taking into account that the transfer of R⁺ through M/w₂ interface also occurs reversibly, and that the current through both interfaces is the same, i.e., $I_1 = I_2 = I$, it can be deduced:

$$E_2 = \Delta_{w_2}^M \phi_{X^+}^{\ominus'} + \frac{RT}{F} \ln\left(\frac{c_{R^+}^*}{\gamma_2 c_{X^+}^*}\right) + \frac{RT}{F} \ln\left(\frac{I_d}{I}\right) \quad (2.77)$$

with

$$\gamma_2 = \sqrt{\frac{D_{X^+}^{w_1}}{D_{R^+}^{w_2}}} \quad (2.78)$$

By subtracting equations for E_1 and E_2 ,

$$E^M = E_2 - E_1 = E_{1/2}^M + \frac{RT}{F} \ln\left(\frac{2(I_N)^2}{1 - I_N}\right) \quad (2.79)$$

where:

$$I_N = \frac{I(t)}{I_d(t)} \quad (2.80)$$

$$E_{1/2}^M = E^{M, \ominus'} + \frac{RT}{F} \ln\left(\frac{1}{\lambda}\right) \quad (2.81)$$

$$\lambda = \frac{2\sqrt{D_{R^+}^{w_2} D_{X^+}^M} c_{R^+}^*}{D_{X^+}^{w_1} c_{X^+}^*} \quad (2.82)$$

$$E^{M, \ominus'} = \Delta_M^{w_1} \phi_{X^+}^{\ominus'} - \Delta_{w_2}^M \phi_{R^+}^{\ominus'} \quad (2.83)$$

Equation (2.79) provides the expression of the membrane potential E^M (applied potential) as a function of the normalized current I_N at this potential (measured current, which is not known). So, by working out the current from the above equation we deduce the following explicit expression for the current obtained in single potential step voltammetry as a function of the applied potential:

$$I = FA \sqrt{\frac{D_{X^+}^w}{\pi t}} c_{X^+}^* g(\eta) \quad (2.84)$$

where $g(\eta)$ is the function that contains the dependence on the applied potential for this kind of membrane systems and it is also fundamental in the current–potential response deduced for any voltammetric technique [30],

$$\left. \begin{aligned} g(\eta) &= \frac{\sqrt{\lambda^2 e^{2\eta} + 8\lambda e^\eta} - \lambda e^\eta}{4} \\ \eta &= \frac{F}{RT} (E^M - E^{M, \ominus'}) \end{aligned} \right\} \quad (2.85)$$

If coupled to the transfer of the target cation, through the outer interface, the anion of the supporting electrolyte of w_2 is transferred through the inner one; Eqs. (2.84) and (2.85) are still valid for changing λ for λ^- ,

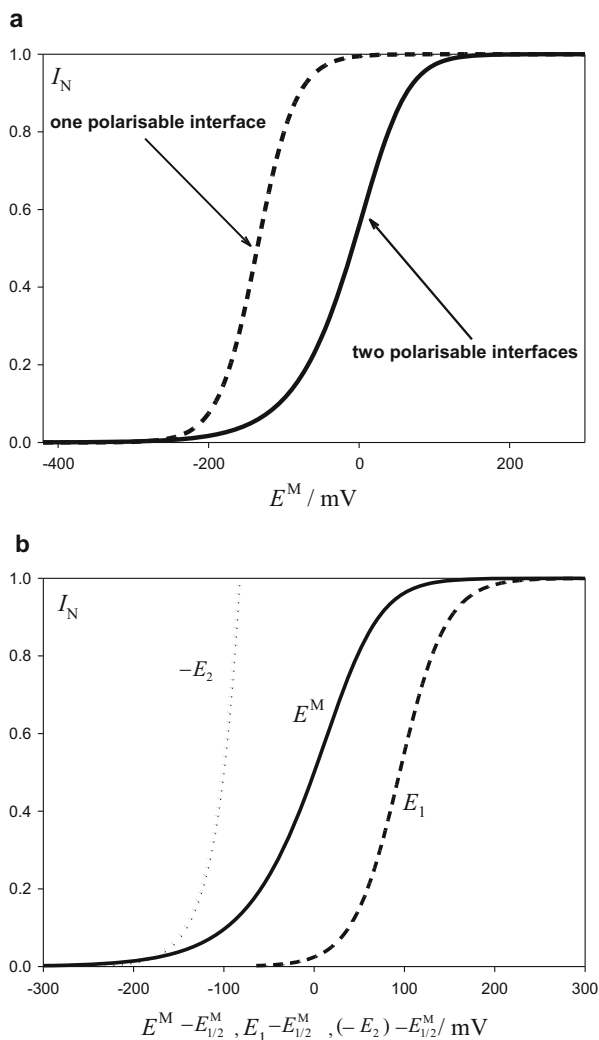
$$\lambda^- = \frac{2\sqrt{D_{R^+}^M D_{X^+}^M} c_{R^+}^*}{D_{X^+}^{w_1} c_{X^+}^*} \quad (2.86)$$

By comparing this solution with that obtained for only one polarized L/L interface (Eq. 2.52), it can be observed that both are formally similar if we change $g(\eta)$ function for the sigmoidal function $\gamma e^\eta / (1 + \gamma e^\eta)$. The different behavior of both responses is shown in Fig. 2.5, which corresponds to the transfer of a target cation X^+ from water to a plasticized polymeric membrane in a system of one and two L/L polarized interfaces (dashed and solid line, respectively). It can be seen in Figure 2.5a that when the two interfaces are polarized, the I/E curve behaves in a similar way to that corresponding to an irreversible process with only one interface. Figure 2.5b also shows how the I/E curve corresponding to the applied potential (or the membrane potential) is the sum of the curves corresponding to the outer and inner potentials.

Note finally that in the case of two-polarized interface systems, the plots of the membrane potential E^M versus $\ln(2(I_N)^2 / (1 - I_N))$ are linear with a slope equal to RT/F and an intercept $E_{1/2}^M$.

Fig. 2.5 (a) Normalized current–potential curves corresponding to a system with two polarizable liquid/liquid interfaces (solid line; see Eq. (2.84)) and to a system with one polarizable interface (dashed line; see Eq. (2.52)). (b) I_N/E^M (solid line), I_N/E_1 (dashed line), and $I_N/(-E_2)$ (dotted line) calculated from Eqs. (2.84), (2.73), and (2.77), respectively.

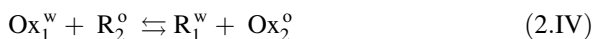
$\Delta_M^{w_1} \phi_{X^+}^{\ominus'} = -224$ mV,
 $\Delta_{w_2}^M \phi_{R^+}^{\ominus'} = -304$ mV,
 $D_{X^+}^{w_1} = D_{R^+}^{w_2} = 10^{-5}$ cm² s⁻¹,
 $D_{X^+}^M = 10^{-8}$ cm² s⁻¹,
 $c_{X^+}^* = 0.1$ mM,
 $c_{R^+}^* = 50$ mM, $T = 298.15$ K.
 Reproduced with permission [30]



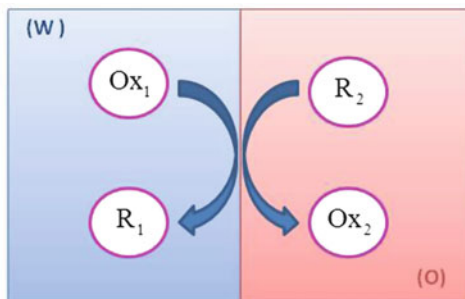
2.3.3 Electron Transfer at the Liquid/Liquid Interface

In this section, we will consider the transfer of electrons between an oxidized species O_1 in an aqueous phase and a reduced species R_1 in an organic phase, as illustrated in reaction Scheme 2.3

The global process can be written as



Scheme 2.3 A schematic view of an heterogeneous redox reaction at a liquid/liquid interface



To solve the mass transport equations corresponding to this process, it is necessary to consider the arrival of two reactants in different phases at the surface and the departure of the two products from it, so four differential equations should be considered [31]: two for the aqueous phase,

$$\left. \begin{aligned} \frac{\partial c_{\text{Ox}_1}}{\partial t} &= D_{\text{O}_1} \frac{\partial^2 c_{\text{Ox}_1}}{\partial x^2} \\ \frac{\partial c_{\text{R}_1}}{\partial t} &= D_{\text{R}_1} \frac{\partial^2 c_{\text{R}_1}}{\partial x^2} \end{aligned} \right\} \quad (2.87)$$

and two for the organic one,

$$\left. \begin{aligned} \frac{\partial c_{\text{Ox}_2}}{\partial t} &= D_{\text{O}_2} \frac{\partial^2 c_{\text{Ox}_2}}{\partial x^2} \\ \frac{\partial c_{\text{R}_2}}{\partial t} &= D_{\text{R}_2} \frac{\partial^2 c_{\text{R}_2}}{\partial x^2} \end{aligned} \right\} \quad (2.88)$$

The boundary value problem is the following:

$$t = 0, \quad \forall x$$

$$\left. \begin{aligned} c_{\text{Ox}_1} &= c_{\text{Ox}_1}^* \\ c_{\text{R}_1} &= c_{\text{R}_1}^* \\ c_{\text{Ox}_2} &= c_{\text{Ox}_2}^* \\ c_{\text{R}_2} &= c_{\text{R}_2}^* \end{aligned} \right\} \quad (2.89)$$

$$t > 0, \quad x \rightarrow -\infty$$

$$\left. \begin{aligned} c_{\text{Ox}_1} &= c_{\text{Ox}_1}^* \\ c_{\text{R}_1} &= c_{\text{R}_1}^* \end{aligned} \right\} \quad (2.90)$$

$t > 0, \quad x \rightarrow \infty$

$$\left. \begin{aligned} c_{\text{O}_2} &= c_{\text{O}_2}^* \\ c_{\text{R}_2} &= c_{\text{R}_2}^* \end{aligned} \right\} \quad (2.91)$$

$t > 0, \quad x = 0$

$$\left. \begin{aligned} D_{\text{Ox}_1} \left(\frac{\partial c_{\text{Ox}_1}}{\partial x} \right)_{x=0} + D_{\text{R}_1} \left(\frac{\partial c_{\text{R}_1}}{\partial x} \right)_{x=0} &= 0 \\ D_{\text{Ox}_2} \left(\frac{\partial c_{\text{Ox}_2}}{\partial x} \right)_{x=0} + D_{\text{R}_2} \left(\frac{\partial c_{\text{R}_2}}{\partial x} \right)_{x=0} &= 0 \end{aligned} \right\} \quad (2.92)$$

The solutions to the four differential equations given by Eqs. (2.87) and (2.88) can be obtained easily by introducing the s_i^p parameter defined in Eq. (2.8). Once this parameter is inserted in the above equations, the following general solution for the concentration profiles is obtained by following a similar procedure to that described in Sect. 2.2:

$$c_i(x, t) = c_i^* + (c_i(0) - c_i^*) \operatorname{erfc}(s_i^p) \quad \text{with } i = \text{Ox}_1, \text{R}_1, \text{Ox}_2, \text{ and } \text{R}_2 \quad (2.93)$$

Note that $\operatorname{erfc}(x) = 1 - \operatorname{erf}(x)$ for $x > 0$ and $\operatorname{erfc}(x) = 1 + \operatorname{erf}(x)$ for $x < 0$.

From this equation, it is possible to calculate the surface gradients of the four species. If we assume that the diffusion coefficients of all of them are equal ($D_{\text{Ox}_1} = D_{\text{R}_1} = D_{\text{Ox}_2} = D_{\text{R}_2} = D$), then,

$$\left. \begin{aligned} \left(\frac{\partial c_{\text{Ox}_1}}{\partial x} \right)_{x=0} &= - \frac{(c_{\text{Ox}_1}(0) - c_{\text{Ox}_1}^*)}{\sqrt{\pi Dt}} \\ \left(\frac{\partial c_{\text{R}_1}}{\partial x} \right)_{x=0} &= - \frac{(c_{\text{R}_1}(0) - c_{\text{R}_1}^*)}{\sqrt{\pi Dt}} \\ \left(\frac{\partial c_{\text{Ox}_2}}{\partial x} \right)_{x=0} &= \frac{(c_{\text{Ox}_2}(0) - c_{\text{Ox}_2}^*)}{\sqrt{\pi Dt}} \\ \left(\frac{\partial c_{\text{R}_2}}{\partial x} \right)_{x=0} &= \frac{(c_{\text{R}_2}(0) - c_{\text{R}_2}^*)}{\sqrt{\pi Dt}} \end{aligned} \right\} \quad (2.94)$$

The current is given by the following relationship:

$$I = FAD \left(\frac{\partial c_{\text{Ox}_1}}{\partial x} \right)_{x=0} \quad (2.95)$$

Taking into account Eqs. (2.92), (2.94), and (2.95), we get the following expressions for the surface concentrations of the four species in terms of the current:

$$\left. \begin{aligned} c_{\text{Ox}_1}(0) &= \frac{-I}{FA\sqrt{\frac{D}{\pi t}}} + c_{\text{Ox}_1}^* \\ c_{\text{R}_1}(0) &= \frac{I}{FA\sqrt{\frac{D}{\pi t}}} + c_{\text{R}_1}^* \\ c_{\text{Ox}_2}(0) &= \frac{I}{FA\sqrt{\frac{D}{\pi t}}} + c_{\text{Ox}_2}^* \\ c_{\text{R}_2}(0) &= \frac{-I}{FA\sqrt{\frac{D}{\pi t}}} + c_{\text{R}_2}^* \end{aligned} \right\} \quad (2.96)$$

The equivalent of the Nernst equation for the above process at the interface is

$$\Delta_o^w \phi = \Delta_o^w \phi^{\ominus'} + \frac{RT}{F} \ln \left(\frac{c_{\text{R}_1}(0)c_{\text{Ox}_2}(0)}{c_{\text{Ox}_1}(0)c_{\text{R}_2}(0)} \right) \quad (2.97)$$

which can be rewritten as

$$e^{\eta} = \frac{c_{\text{R}_1}(0)c_{\text{Ox}_2}(0)}{c_{\text{Ox}_1}(0)c_{\text{R}_2}(0)} = \left(\frac{\left(I_N + \frac{c_{\text{R}_1}^*}{c_{\text{Ox}_1}^*} \right) \left(I_N + \frac{c_{\text{Ox}_2}^*}{c_{\text{Ox}_1}^*} \right)}{(-I_N + 1) \left(-I_N + \frac{c_{\text{R}_2}^*}{c_{\text{Ox}_1}^*} \right)} \right) \quad (2.98)$$

with

$$\eta = \frac{F}{RT} \left(\Delta_o^w \phi - \Delta_o^w \phi^{\ominus'} \right) \quad (2.99)$$

$$I_N = \frac{I}{FAc_{\text{Ox}_1}^* \sqrt{\frac{D}{\pi t}}} \quad (2.100)$$

By working out the current in terms of the potential, the following quadratic equation is obtained:

$$I_N^2 (e^{\eta} - 1) - I_N [e^{\eta} (1 + \beta) + \alpha + \gamma] + e^{\eta} \beta - \alpha \gamma = 0 \quad (2.101)$$

with

$$\left. \begin{aligned} \alpha &= \frac{c_{\text{R}_1}^*}{c_{\text{Ox}_1}^*} \\ \beta &= \frac{c_{\text{R}_2}^*}{c_{\text{Ox}_1}^*} \\ \gamma &= \frac{c_{\text{O}_2}^*}{c_{\text{Ox}_1}^*} \end{aligned} \right\} \quad (2.102)$$

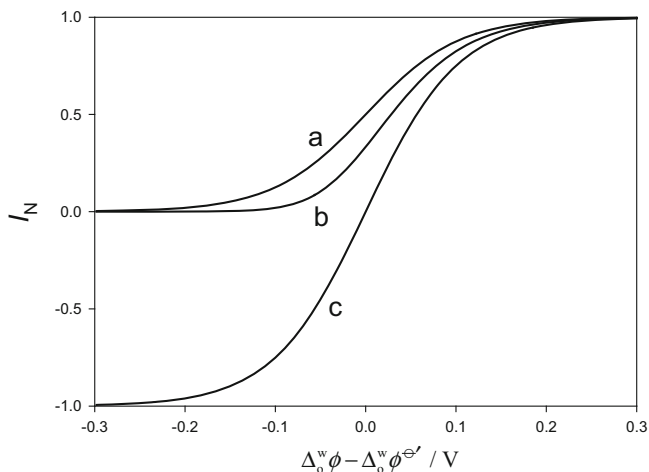


Fig. 2.6 Normalized current–potential curves corresponding to a heterogeneous redox reaction at a liquid/liquid interface calculated from Eqs. (2.102) and (2.103). The values of coefficients α , β , and γ are: (a) 0, 1, and 0; (b) 1, 1, and 0; (c) 1, 1, and 1

Finally, the current corresponds to the following root of Eq. (2.101):

$$I_N = \frac{[e^{\eta}(1 + \beta) + \alpha + \gamma] - \sqrt{[e^{\eta}(1 + \beta) + \alpha + \gamma]^2 - 4(e^{\eta} - 1)(e^{\eta}\beta - \alpha\gamma)}}{2(e^{\eta} - 1)} \quad (2.103)$$

Figure 2.6 plots the NPV response of a redox reaction at a liquid/liquid interface for different values of the ratio of concentrations α , β , and γ (see Eq. 2.102). As can be seen in these curves, the presence of the products of the redox reaction at the aqueous phase R_1 leads to a shift of the response toward more positive potentials (curve b), whereas the presence of species O_2 allows the attainment of negative currents for negative values of $\Delta_0^w\phi - \Delta_0^w\phi^{e'}$.

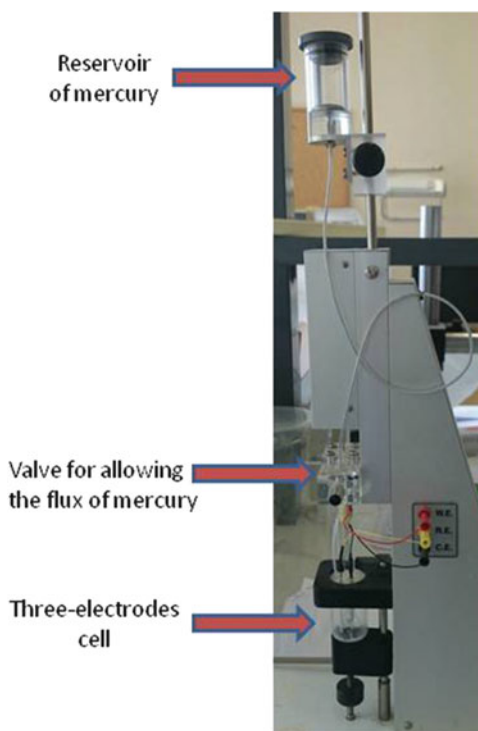
2.4 Dropping Mercury Electrode (DME)

Although nowadays the DME electrode is scarcely employed, it is of a great historical importance since it allowed the development of the first voltammetrical technique, Polarography, designed by Jaroslav Heyrovský (Fig. 2.7). A DME consists of a glass capillary of 0.05–0.1 mm of internal diameter from which mercury flows forming spherical drops (see Fig. 2.8). This electrode has two characteristic parameters: the flow rate m (mass of mercury per unit of time) and the drop life time t_1 . By assuming that the electrode has spherical shape at any

Fig. 2.7 A portrait of Jaroslav Heyrovský, Nobel Prize for Chemistry in 1959 “for his discovery and development of the polarographic methods of analysis.” Source: archiv ÚFCH J. Heyrovského AV ČR, v.v.i. <http://www.jh-inst.cas.cz>



Fig. 2.8 A schematic view of a Dropping Mercury Electrode



moment, the radius and the area of the drop at any instant during its growth are (see Chap. 2 of [3]):

$$r_{\text{DME}} = \left(\frac{3mt}{4\pi\rho} \right)^{1/3} \quad (2.104)$$

$$A(t) = 4\pi r_{\text{DME}}^2 = 4\pi \left(\frac{3mt}{4\pi \times 13.6} \right)^{2/3} = 0.85m^{2/3}t^{2/3} \quad (2.105)$$

with $0 \leq t \leq t_1$, ρ being the mercury density in g cm^{-3} , m being expressed in g s^{-1} , t in s, and the area in cm^2 .

The DME presents special features derived from its homogeneous and isotropic drops, small size, and periodical renewed surface so that the current on each drop rises from zero to its maximum value toward the end of the drop life. Moreover, it is well known that mercury has the highest overpotential for hydrogen evolution, which enables polarization of the electrode to very negative potentials.

Two different ways of operating with a DME will be described in this section. In the first, called “dc Polarography” (dcP), the potential step is applied from the beginning of the drop life with electrolysis taking place during the whole drop life. The other way consists of applying a potential pulse only at the end of the drop life for a short time called pulse time (1–200 ms), after which the potential returns to the initial value. This last technique is called Normal Pulse Polarography (NPP). In the first technique, the voltage varies linearly with time very slowly from an initial value, so it can be considered almost constant for each drop during the whole drop life. The polarographic potential–current curve presents regular oscillations due to the repetitive drop growth and fall. This feature prompted the application of dumping systems, and thus most of the theoretical expressions have been derived for mean currents. As will be seen below, for reversible electrode processes, the instantaneous current during a single drop varies with $t^{1/6}$ following an “Ilkovičian” behavior.

2.4.1 dc Polarography

Theoretically, the modeling of the electrochemical response corresponding to the application of a constant potential to a single drop presents an additional complication over stationary electrodes due to the convection caused by the growth of the mercury drop toward the solution. Under these conditions the temporal variation of the concentration of electroactive species is related both to the diffusion component and to convection. This problem was solved by Koutecký by using the expanding sphere electrode model (see Eq. 2.119), although the first model that treated this electrode was proposed by Ilkovič [32], and is known as the “expanding plane” model, and assumes linear diffusion in the way,

$$\frac{\partial c_i}{\partial t} = D_i \frac{\partial^2 c_i}{\partial x^2} - v_x \frac{\partial c_i}{\partial x} \quad i = \text{O, R} \quad (2.106)$$

with the term $v_x \partial c_i / \partial x$ being related to the convection through the velocity of the solution, v_x (see Sect. 1.8.3). The basic assumption of the model is that the growth of the drop can be described as the movement of an expanding plane toward the solution, so the convection velocity would be only observed in the normal direction to the plane, v_x . Its expression is $v_x = -2x/3t$, such that the mass transport equation becomes [3, 32–34]:

$$\frac{\partial c_i}{\partial t} = D_i \frac{\partial^2 c_i}{\partial x^2} + \frac{2x}{3t} \frac{\partial c_i}{\partial x} \quad i = \text{O, R} \quad (2.107)$$

The applicability of this model is restricted to longer times, i.e., drops of large radius ($r_{\text{DME}} \geq 0.05$ cm for $t = 1$ s). Although this equation is logically more complex than that corresponding to stationary planar electrodes, it can be easily solved in a similar way to that described in Sect. 2.2 (Eqs. 2.8–2.19) by making the following variable change:

$$s_i^{\text{DME}} = \sqrt{\frac{7}{3}} \frac{x}{2\sqrt{D_i t}} = \sqrt{\frac{7}{3}} s_i^{\text{p}} \quad i = \text{O, R} \quad (2.108)$$

By including this new variable in the differential equation system (2.107) and in the initial and limiting conditions, these are transformed into a one-variable problem (s_i^{DME}) of identical form to that given by Eqs. (2.9)–(2.12) for static planar electrodes; that is, c_{O} and c_{R} can be expressed as functions of only one variable, $s_{\text{O}}^{\text{DME}}$ and $s_{\text{R}}^{\text{DME}}$, respectively. Thus, by following the same procedure indicated by Eqs. (2.13)–(2.18), one obtains expressions for the concentration profiles:

$$\left. \begin{aligned} c_{\text{O}}(x, t) &= c_{\text{O}}(s_{\text{O}}^{\text{DME}}) = c_{\text{O}}^* + (c_{\text{O}}^{\text{s,r}} - c_{\text{O}}^*) \operatorname{erfc}(s_{\text{O}}^{\text{DME}}) \\ c_{\text{R}}(x, t) &= c_{\text{R}}(s_{\text{R}}^{\text{DME}}) = c_{\text{R}}^* + (c_{\text{R}}^{\text{s,r}} - c_{\text{R}}^*) \operatorname{erfc}(s_{\text{R}}^{\text{DME}}) \end{aligned} \right\} \quad (2.109)$$

As can be seen, these expressions are formally identical to those deduced for a planar electrode (compare Eqs. (2.109) and (2.19)), with the only difference being the definition of the dimensionless variable: s_i^{p} for planar electrodes and s_i^{DME} for DME. Under these conditions, surface concentrations are also given by Eq. (2.20) and condition (2.22) is also fulfilled.

According to Fick's law the current is

$$I_{\text{dcP}}^{\text{DME}} = FA(t)D_{\text{O}} \left(\frac{\partial c_{\text{O}}}{\partial x} \right)_{x=0} = -FA(t)D_{\text{R}} \left(\frac{\partial c_{\text{R}}}{\partial x} \right)_{x=0} \quad (2.110)$$

with $A(t)$ given by Eq. (2.105). Inserting Eq. (2.109) in Eq. (2.110), gives the following expression for the current:

$$I_{\text{dcP}}^{\text{DME}} = FA(t)D_{\text{O}}\sqrt{\frac{7}{3\pi D_{\text{O}}t}}(c_{\text{O}}^* - c_{\text{O}}^{\text{s,r}}) = -FA(t)D_{\text{R}}\sqrt{\frac{7}{3\pi D_{\text{R}}t}}(c_{\text{R}}^* - c_{\text{R}}^{\text{s,r}}) \quad (2.111)$$

with $c_{\text{O}}^{\text{s,r}}$ and $c_{\text{R}}^{\text{s,r}}$ being the surface concentrations deduced for a plane electrode given by Eq. (2.20).

From Eq. (2.105), (2.111) can be written as

$$\begin{aligned} I_{\text{dcP}}^{\text{DME}} &= 4\pi\left(\frac{3m}{4\pi\rho}\right)^{2/3}FD_{\text{O}}t^{2/3}\sqrt{\frac{7}{3\pi D_{\text{O}}t}}(c_{\text{O}}^* - c_{\text{O}}^{\text{s,r}}) = \\ &= -4\pi\left(\frac{3m}{4\pi\rho}\right)^{2/3}FD_{\text{R}}t^{2/3}\sqrt{\frac{7}{3\pi D_{\text{R}}t}}(c_{\text{R}}^* - c_{\text{R}}^{\text{s,r}}) \end{aligned} \quad (2.112)$$

and on inserting Eq. (2.20) in (2.112),

$$I_{\text{dcP}}^{\text{DME}} = 4\pi\left(\frac{3m}{4\pi\rho}\right)^{2/3}FD_{\text{O}}t^{1/6}\sqrt{\frac{7}{3\pi D_{\text{O}}}}\frac{(c_{\text{O}}^* - c_{\text{R}}^*e^{\eta})}{1 + \gamma e^{\eta}} \quad (2.113)$$

If we consider that the current I is in A, the concentrations c_i^* are in mol cm^{-3} , the diffusion coefficient D_{O} is in $\text{cm}^2 \text{s}^{-1}$, the mercury density ρ in g cm^{-3} , the mercury flow m in g s^{-1} , and time t in s, Eq. (2.113) becomes

$$I_{\text{dcP}}^{\text{DME}} = 0.732FD_{\text{O}}^{1/2}m^{2/3}\frac{(c_{\text{O}}^* - c_{\text{R}}^*e^{\eta})}{1 + \gamma e^{\eta}}t^{1/6} \quad (2.114)$$

From this equation, cathodic and anodic limits are deduced by making $e^{\eta} \rightarrow 0$ and $e^{\eta} \rightarrow \infty$, respectively, giving rise to the well-known Ilkovič equations [32–34]:

$$\left. \begin{aligned} I_{\text{d,c}}^{\text{DME}} &= 0.732FD_{\text{O}}^{1/2}m^{2/3}c_{\text{O}}^*t^{1/6} \\ I_{\text{d,a}}^{\text{DME}} &= -0.732FD_{\text{R}}^{1/2}m^{2/3}c_{\text{R}}^*t^{1/6} \end{aligned} \right\} \quad (2.115)$$

Figure 2.9 plots the time variation of the limiting current $I_{\text{d,c}}^{\text{DME}}$ given by the Eq. (2.115) for five drops. As can be seen in this Figure, the current increases with time until $t = t_1$ when the drop falls and, logically, the current also falls to zero.

Note that for the DME it is fulfilled that

$$\frac{I_{\text{dcP}}^{\text{DME}}}{I_{\text{d,c}}^{\text{DME}}} = \frac{(1 - (c_{\text{R}}^*/c_{\text{O}}^*)e^{\eta})}{1 + \gamma e^{\eta}} \quad (2.116)$$

which can be rewritten as

$$E = E_{1/2}^{\text{r}} + \frac{RT}{F} \ln \left(\frac{I_{\text{d,c}}^{\text{DME}} - I_{\text{dcP}}^{\text{DME}}}{I_{\text{dcP}}^{\text{DME}} - I_{\text{d,a}}^{\text{DME}}} \right) \quad (2.117)$$

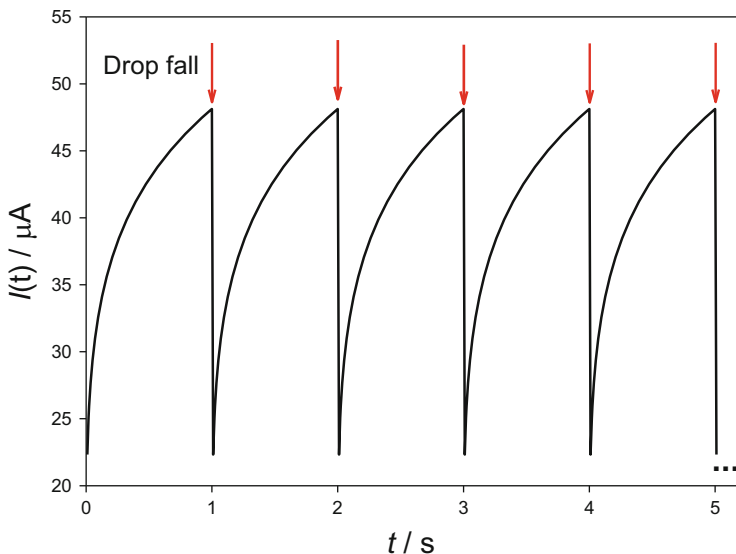


Fig. 2.9 Current–time curves for a DME calculated from Eq. (2.115). $m = 0.1 \text{ g s}^{-1}$, $D_{\text{O}} = 10^{-5} \text{ cm}^2 \text{ s}^{-1}$, $t_1 = 1 \text{ s}$, $c_{\text{O}}^* = 1 \text{ mM}$

Observe that Eqs. (2.116) and (2.117) are identical to (2.27), (2.28) and (2.31) deduced for planar electrodes.

From Eq. (2.111), it can be deduced that the Nernst diffusion layer for a DME is

$$\delta_{\text{DME},i}^r = \sqrt{\frac{3}{7}\pi D_i t} = \sqrt{\frac{3}{7}} \delta_{\text{p},i}^r \quad i = \text{O, R} \quad (2.118)$$

By using the expanding sphere electrode model for the DME, Koutecký obtained the following expression for the instantaneous limiting current [35–37]:

$$I_{\text{dcP}}^{\text{DME}} = 0.732FD_{\text{O}}^{1/2}m^{2/3}c_{\text{O}}^*t^{1/6} \left\{ 1 + 3.9 \frac{D_{\text{O}}^{1/2}t^{1/6}}{m^{1/3}} + 1.5 \left(\frac{D_{\text{O}}^{1/2}t^{1/6}}{m^{1/3}} \right)^2 + \dots \right\} \quad (2.119)$$

2.4.2 Normal Pulse Polarography (NPP)

In this technique, the DME is kept at an initial potential E_1 during a time t_1 at which the electrode reaction cannot occur and then it is polarized by a potential pulse of increasing amplitude, E_2 . The measurement of the current during a short pulse time t_2 at the end of the drop life confers important advantages on NPP over dcP in relation to the elimination of double-layer effects. In any case, this technique is actually a single potential step technique in which the perturbation shown in

Scheme 2.1 is applied to the DME for a very short time interval, t_2 , before which the electrode has an area proportional to $t_1^{2/3}$.

The differential diffusion equations system to solve when a potential pulse E is applied and the corresponding boundary value problem (bvp) when the expanding plane model for the DME is considered are:

$$\frac{\partial c_i}{\partial t_2} = D_i \frac{\partial^2 c_i}{\partial x^2} + \frac{2x}{3(t_1 + t_2)} \frac{\partial c_i}{\partial x} \quad i = \text{O and R} \quad (2.120)$$

$$\left. \begin{array}{l} t_2 \geq 0, \quad x \rightarrow \infty \\ t_2 = 0, \quad x \geq 0 \end{array} \right\} c_{\text{O}} = c_{\text{O}}^*, \quad c_{\text{R}} = c_{\text{R}}^* \quad (2.121)$$

$$t_2 > 0, \quad x \geq 0$$

$$D_{\text{O}} \left(\frac{\partial c_{\text{O}}}{\partial x} \right)_{x=0} = -D_{\text{R}} \left(\frac{\partial c_{\text{R}}}{\partial x} \right)_{x=0} \quad (2.122)$$

$$c_{\text{O}}^{\text{s,r}} = e^{\eta} c_{\text{R}}^{\text{s,r}} \quad (2.123)$$

where t_1 is the constant time previous to the application of the potential pulse and t_2 the variable pulse time, the total time drop life is $t = t_1 + t_2$, and $c_{\text{O}}^{\text{s,r}}$ and $c_{\text{R}}^{\text{s,r}}$ are the surface concentrations deduced for a plane electrode given by Eqs. (2.20).

This problem was addressed by Brikmann and Loss [38] and solved later by Galvez and Serna [39]. More recently, a compact expression as a function of the ratio (t_2/t) for the pulse polarographic wave when the two species are initially present in the solution was obtained [40, 41]. Under these conditions, the current can be expressed as

$$I_{\text{NPP}}^{\text{DME}} = FA(t) \frac{(c_{\text{O}}^* - c_{\text{R}}^* e^{\eta})}{1 + \gamma e^{\eta}} \sqrt{\frac{D_{\text{O}}}{\pi t_2}} h(\alpha) \quad (2.124)$$

with

$$\left. \begin{array}{l} h(\alpha) = \sqrt{\frac{(7/3)\alpha}{1 - (1 - \alpha)^{(7/3)}}} \\ \alpha = \frac{t_2}{t_1 + t_2} \end{array} \right\} \quad (2.125)$$

Note that if $t_1 \rightarrow 0$ (i.e., $t_2 \rightarrow t$ and $\alpha \rightarrow 1$), $h(\alpha) \rightarrow \sqrt{7/3}$ such that Eq. (2.124) presents an ilkovičian behavior (see 2.114):

$$\begin{aligned} I_{\text{NPP}}^{\text{DME}}(t_1 \rightarrow 0) &= FA_0 t^{2/3} \frac{(c_{\text{O}}^* - c_{\text{R}}^* e^{\eta})}{1 + \gamma e^{\eta}} \sqrt{\frac{D_{\text{O}}}{\pi t}} \sqrt{\frac{7}{3}} \\ &= FA_0 \sqrt{\frac{7D_{\text{O}}}{3\pi}} t^{1/6} \frac{(c_{\text{O}}^* - c_{\text{R}}^* e^{\eta})}{1 + \gamma e^{\eta}} \end{aligned} \quad (2.126)$$

where $A_0 = 4\pi(3m/(4\pi\rho))^{2/3}$.

On the other hand, if $t_2 \ll t_1$ (i.e., $\alpha \rightarrow 0$), $h \rightarrow 1$, Eq. (2.124) transforms into

$$I_{\text{NPP}}^{\text{DME}}(t_2 \ll t_1) = FA \frac{(c_{\text{O}}^* - c_{\text{R}}^* e^{\eta})}{1 + \gamma e^{\eta}} \sqrt{\frac{D_{\text{O}}}{\pi t_2}} \quad (2.127)$$

with $A = A_0 t_1^{2/3}$ being constant. The above equation is simply the current–potential relationship corresponding to a planar electrode with the potential pulse time being t_2 (see Eq. 2.27). Therefore, it presents a cotrellian behavior.

In all the above cases, it is possible to rewrite the current–potential expression as

$$E = E_{1/2}^r + \frac{RT}{F} \ln \left(\frac{I_{\text{d,c}} - I_{\text{NPP}}^{\text{DME}}}{I_{\text{NPP}}^{\text{DME}} - I_{\text{d,a}}} \right) \quad (2.128)$$

which is identical to that obtained in a static planar electrode (see Eq. 2.31).

The sensitivity of NPP is greater than that of dcP because the ratio $I_{\text{NPP}}^{\text{DME}}/I_{\text{dcP}}^{\text{DME}} \cong (3t/7t_2)^{1/2}$ is much greater than unity, provided that $t \gg t_2$. Moreover, the pulse current greatly exceeds the charging current as compared to dc current, since the charging current for a DME is given by [1–3]:

$$I_{\text{c}}^{\text{DME}} = 0.567 C_i (E_{\text{PZC}} - E) m^{2/3} t^{-2/3} \propto t^{-2/3} \quad (2.129)$$

where C_i is the integral capacity and E_{PZC} is the potential of zero charge (see Sect. 1.6). Note that C_i is given in F cm^{-1} , m in g s^{-1} , E in V, and the current I_{c} in A. So, for NPP it is fulfilled that

$$I_{\text{NPP}}^{\text{DME}} + I_{\text{c}}^{\text{DME}} \propto t^{-1/2} + t^{-2/3} \cong t^{-1/2} \quad (2.130)$$

The NPP current–potential curves calculated from Eq. (2.124) for $t_1 = 1$ s and different values of t_2 have been plotted in Fig. 2.10. As can be seen from these curves, the decrease of the potential pulse time t_2 leads to an increase of the response (and therefore of its sensitivity), whereas it does not affect the location of the current–potential curve.

2.5 Spherical Electrodes

When the electrode does not have macrometric dimensions (i.e., for a radius smaller than 0.05 cm for a time of experiment of 1 s), the geometry becomes fundamental. In this section, special detail will be paid to spherical geometry. The use of spherical electrodes such that the Static Mercury Drop Electrode (SMDE) offers important advantages over solid electrodes on account of its smooth and

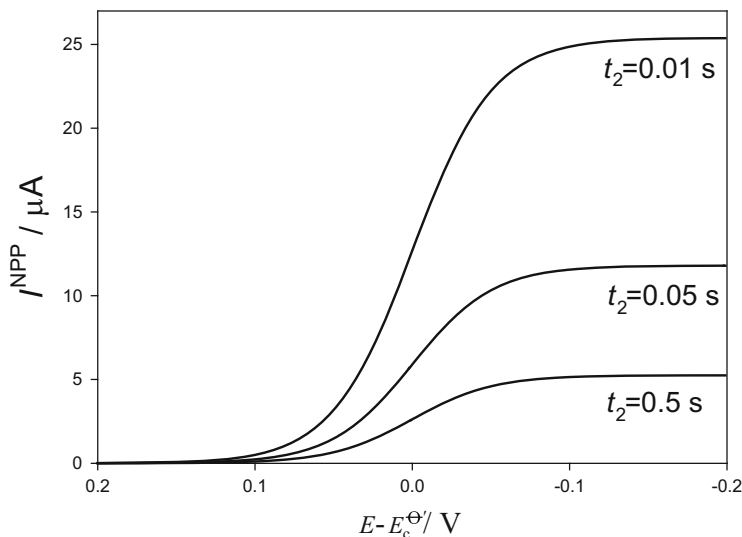


Fig. 2.10 NPP current–potential curves calculated from Eq. (2.124) for a DME with $m = 0.1 \text{ g s}^{-1}$, $D_{\text{O}} = D_{\text{R}} = 10^{-5} \text{ cm}^2 \text{ s}^{-1}$, $c_{\text{O}}^* = 1 \text{ mM}$, $c_{\text{R}}^* = 0$, $t_1 = 1 \text{ s}$, and different values of t_2 indicated in the figure

homogeneous surface and because of the large hydrogen overpotential. This electrode is extensively used in Stripping Analysis by preconcentration of the metal into the small volume of the mercury electrode by cathodic deposition at controlled time and potential [42, 43]. Nowadays gold spherical electrodes and microelectrodes are also widely used [44, 45]. Moreover, the electrode potential can be used to induce uptake or release of species in individual spherical droplets or arrays of droplets and in the monitorization of processes in and around biological cells. In all these examples, the spherical geometry plays an important role [46, 47].

In this section, it will be highlighted that, for nonplanar geometry, finding analytical solutions when the diffusion coefficients of oxidized and reduced species are different is much more complicated than in the planar case, since under these conditions the surface concentrations are time dependent even for reversible processes. However, this situation is of great interest when the ion is transferred between two different phases as in the case of ion transfer between conventional solvents and liquid membranes, or in amalgamation processes. When room temperature ionic liquids (RTILs) are used as solvents, significant differences in the diffusion coefficients of oxidized and reduced species can be also found [48–50], since the electrostatic interactions of the solute with the solvent play an important role in its transport properties, so the different charge of the electroactive species has a significant influence on the magnitude of the diffusion coefficient [49, 51].

2.5.1 Unequal Diffusion Coefficients ($D_O \neq D_R$)

Under these conditions, the diffusion equations to solve are the following:

$$\left. \begin{aligned} \frac{\partial c_O}{\partial t} &= D_O \left(\frac{\partial^2 c_O}{\partial r^2} + \frac{2}{r} \frac{\partial c_O}{\partial r} \right) \\ \frac{\partial c_R}{\partial t} &= D_R \left(\frac{\partial^2 c_R}{\partial r^2} + \frac{2}{r} \frac{\partial c_R}{\partial r} \right) \end{aligned} \right\} \quad (2.131)$$

The boundary value problem (bvp) by considering that the reduced species is initially present in the solution (solution soluble product) or in the electrode (amalgam formation), and that diffusion coefficients of both species are different, is

$$\left. \begin{aligned} t &\geq 0, \quad r \rightarrow \infty \\ t &= 0, \quad r \geq r_s \end{aligned} \right\} \quad c_O = c_O^*, \quad c_R = c_R^* \quad (2.132)$$

for solution soluble product, and

$$\left. \begin{aligned} t &\geq 0, \quad r \rightarrow \infty \\ t &= 0, \quad r \geq r_s \end{aligned} \right\} \quad c_O = c_O^*, \quad c_R = 0 \quad (2.133)$$

$$\left. \begin{aligned} t &\geq 0, \quad r \rightarrow -\infty \\ t &= 0, \quad r \leq r_s \end{aligned} \right\} \quad c_O = 0, \quad c_R = c_R^* \quad (2.134)$$

for amalgam formation

$$t \geq 0, \quad r \geq r_s :$$

$$D_O \left(\frac{\partial c_O}{\partial r} \right)_{r=r_s} = \mp D_R \left(\frac{\partial c_R}{\partial r} \right)_{r=r_s} \quad (2.135)$$

$$c_O^{s, \text{sph}} = e^\eta c_R^{s, \text{sph}} \quad (2.136)$$

with η given by Eq. (2.6) and r_s being the radius of the spherical electrode. In the following and in Eq. (2.135), the upper sign refers to solution soluble product and the lower one to amalgam formation.

By following the procedure indicated in Appendix A, an analytical expression for the current can be deduced:

$$\frac{I^{\text{sph}}}{FA_s D_O c_O^*} = \left(\frac{1 - (c_R^*/c_O^*)e^\eta}{1 + \gamma e^\eta} \right) \left\{ \frac{1}{\sqrt{\pi D_O t}} + \frac{1}{r_s} - \frac{e^\eta \gamma (\gamma \mp 1)}{r_s (\gamma^2 e^\eta \pm 1)} + \frac{e^\eta (\gamma \mp 1)^2}{r_s (\gamma^2 e^\eta \pm 1) (1 + \gamma e^\eta)} H(\xi) \right\} \quad (2.137)$$

with

$$H(\xi) = e^{(\xi/2)^2} \operatorname{erfc}(\xi/2) \quad (2.138)$$

$$\xi = \frac{2\sqrt{D_R t}(\gamma^2 e^\eta \pm 1)}{r_s(1 + \gamma e^\eta)} \quad (2.139)$$

and the time-dependent surface concentrations $c_O^{s,\text{sph}}$ and $c_R^{s,\text{sph}}$ are

$$\left. \begin{aligned} c_O^{s,\text{sph}} &= c_O^{s,r} - \frac{e^\eta \gamma (\gamma \mp 1) (c_O^* - c_O^{s,r})}{(\gamma^2 e^\eta \pm 1)} [H(\xi) - 1] \\ c_R^{s,\text{sph}} &= c_R^{s,r} + \frac{(\gamma \mp 1) (c_R^* - c_R^{s,r})}{(\gamma^2 e^\eta \pm 1)} [H(\xi) - 1] \end{aligned} \right\} \quad (2.140)$$

$c_O^{s,r}$ and $c_R^{s,r}$ are the time-independent surface concentrations found in planar electrodes (Eq. 2.20), and $A_s = 4\pi r_s^2$.

Note that the finite electrode volume has not been considered to deduce Eq. (2.137), i.e., we have used the so-called Koutecký approximation (see Eq. (2.134) and [52]). Therefore, when amalgamation takes place, these equations with the lower sign cannot be used for very small spherical electrodes for which numerical treatments considering null flux at the center of the electrode are needed.

According to Eq. (2.140), the presence of amalgam has no effect on the voltammetric response of planar electrodes since, under these conditions $r_s \rightarrow \infty$ ($\xi \rightarrow 0$; see Eq. (2.139)) and $H(\xi) \rightarrow 1$ (see also Eq. 2.20).

To obtain Eqs. (2.137) and (2.140), the Dimensionless Parameter Method (DPM) has been used as described in Appendix A and expressions of the concentration profiles have been obtained [52]. In the 1960s, a compact analytical solution for the I - E response was obtained by using the Laplace transform method when the oxidized species was the only present in the electrolytic solution, i.e., for a cathodic wave [53, 54], and non-explicit expressions for the concentration profiles and surface concentrations were obtained.

The time variation of the surface concentration of the oxidized species for different values of γ at a potential corresponding to $E - E_c^{\ominus} = -0.05$ V can be seen in Fig. 2.11. It is clear that for the radii considered the surface concentrations of the oxidized species vary with time for $\gamma < 0.7$ and $\gamma > 1.41$, respectively, while remaining almost constant for other values of γ . It is also observed that the further γ is from the unity, the longer it takes to reach a constant value.

In Fig. 2.12, the analytical current-time curves under anodic and cathodic limiting current conditions calculated from Eq. (2.137) (Fig. 2.12a and b, respectively) when species R is soluble in the electrolytic solution (solid curves) and when species R is amalgamated in the electrode (dotted lines) are plotted. In Fig. 2.12a, the amalgamation effect on the anodic limiting current has been analyzed. As expected, when species R is soluble in the electrolytic solution, the absolute value of the current density increases when the electrode radius decreases because of the enhancement of

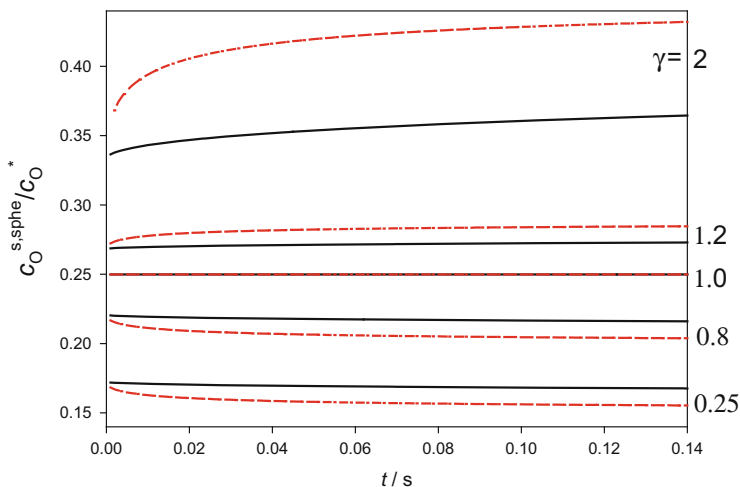


Fig. 2.11 Temporal evolution of the surface concentrations of oxidized species calculated from Eq. (2.140). Two electrode radius values are considered: $r_s = 5 \times 10^{-3}$ cm (solid curves) and $r_s = 5 \times 10^{-4}$ cm (dashed curves), and different γ values indicated in the figure. $E - E_c^{\ominus} = -0.05$ V, $c_O^* = c_R^* = 1$ mM, $D_O = 10^{-5}$ cm² s⁻¹

the diffusive mass transport. On the other hand, for a given electrode radius the amalgam formation leads to a decrease in the absolute value of the current density, and this decrease is more significant when the electrode radius becomes smaller and/or the electrolysis time is longer. Thus, the radius influence is inverted in relation to the solution soluble product case, so a decrease in electrode radius leads to a decrease in the absolute value of the current density (see Fig. 2.12a, dotted lines). This behavior is due to the diffusion of R taking place inside the spherical electrode. As expected, the cathodic limiting current (see Fig. 2.12b) is not influenced by the amalgam formation, since it is only dependent on the species O behavior.

The analytical equations obtained allow us to study the anodic–cathodic wave. The current–potential curves for $\gamma = 0.7$ are plotted in Fig. 2.13 for three values of the electrode radius and for two different initial conditions: when species O is the only one present (Fig. 2.13a), and when both species are present in the system (Fig. 2.13b).

In the first case, when only species O is initially present in the electrolytic solution (Fig. 2.13a), it is observed that the amalgamation of species R leads to a shift of the wave to more negative potential values, and this shift is greater the more spherical the electrode, i.e., when the duration of the experiment increases or the electrode radius decreases. In the second case (Fig. 2.13b), both species are initially present in the system so we can study the anodic–cathodic wave. In the anodic branch of the wave, the amalgamation produces a decrease in the absolute value of the current. As is to be expected, the null current potential, crossing potential, or equilibrium potential (E_{Eq}) is not affected by the diffusion rates (D_O and D_R), by the electrolysis time, by the electrode geometry (r_s), nor by the behavior of species R

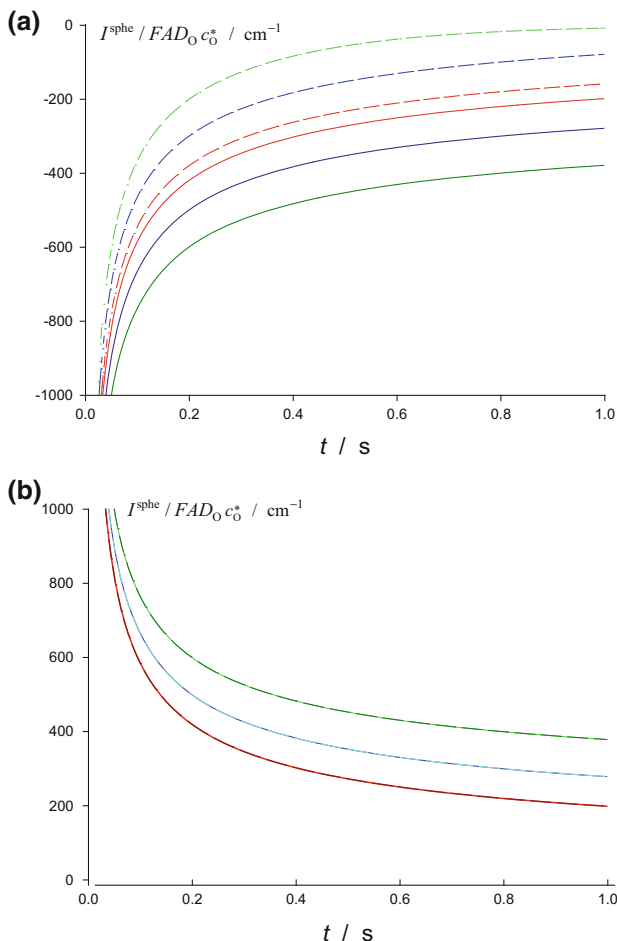


Fig. 2.12 Influence of the electrode radius on the current–time curves under anodic (a) and cathodic (b) limiting conditions (Eq. 2.137) when species R is soluble in the electrolytic solution (solid curves) and when it is amalgamated in the electrode (dashed curves). The electrode radius values (in cm) are: $r_s = 5 \times 10^{-2}$ (red curves), $r_s = 10^{-2}$ (blue curves), and $r_s = 5 \times 10^{-3}$ (green curves). $c_{\text{O}}^* = c_{\text{R}}^* = 1 \text{ mM}$, $D_{\text{O}} = D_{\text{R}} = 10^{-5} \text{ cm}^2 \text{ s}^{-1}$. (The dashed green curve has been calculated numerically for $t > 0.5 \text{ s}$). Reproduced with permission [52]

(soluble in the electrolytic solution or in the electrode) (see Eq. 2.33). On the other hand, the half-wave reversible potential is affected by the diffusional behavior of species O and R and the following is observed for a solution soluble product:

$$E_{1/2}^{\text{r}} \Big|_{\text{sphe}} \begin{cases} > \\ \approx \\ < \end{cases} E_{1/2}^{\text{r}} \Big|_{\text{plane}} \quad \text{if} \quad \gamma \begin{cases} < \\ \approx \\ > \end{cases} 1 \quad (2.141)$$

Note that in this case the determination of the half-wave potential can be made by fitting experimental data to the Eq. (2.137) since Eq. (2.31) is not fulfilled under

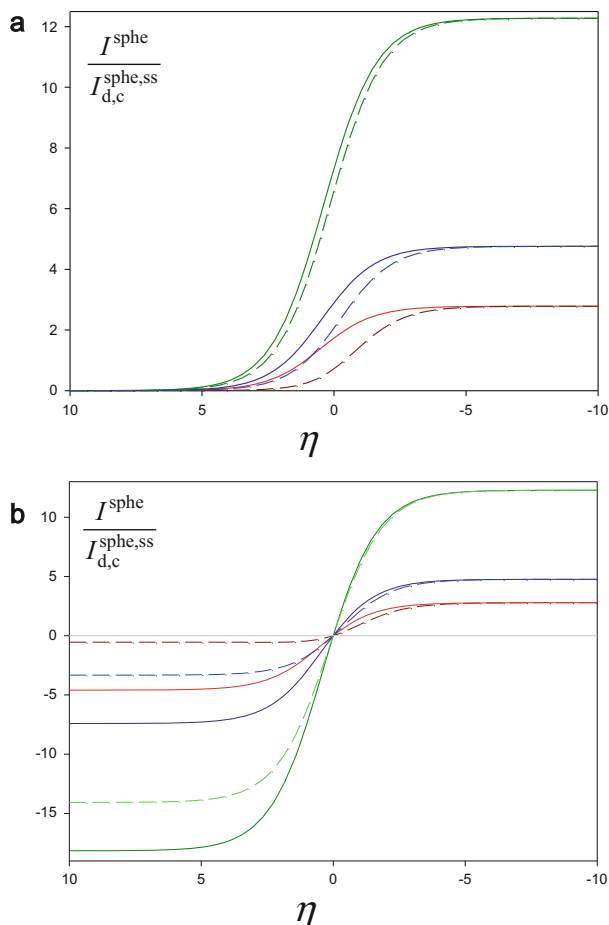


Fig. 2.13 Influence of the c_R^*/c_O^* ratio on the anodic–cathodic waves when species R is soluble in the electrolytic solution (*solid curves*) (Eq. (2.137) considering the upper sign) and when it is amalgamated in the electrode (*dotted curves*) (Eq. (2.137) considering the lower sign). $I_{d,c}^{sphe,ss} = FA_s D_O c_O^*/r_s$ (see Eq. 2.148). Three electrode sphericity values ($\sqrt{D_R t}/r_s$) are considered: 0.071 (*green curves*), 0.214 (*blue curves*), and 0.451 (*red curves*), and two different initial concentration ratios: $c_O^* = 1 \text{ mM}$, $c_R^* = 0$ (**a**), $c_O^* = c_R^* = 1 \text{ mM}$ (**b**). $D_O = 10^{-5} \text{ cm}^2 \text{ s}^{-1}$, $\gamma = 0.7$. Reproduced with permission [52]

these conditions and the plots E vs. $\ln\left(\left(I_{d,c}^{sphe} - I^{sphe}\right)/\left(I^{sphe} - I_{d,a}^{sphe}\right)\right)$ cannot be used as in the case of planar electrodes. This is because under the above conditions the current presents a complex expression which cannot be written as the product of a function of the potential by a function of time, as in the case of the electrodes mentioned above.

2.5.2 Equal Diffusion Coefficients ($D_O = D_R$)

When both diffusion coefficients are equal ($D_O = D_R = D$), and both species are soluble in the electrolytic solution (taking only the upper sign in Eq. (2.135)), Eqs. (2.137) and (2.140) drastically simplify to the following [1–4, 40, 41, 55, 56]:

$$\frac{I^{\text{sphc}}}{FA_s D c_O^*} = \left(\frac{1 - (c_R^*/c_O^*)e^\eta}{1 + e^\eta} \right) \left\{ \frac{1}{\sqrt{\pi D t}} + \frac{1}{r_s} \right\} \quad (2.142)$$

$$\left. \begin{aligned} c_O^{\text{s, sphc}} \Big|_{\gamma=1} &= c_O^{\text{s, r}} \Big|_{\gamma=1} = \frac{e^\eta (c_O^* + c_R^*)}{1 + e^\eta} \\ c_R^{\text{s, sphc}} \Big|_{\gamma=1} &= c_R^{\text{s, r}} \Big|_{\gamma=1} = \frac{c_O^* + c_R^*}{1 + e^\eta} \end{aligned} \right\} \quad (2.143)$$

and the concentration profiles are given by the following equations:

$$\left. \begin{aligned} c_O(r, t) &= c_O^* + \frac{r_s}{r} (c_O^{\text{s, r}} - c_O^*) \operatorname{erfc} \left(\frac{r - r_s}{2\sqrt{Dt}} \right) \\ c_R(r, t) &= c_R^* + \frac{r_s}{r} (c_R^{\text{s, r}} - c_R^*) \operatorname{erfc} \left(\frac{r - r_s}{2\sqrt{Dt}} \right) \end{aligned} \right\} \quad (2.144)$$

Appendix B describes in detail the solution of this problem as an application of the Laplace's Transform method and Eqs. (2.142)–(2.144) have also been deduced.

As can be inferred from Eq. (2.143), under these conditions the surface concentrations of both species are time independent, so the current given by Eq. (2.142) can be written as

$$\begin{aligned} I^{\text{sphc}} &= FA_s D_O (c_O^* - c_O^{\text{s, r}}) \left\{ \frac{1}{\sqrt{\pi D t}} + \frac{1}{r_s} \right\} \\ &= -FA_s D_R (c_R^* - c_R^{\text{s, r}}) \left\{ \frac{1}{\sqrt{\pi D t}} + \frac{1}{r_s} \right\} \end{aligned} \quad (2.145)$$

From Eq. (2.145), it is clear that the diffusion layer thickness in spherical diffusion is (compare Eqs. (2.145) and (2.26)) [12],

$$\delta_{\text{sphc}}^r = \frac{1}{\left\{ \frac{1}{\sqrt{\pi D t}} + \frac{1}{r_s} \right\}} \quad (2.146)$$

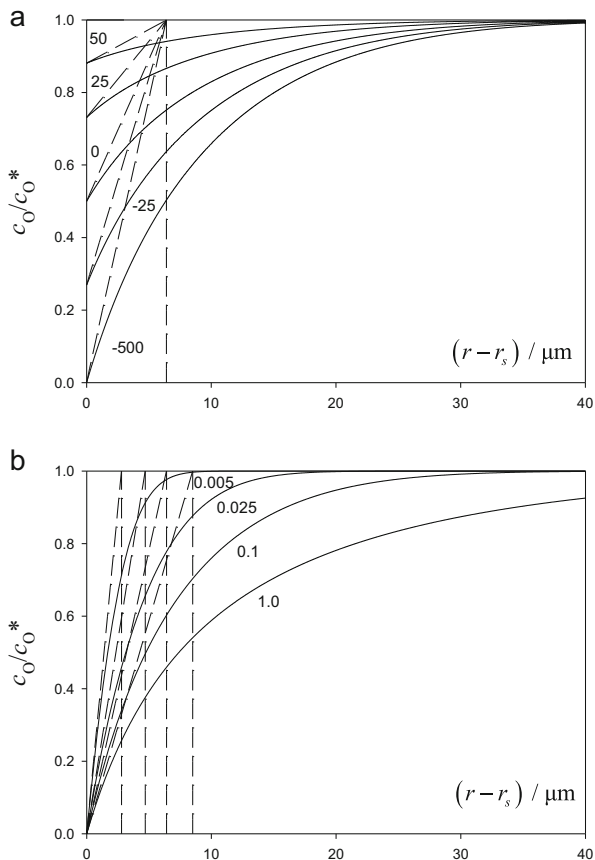
which is independent of the applied potential, as in the case of planar diffusion.

In Fig. 2.14 we have plotted the transient accurate concentration profiles for species O, $c_O(r, t)$ (Eq. 2.144) and the linear concentration profiles $\left(c_O(r, t) = \frac{c_O^* - c_O^{\text{s, r}}}{\delta_{\text{sphc}}^r} (r - r_s) + c_O^{\text{s, r}} \right)$ at a fixed time and different potentials (Fig. 2.14a), and at a fixed potential and different times (Fig. 2.14b).

Fig. 2.14 Concentration profiles of a spherical electrode for the application of a potential pulse for different values of

$(E - E_c^{\phi'})$ (in mV) for a fixed time (a), and different values of time (in s) for a fixed potential (b), shown in the curves. $D_O = D_R = D$. The electrode radius is $10 \mu\text{m}$. Dashed lines correspond to their linear concentration profiles.

$t = 0.1 \text{ s}$ (a) and $(E - E_c^{\phi'}) = -500 \text{ mV}$ (b). Reproduced with permission [12]



When compared with the linear concentration profiles of Fig. 2.1a, it can be observed that, in agreement with Eq. (2.146) for spherical electrodes, the Nernst diffusion layer is, under these conditions, independent of the potential in all the cases. As for the time dependence of the profiles shown in Fig. 2.14b, it can be seen that the Nernst diffusion layer becomes more similar to the electrode size at larger times. Analogous behavior can be observed when the electrode radius decreases.

Expressions for the cathodic and anodic limiting currents can also be easily obtained for spherical electrodes by making $e^{\eta} \rightarrow 0$ and $e^{\eta} \rightarrow \infty$ in Eq. (2.142),

$$\left. \begin{aligned} I_{d,c}^{\text{sph}} &= FA_s D c_O^* \left(\frac{1}{\sqrt{\pi D t}} + \frac{1}{r_s} \right) \\ I_{d,a}^{\text{sph}} &= -FA_s D c_R^* \left(\frac{1}{\sqrt{\pi D t}} + \frac{1}{r_s} \right) \end{aligned} \right\} \quad (2.147)$$

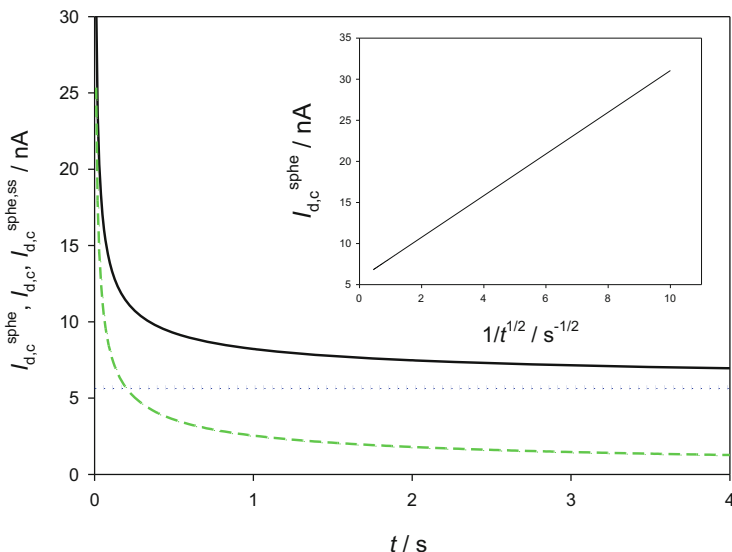


Fig. 2.15 (Solid line) Current–time curves for the application of a constant potential to a spherical electrode calculated from Eq. (2.142). $D_O = D_R = 10^{-5} \text{ cm}^2 \text{ s}^{-1}$, $c_O^* = c_R^* = 1 \text{ mM}$, $r_s = 0.001 \text{ cm}$, $(E - E_c^{\ominus}) = -0.2 \text{ V}$, $T = 298 \text{ K}$. (Dashed line) Current–time curves for the application of a constant potential to a planar electrode of the same area as the spherical one calculated from Eq. (2.28). (Dotted line) Steady-state limiting current for a spherical electrode calculated from Eq. (2.148). The inner figure corresponds to the plot of the current of the spherical electrode versus $1/\sqrt{t}$

The time evolution of the cathodic limiting current (Eq. 2.147) has been plotted in Fig. 2.15 together with that obtained for a planar electrode (Eq. 2.28) and the constant steady-state limiting current for a spherical electrode given by

$$I_{d,c}^{\text{sphe,ss}} = FA_s D c_O^* \frac{1}{r_s} \quad (2.148)$$

From this figure, it can be seen that the current decays with time as in the planar case although this decrease leads to a constant value, $I_{d,c}^{\text{sphe,ss}}$, different from zero, which will be achieved sooner as the electrode radius diminishes. The current for times close to zero is identical to that obtained in a planar electrode given to the prevalence of the term $1/\sqrt{\pi D t}$ over the inverse of the radius. For longer times, the opposite happens and the term $1/r_s$ is dominant.

In order to obtain values for the diffusion coefficient at spherical electrodes, a logarithmic plot of the current versus time would lead to nonlinear dependence (see Eq. 2.147). In this case a plot of the current versus $1/\sqrt{t}$ is more appropriate (see inner curve in Fig. 2.15) and this plot also allows the determination of the electrode radius by combining the values of the slope ($FA_s c_O^* \sqrt{D/\pi}$) and intercept ($FA_s D c_O^*/r_s$).

Finally, from Eq. (2.145), it is clear that the half-wave potential, which under these conditions ($D_O = D_R$) coincides with the formal potential E_c^{\ominus} , can be easily

obtained from the linear analysis of the potential versus $\ln\left(\left(I_{d,c}^{\text{sphc}} - I^{\text{sphc}}\right)/\left(I^{\text{sphc}} - I_{d,a}^{\text{sphc}}\right)\right)$ curves like in the case of a planar electrode or a DME with the expanding plane model since, as in these cases, the current presents the potential and time dependences in separate terms.

2.6 Other Electrodes Geometries

This section addresses other electrode geometries, both uniformly accessible (like cylindrical electrodes) and non-uniformly accessible (like discs and bands) (see Scheme 2.4). Cylindrical electrodes are the best example of electrodes where one dimension (the radius) is much smaller than the other (the length). Under these conditions, edge effects on the current can be considered as negligible and diffusion is mainly radial and therefore only dependent on the distance r to the center of the cylinder [10]. In relation with disc and band electrodes, it is important to highlight that the mass transport of species in solution requires a much more complex mathematical treatment due to their nonuniform accessibility. The theoretical modeling of the mass transport at these electrodes shows that the current is an average quantity resulting from an average mass flux over the electrode surface [10, 57, 58]. Hence, in the case of disc electrodes, depending on the electrode size, the current will be the result of mixed mass transport, with a predominant component that could change from linear (large sizes or short times) to radial (small sizes or long times). This nonuniform accessibility leads to more efficient mass transport to the electrode edge and to a shielding effect of this at the center of the electrode (see Fig. 2.16). Even so, this electrode remains the most popular and practical due to its easy manufacture in a wide range of sizes, and the easy and controlled cleaning of its surface [58, 59].

For the sake of simplicity only electrode processes in which the oxidized and reduced species are soluble in the electrolytic solution and have equal diffusion coefficients will be considered.

Under these conditions, the differential equation systems for the diffusion mass transport of species O and R is given by

$$\left. \begin{aligned} \frac{\partial c_O}{\partial t} &= D\nabla^2 c_O \\ \frac{\partial c_R}{\partial t} &= D\nabla^2 c_R \end{aligned} \right\} \quad (2.149)$$

where ∇^2 is the Laplacian operator given by any equation of Table 2.2. When the flux is conserved in the electrode surface, the following solution for the sum of concentrations of species O and R is obtained (see Appendix in reference [60]):

$$c_O(q, t) + c_R(q, t) = c_O^* + c_R^* \quad (2.150)$$

Scheme 2.4 Most common electrode and microelectrode geometries and their diffusion fields

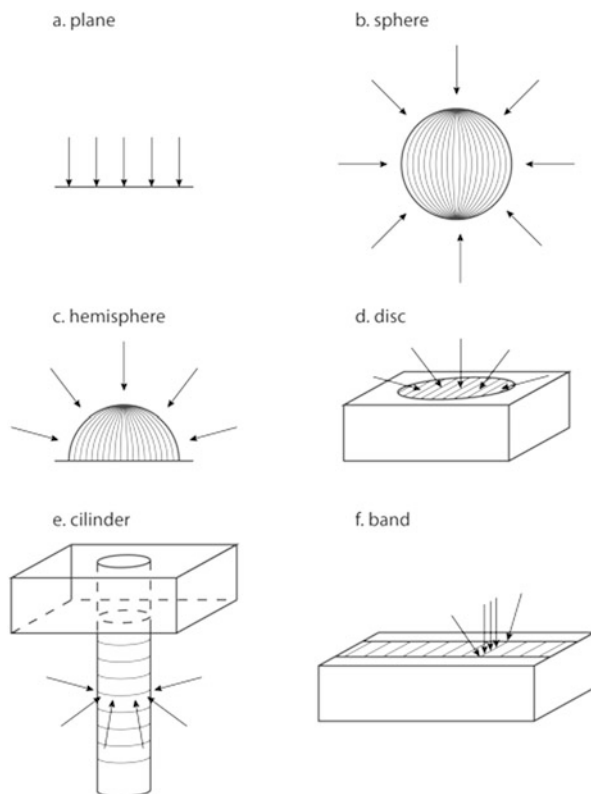


Fig. 2.16 Evolution of the normalized flux at $z = 0$, $J_N = (\partial c_i / \partial z)_{z=0} / (2c_i^* / \pi r_d)$ versus (r/r_d) for a disc electrode calculated from Eq. (C.18) of Appendix C (see Scheme 2.5)

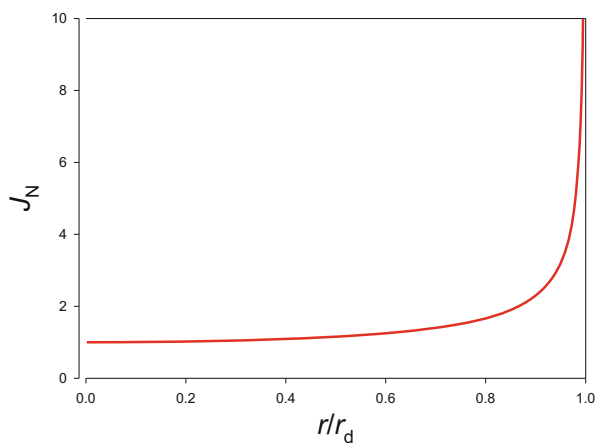


Table 2.2 Expressions for the diffusion mass transport operators given by Fick's second law

Electrode geometry	Laplacian operator ∇^2
Planar	$\left(\frac{\partial^2}{\partial x^2}\right)$
Spherical	$\left(\frac{\partial^2}{\partial r^2} + \frac{2}{r} \frac{\partial}{\partial r}\right)$
Cylindrical	$\left(\frac{\partial^2}{\partial r^2} + \frac{1}{r} \frac{\partial}{\partial r}\right)$
Band	$\left(\frac{\partial^2}{\partial x^2} + \frac{\partial^2}{\partial z^2}\right)$
Disc	$\left(\frac{\partial^2}{\partial r^2} + \frac{1}{r} \frac{\partial}{\partial r} + \frac{\partial^2}{\partial z^2}\right)$

with q and t referring to spatial coordinates and time values, respectively. Equation (2.150) is, of course, fulfilled at the electrode surface, i.e., for $q = q^s$, with q^s being the coordinates at the surface of the electrode.⁵ For nernstian processes, at q^s :

$$c_{\text{O}}^{s,r} = e^{\eta} c_{\text{R}}^{s,r} \quad (2.151)$$

The combination of Eqs. (2.150) and (2.151) transforms the problem of two variables c_{O} and c_{R} into two separate problems of only one variable with constant surface conditions,

$$\left. \begin{array}{l} \frac{\partial c_{\text{O}}}{\partial t} = D \nabla^2 c_{\text{O}} \\ \left. \begin{array}{l} t \geq 0, q \rightarrow \infty \\ t = 0, q \geq q^s \end{array} \right\} c_{\text{O}}(q, t) = c_{\text{O}}^* \\ t \geq 0, q = q^s \quad c_{\text{O}}^{s,r} = \frac{e^{\eta} (c_{\text{O}}^* + c_{\text{R}}^*)}{1 + e^{\eta}} \end{array} \right\} \quad (2.152)$$

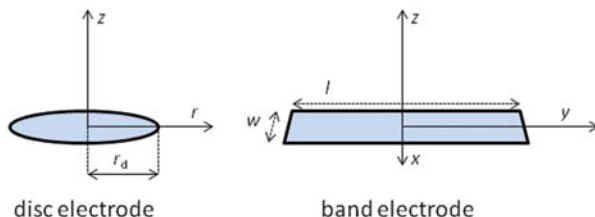
$$\left. \begin{array}{l} \frac{\partial c_{\text{R}}}{\partial t} = D \nabla^2 c_{\text{R}} \\ \left. \begin{array}{l} t \geq 0, q \rightarrow \infty \\ t = 0, q \geq q^s \end{array} \right\} c_{\text{R}}(q, t) = c_{\text{R}}^* \\ t \geq 0, q = q^s \quad c_{\text{R}}^{s,r} = \frac{(c_{\text{O}}^* + c_{\text{R}}^*)}{1 + e^{\eta}} \end{array} \right\} \quad (2.153)$$

with η being given in Eq. (2.6).

The two diffusional problems above are very similar to those corresponding to a process under limiting current conditions but with $c_{\text{O}}^{s,r} \neq 0$ and/or $c_{\text{R}}^{s,r} \neq 0$.

⁵ For a cartesian set of coordinates, like those used for band electrodes, q denotes coordinates x , y , and z , whereas for a cylindrical set of coordinates, like those corresponding to disc electrodes, q denotes coordinates r and z . In both cases, q^s refers to $z=0$.

Scheme 2.5 Disc and band electrodes and relevant coordinates for each geometry (disc area, $A_d = \pi r_d^2$; band area, $A_b = wl$)



Note that at uniformly accessible electrodes, spheres and cylinders, the mass flux is identical at all the points of its surface, whereas at non-uniformly accessible ones, discs and bands, the mass flux varies through the radius and the width, respectively. Therefore, in these cases, the surface gradient should be calculated by integrating the flux over the electrode surface such that the current is given by (see Scheme 2.5):

$$\frac{I^{\text{disc}}}{F} = 2A_d D c_O^* \frac{1}{r_d} \int_{R=0}^{R=1} \left(\frac{\partial C_O}{\partial Z} \right)_{z=0} R dR \quad (2.154)$$

$$\frac{I^{\text{band}}}{F} = 2A_b D c_O^* \frac{1}{w} \int_{X=0}^{X=1/2} \left(\frac{\partial C_O}{\partial Z} \right)_{z=0} dX \quad (2.155)$$

with $C_O = c_O/c_O^*$, $R = r/r_d$, $X = x/w$ and $Z = z/r_d$ (disc) or $Z = z/w$ (band).

It has been verified that the current obtained when a potential step is applied only differs from the corresponding to the limiting cathodic or anodic currents in the constant terms $(c_O^* - c_O^{s,r})$ and $(c_R^* - c_R^{s,r})$ instead of c_O^* and c_R^* , respectively (with $c_i^{s,r}$ being the surface concentration of species i). From Eqs. (2.152) and (2.153), the surface concentrations are independent of the electrode geometrical characteristics under Nernstian conditions [60]. Hence, the average current can be expressed independently of the electrode geometry as the product of a function of the applied potential $(c_O^* - c_O^{s,r})$ and a function of time and the electrode geometry $f_G(t, q_G)$ (with q_G being the characteristic dimension of the electrode), which is given in Table 2.3 for each particular geometry:

$$\begin{aligned} I^G &= FA_G D \times (c_O^* - c_O^{s,r}) \times f_G(t, q_G) = \\ &= -FA_G D \times (c_R^* - c_R^{s,r}) \times f_G(t, q_G) \end{aligned} \quad (2.156)$$

with

$$c_O^* - c_O^{s,r} = -(c_R^* - c_R^{s,r}) = \frac{c_O^* - e^\eta c_R^*}{1 + e^\eta} \quad (2.157)$$

where A_G is the electrode area and q_G the characteristic dimension of the electrode (Table 2.3).

The cathodic and anodic limiting currents for an electrode of a given geometry can be obtained by imposing $\eta \rightarrow \mp\infty$ on (2.156) and (2.157)

Table 2.3 Expressions for functions $f_G(t, q_G)$ and $f_{G,\text{micro}}$ for the four electrode geometries considered. $q_G = r_d$ for discs; $q_G = r_s$ for spheres or hemispheres; $q_G = r_c$ for cylinders; and $q_G = w$ for bands. Note that functions $f_G(t, q_G)$ and $f_{G,\text{micro}}$ have dimensions of 1/length

Electrode	Function $f_G(t, q_G)$	$f_{G,\text{micro}}$
Disc (radius r_d , Area $A_d = \pi r_d^2$)	$\frac{4}{\pi} \frac{1}{r_d} \left(0.7854 + 0.44315 \frac{r_d}{\sqrt{Dt}} + 0.2146 \exp\left(-0.39115 \frac{r_d}{\sqrt{Dt}}\right) \right)$	$\frac{4}{\pi} \frac{1}{r_d}$
Sphere (radius r_s , $A_s = 4\pi r_s^2$)	$\frac{1}{r_s} + \frac{1}{\sqrt{\pi Dt}}$	$\frac{1}{r_s}$
Band (height w , length l , $A_b = wl$)	$\frac{1}{w} + \frac{1}{\sqrt{\pi Dt}} \quad \text{if } Dt/w^2 < 0.4$ $0.25 \sqrt{\frac{\pi}{Dt}} \exp\left(-0.4 \frac{\sqrt{\pi Dt}}{w}\right) + \frac{\pi}{w \ln\left(5.2945 + 5.9944 \frac{\sqrt{Dt}}{w}\right)} \quad \text{if } Dt/w^2 \geq 0.4$	$\frac{1}{w} \frac{2\pi}{\ln[64Dt/w^2]}$
Cylinder (radius r_c , length l , $A_c = 2\pi r_c l$)	$\frac{1}{\sqrt{\pi Dt}} \exp\left(-0.1 \frac{\sqrt{\pi Dt}}{r_c}\right) + \frac{1}{r_c \ln\left(5.2945 + 1.4986 \frac{\sqrt{Dt}}{r_c}\right)}$	$\frac{1}{r_c} \frac{2}{\ln[4Dt/r_c^2]}$

$$\left. \begin{aligned} I_{d,c}^G &= FA_G D \times c_O^* \times f_G(t, q_G) \\ I_{d,a}^G &= -FA_G D \times c_R^* \times f_G(t, q_G) \end{aligned} \right\} \quad (2.158)$$

In order to highlight the non-uniformity of the concentration distribution around the disc, Fig. 2.17 shows the concentration profiles of oxidized species corresponding to the application of a potential step to a disc electrode for three values of r_d (500, 50, and 5 μm), and two values of the applied potential ($E = E_c^{\ominus'}$ and an E value corresponding to limiting current) for a time $t = 0.5$ s. From this figure, it can be deduced that, although the concentration profiles are logically affected by the applied potential, the Nernst diffusion layer thicknesses are independent of it. It can also be observed from this figure that the solution region adjacent to the electrode surface disturbed by the mass transport is much lower than the disc radius for higher values of r_d . Moreover, in this case (see curves with $r_d = 500$ μm in Fig. 2.17a and b), the dominant mass transport is that corresponding to planar diffusion, i.e., practically all the flux at the surface takes place at the normal coordinate z , with the exception of r values close to the edge of the disc. This gives rise to a planar front for δ_d , as seen in Fig. 2.17a and b. As the disc radius decreases (see Fig. 2.17c–f), the linear diffusion layer thickness becomes comparable to or even higher than r_d , showing a continuous variation between the center and the edge of the disc. For a radius $r_d = 5$ μm (see Fig. 2.17e and f), the radial mass transport becomes dominant in the whole response.

A consequence of the temporal independence of the surface concentrations is that under transient conditions, the relation $I^G/I_{d,c}^G$ and the curve E/I

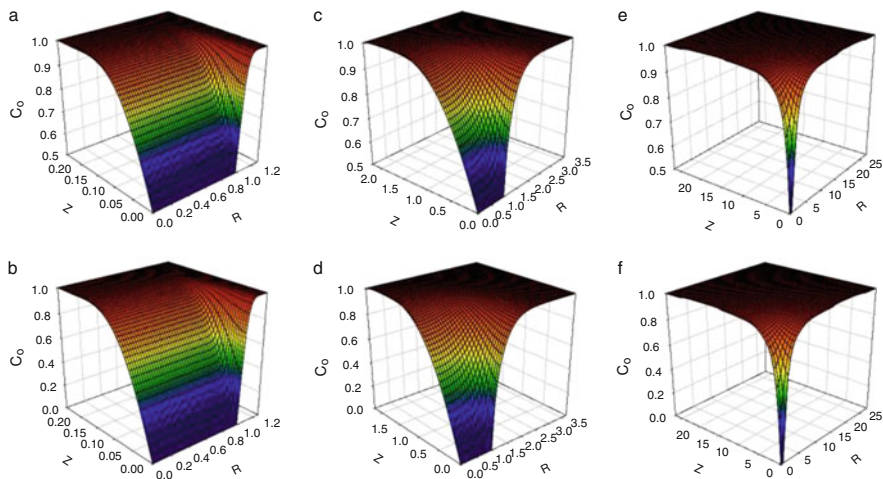


Fig. 2.17 Concentration profiles of oxidized species in reaction Scheme (I) corresponding to the application of a potential step to a disc electrode for three values of r_d (μm): 500 (a, b), 50 (c, d), and 5 (e, f), and two values of the applied potential: $E = E_c^{O'}$ (a, c, and e) and $E = E_c^{O'} - 0.256$ V (b, d, and f). $C_O = c_O/c_O^*$, $R = r/r_d$, and $Z = z/r_d$. These profiles have been numerically obtained by following the procedure described in reference [61] for a time $t = 0.5$ s and $D_O = D_R = 10^{-5}$ $\text{cm}^2 \text{s}^{-1}$. $T = 298.15$ K. Reproduced with permission [59]

$\ln((I_{d,c}^G - I^G)/(I^G - I_{d,a}^G))$ at a fixed time are independent of the electrode geometry,

$$\frac{I^G}{I_{d,c}^G} = \frac{1 - e^{\eta}(c_R^*/c_O^*)}{1 + e^{\eta}} \quad (2.159)$$

or,

$$E - E_c^{O'} = \frac{RT}{F} \ln \left(\frac{I_{d,c}^G - I^G}{I^G - I_{d,a}^G} \right) \quad (2.160)$$

The analysis of the current–time curves at electrodes or microelectrodes of different geometries has also a great interest in detecting the presence of small particles or nanoparticles at its surface or even single nanoparticles events through the current due to the electro-oxidation (or reduction) of the particles (see Fig. 2.18) or to an electrocatalytic reaction on the nanoparticle surface when this comes into contact with the electrode and transiently sticks to it [62–65].

In Fig. 2.19, we have plotted the $(I^G/I_{d,c}^G) - (E - E_c^{O'})$ curves for discs, spheres, bands, and cylinders calculated from Eqs. (2.156) and (2.159) when both species are initially present in the solution in order to show that, for a given process, this ratio is independent of the size and geometry of the electrode considered and independent of the transient or stationary character of the response. On the basis of

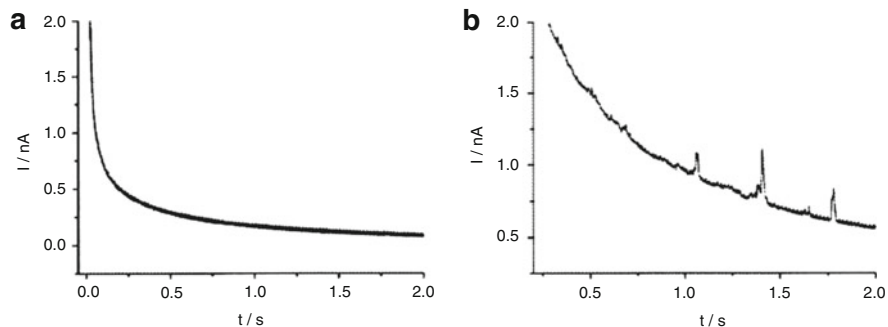


Fig. 2.18 Chronoamperometric profiles showing oxidative faradaic transients of gold nanoparticles at potentials of (a) 0.8 V and (b) 1.1 V at a Glassy Carbon microelectrode of 11 μm of radius. Reproduced from reference [62] with permission

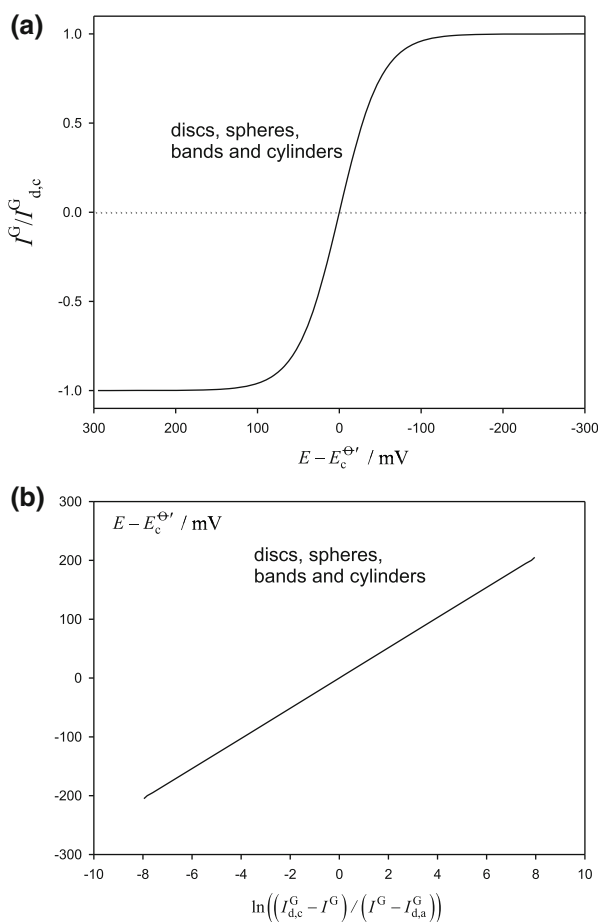


Fig. 2.19 (a) $(I^G/I_{d,c}^G) - (E - E_c^{\ominus'})$ curves and (b) $(E - E_c^{\ominus'}) - \ln((I_{d,c}^G - I^G)/(I^G - I_{d,a}^G))$ for discs, spheres, bands, and cylinders calculated from Eqs. (2.159) and (2.160) when both species are initially present in the solution and $c_R^*/c_O^* = 1$

these results, it is clear that the analysis of the curve $E/\ln((I_{d,c}^G - I^G)/(I^G - I_{d,a}^G))$ is identical to that carried out in the case of planar or spherical electrodes (see for example Eq. 2.31). So, whatever the geometry considered, by combining Eq. (2.156) and

$$I^G = FA_G D \left(\frac{\partial c_O}{\partial q_N} \right)_{q^s} \quad (2.161)$$

with q_N being the normal coordinate value at the electrode surface, the Nernst diffusion layer δ_G^r is easily determined as a function of time, size, and geometry (compare Eq. (2.156) with Eqs. (2.26) and (2.145)):

$$\delta_G^r = \frac{c_O^* - c_O^{s,r}}{I^G / FA_G D c_O^*} = \frac{1}{f_G(t, q_G)} \quad (2.162)$$

with $f_G(t, q_G)$ given in Table 2.3.

Note that if the electrode is not uniformly accessible such as disc and band electrodes, the diffusion layer thickness given by Eq. (2.162) has an average character [59], and in this case it will be denoted $\bar{\delta}_G^r$.

The temporal evolution of $\bar{\delta}_{disc}^r(t)$ and $\bar{\delta}_{band}^r(t)$, calculated from Eq. (2.162) and Table 2.3 for disc (solid lines) and band (solid-dotted lines) electrodes of three sizes ($r_0 = 500, 50,$ and $5 \mu\text{m}$, with r_0 being equal to r_d or $w/2$, respectively), has been plotted in Fig. 2.20. We have compared these curves with those obtained for spherical (dashed lines) and cylindrical (dotted lines) electrodes considering $r_d = r_s = r_c$ (with $\delta_{sph}^r(t)$ and $\delta_{cyl}^r(t)$ being calculated from equations in Table 2.3).

From these curves it can be seen that the Nernst diffusion layer, δ_G^r , increases with time in all cases. Moreover, Fig. 2.20a shows how these curves are all coincident at short times and only small differences appear between the couples “bands and cylinders” and “spheres and discs” at times longer than 0.2 s. This indicates that for this electrode size and time below 0.2 s, the prevalent diffusion field is planar, so the electrode geometry becomes irrelevant. As the electrode size decreases (Fig. 2.20b and c), so does the temporal dependence of δ_G^r and the different curves begin to separate until they reach a steady state in the case of discs and spheres, or a pseudo-steady state in the case of bands and cylinders (Fig. 2.20c). Note that the ratio between the diffusion layers corresponding to small discs and spheres $\delta_{disc}^{r,micro}$ and $\delta_{sph}^{r,micro}$ tends to the value $\pi/4$ (see also Sect. 2.7).

It is worth highlighting that, when different diffusion coefficients are considered, the half-wave potential depends on the characteristics of the diffusive field (geometry and size of the electrode), as indicated in Sect. 2.5.1. The variation of the half-wave potential $E_r^{1/2}$ with the electrode radius for cylindrical and spherical electrodes for $\gamma = 3$ (numerically calculated) has been plotted in Fig. 2.21. The

Fig. 2.20 Temporal evolution of $\bar{\delta}_{disc}^r(t)$ and $\bar{\delta}_{band}^r(t)$, calculated from equations in Table 2.3 for disc (solid lines) and band (solid-dotted lines) electrodes of three sizes ($r_0 = 500, 50,$ and $5 \mu\text{m}$, with r_0 being equal to r_d or $w/2$). These curves have been compared with those obtained for spherical (dashed lines) and cylindrical (dotted lines) electrodes considering $r_d = r_s = r_c$ (with $\delta_{sphe}^r(t)$ and $\delta_{cyl}^r(t)$ is calculated from equations in Table 2.3). Reproduced with permission [59]

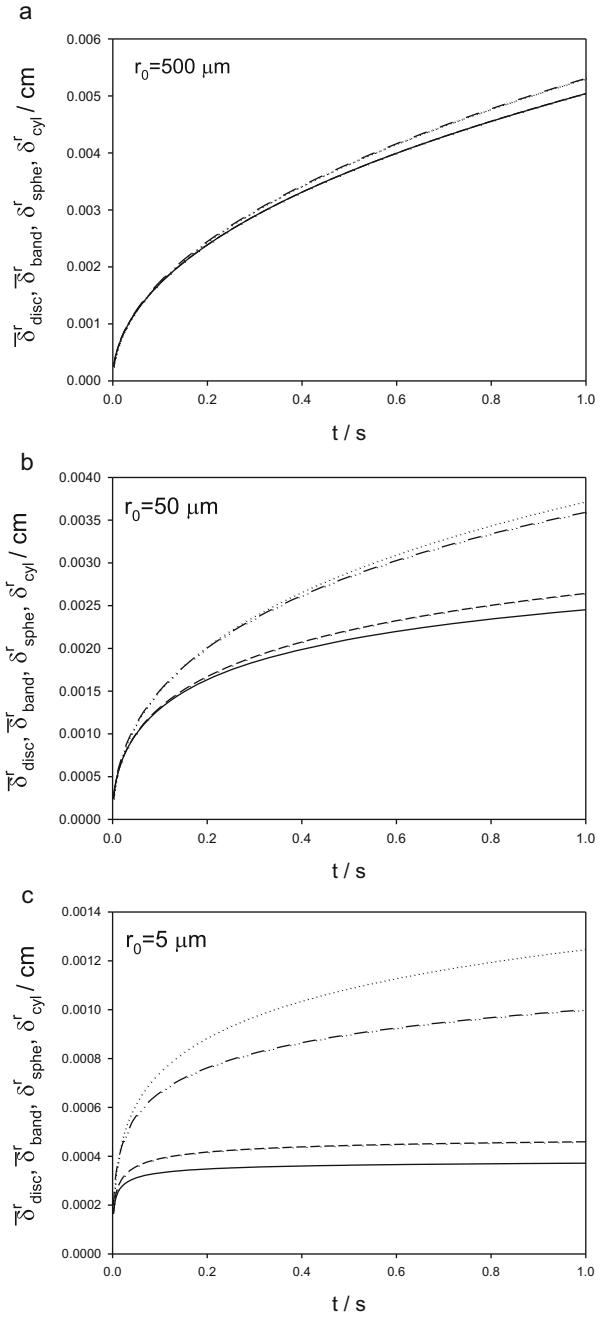
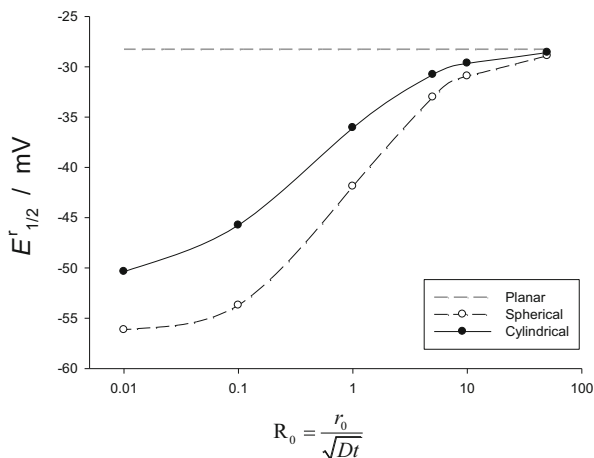


Fig. 2.21 Evolution of the half-wave potential with the electrode size for spherical (white dots) and cylindrical (black dots) electrodes. The value of $E_{1/2}^r$ for a planar electrode has been included for comparison (dashed line). $r_0 = r_s$ for a spherical electrode and $r_0 = r_c$ for a cylindrical one. $D_O = 10^{-5} \text{ cm}^2 \text{ s}^{-1}$, $\gamma = \sqrt{D_O/D_R} = 3$



half-wave potential of planar electrodes is also shown for comparison. As can be seen, the stationary value of $E_{1/2}^r = E_c^{\ominus'} + (RT/F)\ln(1/\gamma^2)$ (see Appendix C and Eq. (2.167)) is reached for spherical electrodes for values of $R_0 = 0.01$, whereas for cylindrical ones a steady-state value is not reached.

2.7 Microelectrodes. Steady-State Voltammetry

A microelectrode is usually defined as an electrode with at least one characteristic dimension (r_G) on the micrometer scale (of tens of micrometers or less). As is well known, the progressive decreasing of the electrode size produces an enhancement of the mass transport between the electrode surface and the bulk of the solution. This leads to important advantages in electrochemistry like fast establishment of stationary response (i.e., independent of time), improved ratio of faradaic to charging currents, decrease of the ohmic drop, short response times, and others derived from its small size: electroanalytical measurements in living organisms, microscopic sensors and arrays, among others. The currents observed at microelectrodes typically lie in the pA to nA range, and are much smaller than those measured with conventional electrodes of millimetric dimensions. It is only since the 1980s that very small electrodes and appropriate instruments to measure such low currents accurately have been available (see [9, 66, 67]). The scarce ohmic drop permits the study of electrochemical processes in high resistance solvents, low supported solutions, solids, and gases. Moreover, the effect of convective flux on mass transport is greatly reduced because the rate of diffusional transport can be several orders of magnitude larger than that attainable at a macro or planar electrode and other modes of transport are masked by the large diffusional contribution. More recently, nanoelectrodes have been developed with their characteristic dimension of a few tens of nanometers, which is comparable to the diffuse double-layer thickness. This can lead to deviations from the classic voltammetric theory [68, 69].

In this section, we will show that the stationary responses obtained at microelectrodes are independent of whether the electrochemical technique employed was under controlled potential conditions or under controlled current conditions, and therefore, they show a universal behavior. In other words, the time independence of the I/E curves yields unique responses independently of whether they were obtained from a voltammetric experiment (by applying any variable on time potential), or from chronopotentiometry (by applying any variable on time current). Hence, the equations presented in this section are applicable to any multipotential step or sweep technique such as Staircase Voltammetry or Cyclic Voltammetry.

Special attention should be paid to spherical geometry, since the mathematical treatment of spherical microelectrodes is the simplest and exemplifies very well the attainment of the steady state observed at microelectrodes of more complex shapes. Indeed, spherical or hemispherical microelectrodes, although difficult to manufacture, are the paragon of mathematical model for diffusion at microelectrodes, to the point that the behavior of other geometries is always compared against them.

The expression for the current of a reversible electrode process corresponding to a microelectrode of a given geometry will be deduced from Eq. (2.156) by making $q_G \ll \sqrt{\pi Dt}$. Under these conditions, a stationary current–potential response will be attained only if $f_{G,\text{micro}}$, defined as

$$f_{G,\text{micro}} = [f_G(t, q_G)]_{q_G \ll \sqrt{\pi Dt}} \quad (2.163)$$

reaches a constant value. The expressions for $f_{G,\text{micro}}$ corresponding to microhemispheres, microdiscs, microcylinders, and microbands are given in Table 2.3. The condition $f_{G,\text{micro}} = \text{constant}$ is only attained at disc and hemispherical electrodes (see Table 2.3). In both cases, the function $f_G(t, q_G)$ becomes independent of time when $q_G \ll \sqrt{\pi Dt}$.

For a spherical electrode, by making $r_s \ll \sqrt{\pi D_O t}$ in Eq. (2.137) (which has been deduced for unequal diffusion coefficients), and considering that both species are soluble in the electrolytic solution (upper sign), one obtains

$$I^{\text{microsphere,ss}} = FA_s D \frac{c_O^* - c_O^{r,s}}{r_s} = FA_s D \frac{c_O^* - e^{\eta} c_R^*}{1 + \gamma^2 e^{\eta}} \frac{1}{r_s} \quad (2.164)$$

or

$$E = E_{1/2}^{r,\text{micro}} + \frac{RT}{F} \ln \left(\frac{I_{d,c}^{\text{microsphere,ss}} - I}{I - I_{d,a}^{\text{microsphere,ss}}} \right) \quad (2.165)$$

where $c_O^{r,s}$ is given by Eq. (C.11) and

$$\left. \begin{aligned} I_{d,c}^{\text{microsphere,ss}} &= FA_s D_O c_O^* \frac{1}{r_s} \\ I_{d,a}^{\text{microsphere,ss}} &= -FA_s D_R c_R^* \frac{1}{r_s} \end{aligned} \right\} \quad (2.166)$$

The reversible half-wave potential is given by

$$E_{1/2}^{r,\text{microsphere}} = E_c^{\ominus'} + \frac{RT}{F} \ln\left(\frac{1}{\gamma^2}\right) \quad (2.167)$$

with $E_{1/2}^{r,\text{microsphere}}$ being the half-wave potential deduced for a microsphere or microhemisphere. As can be expected, the expression for $I_{d,c}^{\text{microsphere,ss}}$ given by Eq. (2.166) coincides with that of $I_{d,c}^{\text{sphere,ss}}$ for a spherical electrode given by Eq. (2.148).

In the case of an ultramicrodisc, the above equations become

$$\left. \begin{aligned} I_{d,c}^{\text{microdisc,ss}} &= 4Fr_d D_O c_O^* \\ I_{d,a}^{\text{microdisc,ss}} &= -4Fr_d D_R c_R^* \end{aligned} \right\} \quad (2.168)$$

It has been verified numerically that, when $D_O \neq D_R$, the stationary current-potential response of a microdisc presents the same half wave potential as that observed for a microsphere, which is given by Eq. (2.167) (see [70] and Appendix C).

Therefore, the stationary I - E response can be written as (Table 2.3)

$$I^{\text{microdisc,ss}} = FA_d D_O \frac{c_O^* - c_O^{r,s}}{r_d} \frac{4}{\pi} = FA_d D_O \frac{c_O^* - e^{\eta} c_R^*}{1 + \gamma^2 e^{\eta}} \frac{4}{\pi r_d} \quad (2.169)$$

where $c_O^{r,s}$ is given by Eq. (C.20).

The current densities ($i = I/A$) obtained for disc and microspheres of the same radius for reversible electrode processes at any value of the applied potential follow the equivalence relationship given by [70, 71]:

$$\frac{i^{\text{microdisc,ss}}}{i^{\text{microsphere,ss}}} = \frac{4}{\pi} \quad (2.170)$$

In the case of microcylinders and microbands, $f_{G,\text{micro}}$ is time dependent (Table 2.3) and only a pseudo-stationary response can be achieved. This is because all the microelectrode dimensions have to fall in the range of the microns to attain a true steady state. The expressions for the pseudo-stationary current-potential responses when the diffusion coefficients of species O and R fulfills $D_O = D_R$ are:

$$I^{\text{microcylinder, pss}} = FA_c D \frac{c_O^* - e^{\eta} c_R^*}{1 + e^{\eta}} \frac{1}{r_c} \frac{2}{\ln\left[\frac{4Dt}{r_c^2}\right]} \quad (2.171)$$

$$I^{\text{microband, pss}} = FA_b D \frac{c_O^* - e^{\eta} c_R^*}{1 + e^{\eta}} \frac{1}{w} \frac{2\pi}{\ln\left[\frac{64Dt}{w^2}\right]} \quad (2.172)$$

Nevertheless, it is possible to obtain a constant relationship between the current at both microelectrodes for certain geometrical conditions. Thus, for microbands and microhemicylinders fulfilling $r_c = w/4$, a constant ratio is obtained, but in this case it is necessary to use the same experimental timescale [10]:

$$\frac{I^{\text{microband, pss}}}{I^{\text{microhemicylinder, pss}}} = 1 \quad (2.173)$$

The solutions of the stationary diffusion equations for spherical and disc microelectrodes are deduced in Appendix C.

It is also of interest to consider the case of a microsphere at a non-electroactive substrate because it is used as a model for spherical nanoparticles (of radius r_{np} and area A_{np}) impacting on a surface [72, 73]. For this case the average stationary current is given by [74]:

$$I^{\text{np, ss}} = A_{\text{np}} DF \frac{c_{\text{O}}^* - c_{\text{O}}^{\text{r, s}}}{r_{\text{np}}} \ln 2 \quad (2.174)$$

Note that, on the basis of Eqs. (2.164), (2.169), and (2.174), it can be concluded that for all these electrode geometries for which it is possible to achieve a true stationary response, Eq. (2.165) could be used by changing $I_{\text{d, c}}^{\text{microsphere, ss}}$ by the corresponding stationary limiting current for the geometry considered. Therefore, in all the previous cases it is fulfilled,

$$E = E_{1/2}^{\text{r, microG}} + \frac{RT}{F} \ln \left(\frac{I_{\text{d, c}}^{\text{microG}} - I^{\text{microG}}}{I^{\text{microG}} - I_{\text{d, a}}^{\text{microG}}} \right) \quad (2.175)$$

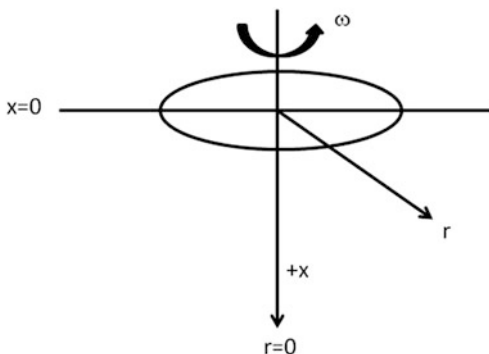
The advantages derived from the use of microelectrodes will be discussed in Sect. 5.4.

2.8 Rotating Disc Electrode

A rotating disc electrode (RDE) is a conductive disc of the material of interest embedded in an inert non-conductive polymer or resin that can be attached to an electric motor which has very fine control of the electrode's rotation rate. During the experiment, the electrode rotates in the solution under study, thus inducing a flux of redox analyte to the electrode [75].

The modeling of the electrochemical response corresponding to the application of a constant potential to an RDE is similar to that discussed in the case of a DME since in this electrode it is imperative to consider the convection caused by the rotation of the electrode. This problem was solved by Levich under stationary conditions [76]. To do this, the starting point is the diffusive–convective differential

Fig. 2.22 Polar coordinates for the rotating disc electrode



equation that describes the mass transport in the normal direction to the electrode surface (see Fig. 2.22),

$$\frac{\partial c_i}{\partial t} = D_i \frac{\partial^2 c_i}{\partial x^2} - v_x \frac{\partial c_i}{\partial x} \quad i = \text{O, R} \quad (2.176)$$

The convection velocity for an RDE is given by the following expression:

$$v_x = -0.51\omega^{3/2}\nu^{-1/2}x^2 \quad (2.177)$$

in which ω is the angular rotation speed (in Hz) and ν the kinematic viscosity (in $\text{m}^2 \text{s}^{-1}$).

Under steady-state conditions, i.e., when $\partial c_i/\partial t = 0$, Eq. (2.176) simplifies to

$$\left. \begin{aligned} \frac{d^2 c_i}{dx^2} &= -\frac{x^2}{B} \frac{dc_i}{dx} \quad i = \text{O, R} \\ B &= \frac{D_i}{0.51\omega^{3/2}\nu^{-1/2}} \end{aligned} \right\} \quad (2.178)$$

By making the change of variable $y = dc_i/dx$, Eq. (2.178) is easily integrated and the following expression is obtained:

$$\frac{dc_i}{dx} = \left(\frac{dc_i}{dx} \right)_{x=0} e^{-\frac{x^2}{3B}} \quad i = \text{O, R} \quad (2.179)$$

Integrating once more, the concentration profile,

$$c_i(x) - c_i(0) = \left(\frac{dc_i}{dx} \right)_{x=0} \int_0^x e^{-\frac{u^2}{3B}} du \quad i = \text{O, R} \quad (2.180)$$

By taking the infinite limit ($x \rightarrow \infty$) in the above equation, it becomes

$$\begin{aligned} c_i^* - c_i(0) &= \left(\frac{dc_i}{dx}\right)_{x=0} \int_0^{\infty} e^{-\frac{u^2}{3B}} du = \\ &= \left(\frac{dc_i}{dx}\right)_{x=0} (3B)^{1/3} \Gamma(3/4) = 1.29B^{1/3} \left(\frac{dc_i}{dx}\right)_{x=0} \end{aligned} \quad (2.181)$$

with $\Gamma(x)$ being the Euler Gamma function. By combining Eqs. (2.180) and (2.181) the following expression for the concentration profile is deduced:

$$c_i(x) - c_i(0) = \frac{c_i^* - c_i(0)}{1.29B^{1/3}} \int_0^x e^{-u^3/3B} du \quad i = O, R \quad (2.182)$$

Moreover, the current is given by

$$\begin{aligned} I^{\text{RDE}} &= FAD_O \left(\frac{dc_O}{dx}\right)_{x=0} = \frac{c_O^* - c_O(0)}{1.29B^{1/3}} = \\ &= 0.620FAD_O^{2/3} \omega^{1/2} \nu^{-1/6} (c_O^* - c_O(0)) \end{aligned} \quad (2.183)$$

which simplifies to the well-known Levich's equation for limiting conditions (i.e., $c_O(0) = 0$):

$$I_{d,c}^{\text{RDE}} = 0.620FAD_O^{2/3} \omega^{1/2} \nu^{-1/6} c_O^* \quad (2.184)$$

From Eqs. (2.183) and (2.184), it is possible to rewrite the expression of the surface concentrations in terms of the current, and the cathodic and anodic limiting currents are as follows:

$$\left. \begin{aligned} \frac{c_O(0)}{c_O^*} &= 1 - \frac{I^{\text{RDE}}}{I_{d,c}^{\text{RDE}}} \\ \frac{c_R(0)}{c_R^*} &= 1 - \frac{I^{\text{RDE}}}{I_{d,a}^{\text{RDE}}} \end{aligned} \right\} \quad (2.185)$$

with $I_{d,a}^{\text{RDE}}$ being identical to that given in Eq. (2.184) by changing D_O and c_O^* by D_R and c_R^* and of negative sign. By combining Eq. (2.185) with the nernstian condition $e^\eta = c_O(0)/c_R(0)$, with η given by Eq. (2.6), the following relationship between current and potential is given by

$$E = E_{1/2}^{\text{r,RDE}} + \frac{RT}{F} \ln \left(\frac{I_{d,c}^{\text{RDE}} - I^{\text{RDE}}}{I^{\text{RDE}} - I_{d,a}^{\text{RDE}}} \right) \quad (2.186)$$

which is formally identical to that obtained at planar electrodes (Eq. 2.31), but the half-wave potential is

$$E_{1/2}^{\text{r,RDE}} = E_c^{\ominus'} + \frac{RT}{F} \ln \left(\frac{D_R}{D_O} \right)^{2/3} \quad (2.187)$$

2.9 Thin Layer Voltammetry

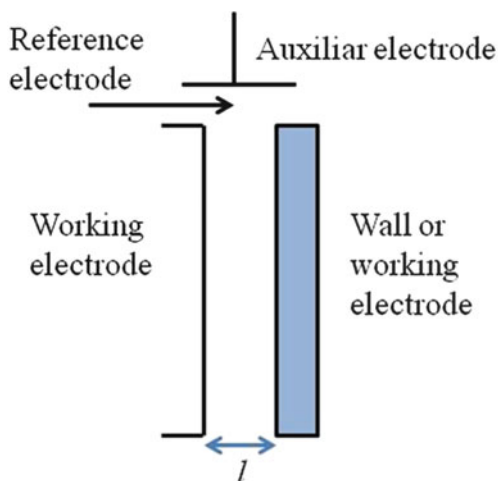
This section analyzes the response of a charge transfer process under conditions of finite linear diffusion which corresponds to a thin layer cell. This type of cell can be achieved by miniaturization process for obtaining a very high Area/Volume ratio, i.e., a maximum distance between the working and counter electrodes that is even smaller than the diffusion layer [31]. In these cells it is easy to carry out a bulk electrolysis of the electroactive species even with no convection. Two different cell configurations can be described: a cell with two working electrodes or a working electrode versus an electro-inactive wall separated at distance l (see Fig. 2.23).

If we consider a thin layer cell where the electrode process given in reaction Scheme (I) takes place, the mass transport differential equation is given by Eq. (2.2) and the boundary conditions corresponding to limiting current are as follows:

$$t = 0, 0 \leq x \leq l \quad c_O = c_O^*, c_R = 0 \quad (2.188)$$

$t > 0$

Fig. 2.23 Diagram of a thin layer cell with a single or two working electrodes



$$\left. \begin{array}{l} c_{\text{O}}(0, t) = c_{\text{O}}(l, t) = 0 \\ \left(\frac{\partial c_{\text{O}}}{\partial x} \right)_{x=l/2} = 0 \end{array} \right\} \text{two working electrodes} \quad (2.189)$$

$$\left. \begin{array}{l} c_{\text{O}}(0, t) = 0 \\ \left(\frac{\partial c_{\text{O}}}{\partial x} \right)_{x=l} = 0 \end{array} \right\} \text{one working electrode} \quad (2.190)$$

The solution to Eq. (2.2) can be deduced by using Laplace transform method (see Appendix B), by obtaining the following expression:

$$\bar{c}_{\text{O}}(x, p) = \frac{c_{\text{O}}(x, 0)}{p} + a_1 e^{\sqrt{\frac{p}{D_{\text{O}}}}x} + a_2 e^{-\sqrt{\frac{p}{D_{\text{O}}}}x} \quad (2.191)$$

In order to determine the values of constants a_1 and a_2 , the derivative of Eq. (2.191) is equated to zero at the corresponding distance ($x = l/2$ or $x = l$) in line with Eqs. (2.189) and (2.190):

$$a_1 e^{\sqrt{\frac{p}{D_{\text{O}}}}\delta} - a_2 e^{-\sqrt{\frac{p}{D_{\text{O}}}}\delta} = 0 \quad (2.192)$$

where $\delta = l/2$ for the two electrodes cell and $\delta = l$ for the one electrode cell. By combining Eq. (2.192) and condition $\bar{c}_{\text{O}}(0, p) = 0$, one obtains

$$a_1 = \frac{-c_{\text{O}}^*}{p} \frac{e^{-\sqrt{\frac{p}{D_{\text{O}}}}\delta}}{e^{\sqrt{\frac{p}{D_{\text{O}}}}\delta} + e^{-\sqrt{\frac{p}{D_{\text{O}}}}\delta}} \quad (2.193)$$

$$a_2 = \frac{-c_{\text{O}}^*}{p} \frac{e^{\sqrt{\frac{p}{D_{\text{O}}}}\delta}}{e^{\sqrt{\frac{p}{D_{\text{O}}}}\delta} + e^{-\sqrt{\frac{p}{D_{\text{O}}}}\delta}} \quad (2.194)$$

The Laplace transform of the current is given by

$$\bar{I}^{\text{TLV}}(p) = FAD_{\text{O}} \left(\frac{\partial \bar{c}_{\text{O}}}{\partial x} \right)_{x=0} = FAD_{\text{O}} \sqrt{\frac{p}{D_{\text{O}}}} [a_1 - a_2] \quad (2.195)$$

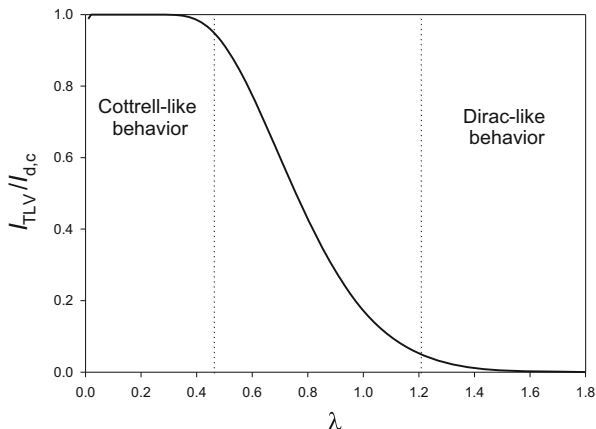
which, by taking into account Eqs. (2.193) and (2.194), becomes [31]:

$$\bar{I}^{\text{TLV}}(p) = FAc_{\text{O}}^* \sqrt{\frac{D_{\text{O}}}{p}} \frac{e^{\sqrt{\frac{p}{D_{\text{O}}}}\delta} - e^{-\sqrt{\frac{p}{D_{\text{O}}}}\delta}}{e^{\sqrt{\frac{p}{D_{\text{O}}}}\delta} + e^{-\sqrt{\frac{p}{D_{\text{O}}}}\delta}} = FA \sqrt{\frac{D_{\text{O}}}{p}} \tan h \left(\sqrt{\frac{p}{D_{\text{O}}}}\delta \right) \quad (2.196)$$

As indicated in reference [77] the inverse transform of Eq. (2.196) leads to

$$\frac{I_{\text{d,c}}^{\text{TLV}}}{I_{\text{d,c}}} = 4\lambda \sum_{m=1}^{\infty} \exp \left[-(2m-1)^2 \pi \lambda^2 \right] \quad (2.197)$$

Fig. 2.24 Variation of the ratio ($I_{\text{TLV}}/I_{\text{d,c}}$) versus λ calculated from Eq. (2.197)



with

$$\lambda = \begin{cases} \frac{\sqrt{\pi D_O t}}{l} & \text{two working electrodes} \\ \frac{\sqrt{\pi D_O t}}{2l} & \text{one working electrode} \end{cases} \quad (2.198)$$

and $I_{\text{d,c}}$ being the diffusion-controlled limiting current (see Eq. 2.28). Equation (2.197) simplifies in two asymptotic cases. When $\lambda \rightarrow 0$ (i.e., $l \gg \sqrt{\pi D_O t}$), the term $4\lambda \sum_{m=1}^{\infty} \exp[-(2m-1)^2 \pi \lambda^2] \rightarrow 1$ in such a way the current becomes identical to $I_{\text{d,c}}$ (that is, the expression corresponding to the semi-infinite approach). In the contrary, i.e., for $\lambda \rightarrow \infty$ (and $l \ll \sqrt{\pi D_O t}$), the current expression simplifies to [31],

$$I_{\lambda \rightarrow \infty}^{\text{TLV}} = FAc_O^* l \times \text{Dirac}(t) \quad (2.199)$$

This result indicates that as l decreases the current takes a very high value at times close to zero and it diminishes very fast (i.e., species O is consumed instantaneously). In order to check the values of parameter λ for which the response evolves from the cottrellian behavior to that given by Eq. (2.199), the behavior of the ratio ($I^{\text{TLV}}/I_{\text{d,c}}$) versus λ has been plotted in Fig. 2.24. From this figure, it can be seen that for $\lambda \leq 0.46$ the current is identical to that obtained with the Cottrell equation (with a maximum relative difference of 5 %). For higher values of λ , the ratio decreases until for $\lambda \geq 1.21$ the current behaves in line with Eq. (2.199) (with a maximum relative difference of 5 %). In practice, that means that the current will be similar to that obtained at a “semi-infinite” cell for times close to zero and it will decrease with time faster, the smaller the value of l (i.e., the faster λ increases) due

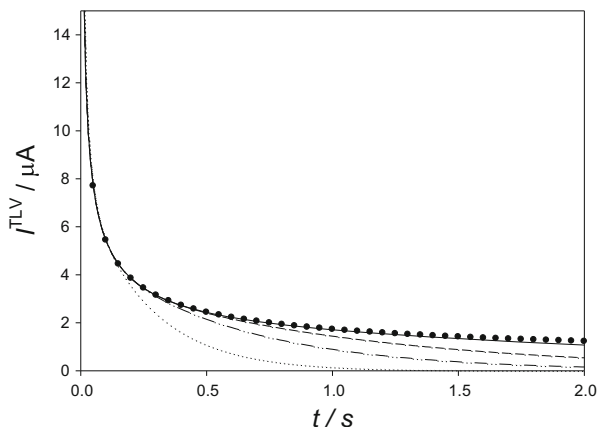


Fig. 2.25 Chronoamperometric responses of a thin layer cell calculated from Eq. (2.197) for different values of l (in μm): 150 (*solid line*); 100 (*dashed line*); 75 (*dashed-dotted line*); and 50 (*dotted line*). The current calculated with Cottrell Eq. (2.28) is also plotted (*black dots*). $D = 10^{-5} \text{ cm}^2 \text{ s}^{-1}$, $A = 0.01 \text{ cm}^2$, $c_0^* = 10^{-6} \text{ mol cm}^{-3}$

to a faster depletion of the oxidized species, which can be seen in Fig. 2.25. For example, for a fixed time of one second, the current obtained for a separation between electrodes of $150 \mu\text{m}$ is undistinguishable from that obtained under semi-infinite linear diffusion whereas it drops 48 % from the cottrellian value when the distance is $l = 75 \mu\text{m}$. This decrease reaches 91 % for the narrower cell ($l = 50 \mu\text{m}$), for which, at this time, the current is very close to zero.

References

1. Galus Z (1993) Fundamentals of electrochemical analysis, 2nd/rev edn. Ellis Horwood series in analytical chemistry. Ellis Horwood, Chichester
2. Bard AJ, Faulkner LR (2001) Electrochemical methods, fundamental and applications. Wiley, New York, NY
3. Heyrovský J (1966) Principles of polarography. Academic, New York, NY
4. MacDonald DD (1958) Transient techniques in electrochemistry. Plenum, New York, NY
5. Barker GC (1958) Anal Chim Acta 18:118–131
6. Barker GC, Gardner AW (1958) Atomic Energy Res Estab Harwell C/R 2297
7. Barker GC, Gardner AW (1960) Z Anal Chem 173:79–83
8. Bard AJ, Inzelt G, Scholz F (eds) (2008) Electrochemical dictionary. Springer, Berlin
9. Montenegro I, Queiros MA, Daschbach JL (eds) (1991) Microelectrodes: theory and applications (Nato Science Series E). Kluwer Academic, Dordrecht
10. Amatore C (1995) In: Rubinstein I (ed) Physical electrochemistry: principles, methods and applications. Marcel Dekker, New York, NY
11. Brett CMA, Brett AMO (1993) Electrochemistry: principles, methods, and applications. Oxford University Press, Oxford

12. Molina A, Gonzalez J, Martinez-Ortiz F, Compton RG (2010) *J Phys Chem C* 114:4093–4099
13. Cottrell FG (1902) *Z Phys Chem* 42:385
14. Gao X, Lee J, White HS (1995) *Anal Chem* 67:1541–15445
15. Amatore C, Knobloch K, Thouin L (2007) *J Electroanal Chem* 601:17–28
16. Amatore C, Pebay C, Thouin L, Wang A (2009) *Electrochem Commun* 11:1269–1272
17. Tomeš J (1937) *Czech Collect Chem Commun* 9:12
18. Koryta J, Vanýsek P, Brezina M (1977) *J Electroanal Chem* 75:211–228
19. Samec Z (2004) *Pure Appl Chem* 76:2147–2180
20. Volkov AG (1988) *Electrochim Acta* 44:139–153
21. Peljo P, Murtomäki L, Kallio T, Xu HJ, Meyer M, Gros CP, Barbe JM, Girault HH, Laasonen K, Kontturi KS (2012) *J Am Chem Soc* 134:5974–5984
22. Molina A, Serna C, Ortuño JA, Torralba E (2012) *Annu Rep Prog Chem Sect C* 108:126–176
23. Gavach C, Młodnicka T, Guastalla J (1968) *C R Acad Sci C* 266:1196–1199
24. Vanýsek P (1995) *Electrochim Acta* 40:2841–2847
25. Shirai O, Kihara S, Yoshida Y, Matsui M (1995) *J Electroanal Chem* 389:61–70
26. Langmaier J, Samec Z (2007) *Electrochem Commun* 9:2633–2638
27. Senda M, Kakiuchi T, Osakai T (1991) *Electrochim Acta* 36:253–262
28. Scholz F (2006) *Annu Rep Prog Chem Sect C* 102:43–70
29. Ortuño J, Serna C, Molina A, Torralba E (2009) *Electroanalysis* 21:2297–2302
30. Molina A, Serna C, Gonzalez J, Ortuño J, Torralba E (2009) *Phys Chem Chem Phys* 11: 1159–1166
31. Girault HH (2004) *Analytical and physical electrochemistry, Fundamental sciences series*. EFPL Press, Lausanne
32. Ilkovič D (1934) *Czech Collect Chem Commun* 6:498–513
33. Kolthoff IM, Lingane JJ (1952) *Polarography*, 2nd edn. Wiley-Interscience, New York, NY
34. Meites L (1958) *Polarographic techniques*, 2nd edn. Wiley-Interscience, New York, NY
35. Koutecký J (1953) *Czech J Phys* 2:50–58
36. Koutecký J, Stackelberg MV (1962) In: Zuman P, Kolthoff IM (eds) *Progress in polarography*, vol I. Wiley-Interscience, New York, NY
37. Newman J (1967) *J Electroanal Chem* 15:309–312
38. Brikmann AAAM, Loss JM (1964) *J Electroanal Chem* 7:171–183
39. Galvez J, Serna A (1976) *J Electroanal Chem* 69:133–143
40. Molina A, Serna C, Camacho L (1995) *J Electroanal Chem* 394:1–6
41. Molina A, Serna C (1999) *J Electroanal Chem* 466:8–14
42. Wang J (2006) *Analytical Electrochemistry*, 3rd edn. Wiley-VCH, New York, NY
43. Lovrić M (2002) *Stripping voltammetry*. In: Scholz F (ed) *Electroanalytical methods: guide to experiments and applications*. Springer, Berlin
44. Demaille C, Brust M, Tsionsky M, Bard AJ (1997) *Anal Chem* 69:2323–2328
45. Amatore C, Maisonhaute E, Schöllhorn B, Wadhawan J (2007) *Chem Phys Chem* 8: 1321–1329
46. Martinez Ortiz F, Laborda E, Limon-Petersen JG, Rogers EI, Serna C, Rees NV, Molina A, Compton RG (2009) *J Phys Chem C* 113:17215–17222
47. Scholz F (2011) *J Solid Stat Electrochem* 15:1699–1702
48. Hapiot P, Lagrost C (2008) *Chem Rev* 108:2238–2264
49. Molina A, Laborda E, Rogers EI, Martinez-Ortiz F, Serna C, Limon-Petersen JG, Rees NV, Compton RG (2009) *J Electroanal Chem* 634:90–97
50. Rogers EI, Silvester DS, Poole DL, Aldous L, Hardacre C, Compton RG (2008) *J Phys Chem C* 112:2729–2735
51. Laborda E, Rogers EI, Martinez-Ortiz F, Limon-Petersen JG, Rees NV, Molina A, Compton RG (2009) *J Electroanal Chem* 634:1–10
52. Molina A, Serna C, Martínez-Ortiz F, Laborda E (2008) *J Electroanal Chem* 617:14–26
53. Delmastro JR, Smith DE (1966) *Anal Chem* 38:169–179
54. Delmastro JR, Smith DE (1967) *J Phys Chem* 71:2138–2149

55. MacGillavry D, Rideal EK (1937) *Recl Trav Chim* 56:1013
56. Polo S, Llopis J, Rius A (1949) *An Quim* 45:1029
57. Saito Y (1968) *Rev Polarograph* 15:177–187
58. Compton RG, Banks CE (2011) *Understanding voltammetry*, 2nd edn. ICP, London
59. Molina A, Gonzalez J, Henstridge M, Compton RG (2011) *Electrochim Acta* 56:4589–4594
60. Molina A, Gonzalez J, Henstridge M, Compton RG (2011) *J Phys Chem C* 115:4054–4062
61. Alden JA, Hutchinson F, Compton RG (1997) *J Phys Chem B* 101:949–958
62. Rees NV, Zhou YG, Compton RG (2012) *RSC Adv* 2:379–384
63. Kwon SJ, Fu-Ren F, Bard AJ (2010) *J Am Chem Soc* 132:13165–13167
64. Hellberg D, Scholz F, Schauer F, Weitschies W (2002) *Electrochem Commun* 4:305–309
65. Hellberg D, Scholz F, Schubert F, Lovrić M, Omanović D, Hernandez VA, Thede R (2005) *J Phys Chem B* 109:14715–14726
66. Forster RJ (2003) Microelectrodes: retrospect and prospect. In: Bard AJ, Stratmann M, Unwin P (eds) *Encyclopedia of electrochemistry*, vol 3, Instrumentation and electroanalytical chemistry. Wiley-VCH, Weinheim, pp 160–195
67. Zoski CG (ed) (2007) *Handbook of electrochemistry*. Elsevier, Amsterdam
68. Wang Y, Velmurugan J, Mirkin MV (2010) *Isr J Chem* 50:291–305
69. Wightman RM, Wipf DO (1988) Voltammetry at Ultramicroelectrodes. In: Bard AJ (ed) *Electroanalytical chemistry*, vol 15. Marcel Dekker, New York, pp 267–353
70. Oldham KB, Zoski CG (1988) *J Electroanal Chem* 256:11–19
71. Amatore CA, Fosset B (1992) *J Electroanal Chem* 328:21–32
72. Henstridge M, Compton RG (2012) *Chem Rec* 12:63–71
73. Bobbert PA, Winf MM, Vlieger J (1987) *Phys A* 141:58–72
74. Molina A, Gonzalez J, Barnes EO, Compton RG (2014) *J Phys Chem C* 118:346–356
75. Newman JS (1991) *Electrochemical Systems*, 2nd edn. Prentice Hall, Englewood Cliffs, NJ, Chaps. 15 and 17
76. Levich VG (1962) *Physicochemical hydrodynamics*. Prentice-Hall, Englewood Cliffs, NJ
77. Hubbard AT, Anson FC (1970) The theory and practice of electrochemistry with thin layer cells. In: Bard AJ (ed) *Electroanalytical chemistry*, vol 4. Marcel Dekker, New York, NY, pp 129–214

Chapter 3

Single Pulse Voltammetry: Non-reversible and Complex Electrochemical Reactions

Contents

3.1	Introduction	134
3.2	Quasi-reversible and Irreversible Electrochemical Reactions	134
3.2.1	Planar Electrodes	135
3.2.2	Dropping Mercury Electrode	152
3.2.3	Spherical Electrodes and Microelectrodes	154
3.2.4	Microdiscs. Steady-State Voltammetry	163
3.2.5	General Expression for the Stationary Current–Potential Response at Microelectrodes	166
3.2.6	Comparison Between Marcus–Hush and Butler–Volmer Kinetics	167
3.3	Multi-electron Electrochemical Reactions	171
3.3.1	Two-Electron Electrochemical Reactions at Planar Electrodes	173
3.3.2	Two-Electron Electrochemical Reactions at Different Electrode Geometries	180
3.3.3	Non-reversible Two-Electron Electrochemical Reactions	183
3.3.4	General Solution for Multi-electron Electrochemical Reactions	185
3.4	First-Order Chemical Reactions Coupled to Charge Transfer Processes	189
3.4.1	Catalytic Mechanism	193
3.4.2	CE Mechanism	196
3.4.3	EC Mechanism	201
3.4.4	Comparison of the Disturbed Regions by Catalytic, CE, and EC Mechanisms ...	203
3.4.5	Comparison Between the Current–Potential Curves Corresponding to Catalytic, CE, and EC Mechanisms	205
3.4.6	Determination of Kinetic Parameters	207
3.4.7	Spherical Electrodes	210
3.4.8	ECE Mechanism and Other More Complex Reaction Schemes	216
3.4.9	Catalytic Mechanism at Disc Electrodes	218
3.4.10	Reversible Charge Transfers Preceded and Followed by Several Complexation Reactions in Equilibrium (Ladder Mechanism)	220
	References	225

3.1 Introduction

This chapter addresses more complex electrode processes than one-electron reversible electrochemical reactions in single potential pulse techniques. The concepts given here set the basis for tackling the current–potential response in multipotential pulse electrochemical techniques (see Chaps. 4–7), which are more powerful, but also present greater theoretical complexity.

In Sect. 3.2, non-reversible charge transfer reactions will be studied, with emphasis on their most characteristic aspects, such as the dependence of the half-wave potential on the heterogeneous charge transfer rate constant and the time of the application of the potential, as well as the size and geometric characteristics of the working electrode.

Multi-electron (multistep) electrode processes will be studied in Sect. 3.3, underlining the key role of the difference of the formal potentials between each two consecutive electrochemical steps on the current–potential curves and also the comproportionation/disproportionation reactions that take place in the vicinity of the electrode surface. In the case of two-step reactions, interesting aspects of the current–potential curves will be discussed and related to the surface concentrations of the participating species.

In Sect. 3.4, the current–potential curves corresponding to electrode processes complicated with homogeneous chemical reactions will be analyzed, highlighting the analogies and differences between the theoretical treatments of the different reaction schemes corresponding to first-order catalytic, CE, and EC mechanisms. These three reaction schemes will be treated rigorously and with different approaches of approximation. Also working curves will be given to obtain equilibrium and chemical rate constants in each case. ECE mechanism and some more complex reaction schemes will also be discussed.

All general typical variables considered in this chapter for a particular reaction scheme, for example the half-wave potential, are of fundamental interest for its characterization in any electrochemical technique. Moreover, as indicated in the previous chapter, all the current–potential expressions deduced here under stationary conditions (when microelectrodes are used) are applicable to any multipotential step or sweep electrochemical techniques like Staircase Voltammetry or Cyclic Voltammetry.

3.2 Quasi-reversible and Irreversible Electrochemical Reactions

In the preceding chapter, single pulse voltammetry and chronoamperometry were applied to the study of reversible electrode reactions of species in solution. Under these conditions, the surface concentrations fulfill Nernst equation and are independent of the duration of the experiment, regardless of the diffusion field

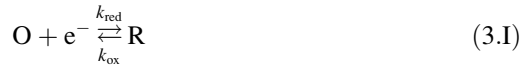
geometry, if the diffusion coefficients are identical, and depend only on the applied potential.

In this section, a non-reversible electrode reaction will be addressed. An exact definition of a slow charge transfer process is not possible because the charge transfer reaction can be reversible, quasi-reversible, or irreversible depending on the duration of the experiment and the mass transport rate. So, an electrode reaction can be slow or non-reversible when the mass transport rate has a value such that the measured current is lower than that corresponding to a reversible process because the rate of depletion of the surface species at the electrode surface is less than the diffusion rate at which it reaches the surface. Under these conditions, the potential values that reduce the O species and oxidize the R species become more negative and more positive, respectively, than those predicted by Nernst equation.

A reversible criterion will be presented in order to clearly establish the experimental conditions for which a charge transfer process can be considered as reversible, quasi-reversible, or fully irreversible. Note that this criterion can be easily extended to any electrochemical technique. This section also analyzes the response of non-reversible electrode processes at microelectrodes, which does not depend on the electrochemical technique employed, as stated in Chap. 2.

3.2.1 Planar Electrodes

A non-reversible electrochemical reaction that occurs on a planar electrode is considered according to the reaction scheme:



The mass transport of the different species in solution is described by the diffusive differential equation system:

$$\begin{aligned} \frac{\partial c_{\text{O}}}{\partial t} &= D_{\text{O}} \frac{\partial^2 c_{\text{O}}}{\partial x^2} \\ \frac{\partial c_{\text{R}}}{\partial t} &= D_{\text{R}} \frac{\partial^2 c_{\text{R}}}{\partial x^2} \end{aligned} \quad (3.1)$$

The boundary conditions for a non-reversible electrochemical reaction are

$$\left. \begin{aligned} t &\geq 0, & x &\rightarrow \infty \\ t &= 0, & x &\geq 0 \end{aligned} \right\} c_{\text{O}} = c_{\text{O}}^*, \quad c_{\text{R}} = c_{\text{R}}^* \quad (3.2)$$

$t > 0, \quad x = 0 :$

$$D_O \left(\frac{\partial c_O}{\partial x} \right)_{x=0} = - D_R \left(\frac{\partial c_R}{\partial x} \right)_{x=0} \quad (3.3)$$

$$D_O \left(\frac{\partial c_O}{\partial x} \right)_{x=0} = k_{\text{red}} c_O^s - k_{\text{ox}} c_R^s \quad (3.4)$$

Taking into account the relationship between the oxidation and reduction rate constants (i.e., $k_{\text{ox}} = k_{\text{red}} e^\eta$ with $\eta = F(E - E_c^{\ominus})/RT$; see Sect. 1.7) whatever the kinetic model considered, Eq. (3.4) becomes

$$D_O \left(\frac{\partial c_O}{\partial x} \right)_{x=0} = k_{\text{red}} [c_O^s - e^\eta c_R^s] \quad (3.5)$$

where c_O^s and c_R^s are the surface concentrations of species O and R.

The above problem is solved using the dimensionless parameter method developed by Koutecký [1–3] (the Laplace transform method has been addressed in reference [4]). First, we insert the dimensionless diffusion parameter s_i^p ($i = O, R$):

$$s_i^p = \frac{x}{2\sqrt{D_i t}} \quad (3.6)$$

such that the boundary value problem becomes

$$s_i^p \rightarrow \infty$$

$$c_O = c_O^*; \quad c_R = c_R^* \quad (3.7)$$

$$s_i^p = 0 :$$

$$\left(\frac{\partial c_O}{\partial s_O^p} \right)_{s_O^p=0} = - \frac{1}{\gamma} \left(\frac{\partial c_R}{\partial s_R^p} \right)_{s_R^p=0} \quad (3.8)$$

$$\left(\frac{\partial c_O}{\partial s_O^p} \right)_{s_O^p=0} = 2k_{\text{red}} \sqrt{\frac{t}{D_O}} [c_O^s - e^\eta c_R^s] \quad (3.9)$$

where

$$\gamma = \sqrt{D_O/D_R} \quad (3.10)$$

Surface condition (3.9) indicates that the surface concentrations of species O and R, c_O^s and c_R^s , are not only functions of variable s_i^p ($i = O, R$), as in the case of Nernstian charge transfer processes, but also time dependent, since their corresponding derivatives at $s_i^p = 0$ are too.

Both surface conditions (3.8) and (3.9) suggest the inclusion of a new time-dependent dimensionless variable:

$$\chi = 2k_{\text{red}} \sqrt{\frac{t}{D_{\text{O}}}} (1 + \gamma e^{\eta}) \quad (3.11)$$

Inserting variables s_i^{p} and χ in Eq. (3.1) gives the differential equation system in Eq. (D.1) of Appendix D, and by following the procedure described in Appendices A and D, the expressions for the concentration profiles are obtained (see Eqs. (D.19) and (D.20)). By making $s_i^{\text{p}} = 0$ in these equations, the following expressions for the surface concentrations are deduced:

$$c_{\text{O}}(0, \chi) = c_{\text{O}}^{\text{s}}(\chi) = c_{\text{O}}^* \left[1 + \left(\frac{1 - (c_{\text{R}}^*/c_{\text{O}}^*)e^{\eta}}{1 + \gamma e^{\eta}} \right) (H(\chi) - 1) \right] \quad (3.12)$$

$$c_{\text{R}}(0, \chi) = c_{\text{R}}^{\text{s}}(\chi) = c_{\text{R}}^* \left[1 - \frac{\gamma}{(c_{\text{R}}^*/c_{\text{O}}^*)} \left(\frac{1 - (c_{\text{R}}^*/c_{\text{O}}^*)e^{\eta}}{1 + \gamma e^{\eta}} \right) (H(\chi) - 1) \right] \quad (3.13)$$

where $H(\chi) = e^{(\chi/2)^2} \text{erfc}(\chi/2)$ (see also Eq. (2.138)).

In what follows, the Butler–Volmer formalism for the electrode kinetics will be assumed (unless otherwise indicated), so the expressions for the rate constants are (see Sect. 1.7.1):

$$\left. \begin{aligned} k_{\text{red}} &= k^0 e^{-\alpha\eta} \\ k_{\text{ox}} &= k_{\text{red}} e^{\eta} \end{aligned} \right\} \quad (3.14)$$

with $\eta = F(E - E_c^{\ominus})/RT$, and k^0 and α being the standard heterogeneous rate constant and charge transfer coefficient. Note that k^0 is the value of the reduction and oxidation rate constants at the formal potential E_c^{\ominus} .

3.2.1.1 Concentration Profiles

The concentration profiles are very sensitive to the kinetics of the electrode reaction. In this context, the determination of the diffusion layer thickness is of great importance in the study of non-reversible charge transfer processes. This magnitude can be defined as the thickness of the region adjacent to the electrode surface where the concentration of electro-active species differs from its bulk value, and it can be accurately calculated from the concentration profiles. In the previous chapter, the extensively used concept of “Nernst diffusion layer” (δ), defined as the distance at which the linear concentration profile (obtained from the straight line tangent to the concentration profile curve at the electrode surface) takes its bulk value, has been explained. In this chapter, we will refer to it as “linear diffusion layer” since the term “Nernst” can be misunderstood when non-reversible processes

are treated. An analytical expression for the linear diffusion layer thickness is provided in Eq. (3.22).

The variation with time of the transient concentration profiles ($c_O(x, t)/c_O^*$ vs. x) and the linear concentration profiles ($c_O(x, t) = ((c_O^* - c_O^s)/\delta_{p,O}^{qr})x + c_O^s$ vs. x is shown in Fig. 3.1, with $\delta_{p,O}^{qr}$ being the linear diffusion layer thickness, see below) of species O when a potential step $E = E_c^{\ominus'} - 0.10$ V is applied for different values of the standard heterogeneous rate constant k^0 and supposing that only species O is initially present in the electrolytic solution. The superscript “qr” in the diffusion layer δ denotes that it corresponds to quasi-reversible processes.

As can be observed from these curves, the rate of variation of linear and real diffusion layer thickness with time increases with k^0 , being maximum for $k^0 \geq 0.1$ cm s⁻¹, which corresponds to the reversible case. From Fig. 3.1a, it can be seen that for reversible processes the surface concentration is independent of time in agreement with Eq. (2.20) (see also Fig. 2.1 in Sect. 2.2.1). However, for non-reversible processes (Fig. 3.1b and c), the time has an important effect on the surface concentration, such that c_O^s decreases as t increases, with this behavior being more marked for intermediate k^0 values (quasi-reversible processes). So, for $k^0 = 10^{-3}$ cm s⁻¹, the surface concentration decreases by 19 % from $t = 0.1$ to 0.4 s, whereas for $k^0 = 10^{-4}$ cm s⁻¹ it only varies 7 %. It is also worth noting that for the reversible case (Fig. 3.1a), the diffusion control ($c_O^s \rightarrow 0$) has practically been reached at the selected potential.

3.2.1.2 Current–Time Curves (Chronoamperometry) and Current–Potential Curves (Voltammetry)

From Eq. (D.19) of Appendix D and (E.6) of Appendix E, the following expression for the current is obtained:

$$\frac{I^{\text{plane}}}{FAD_O} = \frac{1}{2\sqrt{D_O t}} \left(\frac{\partial c_O}{\partial s^p} \right)_{s^p=0} = \frac{c_O^*}{\sqrt{\pi D_O t}} \left(\frac{1 - (c_R^*/c_O^*)e^{\eta}}{1 + \gamma e^{\eta}} \right) F(\chi) \quad (3.15)$$

where F function is defined as (see Appendix E):

$$F(x) = \sum_{j=0}^{\infty} \frac{(-1)^j}{\prod_{h=0}^j p_h} (x)^{j+1} = \sqrt{\pi}(x/2) \exp(x/2)^2 \operatorname{erfc}(x/2) \quad (3.16)$$

By comparing Eq. (3.15) with Eq. (2.27), it can be written that

$$\frac{I^{\text{plane}}}{I^{\text{rev}}} = F(\chi) \quad (3.17)$$

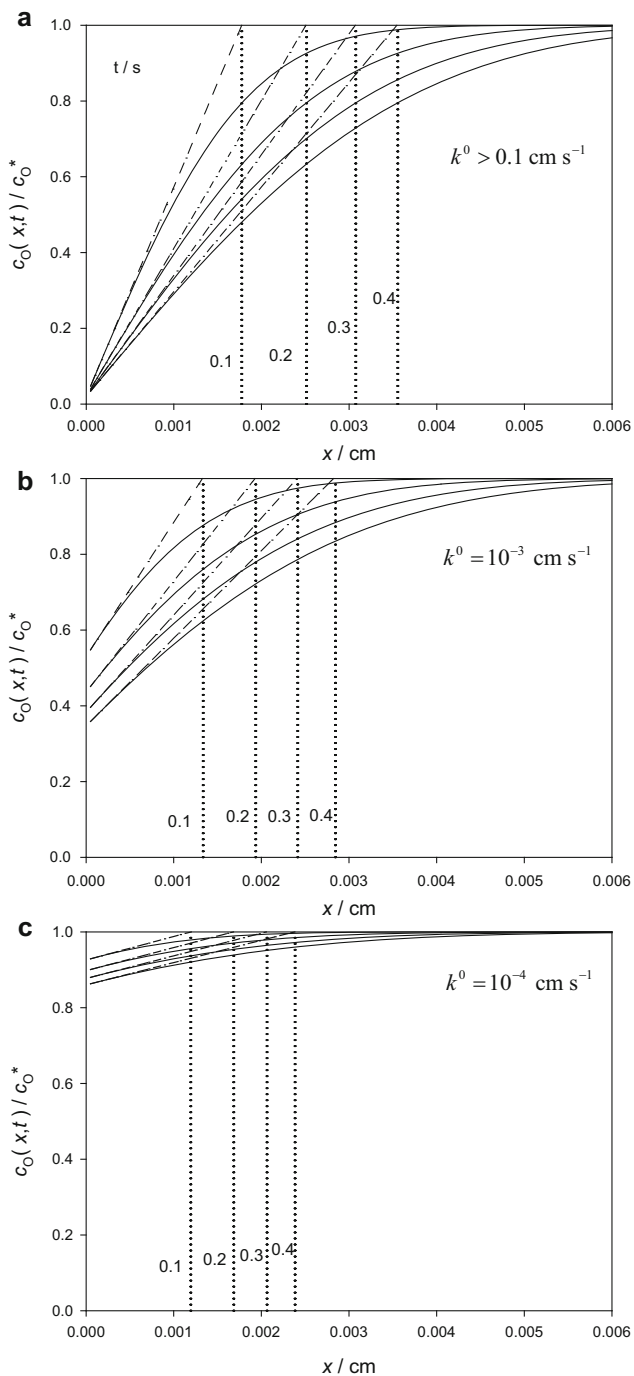


Fig. 3.1 Real concentration profiles (*solid lines*) and linear concentration profiles (*dashed lines*) of the oxidized species at a planar electrode for the application of a potential step, calculated from

or (see Eq. (2.28))

$$\frac{I^{\text{plane}}}{I_{\text{d,c}}^{\text{plane}}} = \frac{1 - (c_{\text{R}}^*/c_{\text{O}}^*)e^{\eta}}{1 + \gamma e^{\eta}} F(\chi) \quad (3.18)$$

with χ given in Eq. (3.11) and

$$I_{\text{rev}}^{\text{plane}} = FA \sqrt{\frac{D_{\text{O}}}{\pi t}} \frac{(c_{\text{O}}^* - c_{\text{R}}^* e^{\eta})}{1 + \gamma e^{\eta}} \quad (3.19)$$

$$I_{\text{d,c}}^{\text{plane}} = FA \sqrt{\frac{D_{\text{O}}}{\pi t}} c_{\text{O}}^* \quad (3.20)$$

The main characteristics of function F are outlined in Appendix E.

Equations (3.17) and (3.18) hold for electrochemical reactions of any reversibility degree. By comparing these equations with Eq. (3.19) corresponding to a reversible process, it can be inferred that the current for a non-reversible process is expressed as the reversible current modulated by F function (that contains the kinetic influence through the dimensionless parameter χ), which increases with χ from zero to the unity (see Fig. E.1 of Appendix E). Hence, small values of χ cause a strong kinetic influence and large values of χ give rise to a reversible behavior.

The faradaic current corresponding to any charge transfer process depends on the surface gradient $(\partial c_{\text{O}}/\partial x)_{x=0}$, which can be expressed as the ratio of the difference between the bulk and surface concentrations of the oxidized species and the linear diffusion layer, $\delta_{\text{p,O}}^{\text{qr}}$,

$$\frac{I^{\text{plane}}}{FAD_{\text{O}}} = \frac{c_{\text{O}}^* - c_{\text{O}}^{\text{s}}}{\delta_{\text{p,O}}^{\text{qr}}} \quad (3.21)$$

By solving for $\delta_{\text{p,O}}^{\text{qr}}$ in Eq. (3.21) and substituting the expressions of the surface concentrations and the current given by Eqs. (3.12) and (3.18), one has [3]:

$$\delta_{\text{p,O}}^{\text{qr}} = G(\chi) \delta_{\text{p,O}}^{\text{r}} \quad (3.22)$$

with

$$G(\chi) = \frac{1}{F(\chi)} - \frac{1}{\chi\sqrt{\pi}/2} \quad (3.23)$$

Fig. 3.1 (continued) Eq. (D.19) $E - E_{\text{c}}^{\ominus'} = -0.1$ V, $\alpha = 0.5$, $D_{\text{O}} = 10^{-5}$ cm² s⁻¹, $\gamma = 1$. $T = 298$ K. The values of time and of the heterogeneous rate constant k^0 are on the curves. *Dotted lines* mark the values of the linear diffusion layer. Reproduced with permission from reference [3]

$$\delta_{p,O}^r = \sqrt{\pi D_0 t} \quad (3.24)$$

and $F(\chi)$ given by Eq. (3.16).

From Eq. (3.22), it can be deduced that function G defines the ratio $\delta_{p,O}^{qr}/\delta_{p,O}^r$ as a function of parameter χ , and leads to the following limits:

$$\frac{2}{\pi} \leq \frac{\delta_{p,O}^{qr}}{\delta_{p,O}^r} \leq 1 \quad (3.25)$$

Note that $\delta_{p,O}^{qr}$, unlike the reversible case, depends on the applied potential, and the more irreversible the process, the smaller the diffusion layer (except under limiting current conditions where the thickness is independent of the electrode kinetics).

For fully irreversible reduction reactions (small values of k^0), the enhancement of k_{red} leads to a progressive decrease of k_{ox} as the potential becomes less than $E_c^{e'}$ such that, under conditions for which the current is measurable, it is fulfilled that $k_{red} \gg k_{ox}$. Under these conditions, $(k_{ox}/k_{red}) = e^{\eta} \rightarrow 0$, and from Eqs. (3.11) and (3.18),

$$\frac{I^{plane}}{I_{d,c}^{plane}} = F(\chi^{irrev}) \quad (3.26)$$

can be easily deduced, where

$$\chi^{irrev} = 2k_{red} \sqrt{\frac{t}{D_0}} \quad (3.27)$$

From Eqs. (3.26) and (3.27), the expression of the half-wave potential for a totally irreversible reaction can be easily deduced since, for $E = E_{1/2}^{irrev}$,

$$\frac{I^{plane}}{I_{d,c}^{plane}} = \frac{1}{2} = F(\chi_{1/2}^{irrev}) \quad (3.28)$$

with

$$\chi_{1/2}^{irrev} = 2k^0 \sqrt{\frac{t}{D_0}} e^{-\frac{aF}{RT} (E_{1/2}^{irrev} - E_c^{e'})} \quad (3.29)$$

Equation (3.28) holds for $\chi_{1/2}^{irrev} = 0.865$. By taking logarithms and solving for $E_{1/2}^{irrev}$, one obtains [4, 5],

$$E_{1/2}^{\text{irrev}} = E_c^{\ominus'} + \frac{RT}{\alpha F} \ln \left(2.309 k^0 \sqrt{\frac{t}{D_O}} \right) \quad (3.30)$$

It is important to highlight that the current for a quasi-reversible or fully irreversible electrode process cannot be expressed as a product of functions depending on the different variables, i.e., applied potential and time (or $k^0 \sqrt{t/D_O}$). Unfortunately, the dimensionless parameter χ is influenced by time, by the kinetic constants and by the applied potential.

3.2.1.2.1 Chronoamperometry

The expression for the current of a non-reversible process given by Eq. (3.18) allows us to obtain those corresponding to cathodic and anodic diffusion-controlled limiting currents, $I_{d,c}^{\text{plane}}$ and $I_{d,a}^{\text{plane}}$ given by Eq. (2.28) by making $e^{\eta} \rightarrow 0$ and $e^{\eta} \rightarrow \infty$, respectively (i.e., $\chi \rightarrow \infty$; see Eqs. (3.11) and (3.14), and Appendix E).

The dependence on time of the current when a constant potential is applied to a plane electrode for different values of the heterogeneous rate constant k^0 ranging from reversible to totally irreversible processes is shown in Fig. 3.2.

From these curves, it can be seen that the current decreases with time in all cases, and more pronounced the higher the rate constant. Moreover, for values of $k^0 \geq 10^{-2} \text{ cm s}^{-1}$, the response becomes independent of the kinetics, i.e., the reversible limit has been reached. The rate constant is related to the kinetic

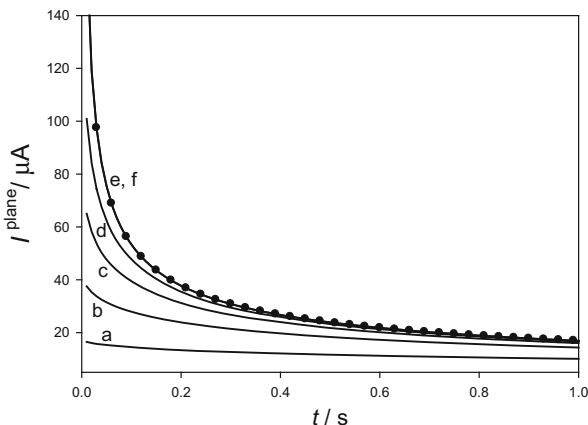


Fig. 3.2 Current–time curves calculated from Eq. (3.18) for a plane electrode with $E - E_c^{\ominus'} = -0.15 \text{ V}$, $A = 0.031 \text{ cm}^2$, $c_O^* = 1 \text{ mM}$, $c_R^* = 0$, $D_O = 10^{-5} \text{ cm}^2 \text{ s}^{-1}$, $\gamma = 1$. The values of the heterogeneous rate constant k^0 (in cm s^{-1}) are: (a) 10^{-4} ; (b) 2.5×10^{-4} ; (c) 5×10^{-4} ; (d) 10^{-3} ; (e) 10^{-2} ; and (f) 0.1. The current corresponding to a reversible process, given by Eq. (2.27), has been included for comparison (*black dots*)

activation that the charge process requires to give rise to measurable values of the current. In this sense it can be seen that, whereas for reversible processes the current tends to infinity when the time tends to zero (see Eq. (2.28)), in the case of non-reversible processes, the current takes a constant value at $t \rightarrow 0$, which decreases with the rate constant. This value can be obtained from the series expansion of function F given in Appendix E for small values of χ (see Eq. (E.6))

$$(I^{\text{plane}})_{t \ll 1} \cong \frac{1 - (c_{\text{R}}^*/c_{\text{O}}^*)e^{\eta}}{1 + \gamma e^{\eta}} FAc_{\text{O}}^*(k_{\text{red}} + \gamma k_{\text{ox}}) \left(1 - \frac{2}{\sqrt{\pi}}(k_{\text{red}} + \gamma k_{\text{ox}}) \sqrt{\frac{t}{D_{\text{O}}}} \right) \quad (3.31)$$

so for $t \rightarrow 0$ the second term in the brackets of the right-hand side vanishes and the current takes the constant value $(1 - (c_{\text{R}}^*/c_{\text{O}}^*)e^{\eta})FAc_{\text{O}}^*(k_{\text{red}} + \gamma k_{\text{ox}})/(1 + \gamma e^{\eta})$, which for a totally irreversible process simplifies to $FAk_{\text{red}}c_{\text{O}}^*$.

3.2.1.2.2 Voltammetry

The shape and location of the current–potential curves are strongly dependent on the kinetics of the electrode reaction through the dimensionless rate constant, defined as

$$\kappa_{\text{plane}}^0 = k^0 \sqrt{t/D_{\text{O}}} \quad (3.32)$$

This dimensionless rate constant contains typical parameters of the process (i.e., the heterogeneous rate constant k^0 , the diffusion coefficient, and the experiment time), thus reflecting that the behavior of the process is the result of a combination of intrinsic (kinetics and diffusion) and extrinsic (time window) effects. The effect of κ_{plane}^0 in the voltammograms obtained when both species (a) or only oxidized species O (b) are initially present can be seen in Fig. 3.3.

The curves in Fig. 3.3a for electrochemical processes of different reversibility degree show how κ_{plane}^0 affects the voltammograms. Note that a decrease of the dimensionless rate constant leads to gentler current–potential curves. In this sense, irreversible processes spread into broader intervals of potential. This can be quantified by calculating the width of the potential region needed to go from, for example, $(1/4)(I^{\text{plane}}/I_{\text{d,c}}^{\text{plane}})$ to $(3/4)(I^{\text{plane}}/I_{\text{d,c}}^{\text{plane}})$ (i.e., the difference $E_{3/4}^{\text{irr}} - E_{1/4}^{\text{irr}}$). For a reversible process, this region has a width of 56 mV (see Eq. (2.36) and Fig. 2.4 of Sect. 2.2.2.2), whereas for a totally irreversible one (i.e., $\kappa_{\text{plane}}^0 \leq 0.01$) it is of 90 mV (see Eq. (3.26) and Fig. 3.4). Moreover, for values of $\kappa_{\text{plane}}^0 \leq 0.01$, the shape of the anodic and cathodic waves remains unchanged although they move toward positive and negative potentials, respectively. This shift is due to the fact that the lower κ_{plane}^0 is, the higher the values of η necessary for χ to have a value for

Fig. 3.3 Normalized current–potential curves calculated from Eq. (3.18) for a plane electrode with $\gamma = 1$, $c_R^* = c_O^*$ (a) and $c_R^* = 0$ (b). The values of the dimensionless rate constant $\kappa_{\text{plane}}^0 = k^0 \sqrt{t/D_O}$ are shown in the curves. The current corresponding to a reversible process, given by Eq. (2.27), has been included for comparison (black dots). $\alpha = 0.5$, $T = 298 \text{ K}$

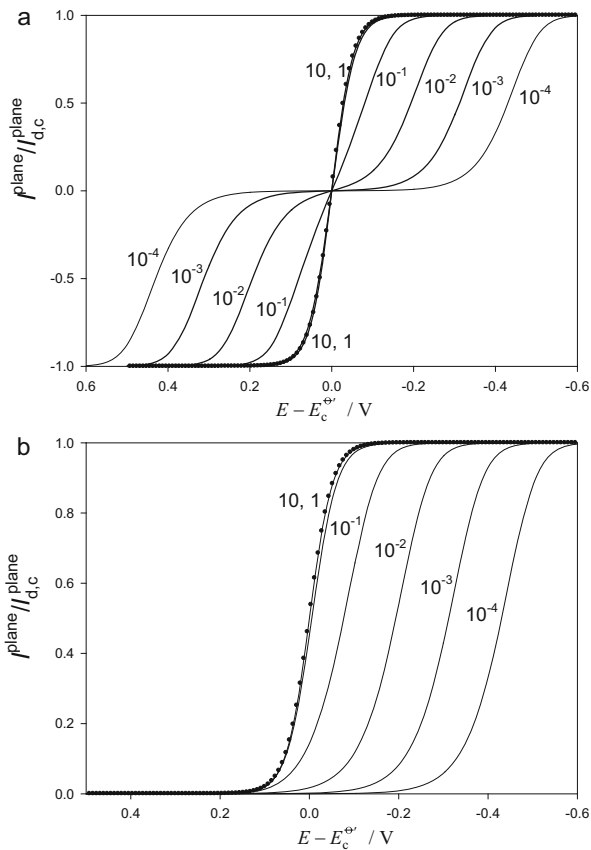
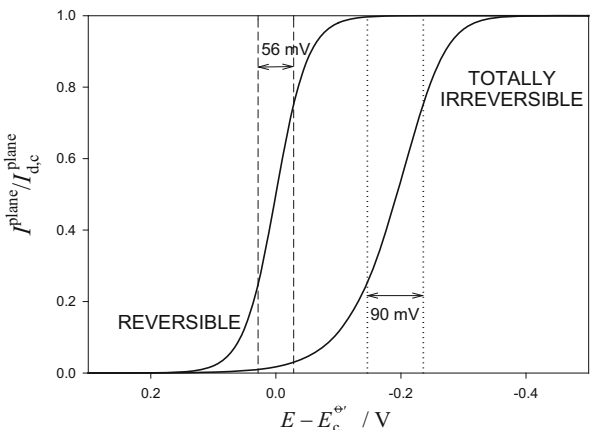


Fig. 3.4 Comparison of the voltammograms corresponding to a reversible process (calculated from Eq. (2.36)) and to a totally irreversible one (calculated from Eq. (3.26)) with $(c_R^*/c_O^*) = 0$, $\alpha = 0.5$, and $\kappa_{\text{plane}}^0 = 0.01$



$F(\chi) \neq 0$. In other words, the electrode reaction presents a stronger kinetic resistance the smaller κ_{plane}^0 is, and, as a consequence, higher η values are required to obtain measurable anodic and cathodic currents.

It is also worth pointing out that a similar result to that shown in Fig. 3.3 is obtained if we analyze the effect of the time in the response of a quasi-reversible charge transfer process, i.e., for a given value of the rate constant k^0 , a decrease of the time leads to a decrease of the dimensionless rate constant κ_{plane}^0 and therefore to a higher irreversible character of the process. This fact can be used to ascertain at a glance if a particular electrode process behaves in a reversible or non-reversible way, since in the first case no influence of time on the normalized current is observed (see Eq. (2.36)).

3.2.1.3 Approximate Treatment

This approximate procedure is similar to that used in references [6–8] applied to the Dropping Mercury Electrode. In this treatment, it is assumed that the concentrations of oxidized and reduced species at the electrode surface can be written in the form given by Eq. (2.30), i.e.,

$$c_{\text{O}}^{\text{s}} = c_{\text{O}}^* \left(\frac{I_{\text{d,c}}^{\text{plane}} - I^{\text{plane}}}{I_{\text{d,c}}^{\text{plane}}} \right) \quad (3.33)$$

$$c_{\text{R}}^{\text{s}} = c_{\text{R}}^* \left(\frac{I_{\text{d,a}}^{\text{plane}} - I^{\text{plane}}}{I_{\text{d,a}}^{\text{plane}}} \right) \quad (3.34)$$

with $I_{\text{d,c}}^{\text{plane}}$ and $I_{\text{d,a}}^{\text{plane}}$ given by Eq. (2.28) of Sect. 2.2.2.1.

As the current for a non-nernstian process is

$$\frac{I^{\text{plane}}}{FA} = k_{\text{red}} c_{\text{O}}^{\text{s}} - k_{\text{ox}} c_{\text{R}}^{\text{s}} \quad (3.35)$$

by inserting Eqs. (3.33), (3.34), and (2.28) in (3.35), the following expression for the current is deduced:

$$I^{\text{plane}} = \frac{\sqrt{\pi t} \left\{ k_{\text{red}} \frac{I_{\text{d,c}}^{\text{plane}}}{\sqrt{D_{\text{O}}}} + k_{\text{ox}} \frac{I_{\text{d,a}}^{\text{plane}}}{\sqrt{D_{\text{R}}}} \right\}}{1 + k_{\text{red}} \sqrt{\frac{\pi t}{D_{\text{O}}}} + k_{\text{ox}} \sqrt{\frac{\pi t}{D_{\text{R}}}}} \quad (3.36)$$

By considering that the current for a reversible process, after arranging Eq. (2.31) of Sect. 2.2.2.2 and taking into account that $e^{\eta} = k_{\text{ox}}/k_{\text{red}}$, it can be written as

$$I_{\text{rev}}^{\text{plane}} = \frac{k_{\text{red}}\sqrt{D_{\text{R}}}I_{\text{d,c}} + k_{\text{ox}}\sqrt{D_{\text{O}}}I_{\text{d,a}}}{k_{\text{red}}\sqrt{D_{\text{R}}} + k_{\text{ox}}\sqrt{D_{\text{O}}}} \quad (3.37)$$

From Eqs. (3.36) and (3.37), we get

$$\frac{I_{\text{rev}}^{\text{plane}}}{I_{\text{rev}}^{\text{plane}}} = \frac{\sqrt{\pi t} \left\{ \frac{k_{\text{red}}}{\sqrt{D_{\text{O}}}} + \frac{k_{\text{ox}}}{\sqrt{D_{\text{R}}}} \right\}}{1 + \sqrt{\pi t} \left\{ \frac{k_{\text{red}}}{\sqrt{D_{\text{O}}}} + \frac{k_{\text{ox}}}{\sqrt{D_{\text{R}}}} \right\}} \quad (3.38)$$

It is important to note that Eq. (3.38) obtained with this treatment (based on the consideration that the diffusion layer corresponding to a non-nernstian electrode process coincides with that corresponding to a reversible one) can also be directly deduced from Eq. (3.17) if $F(\chi)$ is replaced by its simplified form given by Eq. (E.10) (which is valid for $\chi \leq 0.185$ and $\chi \geq 19.7$ with an error smaller than 5 %; see Appendix E):

$$\frac{I_{\text{rev}}^{\text{plane}}}{I_{\text{rev}}^{\text{plane}}} = F(\chi) \approx \frac{(\sqrt{\pi}/2)\chi}{1 + (\sqrt{\pi}/2)\chi} \quad (3.39)$$

So, for an irreversible cathodic electrode reaction ($k_{\text{red}} \gg k_{\text{ox}}$, $e^{\eta} \rightarrow 0$), Eq. (3.38) or (3.39) leads to

$$\frac{I_{\text{d,c}}^{\text{plane}}}{I_{\text{d,c}}^{\text{plane}}} = \frac{\sqrt{\frac{\pi t}{D_{\text{O}}}}k_{\text{red}}}{1 + \sqrt{\frac{\pi t}{D_{\text{O}}}}k_{\text{red}}} \quad (3.40)$$

By expressing k_{red} in terms of the potential through the Butler–Volmer relation ($k_{\text{red}} = k^0 e^{-a\eta}$), it is easily deduced that under suitable conditions in which Eq. (3.40) is applicable, the potential varies linearly with $\ln\left(\left(I_{\text{d,c}}^{\text{plane}} - I^{\text{plane}}\right)/I^{\text{plane}}\right)$:

$$E = E_{1/2} + \frac{RT}{\alpha F} \ln\left(\frac{I_{\text{d,c}}^{\text{plane}} - I^{\text{plane}}}{I^{\text{plane}}}\right) \quad (3.41)$$

with

$$E_{1/2} = E_c^{\text{eff}} + \frac{RT}{\alpha F} \ln\left(\sqrt{\pi}\kappa_p^0\right) \quad (3.42)$$

Note that the expression of $E_{1/2}$ in Eq. (3.42) differs from that obtained from the rigorous expression of $E_{1/2}$ for a fully irreversible electrode process given in Eq. (3.30) (with this difference being $RT\ln(2.309/\sqrt{\pi})/(\alpha F) = 13.6$ mV for $\alpha = 0.5$ and $T = 298$ K).

3.2.1.4 Reversibility Criteria

At this point, a question arises concerning the reversibility degree of the charge transfer process. It was stated in Sect. 3.2 that an exact definition of a slow charge transfer process is not possible. However, is it possible to give a criterion for clearly defining when the electrode process behaves in a reversible or non-reversible way? Attending to the above discussion and to that in Sect. 3.2, this question could be answered by considering the relation between the heterogeneous rate constant and the mass transport coefficient for the oxidized species, m_O , defined as the ratio between the surface flux and the difference of bulk and surface concentrations (see Sect. 1.8.4 and references [4, 9, 10]), i.e.,

$$m_O = \frac{I^{\text{plane}}/FA}{c_O^* - c_O^s} = \frac{D_O}{\delta_{p,O}^{\text{qr}}} \quad (3.43)$$

Note that the usual definition of the mass transfer coefficient is related to limiting diffusion conditions or nernstian conditions ($m_{O,\infty} = \sqrt{D_O/\pi t}$ for a planar electrode; see Sect. 1.8.4). The definition given in Eq. (3.43) is general for any reversibility degree of the electrode process at planar electrodes.

In order to discriminate between reversible and non-reversible regimes, the behavior of the following relation R^0 at the formal potential should be examined:

$$R^0 = \frac{k^0}{m_O^0} = \frac{k^0 \delta_{p,O}^{\text{qr}}(\chi^0)}{D_O} \quad (3.44)$$

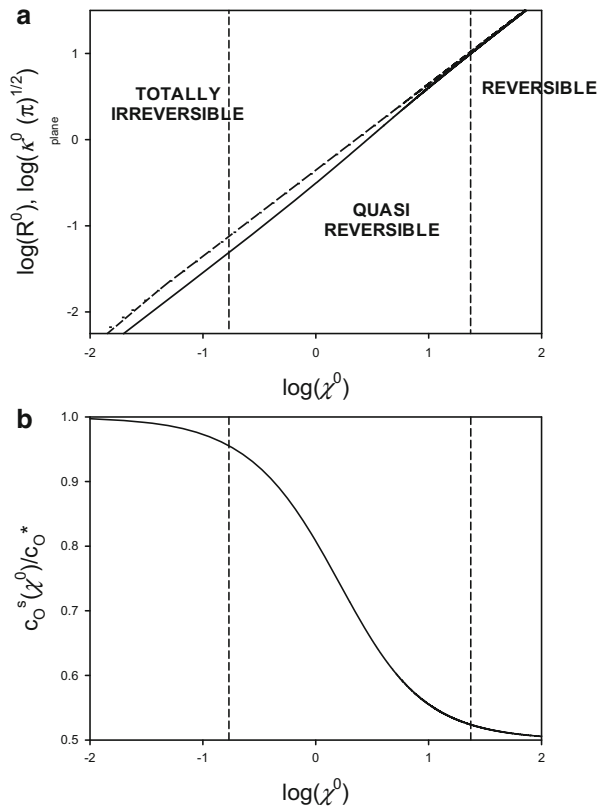
with χ^0 and m_O^0 being the value of χ and m_O at $E = E_c^{\ominus}$. By taking into account Eqs. (3.11), (3.14), and (3.22)–(3.24), R^0 can be written as

$$R^0 = \chi^0 \frac{\sqrt{\pi}}{2(1+\gamma)} G(\chi^0) \quad (3.45)$$

By assuming that a reversible process corresponds to $R^0 > 10$ and a fully irreversible one to $R^0 < 0.05$ (i.e., the heterogeneous rate constant is ten times higher or 20 times smaller than the mass transport coefficient, respectively), in the interval $0.05 \leq R^0 \leq 10$ the process can be considered as quasi-reversible. The variation of $\log(R^0)$ with $\log(\chi^0)$ for $\gamma = 1$ has been plotted in Fig. 3.5, and the three regions have been delimited. From the above criterion, a totally irreversible process is characterized by a value of $\chi^0 < 0.17$ (which corresponds to a dimensionless rate constant $\kappa_{\text{plane}}^0 < 0.042$), and a reversible behavior is attained for $\chi^0 > 23.6$ (i.e., $\kappa_{\text{plane}}^0 > 5.9$).

The figure also includes the variation of the ratio $k^0/m_{O,\infty} = \sqrt{\pi}\kappa_{\text{plane}}^0$ with $\log(\chi^0)$ (dashed line) for comparison. Thus, it can be seen that in the reversible limit, there is a coincidence with the criterion used here, but in the irreversible one, this

Fig. 3.5 Variation of $\log(R^0)$ (a) and of the surface concentration of oxidized species $c_O^s(\chi^0)$ (b) with $\log(\chi^0)$ calculated from Eqs. (3.45) and (3.12) with $c_R^* = 0$, respectively. The variation of the ratio $\sqrt{\pi}\kappa_{\text{plane}}^0$ with $\log(\chi^0)$ (dashed line) has been included in Fig. 3.5a for comparison



relation leads to a value of $\chi^0 = 0.113$ (i.e., $\kappa_{\text{plane}}^0 < 0.03$ if $\gamma = 1$). This smaller value of κ_{plane}^0 is a consequence of the use of the linear diffusion layer for reversible processes instead of that obtained for processes of any reversibility given by Eq. (3.22) (which fulfills $(\delta_{\text{p},\text{O}}^{\text{qr}} / \delta_{\text{p},\text{O}}) \leq 1$).

The criterion discussed above is based on the dependence of the surface concentration of the oxidized species with the reversibility degree of the electrode process. So, for a totally irreversible process, the rate of depletion of the surface concentration c_O^s is much smaller than the mass transport rate process, and therefore, at the formal potential its value should be coincident with the bulk concentration ($c_O^s(\chi^0)/c_O^* \cong 1$). In contrast, for reversible electrode reactions, $c_O^s(\chi^0)/c_O^* = 0.5$ (see Eq. (2.20) of Sect. 2.2 for $c_R^* = 0$ and $\gamma = 1$). In order to verify this behavior, the variation of the surface concentration of species O at the formal potential calculated as a function of χ^0 has been plotted in Fig. 3.5b. From this figure, it can be deduced that at the irreversible limit (i.e., $\chi^0 = 0.17$), $c_O^s(\chi^0)/c_O^* = 0.955$ (around 5 % error), whereas for the reversible limit ($\chi^0 = 23.6$), it is $c_O^s(\chi^0)/c_O^* = 0.524$ (around 5 % error). Both results confirm the accuracy of the chosen limits of χ^0 .

Note that any reversibility criterion can change with the geometry and size of the electrode considered since the expression of the mass transport coefficient depends on these features.

3.2.1.5 Determination of Kinetic Parameters

The characterization of a non-reversible electrode process is logically more complex than that of a reversible one since it implies knowledge of thermodynamic (formal potential) and kinetic (heterogeneous rate constant and charge transfer coefficient) parameters of the process under study.

There are various approaches for determining the kinetic parameters of non-reversible processes. The most common correspond to totally irreversible processes since the expression of the current given by Eq. (3.26) is simpler than that obtained for the general case (Eq. 3.18). Below we present the main features of three ways of determining these parameters.

(a) Determination of k_{red} at any potential value

In agreement with Eq. (3.26), for a totally irreversible process, from a plot of the normalized current $I^{\text{plane}}/I_{\text{d,c}}^{\text{plane}}$ vs. χ^{irrev} (i.e., Fig. E.1 in Appendix E), it is possible to determine the values of parameter χ^{irrev} corresponding to each potential by using the corresponding values of F function. Once the values of χ^{irrev} have been obtained, from Eq. (3.27), k_{red} at each potential follows immediately. A logarithmic plot of the potential versus $\ln(k_{\text{red}})$ will allow us to obtain the values of α from the slope and of k^0 from the intercept if the formal potential is known (see Eq. (3.14)).

(b) Tomeš criterion [11]

As in the reversible case, together with the irreversible half-wave potential, the difference between potentials corresponding to a current $I^{\text{plane}} = (3/4)I_{\text{d,c}}^{\text{plane}}$ and $I^{\text{plane}} = (1/4)I_{\text{d,c}}^{\text{plane}}$, $E_{3/4}^{\text{irr}} - E_{1/4}^{\text{irr}}$, can be used to determine the charge transfer coefficient. Thus, for a quasi-reversible process, this difference is higher than the 56.4 mV value typical of a reversible monoelectronic charge transfer, reaching the value $45/\alpha$ mV for a fully irreversible process (see also Fig. 3.4). By combining this difference with the irreversible half-wave potential given by Eq. (3.30), it is possible to obtain k^0 when the formal potential is known.

(c) Linearized current–potential curves.

The easiest way to obtain thermodynamic information of a reversible electrode process comes from the plots of the potential versus $\ln\left(\left(I_{\text{d,c}}^{\text{plane}} - I^{\text{plane}}\right)/I^{\text{plane}}\right)$, which are linear in agreement with Eq. (2.35) of Sect. 2.2.2.2, and whose intercept coincides with the reversible half-wave potential. In the case of non-reversible processes, it could be thought that these plots would not be linear since this linearity is a direct consequence of

the separation between potential and time dependences in the expression of the reversible current, which does not occur in the case of fully irreversible processes (see Eq. (3.26)). In order to check if this linearity could also be observed for non-reversible processes at planar electrodes, a set of $E - \ln\left(\left(I_{d,c}^{\text{plane}} - I^{\text{plane}}\right)/I^{\text{plane}}\right)$ curves calculated for different values of the dimensionless rate constant κ_{plane}^0 covering all the reversibility degrees of the process is plotted in Fig. 3.6. The plots in this figure for non-reversible processes (i.e., $\kappa_{\text{plane}}^0 < 1$) deviate from linearity, but can be decomposed into three different linear regions corresponding to different potential intervals (which are related with the corresponding values of χ through Eq. (3.11)). The particular case corresponding to $\kappa_{\text{plane}}^0 = 0.1$ is analyzed in detail in Fig. 3.7. The zone labeled 1 corresponds to positive potentials and high values of χ (i.e., $F(\chi) \approx 1$; see Appendix E), for which the process behaves as reversible and the $E - \ln\left(\left(I_{d,c}^{\text{plane}} - I^{\text{plane}}\right)/I^{\text{plane}}\right)$ plot in this region is coincident with that obtained for a reversible process (black dots in Fig. 3.6), thus presenting as intercept the reversible half-wave potential $E_{1/2}^E$ (red dot on Fig. 3.7b). This potential region corresponds to the foot of non-reversible voltammograms (red line in Fig. 3.7) and it will only be useful for quasi-reversible processes ($1 > \kappa_{\text{plane}}^0 > 0.1$) since for irreversible ones it appears at very positive potentials at which the current obtained is indistinguishable from the background current (Fig. 3.7a). For more negative potentials (zone 2 of the voltammogram; see also blue line in Fig. 3.7b), a second zone with a linear dependence of the potential with $\ln\left(\left(I_{d,c}^{\text{plane}} - I^{\text{plane}}\right)/I^{\text{plane}}\right)$ appears. This zone corresponds to small values of χ for which the approximate Eq. (3.40) can be used with small error (see Appendix E). Therefore,

Fig. 3.6 E vs. $\ln\left(\left(I_{d,c}^{\text{plane}} - I^{\text{plane}}\right)/I^{\text{plane}}\right)$ curves calculated from Eq. (3.18) for different values of the dimensionless rate constant κ_{plane}^0 . $c_R^* = 0$, $\alpha = 0.5$. The plot corresponding to a reversible process, given by Eq. (2.35) of Sect. 2.2.2.2, is included for comparison (black dots)

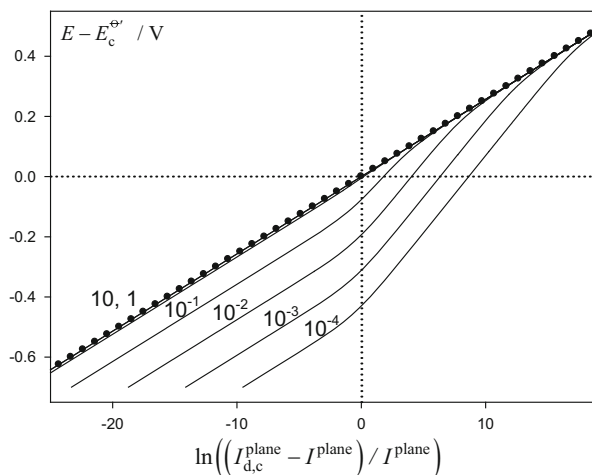
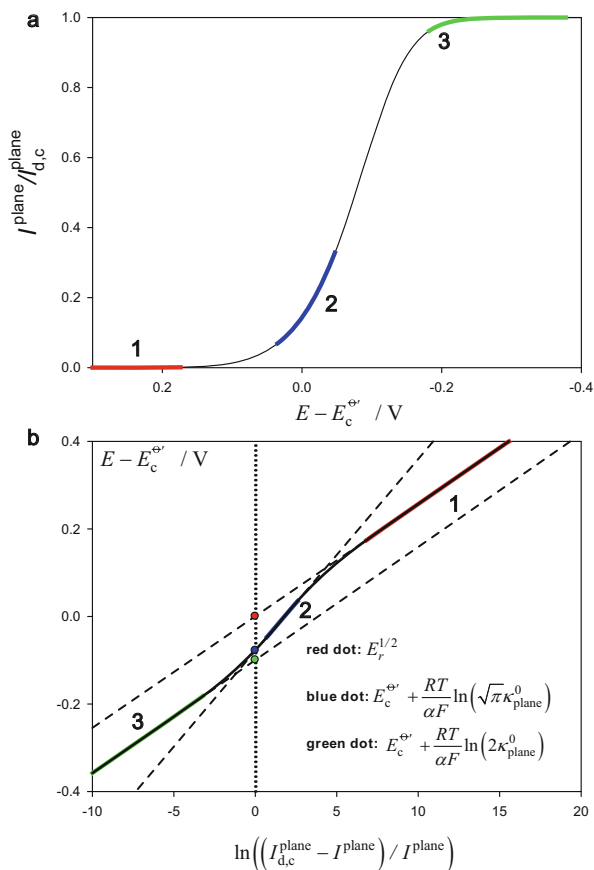


Fig. 3.7 Current–potential (a) and

$(E - E_c^{\ominus'}) - \ln$
 $\left(\frac{I_{d,c}^{\text{plane}} - I^{\text{plane}}}{I^{\text{plane}}}\right)$
 curves (b) calculated from
 Eq. (3.18) for $\kappa_{\text{plane}}^0 = 0.1$.
 $c_R^* = 0$, $\alpha = 0.5$



$$E \cong E_c^{\ominus'} + \frac{RT}{\alpha F} \ln\left(\sqrt{\pi} \kappa_{\text{plane}}^0\right) + \frac{RT}{\alpha F} \ln\left(\frac{I_{d,c}^{\text{plane}} - I^{\text{plane}}}{I^{\text{plane}}}\right) \quad (3.46)$$

is fulfilled.

Note that the range of potentials for which Eq. (3.46) can be applied becomes broader as the rate constant decreases. By using Eq. (3.46), the rate constant k^0 can be determined from the intercept of these plots $(E_c^{\ominus'} + RT \ln(\sqrt{\pi} \kappa_{\text{plane}}^0)/(\alpha F))$, shown as a blue dot in Fig. 3.7b, if the formal potential is known (with negligible errors in the rate constant for $\kappa_{\text{plane}}^0 \leq 10^{-2}$).

Finally, for currents close to the diffusion-limiting current (very cathodic potentials), a new linear region appears (labeled 3 in Fig. 3.7) which, for $\alpha = 0.5$, presents the same slope as the reversible region. The linear dependence found here can be identified using a truncated asymptotic expansion of function F given by Eq. (E.9) of Appendix E

$$F(\chi) \approx 1 - \frac{2}{\chi^2}, \quad \chi > 3.6 \quad (3.47)$$

By inserting Eq. (3.47) into Eq. (3.26) it is found that

$$E \cong E_c^{\ominus'} + \frac{RT}{\alpha F} \ln\left(\sqrt{2}\kappa_{\text{plane}}^0\right) + \frac{RT}{2\alpha F} \ln\left(\frac{I_{\text{d,c}}^{\text{plane}} - I^{\text{plane}}}{I^{\text{plane}}}\right) \quad (3.48)$$

Under these conditions, for $\alpha = 0.5$ the slope coincides with that corresponding to a reversible process and the intercept is $E_c^{\ominus'} + (2RT/F)\ln\left(\sqrt{2}\kappa_{\text{plane}}^0\right)$ (marked as a green dot in Fig. 3.7b). As the current values for this region are close to $I_{\text{d,c}}^{\text{plane}}$, the limiting current needs to be obtained with high accuracy. From a practical point of view, only region 2 will provide good normalized current values for the linear analysis of the non-reversible current potential curves. The usefulness of zones 1 and 3 depends on the accuracy of the experimental values for the current response and on the degree of reversibility of the process. This behavior reflects the complexity of the current–potential response associated with non-reversible processes and the great difficulties involved in the analysis of the kinetic and thermodynamic parameters. For this reason, the common way to proceed in the analysis of the current potential curves of a non-reversible electrode reaction involves the use of numerical fitting procedures to determine the characteristics parameters of the process under study.

3.2.2 Dropping Mercury Electrode

3.2.2.1 dc Polarography

The study of non-reversible processes with dc Polarography was solved by Koutecký [1, 6] by using the dimensionless parameter method and finding the following expression for the current:

$$\frac{I_{\text{dcP}}^{\text{DME}}}{I_{\text{rev}}^{\text{DME}}} = F(\chi_{\text{DME}}) \quad (3.49)$$

where $I_{\text{rev}}^{\text{DME}}$ is given by Eq. (2.113) and $F(\chi_{\text{DME}})$ is the so-called Koutecký function. This function is given in equation (E.1) of Appendix E ($z = 2/3$) by

$$\chi_{\text{DME}} = \sqrt{\frac{3}{7}} 2k_{\text{red}} \sqrt{\frac{t}{D_{\text{O}}}} (1 + \gamma e^{\eta}) = \sqrt{\frac{3}{7}} \chi \quad (3.50)$$

γ and χ are given by Eqs. (3.10) and (3.11). Different approximations to $F(\chi_{\text{DME}})$ are discussed in Appendix E.

The characteristics of the current–potential curves (polarograms) are similar to that discussed in Sect. 3.2.1.2.2 for planar electrodes.

For an irreversible process, the half-wave potential is

$$E_{1/2}^{\text{DME, irrev}} = E_c^{\ominus'} + \frac{RT}{\alpha F} \ln \left(1.33k^0 \sqrt{\frac{t}{D_O}} \right) \quad (3.51)$$

3.2.2.2 Normal Pulse Polarography

The measured current at a short pulse time at the end of the drop life is given by

$$I_{\text{NPP}}^{\text{DME}} = FA(t_1 + t_2) \sqrt{\frac{D_O}{\pi t_2}} c_O^* \frac{G(\alpha, \chi)}{1 + \gamma e^\eta} \quad (3.52)$$

where

$$A(t_1 + t_2) = 4\pi \left(\frac{3m}{4\pi\rho} \right)^{2/3} (t_1 + t_2)^{2/3} \quad (3.53)$$

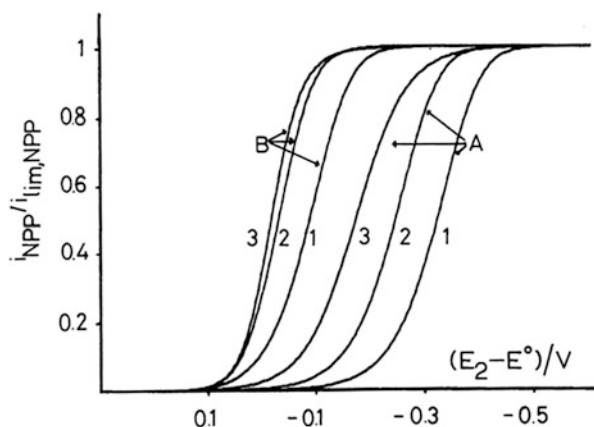
$$\alpha = \frac{t_2}{t_1 + t_2} \quad (3.54)$$

$$\chi = 2k_{\text{red}} \sqrt{\frac{t_2}{D_O}} (1 + \gamma e^\eta) \quad (3.55)$$

$G(\alpha, \chi)$ is defined by Eqs. (A4)–(A5) in reference [12], and m and ρ are the flux and density of the mercury, respectively.

The behavior of the normalized normal pulse polarograms at different pulse time values is shown in Fig. 3.8, which clearly shows the influence of the pulse time on

Fig. 3.8 NPP curves obtained for different values of t_2 for $D_O = 10^{-5} \text{ cm}^2 \text{ s}^{-1}$, $T = 298 \text{ K}$, $\alpha = 0.5$, $t_1 = 1 \text{ s}$, k^0 (in cm s^{-1}): (A) 10^{-2} ; (B) 10^{-4} . t_2 (in s): (1) 0.001; (2) 0.02; (3) 1. Reproduced with permission [12]



the reversibility of the process, with the current potential curve being as more irreversible the smaller the value of t_2 .

3.2.3 Spherical Electrodes and Microelectrodes

As shown in Chap. 2, attaining analytical explicit solutions is considerably more complex for nonplanar geometries. This section studies quasi-reversible and irreversible processes when a potential step is applied to a spherical electrode, since this solution will be very useful for discussing the behavior of these electrode reactions when steady-state conditions are addressed in the next section. Moreover, the treatment of other electrode geometries seldom leads to explicit analytical solutions and it is necessary in most cases to use numerical treatments.

Section 2.5 and Appendix A show (see Eqs. (A.27)–(A.32)) how the change of variable

$$u_i(r, t) = \frac{c_i(r, t)r}{c_O^* r_s} \quad i = O, R \quad (3.56)$$

is very useful when the spherical diffusion operator is considered, and how this change of variable notably simplifies the mass transport equations, although it complicates the boundary conditions. In the case of a non-reversible process, the boundary value problem becomes

$$\left. \begin{aligned} \frac{\partial u_O(r, t)}{\partial t} &= D_O \frac{\partial^2 u_O(r, t)}{\partial r^2} \\ \frac{\partial u_R(r, t)}{\partial t} &= D_R \frac{\partial^2 u_R(r, t)}{\partial r^2} \end{aligned} \right\} \quad (3.57)$$

$$\left. \begin{aligned} t = 0; r \geq r_s \\ t > 0; r \rightarrow \infty \end{aligned} \right\} \quad u_O(r, t) = \frac{r}{r_s}; \quad u_R(r, t) = \frac{c_R^* r}{c_O^* r_s} \quad (3.58)$$

$t > 0; r = r_s$

$$D_O \left(\left(\frac{\partial u_O(r, t)}{\partial r} \right)_{r=r_s} - \frac{u_O(r_s, t)}{r_s} \right) = -D_R \left(\left(\frac{\partial u_R(r, t)}{\partial r} \right)_{r=r_s} - \frac{u_R(r_s, t)}{r_s} \right) \quad (3.59)$$

$$D_O \left(\left(\frac{\partial u_O(r, t)}{\partial r} \right)_{r=r_s} - \frac{u_O(r_s, t)}{r_s} \right) = k_{\text{red}} u_O(r_s, t) - k_{\text{ox}} u_R(r_s, t) \quad (3.60)$$

This problem was solved by Delmastro and Smith by using the Laplace transform method, assuming that only oxidized species O was initially present in the solution [13], and they reported the following analytical solution:

$$I^{\text{sphe}} = FA_s c_{\text{O}}^* \left(\frac{D_{\text{O}}}{D}\right)^{1/2} k_{\text{red}} \left\{ \frac{1}{a-b} \left[a - \frac{D_{\text{O}}^{1/2} + D_{\text{R}}^{1/2}}{r_s} + \frac{D_{\text{O}}^{1/2} D_{\text{R}}^{1/2}}{r_s^2 a} \right] \exp(a^2 t) \operatorname{erfc}(at^{1/2}) - \frac{1}{a-b} \left[b - \frac{D_{\text{O}}^{1/2} + D_{\text{R}}^{1/2}}{r_s} + \frac{D_{\text{O}}^{1/2} D_{\text{R}}^{1/2}}{r_s^2 b} \right] \exp(b^2 t) \operatorname{erfc}(bt^{1/2}) + \frac{D_{\text{O}}^{1/2} D_{\text{R}}^{1/2}}{r_s^2 ab} \right\} \quad (3.61)$$

where

$$2a = \frac{D_{\text{O}}^{1/2} + D_{\text{R}}^{1/2}}{r_s} + \lambda - \left\{ \left[\frac{D_{\text{O}}^{1/2} + D_{\text{R}}^{1/2}}{r_s} + \lambda \right]^2 - 4 \left[\frac{D_{\text{O}}^{1/2} D_{\text{R}}^{1/2}}{r_s^2} + k^0 \frac{(D_{\text{R}}^{1/2} e^{-\alpha\eta} + D_{\text{O}}^{1/2} e^{(1-\alpha)\eta})}{r_s D^{1/2}} \right] \right\} \quad (3.62)$$

$$2b = \frac{D_{\text{O}}^{1/2} + D_{\text{R}}^{1/2}}{r_s} + \lambda + \left\{ \left[\frac{D_{\text{O}}^{1/2} + D_{\text{R}}^{1/2}}{r_s} + \lambda \right]^2 - 4 \left[\frac{D_{\text{O}}^{1/2} D_{\text{R}}^{1/2}}{r_s^2} + k^0 \frac{(D_{\text{R}}^{1/2} e^{-\alpha\eta} + D_{\text{O}}^{1/2} e^{(1-\alpha)\eta})}{D^{1/2} r_s} \right] \right\} \quad (3.63)$$

$$\lambda = k^0 \frac{(e^{-\alpha\eta} + e^{(1-\alpha)\eta})}{D^{1/2}} \quad (3.64)$$

$$D = D_{\text{O}}^{1-\alpha} D_{\text{R}}^{\alpha} \quad (3.65)$$

By supposing that both oxidized and reduced species are initially present in the electrolytic solution and that diffusion coefficients of O and R are equal ($D_{\text{O}} = D_{\text{R}} = D$), the current takes the form [14]:

$$\frac{I^{\text{sphe}}}{I_{\text{d,c}}^{\text{sphe}}} = \frac{\kappa_{\text{sphe}} (1 - (c_{\text{R}}^*/c_{\text{O}}^*) e^{\eta})}{\vartheta (1 + e^{\eta})} \left[1 + \kappa_{\text{sphe}} \left(1 + \frac{2}{\sqrt{\pi}} \frac{\vartheta}{\chi_s} \right) H(\chi_s) \right] \quad (3.66)$$

with

$$H(\chi_s) = 2F(\chi_s)/(\sqrt{\pi}\chi_s) = e^{\chi_s^2/4} \operatorname{erfc}(\chi_s/2) \quad (3.67)$$

$$\vartheta = 1 + \frac{k^0 r_s}{D} \frac{1 + e^{\eta}}{e^{\alpha\eta}} \quad (3.68)$$

$$\chi_s = \frac{2\sqrt{Dt}}{r_s} \vartheta \quad (3.69)$$

$$\kappa_{\text{sphe}} = \kappa_{\text{sphe}}^0 e^{-\alpha\eta} (1 + e^{\eta}) \quad (3.70)$$

$$\kappa_{\text{sph}}^0 = \frac{k^0 r_s}{D} \frac{1}{1 + \frac{r_s}{\sqrt{\pi D t}}} \quad (3.71)$$

$$I_{\text{d,c}}^{\text{sph}} = FADc_{\text{O}}^* \left(\frac{1}{r_s} + \frac{1}{\sqrt{\pi D t}} \right) \quad (3.72)$$

Equation (3.66) coincides with (3.61) if $c_{\text{R}}^* = 0$ and $D_{\text{O}} = D_{\text{R}}$.

The expression for the current given in Eq. (3.66) can be simplified by considering the approximate expression of the F function given in Eq. (E.10):

$$\frac{I_{\text{d,c}}^{\text{sph}}}{I_{\text{d,c}}^{\text{sph}}} \cong \frac{\kappa_{\text{sph}} (1 - (c_{\text{R}}^*/c_{\text{O}}^*)e^{\eta})}{\vartheta(1 + e^{\eta})} \left[1 + \kappa_{\text{sph}} \left[\frac{1 + \frac{\vartheta}{(\sqrt{\pi}/2)\chi_s}}{1 + (\sqrt{\pi}/2)\chi_s} \right] \right] \quad (3.73)$$

For spherical microelectrodes, it is fulfilled that $\chi_s \gg 1$ and $H(\chi_s) \rightarrow 0$ (see Eqs. (3.67)–(3.69)) so the second term in the brackets of Eqs. (3.66) or (3.73) can be neglected, and the following time-independent response is deduced [15, 16]:

$$I_{\text{d,c}}^{\text{sph,ss}} = I_{\text{d,c}}^{\text{sph,ss}} \frac{\kappa_{\text{sph,ss}}^0 e^{-\alpha\eta} (1 - (c_{\text{R}}^*/c_{\text{O}}^*)e^{\eta})}{(1 + \kappa_{\text{sph,ss}}^0 e^{-\alpha\eta} (1 + e^{\eta}))} \quad (3.74)$$

with

$$\kappa_{\text{sph,ss}}^0 = \frac{k^0 r_s}{D} \quad (3.75)$$

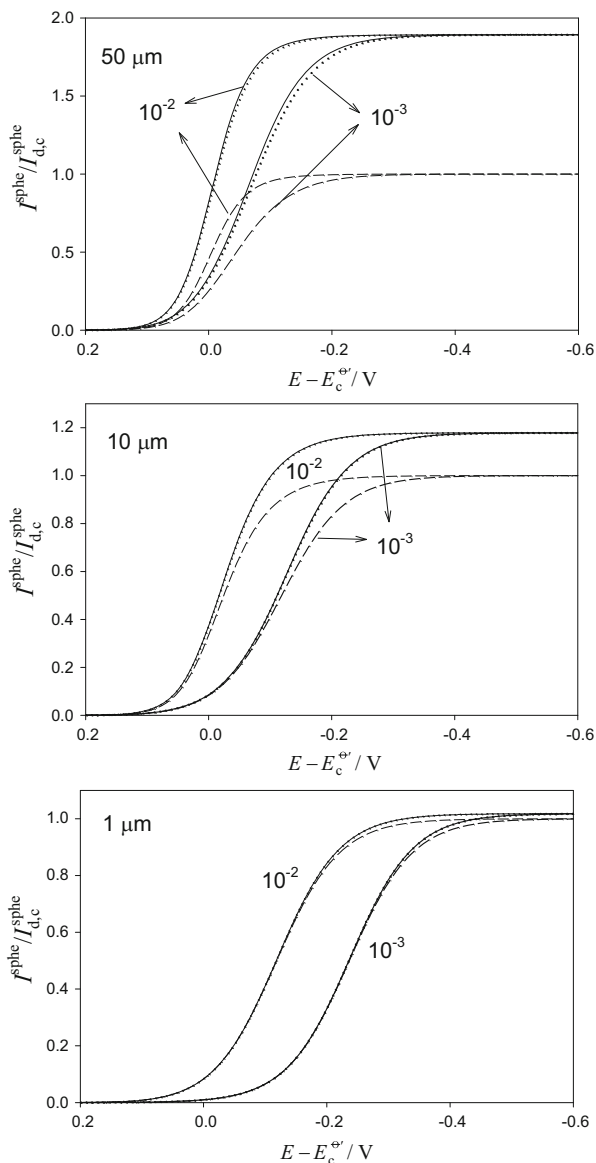
$$I_{\text{d,c}}^{\text{sph,ss}} = FA_s D c_{\text{O}}^* \frac{1}{r_s} \quad (3.76)$$

Equation (3.74) is only applicable to microspheres and microhemispheres, i.e., under steady-state conditions for which $\chi_s \gg 1$ and $r_s \ll \sqrt{\pi D t} \vartheta / (\vartheta - 1)$ in Eq. (3.66). These conditions relate the electrode radius not only to $\sqrt{\pi D t}$, like for a reversible charge transfer process (see Sect. 2.7), but also to the kinetic parameters k^0 and α , and the applied potential E .

In order to analyze the degree of accuracy of Eqs. (3.73) and (3.74), the current–potential curves calculated with rigorous (3.66) (solid lines), approximate quasi-stationary (3.73) (dotted lines), and stationary (3.74) (dashed lines) equations have been plotted in Fig. 3.9 for different values of the electrode radius and two values of k^0 . From this figure, it can be observed that a decrease of the electrode size facilitates the fulfillment of the Eq. (3.73) for a given value of k^0 such that the approximate quasi-stationary solution can be used instead of the rigorous one with an error smaller than 5 % for $r_s < 50 \mu\text{m}$ if $k^0 = 10^{-3} \text{ cm s}^{-1}$ and $t = 1 \text{ s}$. Equation (3.74) is valid for any value of k^0 if $r_s < 3 \mu\text{m}$.

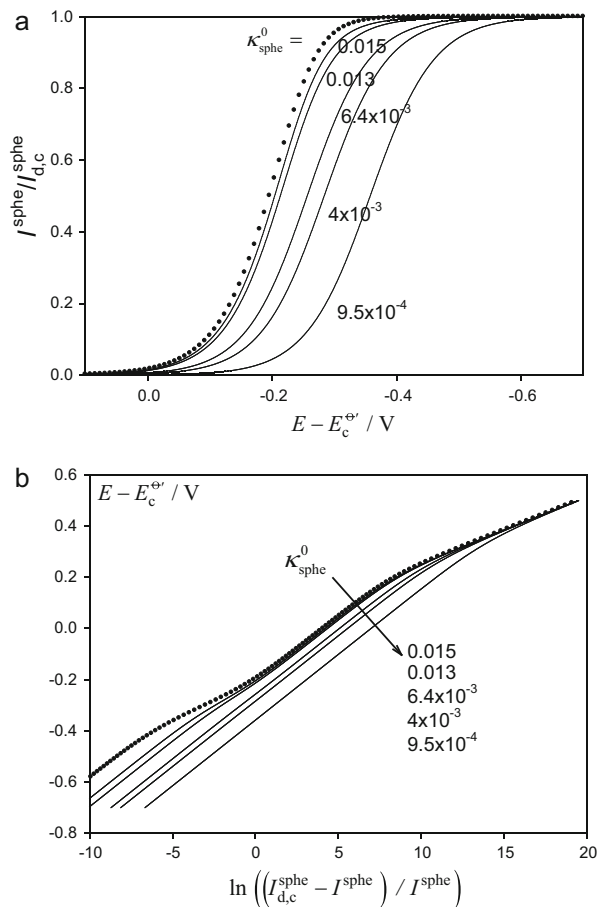
The influence of the kinetics on the voltammograms corresponding to spherical electrodes is conditioned by different variables, and is linked to the electrode size.

Fig. 3.9 Current–potential curves for a slow charge transfer reactions at spherical electrodes calculated from Eqs. (3.66) (solid lines), (3.73) (dotted lines), and (3.74) (dashed lines). The values of k^0 (in cm s^{-1}) and of the electrode radius (in microns) are shown in the curves. $\alpha = 0.5$, $D = 10^{-5} \text{ cm}^2 \text{ s}^{-1}$, $t = 1 \text{ s}$, $T = 298.15 \text{ K}$



This mixed influence can be observed from the expression of χ_s (Eqs. 3.68 and 3.69). In order to analyze the influence of the electrode size, Fig. 3.10a shows the current–potential curves obtained for a charge transfer process with different values of the dimensionless rate constant κ_{spher}^0 for a fixed $k^0 = 10^{-4} \text{ cm s}^{-1}$ in NPV with a time pulse $t = 0.1 \text{ s}$ (i.e., for different values of the electrode radius ranging from 100 to 1 μm). As a limiting case useful for comparison, the current–potential

Fig. 3.10 Current–potential curves (a) and $E - \ln\left(\left(I_{d,c}^{\text{sphc}} - I^{\text{sphc}}\right)/I^{\text{sphc}}\right)$ (b) for a slow electrode process taking place at a spherical electrode, calculated from Eq. (3.66) for different values of κ_{sphc}^0 with $k^0 = 10^{-4} \text{ cm s}^{-1}$, $t = 0.1 \text{ s}$, and $\alpha = 0.5$. The curve corresponding to a plane electrode, calculated from Eq. (3.15) for $\kappa_{\text{plane}}^0 = k^0 \sqrt{t/D} = 0.01$ (black dots), has been included for comparison



response at a planar electrode has been included (black dots). From these curves, it is clear that a decrease of the dimensionless rate constant κ_{sphc}^0 given by Eq. (3.71) mainly affects the irreversible half-wave potential of the responses leading to a shift of the current–potential curves toward more cathodic potentials. This effect can be explained by taking into account that the location of the voltammogram is directly related to κ_{sphc}^0 , which presents the limits:

$$\kappa_{\text{sphc}}^0 = \frac{k^0 r_s}{1 + \frac{r_s}{\sqrt{\pi D t}}} \begin{cases} \text{planar electrodes} \\ (r_s \gg \sqrt{\pi D t}) & \kappa_{\text{sphc}}^0 \cong \sqrt{\pi} \kappa_{\text{plane}}^0 = k^0 \sqrt{\frac{\pi t}{D}} \\ \text{microelectrodes} \\ (r_s \ll \sqrt{\pi D t}) & \kappa_{\text{sphc}}^0 \cong \kappa_{\text{sphc,ss}}^0 = k^0 \frac{r_s}{D} \end{cases} \quad (3.77)$$

For spherical electrodes, κ_{sph}^0 plays an analogous role to κ_{p}^0 (given by Eq. (3.32)) for planar electrodes, i.e., it contains characteristic parameters of the system (the heterogeneous rate constant k^0 , the diffusion coefficient, the time of the experiment, and the electrode radius). According to Eq. (3.77), κ_{sph}^0 tends to κ_{plane}^0 multiplied by $\sqrt{\pi}$ when $r_s \gg \sqrt{\pi Dt}$ (i.e., for $r_s \geq 36\sqrt{Dt}$ for an error lower than 5 %), and $\kappa_{\text{sph}}^0 \cong \kappa_{\text{sph,ss}}^0 = k^0 r_s / D$ when $r_s \ll \sqrt{\pi Dt}$ (i.e., for $r_s \leq 0.1\sqrt{Dt}$ for an error lower than 5 %). These two limiting behaviors are clearly seen in Fig. 3.11.

Concerning the determination of kinetic parameters of the voltammograms of quasi-reversible and irreversible electrode processes, Fig. 3.10b shows the existence of different linear zones in a similar way to that observed for planar electrodes (see Fig. 3.6). For practical purposes, it is helpful to use spherical microelectrodes, for which a broader linear region is obtained under steady-state conditions, since the process behaves as more irreversible as the radius decreases. For fully irreversible charge transfers, Eq. (3.74) simplifies to

$$I_{\text{sph}}^{\text{sphe,ss}} = I_{\text{d,c}}^{\text{sphe,ss}} \frac{\kappa_{\text{sph,ss}}^0 e^{-\alpha\eta}}{1 + \kappa_{\text{sph,ss}}^0 e^{-\alpha\eta}} \quad (3.78)$$

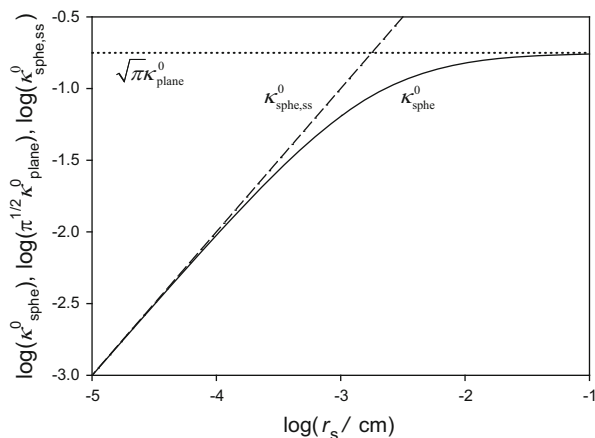
which can be rewritten as

$$E = E_c^{\ominus'} + \frac{RT}{\alpha F} \ln(\kappa_{\text{sph,ss}}^0) + \frac{RT}{\alpha F} \ln\left(\frac{I_{\text{d,c}}^{\text{sphe,ss}} - I_{\text{sph}}^{\text{sphe,ss}}}{I_{\text{sph}}^{\text{sphe,ss}}}\right) \quad (3.79)$$

Equation (3.79) allows us to obtain α and k^0 values from the slope and intercept of the plots of Fig. 3.10b, once the formal potential $E_c^{\ominus'}$ is known.

In order to gain a deeper understanding of the particularities of non-reversible processes at spherical electrodes, it is useful to define the linear diffusion layer

Fig. 3.11 Variation of κ_{sph}^0 with the electrode radius (solid line) calculated from Eq. (3.77). $k^0 = 10^{-3} \text{ cm s}^{-1}$. The variation of $\kappa_{\text{sph,ss}}^0$ (dashed line, Eq. (3.75)) and that of κ_{plane}^0 (dotted line, Eq. (3.32)) have been included for comparison



thickness in an analogous way to that discussed for the case of planar electrodes (see Sect. 3.2.1.2):

$$\delta_{\text{sph}}^{\text{qr}} = \frac{c_{\text{O}}^* - c_{\text{O}}^{\text{s}}}{I_{\text{sph}}^{\text{sphe}}/(FA_s D)} \quad (3.80)$$

By considering that the current I^{sphe} is given by Eq. (3.66) and that the surface concentration of species O when diffusion coefficients are equal is

$$c_{\text{O}}^{\text{s}} = c_{\text{O}}^* \left[1 + \frac{\kappa_{\text{sph}} \left(1 + \frac{2}{\sqrt{\pi}} \frac{\vartheta}{\chi_s} \right) (1 - (c_{\text{R}}^*/c_{\text{O}}^*)e^{\eta})}{\left(1 + \kappa_{\text{sph}} \left(1 + \frac{2}{\sqrt{\pi}} \frac{\vartheta}{\chi_s} \right) \right) (1 + e^{\eta})} (H(\chi_s) - 1) \right] \quad (3.81)$$

it is found that

$$\delta_{\text{sph}}^{\text{qr}} = r_s \left[\frac{1 - H(\chi_s)}{1 + \kappa_{\text{sph}} \left(1 + \frac{2}{\sqrt{\pi}} \frac{\vartheta}{\chi_s} \right) H(\chi_s)} \right] = \frac{r_s (1 - H(\chi_s))}{1 - H(\chi_s) + \frac{2}{\sqrt{\pi}} \frac{\vartheta}{\chi_s} F(\chi_s)} \quad (3.82)$$

with $H(\chi_s)$, χ_s , κ_{sph} , and ϑ given in Eqs. (3.67)–(3.70) and $F(\chi_s)$ by Eq. (3.16).

Note that for reversible processes ($k^0 \rightarrow \infty$, $\chi_s \rightarrow \infty$, $H \rightarrow 0$, and $F \rightarrow 1$), $\delta_{\text{sph}}^{\text{qr}} \rightarrow \delta_{\text{sph}}^{\text{r}} = (1/\sqrt{\pi Dt} + 1/r_s)^{-1}$ (see Eq. (2.146) of Sect. 2.5.2).

For spherical microelectrodes ($r_s \ll \sqrt{\pi Dt}$), $H(\chi_s) \rightarrow 0$ and Eqs. (3.81) and (3.82) convert into

$$c_{\text{O}}^{\text{s}} = \frac{c_{\text{O}}^* + \kappa_{\text{sph},\text{ss}}^0 e^{(1-\alpha)\eta} (c_{\text{O}}^* + c_{\text{R}}^*)}{1 + \kappa_{\text{sph},\text{ss}}^0 e^{-\alpha\eta} (1 + e^{\eta})} \quad (3.83)$$

$$\delta_{\text{sph}}^{\text{qr}} \cong r_s \quad (3.84)$$

with $\kappa_{\text{sph},\text{ss}}^0$ given by Eq. (3.75).

The influence of the electrode radius (through $r_s/\sqrt{\pi Dt}$) and kinetics (through $k^0\sqrt{t/D}$) on the ratio $\delta_{\text{sph}}^{\text{qr}}/\delta_{\text{sph}}^{\text{r}}$ for $E - E_c^{\ominus'} = -150$ mV is summarized in Fig. 3.12. As mentioned in Sect. 3.2.1.2 and in reference [17], $\delta_{\text{sph}}^{\text{qr}}/\delta_{\text{sph}}^{\text{r}}$ is equal to $2/\pi$ at planar electrodes (i.e., macroelectrodes) for totally irreversible systems ($k^0\sqrt{t/D} < 5 \times 10^{-3}$ within 2 % error). For smaller electrodes and/or faster processes, $\delta_{\text{sph}}^{\text{qr}}/\delta_{\text{sph}}^{\text{r}}$ is greater, approaching a limiting value of 1. This value is attained for reversible processes or when microelectrodes are used, given that in the latter situation the thickness of the linear diffusion layer is $\delta_{\text{sph}}^{\text{qr}} \cong r_s$ independently of the reversibility degree.

On the basis of the above, in an analogous way to that discussed for planar electrodes in Sect. 3.2.1.4, a reversibility criterion can be also defined for spherical

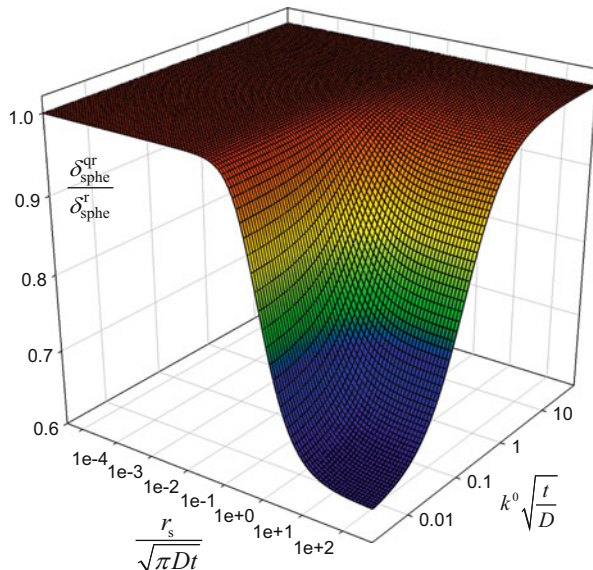
Fig. 3.12 Variation of the ratio between the linear diffusion layer thickness of slow and fast electrode reactions for spherical electrodes, $\delta_{\text{sph}}^{\text{qr}}/\delta_{\text{sph}}^{\text{r}}$, with the electrode kinetics (through the dimensionless parameter $k^0\sqrt{t/D}$) and the electrode size (through $r_s/\sqrt{\pi Dt}$).

$$E - E_c^{\ominus'} = -150 \text{ mV,}$$

$$\alpha = 0.5, t = 1 \text{ s,}$$

$$D = 10^{-5} \text{ cm}^2 \text{ s}^{-1}.$$

Reproduced with permission of reference [17]



electrodes relied on R_{sph}^0 , defined as the ratio between the heterogeneous rate constant and the mass transport coefficient $m^0 = D/\delta_{\text{sph}}^{\text{qr}}$, calculated at the formal potential:

$$R_{\text{sph}}^0 = \frac{k^0}{m^0} = \frac{k^0 \delta_{\text{sph},0}^{\text{qr}}}{D} \quad (3.85)$$

with $\delta_{\text{sph},0}^{\text{qr}}$ defined by Eq. (3.82) at $E = E_c^{\ominus'}$.

For microelectrodes, the ratio R_{sph}^0 becomes (see Eq. (3.84)):

$$R_{\text{micro}}^0 = \kappa_{\text{sph},\text{ss}}^0 = \frac{k^0 r_s}{D_O} \quad (3.86)$$

which is independent of the potential.

As indicated in Sect. 3.2.1.4, it will be assumed that an irreversible process corresponds to $R_{\text{sph}}^0 < 0.05$ and a reversible one to $R_{\text{sph}}^0 > 10$. On the basis of these limits, it is clear that the lower the electrode radius, the higher the value of k^0 needed to consider the process reversible is. For example, for $D = 10^{-5} \text{ cm}^2 \text{ s}^{-1}$, reversible processes are observed in microelectrodes for $k^0 \geq 10^{-4}/r_s$. This means that for $r_s = 10^{-3} \text{ cm}$ a value of $k^0 \geq 0.1 \text{ cm s}^{-1}$ is enough, whereas for $r_s = 10^{-5} \text{ cm}$ it is necessary for $k^0 \geq 10 \text{ cm s}^{-1}$. This behavior is in agreement with the enhanced irreversibility observed for microelectrodes, as discussed above. The accuracy of this approach is based on the dependence of the surface concentration of the oxidized species with the reversibility degree. Under these conditions, at

$E = E_c^{\ominus'}$ (and assuming $c_R^* = 0$), the surface concentration of species O for a microsphere or a microhemisphere is easily deduced from Eq. (3.81):

$$c_O^s(E = E_c^{\ominus'})_{\text{micro}} = c_O^* \frac{1 + \kappa_{\text{sph},\text{ss}}^0}{1 + 2\kappa_{\text{sph},\text{ss}}^0} \quad (3.87)$$

For a totally irreversible process, it should be fulfilled that $c_O^s \cong c_O^*$ (see Eq. (3.81)) whereas for a reversible one $c_O^s = c_O^*/2$ (see Eq. (2.143) of Sect. 2.5.2). These assumptions are satisfied with an error of less than 5 % for the values of R_{micro}^0 considered above.

In reference [18], the authors show the expression for the stationary current obtained at uniformly accessible electrodes in the case in which species R is not initially present in the solution (i.e., $c_R^* = 0$). In the case of spherical electrodes, it can be written:

$$\frac{I^{\text{sph},\text{ss}}}{I_{\text{d,c}}^{\text{sph},\text{ss}}} = \frac{1}{\Theta + \frac{1}{\kappa_{\text{red},\text{sph},\text{ss}}}} \quad (3.88)$$

with

$$\Theta = 1 + \gamma^2 e^{\eta} \quad (3.89)$$

$$\kappa_{\text{red},\text{sph},\text{ss}} = \kappa_{\text{sph},\text{ss}}^0 e^{-\alpha\eta} \quad (3.90)$$

and $\eta = F(E - E_c^{\ominus'})/RT$, $\gamma = \sqrt{D_O/D_R}$, and $\kappa_{\text{sph},\text{ss}}^0$ is given in Eq. (3.75).

If the potential $E_{1/p}$ is considered, where $I^{\text{sph},\text{ss}}/I_{\text{d,c}}^{\text{sph},\text{ss}} = 1/p$, it is fulfilled that

$$\Theta_{1/p} + 1/\kappa_{\text{red},\text{sph},\text{ss},1/p} = p \quad (3.91)$$

Writing Eq. (3.91) for $p = 2, 4$, and $4/3$ (half-wave potential, $E_{1/2}$, quartile potential, $E_{1/4}$, and three-quartile potential, $E_{3/4}$, respectively), and combining these expressions yields

$$\Theta_{1/2} = \frac{3 + \varepsilon_{1/4} - 2\varepsilon_{1/4}^\alpha}{\varepsilon_{1/4} - \varepsilon_{1/4}^\alpha} \quad (3.92)$$

and

$$\varepsilon_{1/4}^\alpha (1 - 3\varepsilon_{3/4}) + 3\varepsilon_{3/4}^\alpha (\varepsilon_{1/4} - 3) + 9\varepsilon_{3/4} - \varepsilon_{1/4} = 0 \quad (3.93)$$

with

$$\varepsilon_{1/p} = \exp\left(\frac{F}{RT}(E_{1/p} - E_{1/2})\right) \quad (3.94)$$

Solving Eq. (3.93) numerically, Bard and Mirkin presented a table with the values of α , k^0 , and $\Delta E^{\ominus'} = E_c^{\ominus'} - E_{1/2}$ for different pairs of values of $E_{1/4} - E_{1/2}$ and $E_{1/2} - E_{3/4}$.

3.2.4 Microdiscs. Steady-State Voltammetry

In this section, microdisc electrodes will be discussed since the disc is the most important geometry for microelectrodes (see Sect. 2.7). Note that discs are not uniformly accessible electrodes so the mass flux is not the same at different points of the electrode surface. For non-reversible processes, the applied potential controls the rate constant but not the surface concentrations, since these are defined by the local balance of electron transfer rates and mass transport rates at each point of the surface. This local balance is characteristic of a particular electrode geometry and will evolve along the voltammetric response. For this reason, it is difficult (if not impossible) to find analytical rigorous expressions for the current analogous to that presented above for spherical electrodes. To deal with this complex situation, different numerical or semi-analytical approaches have been followed [19–25]. The expression most employed for analyzing stationary responses at disc microelectrodes was derived by Oldham [20], and takes the following form when equal diffusion coefficients are assumed:

$$I^{\text{microdisc, ss}} = I_{\text{d,c}}^{\text{microdisc, ss}} \frac{1}{(1 + e^\eta)} \left[1 + \frac{1}{\left(\frac{\kappa_{\text{disc, ss}}^0}{\pi} \right) e^{-\alpha\eta} (1 + e^\eta)} \frac{\kappa_{\text{disc, ss}}^0 \left(\frac{2}{\pi} \right) e^{-\alpha\eta} (1 + e^\eta) + 3}{\kappa_{\text{disc, ss}}^0 \left(\frac{4}{\pi} \right) e^{-\alpha\eta} (1 + e^\eta) + 3\pi} \right]^{-1} \quad (3.95)$$

with

$$\kappa_{\text{disc, ss}}^0 = \frac{k^0 r_d \pi}{D} \frac{\pi}{4} \quad (3.96)$$

$$I_{\text{d,c}}^{\text{microdisc, ss}} = 4FDc_O^* r_d \quad (3.97)$$

In references [20, 25], Oldham establishes that this empirical solution presents a maximum error of 0.3 % versus numerical simulations.

In view of the expressions of the stationary current–potential responses of microspherical and microdisc electrodes (Eqs. (3.74) and (3.95), respectively), it is clear that an equivalence relationship between disc and hemispherical microelectrodes, like that shown for fast charge transfer processes (see Eq. (2.170) of Sect. 2.7), cannot be established in this case.

For discs and bands, it is very difficult to obtain analytical expressions for the steady-state current, although at first sight the theory for steady-state voltammetry

appears simple. When the electrochemical processes are kinetically non-reversible, analytical treatments become very challenging and have hitherto been carried out on a one-by-one basis for each particular electrode geometry of interest. This is why numerical procedures are usually employed for the analysis of these responses. However, an approximate yet accurate alternative general approach can be used. This approach is based on the fact that when the boundary values of the concentrations of electro-active species at the electrode surface and in the bulk are constant, the solution for the diffusion equation at any electrode geometry can be written as [26]:

$$c_i(q, t) = c_i^* + (c_i^s - c_i^*)f(q, t) \quad i = O, R \quad (3.98)$$

where q denotes the required coordinates for the electrode geometry considered and c_i^s and c_i^* are the constant values of the concentration of species i at the electrode surface and at the bulk, respectively. $f(q, t)$ is a continuous function dependent on the particular electrode geometry and on time, t . Equation (3.98) can be rigorously applied in the study of a charge transfer process under transient conditions provided that the charge transfer is reversible and the diffusion coefficients of species O and R are equal (see Eq. (2.144) of Sect. 2.5.2). When either assumption is not fulfilled this equation is not strictly valid, since in this case c_i^s depends on time. As the electrode size diminishes, the electrochemical response of the system tends to become stationary or quasi-stationary such that both the average surface concentrations¹ of electro-active species and the average normal surface gradient become independent of time even for non-reversible electrode processes. Under these conditions, Eq. (3.98) may be again applicable in an approximate way. This is of great interest since, on the basis of this reasoning, it is possible to obtain general, albeit approximate, simple analytical solutions for microelectrodes of different geometries when the steady state is reached.

So, in the case of microdiscs under steady-state conditions, the following general expression for the current can be written:

$$\frac{I^{\text{microdisc, ss}}}{FA_d} = -D \frac{(c_O^* - \tilde{c}_O^s)}{r_d} = (k_{\text{red}} + k_{\text{ox}})\tilde{c}_O^s - k_{\text{ox}}c^* \quad (3.99)$$

with \tilde{c}_O^s being the average surface concentration, A_d the microdisc area, and $c^* = c_O^* + c_R^*$.

By operating on Eq. (3.99), it is possible to obtain an expression for the average surface concentration of oxidized species:

¹ Note that surface concentrations under stationary conditions are not uniform on the disc surface, varying from the center to the edge of the disc. Under these conditions, only the average surface concentrations are constant. For nonstationary conditions even the average surface concentrations are time dependent.

$$\tilde{c}_O^s = c_O^* \frac{1 + \kappa_{\text{disc,ss}}^0 e^{(1-\alpha)\eta}}{1 + \kappa_{\text{disc,ss}}^0 e^{-\alpha\eta} (1 + e^\eta)} \quad (3.100)$$

where κ_{disc}^0 is given in Eq. (3.96).

The general expression for the current can be written in the general way:

$$\frac{I^{\text{microdisc,ss}}}{I_{\text{d,c}}^{\text{microdisc,ss}}} = \frac{\kappa_{\text{disc,ss}}^0 e^{-\alpha\eta} (1 - (c_R^*/c_O^*) e^\eta)}{1 + \kappa_{\text{disc,ss}}^0 e^{-\alpha\eta} (1 + e^\eta)} \quad (3.101)$$

with $I_{\text{d,c}}^{\text{microdisc,ss}}$ given by Eq. (3.97) and $\kappa_{\text{disc,ss}}^0$ being the dimensionless rate constant for a microdisc given by Eq. (3.96).

In order to determine the accuracy of the solution proposed in Eq. (3.101) for the case of a microdisc electrode, in Fig. 3.13 numerical results are compared with this equation and also with the Oldham Eq. (3.95). Fully reversible, $\kappa_{\text{disc,ss}}^0 = 1000\pi/4$, quasi-reversible, $\kappa_{\text{disc,ss}}^0 = \pi/4$, and fully irreversible, $\kappa_{\text{disc,ss}}^0 = 0.001\pi/4$, heterogeneous kinetics were considered under steady-state behavior. It is seen that, for fully reversible kinetics, both equations give almost identical results which are in good agreement with the simulated values. As the kinetics becomes less reversible, however, the results given by the two equations diverge from each other, with the simulated result lying between them. The maximum error in the Oldham equation is 0.5 %, and for Eq. (3.101), the maximum error is 3.6 %.

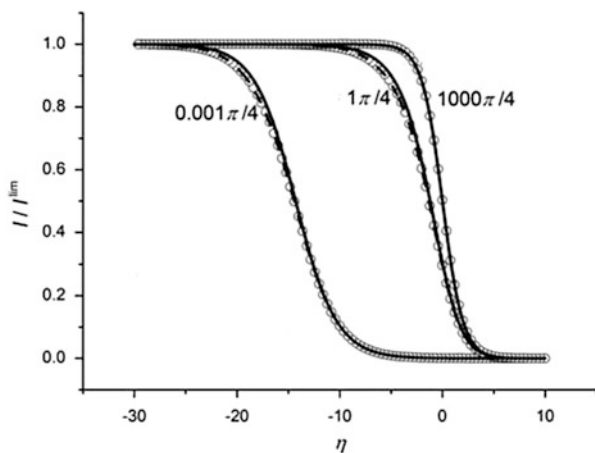


Fig. 3.13 Simulated (white dots) and analytical steady-state voltammograms for the reduction of a single electro-active species at a microdisc electrode for reversible, quasi-reversible, and irreversible kinetics calculated from Eqs. (3.101) (solid line) and (3.95) (dashed line). $I/I_{\text{lim}} = I^{\text{microdisc,ss}}/I_{\text{d,c}}^{\text{microdisc,ss}}$. The values of $\kappa_{\text{disc,ss}}^0$ appear on the curves. In all cases, $\alpha = 0.5$, and $D_O = D_R$. Reproduced with permission of reference [26]

3.2.5 General Expression for the Stationary Current–Potential Response at Microelectrodes

Although Eq. (3.101) has been written for microdiscs, it can be applied to any particular electrode geometry by changing $I_{d,c}^{\text{microdisc,ss}}$ and $\kappa_{\text{disc,ss}}^0$ for the corresponding steady-state limiting current and dimensionless rate constant. Thus, the general expression for the current–potential response at a microelectrode of geometry G is

$$\frac{I_{d,c}^{\text{G,ss}}}{I_{d,c}^{\text{G,ss}}} = \frac{\kappa_{\text{G,ss}}^0 e^{-\alpha\eta} (1 - (c_{\text{R}}^*/c_{\text{O}}^*)e^{\eta})}{1 + \kappa_{\text{G,ss}}^0 e^{-\alpha\eta} (1 + e^{\eta})} \quad (3.102)$$

Another situation of interest in which this equation is applicable is that of a single conductive sphere (or nanoparticle) on an electro-inactive surface (np) since it can be considered as a model system for the study of the voltammetric behavior of spherical nanoparticles adhered to a support [26, 27]. In this last case, the expression for the current–potential curve is identical to Eq. (3.101) by using

$$I_{d,c}^{\text{np,ss}} = FA_{\text{np}}Dc_{\text{O}}^* \frac{\ln(2)}{r_{\text{np}}} \quad (3.103)$$

and

$$\kappa_{\text{np,ss}}^0 = \frac{k^0 r_{\text{np}}}{D \ln(2)} \quad (3.104)$$

with r_{np} and A_{np} being the radius and area of the nanoparticle. For this particular geometry, Eq. (3.102) has a maximum error of 2.6 % [26].

In Eq. (3.102), G = s for microspheres, G = d for microdiscs, and G = np for single conductive spheres. Moreover, the expressions of $\kappa_{\text{sph,ss}}^0$ (microspheres) and $\kappa_{\text{disc,ss}}^0$ (microdiscs) are given in Eqs. (3.75) and (3.96), respectively.

Equation (3.102) can be rewritten as [15, 20, 25] (see also Sect. 1.8.4):

$$\frac{1}{I_{d,c}^{\text{G,ss}}} = \frac{1}{I^{\text{kin}}} + \frac{1}{I_{d,c}^{\text{G,ss}}} + \frac{1}{I_{d,N}^{\text{G}}} \quad (3.105)$$

with

$$I^{\text{kin}} = A_G F c_{\text{O}}^* k_{\text{red}} \quad \text{for any geometry} \quad (3.106)$$

$$\left. \begin{aligned} I_{d,N}^{\text{microdisc}} &= 4FDc_{\text{O}}^* r_{\text{d}} e^{-\eta} \\ I_{d,N}^{\text{microsphere}} &= 2\pi FDc_{\text{O}}^* r_{\text{s}} e^{-\eta} \\ I_{d,N}^{\text{np}} &= 4\pi \ln(2) FDc_{\text{O}}^* r_{\text{np}} e^{-\eta} \end{aligned} \right\} \quad (3.107)$$

and $I_{d,c}^{G,ss}$ given by Eqs. (3.76), (3.97), and (3.103) for microspheres, microdiscs, and single conductive spheres, respectively.

Equations (3.105)–(3.107) point out the existence of three different polarization causes. So, I^{kin} is a kinetically controlled current which is independent of the diffusion coefficient and of the geometry of the diffusion field, i.e., it is a pure kinetic current. The other two currents have a diffusive character, and, therefore, depend on the geometry of the diffusion field. $I_{d,c}^{G,ss}$ corresponds to the maximum current achieved for very negative potentials and $I_{d,N}^G$ is a current controlled by diffusion and by the applied potential which has no physical meaning since it exceeds the limiting diffusion current $I_{d,c}^{G,ss}$ when the applied potential is lower than the formal potential ($E < E_c^{\ominus'}$). This behavior is indicated by Oldham in the case of spherical microelectrodes [15, 20, 25].

3.2.6 Comparison Between Marcus–Hush and Butler–Volmer Kinetics

Up to now, the treatment of non-reversible electrode process has focused on the usual Butler–Volmer kinetics for which the rate constants take the form (see Sect. 1.7.1):

$$\left. \begin{aligned} k_{red}^{BV} &= k^0 e^{-\alpha\eta} \\ k_{ox}^{BV} &= k^0 e^{(1-\alpha)\eta} \end{aligned} \right\} \quad (3.108)$$

where $\eta = F(E - E_c^{\ominus'})/RT$ and α and $(1 - \alpha)$ are the transfer coefficients that are related to the symmetry of the energy barrier, that is, if the transition state is reactant or product like. As has been indicated in Sect. 1.7.2, together with Butler–Volmer approach the symmetric Marcus–Hush one is the most employed kinetic schemes. For this model, the expressions of the heterogeneous rate constants are [28, 29]:

$$\left. \begin{aligned} k_{red}^{MH} &= k^0 e^{-\eta/2} \frac{I(\eta, \Lambda)}{I(0, \Lambda)} \\ k_{ox}^{MH} &= k^0 e^{\eta/2} \frac{I(\eta, \Lambda)}{I(0, \Lambda)} \end{aligned} \right\} \quad (3.109)$$

where $\Lambda = \lambda F/RT$, with λ being the reorganization energy, and $I(\eta, \Lambda)$ is an integral of the form:

$$I(\eta, \Lambda) = \int_{-\infty}^{\infty} \frac{\exp\left[\frac{-(\varepsilon-\eta)^2}{4\Lambda}\right]}{2 \cosh(\varepsilon/2)} d\varepsilon \quad (3.110)$$

where ε is an integral variable. The value of the reorganization energy (λ) corresponds to the energy necessary to adjust the configurations of the reactant and solvent to those of the product state. At the limit $\Lambda \rightarrow \infty$ Eqs. (3.109) reduce to (3.108) when $\alpha = 1/2$, i.e., the effectiveness of Butler–Volmer formalism as an approximation of the Marcus–Hush one improves as Λ increases.

In this section, both approaches will be compared in chronoamperometry under limiting current conditions at spherical electrodes and microelectrodes. As is well known, for spherical electrodes and taking into account the Butler–Volmer model, the value of the diffusion-controlled reduction current at large overpotentials, $I_{d,c}^{\text{sph},\text{BV}}$, is given by the following expression (see Eq. (2.147) of Sect. 2.5.2):

$$I_{d,c}^{\text{sph},\text{BV}} = FA_s D_O c_O^* \left(\frac{1}{\sqrt{\pi D_O t}} + \frac{1}{r_s} \right) \quad (3.111)$$

which is exclusively controlled by the diffusion transport of species O toward the electrode surface and independent of the electrochemical reversibility of the process.

When the Marcus–Hush treatment is considered, the reduction rate constant is not predicted to increase continuously with the applied potential, but rather a maximum value exists. A simple expression for this value of the rate constant was given in reference [29]:

$$k_{\text{max}}^{\text{MH}} = k^0 \frac{\sqrt{4\pi\Lambda} \exp(\Lambda/4)}{\pi - \frac{\pi^3}{4(\Lambda+4.31)}} \quad (2.5 \leq \Lambda \leq 80) \quad (3.112)$$

By inserting Eq. (3.112) in (3.66) under limiting current conditions at spherical electrodes (i.e., $E \ll E_c^{\ominus'}$) and taking into account that now $\vartheta = 1 + K_{\text{max}}^{\text{MH}}$ and $\kappa_{\text{sph}} = K_{\text{max}}^{\text{MH}} / (1 + r_s / \sqrt{\pi D t})$, the following solution is derived:

$$\begin{aligned} \frac{I_{d,c}^{\text{sph},\text{MH}}}{FA_s D_O c_O^* \frac{1}{r_s}} &= \\ &= \left(\frac{K_{\text{max}}^{\text{MH}}}{1 + K_{\text{max}}^{\text{MH}}} \right) \left[1 + K_{\text{max}}^{\text{MH}} \exp \left(\frac{\sqrt{D_O t}}{r_s} (1 + K_{\text{max}}^{\text{MH}}) \right)^2 \operatorname{erfc} \left(\frac{\sqrt{D_O t}}{r_s} (1 + K_{\text{max}}^{\text{MH}}) \right) \right] \end{aligned} \quad (3.113)$$

where $K_{\text{max}}^{\text{MH}} = k_{\text{max}}^{\text{MH}} r_s / D_O$. Note that the value of the dimensionless heterogeneous rate constant $K_{\text{max}}^{\text{MH}}$ increases with the standard rate constant k^0 , the reorganization energy, and the electrode radius, and it decreases with the diffusion coefficient. This expression leads to accurate results (error smaller than 1 % with respect to

Eq. (3.109) for the rate constants) in a wide range of values of the reorganization energy, $2.5 \leq \Lambda \leq 80$.

According to Eq. (3.113), the limiting current depends not only on the diffusion transport but also on the electrode kinetics, so it is a function of the reorganization energy and the heterogeneous rate constant. These parameters set the discrepancy in the value of the limiting current between the two kinetic models such that greater differences are expected for small k^0 and/or λ values, short t values, and small electrode radius.

Under steady-state conditions, the expressions for the limiting current simplify to

$$I_{d,c}^{\text{sphe,ss,BV}} = \frac{FAD_0 c_O^*}{r_s} \quad (3.114)$$

$$I_{d,c}^{\text{sphe,ss,MH}} = I_{d,c}^{\text{sphe,ss,BV}} \left(\frac{K_{\text{max}}^{\text{MH}}}{1 + K_{\text{max}}^{\text{MH}}} \right) \quad (3.115)$$

The difference between the BV and MH expressions is the term $K_{\text{max}}^{\text{MH}}/1 + K_{\text{max}}^{\text{MH}}$, which tends to unity for large $K_{\text{max}}^{\text{MH}}$ values, so both solutions coincide. Otherwise, this term is smaller than the unity and the stationary current predicted by Marcus–Hush is less than by Butler–Volmer; the smaller the electrode radius (i.e., the smaller the $K_{\text{max}}^{\text{MH}}$ value), the greater the difference between both solutions.

In Fig. 3.14a, the dimensionless limiting current $I_{d,c}^{\text{plane}}(t)/I_{d,c}^{\text{plane}}(t_p)$ (where t_p is the total duration of the potential step) at a planar electrode is plotted versus $1/\sqrt{t}$ under the Butler–Volmer (solid line) and Marcus–Hush (dashed lines) treatments for a fully irreversible process with $k^0 = 10^{-4} \text{ cm s}^{-1}$, where the differences between both models are more apparent according to the above discussion. Regarding the BV model, a unique curve is predicted independently of the electrode kinetics with a slope unity and a null intercept. With respect to the MH model, for typical values of the reorganization energy ($\lambda = 0.5 - 1 \text{ eV}$, $\Lambda \approx 20 - 40$ [4]), the variation of the limiting current with time compares well with that predicted by Butler–Volmer kinetics. On the other hand, for small λ values ($\Lambda < 20$) and short times, differences between the BV and MH results are observed such that the current expected with the MH model is smaller. In addition, a nonlinear dependence of $I_{d,c}^{\text{plane}}(t)/I_{d,c}^{\text{plane}}(t_p)$ with $1/\sqrt{t}$ is predicted, and any attempt at linearization would result in poor correlation coefficient and a slope smaller than unity and non-null intercept.

The differences between BV and MH also have implications in the concentration profiles of the electro-active species. Thus, whereas the BV model predicts a zero surface concentration of the oxidized species at the electrode surface, in the Marcus–Hush model the surface concentration of species O also depends on the electrode kinetics such that for small values of the heterogeneous

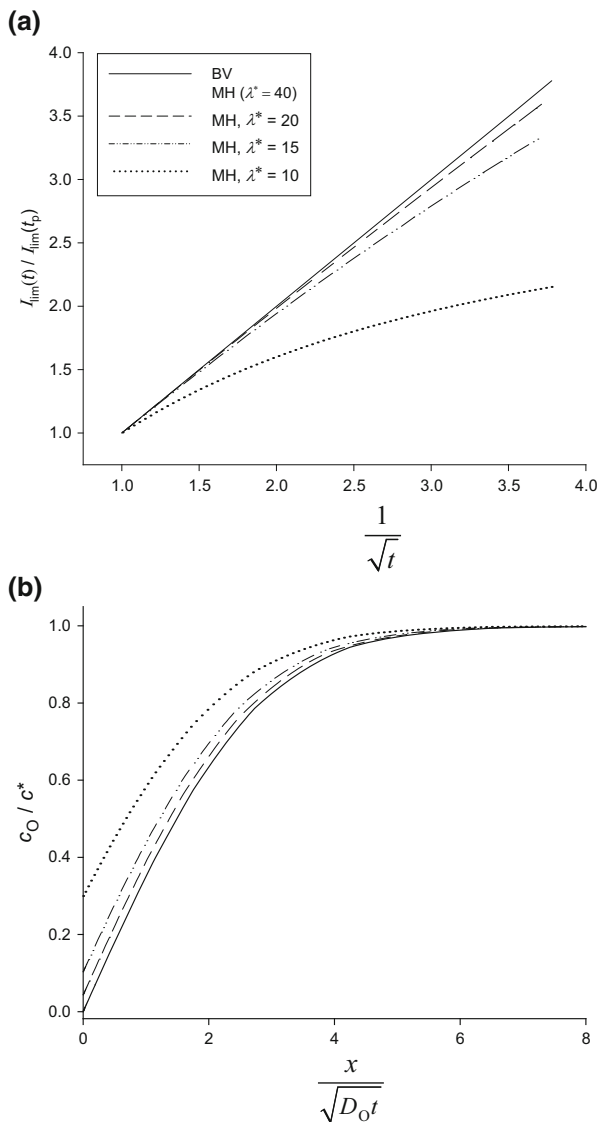


Fig. 3.14 Single potential step chronoamperometry at large overpotentials. (a) Variation of the limiting current with time; (b) concentration profiles at the end of the pulse. Planar electrode. $I_{\text{lim}}(t)/I_{\text{lim}}(t_p) = I_{\text{d,c}}^{\text{plane}}(t)/I_{\text{d,c}}^{\text{plane}}(t_p)$ for the two kinetic models considered. $k^0 = 10^{-4}$ cm/s. Reproduced with permission of reference [30]. In this Figure $\lambda^* = \Lambda$.

rate constant and reorganization energy, this is not zero (see Fig. 3.14b); the smaller the reorganization energy, the greater the surface concentration of the reacting species.

3.3 Multi-electron Electrochemical Reactions

There are a number of molecules for which two- or more electron transfers can be detected (i.e., stepwise processes). For molecules capable of giving two-electron transfer reactions (EE mechanism; see reaction scheme (3.II)), the addition of the second electron occurs, in the more typical case, with greater difficulty than the first, so the single pulse voltammogram presents two well-separated waves because of the difference between the two formal potentials defined as

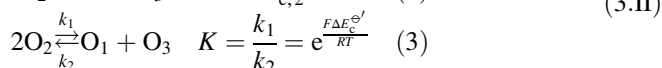
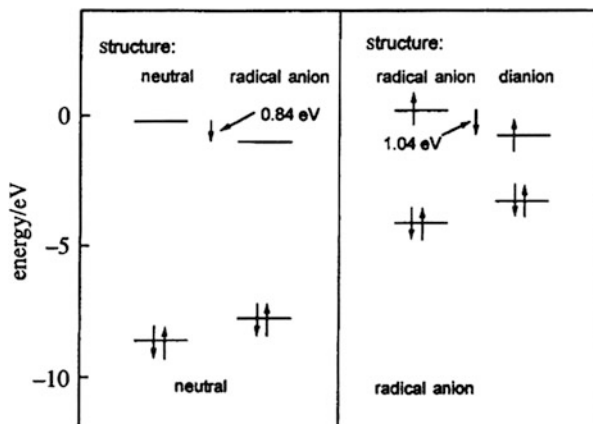
$$\Delta E_c^{\ominus'} = E_{c,2}^{\ominus'} - E_{c,1}^{\ominus'} \quad (3.116)$$

is negative enough (i.e., $\Delta E_c^{\ominus'} \leq -200$ mV; see below). This behavior is very common in electrochemical reactions of alkylviologens and metallocenes where the first electron transfer does not give rise to large changes in the molecule and the second electron transfer is thermodynamically more difficult than the first [4, 31]. In any case this behavior leads to a very stable intermediate redox state of the molecule. Under these conditions, one can speak of a “normal” potential difference [31, 32], repulsive or negative interactions [4, 33, 34], or high anti-cooperativity degree between the two charge transfers [35].

For $\Delta E_c^{\ominus'} \geq -71.2$ mV, one wave is observed in the current–potential curve. Under these conditions, low anti-cooperativity degree ($-71.2 \leq \Delta E_c^{\ominus'} < -35.6$ mV) [35], cooperativity and attractive (or positive) interactions ($\Delta E_c^{\ominus'} > -35.6$ mV) [4, 33, 35], and “inverted” potential difference ($\Delta E_c^{\ominus'} > 0$ mV) [31, 32] denominations are used for an increasingly unstable intermediate (see below). This last denomination refers to the fact that, after the first transfer, there is an important change in the molecular structure that leads to a modification of the frontier orbitals or, alternatively, there are changes in solvation or ion pairing formation. Examples of the potential inversion are the case of several reversible electrode reductions in aqueous solutions of ions as $\text{Cd}^{2+} + 2e^- \rightleftharpoons \text{Cd}$, Molybdenum polyoxometalates, and a number of aromatic species like derivatives of tetraphenylethylene [31, 36]. In this last case, the structural changes accompanying the inclusion of electrons into the sterically congested neutral species lead to the LUMO energy of this decreasing. In the same way the SOMO energy of the radical anion diminishes as it adopts the structure of the di-anion [37]. This behavior could justify the inversion of the formal potentials in these species (see Fig. 3.15).

In this section, the electrochemical behavior of an EE mechanism with two reversible electron transfer reactions will be studied. It will also be shown that for this electrode process (given in reaction scheme (3.II)) in both cases, i.e., normal ordering and potential inversion, the disproportionation/comproportionation reaction (3) can take place in the diffusion layer.

Fig. 3.15 Orbital energies for the neutral and radical anion forms of tetraphenylethylene, each in two different structures. Note the lowering of the LUMO energy of the neutral form when it is converted to the structure of the radical anion and also the lowering of the SOMO energy of the radical anion as it adopts the structure of the di-anion. Reproduced from reference [37] with permission



Reaction Scheme (3.II) $E_{c,j}^{\ominus'}$ with $j = 1, 2$ are the formal potentials of each electron transfer step. k_1, k_2 , and K are the rate and equilibrium constants, respectively, of the disproportionation reaction (3).

Reaction (3) has no effect on the electrochemical response when both electron transfers are reversible, diffusion is the only transport mechanism, the diffusion coefficients of all species are equal and there are no solution phase reactions in the vicinity of the electrode surface other than disproportionation/comproportionation ones (although it cannot be ignored for obtaining the concentration profiles). It will be shown in this section that this behavior occurs independently of the electrochemical technique employed and also of the geometry and size of the electrode [30, 33]. Under these conditions, experimental methods other than electrochemical must be used to characterize the kinetics of the disproportionation reaction in reaction scheme (3.II). Reaction (3) can be detected from electrochemical measurements when diffusion coefficients are not identical (although these effects are not very significant), when the concentration of supporting electrolyte becomes small enough to have to consider mass transport by electrical migration, when other homogeneous chemical reactions take place, or when one or both electron transfers are quasi-reversible [31, 38, 39].

3.3.1 Two-Electron Electrochemical Reactions at Planar Electrodes

The reduction of a soluble molecule O_1 with initial concentration $c_{O_1}^*$ to the different two oxidation states O_2 and O_3 , as shown in reaction scheme (3.II), is considered under the above mentioned conditions in which, as can be seen below, reaction (3) has no effect on the electrochemical response. Thus, when a constant potential is applied, the formulation of the problem is as follows [33, 34, 39]:

$$\left. \begin{aligned} \frac{\partial c_{O_1}}{\partial t} &= D_{O_1} \frac{\partial^2 c_{O_1}}{\partial x^2} + k_1 c_{O_2}^2 - k_2 c_{O_1} c_{O_3} & (a) \\ \frac{\partial c_{O_2}}{\partial t} &= D_{O_2} \frac{\partial^2 c_{O_2}}{\partial x^2} - 2k_1 c_{O_2}^2 + 2k_2 c_{O_1} c_{O_3} & (b) \\ \frac{\partial c_{O_3}}{\partial t} &= D_{O_3} \frac{\partial^2 c_{O_3}}{\partial x^2} + k_1 c_{O_2}^2 - k_2 c_{O_1} c_{O_3} & (c) \end{aligned} \right\} \quad (3.117)$$

$$\left. \begin{aligned} t &\geq 0, \quad x \rightarrow \infty \\ t &= 0, \quad x \geq 0 \end{aligned} \right\} \quad c_{O_1} = c_{O_1}^*, \quad c_{O_2} = 0, \quad c_{O_3} = 0 \quad (3.118)$$

$$t > 0, \quad x = 0$$

$$D_{O_1} \left(\frac{\partial c_{O_1}}{\partial x} \right)_{x=0} + D_{O_2} \left(\frac{\partial c_{O_2}}{\partial x} \right)_{x=0} + D_{O_3} \left(\frac{\partial c_{O_3}}{\partial x} \right)_{x=0} = 0 \quad (3.119)$$

$$c_{O_1}^s = e^{\eta_1} c_{O_2}^s \quad (3.120)$$

$$c_{O_2}^s = e^{\eta_2} c_{O_3}^s \quad (3.121)$$

with

$$\eta_j = \frac{F}{RT} (E - E_{c,j}^{\ominus'}) \quad j = 1, 2 \quad (3.122)$$

From Eqs. (3.120)–(3.122), it can be deduced that

$$\frac{c_{O_1}^s}{c_{O_3}^s} = e^{\bar{\eta}^2} \quad (3.123)$$

with

$$\bar{\eta} = \frac{F}{RT} (E - \bar{E}_c^{\ominus'}) \quad (3.124)$$

and $\bar{E}_c^{\ominus'}$ being the average formal potential defined as

$$\bar{E}_c^{\ominus'} = \frac{E_{c,1}^{\ominus'} + E_{c,2}^{\ominus'}}{2} \quad (3.125)$$

and the current is given by (see Eq. (3.119)):

$$\begin{aligned} \frac{I^{\text{EE, plane}}}{FA} &= D_{\text{O}_1} \left(\frac{\partial c_{\text{O}_1}}{\partial x} \right)_{x=0} - D_{\text{O}_3} \left(\frac{\partial c_{\text{O}_3}}{\partial x} \right)_{x=0} \\ &= 2D_{\text{O}_1} \left(\frac{\partial c_{\text{O}_1}}{\partial x} \right)_{x=0} + D_{\text{O}_2} \left(\frac{\partial c_{\text{O}_2}}{\partial x} \right)_{x=0} \end{aligned} \quad (3.126)$$

An analytical solution has not been found for this problem, which has, instead, been solved numerically in a number of papers [40, 41]. However, if the diffusion coefficients of the different oxidation states O_1 , O_2 , and O_3 are equal, i.e., $D_{\text{O}_1} = D_{\text{O}_2} = D_{\text{O}_3} = D$, important simplifications can be made as indicated in [34, 39].

In this situation, the addition of equations (a), (b), and (c) in (3.117) gives rise to

$$\frac{\partial Y}{\partial t} = D \frac{\partial^2 Y}{\partial x^2} \quad (3.127)$$

$$\left. \begin{array}{l} t \geq 0, \quad x \rightarrow \infty \\ t = 0, \quad x \geq 0 \end{array} \right\} Y = c_{\text{O}_1}^* \quad (3.128)$$

$t > 0, \quad x = 0$:

$$\left(\frac{\partial Y}{\partial x} \right)_{x=0} = 0 \quad (3.129)$$

where

$$Y = c_{\text{O}_1}(x, t) + c_{\text{O}_2}(x, t) + c_{\text{O}_3}(x, t) \quad (3.130)$$

The solution of this simple problem leads to the following solution, independently of the electrode geometry (see below):

$$c_{\text{O}_1}(x, t) + c_{\text{O}_2}(x, t) + c_{\text{O}_3}(x, t) = c_{\text{O}_1}^* \quad (3.131)$$

By combining Eq. (3.131) for $x = 0$ with surface conditions (3.120)–(3.121), the following expressions for the surface concentrations are found:

$$\left. \begin{array}{l} c_{\text{O}_1}^{\text{S}} = \frac{e^{\eta_1} e^{\eta_2}}{1 + e^{\eta_2} + e^{\eta_1} e^{\eta_2}} c_{\text{O}_1}^* \\ c_{\text{O}_2}^{\text{S}} = \frac{e^{\eta_2}}{1 + e^{\eta_2} + e^{\eta_1} e^{\eta_2}} c_{\text{O}_1}^* \\ c_{\text{O}_3}^{\text{S}} = \frac{1}{1 + e^{\eta_2} + e^{\eta_1} e^{\eta_2}} c_{\text{O}_1}^* \end{array} \right\} \quad (3.132)$$

which can be rewritten in terms of the average formal potential as

$$\left. \begin{aligned} c_{O_1}^s &= \frac{\sqrt{K}e^{2\bar{\eta}}}{\sqrt{K} + e^{\bar{\eta}} + \sqrt{K}e^{2\bar{\eta}}} c_{O_1}^* \\ c_{O_2}^s &= \frac{e^{\bar{\eta}}}{\sqrt{K} + e^{\bar{\eta}} + \sqrt{K}e^{2\bar{\eta}}} c_{O_1}^* \\ c_{O_3}^s &= \frac{\sqrt{K}}{\sqrt{K} + e^{\bar{\eta}} + \sqrt{K}e^{2\bar{\eta}}} c_{O_1}^* \end{aligned} \right\} \quad (3.133)$$

with

$$K = e^{\frac{F\Delta E_c^{\ominus'}}{RT}} \quad (3.134)$$

It is notable that surface concentrations are only dependent on the applied potential and independent of the time and of the values of k_1 and k_2 . Therefore, they are independent of the existence of the disproportionation/comproportionation in solution (see reaction scheme (3.II)).

The following linear combination is now considered:

$$W = 2c_{O_1}(x, t) + c_{O_2}(x, t) \quad (3.135)$$

which fulfills

$$\frac{\partial W}{\partial t} = D \frac{\partial^2 W}{\partial x^2} \quad (3.136)$$

with the boundary conditions

$$\left. \begin{aligned} t \geq 0, \quad x \rightarrow \infty \\ t = 0, \quad x \geq 0 \end{aligned} \right\} W = W^* = 2c_{O_1}^* \quad (3.137)$$

$t > 0, \quad x = 0$

$$W^s = 2c_{O_1}^s + c_{O_2}^s = \frac{2\sqrt{K}e^{2\bar{\eta}} + e^{\bar{\eta}}}{\sqrt{K} + e^{\bar{\eta}} + \sqrt{K}e^{2\bar{\eta}}} c_{O_1}^* \quad (3.138)$$

By following an identical procedure to that indicated in Sect. 2.2, it can be easily demonstrated that the solution of this other simple problem is

$$W(x, t) = W^* + (W^s - W^*)\operatorname{erfc}(s) \quad (3.139)$$

with s given by Eq. (2.8) of Sect. 2.2, such that the current corresponding to a two-electron electrochemical reaction (EE mechanism) is given by (see Eqs. (3.126) and (3.135)):

$$\frac{I^{\text{EE, plane}}}{FAD} = \left(\frac{\partial W}{\partial x} \right)_{x=0} = \frac{W^* - W^s}{\sqrt{\pi Dt}} = \frac{c_{\text{O}_1}^*}{\sqrt{\pi Dt}} \frac{2\sqrt{K} + e^{\bar{\eta}}}{\sqrt{K} + e^{\bar{\eta}} + \sqrt{K}e^{2\bar{\eta}}} \quad (3.140)$$

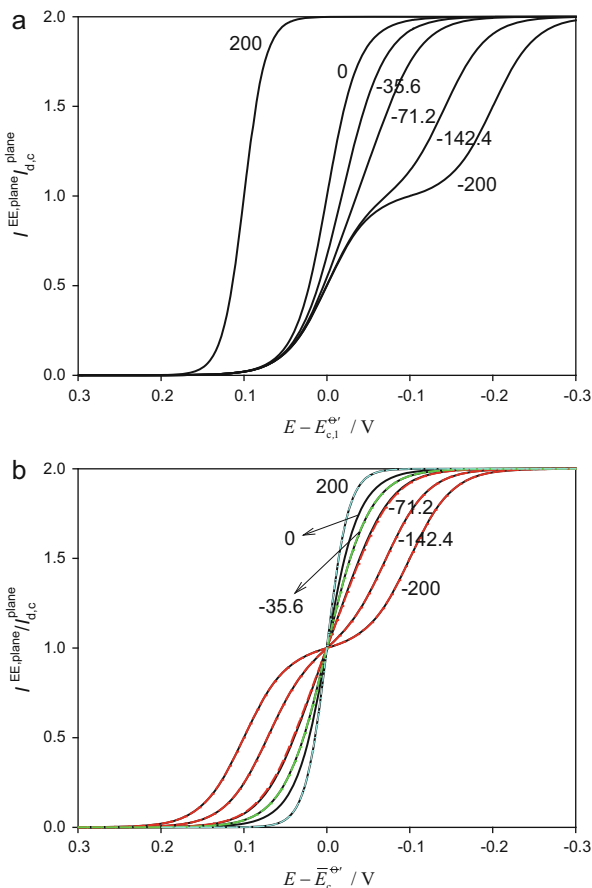
This equation can be written in a normalized way:

$$\frac{I^{\text{EE, plane}}}{I_{\text{d,c}}^{\text{plane}}} = \frac{2\sqrt{K} + e^{\bar{\eta}}}{\sqrt{K} + e^{\bar{\eta}} + \sqrt{K}e^{2\bar{\eta}}} \quad (3.141)$$

with $I_{\text{d,c}}^{\text{plane}} = FAC_{\text{O}_1}^* \sqrt{D/\pi t}$ (Eq. 3.20), being the diffusion-controlled limiting current for a single charge transfer.

Equation (3.140) shows that the electrochemical response of an EE mechanism depends on the difference between the formal potentials $\Delta E_c^{\ominus'}$ and is not influenced by the homogeneous reaction. This behavior is shown in Fig. 3.16 where the current for an EE mechanism versus $E - E_{\text{c},1}^{\ominus'}$ (Fig. 3.16a) and versus $E - \bar{E}_c^{\ominus'}$ (Fig. 3.16b)

Fig. 3.16 Current for an EE mechanism vs. $E - E_{\text{c},1}^{\ominus'}$ (a) and vs. $E - \bar{E}_c^{\ominus'}$ (b) calculated from Eq. (3.141) for different values of $\Delta E_c^{\ominus'}$ (shown in the curves). (b) Includes the response of two independent E mechanisms for the values of $\Delta E_c^{\ominus'}$ (in mV) -200 , -142.4 , and -71.2 (dashed red curves), for $\Delta E_c^{\ominus'} = 0$ mV (dashed green curve), calculated from Eq. (20) in reference [42], and also for a simple di-electronic charge transfer (dashed blue curve) calculated from Eq. (2.34) of Sect. 2.2.2.2. $I_{\text{d,c}}^{\text{plane}} = FAC_{\text{O}_1}^* \sqrt{D/\pi t}$ (Eq. 3.20)



has been plotted for different values of $\Delta E_c^{\ominus'}$. In all the cases, the current–potential curves are symmetrical with respect to the average formal potential $\bar{E}_c^{\ominus'}$ as shown in Fig. 3.16b (i.e., all of them present a symmetry center located at the point $(I^{EE, \text{plane}}/I_{d,c}^{\text{plane}} = 1, \bar{E}_c^{\ominus'})$).

As can be observed in this figure (see also Table 3.1), for $\Delta E_c^{\ominus'} \leq -142.4$ mV ($K = 1/2^8$), the normal pulse voltogram presents two well-resolved waves whose half-wave potentials exactly match with the corresponding formal potentials $E_{c,1}^{\ominus'}$ and $E_{c,2}^{\ominus'}$ (for $(-142.4 < \Delta E_c^{\ominus'} < -71.2)$ mV, two non-well-resolved waves are observed, whose half-wave potentials are not coincident with the corresponding individual formal potentials, Fig. 3.16a. For $\Delta E_c^{\ominus'} \geq -71.2$ mV ($K \geq 1/2^4$), only one wave is obtained with the half-wave potential being $E_r^{1/2} = \bar{E}_c^{\ominus'}$ (thus, at $\Delta E_c^{\ominus'} = -71.2$ mV the transition two waves \rightarrow one wave takes place).

For $\Delta E_c^{\ominus'} = -35.6$ mV ($K = 1/2^2$), one wave with identical shape to that of an E process but with double height is observed. Finally, for very positive values of $\Delta E_c^{\ominus'}$ (see curves with $\Delta E_c^{\ominus'} = 200$ mV in Fig. 3.16a and b), the response of the EE mechanism is indistinguishable from that obtained for a single charge transfer of two electrons (see dashed blue curve).

The voltammetric response of the EE mechanism can be compared with those for two independent reversible charge transfers (two reversible independent E processes or E + E mechanism) with identical bulk concentrations of oxidized species (c^*) by assuming that the diffusion coefficients of all species are equal, that is,

Table 3.1 Analytical expressions for the roots with physical meaning of the second derivative of the current of an EE mechanism given by Eq. (3.141) [43]

$$\left. \begin{aligned} E_I &= \bar{E}_c^{\ominus'} + \frac{RT}{F} \ln \left(-4\sqrt{K} + \frac{1 - \sqrt{(4K-1)(16K-1)}}{2\sqrt{K}} \right) \\ E_{II} &= \bar{E}_c^{\ominus'} + \frac{RT}{F} \ln \left(-4\sqrt{K} + \frac{1 + \sqrt{(4K-1)(16K-1)}}{2\sqrt{K}} \right) \end{aligned} \right\} K < (1/16) \quad (\Delta E_c^{\ominus'} < -71.2 \text{ mV})$$

Note that

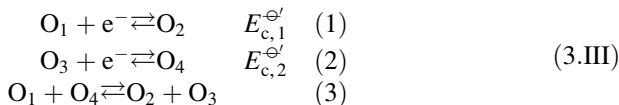
$$\left. \begin{aligned} E_I &= E_{c,1}^{\ominus'} \\ E_{II} &= E_{c,2}^{\ominus'} \end{aligned} \right\} \text{for } K \leq (1/256) \quad (\Delta E_c^{\ominus'} \leq -142.4 \text{ mV})$$

E_I and E_{II} coincide with the reversible half-wave potentials of the individual waves, $E_{1/2,1}^r$ and $E_{1/2,2}^r$, respectively

$$E_{III} = \bar{E}_c^{\ominus'} \text{ For } K \left\{ \begin{array}{l} < (1/16) \quad (\Delta E_c^{\ominus'} < -71.2 \text{ mV}) \\ E_{III} \text{ corresponds to the inflexion point between the two waves} \\ \geq (1/16) \quad (\Delta E_c^{\ominus'} \geq -71.2 \text{ mV}) \\ E_{III} \text{ corresponds to the half-wave potential of the single wave} \end{array} \right.$$

$$E_I = E_{II} = E_{III} = \bar{E}_c^{\ominus'} \text{ for } K = (1/16) \quad (\Delta E_c^{\ominus'} = -71.2 \text{ mV})$$

Transition 2 waves—1 wave



with $c_{\text{O}_1} + c_{\text{O}_2} = c_{\text{O}_3} + c_{\text{O}_4} = c^*$. Under these conditions, it is fulfilled that

$$\begin{aligned}
 E = E_{c,1}^{\ominus'} &\Rightarrow c_{\text{O}_1}^s = c_{\text{O}_2}^s = c^*/2 \\
 E = E_{c,2}^{\ominus'} &\Rightarrow c_{\text{O}_3}^s = c_{\text{O}_4}^s = c^*/2
 \end{aligned}
 \tag{3.142}$$

Conditions (3.142) are independent of the difference between the formal potentials of both processes 1 and 2, $\Delta E_c^{\ominus'} = E_{c,2}^{\ominus'} - E_{c,1}^{\ominus'}$. In Fig. 3.16b, it can be seen the coincidence between the responses of EE and E+E mechanisms for $\Delta E_c^{\ominus'} < -71.2$ mV (two waves in the voltogram; see dashed red lines). The EE mechanism with $\Delta E_c^{\ominus'} = -35.6$ mV behaves as two independent E mechanisms with $\Delta E_c^{\ominus'} = 0$ mV (see dashed green curve in Fig. 3.16b).

In order to clarify the influence of $\Delta E_c^{\ominus'}$ on the electrochemical response of an EE mechanism, in Fig. 3.17 the dependence of the normalized surface concentrations of species O_1 , O_2 , and O_3 ($c_{\text{O}_i}^s/c_{\text{O}_i}^*$ $i = 1, 2, 3$) with $E - \bar{E}_c^{\ominus'}$ given by Eq. (3.133) has been plotted for the same values of $\Delta E_c^{\ominus'}$ appearing in Fig. 3.16.

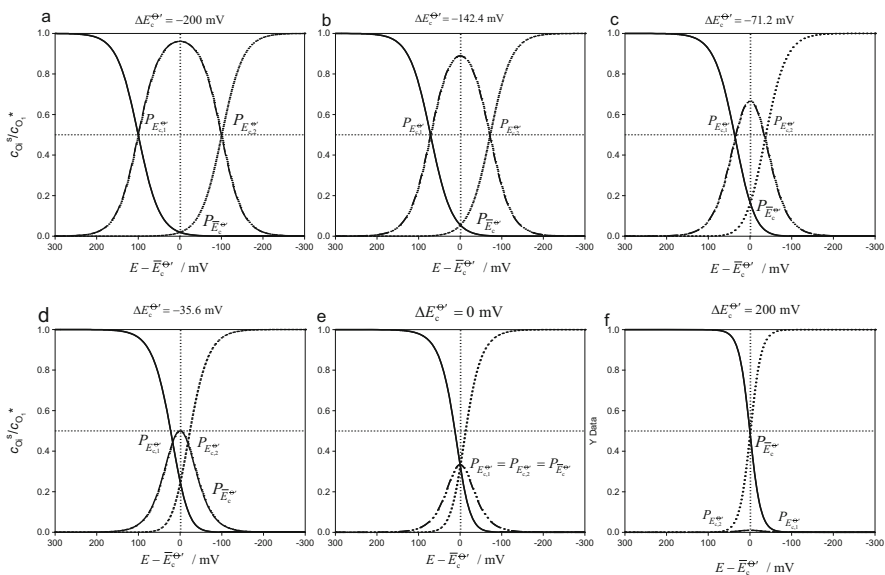


Fig. 3.17 Variation of the normalized surface concentrations $c_{\text{O}_1}^s/c_{\text{O}_1}^*$ (solid lines), $c_{\text{O}_2}^s/c_{\text{O}_1}^*$ (dashed-dotted lines), and $c_{\text{O}_3}^s/c_{\text{O}_1}^*$ (dotted lines) corresponding to a reversible EE mechanism, with $E - \bar{E}_c^{\ominus'}$ (mV) (Eq. 3.133) for different values of $\Delta E_c^{\ominus'}$ (shown in the Figure). $P_{E_{c,1}^{\ominus'}}$, $P_{E_{c,2}^{\ominus'}}$, and $P_{\bar{E}_c^{\ominus'}}$ denote the cross points. Reproduced with permission of [43]

In this figure, three characteristic cross points for the surface concentrations can be observed: $P_{E_{c,1}^{\ominus'}}$ ($c_{O_1}^s = c_{O_2}^s$, Eq. (3.120)), $P_{E_{c,2}^{\ominus'}}$ ($c_{O_2}^s = c_{O_3}^s$, Eq. (3.121)), and $P_{\bar{E}_c^{\ominus'}}$ ($c_{O_1}^s = c_{O_3}^s$, Eq. (3.123)), located respectively (see dotted vertical lines) at $E = E_{c,1}^{\ominus'}$ ($E - \bar{E}_c^{\ominus'} = -\Delta E_c^{\ominus'}/2$), $E = E_{c,2}^{\ominus'}$ ($E - \bar{E}_c^{\ominus'} = \Delta E_c^{\ominus'}/2$), and $E = \bar{E}_c^{\ominus'}$, regardless of the difference between the formal potentials $\Delta E_c^{\ominus'}$. Note that when $\Delta E_c^{\ominus'}$ increases from -200 mV (Fig. 3.17a) to 200 mV (Fig. 3.17f), the values of the normalized surface concentrations at $P_{E_{c,1}^{\ominus'}}$ and $P_{E_{c,2}^{\ominus'}}$ vary between 0.5 (i.e., as corresponds to a simple E mechanism) and 0 , and contrarily, between 0 and 0.5 at $P_{\bar{E}_c^{\ominus'}}$.

Thus, the behavior of the $(I^{EE, \text{plane}}/I_{d,c}^{\text{plane}}) - (E - \bar{E}_c^{\ominus'})$ curves in Fig. 3.16 can be understood in terms of the surface concentrations, taking into account that the values of $(c_{O_2}^s/c_{O_1}^*)_{\bar{E}_c^{\ominus'}}$ and $((c_{O_1}^s + c_{O_3}^s)/c_{O_1}^*)_{\bar{E}_c^{\ominus'}}$ are indicative of the percentage of character $E_{1e^-}E_{1e^-}$ and of character E_{2e^-} , respectively, of the EE mechanism [43]. Indeed, for $\Delta E_c^{\ominus'} \leq -200$ mV, $(c_{O_2}^s/c_{O_1}^*)_{\bar{E}_c^{\ominus'}} \cong 1$ (see Fig. 3.17a), and this limiting situation corresponds to a genuine 100% $E_{1e^-}E_{1e^-}$ mechanism with a totally stable intermediate (0% character E_{2e^-}), i.e., two totally separate waves appear in the voltogram with the half-wave potential of each individual wave being coincident with the formal potential of each process (Fig. 3.16a). For $\Delta E_c^{\ominus'} = -142.4$ mV (Fig. 3.17b), a less stable intermediate leads to the appearance of two non-totally separate waves in the response (89% character $E_{1e^-}E_{1e^-}$ and 11% character E_{2e^-}), although the half-wave potential of each individual wave remains coincident with the formal potential of each process. For $\Delta E_c^{\ominus'} = -71.2$ mV (Fig. 3.17c), it is fulfilled that $(c_{O_2}^s/c_{O_1}^*)_{\bar{E}_c^{\ominus'}} = 0.666$ (66.7% character $E_{1e^-}E_{1e^-}$), i.e., the transition two waves—one wave in the voltogram takes place, but the intermediate O_2 is still stable.

Note that for $\Delta E_c^{\ominus'} \leq -71.2$ mV, $(c_{O_i}^s/c_{O_1}^*) \cong 0.5$ with $i = 1, 2$, at the cross point $P_{E_{c,1}^{\ominus'}}$ and $i = 2, 3$ at $P_{E_{c,2}^{\ominus'}}$, and, therefore, the EE mechanism practically behaves like the E + E mechanism (see dashed red lines in Fig. 3.16b).

The value $\Delta E_c^{\ominus'} = -35.6$ mV has the particular interest of corresponding to a 50% of character $E_{1e^-}E_{1e^-}$ and E_{2e^-} . At the average formal potential $\bar{E}_c^{\ominus'}$, the intermediate species reaches half of its maximum value and, hence, at this $\Delta E_c^{\ominus'}$ species O_2 may or may not gain a second electron (and as a direct consequence, for higher $\Delta E_c^{\ominus'}$ it will be considered that the intermediate species is no more stable at the average formal potential). So, this $\Delta E_c^{\ominus'}$ could be considered as the boundary between anti-cooperative and cooperative behavior of both electron transfer reactions [35, 43]. Indeed, it is well known that the voltamogram of an EE mechanism under these conditions is identical to that of an E mechanism multiplied by a factor

2 (as the case of two independent monoelectronic charge transfers with identical formal potentials, $\Delta E_c^{\ominus'} = 0$; see dashed green curves in Fig. 3.16b). For $\Delta E_c^{\ominus'} = 0$ mV (Fig. 3.17e), $P_{E_{c,1}^{\ominus'}}$, $P_{E_{c,2}^{\ominus'}}$, and $P_{E_c^{\ominus'}}$ become coincident and $\left(c_{O_2}^s/c_{O_1}^*\right)_{E_c^{\ominus'}} = 0.333$ (66.7 % character E_{2e^-}). For $\Delta E_c^{\ominus'} \geq 200$ mV (Fig. 3.17f), the intermediate practically disappears and $\left(c_{O_1}^s/c_{O_1}^*\right)_{E_c^{\ominus'}} = \left(c_{O_3}^s/c_{O_1}^*\right)_{E_c^{\ominus'}} = 0.5$. Thus, the typical behavior of surface concentrations for a two-electron E mechanism is observed (100 % character E_{2e^-}), and hence the corresponding typical voltogram is obtained (see dashed blue curve in Fig. 3.16b).

In line with the above discussion, the term “effective electron number”, n_{eff} , defined as

$$n_{\text{eff}} = (1 + \% \text{ character } E_{2e^-} / 100) = 2 \left(c_{O_2}^s / c_{O_1}^* \right)_{E_c^{\ominus'}} \quad (3.143)$$

is introduced. Thus, $n_{\text{eff}} = 1$ for $\Delta E_c^{\ominus'} \leq -200$ mV, $n_{\text{eff}} = 1.333$ for $\Delta E_c^{\ominus'} = -71.2$ mV, $n_{\text{eff}} = 1.5$ for $\Delta E_c^{\ominus'} = -35.6$ mV, and $n_{\text{eff}} = 2$ for $\Delta E_c^{\ominus'} \geq 200$ mV [43].

Table 3.1 shows the analytical expressions for the roots with physical meaning of the second derivative of the current expression given by Eq. (3.141) with respect to the potential (E_I , E_{II} , and E_{III}), which correspond to the inflexion points of the current–potential curves shown in Fig. 3.16, given as a function of K .

3.3.2 Two-Electron Electrochemical Reactions at Different Electrode Geometries

When nonplanar geometries are considered for the reaction scheme (3.II), the following diffusive-kinetic differential equations must be solved:

$$\left. \begin{aligned} \frac{\partial c_{O_1}}{\partial t} &= D_{O_1} \nabla^2 c_{O_1} + k_1 c_{O_2}^2 - k_2 c_{O_1} c_{O_3} & \text{(a)} \\ \frac{\partial c_{O_2}}{\partial t} &= D_{O_2} \nabla^2 c_{O_2} - 2k_1 c_{O_2}^2 + 2k_2 c_{O_1} c_{O_3} & \text{(b)} \\ \frac{\partial c_{O_3}}{\partial t} &= D_{O_3} \nabla^2 c_{O_3} + k_1 c_{O_2}^2 - k_2 c_{O_1} c_{O_3} & \text{(c)} \end{aligned} \right\} \quad (3.144)$$

where ∇^2 is the Laplacian operator for the geometry considered given in Table 2.2 of Sect. 2.6. If only species O_1 is initially present with a concentration $c_{O_1}^*$, the boundary value problem is

$$\left. \begin{aligned} t = 0, q \geq q^s \\ t > 0, q \rightarrow \infty \end{aligned} \right\} \quad c_{O_1} = c_{O_1}^*; \quad c_{O_2} = c_{O_3} = 0 \quad (3.145)$$

$t > 0, q = q^s :$

$$D_{O_1} \left(\frac{\partial c_{O_1}}{\partial q_N} \right)_{q^s} + D_{O_2} \left(\frac{\partial c_{O_2}}{\partial q_N} \right)_{q^s} + D_{O_3} \left(\frac{\partial c_{O_3}}{\partial q_N} \right)_{q^s} = 0 \quad (3.146)$$

$$\left. \begin{aligned} c_{O_1}^s &= e^{\eta_1} c_{O_2}^s \\ c_{O_2}^s &= e^{\eta_2} c_{O_3}^s \end{aligned} \right\} \quad (3.147)$$

where η_j ($j = 1, 2$) is given in Eq. (3.122), q^s is the value of the coordinates at the electrode surface, and q_N is the normal coordinate value at the electrode surface.

By assuming that the diffusion coefficients of the different oxidation states O_1 , O_2 , and O_3 are equal, i.e., $D_{O_1} = D_{O_2} = D_{O_3} = D$, function $Y = c_{O_1}(q, t) + c_{O_2}(q, t) + c_{O_3}(q, t)$ can be used to solve the above problem and the general solution given by Eq. (3.131) remains valid, independently of the electrode geometry. By combining Eq. (3.131) with the nernstian conditions (3.147), identical expressions to those given by Eqs. (3.132) or (3.133) are obtained for the surface concentrations. Under these conditions, the current can be written, regardless of the electrode geometry (see Eq. (3.126)) as

$$\frac{I^{EE,G}}{F A_G D} = \left(\frac{\partial W}{\partial q_N} \right)_{q^s} \quad (3.148)$$

where

$$W = 2c_{O_1}(q, t) + c_{O_2}(q, t) \quad (3.149)$$

and A_G is the electrode area in the corresponding geometry. The current can be expressed as a product of two functions which depend on the potential and on time and electrode geometry, respectively, as occurs for a reversible E process (see Eq. (2.156) of Sect. 2.6) [44–46]:

$$I^{EE,G} = F A_G D f_G(t, q_G) (W^* - W^s) \quad (3.150)$$

with $f_G(t, q_G)$ given in Table 2.3 of Sect. 2.6 for each geometry and (see Eq. 3.140)

$$W^* - W^s = c_{O_1}^* \frac{2\sqrt{K} + e^{\eta}}{\sqrt{K} + e^{\eta} + \sqrt{K}e^{2\eta}} \quad (3.151)$$

Equation (3.150) can be also written in a dimensionless form as

$$\frac{I^{EE,G}}{I_{d,c}^G} = \frac{W^* - W^s}{c_{O_1}^*} \quad (3.152)$$

with $I_{d,c}^G$ being the diffusion-controlled limiting current for the geometry considered given by

$$I_{d,c}^G = FA_G D c_{O_1}^* f_G(t, q_G) \quad (3.153)$$

Note that function $f_G(t, q_G)$ is identical to that appearing in the case of an E mechanism. Moreover, Eqs. (3.151) and (3.152) are identical to that corresponding to a planar electrode (Eq. 3.141).

In the case of non-uniformly accessible electrodes, the currents given by Eqs. (3.150) or (3.153) are an average current [46].

3.3.2.1 Microelectrodes. Steady-State Voltammetry

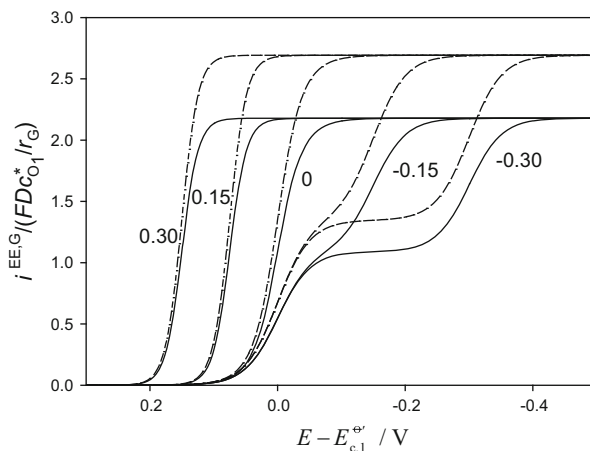
The current for a reversible EE mechanism can achieve a stationary feature when microelectrodes are used since in these conditions the function $f_G(t, q_G)$ that appears in Eq. (3.150) transforms into $f_{G,\text{micro}}$ given in Table 2.3 of Sect. 2.6. For microelectrode geometries for which $f_{G,\text{micro}}$ is constant, the current–potential responses have a stationary character, which for microdiscs and microspheres can be written as [16]:

$$\begin{aligned} I^{EE, \text{microdisc, ss}} &= FA_d D c_{O_1}^* \frac{4}{\pi r_d} \frac{1}{\sqrt{K} + e^{\eta} + \sqrt{K} e^{2\eta}} \\ I^{EE, \text{microsphere, ss}} &= FA_s D c_{O_1}^* \frac{1}{r_s} \frac{1}{\sqrt{K} + e^{\eta} + \sqrt{K} e^{2\eta}} \end{aligned} \quad (3.154)$$

In Fig. 3.18, it is shown the response of an EE mechanism at microdiscs and microspheres for different values of $\Delta E_c^{\ominus'}$.

Obviously the equivalence relationship for microspheres and microdiscs established for a single charge transfer process (see Eq. (2.170) of Sect. 2.7) also holds in this case (Fig. 3.18).

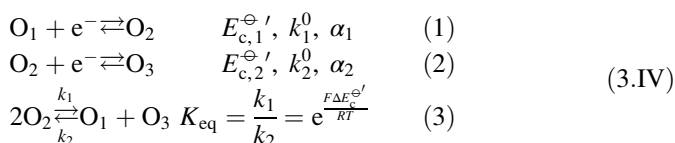
Fig. 3.18 Current density–potential curves for two-electron transfer processes at disc (solid line) and spherical (dashed line) microelectrodes of the same radius. The values of the difference between the formal potentials of the redox centers, $\Delta E_c^{\ominus'}$ (in V), are indicated on the curves. These curves have been calculated with Eq. (3.154) by assuming $r_G = r_d = r_s = 5 \mu\text{m}$, $t = 1 \text{ s}$, $D = 10^{-5} \text{ cm}^2 \text{ s}^{-1}$, $T = 298 \text{ K}$



For microelectrodes like microbands or microcylinders for which $f_{G,\text{micro}}$ is not constant, only pseudo-stationary behavior can be achieved.

3.3.3 Non-reversible Two-Electron Electrochemical Reactions

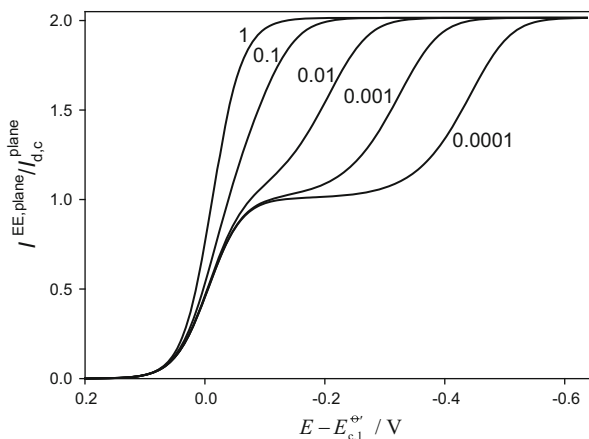
The treatment of non-reversible two-electron electrochemical reactions is much more complex than the reversible one. The general scheme of the process is



with k_j^0 and α_j , $j = 1, 2$, being the rate constants and charge transfer coefficients of the step j .

Even in the simplest situation for which $\alpha_1 = \alpha_2 = 0.5$, the global behavior of the response depends upon three parameters, the difference between the formal potentials $\Delta E_c^{\ominus'}$, and the rate constants of both steps k_1^0 and k_2^0 . Thus, the observed current–potential curves are the result of the interaction of thermodynamic and kinetic effects so the appearance of two or one waves would not be due solely to thermodynamic stability or instability of the intermediate species but also to a kinetic stabilization or destabilization of the same [4, 31]. This can be seen in Fig. 3.19 in which the current–potential curves of an EE process with $\Delta E_c^{\ominus'} = 0$ mV taking place at a planar electrode with a reversible first step ($\kappa_{\text{plane},1}^0 = k_1^0 \sqrt{t/D} = 1$) and a second step with different reversibility degree

Fig. 3.19 Current–potential responses for an EE mechanism at a plane electrode calculated by following the numerical procedure described in reference [47] $\Delta E_c^{\ominus'} = 0$ mV. $\kappa_{\text{plane},1}^0 = k_1^0 \sqrt{t/D} = 1$ and $\alpha_1 = \alpha_2 = 0.5$. The values of $\kappa_{\text{plane},2}^0 = k_2^0 \sqrt{t/D}$ appear on the curves



have been plotted. The voltammogram for a second reversible step shows a single wave in line with results shown in Fig. 3.16. As the second charge transfer becomes more irreversible, the increasing kinetic stabilization of the intermediate leads to the appearance of a second wave that shifts toward more negative potentials as $k_{\text{plane},2}^0 = k_2^0 \sqrt{t/D}$ decreases.

Moreover, the current–potential curves are affected by the disproportionation reaction; therefore, other variables (the rate constant for the disproportionation reaction) must be taken into account. Since experimental results for many interesting systems show clear evidence of slow kinetics, ad hoc simulation procedures have typically been used for the analysis of the resulting current–potential curves [31, 38, 41, 48]. As an example, in reference [38], it is reported that a clear comproportionation influence is observed for an EE mechanism with normal ordering of potentials and an irreversible second charge transfer step. In this case, the second wave is clearly asymmetric, showing a sharp rise near its base. This result was observed experimentally for the reduction of 7,7,8,8-tetracyanoquinodimethane in acetonitrile at platinum electrodes (see Fig. 3.20). In order to fit the experimental results, a comproportionation rate constant $k_{\text{comp}} = 10^8 \text{ M}^{-1} \text{ s}^{-1}$ should be introduced.

References [40, 41] report the chronoamperometric analysis of the response of an EE mechanism with non-reversible charge transfer processes including the consideration of a fast comproportionation step [40], indicating that strong differences in the diffusion coefficients of the different species are needed to cause a clear influence of the comproportionation process in the electrochemical response.

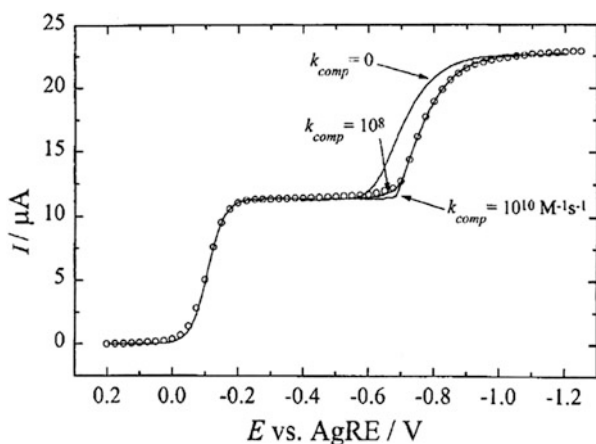
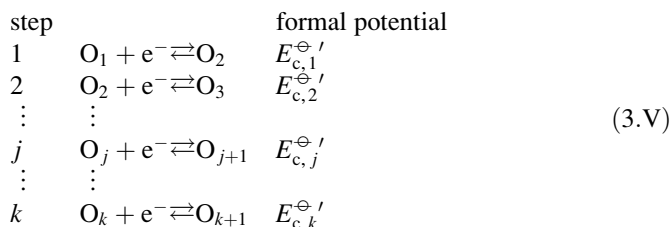


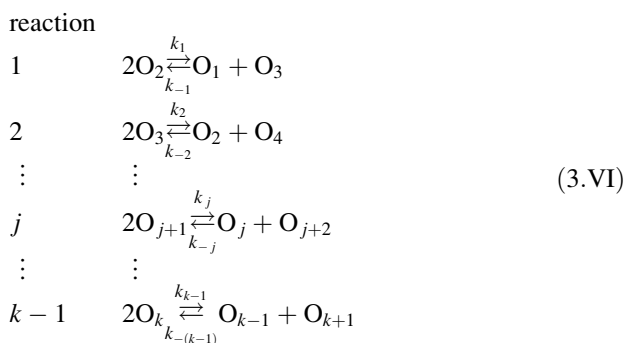
Fig. 3.20 Normal Pulse Voltammograms for the reduction of $6.9 \times 10^{-4} \text{ M}$ tetracyanoquinodimethane (TCNQ) in acetonitrile with $0.10 \text{ NBU}_4\text{NPF}_6$ at 293 K (platinum disc electrode with diameter 0.31 cm). Pulse duration: 0.050 s. Lines are simulations with the following input parameters: $E_{\text{c},1}^{\ominus'}$ = -0.107 V , $\Delta E_{\text{c}}^{\ominus'}$ = -0.551 V , $k_1^0 = 10^4 \text{ cm s}^{-1}$, $\alpha_1 = 0.5$, $\alpha_2 = 0.35$, $k_2^0 = 6.5 \times 10^{-3} \text{ cm s}^{-1}$, diffusion coefficients of neutral, anion, and di-anion are: 1.44×10^{-5} , 1.35×10^{-5} , and $9.1 \times 10^{-6} \text{ cm}^2 \text{ s}^{-1}$, respectively. Reproduced from reference [38] with permission

3.3.4 General Solution for Multi-electron Electrochemical Reactions

In this section, the results corresponding to an EE process are generalized for a multi-electron electrochemical reaction of k steps (multi-E process) in agreement with the reaction scheme:



where $E_{c,j}^{\ominus'}$ ($j = 1, 2, \dots, k$) is the formal potential of each step. The above general reaction scheme must be considered together with $(k - 1)$ homogeneous chemical reactions of disproportionation, coupled to the k heterogeneous steps of the electrochemical process given in scheme (3.V):²



whose equilibrium constants, K_j ($j = 1, 2, \dots, k - 1$), are determined by the difference between the formal potential of the redox couples implied in each chemical reaction:

$$\begin{aligned}
 K_j &= \frac{c_{\text{eq}, O_j} c_{\text{eq}, O_{j+2}}}{c_{\text{eq}, O_{j+1}}^2} = \exp\left(\frac{(E_{c,j+1}^{\ominus'} - E_{c,j}^{\ominus'})}{RT}\right) \\
 &= \exp\left(\frac{\Delta E_{c,j}^{\ominus'}}{RT}\right) \quad (j = 1, 2, \dots, k - 1)
 \end{aligned}
 \tag{3.155}$$

²For sake of simplicity, only homogeneous, independent chemical reactions are considered in scheme (3.VI)

In the vicinity of the electrode, the homogeneous chemical reactions inevitably take place since, when the electrode process given in reaction scheme (3.V) occurs, all species O_i ($i = 1, 2, \dots, k + 1$) are being generated at the electrode surface.

By considering the chemical reactions of reaction scheme (3.VI), the differential equation system that describes the mass transport of the ($k + 1$) species involved is

$$\left. \begin{aligned} \frac{\partial c_{O_1}}{\partial t} &= D_{O_1} \nabla^2 c_{O_1} - k_{-1} c_{O_1} c_{O_3} + k_1 c_{O_2}^2 \\ \frac{\partial c_{O_2}}{\partial t} &= D_{O_2} \nabla^2 c_{O_2} + 2k_{-1} c_{O_1} c_{O_3} - 2k_1 c_{O_2}^2 - k_{-2} c_{O_2} c_{O_4} + k_2 c_{O_3}^2 \\ &\vdots \\ \frac{\partial c_{O_i}}{\partial t} &= D_{O_i} \nabla^2 c_{O_i} + 2k_{-(i-1)} c_{O_{i-1}} c_{O_{i+1}} - 2k_{(i-1)} c_{O_i}^2 - k_{-(i-2)} c_{O_{i-2}} c_{O_i} + k_{(i-2)} c_{O_{i-1}}^2 \\ &\quad - k_{-i} c_{O_i} c_{O_{i+2}} + k_i c_{i+1}^2 \\ &\vdots \\ \frac{\partial c_{O_k}}{\partial t} &= D_{O_k} \nabla^2 c_{O_k} + 2k_{-(k-1)} c_{O_{k-1}} c_{O_{k+1}} - 2k_{(k-1)} c_{O_k}^2 - k_{-(k-2)} c_{O_{k-2}} c_{O_k} + k_{(k-2)} c_{O_{k-1}}^2 \\ \frac{\partial c_{O_{k+1}}}{\partial t} &= D_{O_k} \nabla^2 c_{O_{k+1}} - k_{-(k-1)} c_{O_{k-1}} c_{O_{k+1}} + k_{(k-1)} c_{O_k}^2 \end{aligned} \right\} \quad (3.156)$$

where c_{O_i} ($i = 1, 2, \dots, k + 1$) are the concentration of each species O_i , and k_j and k_{-j} ($j = 1, 2, \dots, k - 1$) the rate constants corresponding to the j th chemical step in reaction scheme (3.VI). The expressions for the laplacian operator ∇^2 corresponding to the most usual electrode geometries are given in Table 2.2 of Sect. 2.6.

As discussed in Sects. 3.3.1 and 3.3.2, the presence of disproportionation reactions has no effect on the current when all the heterogeneous steps are reversible and the diffusion coefficients of each species O_i are assumed to be equal. To test this, it should be first considered that the initial and limiting conditions for the stepwise process given in reaction scheme (3.V) are

$$\left. \begin{aligned} t = 0, \quad q \geq q^s \\ t > 0, \quad q \rightarrow \infty \end{aligned} \right\} \quad c_{O_1} = c_{O_1}^*, \quad c_{O_i} = 0 \quad (i = 2, \dots, k + 1) \quad (3.157)$$

$$t > 0, \quad q = q^s$$

$$\sum_{i=1}^{k+1} \left(\frac{\partial c_{O_i}(q, t)}{\partial q_N} \right)_{q^s} = 0 \quad (3.158)$$

$$c_{O_i}^s = e^{\frac{F}{RT}(E - E_{c,i}^{\theta'})} c_{O_{i+1}}^s \quad (i = 1, 2, \dots, k) \quad (3.159)$$

where q^s denotes the value of the coordinates at the electrode surface and q_N is the normal coordinate value at the electrode surface.

The expression of the total current is the sum of the partial currents corresponding to the different steps is:

$$I^{\text{multi-E,G}} = \sum_{j=1}^k I_j^{\text{multi-E,G}} \quad (3.160)$$

The partial currents $I_j^{\text{multi-E,G}}$ are calculated by taking into account that for reaction scheme (3.V) the following relationships hold:

$$\left. \begin{aligned} \frac{I_1^{\text{multi-E,G}}}{FA_G} &= D \left(\frac{\partial c_{O_1}}{\partial q_N} \right)_{q^s} \\ \frac{I_2^{\text{multi-E,G}} - I_1^{\text{multi-E,G}}}{FA_G} &= D \left(\frac{\partial c_{O_2}}{\partial q_N} \right)_{q^s} \\ &\vdots \\ \frac{I_k^{\text{multi-E,G}} - I_{k-1}^{\text{multi-E,G}}}{FA_G} &= D \left(\frac{\partial c_{O_k}}{\partial q_N} \right)_{q^s} \\ \frac{I_k^{\text{multi-E,G}}}{FA_G} &= -D \left(\frac{\partial c_{O_{k+1}}}{\partial q_N} \right)_{q^s} \end{aligned} \right\} \quad (3.161)$$

From Eq. (3.161), it is deduced that for the j th step the partial current can be written as

$$I_j^{\text{multi-E,G}} = FA_G D \sum_{i=1}^j \left(\frac{\partial c_{O_i}}{\partial q_N} \right)_{q^s} \quad (3.162)$$

and by combining Eqs. (3.160) and (3.162), the following expression for the current is deduced:

$$I^{\text{multi-E,G}} = FA_G D \sum_{j=1}^k (k-j+1) \left(\frac{\partial c_{O_j}}{\partial q_N} \right)_{q^s} \quad (3.163)$$

Equations (3.158) and (3.163) suggest the inclusion of the linear combinations:

$$Y(q, t) = \sum_{j=1}^{k+1} c_{O_j}(q, t) \quad (3.164)$$

$$W(q, t) = \sum_{j=1}^k (k-j+1) c_{O_j}(q, t) \quad (3.165)$$

for which the differential equations that described the mass transport become

$$\left. \begin{aligned} \frac{\partial Y(q, t)}{\partial t} &= D \nabla^2 Y(q, t) \\ \frac{\partial W(q, t)}{\partial t} &= D \nabla^2 W(q, t) \end{aligned} \right\} \quad (3.166)$$

From Eqs. (3.157), (3.158), and (3.166), it can be easily demonstrated that

$$Y(q, t) = c_{O_1}^* \quad \forall q, t \quad (3.167)$$

The current can be written as

$$I^{\text{multi-E,G}} = F A_G D \left(\frac{\partial W(q, t)}{\partial q_N} \right)_{q^s} \quad (3.168)$$

and it is not sensitive to the presence of coupled reactions to the charge transfer processes under the above conditions.

The surface concentrations of species O_i with $(i = 1, 2, \dots, k + 1)$ are obtained by combining Eqs. (3.159) and (3.167) [42]:

$$\left. \begin{aligned} c_{O_i}^s &= c_{O_1}^* \frac{\prod_{h=i}^k e^{\eta_h}}{1 + \sum_{m=1}^k \prod_{h=m}^k e^{\eta_h}} \quad i = 1, 2, \dots, k \\ c_{O_{k+1}}^s &= c_{O_1}^* \frac{1}{1 + \sum_{m=1}^k \prod_{h=m}^k e^{\eta_h}} \end{aligned} \right\} \quad (3.169)$$

with

$$\eta_j = \frac{F}{RT} (E - E_{c,j}^{\ominus'}) \quad j = 1, 2, \dots, k \quad (3.170)$$

As in the case of an EE process, the total current for a molecule capable of producing k electron transfers (reaction scheme (3.V)) can be expressed as a product of two functions which depend on the potential and on time and electrode geometry, respectively:

$$I^{\text{multi-E,G}} = F A_G D c_{O_1}^* f_G(t, q_G) (W^* - W^s) \quad (3.171)$$

with

$$W^* - W^s = c_{O_1}^* \frac{k + \sum_{s=1}^{k-1} \left(s \prod_{m=s+1}^k e^{\eta_m} \right)}{1 + \sum_{s=1}^k \prod_{m=s}^k e^{\eta_m}} \quad (3.172)$$

and $f_G(t, q_G)$ given in Table 2.3 of Sect. 2.6 with q_G being the characteristic dimension of the electrode considered.

3.4 First-Order Chemical Reactions Coupled to Charge Transfer Processes

In the previous sections, only fast or slow charge transfer reactions (one-electron or multi-electron) have been considered. As occurs with a chemical reaction, an electrochemical reaction can be complicated by the coupling of homogeneous chemical reactions where one or both electro-active species participate. In this section, only some of the more important electrode reaction schemes are studied. Of course, many more reaction schemes than those we discuss below could be considered by adding chemical homogeneous reactions or varying the reversibility degree of the electron transfer reaction, but in this book only the more usual reaction schemes will be treated in order to discuss the elucidation of the different mechanisms by using electrochemical methods.

Sometimes the oxidized species can exist in two forms in chemical equilibrium, with one of them electro-inactive in the potential range where the electrochemical process occurs. This type of reaction pathway is known as a CE mechanism because a homogeneous chemical reaction (C) precedes the heterogeneous electrochemical process (E). If the chemical step is of first or pseudo-first order, the process can be expressed by the reaction scheme:



Examples of these reactions are the reduction of the non-hydrated form of formaldehyde or that of acetic acid in aqueous solution at a mercury electrode [9] as well as the reduction of many inorganic ions in their complexed forms [49]. Among organic species there are also many examples of this reaction scheme like the reduction of benzoic acid at room temperature ionic liquids [50] or that of the oxidation of ferrocenecarboxylate in the presence of a β -cyclodextrin host (see Fig. 3.21) [51].

Sometimes the electrochemical reaction product is not stable and it reacts with any species present in the solution to produce a non-electro-active species at the

Fig. 3.21 CE mechanism for the oxidation of ferrocenecarboxylate in the presence of a β -cyclodextrin host. Reproduced with permission of reference [51]

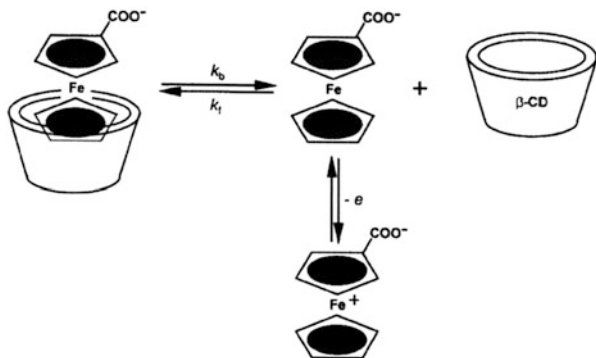
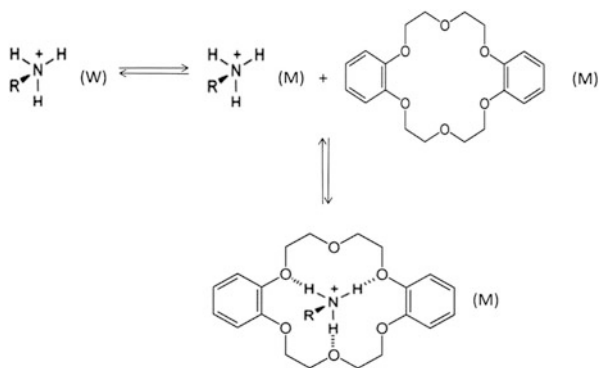
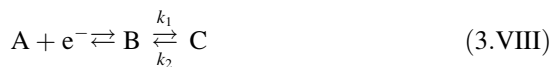


Fig. 3.22 Interaction between DB18C6 and alkylammonium cations [52]



potential range where the electrochemical process occurs. This reaction scheme (pseudo-first-order EC mechanism) is



Examples of these processes are the oxidation of *p*-aminophenol at platinum electrodes in aqueous acidic solution, the reduction of dopamine at glassy carbon electrodes or that of the cation 2,6-diphenylpyrylium in acetonitrile [9]. Another interesting example arises from the facilitated ion transfer of amines from aqueous to organic media in the presence of crown ethers like the dibenzo-18-crown-6 [52, 53] (see Fig. 3.22).

In a catalytic process, the product of an electrochemical reaction B reduces an electro-inactive species Z and is regenerated to its oxidized state C, in line with the following reaction scheme:

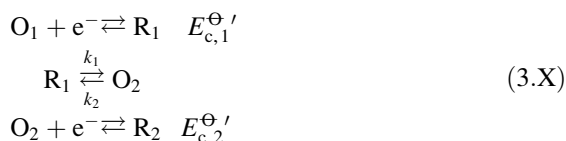


where species Z is present in a large excess so the reaction is of pseudo-first order, with the pseudo-first-order rate constants being $k_1 = k'_1 c_Z^*$ and $k_2 = k'_2 c_P^*$. It can be considered that the redox couple C/B is a catalyst and Z is the species that is catalytically reduced. In this reaction scheme, the direct reduction of species Z at the electrode surface occurs with great difficulty, and is facilitated through its reaction with species B. In most cases, homogeneous reaction in scheme (IXa) is irreversible and can be written as



In this case, the above process is called EC' mechanism. Examples of this reaction scheme are the reduction of Ti(IV) in the presence of Hydroxylamine, the reduction of Fe^{3+} in the presence of H_2O_2 (Fenton reaction) [2, 4, 6], or the mediated reduction of oxygen via the reduced form of methyl viologen at a boron doped diamond electrode [54].

Multistep electrode reactions can also be complicated by homogeneous chemical reactions. The most studied case is that the product of a first electron transfer undergoes a homogeneous chemical transformation with an electro-inactive species present in a large excess; under these conditions, the reaction scheme is that corresponding to a pseudo-first-order ECE mechanism given by



Examples of this mechanism are the reduction of *o*-nitrophenol, *p*-nitrosophenol, uranium complexes, and tocopherols, among many others [55], and also proteins containing two redox sites including the possibility of an intramolecular electron transfer [35].

In single step voltammetry, the existence of chemical reactions coupled to the charge transfer can affect the half-wave potential $E_{1/2}$ and the limiting current I_1 . For an in-depth characterization of these processes, we will study them more extensively under planar diffusion and, then, under spherical diffusion and so their characteristic steady state current potential curves. These are applicable to any electrochemical technique as previously discussed (see Sect. 2.7). In order to distinguish the different behavior of catalytic, CE, and EC mechanisms (the ECE process will be analyzed later), the boundary conditions of the three processes will be given first in a comparative way to facilitate the understanding of their similarities and differences, and then they will be analyzed and solved one by one. The first-order catalytic mechanism will be described first, because its particular reaction scheme makes it easier to study.

Boundary Value Problem for Catalytic, CE, and EC Mechanisms

If we consider a planar electrode and assume that the chemical reaction in reaction schemes (3.VII)–(3.IXa, 3.IXb) is of first or pseudo-first order, the differential equation systems that should be solved together with the initial and surface concentrations in the three reaction schemes considered are given in Table 3.2.

Table 3.2 Boundary value problem corresponding to Catalytic, CE, and EC mechanisms

Mass transport differential equations		
Catalytic	CE	EC
$\left. \begin{aligned} \hat{\delta}_p c_B &= -k_1 c_B + k_2 c_C \\ \hat{\delta}_p c_C &= k_1 c_B - k_2 c_C \end{aligned} \right\} \quad (3.173a)$	$\left. \begin{aligned} \hat{\delta}_p c_B &= -k_1 c_B + k_2 c_C \\ \hat{\delta}_p c_C &= k_1 c_B - k_2 c_C \\ \hat{\delta}_p c_D &= 0 \end{aligned} \right\} \quad (3.173b)$	$\left. \begin{aligned} \hat{\delta}_p c_A &= 0 \\ \hat{\delta}_p c_B &= -k_1 c_B + k_2 c_C \\ \hat{\delta}_p c_C &= k_1 c_B - k_2 c_C \end{aligned} \right\} \quad (3.173c)$
Initial and boundary conditions		
$\left. \begin{aligned} t &= 0, x \geq 0 \\ t &> 0, x \rightarrow \infty \end{aligned} \right\}$		
$\left. \begin{aligned} c_B &= c_B^* \\ c_C &= c_C^*; K = \frac{c_B^*}{c_C^*} \end{aligned} \right\} \quad (3.174a)$	$\left. \begin{aligned} c_C &= c_C^* \\ c_B &= c_B^*; K = \frac{c_B^*}{c_C^*} \\ c_D &= 0 \end{aligned} \right\} \quad (3.174b)$	$\left. \begin{aligned} c_A &= c_A^* \\ c_B &= c_C = 0 \end{aligned} \right\} \quad (3.174c)$
$t > 0, x = 0,$		
$D_C \left(\frac{\partial c_C}{\partial x} \right)_{x=0} = -D_B \left(\frac{\partial c_B}{\partial x} \right)_{x=0} \quad (3.175a)$	$D_C \left(\frac{\partial c_C}{\partial x} \right)_{x=0} = -D_D \left(\frac{\partial c_D}{\partial x} \right)_{x=0} \quad (3.175b)$	$D_A \left(\frac{\partial c_A}{\partial x} \right)_{x=0} = -D_B \left(\frac{\partial c_B}{\partial x} \right)_{x=0} \quad (3.175c)$
$c_C^s = e^\eta c_B^s \quad (3.176a)$	$D_B \left(\frac{\partial c_B}{\partial x} \right)_{x=0} = 0 \quad (3.176b)$	$D_C \left(\frac{\partial c_C}{\partial x} \right)_{x=0} = 0 \quad (3.176c)$
	$c_C^s = e^\eta c_D^s \quad (3.177b)$	$c_A^s = e^\eta c_B^s \quad (3.177c)$

with $\eta = F(E - E_c^{\text{ref}})/RT$ and E_c^{ref} being the formal potential of the electro-active couple on each of the three mechanisms. Note that conditions (3.176b) and (3.176c) are related with the fact that species B and C are electro-inactive in the CE and EC mechanisms, respectively. K in Eqs. (3.174a) and (3.174b) is the inverse of the equilibrium constant, K_{eq}

In Eqs. (3.173a)–(3.173c), $\hat{\delta}_p$ is the mass transport operator corresponding to linear diffusion given by

$$\hat{\delta}_p = \frac{\partial}{\partial t} - D_i \frac{\partial^2}{\partial x^2} \quad (\text{with } i = A, B, C, \text{ or } D) \quad (3.178)$$

In order to ease the resolution of these problems, it is useful to assume that all diffusion coefficients are equal and make the following variable changes:

$$\zeta = c_B + c_C \quad (3.179)$$

$$\phi = (c_B - K c_C) e^{\zeta} \quad (3.180)$$

with

$$\chi = (k_1 + k_2)t \quad (3.181)$$

By inserting Eqs. (3.179) and (3.180) into (3.173a)–(3.173c), it is fulfilled that

$$\hat{\delta}_p \zeta = 0 \quad (3.182)$$

$$\hat{\delta}_p \phi = 0 \quad (3.183)$$

and

$$c_C = \frac{\zeta - \phi e^{-\chi}}{1 + K} \quad (3.184)$$

$$c_B = \frac{K\zeta + \phi e^{-\chi}}{1 + K} \quad (3.185)$$

Now we will insert Eqs. (3.179)–(3.183) in the boundary value problem of the three reaction schemes considered. The first-order catalytic mechanism will be considered first.

3.4.1 Catalytic Mechanism

By inserting Eq. (3.179) into Eq. (3.174a)–(3.175a) and assuming that $D_B = D_C = D$ it is obtained that

$$\left. \begin{array}{l} t = 0, x \geq 0 \\ t > 0, x \rightarrow \infty \end{array} \right\} \zeta = \zeta^* = c_C^*(1 + K), K = \frac{c_B^*}{c_C^*} = \frac{1}{K_{\text{eq}}} \quad (3.186a)$$

$t > 0, x = 0,$

$$\left(\frac{\partial \zeta}{\partial x} \right)_{x=0} = 0 \quad (3.187a)$$

Equation (3.182) with conditions (3.186a)–(3.187a) implies that

$$\zeta(x, t) = c_B(x, t) + c_C(x, t) = \zeta^* \quad \forall x, t \quad (3.188a)$$

Moreover, from Eqs. (3.176a) and (3.188a), it is easily deduced that

$$c_B^s = \frac{\zeta^*}{1 + e^{\eta}} \quad (3.189a)$$

$$c_C^s = \frac{\zeta^* e^\eta}{1 + e^\eta} \quad (3.190a)$$

It is clear that the resolution of this problem is reduced to solving the differential Eq. (3.183) with the following boundary conditions:

$$\left. \begin{array}{l} t = 0, x \geq 0 \\ t > 0, x \rightarrow \infty \end{array} \right\} \phi = 0 \quad (3.191a)$$

$t > 0, x = 0$,³

$$e^{-\chi} \phi^s = \frac{1 - Ke^\eta}{1 + e^\eta} \zeta^* \quad (3.192a)$$

with ϕ^s the value of variable ϕ given by Eq. (3.180) at the electrode surface.

Equation (3.192a) has been obtained by inserting Eqs. (3.184), (3.185), and (3.188a) into Eq. (3.176a).

Rigorous Solution

The current corresponding to the catalytic mechanism is given by (see Eqs. (3.184) and (3.188a)):

$$\frac{I^{\text{cat, plane}}}{FAD} = \left(\frac{\partial c_C}{\partial x} \right)_{x=0} = -\frac{e^{-\chi}}{1 + K} \left(\frac{\partial \phi}{\partial x} \right)_{x=0} \quad (3.193a)$$

This problem was solved in Chronoamperometry in references [56, 57] and in Polarography in reference [58–62] (see Appendix D)

$$\frac{I^{\text{cat, plane}}}{FAD\zeta^*} = \frac{1 - Ke^\eta}{(1 + K)(1 + e^\eta)} \left[\left(\frac{e^{-\chi}}{\sqrt{\pi\chi}} + \text{erf}(\sqrt{\chi}) \right) \sqrt{\frac{k_1 + k_2}{D}} \right] \quad (3.194a)$$

From Eq. (3.194a) it can be deduced that for $E \ll E_c^{\Theta\prime}$ (i.e., $e^\eta \rightarrow 0$), the cathodic limiting current is

$$\frac{I_{1,c}^{\text{cat, plane}}}{FAD\zeta^*} = \frac{1}{1 + K} \left[\left(\frac{e^{-\chi}}{\sqrt{\pi\chi}} + \text{erf}(\sqrt{\chi}) \right) \sqrt{\frac{k_1 + k_2}{D}} \right] \quad (3.195a)$$

whereas for $E \gg E_c^{\Theta\prime}$ (i.e., $e^\eta \rightarrow \infty$), the anodic limiting current is

$$\frac{I_{1,a}^{\text{cat, plane}}}{FAD\zeta^*} = \frac{-K}{1 + K} \left[\left(\frac{e^{-\chi}}{\sqrt{\pi\chi}} + \text{erf}(\sqrt{\chi}) \right) \sqrt{\frac{k_1 + k_2}{D}} \right] \quad (3.196a)$$

³ Note that, according with Eq. (3.180)–(3.181), surface condition (3.192a) is independent on time, since it can be written as $c_B^s - Kc_C^s = \frac{1 - Ke^\eta}{1 + e^\eta} \zeta^*$.

Note that

$$\frac{|I_{1,a}^{\text{cat,plane}}|}{I_{1,c}^{\text{cat,plane}}} = K = \frac{1}{K_{\text{eq}}} \quad (3.197\text{a})$$

Moreover, from Eqs. (3.194a)–(3.196a), it is deduced that

$$E = E_c^{\Theta'} + \frac{RT}{F} \ln \left(\frac{I_{1,c}^{\text{cat,plane}} - I^{\text{cat,plane}}}{I^{\text{cat,plane}} - I_{1,a}^{\text{cat,plane}}} \right) \quad (3.198\text{a})$$

Kinetic Steady-State Conditions (kss)

This treatment makes the assumption that the equilibrium perturbation given by

$$\phi_{\text{ss}} = c_B - Kc_C \quad (3.199\text{a})$$

is independent of time. So, by inserting Eq. (3.199a) in Eq. (3.183), one has

$$\frac{\partial \phi_{\text{ss}}}{\partial t} = 0 = D \frac{\partial^2 \phi_{\text{ss}}}{\partial x^2} - (k_1 + k_2) \phi_{\text{ss}} \quad (3.200\text{a})$$

The solution to Eq. (3.200a) is [2, 63, 64]:

$$\phi_{\text{ss}} = \phi_{\text{ss}}^s e^{-\sqrt{\frac{k_1+k_2}{D}}x} \quad (3.201\text{a})$$

with ϕ_{ss}^s being the value of ϕ_{ss} at the electrode surface, which is easily obtained by combining Eqs. (3.189a), (3.190a), and (3.199a):

$$\phi_{\text{ss}}^s = \frac{1 - Ke^{\eta}}{1 + e^{\eta}} \zeta^* \quad (3.202\text{a})$$

From Eqs. (3.193a), (3.199a), and (3.201a), we deduce the stationary (independent of time) kinetic current, which can be written as

$$\frac{I^{\text{cat,plane,ss}}}{FAD} = -\frac{1}{1+K} \frac{\phi_{\text{ss}}(\infty) - \phi_{\text{ss}}^s}{\delta_r} \quad (3.203\text{a})$$

with $\phi_{\text{ss}}(\infty)$ being the value of ϕ_{ss} at the bulk, which in line with Eq. (3.201a) is $\phi_{\text{ss}}(\infty) = 0$, and δ_r the reaction layer thickness for a planar electrode given by [6, 65–67]:

$$\delta_r = \sqrt{\frac{D}{k_1 + k_2}} \quad (3.204\text{a})$$

Therefore, Eq. (3.203a) can be rewritten as

$$\frac{I^{\text{cat, plane, ss}}}{FAD\zeta^*} = \frac{1 - Ke^{\eta}}{(1 + K)(1 + e^{\eta})} \frac{1}{\delta_r} \quad (3.205a)$$

If the homogeneous reaction is irreversible $K \rightarrow 0$, $\zeta^* = c_C^*(1 + K) \rightarrow c_C^*$, and Eq. (3.205a) simplifies to

$$\frac{I^{\text{cat, plane, ss}}}{FAD\zeta^*} = \frac{1}{1 + e^{\eta}} \sqrt{\frac{k_1 + k_2}{D}} \quad (3.206a)$$

Note that from Eq. (3.194a) under transient conditions or from Eq. (3.205a) corresponding to a stationary response, it is easily deduced that the variation of the potential with $\ln\left(\left(I_{1,c}^{\text{cat, plane}} - I^{\text{cat, plane}}\right) / \left(I^{\text{cat, plane}} - I_{1,a}^{\text{cat, plane}}\right)\right)$ is linear as in the case of a reversible single charge transfer reaction (E mechanism), although here the cathodic limiting current increases with $\sqrt{k_1 + k_2}$ (see Eqs. (3.194a) and (3.206a)).

3.4.2 CE Mechanism

To solve this problem using the variables ζ and ϕ given by Eqs. (3.179) and (3.180) when assuming that all diffusion coefficients are equal ($D_B = D_C = D_D = D$), the following differential equation system must be tackled:

$$\hat{\delta}_p \zeta = 0 \quad (3.186b)$$

$$\hat{\delta}_p \phi = 0 \quad (3.187b)$$

$$\hat{\delta}_p c_D = 0 \quad (3.188b)$$

with the following boundary conditions (see Eqs. (3.174b)–(3.177b) and (3.184)–(3.185)):

$$\left. \begin{array}{l} t = 0, x \geq 0 \\ t > 0, x \rightarrow \infty \end{array} \right\} \begin{array}{l} \zeta = \zeta^* = c_C^*(1 + K), \\ \phi = 0 \quad c_D = 0 \end{array} \quad K = \frac{c_B^*}{c_C^*} = \frac{1}{K_{\text{eq}}} \quad (3.189b)$$

$t > 0, x = 0,$

$$D \left(\frac{\partial \zeta}{\partial x} \right)_{x=0} = -D \left(\frac{\partial c_D}{\partial x} \right)_{x=0} \quad (3.190b)$$

$$-K \left(\frac{\partial \zeta}{\partial x} \right)_{x=0} = e^{-\chi} \left(\frac{\partial \phi}{\partial x} \right)_{x=0} \quad (3.191b)$$

$$\zeta^s - \phi^s e^{-\chi} = (1 + K) e^{\eta} c_D^s \quad (3.192b)$$

with the current given by (see Eqs. (3.176b) and (3.179)):

$$\frac{I^{\text{CE, plane}}}{FAD} = \left(\frac{\partial \zeta}{\partial x} \right)_{x=0} \quad (3.193b)$$

Rigorous Solution

Finding the rigorous solution of the problem is much more complicated than that corresponding to a catalytic mechanism (see reaction scheme 3.VII), and it is given by [68]:

$$\frac{I^{\text{CE, plane}}}{I_{d,c}^{\text{plane}}(\zeta^*)} = \frac{1}{(1 + K)(1 + e^{\eta})} \left[1 + \frac{KS^{\text{CE}}}{(1 + K)(1 + e^{\eta})} \right] \quad (3.194b)$$

with

$$I_{d,c}^{\text{plane}}(\zeta^*) = FA\zeta^* \sqrt{\frac{D}{\pi t}} \quad (3.195b)$$

$$S^{\text{CE}} = \sum_{j=1}^{\infty} \varepsilon_j^{\text{CE}} \chi^j \quad (3.196b)$$

where χ is given by Eq. (3.181) and the coefficients $\varepsilon_j^{\text{CE}}$ of the functional series S^{CE} are defined in Appendix D in a recurrent way (see Eq. (D.61)).

In order to try to get a simpler response, it is advisable to use the kinetic steady-state approximation.

Kinetic Steady-State Conditions (kss)

In this case, the variables ζ given by Eq. (3.179) and ϕ_{ss} (see Eq. (3.199a)) are used. So, Eqs. (3.186b) and (3.188b) are still satisfied and

$$\hat{\delta}_p \phi_{ss} = -(k_1 + k_2) \phi_{ss} \quad (3.197b)$$

The boundary conditions are

$$\left. \begin{array}{l} t = 0, x \geq 0 \\ t > 0, x \rightarrow \infty \end{array} \right\} \zeta = \zeta^* \quad \phi_{ss} = 0 \quad c_D = 0 \quad (3.198b)$$

$t > 0, x = 0,$

$$D \left(\frac{\partial \zeta}{\partial x} \right)_{x=0} = -D \left(\frac{\partial c_D}{\partial x} \right)_{x=0} \quad (3.199b)$$

$$-K \left(\frac{\partial \zeta}{\partial x} \right)_{x=0} = \left(\frac{\partial \phi_{ss}}{\partial x} \right)_{x=0} \quad (3.200b)$$

$$\zeta^s - \phi_{ss}^s = (1 + K)e^{\eta} c_D^s \quad (3.201b)$$

The kinetic steady-state assumption implies that the equilibrium perturbation function ϕ_{ss} is independent of time, so

$$\frac{\partial \phi_{ss}}{\partial t} = 0 \quad (3.202b)$$

Therefore, the solution of Eq. (3.197b) with this restriction is

$$\phi_{ss} = \phi_{ss}^s e^{-\sqrt{\frac{k_1+k_2}{D}}x} \quad (3.203b)$$

By inserting Eq. (3.203b) into (3.200b) and (3.201b), these boundary conditions become

$$\zeta^s - K \sqrt{\frac{D}{k_1 + k_2}} \left(\frac{\partial \zeta}{\partial x} \right)_{x=0} = (1 + K)e^{\eta} c_D^s \quad (3.204b)$$

To summarize, this problem has now been reduced to the following one, depending on the variables ζ and c_D :

$$\hat{\delta}_p \zeta = 0 \quad (3.205b)$$

$$\hat{\delta}_p c_D = 0 \quad (3.206b)$$

$$\left. \begin{array}{l} t = 0, x \geq 0 \\ t > 0, x \rightarrow \infty \end{array} \right\} \zeta = \zeta^* \quad c_D = 0 \quad (3.207b)$$

$t > 0, x = 0,$

$$D \left(\frac{\partial \zeta}{\partial x} \right)_{x=0} = -D \left(\frac{\partial c_D}{\partial x} \right)_{x=0} \quad (3.208b)$$

$$\left(\frac{\partial \zeta}{\partial x} \right)_{x=0} = \frac{1}{K} \sqrt{\frac{k_1 + k_2}{D}} [\zeta^s - (1 + K)e^{\eta} c_D^s] \quad (3.209b)$$

Note that Eq. (3.209b) is merely manipulation of Eq. (3.204b).

It is important to highlight that “by chance” the problem given by Eqs. (3.205b)–(3.209b) is identical to that previously solved for a non-reversible process (see

Eq. (3.5)) by changing $\sqrt{k/D}/K$ by $k_{\text{red}}/D_{\text{O}}$, $(1+K)e^{\eta}$ by e^{η} , and ζ^{s} and c_{D}^{s} by c_{O}^{s} and c_{R}^{s} .

So it is very easy to verify that the current of a CE mechanism under kinetic steady-state conditions is given by [63–65]:

$$\frac{I_{\text{d,c}}^{\text{CE,plane,kss}}}{I_{\text{d,c}}^{\text{plane}}(\zeta^*)} = \frac{F(\chi_{\text{kss}}^{\text{CE}})}{1 + (1+K)e^{\eta}} \quad (3.210\text{b})$$

with

$$\chi_{\text{kss}}^{\text{CE}} = \frac{2\sqrt{\chi}}{K} [1 + (1+K)e^{\eta}] \quad (3.211\text{b})$$

and F function and $I_{\text{d,c}}^{\text{plane}}(\zeta^*)$ given by Eqs. (3.16) and (3.195b), respectively. The solution given by Eq. (3.210b) only coincides with the rigorous one Eq. (3.194b) when $\chi > 5$ for any value of K .

As can be seen in Eq. (3.211b), $\chi_{\text{kss}}^{\text{CE}}$ is influenced not only by the rate constants of the chemical step but also by the equilibrium constant ($K_{\text{eq}} = 1/K$), since any significant influence of the chemical reaction requires large values of χ and small equilibrium constants (i.e., large K values).

The limiting current is deduced from Eqs. (3.210b) and (3.211b) by making $e^{\eta} \rightarrow 0$

$$\frac{I_{\text{l,c}}^{\text{CE,plane,kss}}}{I_{\text{d,c}}^{\text{plane}}(\zeta^*)} = F\left(\frac{2\sqrt{\chi}}{K}\right) \quad (3.212\text{b})$$

with χ given by Eq. (3.181).

As $0 \leq F \leq 1$, as indicated in Appendix E, the limiting current of a CE mechanism is always less than that obtained for a single charge transfer reaction.

Equations (3.210b)–(3.212b) indicate that under kinetic steady-state conditions the single pulse voltammograms obtained for a CE mechanism depend on the kinetic constants and time, unlike to that deduced for a catalytic mechanism, for which a time-independent current–potential curve was obtained under these conditions (see Eqs. (3.205a)–(3.206a)).

Kinetic Steady-State Conditions by Assuming a Purely Diffusive Behavior for Species ζ and D (Diffusive-Kinetic Steady State, dkss)

In this section, new assumptions are introduced which will be fundamental for the general definition and understanding of reaction and diffusion layers. We will consider that variable ϕ_{ss} retains the form given by Eq. (3.203b) deduced under kinetic steady-state approximation (i.e., by supposing that $\partial\phi_{\text{ss}}/\partial t = \partial(c_{\text{B}} - Kc_{\text{C}})/\partial t = 0$). In relation to the variables ζ and c_{D} , it is assumed that their profiles have the same form as that for species that would only suffer diffusion and would keep time-independent values at the electrode surface, i.e., [63]:

$$\zeta = \zeta^* + (\zeta^s - \zeta^*) \operatorname{erfc}\left(\frac{x}{2\sqrt{Dt}}\right) \quad (3.213b)$$

$$c_D = c_D^s \operatorname{erfc}\left(\frac{x}{2\sqrt{Dt}}\right) \quad (3.214b)$$

By inserting Eqs. (3.203b), (3.213b), and (3.214b) into Eqs. (3.199b)–(3.201b), the following expression for the current is deduced:

$$\frac{I^{\text{CE, plane, dkss}}}{FAD} = \left(\frac{\partial \zeta}{\partial x}\right)_{x=0} = \frac{\zeta^* - \zeta^s}{\delta} \quad (3.215b)$$

or

$$\frac{I^{\text{CE, plane, dkss}}}{FAD} = -\frac{1}{K} \left(\frac{\partial \phi_{ss}}{\partial x}\right)_{x=0} = -\frac{1}{K} \frac{\phi_{ss}(\infty) - \phi_{ss}^s}{\delta_r} \quad (3.216b)$$

with $\phi_{ss}(\infty) = 0$, and δ and δ_r are the diffusion and reaction layer thickness for planar electrodes, respectively, with (see also Eq. (2.25) of Sect. 2.2.1):

$$\delta = \sqrt{\pi Dt} \quad (3.217b)$$

and δ_r given in Eq. (3.204a).

The expressions of ζ^s or ϕ_{ss}^s can be obtained from conditions (3.199b)–(3.201b) and the current for a CE mechanism can be written as

$$\frac{I^{\text{CE, plane, dkss}}}{I_{d,c}^{\text{plane}}(\zeta^*)} = \frac{1}{K(\delta_r/\delta) + (1 + (1 + K)e^\eta)} \quad (3.218b)$$

and the cathodic limiting current ($e^\eta \rightarrow 0$) is

$$\frac{I_{1,c}^{\text{CE, plane, dkss}}}{I_{d,c}^{\text{plane}}(\zeta^*)} = \frac{1}{K(\delta_r/\delta) + 1} = \frac{\sqrt{\pi(k_1 + k_2)t}}{K + \sqrt{\pi(k_1 + k_2)t}} \quad (3.219b)$$

The expression of the current given by Eqs. (3.218b) or (3.219b) only coincides with the rigorous one (Eq. 3.194b) for $\chi^{\text{CE}} > 10$ with an error smaller than 5 %.

From Eqs. (3.218b) and (3.219b), it is easily deduced that under these conditions the applied potential varies linearly with $\ln\left(\left(\frac{I_{1,c}^{\text{CE, plane, dkss}}}{I_{d,c}^{\text{plane}}(\zeta^*)} - I^{\text{CE, plane, dkss}}\right) / I^{\text{CE, plane, dkss}}\right)$:

$$E = E_{1/2}^{\text{CE}} + \frac{RT}{F} \ln\left(\frac{I_{1,c}^{\text{CE, plane, dkss}} - I^{\text{CE, plane, dkss}}}{I^{\text{CE, plane, dkss}}}\right) \quad (3.220b)$$

being

$$E_{1/2}^{\text{CE}} = E_c^{\ominus'} + \frac{RT}{F} \ln \left(\frac{1 + K(\delta_r/\delta)}{1 + K} \right) \quad (3.221b)$$

3.4.3 EC Mechanism

In this case (see reaction scheme (3.VIII)), the following problem should be solved:

$$\hat{\delta}_p c_A = 0 \quad (3.186c)$$

$$\hat{\delta}_p \zeta = 0 \quad (3.187c)$$

$$\hat{\delta}_p \phi = 0 \quad (3.188c)$$

with the following boundary conditions (see Eqs. (3.174c)–(3.177c) and (3.179)–(3.181)):

$$\left. \begin{array}{l} t = 0, x \geq 0 \\ t > 0, x \rightarrow \infty \end{array} \right\} c_A = c_A^* \quad \zeta = 0 \quad \phi = 0 \quad (3.189c)$$

$t > 0, x = 0,$

$$D \left(\frac{\partial c_A}{\partial x} \right)_{x=0} = -D \left(\frac{\partial \zeta}{\partial x} \right)_{x=0} \quad (3.190c)$$

$$\left(\frac{\partial \zeta}{\partial x} \right)_{x=0} = e^{-\chi} \left(\frac{\partial \phi}{\partial x} \right)_{x=0} \quad (3.191c)$$

$$K\zeta^s + \phi^s e^{-\chi} = \frac{(1 + K)c_A^s}{e^{\eta}} \quad (3.192c)$$

and the current is

$$\frac{I^{\text{EC, plane}}}{FAD} = \left(\frac{\partial c_A}{\partial x} \right)_{x=0} \quad (3.193c)$$

By comparing the problem given by Eqs. (3.186b)–(3.193b) for a CE mechanism with Eqs. (3.186c)–(3.193c) for an EC mechanism, it can be easily inferred that the current corresponding to the EC process can be deduced with a similar procedure to that followed for a CE one (see Appendix D). So, the solution is:

Rigorous Solution

$$\frac{I^{\text{EC, plane}}}{I_{\text{d,c}}^{\text{plane}}(c_A^*)} = \frac{1}{1 + e^\eta} \left[1 + \frac{e^\eta S^{\text{EC}}}{(1 + K)(1 + e^\eta)} \right] \quad (3.194\text{c})$$

with

$$I_{\text{d,c}}^{\text{plane}}(c_A^*) = FAc_A^* \sqrt{\frac{D}{\pi t}} \quad (3.195\text{c})$$

$$S^{\text{EC}} = \sum_{j=1}^{\infty} \varepsilon_j^{\text{EC}} \chi^j \quad (3.196\text{c})$$

where χ is given in Eq. (3.181) and the expression of coefficients $\varepsilon_j^{\text{EC}}$ is given in Appendix D (see Eq. (D.63)).

Contrarily to the CE mechanism, in this case the current–potential curve is more affected by the chemical reaction the higher the rate and the equilibrium constants χ and $K_{\text{eq}} = 1/K$.

Kinetic Steady State (kss)

In this case, the following expression for the current is obtained:

$$\frac{I^{\text{EC, plane, kss}}}{I_{\text{d,c}}^{\text{plane}}(c_A^*)} = \frac{(1 + K)F(\chi_{\text{kss}}^{\text{EC}})}{1 + K + Ke^\eta} \quad (3.197\text{c})$$

with $I_{\text{d,c}}^{\text{plane}}$ given by Eq. (3.195c). Function F is given in Appendix E and

$$\chi_{\text{kss}}^{\text{EC}} = \frac{2\sqrt{\chi}}{e^\eta} [1 + K + Ke^\eta] \quad (3.198\text{c})$$

Kinetic Steady State Assuming Purely Diffusive Behavior for A and ζ Species (Diffusive-Kinetic Steady State, dkss)

Under these conditions, the current is

$$\frac{I^{\text{EC, plane, dkss}}}{I_{\text{d,c}}^{\text{plane}}(c_A^*)} = \frac{1 + K}{1 + K + e^\eta(K + \delta_r/\delta)} \quad (3.199\text{c})$$

or

$$E = E_{1/2}^{\text{EC}} + \frac{RT}{F} \ln \left(\frac{I_{1,c}^{\text{EC, plane, dkss}} - I^{\text{EC, plane, dkss}}}{I^{\text{EC, plane, dkss}}} \right) \quad (3.200\text{c})$$

being

$$E_{1/2}^{\text{EC}} = E_c^{\Theta'} + \frac{RT}{F} \ln \left(\frac{1+K}{K + (\delta_r/\delta)} \right) \quad (3.201c)$$

where δ and δ_r are given in Eqs. (3.217b) and (3.204a), respectively.

From Eqs. (3.194c), (3.197c), and (3.199c) corresponding to rigorous and approximate treatments, it can be deduced that under limiting conditions (i.e., $E \ll E_c^{\Theta'}$ or $e^{\eta} \rightarrow 0$), the expression for the current coincides with that corresponding to a single charge transfer process (E mechanism):

$$I_{1,c}^{\text{EC, plane}}(c_A^*) = I_{d,c}^{\text{plane}}(c_A^*) \quad (3.202c)$$

with $I_{d,c}^{\text{plane}}(c_A^*)$ given by Eq. (3.195c).

An important particular situation of an EC mechanism corresponds to the case $K = 0$ ($K_{\text{eq}} \rightarrow \infty$), for which the chemical reaction has its greatest influence. Under these conditions, Eqs. (3.199c) and (3.201c) transform, respectively, to

$$\frac{I_{d,c}^{\text{EC, plane}}}{I_{d,c}^{\text{plane}}(c_A^*)} = \frac{1}{1 + e^{\eta}(\delta_r/\delta)} \quad (3.203c)$$

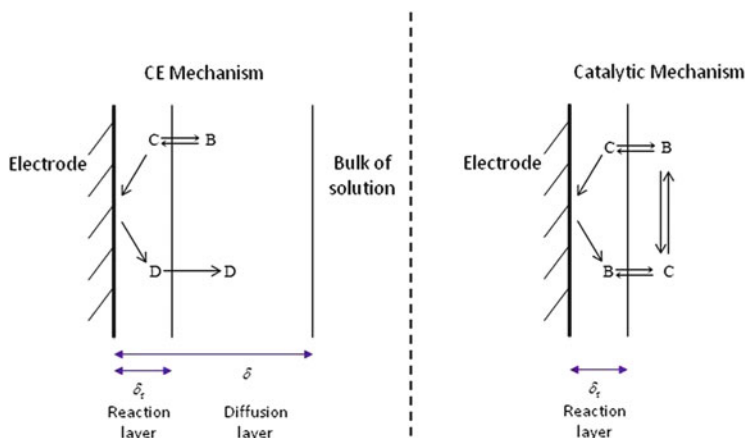
$$E_{1/2}^{\text{EC}} = E_c^{\Theta'} + \frac{RT}{F} \ln \left(\frac{\delta}{\delta_r} \right) = E_c^{\Theta'} + \frac{RT}{2F} \ln(\pi k_1 t) \quad (3.204c)$$

Under these conditions, $E_{1/2}^{\text{EC}}$ is dependent on k_1 , and is shifted toward more anodic potentials as k_1 increases.

3.4.4 Comparison of the Disturbed Regions by Catalytic, CE, and EC Mechanisms

In this section, the different behavior of processes with coupled noncatalytic homogeneous reactions (CE and EC mechanisms) is discussed in comparison with a catalytic process. We will consider that the chemical kinetics is fast enough and in the case of CE and EC mechanisms $K (= c_B^*/c_C^*)$ fulfills $K \gg 1$ so that the kinetic steady-state and even diffusive-kinetic steady-state approximation can be applied.

Indeed, from Eq. (3.205a) for a catalytic process (under kss conditions) and Eqs. (3.218b) and (3.199c) for CE and EC processes (under the more restrictive dkss conditions), it can be inferred that a true stationary (independent of time) current–potential response for a catalytic reaction (reaction scheme (3.IXa, 3.IXb)) can be reached even for large electrodes (planar diffusion), whereas for CE and EC



Scheme 3.1 Steady-state diffusion and reaction layers for CE and catalytic mechanisms

processes (schemes (3.VII) and (3.VIII)), it is not possible to find a true stationary current–potential response under these conditions, as is shown from Eqs. (3.218b) and (3.199c) obtained under the dkss assumption (this is also impossible for an E process). This different behavior is outlined in Scheme 3.1 [63].

This different behavior can be explained by considering that for a CE mechanism (the reasoning is similar for an EC one), C species is required by the chemical reaction whose equilibrium is distorted in the reaction layer (whose thickness in the simplified dkss treatment is $\delta_r = \sqrt{D/(k_1 + k_2)}$) and by the electrochemical reaction, which is limited by the diffusion layer (of thickness $\delta = \sqrt{\pi Dt}$). For a catalytic mechanism, C species is also required for both the chemical and the electrochemical reactions, but this last stage gives the same species B, which is demanded by the chemical reaction such that only in the reaction layer do the concentrations of species B and C take values significantly different from those of the bulk of the solution. In summary, the catalytic mechanism can reach a true steady-state current–potential response under planar diffusion because its perturbed zone is restricted to the reaction layer δ_r , which is independent of time, whereas the distortion of CE (or EC) mechanism is extended until the diffusion layer δ , which depends on time, and a stationary current–potential response will not be reached under these conditions.

It is interesting to point out that if we write Eqs. (3.218b) and (3.199c) corresponding to CE and EC processes as

$$\frac{I^{\text{CE, plane, dkss}}}{FAD\zeta^*} = \frac{1}{K(\delta_r/\delta) + (1 + (1 + K)e^\eta)\delta} \quad (3.222)$$

$$\frac{I^{\text{EC, plane, dkss}}}{FADc_A^*} = \frac{(1 + K)}{1 + K + e^\eta(K + (\delta_r/\delta))\delta} \quad (3.223)$$

by making $\delta = \delta_r$ (and $c_D^* = c_B^*$ in Eq. (3.222) and $c_A^* = c_C^*$ in Eq. (3.223)), both equations convert to that corresponding to a catalytic mechanism with $K = 0$ when diffusion and reaction layers become coincident, i.e.,

$$I^{\text{CE, plane, dkss}} \Big|_{c_D^* = c_B^*} = I^{\text{EC, plane, dkss}} \Big|_{c_A^* = c_C^*} = I^{\text{cat, plane, kss}} \quad \text{if } \delta \rightarrow \delta_r \quad (3.224)$$

3.4.5 Comparison Between the Current–Potential Curves Corresponding to Catalytic, CE, and EC Mechanisms

Before studying the influence of the different kinetic parameters on the single potential step or normal pulse voltammograms corresponding to these three reaction mechanisms, it is of great interest to point out some features of these curves, which can be directly deduced from the equations presented in the previous sections corresponding to the dependence of the limiting current and of the half-wave potential with the characteristic parameters when diffusion coefficients of species B and C are assumed equal.

The single pulse voltammograms of a pseudo-first-order catalytic process are easily characterized by the increase of the limiting current with the time or the chemical kinetic constants, whereas its half-wave potential remains unchanged.

For a pseudo-first-order CE mechanism, both the limiting current (which is always less than that corresponding to an E mechanism) and the half-wave potential are affected by the equilibrium and rate constants.

In the case of a pseudo-first-order EC mechanism, only the half-wave potential depends on time and the equilibrium and rate constants, with the limiting current remaining unaltered with the variation of these parameters—identical to that corresponding to an E mechanism.

The influence of the ratio $K = c_B^*/c_C^*$ on the normalized single pulse voltammograms corresponding to $\chi = (k_1 + k_2)t = 30$ for the three mechanisms (note that K is the inverse of the equilibrium constant, i.e., $K = (1/K_{\text{eq}})$) can be seen in Fig. 3.23. An increase of K does not affect the location of the voltammograms in the potential axis in the case of the catalytic mechanism (Fig. 3.23a), whereas it causes a shift of the current–potential curves for both CE and EC mechanisms toward more negative potentials (Fig. 3.23b and c). Concerning the influence of $K (= 1/K_{\text{eq}})$ in the limiting currents, for a catalytic mechanism the increase of this ratio leads to a decrease of the cathodic limiting current and to an increase of the anodic one in absolute value (in line with Eqs. (3.195a) and (3.196a)). The cathodic limiting current of the CE mechanism also decreases with the increase of K (see Eq. (3.212b)), whereas it does not affect that corresponding to an EC mechanism (see Eq. (3.202c)). In the case of a CE mechanism, the behavior corresponding to a simple charge transfer without chemical complications (dotted line in Figure b) refers to the sum of concentrations of species B and C (labile equilibrium) for $K \rightarrow 0$ and only to the concentration of

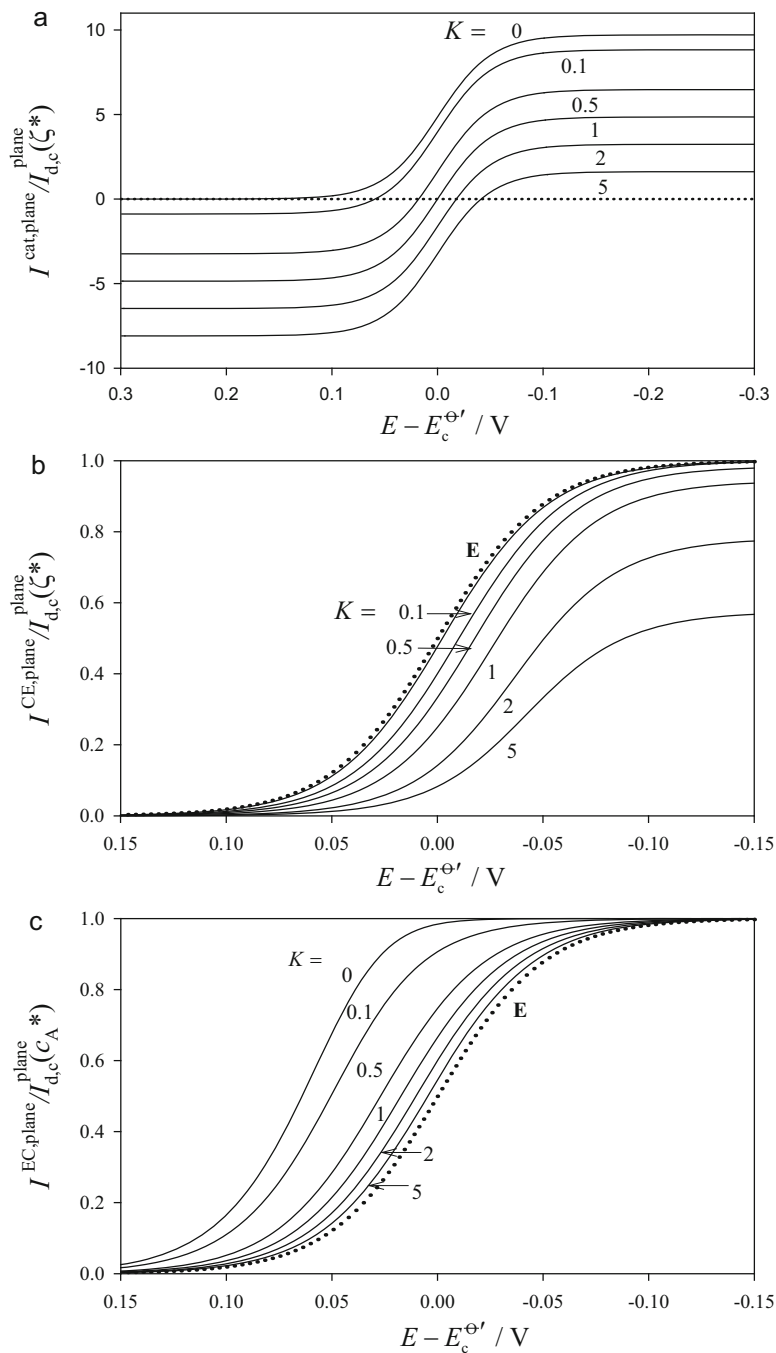


Fig. 3.23 Influence of $K (= 1/K_{\text{eq}})$ on the normalized voltammograms corresponding to a catalytic (a, Eqs. (3.194a) and (3.195b)), CE (b, Eqs. (3.194b) and (3.195b)), and EC mechanism

species C (non-labile equilibrium) for $K \gg 1$ [69]. An EC mechanism behaves like an E process only if $K \gg 1$ (see Fig. 3.23c).

The variation of the normalized single pulse voltammograms of the three reaction mechanisms with χ for $K=1$ (CE mechanism, Figure b) and $K=0$ (catalytic and EC mechanism, Figures a and c, respectively) is plotted in Fig. 3.24. From these curves, it can be observed that an increase of χ does not affect the location of the voltammetric responses of a catalytic process (Fig. 3.24a), whereas it causes a slight shift toward more negative potentials in the case of a CE process (Fig. 3.24b) and a more notable shift toward more positive potentials for an EC one (Fig. 3.24c). The influence of χ in the limiting current is restricted to catalytic and CE mechanism (since it does not affect the limiting current of the EC one), being stronger in the former case since $I_{1,c}^{\text{cat,plane}}/I_{d,c}^{\text{plane}}(\zeta^*)$ is proportional to $\sqrt{\chi}$ (see Eqs. (3.225) and (3.226)).

3.4.6 Determination of Kinetic Parameters

From the Limiting Currents

In the case of a catalytic mechanism, the normalized limiting current $I_{1,c}^{\text{cat,plane}}/I_{d,c}^{\text{plane}}(\zeta^*)$ is

$$I_N^{\text{cat,plane}} = \frac{I_{1,c}^{\text{cat,plane}}}{I_{d,c}^{\text{plane}}(\zeta^*)} = \left[\left(\frac{e^{-\chi}}{\sqrt{\pi\chi}} + \text{erf}(\sqrt{\chi}) \right) \sqrt{\pi\chi} \right] \frac{1}{1+K} \quad (3.225)$$

with $I_{d,c}^{\text{plane}}(\zeta^*) = FA\zeta^* \sqrt{D/(\pi t)}$ and χ given by Eq. (3.181). So, a set of plots of $I_N^{\text{cat,plane}}$ vs. $\sqrt{\chi}$ for different values of K can be used as working curves to determine k_1 and k_2 from experimental values of $I_N^{\text{cat,plane}}$ once the value of D is known (see Fig. 3.25). The value of K can be obtained by linear extrapolation of these curves to $\chi \rightarrow 0$ (see dashed lines) [4]. Note that for $\chi > 1.5$ the kinetic steady state is applicable and these plots are linear since the term $(e^{-\chi}/\sqrt{\pi\chi} + \text{erf}(\sqrt{\chi})) \rightarrow 1$ and

$$I_N^{\text{cat,plane}} \Big|_{\chi > 1.5} \cong \frac{\sqrt{\pi\chi}}{1+K} \quad (3.226)$$

For a CE mechanism, the curves $I_N^{\text{CE,plane}} = I_{1,c}^{\text{CE,plane}}/I_{d,c}^{\text{plane}}(\zeta^*)$ vs. χ calculated from Eqs. (3.194b) and (3.195b) are plotted in Fig. 3.26.

Fig. 3.23 (continued) (c, Eqs. (3.194c) and (3.195c)). The values of $K = 1/K_{\text{eq}}$ appear on the curves. $\chi = 30$. $T = 293.15$ K. *Dotted lines* in Figures b and c correspond to a charge transfer without chemical complications (E mechanism; see Eq. (2.36))

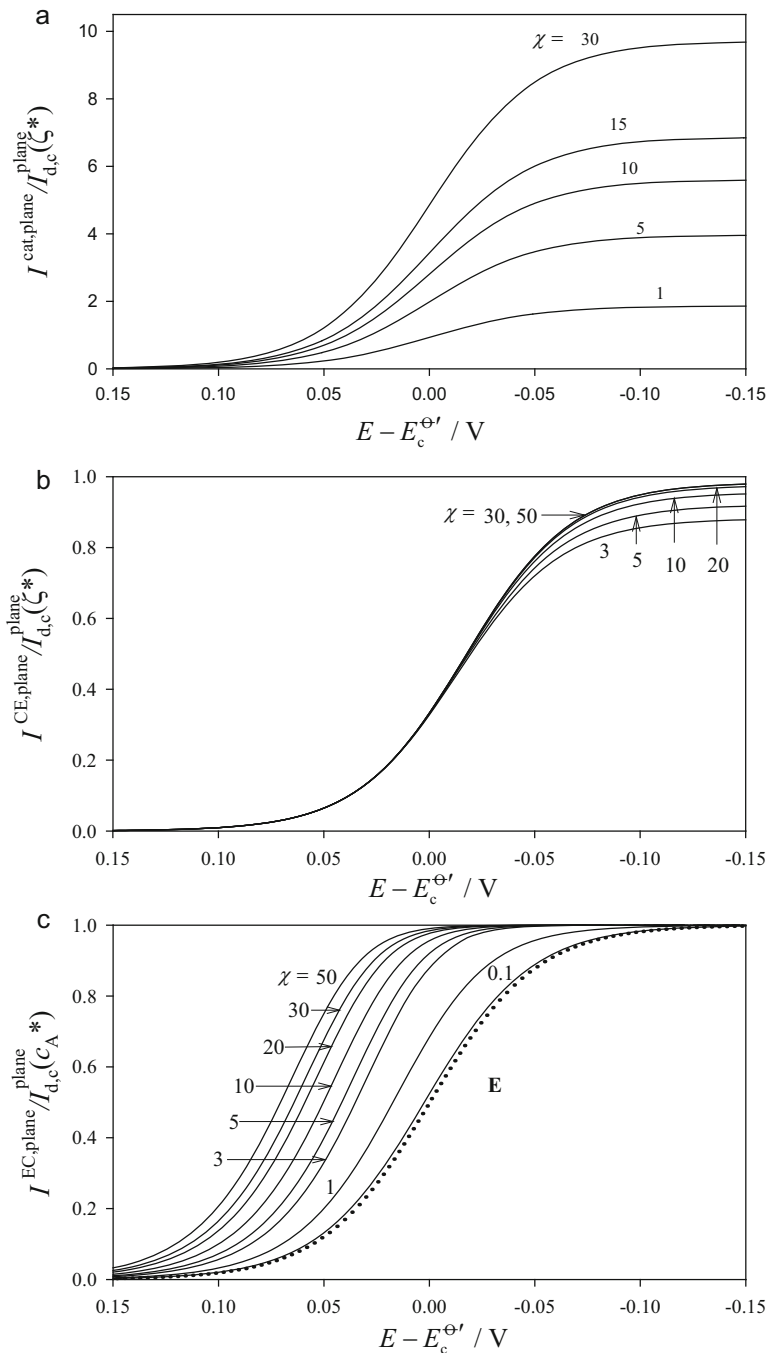


Fig. 3.24 Influence of χ on the normalized voltammograms corresponding to a catalytic (a, Eqs. (3.194a) and (3.195b)), CE (b, Eqs. (3.194b) and (3.195b)), and EC mechanism (c,

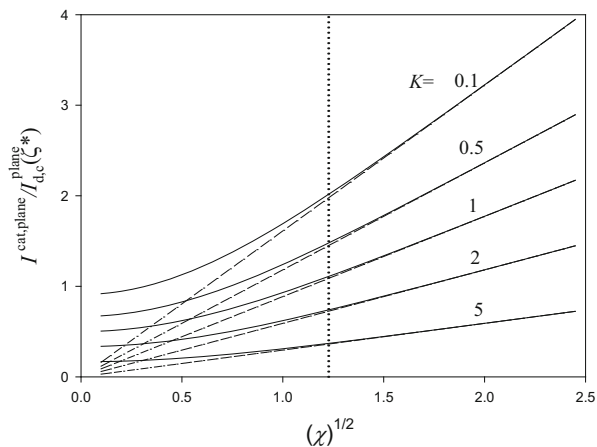


Fig. 3.25 Variation of the normalized current of a first-order catalytic mechanism versus $\sqrt{\chi}$ calculated from Eq. (3.225) with $K = 1/K_{\text{eq}}$, $E - E_c^{\Theta'} = -0.3$ V, $T = 298.15$ K. Dashed lines correspond to the limiting behavior of the normalized current given by Eq. (3.226). A vertical dotted line has been plotted at $\chi = 1.5$

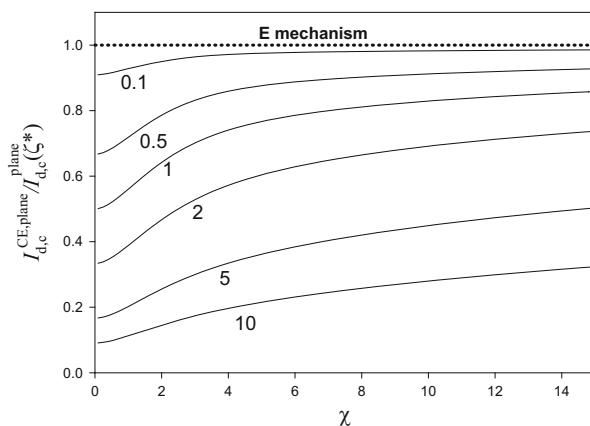


Fig. 3.26 Variation of the normalized current of a CE mechanism versus χ calculated from Eqs. (3.194b) under limiting current conditions and (3.195b). The values of $K = 1/K_{\text{eq}}$ are on the curves. $E - E_c^{\Theta'} = -0.3$ V, $T = 298.15$ K. Dashed lines correspond to the behavior of a simple charge transfer without chemical complications (E mechanism; see Eq. (2.36))

Fig. 3.24 (continued) Eqs. (3.194c) and (3.195c)). The values of χ appear on the curves. For the catalytic and EC mechanism $K = 1/K_{\text{eq}} = 0$ and for the CE one $K = 1/K_{\text{eq}} = 1$. $T = 293.15$ K. Dotted lines in Figure c correspond to a charge transfer without chemical complications (E mechanism, see Eq. (2.36))

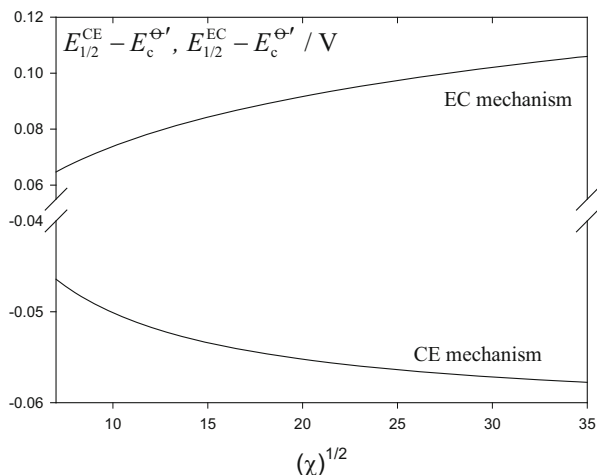


Fig. 3.27 Variation of the half-wave potential with $\sqrt{\chi}$ for a CE (Eq. 3.221b) and EC (Eq. 3.201c) mechanism. $K = 0$ (EC mechanism) and $K = 10$ (CE mechanism) with $K (= 1/K_{\text{eq}})$

From these curves, by knowing the experimental values of $I_N^{\text{CE,plane}}$, it is possible to determine k_1 and k_2 once K is known. Moreover the lower bound of the equilibrium constant of the chemical reaction can be determined (note that if $I_N^{\text{CE,plane}}(t \rightarrow 0) \leq 0.5$, $K \geq 1$). The value of K can be also calculated by extrapolation of these curves for small values of χ (i.e., for $\chi \rightarrow 0$) since $I_N^{\text{CE,plane}}(t \rightarrow 0) = 1/(1 + K)$ [68].

The limiting current of an EC mechanism is independent of χ and its value cannot be used to obtain the parameters of the chemical reaction.

From the Half-Wave Potentials

The variation of the half-wave potentials with $\sqrt{\chi} = \sqrt{(k_1 + k_2)t}$ for CE (see Eq. (3.221b)) and EC (see Eq. (3.201c)) mechanisms is plotted in Fig. 3.27. From this figure, it can be seen that the half-wave potential shifts toward more anodic (EC) or cathodic (CE) potentials when χ increases, respectively, whereas the half-wave potentials of catalytic and E mechanisms are independent of χ .

3.4.7 Spherical Electrodes

Catalytic Mechanism

As discussed in Sect. 3.4.1, finding the single step voltammetric curve of this mechanism is much easier than finding those corresponding to EC and CE mechanisms in planar electrodes because the surface concentrations of the participating species are independent of time. In this case, finding the voltammogram for a

spherical electrode of any size is not very difficult and is given in references [59, 63, 64, 70], and the current can be written as

$$\frac{I^{\text{cat, sphe}}}{FA_s D \zeta^*} = \frac{1 - Ke^\eta}{(1 + K)(1 + e^\eta)} \left[\sqrt{\frac{k_1 + k_2}{D}} \left(\frac{e^{-\chi}}{\sqrt{\pi\chi}} + \text{erf}(\sqrt{\chi}) \right) + \frac{1}{r_s} \right] \quad (3.227)$$

with χ given in Eq. (3.181) and r_s being the electrode radius.

Under kinetic steady-state conditions ($\chi > 1.5$), Eq. (3.227) becomes

$$\frac{I^{\text{cat, sphe, kss}}}{FA_s D \zeta^*} = \frac{1 - Ke^\eta}{(1 + K)(1 + e^\eta)} \left(\sqrt{\frac{k_1 + k_2}{D}} + \frac{1}{r_s} \right) \quad (3.228)$$

By comparing Eq. (3.228) with (3.205a) for planar electrodes, it can be easily inferred that the reaction layer in this case is

$$\delta_r^{\text{sphe}} = \frac{1}{\sqrt{\frac{k_1 + k_2}{D}} + \frac{1}{r_s}} \quad (3.229)$$

CE and EC Mechanisms

Finding rigorous analytical expressions for the single potential step voltammograms of these reaction mechanisms in a spherical diffusion field is not easy. However, they can be found in reference [63, 64, 71–73] for the complete current–potential curve of CE and EC mechanisms. The solutions of CE and EC processes under kinetic steady state can be found in references [63, 64] and the expression of the limiting current in reference [74]. Both rigorous and kinetic steady state solutions are too complex to be treated within the scope of this book. Thus, the analysis of these processes in spherical diffusion will be restricted to the application of diffusive-kinetic steady-state treatment.

For this purpose, we will consider a CE mechanism (reaction scheme (3.VII)), since the derivation of the expressions for an EC process can be carried out by following a similar procedure to that of a CE process. In this case, as previously, we will consider that the pseudo-species $\zeta (= c_B + c_C)$ and species c_D have a purely diffusive behavior. So, it is also supposed that $\partial\phi_{ss}/\partial t = 0$ ($\phi_{ss} = c_B - Kc_C$), which fulfills, in a spherical diffusion field:

$$\frac{\partial^2 \phi_{ss}}{\partial r^2} + \frac{2}{r} \frac{\partial \phi_{ss}}{\partial r} = \frac{k_1 + k_2}{D} \phi_{ss} \quad (3.230)$$

The solution of this differential equation is

$$\phi_{ss} = \frac{r_s}{r} \phi_{ss}^s e^{-\sqrt{\frac{k_1 + k_2}{D}} (r - r_s)} \quad (3.231)$$

then,

$$\left(\frac{\partial \phi_{ss}}{\partial r}\right) = -\frac{r_s}{r} \phi_{ss}^s e^{-\sqrt{\frac{k_1+k_2}{D}}(r-r_s)} \left[\frac{1}{r} + \sqrt{\frac{k_1+k_2}{D}}\right] \quad (3.232)$$

which takes the following expression at the electrode surface:

$$\left(\frac{\partial \phi_{ss}}{\partial r}\right)_{r=r_s} = \frac{-\phi_{ss}^s}{\delta_r^{\text{sph}}} \quad (3.233)$$

with δ_r^{sph} given by Eq. (3.229).

Moreover, it is assumed that in spherical diffusion the concentration profiles of ζ and c_D are given by (see Eq. (2.144) of Sect. 2.5.2):

$$\zeta = \zeta^* - \frac{r_s}{r}(\zeta^* - \zeta^s) \operatorname{erfc}\left(\frac{r-r_s}{2\sqrt{Dt}}\right) \quad (3.234)$$

$$c_D = c_D^s \frac{r_s}{r} \operatorname{erfc}\left(\frac{r-r_s}{2\sqrt{Dt}}\right) \quad (3.235)$$

then,

$$\left(\frac{\partial \zeta}{\partial r}\right)_{r=r_s} = \frac{\zeta^* - \zeta^s}{\delta^{\text{sph}}} \quad (3.236)$$

$$\left(\frac{\partial c_D}{\partial r}\right)_{r=r_s} = -\frac{c_D^s}{\delta^{\text{sph}}} \quad (3.237)$$

with δ^{sph} being the diffusion layer thickness for spherical electrodes (see Eq. (2.146) of Sect. 2.5.2):

$$\delta^{\text{sph}} = \frac{1}{\frac{1}{r_s} + \frac{1}{\sqrt{\pi Dt}}} \quad (3.238)$$

By inserting Eqs. (3.231)–(3.238) in the surface conditions of a CE process (see Eqs. (3.174b)–(3.177b)) and considering spherical diffusion, it is easily deduced that

$$\frac{I^{\text{CE, sphe, dkss}}}{I_{d,c}^{\text{sph}}(\zeta^*)} = \frac{1}{K(\delta_r^{\text{sph}}/\delta^{\text{sph}}) + (1 + (1 + K)e^\eta)} \quad (3.239)$$

$$\frac{I^{\text{EC, sphe, dkss}}}{I_{d,c}^{\text{sph}}(c_A^*)} = \frac{1 + K}{1 + K + e^\eta(K + \delta_r^{\text{sph}}/\delta^{\text{sph}})} \quad (3.240)$$

with

$$I_{d,c}^{\text{sph}}(c^*) = FA_s D c^* \left(\frac{1}{r_s} + \frac{1}{\sqrt{\pi D t}} \right) \quad (3.241)$$

with $c^* = \zeta^*$ or $c^* = c_A^*$ in Eqs. (3.239) and (3.240), respectively.

By comparing Eqs. (3.239) and (3.240) with Eqs. (3.218b) and (3.199c) previously deduced for planar electrodes, it can be verified that they are identical if we change in Eqs. (3.239) and (3.240) δ_r^{sph} for δ_r and δ^{sph} for δ . So, all equations deduced for planar electrodes under dkss conditions can be transferred to spherical diffusion merely by making these changes. This is also applicable to a catalytic mechanism under kinetic steady-state conditions (compare Eqs. (3.205a) and (3.228)).

Microspherical Electrodes (Total Steady State)

If the electrode radius r_s is restricted to the interval $\sqrt{D/(k_1 + k_2)}/10 \leq r_s \leq \sqrt{\pi D t}/20$, the spherical diffusion and reaction layer thicknesses given by Eq. (3.229) or (3.238) simplifies to

$$\left. \begin{aligned} \delta^{\text{microsphe}} &= r_s \\ \delta_r^{\text{microsphe}} &= \delta_r^{\text{sph}} \end{aligned} \right\} \quad (3.242)$$

Under these conditions, the voltammetric response of a catalytic mechanism given by Eq. (3.228) remains valid since it is independent of time. This expression can be normalized by the diffusion-controlled limiting current at microspheres:

$$\frac{I^{\text{cat, sph}}}{I_{d,c}^{\text{microsphe}}(\zeta^*)} = \frac{1 - Ke^\eta}{(1 + K)(1 + e^\eta)} \left(r_s \sqrt{\frac{k_1 + k_2}{D}} + 1 \right) \quad (3.243)$$

with

$$I_{d,c}^{\text{microsphe}}(\zeta^*) = 4\pi F r_s D \zeta^* \quad (3.244)$$

Equation (3.243) shows that for pseudo-first-order catalytic mechanism, the normalized current varies linearly with the radius for any value of the applied potential and the term $(k_1 + k_2)$ can be calculated from the slope provided the equilibrium constant and the diffusion coefficients are known.

The current–potential curves corresponding to CE and EC mechanisms become independent of time under these conditions, and Eqs. (3.239)–(3.240) can be used by changing δ^{sph} for $\delta^{\text{microsphe}}$.

So, the half-wave potentials for these mechanisms at spherical microelectrodes are

$$E_{1/2}^{\text{CE}} = E_c^{\Theta'} + \frac{RT}{F} \ln \left(\frac{1 + K(\delta_r^{\text{sphe}}/r_s)}{1 + K} \right) \quad (3.245)$$

$$E_{1/2}^{\text{EC}} = E_c^{\Theta'} + \frac{RT}{F} \ln \left(\frac{1 + K}{K + (\delta_r^{\text{sphe}}/r_s)} \right) \quad (3.246)$$

The solutions found under these conditions are equivalent to the simultaneous establishment of the three assumptions:

$$\left(\frac{\partial \zeta}{\partial t} \right) = \left(\frac{\partial c_D}{\partial t} \right) = \left(\frac{\partial \phi_{\text{ss}}}{\partial t} \right) = 0 \quad (3.247)$$

for a CE mechanism and

$$\left(\frac{\partial \zeta}{\partial t} \right) = \left(\frac{\partial c_A}{\partial t} \right) = \left(\frac{\partial \phi_{\text{ss}}}{\partial t} \right) = 0 \quad (3.248)$$

for an EC mechanism.

The use of microelectrodes under total steady-state conditions is very advantageous in determining kinetic constants of very fast chemical reactions. To show this, in Fig. 3.28, we show the time influence at different values of r_s on the normalized limiting current of a CE mechanism (Eq. 3.249) compared with the time-independent solution (dashed lines and Eq. (3.250)):

$$\frac{I_{l,c}^{\text{CE, sphe, dkss}}}{I_{d,c}^{\text{sphe}}(\zeta^*)} = \frac{1}{K(\delta_r^{\text{sphe}}/\delta^{\text{sphe}}) + 1} \quad (3.249)$$

with the time-independent solution given by ($\delta^{\text{sphe}} \rightarrow r_s$):

$$\frac{I_{l,c}^{\text{CE, microsphe}}}{I_{d,c}^{\text{micro}}(\zeta^*)} = \frac{1}{K(\delta_r^{\text{sphe}}/r_s) + 1} \quad (3.250)$$

and $I_{d,c}^{\text{sphe}}(\zeta^*)$ and $I_{d,c}^{\text{microsphe}}(\zeta^*)$ given by Eqs. (3.241) and (3.244), respectively.

It is clearly shown in this figure that time has a great effect on the current and that this influence decreases with r_s . Figure 3.28b ($K = 10^2$ and $k_1 + k_2 = 10^2 \text{ s}^{-1}$) shows that Eq. (3.250) can be applied for $t = 1 \text{ s}$ only if $r_s < 10^{-3} \text{ cm}$.

Both Eqs. (3.243) and (3.250) for catalytic and CE mechanisms, respectively, convert into that corresponding to an E process when $(k_1 + k_2) \ll D/r_s^2$, since under these conditions the chemical reaction is masked and the use of microelectrodes is not appropriate for determining kinetic rate constants.

The analysis of the EC and CE mechanisms under steady-state conditions at other microelectrode geometries is much more complex. In the case of microdiscs,

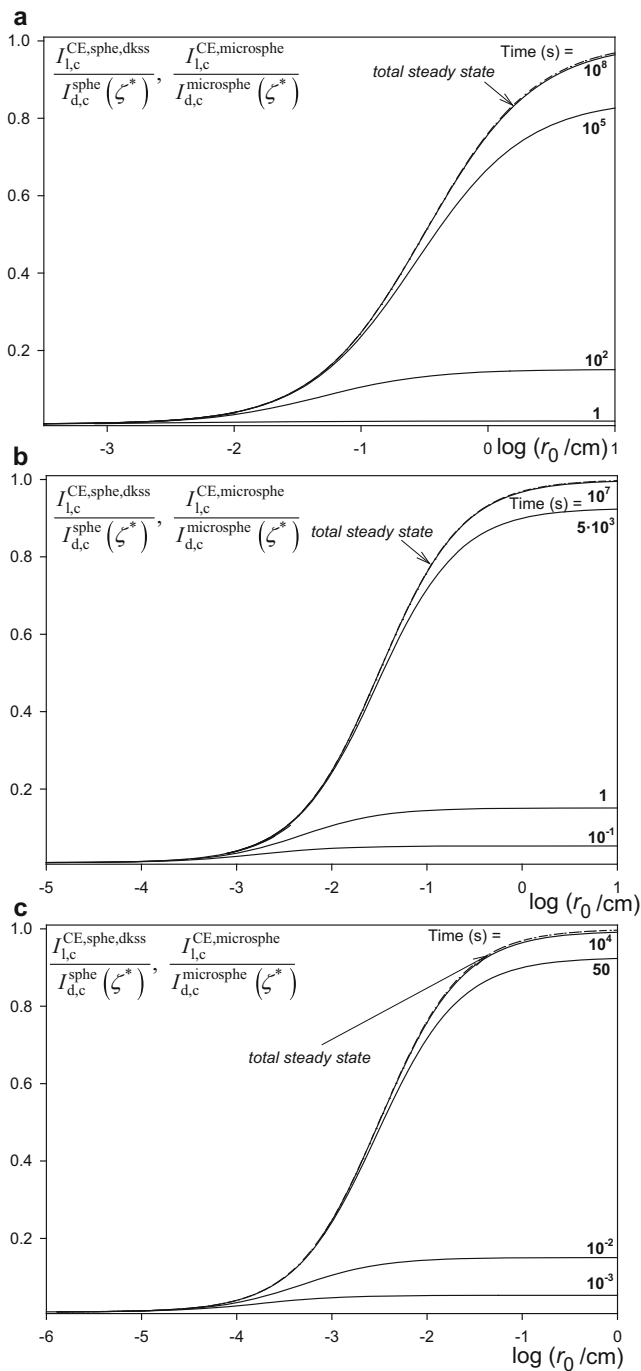


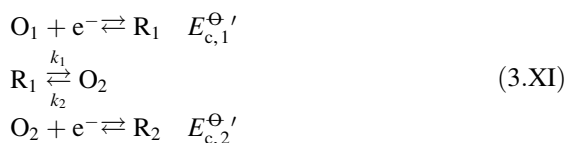
Fig. 3.28 Time influence at different values of r_s on the normalized limiting current of a CE mechanism (Eqs. 3.249 and 3.241) compared with the time-independent solution (*dashed lines* and

some authors have proposed approximate equations analogous to those given in Eqs. (3.239) and (3.240) by taking as valid the analogy between the disc and sphere radius, i.e., by making the change $r_s = \pi r_d/4$ in the expressions of the diffusion and reaction layers given by Eqs. (3.229) and (3.238) (see [76, 77] and Sect. 2.7). Under these conditions, the approximate expressions of the reaction and diffusion layers are

$$\left. \begin{aligned} \delta_r^{\text{disc}} &= \frac{1}{\sqrt{\frac{k_1 + k_2}{D} + \frac{4}{\pi r_d}}} \\ \delta^{\text{microdisc}} &= \frac{\pi}{4} r_d \end{aligned} \right\} \quad (3.251)$$

3.4.8 ECE Mechanism and Other More Complex Reaction Schemes

When there is a chemical reaction between two electrochemical steps, the mechanism is called ECE. This process, when the second electrochemical step is further reduced, is also denoted $\vec{E}\vec{C}\vec{E}$ and can be schematized



As in the case of two electrochemical steps (EE mechanism), the following reaction occurs:



If $E_{c,2}^{\ominus'} > E_{c,1}^{\ominus'}$, then the disproportionation step (3.XII) is thermodynamically viable. The source of the second electron transfer may then be either the second

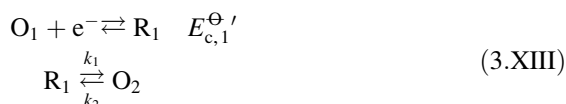
Fig. 3.28 (continued) Eqs. (3.250) and (3.244)). Three values of $(k_1 + k_2)$ (in s^{-1}) are considered: 1 (a); 10^2 (b); and 10^4 (c). r_0 is the radius of the spherical electrode. Time values are indicated on the curves. $K = 1/K_{\text{eq}} = 10^2$. Taken from [75] with permission

electron transfer reaction (ECE mechanism) or the chemical reaction (3.XII) (DISP1 mechanism if the intermediate chemical reaction in (3.XI) is rate limiting, or the DISP2 mechanism if reaction (3.XII) is rate limiting). While DISP2 is distinguished from the other mechanisms with relative ease, discrimination between ECE and DISP1 is more difficult [78, 79]. At high concentrations of supporting electrolyte, careful analysis of voltammetric wave shape over a range of scan rates can in some circumstances be used [80].

Throughout this book, a negligible interference of reaction (3.XII) is considered. The reader can find an extensive analysis of its influence on the response in references [79, 81].

If the second electrochemical step corresponds to the oxidation of the chemical reaction product, this process is called parallel ECE mechanism and is denoted $\vec{\text{ECE}}$.

The voltammetric response for the reaction scheme (3.XI) depends on the difference between the formal potentials of both electrochemical steps, $\Delta E_c^{\ominus'}$, and on the equilibrium and kinetic constants of the intermediate chemical reaction. If $\Delta E_c^{\ominus'} = E_{c,2}^{\ominus'} - E_{c,1}^{\ominus'} \ll 0$ (i.e., $E_{c,2}^{\ominus'}$ is much more negative than $E_{c,1}^{\ominus'}$), two well-resolved waves are observed, with the first corresponding to the EC process:

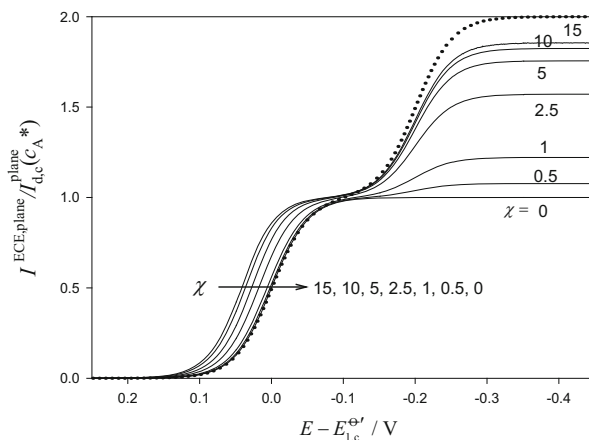


giving rise to a first plateau of current independent of the chemical reaction which is defined by the diffusion-controlled current of the first electron transfer. The limiting current corresponding to the second wave is obviously less than that which would correspond to the diffusion-controlled current of the second electron transfer, since it is conditioned by the chemical reaction. However, this limiting current, while presenting certain similarities, does not coincide exactly with that deduced for a CE mechanism, because for an irreversible chemical reaction ($K=0$), the second limiting current of an $\vec{\text{ECE}}$ process is less than the diffusion-controlled current except for very large values of $\chi = k_1 t$, contrary to that predicted for a CE mechanism, since the second wave depends on the previous step, as can be seen in Fig. 3.29.

The limiting current corresponding to the second electron transfer of an $\vec{\text{ECE}}$ mechanism is given by [82]:

$$\frac{I_{1,c}^{\vec{\text{ECE}},\text{plane}}}{I_{d,c}^{\text{plane}}(\zeta^*)} = 1 + \frac{S_1^{\text{CE}}}{1+K} \quad (3.252)$$

Fig. 3.29 Influence of χ on the normalized voltammograms corresponding to an ECE mechanism (see Eqs. (40)–(42) in reference [82]). The values of χ appear on the curves. $K = 1/K_{\text{eq}} = 0$, $T = 298.15$ K, $\Delta E_c^{\text{O}'} = -0.200$ V. Dotted lines correspond to simple EE mechanism (calculated from Eq. (3.133))



with S_1^{CE} being coincident with the series corresponding to a CE mechanism only under limiting current conditions (see Eq. (3.196b) in Sect. 3.4.2). The limiting current of a CE process is

$$\frac{I_{1,c}^{\text{CE,plane}}}{I_{d,c}^{\text{plane}}(\zeta^*)} = \frac{1}{1+K} \left[1 + \frac{KS_1^{\text{CE}}}{1+K} \right] \quad (3.253)$$

Second-Order Catalytic Mechanism

The theoretical study of other electrode processes as a reduction followed by a dimerization of the reduced form or a second-order catalytic mechanism (when the concentration of species Z in scheme (3.IXa, 3.IXb) is not too high) requires the direct use of numerical procedures to obtain their voltammetric responses, although approximate solutions for a second-order catalytic mechanism have been given [83–85]. An approximate analytical expression for the normalized limiting current of this last mechanism with an irreversible chemical reaction is obtained in reference [86] for spherical microelectrodes, and is given by

$$\frac{I_{1,c}^{\text{cat,microsphe}}}{I_{d,c}^{\text{microsphe}}(\zeta^*)} = 1 - \frac{k_1 r_s^2 c_C^*}{2D} + \frac{1}{2} \left[\left(\frac{k_1 r_s^2 c_C^*}{D} \right)^2 + \frac{4k_1 r_s^2 c_Z^*}{D} \right]^{1/2} \quad (3.254)$$

with k_1 being the rate constant of the irreversible chemical reaction.

3.4.9 Catalytic Mechanism at Disc Electrodes

The special characteristics of the first-order catalytic mechanism make it possible to obtain an explicit analytical expression for its transient voltammetric response at

disc microelectrodes [87, 88]. Indeed, by considering a nernstian behavior for the electrochemical reaction, the surface concentrations are constant and only depend on the applied potential, and the current can be written as

$$\frac{I^{\text{cat,disc}}}{FA_d D \zeta^*} = \frac{1 - Ke^\eta}{(1 + K)(1 + e^\eta)} f_{\text{disc}}^{\text{cat}}(r_d, \chi) \quad (3.255)$$

being

$$f_{\text{disc}}^{\text{cat}}(r_d, \chi) = \frac{1}{r_d} + \sqrt{\frac{k_1 + k_2}{D}} T^{\text{disc}}(\chi, \xi) \quad (3.256)$$

with

$$T^{\text{disc}}(\chi, \xi) = T(\chi) + 0.2732 \frac{\sqrt{\chi}}{\xi} \int_0^{\xi^2} \exp\left[-\frac{0.39115}{\sqrt{u}} - \frac{\chi}{\xi^2} u\right] du + \quad (3.257)$$

$$+ 0.2732 \frac{\xi}{\sqrt{\chi}} \exp\left(-\chi - \frac{0.39115}{\xi}\right)$$

$$T(\chi) = \frac{e^{-\chi}}{\sqrt{\pi\chi}} + \text{erf}(\sqrt{\chi}) \quad (3.258)$$

$$\xi = \frac{\sqrt{Dt}}{r_d} \quad (3.259)$$

with χ given in Eq. (3.181) and r_d being the radius of the disc electrode.

Steady-State Conditions

Inserting the condition $\chi > 1.5$ in Eqs. (3.255)–(3.258), one obtains

$$\frac{I^{\text{cat,microdisc}}}{FA_d D \zeta^*} = \frac{1 - Ke^\eta}{(1 + e^\eta)(1 + K)} \times \left\{ \frac{1}{r_d} + \sqrt{\frac{k_1 + k_2}{D}} + 0.5465 \sqrt{\frac{k_1 + k_2}{D}} \frac{\sqrt{\chi}}{\xi} \int_0^\infty u \exp\left(-\frac{0.39115}{\sqrt{u}} - \frac{\chi}{\xi^2} u^2\right) du \right\} \quad (3.260)$$

When the condition $(k_1 + k_2) \ll D/r_d^2$ is fulfilled, the enhancement of the diffusion transport freezes the chemical reaction, so the response is that corresponding to a simple charge transfer process and therefore does not contain any information about the chemical kinetics. So, Eq. (3.260) under these conditions becomes

$$\frac{I^{\text{cat,microdisc}}}{FA_d D \zeta^*} \Big|_{(k_1 + k_2) \ll D/r_d^2} = \frac{1 - Ke^\eta}{(1 + e^\eta)(1 + K)} \frac{4}{\pi r_d} \quad (3.261)$$

It is interesting to highlight that Eqs. (3.255), (3.260), and (3.261) deduced in this section fulfill that

$$\frac{I^{\text{cat, disc}}}{I_{1,c}^{\text{cat, disc}}(\zeta^*)} = \frac{1 - Ke^{\eta}}{(1 + e^{\eta})(1 + K)} \quad (3.262)$$

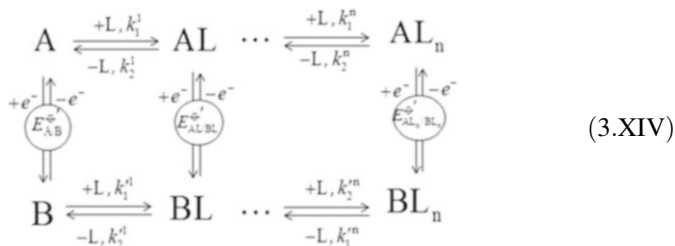
since the applied potential only affects the surface concentrations which are independent of time.

For a second-order catalytic mechanism with an irreversible chemical reaction, an approximate analytical solution has been reported [86]:

$$\frac{I_1^{\text{cat, microdisc}}}{I_{d,c}^{\text{microdisc}}(\zeta^*)} = 1 - \frac{k_1 \pi r_d^2 c_C^*}{32D} + \frac{1}{2} \left[\left(\frac{k_1 \pi^2 r_d^2 c_C^*}{16D} \right)^2 + \frac{k_1 \pi^2 r_d^2 c_Z^*}{4D} \right]^{1/2} \quad (3.263)$$

3.4.10 Reversible Charge Transfers Preceded and Followed by Several Complexation Reactions in Equilibrium (Ladder Mechanism)

Another very common situation is produced when a species A is electro-reduced to B with both species taking part in a number of chemical equilibria in solution which may refer to their complexation with a ligand L [89, 90], protonation [91, 92] or formation of ion pairs [93, 94], or association of charged species with DNA [95], the products of which (AL, BL, ... AL_n, BL_n) are also electro-active in line with the following reaction scheme:



Ligand L is assumed to be present at high concentration ($c_L^* \gg c_A^*, c_B^*, c_{AL_j}^*, c_{BL_j}^*$) and k_j^i and k_j^i ($j=1, 2; i=1, 2 \dots n$) represent the (pseudo)first-order forward and backward rate constants of the chemical reactions. Note that this reaction scheme covers different common mechanisms that can be

studied by adjusting the values of the formation equilibrium constants. Thus, the situation where only the oxidized (A) or the reduced (B) species is involved in the homogeneous chemical equilibria (i.e., only one species reacts in solution) can be studied by setting to zero the equilibrium constant(s) of the other species (C_n^{eq} E^{rev} - or E^{rev} C_n^{eq} -type mechanisms). The E^{rev} C_n^{eq} mechanism is very usual in real systems since the electron transfer generally increases the instability and reactivity of the chemical species, for example, by forming radicals.

When a constant potential, E , is applied to the electrode immersed in the solution containing species A and L such that the electron transfer reactions take place, the mass transport supposed by pure diffusion to and from the electrode surface, in the presence of an excess of supporting electrolyte, is described by the following differential diffusive-kinetic equations system:

$$\left. \begin{aligned} \frac{\partial c_{\text{AL}_i}}{\partial t} &= D_{\text{AL}_i} \nabla^2 c_{\text{AL}_i} + k_1^i c_{\text{AL}_{i-1}} - (k_2^i + k_1^{i+1}) c_{\text{AL}_i} + k_2^{i+1} c_{\text{AL}_{i+1}} \\ \frac{\partial c_{\text{BL}_i}}{\partial t} &= D_{\text{BL}_i} \nabla^2 c_{\text{BL}_i} + k_1^i c_{\text{BL}_{i-1}} - (k_2^i + k_1^{i+1}) c_{\text{BL}_i} + k_2^{i+1} c_{\text{BL}_{i+1}} \end{aligned} \right\} \quad (3.264)$$

where ∇^2 is the Laplacian operator given in Table 2.2 of Sect. 2.6 for the main electrode geometries, $0 \leq i \leq n$ for the different complexes, $\text{AL}_0 = \text{A}$, $\text{BL}_0 = \text{B}$, $k_j^0 = k_j^{n+1} = 0$, $k_j^0 = k_j^{n+1} = 0$ ($j = 1, 2$).

The boundary value problem associated with the reduction of A is given by

$$\left. \begin{aligned} & \left. \begin{aligned} t = 0, \quad q \geq q^s \\ t \geq 0, \quad q \rightarrow \infty \end{aligned} \right\} \\ c_{\text{A}}(q, 0) = c_{\text{A}}(\infty, t) &= \frac{c^*}{1 + \sum_{s=1}^n \beta_s} \quad ; \quad c_{\text{AL}_i}(q, 0) = c_{\text{AL}_i}(\infty, t) = \frac{c^* \beta_i}{1 + \sum_{s=1}^n \beta_s} \\ c_{\text{B}}(q, 0) = c_{\text{B}}(\infty, t) &= 0 \quad ; \quad c_{\text{BL}_i}(q, 0) = c_{\text{BL}_i}(\infty, t) = 0 \end{aligned} \right\} \quad (3.265)$$

$$t > 0, \quad q = q^s$$

$$D_{\text{A}} \left(\frac{\partial c_{\text{A}}}{\partial q_{\text{N}}} \right)_{q=q^s} = -D_{\text{B}} \left(\frac{\partial c_{\text{B}}}{\partial q_{\text{N}}} \right)_{q=q^s} \quad (3.266)$$

$$D_{\text{AL}_i} \left(\frac{\partial c_{\text{AL}_i}}{\partial q_{\text{N}}} \right)_{q=q^s} = -D_{\text{BL}_i} \left(\frac{\partial c_{\text{BL}_i}}{\partial q_{\text{N}}} \right)_{q=q^s} \quad ; \quad 1 \leq i \leq n \quad (3.267)$$

$$c_{\text{A}}(q^s) = c_{\text{B}}(q^s) e^{\eta_{\text{A/B}}} \quad (3.268)$$

$$c_{AL_i}(q^s) = c_{BL_i}(q^s) e^{\eta_{AL_i/BL_i}} \quad ; \quad 1 \leq i \leq n \quad (3.269)$$

with

$$\eta_{A/B} = F(E - E_{A/B}^{\ominus})/RT \quad (3.270)$$

$$\eta_{AL_i/BL_i} = F(E - E_{AL_i/BL_i}^{\ominus})/RT \quad ; \quad 1 \leq i \leq n \quad (3.271)$$

where q and t refer to the spatial coordinate and time values, q^s to the coordinates at the electrode surface, q_N is the normal coordinate value at the surface of the electrode, and β_i represents the overall formation constant for the different complexes of species A initially present in solution (see Eq. (3.272)).

It will be assumed that the rates of formation and dissociation of the different complexes (k_1^i , k_1^i , k_2^i , and k_2^i) are sufficiently fast in comparison to the diffusion rate so that the complex formations and dissociations are at equilibrium even when current is flowing, i.e., that chemical equilibrium conditions are maintained at any position and time of the experiment [90]:

$$\left. \begin{aligned} \beta_i &= \prod_{m=1}^i K_m c_L^* = \frac{c_{AL_i}(q, t)}{c_A(q, t)} \\ \beta_i' &= \prod_{m=1}^i K_m' c_L^* = \frac{c_{BL_i}(q, t)}{c_B(q, t)} \end{aligned} \right\} \quad \forall q, t \quad ; \quad i \geq 1 \quad ; \quad (3.272)$$

with K_m and K_m' being

$$\begin{aligned} K_m &= \frac{c_{AL_m}(q, t)}{c_{AL_{m-1}}(q, t) c_L^*} \\ K_m' &= \frac{c_{BL_m}(q, t)}{c_{BL_{m-1}}(q, t) c_L^*} \end{aligned} \quad (3.273)$$

To solve the problem defined above, the new variables c_T^A and c_T^B are defined as

$$c_T^A(q, t) = c_A(q, t) + \sum_{i=1}^n c_{AL_i}(q, t) \quad (3.274)$$

$$c_T^B(q, t) = c_B(q, t) + \sum_{i=1}^n c_{BL_i}(q, t) \quad (3.275)$$

which relate to the total concentration of species A and B. Taking into account Eq. (3.272), it is possible to establish the following relationships:

$$\left. \begin{aligned} c_A(q, t) &= \frac{c_T^A(q, t)}{1 + \sum_{m=1}^n \beta_m} & ; & \quad c_{AL_i}(q, t) = \frac{c_T^A(q, t) \beta_i}{1 + \sum_{m=1}^n \beta_m} \\ c_B(q, t) &= \frac{c_T^B(q, t)}{1 + \sum_{m=1}^n \beta_m'} & ; & \quad c_{BL_i}(q, t) = \frac{c_T^B(q, t) \beta_i'}{1 + \sum_{m=1}^n \beta_m'} \end{aligned} \right\} \quad (3.276)$$

By introducing the new variables c_T^A and c_T^B (given by Eqs. (3.274) and (3.275)) and the relationships given by Eq. (3.276) in Eqs. (3.264)–(3.269), the diffusive-kinetic differential equation system and boundary value problem simplifies to

$$\left. \begin{aligned} \frac{\partial c_T^A}{\partial t} &= D_{\text{eff}}^A \nabla^2 c_T^A \\ \frac{\partial c_T^B}{\partial t} &= D_{\text{eff}}^B \nabla^2 c_T^B \end{aligned} \right\} \quad (3.277)$$

$$\left. \begin{aligned} t = 0, & \quad q \geq q^s \\ t \geq 0, & \quad q \rightarrow \infty \end{aligned} \right\}$$

$$\left. \begin{aligned} c_T^A(q, 0) &= c_T^A(\infty, t) = c^* \\ c_T^B(q, 0) &= c_T^B(\infty, t) = 0 \end{aligned} \right\} \quad (3.278)$$

$$t > 0, \quad q = q^s$$

$$D_{\text{eff}}^A \left(\frac{\partial c_T^A}{\partial q_N} \right)_{q=q^s} = -D_{\text{eff}}^B \left(\frac{\partial c_T^B}{\partial q_N} \right)_{q=q^s} \quad (3.279)$$

$$c_T^A(q^s) = c_T^B(q^s) \omega e^{\eta_{A/B}} \quad (3.280)$$

where $c_T^A(q^s)$ and $c_T^B(q^s)$ are the total surface concentrations of species A and B (see Eqs. (3.274) and (3.275), respectively), ω is given by

$$\omega = \frac{1 + \sum_{i=1}^n \beta_i}{1 + \sum_{i=1}^n \beta_i'} \quad (3.281)$$

and D_{eff}^A and D_{eff}^B are the effective diffusion coefficients of the pseudo-species A_T and B_T , respectively:

$$D_{\text{eff}}^{\text{A}} = \frac{D_{\text{A}} + \sum_{i=1}^n D_{\text{AL}_i} \beta_i}{1 + \sum_{i=1}^n \beta_i} \quad (3.282)$$

$$D_{\text{eff}}^{\text{B}} = \frac{D_{\text{B}} + \sum_{i=1}^n D_{\text{BL}_i} \beta'_i}{1 + \sum_{i=1}^n \beta'_i} \quad (3.283)$$

In this particular situation where the concentration of all the species satisfies the chemical equilibrium (Eqs. (3.272)–(3.273)), $D_{\text{eff}}^{\text{A/B}}$ is simply equal to a mole fraction weighted average [96]. Note that Eqs. (3.278)–(3.280) are a set of initial and boundary conditions formally identical to those of a simple reversible electron transfer process for the pseudo-species c_{T}^{A} and c_{T}^{B} at electrodes of the different geometries considered. By assuming that $D_{\text{eff}}^{\text{A}} = D_{\text{eff}}^{\text{B}} = D$, which does not mean that the diffusivities of the free and complexed species are the same and it is reasonable to have a great variety of experimental systems in conventional solvents [4], it can be deduced that for any values of q and t it is fulfilled that [97]

$$c_{\text{T}}^{\text{A}}(q, t) + c_{\text{T}}^{\text{B}}(q, t) = c^* \quad (3.284)$$

The combination of Eqs. (3.280) and (3.284) at $q = q^{\text{s}}$ turns the problem of two variables c_{T}^{A} and c_{T}^{B} into two separate problems of only one variable with constant limit and surface conditions

$$\left. \begin{array}{l} \frac{\partial c_{\text{T}}^{\text{A}}}{\partial t} = D \nabla^2 c_{\text{T}}^{\text{A}} \\ t \geq 0, q \rightarrow \infty \\ t = 0, q \geq q^{\text{s}} \end{array} \right\} c_{\text{T}}^{\text{A}}(q, t) = c^* \quad (3.285)$$

$$\left. \begin{array}{l} t \geq 0, q = q^{\text{s}} \\ c_{\text{T}}^{\text{A}}(q^{\text{s}}) = \frac{c^* \omega e^{\eta_{\text{A/B}}}}{1 + \omega e^{\eta_{\text{A/B}}}} \end{array} \right\}$$

$$\left. \begin{array}{l} \frac{\partial c_{\text{T}}^{\text{B}}}{\partial t} = D \nabla^2 c_{\text{T}}^{\text{B}} \\ t \geq 0, q \rightarrow \infty \\ t = 0, q \geq q^{\text{s}} \end{array} \right\} c_{\text{T}}^{\text{B}}(q, t) = 0 \quad (3.286)$$

$$\left. \begin{array}{l} t \geq 0, q = q^{\text{s}} \\ c_{\text{T}}^{\text{B}}(q^{\text{s}}) = \frac{c^*}{1 + \omega e^{\eta_{\text{A/B}}}} \end{array} \right\}$$

with $\eta_{\text{A/B}}$ being given in Eq. (3.270).

The above differential equation problems (Eqs. 3.285 and 3.286) are mathematically analogous to the problem corresponding to the application of a potential pulse under limiting current conditions given that the boundary conditions are time

independent. Therefore, the solutions of both problems are identical except for the constant surface concentration values. So, the expression for the current for any value of the applied potential in the different geometries considered can be written in the following general form:

$$\frac{I^G}{FA_G D} = (c^* - c_T^A(q^s))f_G(t, q_G) = c_T^B(q^s)f_G(t, q_G) \quad (3.287)$$

where $f_G(t, q_G)$ is a function of time and the electrode geometry, given in Table 2.3 of Sect. 2.6 for the most commonly used electrodes, and A_G is the electrode area.

Equation (3.287) can also be written as

$$E = E_{1/2} + \frac{RT}{F} \ln \left(\frac{I_{1,c}^G - I^G}{I^G} \right) \quad (3.288)$$

where $E_{1/2}$ is the half-wave potential of the process

$$E_{1/2} = E_{A/B}^{\ominus'} + \frac{RT}{F} \ln \left(\frac{1 + \sum_{i=1}^n \beta'_i}{1 + \sum_{i=1}^n \beta_i} \right) \quad (3.289)$$

and $I_{1,c}^G$ is given by

$$I_{1,c}^G = FA_G \sqrt{\frac{D_{\text{eff}}^A}{\pi t}} c^* \quad (3.290)$$

From Eqs. (3.287) and (3.290), it can be inferred that, when total equilibrium conditions are considered for the precedent and subsequent chemical reactions to the charge transfer reaction, the shape and height of the voltammetric curve are not affected although the half-wave potential shifts toward more cathodic or anodic

potentials depending on the term $\left(1 + \sum_{i=1}^n \beta'_i\right) / \left(1 + \sum_{i=1}^n \beta_i\right)$.

References

1. Koutecký J (1953) Collect Czech Chem Commun 18:597–610
2. Galus Z (1993) Fundamentals of electrochemical analysis, 2nd/rev edn. Ellis Horwood series in analytical chemistry. Ellis Horwood, Chichester
3. Molina A, Gonzalez J, Laborda E, Compton RG (2013) Phys Chem Chem Phys 15:2381–2388

4. Bard AJ, Faulkner LR (2001) *Electrochemical methods, fundamental and applications*. Wiley, New York, NY
5. Zoski CG (ed) (2007) *Handbook of electrochemistry*. Elsevier, Amsterdam
6. Heyrovský J (1966) *Principles of polarography*. Academic, New York, NY
7. Kůta J (1951) *Collect Czech Chem Commun* 16:1
8. Delahay P, Strassner JE (1951) *J Am Chem Soc* 73:5218
9. Compton RG, Banks CE (2011) *Understanding voltammetry*, 2nd edn. ICP, London
10. Gileadi E (2011) *Physical electrochemistry*. Wiley-VCH, Weinheim
11. Tomeš J (1937) *Collect Czech Chem Commun* 9:12, and 9:150
12. Galvez J, Zapata J, Serna C (1986) *J Electroanal Chem* 205:21–34
13. Delmastro JR, Smith DE (1966) *Anal Chem* 28:169–179
14. Molina A, Martinez-Ortiz F, Laborda E, Compton RG (2010) *Electrochim Acta* 55:5163–5172
15. Bond AM, Oldham KB, Zoski CG (1989) *Anal Chim Acta* 216:177–230
16. Molina A, Gonzalez J (2012) In: Kaufmann EN (ed) *Characterization of materials*, 2nd edn. Hoboken, Wiley
17. Molina A, Laborda E, Gonzalez J, Compton RG (2013) *Phys Chem Chem Phys* 15:7106–7113
18. Mirkin MV, Bard AJ (1992) *Anal Chem* 64:2293–2302
19. Streeter I, Compton RG (2007) *J Phys Chem C* 111:18049–18054
20. Oldham KB, Zoski CG (1991) *J Electroanal Chem* 313:17–28
21. Bobbert PA, Wind MM, Vlieger J (1987) *Physica* 141A:58–72
22. Molina A, Gonzalez J, Henstridge MC, Compton RG (2011) *Electrochim Acta* 56:4589–4594
23. Phillips CG (1990) *J Electroanal Chem* 291:251–256
24. Xiaoping L, Juntao L, Chuansin C (1990) *J Electroanal Chem* 295:15–23
25. Oldham KB (1992) *J Electroanal Chem* 323:53–76
26. Molina A, Gonzalez J, Barnes EO, Compton RG (2014) *J Phys Chem C* 118:346–356
27. Ward KR, Lawrence NS, Hartshorne RS, Compton RG (2012) *J Electroanal Chem* 683:37–42
28. Chidsey CED (1991) *Science* 251:919–922
29. Feldberg SW (2010) *Anal Chem* 82:5176–5183
30. Laborda E, Henstridge M, Molina A, Martinez-Ortiz F, Compton RG (2011) *J Electroanal Chem* 660:169–177
31. Evans DH (2008) *Chem Rev* 108:2113–2144
32. Evans DH, Lehmann MW (1999) *Acta Chim Scan* 53:765–774
33. Molina A, Serna C, Lopez-Tenes M, Moreno MM (2005) *J Electroanal Chem* 576:9–19
34. Hale JM (1964) *J Electroanal Chem* 8:181–199
35. Leger C, Bertrand P (2008) *Chem Rev* 108:2379–2438
36. Sadakane M, Steckhan E (1998) *Chem Rev* 98:219–237
37. Evans DH, Hu K (1996) *J Chem Soc Faraday Trans* 92:3893–3890
38. Lehmann MW, Evans DH (1999) *Anal Chem* 71:1947–1950
39. Andrieux CP, Saveant J (1970) *J Electroanal Chem* 28:339–348
40. Klymenko OV, Svir I, Amatore C (2010) *Electrochem Commun* 12:1378–1382
41. Belding S, Baron R, Dickinson E, Compton RG (2009) *J Phys Chem C* 113:16042–16050
42. Serna C, Lopez-Tenes M, Gonzalez J, Molina A (2001) *Electrochim Acta* 46:2699–2709
43. Lopez-Tenes M, Gonzalez J, Molina A (2014) *J Phys Chem C* 118:12312–12324
44. Lopez-Tenes M, Molina A, Serna A, Moreno MM, Gonzalez J (2007) *J Electroanal Chem* 603:249–259
45. Molina A, Gonzalez J, Laborda E, Compton RG (2012) *Int J Electrochem Sci* 7:5765–5778
46. Molina A, Serna C, Laborda E, Li Q, Batchelor-McAuley C, Compton RG (2012) *J Phys Chem C* 116:1070–1079
47. Molina A, Serna C, Martinez-Ortiz F, Laborda E (2008) *J Electroanal Chem* 617:14–26
48. Hapiot P, Kispert LD, Konovalov VV, Saveant JM (2001) *J Am Chem Soc* 123:6669–6677
49. Zanello P (2003) *Inorganic electrochemistry: theory, practice and application*. Royal Society of Chemistry, Oxford
50. Silvester DS, He W, Aldous L, Hardacre C, Compton RG (2008) *J Phys Chem C* 112:12966–12973

51. Cardona CM, Mendoza S, Kaifer AE (2000) *Chem Soc Rev* 29:37–42
52. Torralba E, Ortuño J, Molina A, Serna C, Karimian F (2014) *Anal Chim Acta* 826:12–20
53. Zhan D, Mao S, Zhao Q, Chen Z, Hu H, Jing P, Zhang M, Zhu Z, Shao Y (2004) *Anal Chem* 76:4128–4136
54. Lin Q, Batchelor-MacAuley C, Compton RG (2013) *Phys Chem Chem Phys* 15:7760–7767
55. Komorsky-Lovrić S, Lovrić M (2013) *Anal Bioanal Electrochem* 5:291–304
56. Delahay P, Stiehl GL (1952) *J Am Chem Soc* 74:3500–3505
57. Miller SL (1952) *J Am Chem Soc* 74:4130–4134
58. Koutecký J (1953) *Chem List* 47:323–333
59. Weber J (1958) *Chem List* 52:1888–1898
60. Brdička R, Wiesner K (1947) *Collect Czech Chem Commun* 12:39–63
61. Koutecký J, Brdička R, Hanuš V (1953) *Collect Czech Chem Commun* 18:611–622
62. Koutecký J, Čížek J (1956) *Collect Czech Chem Commun* 21:1063–1065
63. Molina A, Morales I (2005) *J Electroanal Chem* 583:193–202
64. Molina A, Morales I, Lopez-Tenes M (2006) *Electrochem Commun* 8:1062–1070
65. Koutecký J (1954) *Collect Czech Chem Commun* 19:1093–1098
66. Čížek J, Koutecký J (1963) *Collect Czech Chem Commun* 28:2808–2810
67. Čížek J, Koryta J, Koutecký J (1959) *Collect Czech Chem Commun* 24:663–670
68. Galvez J, Serna A, Molina A, Marin D (1979) *J Electroanal Chem* 102:277–288
69. Molina A, Martinez-Ortiz F, Laborda E, Puy J (2010) *Phys Chem Chem Phys* 12:5396–5404
70. Molina A (1998) *J Electroanal Chem* 443:163–167
71. Morales I, Molina A (2006) *Electrochem Commun* 8:1453–1460
72. Molina A, Martinez-Ortiz F, Laborda E, Morales I (2009) *J Electroanal Chem* 633:7–14
73. Lovrić M, Tur'yan YI (2003) *Croat Chem Acta* 76:189–197
74. Budyevskii E, Desimirov G (1963) *Dokl Akad Nauk SSSR* 149:120–123
75. Molina A, Martinez-Ortiz F, Laborda E (2009) *Electrochem Commun* 11:562–565
76. Fleischmann M, Lasserre F, Robinson J, Swan D (1984) *J Electroanal Chem* 177:97–114
77. Alden JA, Hakoura S, Compton RG (1999) *Anal Chem* 71:806–810
78. Müller R, Lamberts L, Evers M (1996) *J Electroanal Chem* 417:35–43
79. Amatore CA, Saveánt JM (1978) *J Electroanal Chem* 86:227–232
80. Barnes EO, Wang Y, Limon-Petersen JG, Belding SR, Compton RG (2011) *J Electroanal Chem* 659:25–35
81. Amatore C, Gareil M, Saveánt JM (1983) *J Electroanal Chem* 147:1–38
82. Galvez J, Molina A (1980) *J Electroanal Chem* 110:49–68
83. Koutecký J (1954) *Chem List* 48:116–123
84. Che GL, Dong SJ (1992) *Electrochim Acta* 37:2695–2699
85. Wang Y, Laborda E, Compton RG (2012) *J Electroanal Chem* 670:56–71
86. Denault G, Fleischmann M, Pletcher D, Tutty OR (1990) *J Electroanal Chem* 280:243–254
87. Molina A, Gonzalez J, Laborda E, Henstridge M, Compton R (2011) *Electrochim Acta* 56:7404–7410
88. Galceran J, Taylor SL, Bartlett PN (1999) *J Electroanal Chem* 466:15–25
89. Beer PD, Gale PA, Chen GZ (1999) *Coord Chem Rev* 185:3–36
90. Molina A, Torralba E, Serna C, Ortuño JA (2013) *Electrochim Acta* 106:244–257
91. Alligrant TM, Alvarez JC (2011) *J Phys Chem C* 115:10797–10805
92. Weinberg DR, Gagliardi CJ, Hull JF, Murphy CF, Kent CA, Westlake BC, Paul A, Ess DH, McCafferty DG, Meyer TJ (2012) *Chem Rev* 112:4016–4093
93. Atifi A, Ryan MD (2014) *Anal Chem* 86:6617–6625
94. Savéant JM (2008) *J Am Chem Soc* 130:4732–4741
95. De Rache A, Buess-Herman C, Doneux T (2015) *J Electroanal Chem*. doi:10.1016/j.jelechem.2015.1003.1014
96. Texter J (1991) *J Electroanal Chem* 304:257–262
97. Molina A, Gonzalez J, Henstridge M, Compton RG (2011) *J Phys Chem C* 115:4054–4062

Chapter 4

Double Pulse Voltammetries

Contents

4.1	Introduction	229
4.2	Reversible Electrochemical Reactions	233
4.2.1	Application of a Double Potential Pulse to Electrodes and Microelectrodes of Any Geometry	234
4.2.2	Double Pulse Chronoamperometry and Chronocoulometry	239
4.2.3	Reverse Pulse Voltammetry	247
4.2.4	Differential Double Pulse Voltammetry	252
4.2.5	Differential Normal Double Pulse Voltammetry	260
4.2.6	Additive Differential Double Pulse Voltammetry	260
4.3	Nonreversible Electrochemical Reactions	264
4.3.1	Application of a Double Potential Pulse to Planar and Spherical Electrodes ...	264
4.3.2	Reverse Pulse Voltammetry	266
4.3.3	Differential Double Pulse Voltammetry	270
4.3.4	Additive Double Differential Pulse Voltammetry	274
4.4	Multi-electron Electrochemical Reactions	278
4.4.1	Application of a Double Potential Pulse to Electrodes of Any Geometry	278
4.4.2	Differential Double Pulse Voltammetry	282
4.4.3	Additive Differential Double Pulse Voltammetry	287
4.5	First-Order Chemical Reactions Coupled to Charge Transfer Processes	291
4.5.1	Catalytic Mechanism at Disc, Spherical, and Planar Electrodes	291
4.5.2	CE and EC Mechanisms at Planar Electrodes	301
4.6	Triple Pulse Voltammetries	311
4.6.1	Reverse Differential Pulse Voltammetry	311
4.6.2	Double Differential Triple Pulse Voltammetry	313
	References	314

4.1 Introduction

Double Potential Pulse Electrochemical Techniques combine the faradaic currents at two successive potential pulses recovering then the initial equilibrium conditions (in the case of a DME the two successive potentials are applied to the same drop).

They are applicable to electrodes of any shape and size and are extensively employed in electroanalysis due to their high sensitivity, good definition of signals, and minimization of double layer and background currents. In these techniques, both the theoretical treatments and the interpretation of the experimental results are easier than those corresponding to the multipulse techniques treated in the following chapters. Four double potential pulse techniques are analyzed in this chapter: Double Pulse Chronoamperometry (DPC), Reverse Pulse Voltammetry (RPV), Differential Double Pulse Voltammetry (DDPV), and a variant of this called Additive Differential Double Pulse Voltammetry (ADDPV). A brief introduction to two triple pulse techniques (Reverse Differential Pulse Voltammetry, RDPV, and Double Differential Triple Pulse Voltammetry, DDTPV) is also given in Sect. 4.6.

The general features of the potential waveform applied and of the output currents of these double pulse techniques are shown.

Double Potential Chronoamperometry

Among double pulse techniques, the simplest case is recording the current–time curves obtained when the two successive potential pulses are applied. Usually, the first is set at values corresponding to limiting current conditions for the reactant, $E_1 \ll E_c^{\Theta'}$, for a time $0 \leq t_1 \leq \tau_1$ and the second to limiting current conditions for the electrogenerated product, $E_2 \gg E_c^{\Theta'}$, for a time $0 \leq t_2 \leq \tau_2$ as shown in Scheme 4.1.

Reverse Pulse Voltammetry

In this voltammetric technique, introduced by Oldham and Parry by using the DME [1], the product species of an electrochemical reaction is electrogenerated under diffusion-limited conditions by applying a first potential $E_1 \ll E_c^{\Theta'}$ in the first period $0 \leq t_1 \leq \tau_1$, and the value of the second one, E_2 , varying toward anodic potentials during the second period $0 \leq t_2 \leq \tau_2$. The current is sampled at the end of the second pulse, $I_2(\tau_2)$, and plotted versus E_2 values (Scheme 4.2).

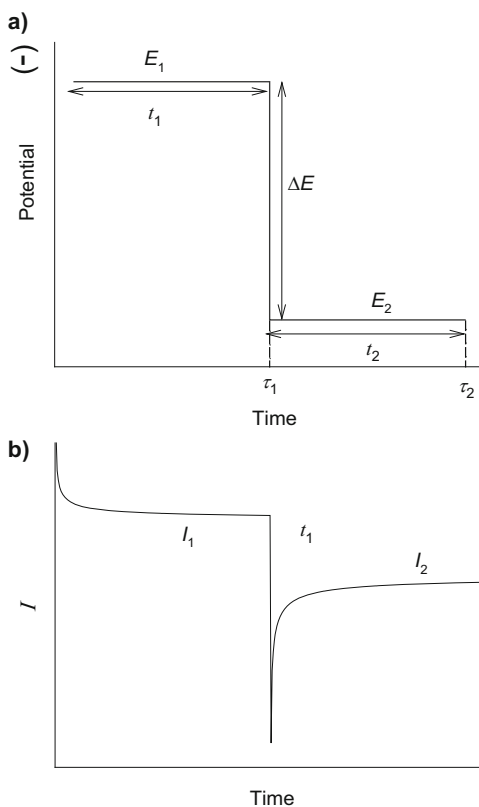
Differential Double Pulse Voltammetry

This technique is based on the derivative of the NPV curve introduced by Barker and Gardner [2]. In DDPV, two consecutive potentials E_1 and E_2 are applied during times $0 \leq t_1 \leq \tau_1$ and $0 \leq t_2 \leq \tau_2$, respectively, with the length of the second pulse being much shorter than the first ($\tau_1/\tau_2 \cong 50 - 100$). The difference $\Delta E = E_2 - E_1$ is kept constant during the experiment and the difference $\Delta I_{\text{DDPV}} = I_2 - I_1$ is plotted versus E_1 or versus an average potential $E_{1,2} = (E_1 + E_2)/2$. When the two pulses are of similar duration, the technique is known as Differential Normal Double Pulse Voltammetry (DNDPV) (Scheme 4.3).

Additive Differential Double Pulse Voltammetry

This double pulse technique is a modification of the DDPV one based on obtaining two differential signals corresponding to the same first potential, E_1 (see Scheme 4.4) [3],

Scheme 4.1 Double Pulse Chronoamperometry. **(a)** Potential–time program; **(b)** DPC response



$$\Delta I_{\text{DDPV}}^c = I_2^c(E_2^c) - I_1(E_1) \quad (4.1)$$

$$\Delta I_{\text{DDPV}}^a = I_2^a(E_2^a) - I_1(E_1) \quad (4.2)$$

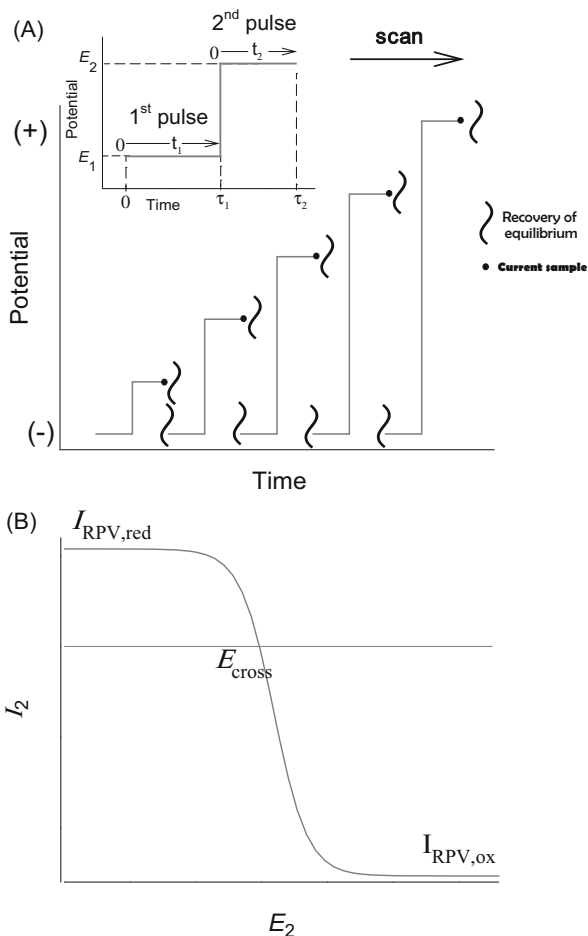
with $|\Delta E| = -(E_2^c - E_1) = E_2^a - E_1$, being $\Delta E < 0$ in Eq. (4.1) and $\Delta E > 0$ in Eq. (4.2). The additive response is obtained by adding both differential signals ΔI^c and ΔI^a , such that

$$I_{\text{ADDPV}} = \Delta I_{\text{DDPV}}^c + \Delta I_{\text{DDPV}}^a = I_2^c - 2I_1 + I_2^a \quad (4.3)$$

and I_{ADDPV} is plotted versus E_1 . In this technique, the length of the second pulse is much shorter than the first one. The recorded ADDPV signal is shown in Scheme 4.4.

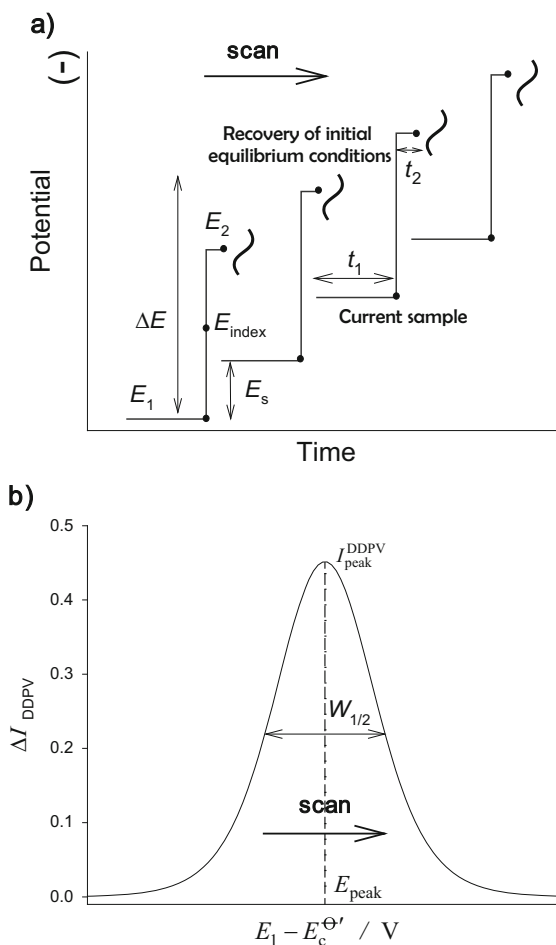
It is necessary to mention that there is no universal and unambiguous nomenclature for the different differential pulse techniques, something which can lead to inaccurate analyses and misinterpretations. The DDPV technique is usually called ‘‘Differential Pulse Voltammetry’’ (DPV) referring to the double pulse

Scheme 4.2 Reverse Pulse Voltammetry. (a) Potential–time program; (b) RPV response. $I_{\text{RPV,red}}$ and $I_{\text{RPV,ox}}$ are the limiting currents corresponding to very negative ($E_2 \ll E_c^{\theta'}$) and positive ($E_2 \gg E_c^{\theta'}$) potentials, respectively. E_{cross} is the potential of null current



program [4–9], although some authors and most of the commercial software available in Electrochemistry use the term DPV for the multipulse variant [10–15] where the equilibrium is fully regained only at the end of the experiment (see Sect. 5.1). The origin of this confusion may be that most of these electrochemical methods were designed for the dropping mercury electrode (DME) where the renewal of the equilibrium conditions is easily achieved once the drop releases, meaning that each drop can be treated as a new experiment. However, the recovery of equilibrium conditions at stationary electrodes can be time-consuming, especially in the case of macroelectrodes. For these reasons and in order to distinguish clearly between double and multipulse mode, in this book the term “Differential Double Pulse Voltammetry” (DDPV) will be employed for the double pulse technique and the term “Differential Multipulse Voltammetry” (DMPV) for the multipulse one which will be analyzed in the chapter (see also Sect. 7.2.2), in order

Scheme 4.3 Differential Double Pulse Voltammetry: (a) Potential–time program; (b) DDPV response. $I_{\text{DDPV}}^{\text{peak}}$, E_{peak} , and $W_{1/2}$ denote the peak parameters of the DDPV signal, peak current, peak potential, and half-peak width, respectively

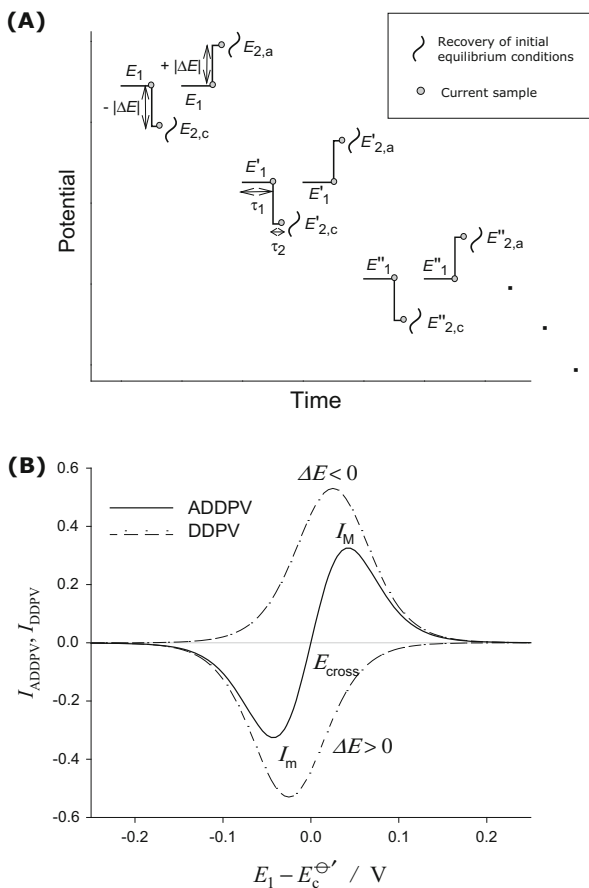


that these two modes can be clearly distinguished. Note that, although DDPV and DMPV can lead to similar responses in the case of reversible electrode processes because the length of the first pulse, t_1 , is much longer than the second one, t_2 . This does not occur in the case of nonreversible electrode processes, since re-establishment of the equilibrium is not generally possible during t_1 in the multipulse mode.

4.2 Reversible Electrochemical Reactions

In this section only very fast charge transfer reactions will be considered in order to analyze their response in the different double pulse techniques considered in Sect. 4.1.

Scheme 4.4 Additive Differential Pulse Voltammetry: (a) Potential waveform, (b) Signal. I_M and I_m denote the maximum and minimum values of the ADDPV current and E_{cross} is the potential of null current. Dashed lines in Figure (b) correspond to the DDPV curves that are combined to obtain the ADDPV one



4.2.1 Application of a Double Potential Pulse to Electrodes and Microelectrodes of Any Geometry

Let us consider the fast electrode reaction



and application of two successive potentials E_1 and E_2 to an electrode of any geometry for the periods $0 \leq t_1 \leq \tau_1$ and $0 \leq t_2 \leq \tau_2$, respectively, when both electroactive species are initially present and the condition $D_O = D_R = D$ holds. The current obtained when the first potential step E_1 is applied is given by Eq. (2.156) of Sect. 2.6.

If at a time $t = \tau_1$ the potential is stepped to a value E_2 over an interval $0 \leq t_2 \leq \tau_2$, with the total time of the experiment being $t = \tau_1 + t_2$, the mass transport of species O and R is described by the differential equations

$$\frac{\partial c_{\text{O}}^{(2)}}{\partial t_2} = D \nabla^2 c_{\text{O}}^{(2)} \quad (4.4)$$

$$\frac{\partial c_{\text{R}}^{(2)}}{\partial t_2} = D \nabla^2 c_{\text{R}}^{(2)} \quad (4.5)$$

with ∇^2 being the Laplace operator given in Table 2.2 of Sect. 2.6, and $c_{\text{O}}^{(2)}$ and $c_{\text{R}}^{(2)}$ the solutions of Eqs. (4.4) and (4.5). The boundary value problem is given by

$$\left. \begin{array}{l} t_2 \geq 0, q \rightarrow \infty \\ t_2 = 0, q \geq q^s \end{array} \right\} c_{\text{O}}^{(2)} = c_{\text{O}}^{(1)}, c_{\text{R}}^{(2)} = c_{\text{R}}^{(1)} \quad (4.6)$$

$$t_2 > 0, q = q^s,$$

$$c_{\text{O}}^{(2,s)} + c_{\text{R}}^{(2,s)} = c_{\text{O}}^* + c_{\text{R}}^* \quad (4.7)$$

$$c_{\text{O}}^{(2,s)} = e^{\eta_2} c_{\text{R}}^{(2,s)} \quad (4.8)$$

with

$$\eta_2 = \frac{F}{RT} (E_2 - E_c^{\Theta'}) \quad (4.9)$$

$c_{\text{O}}^{(2,s)}$ and $c_{\text{R}}^{(2,s)}$ are the surface concentrations of species O and R corresponding to the application of potential E_2 , and c_{O}^* and c_{R}^* the initial concentrations of these species. q refers to spatial coordinates (r in the case of spheres and cylinders, x and y in the case of bands, and r and z in the case of discs), q^s to the value of q at the electrode surface, and $c_{\text{O}}^{(1)}$ and $c_{\text{R}}^{(1)}$ are the solutions corresponding to the application of the first potential E_1 . Note that condition (4.7) is a consequence of the flux conservation at the electrode surface when equidiffusivity is assumed for both O and R species [16].

Since the operators of Fick's second law are linear, the expressions for the concentrations $c_{\text{O}}^{(2)}$ and $c_{\text{R}}^{(2)}$ can be written as

$$c_{\text{O}}^{(2)}(q, t) = c_{\text{O}}^{(1)}(q, t) + \tilde{c}_{\text{O}}^{(2)}(q, t_2) \quad (4.10)$$

$$c_{\text{R}}^{(2)}(q, t) = c_{\text{R}}^{(1)}(q, t) + \tilde{c}_{\text{R}}^{(2)}(q, t_2) \quad (4.11)$$

where $\tilde{c}_{\text{O}}^{(2)}(q, t_2)$ and $\tilde{c}_{\text{R}}^{(2)}(q, t_2)$ are unknown functions to be determined.

It should be noted that for any value of t (with $0 \leq t \leq (\tau_1 + t_2)$), $c_{\text{O}}^{(1)}$ and $c_{\text{R}}^{(1)}$ fulfill the equations:

$$\frac{\partial c_i^{(1)}}{\partial t} = D \nabla^2 c_i^{(1)} \quad i = \text{O, R} \quad (4.12)$$

$$\left. \begin{array}{l} t \geq 0, q \rightarrow \infty \\ t = 0, q \geq q^s \end{array} \right\} c_{\text{O}}^{(1)} = c_{\text{O}}^*, c_{\text{R}}^{(1)} = c_{\text{R}}^* \quad (4.13)$$

$$t > 0, q = q^s,$$

$$c_{\text{O}}^{(1,s)} + c_{\text{R}}^{(1,s)} = c_{\text{O}}^* + c_{\text{R}}^* \quad (4.14)$$

$$c_{\text{O}}^{(1,s)} = e^{\eta_1} c_{\text{R}}^{(1,s)} \quad (4.15)$$

with

$$\eta_1 = \frac{F}{RT} (E_1 - E_c^{\theta'}) \quad (4.16)$$

and, from Eqs. (4.14) and (4.15), the surface concentrations $c_{\text{O}}^{(1,s)}$ and $c_{\text{R}}^{(1,s)}$ can be directly deduced (see also Eqs. (2.152) and (2.153) in Sect. 2.6),

$$c_{\text{O}}^{(1,s)} = \frac{e^{\eta_1}}{1 + e^{\eta_1}} (c_{\text{O}}^* + c_{\text{R}}^*) \quad (4.17)$$

$$c_{\text{R}}^{(1,s)} = \frac{c_{\text{O}}^* + c_{\text{R}}^*}{1 + e^{\eta_1}} \quad (4.18)$$

By inserting Eqs. (4.10)–(4.11) into Eqs. (4.4)–(4.8) and taking into account Eqs. (4.12)–(4.18), it is possible to express the boundary value problem in this second pulse only in terms of the new unknowns $\tilde{c}_{\text{O}}^{(2)}(q, t_2)$ and $\tilde{c}_{\text{R}}^{(2)}(q, t_2)$,

$$\frac{\partial \tilde{c}_i^{(2)}}{\partial t_2} = D \nabla^2 \tilde{c}_i^{(2)} \quad i = \text{O, R} \quad (4.19)$$

$$\left. \begin{array}{l} t_2 \geq 0, q \rightarrow \infty \\ t_2 = 0, q \geq q^s \end{array} \right\} \tilde{c}_{\text{O}}^{(2)} = \tilde{c}_{\text{R}}^{(2)} = 0 \quad (4.20)$$

$$t_2 > 0, q = q^s,$$

$$\tilde{c}_{\text{O}}^{(2,s)} + \tilde{c}_{\text{R}}^{(2,s)} = 0 \quad (4.21)$$

$$\tilde{c}_{\text{O}}^{(2,s)} = e^{\eta_2} \tilde{c}_{\text{R}}^{(2,s)} + \frac{e^{\eta_1} - e^{\eta_2}}{1 + e^{\eta_1}} (c_{\text{O}}^* + c_{\text{R}}^*) \quad (4.22)$$

By comparing Eqs. (4.13)–(4.15) and (4.20)–(4.22), it is clear that this second problem is quite similar to that solved when the first potential pulse is applied but with null initial conditions. At the electrode surface $\tilde{c}_{\text{O}}^{(2,s)}$ and $\tilde{c}_{\text{R}}^{(2,s)}$, take the following constant values:

$$\tilde{c}_{\text{O}}^{(2,\text{s})} = \frac{e^{\eta_1} - e^{\eta_2}}{(1 + e^{\eta_1})(1 + e^{\eta_2})} (c_{\text{O}}^* + c_{\text{R}}^*) \quad (4.23)$$

$$\tilde{c}_{\text{R}}^{(2,\text{s})} = -\frac{e^{\eta_1} - e^{\eta_2}}{(1 + e^{\eta_1})(1 + e^{\eta_2})} (c_{\text{O}}^* + c_{\text{R}}^*) \quad (4.24)$$

By inserting Eqs. (4.23) and (4.24) in Eqs. (4.10)–(4.11), and taking into account Eqs. (4.17) and (4.18), the surface concentrations corresponding to this second potential pulse are obtained

$$c_{\text{O}}^{(2,\text{s})} = c_{\text{O}}^{(1,\text{s})} + \tilde{c}_{\text{O}}^{(2,\text{s})} = \frac{e^{\eta_2}}{1 + e^{\eta_2}} (c_{\text{O}}^* + c_{\text{R}}^*) \quad (4.25)$$

$$c_{\text{R}}^{(2,\text{s})} = c_{\text{R}}^{(1,\text{s})} + \tilde{c}_{\text{R}}^{(2,\text{s})} = \frac{c_{\text{O}}^* + c_{\text{R}}^*}{1 + e^{\eta_2}} \quad (4.26)$$

being $c_{\text{O}}^{(2,\text{s})}$ and $c_{\text{R}}^{(2,\text{s})}$ only dependent of potential E_2 , as expected (see Eqs. (4.7) and (4.8)).

After demonstrating the similarity between the boundary value problem of the first and second potential pulses, the current corresponding to the second potential pulse at an electrode of any geometry can be written as (see Eq. (4.10))

$$\begin{aligned} \frac{I_2^{\text{G}}}{FA_{\text{G}}D} &= \left(\frac{\partial c_{\text{O}}^{(2)}}{\partial q_{\text{N}}} \right)_{q^{\text{s}}} = \left(\frac{\partial c_{\text{O}}^{(1)}}{\partial q_{\text{N}}} \right)_{q^{\text{s}}} + \left(\frac{\partial \tilde{c}_{\text{O}}^{(2)}}{\partial q_{\text{N}}} \right)_{q^{\text{s}}} = I_1^{\text{G}}(\tau_1 + t_2) + I_2^{\text{G}}(t_2) = \\ &= (c_{\text{O}}^* - c_{\text{O}}^{(1,\text{s})}) f_{\text{G}}(\tau_1 + t_2, q_{\text{G}}) - \tilde{c}_{\text{O}}^{(2,\text{s})} f_{\text{G}}(t_2, q_{\text{G}}) \end{aligned} \quad (4.27)$$

with f_{G} given in Table 2.3 of Sect. 2.6 for several electrode geometries. By taking into account that (see Eqs. (2.156) and (2.157) of Sect. 2.6),

$$\frac{I_1^{\text{G}}(\tau_1 + t_2)}{FA_{\text{G}}Dc_{\text{O}}^*} = \frac{1 - e^{\eta_1} (c_{\text{R}}^*/c_{\text{O}}^*)}{1 + e^{\eta_1}} f_{\text{G}}(\tau_1 + t_2, q_{\text{G}}) \quad (4.28)$$

and inserting the expressions of $c_{\text{O}}^{(1,\text{s})}$ and $\tilde{c}_{\text{O}}^{(2,\text{s})}$ given by Eqs. (4.17) and (4.23), into Eq. (4.27)

$$\frac{I_2^G}{FA_G D c_O^*} = \frac{1 - e^{\eta_1} (c_R^*/c_O^*)}{1 + e^{\eta_1}} f_G(\tau_1 + t_2, q_G) + (1 + (c_R^*/c_O^*)) \left(\frac{1}{1 + e^{\eta_2}} - \frac{1}{1 + e^{\eta_1}} \right) f_G(t_2, q_G) \quad (4.29)$$

is finally obtained

It is worth recalling that, as was indicated in Sect. 2.6, in the cases of non-uniformly accessible electrodes (discs and bands), the current is an average quantity resulting from an average flux over the electrode surface (see for example [17–19]).

4.2.1.1 Planar Electrodes

Equation (4.29) is applicable when both species are initially present in the solution independently of the geometry and size of the working electrode. In the case of planar electrodes

$$\frac{I_2^{\text{plane}}}{FA_s D c_O^*} = \frac{1}{1 + e^{\eta_1}} \frac{1}{\sqrt{\pi D (\tau_1 + t_2)}} + \left(\frac{1}{1 + e^{\eta_2}} - \frac{1}{1 + e^{\eta_1}} \right) \frac{1}{\sqrt{\pi D t_2}} \quad (4.30)$$

is obtained

It is also possible to deduce the expression of I_2^{plane} for the case of different diffusion coefficients, since the surface concentrations $c_O^{(1,s)}$ and $c_R^{(1,s)}$ are also constant at macroelectrodes when $D_O \neq D_R$ (see Eq. (2.20)). Under these conditions the current is given by [20, 21]:

$$\frac{I_2^{\text{plane}}}{FA c_O^* D_O \frac{1}{\sqrt{\pi D_O t_2}}} = \sqrt{\frac{t_2}{\tau_1 + t_2}} \frac{1 - e^{\eta_1} (c_R^*/c_O^*)}{1 + \gamma e^{\eta_1}} + \left(\frac{1}{1 + \gamma e^{\eta_2}} - \frac{1}{1 + \gamma e^{\eta_1}} \right) \left[1 + \frac{c_R^*}{\gamma c_O^*} \right] \quad (4.31)$$

with

$$\gamma = \sqrt{\frac{D_O}{D_R}} \quad (4.32)$$

4.2.1.2 Spherical Electrodes

For spherical electrodes, given that (see Table 2.3 of Sect. 2.6),

$$f_s(t, r_s) = \frac{1}{r_s} + \frac{1}{\sqrt{\pi Dt}} \quad (4.33)$$

by inserting Eq. (4.33) into Eq. (4.29) for the most usual case in which only species O is initially present (i.e., $c_R^* = 0$),

$$\begin{aligned} \frac{I_2^{\text{sph}}}{FA_s D c_O^*} &= \left(\frac{1}{1 + e^{\eta_1}} \right) \frac{1}{\sqrt{\pi D (\tau_1 + t_2)}} + \left(\frac{1}{1 + e^{\eta_2}} - \frac{1}{1 + e^{\eta_1}} \right) \frac{1}{\sqrt{\pi D t_2}} + \left(\frac{1}{1 + e^{\eta_2}} \right) \frac{1}{r_s} = \\ &= \frac{I_2^{\text{plane}}}{FA_s D c_O^*} + \frac{I_2^{\text{microsphe}}}{FA_s D c_O^*} \end{aligned} \quad (4.34)$$

is obtained

with r_s and A_s being the radius and area of the spherical electrode, I_2^{plane} is given by Eq. (4.30), and

$$\frac{I_2^{\text{microsphe}}}{FA_s D c_O^*} = \left(\frac{1}{1 + e^{\eta_2}} \right) \frac{1}{r_s} \quad (4.35)$$

The case of different diffusion coefficients of the electroactive species has been also considered for spherical electrodes, with the current corresponding to the second potential being much more complex (see Eq. (F.43) in Appendix F and reference [20]).

4.2.2 Double Pulse Chronoamperometry and Chronocoulometry

This section considers that the first potential pulse is set at values corresponding to diffusion-controlled cathodic limiting current conditions for the reactant ($E_1 \ll E_c^{\ominus'}$, $0 \leq t_1 \leq \tau_1$) and the second to diffusion-controlled anodic limiting current conditions for the electrogenerated product ($E_2 \gg E_c^{\ominus'}$, $0 \leq t_2 \leq \tau_2$), see Scheme 4.1. The use of these diffusion-controlled limiting currents, for which no kinetic influence is present, is very useful in the determination of diffusion coefficients of both oxidized and reduced species.

By making $e^{\eta_1} \rightarrow 0$ and $e^{\eta_2} \rightarrow \infty$ in Eq. (4.29), one obtains (see also Eq. (2.158) of Sect. 2.6),

$$\frac{I_{d,1}^G}{FA_G D c_O^*} = f_G(t_1, q_G), \quad 0 \leq t_1 \leq \tau_1 \quad (4.36)$$

$$\frac{I_{d,2}^G}{FA_G D c_O^*} = f_G(\tau_1 + t_2, q_G) - (1 + (c_R^*/c_O^*))f_G(t_2, q_G), \quad 0 \leq t_2 \leq \tau_2 \quad (4.37)$$

with $f_G(t, q_G)$ given in Table 2.3 of Sect. 2.6.

In the case of unequal diffusion coefficients, when spherical electrodes are considered, the currents of the first and second potential pulses under the above conditions are (see also Eq. (2.147) of Sect. 2.5.2 and Appendix F),

$$\frac{I_{d,1}^{\text{sph}}}{FA_s D_O c_O^*} = \frac{1}{\sqrt{\pi D_O t_1}} + \frac{1}{r_s} \quad 0 \leq t_1 \leq \tau_1 \quad (4.38)$$

$$\begin{aligned} \frac{I_{d,2}^{\text{sph}}}{FA_s D_O c_O^*} = & \left[\frac{1}{r_s} + \frac{1}{\sqrt{\pi D_O (\tau_1 + t_2)}} \right] - \frac{1}{\sqrt{\pi D_O t_2}} \left[1 + \frac{c_R^*}{\gamma c_O^*} \right] (1 \pm \xi_2) - \\ & - (\gamma \mp 1) \frac{1}{\sqrt{\pi D_O t_2}} \left\{ (\xi_2 \pm 1) [1 - H(\xi_1)] + \frac{\xi_1}{\sqrt{\pi}} [G(\beta) - 1] + \right. \\ & \left. + \frac{\gamma \xi_2}{\sqrt{\pi}} S(\beta, \xi_1) \right\} \quad 0 \leq t_2 \leq \tau_2 \end{aligned} \quad (4.39)$$

with

$$\xi_1 = \frac{2\sqrt{D_R(\tau_1 + t_2)}}{r_s} \quad (4.40)$$

$$\xi_2 = \frac{2\sqrt{D_R t_2}}{r_s} \quad (4.41)$$

$$\beta = \sqrt{\frac{t_2}{\tau_1 + t_2}} \quad (4.42)$$

$$G(\beta) = \beta \arcsin(\beta) + \sqrt{1 - \beta^2} \quad (4.43)$$

$$H(\xi_1) = \exp\left(\frac{(\xi_1)^2}{4}\right) \operatorname{erfc}(\xi_1/2) \quad (4.44)$$

$$S(\beta, \xi_1) = \sum_{\substack{i=1 \\ j=0}}^{\infty} \left[\frac{(-1)^{j+i} (\xi_1)^i \beta^{2j+1} p_i \prod_{l=0}^j (i - 2l + 1)}{(i+1)(2j+1)2^j(j+1)! \prod_{l=1}^i p_l} \right] \quad (4.45)$$

$$p_l = \frac{2\Gamma(1 + \frac{l}{2})}{\Gamma(\frac{l+1}{2})} \quad (4.46)$$

In Eq. (4.39), the upper sign refers to solution soluble product and the lower one to amalgam formation. When species R is amalgamated inside the electrode, the applicability of this analytical equation is limited by Koutecký approximation, which considers semi-infinite diffusion inside the electrode, neglecting its finite size and simplifying the calculations. Due to the limitations of this approximation, the analytical and numerical results coincide only for $\xi_1 < 1$ with a relative difference $\leq 1.7\%$ [20]. For higher values of ξ_1 , a numerical solution obtained with the condition $(\partial c_R / \partial r)_{r=0} = 0$ should be used.

Equations (4.38) and (4.39) are greatly simplified for the case of spherical ultramicroelectrodes. By making $r_s \ll \sqrt{\pi D_O t}$ in the expressions of $I_{d,1}^{\text{sph}}$ and $I_{d,2}^{\text{sph}}$ is deduced

$$\frac{I_{d,1}^{\text{microsphe}}}{FA_s D_O c_O^*} = \frac{1}{r_s} \quad 0 \leq t_1 \leq \tau_1 \quad (4.47)$$

$$\frac{I_{d,2}^{\text{microsphe}}}{FA_s D_O c_O^*} \cong -\frac{1}{r_s} \frac{c_R^*}{\gamma^2 c_O^*} \quad 0 \leq t_2 \leq \tau_2 \quad (4.48)$$

with γ given by Eq. (4.32).

Note that under steady-state conditions the second response will only exist if the reduced species is initially present ($c_R^* \neq 0$).

For planar electrodes, by making $E_1 - E_c^{\Theta'} \rightarrow -\infty$ in Eq. (2.34) of Sect. 2.2.2.2 and $E_2 - E_c^{\Theta'} \rightarrow \infty$ in Eq. (4.31) it is deduced

$$\frac{I_{d,1}^{\text{plane}}}{FAD_O c_O^*} = \frac{1}{\sqrt{\pi D_O t_1}} \quad 0 \leq t_1 \leq \tau_1 \quad (4.49)$$

$$\frac{I_{d,2}^{\text{plane}}}{FAD_O c_O^*} = \frac{1}{\sqrt{\pi D_O (\tau_1 + t_2)}} - \frac{1}{\sqrt{\pi D_O t_2}} \left[1 + \frac{c_R^*}{\gamma c_O^*} \right] \quad 0 \leq t_2 \leq \tau_2 \quad (4.50)$$

Equation (4.50) for the particular case of equal diffusion coefficients and $c_R^* = 0$ was deduced by Kambara [22] by applying the Superposition Principle.

The use of double potential pulse chronoamperometry is of great interest in electrochemistry for an accurate determination of both diffusion coefficients D_O and D_R , and this interest is enhanced when this technique is applied to small size spherical electrodes like the SMDE or gold microhemispheres or microspheres. There is a great number of redox couples for which highly unequal diffusion coefficients appear such as room temperature ionic liquids [23], ferrocene/

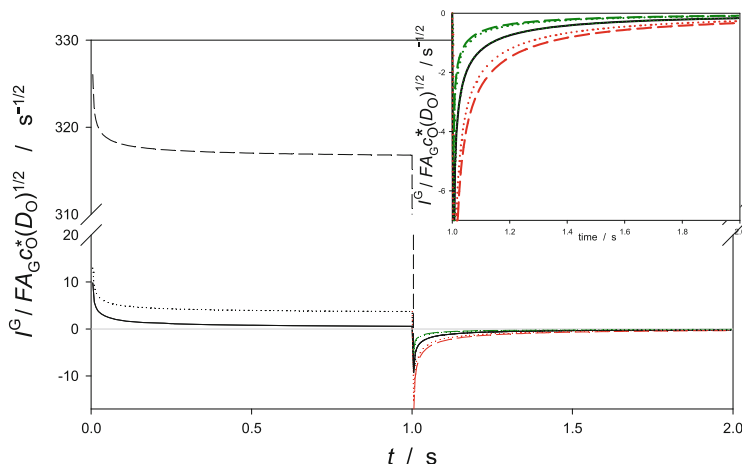


Fig. 4.1 Current density–time curves when both species are soluble in the electrolytic solution and only species O is initially present. Three electrode sizes are considered: planar electrode (*solid lines*), spherical electrode with $r_s = 10^{-3}$ cm (*dotted lines*), and spherical ultramicroelectrode with $r_s = 10^{-5}$ cm (*dashed lines*), and three γ values: $\gamma = 0.5$ (*green curves*), $\gamma = 1.0$ (*black curves*), and $\gamma = 2.0$ (*red curves*). The applied potential sequences are $E_1 - E_c^{\Theta'} \rightarrow -\infty$, $E_2 - E_c^{\Theta'} \rightarrow +\infty$. $\tau_1 = \tau_2 = 1$ s, $c_O^* = 1$ mM, $c_R^* = 0$, $D_O = 10^{-5}$ cm² s⁻¹. Taken from [20] with permission

ferrocinium ($\gamma = 0.89$ in acetonitrile [24]), *p*-benzoquinone and its cation radical ($\gamma = 0.84$ in acetonitrile [24]), ferrocyanide/ferricyanide ($\gamma = 1.08$ in aqueous solution [24, 25]), aromatic compounds with their corresponding cation radicals ($\gamma = 0.71 - 0.93$ in different organic solvents [26, 27]), or redox systems incorporated into polymeric matrices [28].

In order to establish the most appropriate conditions for the determination of the diffusion coefficients of both electroactive species by using Eqs. (4.38) and (4.39), it has been reported that when the reaction product is absent (i.e., $c_R^* = 0$) neither planar electrodes nor ultramicroelectrodes can be used in DPC for determining diffusion coefficients (see Eqs. (4.48) and (4.50)) because in these situations the anodic limiting current is either independent of D_R or null, respectively.

To check this, in Fig. 4.1 the influence of the electrode size on *current density–time* curves is shown for different γ values when both species are soluble in the electrolytic solution, with only species O initially present. As can be observed, the electrode radius has a great influence on the current density corresponding to the first potential pulse, increasing its value when the electrode size decreases as is well known.

It is interesting to highlight the case in which $D_O = D_R = D$ (i.e., $\gamma = 1$) since, surprisingly, in this situation the current density corresponding to the second potential pulse remains unaltered when the electrode radius varies from $r_s \rightarrow \infty$ (planar electrode) up to $r_s \rightarrow 0$ (ultramicroelectrodes). This can be easily

demonstrated from the analytical results, since from Eq. (4.39) it is deduced that the current density corresponding to the second pulse for any r_s value is given by

$$\frac{I_{d,2}^{\text{sph}}(\gamma = 1)}{A_s} = \frac{Fc_O^*\sqrt{D}}{\sqrt{\pi t_2}} \left[\left(\sqrt{\frac{t_2}{\tau_1 + t_2}} - 1 \right) - (c_R^*/c_O^*) \left(1 + \frac{\sqrt{\pi D t_2}}{r_s} \right) \right] \quad (4.51)$$

Thus, second pulse current density becomes independent of electrode radius when the reaction product is not initially present ($c_R^* = 0$):

$$\frac{I_{d,2}^{\text{sph}}(\gamma = 1)}{A_s} = \frac{Fc_O^*\sqrt{D}}{\sqrt{\pi t_2}} \left(\sqrt{\frac{t_2}{\tau_1 + t_2}} - 1 \right) \quad (4.52)$$

When $D_O \neq D_R$ ($\gamma \neq 1$) the current density corresponding to the second potential pulse is much less affected by the electrode size than that corresponding to the first potential. Regarding the γ influence, it is observed that *current density–time* curves corresponding to the first potential pulse are independent of D_R value, since cathodic limiting conditions are imposed. In contrast, γ value has a meaningful effect on the curves corresponding to the second potential pulse at spherical electrodes, so that the greater the D_R value the lower current density. This effect is more noticeable when the electrode radius decreases. However, a practical limit appears as a consequence of the decrease of the ratio $I_{d,2}^{\text{sph}}/I_{d,1}^{\text{sph}}$ at small electrodes, which makes it difficult to determine a small current density ($I_{d,2}^{\text{sph}}/A_s$) after a big current density ($I_{d,1}^{\text{sph}}/A_s$) in the same experiment. By studying the behavior of the ratio $I_{d,2}^{\text{sph}}/I_{d,1}^{\text{sph}}$, it is concluded that values of $\sqrt{D_O\tau_1}/r_s$ in the range $0.5 < \sqrt{D_O\tau_1}/r_s < 1.25$ are optimum for this purpose since the ratio $I_{d,2}^{\text{sph}}/I_{d,1}^{\text{sph}}$ is adequate, and $I_{d,2}^{\text{sph}}$ is sensitive to D_R ; for example, for $D_O = 10^{-5} \text{ cm}^2 \text{ s}^{-1}$ and $t_1 = 1 \text{ s}$ the optimum electrode radius is 25–65 μm . At planar electrodes the second potential *current density–time* curve is not sensitive to species R diffusion coefficient under these conditions ($c_R^* = 0$), as can be deduced from Eq. (4.50):

$$\frac{I_{d,2}^{\text{plane}}(\gamma \neq 1)}{A} = \frac{Fc_O^*\sqrt{D_O}}{\sqrt{\pi t_2}} \left(\sqrt{\frac{t_2}{\tau_1 + t_2}} - 1 \right) \quad (4.53)$$

which coincides with the current density at a spherical electrode when both diffusion coefficients are equal (see Fig. 4.1).

So, it can be concluded that, when reaction product is not initially present, DPC of limiting currents can only be used for determining both diffusion coefficients when spherical electrodes are used. The use of planar electrodes or ultramicroelectrodes for calculating D_R needs species R to be initially present.

The current–time curve corresponding to the application of the second potential is very sensitive to the presence of assimilation or amalgamation processes at spherical electrodes. In order to check this in Fig. 4.2, it can be seen the

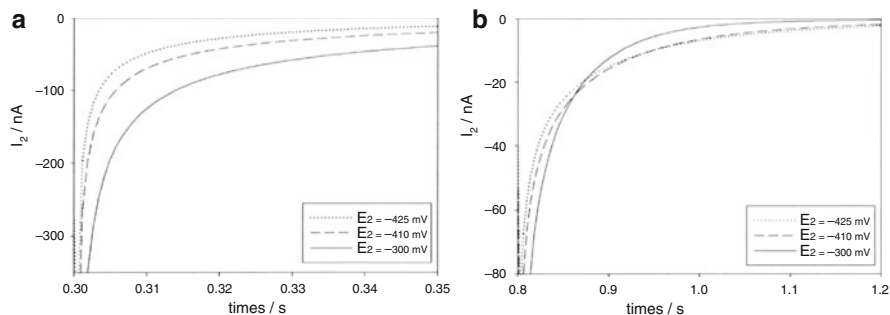


Fig. 4.2 Experimental chronoamperometric curves of the second pulse for different E_2 values corresponding to the re-oxidation of Tl(Hg) on a hemispherical mercury electrode with: (a) $r_s = 50 \mu\text{m}$; $\tau_1 = 300 \text{ ms}$; (b) $r_s = 25 \mu\text{m}$; $\tau_1 = 800 \text{ ms}$; 0.2 mM TlNO_3 , 0.1M KNO_3 . Reproduced with permission of reference [29]

chronoamperometric curves corresponding to the second potential pulse for different E_2 values for the reduction of Tl^+ at hemispherical mercury electrodes of two different sizes ($r_s = 50 \mu\text{m}$, Fig. 4.2a, and $r_s = 25 \mu\text{m}$, Fig. 4.2b). As shown in Fig. 4.2a, when the electrode size increases the “usual” behavior of the current–potential curves is observed, so the less positive the E_2 value, the smaller the oxidation current at any time. In contrast, for the smaller radius (Fig. 4.2b), the decrease of the current under anodic limiting conditions is very fast as a consequence of the depletion of the reduced species during the release/re-oxidation step. Unlike what happens with medium-sized electrodes, this gives rise to the crossing of the chronoamperometric curves at a given time (crossing time) and after this time the limiting current is smaller than that corresponding to a less anodic potential. This behavior occurs because at the less positive potential the depletion of species R is slower and so is the decay of the current with time [29].

Although present study has so far the been focused on current–potential curves, there are some experimental situations in which it is of interest to analyze the charge–potential ones. Chronocoulograms can be obtained from the integration of the corresponding chronoamperograms. Under limiting condition like those discussed in this section, the expressions of the charge–time curves corresponding to the application of the first and second potential pulses when the diffusion coefficients of species O and R are assumed equals and $c_R^* = 0$ are given by (see Eqs. (4.36) and (4.37)):

$$\frac{Q_{d,1}^G}{FA_G D C_O^*} = \text{integral } f_{t_1,G} \quad 0 \leq t_1 \leq \tau_1 \quad (4.54)$$

$$\frac{Q_{d,2}^G}{FA_G D C_O^*} = \left[\text{integral } f_{(\tau_1+t_2),G} - \text{integral } f_{t_2,G} \right] \quad 0 \leq t_2 \leq \tau_2 \quad (4.55)$$

with

$$\left. \begin{aligned} \text{integral } f_{t_1, G} &= \int_0^{t_1} f_G(u, q_G) du \\ \text{integral } f_{(\tau_1+t_2), G} &= \int_0^{\tau_1+t_2} f_G(u, q_G) du \\ \text{integral } f_{t_2, G} &= \int_0^{t_2} f_G(u, q_G) du \end{aligned} \right\} \quad (4.56)$$

and $f_G(t, q_G)$ given in Table 2.3 of Sect. 2.6.

For a planar electrode it is fulfilled that for a given value of t (see [30]),

$$\text{integral } f_{t, \text{plane}} = \frac{2\sqrt{t}}{\sqrt{\pi D}} \quad (4.57)$$

and Eqs. (4.54) and (4.55) can be written as

$$Q_{d,1}^{\text{plane}} = FADc_O^* \frac{2\sqrt{t_1}}{\sqrt{\pi D}} \quad (4.58)$$

$$Q_{d,2}^{\text{plane}} = FADc_O^* \frac{2}{\sqrt{\pi D}} [\sqrt{\tau_1 + t_2} - \sqrt{t_2}] \quad (4.59)$$

In the case of spherical electrodes for a given value of t ,

$$\text{integral } f_{t, \text{sphe}} = \frac{2\sqrt{t}}{\sqrt{\pi D}} + \frac{t}{r_s} \quad (4.60)$$

and, therefore, the charge–time response can be written as,

$$Q_{d,1}^{\text{sphe}} = FA_s D c_O^* \left(\frac{2\sqrt{t_1}}{\sqrt{\pi D}} + \frac{t_1}{r_s} \right) \quad (4.61)$$

$$Q_{d,2}^{\text{sphe}} = FA_s D c_O^* \left[\frac{2}{\sqrt{\pi D}} (\sqrt{\tau_1 + t_2} - \sqrt{t_2}) + \frac{\tau_1}{r_s} \right] \quad (4.62)$$

The time variation of the normalized converted charges for planar, spherical, and disc electrodes can be seen in Fig. 4.3, for which a radius of 10 μm has been assumed for the spherical and disc electrodes. $Q_{\tau_1}^G$ is the maximum converted charge for the first potential pulse corresponding to a time $t_1 = \tau_1$, and is given by

$$\frac{Q_{\tau_1}^G}{FA_G D c_O^*} = \text{integral } f_{\tau_1, G} \quad (4.63)$$

with $\text{integral } f_{\tau_1, G} = \int_0^{\tau_1} f_G(u, q_G) du$.

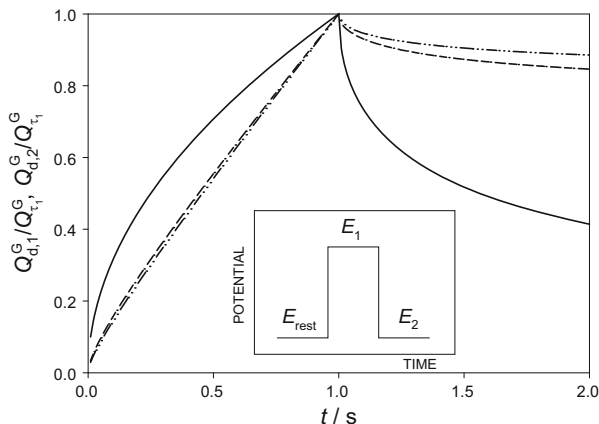


Fig. 4.3 Normalized charge–time curves for a double potential step with $E_1 \ll E_c^{\Theta'}$ ($0 \leq t_1 \leq \tau_1$) and $E_2 \gg E_c^{\Theta'}$ ($\tau_1 \leq t \leq (\tau_1 + \tau_2)$), calculated from Eqs. (4.54) and (4.55) for planar (solid lines), spherical (dashed lines), and disc (dashed-dotted lines) electrodes. $Q_{r,1}$ is given by Eq. (4.63). In the inner figure, the potential perturbation has been plotted with E_{rest} being the resting potential of null current previous to the application of E_1 and $E_2 = E_{\text{rest}}$. $D = 10^{-5} \text{ cm}^2 \text{ s}^{-1}$, $\tau_1 = \tau_2 = 1 \text{ s}$

It is clear from Fig. 4.3 that the temporal evolution of the converted charge is electrode-size and shape depending. For spherical and disc electrodes, the evolution of $(Q_{d,1}^G/Q_{r,1}^G)$ is quasi-linear (since for this radius $Q_{d,1}^{\text{sph}} \cong Q_{d,1}^{\text{disc}} \approx t_1/\tau_1$; see Eq. (4.61) and Table 2.3 of Sect. 2.6), whereas for the second potential pulse the amount of converted charge is much smaller than that obtained at a planar electrode (macroelectrode). Indeed, when the electrode radius becomes small enough the converted charge for the second potential pulse is constant and coincides with $Q_{r,1}^G$ (for example, from Eq. (4.62) in the limit $r_s \ll \sqrt{\pi D t_1}$ the expression $Q_{d,2}^{\text{sph}} \cong F A_s D c_O^* \tau_1 / r_s$ is obtained). This result is in line with those plotted in Fig. 4.1 for the current–time curves.

Note that, in agreement with Eq. (4.55) and due to its cumulative character, the charge corresponding to the second potential pulse tends to $Q_{r,1}^G$ when $t_2 \rightarrow 0$. Therefore, the reverse charge due solely to the second potential, $Q_{r,2}^G$, is given as,

$$\begin{aligned} Q_{r,2}^G &= Q_{r,1}^G - Q_{d,2}^G \\ &= F A_G D c_O^* \left[\text{integral } f_{\tau_1, G} - \text{integral } f_{(\tau_1+t_2), G} + \text{integral } f_{t_2, G} \right] \quad (4.64) \end{aligned}$$

Equations (4.54) and (4.55) only consider the “faradaic” charge, that is, only the converted charge due to the redox conversion of species O and R. The total converted charge should contain also a contribution due to the double layer charging process (Q_c) and, if there is adsorption of redox species, an addend which accounts the charge due to the reduction of these immobilized molecules

($Q_a = FAF_T$, with F_T being the total excess of redox species). In absence of adsorption of reactants, and assuming that the second potential pulse returns to the initial resting value E_{rest} (see Fig. 4.3), Eqs. (4.54) and (4.64) can be written as

$$\left. \begin{aligned} Q_{d,1}^G &= FA_G D c_O^* \int f_{t_1,G} + Q_c \\ Q_{r,2}^G &= FA_G D c_O^* \left[\int f_{\tau_1,G} - \int f_{(\tau_1+t_2),G} + \int f_{t_2,G} \right] + Q_c \end{aligned} \right\} \quad (4.65)$$

in such a way that the plot of $Q_{d,1}^G$ versus $\int f_{t_1,G}$ and of $Q_{r,2}^G$ versus $\left[\int f_{\tau_1,G} - \int f_{(\tau_1+t_2),G} + \int f_{t_2,G} \right]$ should be linear with the intercept of both lines being equal to Q_c in agreement with the potential perturbation applied. Note also that when adsorption of redox species takes place the intercept reflects the value of the adsorbed charge Q_a (for a detailed discussion of the different possibilities, see [31]).

The charge is a valuable magnitude for identifying the presence of homogeneous chemical reactions or, in general, deviations from a pure faradaic behavior. Thus, in absence of adsorption of redox species, the normalized charge-time curves can be written as

$$\left. \begin{aligned} \frac{Q_{d,1}^{G,n}}{Q_{\tau_1}^G} &= \frac{\int f_{t_1,G}}{\int f_{\tau_1,G}} \\ \frac{Q_{r,2}^{G,n}}{Q_{\tau_1}^G} &= 1 - \frac{\int f_{(\tau_1+t_2),G}}{\int f_{\tau_1,G}} + \frac{\int f_{t_2,G}}{\int f_{\tau_1,G}} \end{aligned} \right\} \quad (4.66)$$

The ratios given in Eq. (4.66) are only dependent on the electrode shape and size but not on parameters related to the electrode reaction, like the number of transferred electrons, the initial concentration of oxidized species, or the diffusion coefficient D . For fixed time and size, the values of $Q_{d,1}^{G,n}$ or $Q_{r,2}^{G,n}$ are characteristic for a simple charge transfer (see Fig. 4.4 for the plot of $Q_{r,2}^{G,n}$ calculated at time $(\tau_1 + \tau_2)$ for planar, spherical, and disc electrodes) and, as a consequence, deviations from this value are indicative of the presence of lateral processes (chemical instabilities, adsorption, non-idealities, etc.) [4, 32]. Additionally, for nonplanar electrodes, these values allow to the estimation of the electrode radius when simple electrode processes are considered.

4.2.3 Reverse Pulse Voltammetry

As stated in Sect. 4.1, in RPV a series of double potential pulses are applied where the product is generated always in the first one under diffusion-controlled conditions whereas the second potential pulse is set at different values (E_2) and the current is recorded at the end of this second pulse (I_2^G , measured at $t_2 = \tau_2$) (see Scheme 4.2).

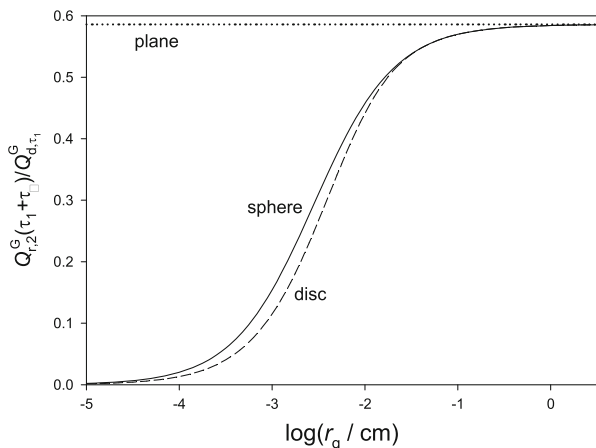


Fig. 4.4 Normalized net charge, corresponding to the second potential pulse applied, calculated from Eq. (4.66) for a time $t = (\tau_1 + \tau_2)$ for planar (dotted line), spherical (solid line), and disc (dashed line) electrodes as a function of the electrode radius r_G (with $r_G = r_s$ for a spherical electrode and $r_G = r_d$ for a disc one). $Q_{\tau_1}^G$ is given by Eq. (4.63). $D = 10^{-5}$ cm² s⁻¹, $\tau_1 = \tau_2 = 1$ s

Thus, apart from information about the mass transport and reactivity of the product (analogously to DPC), the thermodynamics and kinetics of the electron transfer can be studied from the position and shape of the RPV curve: I_2^G versus E_2 .

The expression for the current in this technique, valid for any electrode geometry when the diffusion coefficients of species O and R are assumed as equal, can be obtained from Eq. (4.29) by making $e^{\eta_1} \rightarrow 0$ and assuming $c_R^* = 0$ for the sake of simplicity,

$$\frac{I_{\text{RPV}}^G}{FA_G D c_O^*} = f_G(\tau_1 + \tau_2, q_G) - \frac{e^{\eta_2}}{1 + e^{\eta_2}} f_G(\tau_2, q_G) \quad (4.67)$$

Equation (4.67) takes the following expressions for disc, spherical, and planar electrodes:

$$I_{\text{RPV,N}}^{\text{disc}} = \frac{I_{\text{RPV}}^{\text{disc}}}{I_{\text{d,1}}^{\text{plane}}(\tau_2)} = \sqrt{\pi D \tau_2} \left(f_d(\tau_1 + \tau_2, r_d) - \frac{e^{\eta_2}}{1 + e^{\eta_2}} f_d(\tau_2, r_d) \right) \quad (4.68)$$

$$I_{\text{RPV,N}}^{\text{sph}} = \frac{I_{\text{RPV}}^{\text{sph}}}{I_{\text{d,1}}^{\text{plane}}(\tau_2)} = \frac{\sqrt{\pi D \tau_2}}{r_s} + \sqrt{\frac{\tau_2}{\tau_1 + \tau_2}} - \frac{e^{\eta_2}}{1 + e^{\eta_2}} \left(\frac{\sqrt{\pi D \tau_2}}{r_s} + 1 \right) \quad (4.69)$$

$$I_{\text{RPV,N}}^{\text{plane}} = \frac{I_{\text{RPV}}^{\text{plane}}}{I_{\text{d,1}}^{\text{plane}}(\tau_2)} = \sqrt{\frac{\tau_2}{\tau_1 + \tau_2}} - \frac{e^{\eta_2}}{1 + e^{\eta_2}} \quad (4.70)$$

with η_2 given in Eq. (4.9) and f_d being a function of time and of the disc radius r_d given in Table 2.3 of Sect. 2.6 and $I_{\text{d,1}}^{\text{plane}}(\tau_2)$ given by Eq. (4.49) with $t_1 = \tau_2$ and $D_0 = D$.

From Eq. (4.67), it is possible to obtain an expression for the cross potential (null current potential) of the RPV curve valid for any electrode geometry

$$E_{\text{cross}} = E_c^{\Theta'} + \frac{RT}{F} \ln \left(\frac{f_G(\tau_1 + \tau_2, q_G)}{f_G(\tau_2, q_G) - f_G(\tau_1 + \tau_2, q_G)} \right) \quad (4.71)$$

From Eqs. (4.68)–(4.70), it is clear that the anodic normalized limiting currents (corresponding to $e^{\eta/2} \rightarrow \infty$) obtained for planar and spherical electrodes have an identical expression, and are only dependent on the ratio between the time lengths of the first and second potential pulse, τ_1 and τ_2 ,

$$I_{\text{RPV,N}}^{\text{plane}}(E_2 \gg E_c^{\Theta'}) = I_{\text{RPV,N}}^{\text{sph}}(E_2 \gg E_c^{\Theta'}) = \sqrt{\frac{\tau_2}{\tau_1 + \tau_2}} - 1 \quad (4.72)$$

In the case of disc electrodes, the anodic normalized limiting current depends on the disc radius through the function f_d , which is independent of the potential (see Table 2.3 of Sect. 2.6). Therefore, the inflection point of the $I_{\text{RPV}}^G - E_2$ curve of the RPV curve (mid-wave potential, $E_{\text{mid,RPV}}$) coincides with the half wave potential, which can be obtained from Eq. (4.67) independently of the electrode geometry and is given by,

$$E_{\text{mid,RPV}} = E_{1/2}^r = E_c^{\Theta'} \quad (4.73)$$

In Fig. 4.5 it can be seen the influence of τ_2 on the normalized RPV curves calculated from planar, spherical, and disc electrodes from Eqs. (4.67) and (4.36). From these curves, it can be observed that the decrease of τ_2 causes an increase of the anodic limiting current (with this increase being more noticeable in the case of planar electrodes), whereas it has no effect on the half-wave potential of the responses (marked as a vertical dotted line).

When the diffusion coefficients of both electroactive species are assumed as different, a general solution for the RPV response at any electrode geometry has not been found. In the case of spherical electrodes, the response is rather complex and it can be found in reference [33] (see also Eq. (F.42) in Appendix F). From this solution, the particular cases of planar and spherical ultramicroelectrodes can be directly obtained,

$$I_{\text{RPV,N}}^{\text{plane}} = \sqrt{\frac{\tau_2}{\tau_1 + \tau_2}} - \frac{\gamma e^{\eta/2}}{1 + \gamma e^{\eta/2}} \quad (4.74)$$

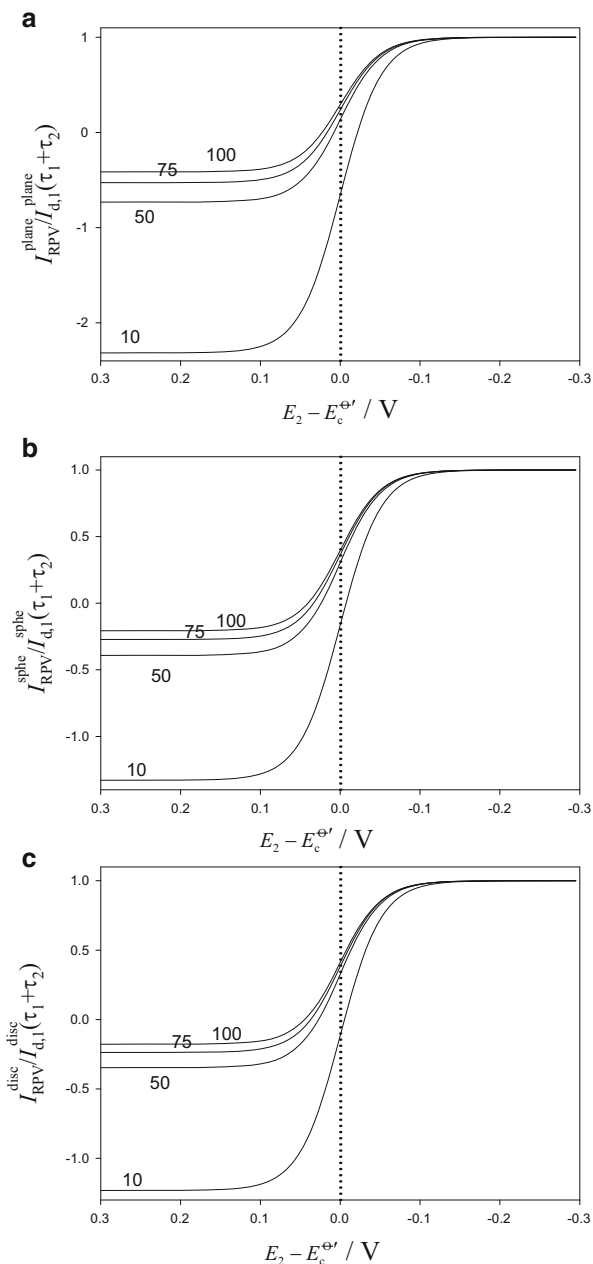
$$I_{\text{RPV,N}}^{\text{microsphe}} = \frac{I_{\text{RPV}}^{\text{microsphe}}}{I_{\text{d,c}}^{\text{sph,ss}}} \rightarrow \frac{1}{1 + \gamma^2 e^{\eta/2}} \quad (4.75)$$

with

$$I_{\text{d,c}}^{\text{sph,ss}} = FA_s D_{\text{O}} c_{\text{O}}^* \frac{1}{r_s} \quad (4.76)$$

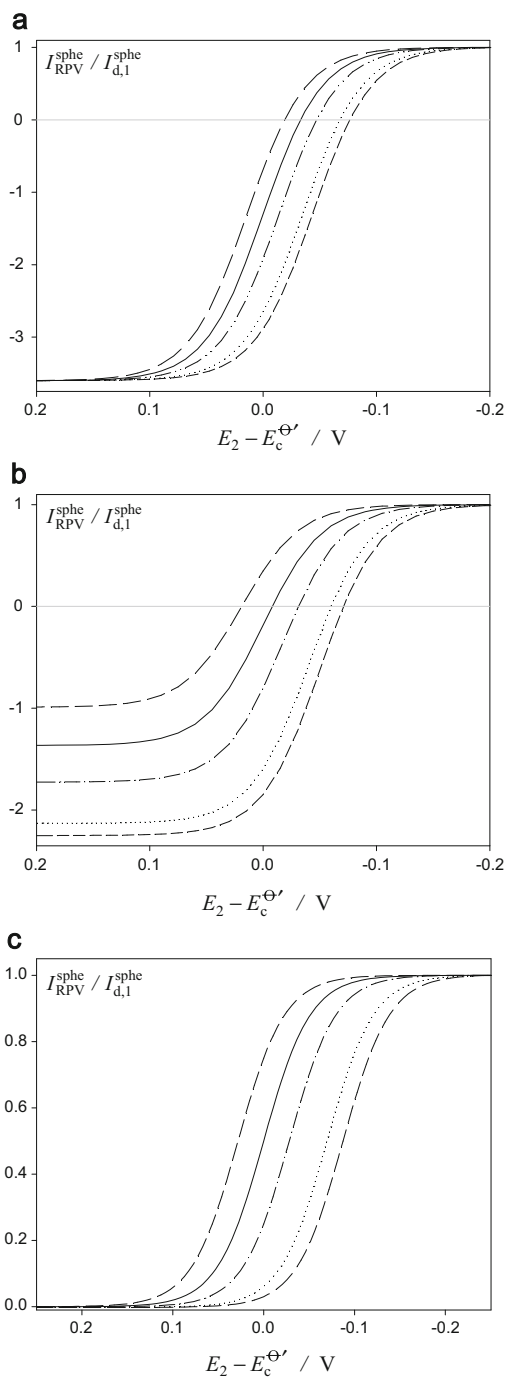
Fig. 4.5 Influence of τ_2 on the normalized RPV curves calculated from planar (a), spherical (b) and disc (c) electrodes from Eqs. (4.67) and (4.36).

$r_s = r_d = 25 \mu\text{m}$,
 $D = 10^{-5} \text{ cm}^2 \text{ s}^{-1}$,
 $\tau_1 = 1 \text{ s}$. The values of τ_2 (in ms) appear on the curves. Vertical dotted lines mark the mid-wave potential



The effect of the electrode radius and of D_R on the RPV curves can be seen in Fig. 4.6. It is observed that an increase of D_R gives rise to a shift of the RPV curve toward more positive potentials regardless of the electrode size. Nevertheless, the influence of D_R on the anodic limiting current depends on the electrode size. Thus,

Fig. 4.6 Normalized RPV curves when only species O is initially present for three electrode sizes: planar electrode (a), spherical electrode with $r_s = 3 \times 10^{-3}$ cm (b), and ultramicroelectrode with $r_s < 10^{-6}$ cm (c) calculated from Eq. (F.43) of Appendix F. $I_{d,1}^{\text{sphe}} = FA_s D_O c_O^* (1 / \sqrt{\pi D_O (\tau_1 + \tau_2)} + 1 / r_s)$ (see Eq. (4.36)). Five γ values are considered: $\gamma^2 = 1/10$ (long dashed line), $\gamma^2 = 1/3$ (dash-dotted line), $\gamma^2 = 1$ (solid line), $\gamma^2 = 3$ (dotted line), and $\gamma^2 = 10$ (dashed line). $\tau_1 = 1$ s, $\tau_2 = 0.05$ s, $c_O^* = 1$ mM, $c_R^* = 0$, $D_O = 10^{-5}$ cm² s⁻¹. Reproduced with permission of [33]



this influence is null for planar electrodes (Fig. 4.6a), meaningful at microelectrodes ($r_s \sim 3 \times 10^{-3}$ cm) and again negligible at spherical ultramicroelectrodes. These conclusions can be extended for other microelectrode geometries (Fig 4.6b, c). Under the conditions considered in the figure, which are typical of aqueous solutions ($D_O = 10^{-5}$ cm² s⁻¹, $\tau_1 = 1$ s), electrode radii between 25 and 65 μ m are optimum for the determination of D_R from the anodic limiting current values [20] (besides, the ratio between the limiting currents may offer better tolerance to possible uncertainties in the values of the bulk concentration and/or the electrode radius). Therefore, in conventional solvents ordinary microelectrodes are very appropriate for the measurement of both diffusion coefficients of the redox couple in the same experiment with RPV. In other media like, for example, ionic liquids, the diffusion coefficients of the electroactive species are significantly smaller ($D_R \sim 10^{-7}$ cm² s⁻¹ [23, 33, 34]) so ultramicroelectrodes must be used to have a good sensitivity. The decrease of the anodic limiting current when the diffusion coefficient of the reduced species increases is due to the greater diffusion of species R toward the bulk solution.

4.2.4 Differential Double Pulse Voltammetry

In the differential double pulse techniques, the current response is the difference $\Delta I^G = I_2^G - I_1^G$ obtained when two consecutive potentials E_1 and E_2 are applied (with the difference $\Delta E = E_2 - E_1$ called pulse amplitude being constant during each experiment; see Scheme 4.3). The theoretical expressions for the $\Delta I^G - E_1$ curve of reversible processes under planar diffusion were given by Parry and Osteryoung [35] and Ruzic and Sluyter-Rehbach [36].

The subtractive nature of signal and the rapid decay of the charging current in a constant potential pulse give rise to well-defined peak-shaped curves that can be characterized through the peak current ($\Delta I^{G,\text{peak}}$), the peak potential ($E_{1,2}^{G,\text{peak}}$), and the half peak width, $W^{1/2}$. Differential double pulse techniques emulate the first derivative of the NPV curve and the signal coincides with it for small values of ΔE (i.e., for $\Delta E \ll RT/F$) [37]. Thus, by subtracting the expressions of I_1^G and I_2^G measured at the end of their respective potential pulses given by Eqs. (4.28) and (4.29), respectively, valid for any electrode geometry when the diffusion coefficients of species O and R are assumed as equal (with $c_R^* = 0$), we get

$$\begin{aligned} \Delta I^G = I_2^G(\tau_1 + \tau_2) - I_1^G(\tau_1) = FA_G D c_O^* & \left(\frac{1}{1 + e^{\eta_1}} f_G(\tau_1 + \tau_2, q_G) + \right. \\ & \left. + \left(\frac{1}{1 + e^{\eta_2}} - \frac{1}{1 + e^{\eta_1}} \right) f_G(\tau_2, q_G) - \frac{1}{1 + e^{\eta_1}} f_G(\tau_1, q_G) \right) \end{aligned} \quad (4.77)$$

In DDPV, the duration of the second pulse is much shorter than the first one $\tau_1/\tau_2 = 50 - 100$ such that it can be assumed that $f_G(\tau_1 + \tau_2, q_G) \cong f_G(\tau_1, q_G)$ and, therefore, Eq. (4.77) simplifies to

$$\Delta I_{\text{DDPV}}^G = FA_G D c_O^* \left(\frac{1}{1 + e^{\eta_2}} - \frac{1}{1 + e^{\eta_1}} \right) f_G(\tau_2, q_G). \quad (4.78)$$

The applicability of Eq. (4.78) is dependent on the ratio τ_1/τ_2 , and on the electrode size. So, the radius range of validity of this expression broadens when the ratio τ_1/τ_2 increases.

Equation (4.78) takes the following expressions for disc, spherical, and planar electrodes,

$$\Delta I_{\text{DDPV,N}}^{\text{disc}} = \frac{\Delta I_{\text{DDPV}}^{\text{disc}}}{I_{\text{d},1}^{\text{plane}}(\tau_2)} = \sqrt{\pi D \tau_2} \left(\frac{1}{1 + e^{\eta_2}} - \frac{1}{1 + e^{\eta_1}} \right) f_d(\tau_2, r_d) \quad (4.79)$$

$$\Delta I_{\text{DDPV,N}}^{\text{sph}} = \frac{\Delta I_{\text{DDPV}}^{\text{sph}}}{I_{\text{d},1}^{\text{plane}}(\tau_2)} = \left(\frac{1}{1 + e^{\eta_2}} - \frac{1}{1 + e^{\eta_1}} \right) \left(\frac{\sqrt{\pi D \tau_2}}{r_s} + 1 \right) \quad (4.80)$$

$$\Delta I_{\text{DDPV,N}}^{\text{plane}} = \frac{\Delta I_{\text{DDPV}}^{\text{plane}}}{I_{\text{d},1}^{\text{plane}}(\tau_2)} = \left(\frac{1}{1 + e^{\eta_2}} - \frac{1}{1 + e^{\eta_1}} \right) \quad (4.81)$$

with η_2 and η_1 given by Eqs. (4.9) and (4.16), respectively, $I_{\text{d},1}^{\text{plane}}(\tau_2)$ given by Eq. (4.49) with $t_1 = \tau_2$ and $D_O = D$. Note that Eq. (4.80) for spherical electrodes is generally applicable for $\tau_1/\tau_2 \geq 50$ with an error lower than 0.2 % in the region around DDPV peak for any electrode size.

When different diffusion coefficients are considered, the expression for spherical electrodes is given in Eq. (4) of reference [38]. From this equation, the particular cases of planar and spherical ultramicroelectrodes can be directly obtained,

$$\Delta I_{\text{DDPV,N}}^{\text{plane}} = \frac{\Delta I_{\text{DDPV}}^{\text{plane}}}{I_{\text{d},1}^{\text{plane}}(\tau_2)} = \gamma \left(\frac{1}{1 + \gamma e^{\eta_2}} - \frac{1}{1 + \gamma e^{\eta_1}} \right) \quad (4.82)$$

$$\Delta I_{\text{DDPV,N}}^{\text{microsph}} = \frac{\Delta I_{\text{DDPV}}^{\text{microsph}}}{I_{\text{d},c}^{\text{sph,ss}}} = \gamma^2 \left(\frac{1}{1 + \gamma^2 e^{\eta_2}} - \frac{1}{1 + \gamma^2 e^{\eta_1}} \right) \quad (4.83)$$

with γ and $I_{\text{d},c}^{\text{sph,ss}}$ given by Eqs. (4.32) and (4.76), respectively.

In this section, we use the average of the two stepped potentials as potential axis

$$\left. \begin{aligned} E_{1,2} &= \frac{E_1 + E_2}{2} \\ \eta_{1,2} &= \frac{F}{RT} (E_{1,2} - E_c^{\ominus}) \end{aligned} \right\} \quad (4.84)$$

instead of the usual E_1 -value.¹ Note that this choice gives the advantage that the peak potential coincides with the half-wave potential when both diffusion coefficients are equal, regardless of the electrode size and shape. Moreover, for a given experimental system (electrode geometry, diffusion coefficients) the DDPV curves corresponding to a negative pulse height ($\Delta E < 0$, normal mode) and to a positive one ($\Delta E > 0$, reverse mode) are fully symmetrical with respect to the potential axis for electrodes of any geometry and size (Eqs. 4.78–4.83).

For the particular cases studied here, it is possible to deduce simple analytical expressions for the values of peak potential and peak current. The peak potential ($E_{1,2}^{G,\text{peak}}$) is obtained by equaling the derivative $d\Delta I_{\text{DDPV}}^G/dE_{1,2}$ to zero. Next, by substituting $E_{1,2}^{G,\text{peak}}$ in the expression for ΔI_{DDPV}^G , the peak current ($\Delta I_{\text{DDPV}}^{G,\text{peak}}$) is immediately deduced.

In all the cases, the expression for the current separates into two factors, one dependent on τ_2 and/or r_s or r_d , and another dependent on γ ($= \sqrt{D_O/D_R}$) (in the case of planar electrodes), E_1 and E_2 . As only the second factor varies “along” DDPV scan, the peak potential is only a function of the parameters included in this factor, and so is independent of time and electrode geometry.

– *Peak parameters for any electrode geometry by assuming $D_O = D_R = D$:*

$$E_{1,2}^{G,\text{peak}} = E_{1/2}^r = E_c^{\phi'} \quad (4.85)$$

$$\Delta I_{\text{DDPV}}^{G,\text{peak}} = FA_G D c_O^* f_G(\tau_2, q_G) \tanh\left(\frac{F}{RT} \frac{|\Delta E|}{4}\right) \quad (4.86)$$

Note that Eq. (4.85) is fulfilled for the $\Delta I_{\text{DDPV}}^G - E_{1,2}$ curve whereas for the $\Delta I_{\text{DDPV}}^G - E_1$ one, the expression of the peak potential is $E_1^{G,\text{peak}} = E_c^{\phi'} - |\Delta E|/2$ [38].

Under these conditions, the peak potential is independent of the electrode geometry considered. For small values of the pulse amplitude ($|\Delta E| \ll RT/F$) the DDPV current coincides with the derivative of the Normal Pulse Voltammetric curve at τ_2 , being in these conditions $\tanh(F|\Delta E|/(4RT)) \cong F|\Delta E|/(4RT)$ and the peak current [37, 39],

$$\left(\frac{\Delta I_{\text{DDPV}}^{G,\text{peak}}}{(F|\Delta E|/(RT))}\right)_{|\Delta E| \ll RT/F} = \frac{1}{4} FA_G D c_O^* f_G(\tau_2, q_G) \quad (4.87)$$

¹ The expression $\left(\frac{1}{1+\gamma e^{\eta_2}} - \frac{1}{1+\gamma e^{\eta_1}}\right)$, which depends on E_1 and E_2 through η_1 and η_2 , can be written as a function of $E_{1,2}$ and ΔE , since $\exp(\eta_1) = \exp(\eta_{1,2})/\exp(F\Delta E/2RT)$ and $\exp(\eta_2) = \exp(\eta_{1,2})\exp(F\Delta E/2RT)$. Note that the peak current and the half peak width are not affected by this change.

– *Peak parameters for planar electrodes* ($D_O \neq D_R$):

When the diffusion coefficients are different, the peak potential coincides with the “reversible” half-wave potential ($E_{1,2}^r$), whose value depends on γ ($= \sqrt{D_O/D_R}$), enabling determination of D_R once D_O is known,

$$E_{1,2}^{\text{plane, peak}} = E_{1/2}^{\text{r, plane}} = E_c^{\Theta'} + \frac{RT}{F} \ln\left(\frac{1}{\gamma}\right) \quad (4.88)$$

$$\Delta I_{\text{DDPV}}^{\text{plane, peak}} = \frac{FA\sqrt{D_O c_O^*}}{\sqrt{\pi\tau_2}} \tanh\left(\frac{F}{RT} \frac{|\Delta E|}{4}\right) \quad (4.89)$$

Again, for the $\Delta I_{\text{DDPV}}^{\text{plane}} - E_{1,2}$ curve the expression of the peak potential is $E_{1,2}^{\text{plane, peak}} = E_{1/2}^{\text{r, plane}}$ [4, 35, 36].

– *Peak parameters for microspheres and microdiscs*:

At spherical and disc ultramicroelectrodes under steady-state conditions the peak potential coincides with the “reversible” half-wave potential ($E_{1/2}^{\text{micro}}$),

$$E_{1,2}^{\text{microsphe, peak}} = E_{1,2}^{\text{microdisc, peak}} = E_{1/2}^{\text{r, micro}} = E_c^{\Theta'} + \frac{RT}{F} \ln\left(\frac{1}{\gamma^2}\right) \quad (4.90)$$

and the peak current is

$$\left. \begin{aligned} \Delta I_{\text{DDPV}}^{\text{microsphe, peak}} &= F4\pi r_s D_O c_O^* \tanh\left(\frac{F}{RT} \frac{|\Delta E|}{4}\right) \\ \Delta I_{\text{DDPV}}^{\text{microdisc, peak}} &= 4F r_d D_O c_O^* \tanh\left(\frac{F}{RT} \frac{|\Delta E|}{4}\right) \end{aligned} \right\} \quad (4.91)$$

Note that the peak current densities ($\Delta i_{\text{DDPV}}^{\text{G, peak}} = \Delta I_{\text{DDPV}}^{\text{G, peak}}/A_G$) of microspheres and microdiscs of the same radius fulfill $\Delta i_{\text{DDPV}}^{\text{microsphe, peak}} = (\pi/4)\Delta i_{\text{DDPV}}^{\text{microdisc, peak}}$.

As the half-wave potential depends on the geometry and size of the electrode considered, in the case of spherical or disc electrodes under transient conditions, it is deduced that the peak potentials are comprised between $E_{1/2}^{\text{r, micro}}$ for $r_G \ll \sqrt{\pi D_O t}$ (see Eq. (4.90)) and $E_{1/2}^{\text{r, plane}}$ for $r_G \gg \sqrt{\pi D_O t}$ (see Eq. (4.88)).

In Fig. 4.7, the peak potential and the half-wave potential corresponding to a spherical electrode are plotted versus the sphericity factor $R_0 = r_s/\sqrt{D_O\tau_2}$ using three values of γ (5, 1, and 0.2). As expected, the $E_{1,2}^{\text{sph, peak}}$ and $E_{1/2}^{\text{r, sph}}$ values coincide for planar and ultramicroelectrodes, whereas for spherical microelectrodes the discrepancy is significant when $\gamma \neq 1$, with a maximum difference of ≈ 11 mV for $r_s/\sqrt{D_{\text{max}}\tau_2} \approx 2$ (where D_{max} is the largest diffusion coefficient of the redox pair) that increases as γ moves away from 1 and the ratio τ_1/τ_2 is higher. This alerts against the identification of the peak potential as the half-wave potential when microelectrodes are employed and the diffusion coefficients differ significantly.

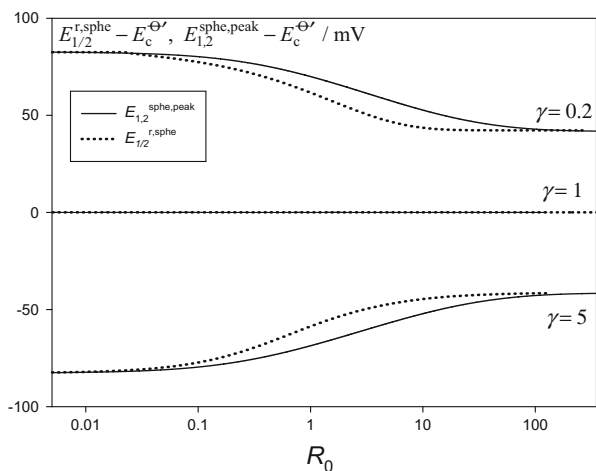


Fig. 4.7 Variation of the DDPV peak potential (*solid line*) and the half-wave potential (*dotted line*) with respect to the formal potential with the electrode sphericity parameter corresponding to the second pulse ($R_0 = r_s / \sqrt{D_O \tau_2}$) for different values of γ indicated on the graph. $\Delta E = -50$ mV, $\tau_1 = 5$ s, $\tau_2 = 0.025$ s

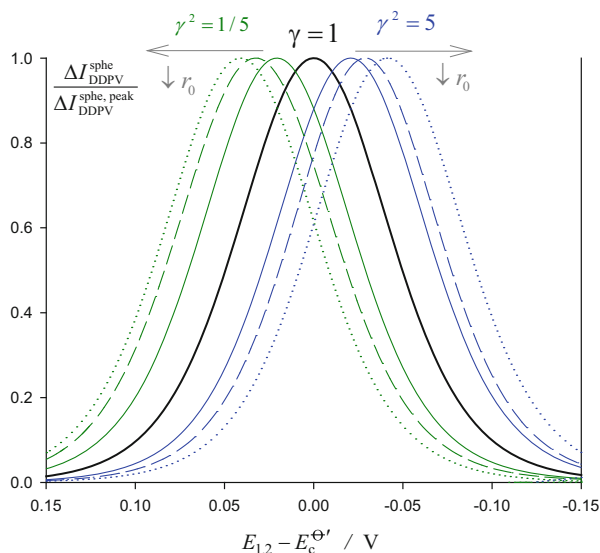


Fig. 4.8 Influence of electrode radius on the peak potential of the DDPV responses. Three electrode sizes are considered: planar electrode (*solid line*, from Eq. (4.82)), $r_s = 2 \times 10^{-3}$ cm (*dashed line*, from Eq. (4) of reference [38]), $r_s = 5 \times 10^{-6}$ cm (*dotted line*, from Eq. (4.83)). γ values are marked on the curves. $\Delta E = -50$ mV, $E_{1,2}^{\text{initial}} - E_c^{\Theta'} = +150$ mV, $E_{1,2}^{\text{final}} - E_c^{\Theta'} = -150$ mV, number of points = 50. $\tau_1 = 1$ s, $\tau_2 = 0.02$ s, $c_O^* = 1$ mM, $c_R^* = 0$, $D_O = 10^{-5}$ cm² s⁻¹, $r_0 = r_s$. Reproduced from [38] with permission

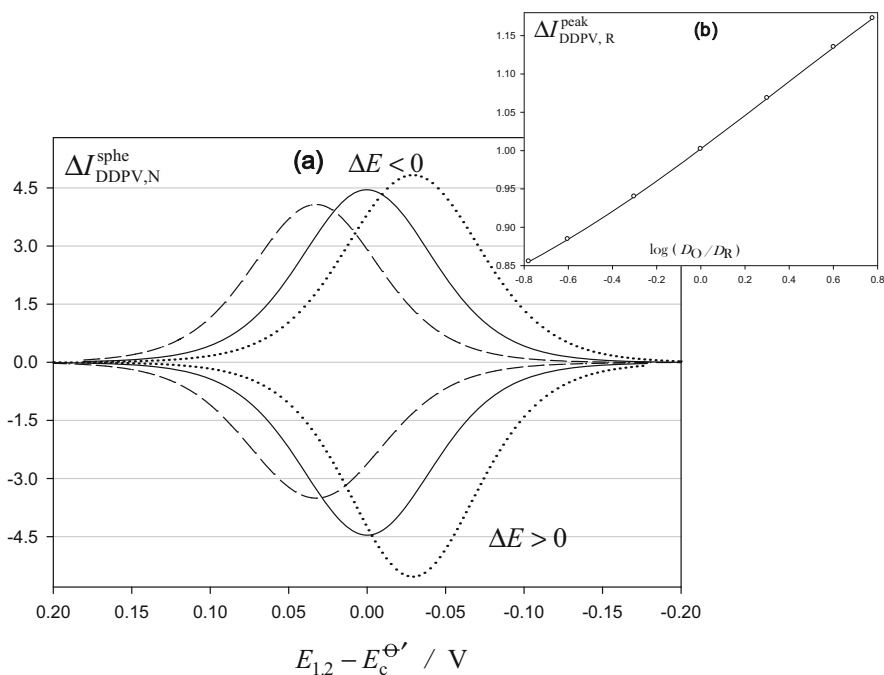


Fig. 4.9 (a) Normalized DDPV curves ($\Delta I_{\text{DDPV}}^{\text{sphe}}/I_{\text{d},1}^{\text{plane}}(\tau_1)$) corresponding to a scan in normal mode ($\Delta E = -50$ mV) and in reverse mode ($\Delta E = 50$ mV) at a spherical electrode ($r_s = 2 \times 10^{-3}$ cm), from Eq. (4) of reference [38]. Three γ values are considered: $\gamma^2 = 1/5$ (dashed line), $\gamma^2 = 1$ (solid line), and $\gamma^2 = 5$ (dotted line); (b) Variation of $\Delta I_{\text{DDPV,R}}^{\text{sphe,peak}}$ with the ratio of diffusion coefficients. $E_{1,2}^{\text{initial}} - E_c^{\Theta'} = +200$ mV, $E_{1,2}^{\text{final}} - E_c^{\Theta'} = -200$ mV, number of points = 70. Taken from [38] with permission

In Fig. 4.8, the influence of the electrode radius of spherical electrodes on the peak potential can be seen. The DPV curves are normalized in order to show better the radius effect, i.e., $\Delta I_{\text{DDPV}}^{\text{sphe}}/\Delta I_{\text{DDPV}}^{\text{sphe,peak}}$. When $\gamma > 1$ a decrease of electrode radius gives rise to a shift of the peak potential toward more negative potentials, whereas when $\gamma < 1$ the shift is toward more positive potentials. For $\gamma = 1$, the peak potential is independent of the electrode size and equal to the formal potential (Eq. 4.85). Under the conditions considered in the figure ($\gamma^2 = 5, 1/5$), the absolute value of the difference between the peak potential at planar electrode and spherical (or disc) ultramicroelectrodes is $|E_{1/2}^{\text{r,micro}} - E_{1/2}^{\text{r,plane}}| \approx 20.7$ mV.

The DDPV curves corresponding to a negative pulse height ($\Delta E < 0$) and to a positive one ($\Delta E > 0$) for three γ values at a spherical electrode can be seen in Fig. 4.9. For any γ value, the peak potential is the same for normal and reverse modes when $E_{1,2}$ is chosen as the x -axis. The sign of ΔE has an influence on $\Delta I_{\text{DDPV}}^{\text{sphe,peak}}$, and this depends on the ratio of the diffusion coefficients of electroactive species. It can be defined the following ratio:

$$\Delta I_{\text{DDPV,R}}^{\text{sphe,peak}} = \left| \frac{\Delta I_{\text{DDPV}}^{\text{sphe,peak}}(\Delta E > 0)}{\Delta I_{\text{DDPV}}^{\text{sphe,peak}}(\Delta E < 0)} \right| \quad (4.92)$$

As can be inferred from Fig. 4.9, $\Delta I_{\text{DDPV,R}}^{\text{sphe,peak}} = 1$ when both diffusion coefficients are equal ($D_{\text{O}} = D_{\text{R}}$) (see Eq. (4.86)). When $D_{\text{O}} > D_{\text{R}}$, $\Delta I_{\text{DDPV,R}}^{\text{sphe,peak}} > 1$, whereas when $D_{\text{O}} < D_{\text{R}}$ we find that $\Delta I_{\text{DDPV,R}}^{\text{sphe,peak}} < 1$. Hence, this ratio is sensitive to the γ value and, therefore, is very useful for the determination of diffusion coefficients (in the optimum range $0.5 \leq r_s/\sqrt{D_{\text{max}}\tau_2} \leq 3.5$, with D_{max} being the largest diffusion coefficient of the redox pair).

4.2.4.1 Ion Transfer Through Liquid Membranes

DDPV technique has been also applied to the study of the ion transfer processes in systems with one and two liquid/liquid polarizable interfaces [40–42]. The expression for the current corresponding to the transfer of ion X^+ is:

$$\frac{\Delta I_{\text{DDPV}}}{FAC_{X^+}^* \sqrt{D_{X^+}^w/\pi\tau_2}} = \frac{1}{1 + e^{\eta_2}} - \frac{1}{1 + e^{\eta_1}} \quad \text{one polarizable interface} \quad (4.93)$$

$$\frac{\Delta I_{\text{DDPV}}}{FAC_{X^+}^* \sqrt{D_{X^+}^w/\pi\tau_2}} = g(\eta_{\text{M},2}) - g(\eta_{\text{M},1}) \quad \text{two polarizable interfaces} \quad (4.94)$$

with

$$g(\eta_{\text{M},j}) = \frac{\sqrt{(\lambda^+ e^{\eta_{\text{M},j}})^2 + 8\lambda^+ e^{\eta_{\text{M},j}} - \lambda^+ e^{\eta_{\text{M},j}}}}{4} \quad j = 1, 2 \quad (4.95)$$

$$\left. \begin{aligned} \eta_{\text{M},j} &= \frac{F}{RT} (E^{\text{M},j} - E^{\text{M},\Theta'}) \\ E^{\text{M},j} &= E_{\text{out},j} - E_{\text{inn},j} \end{aligned} \right\} \quad j = 1 \text{ or } 2 \quad (4.96)$$

$$E^{\text{M},\Theta'} = \Delta_{\text{M}}^w \phi_{X^+}^{\Theta'} - \Delta_{w_2}^{\text{M}} \phi_{R^+}^{\Theta'} \quad (4.97)$$

$$\lambda^+ = \frac{2\sqrt{D_{R^+}^{w_2} D_{X^+}^{\text{M}}}}{D_{X^+}^{w_1}} \frac{c_{R^+}^*}{c_{X^+}^*} \quad (4.98)$$

$E_{\text{out},j}$ and $E_{\text{inn},j}$ are the individual potential drops at each interface caused by the application of the first and second potential steps. $\Delta_{\text{M}}^w \phi_{X^+}^{\Theta'}$ and $\Delta_{w_2}^{\text{M}} \phi_{R^+}^{\Theta'}$ are the formal ion transfer potentials for the target ion X^+ and for the membrane electrolyte cation R^+ , respectively, $c_{R^+}^*$ is the concentration of the membrane electrolyte cation, R^+ , and $D_{X^+}^{\text{M}}$ and $D_{R^+}^{w_2}$ are the diffusion coefficients of X^+ in the membrane (M phase) and R^+ in the inner aqueous solution (w_2 phase), respectively.

The half-wave potential, $E_{1/2}^{\text{M}}$, is given by

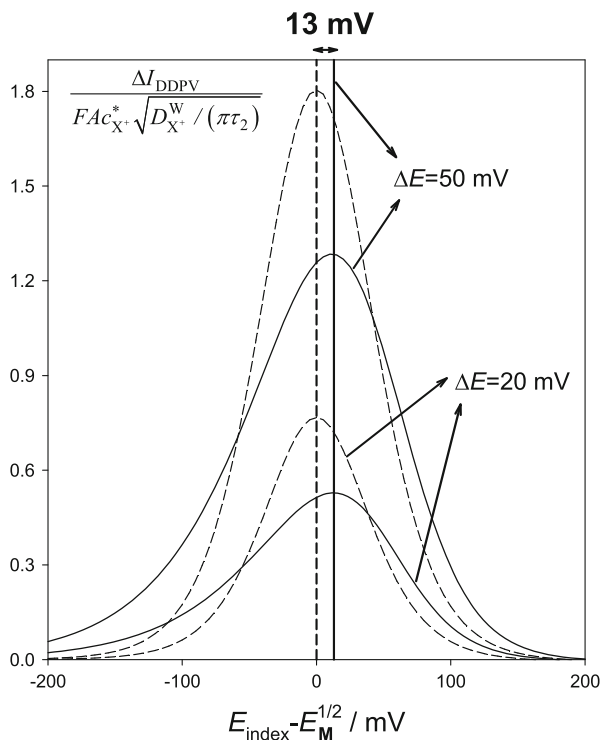


Fig. 4.10 Normalized $\Delta I_{DDPV} / (F A c_{X^+}^* \sqrt{D_{X^+}^w / \pi \tau_2}) - (E_{index} - E_{1/2}^M)$ curves calculated from Eqs. (4.93) (dashed lines) and (4.94) (solid lines). The values of ΔE are on the curves. $\Delta_M^w \phi_{X^+}^{\ominus'} = -200$ mV, $\Delta_{w_2}^M \phi_{R^+}^{\ominus'} = -350$ mV, $\tau_1 = 12.5$ s, $\tau_2 = 0.25$ s, $D_{X^+}^w = D_{R^+}^w = 10^{-5}$ cm² s⁻¹, $D_{X^+}^M = 10^{-8}$ cm² s⁻¹, $c_{X^+}^* = 0.1$ mM, $c_{R^+}^* = 50$ mM, $T = 298.15$ K. Taken from [42] with permission

$$E_{1/2}^M = E^{M, \ominus'} - \frac{RT}{F} \ln \lambda^+ \quad (4.99)$$

In Fig. 4.10, the DDPV curves corresponding to a membrane system with two polarizable interfaces (solid lines) and also to a system with a single polarizable interface (dashed lines), obtained for two values of the pulse amplitude ΔE , are shown. The current ΔI_{DDPV} has been plotted in all the cases versus the difference $(E_{index} - E_{1/2}^M)$, with $E_{index} = (E^{M,1} + E^{M,2})/2$. The use of E_{index} instead of the usual $E^{M,1}$ is of great interest since, as has been indicated above, the $\Delta I_{DDPV} - E_{index}$ plots are centred about the half-wave potential in the case of a single polarizable interface system (see dashed curves). As can be seen in this Figure, the DDPV peaks obtained for the liquid membrane system with two polarizable interfaces are shifted 13 mV with respect to those obtained when only one polarizable interface is used, in agreement with Eq. (4.94). Moreover, in the

first case the $\Delta I_{\text{DDPV}} - E_{\text{index}}$ curves are lower (around 40–45 %) and wider than those obtained in the second case (with a half peak width $W_{\text{DDPV}}^{1/2} \simeq 131$ mV versus the $\simeq 90$ mV observed when only one interface is considered).

4.2.5 Differential Normal Double Pulse Voltammetry

Equation (4.77) corresponds to the normal mode of Differential Double Pulse Voltammetry for which the duration of the second applied pulse is not restricted as in the case of DDPV [35]. From this equation, the expression of the current $\Delta I_{\text{DNDPV}}^{\text{G}}$ at very negative and positive potentials valid for any electrode geometry can be directly obtained,

$$\Delta I_{\text{DNDPV}}^{\text{G}}(E_1 \rightarrow -\infty, E_2 \rightarrow -\infty) = F A_G D c_O^* (f_G(\tau_1 + \tau_2, q_G) - f_G(\tau_1, q_G)) \quad (4.100)$$

$$\Delta I_{\text{DNDPV}}^{\text{G}}(E_1 \rightarrow \infty, E_2 \rightarrow \infty) = 0 \quad (4.101)$$

In the case of planar electrodes, from Eq. (4.100) and Table 2.3 of Sect. 2.6, it is immediately deduced that

$$\frac{\Delta I_{\text{DNDPV}}^{\text{plane}}(E_1 \rightarrow -\infty, E_2 \rightarrow -\infty)}{F A D c_O^*} = \frac{1}{\sqrt{\pi D}} \left(\frac{1}{\sqrt{\tau_1 + \tau_2}} - \frac{1}{\sqrt{\tau_1}} \right) \quad (4.102)$$

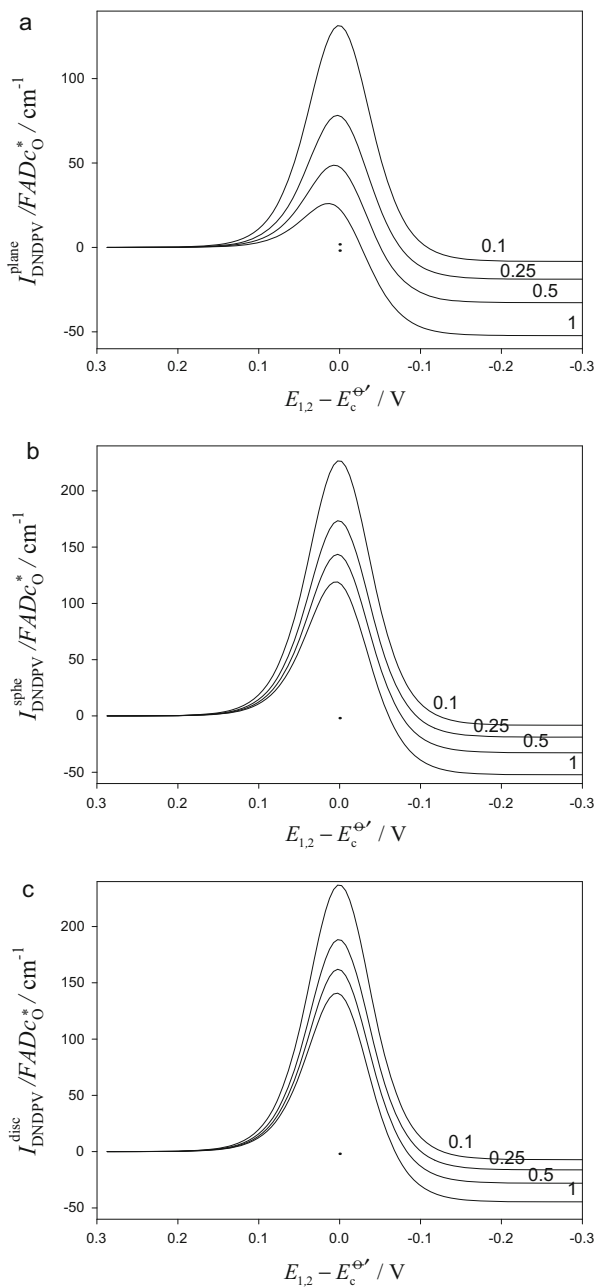
In order to check this behavior, in Fig. 4.11 it can be seen the influence of τ_2 on the DNDPV curves calculated from planar, spherical, and disc electrodes from Eq. (4.77). From these curves, it can be observed that the increase of τ_2 causes a decrease of the peak current in all the cases, which is much more pronounced in the case of planar electrodes (a). The current at very negative potentials increases in absolute value with τ_2 which is in agreement with Eq. (4.100). The peak potential of the DNDPV curves of spherical and disc electrodes is not practically affected by the value of τ_2 but in the case of a plane electrode is shifted toward more positive values as τ_2 increases.

4.2.6 Additive Differential Double Pulse Voltammetry

As established in Sect. 4.1, two DDPV recordings, $\Delta I_{\text{DDPV}}^{\text{G,c}} = I_2^{\text{G,c}}(E_2^{\text{c}}) - I_1^{\text{G}}(E_1)$, where $E_2^{\text{c}} = E_1 - |\Delta E|$ and $\Delta I_{\text{DDPV}}^{\text{G,a}} = I_2^{\text{G,a}}(E_2^{\text{a}}) - I_1^{\text{G}}(E_1)$ where $E_2^{\text{a}} = E_1 + |\Delta E|$, enables us to analyze the influence of different parameters on the charge transfer reaction. In Scheme 4.4, it has been shown this new technique consisting in the addition of the signals $\Delta I_{\text{DDPV}}^{\text{G,c}}$ and $\Delta I_{\text{DDPV}}^{\text{G,a}}$ [3]

Fig. 4.11 Influence of τ_2 on the DNDPV curves calculated from planar (a), spherical (b), and disc electrodes (c), from Eq. (4.77).

$r_s = r_d = 25 \mu\text{m}$,
 $D = 10^{-5} \text{ cm}^2 \text{ s}^{-1}$,
 $\tau_1 = 1 \text{ s}$. The values of τ_2 (in s) appear on the curves



$$I_{\text{ADDPV}}^{\text{G}} = I_2^{\text{G},c}(E_2^c) - 2I_1^{\text{G}}(E_1) + I_2^{\text{G},a}(E_2^a). \quad (4.103)$$

This technique can be considered as a natural extension of DDPV and it offers, among others, the following advantages:

- ADDPV behaves as the Double Derivative Voltammetry for $\Delta E \ll RT/F$.
- The ADDPV curves present a zero current potential, E_{cross} , which can be measured with great accuracy. It coincides with the half-wave potential of a reversible electrode process in planar electrodes and with the formal potential independently of the electrode geometry when the diffusion coefficients of both species are assumed as equal.
- The charge current is minimized to a large extent with respect to other double pulse techniques including DDPV, a feature which gives it great analytical usefulness.
- ADDPV allows diagnostic criteria to be given about reaction mechanisms based on the maximum and minimum peak current and peak potential measurements, I_{M}^{G} and E_{M} , and I_{m}^{G} and E_{m} (see Scheme 4.4).
- The analytical expressions of the ADDPV signals are easily obtained from the expression corresponding to DDPV ones, given in Sect. 4.2.4.

Using the expressions of the currents corresponding to the first and second potentials applied given by Eqs. (4.28) and (4.29), the expression of the current in ADDPV at any electrode geometry assuming equal diffusion coefficients for species O and R and $c_{\text{R}}^* = 0$ is

$$\frac{I_{\text{ADDPV}}^{\text{G}}}{FADc_{\text{O}}^*} = \left(\frac{1}{1 + e^{\eta_{2,c}}} - \frac{2}{1 + e^{\eta_1}} + \frac{1}{1 + e^{\eta_{2,a}}} \right) f_{\text{G}}(t_2, q_{\text{G}}) \quad (4.104)$$

with

$$\left. \begin{aligned} \eta_{2,c} &= \frac{RT}{F} (E_2^c - E_c^{\Theta'}) = \frac{RT}{F} (E_1 - |\Delta E| - E_c^{\Theta'}) \\ \eta_{2,a} &= \frac{RT}{F} (E_2^a - E_c^{\Theta'}) = \frac{RT}{F} (E_1 + |\Delta E| - E_c^{\Theta'}) \end{aligned} \right\} \quad (4.105)$$

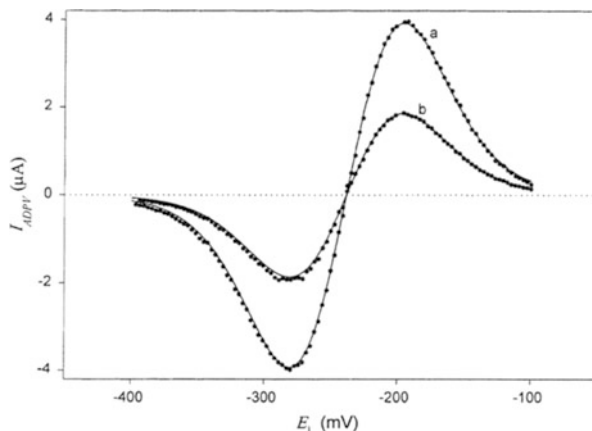
In the case of planar electrodes, when different diffusion coefficients are assumed, the expression of the ADDPV response is [3]:

$$\frac{I_{\text{ADDPV}}^{\text{plane}}}{FADc_{\text{O}}^*} = \left(\frac{1}{1 + \gamma e^{\eta_{2,c}}} - \frac{2}{1 + \gamma e^{\eta_1}} + \frac{1}{1 + \gamma e^{\eta_{2,a}}} \right) \frac{1}{\sqrt{\pi D_{\text{O}} t_2}} \quad (4.106)$$

where γ is given by Eq. (4.32).

Equation (4.104) is fulfilled independently of the electrode size and shape whenever $\tau_1 \gg \tau_2$. Therefore, under these conditions the peaks and cross potentials of the $I_{\text{ADDPV}}^{\text{G}} - E_1$ curve are independent of the electrode geometry and of t_2 . Moreover, from Eq. (4.104) it can be deduced that $E_{\text{M}} - E_c^{\Theta'} = -(E_{\text{m}} - E_c^{\Theta'})$ and

Fig. 4.12 Experimental (symbols) and theoretical (solid lines, Eq. (4.104) with $f_G = f_s$) $I_{\text{ADDPV}}^{\text{sphe}} - E_1$ for 1 mM Fe^{3+} in 0.5 M $\text{K}_2\text{C}_2\text{O}_4$, pH = 4.45 at an SMDE. $|\Delta E| = 50$ mV, $\tau_1 = 3$ s, $t_2 = 0.03$ s, $T = 291$ K, $D = 5.9 \times 10^{-6}$ $\text{cm}^2 \text{s}^{-1}$, $E_c^{\Theta'} = -238$ mV. The values of the electrode radii (in cm) are (a) 0.038, (b) 0.026. (Reproduced with permission of reference [3])



$$\left| \frac{I_M^G}{I_m^G} \right| = 1 \quad (4.107)$$

By equating Eq. (4.104) to zero, the expression of the cross potential is immediately deduced,

$$E_{\text{cross}} = E_c^{\Theta'} \quad (4.108)$$

The difference between potentials E_M and E_m can be also obtained, and it is given by

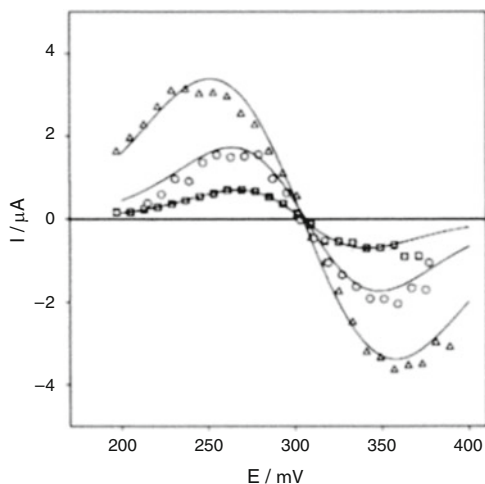
$$E_M - E_m \cong 68 + 7.45 \times 10^{-3} |\Delta E|^2 - 2.54 \times 10^{-7} |\Delta E|^4 \text{ mV} \quad \text{for } |\Delta E| > 20 \text{ mV} \quad (4.109)$$

$$E_M - E_m \cong 68 \text{ mV} \quad \text{for } |\Delta E| < 10 \text{ mV} \quad (4.110)$$

This last value coincides with that deduced previously for Double Derivative Voltammetry [43] as indicated.

In Fig. 4.12, it can be seen the theoretical and experimental ADDPV curves obtained for the system Fe(III) in oxalate for two different radii of an SMDE. It is clear that the agreement between both sets of results is very good. The cross potential, which coincides with $E_c^{\Theta'}$, is not affected by the variation of the electrode size in line with Eq. (4.108). ADDPV has also been applied to study ion transfer across the water-solvent polymeric membrane interface [41]. In Fig. 4.13, the morphology of the background subtracted ADDPV curve obtained for the transfer of tetraalkylammonium (TEA^+) for $|\Delta E| = 30, 50,$ and 80 mV is shown. The experimental data were fitted to Eq. (4.106) by using the half-wave potential and the term $A(D_{X^+}^W)^{1/2}$ as adjustable parameters ($D_{X^+}^W$ is the diffusion coefficient of the TEA^+ cation in aqueous media). It can be seen that the cross potential does not depend on the value of $|\Delta E|$ and it can be measured with high accuracy by making a

Fig. 4.13 background subtracted ADDPV curves obtained for 10^{-4} M TEA⁺ at the following $|\Delta E|$ values: 30 (squares); 50 (circles), and 80 mV (triangles). (Reproduced with permission of reference [41])



linear interpolation of the central zone of the ADDPV curves. The half-wave potential obtained was 305 ± 1 mV [41].

4.3 Nonreversible Electrochemical Reactions

In contrast with the behavior discussed in Sect. 4.2, in the case of non-reversible electrode processes, a general treatment valid for any electrode geometry when a second potential pulse is applied, as that discussed in Sect. 3.2, has not been found, even when the diffusion coefficients are considered as equal. In this case analytical treatments become very challenging, and numerical approaches are the most used for analyzing the electrochemical responses. In this section, two analytical solutions corresponding to spherical electrodes will be presented and discussed in RPV and DDPV (the limiting behavior corresponding to planar electrodes will also be presented).

4.3.1 Application of a Double Potential Pulse to Planar and Spherical Electrodes

The following charge transfer reaction taking place at a spherical electrode will be considered:



with k_{red} and k_{ox} being the rate constants for the electro-reduction and electro-oxidation processes. The general approach for solving this process in double pulse techniques at spherical electrodes is:

- The first applied potential is set at a value E_1 at a stationary spherical electrode during the interval $0 \leq t_1 \leq \tau_1$. The diffusion mass transport of the electroactive species toward or from the electrode surface is described by the following differential equation system:

$$\hat{\delta} c_{\text{O}}^{(1)}(r, t) = \hat{\delta} c_{\text{R}}^{(1)}(r, t) = 0 \quad (4.111)$$

with

$$\hat{\delta} = \frac{\partial}{\partial t} - D \left(\frac{\partial^2}{\partial r^2} + \frac{2}{r} \frac{\partial}{\partial r} \right) \quad (4.112)$$

where it is assumed that both electroactive species have the same diffusion coefficient ($D_{\text{O}} = D_{\text{R}} = D$) and a Butler–Volmer kinetic scheme for the charge transfer (see Sect. 1.7).

The boundary conditions to be fulfilled by the solutions of the differential equations are given by

$$\left. \begin{array}{l} t_1 \geq 0, r \rightarrow \infty \\ t_1 = 0, r \geq r_s \end{array} \right\} c_{\text{O}}^{(1)} = c_{\text{O}}^*, c_{\text{R}}^{(1)} = c_{\text{R}}^* \quad (4.113)$$

$$t_1 > 0, r = r_s : \left(\frac{\partial c_{\text{O}}^{(1)}}{\partial r} \right)_{r=r_s} = - \left(\frac{\partial c_{\text{R}}^{(1)}}{\partial r} \right)_{r=r_s} \quad (4.114)$$

$$D \left(\frac{\partial c_{\text{O}}^{(1)}}{\partial r} \right)_{r=r_s} = k^0 e^{-\alpha n_1} c_{\text{O}}^{(1)}(r_s, t) - k^0 e^{(1-\alpha) n_1} c_{\text{R}}^{(1)}(r_s, t) \quad (4.115)$$

where $\eta_1 = F(E_1 - E_c^{\ominus})/RT$ (see Eq. (4.16)).

Using the mathematical procedure described in Appendix G, the expression for the current I_1^{sph} given by Eq. (G.21) is derived.

At time $t \geq \tau_1$, the applied potential is stepped from E_1 to E_2 and the mass transport of species O and R during this second period ($t = \tau_1 + t_2$; $0 \leq t_2 \leq \tau_2$) described by

$$\hat{\delta} c_{\text{O}}^{(2)}(r, t) = \hat{\delta} c_{\text{R}}^{(2)}(r, t) = 0 \quad (4.116)$$

with the following boundary value problem:

$$\left. \begin{array}{l} t_2 \geq 0, r \rightarrow \infty \\ t_2 = 0, r \geq r_s \end{array} \right\} c_{\text{O}}^{(2)} = c_{\text{O}}^{(1)}, c_{\text{R}}^{(2)} = c_{\text{R}}^{(1)} \quad (4.117)$$

$$t_2 > 0, r = r_s : \left(\frac{\partial c_O^{(2)}}{\partial r} \right)_{r=r_s} = - \left(\frac{\partial c_R^{(2)}}{\partial r} \right)_{r=r_s} \quad (4.118)$$

$$D \left(\frac{\partial c_O^{(2)}}{\partial r} \right)_{r=r_s} = k^0 e^{-\alpha \eta_2} c_O^{(2)}(r_s, t) - k^0 e^{(1-\alpha)\eta_2} c_R^{(2)}(r_s, t) \quad (4.119)$$

with $\eta_2 = F(E_2 - E_c^\ominus)/RT$ (Eq. (4.9)).

Equation (4.119) assumes, as in previous chapter 3, that the transition state does not change with potential and so the same value of α applies to forward and reverse processes.

The resolution of Eq. (4.116) is given in Appendix G and the conditions of validity of the expressions for the current corresponding to RPV and DDPV are deduced.

4.3.2 Reverse Pulse Voltammetry

As discussed in Sect. 4.1, the solution for the first potential pulse in RPV corresponds to the well-known situation for a charge transfer process at a spherical electrode under limiting conditions, with the current–time expression given by Eq. (4.38). By following the mathematical procedure detailed in Appendix G, the following expression for the current–potential response at the second potential pulse under RPV conditions is obtained [44]:

$$I_{\text{RPV}}^{\text{sph}} = I_{\text{d},1}^{\text{sph}}(\tau_1 + \tau_2) + \frac{I_{\text{d},1}^{\text{plane}}(\tau_2)}{1 + \kappa_{\text{sph},\text{ss}}^0 e^{-\alpha \eta_2} (1 + e^{\eta_2})} \times \left\{ \frac{\sqrt{\pi}}{2} Z \chi_{s,2} - \beta^{1/2} + \kappa_{\text{sph},\text{ss}}^0 e^{-\alpha \eta_2} (1 + e^{\eta_2}) [ZF(\chi_{s,2}) + YG(\chi_{s,2}, \beta)] \right\} \quad (4.120)$$

with η_2 , $I_{\text{d},1}^{\text{sph}}$, and $I_{\text{d},1}^{\text{plane}}$ given by Eqs. (4.9), (4.38), and (4.49), respectively. Moreover,

$$\kappa_{\text{sph},\text{ss}}^0 = \frac{k^0 r_s}{D} \quad (4.121)$$

$$Z = - \frac{1 + \kappa_{\text{sph},\text{ss}}^0 e^{(1-\alpha)\eta_2} \left(1 + \frac{c_R^*}{c_O^*} \right)}{1 + \kappa_{\text{sph},\text{ss}}^0 e^{-\alpha \eta_2} (1 + e^{\eta_2})} \quad (4.122)$$

$$\chi_{s,2} = \frac{2\sqrt{D\tau_2}}{r_s} + 2\sqrt{\frac{\tau_2}{D}} k^0 e^{-\alpha \eta_2} (1 + e^{\eta_2}) \quad (4.123)$$

$$\beta = \frac{\tau_2}{\tau_1 + \tau_2} \quad (4.124)$$

$$F(\chi_{s,2}) = \frac{\sqrt{\pi}}{2} \chi_{s,2} \exp(\chi_{s,2}/2)^2 \operatorname{erfc}(\chi_{s,2}/2) \quad (4.125)$$

$$Y = -\frac{2}{\chi_{s,2}} \sqrt{\frac{\beta}{\pi}} \quad (4.126)$$

$$G(\chi_{s,2}, \beta) = \begin{cases} \sum_{i=0}^{\infty} \frac{(-1)^i \chi_{s,2}^{i+1}}{\prod_{l=0}^i p_l} \left\{ 1 + \sum_{k=1}^{\infty} \frac{(2k-1)! \beta^k}{2^{2k-1} k! (k-1)! (i+2k)} \right\} & \text{for } \chi_{s,2} < 10 \\ \sqrt{1-\beta} + \sqrt{\pi} \sum_{k=1}^{\infty} \frac{(-1)^{k-1} (2k-1)! \beta^k}{(k-1)! \chi_{s,2}^{2k-1}} + \\ + \sum_{i=1}^{\infty} \frac{(-1)^i 2(2i-1)!}{(i-1)! \chi_{s,2}^{2i}} \left(1 - \sum_{k=1}^{\infty} \frac{2^{1-2k} (2k-1)! (2i+1) \beta^k}{k! (k-1)! (2k-2i-1)} \right) & \text{for } \chi_{s,2} > 10 \end{cases} \quad (4.127)$$

$$I_{d,1}^{\text{sph}}(\tau_1 + \tau_2) = FA_s D c_O^* \left(\frac{1}{\sqrt{\pi D (\tau_1 + \tau_2)}} + \frac{1}{r_s} \right) \quad (4.128)$$

with p_l given by Eq. (4.46).

The validity of analytical solution (4.120) has been studied by comparison with numerical calculations [45] and an excellent agreement between analytical and numerical results was obtained for any electrode size, for any length of the potential pulses, and whatever the reversibility degree of the electrode process.

From Eq. (4.120), some particular cases of interest can be deduced:

– *Planar electrodes* ($r_s \rightarrow \infty$) [46]:

$$I_{\text{RPV}}^{\text{plane}} = I_{d,1}^{\text{plane}}(\tau_1 + \tau_2) + I_{d,1}^{\text{plane}}(\tau_2) [Z^{\text{P}} F(\chi_{p,2}) + YG(\chi_{p,2}, \beta)] \quad (4.129)$$

with

$$Z^{\text{P}} = -\frac{e^{\eta_2}}{1 + e^{\eta_2}} \quad (4.130)$$

$$\chi_{p,2} = 2\sqrt{\frac{\tau_2}{D}} k^0 e^{-\alpha \eta_2} (1 + e^{\eta_2}) \quad (4.131)$$

– *Ultramicroelectrodes* ($r_s \ll \sqrt{\pi D \tau_2}$) [44, 47]:

$$I_{\text{RPV}}^{\text{microsph}} = I_{d,c}^{\text{sph,ss}} \frac{\kappa_{\text{sph,ss}}^0 e^{-\alpha \eta_2}}{1 + \kappa_{\text{sph,ss}}^0 e^{-\alpha \eta_2} (1 + e^{\eta_2})} \quad (4.132)$$

with $I_{d,c}^{\text{sph,ss}}$ given by Eq. (4.76).

In Fig. 4.14, the influence of different parameters like the duration of the second potential pulse (τ_2 , Fig. 4.14a), the heterogeneous rate constant (k^0 , Fig. 4.14b), and the electrode size (through r_s , Fig. 4.14c) on the RPV responses of planar and spherical electrodes is shown. It is important to highlight that for irreversible processes the RPV curve presents two branches (cathodic and anodic), the null current plateau between them being wider the smaller k^0 is.

Concerning the influence of τ_2 in the case of large electrodes, a striking peak is found in the anodic wave of the RPV curve for quasireversible and irreversible systems when τ_2 is sufficiently large (see Fig. 4.14a). This atypical anodic peak is characteristic, and so indicative, of slow charge transfer processes ($k^0 < 10^{-3} \text{ cm s}^{-1}$), and is not found for reversible ones as can be seen in Fig. 4.14c. In this figure, it can be also observed that the peak increases as k^0 diminishes up to a limiting situation corresponding to totally irreversible systems for which the magnitude of the peak is independent of k^0 whereas its position shifts toward more positive potentials as k^0 value diminishes.

Note that the appearance of the anodic peak implies that, beyond the peak potential, smaller anodic currents are obtained at more anodic potentials. This situation is shown in Fig. 4.14b where it can be seen that at a given time there is a crossing of the chronoamperograms so that the current corresponding to the peak ($E_2 - E_c^{\theta'} = 300 \text{ mV}$, black curve) becomes greater than the anodic limiting current ($E_2 - E_c^{\theta'} = 700 \text{ mV}$, blue curve). The appearance of a peak in the anodic branch of RPV and Normal Pulse Voltammetry curves has also been described in amalgam systems when small sized electrodes are used [21, 29], although in that case the phenomenon is related to the depletion of species R whereas in the present case it is related to the reversibility of the electrode process.

This unusual feature in RPV response is more apparent the longer the duration of the second pulse (see Fig. 4.14a) and it is promoted by large electrodes, so that the greatest peak is obtained at planar electrodes whereas it is not observed at micro-electrodes (see Fig. 4.14d).

The shape and symmetry of the RPV curve give information about the kinetics of the electrode process. This feature can be used for the extraction of kinetic parameters by defining the parameter

$$\Delta E_{\text{mid,RPV}} = E_{\text{mid}}^{\text{an}} - E_{\text{mid}}^{\text{cath}} \quad (4.133)$$

where $E_{\text{mid}}^{\text{cath}}$ is the potential at which the current takes the half value of the cathodic limiting current (i.e., $I_{\text{RPV}}^{\text{G}}(E_{\text{mid}}^{\text{cath}}) = I_{\text{d},1}^{\text{G}}/2$) and $E_{\text{mid}}^{\text{an}}$ the potential at which the current takes the half value of the anodic limiting current (i.e., $I_{\text{RPV}}^{\text{G}}(E_{\text{mid}}^{\text{an}}) = I_{\text{RPV}}^{\text{G}}(\eta_2 \rightarrow \infty)/2$).

$\Delta E_{\text{mid,RPV}}$ is directly related to the shape of RPV curves and so is very useful for the quantitative study of the system kinetics. Thus, it is related to the separation of the cathodic and anodic branches of the RPV curve, so its value increases as the system behavior is more irreversible (see Fig. 4.15). Another interesting parameter

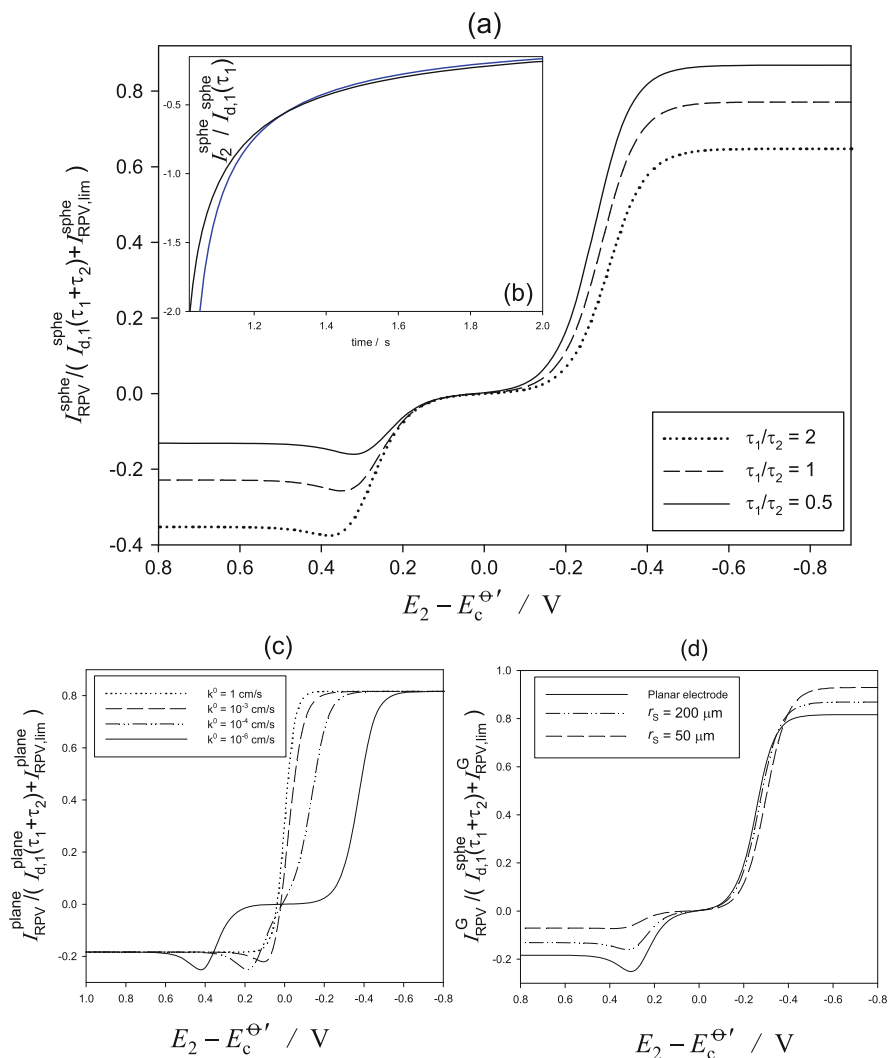
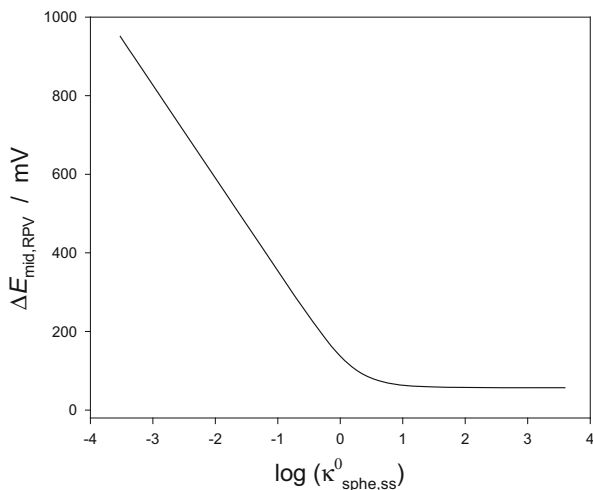


Fig. 4.14 (a) Variation of RPV curve with τ_2 for an irreversible system ($k^0 = 10^{-5} \text{ cm s}^{-1}$) at a spherical electrode with $r_s = 200 \mu\text{m}$ (Eq. 4.120). τ_2 values indicated on the graph; (b) $I_2 - t_2$ chronoamperograms for two values of the second potential pulse: $E_2 - E_c^{\Theta'} = 300 \text{ mV}$ (black line) and $E_2 - E_c^{\Theta'} = 700 \text{ mV}$ (blue line); (c) RPV curves for different values of k^0 (indicated on the graph) at a planar electrode (Eq. 4.129) with $\tau_2 = 2\tau_1$; (d) RPV curves for different electrode radius (r_s values indicated on the graph) for an irreversible system ($k^0 = 10^{-5} \text{ cm s}^{-1}$) with $\tau_2 = 2\tau_1$ (Eq. 4.120). $\tau_1 = 1 \text{ s}$, $D = 10^{-5} \text{ cm}^2 \text{ s}^{-1}$, $c_R^* = 0$. $I_{\text{RPV,lim}}^{\text{G}} = I_{\text{RPV}}^{\text{G}}(\eta_2 \rightarrow \infty)$. Taken from [44] with permission

Fig. 4.15 Variation of $\Delta E_{\text{mid,RPV}}$ with $\kappa_{\text{sph,ss}}^0$ for $\alpha = 0.5$, $2\sqrt{D\tau_2}/r_s = 0.45$, $\tau_1/\tau_2 = 20$



directly related to the symmetry of the RPV curves is $\Sigma E_{\text{mid,RPV}} = E_{\text{mid}}^{\text{an}} + E_{\text{mid}}^{\text{cath}}$. By combining the simultaneous analysis of the variation of $\Sigma E_{\text{mid,RPV}}$ and $\Delta E_{\text{mid,RPV}}$ with the duration of the second potential pulse, a complete characterization of the redox system is feasible with RPV as discussed in [44], so allowing the determination of the heterogeneous rate constant, the electron transfer coefficient, and the formal potential. In [48], this analysis is carried out for the reduction of three different redox systems covering a wide range of electrode kinetics (3-nitrophenolate^{-/2-•}, 3-nitrophthalate^{2-/3-•} and Eu^{3+/2+}) taking place at mercury hemispherical electrodes of ca. 25 μm radius, and experimental values for the above parameters have been obtained (see Table 4.1).

4.3.3 Differential Double Pulse Voltammetry

From the mathematical procedure given in Appendix G when $\tau_1 \gg \tau_2$, the expression for the current of the second potential pulse is obtained:

$$I_2^{\text{sphe}} = I_1^{\text{sphe}}(\tau_1 + \tau_2) + I_{\text{d,c}}^{\text{sphe,ss}} \frac{(\theta_2 - 1)g(\chi_{s,1})}{\theta_2(1 + e^{\eta_2})} [1 + (\theta_2 - 1)H(\chi_{s,2})] \quad (4.134)$$

with $I_1^{\text{sphe}}(\tau_1 + \tau_2)$ given in Eq. (G.21) of Appendix G (see also Eqs. (3.66) and (3.76) in Sect. 3.2.3), and $\chi_{s,2}$ given in Eq. (4.123). Moreover,

Table 4.1 Heterogeneous rate constant (k^0), electron transfer coefficient (α), and formal potential ($E_c^{\theta'}$) corresponding to the best fit of theoretical working curves (Eq. 4.120) to the RPV experimental results [48]

Redox couple	Medium ^a	$k^0 / \text{cm s}^{-1}$	α	$E_c^{\theta'} / \text{V}$
3-Nitrophenolate ^{-/2-} •	0.1 M Bu ₄ NPF ₆ , DMSO	1.6×10^{-2}	0.46 ^d	-1.410 ^{c,d}
3-Nitrophenolate ^{2-/3-} •	0.1 M Bu ₄ NPF ₆ , DMSO	1.7×10^{-3}	0.40	-1.515 ^c
Eu ^{3+/2+}	0.1 M NaClO ₄ , H ₂ O (pH = 4.5)	1.4×10^{-4}	0.72	-0.643 ^b

^aConcentration substrate: 1 mM of 3-nitrophenolate⁻, 3-nitrophenolate²⁻, Eu³⁺

^bvs SCE reference electrode

^cvs Ag/Ag⁺ reference electrode

^dValues calculated from the fit of the complete RPV curve

$$\chi_{s,1} = \frac{2\sqrt{D(\tau_1 + \tau_2)}}{r_s} + 2\sqrt{\frac{(\tau_1 + \tau_2)}{D}}k^0e^{-\alpha\eta_1}(1 + e^{\eta_1}) \quad (4.135)$$

$$g(x) = 1 - \left(\frac{e^{\eta_2}}{e^{\eta_1}}\right)^\alpha \left[\frac{\theta_2}{\theta_1} + \left(1 - \frac{\theta_2}{\theta_1}\right)H(x) \right] \quad (4.136)$$

$$H(x) = \exp(x/2)^2 \operatorname{erfc}(x/2) \quad (4.137)$$

$$\theta_2 = 1 + \kappa_{\text{sph},\text{ss}}^0 e^{-\alpha\eta_2}(1 + e^{\eta_2}) \quad (4.138)$$

$$\theta_1 = 1 + \kappa_{\text{sph},\text{ss}}^0 e^{-\alpha\eta_1}(1 + e^{\eta_1}) \quad (4.139)$$

with $\kappa_{\text{sph},\text{ss}}^0$ given in Eq. (4.121).

As mentioned in Sect. 4.1, in DDPV technique initial equilibrium conditions are reestablished before the application of each double potential pulse, for example, by renewal of the electrode (mercury drop electrode) or by open circuiting the working electrode for a waiting period. Lovrić shows [49], and it is proved by numerical simulations in [5] that for a reversible process a waiting period of $\leq 5\tau_1$ is long enough to achieve this condition at spherical electrodes; the smaller the electrode radius, the shorter the waiting period required. So, the expression for DDPV response, for which $\tau_1 \gg \tau_2$, is immediately particularized from Eq. (4.134) and the expression of $I_1^{\text{sph}}(\tau_1)$ (Eq. (G.21)),

$$\frac{\Delta I_{\text{d,c}}^{\text{sph}}}{I_{\text{d,c}}^{\text{sph},\text{ss}}} = \frac{(\theta_2 - 1)g(\chi'_{s,1})}{\theta_2(1 + e^{\eta_2})} [1 + (\theta_2 - 1)H(\chi_{s,2})] \quad (4.140)$$

where

$$\chi'_{s,1} = \frac{2\sqrt{D\tau_1}}{r_s} + 2\sqrt{\frac{\tau_1}{D}}k^0e^{-\alpha\eta_1}(1 + e^{\eta_1}) \quad (4.141)$$

From Eq. (4.140), expressions under some interesting conditions can be derived:

– *Planar electrodes* ($r_s \rightarrow \infty$). In this situation, expression (4.140) becomes:

$$\begin{aligned} \frac{\Delta I_{\text{d,1}}^{\text{plane}}}{I_{\text{d,1}}^{\text{plane}}(\tau_2)} &= \sqrt{\frac{\pi\tau_2}{D}}k^0e^{-\alpha\eta_2}F(\chi_{p,2}) \times \\ &\times \left\{ 1 - \left(\frac{1 + e^{\eta_2}}{1 + e^{\eta_1}}\right) \left[1 + \left(\frac{1 + e^{\eta_2}}{1 + e^{\eta_1}}\right)^\alpha \left(\frac{e^{\eta_2}}{e^{\eta_1}}\right)^\alpha - 1 \right] H(\chi_{p,1}) \right\} \end{aligned} \quad (4.142)$$

with function F given in Eq. (4.125), $I_{\text{d,1}}^{\text{plane}}$ by Eq. (4.49) and

$$\chi_{p,1} = 2\sqrt{\frac{(\tau_1 + \tau_2)}{D}}k^0 e^{-\alpha\eta_1} (1 + e^{\eta_1}) \quad (4.143)$$

$$\chi_{p,2} = 2\sqrt{\frac{\tau_2}{D}}k^0 e^{-\alpha\eta_2} (1 + e^{\eta_2}) \quad (4.144)$$

– *Ultramicroelectrodes.* When $r_s \ll \sqrt{\pi D\tau_2}$, Eq. (4.140) tends to:

$$\frac{\Delta I_{\text{DDPV}}^{\text{microsphe}}}{I_{\text{d,c}}^{\text{sphc,ss}}} = \kappa_{\text{sphc,ss}}^0 \left[\frac{e^{-\alpha\eta_2}}{\theta_2} - \frac{e^{-\alpha\eta_1}}{\theta_1} \right] \quad (4.145)$$

which, in the case of reversible systems ($k^0 \rightarrow \infty$), is equivalent to that obtained in Square Wave Voltammetry under steady-state conditions [47]. Note that the use of this equation is quite restricted since attaining steady-state conditions in DDPV requires very small electrodes because of the very short duration of the second potential pulse (t_2).

As discussed in Appendix G, for the resolution of the problem we have supposed that the mathematical concentration profiles of the first pulse for the total time $\tau_1 + \tau_2$ are not disturbed by the application of the second one. This assumption is fully valid for any electrode radius in DDPV technique, where the duration of the second pulse is much shorter than that of the first one ($\tau_1 \gg \tau_2$). It has been confirmed the validity of the analytical Eq. (4.134) in DDPV conditions by comparison with numerical results [45], since nonsignificant deviations are obtained (less than 0.5 %) around the peak potential when $\tau_1/\tau_2 > 50$.

In Fig. 4.16, the effect of the reversibility of the electron transfer process on DDPV peaks is studied at conventional spherical microelectrodes (electrode radius $r_s = 30 \mu\text{m}$ for $t_2 = 10 \text{ ms}$ and $D = 10^{-5} \text{ cm}^2 \text{ s}^{-1}$).

As previously depicted for planar electrodes in reference [50], the decrease of the heterogeneous rate constant gives rise to the decrease of the peak current, the increase of the peak half width and the shift of the peak potential toward more negative values. For fully irreversible systems (very small k^0 values), it is observed that the current peak and the peak half width become independent of the rate constant, and only the position of the peak (i.e., the peak potential $E^{\text{G,peak}}$) changes with k^0 .

For the above study the usual value of the transfer coefficient $\alpha = 0.5$ has been considered. With small α values, DDPV peaks are found to show a special shape under certain conditions. As can be seen in Fig. 4.17a, for $\alpha < 0.3$ the DDPV curves corresponding to quasireversible processes with $k^0 \sim 10^{-3} \text{ cm s}^{-1}$ present a striking splitting of the peak, with a sharper peak appearing at more anodic potentials. This phenomenon is promoted by small transfer constants and is more obvious for positive pulse heights ($\Delta E > 0$, reverse mode, where the anodic peak is even greater than the cathodic one) and at planar electrodes, since it becomes less apparent as the electrode size is reduced (see Fig. 4.17b). The description of this phenomenon is of great interest since this could lead to erroneous interpretation of

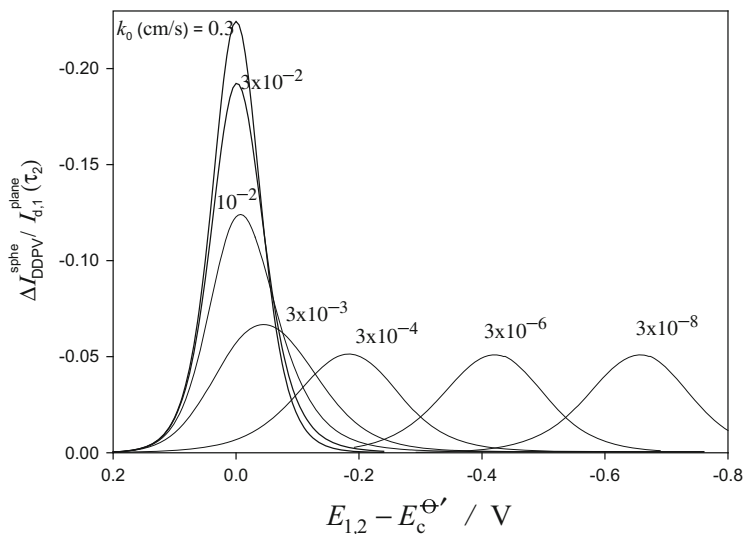


Fig. 4.16 Influence of the heterogeneous rate constant k^0 on DDPV curves [calculated from Eq. (4.140)]. The values of the heterogeneous rate constant k^0 are marked on the curves. $r_s = 30 \mu\text{m}$, $\alpha = 0.5$, $\Delta E = 20 \text{ mV}$, $\tau_1 = 1 \text{ s}$, $\tau_1/\tau_2 = 100$, $D = 10^{-5} \text{ cm}^2 \text{ s}^{-1}$. Taken from [5] with permission

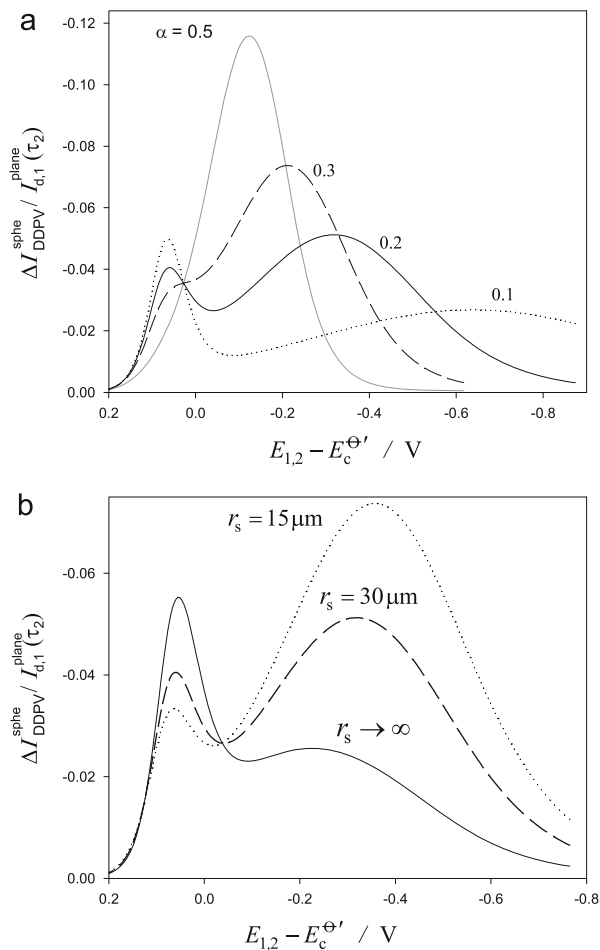
experimental data for real quasireversible systems with low α values [51, 52]. It is worth highlighting that this anomalous behaviour is characteristic of quasireversible processes with $k^0 \sim 10^{-3} \text{ cm s}^{-1}$, and the splitting is not observed for greater ($k^0 \geq 10^{-2} \text{ cm s}^{-1}$) or smaller ($k^0 \leq 10^{-4} \text{ cm s}^{-1}$) rate constants, where the usual single peak is obtained regardless of α value. This splitting has been observed experimentally for the case of the reduction of zinc (II) at mercury electrodes [53] as well as in other electrochemical techniques like Square Wave Voltammetry [54] and Double Differential Triple Pulse Voltammetry (see Sect. 4.6.2).

To determine kinetic parameters with DDPV, the variation of the peak potential and the normalized peak current $\Delta I_{\text{DDPV}}^{\text{spher,peak}}/I_{d,1}^{\text{plane}}(\tau_2)$ with the dimensionless parameters $2\sqrt{D\tau_2}/r_s$ and $\kappa_{\text{spher,ss}}^0$ are proposed as working surfaces from which the kinetic parameters are easily obtained, once D value is known, by measuring both peak parameters for different values of the double pulse duration, and keeping the ratio τ_1/τ_2 constant [5].

4.3.4 Additive Double Differential Pulse Voltammetry

From the analytical expressions obtained for DDPV (given by Eq. (4.140)), an explicit analytical solution for the ADDPV current is immediately deduced, which is valid for spherical electrodes of any size and whatever the kinetics of the electrode process [55]:

Fig. 4.17 Anomalous behavior of DDPV curves for small values of the transfer coefficient (Eq. 4.140). $\Delta E = 50$ mV. (a) different α values are considered (marked on the curves); $r_s = 30 \mu\text{m}$; (b) different electrode sizes are considered (marked on the curves); $k^0 = 10^{-3} \text{ cm s}^{-1}$, $\alpha = 0.2$, $\tau_1 = 1 \text{ s}$, $\tau_1/\tau_2 = 100$, $D = 10^{-5} \text{ cm}^2 \text{ s}^{-1}$. Taken from [5] with permission



$$\frac{I_{\text{ADDPV}}^{\text{sphe}}}{I_{d,c}^{\text{sphe,ss}}} = \kappa_0^{\text{ss}} \left\{ \frac{g_c(\chi_{s,1}) e^{-a\eta_{2,c}}}{\theta_{2,c}} (1 + (\theta_{2,c} - 1)H(\chi_{s,2,c})) + \frac{g_a(\chi_{s,1}) e^{-a\eta_{2,a}}}{\theta_{2,a}} (1 + (\theta_{2,a} - 1)H(\chi_{s,2,a})) \right\} \quad (4.146)$$

where $I_{d,c}^{\text{sphe,ss}}$ is given by Eq. (4.76), the subscripts “c” and “a” refer to the normal and reverse mode, respectively, so the potential for the former is $E_{2,c} = E_1 - |\Delta E|$ and for the latter $E_{2,a} = E_1 + |\Delta E|$, and

$$g_m(x) = 1 - \left(\frac{e^{\eta_{2,m}}}{e^{\eta_1}} \right)^\alpha \left[\frac{\theta_{2,m}}{\theta_1} + \left(1 - \frac{\theta_{2,m}}{\theta_1} \right) H(x) \right], \quad m = c, a \quad (4.147)$$

$$\theta_{2,m} = 1 + \kappa_{\text{sph},\text{ss}}^0 e^{-\alpha\eta_{2,m}} (1 + e^{\eta_{2,m}}), \quad m = c, a \quad (4.148)$$

$$\chi_{s,2,m} = \frac{2\sqrt{D}\tau_2}{r_s} + 2\sqrt{\frac{\tau_2}{D}} k^0 e^{-\alpha\eta_{2,m}} (1 + e^{\eta_{2,m}}), \quad m = c, a \quad (4.149)$$

$\chi_{s,1}$, $H(x)$, and θ_1 are given in Eqs. (4.135), (4.137), and (4.139), respectively.

For the case of reversible processes (large k^0 values), the above expression for the ADDPV current simplifies to Eq. (4.104) with $f_G = f_s$.

Particular Cases

From Eq. (4.146), the following asymptotic expressions can be derived:

– *Planar electrodes* ($r_s \rightarrow \infty$). Expression (4.146) becomes:

$$\begin{aligned} \frac{I_{\text{ADDPV}}^{\text{plane}}}{I_{d,1}^{\text{plane}}(\tau_2)} &= \\ &= \pi^{1/2} k^0 (g_c^p(\chi_{p,1}) e^{-\alpha\eta_{2,c}} H(\chi_{p,2,c}) + g_a^p(\chi_{p,1}) e^{-\alpha\eta_{2,a}} H(\chi_{p,2,a})) \end{aligned} \quad (4.150)$$

with $\chi_{p,1}$ given in Eq. (4.143) and

$$g_m^p(x) = 1 - \left(\frac{1 + e^{\eta_{2,m}}}{1 + e^{\eta_1}} \right)^\alpha \left[1 + \left(\frac{1 + e^{\eta_1}}{1 + e^{\eta_{2,m}}} \left(\frac{e^{\eta_{2,m}}}{e^{\eta_1}} \right)^\alpha - 1 \right) H(x) \right], \quad m = c, a \quad (4.151)$$

$$\chi_{p,2,m} = 2\sqrt{\frac{\tau_2}{D}} k^0 e^{-\alpha\eta_{2,m}} (1 + e^{\eta_{2,m}}), \quad m = c, a \quad (4.152)$$

and $I_{d,1}^{\text{plane}}(\tau_2)$ given by Eq. (4.49).

– *Ultramicroelectrodes* (UME). When $r_s \ll \sqrt{\pi D \tau_2}$, Eq. (4.146) tends to:

$$\frac{I_{\text{ADDPV}}^{\text{microspher}}}{I_{d,c}^{\text{spher,ss}}} = \kappa_{\text{spher,ss}}^0 \left[\frac{e^{-\alpha\eta_{2,c}}}{\theta_{2,c}} + \frac{e^{-\alpha\eta_{2,a}}}{\theta_{2,a}} - 2 \frac{e^{-\alpha\eta_1}}{\theta_1} \right] \quad (4.153)$$

so a time-independent response is obtained under these conditions.

In Fig. 4.18, the influence of the kinetic parameters (k^0 , α) on the ADDPV curves is modeled at a spherical microelectrode ($2\sqrt{D}\tau_2/r_s = 0.2$). In general terms, the peak currents decrease and the crossing and peak potentials shift toward more negative values as the electrode processes are more sluggish (see Fig. 4.18a). For quasireversible systems ($k^0 \sim 10^{-2} - 10^{-4} \text{ cm s}^{-1}$), the peak currents are very sensitive to the value of the heterogeneous rate constant (k^0) whereas the variation of the crossing potential is less apparent. On the other hand, for totally irreversible

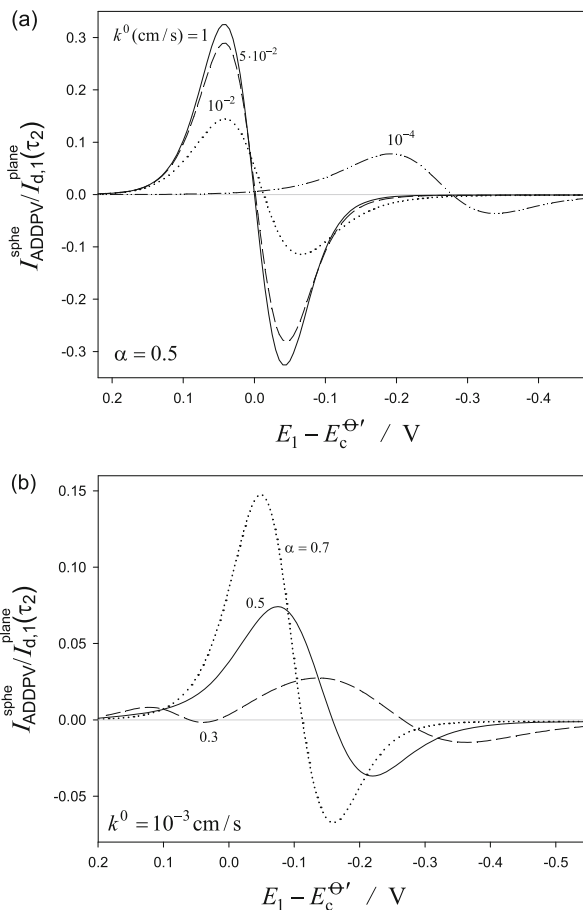
Fig. 4.18 Influence of the value of the heterogeneous rate constant (k^0 , **a**) and the transfer coefficient (α , **b**) on the ADDPV curves (Eq. 4.146).

$$2\sqrt{D}\tau_2/r_s = 0.2,$$

$$|\Delta E| = 50 \text{ mV},$$

$$\tau_1/\tau_2 = 100, k^0, \text{ and } \alpha$$

values indicated on the graphs. Reproduced with permission [55]



processes ($k^0 < 10^{-4}$ cm s $^{-1}$), the crossing potential significantly shifts toward more negative values, whereas the peak currents are independent of the k^0 value.

The relative symmetry of the peaks also indicates the degree of reversibility; thus, for reversible systems, symmetrical peaks are obtained (i.e., $|I_{\text{M}}^{\text{splane}} / I_{\text{m}}^{\text{splane}}| = 1$) whereas for quasireversible and irreversible processes $|I_{\text{M}}^{\text{splane}} / I_{\text{m}}^{\text{splane}}| > 1$.

In Fig. 4.18b, the effects of the electron transfer coefficient (α) on the ADDPV curves is shown. A decrease of α leads to the decrease of the peak currents together with the shift of the peak and crossing potentials toward more negative values. The ratio of the peak currents ($|I_{\text{M}}^{\text{splane}} / I_{\text{m}}^{\text{splane}}|$) also varies with α , and the greater the α value, the greater the $|I_{\text{M}}^{\text{splane}} / I_{\text{m}}^{\text{splane}}|$ ratio. It is worth highlighting the anomalous

shape of the ADDPV signal found for small α values (see curve for $\alpha = 0.3$ in Fig. 4.18b). Under this situation, two pairs of peaks are found, a small one situated at more positive values than the formal potential and a larger one at more negative values. Thus, two peaks with $I_{\text{ADDPV}}^{\text{sph}} > 0$, two peaks with $I_{\text{ADDPV}}^{\text{sph}} < 0$, and three crossing potentials are obtained. The appearance of a new signal at more positive potentials is related to the great influence of the anodic contribution when the α value is very small. The split into two of the response for quasireversible systems is typical of differential techniques and it has been previously described for Differential Double Pulse Voltammetry (DDPV) at which a double peak is obtained for small α values ($\alpha \leq 0.3$) (see Fig. 4.17) [5].

4.4 Multi-electron Electrochemical Reactions

Multi-electronic processes (like those consisting of two-electron transfers, EE mechanism) have been widely treated in the literature, both in their theoretical and applied aspects [4, 10, 56–68]. This high productivity measures in some way the great presence and relevance of these processes in many fields, and hence the importance of understanding them.

Among the double pulse techniques, DDPV is very attractive for the characterization of multi-electron transfer processes. Besides the reduction of undesirable effects, this technique gives well-resolved peak-shaped signals which are much more advantageous for the elucidation of these processes than the sigmoidal voltammograms obtained in Normal Pulse Voltammetry and discussed in Sect. 3.3.

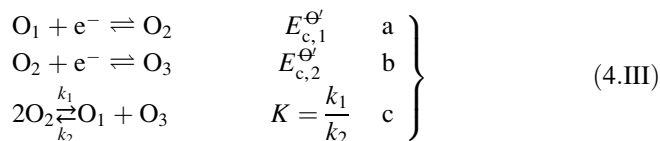
In this section, it will be shown that, when the electron transfer processes behave as reversible, the DDPV curves (properly normalized) are independent of the electrode size and geometry in such a way that the responses obtained in this technique by using macroelectrodes are indistinguishable from those obtained with microelectrodes under transient or stationary conditions.

When any of the electron transfer is slow the situation is much more complex and the geometry of the diffusive field plays a relevant role in the electrochemical response [4, 10].

4.4.1 Application of a Double Potential Pulse to Electrodes of Any Geometry

For the sake of simplicity, only two-electron transfer processes are discussed in this section. The theory corresponding to multielectronic transfer processes can be easily generalized from that presented here and is discussed in detail in [60–62].

For reversible electrode reactions and no solution phase reactions other than disproportionation, the following reaction scheme (EE mechanism) applies (see also Sect. 3.3):



where $E_{c,j}^{\Theta'}$ ($j=1, 2$) are the formal potentials of each electron transfer process and K the disproportionation constant. When the diffusion coefficients of O_1 , O_2 , and O_3 are assumed as equal, the side reaction given by reaction Scheme (4.111c) does not affect the voltammetric response in any single or multipotential technique as has been discussed in Sect. 3.3 (although its influence cannot be discarded in the concentration profiles).

When we consider the problem corresponding to the application of the second potential pulse, E_2 , to the electrode process given by Scheme (4.111) at an electrode of any geometry, the formulation of the problem in such conditions is the following:

$$\left. \begin{array}{l} \frac{\partial c_{\text{O}_1}^{(2)}}{\partial t_2} = D_{\text{O}_1} \nabla^2 c_{\text{O}_1}^{(2)} + k_1 (c_{\text{O}_2}^{(2)})^2 - k_2 c_{\text{O}_1}^{(2)} c_{\text{O}_3}^{(2)} \quad (\text{a}) \\ \frac{\partial c_{\text{O}_2}^{(2)}}{\partial t_2} = D_{\text{O}_2} \nabla^2 c_{\text{O}_2}^{(2)} - 2k_1 (c_{\text{O}_2}^{(2)})^2 + 2k_2 c_{\text{O}_1}^{(2)} c_{\text{O}_3}^{(2)} \quad (\text{b}) \\ \frac{\partial c_{\text{O}_3}^{(2)}}{\partial t_2} = D_{\text{O}_3} \nabla^2 c_{\text{O}_3}^{(2)} + k_1 (c_{\text{O}_2}^{(2)})^2 - k_2 c_{\text{O}_1}^{(2)} c_{\text{O}_3}^{(2)} \quad (\text{c}) \end{array} \right\} \quad (4.154)$$

$$\left. \begin{array}{l} t_2 = 0, q \geq q^s \\ t_2 > 0, q \rightarrow \infty \end{array} \right\} c_{\text{O}_i}^{(2)} = c_{\text{O}_i}^{(1)}; \quad i = 1, 2, 3 \quad (4.155)$$

$$t_2 > 0, q = q^s : \quad \left(\frac{\partial c_{\text{O}_1}^{(2)}}{\partial q_N} \right)_{q^s} + \left(\frac{\partial c_{\text{O}_2}^{(2)}}{\partial q_N} \right)_{q^s} + \left(\frac{\partial c_{\text{O}_3}^{(2)}}{\partial q_N} \right)_{q^s} = 0 \quad (4.156)$$

$$\left. \begin{array}{l} c_{\text{O}_1}^{(2,s)} = e^{\eta_1^{(2)}} c_{\text{O}_2}^{(2,s)} \\ c_{\text{O}_2}^{(2,s)} = e^{\eta_2^{(2)}} c_{\text{O}_3}^{(2,s)} \end{array} \right\} \quad (4.157)$$

with ∇^2 being the Laplacian operator for the particular electrode geometry under study given in Table 2.3 of Sect. 2.6, $c_{\text{O}_i}^{(2,s)}$ the surface concentrations of species O_i ($i = 1, 2, 3$) for the application of the second potential pulse, and

$$\eta_j^{(2)} = \frac{F(E_2 - E_{c,j}^{\Theta'})}{RT} \quad j = 1, 2 \quad (4.158)$$

The problem given by Eqs. (4.154)–(4.157) cannot be solved analytically. However, by assuming that the diffusion coefficients of the different species are equal ($D_{O_1} = D_{O_2} = D_{O_3} = D$), an expression for the current can be deduced, in a similar way to that indicated for the first potential pulse (see Eqs. (3.117)–(3.126) in Sect. 3.3.1), by using the following linear combination:

$$Y^{(2)} = c_{O_1}^{(2)} + c_{O_2}^{(2)} + c_{O_3}^{(2)} = c_{O_1}^* \quad (4.159)$$

So, by combining Eqs. (4.157) and (4.159), the following time-independent expressions are obtained for the surface concentrations of the electroactive species during the second pulse:

$$\left. \begin{aligned} c_{O_1}^{(2,s)} &= \frac{\sqrt{K} e^{2\bar{\eta}^{(2)}}}{\sqrt{K} + e^{\bar{\eta}^{(2)}} + \sqrt{K} e^{2\bar{\eta}^{(2)}}} c_{O_1}^* \\ c_{O_2}^{(2,s)} &= \frac{e^{\bar{\eta}^{(2)}}}{\sqrt{K} + e^{\bar{\eta}^{(2)}} + \sqrt{K} e^{2\bar{\eta}^{(2)}}} c_{O_1}^* \\ c_{O_3}^{(2,s)} &= \frac{\sqrt{K}}{\sqrt{K} + e^{\bar{\eta}^{(2)}} + \sqrt{K} e^{2\bar{\eta}^{(2)}}} c_{O_1}^* \end{aligned} \right\} \quad (4.160)$$

with

$$K = \exp\left(\frac{F\Delta E_c^{\Theta'}}{RT}\right) \quad (4.161)$$

$$\bar{\eta}^{(2)} = \frac{F}{RT}(E_2 - \bar{E}_c^{\Theta'}) \quad (4.162)$$

$$\bar{E}_c^{\Theta'} = \frac{E_{c,1}^{\Theta'} + E_{c,2}^{\Theta'}}{2} \quad (4.163)$$

$$\Delta E_c^{\Theta'} = E_{c,2}^{\Theta'} - E_{c,1}^{\Theta'} \quad (4.164)$$

As in the case of the first potential pulse (see Sect. 3.4.1), the following linear combination can be used,

$$W^{(2)} = 2c_{O_1}^{(2)}(q, t) + c_{O_2}^{(2)}(q, t) \quad (4.165)$$

which fulfills

$$\frac{\partial W^{(2)}}{\partial t_2} = D\nabla^2 W^{(2)} \quad (4.166)$$

Function $W^{(2)}$ can be written

$$W^{(2)} = W^{(1)} + \tilde{W}^{(2)} \quad (4.167)$$

with $W^{(1)} = 2c_{\text{O}_1}^{(1)}(q, t) + c_{\text{O}_2}^{(1)}(q, t)$ (see also Eq. (3.135)). By inserting Eqs. (4.167) into (4.166) and taking into account Eqs. (3.136)–(3.138) of Sect. 3.3.1, it is found the following boundary value problem for $\tilde{W}^{(2)}$:

$$\frac{\partial \tilde{W}^{(2)}}{\partial t_2} = D\nabla^2 \tilde{W}^{(2)} \quad (4.168)$$

$$\left. \begin{array}{l} t_2 = 0, q \geq q^s \\ t_2 > 0, q \rightarrow \infty \end{array} \right\} \tilde{W}^{(2)} = 0 \quad (4.169)$$

$$t_2 > 0, q = q^s : \quad \tilde{W}^{(2,s)} = W^{(2,s)} - W^{(1,s)} \quad (4.170)$$

From Eqs. (4.165)–(4.170) and following a procedure analogous to that described in Sect. 3.3.2 for the first potential pulse, the expression for current corresponding to the second potential pulse can be obtained,

$$\begin{aligned} I_2^G &= FA_G D \left(\frac{\partial W^{(2)}}{\partial q_N} \right)_{q^s} \\ &= I_1^G(\tau_1 + t_2) + FA_G D f_G(t_2, q_G) (W^{(1,s)} - W^{(2,s)}) \end{aligned} \quad (4.171)$$

where:

$$I_1^G(t) = FA_G D f_G(\tau_1 + t_2, q_G) (W^* - W^{(1,s)}) \quad (4.172)$$

$$W^{(j,s)} = \frac{2\sqrt{K}e^{2\bar{\eta}^{(j)}} + e^{\bar{\eta}^{(j)}}}{\sqrt{K} + e^{\bar{\eta}^{(j)}} + \sqrt{K}e^{2\bar{\eta}^{(j)}}} c_{\text{O}_1}^*; \quad j = 1, 2 \quad (4.173)$$

$$W^* = 2c_{\text{O}_1}^* \quad (4.174)$$

$$\bar{\eta}^{(j)} = \frac{F}{RT} (E_j - \bar{E}_c^{\theta'}); \quad j = 1, 2 \quad (4.175)$$

Function $f_G(t, q_G)$ is characteristic of each electrode geometry and is given in Table 2.3 of Sect. 2.6.

4.4.2 Differential Double Pulse Voltammetry

In this section, the analytical expressions given by Eqs. (4.171) and (4.172) are applied to differential double pulse voltammetry (DDPV) [63, 64]. In this technique the duration of the second pulse is usually much shorter than that of the first: $\tau_1 \geq 50 \times \tau_2$. Under these conditions, $f_G(\tau_1 + \tau_2, q_G) \approx f_G(\tau_1, q_G)$ so equation for ΔI_{DDPV}^G simplifies to:

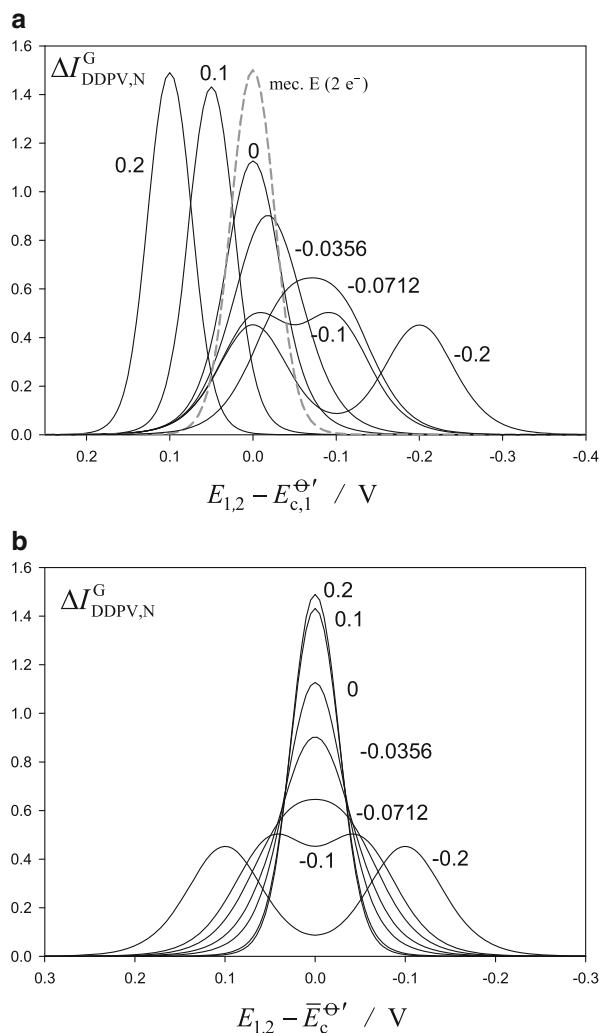
$$\frac{\Delta I_{\text{DDPV}}^G}{FA_G D c_{O_1}^*} = f_G(\tau_2, q_G) \left(\frac{W^{(1,s)} - W^{(2,s)}}{c_{O_1}^*} \right) \quad (4.176)$$

where $(W^{(1,s)} - W^{(2,s)})$ is only dependent on the applied double pulse waveform (E_1 and E_2), see Eqs. (4.173) and (4.175).

According to the definition of K given in Eq. (4.161), when the formal potential of the first step is much larger than that of the second, $\Delta E_c^{\theta'} \leq -200$ mV, the intermediate oxidation state, O_2 , is stable. As can be seen in Fig. 4.19, under these conditions two well-separate peaks are obtained, centred on the formal potential of each process and with the same features of the signal corresponding to a simple one-electron reaction. As the $\Delta E_c^{\theta'}$ value increases, the peaks get closer since the intermediate species is less stable. Thus, a transition from two peaks to a single peak is found. The DDPV response, independently of the $\Delta E_c^{\theta'}$ value and the form of the signal, is symmetrical with respect to the average value of the formal potentials, $\bar{E}_c^{\theta'}$ (see Fig. 4.19b). This value corresponds to the valley between peaks for very negative values of $\Delta E_c^{\theta'}$ and to the peak potential for $\Delta E_c^{\theta'} > -71.2$ mV (for small values of ΔE). This behavior is independent of the electrode size and geometry and of the pulse durations. Eventually, when the formal potential of the second step is much larger than that of the first one, $\Delta E_c^{\theta'} \geq 200$ mV, the system behaves in an identical way to a simple charge transfer process of two electrons (grey dotted curve in Fig. 4.19a).

The electrode size is another important variable to analyze since the use of microelectrodes is very relevant for experimental electrochemical studies enabling the reduction of capacitive and ohmic drop effects, as indicated in Sect. 2.7. Specifically, it is of great interest to check the behavior of the system when the size of the electrode is reduced. In Fig. 4.20, the influence of the electrode radius on the DDPV curves is shown for spherical and disc electrodes and different $\Delta E_c^{\theta'}$ values. As can be seen, independently of the electrode size, a peak-shaped response is obtained with the same peak potential and width (see the superimposed $\Delta I_{\text{DDPV}}^G / \Delta I_{\text{DDPV}}^{G,\text{peak}} - E$ curves in the inserted Figures) since these responses are independent of the electrode geometry (see Eqs. (4.173) and (4.176)). This is a notable advantage over Cyclic Voltammetry where sigmoidal curves are obtained when small electrodes are employed which makes data analysis more difficult and less

Fig. 4.19 Variation of the normalized DDPV curves versus $E - E_{c,1}^{\ominus'}$ (a) or $E - \bar{E}_c^{\ominus'}$ (b) (with $\Delta I_{\text{DDPV},N}^G = \Delta I_{\text{DDPV}}^G / (FA_G D c_{O_1}^* f_G(\tau_2, q_G))$, with the difference between the formal potentials of the redox centers, $\Delta E_c^{\ominus'}$ (values in V indicated on the curves) calculated from Eq. (4.176). The case corresponding to a two-electron E process is also plotted (gray dotted line). $\Delta E = -50$ mV, $\tau_1/\tau_2 = 50$, $\tau_1 = 1$ s. $T = 298$ K



precise (see Sect. 6.2.1). Moreover, given that the peak position and width are independent of the electrode size, the criteria for the characterization of these molecules based on these DDPV peak parameters are very general and can be applied to any electrode. It is important to highlight that, as expected, for ultramicroelectrodes (see curves with $r_s = 5 \mu\text{m}$ in Fig. 4.20 for which the steady state has been almost reached), the ratio between the current densities Δi_{DDPV}^G ($= \Delta I_{\text{DDPV}}^G / A_G$) for disc and spheres (solid and dashed lines, respectively) tends to $4/\pi$ since under these conditions it can be deduced from Eq. (4.176) and Table 2.3 of Sect. 2.6:

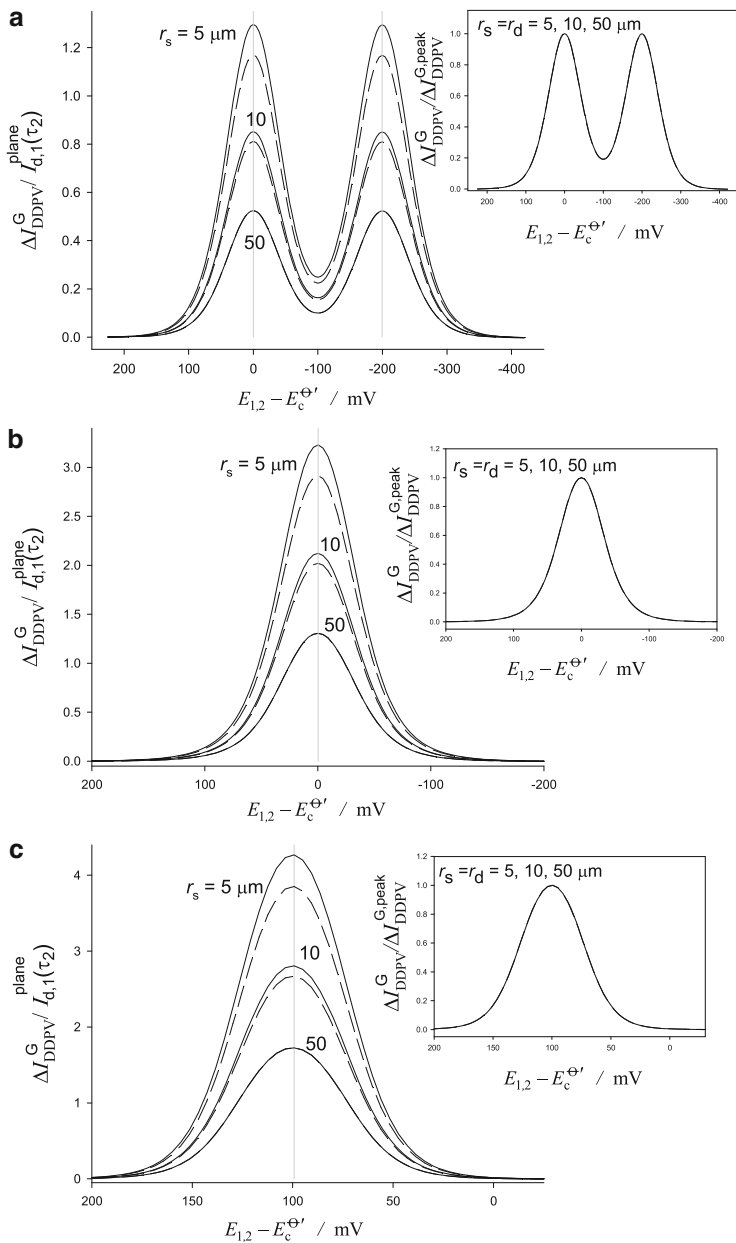


Fig. 4.20 Influence of the electrode radius (r_s and r_d values indicated on the curves) on DDPV curves for disc (solid line) and spherical (dashed line) electrodes with $r_s = r_d$ in all the cases. Three different $\Delta E_c^{\Theta'}$ values are considered: (a) -200 mV, (b) 0 mV, and (c) $+200$ mV. The curves normalized with respect to the peak current are also shown in the inserted graphs. $\tau_1/\tau_2 = 50$, $\Delta E = -50$ mV, $\tau_1 = 1$ s. $T = 298$ K. $I_{d,1}^{\text{plane}}$ is given in Eq. (4.49). Reproduced with permission of [64]

$$\frac{\Delta I_{\text{DDPV}}^{\text{disc,ss}}}{FDc_{\text{O}_1}^*} = \frac{4}{\pi r_d} \left(\frac{W^{(1,s)} - W^{(2,s)}}{c_{\text{O}_1}^*} \right) \quad (4.177)$$

$$\frac{\Delta I_{\text{DDPV}}^{\text{sphe,ss}}}{FDc_{\text{O}_1}^*} = \frac{1}{r_s} \left(\frac{W^{(1,s)} - W^{(2,s)}}{c_{\text{O}_1}^*} \right) \quad (4.178)$$

in such a way that for $r_d = r_s$:

$$\frac{\Delta I_{\text{DDPV}}^{\text{disc,ss}}}{\Delta I_{\text{DDPV}}^{\text{sphe,ss}}} = \frac{4}{\pi} \quad (4.179)$$

By equating to zero the derivative of Eq. (4.176) with respect to $E_{1,2}(= (E_1 + E_2)/2)$, a eighth degree polynomial is obtained, for which the following three real positive roots for $E_{1,2}$ corresponding to the peak and valley potentials are deduced [64]:

$$\left. \begin{aligned} E_{\text{I}} &= E_{\text{c},1}^{\ominus'} + \frac{RT}{F} \ln(\sqrt{K}) && \text{any value of } K \quad (\text{a}) \\ E_{\text{II}} &= E_{\text{c},1}^{\ominus'} + \frac{RT}{F} \ln \left(-\frac{2K - \sqrt{f_2(K)} - A\sqrt{f_1(K)} + 2A^2K}{2A} \right) && (\text{b}) \\ E_{\text{III}} &= E_{\text{c},1}^{\ominus'} + \frac{RT}{F} \ln \left(-\frac{2K + \sqrt{f_2(K)} - A\sqrt{f_1(K)} + 2A^2K}{2A} \right) && (\text{c}) \end{aligned} \right\} \begin{aligned} &K < ca. 0.06 \\ &\Delta E_{\text{c}}^{\ominus'} < ca. -71.2 \text{ mV} \\ &\text{for } \Delta E \leq 30 \text{ mV} \end{aligned} \quad (4.180)$$

with K given in Eq. (4.161) and

$$f_1(K) = \frac{(4K - 1)(K - A^2 + 2A^2K + A^4K)}{A^2} \quad (4.181)$$

$$f_2(K) = A^2 - K + 8K^2 + 16A^2K^2 + 8A^4K^2 - 10A^2K - A^4K - 4AK\sqrt{f_1(K)} - 4A^3K\sqrt{f_1(K)} \quad (4.182)$$

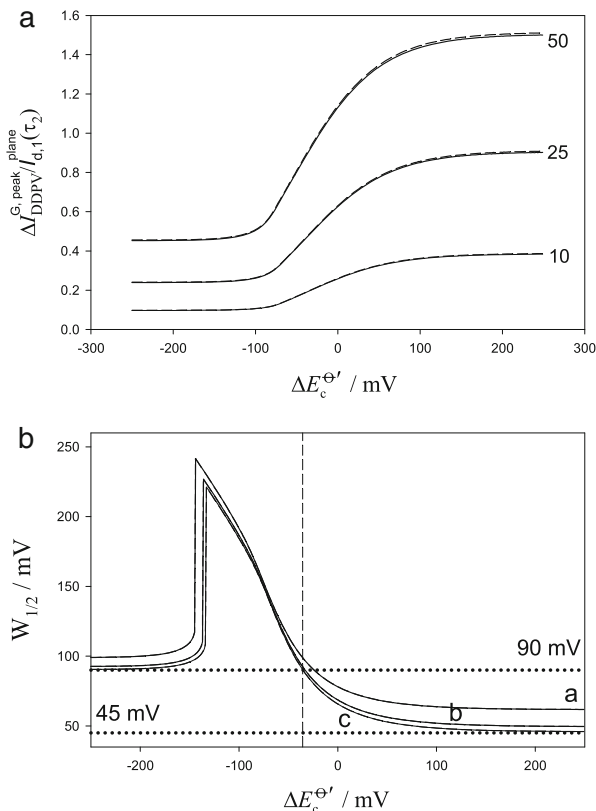
$$A = \exp \left(\frac{F}{2RT} |\Delta E| \right) \quad (4.183)$$

From Eqs. (4.180)–(4.183), it can be shown that these roots depend on $\Delta E_{\text{c}}^{\ominus'}$ (through K) and on the pulse amplitude $|\Delta E|$ (through A). The first root (E_{I}) is valid for any $\Delta E_{\text{c}}^{\ominus'}$ value and corresponds to the average potential

$$E_{\text{I}} = \bar{E}_{\text{c}}^{\ominus'} \quad (4.184)$$

The physical meaning of E_{I} depends on the K value considered. For $K > 0.06$ ($\Delta E_{\text{c}}^{\ominus'} \geq -71.2 \text{ mV}$), it corresponds to the peak potential of the single peak obtained

Fig. 4.21 Evolution of the DDPV dimensionless peak height $\Delta I_{\text{DDPV}}^{\text{G,peak}}/I_{\text{d},1}^{\text{plane}}(\tau_2)$ and of the half-peak width $W_{1/2}$ with $\Delta E_c^{\Theta'}$, corresponding to a two-electron reducible molecule at disc (*solid line*) and spherical (*dashed line*) electrodes. $r_s = r_d = 1 \mu\text{m}$. $I_{\text{d},1}^{\text{plane}}$ is given in Eq. (4.49). ΔE values (in mV) are marked on the graphs in Figure A and are (a) 50 mV, (b) 25 mV, and (c) 10 mV in Figure B. $\tau_1 = 1 \text{ s}$, $\tau_1/\tau_2 = 50$. $T = 298 \text{ K}$. *Dashed line* in Figure B marks the value $\Delta E_c^{\Theta'} = -35.6 \text{ mV}$. Reproduced with permission of [64]



(see Fig. 4.19). For $\Delta E_c^{\Theta'} < -71.2 \text{ mV}$ ($K < 0.06$, separated peaks), E_1 corresponds to the potential of the valley between the two peaks. The roots E_{II} and E_{III} , only operative for $\Delta E_c^{\Theta'} < -71.2 \text{ mV}$, correspond to the peak potentials of separate signals (i.e., to $E_{\text{c},1}^{\Theta'}$ and $E_{\text{c},2}^{\Theta'}$) when $\Delta E_c^{\Theta'} < -142 \text{ mV}$. In these conditions, the peak heights tend to that corresponding to a single electron E mechanism (see also Fig. 4.19). When the pulse amplitude tends to zero (and the response of DDPV becomes coincident with the derivative of the Normal Pulse Voltammogram), the expressions of the three roots are coincident with those given in Table 3.1 of Sect. 3.3.1 for the inflection points of the NPV responses.

The evolution of the DDPV dimensionless peak height $h_{\text{peak}} = \Delta I_{\text{DDPV}}^{\text{G,peak}}/I_{\text{d},1}^{\text{plane}}(\tau_2)$ (a) and half peak width $W_{1/2}$ (b) with $\Delta E_c^{\Theta'}$ calculated from Eq. (4.176) for a disc and a spherical electrode of radius $r_s = r_d = 1 \mu\text{m}$ and three values of the potential pulse amplitudes $\Delta E = E_2 - E_1$ can be seen in Fig. 4.21.

The peak height, $\Delta J_{\text{DDPV}}^{\text{G,peak}}$, always increases with $\Delta E_c^{\Theta'}$ from the value corresponding to one-electron charge transfers for $\Delta E_c^{\Theta'} < -120$ mV, until it reaches that corresponding to an apparent simultaneous two-electron charge transfers for $\Delta E_c^{\Theta'} > 200$ mV (see Fig. 4.21a). Note that the peak height increases with the potential amplitude for both geometries. Concerning the variation of the DDPV half-peak width $W_{1/2}$ (calculated for $T = 298$ K), the curves for discs and spherical electrodes are superimposed since the value of the peak width is independent of the electrode size and shape, being determined by the pulse amplitude $|\Delta E|$ and the difference between the formal potentials $\Delta E_c^{\Theta'}$. Therefore, the results presented in this Figure are very general and enable the characterization of two-electron reducible molecule whatever the electrode employed. As can be observed, $W_{1/2}$ takes a constant value close to 90 mV ($W_{1/2} \leq 99$ mV for $|\Delta E| \leq 50$ mV) when two separate monoelectronic peaks are obtained for $\Delta E_c^{\Theta'} < -140$ mV, showing a sharp jump at $\Delta E_c^{\Theta'}$ around -140 mV. This value corresponds to the case at which the height of the central valley coincides with the half-peak height. For $\Delta E_c^{\Theta'} > -140$ mV, two unresolved peaks or a single peak are obtained, and $W_{1/2}$ decreases with $\Delta E_c^{\Theta'}$ until it reaches a value close to 45 mV, corresponding to an apparently simultaneous two-electron E mechanism. A special case is $\Delta E_c^{\Theta'} = -35.6$ mV ($K = 1/4$), for which $W_{1/2}$ is the same as that corresponding to a simple one-electron charge transfer (see dashed line in the Figure) whereas the response has double the height. In line with references [4, 61, 65, 66], this particular case corresponds to the absence of interactions between the two redox centers and it applies for any electrochemical technique and for any electrode geometry (see also Fig. 4.19 and [61]).

4.4.3 Additive Differential Double Pulse Voltammetry

This section addresses the application of additive differential double pulse voltammetry (ADDPV) to the study of a reversible two-electron transfer reaction. As indicated in Sect. 4.1, in this technique two differential double pulse voltammetry (DDPV) experiments are performed with the same absolute value of the pulse amplitude (ΔE) but with opposite signs. Depending on the difference between the formal potentials between the two steps of the whole process, ADDPV voltammograms can show two or more peaks and one or more crossing points corresponding to the intersection of the current with the potential axis. This offers a very valuable procedure for the determination of the formal potentials since, besides its simplicity, the crossing potentials can often be measured experimentally with greater precision than the peak potentials and widths in other differential techniques. Moreover, their value is independent of the electrode geometry and is

not affected by uncertainties in experimental variables such as the electrode size, the concentration of electroactive species, or the diffusion coefficient.

By taking into account the expression of the currents for the first and second potential pulses applied given by Eqs. (4.171) and (4.172) and that corresponding to the response of the ADDPV technique (Eq. 4.3), the expression of the current is [62, 67],

$$\frac{\Delta I_{\text{ADDPV}}^G}{FADc_{\text{O}_1}^*} = \frac{f_G(\tau_2, q_G)}{c_{\text{O}_1}^*} \left((W^{(1,s)} - W^{(2,s)})_c - (W^{(1,s)} - W^{(2,s)})_a \right) \quad (4.185)$$

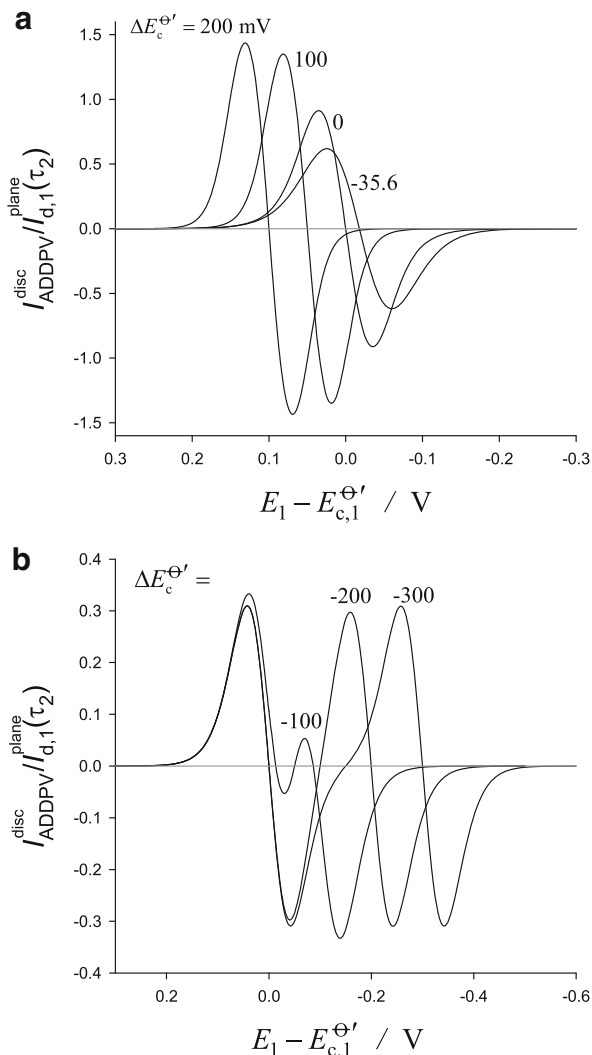
with $(W^{(1,s)} - W^{(2,s)})_c$ and $(W^{(1,s)} - W^{(2,s)})_a$ given by Eq. (4.173) with $E_2 = E_1 - |\Delta E|$ and $E_2 = E_1 + |\Delta E|$, respectively. Thus, the ADDPV voltammogram has a symmetry center for any value of the difference between the formal potentials which corresponds to null current and a potential value given by [67]:

$$E_{\text{cross}}^{\text{sim}} = \bar{E}_c^{\ominus'} = \frac{E_{c,1}^{\ominus'} + E_{c,2}^{\ominus'}}{2} \quad (4.186)$$

The dimensionless theoretical ADDPV curves for a reversible EE mechanism at a disc electrode of radius $r_d = 50 \mu\text{m}$, with a pulse amplitude $|\Delta E| = 50 \text{ mV}$ and different values of the difference between the formal potentials of both electrochemical steps, can be seen in Fig. 4.22. In all cases, ADDPV curves have a center of symmetry at the crossing potential, $E_{\text{cross}}^{\text{sim}}$ given by Eq. (4.186). So, the determination of this point helps to extract the formal potentials accurately. Besides being easier to measure than the potential or width of a peak, the $E_{\text{cross}}^{\text{sim}}$ value is independent of the pulse amplitude, the electrode size and shape, and the difference between the formal potentials, so this diagnosis criterion is very general.

For the $\Delta E_c^{\ominus'}$ values considered in Fig. 4.22a, ADDPV curves show two peaks (a maximum and a minimum) of the same height that increase with $\Delta E_c^{\ominus'}$ until reaching a maximum value for $\Delta E_c^{\ominus'} \geq 200 \text{ mV}$ corresponding to an apparent simultaneous two-electron E process of (see also Sect. 3.3). The $E_{\text{cross}}^{\text{sim}}$ value moves continuously toward more positive potentials as $\Delta E_c^{\ominus'}$ increases. For more negative $\Delta E_c^{\ominus'}$ values, the ADDPV voltammogram splits into two as the stability of the intermediate species O_2 increases, being the limiting value of $\Delta E_c^{\ominus'}$ required for this split function of the pulse amplitude ΔE values ($\Delta E_c^{\ominus'} \leq -100 \text{ mV}$ in the conditions considered in Fig. 4.22b). As a result, four peaks (two maxima and two minima) and three crossing potentials ($E_{c,1}$, $E_{\text{cross}}^{\text{sim}}$, and $E_{c,2}$) can be identified. Expressions for the values of these potentials are obtained from Eq. (4.185) by finding the roots of the equation for the ADDPV current [62]:

Fig. 4.22 Influence of $\Delta E_c^{\ominus'}$ on the dimensionless ADDPV curves ($\tau_1/\tau_2 = 100$) for a reversible EE mechanism (calculated from Eq. (4.185)) at a disc electrode of radius $r_d = 50 \mu\text{m}$, $|\Delta E| = 50 \text{ mV}$, $\tau_2 = 10 \text{ ms}$, $D = 10^{-5} \text{ cm}^2 \text{ s}^{-1}$, $E_{c,1}^{\ominus'} = 0 \text{ V}$, $T = 298 \text{ K}$. The values of the difference between the formal potentials of both electrochemical steps are shown on the curves. Reproduced with permission of [62]



$$\left. \begin{aligned}
 E_{\text{cross}}^{\text{sim}} &= \bar{E}_c^{\ominus'} \\
 E_{c,1} &= E_{c,1}^{\ominus'} + \frac{RT}{F} \ln \left(\frac{-K + \frac{A^2}{2} + \frac{\sqrt{g(K,A)}}{2} - KA^4 - 2KA^2}{A^2} \right) \\
 E_{c,2} &= E_{c,1}^{\ominus'} + \frac{RT}{F} \ln \left(\frac{-2K + A^2 - \sqrt{g(K,A)} - 2KA^4 - 4KA^2}{2A^2} \right)
 \end{aligned} \right\} (4.187)$$

with:

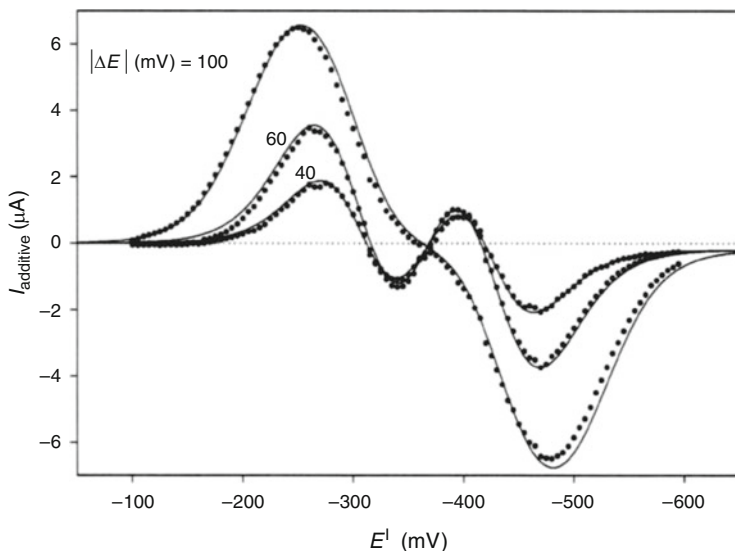


Fig. 4.23 Comparison between experimental curves for 1.25 mM pyrazine at an SMDE at pH = 1.0 in HClO₄ + NaClO₄ adjusted to ionic strength 1.0 M (dotted lines) and theoretical curves for an EE mechanism with $\Delta E_c^{\theta'} = -117$ mV (see Eq. (4.185)) for a spherical electrode, solid lines), for different values of the pulse amplitude $|\Delta E|$ (shown in the Figure). $\tau_1 = 1$ s, $\tau_2 = 0.05$ s, $T = 298.15$ K, $A = 0.011$ cm², $D = 0.781 \times 10^{-5}$ cm² s⁻¹. Reproduced with permission of reference [67]

$$g(K, A) = 4K^2A^8 + 16K^2A^6 + 24K^2A^4 + 16K^2A^2 + 4K^2 + A^4 - 4KA^6 - 12KA^4 - 4KA^2 \quad (4.188)$$

and A given in Eq. (4.183).

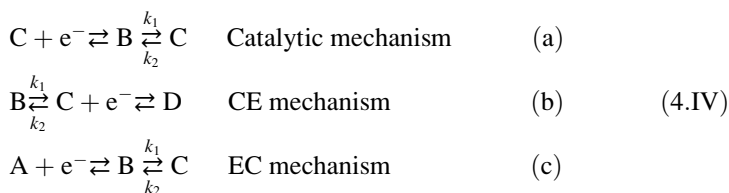
The extreme crossing potentials $E_{c,1}$ and $E_{c,2}$ do depend on the difference between the formal potentials (through K) and the pulse amplitude employed (through A) and they move apart when K decreases. When the ADDPV curve shows three crossing points, the values of the formal potentials can be easily and accurately extracted from the analysis of the $E_{c,1}$, $E_{\text{cross}}^{\text{sim}}$, and $E_{c,2}$ values. For very negative values of $\Delta E_c^{\theta'}$ the determination is immediate since two well-resolved signals are obtained with the characteristics of the ADDPV voltammograms of one-electron reversible processes. Thus, the extreme potentials coincide with the corresponding formal potentials: $E_{c,1}(K \rightarrow 0) \rightarrow E_{c,1}^{\theta'}$ and $E_{c,2}(K \rightarrow 0) \rightarrow E_{c,2}^{\theta'}$. When only one cross potential is obtained, the formal potentials of both steps can be obtained by fitting the experimental ADDPV voltammograms with theoretical curves calculated for different values of $\Delta E_c^{\theta'}$, once the value of $\bar{E}_c^{\theta'}$ has been determined from $E_{\text{cross}}^{\text{sim}}$.

An experimental example of the application of ADDPV to the determination of the formal potentials of the two steps can be seen in Fig. 4.23, corresponding to the

reduction of pyrazine at an SMDE in aqueous acidic media for pulse times $\tau_1 = 1$ s and $\tau_2 = 0.05$ s and different values of the pulse amplitude. All the curves shown in this figure are, as expected, coincident at the symmetry center, $E_{\text{cross}}^{\text{sim}}$, independently of the pulse amplitude $|\Delta E|$. It is also observed how only two peaks are obtained for high values of $|\Delta E|$, but the typical behavior of four peaks described above is achieved by decreasing $|\Delta E|$. These curves provide the value $E_{\text{cross}}^{\text{sim}} = -367$ mV and from the difference between the extreme crossing potentials a value of $\Delta E_c^{\Theta'}$ = -117 mV is obtained, from which it is immediately deduced that $E_{c,1}^{\Theta'} = -308.5$ mV and $E_{c,2}^{\Theta'} = -425.5$ mV vs. Ag/AgCl, KCl (1.0 M).

4.5 First-Order Chemical Reactions Coupled to Charge Transfer Processes

As discussed in Sect. 3.4, the study of electrode processes coupled with homogeneous chemical reactions is frequent in different fields like organic electrosynthesis, ecotoxicity, biosciences, environmental studies, etc. [4, 10, 68–70]. In this section, double pulse techniques will be applied to the study of these processes. These techniques present important advantages like their great sensitivity and the significative reduction of capacitative and background currents, which allow an enhanced resolution of the registered signals [4, 10]. Among the wide range of this type of processes, our study will focused on three reaction mechanisms (see Scheme 4.IV), the first- or pseudo-first- order catalytic, EC and CE processes for which analytical expressions for the current in these double pulse techniques can be obtained when planar or spherical electrodes are considered.



4.5.1 Catalytic Mechanism at Disc, Spherical, and Planar Electrodes

The current corresponding to a catalytic mechanism (reaction scheme 4.IV a) when a potential pulse E_1 is applied to a planar electrode for a time $0 \leq t_1 \leq \tau_1$ when the diffusion coefficients of both species B and C are assumed as equal was deduced in Sect. 3.4.1 and is given by [71, 72]:

$$\frac{I_1^{\text{cat, plane}}}{FAD} = \frac{\zeta^*}{1+K} Z_1^{\text{cat}} f_{\text{plane}}^{\text{cat}}(\chi_1) \quad (4.189)$$

with

$$Z_1^{\text{cat}} = \frac{1 - Ke^{\eta_1}}{1 + e^{\eta_1}} \quad (4.190)$$

$$f_{\text{plane}}^{\text{cat}}(\chi_1) = \left(\frac{e^{-\chi_1}}{\sqrt{\pi\chi_1}} + \text{erf}(\sqrt{\chi_1}) \right) \sqrt{\frac{k_1 + k_2}{D}} \quad (4.191)$$

$$K = \frac{c_{\text{B}}^*}{c_{\text{C}}^*} \quad (4.192)$$

$$\zeta^* = c_{\text{C}}^*(1 + K) \quad (4.193)$$

$$\chi_1 = (k_1 + k_2)t_1 \quad (4.194)$$

and $\eta_1 = F(E_1 - E_c^{\Theta'})/(RT)$. Note that K is the inverse of the equilibrium constant (see also Sect. 3.4).

When a second potential pulse E_2 is applied for a time $0 \leq t_2 \leq \tau_2$, due to the linearity of the mass transport operator, the solutions can be written as

$$\left. \begin{aligned} c_{\text{B}}^{(2)}(x, t) &= c_{\text{B}}^{(1)}(x, t) + \tilde{c}_{\text{B}}^{(2)}(x, t_2) \\ c_{\text{C}}^{(2)}(x, t) &= c_{\text{C}}^{(1)}(x, t) + \tilde{c}_{\text{C}}^{(2)}(x, t_2) \end{aligned} \right\} \quad (4.195)$$

where $c_{\text{B}}^{(1)}(x, t)$ and $c_{\text{C}}^{(1)}(x, t)$ are the solutions corresponding to the first potential pulse (for $t = \tau_1 + t_2$) and $\tilde{c}_{\text{B}}^{(2)}(x, t_2)$ and $\tilde{c}_{\text{C}}^{(2)}(x, t_2)$ are the new unknown partial solutions. The boundary value problem for this second potential is

$$\left. \begin{aligned} t_2 = 0, x \geq 0 \\ t_2 > 0, x \rightarrow \infty \end{aligned} \right\} \left. \begin{aligned} c_{\text{B}}^{(2)}(x, t) &= c_{\text{B}}^{(1)}(x, t) \\ c_{\text{C}}^{(2)}(x, t) &= c_{\text{C}}^{(1)}(x, t) \end{aligned} \right\} \quad (4.196)$$

$$\begin{aligned} t_2 > 0, x = 0, \\ c_{\text{C}}^{(2,s)} &= e^{\eta_2} c_{\text{B}}^{(2,s)} \end{aligned} \quad (4.197)$$

with $c_i^{(2,s)}$ being the surface concentration of species i (with $i = \text{C}$ or B) for the second potential pulse and $\eta_2 = F(E_2 - E_c^{\Theta'})/(RT)$.

As in the case of the first potential pulse (see Sect. 3.4.1), it is convenient to introduce the variables $\phi^{(2)}$ and $\zeta^{(2)}$,

$$\left. \begin{aligned} \phi^{(2)}(x, t) &= \phi^{(1)}(x, t) + \tilde{\phi}^{(2)}(x, t_2) \\ \zeta^{(2)}(x, t) &= \zeta^{(1)}(x, t) + \tilde{\zeta}^{(2)}(x, t_2) = \zeta^* \end{aligned} \right\} \quad (4.198)$$

with $\phi^{(1)}$ and $\zeta^{(1)}$ being the solutions found for the first potential step (see Eqs. (3.180), (3.184), (3.185) and (3.188a)), and $\tilde{\phi}^{(2)}$ and $\tilde{\zeta}^{(2)}$ are given by

$$\tilde{\phi}^{(2)} = \left(\tilde{c}_B^{(2)}(x, t_2) - K \tilde{c}_C^{(2)}(x, t_2) \right) e^{(k_1+k_2)(\tau_1+t_2)} \quad (4.199)$$

$$\tilde{\zeta}^{(2)} = \tilde{c}_B^{(2)}(x, t_2) + \tilde{c}_C^{(2)}(x, t_2) = 0 \quad (4.200)$$

From Eqs. (4.197) and (4.198), it can be deduced that

$$\left. \begin{aligned} c_B^{(2,s)} &= \frac{e^{\eta_2 \zeta^*}}{1 + e^{\eta_2}} \\ c_C^{(2,s)} &= \frac{\zeta^*}{1 + e^{\eta_2}} \end{aligned} \right\} \quad (4.201)$$

$$e^{-(k_1+k_2)(\tau_1+t_2)} \phi^{(2,s)} = \frac{1 - Ke^{\eta_2}}{1 + e^{\eta_2}} \zeta^* \quad (4.202)$$

with $\phi^{(2,s)}$ being the value of $\phi^{(2)}$ at the electrode surface.

Note that the expressions for the surface concentrations of species B and C given by Eq. (4.201) are similar to those corresponding to species O and R of a simple charge transfer (see Eqs. (4.25) and (4.26)), (although in the case of a catalytic mechanism K refers to the inverse of the chemical equilibrium constant of species B and C).

The boundary value problem for the second potential pulse can be written solely in terms of the function $\tilde{\phi}^{(2)}$,

$$\left. \begin{aligned} t_2 = 0, x \geq 0 \\ t_2 > 0, x \rightarrow \infty \end{aligned} \right\} \tilde{\phi}^{(2)} = 0 \quad (4.203)$$

$$t_2 > 0, x = 0,$$

$$e^{-(k_1+k_2)t_2} \tilde{\phi}^{(2,s)} = e^{(k_1+k_2)\tau_1} \left(\frac{1 - Ke^{\eta_2}}{1 + e^{\eta_2}} - \frac{1 - Ke^{\eta_1}}{1 + e^{\eta_1}} \right) \zeta^* \quad (4.204)$$

Equations (4.203) and (4.204) are analogous to Eqs. (3.191a)–(3.192a) of Sect. 3.4.1 corresponding to the first potential pulse applied (by changing $\tilde{\phi}^{(2,s)}$ by $\phi^{(s)}$), except in the value of the constant in the surface condition which is given by $\zeta^*(1 - Ke^{\eta_1})/(1 + e^{\eta_1})$ in the first case (Eq. 3.192a) and by

$e^{(k_1+k_2)\tau_1} \left(\frac{1-Ke^{\eta_2}}{1+e^{\eta_2}} - \frac{1-Ke^{\eta_1}}{1+e^{\eta_1}} \right) \zeta^*$ in the second (Eq. 4.204). It is clear that the mathematical expression of $e^{-(k_1+k_2)t_2} \tilde{\phi}^{(2)}$ will be identical to that obtained for $e^{-(k_1+k_2)(\tau_1+t_2)} \phi^{(s)}$ (Eq. (3.192a) of Sect. 3.4.1) except in the value of this constant.

Thus, the current for the second potential pulse is given by

$$\begin{aligned} \frac{I_2^{\text{cat, plane}}}{FAD} &= \left(\frac{\partial c_C^{(2)}}{\partial x} \right)_{x=0} = \\ &= -\frac{1}{1+K} \left[e^{-(k_1+k_2)(\tau_1+t_2)} \left(\frac{\partial \phi^{(1)}}{\partial x} \right)_{x=0} + e^{-(k_1+k_2)(\tau_1+t_2)} \left(\frac{\partial \tilde{\phi}^{(2)}}{\partial x} \right)_{x=0} \right], \end{aligned} \quad (4.205)$$

It can be deduced easily that the rigorous expression of the current is

$$\frac{I_2^{\text{cat, plane}}}{FAD} = \frac{\zeta^*}{1+K} \left[Z_1^{\text{cat}} f_{\text{plane}}^{\text{cat}}(\chi_1) + Z_2^{\text{cat}} f_{\text{plane}}^{\text{cat}}(\chi_2) \right] \quad (4.206)$$

with

$$Z_2^{\text{cat}} = (1+K) \left(\frac{1}{1+e^{\eta_2}} - \frac{1}{1+e^{\eta_1}} \right) \quad (4.207)$$

$$\chi_2 = (k_1+k_2)t_2 \quad (4.208)$$

and Z_1^{cat} and $f_{\text{plane}}^{\text{cat}}$ given by Eqs. (4.190) and (4.191), respectively, but with $\chi_1 = (k_1+k_2)(\tau_1+t_2)$ in this case.

Equations (4.189) and (4.206) for $I_1^{\text{cat, plane}}$ and $I_2^{\text{cat, plane}}$ at a planar electrode can be extended to spherical and disc electrodes by changing the expression of the electrode area and function $f_{\text{plane}}^{\text{cat}}$ by the corresponding $f_{\text{sph}}^{\text{cat}}$ and $f_{\text{disc}}^{\text{cat}}$, being [73, 74]

$$f_{\text{sph}}^{\text{cat}}(\chi_m, r_s) = \frac{1}{r_s} + f_{\text{plane}}^{\text{cat}}(\chi_m) \quad m = 1, 2 \quad (4.209)$$

$$f_{\text{disc}}^{\text{cat}}(\chi_m, r_d) = \frac{1}{r_d} + \sqrt{\frac{k_1+k_2}{D}} T^{\text{disc}}(\chi_m, \xi_m) \quad m = 1, 2 \quad (4.210)$$

with

$$T^{\text{disc}}(\chi_m, \xi_m) = \frac{e^{-\chi_m}}{\sqrt{\pi\chi_m}} + \text{erf}(\sqrt{\chi_m}) + 0.2732 \frac{\sqrt{\chi_m}}{\xi_m} \int_0^{\xi_m^2} \exp\left[-\frac{0.39115}{\sqrt{u}} - \frac{\chi_m}{\xi_m^2} u\right] du +$$

$$+ 0.2732 \frac{\xi_m}{\sqrt{\chi_m}} \exp\left(-\chi_m - \frac{0.39115}{\xi_m}\right) \quad m = 1, 2 \quad (4.211)$$

$$\left. \begin{aligned} \xi_1 &= \frac{\sqrt{D(\tau_1 + t_2)}}{r_d} \\ \xi_2 &= \frac{\sqrt{Dt_2}}{r_d} \end{aligned} \right\} \quad (4.212)$$

$$\left. \begin{aligned} \chi_1 &= (k_1 + k_2)(\tau_1 + t_2) \\ \chi_2 &= (k_1 + k_2)t_2 \end{aligned} \right\} \quad (4.213)$$

Under conditions of kinetic steady state (i.e., by making $\partial\phi/\partial t = 0$ which is fulfilled for $(k_1 + k_2)t_2 > 1.5$ [73]), the expressions of the current for the first and second potential pulses become

$$\left. \begin{aligned} \frac{I_1^{\text{cat, G, ss}}}{FA_G D} &= \frac{\zeta^*}{1 + K} \frac{1 - Ke^{\eta_1}}{1 + e^{\eta_1}} \frac{1}{\delta_r^G} \\ \frac{I_2^{\text{cat, G, ss}}}{FA_G D} &= \frac{\zeta^*}{1 + K} \frac{1 - Ke^{\eta_2}}{1 + e^{\eta_2}} \frac{1}{\delta_r^G} \end{aligned} \right\} \quad (4.214)$$

where

$$\delta_r^{\text{plane}} = \sqrt{\frac{D}{k_1 + k_2}} \quad (4.215)$$

$$\delta_r^{\text{sphc}} = \frac{1}{\sqrt{\frac{k_1 + k_2}{D} + \frac{1}{r_s}}} \quad (4.216)$$

$$\delta_r^{\text{disc}} = \left[\frac{1}{r_d} + \sqrt{\frac{k_1 + k_2}{D}} + 0.5465 \sqrt{\frac{k_1 + k_2}{D}} \frac{\sqrt{\chi}}{\xi} \int_0^{\xi^2} u \exp\left(-\frac{0.39115}{\sqrt{u}} - \frac{\chi}{\xi^2} u^2\right) du \right]^{-1} \quad (4.217)$$

In the case of disc electrodes, the reaction layer given by Eq. (4.217) is an average value.

4.5.1.1 Reverse Pulse Voltammetry

In RPV technique, the second potential pulse is applied after a first potential pulse under limiting conditions (i.e., $E_1 \rightarrow -\infty$, $Z_1 \rightarrow 1$; see Eq. (4.190)), with E_2 being

scanned in the positive direction. With these conditions in Eq. (4.206), it is obtained [75],

$$\frac{I_{\text{RPV}}^{\text{cat,G}}}{FA_G D} = \frac{\zeta^*}{1+K} [f_G^{\text{cat}}(\chi_1) + Z_2^{\text{cat}} f_G^{\text{cat}}(\chi_2)] \quad (4.218)$$

with χ_1 and χ_2 given by Eq. (4.213), ζ^* by Eq. (4.193) and $f_G^{\text{cat}}(\chi_1)$ and $f_G^{\text{cat}}(\chi_2)$ by Eq. (4.191) for planar electrodes ($G = p$), by Eq. (4.209) for spherical electrodes ($G = s$), and by Eq. (4.210) for disc electrodes ($G = d$). The cathodic and anodic limiting currents are

$$\frac{I_{\text{RPV,l,c}}^{\text{cat,G}}}{FA_G D} = \frac{\zeta^*}{1+K} f_G^{\text{cat}}(\chi_1) \quad (4.219)$$

$$\frac{I_{\text{RPV,l,a}}^{\text{cat,G}}}{FA_G D} = \frac{\zeta^*}{1+K} [f_G^{\text{cat}}(\chi_1) - (1+K)f_G^{\text{cat}}(\chi_2)] \quad (4.220)$$

which, for the particular case of a spherical electrode, can be written as,

$$\frac{I_{\text{RPV,l,c}}^{\text{cat,sphe}}}{FA_s D} = \frac{\zeta^*}{1+K} \left(\frac{1}{r_s} + \sqrt{\frac{k_1+k_2}{D}} f_{\text{plane}}^{\text{cat}}(\chi_1) \right) \quad (4.221)$$

$$\frac{I_{\text{RPV,l,a}}^{\text{cat,sphe}}}{FA_s D} = \zeta^* \left(-\frac{K}{1+K} \left(\frac{1}{r_s} \right) + \sqrt{\frac{k_1+k_2}{D}} \left(\frac{f_{\text{plane}}^{\text{cat}}(\chi_1)}{1+K} - f_{\text{plane}}^{\text{cat}}(\chi_2) \right) \right) \quad (4.222)$$

From Eqs. (4.221) and (4.222), it is clear that both limiting currents increase when the electrode radius decreases and, when the chemical reaction is irreversible ($K = 0$), the anodic limiting current $I_{\text{RPV,l,a}}^{\text{cat,sphe}}$ is independent of the electrode size.

The formal potential of the electroactive couple can be obtained as the value of the potential E_2 at which

$$I_{\text{RPV}}^{\text{cat,sphe}}(E_c^{\Theta'}) = \frac{1}{2} [I_{\text{RPV,l,c}}^{\text{cat,sphe}} - |I_{\text{RPV,l,a}}^{\text{cat,sphe}}|] \quad (4.223)$$

and by combining Eqs. (4.221) and (4.222)

$$I_{\text{RPV,l,c}}^{\text{cat,sphe}} + |I_{\text{RPV,l,a}}^{\text{cat,sphe}}| = \frac{1}{r_s} + \sqrt{\frac{k_1+k_2}{D}} f_{\text{plane}}^{\text{cat}}(\chi_2) \quad (4.224)$$

is obtained.

Under conditions of a kinetic steady state with $\chi_2 > 1.5$, Eq. (4.218) simplifies to

$$\frac{I_{\text{RPV}}^{\text{cat,G,ss}}}{FA_G D} = \frac{\zeta^*}{1+K} [1+Z_2] \frac{1}{\delta_r^G} \quad (4.225)$$

and the limiting currents (Eqs. (4.219) and (4.220)) become

$$\frac{I_{\text{RPV,1,c}}^{\text{cat,G,ss}}}{FA_G D} = \frac{\zeta^*}{1+K} \frac{1}{\delta_r^G} \quad (4.226)$$

$$\frac{I_{\text{RPV,1,a}}^{\text{cat,G,ss}}}{FA_G D} = \frac{-K\zeta^*}{1+K} \frac{1}{\delta_r^G} \quad (4.227)$$

Thus, independently of the electrode geometry, the sum of Eqs. (4.226) and (4.227) leads to

$$\frac{I_{\text{RPV,1,c}}^{\text{cat,G,ss}}}{FA_G D} + \left| \frac{I_{\text{RPV,1,a}}^{\text{cat,G,ss}}}{FA_G D} \right| = \frac{1}{\delta_r^G} \quad (4.228)$$

where δ_r^G is given by Eqs. (4.215), (4.216) and (4.217) for planar, spherical, and disc electrodes, respectively

The influence of the duration of the second potential pulse τ_2 on the experimental RPV voltammograms corresponding to the catalytic process of Ti(IV) in the presence of hydroxylamine at an SMDE electrode can be seen in Fig. 4.24. These curves show the evident influence of τ_2 on the anodic currents owing to the presence of the catalytic process is evident. By using Eq. (4.224) by supposing that the chemical step is irreversible (i.e., $K = 1/K_{\text{eq}} = 0$), the value of the rate constant $k_1 = (1.90 \pm 0.05) \text{ s}^{-1}$ has been reported [75].

4.5.1.2 Differential Double Pulse Voltammetry

The response corresponding to DDPV technique can be obtained by subtracting the expressions of $I_1^{\text{cat,G}}$ and $I_2^{\text{cat,G}}$ given by Eqs. (4.189) and (4.206), respectively, by making $\tau_1 \gg \tau_2$, such that

$$\frac{\Delta I_{\text{DDPV}}^{\text{cat,G}}}{FA_G D} = \frac{\zeta^*}{1+K} Z_2^{\text{cat}} f_G^{\text{cat}}(\chi_2, q_G) \quad (4.229)$$

with $f_G^{\text{cat}}(\chi_2, q_G)$ being the function corresponding to planar, spherical, or disc electrode given by Eqs. (4.191), (4.209), or (4.210), respectively, for $\chi = \chi_2$ and $q_G = r_s$ or $q_G = r_d$ for spherical or disc electrodes, respectively. The DDPV voltammograms thus obtained are peak shaped being the peak potential (when the current is plotted versus the average potential $E_{1,2} = (E_1 + E_2)/2$) and the peak height,

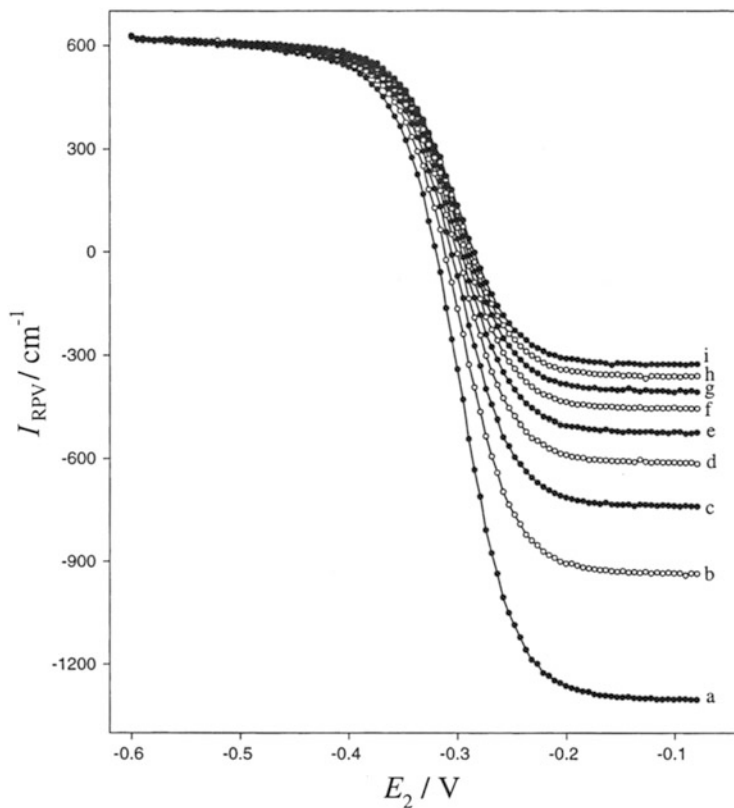


Fig. 4.24 Experimental RPV voltammograms for 1.04 mM Ti(IV) in 0.2 H₂C₂O₄ + 0.07 M HCl + 0.1 M NH₂OH. The radius of the SMDE is $r_s = 0.0226$ cm, $\tau_1 = 1.5$ s, $T = 298$ K. The values of τ_2 (in s) are (a) 0.020, (b) 0.030, (c) 0.040, (d) 0.050, (e) 0.060, (f) 0.070, (g) 0.080, (h) 0.090, and (i) 0.100. Reproduced from reference [75] with permission

$$E_{\text{DDPV}}^{\text{cat, peak}} = E_c^{\Theta'} \quad (4.230)$$

$$\Delta I_{\text{DDPV}}^{\text{cat, peak}} = FA_G D \frac{\zeta^*}{1+K} f_G^{\text{cat}}(\chi_2, q_G) \tanh\left(\frac{F}{4RT} |\Delta E|\right) \quad (4.231)$$

Under kinetic steady state conditions, the expression of the DDPV current becomes

$$\frac{\Delta I_{\text{DDPV}}^{\text{cat, G, ss}}}{FA_G D} = \frac{\zeta^*}{1+K} Z_2^{\text{cat}} \frac{1}{\delta_r^{\text{G}}} \quad (4.232)$$

with δ_r^{G} given by Eqs. (4.215)–(4.217) for the three-electrode geometries considered here.

The voltammetric behavior of the first-order catalytic process in DDPV for different values of the kinetic parameter $\chi_2 (= (k_1 + k_2)\tau_2)$ at spherical and disc electrodes with radius ranging from 1 to 100 μm can be seen in Fig. 4.25. For this mechanism, the criterion for the attainment of a kinetic steady state is $\chi_2 \geq 1.5$ (Eq. 4.232) [73–75]. In both transient and stationary cases, the response is peak-shaped and increases with χ_2 . It is important to highlight that the DDPV response loses its sensitivity toward the kinetics of the chemical step as the electrode size decreases (compare the curves in Fig. 4.25a, c). For the smallest electrode ($r_d = r_s = 1 \mu\text{m}$, Fig. 4.25c), only small differences in the peak current can be observed in all the range of constants considered. Thus, the rate constants that can be determined in DDPV if conditions $r_d \geq \sqrt{D/(k_1 + k_2)}(T^{\text{disc}}(\chi_2, \xi_2))^{-1}$ for a disc electrode or $r_s \geq \sqrt{D/(k_1 + k_2)}(f_{\text{plane}}^{\text{cat}}(\chi_2))^{-1}$ for a spherical one are fulfilled (see Eqs. (4.191), (4.209)–(4.211)).

In all the cases shown in Fig. 4.25, the peak potential corresponds to the formal potential of the charge transfer process, $E_{1,2}^{\text{cat,peak}} = E_c^{\theta'}$, with this behavior being characteristic of the catalytic mechanism and of reversible charge transfer processes (reversible E mechanism; see Eq. (4.85)). The half-peak width ($W_{1/2}$) is independent of the electrode geometry and size and the catalytic rate constants and is given by

$$W_{1/2} = \frac{RT}{F} \ln \left(\frac{1 + A^2 + 4A + \sqrt{(1 + A^2 + 4A)^2 - 4A^2}}{1 + A^2 + 4A - \sqrt{(1 + A^2 + 4A)^2 - 4A^2}} \right) \quad (4.233)$$

with $A = \exp(F|\Delta E|/2RT)$ (see Eq. (4.183)).

The peak height of the DDPV curves is highly sensitive to the parameter $\Lambda (= r_G^2(k_1 + k_2)/D)$ value which can be used for the determination of the catalytic rate constants. In the case of spherical and disc electrodes, the expression of the peak height can be written as [73, 75]

$$\frac{\Delta I_{\text{DDPV}}^{\text{cat, sphe, peak}}}{FA_s D \frac{\zeta^*}{1+K} \frac{1}{\sqrt{\pi D \tau_2}}} = \frac{\sqrt{\pi D \tau_2}}{r_s} \left(1 + \sqrt{\Lambda} \left(\frac{e^{-\chi_2}}{\sqrt{\pi \chi_2}} + \text{erf}(\sqrt{\chi_2}) \right) \right) \tanh \left(\frac{F}{4RT} |\Delta E| \right) \quad (4.234)$$

$$\frac{\Delta I_{\text{DDPV}}^{\text{cat, disc, peak}}}{FA_d D \frac{\zeta^*}{1+K} \frac{1}{\sqrt{\pi D \tau_2}}} = \frac{\sqrt{\pi D \tau_2}}{r_d} \left(1 + \sqrt{\Lambda} T^{\text{disc}}(\chi_2, \xi_2) \right) \tanh \left(\frac{F}{4RT} |\Delta E| \right) \quad (4.235)$$

Thus, in Fig. 4.26 working curves corresponding to the variation of the dimensionless peak current of the catalytic mechanism for spherical and disc electrodes with the parameter $\xi_2 = \sqrt{D\tau_2}/r_G$ are plotted. For a given experimental system,

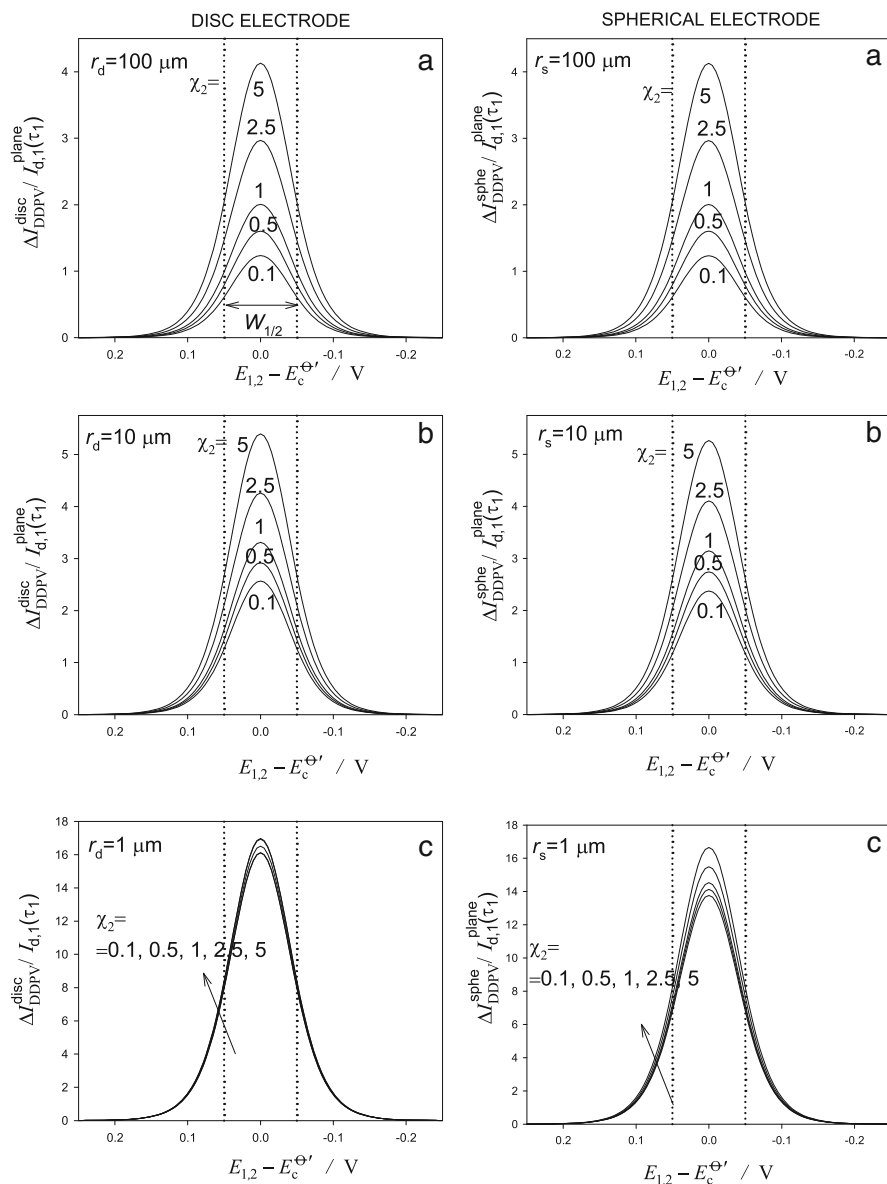


Fig. 4.25 Effect of the electrode radius and the chemical kinetics on the DDV responses of a catalytic mechanism calculated from Eq. (4.229) for disc and spherical electrodes. $|\Delta E| = 50 \text{ mV}$, $\tau_1 = 1 \text{ s}$, $\tau_2 = 0.050 \text{ s}$, $K = 1/K_{\text{eq}} = 1$, $T = 298.15 \text{ K}$, and $D = 10^{-5} \text{ cm}^2 \text{ s}^{-1}$. The values of the electrode radius $r_d = r_s$ and $\chi_2 = (k_1 + k_2)\tau_2$ are indicated on the graphs. Dotted lines mark the potential values where the response equals to the half of the peak height

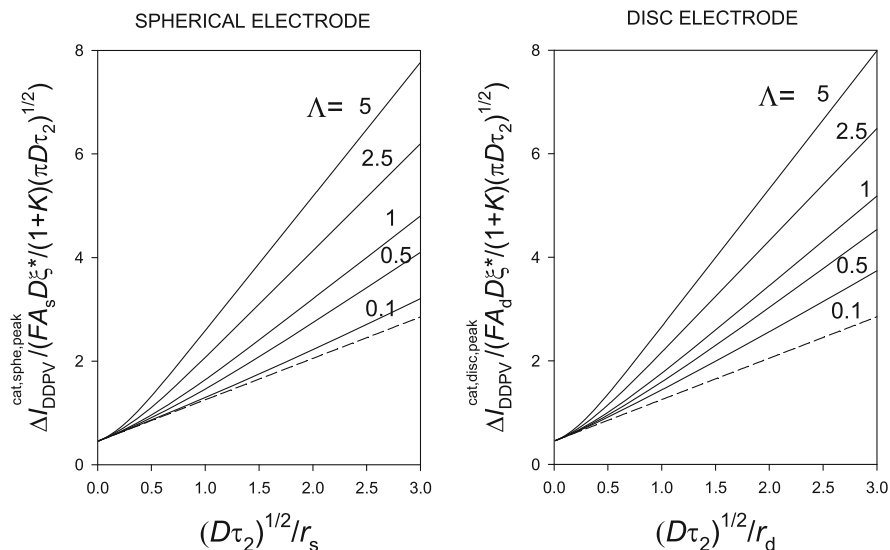


Fig. 4.26 Variation of the dimensionless peak current of a catalytic mechanism (*solid lines*) and of a reversible E mechanism (*dashed line*) for spherical and disc electrodes with the parameter $\sqrt{D\tau_2}/r_G$, with r_G being the sphere or disc radius. The values of $\Lambda (= r_G^2(k_1 + k_2)/D)$ are indicated on the curves. $|\Delta E| = 50 \text{ mV}$, $\tau_1 = 1 \text{ s}$, $\tau_2 = 0.050 \text{ s}$, $K = 1/K_{\text{eq}} = 1$, $T = 298.15 \text{ K}$, and $D = 10^{-5} \text{ cm}^2 \text{ s}^{-1}$

when the electrode radius and the diffusion coefficients are known, these working curves help to determine the rate constants ($k_1 + k_2$) from the value of the dimensionless peak current. The case $k_1 + k_2 = 0$ corresponds to a reversible E mechanism (dashed line), which shows the linear dependence of the peak height with ξ_2 at spherical and disc electrodes.

4.5.2 CE and EC Mechanisms at Planar Electrodes

Unlike the case of catalytic mechanism discussed in the previous section, the theoretical study of CE and EC mechanisms (see reaction scheme 4.IVb, c) in double potential pulse techniques is much more complex than that corresponding to a single potential pulse since the surface concentrations of the species involved in these reaction schemes corresponding to the application of the first potential pulse are time dependent (see also Sects. 3.4.2 and 3.4.3). Due to this, only simplified situations of these mechanisms are considered in this section under planar diffusion conditions. The treatment of both mechanisms at other geometries can be found in [76–79].

4.5.2.1 Reverse Pulse Voltammetry

This section deals with the solution corresponding to an EC mechanism (see reaction scheme 4.IVc) in Reverse Pulse Voltammetry technique under conditions of kinetic steady state (i.e., the perturbation of the chemical equilibrium is independent of time; see Sect. 3.4.3). In this technique, the product is electrogenerated under diffusion-limited conditions in the first period ($0 \leq t_1 \leq \tau_1$) and then examined electrochemically during the second one ($0 \leq t_2 \leq \tau_2$; see Scheme 4.2). Therefore, this method is applicable to obtain information about the product of the electrode reaction. Moreover, under RPV conditions, the first potential pulse corresponds to diffusion-limited current conditions for the electroreduction of species A and the expression of the current for planar electrodes is given by [79],

$$I_{\text{RPV}}^{\text{EC, plane}} = I_{\text{d},1}^{\text{plane}}(\tau_1 + \tau_2) - I_{\text{d},1}^{\text{plane}}(\tau_2) \left[\frac{K e^{\eta_2}}{1 + K + K e^{\eta_2}} F(\chi_2^{\text{EC, p}}) + \frac{2}{\chi_2^{\text{EC, p}}} \sqrt{\frac{\beta}{\pi}} M(\chi_2^{\text{EC, p}}, \beta) \right], \quad (4.236)$$

where $\eta_2 = F(E_2 - E_c^\ominus)/(RT)$ and

$$\chi_2^{\text{EC, p}} = \frac{2\sqrt{D\tau_2}}{K\delta_r^{\text{plane}}} \left(1 + \frac{1+K}{K e^{\eta_2}} \right) \quad (4.237)$$

$$\beta = \frac{\tau_2}{\tau_1 + \tau_2} \quad (4.238)$$

$$F(x) = \frac{\sqrt{\pi}}{2} x \exp(x/2)^2 \operatorname{erfc}(x/2) \quad (4.239)$$

$$M(x, \beta) = \sum_{i=0}^{\infty} \frac{(-1)^i x^{i+1}}{\prod_{l=0}^i p_l} \left\{ 1 + \sum_{k=1}^{\infty} \frac{(2k-1)! i \beta^k}{2^{2k-1} k!(k-1)!(i+2k)} \right\} \quad \text{for } x < 10 \quad (4.240)$$

$$M(x, \beta) = \sqrt{1-\beta} + \sqrt{\pi} \sum_{k=1}^{\infty} \frac{(-1)^{k-1} (2k-1)! \beta^k}{(k-1)! x^{2k-1}} + \sum_{i=1}^{\infty} \frac{(-1)^i 2(2i-1)!}{(i-1)! x^{2i}} \left(1 - \sum_{k=1}^{\infty} \frac{2^{1-2k} (2k-1)! (2i+1) \beta^k}{k!(k-1)!(2k-2i-1)} \right) \quad \text{for } x > 10 \quad (4.241)$$

and $I_{\text{d},1}^{\text{plane}}$ and δ_r^{plane} are given in Eqs. (4.49) and (4.215), respectively.

The oxidative limiting current in linear diffusion ($e^{\eta_2} \rightarrow \infty$) is given by

$$I_{\text{RPV},1,a}^{\text{EC,plane}} = I_{\text{d},1}^{\text{plane}} (\tau_1 + \tau_2) - I_{\text{d},1}^{\text{plane}} (\tau_2) \left[F(\chi_{2,\text{ox}}^{\text{EC,p}}) + \frac{2}{\chi_{2,\text{ox}}^{\text{EC,p}}} \sqrt{\frac{\beta}{\pi}} M(\chi_{2,\text{ox}}^{\text{EC,p}}, \beta) \right] \quad (4.242)$$

with

$$\chi_{2,\text{ox}}^{\text{EC,p}} = \frac{2K\sqrt{D}\tau_2}{\delta_{\text{r}}^{\text{plane}}} \quad (4.243)$$

When the kinetics of the chemical reaction in solution is very fast with respect to the diffusion transport, the resolution of the problem can be simplified by noting that the concentrations of species B and C are in equilibrium at any point and time ($c_{\text{B}}(r, t) = c_{\text{B}}^*$, $c_{\text{C}}(r, t) = c_{\text{C}}^*$) and the reaction layer thickness ($\delta_{\text{r}}^{\text{plane}}$) tends to zero. Taking into account these considerations, the RPV current for the EC mechanism is given by

$$I_{\text{RPV}}^{\text{EC fast,plane}} = I_{\text{d},1}^{\text{plane}} (\tau_1 + \tau_2) - I_{\text{d},1}^{\text{plane}} (\tau_2) \left(\frac{e^{\eta_{1/2}}}{1 + e^{\eta_{1/2}}} \right) \quad (4.244)$$

with $\eta_{1/2} = \frac{F}{RT}(E - E_{\text{mid,RPV}}^{\text{fast}})$ and $E_{\text{mid,RPV}}^{\text{fast}}$ being the mid-wave potential in the limit of very fast chemical kinetics,

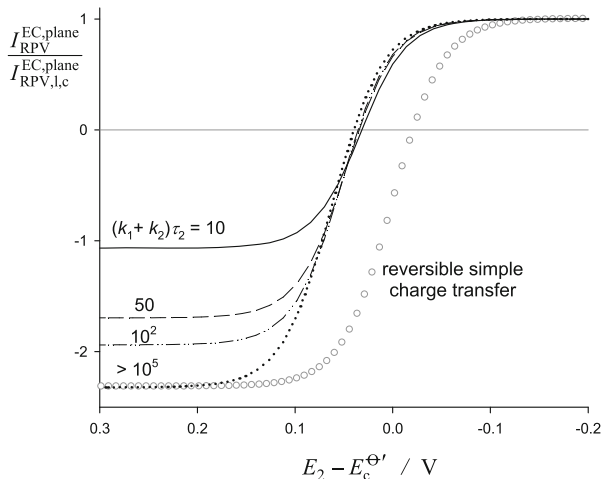
$$E_{\text{mid,RPV}}^{\text{fast}} = E_{\text{c}}^{\ominus'} + \frac{RT}{F} \ln \left(\frac{1+K}{K} \right). \quad (4.245)$$

Note that in this limiting case, the oxidative limiting current of the EC mechanism is the same as for the E mechanism given by Eq. (4.72).

The conditions where Eq. (4.236) provides good results have been examined by comparison with those obtained from digital simulation in [79] and it is concluded that this solution gives rise to accurate results in RPV for $(k_1 + k_2)\tau_2 \geq 5$ (with τ_2 being the duration of the second pulse), with the error decreasing as K increases and always less than 5 % for the value of the oxidative limiting current.

The influence of the rate constants ($k_1 + k_2$) of an EC mechanism with an equilibrium constant $K = 1/K_{\text{eq}} = 0.1$ is shown in Fig. 4.27. As expected, when the second potential is set, like the first one, under diffusion-limited conditions for the electroreduction of species A (i.e., $E_2 - E_{\text{c}}^{\ominus'} \ll 0$, $e^{\eta_2} \rightarrow 0$), the corresponding reductive limiting current $I_{\text{RPV},1,c}^{\text{EC,plane}}$ is independent of the behavior of the product species. At other E_2 values, the RPV current is affected by the coupled chemical process. Hence for the range of $(k_1 + k_2)$ values considered in the figure, the

Fig. 4.27 Influence of the chemical kinetics ($k_1 + k_2$) τ_2 on the RPV curves calculated from Eq. (4.236). The values of ($k_1 + k_2$) (in s^{-1}) appear in the curves. $\tau_1 = 1 \text{ s}$, $\tau_1/\tau_2 = 10$, $K = (1/K_{\text{eq}}) = 0.1$. Taken from [79] with permission



oxidative limiting current ($I_{\text{RPV},1,a}^{\text{EC,plane}}$) increases in absolute value with the rate constants.

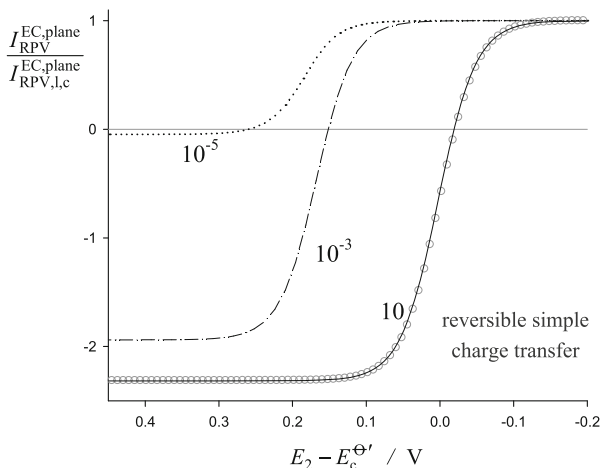
The position of the voltammogram is also affected by the homogeneous chemical reaction. Thus, the reductive RPV curve shifts toward more positive potentials as species B is consumed faster by the chemical process. This shift can be easily monitored by means of the mid-wave potential ($E_{\text{mid,RPV}}^{\text{fast}}$), which helps to characterize the chemical reaction as well as to determine the formal potential of the electrode reaction, $E_c^{\Theta'}$.

For the limit of very fast kinetics, the RPV response is analogous to that of the E mechanism but shifted toward more positive potentials (in the case of a reduction process), the shift magnitude being dependent on the value of the equilibrium constant. This can be observed clearly in Fig. 4.27 by comparing the curve for $(k_1 + k_2)\tau_2 > 10^5$ and for the E mechanism (empty points). From Eq. (4.245) it can be inferred that the mid-potential value $E_{\text{mid,RPV}}$ only depends on the equilibrium constant, and is independent of geometric and kinetic parameters and coincident with $E_{1/2}^{\text{E}}$ [80].

The influence of $K = 1/K_{\text{eq}}$ on the RPV curves is shown in Fig. 4.28. The incidence of the chemical reaction on the voltammograms is more apparent as the chemical equilibrium shifts toward the electroinactive species C, that is, for small K values. Thus, the oxidative limiting current decreases and the voltammogram shifts toward more positive potentials as K decreases. On the other hand, for high K values the effect of the chemical step vanishes and the response of the EC mechanism tends to that of a simple E process (open circles).

As can be deduced from Figs. 4.27 and 4.28, the value of the oxidative limiting current provides a simple criterion to distinguish between the EC and E mechanisms independently of the reversibility degree of the latter. Thus, when a follow-up

Fig. 4.28 Influence of $K = 1/K_{\text{eq}}$ on the RPV curves calculated from Eq. (4.236). The values of K appear in the curves. $(k_1 + k_2)\tau_2 = 10^6$, $\tau_1 = 1$ s, $\tau_1/\tau_2 = 10$. Taken from [79] with permission



chemical reaction occurs, the $I_{\text{RPV,ox}}$ absolute value is smaller (or much smaller for $K \ll 1$) than that expected for a simple charge transfer process.

According to these results, the characterization of the subsequent coupled chemical reaction of the EC mechanism can be achieved with RPV by examining the oxidative limiting current. The half-wave potential is also interesting in order to determine the formal potential of the electrode process [79].

4.5.2.2 Differential Double Pulse Voltammetry

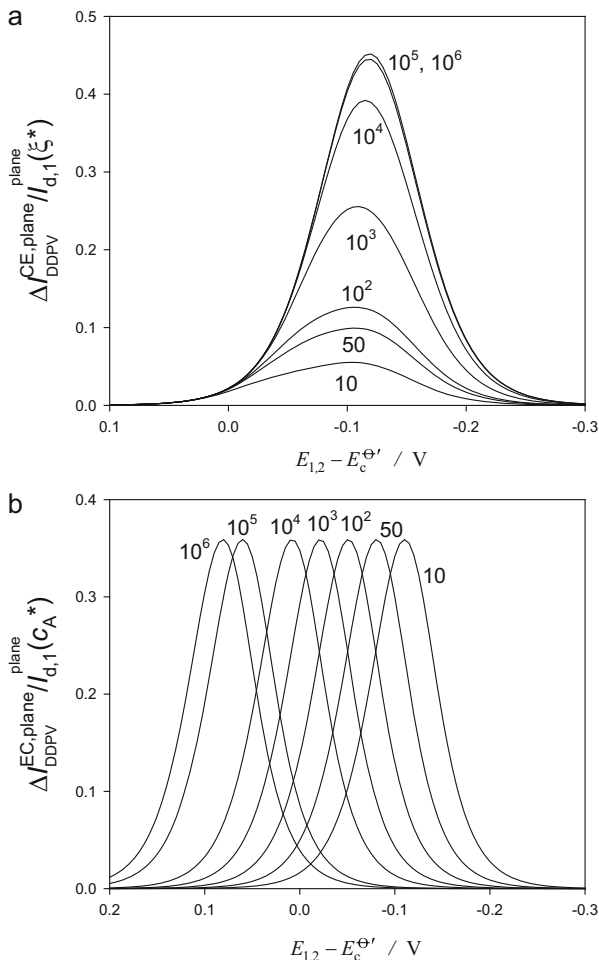
This section presents the solutions for CE and EC mechanism in DDPV technique at planar electrodes under the approximation of kinetic steady state, which are applicable to fast chemical reactions [72]. To obtain these solutions, a mathematical procedure similar to that presented in Sects. 3.4.2 and 3.4.3 has been followed for which it has been assumed that the perturbation of the chemical equilibrium is independent of time (i.e., $\partial\phi_{\text{ss}}/\partial t = \partial(c_{\text{B}} - Kc_{\text{C}})/\partial t = 0$) such that the expression of the current for both mechanisms in DDPV ($\tau_2 \ll \tau_1$) is [77]

$$\frac{\Delta I_{\text{DDPV}}^{\text{CE,plane}}}{I_{\text{d},1}^{\text{plane}}(c_A^*)} = \frac{\sqrt{\pi D \tau_1}}{K \delta_{\text{r}}^{\text{plane}}} \left(\frac{(1+K)(e^{\eta_1} - e^{\eta_2})}{1 + (1+K)e^{\eta_1}} \right) (1 + H(\chi_1^{\text{CE}})) H(\chi_2^{\text{CE}}) \quad (4.246)$$

$$\frac{\Delta I_{\text{DDPV}}^{\text{EC,plane}}}{I_{\text{d},1}^{\text{plane}}(c_A^*)} = \frac{\sqrt{\pi D \tau_1}}{e^{\eta_2} \delta_{\text{r}}^{\text{plane}}} \left(\frac{(1+K)(e^{\eta_1} - e^{\eta_2})}{1 + K + Ke^{\eta_1}} \right) \left(K + \frac{(1+K)}{e^{\eta_1}} H(\chi_1^{\text{EC}}) \right) H(\chi_2^{\text{EC}}) \quad (4.247)$$

where $I_{\text{d},1}^{\text{plane}}$, $H(x)$, and $\delta_{\text{r}}^{\text{plane}}$ are given in Eqs. (4.49), (4.137), and (4.215), respectively. Moreover,

Fig. 4.29 Influence of the chemical kinetics (χ_2) on DDPV curves for (a) a CE mechanism ($K = (1/K_{\text{eq}}) = 10^2$) and (b) an irreversible EC mechanism ($K = (1/K_{\text{eq}}) = 0$) calculated from Eqs. (4.246)–(4.247). χ_2 values are marked on the curves. $\Delta E = -50$ mV. $\tau_1 = 1$ s, $\tau_1/\tau_2 = 20$



$$\chi_m^{\text{CE}} = \frac{2\sqrt{D}\tau_m}{K\delta_{\text{T}}^{\text{plane}}} (1 + (1 + K)e^{\eta_m}) \quad m = 1, 2 \quad (4.248)$$

$$\chi_m^{\text{EC}} = \frac{2\sqrt{D}\tau_m}{e^{\eta_m}\delta_{\text{T}}^{\text{plane}}} (1 + K + Ke^{\eta_m}) \quad m = 1, 2 \quad (4.249)$$

$$\tau_m = \sum_{h=1}^m \tau_h \quad (4.250)$$

$$K = \frac{c_{\text{B}}^*}{c_{\text{C}}^*} = \frac{1}{K_{\text{eq}}} \quad (4.251)$$

As shown in Sects. 3.4.2 and 3.4.3, for the NPV response the condition $\partial\phi_{\text{ss}}/\partial t = 0$ is not sufficient to obtain a time-independent current as in the case of a catalytic mechanism. The DDPV curves for different values of the dimensionless rate constant $\chi_2 = (k_1 + k_2)\tau_2$ are displayed in Fig. 4.29. As can be seen, the

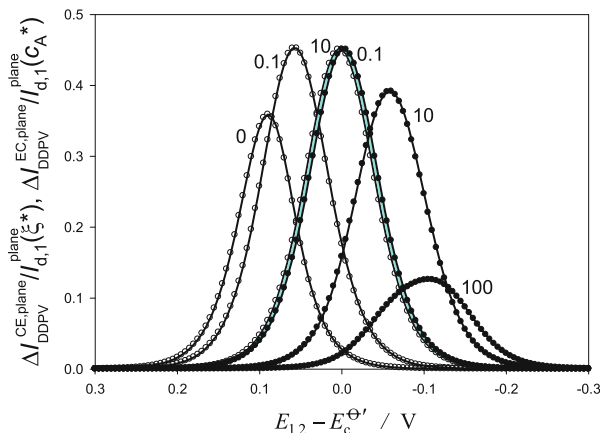


Fig. 4.30 Influence of the inverse of the equilibrium constant (K) on DDPV curves for a CE mechanism (filled circle) and an EC mechanism (open circle) calculated from Eqs. (4.246)–(4.247). K values are marked on the curves. $\chi_2 = 10^2$, $\Delta E = -50$ mV. $\tau_1 = 1$ s, $\tau_1/\tau_2 = 20$. The DDPV response corresponding to a simple reversible electron transfer calculated from Eq. (4.81) is also plotted (blue line). Taken from [77] with permission

behavior both of the peak current and of the peak potential is different for a CE and an irreversible EC mechanism so that the reaction mechanism can be established by changing the dimensionless rate constants through the experimental conditions, for example, the pH in the case of the reduction of an acid or the ligand concentration in the case of the reduction of a metal complex. For a preceding chemical reaction (CE mechanism, Fig. 4.29a), the faster the chemical kinetics (i.e., the greater χ_2^{CE} value), the greater the $\Delta I_{DDPV}^{\text{CE,plane,peak}} / I_{d,1}^{\text{plane}}(\zeta^*)$, while the DDPV peak moves toward more negative potentials. On the other hand, for the case of an irreversible EC mechanism (Fig. 4.29b) the peak potential moves toward more positive values as χ_2^{EC} increases, whereas $\Delta I_{DDPV}^{\text{EC,plane,peak}} / I_{d,1}^{\text{plane}}(c_A^*)$ remains practically constant for all the χ_2^{EC} values considered.

The influence of the equilibrium constant on DDPV curves is shown in Fig. 4.30. DDPV current increases and peak position approaches $E_c^{\Theta'}$ as the chemical equilibrium shifts toward the electroactive species ($K \ll 1$ ($k_2 \ll k_1$) for CE mechanism and $K \gg 1$ ($k_2 \gg k_1$) for EC one with $K = (1/K_{\text{eq}})$), up to a situation at which the responses of both mechanisms overlap, being equivalent to that obtained for a simple reversible E mechanism (blue line) since the effect of the chemical step vanishes.

The complete characterization of the coupled chemical reaction can be performed through the analysis of the peak current and peak potentials for different values of $(\tau_1 + \tau_2)$ and hence the rate constants of the chemical step for a given value of K can be obtained [77].

4.5.2.3 Additive Differential Double Pulse Voltammetry

The response of CE and EC mechanisms (see reaction scheme 4.IVb, c) in ADDPV is the sum of the responses obtained in two DDPV experiments performed with the same value of the pulse height and opposite sign,

$$\frac{I_{\text{ADDPV}}^{\text{CE, plane}}}{I_{\text{d,1}}^{\text{plane}}(\zeta^*)} = \frac{\sqrt{\pi D \tau_1}}{K \delta_r^{\text{plane}}} \left\{ \left(\frac{(1+K)(e^{\eta_1} - e^{\eta_{2,c}})}{1 + (1+K)e^{\eta_1}} \right) (1 + H(\chi_1^{\text{CE}})) H(\chi_{2,c}^{\text{CE}}) + \right. \\ \left. + \left(\frac{(1+K)(e^{\eta_1} - e^{\eta_{2,a}})}{1 + (1+K)e^{\eta_1}} \right) (1 + H(\chi_1^{\text{CE}})) H(\chi_{2,a}^{\text{CE}}) \right\} \quad (4.252)$$

$$\frac{I_{\text{ADDPV}}^{\text{EC, plane}}}{I_{\text{d,1}}^{\text{plane}}(C_A^*)} = \frac{\sqrt{\pi D \tau_1}}{e^{\eta_{2,c}} \delta_r^{\text{plane}}} \left(\frac{(1+K)(e^{\eta_1} - e^{\eta_{2,c}})}{1 + K + Ke^{\eta_1}} \right) \left(K + \frac{(1+K)}{e^{\eta_1}} H(\chi_1^{\text{EC}}) \right) H(\chi_{2,c}^{\text{EC}}) + \\ + \frac{\sqrt{\pi D \tau_1}}{e^{\eta_{2,a}} \delta_r^{\text{plane}}} \left(\frac{(1+K)(e^{\eta_1} - e^{\eta_{2,a}})}{1 + K + Ke^{\eta_1}} \right) \left(K + \frac{(1+K)}{e^{\eta_1}} H(\chi_1^{\text{EC}}) \right) H(\chi_{2,a}^{\text{EC}}) \quad (4.253)$$

where planar electrodes under the approximation of kinetic steady state have been assumed and $E_{2,c} = E_1 - |\Delta E|$ and $E_{2,a} = E_1 + |\Delta E|$, respectively.

For high values of the chemical rate constant, i.e., under conditions of a diffusive-kinetic steady state ($\partial \phi_{\text{ss}} / \partial t = 0$ and consideration that diffusion only acts on variable ζ ; see Sects. 3.4.2 and 3.4.3), it is possible to find simple expressions for the cross potentials of the ADDPV curves,

$$E_{\text{cross}}^{\text{CE}}(\chi_{2,\text{lim}}^{\text{CE}} > 40) = E_c^{\Theta'} + \frac{RT}{F} \ln \left(\frac{\frac{K}{\sqrt{\pi(k_1+k_2)\tau_2}} + 1}{(1+K)} \right) \quad (4.254)$$

$$E_{\text{cross}}^{\text{EC}}(\chi_{2,\text{lim}}^{\text{EC}} > 40) = E_c^{\Theta'} + \frac{RT}{F} \ln \frac{(1+K)}{\frac{1}{\sqrt{\pi(k_1+k_2)\tau_2}} + K} \quad (4.255)$$

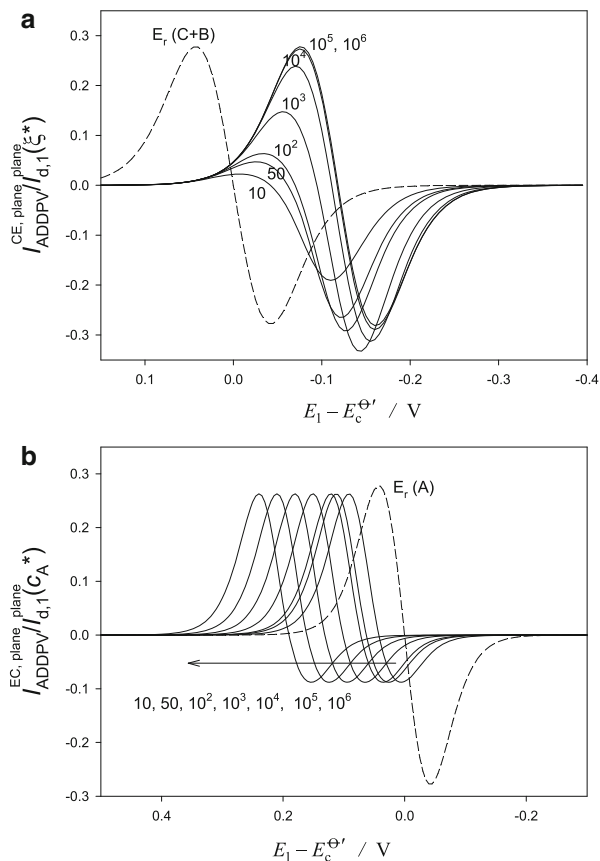
with

$$\chi_{2,\text{lim}}^{\text{CE}} = \frac{2\sqrt{D\tau_2}}{K \delta_r^{\text{plane}}} \quad (4.256)$$

$$\chi_{2,\text{lim}}^{\text{EC}} = \frac{2\sqrt{D\tau_2}}{\delta_r^{\text{plane}}} K \quad (4.257)$$

and δ_r^{plane} given by Eq. (4.215). According to Eqs. (4.254) and (4.255), in the case of very fast kinetics ($k_1 + k_2 \rightarrow \infty$) the cross potential tends to a value which only depends on the equilibrium constant [78]:

Fig. 4.31 Influence of the chemical kinetics on the ADDPV curves for (a) a CE mechanism ($K = 100$, Eq. (4.252)) and (b) an EC mechanism with an irreversible homogeneous chemical reaction ($K = (1/K_{\text{eq}}) = 0$, Eq. (4.253)). χ_2 values are indicated on the curves. The curves corresponding to a reversible charge transfer process (E_r) are plotted for comparison (dashed line, Eq. (4.106)) with the bulk concentration of the electroactive species being (a) $c^* = \zeta^* = c_B^* + c_C^*$ and (b) $c^* = c_A^*$. $|\Delta E| = 50 \text{ mV}$, $\tau_1 = 1 \text{ s}$, $\tau_1/\tau_2 = 20$



$$E_{\text{cross}}^{\text{CE}}((k_1 + k_2) \rightarrow \infty) = E_c^{\Theta'} + \frac{RT}{F} \ln \left(\frac{1}{1 + K} \right) \quad (4.258)$$

$$E_{\text{cross}}^{\text{EC}}((k_1 + k_2) \rightarrow \infty) = E_c^{\Theta'} + \frac{RT}{F} \ln \left(\frac{1 + K}{K} \right) \quad (4.259)$$

The influence of the chemical kinetics is analyzed in Fig. 4.31 where ADDPV curves are plotted for different values of the dimensionless rate constant $\chi_2 (= (k_1 + k_2) \tau_2)$. For comparison, the curve corresponding to a simple, reversible charge transfer process (E_r) of species “C + B” for the CE mechanism and of species A for the EC one has also been plotted (dashed line in Fig. 4.31a, b). As can be observed, the behavior of ADDPV curves with χ_2 is very different depending on the reaction scheme. For the CE mechanism with $K = (1/K_{\text{eq}}) = 100$ (Fig. 4.31a), the peak current increases and the peak potential shifts toward more negative values as the kinetics is faster, that is, as χ_2 increases. For very fast chemical reactions, the ADDPV signal is equivalent to that of a reversible E mechanism (E_r) with

$\zeta^* = c_C^* + c_B^*$ although located at more negative potentials. A good agreement is found between the value of the crossing potential of the ADDPV curves and that predicted by Eq. (4.254) (error smaller than 3 mV for $\chi_2 > 10^2$).

For an electrode process followed up by an irreversible homogeneous chemical reaction ($K = 0$, Fig. 4.31b), the peak currents are independent of the chemical kinetics whereas the peak potential takes more positive values as χ_2 increases because the chemical reaction facilitates the reduction process by removal of species B. In all cases plotted in this figure, the value of the crossing potential can be evaluated with good accuracy from Eq. (4.255) (error smaller than 3 mV for $\chi_2 > 10^2$). With respect to the E mechanism of species A, in the EC response both peak currents are smaller, and this effect is especially noticeable in the minimum which is more affected by the follow-up reaction.

Therefore, we can identify the reaction scheme by studying the variation of the ADDPV response when the χ_2 value is modified through the experimental conditions (for example, the pH or the ligand concentration) or the pulse duration.

The relative magnitude of the peaks of the ADDPV curve is also very informative about the electrode process [55, 81, 82]. It can be observed that for the CE mechanism it is fulfilled that $I_M^{\text{plane}} < |I_m^{\text{plane}}|$ whereas for the EC one $I_M^{\text{plane}} > |I_m^{\text{plane}}|$. This behavior contrasts with the case of the first-order catalytic mechanism and with the reversible E mechanism for which the value of the peak currents is equal ($I_M^{\text{plane}} = |I_m^{\text{plane}}|$). Therefore, this simple criterion allows us to discriminate between these mechanisms.

The chemical kinetics (χ_2), has no effect on the symmetry of the peaks in the case of the irreversible EC mechanism ($K = 0$) under kinetic steady-state conditions. On the other hand, for the CE mechanism the $I_M^{\text{plane}}/|I_m^{\text{plane}}|$ value does depend on χ_2 and it tends to $I_M^{\text{plane}}/|I_m^{\text{plane}}| \rightarrow 1$ in the limiting case of very fast chemical reactions (see Fig. 4.31a).

The influence of the equilibrium constant on the ADDPV curves for the CE and irreversible EC mechanisms can be seen in Fig. 4.32. For a given χ_2 value, the magnitude of the signal diminishes and it shifts away from the formal potential as the equilibrium is displaced toward the electroinactive species, that is, for large K values in the CE mechanism and for small K values in the EC mechanism. In the opposite limiting case, that is, when the chemical equilibrium is fully displaced toward the electroactive species, the kinetic effects disappear and obviously the signal coincides with that of a reversible charge transfer process (grey line).

The quantitative determination of the homogeneous rate constants can be easily carried out from the values of the peak currents and the crossing potential of the ADDPV curves [78]. The use of the crossing potential is very helpful since this parameter does not depend on the pulse height (ΔE) employed and so can be measured with good accuracy from several ADDPV curves obtained with different ΔE values. In addition, for fast kinetics the simple analytical expressions that are available for E_{cross} (Eqs. (4.254) and (4.255)) allow a direct determination of the rate constants of the chemical reaction.

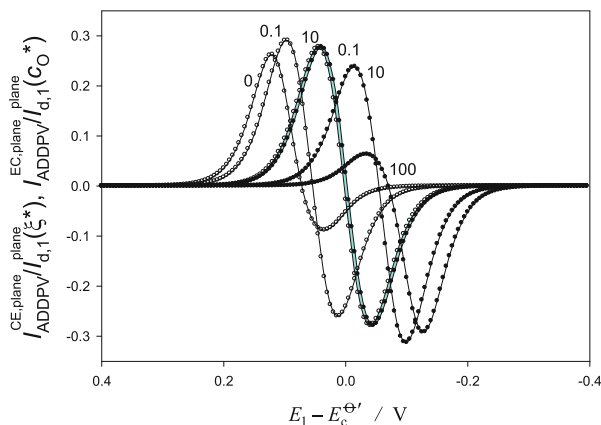


Fig. 4.32 Influence of the inverse of the equilibrium constant $K = 1/K_{\text{eq}}$ on the ADDPV curves for a CE mechanism [filled circle, Eq. (4.252)] and an EC mechanism [open circle, Eq. (4.253)]. $\chi_2 = 100$. The curve corresponding to a reversible charge transfer process (E_r) is also plotted for comparison [gray line, Eq. (4.106)]. $|\Delta E| = 50\text{mV}$, $\tau_1 = 1\text{ s}$, $\tau_1/\tau_2 = 20$. Taken from [78] with permission

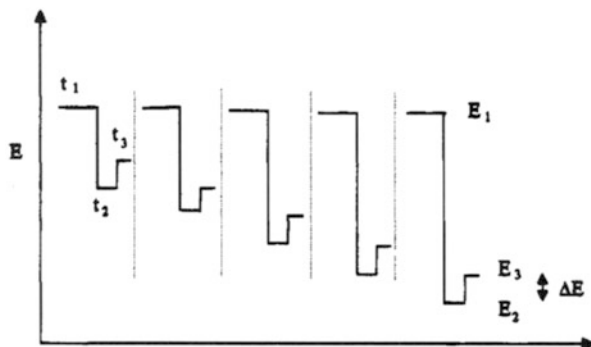
4.6 Triple Pulse Voltammetries

As highlighted in previous sections, double pulse techniques offer some advantages over single potential pulse techniques by providing increased signal sensitivity and eliminating most of the charge current. Multipotential pulse techniques exploit these advantages, but the complexity of the diffusional-kinetic problem compels the use of numerical methods to obtain the theoretical solutions in many cases. Due to this, triple potential pulse techniques are an interesting alternative, for which a brief introduction will be given in the present section. These techniques present the advantage of a simple theoretical evaluation of their response together with a higher versatility. Two triple potential pulse techniques will be presented, Reverse Differential Pulse Voltammetry (RDPV), which is a modification of the Reverse Pulse technique proposed by Brumleve et al. [83], and Double Differential Triple Pulse Voltammetry (DDTPV) [84–86].

4.6.1 Reverse Differential Pulse Voltammetry

Among double pulse techniques, RPV is the most powerful from the kinetic point of view, due to the information it provides on the degree of reversibility of the electrode process. This information is similar to that which can be obtained from

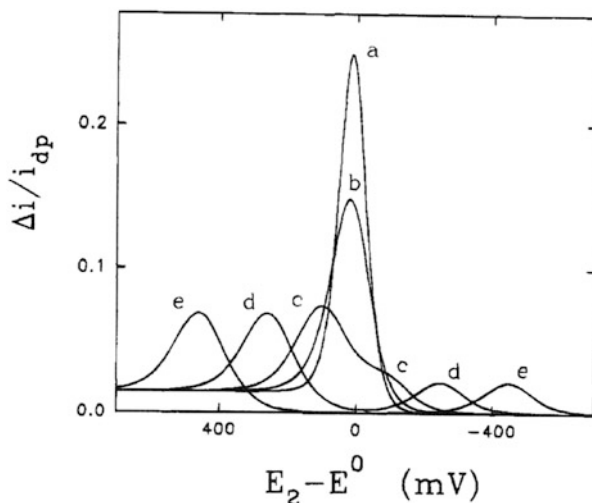
Scheme 4.5 Potential–time waveform corresponding to RDPV



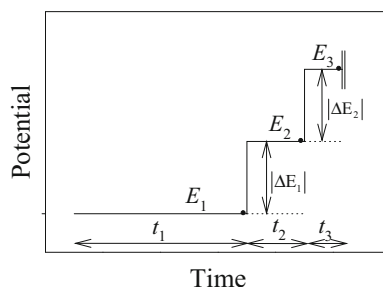
Cyclic Voltammetry. However, experimental use of this technique has been restricted almost exclusively to the analysis of the limiting currents of the signals obtained. One reason for this could be that when a quasi-reversible electronic transfer is analyzed in RPV, two very close waves are obtained, which are difficult to resolve from an experimental viewpoint. This problem can be eliminated by using the triple pulse technique Reverse Differential Pulse Voltammetry (RDPV), proposed in references [80, 84, 85] and based in the application of the waveform presented in Scheme 4.5.

Potentials E_1 and E_2 are chosen as in RDP technique, i.e., E_1 is constant and it corresponds to a potential value at which the reduction process is controlled by diffusion, whereas E_2 shifts to positive potentials. In RDPV, a potential E_3 is chosen such that $\Delta E = E_3 - E_2$ is constant. I_1^G , I_2^G , and I_3^G are designed as the faradaic responses corresponding to each of the potentials E_1 , E_2 , and E_3 , which are applied during times $0 \leq t_1 \leq \tau_1$, $0 \leq t_2 \leq \tau_2$, and $0 \leq t_3 \leq \tau_3$, respectively. In RDPV, the representation of $\Delta I^G = I_3^G - I_2^G$ versus E_2 is carried out, with I_3^G and I_2^G being measured at times τ_3 and τ_2 , respectively, and with the additional condition $\tau_1 \gg (\tau_2 + \tau_3)$ [87]. The records obtained are peak shaped, in contrast to the waves obtained in RPV, with the corresponding analytical advantage that this implies. In RDPV, the appearance of two peaks can be observed for an irreversible simple electronic transfer. One of the peaks appears at more positive potentials and the other at more negative potentials than the formal potential $E_c^{\theta'}$. The difference between the potentials of these peaks enables an approximate determination of the value of the rate constant of the electrode reaction k^0 , while the sum of these peak potentials is proportional to $E_c^{\theta'}$. Finally, the half-width of the peak allows an approximate calculation of the values of the transfer coefficient of the cathodic process, α , in the peak which appears at more negative potentials than $E_c^{\theta'}$ and of that corresponding to the anodic process, $(1 - \alpha)$, in the peak that appears at more positive values than $E_c^{\theta'}$. Some examples of this behavior can be seen in Fig. 4.33, obtained for different values of k^0 with $\tau_1 = 3$ s, $\tau_2 = 0.3$ s, and $\tau_3 = 0.03$ s and $\Delta E = -25$ mV. For $k^0 \geq 0.1$ cm s⁻¹ only one

Fig. 4.33 Plot of $\Delta I_{\text{RDPV}}^{\text{plane}} / I_{\text{d,c}}^{\text{plane}}(t_3)$ versus $E_2 - E_c^{\ominus}$, with $I_{\text{d,c}}^{\text{plane}}(t_3) = FADc_O^* / \sqrt{\pi D t_3}$ calculated from Eq. (1) of reference [87] with $z=0$, $\alpha=0.5$, $D_O = D_R = 10^{-5} \text{ cm}^2 \text{ s}^{-1}$, $\tau_1 = 3 \text{ s}$, $\tau_2 = 0.3 \text{ s}$, $\tau_3 = 0.03 \text{ s}$, and $\Delta E = -25 \text{ mV}$. The values of k^0 (in cm s^{-1}) are (a) 1; (b) 5×10^{-3} ; (c) 10^{-3} ; (d) 5×10^{-5} and (e) 10^{-6} . Taken from [87] with permission



Scheme 4.6 Potential–time waveform corresponding to DDTPV



peak appears and its position and height are independent of the k^0 value, i.e., under these experimental conditions, the electronic transfer can be considered as reversible. For $k^0 < 5 \times 10^{-4} \text{ cm s}^{-1}$ two well-developed peaks can be observed.

4.6.2 Double Differential Triple Pulse Voltammetry

In this technique, three potential steps, E_1 , E_2 , and E_3 are successively applied during times $0 \leq t_1 \leq \tau_1$, $0 \leq t_2 \leq \tau_2$, and $0 \leq t_3 \leq \tau_3$, respectively, with the condition $\tau_1 \gg (\tau_2 + \tau_3)$, and the differences $\Delta E_1 = E_2 - E_1$ and $\Delta E_2 = E_3 - E_2$ are of equal sign (see Scheme 4.6). Thus, $\Delta I_1^G = I_2^G - I_1^G$ and $\Delta I_2^G = I_3^G - I_2^G$ also result in the same sign. The signal registered in DDTPV is [84–86]:

$$I_{\text{DDTPV}}^{\text{G}} = \Delta I_2^{\text{G}} - \Delta I_1^{\text{G}} = I_3^{\text{G}} - 2I_2^{\text{G}} + I_1^{\text{G}} \quad (4.260)$$

which is plotted vs. E_2 .

The form of the signal is similar to the second derivative of the NPV curve and when the time duration of the second and third potential pulses fulfills $\tau_3 = 2\tau_2/3$, the DDTPV response coincides with that obtained in ADDPV for reversible charge transfer processes [88].

References

1. Oldham KB, Parry EP (1970) *Anal Chem* 42:229–233
2. Barker GC, Gardner AW (1960) *Z Anal Chem* 173:79–83
3. Molina A, Moreno MM, Serna C, Camacho L (2001) *Electrochem Commun* 3:324–329
4. Bard AJ, Faulkner LR (2001) *Electrochemical Methods. Fundamentals and Applications*, 2nd edn. Wiley, New York, NY
5. Molina A, Martínez-Ortiz F, Laborda E, Compton RG (2010) *Electrochim Acta* 55:5163–5172
6. Serna C, Moreno MM, Molina A, Gonzalez J (2000) In: *Transworld Research Network* (ed) Recent research developments in electrochemistry, vol 3. Transworld Research Network, Trivandrum, pp 29–42
7. Lovrić M, O’Dea JJ, Osteryoung J (1983) *Anal Chem* 55:704–708
8. Aoki K, Osteryoung J, Osteryoung RA (1980) *J Electroanal Chem* 110:1–18
9. Lovrić M, Osteryoung J (1982) *Electrochim Acta* 27:963–968
10. Compton RG, Banks CE (2007) *Understanding voltammetry*. World Scientific, Singapore
11. Laborda E, Gonzalez J, Molina A (2014) *Electrochem Commun* 43:25–30
12. Melville JL, Compton RG (2001) *Electroanalysis* 13:123–130
13. Rifkin SC, Evans DH (1976) *Anal Chem* 48:1616–1618
14. Rifkin SC, Evans DH (1976) *Anal Chem* 48:2174–2180
15. Thormann W, Bixler JW, Mann TF, Bond AM (1988) *J Electroanal Chem* 241:1–15
16. Molina A, Gonzalez J, Henstridge M, Compton RG (2011) *J Phys Chem C* 115:4054–4062
17. Montenegro MI, Queirós MA, Daschbach JL (eds) (1991) *Microelectrodes: theory and applications*. Kluwer, Dordrecht
18. Ahmed Basha C, Rajendran L (2006) *Int J Electrochem Sci* 1:268–282
19. Molina A, Gonzalez J, Henstridge M, Compton RG (2011) *Electrochim Acta* 56:4589–4594
20. Molina A, Compton RG, Serna C, Martinez-Ortiz F, Laborda E (2009) *Electrochim Acta* 54:2320–2328 and references therein
21. Serna C, Molina A (1999) *J Electroanal Chem* 466:8–14
22. Kambara T (1954) *Bull Chem Soc Jpn* 27:523–525
23. Buzzeo MC, Klimentko OV, Wadhawan JD, Hardacre C, Seddon KR, Compton RG (2003) *J Phys Chem A* 107:8872–8878
24. Martin RD, Unwin PR (1998) *Anal Chem* 70:276–284
25. Garay F, Barbero CA (2006) *Anal Chem* 78:6740–6746
26. Svanholm U, Parker VD (1975) *J Chem Soc Perkin Trans II* 7:755–757
27. Wang RL, Tam KY, Compton RG (1997) *J Electroanal Chem* 434:105–114
28. Michael AC, Wightman RM, Amatore CA (1989) *J Electroanal Chem* 267:33–45
29. Martinez-Ortiz F, Laborda E, Limon-Petersen JG, Rogers EI, Serna C, Rees NV, Molina A, Compton RG (2009) *J Phys Chem C* 113:17215–17222
30. Anson FC (1966) *Anal Chem* 38:54–57
31. Christie JH, Osteryoung RA, Anson FC (1967) *J Electroanal Chem* 13:236–244
32. Yu J-S, Zhang Z-X (1997) *J Electroanal Chem* 439:73–80

33. Laborda E, Rogers EI, Martínez-Ortiz F, Limón-Petersen JG, Rees NV, Molina A, Compton RG (2009) *J Electroanal Chem* 634:1–10
34. Zigah D, Ghilane J, Lagrost C, Hapiot P (2008) *J Phys Chem B* 112:14952–14958
35. Parry EA, Osteryoung RA (1965) *Anal Chem* 37:1634–1637
36. Ružič I, Sluyters-Rehbach M (1978) *Anal Chim Acta* 99:177–182
37. Molina A, Morales I (2007) *Int J Electrochem Sci* 2:386–405
38. Molina A, Laborda E, Rogers EI, Martínez-Ortiz F, Serna C, Limon-Petersen JG, Rees NV, Compton RG (2009) *J Electroanal Chem* 634:73–81
39. Gonzalez J, Molina A, López-Tenés M, Serna C (2000) *J Electrochem Soc* 147:3429–3435
40. Qian Q, Wilson GS, Bowman-James K, Girault HH (2001) *Anal Chem* 73:491–503
41. Ortuño JA, Serna C, Molina A, Gil A (2006) *Anal Chem* 78:8129–8133
42. Molina A, Serna C, Ortuño JA, Gonzalez J, Torralba E, Gil A (2009) *Anal Chem* 81:4220–4225
43. Kim M, Smith VP, Hong T (1993) *J Electrochem Soc* 140:712–721
44. Molina A, Martínez-Ortiz F, Laborda E, Compton RG (2010) *J Electroanal Chem* 648:67–77
45. Martínez-Ortiz F, Zoroa N, Molina A, Serna C, Laborda E (2009) *Electrochim Acta* 54:1042–1055
46. Camacho L, Ruiz JJ, Serna C, Molina A, Martínez-Ortiz F (1994) *Can J Chem* 72:2369–2377
47. Molina A, Serna C, Camacho L (1995) *J Electroanal Chem* 394:1–6
48. Laborda E, Rogers EI, Martínez-Ortiz F, Molina A, Compton RG (2010) *Electrochim Acta* 55:6577–6585
49. Lovrić M (1999) *Electroanalysis* 11:1089–1093
50. Birke RL (1978) *Anal Chem* 50:1489–1496
51. Birke RL, Kim M-H, Strassfeld M (1981) *Anal Chem* 53:852–856
52. Abrantes LM, Gonzalez J, Molina A, Saavedra F (1999) *Electrochim Acta* 45:457–468
53. Go WS, O’Dea JJ, Osteryoung J (1988) *J Electroanal Chem* 255:21–44
54. Miřeski V, Komorsky-Lovrić S, Lovrić M (2007) *Square wave voltammetry*. Springer, Berlin
55. Laborda E, Rogers EI, Martínez-Ortiz F, Molina A, Compton RG (2010) *Electroanalysis* 22:2784–2793
56. Bartlett PN (2008) *Bioelectrochemistry, fundamentals, experimental techniques and applications*. Wiley, Chichester
57. Evans DH (2008) *Chem Rev* 108:2113–2144
58. Leger C, Bertrand P (2008) *Chem Rev* 108:2379–2438
59. Gulaboski R, Miřeski V, Bogeski I, Hoth M (2012) *J Sol Stat Electrochem* 16:2315–2328
60. Serna C, Molina A, Moreno MM, Lopez-Tenes M (2003) *J Electroanal Chem* 546:97–108
61. Molina A, Serna C, Lopez-Tenes M, Moreno MM (2005) *J Electroanal Chem* 576:9–19
62. Molina A, Gonzalez J, Laborda E, Compton RG (2012) *Int J Electrochem Sci* 7:5765–5778
63. Lopez-Tenes M, Moreno MM, Serna C, Molina A (2002) *J Electroanal Chem* 528:159–169
64. Molina A, Gonzalez J, Laborda E, Li Q, Batchelor-McAuley C, Compton RG (2012) *J Phys Chem C* 116:1070–1079
65. Hale JM (1964) *J Electroanal Chem* 8:181–199
66. Flanagan JB, Margel S, Bard AJ, Anson FC (1978) *J Am Chem Soc* 100:4248–4253
67. Molina A, Moreno MM, Lopez-Tenes M, Serna C (2002) *Electrochem Commun* 4:457–461
68. Lund H, Hammerich O (2000) *Organic electrochemistry*, vol 4. Marcel Dekker, New York, NY
69. Buffle J, Startchev K, Galceran J (2007) *Phys Chem Chem Phys* 9:2844–2855
70. van Leeuwen HP, Town RM, Buffle J, Cleven RFMJ, Davison W, Puy J, van Riemsdijk WH, Sigg L (2005) *Environ Sci Technol* 39:8545–8556
71. Molina A (1999) *J Electroanal Chem* 443:163–167
72. Galus Z (1993) *Fundamentals of electrochemical analysis*, 2nd/rev edn. Ellis Horwood series in analytical chemistry. Ellis Horwood, Chichester
73. Molina A, Gonzalez J, Laborda E, Henstridge M, Compton RG (2011) *Electrochim Acta* 56:7404–7410
74. Molina A, Serna C, Gonzalez J (1998) *J Electroanal Chem* 454:15–31
75. Serna C, Molina A, Martínez-Ortiz F, Gonzalez J (1999) *J Electroanal Chem* 468:158–169

76. Molina A, Martínez-Ortiz F, Laborda E, Morales I (2009) *J Electroanal Chem* 633:7–14
77. Laborda E, Martínez-Ortiz F, Molina A (2010) *Electroanalysis* 22:1857–1866
78. Laborda E, Martínez-Ortiz F, Molina A (2011) *Electrochim Acta* 56:5335–5342
79. Molina A, Laborda E, Martínez-Ortiz F, Torralba E, Compton RG (2013) *Electrochim Acta* 87:416–424
80. Molina A, Moreno MM, Serna C, Martínez-Ortiz F (2003) *Electroanalysis* 15:254–262
81. Kim M-H, Yan L, Birke RL, Czae M-Z (2003) *Electroanalysis* 15:1541–1553
82. Molina A, Martínez-Ortiz F, Laborda E (2009) *Int J Electrochem Sci* 4:1395–1406
83. Brumleve TR, Osteryoung RA, Osteryoung J (1982) *Anal Chem* 54:782–787
84. Serna C, Molina A, Camacho L, Ruiz JJ (1993) *Anal Chem* 65:215–222
85. Camacho L, Ruiz JJ, Molina A, Serna C (1994) *J Electroanal Chem* 365:97–105
86. Molina A, Martínez-Ortiz F, Serna C, Camacho L, Ruiz JJ (1996) *J Electroanal Chem* 408:33–45
87. Camacho L, Ruiz JJ, Serna C, Martínez-Ortiz F, Molina A (1995) *Anal Chem* 67:2619–2624
88. Molina A, López-Tenes M, Serna C, Moreno MM, Rueda M (2005) *Electrochem Commun* 7:751–761

Chapter 5

Multipulse and Sweep Voltammetries I

Contents

5.1	Introduction	317
5.2	Reversible Electrochemical Reactions	321
5.2.1	Application of a Multipulse Sequence to Electrodes and Microelectrodes of Any Geometry	322
5.2.2	Multipulse Chronoamperometry	325
5.2.3	Cyclic Staircase Voltammetry and Cyclic Voltammetry at Electrodes and Microelectrodes of Any Geometry	328
5.3	Non-reversible Electrochemical Reactions	349
5.3.1	Planar Electrodes	349
5.3.2	Reversibility Criteria	352
5.3.3	Other Electrode Geometries: Microelectrodes and Steady-State Voltammetry	354
5.3.4	Marcus–Hush Kinetics	356
5.4	Advantages of Using Microelectrodes	358
5.4.1	Reduction of Ohmic Drop and Capacitive Effects	359
5.4.2	Neglecting Convection	361
5.4.3	Ultrafast Voltammetry	361
5.4.4	Microelectrode Arrays	362
5.4.5	Nanoelectrodes	364
5.5	Ion Transport Through Liquid Membranes	365
5.5.1	One Polarized Interface	365
5.5.2	Two Polarized Interfaces	367
5.5.3	Micro-ITIES and Asymmetrical Diffusion	369
	References	373

5.1 Introduction

In Multipulse techniques, the potential waveform consists of a sequence of potential pulses E_1, E_2, \dots, E_p , and the initial conditions of the system are only regained after the application of the last potential step [1–6]. When the potential waveform is a staircase of constant pulse amplitude $|\Delta E|$, the perturbation includes as a limiting

situation a potential sweep (obtained when $|\Delta E| \rightarrow 0$ at a given scan rate; see below). Therefore, the case of sweep techniques (like Linear Sweep Voltammetry, LSV, and Cyclic Voltammetry, CV) is considered here as a limiting behavior of the potential staircase.¹ The application of a multipulse perturbation enables us to reduce the experimental time necessary to obtain a whole current–potential response, but makes the theoretical treatment more complex. These methods offer a number of advantages for quantitative studies, mainly well-defined and mostly peak-shaped responses where undesirable effects are greatly minimized. Thus, these techniques are highly valuable in mechanistic and kinetic quantitative studies using the broad theoretical framework available.

In this chapter, several Multipulse techniques are analyzed: Multipulse Chronoamperometry (and Chronocoulometry), Staircase Voltammetry (SCV), and Linear Sweep Voltammetry (LSV). Both SCV and LSV techniques can be used in cyclic mode, giving rise to Cyclic Staircase Voltammetry (CSCV) and Cyclic Linear Sweep Voltammetry, commonly denoted as Cyclic Voltammetry (CV). Note that both SCV and LSV register the current–potential signal, but they can also be used to register the charge–potential signal in the Voltcoulometric modalities of these techniques (although the current is the usual magnitude to be recorded and the charge has been only used for some particular situations, mainly for immobilized molecules).

It is of interest at this point to compare the study of Multipulse Chronoamperometry and Staircase Voltammetry with those corresponding to Single Pulse Chronoamperometry and Normal Pulse Voltammetry (NPV) developed in Chaps. 2 and 3 in order to understand how the same perturbation (i.e., a staircase potential) leads to a sigmoidal or a peak-shaped current–potential response as the equilibrium between two consecutive potential pulses is restored, or not. This different behavior is due to the fact that in SCV the current corresponding to a given potential pulse depends on the previous potential pulses, i.e., its history. In contrast, in NPV, since the equilibrium is restored, for a reversible process the current–potential curve is similar to a stationary one, because in this last technique the current corresponding to any potential pulse is independent of its history [8].

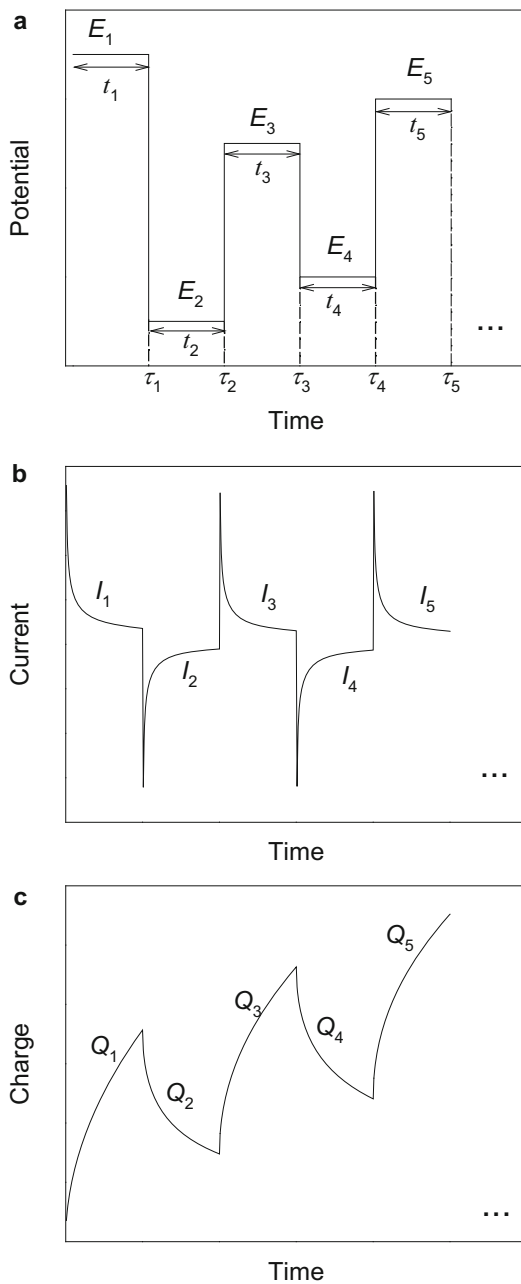
General features of the potential–time perturbation and of the current–potential responses characteristic of these techniques are:

Multipulse Chronoamperometry and Chronocoulometry

The simplest case of a multipulse technique corresponds to the record of the current time (chronoamperometry) or the charge time (chronocoulometry) curves obtained when a given sequence of successive potential pulses E_1, E_2, \dots, E_p is applied for times $0 \leq t_n \leq \tau_n$, with $n = 1, 2, \dots, p$, as shown in Scheme 5.1.

¹ Note that digital instrumentation approximates the linear potential ramp as a staircase waveform [3, 6, 7]. There is a good agreement between the linear and staircase currents for $t_s/\tau = 0.25 - 0.30$ for reversible processes (with t_s being the time between the application of the potential pulse and the current sampling), if the potential step ΔE is less than 8 mV.

Scheme 5.1 Multipulse Chronoamperometry and Chronocoulometry. (a) Potential–time program; (b) Current–time response; (c) Charge–time response



Staircase Voltammetry and Linear Sweep Voltammetry in Single and Cyclic Modes

In Staircase Voltammetry (SCV), a sequence of potential pulses of identical time length τ defining a “staircase” of potentials is applied to the system with no recovery of the initial equilibrium at any moment of the experiment (see Scheme 5.2). In this technique, the difference between two consecutive potential pulses, $|\Delta E|$, is constant, and the ratio $\nu = \Delta E/\tau$ is defined as the scan rate.

When the pulse amplitude, ΔE , tends to zero and the scan rate is held constant (i.e., the pulse duration also tends to zero in order to keep the ratio $\nu = \Delta E/\tau$ constant), the potential–time perturbation applied in SCV becomes a continuous ramp of potentials and so can be identified with the potential–time perturbation applied in Linear Sweep Voltammetry (LSV,²; see Scheme 5.2).

If the potential is inverted at a given value (inversion or final potential) until the initial potential is reached again, the two above techniques are denoted Cyclic Staircase Voltammetry (CSCV) and Cyclic Voltammetry (CV), respectively (see Scheme 5.3). The potential waveform in CV can be written as a continuous function of time

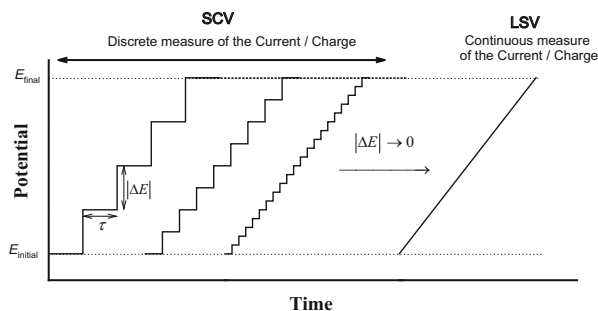
$$\left. \begin{aligned} E(t) &= E_{\text{initial}} - \nu t & \text{for } t \leq t_{\text{inv}} \\ E(t) &= E_{\text{final}} + \nu t & \text{for } t > t_{\text{inv}} \end{aligned} \right\} \quad (5.1)$$

where t_{inv} is the time at which the scan is inverted and the scan rate is $\nu = dE/dt$. This waveform can be obtained as a limit of the discrete perturbation applied in CSCV, which is given by

$$\left. \begin{aligned} E_j &= E_{\text{initial}} - (j-1)\Delta E & \text{for } j = 1, 2, \dots, N/2 \\ E_j &= E_{\text{final}} + \left(j - \frac{N}{2}\right)\Delta E & \text{for } j > N/2 \end{aligned} \right\} \quad (5.2)$$

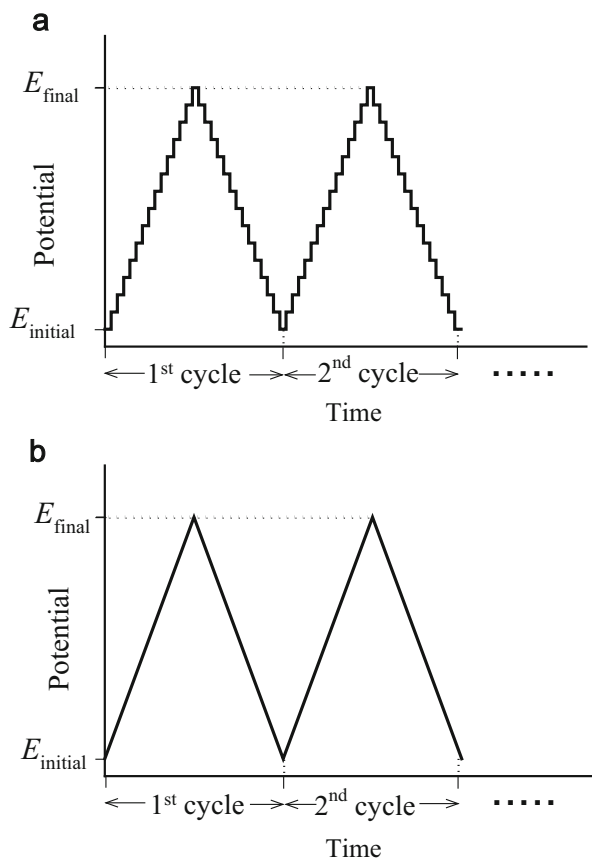
where ΔE is the constant difference between two potential pulses denoted as “pulse amplitude” and N the total number of potential pulses applied in the cyclic scan. In a general way, a good coincidence is obtained between CSCV and CV for $|\Delta E| \rightarrow 0$ mV [5]. It is important to highlight that a true linear sweep or cyclic voltammetry is not applied in modern digital potentiostats for which the real

Scheme 5.2 Potential waveform applied in SCV and LSV (limiting behavior obtained when $|\Delta E| \rightarrow 0$ for a fixed scan rate)



²This technique was originally called “Stationary Electrode Polarography” [9, 10].

Scheme 5.3 Potential waveform applied in (a) CSCV and (b) CV



perturbation is that given by Eq. (5.2) [3, 4, 6, 10]. A comparison between CVSC and CV is made in Sect. 5.2.3.1 in order to analyze the effect of the discretization of the potential perturbation.

In the following sections, the behavior of soluble solution species giving rise to simple charge transfer reactions (electronic and ionic) is analyzed. The case corresponding to more complex reaction mechanisms is the subject of Chap. 6.

5.2 Reversible Electrochemical Reactions

Let us consider the fast electrode reaction



when species O and R are soluble in the electrolytic solution. In this section, the response of this electrode process in the different multipulse techniques described in Sect. 5.1 is analyzed.

5.2.1 Application of a Multipulse Sequence to Electrodes and Microelectrodes of Any Geometry

The expressions for the current–potential response of the electrode process given in reaction scheme 5.1 when a single potential pulse and two successive potential pulses are applied at electrodes of any geometry are given in Sects. 2.6 and 4.2.1, respectively.

Let us consider now a potential waveform consisting of a potential pulses sequence E_1, E_2, \dots, E_p , with each pulse of the sequence E_p being applied to an electrode of any geometry G over the interval $0 \leq t_p \leq \tau_p$. The total time of the experiment is

$$t = \sum_{m=1}^{p-1} \tau_m + t_p \quad (5.3)$$

In the following, it is considered that the diffusion coefficients of species O and R are equal ($D_O = D_R = D$), except in the case of macroelectrodes (planar electrodes).

The mass transport of species O and R is described by the differential equations:

$$\frac{\partial c_O^{(p)}}{\partial t_p} = D \nabla^2 c_O^{(p)} \quad (5.4)$$

$$\frac{\partial c_R^{(p)}}{\partial t_p} = D \nabla^2 c_R^{(p)} \quad (5.5)$$

with ∇^2 being the Laplacian operator given in Table 2.2 and $c_O^{(p)}$ and $c_R^{(p)}$ the solutions of Eqs. (5.4)–(5.5). The boundary value problem is given by

$$\left. \begin{array}{l} t_p \geq 0, q \rightarrow \infty \\ t_p = 0, q \geq q^s \\ t_p > 0, q = q^s, \end{array} \right\} \left. \begin{array}{l} c_O^{(1)} = c_O^*, c_R^{(1)} = c_R^* \\ c_O^{(p)} = c_O^{(p-1)}, c_R^{(p)} = c_R^{(p-1)} \quad p > 1 \end{array} \right\} \quad (5.6)$$

$$c_O^{(p,s)} + c_R^{(p,s)} = c_O^* + c_R^* \quad (5.7)$$

$$c_O^{(p,s)} = e^{\eta_p} c_R^{(p,s)} \quad (5.8)$$

with

$$\eta_p = \frac{F}{RT} (E_p - E_c^{\Theta'}) \quad (5.9)$$

$c_O^{(p,s)}$ and $c_R^{(p,s)}$ are the surface concentrations of species O and R corresponding to the application of potential E_p , and c_O^* and c_R^* the initial concentrations of these

species. Since no restrictions have been considered in the electrode geometry, q refers to spatial coordinates (e.g., r in the case of spheres and cylinders, x and y in the case of bands, and r and z in the case of discs), q^s to the value of q at the electrode surface, and $c_O^{(p-1)}$ and $c_R^{(p-1)}$ are the solutions corresponding to the application of the $(p-1)$ potential, E_{p-1} .

Given that the operators of Fick's second law are linear, the expressions for the concentration profiles of species O and R corresponding to the p th potential pulse of the perturbation can be written as a linear combination of solutions:

$$c_i^{(p)}(q, t) = c_i^{(p-1)}(q, t) + \tilde{c}_i^{(p)}(q, t), \quad \begin{array}{l} i \equiv \text{O, R} \\ p = 2, 3, \dots \end{array} \quad (5.10)$$

where $\tilde{c}_i^{(p)}(q, t)$ are unknown functions of coordinates and time to be determined and

$$c_i^{(p-1)} = c_i^{(1)}(q, t) + \sum_{m=2}^{p-1} \tilde{c}_i^{(m)}(q, t), \quad \begin{array}{l} i \equiv \text{O, R} \\ p = 2, 3, \dots \end{array} \quad (5.11)$$

By taking into account Eqs. (2.149)–(2.153) for the application of the first potential pulse, Eqs. (4.4)–(4.22) for the application of the second one, and applying the Induction Principle, it is possible to express the boundary value problem for any potential p of the applied sequence in terms of the unknown functions $\tilde{c}_i^{(p)}(q, t)$, in the following general way:

$$\left. \begin{array}{l} \frac{\partial \tilde{c}_O^{(p)}}{\partial t_p} = D \nabla^2 \tilde{c}_O^{(p)} \\ \frac{\partial \tilde{c}_R^{(p)}}{\partial t_p} = D \nabla^2 \tilde{c}_R^{(p)} \end{array} \right\} \quad (5.12)$$

$$\left. \begin{array}{l} t_p = 0, \quad q \geq q^s \\ t_p > 0, \quad q \rightarrow \infty \end{array} \right\}$$

$$\tilde{c}_O^{(p)}(q, t) = \tilde{c}_R^{(p)}(q, t) = 0 \quad (5.13)$$

$$t_p > 0, \quad q = q^s :$$

$$\tilde{c}_O^{(p,s)} + \tilde{c}_R^{(p,s)} = 0 \quad (5.14)$$

$$\tilde{c}_O^{(p,s)} = e^{\eta_p} \tilde{c}_R^{(p,s)} + \frac{e^{\eta_{p-1}} - e^{\eta_p}}{1 + e^{\eta_{p-1}}} (c_O^* + c_R^*) \quad (5.15)$$

Moreover, for any potential pulse E_p , the following is fulfilled (see Eqs. (5.7) and (5.8)):

$$\left. \begin{aligned} c_{\text{O}}^{(p,s)} &= \frac{e^{\eta_p} (c_{\text{O}}^* + c_{\text{R}}^*)}{1 + e^{\eta_p}} \\ c_{\text{R}}^{(p,s)} &= \frac{c_{\text{O}}^{(p,s)}}{e^{\eta_p}} \end{aligned} \right\} \quad (5.16)$$

Eqs. (5.12)–(5.15) show that the boundary value problem has the same general form for any pulse potential p , whatever the geometry of the electrode.

This generalization clearly demonstrates that the superposition principle can be rigorously applied whatever the electrode geometry [5, 8]. The expression for the current corresponding to the application of the p th potential pulse E_p can be written as (see Eqs. (5.10)–(5.11))

$$\frac{I_p^{\text{G}}}{FA_{\text{GD}}} = \left(\frac{\partial c_{\text{O}}^{(p)}}{\partial q_{\text{N}}} \right)_{q^s} = \left(\frac{\partial c_{\text{O}}^{(1)}}{\partial q_{\text{N}}} \right)_{q^s} + \sum_{m=2}^p \left(\frac{\partial \tilde{c}_{\text{O}}^{(m)}}{\partial q_{\text{N}}} \right)_{q^s} \quad (5.17)$$

with q^s and q_{N} being the coordinates at the electrode surface and the normal coordinate, respectively.

Equation (5.17) shows that the current I_p^{G} can be written as a sum of contributions due to the different potential pulses of the sequence which are only effective from the moment when each particular potential pulse is applied. By taking into account Eq. (2.156), Eq. (4.29), and Eqs. (5.10)–(5.16), it is possible to rewrite Eq. (5.17) as

$$\frac{I_p^{\text{G}}}{FA_{\text{GD}}} = \sum_{m=1}^p \left(c_{\text{O}}^{(m-1,s)} - c_{\text{O}}^{(m,s)} \right) f_{\text{G}}(t_{m,p}, q_{\text{G}}) \quad (5.18)$$

where

$$c_{\text{O}}^{(0,s)} = c_{\text{O}}^* \quad (5.19)$$

Superindex “G” refers to the particular electrode geometry considered, q_{G} to the characteristic dimension of the electrode considered, and f_{G} is given in Table 2.3 for several electrode geometries. $t_{m,p}$ is given by

$$t_{m,p} = \sum_{j=m}^{p-1} \tau_j + t_p \quad (5.20)$$

From Eqs. (5.16) and (5.18), the variable Z_m , which is independent of the electrode geometry, can be defined as

$$Z_m = \frac{c_{\text{O}}^{(m-1,s)} - c_{\text{O}}^{(m,s)}}{c_{\text{O}}^* + c_{\text{R}}^*} = \frac{1}{1 + e^{\eta_m}} - \frac{1}{1 + e^{\eta_{m-1}}} \quad m \geq 1 \quad (5.21)$$

with

$$e^{\eta_0} = \exp\left(\frac{F}{RT}(E_{\text{eq}} - E_c^{\ominus'})\right) = \frac{c_{\text{O}}^*}{c_{\text{R}}^*} \quad (5.22)$$

E_{eq} is the equilibrium potential given by Nernst's equation. From Eqs. (4.28)–(4.29) and Eqs. (5.19) and (5.21)–(5.22), the current I_p^{G} can be written as

$$\frac{I_p^{\text{G}}}{FA_G D c_{\text{O}}^*} = (1 + c_{\text{R}}^*/c_{\text{O}}^*) \sum_{m=1}^p Z_m f_{\text{G}}(t_m, p, q_{\text{G}}) \quad (5.23)$$

5.2.2 Multipulse Chronoamperometry

In this technique, the analysis of the current–time responses corresponding to the application of a sequence of potential pulses without the reestablishment of the equilibrium between them is carried out. The usefulness of this technique lies mainly in the determination of diffusion coefficients of the electroactive species when only two potentials are applied, as discussed in Sect. 4.2.2. Nevertheless, there are also other analytical applications, which are presented in this section.

5.2.2.1 Planar Electrodes

In planar geometry, the condition of surface concentrations of species O and R when they are only potential dependent remains valid for any potential pulse of the sequence, even when the diffusion coefficients of species O and R are different (see Sect. 2.2 and [1, 5, 8]). Thus, it is possible to deduce the following simple expression for the concentration profiles of species O and R for any potential pulse of the sequence under these conditions:

$$\left. \begin{aligned} c_i^{(1)}(x, t) &= c_i^* + (c_i^{(1,s)} - c_i^*) \operatorname{erfc}\left(\frac{x}{2\sqrt{D_{\text{O}}t}}\right) \\ c_i^{(p)}(x, t) &= \sum_{m=1}^p \left((c_i^{(m,s)} - c_i^{(m-1,s)}) \operatorname{erfc}\left(\frac{x}{2\sqrt{D_{\text{R}}t_m, p}}\right) \right) \quad p > 1 \end{aligned} \right\} \quad i = \text{O, R} \quad (5.24)$$

with $c_i^{(m,s)}$ ($i = \text{O}$ and R) given by Eq. (5.16), $c_{\text{O}}^{(0,s)}$ by Eq. (5.19), $c_{\text{R}}^{(0,s)} = c_{\text{R}}^*$, $\operatorname{erfc}(x) = 1 - \operatorname{erf}(x)$, and $\operatorname{erf}(x)$ is the error function. The expression of the current under these conditions is

$$\frac{I_p^{\text{plane}}}{FAD_O c_O^*} = \frac{(\gamma + c_R^*/c_O^*)}{\gamma} \sum_{m=1}^p \frac{Z_m}{\sqrt{\pi D_O t_{m,p}}} \quad (5.25)$$

with

$$Z_m = \frac{1}{1 + \gamma e^{\eta_m}} - \frac{1}{1 + \gamma e^{\eta_{m-1}}} \quad m = 1, 2, \dots, p \quad (5.26)$$

$$\gamma = \sqrt{\frac{D_O}{D_R}} \quad (5.27)$$

and e^{η_0} given in Eq. (5.22)

A situation of special interest corresponds to the application of a “square wave” (SW) potential of the form,

$$E = \begin{cases} -E_{\text{abs}} & \text{odd steps} \\ E_{\text{abs}} & \text{even steps} \end{cases} \quad (5.28)$$

with E_{abs} being the absolute value of the potential applied. When $E \rightarrow \mp\infty$ (with the upper sign referring to the odd steps and the lower one to the even steps), the response corresponds to a diffusion-controlled process for the cathodic and anodic currents, and Eq. (5.25) is simplified to

$$\frac{I_p^{\text{plane,SW}}}{FAD_O c_O^*} = \frac{(\gamma + c_R^*/c_O^*)}{\gamma} \sum_{m=1}^p \frac{(-1)^{m+1}}{\sqrt{\pi D_O t_{m,p}}} \quad (5.29)$$

with

$$t_{m,p} = (p - m + 1)\tau \quad (5.30)$$

when all the pulses have the same length. The influence of the presence of the reaction product R on the currents obtained for the application of six potentials can be seen in Fig. 5.1.

From this figure it can be seen that the presence of species R only affects the second and subsequent transient currents by causing an increase of the absolute value of the current with (c_R^*/c_O^*) .

If the length of all the pulses is the same, and the current is measured at the end of each pulse, the expression of the current is [1, 5, 8, 11],

$$\frac{I_p^{\text{plane,SW}}}{FAD_O c_O^*} = \frac{(1 + (c_R^*/c_O^*)/\gamma)}{\sqrt{\pi D_O \tau}} \sum_{m=1}^p \frac{(-1)^{m+1}}{\sqrt{p - m + 1}} \quad p = 1, 2, \dots \quad (5.31)$$

If the number of potential steps p is high enough, the sum of terms in Eq. (5.31) tends to a constant value (0.6045 for odd pulses and -0.6050 for even ones). Thus,

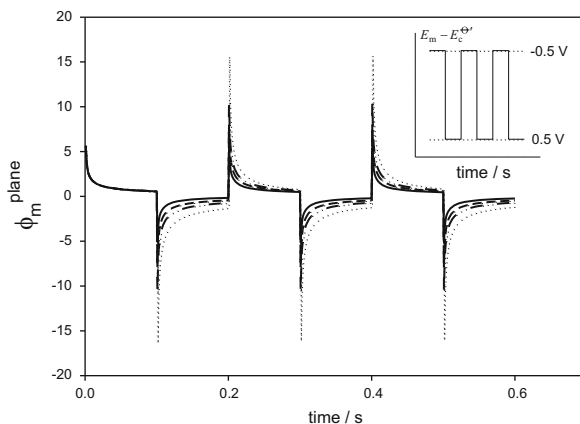


Fig. 5.1 Current–time response calculated from Eq. (5.29), with $\phi_m^{\text{plane}} = J_m^{\text{plane}} / (FA\sqrt{D_O}c_O^*/\sqrt{\tau})$, corresponding to the application of six potentials with $|E_{\text{abs}} - E_c^{\text{O/R}}| = 0.5$ V. The values of the ratio (c_R^*/c_O^*) are: 0, *solid line*; 0.5, *dashed line*; 1, *dashed-dotted line*; 2, *dotted line*. $D_O = D_R$, $\tau_1 = \dots = \tau_6 = \tau = 0.1$ s. The potential waveform applied has been plotted in the inner figure

under these conditions, the cathodic and anodic responses will be repetitive, i.e., an “ultimate state” is achieved, and under these conditions, the bulk concentrations of species O and R can be easily determined [1, 12].

5.2.2.2 Spherical Electrodes and Microelectrodes

For spherical geometry when diffusion coefficients of species O and R are identical, the following analytical and explicit expression for the concentration profiles of species O and R can be obtained,

$$\left. \begin{aligned} c_i^{(1)}(r, t) &= c_i^* + (c_i^{(1,s)} - c_i^*) \frac{r_s}{r} \operatorname{erfc} \left(\frac{r - r_s}{2\sqrt{Dt}} \right) \\ c_i^{(p)}(r, t) &= \sum_{m=1}^p \left((c_i^{(m,s)} - c_i^{(m-1,s)}) \frac{r_s}{r} \operatorname{erfc} \left(\frac{r - r_s}{2\sqrt{Dt_{m,p}}} \right) \right) \quad p > 1 \end{aligned} \right\} \quad i = \text{O, R} \quad (5.32)$$

with $c_i^{(m,s)}$ ($i = \text{O, R}$) given by Eq. (5.16). For this electrode geometry, the expression of the current can be written as

$$\frac{I_p^{\text{sphe}}}{FA_s D c_O^*} = \frac{I_p^{\text{plane}}}{FA_s D c_O^*} + \frac{I_p^{\text{sphe,ss}}}{FA_s D c_O^*} \quad (5.33)$$

with

$$\frac{I_p^{\text{plane}}}{FA_s D c_O^*} = (1 + c_R^*/c_O^*) \sum_{m=1}^p \frac{Z_m}{\sqrt{\pi D t_{m,p}}} \quad (5.34)$$

$$\frac{I_p^{\text{sph,ss}}}{FA_s D c_O^*} = \left(\frac{1}{r_s}\right) \frac{1 - (c_R^*/c_O^*)e^\eta}{1 + e^\eta} \quad (5.35)$$

In the case of the square wave perturbation presented in the previous section, I_p^{plane} is given by Eq. (5.29) with $\gamma = 1$ and

$$\left. \begin{aligned} \frac{I_{\text{odd}}^{\text{sph,ss}}}{FA_s D c_O^*} &= \frac{1}{r_s} \\ \frac{I_{\text{even}}^{\text{sph,ss}}}{FA_s D c_O^*} &= \frac{-(c_R^*/c_O^*)}{r_s} \end{aligned} \right\} \quad (5.36)$$

For very small electrodes, the response attains a stationary character, since the second term in the right-hand side of Eq. (5.33) becomes dominant.

The influence of the electrode size on the current–time curves calculated from Eq. (5.33) for two values of the ratio (c_R^*/c_O^*) is shown in Fig. 5.2. Thus, when species R is not present in the solution, the anodic chronoamperograms tend to zero very quickly, whereas when (c_R^*/c_O^*) = 1 both cathodic and anodic chronoamperograms increase in absolute value as the electrode radius decreases, and their values are coincident with the respective cathodic or anodic stationary values (Eq. (5.36)) and this becomes faster the smaller the size of the electrode.

5.2.3 Cyclic Staircase Voltammetry and Cyclic Voltammetry at Electrodes and Microelectrodes of Any Geometry

In this section, general Eq. (5.23) will be applied to Cyclic Staircase Voltammetry (CSCV) and Cyclic Voltammetry (CV). Note that for CSCV the length of each potential pulse is identical, i.e., $\tau_1 = \tau_2 = \dots = \tau_p = \tau$, and the current is usually measured at the end of the application of each pulse in such a way that the time elapsed between the measurement of m th and p th currents is given by Eq. (5.30).

Moreover, it is more convenient to write a dimensionless expression for the current as

$$\psi_p^G = \frac{I_p^G}{FA_G c_O^* \sqrt{aD}} \quad (5.37)$$

with

$$a = \frac{Fv}{RT} \quad (5.38)$$

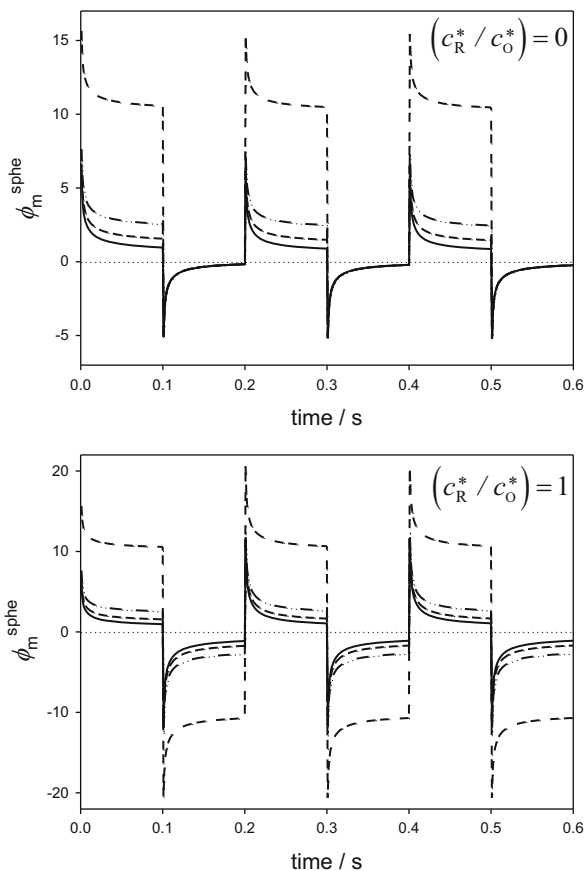


Fig. 5.2 Current–time response calculated from Eq. (5.33), with $\phi_m^{\text{sphc}} = I_m^{\text{sphc}} / (FA_s \sqrt{D_O c_O^*} / \sqrt{\tau})$, corresponding to the application of six potentials with $|E_{\text{abs}} - E_c^{\ominus'}| = 0.5 \text{ V}$. The values of the ratio (c_R^*/c_O^*) are 0 and 1. The values of the radius of the spherical electrode (in microns) are: 25, solid line; 10, dashed line; 5, dashed-dotted line; 1, dotted line. $D_O = D_R$, $\tau_1 = \dots = \tau_6 = \tau = 0.1 \text{ s}$

where v is the scan rate. By inserting Eqs. (5.30) and (5.37) in Eq. (5.23), the expression for the current in CSCV is

$$\psi_p^G = \sqrt{\frac{D}{a}} (1 + c_R^*/c_O^*) \sum_{m=1}^p Z_m f_G((p - m + 1)\tau, q_G) \quad (5.39)$$

where function f_G corresponding to the m th potential pulse (see Table 2.3) has to be calculated for each time $(p - m + 1)\tau$ (with $1 \leq m \leq p$). A complete C++ code to calculate the response of reversible charge transfer processes in Cyclic Staircase Voltammetry at disc, spherical, and cylindrical electrodes of any radius is given in Appendix J.

Equation (5.39) is valid both for CSCV (in which the current is measured in a “discrete” way) and for CV (in which the current is measured as a “continuous” function of potential or time; see Eq. (5.1)). Eq. (5.39) allows us to give the current as a function of time instead of the more usual potential dependence. In order to use this equation in terms of the potential, it has been considered that

$$t_{m,p} = (p - m + 1)\tau = \frac{E_{p-m+1} - E_{\text{initial}}}{v} \quad (5.40)$$

and in this way one obtains

$$\psi_p^G = (1 + c_R^*/c_O^*) \sum_{m=1}^p Z_m f_G(\vartheta_{m,p}, \xi_G) \quad (5.41)$$

with

$$\xi_G = \sqrt{\frac{D}{aq_G^2}} \quad (5.42)$$

$$Z_m = \frac{1}{1 + e^{\vartheta_m} e^{\vartheta_{\text{in}}}} - \frac{1}{1 + e^{\vartheta_{m-1}} e^{\vartheta_{\text{in}}}} \quad (5.43)$$

$$\vartheta_{m,p} = \begin{cases} \frac{F}{RT}(E_{p-m+1} - E_{\text{initial}}) & m \leq N/2 \\ \frac{F}{RT}(E_{p-m+1} - E_{\text{initial}} + 2E_{\text{final}}) & m > N/2 \end{cases} \quad (5.44)$$

$$\vartheta_m = \frac{F}{RT}(E_m - E_{\text{initial}}) \quad (5.45)$$

$$\vartheta_{\text{in}} = \frac{F}{RT}(E_{\text{initial}} - E_c^{\Theta'}) \quad (5.46)$$

with $(N/2)$ being the number of pulses of each scan. G refers to the geometry of the diffusion field considered and q_G is the characteristic dimension of the electrode. The parameter ξ_G depends on the electrode geometry through q_G . The expression of $f_G(\vartheta_{m,p}, \xi_G)$ is given in Table 5.1 for different electrode geometries. Note that the calculation of ψ_p^G with Eq. (5.39) (in terms of time) or Eq. (5.41) (in terms of potential) is equivalent.

Under CV conditions ($|\Delta E| \rightarrow 0$, i.e., for pulse amplitudes which fulfill $|\Delta E| < 0.01$ mV), in Eq. (5.18), it can be written

$$\frac{c_O^{(m-1,s)} - c_O^{(m,s)}}{\Delta E} = \frac{\Delta c_O^{(m,s)}}{\Delta E} \cong \frac{dc_O^{(m,s)}}{dE} = \frac{F}{RT}(c_O^* + c_R^*) \frac{e^{\vartheta_m} e^{\vartheta_{\text{in}}}}{(1 + e^{\vartheta_m} e^{\vartheta_{\text{in}}})^2} \quad m > 1 \quad (5.47)$$

Using this mathematical identity and Eq. (5.43), it is possible to rewrite Eq. (5.41) as

Table 5.1 Expressions for functions $f_G(\theta_{m,p}, \xi_G)$ and $f_{G,\text{micro}}$ for the four electrode geometries considered

Electrode	$f_G(\theta_{m,p}, \xi_G)$	$f_{G,\text{micro}}$
Disc (radius r_d , Area $A_d = \pi r_d^2$)	$\frac{4\xi}{\pi\xi_d} \left(0.7854 + \frac{0.44315}{\xi_d \sqrt{\theta_{m,p}}} + 0.2146 \exp\left(-\frac{0.39115}{\xi_d \sqrt{\theta_{m,p}}} \right) \right)$, $\xi_d = \sqrt{\frac{D}{ar_d^2}}$	$\frac{4\xi}{\pi} \xi_d$
Sphere (radius r_s , Area = $4\pi r_s^2$)	$\xi_s + \frac{1}{\sqrt{\pi \theta_{m,p}}}$, $\xi_s = \sqrt{\frac{D}{ar_s^2}}$	ξ_s
Band (height w , length l , Area = wl)	$\xi_b + \frac{1}{\sqrt{\pi \theta_{m,p}}}$ if $(\xi_b^2 \theta_{m,p}) < 0.4$ $0.25 \sqrt{\frac{\pi}{\theta_{m,p}}} e^{-0.4 \sqrt{\pi \theta_{m,p}} \xi_b} + \frac{\pi \xi_b}{\ln(5.2945 + 5.9944 \sqrt{\theta_{m,p}} \xi_b)}$ if $(\xi_b^2 \theta_{m,p}) \geq 0.4$	$\frac{2\pi \xi_b}{\ln[4\xi_b^2 \theta_{m,p}]}$
Cylinder (radius r_c , length l , Area = $2\pi r_c l$)	$\frac{1}{\sqrt{\pi \theta_{m,p}}} e^{-0.1 \sqrt{\pi \theta_{m,p}} \xi_c} + \frac{\xi_c}{\ln(5.2945 + 1.4986 \sqrt{\theta_{m,p}} \xi_c)}$, $\xi_c = \sqrt{\frac{D}{ar_c^2}}$	$\frac{2\xi_c}{\ln[4\xi_c^2 \theta_{m,p}]}$

$q_G = r_d$ for discs; $q_G = r_s$ for spheres or hemispheres; $q_G = r_c$ for cylinders; and $q_G = w$ for bands. $\theta_{m,p}$ is given in Eq. (5.44) [13–20]. Note that $f_G(\theta_{m,p}, \xi_G)$ and $f_{G,\text{micro}}$ are dimensionless

$$\psi_{CV}^G = \frac{1 - (c_R^*/c_O^*)e^{\vartheta_1}e^{\vartheta_{in}}}{1 + e^{\vartheta_1}e^{\vartheta_{in}}} f_G(\vartheta_{1,p}, \xi_G) + (1 + c_R^*/c_O^*) \sum_{m=2}^p \left(\frac{\Delta\vartheta e^{\vartheta_m}e^{\vartheta_{in}}}{(1 + e^{\vartheta_m}e^{\vartheta_{in}})^2} f_G(\vartheta_{m,p}, \xi_G) \right) \quad (5.48)$$

with

$$\Delta\vartheta = \frac{F}{RT} |\Delta E| \quad (5.49)$$

Note that Eqs. (5.41) or (5.48) should be used for $\Delta\vartheta$ values below 3.8×10^{-4} (i.e., for $|\Delta E| < 0.01$ mV and $T = 298$ K). In the following sections, when this condition is assumed, the current is denoted as ψ_{CV}^G .

5.2.3.1 Planar Electrodes

Equation (5.41) is applicable to any electrode geometry when $D_O = D_R$. In the case of planar electrodes, it becomes

$$\psi_p^{\text{plane}} = (1 + c_R^*/c_O^*) \sum_{m=1}^p Z_m \frac{1}{\sqrt{\pi} \vartheta_{m,p}} \quad (5.50)$$

To use Eq. (5.50) under CV conditions, values of $|\Delta E| < 0.01$ mV must be used.

Unequal Diffusion Coefficients

It is possible to deduce an analytical expression for the CSCV or CV current-potential response at planar electrodes when $D_O \neq D_R$ by following a procedure analogous to that presented in Sect. 5.2.1. In this case it is obtained

$$\psi_p^{\text{plane}} = \frac{I_p^{\text{plane}}}{FAc_O^* \sqrt{aD_O}} = \frac{(\gamma + c_R^*/c_O^*)}{\gamma} \sum_{m=1}^p \left(\frac{1}{1 + \gamma e^{\vartheta_m}e^{\vartheta_{in}}} - \frac{1}{1 + \gamma e^{\vartheta_{m-1}}e^{\vartheta_{in}}} \right) \frac{1}{\sqrt{\pi} \vartheta_{m,p}} \quad (5.51)$$

with $\vartheta_{m,p}$ given in Eq. (5.44) and $\gamma = \sqrt{D_O/D_R}$.

This is the only case in which a rigorous explicit expression of the cyclic voltammogram has been deduced by considering unequal diffusion coefficients for species O and R. When the electrode geometry is considered, it has not been possible to obtain an explicit solution and Fick's second law differential equations need to be solved using numerical procedures.

When $c_R^* = 0$ Eq. (5.51) coincides with the following well-known expression (deduced by Nicholson and Shain at planar electrodes using Laplace transform method; see Appendix H and [9]):

$$\psi_{CV}^{\text{plane}} = \frac{I_{CV}^{\text{plane}}}{FAc_O^* \sqrt{aD_O}} = \sqrt{\frac{\pi}{a}} \chi(at) \quad (5.52)$$

with

$$at = \frac{F}{RT}(E_{\text{initial}} - E(t)) \quad (5.53)$$

with $E(t)$ given by Eq. (5.1). Function $\chi(at)$ can be obtained by solving numerically the following integral equation:

$$\int_0^{at} \frac{\chi(z)}{\sqrt{at-z}} dz = \frac{1}{1 + \gamma\theta e^{-(at)}} \quad (5.54)$$

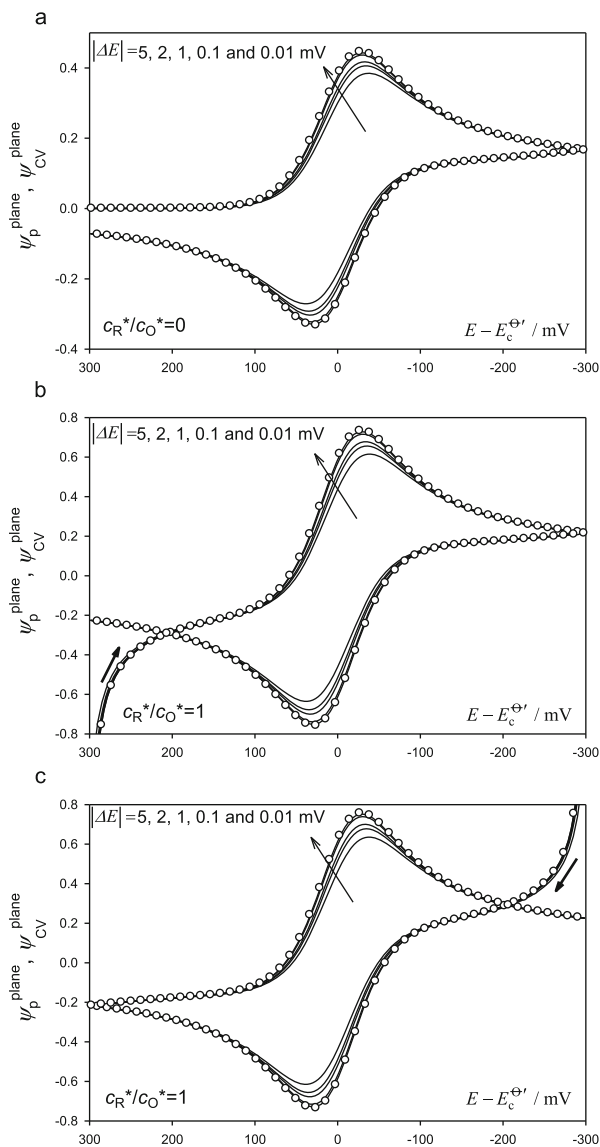
with $\theta = \exp\left(F(E_{\text{initial}} - E_c^{\Theta'})/RT\right)$.

Several examples of applications of Eq. (5.50) valid for CSCV and CV are shown in Fig. 5.3. The influence of the pulse amplitude ΔE (with $\Delta E \geq 0.01$ mV) at planar electrodes with a scan rate $v = 50$ mV s⁻¹, where only the oxidized species (Fig. 5.3a) or both species (Fig. 5.3b, c) are initially present in the electrolyte solution, can be clearly seen. The CV curves (white dots) have been included for comparison.

From these figures, it can be observed that the transient current–potential response corresponding to a Nernstian charge transfer process at a planar electrode presents a pair of peaks, one for the first scan and another for the second, whose separation increases and whose height decreases as $|\Delta E|$ increases. Figure 5.3b, c show that this effect is similar when both species are initially present. In this case an initial anodic (Fig. 5.3b) or cathodic (Fig. 5.3c) current can also be observed in the cyclic voltammograms when sweeping toward cathodic or anodic potentials, respectively. It is notable that for $|\Delta E| = 0.01$ mV there are negligible differences between the SCV curve calculated from Eq. (5.50) and the CV one (Eqs. (5.52)–(5.53) with $c_R^* = 0$, white dots) in all the situations considered. This confirms the validity of Eq. (5.50) to analyze SCV and CV curves. In order to compare experimental and theoretical data, this equation allows us to fit experimental results to any staircase waveform, instead of that given by Eq. (5.52), which is valid only for Cyclic Voltammetry.

The expressions of the peak parameters are

Fig. 5.3 Application of Eq. (5.50) to the study of the influence of ΔE (with $\Delta E \geq 0.01$ mV) on the $\psi_p^{\text{plane}} - E$ curves with $v = 50$ mV s⁻¹, where only the oxidized species (a) or both species (b and c) are initially present in the electrolyte solution. *White dots* correspond to the $\psi_{CV}^{\text{plane}} - E$ curve calculated from Eq. (5.52) for $c_R^* = 0$ and numerically by following the procedure given in [21, 22] for $c_R^* \neq 0$. The values of $|\Delta E|$ appear on the curves. E_{initial} (in V) = 0.3 (a, b) and -0.3 (c). $D_O = D_R = 10^{-5}$ cm² s⁻¹. Reproduced from [8] with permission



– Peak current

$$j_{CV}^{\text{plane, peak}} = 0.446FAC_O^* \sqrt{aD_O} = 0.446FAC_O^* \sqrt{\frac{FD_O}{RT}} v \quad (5.55)$$

This is the well-known Randles–Ševčík equation, which establishes a linear dependence between the peak current and the square root of the scan rate for a reversible process under linear diffusion conditions [23, 24]. For a typical value

of $T = 298 \text{ K}$, A in cm^2 , D in $\text{cm}^2 \text{ s}^{-1}$, c_{O}^* in mol cm^{-3} , v in V s^{-1} , and $I_{\text{CV}}^{\text{plane,peak}}$ in A, Eq. (5.55) becomes

$$I_{\text{CV}}^{\text{plane,peak}} = (2.69 \times 10^5) A \sqrt{D_{\text{O}}} c_{\text{O}}^* \sqrt{v} \quad (5.56)$$

– Forward peak potential, $E_{\text{peak,f}}^{\text{plane}}$

$$E_{\text{peak,f}}^{\text{plane}} = E_{1/2}^{\text{r}} - 1.109 \frac{RT}{F} = E_{1/2}^{\text{r}} - 28 \text{ mV} \quad (T = 298 \text{ K}) \quad (5.57)$$

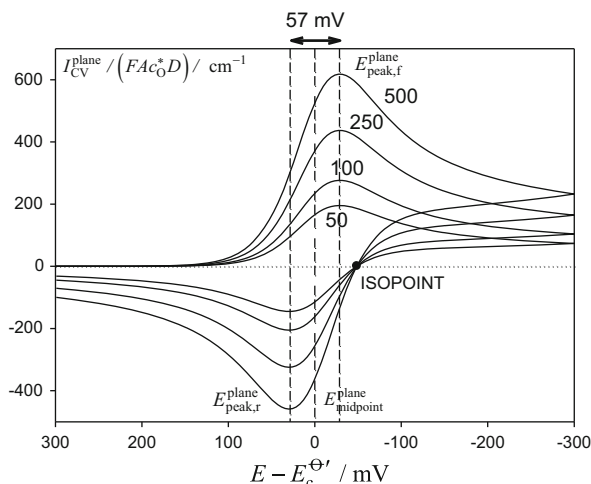
with $E_{1/2}^{\text{r}}$ being the half-wave reversible potential for planar diffusion given by Eq. (2.32) ($= E_{\text{c}}^{\ominus'} + \frac{RT}{F} \ln \sqrt{D_{\text{R}}/D_{\text{O}}}$). Another interesting point of the voltammogram is the half peak potential, which is the potential at which the current is the half of the peak current. This value is of importance when the peak of the I - E curve is very broad and/or badly defined, and it is given by

$$E_{\text{p}/2}^{\text{plane}} = E_{1/2}^{\text{r}} + 1.09 \frac{RT}{F} = E_{1/2}^{\text{r}} + 28 \text{ mV} \quad (T = 298 \text{ K}) \quad (5.58)$$

Note that both the peak and half peak potentials are independent of the scan rate in agreement with Eqs. (5.57)–(5.58). This behavior can be seen in Fig. 5.4, where the voltammograms corresponding to a Nernstian process for different scan rates in the range 50–500 mV s^{-1} have been plotted.

Concerning the peak potential and peak current of the reverse (second) scan, it is important to take into account that the shape of the reverse current depends on the switching potential (i.e., the last potential of the first scan, E_{final}). This especially affects the measurement of the reverse peak current, for which different criteria have been reported [9]. It should be noted that these criteria are ambiguous and it is

Fig. 5.4 Influence of the scan rate on the voltammograms corresponding to a planar electrode calculated from Eq. (5.50) with $\Delta E = 0.01 \text{ mV}$ for different values of the scan rate (shown in the Fig. in mV s^{-1}). $D_{\text{O}} = D_{\text{R}} = 10^{-5} \text{ cm}^2 \text{ s}^{-1}$, $c_{\text{R}}^* = 0$. Vertical dashed lines mark the location of the anodic and cathodic peak potentials. The black dot corresponds to the so-called isopoint



more appropriate to focus on the measurement of the reverse peak potential, $E_{\text{peak,r}}^{\text{plane}}$. If the potential is inverted at a value $|E_{\text{final}}| > \left| E_{\text{peak,f}}^{\text{plane}} \right| + 35 \text{ mV}$, the second peak potential will be unaffected by the switching potential [9, 25]. Under these conditions, the difference between the peak potentials of both scans corresponding to planar electrodes is

$$\Delta E_{\text{peak}}^{\text{plane}} = 2.218 \frac{RT}{F} = 57 \text{ mV} \quad (T = 298 \text{ K}) \quad (5.59)$$

From Eqs. (5.57) and (5.59), it follows immediately that the midpoint between cathodic and anodic peak potentials coincides with the half-wave potential (see also Fig. 5.4):

$$E_{\text{midpoint}}^{\text{plane}} = \frac{E_{\text{peak,f}}^{\text{plane}} + E_{\text{peak,r}}^{\text{plane}}}{2} = E_{1/2}^{\text{r}} \quad (5.60)$$

There is another characteristic point in the voltammogram known as the “isopoint” [25, 26]. At the isopoint, the current is zero regardless of the scan rate (see black dot in Fig. 5.4). In reference [26], the following numerical expression was reported to determine the difference between the peak potential of the forward scan, $E_{\text{peak,f}}^{\text{plane}}$, and the potential of the isopoint, $E_{\text{iso}}^{\text{plane}}$, in terms of the switching potential E_{final} :

$$E_{\text{peak,f}}^{\text{plane}} - E_{\text{iso}}^{\text{plane}} = 0.60 \frac{RT}{F} \ln \left(\frac{F}{RT} \left| E_{\text{final}} - E_{\text{peak,f}}^{\text{plane}} \right| \right) - 1.609 \frac{RT}{F} \quad (5.61)$$

5.2.3.2 Spherical Electrodes

The expression of the dimensionless current obtained for a Nernstian process at spherical electrodes can be deduced from Eq. (5.39) (see also Table 5.1),

$$\begin{aligned} \psi_{\text{CV}}^{\text{sph}} &= \psi_{\text{CV}}^{\text{plane}} + \psi_{\text{CV}}^{\text{sph,ss}} = \\ &= (1 + c_{\text{R}}^*/c_{\text{O}}^*) \sum_{m=1}^p Z_m \frac{1}{\sqrt{\pi} \vartheta_{m,p}} + \xi_s \frac{1 - e^{\vartheta_p} e^{\vartheta_{\text{in}}} (c_{\text{R}}^*/c_{\text{O}}^*)}{(1 + e^{\vartheta_p} e^{\vartheta_{\text{in}}})} \end{aligned} \quad (5.62)$$

with ϑ_{in} , Z_m , ϑ_p and $\psi_{\text{CV}}^{\text{plane}}$ given by Eq. (5.43), (5.45), (5.46) and (5.50), respectively. Moreover,

$$\psi_{\text{CV}}^{\text{sph,ss}} = \xi_s \frac{1 - e^{\vartheta_p} e^{\vartheta_{\text{in}}} (c_{\text{R}}^*/c_{\text{O}}^*)}{(1 + e^{\vartheta_p} e^{\vartheta_{\text{in}}})} \quad (5.63)$$

In the most usual case where only the oxidized species O is initially present ($c_R^* = 0$) and the potential scan starts at $E_{\text{initial}} \gg E_c^{\Theta'}$ (i.e., $e^{\eta_1} \rightarrow \infty$), Eq. (5.62) is simplified to,

$$\psi_{\text{CV}}^{\text{sphe}} = \sum_{m=2}^p Z_m \frac{1}{\sqrt{\pi \vartheta_{m,p}}} + \xi_s \frac{1}{(1 + e^{\vartheta_p} e^{\vartheta_m})} \quad (5.64)$$

with ξ_s given in Eq. (5.42) and in Table 5.1.

Equation (5.64) is equivalent to the following expression deduced by Reinmuth by using Laplace transform and assuming equal diffusion coefficients of species O and R and $c_R^* = 0$ [27],

$$I_{\text{CV}}^{\text{sphe}} = I_{\text{CV}}^{\text{plane}} + FA_s c_O^* \frac{D}{r_s} \frac{1 - e^{-at}}{1 + \theta e^{-at}} \quad (5.65)$$

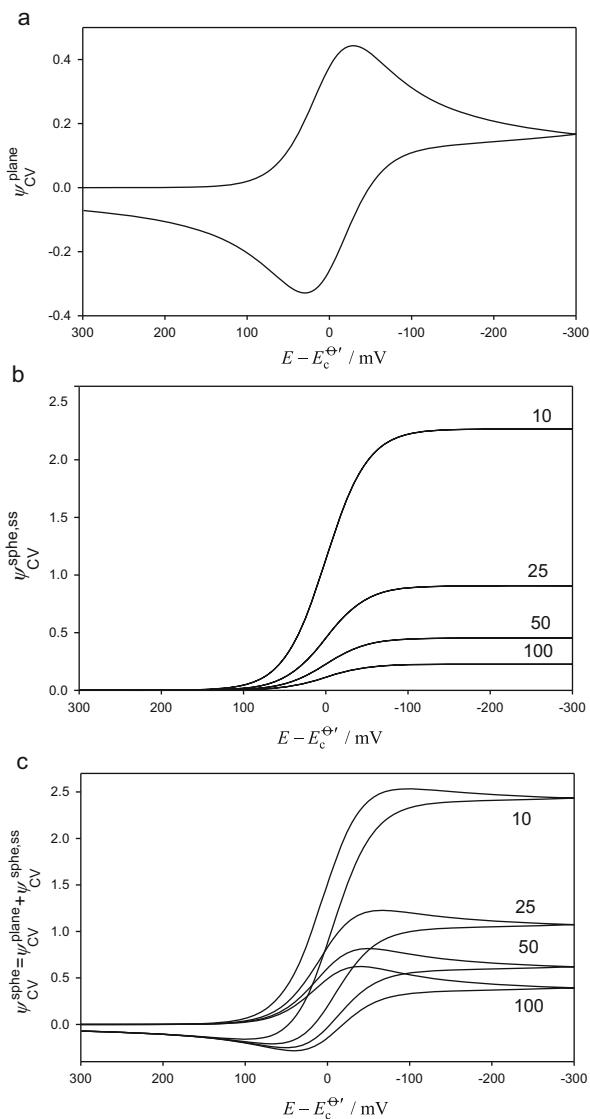
with $\theta = \exp(F(E_{\text{initial}} - E_c^{\Theta'})/(RT))$, see Appendix H, and $I_{\text{CV}}^{\text{plane}}$ and at given in Eqs. (5.52) and (5.53), respectively.

From Eq. (5.62) or (5.65) it is clear that when the electrode radius decreases the second term in the right-hand side of both equations becomes dominant and the current becomes stationary (see below). Thus, the typical peak-shaped signal of macroelectrodes evolves toward a sigmoidal or quasi-sigmoidal shape, indicative of stationary or quasi-stationary behavior, and therefore, under these conditions, the peak is no longer an important feature of the signal.

To check this behavior, in Fig. 5.5 are plotted the voltammograms corresponding to a planar electrode calculated from Eq. (5.50) (Fig. 5.5a), those calculated from Eq. (5.63) for different values of the electrode radius (Fig. 5.5b), and, finally, the current corresponding to a spherical electrode, calculated as the sum of these two contributions (Fig. 5.5c). Thus, the decrease of the electrode size leads to an increase of the dimensionless current of the spherical electrode and to a change of the voltammogram shape in the way indicated above. For small electrodes (see curves in Fig. 5.5c for a radius $r_s = 10$ microns), the peak of the second scan has disappeared and that corresponding to the first scan is poorly defined. Therefore, in these conditions the determination of thermodynamic parameters of the experimental systems under study lies in the study of the half-wave potential of the voltammograms (see below).

Expressions for the peak parameters similar to Eqs. (5.55)–(5.57) have not been reported since, in this case, they also depend on the electrode size. Thus, the separation between cathodic and anodic peaks increases as the electrode radius diminishes (for example, $\Delta E_{\text{peak}}^{\text{sphe}} = 73 \text{ mV}$ ($T = 298 \text{ K}$) for $r_s = 0.01 \text{ cm}$) [25]. The usual approach for spherical or, in general, nonplanar electrode geometries is to use numerical simulations to get an optimal fitting of a particular experimental voltammogram with a given set of parameters (formal potential, diffusion coefficients, etc.).

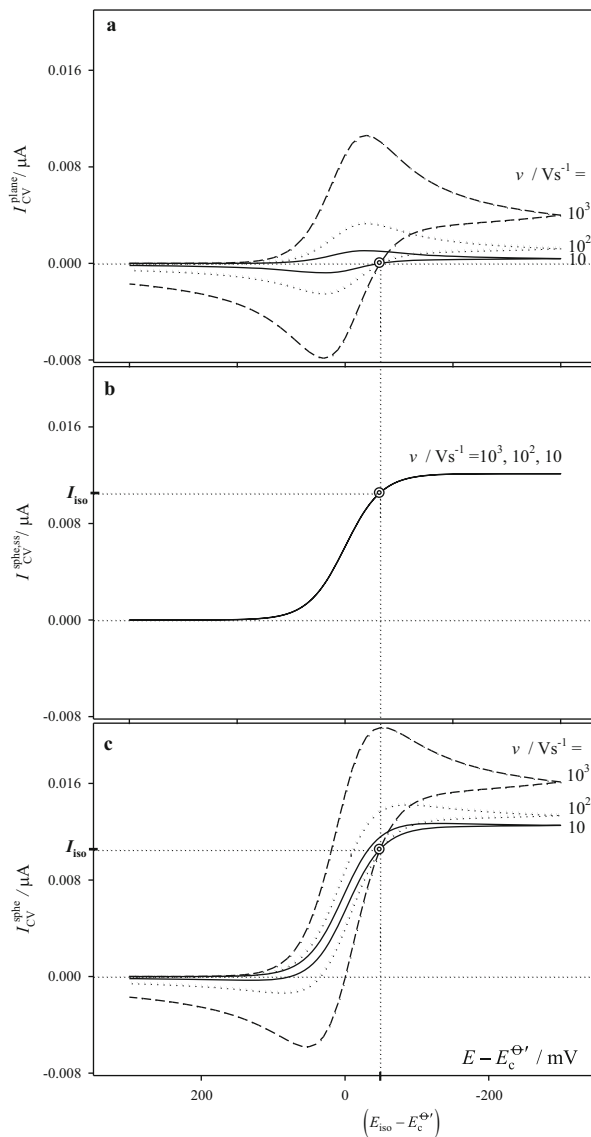
Fig. 5.5 $\psi_{CV}^G - E$ responses calculated with $\Delta E = 0.01$ mV from Eq. (5.50) (a, planar electrode), Eq. (5.63) (b, stationary contribution to the response of a spherical electrode), and Eq. (5.62) (c, spherical electrode). $\nu = 50$ mV s⁻¹, $D = 10^{-5}$ cm² s⁻¹. The values of the electrode radius (in microns) appear on the curves of figures (b) and (c)



Although it is not possible to deduce analytical expressions for the peak currents and potentials for spherical electrodes, the “isopoint” can be analytically characterized, as in the case of planar electrodes (see Sect. 5.2.3.1).

The cyclic voltammograms corresponding to a spherical electrode of radius $r_s = 10$ microns by using three values for the scan rate (10^3 , 10^2 , and 10 mV s⁻¹) are shown in Fig. 5.6. Figure 5.6a, b shows the planar (I_{CV}^{plane} ; see Eqs. (5.37) and (5.50)) and stationary ($I_{CV}^{sphe,ss}$; see Eq. (5.63)) contributions, respectively. Figure 5.6c

Fig. 5.6 Current–potential curves for a Nernstian process in Cyclic Voltammetry. (a) planar contribution, Eqs. (5.37) and (5.50); (b) stationary contribution, Eqs. (5.37) and (5.63); (c) spherical electrodes, Eqs. (5.37) and (5.62). $r_s = 10$ microns, $D = 10^{-5} \text{ cm}^2 \text{ s}^{-1}$, $T = 298.15 \text{ K}$, $c_R^* = 0$, $|\Delta E| = 0.01 \text{ mV}$. The values of the scan rate (in mV s^{-1}) appear in the curves. The coordinates of the nonzero current isopoint ($E_{\text{iso}}^{\text{plane}} - E_c^{\Theta'}$, I_{iso}) are shown in figure (c). Reproduced with permission from [25]



corresponds to the real current that would be expected for a spherical electrode (Eq. (5.62)). As can be seen, planar and spherical curves present a common point in the reverse branches of the current–potential curves obtained at different scan rates which corresponds to the “isopoint.” The current corresponding to this point, regardless of the scan rate value and unlike the case of planar diffusion, corresponds to a nonzero reverse current which is due solely to the stationary contribution, which is independent of the scan rate (see Fig. 5.6b), i.e., $I_{\text{CV}}^{\text{sphe, iso}} = I_{\text{CV}}^{\text{sphe, ss}}(E_{\text{iso}})$. In

this case, the expression of $I_{CV}^{sphe,iso}$ can be easily calculated by making $I_{CV}^{plane,iso} = 0$ in Eqs. (5.62) or (5.65). So it is deduced that

$$I_{CV}^{sphe,iso} = \frac{FA_s D c_O^*}{r_s} \frac{1}{(1 + e^{\theta_{iso}} e^{\theta_{in}})} \quad (5.66)$$

where

$$\theta_{iso} = \frac{F}{RT} (E_{iso}^{sphe} - E_{initial}) \quad (5.67)$$

Equation (5.62) for the current–potential response in CV has been deduced by assuming that the diffusion coefficients of species O and R fulfill the condition $D_O = D_R = D$. If this assumption cannot be fulfilled, this equation is not valid since in this case the surface concentrations are not constant and it has not been possible to obtain an explicit solution. Under these conditions, the CV curves corresponding to Nernstian processes have to be obtained by using numerical procedures to solve the diffusion differential equations (finite differences, Crank–Nicholson methods, etc.; see Appendix I and ([28])³.

The influence of the diffusion coefficients in the voltammograms corresponding to planar (a) and spherical (b) electrodes can be seen in Fig. 5.7, which has been obtained by following the numerical procedure described in [21, 22]. It can be seen in these figures that for planar electrodes the variation of $\gamma = \sqrt{D_O/D_R}$ only causes a shift of the voltammogram toward more negative potentials as γ increases, but has no influence on the peak current, in line with Eqs. (5.55)–(5.56). In the case of spherical electrodes, it can be observed that, together with the shift of the curves toward more negative potentials, there is an increase of the peak current of the second scan, which is more evident as the electrode size or the scan rate decreases.

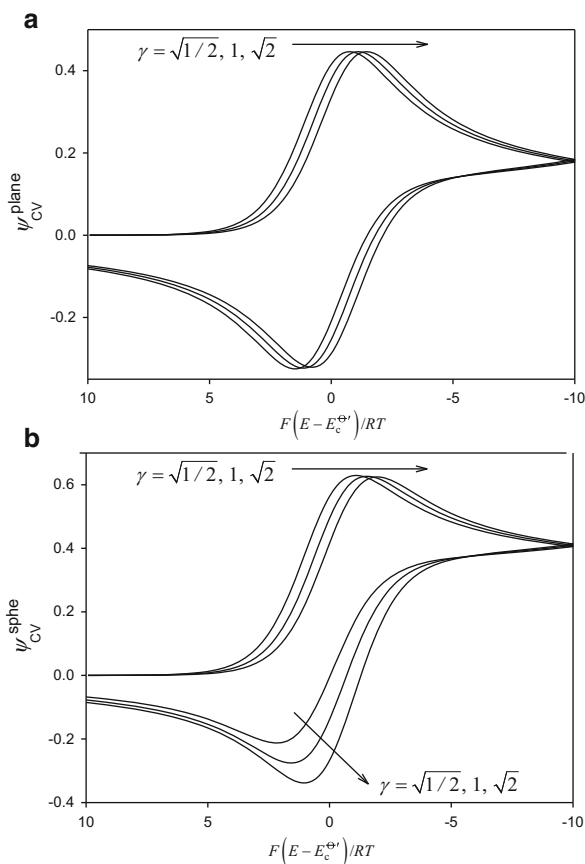
5.2.3.3 Other Electrode Geometries: Microelectrodes and Stationary Voltammetry

For electrode geometries other than planar or spherical, the expression of the SCV current is given, in general, by Eq. (5.41). For CV conditions, the current can be obtained from Eq. (5.41) with $|\Delta E| \leq 0.01$ mV.

The effects of the pulse amplitude $|\Delta E|$ on the values of the peak potential of the forward scan ($E_{peak, f}^G - E_c^{\phi'}$) and the peak-to-peak distance (ΔE_{peak}^G) of the voltammograms calculated at discs (circles), spheres (squares), bands (hexagons), and cylinders (triangles) for three different values of the scan rate are shown in Fig. 5.8.

³ See also: <http://www.basinc.com/products/ec/digisim/> and <http://www.gamry.com/products/digielch-electrochemical-simulation-software/>

Fig. 5.7 Dimensionless current–potential response of a Nernstian process in CV calculated for planar (a) and spherical (b) electrode by using the numerical procedure proposed in [21, 22] (see also Appendix I). The values of the ratio $\gamma = \sqrt{D_O/D_R}$ appear on the curves. $r_s = 100 \mu\text{m}$, $\nu = 50 \text{ mV s}^{-1}$



From these curves, it can be seen that in all the cases ΔE_{peak}^G increases and $E_{\text{peak},f}^G$ is shifted toward more negative potentials as $|\Delta E|$ increases.

Concerning the influence of the scan rate, for $\nu = 1.0 \text{ V s}^{-1}$, no significant differences are observed between the four geometries. These results indicate that for high scan rates (i.e., low values of τ for a fixed $|\Delta E|$), the diffusional behavior can be considered as almost planar, so the particular electrode geometry incorporates only small differences in the current. An additional confirmation of this point is that, as $|\Delta E| \rightarrow 0$ and the SCV voltammograms behave as CV (vertical dotted lines), $E_{\text{peak},f}^G - E_c^{\ominus'}$ and ΔE_{peak}^G approach the values observed in this technique for a planar electrode (-28 and 57 mV , respectively; see Eqs. (5.57) and (5.59)).

However, when ν decreases (i.e., τ increases for a given $|\Delta E|$), the peak potential and peak-to-peak distance show a strong dependence on the electrode geometry, which clearly indicates that the values of f_G function are very different for the four geometries.

The influence of the electrode radius on the cyclic voltammograms ($\Psi^G - E$ curves) obtained for discs, spheres, bands, and cylinders in the more general case in which both species are initially present in the electrolytic solution ($c_R^*/c_O^* = 1$) is

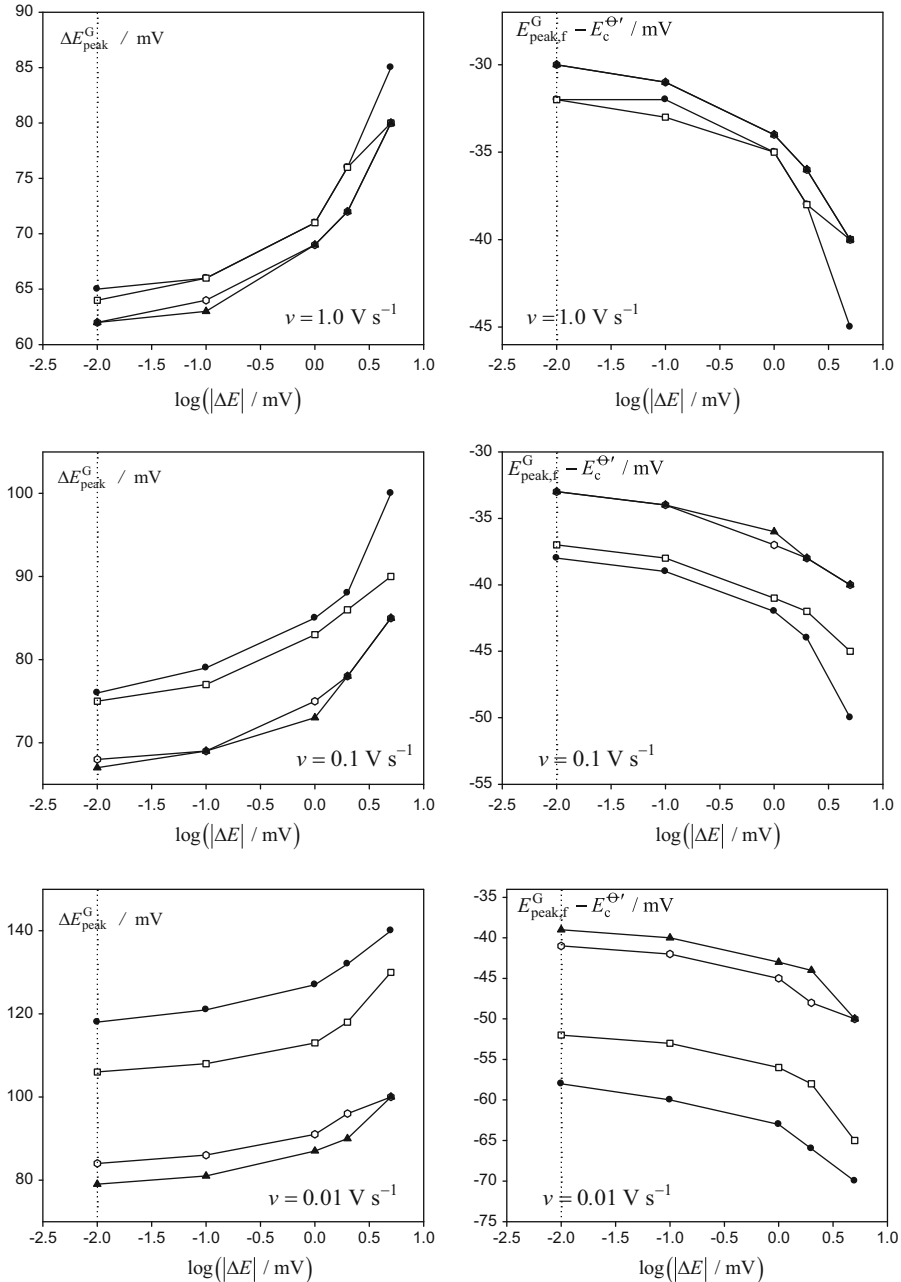


Fig. 5.8 Influence of the pulse amplitude $|\Delta E|$ on the values of the peak potential ($E_{\text{peak},f}^G - E_c^{\Theta'}$) and the peak-to-peak distance (ΔE_{peak}^G) of the voltammograms calculated from Eq. (5.41) for discs (circles), spheres (squares), bands (hexagons), and cylinders (triangles), for three different values of the scan rate. $r_d = r_s = (w/2) = r_c = 0.01 \text{ cm}$, $c_R^*/c_O^* = 0$. $\tau = 50 \text{ ms}$, $D = 10^{-5} \text{ cm}^2 \text{ s}^{-1}$. Vertical dotted lines mark the CV limits, i.e., the response of SCV with $|\Delta E| = 0.01 \text{ mV}$, which can be considered as indistinguishable from that of CV. Taken from [8] with permission

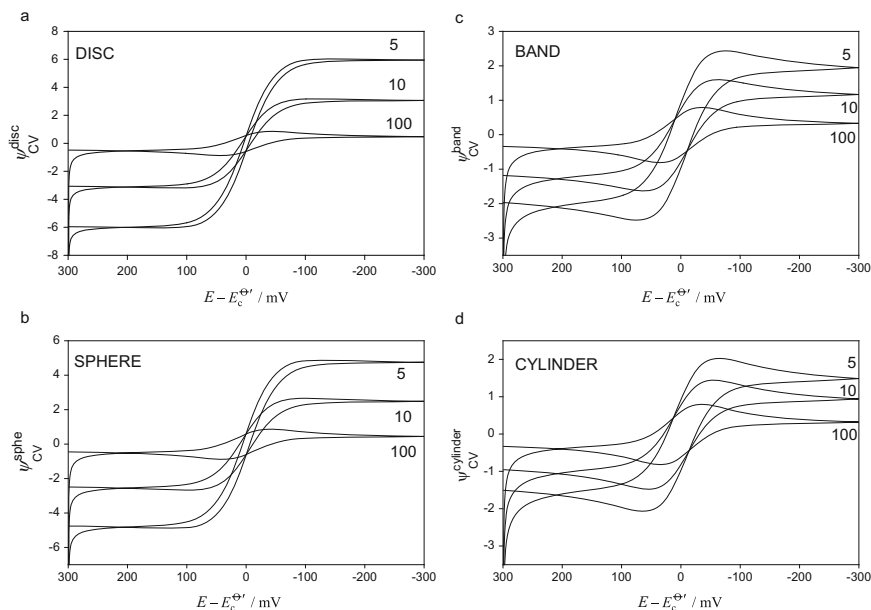


Fig. 5.9 Influence of the electrode radius on the cyclic voltammograms ($\psi_{CV}^G - E$ curves) obtained from Eq. (5.41) for discs, spheres, bands, and cylinders in the more general case in which both species are initially present in the electrolytic solution ($c_R^*/c_O^* = 1$). The values of $r_d = r_s = (w/2) = r_c$ (in microns) are shown in the figures. $\nu = 50 \text{ mV s}^{-1}$. $\tau = 50 \text{ ms}$, $D = 10^{-5} \text{ cm}^2 \text{ s}^{-1}$. Taken from [8] with permission

shown in Fig. 5.9. In order to analyze the effects of the electrode geometry on the dimensionless voltammetric current, discs, spheres, and cylinders with equal radii have been chosen, as well as a band whose semi-width is identical to the cylinder radius.

As can be deduced from these curves, the voltammograms present a more sigmoidal shape as the electrode size decreases, such that for a small enough radius a stationary $I - E$ curve is reached at discs and spheres and, therefore, the current is given by

$$\psi_{CV}^{G,ss} = \frac{1 - e^{\eta_p} (c_R^*/c_O^*)}{1 + e^{\eta_p}} f_{G,micro} \quad (5.68)$$

or, alternatively,

$$\psi_{CV}^{G,ss} = \frac{1 - e^{\vartheta_p} e^{\vartheta_{in}} (c_R^*/c_O^*)}{1 + e^{\vartheta_p} e^{\vartheta_{in}}} f_{G,micro} \quad (5.69)$$

with $\eta_p = F/(RT)(E_p - E_c^{\Theta'})$. ϑ_p and ϑ_{in} are given in Eqs. (5.45)–(5.46) and $f_{G,micro}$ is given in Table 5.1 for different electrode geometries.

By comparing Eq. (5.68) for the CV steady-state currents and Eq. (2.159) for NPV under transient conditions, it can be deduced that at those electrodes where a true steady-state response can be attained (spheres and discs) it holds that

$$\frac{\psi_{CV}^{G,ss}}{\psi_{CV,d,c}^{G,ss}} = \frac{I_{NPV}}{I_{d,c}} = \frac{1 - e^{\eta} (c_R^*/c_O^*)}{1 + e^{\eta}} \quad G = \text{sphere, disc} \quad (5.70)$$

where $\psi_{CV,d,c}^{G,ss}$ is the value of $\psi_{CV}^{G,ss}$ for $E \rightarrow -\infty$ (i.e., $\psi_{CV,d,c}^{G,ss} = f_{G,\text{micro}}$).

This behavior is not expected for microcylinders and microbands, for which only quasi-steady-state curves are obtained (see Fig. 5.9c, d and Table 5.1).

In order to evaluate the conditions under which it is possible to achieve a stationary cyclic voltammogram, a key parameter is Nernst diffusion layer thickness, δ_G^r , which was introduced in Sect. 2.2.1 for reversible processes when a single potential pulse is applied. It is possible to extend the definition of δ_G^r to a multipulse sequence, $\delta_G^{r,p}$, as

$$\delta_G^{r,p} = \frac{\Delta c_O^{(p)}}{I_p^G / (FA_G D c_O^*)} \quad (5.71)$$

with

$$\Delta c_O^{(p)} = 1 - \frac{c_O^{(p,s)}}{c_O^*} = \frac{1 - e^{\eta_p} (c_R^*/c_O^*)}{1 + e^{\eta_p}} \quad (5.72)$$

and I_p^G given in Eq. (5.23) (with $|\Delta E| \leq 0.01$ mV for CV), which is applicable to any electrode geometry.

In the case of spherical electrodes, Nernst diffusion layer thickness reaches the following limiting behaviors:

$$\left. \begin{array}{l} \text{anodic limit} \quad \left(\delta_{\text{sph}}^{r,p} \right)_{E \gg E_c^{\Theta'}} = \frac{1}{\frac{1}{r_s} + \sqrt{\frac{a}{D}}} \\ \text{cathodic limit} \quad \left(\delta_{\text{sph}}^{r,p} \right)_{E \ll E_c^{\Theta'}} = \frac{1}{\frac{1}{r_s} + \sqrt{\frac{v}{\pi D E_p}}} \end{array} \right\} \quad (5.73)$$

For planar electrodes, the limits of the diffusion layer thickness are

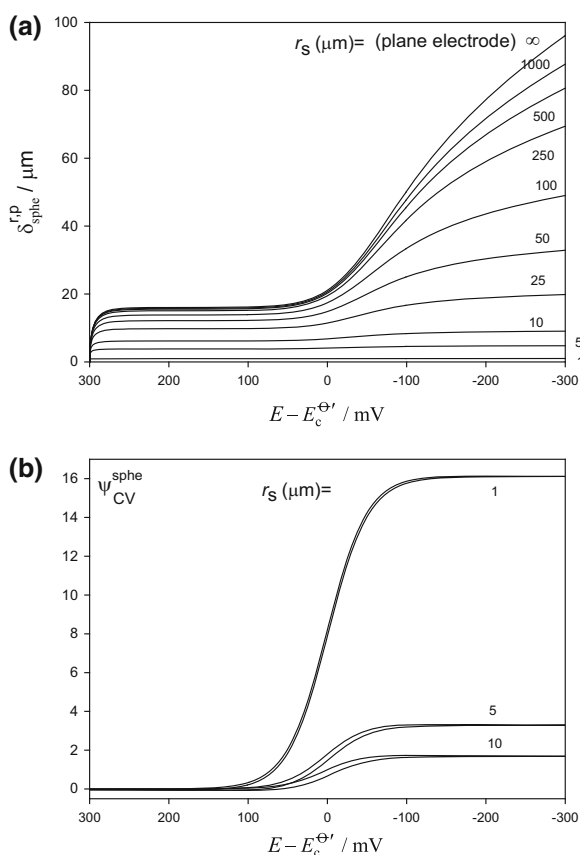
$$\left. \begin{array}{l} \text{anodic limit} \quad \left(\delta_{\text{plane}}^{r,p} \right)_{E \gg E_c^{\Theta'}} = \sqrt{\frac{D}{a}} \\ \text{cathodic limit} \quad \left(\delta_{\text{sph}}^{r,p} \right)_{E \ll E_c^{\Theta'}} = \sqrt{\frac{\pi D E_p}{v}} \end{array} \right\} \quad (5.74)$$

The anodic limiting behavior of Eq. (5.73) is observed for $E - E_c^{\Theta'} \geq 95 \text{ mV}$, whereas the cathodic limiting behavior is observed for $E - E_c^{\Theta'} \leq -230 \text{ mV}$ with errors below 1 % in both cases. From Eq. (5.73), it is clear that for $E \ll E_c^{\Theta'}$, $\delta_{\text{sph}}^{r,p}$ has a dependence on the electrode radius and time ($= (E(t) - E_{\text{initial}})/\nu$) similar to that obtained when only one potential step is applied (see Eq. (2.146)).

It is also possible to find expressions analogous to those given in Eqs. (5.71) for the limiting values of the diffusion layer thickness for other electrode geometries like disc or band electrodes [29, 30].

The variation of $\delta_{\text{sph}}^{r,p}$ with the potential for different values of the electrode radius obtained in CV with spherical electrodes, including the limiting case of a planar electrode ($r_s \rightarrow \infty$), can be seen in Fig. 5.10a. From these curves, which have been calculated using Eq. (5.71) for a sweep rate $\nu = 0.1 \text{ V s}^{-1}$, it can be observed that the diffusion layer thickness decreases with the electrode radius and the constant value $\delta_{\text{sph}}^{r,p} = r_s$ is reached when $r_s \leq 5 \mu\text{m}$ (i.e., a truly stationary $I-E$ response is obtained as can be seen in Fig. 5.10b).

Fig. 5.10 Nernst diffusion layer thickness $\delta_{\text{sph}}^{r,p}$ obtained in LSV (a) and Cyclic Voltammograms (b) corresponding to a spherical electrode. These curves have been calculated from Eq. (5.71)–(5.72) and (5.23) for $|\Delta E| = 10^{-5} \text{ mV}$ and $\nu = 100 \text{ mV s}^{-1}$. The values of the electrode radii appear on the curves. Reproduced with permission [29]



In the case of disc electrodes, a similar behavior to that observed for spherical ones is obtained (although in this case the diffusion layer thickness is an average magnitude), whereas for band or cylinder electrodes, the diffusion layer thickness is always potential dependent, and no constant limit is achieved, even for very small values of the electrode characteristic dimension, confirming the impossibility of these electrodes achieving a true stationary response [5, 8, 16, 29, 30].

5.2.3.4 Effect of the Uncompensated Resistance and of the Double-Layer Charging

One of the main disadvantages of voltammetric techniques like CV is the distortion caused by the combination of the double-layer charging process with the ohmic drop, related to the uncompensated resistance of the solution, R_u (see Sect. 1.9). This distortion can be very significant for macroelectrodes.

The ohmic drop causes the potential imposed between the working electrode and the reference one (E') to differ from the applied potential (E), according to $E' = E - IR_u$. Moreover, it can be assumed, at least approximately, that the current can be expressed as the sum of a pure faradaic current because of the charge transfer process plus a charging current

$$I = I_{\text{faradaic}} + I_c \quad (5.75)$$

For CV, the charging component is a function of the applied potential given by [31]

$$I_{\text{CV},c} = \begin{cases} C_{\text{dl}} \nu \left(1 - e^{-\left(\frac{E_{\text{initial}} - E}{\nu R_u C_{\text{dl}}}\right)} \right) & \text{direct scan} \\ C_{\text{dl}} \nu \left(1 - 2e^{-\left(\frac{E - E_{\text{final}}}{\nu R_u C_{\text{dl}}}\right)} \right) & \text{reverse scan} \end{cases} \quad (5.76)$$

with C_{dl} being the double-layer capacitance, whereas in multipulse techniques like SCV it takes the form (see Eq. (1.203))

$$I_{\text{SCV},c} = \pm \frac{\Delta E}{R_u} e^{-\left(\frac{\tau}{R_u C_{\text{dl}}}\right)} \quad (5.77)$$

with the double sign referring to the direct (upper) and reverse (lower) scans. To deduce Eqs. (5.76)–(5.77), it has been assumed that C_{dl} is potential independent.

The main difference between expressions (5.76) and (5.77) lies in the way the current is measured in each technique. As stated in Sect. 5.1, in CV the current is

measured as a continuous function of potential (or time, since both magnitudes are proportional in line with Eq. (5.1)). In this sense, the charging current is also a continuous function of the potential which is proportional to the scan rate (see Eq. (5.76)), whereas the faradaic current depends linearly on the square root of the scan rate when a planar electrode (i.e., a macroelectrode) is considered (see Eqs. (5.55)–(5.56)). However, in SCV the current is measured in a discrete way at particular values of time (typically at the end of the application of each potential pulse of the perturbation waveform). The expression of the charging current given by Eq. (5.77) has been deduced in agreement with the waveform of SCV perturbation (see Scheme 5.2 and Eq. (5.2)).

Note that for typical electrodes for which the $R_u C_{dl}$ term is in the range of 10–100 μs , it is possible to decouple the charging component of the current from the faradaic one in the case of SCV, since for pulse times of the order of milliseconds, it is fulfilled that $I_{\text{faradaic}} \gg I_c$, and the distortion caused by I_c is much less significant than that observed in CV, where this condition is not fulfilled.

In order to confirm this behavior, the cyclic voltammograms obtained at a planar electrode in CV and SCV (for $|\Delta E| = 5 \text{ mV}$) for a Nernstian charge transfer process at different values of the scan rate are shown in Fig. 5.11. The effect of the ohmic drop and charging current has been considered by including an uncompensated resistance $R_u = 0.1 \text{ K}\Omega$ and a double-layer capacitance $C_{dl} = 20 \mu\text{F cm}^{-2}$.

As can be seen in this figure, the combined effect of ohmic drop and double-layer capacitance is much more serious in the case of CV. The increase of the scan rate (and therefore of the current) causes a shift of the peak potentials which is 50 mV for the direct peak in the case of the CV with $\nu = 100 \text{ V s}^{-1}$ with respect to a situation with $R_u = 0$ (this shift can be erroneously attributed to a non-reversible character of the charge transfer process; see Sect. 5.3.1). Under the same conditions the shift in the peak potential observed in SCV is 25 mV. Concerning the increase of the current observed, in the case of CV the peak current has a value 26 % higher than that in the absence of the charging current for $\nu = 100 \text{ V s}^{-1}$, whereas in SCV this increase is 11 %. In view of these results, it is evident that these undesirable effects in the current are much less severe in the case of multipulse techniques, due to the discrete nature of the recorded current. The CV response can be greatly distorted by the charging and double-layer contributions (see the CV response for $\nu = 500 \text{ V s}^{-1}$) and their minimization is advisable where possible.

In order to avoid the distortion caused by these two effects, the usual approach is to compensate the resistance R_u by a positive feedback loop (this is imperative in systems like plasticized membranes for which the uncompensated resistance can be of the order of megaohms [32–34]). Another possibility is to use microelectrodes, for which a decrease in the measured current is obtained which minimizes the ohmic drop and charging current distortion (see Sects. 2.7 and 5.4.1).

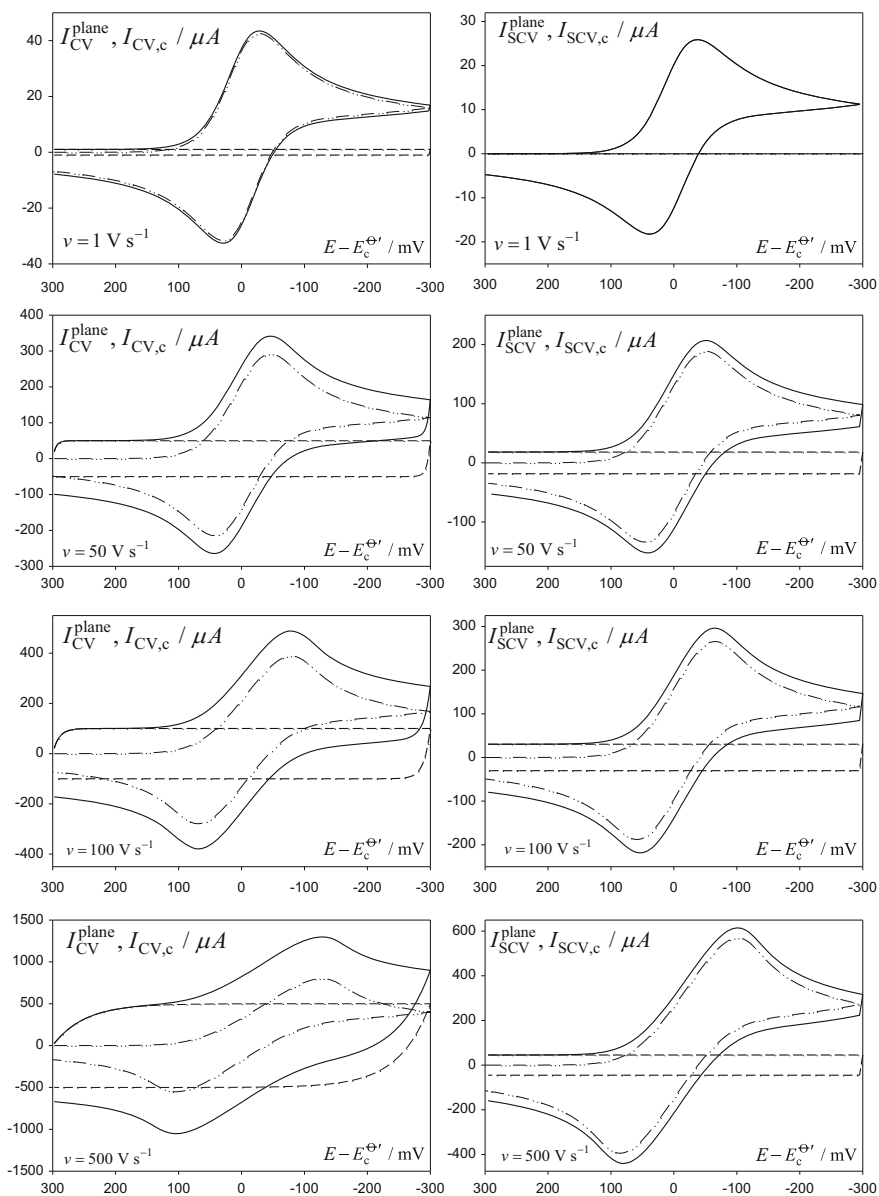


Fig. 5.11 Current–potential response of CV and SCV (for $|\Delta E| = 5$ mV) for a Nernstian charge transfer process taking place at a planar electrode for different values of the scan rate (shown in the figure). *Dashed-dotted lines*: Pure faradaic component (SCV and CV) calculated by using the numerical procedure proposed in [21, 22]. *Dashed lines*: Charging current calculated from Eqs. (5.77) (SCV) and (5.76) (CV). *Solid lines*: total current calculated as indicated in Eq. (5.75). $R_u = 0.1$ k Ω , $C_{dl} = 20$ μ F cm $^{-2}$, Area = 0.05 cm 2 , $c_O^* = 1$ mM, $c_R^* = 0$, $D_O = D_R = 10^{-5}$ cm 2 s $^{-1}$

5.3 Non-reversible Electrochemical Reactions

In this section, a non-reversible electrochemical reaction is considered according to the reaction scheme:



where k_{red} and k_{ox} are the rate constants for the electro-reduction and electro-oxidation charge transfer processes, respectively. The particular expression of the rate constants depends on the kinetic model considered (Butler–Volmer or Marcus–Hush; see Sect. 1.7).

Due to the complexity of this situation, a rigorous explicit solution for the CV current is not available, even for the simplest case of a totally irreversible process. The case corresponding to a planar electrode is treated in detail and that corresponding to nonplanar geometry is addressed briefly.

5.3.1 Planar Electrodes

The expression of the boundary value problem for reaction (5.11) corresponding to the application of a sequence of potential pulses E_1, E_2, \dots, E_p to a planar electrode is

$$\left. \begin{aligned} \frac{\partial c_{\text{O}}^{(p)}}{\partial t_p} &= D_{\text{O}} \frac{\partial^2 c_{\text{O}}^{(p)}}{\partial x^2} \\ \frac{\partial c_{\text{R}}^{(p)}}{\partial t_p} &= D_{\text{R}} \frac{\partial^2 c_{\text{R}}^{(p)}}{\partial x^2} \end{aligned} \right\} \quad (5.78)$$

$$\left. \begin{aligned} t_p \geq 0, \quad x \rightarrow \infty \} & c_{\text{O}}^{(1)} = c_{\text{O}}^*, \quad c_{\text{R}}^{(1)} = 0 \\ t_p = 0, \quad x \geq 0 \} & c_{\text{O}}^{(p)} = c_{\text{O}}^{(p-1)}, \quad c_{\text{R}}^{(p)} = c_{\text{R}}^{(p-1)}, \quad p > 1 \end{aligned} \right\} \quad (5.79)$$

$$t_p > 0, \quad x = 0 :$$

$$D_{\text{O}} \left(\frac{\partial c_{\text{O}}^{(p)}}{\partial x} \right)_{x=0} = - D_{\text{R}} \left(\frac{\partial c_{\text{R}}^{(p)}}{\partial x} \right)_{x=0} \quad (5.80)$$

$$D_{\text{O}} \left(\frac{\partial c_{\text{O}}^{(p)}}{\partial x} \right)_{x=0} = k_{\text{red}, p} c_{\text{O}}^{(p,s)} - k_{\text{ox}, p} c_{\text{R}}^{(p,s)} \quad (5.81)$$

Taking into account the relationship between the oxidation and reduction rate constants (i.e., $k_{\text{ox}, p} = k_{\text{red}, p} e^{\eta_p}$ with $\eta_p = F(E_p - E_c^{\Theta'})/RT$) whatever the kinetic model considered, Eq. (5.81) becomes

$$D_O \left(\frac{\partial c_O^{(p)}}{\partial x} \right)_{x=0} = k_{\text{red}, p} \left[c_O^{(p,s)} - e^{\eta_p} c_R^{(p,s)} \right] \quad (5.82)$$

To date, there has been no explicit solution for this problem for $p > 3$, since the surface concentrations of electroactive species O and R are time dependent and therefore the Superposition Principle cannot be applied (see also Sect. 4.3) [1, 5]. In these conditions, a non-explicit integral solution has been deduced using the Laplace transform method (see Appendix H).

Simple expressions for the peak parameters have been deduced by assuming a totally irreversible reaction (i.e., $k_{\text{red}, p} \gg k_{\text{ox}, p}$). Considering the Butler–Volmer kinetic scheme, the peak parameters are given by [9]:

– Peak current

$$I_{\text{CV}}^{\text{plane, peak}} = (2.99 \times 10^5) \sqrt{\alpha D_O A c_O^* \nu} \quad (5.83)$$

which corresponds to a temperature $T = 298$ K, with A in cm^2 , D in $\text{cm}^2 \text{s}^{-1}$, c_O^* in mol cm^{-3} , and ν in V s^{-1} . In Eq. (5.83), α is the charge transfer coefficient.

– Peak potential

$$E_{\text{peak, f}}^{\text{plane}} = E_c^{\ominus'} - \frac{RT}{\alpha F} \left(0.78 + \ln \left(\frac{\sqrt{\alpha}}{\kappa_{\text{plane}}^0} \right) \right) \quad (5.84)$$

with κ_{plane}^0 being the dimensionless rate constant of the process for CV,

$$\kappa_{\text{plane}}^0 = \frac{k^0}{\sqrt{Da}} = \frac{k^0}{\sqrt{\frac{DF\nu}{RT}}} \quad (5.85)$$

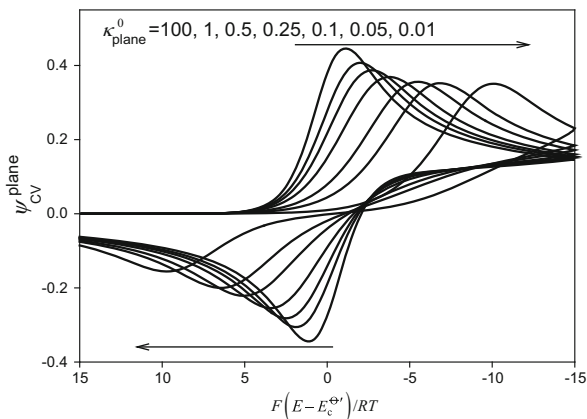
and k^0 is the standard heterogeneous rate constant for the charge transfer reaction. Also of interest is the difference between the peak potential and the half peak potential,

$$E_{\text{peak, f}}^{\text{plane}} - E_{\text{p/2}}^{\text{plane}} = 1.857 \frac{RT}{\alpha F} = \frac{47.7}{\alpha} \text{ mV} \quad (T = 298 \text{ K}) \quad (5.86)$$

The peak parameters of the second scan are logically affected by the inversion potential, as discussed for the case of the Nernstian process. If the switching of the potential for the reverse scan is taken at $|E_{\text{final}}| \geq |E_{\text{peak, f}}| + 90 \text{ mV}$, the peak potential of the second scan is independent of E_{final} and in these conditions it is fulfilled that the difference between both peak potentials is

$$\Delta E_{\text{peak}} = \frac{RT}{\alpha F} \ln(\nu) + \text{constant} \quad (5.87)$$

Fig. 5.12 CV response corresponding to a charge transfer process of different reversibility degrees taking place at a planar electrode, calculated numerically by following the procedure given in [21, 22]. The values of the voltammetric dimensionless rate constant κ_{plane}^0 appear in the figure $\alpha = 0.5$

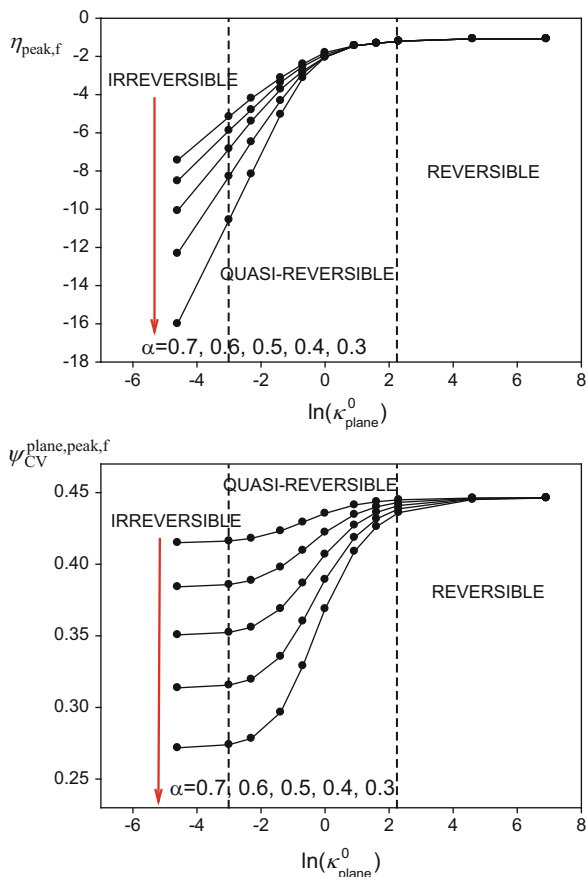


A detailed numerical analysis of the influence of the reversibility of the charge transfer process on the peak parameters for planar electrodes was reported in [35].

The voltammograms corresponding to a charge transfer process with different reversibility degree taking place at a planar electrode are shown in Fig. 5.12. These curves have been calculated for different values of κ_{plane}^0 . In agreement with Eq. (5.85), a decrease of the electrochemical reversibility (i.e., of κ_{plane}^0) is related to intrinsic parameters (a decrease of the heterogeneous rate constant of the electrode process, k^0) and/or extrinsic ones (an increase of the scan rate, ν). In line with the curves in Fig. 5.12, non-reversible processes will lead to voltammetric responses exhibiting lower and wider peaks (a much more marked trend in the peak of the reverse scan), for which the distance between cathodic and anodic peaks increases. For totally irreversible processes, the peak current becomes independent of the value of κ_{plane}^0 , in agreement with Eq. (5.83) and peak potential for the forward scan varies linearly with the logarithm of κ_{plane}^0 , as can be seen from Fig. 5.13. The curves shown in this figure can be used as working curves to determine α and k^0 once the formal potential is known.

Equations (5.83) and (5.84) and the curves in Fig. 5.12 indicate that both peak current and potential of the CV curves change with the scan rate, a feature which is not observed for the peak potential of reversible processes (see Eq. (5.57)). However, the experimental evidence that for a given system the potential peak of the cathodic CV curves shifts to more negative values with increasing scan rate should be used with caution when assigning a non-reversible behavior to the system since, similar displacements can be observed for Nernstian systems when the ohmic drop has an important effect (see Fig. 5.11). Thus, the shift of the CV peak potential with the scan rate is not always a guarantee of a non-reversible charge transfer process.

Fig. 5.13 Dimensionless peak potentials $\eta_{\text{peak},f} = F(E_{\text{peak},f} - E_c^{\ominus'})/RT$ and peak currents ($\psi_{\text{CV}}^{\text{plane,peak},f}$) of the CV curves obtained for a charge transfer process taking place at a planar electrode for different values of the dimensionless rate constant κ_{plane}^0 and of the charge transfer coefficient (α , indicated on the curves)



5.3.2 Reversibility Criteria

From the voltammograms of Fig. 5.12, the evolution of the response from a reversible behavior for values of $\kappa_{\text{plane}}^0 > 10$ to a totally irreversible one (for $\kappa_{\text{plane}}^0 < 0.05$) can be observed. The limits of the different reversibility zones of the charge transfer process depend on the electrochemical technique considered. For Normal or Single Pulse Voltammetry, this question was analyzed in Sect. 3.2.1.4, and the relation between the heterogeneous rate constant and the mass transport coefficient, m^0 , defined as the ratio between the surface flux and the difference of bulk and surface concentrations evaluated at the formal potential of the charge transfer process was considered [36, 37]. The expression of m^0 depends on the electrochemical technique considered (see for example Sect. 1.8.4). For CV or SCV it takes the form

$$m_{CV}^0 = \left(\frac{I_p / FA}{c_O^* - c_O^{(p,s)}} \right)_{E_c^{\Theta'}} = \frac{D}{(\delta_O^{qr,p})_{E_c^{\Theta'}}} \quad (5.88)$$

with I_p and $c_O^{(p,s)}$ being the current and surface concentration of species O corresponding to the application of potential E_p , and $(\delta_O^{qr,p})_{E_c^{\Theta'}}$ the diffusion layer thickness corresponding to a charge transfer process of any reversibility degree calculated at $E_c^{\Theta'}$. In the case of SCV or CV, it is not possible to obtain an analytical expression for $\delta_O^{qr,p}$. However, in the absence of reduced species R, when $E_p \gg E_c^{\Theta'}$, the charge transfer process does not occur, and under these conditions, the diffusion layer thickness is independent of the reversibility of the process and takes the limiting value given in Eq. (5.74) $(\delta_{plane}^{r,p})_{E \gg E_c^{\Theta'}} = \sqrt{D/a}$. By inserting Eq. (5.74) into (5.88), one obtains

$$m_{CV} = \sqrt{Da} \quad (5.89)$$

In order to discriminate between reversible and non-reversible regimes, the relation between the heterogeneous rate constant and the mass transport coefficient can be defined:

$$R = \frac{k^0}{m_{CV}} = \frac{k^0}{\sqrt{Da}} = \kappa_{plane}^0 \quad (5.90)$$

which provides an approximate reversibility criterion. Thus, in line with the discussion in Sect. 3.2.1.4, the following approximate limits are suggested:

$$\begin{array}{ll} \kappa_{plane}^0 \geq 10 & \text{Reversible process} \\ 0.05 \leq \kappa_{plane}^0 < 10 & \text{Quasi-reversible process} \\ \kappa_{plane}^0 < 0.05 & \text{Totally irreversible process} \end{array} \quad (5.91)$$

These regions have been indicated in Fig. 5.13 for $\alpha = 0.5$. Matsuda and Ayabe suggest the following ranges for classifying the electrode process [35]: $\kappa_{plane}^0 \geq 15$, Reversible process; $10^{-3} \leq \kappa_{plane}^0 < 15$, Quasi-reversible process; $\kappa_{plane}^0 < 10^{-3}$, Totally irreversible process. The reversible limit is similar to that proposed here, but the totally irreversible one is clearly excessive (see Fig. 5.13). In any case, this criterion has only an approximate character.

For other electrode geometries and sizes, the expression of the mass transport coefficient is different because the electrode size becomes relevant and the values of the dimensionless rate constant changes (see below).

5.3.3 Other Electrode Geometries: Microelectrodes and Steady-State Voltammetry

For nonplanar electrodes there are no analytical expressions for the CV or SCV curves corresponding to non-reversible (or even totally irreversible) electrode processes, and numerical simulation methods are used routinely to solve diffusion differential equations. The difficulties in the analysis of the resulting responses are related to the fact that the reversibility degree for a given value of the charge transfer coefficient α depends on the rate constant, the scan rate (as in the case of Nernstian processes) and also on the electrode size. For example, for spherical electrodes the expression of the dimensionless rate constant is

$$\kappa_{\text{sph}}^0 = \frac{k^0}{r_s + \sqrt{aD}} \quad (5.92)$$

Equation (5.92) can be rewritten as

$$\frac{1}{\kappa_{\text{sph}}^0} = \frac{1}{\kappa_{\text{plane}}^0} + \frac{1}{\kappa_{\text{sph,ss}}^0} \quad (5.93)$$

with κ_{plane}^0 given in Eq. (5.85) and

$$\kappa_{\text{sph,ss}}^0 = \frac{k^0 r_s}{D} \quad (5.94)$$

Note that the stationary dimensionless rate constant, $\kappa_{\text{sph,ss}}^0$, deduced for CV (Eq. (5.94)) logically coincides with that obtained in SCV and also in NPV (see Eq. (3.74)).

From Eqs. (5.92)–(5.94), it is clear that $\kappa_{\text{sph,ss}}^0 \leq \kappa_{\text{sph}}^0 \leq \kappa_{\text{plane}}^0$, that is, the maximum value of the dimensionless rate constant is that corresponding to a planar electrode (macroelectrode). For smaller electrodes, κ_{sph}^0 decreases until it becomes identical to the value corresponding to a stationary response, $\kappa_{\text{sph,ss}}^0$. In practice, this means that the decrease of the electrode size will lead to the decrease of the reversibility degree of the observed signal. It can be seen in the CV curves of Fig. 5.14, calculated for $k^0 = 10^{-3} \text{ cm s}^{-1}$ and $v = 0.1 \text{ V s}^{-1}$, that the decrease of r_s causes an increase and distortion of the dimensionless current similar to that observed for Nernstian processes (see Fig. 5.5), but there is also a shift of the curve toward more negative potentials (which can be clearly seen in Fig. 5.14b).

The voltammograms present a stationary behavior when the electrode size decreases, and under these conditions, the following current–potential curves are obtained for a microelectrode of geometry G when only oxidized species is initially present [38]:

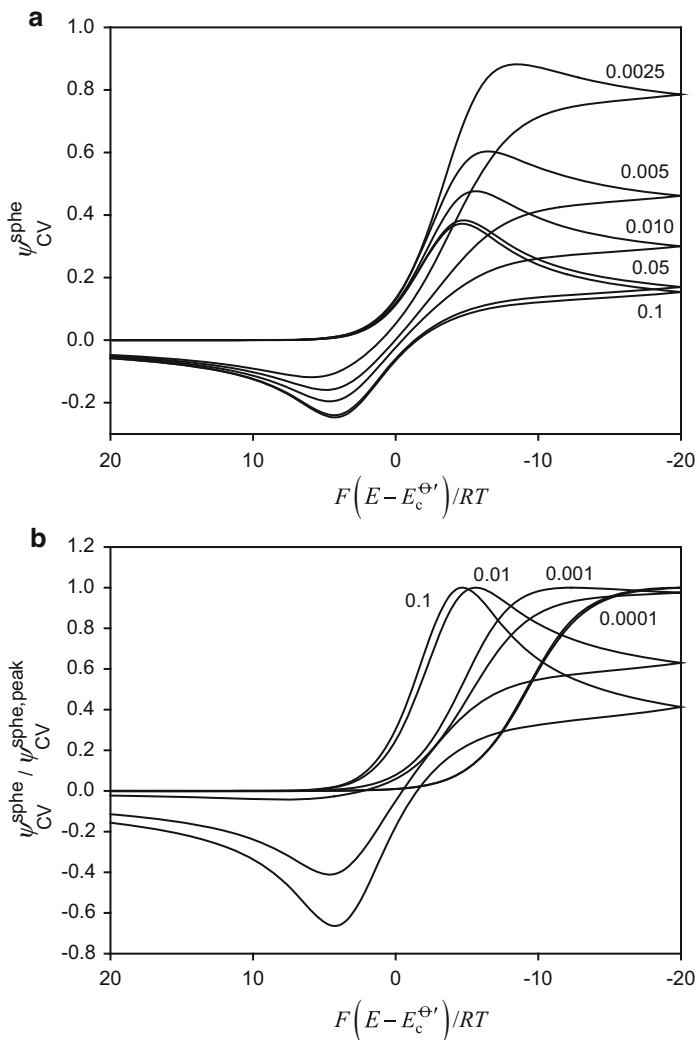


Fig. 5.14 CV responses corresponding to a non-Nernstian charge transfer process at a spherical electrode, calculated by following the numerical procedure discussed in [21, 22]. $\nu = 0.1 \text{ V s}^{-1}$, $k^0 = 10^{-3} \text{ cm s}^{-1}$, $\alpha = 0.5$, $c_O^* = 1 \text{ mM}$, $c_R^* = 0$, $D_O = D_R = 10^{-5} \text{ cm}^2 \text{ s}^{-1}$. The values of the electrode radius (in cm) appear in the figure

$$\psi_{CV}^{G,ss} = \frac{I_p^{G,ss}}{FA_G c_O^* \sqrt{aD}} = \xi_G \frac{\kappa_{G,ss}^0 e^{-a\eta}}{1 + \kappa_{G,ss}^0 e^{-a\eta} (1 + e^\eta)} \quad (5.95)$$

with ξ_G given by Eq. (5.42). For the case of a microsphere (s, radius r_s), a microdisc (d, radius r_d), and a spherical nanoparticle (snp) adhered to a support (snp, radius r_{snp}), the expression of $\kappa_{G,ss}^0$ is (see also Sect. 3.2.5)

$$\left. \begin{aligned} \kappa_{\text{sph},\text{ss}}^0 &= \frac{k^0 r_s}{D} \\ \kappa_{\text{disc},\text{ss}}^0 &= \frac{k^0 r_d \pi}{D 4} \\ \kappa_{\text{np},\text{ss}}^0 &= \frac{k^0 r_{\text{snp}}}{D} \frac{1}{\ln(2)} \end{aligned} \right\} \quad (5.96)$$

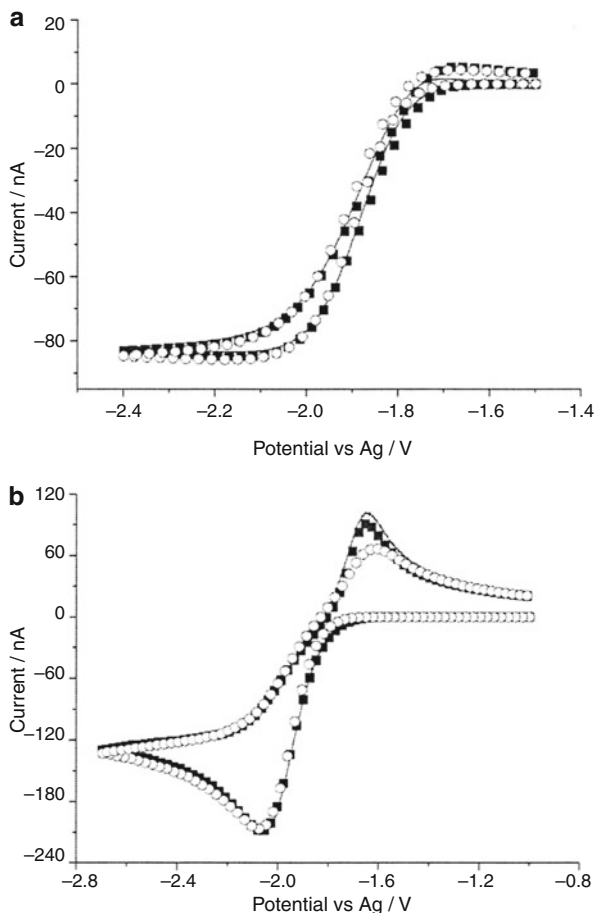
5.3.4 Marcus–Hush Kinetics

In Sect. 3.2.6, the application of the Marcus–Hush formalist (MH) for the electrode kinetics to Single Pulse Voltammetry was discussed. In Cyclic Voltammetry, most researchers have used the Butler–Volmer kinetic model (BV) due to its greater simplicity and to the vast body of data for the rate constant k^0 and the charge transfer coefficient α of a huge number of experimental systems. More recently, there have been several theoretical and experimental attempts to analyze the application of MH to the electrochemical behavior of solution soluble molecules at different electrodes or microelectrodes [39, 40]. For example, it has been shown that this model does not conform to the Randles–Ševčík equation for irreversible kinetics, given in Eq. (5.83), which predicts a linear dependence of the peak current with the square root of the scan rate [39]. The peak currents deduced by using MH are smaller than those calculated with the BV, an effect which increases for lower reorganization energies.

Different electrode processes have been analyzed with both MH and BV models, and it has been concluded that MH is, at best, indistinguishable from BV for those systems for which the charge transfer coefficient α is around 0.5. However, for those systems for which BV predicts values of α other than 0.5, the MH kinetics has been unable to provide good fittings to the experimental CV curves of a number of experimental systems (see, for example, Fig. 5.15 corresponding to the comparison of the voltammograms for the reduction of 2-methyl-2-nitropropane at a platinum electrode). This weakness of MH formalism arises from the use of a symmetrized form of the Marcus theory, which assumes that the Gibbs energy curves of both O and R species have the same curvature (and hence the reduction and electro-oxidation reactions will have the same reorganization energy). In order to overcome this limitation, a nonsymmetrical MH formalism has been presented [42] which incorporates four parameters to model the potential dependence of the response: the formal potential ($E_c^{\ominus'}$), the rate constant (k^0), the reorganization energy (λ), and a “symmetry parameter” (Ξ).

With the asymmetric MH model, it has been possible to find a relationship between the charge transfer coefficient α and the reorganization energy and symmetry factor:

Fig. 5.15 Comparison of experimental voltammograms for the reduction of 2-methyl-2-nitropropane at a platinum electrode (*solid lines*) with best fit simulations using BV (*black squares*) and MH (*white circles*) kinetics at two scan rates: (a) 50 mV s^{-1} ; (b) 5000 mV s^{-1} . Reproduced with permission [41]



$$\alpha(E_c^{\Theta'}) = \frac{1}{2} + \Xi \left(\frac{1}{4} - \frac{1.267}{(F\lambda/(RT) + 3.353)} \right) \quad (5.97)$$

Moreover, it has been also possible to obtain the kinetic parameters of different electrochemical systems (see Table 5.2) derived from very good fittings. The evaluation of the reorganization energy is not accurate since the experimental voltammograms are relatively insensitive to λ , with Ξ being the main fitting parameter within the asymmetric MH model. The fittings obtained with the asymmetric MH model were in all cases indistinguishable from those produced using the BV model (with both models being exactly equivalent in the limit of large reorganization energies). Due to its easier nature, the BV model should be used for the analysis of the voltammograms of solution soluble species [42].

Table 5.2 Kinetic parameters obtained from the fitting of experimental voltammetry at mercury hemispherical microelectrode and platinum disc microelectrode with the asymmetric MH model

Redox couple	Microelectrode	Conditions	Kinetic parameters k^0 (in cm s^{-1}) and Ξ
MeNP/MeNP ^{•-}	Hg (25.0 μm)	0.1 M TBAP, MeCN 25 \pm 0.2 $^\circ\text{C}$	$k^0 = 3.0 \times 10^{-3}$ $\Xi = -0.31$
NPent/NPent ^{•-}	Hg (28.5 μm)	0.1 M TBAP, MeCN 26 \pm 0.1 $^\circ\text{C}$	$k^0 = 1.3 \times 10^{-2}$ $\Xi = -0.14$
NPh ⁻ /NPh ²⁻	Hg (23.0 μm)	0.1 M TBAP, DMSO 24 \pm 0.1 $^\circ\text{C}$	$k^0 = 2.0 \times 10^{-2}$ $\Xi = -0.42$
COT/COT ^{•-}	Hg (50.0 μm)	0.1 M TEABr, DMSO 25 \pm 0.2 $^\circ\text{C}$	$k^0 = 1.1 \times 10^{-2}$ $\Xi = -0.22$
TPE ⁺ /TPE	Pt (25.0 μm)	0.1 M TBAPF ₆ , DCM 25 \pm 0.2 $^\circ\text{C}$	$k^0 = 0.15$ $\Xi = +0.55$
Eu ³⁺ /Eu ²⁺	Hg (50.0 μm)	0.4 M KCl, H ₂ O 25 \pm 0.2 $^\circ\text{C}$	$k^0 = 1.7 \times 10^{-4}$ $\Xi = +0.55$

MeNP, 2-methyl-2-nitropropane; NPent, 1-nitropentane; NPh, 3-nitrophenol; COT, cyclooctatetraene; TPE, tetraphenylethylene; TBAP, tetrabutylammonium perchlorate; TEABr, tetraethylammonium bromide; TBAPF₆, Tetrabutylammonium hexafluorophosphate; MeCN, acetonitrile; DMSO, dimethylsulfoxide; DCM, dichloromethane [42]

5.4 Advantages of Using Microelectrodes

As is well known, the steady-state behavior of (spherical and disc) microelectrodes enables the generation of a unique current–potential relationship since the response is independent of the time or frequency variables [43]. This feature allows us to obtain identical I – E responses, independently of the electrochemical technique, when a voltammogram is generated by applying a linear sweep or a sequence of discrete potential steps, or a periodic potential. From the above, it can also be expected that the same behavior will be obtained under chronopotentiometric conditions when any current time function $I(t)$ is applied, i.e., the steady-state $I(t)$ – E curve (with E being the measured potential) will be identical to the voltammogram obtained under controlled potential–time conditions [44, 45].

However, the stationary behavior cannot be established immediately and there is always a time span necessary to reach it (see [16, 43]). Oldham theoretically established that the time taken to attain a voltammetric steady state within an error $\varepsilon\%$ is given by the ratio $10^4 d^2/(\pi^3 \varepsilon^2 D)$ for fast charge transfer processes, at both hemispherical or disc microelectrodes, independently of whether the route to the steady state is potentiostatic or galvanostatic (with d being the surface diameter of the microelectrode, $d = \pi r_s$ for a microhemisphere, and $d = 2r_d$ for a microdisc) [46]. From the above statement, in order to obtain stationary I – E curves with an error lower than 5 %, experimental times higher than 25 ms are required for microelectrodes of radii above 1 μm for a value of the diffusion coefficient of $10^{-5} \text{ cm}^2 \text{ s}^{-1}$. In the case of slow charge transfer processes, the time that must elapse before an $\varepsilon\%$ approach to the steady state is attained at a spherical

microelectrode is $10^4 \times u^2 \times d^2 / (\pi^3 \epsilon^2 D)$, with u being the normalized steady-state current given by Eq. (3.74) in the case of hemispherical microelectrodes [38, 47].

The use of electrodes of small size brings great benefits associated with the elimination of undesirable effects. Some of these advantages are discussed in the following sections.

5.4.1 Reduction of Ohmic Drop and Capacitive Effects

As stated in Sect. 5.2.3.4, there is always a potential difference generated by the flow of faradaic current I through an electrochemical cell, which is related to the uncompensated resistance of the whole cell (R_u). This potential drop (equal to IR_u) can greatly distort the voltammetric response. At microelectrodes, the ohmic drop of potential decreases strongly compared to macroelectrodes. The resistances for a disc or spherical microelectrode of radius r_d or r_s are given by (see Sect. 1.9 and references [43, 48–50]).

$$\left. \begin{aligned} R_u)_{\text{disc}} &= \frac{1}{4\kappa r_d} \\ R_u)_{\text{sphere}} &= \frac{1}{2\pi\kappa r_s} \end{aligned} \right\} \quad (5.98)$$

where κ is the conductivity of the solution. Therefore, R_u would increase as the electrode radius decreases. However, the currents observed at microelectrodes are typically six orders of magnitude smaller than those observed at macroelectrodes. These small currents often completely eliminate the ohmic drop effects even in organic solvents. As an example, for a solution with a typical value of specific conductance of $0.01 \Omega^{-1} \text{ cm}^{-1}$, the ohmic drop of a conventional macroelectrode for a 1.0 mM solution of ferrocene is of the order of 5–10 mV, whereas for a microdisc of 5 μm radius (i.e., $R_u = 50 \text{ K}\Omega$ in line with Eq. (5.98)), the IR_u value is lower than 0.1 mV [47].

Moreover, under steady-state conditions, the current obtained at disc or spherical electrodes linearly depends on the radius, so the ohmic drop can be written as:

$$I^{ss} R_u = \frac{F c_O^* D O}{\kappa} \quad (5.99)$$

Note that Eq. (5.99) does not contain parameters related to the microelectrode itself. Therefore, this equation applies to any steady-state microelectrode cell, regardless of the shape and size of the electrode, and with the sole provision that the cell has a geometry that permits a diffusive steady state and that the auxiliary electrode is large enough to remain depolarized.

Another distortion reason is related to the charging of the “double layer” formed at the electrode–solution interphase. The reorganization of solvent dipoles and ions at the solution phase layer adjacent to the electrode as a response to the application

of a potential to the electrode causes a charge reorganization leading to a capacitive contribution to the response (I_c). While the steady-state faradaic current is proportional to the characteristic dimension of the microelectrode, the double-layer capacitance is proportional to the electrode area (for example, for a disc electrode is given by $C = \pi r_d^2 C_{dl}$, with C_{dl} being the double-layer capacitance per area unit). A decrease of the electrode area would logically lead to a decrease of the capacitance and, therefore, the I/I_c ratio will increase with the reciprocal of the characteristic dimension. From the above, it can be concluded that it is possible to carry out electrochemical measurements in much shorter time windows than those typical for macroelectrodes. All the electrochemical measurements present a time-scale limit imposed by the $R_u C$ cell time constant. For the application of a constant potential to a solution that does not contain any electroactive species, the charging current is proportional to $e^{-t/(R_u C)}$ [49]. Hence, electrochemical data with faradaic significance can only be extracted from an experiment after five to ten times the cell constant. For a disc electrode, this is given by (see Eq. (5.98)),

$$R_u C = \frac{\pi r_d C_{dl}}{4\kappa} \quad (5.100)$$

On the basis of this equation, the $R_u C$ constant decreases linearly with the radius from values of 10–100 ms for a conventional macrodisc (with r_d being of the order of millimeters) to 20 ns for a disc of $r_d = 1 \mu\text{m}$.

In the case of a linear sweep potential of slope v , the charging current density is given by (see Eq. (5.76))

$$i_c = vC \left(1 - e^{-4(E(t) - E_{\text{initial}})\kappa / v\pi r_d C_{dl}} \right) \quad (5.101)$$

The potential across the cell can be written as,

$$E(t) = E_{\text{initial}} + vt - v \left(1 - e^{-(E(t) - E_{\text{initial}})/vR_u C} \right) R_u C \quad (5.102)$$

The lag of potential of the working electrode is directly related to the cell time constant. For a disc macroelectrode ($r_d = 1 \text{ mm}$, $R_u C = 50 \text{ ms}$), Eq. (5.102) fixes a practical scan rate limit of around 400 V s^{-1} . This limiting scan rate can be considerably higher in the case of microelectrodes (i.e., kilovolts-per-second or even megavolts-per-second [50]).

Another useful conclusion is that it is possible to carry out electrochemical measurements in much shorter time windows than those typical for macroelectrodes.

The above mentioned advantages mean micro and ultramicroelectrodes can be used in very low supported media.

5.4.2 Neglecting Convection

Convection is often neglected at electrodes of micrometric dimensions in macroscopically quiescent solutions. However, depending on the size of these electrodes and timescale of the experiments, convective fluxes due to natural convection may still compete with diffusional fluxes in motionless solutions. These situations arise as soon as the thickness of the diffusion layer becomes comparable to the thickness of the convection-free domain. Under such conditions, the responses do not follow the classical relationships given for currents in transient and steady-state regimes. Therefore, under given experimental conditions, it is of importance to decide the largest size of an electrode to eliminate any influence of natural convection. Amatore has proposed a model to evaluate the influence of convection through an apparent diffusion coefficient, D_{app} , [51]. From his results, it is concluded that the microelectrode properties are achieved for a ratio $(r_G/\delta_{conv}) < 0.2$ where δ_{conv} is the thickness of the convection-free layer.

5.4.3 Ultrafast Voltammetry

When the electrochemical properties of some materials are analyzed, the timescale of the phenomena involved requires the use of ultrafast voltammetry. Microelectrodes play an essential role for recording voltammograms at scan rates of megavolts-per-seconds, reaching nanoseconds timescales for which the perturbation is short enough, so it propagates only over a very small zone close to the electrode and the diffusion field can be considered almost planar. In these conditions, the current and the interfacial capacitance are proportional to the electrode area, whereas the ohmic drop and the cell time constant decrease linearly with the electrode characteristic dimension. For Cyclic Voltammetry, these can be written in terms of the dimensionless parameters γ_u and θ given by

$$\left. \begin{aligned} \gamma_u &= \left(\frac{F}{RT}\right)^{3/2} (D\nu)^{1/2} F A_G c_O^* R_u \\ \theta &= \frac{F}{RT} \nu R_u C \end{aligned} \right\} \quad (5.103)$$

If $\gamma_u < 0.1$ and $\theta < 1$, the distortion of the voltammogram will be minimal [50, 52].

Now it is possible to assemble microelectrodes with extremely short response times. Nevertheless, an additional problem for the reduction of the ohmic drop is that for short times high currents arise from the large concentration surface gradients. This leads to the use of on-line and real-time electronic compensation of the cell resistance combined with the use of microelectrodes [53].

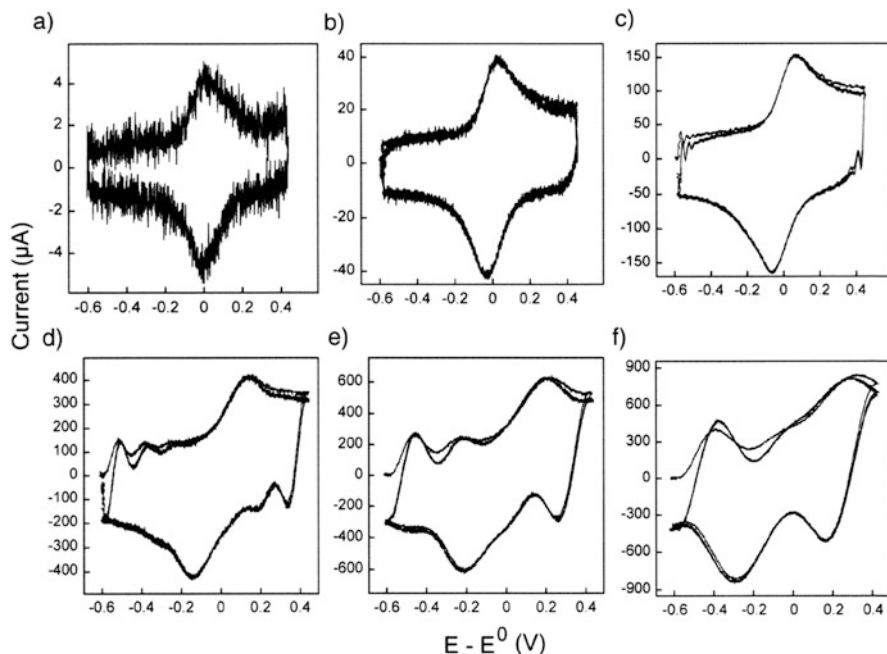


Fig. 5.16 Voltammograms obtained in the Polydimethylsiloxane (PDMS) cell for a ferrocenyl oligo (phenylenevinylene) molecular wire in acetonitrile + 1 M tetraethylammonium tetrafluoroborate at (a) 2085 V s^{-1} ; (b) 20.7 KV s^{-1} ; (c) 103 KV s^{-1} ; (d) 412 KV s^{-1} ; (e) 727 KV s^{-1} ; (f) 1.150 KV s^{-1} . Electrode area (A): $3.75 \times 10^{-9} \text{ m}^2$, surface coverage $f = 8 \times 10^{-7} \text{ mol m}^{-2}$. Reproduced from [54] with permission

Ultrafast voltammetry has a crucial role for investigating the kinetics of very fast reactions, although for very small sizes the kinetics would be masked since the system would be under diffusion control.

The heterogeneous electron transfer dynamics of a diverse range of organic and inorganic species and also the dynamics and energetics of ultrafast heterogeneous electron transfer dynamics of immobilized electroactive species on an electrode surface have been investigated with ultrafast voltammetry under a wide variety of experimental conditions of timescale, temperature, solvent, and electrolyte (see for example Fig. 5.16, obtained from [54]).

5.4.4 Microelectrode Arrays

A microelectrode array consists of a series of microelectrodes separated by an insulating material [36]. The microelectrodes can be regularly or randomly distributed (in the latter case the term “ensemble” is also used). Arrays containing hundreds or even thousands of microelectrodes wired in parallel have been

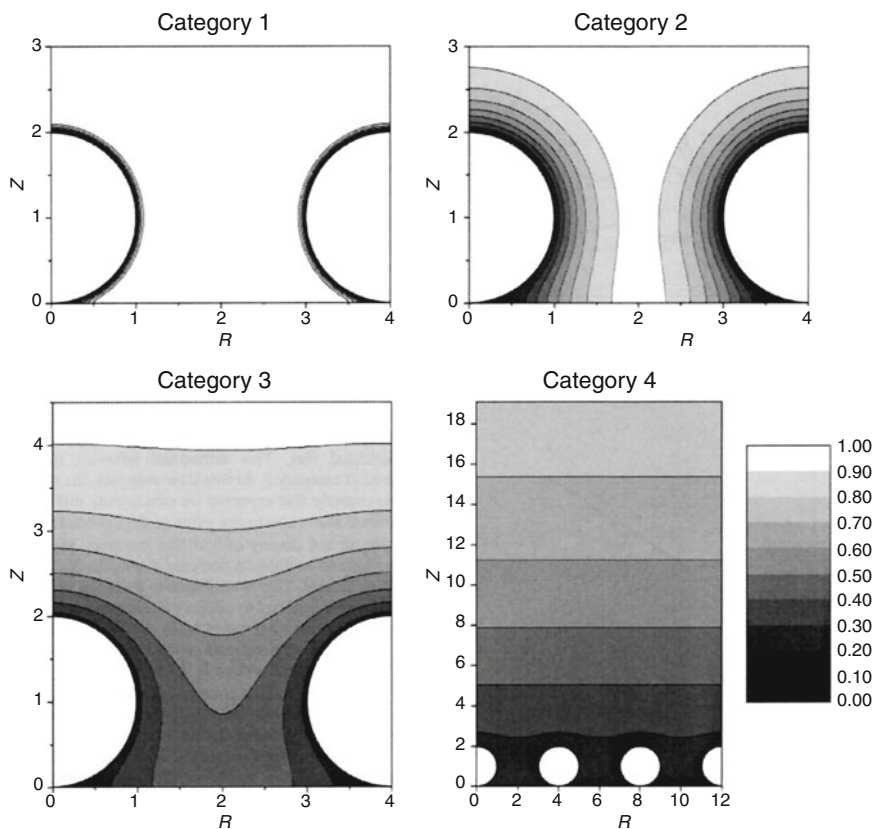


Fig. 5.17 Simulated concentration profiles at a diffusion domain containing a spherical particle. Category 1: $\xi_s^2 = 10^{-3}$. Category 2: $\xi_s^2 = 0.1$. Category 3: $\xi_s^2 = 1$. Category 4: $\xi_s^2 = 100$. For all categories, the distance between particles is two times the radius. Reproduced from [57] with permission

extensively used in electrochemical analysis for sensing multiple reactive species and probing signal transformation in a network of biological cells [36, 55, 56]. These devices comprehend most of the advantages of microelectrodes but add several more: high amplification of the current, adequate output signals, and an improved ratio of the faradaic to charging current. Various types of array electrodes have been made, including planar or recessed microdiscs, microbands, interdigitated microelectrodes, linear microelectrodes, and 3D microelectrodes.

A voltammetric experiment in a microelectrode array is highly dependent on the thickness of the individual diffusion layers, δ , compared with the size of the microelectrodes themselves, and with the interelectrode distance and the time experiment or the scan rate. In order to visualize the different behavior of the mass transport to a microelectrode array, simulated concentration profiles to spherical microelectrodes or particles calculated for different values of the parameter $\xi_s^2 = \sqrt{D/a}/r_s$ can be seen in Fig. 5.17 [57] when the separation between centers of

two adjacent spherical microelectrodes is $4r_s$. Different categories of diffusion can be defined from this figure. For Category 1 (very high scan rates or short time experiments), the particles/microelectrodes must be diffusionally independent (i.e., the diffusion layer thickness is much smaller than the microelectrode size and diffusion is approximately planar). When the scan rate decreases the perturbed zone grows (Category 2) until overlap of the diffusion fields occurs (Category 3) and the microelectrodes suffer a shielding effect from their neighbors. The limiting situation of this effect can be seen in Category 4 for which the overall concentration profile can be considered as planar (i.e., concentration profiles become independent on R coordinate).

For shallow recessed microdisc electrode arrays, the hemispherical diffusion is larger than that for coplanar microdisc arrays. The minimum interelectrode distance necessary for hemispherical diffusion becomes smaller as recess depth increases [58].

Different theories have been developed to characterize the electrochemical responses of arrays. The great majority of theoretical treatments of arrays consider a large number of microelectrodes on an infinite electroinactive plane surface [36].

5.4.5 *Nanoelectrodes*

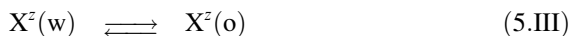
In the case of nanoelectrodes or nanodes, it is important to consider that their small dimensions lead to deviations from the “classical” voltammetry theory. An implicit assumption in electrochemical theory is that the electrode dimensions are much larger than the thickness of the diffuse double layer and incomparably larger than the radii of the species involved in the charge transfer. A number of theoretical and experimental studies have focused on possible deviations from conventional electrochemical theory at nanometer-sized electrodes in recent years [59]. The effect of diffuse layer on mass transfer is the most extensively discussed, and it is expected to be significant if the depletion layer thickness caused by the faradaic process is comparable to that of the diffuse double layer (see [60, 61]). The extent of this effect and its influence on the values of kinetic parameters extracted depend on several factors including the charge of electroactive species, their standard potential (with respect to the potential of zero charge), and the ionic strength of solution. In most cases, the predicted deviations should be more significant at radii below 10 nm. Other size-related electrochemical phenomena and their effects on the rates of the charge transfer process have yet to be explored, such as the stochastic character of the charge transfer events at nanointerfaces, the more rapid potential drops within the diffuse double layer at spherical electrodes smaller than 50–100 nm, or the effect of charges situated on the insulating surface in the mass transfer at glass-sealed nanoelectrodes, among others [62]. The relative importance of each effect remains incompletely understood. To observe and quantitatively evaluate major deviations from conventional theory, electrodes smaller than ~5 nm radius with well-characterized geometry should be required.

5.5 Ion Transport Through Liquid Membranes

In Sects. 2.3 and 4.2.4.1, the electrochemical response corresponding to ion transfer processes through liquid membranes in single potential pulse and double potential pulse techniques has been discussed. In this section, these processes are analyzed with multipulse techniques, mostly with Staircase Voltammetry and Cyclic Voltammetry.

5.5.1 One Polarized Interface

Let us consider the reversible transfer of ion X^z through the interface between an aqueous electrolyte solution (w phase) and an organic one (o phase), which takes place by polarizing the interface,



where z is the positive or negative charge number.

Under the appropriate conditions, the mass transport can be mathematically modeled as a linear diffusion problem to the spatial domains shown in Scheme 5.4,

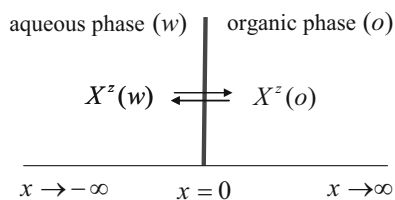
When p successive potential pulses (E_1, E_2, \dots, E_p) of the same length τ are applied, the mass transport during the p th potential pulse in the presence of sufficient amounts of supporting electrolyte in both phases is described by the following differential equations system:

$$\left. \begin{aligned} \frac{\partial c_o^{(p)}}{\partial \tau} - D_o \frac{\partial^2 c_o^{(p)}}{\partial x^2} &= 0 \quad (a) \\ \frac{\partial c_w^{(p)}}{\partial \tau} - D_w \frac{\partial^2 c_w^{(p)}}{\partial x^2} &= 0 \quad (b) \end{aligned} \right\} \quad (5.104)$$

with $c_{ph}^{(p)}(x, t)$ and D_{ph} being the concentration and the diffusion coefficient, respectively, of ion X^z in the ph phase (ph = w, o).

As in the case of single potential pulse and double potential pulse techniques, from the transposition of the theory of multipulse techniques to the ion transfer processes taking place at macro-ITIES, the theoretical expressions obtained with

Scheme 5.4 Spatial domains for the diffusion of X^z ion in the aqueous and organic phases



the semi-infinite diffusion model for electron transfer processes can be used to quantify the current response of the ion transfer. Thus, by following a procedure analogous to that presented in Sect. 5.2.1, an expression for the current of any potential pulse analogous to that corresponding to electron transfer processes taking place at planar electrodes (Eq. (5.25)) is obtained:

$$\begin{aligned} I_p &= zFA \sqrt{\frac{D_w}{\pi\tau}} \sum_{m=1}^p \frac{1}{\sqrt{p-m+1}} \left(c_{X^z}^{(m-1)}(0) - c_{X^z}^{(m)}(0) \right) = \\ &= zFAc_{X^z}^* \sqrt{\frac{D_w}{\pi\tau}} \sum_{m=1}^p \frac{1}{\sqrt{p-m+1}} \left(\frac{1}{1+\gamma e^{\eta_{m-1}}} - \frac{1}{1+\gamma e^{\eta_m}} \right) \end{aligned} \quad (5.105)$$

with $c_{X^z}^*$ being the bulk concentration of ion X^z in the aqueous phase, $\eta_m = F(E_m - \Delta_o^w \phi_{X^z}^{\Theta'}) / RT$ and

$$\gamma = \sqrt{\frac{D_o}{D_w}} \quad (5.106)$$

5.5.1.1 Cyclic Staircase Voltammetry and Cyclic Voltammetry

Cyclic Voltammetry is the most widely used technique for acquiring qualitative information about electrochemical processes and it has also proved to be very useful for the study of ion transfer across bulk, supported, or polymer composite membranes [63]. The expression for the current in CV can be obtained from Eq. (5.105) by considering the potential waveform given in (5.1),

$$\begin{aligned} \psi_{CV} &= \frac{I\sqrt{\pi}}{zFAc_{X^z}^* \sqrt{aD_{X^z}^w}} \\ &= \sum_{m=1}^p \left(\left(\frac{1}{1+\gamma e^{\vartheta_{m-1}} e^{\vartheta_{in}}} - \frac{1}{1+\gamma e^{\vartheta_m} e^{\vartheta_{in}}} \right) \frac{1}{\sqrt{\pi\vartheta_{m,p}}} \right) \end{aligned} \quad (5.107)$$

with

$$\left. \begin{aligned} \vartheta_m &= \frac{zF}{RT} (E_m - E_{\text{initial}}) \\ \vartheta_{in} &= \frac{zF}{RT} (E_{\text{initial}} - \Delta_o^w \phi_{X^z}^{\Theta'}) \end{aligned} \right\} \quad (5.108)$$

where a and $\vartheta_{m,p}$ are given by Eqs. (5.38) and (5.44), respectively, $\Delta_o^w \phi_{X^z}^{\Theta'}$ is the formal ion transfer potential, and F , R , and T have their usual meaning.

5.5.2 Two Polarized Interfaces

In these kinds of systems, the polarization phenomenon is effective at the two interfaces involved (see also Sect. 2.3.2). Specifically, in membrane systems comprising two ITIES, this behavior is achieved when the membrane contains a hydrophobic supporting electrolyte and the sample aqueous solution (the inner one) contains hydrophilic supporting electrolytes, and there is no common ion between any of the adjacent phases. In this case, the potential drop cannot be controlled individually and the processes taking place at both interfaces are linked to each other by virtue of the same electrical current intensity.

5.5.2.1 Cyclic Staircase Voltammetry and Cyclic Voltammetry

As for single polarized interface systems, an explicit analytical equation for the CV response for systems with two L/L polarizable interfaces is derived from that corresponding to CSCV when the pulse amplitude ΔE approaches zero (see also Appendix H). For the case corresponding to the transfer of a cation X^+ , one obtains

$$\psi_{CV} = \frac{I\sqrt{\pi}}{zFAc_{X^+}^* \sqrt{aD_{X^+}^w}} = \sum_{m=1}^p \left((g_{m-1} - g_m) \frac{1}{\sqrt{\pi\vartheta_{m,p}}} \right) \quad (5.109)$$

where g_m is given by

$$\left. \begin{aligned} g_m &= \frac{\sqrt{\lambda^2 e^{2\vartheta_m \vartheta_{in}} + 8\lambda e^{\vartheta_m \vartheta_{in}} - \lambda e^{\vartheta_m \vartheta_{in}}}}{4} \\ \vartheta_m &= \frac{F}{RT} (E_m^M - E_{initial}) \\ \vartheta_{in} &= \frac{F}{RT} (E_{initial} - E^{M, \Theta'}) \end{aligned} \right\} \quad (5.110)$$

and $g_0 = 0$. Moreover,

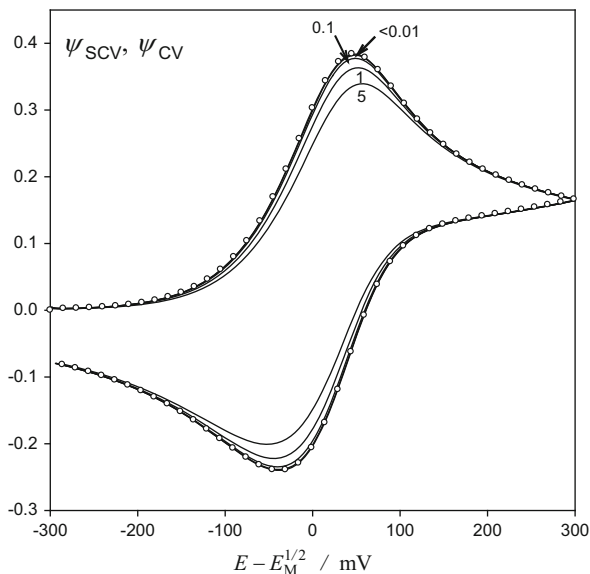
$$\lambda = \frac{2\sqrt{D_{R^+}^{w_2} D_{X^+}^M} c_{R^+}^*}{D_{X^+}^{w_1} c_{X^+}^*} \quad (5.111)$$

$$E^{M, \Theta'} = \Delta_M^{w_1} \phi_{X^+}^{\Theta'} - \Delta_{w_2}^M \phi_{R^+}^{\Theta'} \quad (5.112)$$

The current corresponding to the reverse scan is obtained by taking into account Eq. (5.1).

The $\psi_{CV}-E$ curves (Eq. (5.109)) for different values of ΔE (SCV), including the limiting case of CV ($|\Delta E| < 10^{-2}$ mV), can be shown in Fig. 5.18, in which the $\psi_{CV}-E$ curve calculated from Eq. (12) of reference [64] (circles) is also included.

Fig. 5.18 (solid lines) $\psi_{CV}/E - E^M$ curves calculated from Eq. (5.109) (SCV). The values of the pulse amplitude ΔE (in mV) appear on the curves. (circles) ψ_{CV}/E_M curve calculated from Eq. (12) of reference [64].
 $E_{\text{initial}} - E_M^{1/2} = -300 \text{ mV}$,
 $E_{\text{final}} - E_M^{1/2} = 300 \text{ mV}$.
 Reproduced from [65] with permission



From this figure, it can be seen that the decrease of ΔE causes an increase of the current together with an approach of both peaks until their difference reaches the CV limit $\Delta E_{\text{peak}} \approx 90 \text{ mV}$, in contrast with the 57 mV found in the case of only one polarizable interface. These values are in agreement with those obtained in reference [64] using the Nicholson and Shain method [9].

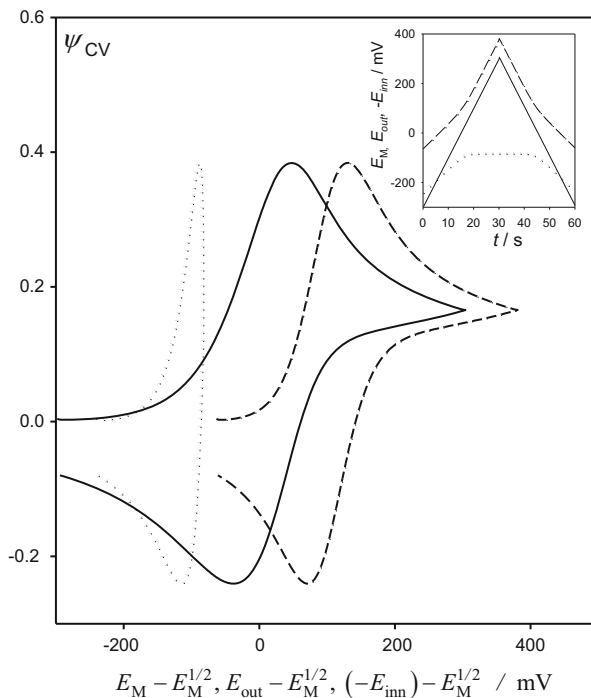
In line with what is observed for other techniques, the response obtained in CV for a system with two liquid/liquid polarizable interfaces is lower and broader than that obtained for ion transfers at a single water/organic interface. This has been attributed to different polarization rates at the outer and inner interfaces [66].

In Fig. 5.19, the cyclic voltammogram versus the membrane potential E^M (given in Eq. (2.79)) obtained for a system with two polarizable interfaces (solid line) is presented. The ψ_{CV} curve has been also plotted versus the outer interface E_{out} (dashed line) and the inner interface potential E_{inn} (dotted line) with E_{out} and E_{inn} given by

$$\left. \begin{aligned} E_{\text{out}} &= \Delta_M^{w_1} \phi_{X^+}^{\Theta'} + \frac{RT}{F} \ln \sqrt{\frac{D_{X^+}^{w_1}}{D_{X^+}^M}} + \frac{RT}{F} \ln \left(\frac{g_m}{1 - g_m} \right) \\ E_{\text{inn}} &= \Delta_M^{w_2} \phi_{R^+}^{\Theta'} + \frac{RT}{F} \ln \left(\sqrt{\frac{D_{R^+}^{w_2} c_{R^+}^*}{D_{X^+}^{w_1} c_{X^+}^*}} \right) - \frac{RT}{F} \ln(g_m) \end{aligned} \right\} \quad (5.113)$$

From these curves, it is clear that the difference between peak potentials for the $\psi_{CV}-E^M$ curve ($\Delta E_p = 88 \text{ mV}$) is equal to the sum of those obtained from the cyclic voltammograms plotted versus E_{out} and E_{inn} (61 mV and 27 mV , respectively). The different voltammetric responses obtained at outer and inner interfaces are the result of different potential drops at each of them, in agreement with Eq. (5.113).

Fig. 5.19 ψ_{CV}/E^M (solid line), ψ_{CV}/E_{out} (dashed line), and $\psi_{CV}/(-E_{inn})$ (dotted line) curves calculated from Eqs. (5.109)–(5.113) with $|\Delta E| = 10^{-4}$ mV and $v = 0.01$ V s $^{-1}$ (see also [67]). Insert figure: time evolution of the potentials E^M (solid), E_{out} (dashed), and $(-E_{inn})$ (dotted). Reproduced from [65] with permission

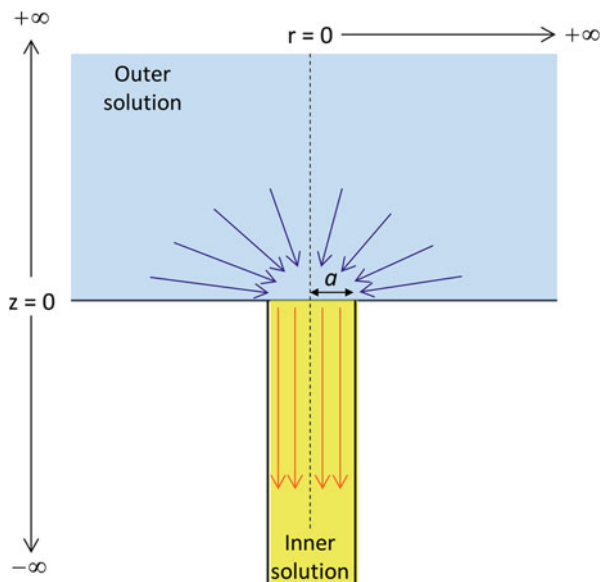


This is confirmed by the insert figure, in which we have plotted the time evolution of E_{out} (dashed line), E_{inn} (dotted line), and E^M (solid line). Note that, with the exception of limiting cathodic and anodic regions, the time variation of E_{out} is similar to that of E^M (although shifted toward more positive potentials), such that a voltammogram similar to those of a single water/organic interface is obtained (with $\Delta E_{peak} \cong 60$ mV). In contrast, E_{inn} remains almost constant for the central part of the sweep (thus presenting a behavior similar to that of a non-polarizable interface). This constant value causes a sharp fall in the current (see ψ_{CV}/E_{inn} curve) and, therefore, a narrow response ($\Delta E_{peak} = 27$ mV).

5.5.3 Micro-ITIES and Asymmetrical Diffusion

In the last 30 years, the manufacturing and use of micrometer- and nanometer-sized electrochemical interfaces, microelectrodes, and micro-ITIES have been widely extended. The main advantages associated with the reduction of the size of the interface are the fast achievement of a time-independent current–potential response (independent of the electrochemical technique employed), the decrease of the ohmic drop, the improvement of the ratio of faradaic to charge current, and the enhancement of the mass transport. Their small size has played an important role in

Fig. 5.20 Problem corresponding to a liquid|liquid interface supported on a microcapillary of radius a . Reproduced from [73] with permission



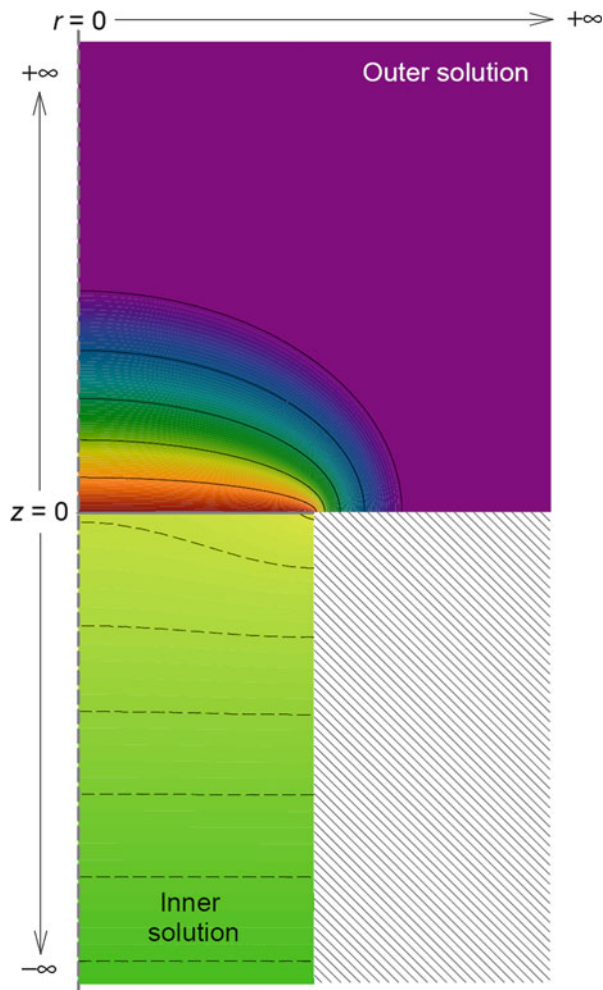
the electrochemical expansion of the use of small sample volumes like microliter and even nanoliter, which accounts for their good performance as sensors in living organisms [66–70].

The first micro-ITIES were introduced in 1986, using a glass micropipette which was pulled down to a fine tip of around $25\ \mu\text{m}$ to support the interface [66–71]. The smaller size of micropipettes or microcapillaries is advantageous for sensor applications, providing the possibility of studying microenvironments as living cells, and it can also be used as a probe in scanning electrochemical microscopy (SECM) [72].

Among the different approaches to these systems, pores, pipettes, and capillaries have been considered to support such small liquid|liquid interfaces, as well as arrays of them in order to amplify the electrochemical signal while retaining the benefits mentioned above. The theoretical treatment and analysis of the results of investigation of ion transfer through these interfaces is not straightforward given the asymmetry of the diffusion fields inside and outside the pore or pipette. Thus, as can be seen in Fig. 5.20, while diffusion can be approximated as linear in the inner phase, radial diffusion is significant in the outer phase, especially when the size of the capillary is decreased [73].

As a result, a stationary voltammogram cannot be expected under these conditions since it shows a behavior similar to that of a macrointerface with respect to the egress of the ion, and features of radial diffusion for the ingress process, reaching a time-independent response [73, 74]. Both are consequences of the markedly different diffusion fields inside and outside the capillaries which give rise to very different concentration profiles (see Fig. 5.21). A similar voltammetric behavior has been reported for electron transfer processes at electrode|solution interfaces where the diffusion fields of the reactant and product species differ greatly.

Fig. 5.21 Diffusion fields corresponding to an ion transfer across a liquid|liquid interface supported on a micro/nanocapillary of radius a . Reproduced from [73] with permission



CV curves corresponding to an ion transfer process at a microcapillary under different experimental situations with respect to the initial presence of the target ion in the inner and outer solution are shown in Fig. 5.22 [74].

When the ion is initially present in the outer solution the forward scan toward negative potentials leads to a sigmoidal curve associated with the ion ingress under strongly convergent diffusion due to the small size of the capillary. On the other hand, the linear-like diffusion that dominates inside the capillary leads to a peak in the reverse scan related to the ion egress. Under these conditions, the ion egress is controlled by the amount of ion ingressed in the forward scan rather than the amount initially present in the inner solution.

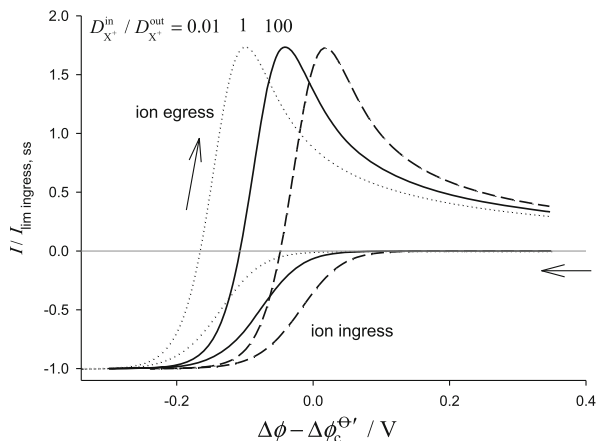
Fig. 5.22 Analytical and numerical cyclic voltammograms for different situations with respect to the bulk concentrations of the ion.

$$r_c \sqrt{a/D_X^{\text{out}}} = 0.1,$$

$$T = 298 \text{ K},$$

$$\psi = I / zF\pi r_c^2 c_X^{*\text{in}} \sqrt{aD_X^{\text{in}}}.$$

Reproduced from [74] with permission



Other authors have incorporated a microhole in a thin inert membrane. This micro-ITIES has the advantage of symmetry of the diffusion fields on both sides of the micro-orifice, which simplifies the theoretical treatment. Nevertheless, this advantage is lost when the thickness of the membrane cannot be neglected. In this case, it is assumed that the microhole is cylindrical and filled with the organic phase, so, a planar L/L interface separates the aqueous and organic phases. Converging diffusion outside the orifice and practically linear diffusion inside the pore are assumed, with the solution depending on the location of the interface inside the hole [70, 75, 76]. This problem can be rigorously treated by transposing the theory developed for microdiscs and recessed microdiscs, which shows that the cottrellian current decays for deep recess microdiscs, showing that at short times linear diffusion dominates, while at long times, the current tends to steady-state value. This steady state response decreases as the recess depth (thickness of the membrane) increases [77, 78].

In summary, although the construction of micro-ITIES is, in general, simpler than that of microelectrodes, their mathematical treatment is always more complicated for two reasons. First, in micro-ITIES the participating species always move from one phase to the other, while in microelectrodes they remain in the same phase. This leads to complications because in the case of micro-ITIES the diffusion coefficients in both phases are different, which complicates the solution when nonlinear diffusion is considered. Second, the diffusion fields of a microelectrode are identical for oxidized and reduced species, while in micro-ITIES the diffusion fields for the ions in the aqueous and organic phases are not usually symmetrical. Moreover, as a stationary response requires $\sqrt{Dt} \gg r_0$ (where D is the diffusion coefficient, r_0 is the critical dimension of the microinterface, and t is the experiment time), even in L/L interfaces with symmetrical diffusion field it may occur that the stationary state has been reached in one phase (aqueous) and not in the other (organic) at a given time, so a transient behavior must be considered.

References

1. Kambara T (1954) *Bull Chem Soc Jpn* 27:523–536, 527–529 and 529–534
2. Christie JH, Lingane PJ (1965) *J Electroanal Chem* 10:176–182
3. Seralathan M, Osteryoung R, Osteryoung J (1986) *J Electroanal Chem* 214:141–156
4. Serna C, Moreno MM, Molina A, Gonzalez J (2000) *Recent Res Devel Electrochem* 3:29–42
5. Molina A, Serna C, Camacho L (1995) *J Electroanal Chem* 394:1–6
6. Laborda E, Gonzalez J, Molina A (2014) *Electrochem Commun* 43:25–30
7. Barnes AS, Streeter I, Compton RG (2008) *J Electroanal Chem* 623:129–133
8. Molina A, Gonzalez J, Henstridge M, Compton RG (2011) *J Phys Chem C* 115:4054–4062
9. Nicholson RS, Shain I (1964) *Anal Chem* 36:706–723
10. Delahay P (1954) *New instrumental methods in electrochemistry*. Interscience, New York (Chapter 3)
11. Serna C, Molina A (1999) *J Electroanal Chem* 466:8–14
12. Oldham KB (2013) *J Solid State Electrochem* 17:2749–2756, 2757–2769
13. Shoup D, Zsabo A (1982) *J Electroanal Chem* 140:237–245
14. Cope DK, Tallman DE (1991) *J Electroanal Chem* 303:1–15
15. Zsabo A, Cope DK, Tallman DE, Kovach PM, Wightman RM (1987) *J Electroanal Chem* 217:417–423
16. Amatore C (1995) In: Rubinstein I (ed) *Physical electrochemistry: principles, methods and applications*. Marcel Dekker, New York (Chapter 4)
17. Cope DK, Skott CH, Kalapathy U, Tallman DE (1990) *J Electroanal Chem* 280:27–35
18. Oldham KB, Zoski CG (1988) *J Electroanal Chem* 256:11–19
19. Aoki K (1993) *Electroanalysis* 5:627–639
20. Aoki K, Honda K, Tokuda K, Matsuda H (1985) *J Electroanal Chem* 182:267–279
21. Molina A, Serna C, Martinez-Ortiz F, Laborda E (2008) *J Electroanal Chem* 617:14–26
22. Martinez-Ortiz F, Molina A, Laborda E (2011) *Electrochim Acta* 56:5707–5716
23. Randles JEB (1948) *Trans Faraday Soc* 44:327–338
24. Ševčík A (1948) *Collect Czech Chem Commun* 13:349
25. Moreno MM, Molina A (2005) *Collect Czech Chem Commun* 70:133–154
26. Paul HJ, Leddy J (1995) *Anal Chem* 67:1661–1668
27. Reinmuth WH (1957) *J Am Chem Soc* 79:6358–6360
28. Britz D (2005) *Digital simulation in electrochemistry*, 3rd edn. Springer, Berlin
29. Molina A, Gonzalez J, Martinez-Ortiz F, Compton RG (2010) *J Phys Chem C* 114:4093–4099
30. Molina A, Gonzalez J, Henstridge M, Compton RG (2011) *Electrochim Acta* 56:4589–4594
31. Marken F, Neudeck A, Bond AM (2002) *Cyclic voltammetry*. In: Scholz F (ed) *Electro-analytical methods. Guide to experiments and applications*. Springer, Berlin
32. Samec Z, Langmaier J, Trojánek A (1999) *J Electroanal Chem* 463:232–241
33. Jadhav S, Bakker E (1999) *Anal Chem* 71:3657–3664
34. Armstrong RD, Horvai G (1990) *Electrochim Acta* 35:1–7
35. Matsuda H, Ayabe Y (1955) *Z Elektrochem* 59:494–503
36. Compton RG, Banks CE (2011) *Understanding voltammetry*, 2nd edn. ICP, London
37. Gileadi E (2011) *Physical electrochemistry*. Wiley-VCH, Weinheim
38. Molina A, Gonzalez J, Barnes EO, Compton RG (2014) *J Phys Chem C* 118:346–356
39. Henstridge M, Laborda E, Rees NV, Compton RG (2012) *Electrochim Acta* 84:12–20
40. Feldberg SW (2010) *Anal Chem* 82:5176–5183
41. Henstridge M, Wang Y, Limon-Petersen JG, Laborda E, Compton RG (2011) *Chem Phys Lett* 517:29–35
42. Laborda E, Henstridge M, Batchelor-McAuley C, Compton RG (2013) *Chem Soc Rev* 42:4894–4905
43. Oldham KB (1990) In: Montenegro MI, Queirós MA, Daschbach JL (eds) *Microelectrodes: theory and applications*. Kluwer Academic Press, Dordrecht, pp 35–50, 83–98
44. Molina A, Gonzalez J, Morales I (2004) *J Electroanal Chem* 569:185–195

45. Molina A, Gonzalez J (1999) *Electrochem Commun* 1:477–482
46. Zoski CG, Bond AM, Allison ET, Oldham KB (1990) *Anal Chem* 62:37–45
47. Molina A, Gonzalez J (2012) In: Kaufmann EN (ed) *Characterization of materials*, 2nd edn. Wiley, New York
48. Newman J (1968) *J Electrochem Soc* 113:501–502
49. Bard AJ, Faulkner LR (2000) *Electrochemical methods: fundamental and applications*, 2nd edn. Wiley, New York
50. Wightman RM, Wipf DO (1988) In: Bard AJ (ed) *Electroanalytical chemistry*, vol 15. Marcel Dekker, New York, pp 267–353
51. Amatore C, Pebay C, Thouin L, Wang A, Warczok J-S (2011) *Anal Chem* 82:6933–6939
52. Imbeaux JC, Savéant JM (1970) *J Electroanal Chem* 28:325–338
53. Amatore C, Arbault S, Maisonhaute E, Szunerits S, Thouin L (2004) In: Amatore C, Pombeiro AJL (eds) *Trends in molecular electrochemistry*. Marcel Dekker, New York, pp 385–412
54. Fortgang P, Amatore C, Maisonhaute E, Schöllhorn B (2010) *Electrochem Commun* 12: 897–900
55. Zoski CG, Wijensinghe M (2010) *Isr J Chem* 50:347–359
56. Huang X-J, O'Mahony AM, Compton RG (2009) *Small* 5:776–788
57. Streeter I, Baron R, Compton RG (2007) *J Phys Chem C* 111:17008–17014
58. Guo J, Lindner E (2009) *Anal Chem* 81:130–138
59. Smith CP, White HS (1993) *Anal Chem* 65:3343–3353
60. Dickinson EJF, Limon-Petersen JG, Compton RG (2011) *J Solid State Electrochem* 15: 1335–1345
61. Liu Y, He R, Zhang Q, Chen S (2010) *J Phys Chem C* 114:10812–10822
62. Wang Y, Velmurugan J, Mirkin MV (2010) *Isr J Chem* 50:291–305
63. Molina A, Serna C, Ortuño JA, Torralba E (2012) *Ann Rep section C (RSC)* 108:126–176
64. Samec Z, Trojanek A, Langmaier J, Samcova E (2000) *J Electroanal Chem* 481:1–6
65. Molina A, Serna C, Gonzalez J, Ortuño JA, Torralba E (2009) *Phys Chem Chem Phys* 11: 1159–1166
66. Ichieda N, Shirai O, Kasuno M, Banu K, Uehara A, Yoshida Y, Kihara S (2003) *J Electroanal Chem* 542:97–107
67. Kakiuchi T (1988) *Electrochim Acta* 44:171–179
68. Wilke S, Osborne MD, Girault HH (1997) *J Electroanal Chem* 436:53–64
69. Liu B, Mirkin MV (2002) *Electroanalysis* 12:1433–1446
70. Liu S, Li Q, Shao Y (2011) *Chem Soc Rev* 40:2236–2253
71. Taylor G, Girault HH (1986) *J Electroanal Chem* 208:179–183
72. Laforge FO, Velmurugan J, Wang YX, Mirkin MV (2009) *Anal Chem* 81:3143–3150
73. Molina A, Laborda E, Compton RG (2014) *Chem Phys Lett* 597:126–133
74. Molina A, Laborda E, Compton RG (2014) *J Phys Chem C* 118:18249–18256
75. Campbell JA, Girault HH (1989) *J Electroanal Chem* 266:465–469
76. Jossierand J, Morandini J, Lee HJ, Girault HH (1999) *J Electroanal Chem* 468:42–52
77. Barlett PN, Taylor SL (1998) *J Electroanal Chem* 453:49–60
78. Amatore C, Oleinick AI, Svir I (2009) *Anal Chem* 81:4397–4405

Chapter 6

Multipulse and Sweep Voltammetries II

Contents

6.1	Introduction	375
6.2	Multi-electron Electrochemical Reactions	376
6.2.1	Application of a Multipulse Sequence to Electrodes and Microelectrodes of Any Geometry	376
6.3	First-Order Chemical Reactions Coupled with the Charge Transfer	390
6.3.1	Catalytic Mechanism	391
6.3.2	CE and EC Mechanisms	401
6.3.3	ECE Mechanism	407
6.3.4	Reversible Charge Transfers Preceded and Followed by Several Complexation Reactions in Equilibrium at Electrodes of Any Geometry ("Ladder" Mechanism)	410
6.4	Surface-Bound Molecules	415
6.4.1	One-Electron Electrochemical Reactions: Statement of the Problem	416
6.4.2	One-Electron Electrochemical Reactions: Cyclic Voltammetry	433
6.4.3	Two-Electron Electrochemical Reactions	440
6.4.4	Electrocatalytic Processes at Modified Electrodes	448
	References	460

6.1 Introduction

This chapter offers a study of the application of the multipulse and sweep techniques Cyclic Staircase Voltammetry (CSCV) and Cyclic Voltammetry (CV) to the study of more complex electrode processes than single charge transfer reactions (electronic or ionic), which were addressed in Chap. 5.

In Sect. 6.2, multi-electron (multistep) electrochemical reactions are surveyed, especially two-electron reactions. It is shown that, when all the electron transfer reactions behave as reversible and the diffusion coefficients of all species are equal, the CSCV and CV curves of these processes are expressed by explicit analytical equations applicable to any electrode geometry and size. The influence of the difference between the formal potentials of the different electrochemical reactions on these

responses is also discussed. Non-reversible electron transfer reactions are also considered.

In Sect. 6.3, the application of SCV and CV techniques is discussed with respect to reversible charge transfer reactions complicated with homogeneous chemical reactions. It is highlighted that, except in the case of a first-order catalytic mechanism, relatively simple analytical general expressions for the current potential response of CE, EC, or ECE mechanisms have not been found. Numerical procedures have been applied to analyze the influence of kinetic parameters of the homogeneous reactions on these curves.

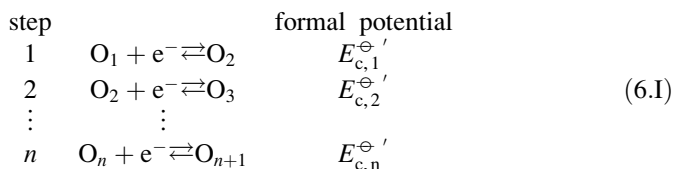
The general electrochemical behavior of surface-bound molecules is treated in Sect. 6.4. The response of a simple electron transfer reaction in Multipulse Chronoamperometry and Chronocoulometry, CSCV, CV, and Cyclic Staircase Voltcoulometry and Cyclic Voltcoulometry is also presented. Multielectronic processes and first- and second-order electrocatalytic reactions at modified electrodes are also discussed extensively.

6.2 Multi-electron Electrochemical Reactions

In this section, the current–potential curves of multi-electron transfer electrode reactions (with special emphasis on the case of a two-electron transfer process or EE mechanism) are analyzed for CSCV and CV. As in the case of single and double pulse potential techniques (discussed in Sects. 3.3 and 4.4, respectively), the equidiffusivity of all electro-active species is assumed, which avoids the consideration of the influence of comproportionation/disproportionation kinetics on the current corresponding to reversible electron transfers. A general treatment is presented and particular situations corresponding to planar and nonplanar diffusion and microelectrodes are discussed later.

6.2.1 Application of a Multipulse Sequence to Electrodes and Microelectrodes of Any Geometry

Let us consider the following reversible multielectronic charge transfer process:



where $E_{c,n}^{\ominus'}$ ($i = 1, 2, \dots, n$) are the formal potentials of each individual electron transfer and n the number of electrochemical steps.

As discussed in Sect. 3.3.4, the incidence of comproportionation reactions on the voltammetric response can be disregarded if diffusion is the only mass transport

mechanism, the diffusion coefficients of all species O_i are equal, the electron transfers are reversible, and any other chemical reactions are absent [1–4]. However, it must be taken into account that comproportionation will indeed have effects on the concentration profiles of the different species and that no analytical solution has been found for them even when a constant potential is applied. Nevertheless, the current–potential response corresponding to a sequence of successive potential pulses E_1, E_2, \dots, E_p applied to an electrode of any geometry can be obtained by introducing the following linear combinations of the concentrations of the different species for any potential pulse p :

$$\left. \begin{aligned} Y^{(p)} &= \sum_{i=1}^{n+1} c_{O_i}^{(p)}(q, t) \\ W^{(p)} &= \sum_{i=1}^n (n-i+1)c_{O_i}^{(p)}(q, t) \end{aligned} \right\} \quad (6.1)$$

with q and t referring to spatial coordinates and time, respectively (with t being in this case $t = \sum_{j=m}^p \tau_j + t_p$ with $m=1, 2, 3, \dots, p-1$), and $c_{O_i}^{(p)}(q, t)$ ($i=1, 2, \dots, n+1$) are the concentration profiles of species O_i corresponding to the p th potential pulse applied.

Both $Y^{(p)}$ and $W^{(p)}$ functions fulfill

$$\left. \begin{aligned} \frac{\partial Y^{(p)}(q, t)}{\partial t_p} &= D \nabla^2 Y^{(p)}(q, t) \\ \frac{\partial W^{(p)}(q, t)}{\partial t_p} &= D \nabla^2 W^{(p)}(q, t) \end{aligned} \right\} \quad (6.2)$$

where ∇^2 is the Laplace operator for mass transport given in Table 2.2 for the more usual electrode geometries. Superindex “ p ” refers to the p th potential pulse applied. Moreover, $Y^{(p)}$ holds for any potential pulse:

$$Y^{(p)} = c_{O_1}^* \quad (6.3)$$

The combination of Eq. (6.3) with Nernst’s law corresponding to the n redox couples for any potential pulse E_p leads to the following expressions for the surface concentrations of the different $(n+1)$ species:

$$\left. \begin{aligned} c_{O_i}^{(p,s)} &= \frac{c_{O_1}^* \prod_{j=i}^n e^{\eta_{p,j}}}{1 + \sum_{k=1}^n \left(\prod_{j=k}^n e^{\eta_{p,j}} \right)}, \quad i = 1, 2, \dots, n \\ c_{O_{n+1}}^{(p,s)} &= \frac{c_{O_1}^*}{1 + \sum_{k=1}^n \left(\prod_{j=k}^n e^{\eta_{p,j}} \right)} \end{aligned} \right\} \quad (6.4)$$

$$c_{O_1}^{(0,s)} = c_{O_1}^*; \quad c_{O_{i \geq 2}}^{(0,s)} = 0 \quad (6.5)$$

with

$$\eta_{p,j} = \frac{F(E_p - E_{c,j}^{\ominus'})}{RT} \quad (6.6)$$

The linear combination $W^{(p)}$ given in Eq. (6.1) fulfills Eq. (6.2) accompanied by these initial and boundary conditions:

$$\left. \begin{array}{l} t_p = 0, q \geq q^s \\ t_p > 0, q \rightarrow \infty \end{array} \right\} W^{(p)} = W^{(p-1)} \quad (6.7)$$

$$t_p > 0, q = q^s$$

$$W^{(p,s)} = \sum_{i=1}^n (n-i+1)c_{O_i}^{(p,s)} \quad (6.8)$$

with $W^{(0)} = 2c_{O_1}^*$.

Note that $W^{(p,s)}$ is only dependent on the applied potential E_p . Function $W^{(p)}$ can be written as a linear combination of the solutions corresponding to the previous pulses as

$$\left. \begin{array}{l} W^{(p)} = W^{(p-1)} + \tilde{W}^{(p)} \\ \tilde{W}^{(p)} = W^{(1)} + \sum_{j=2}^{p-1} \tilde{W}^{(j)} \end{array} \right\} \quad (6.9)$$

where

$$\left. \begin{array}{l} W^{(1)} = \sum_{i=1}^n (n-i+1)c_{O_i}^{(1)}(q,t) \\ \tilde{W}^{(j)} = W^{(j)} - W^{(j-1)} \end{array} \right\} \quad (6.10)$$

with $c_{O_i}^{(1)}(q,t)$ being the solution for the first potential pulse applied and $\tilde{c}_{O_i}^{(j)} (= c_{O_i}^{(j)} - c_{O_i}^{(j-1)})$ the partial solutions for the 2nd, 3rd, ..., p th successive potential pulses.

By inserting Eq. (6.9) into (6.2) and taking into account equations (6.7)–(6.9), it is possible to express the problem in terms only of the unknown function $\tilde{W}^{(p)}$ (see also Sect. 4.4.1):

$$\frac{\partial \tilde{W}^{(p)}(q,t)}{\partial t_p} = D \nabla^2 \tilde{W}^{(p)}(q,t) \quad (6.11)$$

$$\left. \begin{array}{l} t_p = 0, q \geq q^s \\ t_p > 0, q \rightarrow \infty \end{array} \right\} \tilde{W}^{(p)} = 0 \quad (6.12)$$

$$t_p > 0, q = q^s : \quad \tilde{W}^{(p,s)} = \sum_{i=1}^n (n-i+1) \left(c_{O_i}^{(p,s)} - c_{O_i}^{(p-1,s)} \right) \quad (6.13)$$

The current of the multielectronic process can be obtained as

$$I_p^{\text{multi E,G}} = FA_G D \left(\frac{\partial W^{(p)}(q, t)}{\partial q_N} \right)_{q^s} \quad (6.14)$$

with q^s referring to coordinates at the surface and q_N to normal surface coordinate.

By following a procedure similar to that discussed in Sects. 3.3.4 and 4.4.1, the following expression for the current at the p th potential pulse is [5, 6]:

$$I_p^{\text{multi E,G}} = FA_G D \left\{ \sum_{m=1}^p \left[\left(W^{(m-1,s)} - W^{(m,s)} \right) f_G(t_{m,p}, q_G) \right] \right\} \quad (6.15)$$

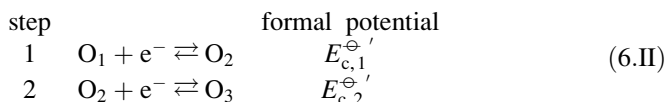
where

$$\left. \begin{aligned} W^{(m,s)} &= c_{O_1}^* \frac{\sum_{i=1}^n \left((n-i+1) \left(\prod_{j=i}^n e^{\eta_{m,j}} \right) \right)}{1 + \sum_{k=1}^n \prod_{h=k}^n e^{\eta_{m,h}}} \quad m = 1, 2, \dots, p \\ W^{(0,s)} &= W^* = n c_{O_1}^* \end{aligned} \right\} \quad (6.16)$$

where A_G is the electrode area corresponding to G geometry, q_G the characteristic dimension of the electrode, $t_{m,p} = \sum_{j=m}^{p-1} \tau_j + t_p$ (see Eq. (5.20)), and function $f_G(t_{m,p}, q_G)$ is given in Table 2.3.

Note that the expression of the current given by Eq. (6.15) is formally identical to that corresponding to a simple charge transfer process (Eq. (5.18)) by simply changing $(c_O^{(m-1,s)} - c_O^{(m,s)})$ in the former for $(W^{(m-1,s)} - W^{(m,s)})$.

In the particular case of an EE mechanism given by the reaction scheme:



$W^{(m)}$ takes the form (see Eq. (6.1)):

$$W^{(m)} = 2c_{O_1}^{(m)} + c_{O_2}^{(m)} \quad (6.17)$$

By inserting Eq. (6.4) for $n=2$ into (6.17) at the surface of the electrode ($q = q^s$), we obtain

$$\left. \begin{aligned} W^{(m,s)} &= c_{O_1}^* \frac{2e^{\eta_{1,m}} e^{\eta_{2,m}} + e^{\eta_{2,m}}}{1 + e^{\eta_{2,m}} + e^{\eta_{1,m}} e^{\eta_{2,m}}} \quad m = 1, 2, \dots, p \\ W^{(0,s)} &= W^* = 2c_{O_1}^* \end{aligned} \right\} \quad (6.18)$$

Equation (6.18) can be rewritten in terms of the average formal potential $\bar{E}_c^{\ominus'}$ and the equilibrium constant of the disproportionation reaction K (see Sects. 3.3.1 and 4.4.1):

$$W^{(m,s)} = \frac{2\sqrt{K}e^{2\bar{\eta}_m} + e^{\bar{\eta}_m}}{\sqrt{K} + e^{\bar{\eta}_m} + \sqrt{K}e^{2\bar{\eta}_m}} c_{O_1}^* \quad m = 1, 2, \dots, p \quad (6.19)$$

with

$$\bar{\eta}_m = \frac{F}{RT} (E_m - \bar{E}_c^{\ominus'}); \quad m = 1, 2, \dots, p \quad (6.20)$$

$$\bar{E}_c^{\ominus'} = \frac{E_{c,1}^{\ominus'} + E_{c,2}^{\ominus'}}{2} \quad (6.21)$$

$$K = \exp\left(\frac{F\Delta E_c^{\ominus'}}{RT}\right) \quad (6.22)$$

$$\Delta E_c^{\ominus'} = E_{c,2}^{\ominus'} - E_{c,1}^{\ominus'} \quad (6.23)$$

6.2.1.1 Cyclic Staircase Voltammetry and Cyclic Voltammetry

In this section, the general analytical expression for the current–potential response (Eq. (6.15)) is particularized for the electrochemical techniques Cyclic Staircase Voltammetry (CSCV) and Cyclic Voltammetry (CV). Thus, the expression for the CSCV and CV currents of multi-electron processes at electrodes of any geometry and size is

$$\psi_p^{\text{multi E,G}} = \frac{I_p^{\text{multi E,G}}}{F A_G c_{O_1}^* \sqrt{aD}} = \frac{1}{c_{O_1}^*} \sum_{m=1}^p \left((W^{(m-1,s)} - W^{(m,s)}) f_G(\xi_G, \vartheta_{m,p}) \right) \quad (6.24)$$

where

$$a = \frac{Fv}{RT} \quad (6.25)$$

$W^{(m,s)}$ is given by Eq. (6.16) or (6.19) for multi-electron or two-electron processes, respectively, and $f_G(\xi_G, \vartheta_{m,p})$ in Table 5.1, and

$$\xi_G = \sqrt{\frac{D}{aq_G^2}} \quad (6.26)$$

$$\vartheta_{m,p} = \begin{cases} \frac{F}{RT}(E_{p-m+1} - E_{\text{initial}}) = a(p-m+1)\tau & m \leq N/2 \\ \frac{F}{RT}(E_{p-m+1} - E_{\text{initial}} + 2E_{\text{final}}) & m > N/2 \end{cases} \quad (6.27)$$

with $(N/2)$ being the number of pulses of each scan.

In the particular case of two-electron transfer processes (i.e., EE mechanism), Eq. (6.24) can be simplified to [5, 6]:

$$\psi_p^{\text{EE,G}} = \sum_{m=1}^p Z_m^{\text{EE}} f_G(\xi_G, \vartheta_{m,p}) \quad (6.28)$$

$$\begin{aligned} Z_m^{\text{EE}} &= \frac{W^{(m-1,s)} - W^{(m,s)}}{c_{\text{O}_1}^*} \\ &= \frac{2\sqrt{K}e^{2\bar{\eta}_{m-1}} + e^{\bar{\eta}_{m-1}}}{\sqrt{K} + e^{\bar{\eta}_{m-1}} + \sqrt{K}e^{2\bar{\eta}_{m-1}}} - \frac{2\sqrt{K}e^{2\bar{\eta}_m} + e^{\bar{\eta}_m}}{\sqrt{K} + e^{\bar{\eta}_m} + \sqrt{K}e^{2\bar{\eta}_m}} \end{aligned} \quad (6.29)$$

or

$$Z_m^{\text{EE}} = \frac{2\sqrt{K}e^{2\vartheta_{m-1}\bar{\vartheta}_{\text{in}}} + e^{\vartheta_{m-1}\bar{\vartheta}_{\text{in}}}}{\sqrt{K} + e^{\vartheta_{m-1}\bar{\vartheta}_{\text{in}}} + \sqrt{K}e^{2\vartheta_{m-1}\bar{\vartheta}_{\text{in}}}} - \frac{2\sqrt{K}e^{2\vartheta_m\bar{\vartheta}_{\text{in}}} + e^{\vartheta_m\bar{\vartheta}_{\text{in}}}}{\sqrt{K} + e^{\vartheta_m\bar{\vartheta}_{\text{in}}} + \sqrt{K}e^{2\vartheta_m\bar{\vartheta}_{\text{in}}}} \quad (6.30)$$

$$\vartheta_m = \frac{F}{RT}(E_m - E_{\text{initial}}) \quad (6.31)$$

$$\bar{\vartheta}_{\text{in}} = \frac{F}{RT}(E_{\text{initial}} - \bar{E}_c^{\Theta'}) \quad (6.32)$$

with $\vartheta_m\bar{\vartheta}_{\text{in}} = \bar{\eta}_m$.

A C++ code to calculate the response of two-electron reversible electrode processes in Staircase Voltammetry at disc, (hemi)spherical, and cylindrical electrodes of any radius can be found in Appendix J

Under CV conditions, Eq. (6.28) should be used with $|\Delta E| \leq 0.01$ mV. In the following sections, the discussion focuses on the EE mechanism, although the results can be easily extrapolated to a multielectronic electrode reaction.

6.2.1.1.1 Planar Electrodes

For the particular case of planar electrodes, Eq. (6.28) simplifies to

$$\psi_{\text{CV}}^{\text{EE,plane}} = \sum_{m=1}^p Z_m^{\text{EE}} \frac{1}{\sqrt{\vartheta_{m,p}}} \quad (6.33)$$

with $\vartheta_{m,p}$ and Z_m^{EE} given in Eqs. (6.27) and (6.29)–(6.30).

Using the Laplace Transform method, this expression can be compared with that deduced by Polcyn and Shain for CV [7]:

$$I_{CV}^{EE, \text{plane}} = 2I^{EE, 1}(\zeta) + I^{EE, 2}(\chi) \quad (6.34)$$

with

$$\begin{aligned} I^{EE, 1}(\zeta) &= FAc_{O_1}^* \sqrt{\pi Da} \zeta(at) \\ I^{EE, 2}(\chi) &= FAc_{O_1}^* \sqrt{\pi Da} \chi(at) \end{aligned} \quad (6.35)$$

where functions $\zeta(at)$ and $\chi(at)$ are non-explicit functions obtained from integral equations and given by equations (9) and (10) of [7]. On comparing Eqs. (6.35) and (6.33) in the limit corresponding to CV by applying the derivative definition in the way of Eq. (5.47) (and taking into account that $|\Delta E| \leq 0.01 \text{ mV}$), it can be concluded that

$$\zeta(at) = \sum_{m=1}^p \left(\frac{2K^{3/2} e^{\theta_m \bar{\vartheta}_{in}} + 2K^2 e^{2\theta_m \bar{\vartheta}_{in}}}{\left(K + K^{1/2} e^{\theta_m \bar{\vartheta}_{in}} + K e^{2\theta_m \bar{\vartheta}_{in}} \right)^2} \right) \quad (6.36)$$

$$\chi(at) = \sum_{m=1}^p \left(\frac{-K^{3/2} e^{\theta_m \bar{\vartheta}_{in}} + K^{3/2} e^{3\theta_m \bar{\vartheta}_{in}}}{\left(K + K^{1/2} e^{\theta_m \bar{\vartheta}_{in}} + K e^{2\theta_m \bar{\vartheta}_{in}} \right)^2} \right) \quad (6.37)$$

Therefore, the classical Polcyn and Shain expression can be still used but with the advantage of having explicit expressions instead of the awkward integral equations for functions $\zeta(at)$ and $\chi(at)$.

The influence of the difference between the formal potentials of the first- and second-electron transfer, $\Delta E_c^{\ominus'}$, on the voltammograms corresponding to an EE mechanism at a plane electrode calculated from Eq. (6.33) can be seen in Fig. 6.1, in which the current has been plotted versus $E - E_{c,1}^{\ominus'}$ (a) and $E - \bar{E}_c^{\ominus'}$ (b). From these curves, it can be observed that the response shows two pair of peaks for very negative values of $\Delta E_c^{\ominus'}$, which approach as this parameter increases until for $\Delta E_c^{\ominus'} \geq -71.2 \text{ mV}$ a single pair of peaks is obtained, although the intermediate species remain stable (see Sect. 3.3.1 for an extensive discussion about this point). For $\Delta E_c^{\ominus'} \geq 200 \text{ mV}$, the response is indistinguishable from that corresponding to an apparently simultaneous di-electronic charge transfer.

In the case of two separate peaks, the difference between the peak potentials coincides with the difference between the formal potentials for $\Delta E_c^{\ominus'} < -142 \text{ mV}$. Under these conditions, the value of the formal potentials can be extracted from the average value of the peak potentials of the forward and backward scans:

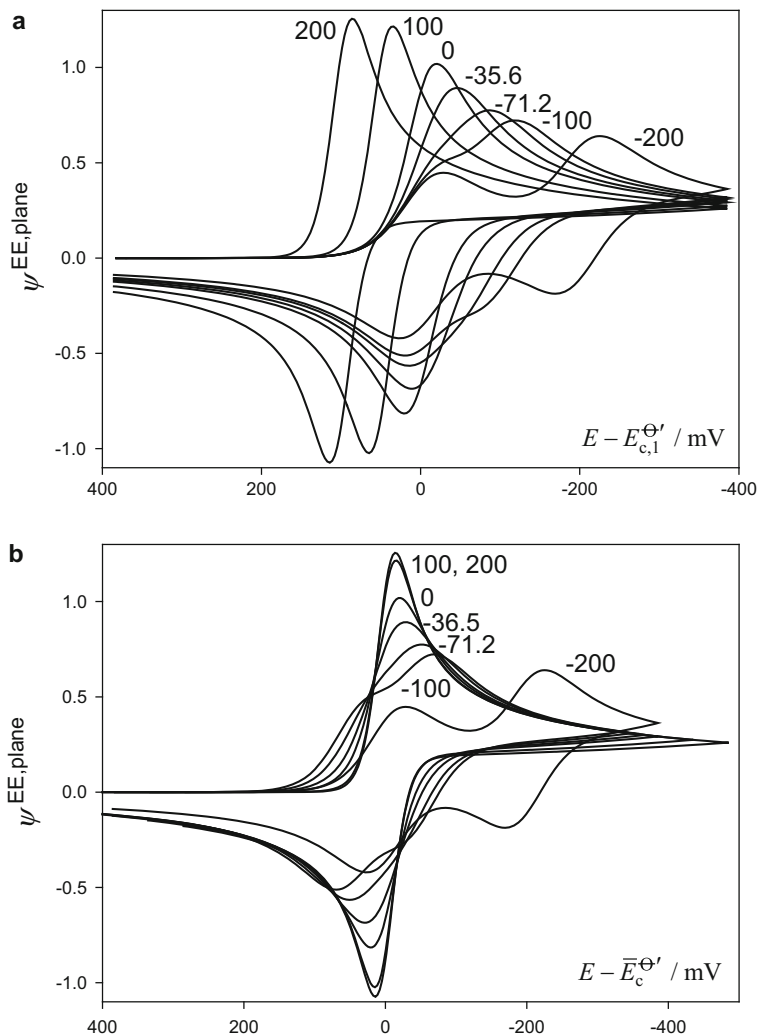


Fig. 6.1 Cyclic voltammograms corresponding to an EE mechanism at planar electrodes (current versus $E - E_{c,1}^{\ominus'}$ (a), and versus $E - \bar{E}_c^{\ominus'}$ (b), calculated from Eq. (6.33) for different values of the difference between formal potentials $\Delta E_c^{\ominus'}$ (values in mV shown in the curves). $E_{c,1}^{\ominus'} = 0$ mV, $T = 298$ K

$$\begin{aligned}
 E_{c,1}^{\ominus'} &= \frac{E_{\text{peak}, f, 1} + E_{\text{peak}, r, 1}}{2} \\
 E_{c,2}^{\ominus'} &= \frac{E_{\text{peak}, f, 2} + E_{\text{peak}, r, 2}}{2}
 \end{aligned}
 \tag{6.38}$$

When a single peak is obtained, the average value of the forward and backward peak potentials corresponds to the average formal potential, $\bar{E}_c^{\ominus'}$, Eq. (6.21) (Fig. 6.1b):

$$\bar{E}_c^{\ominus'} = \frac{E_{\text{peak, f}} + E_{\text{peak, r}}}{2} \quad (6.39)$$

6.2.1.1.2 Spherical Electrodes and Microelectrodes and Other Electrode Geometries

For spherical electrodes, the expression for the SCV current can be written in terms of the planar solution given by Eq. (6.33) as [5, 6]:

$$\psi_{\text{CV}}^{\text{EE, sphe}} = \sum_{m=1}^p \left(Z_m^{\text{EE}} \frac{1}{\sqrt{\pi \vartheta_{m, p}}} \right) + \xi_s \frac{W^{(p, s)}}{c_{\text{O}_1}^*} = \psi_{\text{CV}}^{\text{EE, plane}} + \xi_s \frac{W^{(p, s)}}{c_{\text{O}_1}^*} \quad (6.40)$$

with $W^{(p, s)}$, ξ_s , and Z_m^{EE} given by Eqs. (6.19), (6.26), (6.29), and (6.30) (with $q_G = r_s$), respectively.

This can be extended to other electrode geometries, and, for example, the expression for disc electrodes becomes [5]:

$$\psi_{\text{CV}}^{\text{EE, disc}} = \psi_{\text{CV}}^{\text{EE, plane}} + \xi_d \left(\frac{W^{(p, s)}}{c_{\text{O}_1}^*} + 0.2732 \sum_{m=1}^p Z_m^{\text{EE}} \exp \left(-\frac{0.39115}{\xi_d \sqrt{\vartheta_{m, p}}} \right) \right) \quad (6.41)$$

with ξ_d given by Eq. (6.26) (with $q_G = r_d$).

In both cases, it is clear that the response can be expressed as the sum of the solution for planar electrodes given by Eq. (6.33) and a contribution related to the electrode size (the second addend in the right-hand side of Eqs. (6.40) and (6.41)). When the electrode radius decreases, the current evolves from the transient peak-shaped response to a sigmoidal stationary one in the same way as observed for a simple charge transfer process (see Sects. 5.2.3.2 and 5.2.3.3). For small values of the electrode radius, the planar term in (6.40) and (6.41) becomes negligible and the current simplifies to

$$\left. \begin{aligned} \psi_{\text{CV}}^{\text{EE, sphe, ss}} &= \xi_s \frac{W^{(p, s)}}{c_{\text{O}_1}^*} \\ \psi_{\text{CV}}^{\text{EE, disc, ss}} &= \frac{4}{\pi} \xi_d \frac{W^{(p, s)}}{c_{\text{O}_1}^*} \end{aligned} \right\} \quad (6.42)$$

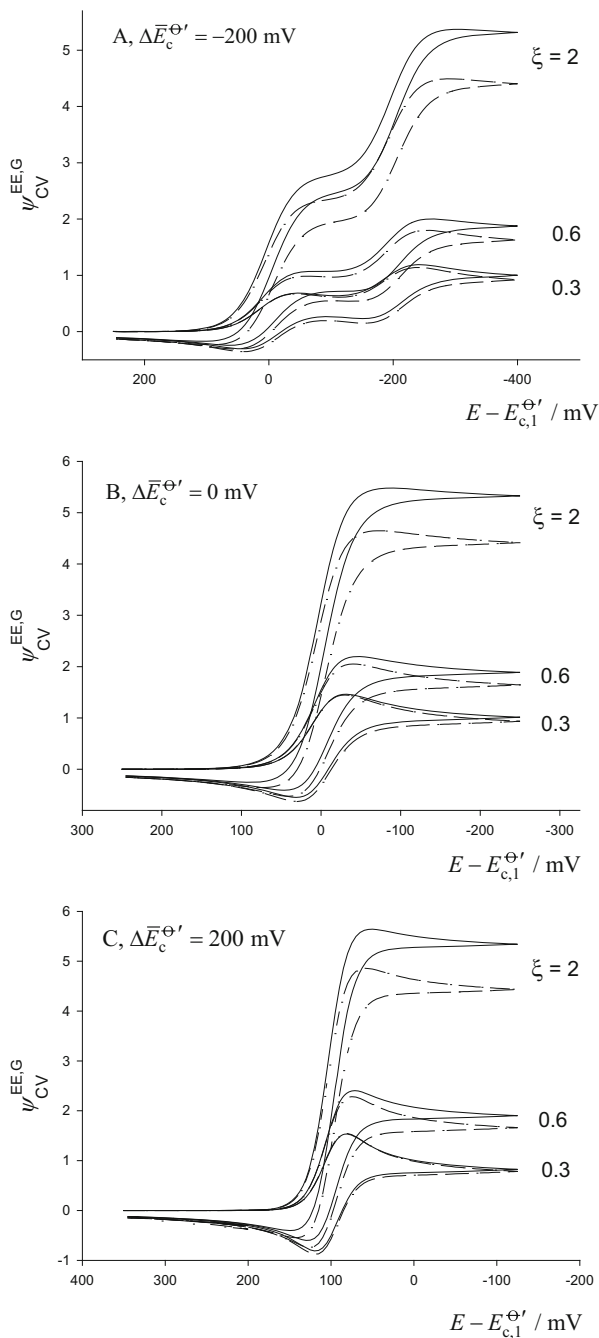
with $W^{(p, s)}$ given by Eq. (6.19).

Equation (6.42) clearly shows that the CV stationary responses of disc and spherical electrodes hold the same equivalence relationship as that observed for a simple charge transfer process:

$$\psi_{\text{CV}}^{\text{EE, disc, ss}} = \frac{4}{\pi} \psi_{\text{CV}}^{\text{EE, sphe, ss}} \quad (6.43)$$

The effects of the scan rate and electrode radius on cyclic voltammograms of different EE processes are analyzed in Fig. 6.2 through the dimensionless

Fig. 6.2 Influence of the scan rate and electrode radius (through the dimensionless parameter $\xi_G = \sqrt{(DRT)/(r_G^2 Fv)}$) on the CV voltammograms of an EE mechanism at disc (*solid line*) and hemispherical (*dashed line*) microelectrodes. Different $\Delta E_c^{\ominus'}$ values are considered: (A) -200 mV, (B) 0 mV, and (C) $+200$ mV. Reproduced from [5] with permission



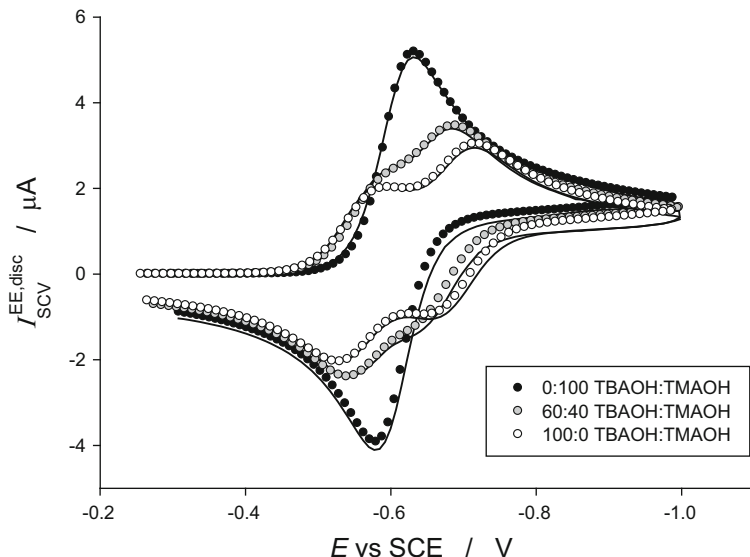


Fig. 6.3 Experimental blank-subtracted (*solid line*) and best-fit theoretical (*points*) SCV voltammograms of 0.5 mM AQ/H₂O solutions supported with [TMAOH] + [TBAOH] = 0.1 M on a gold disc macroelectrode of 0.9 mm radius. The proportion [TBAOH]:[TMAOH] is indicated on the graph. $\nu = 100 \text{ mV s}^{-1}$, $|\Delta E| = 1.06 \text{ mV}$, $T = 298 \text{ K}$. Reproduced with permission from [5]

parameter, ξ_G , defined in Eq. (6.26). According to the definition, large values of parameter ξ_G are associated with small electrode radii and/or slow scan rates. Therefore, as ξ_G is increased, the dimensionless current of the forward scan increases, whereas the backward peaks decrease due to diffusion of the electrogenerated species toward the bulk solution. Moreover, the shape of the forward voltammogram varies from peak to sigmoid shaped as the steady state is reached.

For large electrodes and/or fast scan rates, the voltammograms obtained at disc and (hemi)spherical electrodes coincide (with a difference in the peak current of less than 5 % for $\xi_G < 0.3$). Under these conditions, the diffusion is almost linear, so the current density is the same as on macroelectrodes. On the other hand, the larger the ξ_G value (i.e., the smaller the electrode and/or the slower the scan rate), the more apparent the differences are between the responses at electrodes of different shapes. In these conditions, the diffusion domains at disc and (hemi)spherical electrodes differ significantly, with the current density being greater at discs. At the limit of steady-state conditions, the dimensionless currents for any value of the potential, in any (direct or differential) electrochemical technique, and whatever the number of electrochemical steps is related by $\psi_{CV}^{EE, disc, ss} / \psi_{CV}^{EE, sphe, ss} = 4/\pi$.

Equation (6.41) for the current–potential response has been applied to the analysis of different experimental systems of interest. For example, the experimental SCV voltammograms of the two-electron reduction of anthraquinone-2-sulfonate (AQ) in different mixtures of alkylammonium salts obtained at a gold macroelectrode (radius = 0.9 mm) with a scan rate $\nu = 100 \text{ mV s}^{-1}$ are shown in Fig. 6.3 when a staircase

Table 6.1 Difference between the formal potentials and formal potential of the first electrochemical step obtained from the best fit of staircase cyclic voltammograms at a gold disc macroelectrode ($r_0 = 0.9\text{ mm}$) of 0.5 mM AQ/H₂O solutions in different supporting electrolytes (see Fig. 6.3). $T = 298\text{ K}$ [5]

Electrolyte ($I = 0.1\text{ M}$)	100 % TBAOH	(60 + 40) % TBAOH + TMAOH	100 % TMAOH
$\Delta E_c^{\ominus'} = E_{c,2}^{\ominus'} - E_{c,1}^{\ominus'}\text{ mV}$	-135	-100	-20
$E_{c,1}^{\ominus'}\text{ mV}^a$	-555	-564	-597
$D \times 10^6\text{ cm}^2\text{ s}^{-1b}$	3.0	3.5	5.3

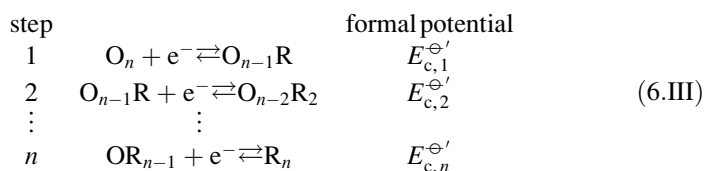
^aVs SCE

^bValues obtained from the steady-state limiting current

potential of pulse amplitude $\Delta E = 1.06\text{ mV}$ is applied. It has been reported in references [8, 9] that tuning the apparent formal potentials of this redox system can be done by varying the electrolyte composition. The semiquinone intermediate is stabilized by ion pairing with the tetra-*n*-butylammonium cation, and, consequently, the difference between the apparent formal potentials of the electron transfers increases. This effect enables the study of a range of $\Delta E_c^{\ominus'}$ values by simply changing the proportion of TBAOH in solution. The values of the formal potentials of the two-electron processes were extracted from the best fit of the experimental data with the analytical expressions given by Eq. (6.41) (see Table 6.1).

6.2.1.1.3 Multicenter Molecules with Non-interacting Redox Centers

The multielectronic process presented in reaction scheme (6.I) is formally equivalent to that corresponding to the reduction of a molecule containing n electroactive redox centers:



such that there are n redox couples $\text{O}_{n-j+1}\text{R}_{j-1}/\text{O}_{n-j}\text{R}_j$ with formal potentials $E_{c,j}^{\ominus'}$ ($j = 1, 2, \dots, n$) and $(n + 1)$ possible redox states O_{n-j}R_j (with subscript j denoting the number of reduced sites of the molecule). This is a very frequent situation (for example in dendrimers or linear polymers) [10], and it has been the subject of several studies [4, 10–13].

In references [10, 12], the particular case was studied of the successive electron transfers of a molecule with n identical and non-interacting centers by following an

equilibrium statistical treatment, from which it is deduced that the difference between the formal potentials of the first and any j oxidation states pair is given by

$$E_{c,1}^{\ominus'} - E_{c,j}^{\ominus'} = \frac{RT}{F} \ln \left(\frac{jn}{n-j+1} \right) \quad (6.44)$$

From this equation, it can be immediately inferred that the difference between the formal potentials of two states j and $(j+1)$ is

$$\Delta E_{c,j}^{\ominus'} = E_{c,j+1}^{\ominus'} - E_{c,j}^{\ominus'} = \frac{RT}{F} \ln \left(\frac{j(n-j)}{(j+1)(n-j+1)} \right) \quad j = 1, 2, \dots, n-1 \quad (6.45)$$

For the particular case of a two-center molecule ($n=2, j=1$), this value is (see Sects. 6.2.1.1.1 and 6.2.1.1.2)

$$\Delta E_{c,1}^{\ominus'} = E_{c,2}^{\ominus'} - E_{c,1}^{\ominus'} = \frac{RT}{F} \ln \left(\frac{1}{4} \right) = -35.6 \text{ mV} \quad (6.46)$$

In the case of a four-center molecule ($n=4, j=1, 2, 3$), it is obtained that

$$\begin{aligned} \Delta E_{c,1}^{\ominus'} &= E_{c,2}^{\ominus'} - E_{c,1}^{\ominus'} = \frac{RT}{F} \ln \left(\frac{3}{8} \right) = -25.1 \text{ mV} \\ \Delta E_{c,2}^{\ominus'} &= E_{c,3}^{\ominus'} - E_{c,2}^{\ominus'} = \frac{RT}{F} \ln \left(\frac{4}{9} \right) = -20.7 \text{ mV} \\ \Delta E_{c,3}^{\ominus'} &= E_{c,4}^{\ominus'} - E_{c,3}^{\ominus'} = \frac{RT}{F} \ln \left(\frac{3}{8} \right) = -25.1 \text{ mV} \end{aligned} \quad (6.47)$$

By inserting Eq. (6.45) in the expression of the surface concentrations (which are analogous to that given in Eq. (6.4)), the following expression for the particular case of n non-interacting centers is found:

$$\frac{c_{O_j}^{(m,s)}}{c^*} = f_j^m \quad (6.48)$$

with c^* being the initial concentration of the multicenter molecule, and f_j^m can be written as the j th coefficient of the binomial distribution

$$f_j^m = \binom{n}{j} \left(\frac{e^{\bar{\eta}_m}}{1 + e^{\bar{\eta}_m}} \right)^{n-j} \left(\frac{1}{1 + e^{\bar{\eta}_m}} \right)^j \quad (6.49)$$

where $\bar{\eta}_m = F(E_m - \bar{E}_c^{\ominus'})/RT$ (Eq. (6.20)) and $\bar{E}_c^{\ominus'}$ is the “common standard potential relating each microscopic center that is in its oxidized state to its reduced counterpart no matter what the overall oxidation state of the molecule happens to

be” [10], whose numerical value coincides with the average formal potential of all pairs of oxidation states:

$$\bar{E}_c^{\ominus'} = \frac{1}{n} \sum_{j=1}^n E_{c,j}^{\ominus'} \quad (6.50)$$

For example, under these conditions a redox bicentric molecule behaves as two separate mono-redox center ones with identical formal potentials equal to $\bar{E}_c^{\ominus'}$.

The expression for the current of a bicenter molecule in the absence of interactions (i.e., for $\Delta E_{c,1}^{\ominus'} = -35.6\text{mV}$) is double that obtained for a single charge transfer given by Eq. (5.24):

$$\frac{I_p^{2 \text{ centers, G}}}{F A_G D c_O^*} = 2 \left[\sum_{m=1}^p \left(\frac{e^{\bar{\eta}_{m-1}}}{1 + e^{\bar{\eta}_{m-1}}} - \frac{e^{\bar{\eta}_m}}{1 + e^{\bar{\eta}_m}} \right) f_G(t_m, p, q_G) \right] \quad (6.51)$$

Thus, Eqs. (6.44)–(6.51) clearly demonstrate that the whole current–potential curve corresponding to a molecule with n non-interacting centers is n times that corresponding to a molecule with only one redox center for the same concentration and diffusion coefficients and in any single or multipulse electrochemical technique, independently of the electrode geometry [12].

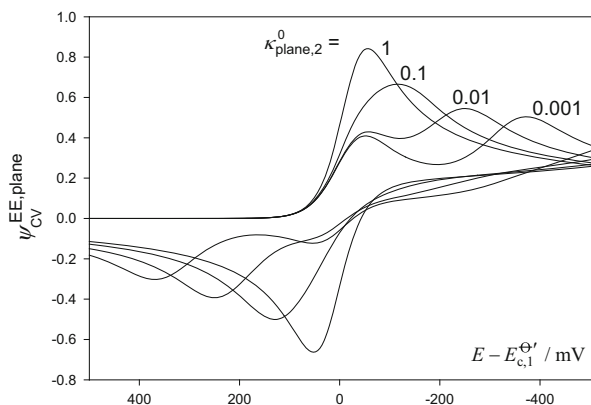
6.2.1.1.4 Non-reversible Two-Electron Electrochemical Reactions

This case is much more complex than the reversible one since the SCV and CV currents depend not only on the difference between formal potentials $\Delta E_c^{\ominus'}$ but also on the particular value of the rate constants for the first and second charge transfer steps, $\kappa_{\text{plane},1}^0$ and $\kappa_{\text{plane},2}^0$, or on one of the rate constants and the ratio between them, with

$$\left. \begin{aligned} \kappa_{\text{plane},1}^0 &= \frac{k_1^0}{\sqrt{aD}} \\ \kappa_{\text{plane},1}^0 &= \frac{k_2^0}{\sqrt{aD}} \end{aligned} \right\} \quad (6.52)$$

Thus, the number of peaks is not merely a function of $\Delta E_c^{\ominus'}$, as in the reversible case. As an example, the CV curves corresponding to a two-electron non-reversible charge transfer calculated for $\Delta E_c^{\ominus'} = 0\text{V}$ and $\kappa_{\text{plane},1}^0 (=1)$ and different values of $\kappa_{\text{plane},2}^0$ have been plotted in Fig. 6.4. From these curves, it is clear that the morphology of the voltammograms evolves from a single pair of peaks for the case in which $\kappa_{\text{plane},1}^0 = \kappa_{\text{plane},2}^0$ to the appearance of a second pair of peaks which are

Fig. 6.4 CV curves corresponding to an EE process with $\Delta E_c^{\Theta'} = 0$ V, $\kappa_{\text{plane},1}^0 = 1$, and different values of $\kappa_{\text{plane},2}^0$ (shown in the curves). $\alpha = 0.5$



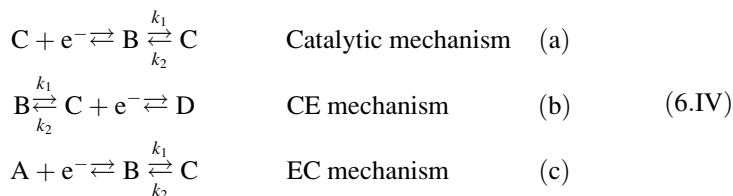
shifted toward more negative and positive potentials in the direct and reverse scans, respectively, as $\kappa_{\text{plane},2}^0$ decreases.

Under these conditions, it is difficult to obtain criteria to characterize the response, although some attempts have been made [14].

6.3 First-Order Chemical Reactions Coupled with the Charge Transfer

As discussed in Sects. 3.4 and 4.5, electrode processes coupled with homogeneous chemical reactions are very frequent and their study is of interest in many applied fields, such as organic electrosynthesis, ecotoxicity, biosciences, environmental studies, among others [15–17]. In this section, multipulse techniques (with a special focus on Cyclic Voltammetry) are applied to the study of the reaction kinetics and mechanisms of electrogenerated species.

Of the wide range of these types of processes, this study focuses mainly on three first- or pseudo-first-order reaction mechanisms (see reaction scheme (6.IV)): catalytic, EC, and CE processes which are the most analyzed in the Electrochemistry literature.



A brief discussion concerning more complex reaction schemes like the ECE mechanism follows.

In these electrode processes, the use of macroelectrodes is recommended when the homogeneous kinetics is slow in order to achieve a commitment between the diffusive and chemical rates. When the chemical kinetics is very fast with respect to the mass transport and macroelectrodes are employed, the electrochemical response is insensitive to the homogeneous kinetics of the chemical reactions—except for first-order catalytic reactions and irreversible chemical reactions follow up the electron transfer—because the reaction layer becomes negligible compared with the diffusion layer. Under the above conditions, the equilibria behave as fully labile and it can be supposed that they are maintained at any point in the solution at any time and at any applied potential pulse. This means an independent of time (stationary) response cannot be obtained at planar electrodes except in the case of a first-order catalytic mechanism. Under these conditions, the use of microelectrodes is recommended to determine large rate constants. However, there is a range of microelectrode radii with which a kinetic-dependent stationary response is obtained; beyond the upper limit, a transient response is recorded, whereas beyond the lower limit, the steady-state response is insensitive to the chemical kinetics because the kinetic contribution is masked by the diffusion mass transport. In the case of spherical microelectrodes, the lower limit corresponds to the situation where the reaction layer thickness does not exceed 80 % of the diffusion layer thickness.

6.3.1 Catalytic Mechanism

As shown in Sects. 3.4.1 and 4.5.1, the first-order catalytic mechanism is much simpler to study than the first CE and EC mechanisms. Thus, when any sequence of potential pulses E_1, E_2, \dots, E_p is applied and diffusion coefficients of species B and C in reaction scheme (6.IV) are assumed equal, it is fulfilled that

$$c_B^{(p)}(q, t) + c_C^{(p)}(q, t) = c_B^* + c_C^* = \xi^* \quad \forall q, t \quad (6.53)$$

for any electrode geometry with $t = \sum_{j=1}^{p-1} \tau_j + t_p$ and q referring to spatial coordinates. This condition means the mathematical treatment of this process is greatly simplified. So, only the variable $\phi^{(p)} \left(= \left(c_B^{(p)} - K c_C^{(p)} \right) e^{-(k_1+k_2)t} \right)$ works

$$\phi^{(p)} = \phi^{(p-1)} + \tilde{\phi}^{(p)} \quad (6.54)$$

where $\phi^{(p-1)}$ is the already known function ϕ corresponding to the previous potential pulse ($p - 1$) at time t and $\tilde{\phi}^{(p)}$ the unknown function to determine.

Under these conditions (see Eqs. (4.199)–(4.202)), it can be easily demonstrated that the Superposition Principle can be applied and the diffusion differential equation and the boundary value problem of this process, independently of the electrode geometry, are simplified to

$$\frac{\partial \tilde{\phi}^{(p)}(q, t)}{\partial t_p} = D \nabla^2 \tilde{\phi}^{(p)}(q, t) \quad (6.55)$$

$$\left. \begin{array}{l} t_p = 0, q \geq q^s \\ t_p > 0, q \rightarrow \infty \end{array} \right\} \tilde{\phi}^{(p)} = 0 \quad (6.56)$$

$$t_p > 0, q = q^s,$$

$$e^{-(k_1+k_2)t_p} \tilde{\phi}^{(p,s)} = e^{(k_1+k_2)\tau_{1,p-1}} \left(\frac{1 - Ke^{\eta_p}}{1 + e^{\eta_p}} - \frac{1 - Ke^{\eta_{p-1}}}{1 + e^{\eta_{p-1}}} \right) \zeta^* \quad (6.57)$$

where $K(=k_2/k_1)$ is the inverse of the chemical equilibrium constant and

$$\tau_{1,p-1} = \sum_{i=1}^{p-1} \tau_i \quad (6.58)$$

$$\tilde{\phi}^{(p,s)} = \left(\tilde{c}_B^{(p,s)} - K \tilde{c}_C^{(p,s)} \right) e^{(k_1+k_2)(\tau_1+\dots+\tau_{p-1}+t_p)} \quad (6.59)$$

$$\left. \begin{array}{l} c_B^{(p)} = c_B^{(1)} + \sum_{j=2}^p \tilde{c}_B^{(j)} \\ c_C^{(p)} = c_C^{(1)} + \sum_{j=2}^p \tilde{c}_C^{(j)} \end{array} \right\} \quad (6.60)$$

and

$$\phi^{(p)} = \phi^{(1)} + \sum_{j=2}^p \tilde{\phi}^{(j)} \quad (6.61)$$

Thus, the expression of the current is

$$\frac{I_p^{\text{cat,G}}}{FAGD} = \left(\frac{\partial c_C^{(p)}}{\partial q_N} \right)_{q^s} = e^{-kt_{1,p}} \left(\frac{\partial \phi^{(1)}}{\partial q_N} \right)_{q^s} + \sum_{m=2}^p \left(e^{-kt_{m,p}} \left(\frac{\partial \tilde{\phi}^{(m)}}{\partial q_N} \right)_{q^s} \right) \quad (6.62)$$

with $t_{m,p}$ being

$$t_{m,p} = \sum_{i=m}^{p-1} \tau_i + t_p \quad (6.63)$$

and q^s and q_N are the coordinates at the electrode surface and the normal coordinate, respectively. By proceeding as in Sect. 4.5.1 (see also [18–21]), one obtains

$$\frac{I_p^{\text{cat,G}}}{FA_G D} = \frac{\zeta^*}{(1+K)} \sum_{m=1}^p (Z_m^{\text{cat}} f_G^{\text{cat}}(\chi_{m,p}, q_G)) \quad (6.64)$$

where

$$Z_m^{\text{cat}} = \begin{cases} \frac{1 - Ke^{\vartheta_1} e^{\vartheta_{\text{in}}}}{1 + e^{\vartheta_1} e^{\vartheta_{\text{in}}}} & m = 1 \\ (1+K) \left(\frac{1}{1 + e^{\vartheta_m} e^{\vartheta_{\text{in}}}} - \frac{1}{1 + e^{\vartheta_{m-1}} e^{\vartheta_{\text{in}}}} \right) & m > 1 \end{cases} \quad (6.65)$$

$$\chi_{m,p} = (k_1 + k_2)t_{m,p} \quad (6.66)$$

$e^{\eta_0} = \exp(F(E_{\text{eq}} - E_c^{\Theta'})/RT) = c_B^*/c_C^* = K = 1/K_{\text{eq}}$, and ξ_G , ϑ_m , and ϑ_{in} are given by Eqs. (6.26), (6.31), and (6.32), respectively. Function $f_G^{\text{cat}}(\chi_{m,p}, q_G)$ depends on the electrode geometry (see Table 6.2 for planar, spherical, and disc electrodes with q_G being the characteristic dimension of the electrode of geometry G).

Under CV conditions (i.e., for $|\Delta E| < 0.01$ mV), Eq. (6.64) can be rewritten as

$$\psi_{\text{CV}}^{\text{cat,G}} = \frac{1}{1+K} \sum_{m=1}^p (Z_m^{\text{cat}} f_G^{\text{cat}}(\vartheta_{m,p}, \xi_G)) \quad (6.67)$$

with $\psi_{\text{CV}}^{\text{cat,G}} = I_p^{\text{cat,G}} / (FA_G \sqrt{aD} \zeta^*)$ and

$$\chi_{m,p} = \chi^{\text{CV}} \vartheta_{m,p} \quad (6.68)$$

$$\chi^{\text{CV}} = \frac{k_1 + k_2}{a} \quad (6.69)$$

where a , $\vartheta_{m,p}$, and Z_m^{cat} are given by Eqs. (6.25), (6.27), and (6.65), respectively.

6.3.1.1 Planar Electrodes

In this case, Eq. (6.67) becomes [18, 19]:

$$\psi_{\text{CV}}^{\text{cat,plane}} = \frac{1}{1+K} \sum_{m=1}^p (Z_m^{\text{cat}} f_{\text{plane}}^{\text{cat}}(\vartheta_{m,p})) \quad (6.70)$$

with $f_{\text{plane}}^{\text{cat}}(\vartheta_{m,p})$ given in Table 6.2.

Since the characteristic time corresponding to CV is given by the variable $1/a$ (with $a = Fv/RT$), it is interesting to analyze the influence of the chemical kinetics on the voltogram by using the variable χ^{CV} given by Eq. (6.69). This influence can

Table 6.2 Expressions for functions $f_G^{\text{cat}}(\chi_{m,p}, q_G)$ and $f_G^{\text{cat}}(Q_G, \Lambda_G, \vartheta_{m,p})$ for planar, spherical, and disc electrodes [18–21]. $G = d$ for discs and s for spheres or hemispheres. The dimension of $f_G^{\text{cat}}(\chi_{m,p}, q_G)$ is l/length whereas $f_G^{\text{cat}}(Q_G, \Lambda_G, \vartheta_{m,p})$ is dimensionless

Electrode	$f_G^{\text{cat}}(\chi_{m,p}, q_G)$	$f_G^{\text{cat}}(Q_G, \Lambda_G, \vartheta_{m,p})$
Planar	$\sqrt{\frac{k_1+k_2}{D}} \left[\frac{e^{-\chi_{m,p}}}{\sqrt{\beta_{m,p}}} + \text{erf}(\sqrt{\beta_{m,p}}) \right]$	$\sqrt{\chi^{\text{CV}}} \left[\frac{e^{-\chi^{\text{CV}} \vartheta_{m,p}}}{\sqrt{\beta_{m,p}}} + \text{erf}(\sqrt{\chi^{\text{CV}} \vartheta_{m,p}}) \right]$
Sphere	$\frac{1}{r_s} + \sqrt{\frac{k_1+k_2}{D}} \left[\frac{e^{-\chi_{m,p}}}{\sqrt{\beta_{m,p}}} + \text{erf}(\sqrt{\beta_{m,p}}) \right]$	$\sqrt{\chi^{\text{CV}}} \left(\frac{1}{\sqrt{\Lambda_s}} + \frac{e^{-\chi^{\text{CV}} \vartheta_{m,p}}}{\sqrt{\beta_{m,p}}} + \text{erf}(\sqrt{\chi^{\text{CV}} \vartheta_{m,p}}) \right)$
Disc	$\frac{1}{r_d} + \sqrt{\frac{k_1+k_2}{D}} \left[\text{erf}(\sqrt{\beta_{m,p}}) + 0.2732 \frac{\sqrt{\beta_{m,p}}}{\xi_d} \int_0^{\xi_d} \frac{1}{\sqrt{u}} \exp \left[-\frac{0.39115}{\sqrt{u}} - \frac{\chi_{m,p}}{\xi_d} \right] du + e^{-\chi_{m,p}} \left[0.2732 \frac{\xi_d}{\sqrt{\beta_{m,p}}} \exp \left(-\frac{0.39115}{\xi_d} \right) + \frac{1}{\sqrt{\beta_{m,p}}} \right] \right]$	$\sqrt{\chi^{\text{CV}}} \left(\frac{1}{\sqrt{\Lambda_d}} + \text{erf}(\sqrt{\chi^{\text{CV}} \vartheta_{m,p}}) + 0.2732 \sqrt{\Lambda_d} \int_0^{\vartheta_{m,p}/Q_d^2} \frac{1}{\sqrt{u}} \exp \left[-\frac{0.39115}{\sqrt{u}} - \Lambda_d u \right] du + \frac{0.2732}{\sqrt{\Lambda_d}} \exp \left(-\frac{\Lambda_d \vartheta_{m,p}}{Q_d^2} - \frac{0.39115 Q_d}{\sqrt{\beta_{m,p}}} \right) \right)$

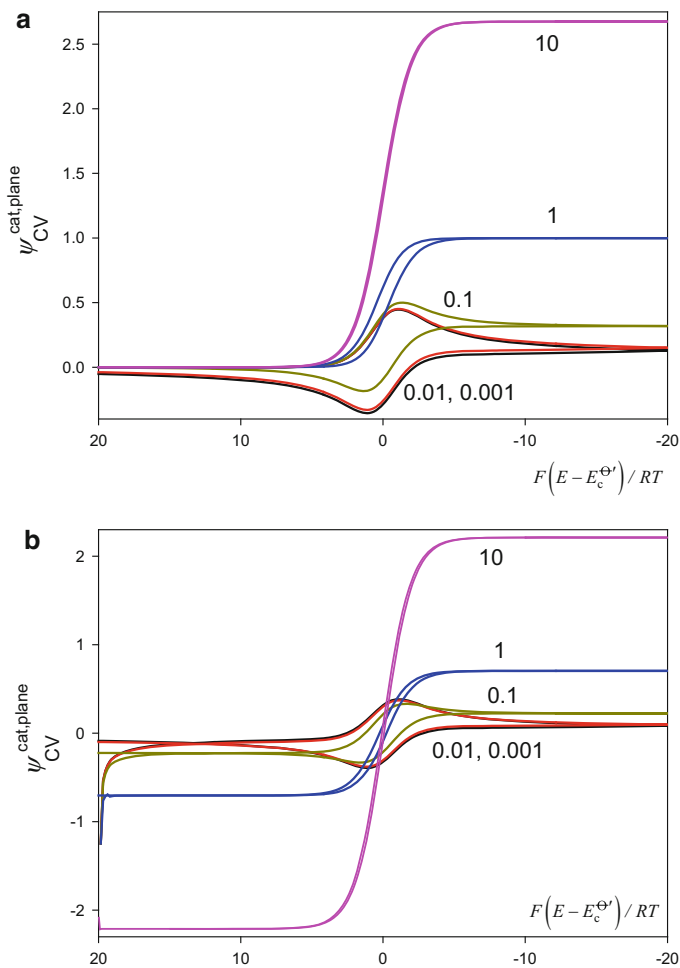


Fig. 6.5 CV curves for a catalytic mechanism at planar electrodes calculated from Eq. (6.70). The values of the inverse of the equilibrium constant are: (a) $K=0$, (b) $K=1$. The values of the rate constant χ^{CV} are 10 (pink), 1 (blue), 0.1 (dark yellow), 0.01 (red), and 0.001 (black). $T=298$ K

be seen in Fig. 6.5 for two values of K (0 and 1). In the case of an irreversible chemical reaction (Fig. 6.5a), the curves calculated for small values of χ^{CV} are practically coincident with those corresponding to a simple charge transfer. The catalysis is more effective, the higher χ^{CV} is, leading to an increase of the current and an evolution from transient peak-shaped curves obtained for small χ^{CV} to sigmoidal stationary ones corresponding to $\chi^{\text{CV}} > 1$. Under these conditions, $f_{\text{plane}}^{\text{cat}}(\chi_{p,m}) \rightarrow 1$ and the current is

$$\psi_{CV}^{\text{cat, plane, ss}} = \frac{\sqrt{\chi^{\text{CV}}}}{1+K} \frac{1 - Ke^{\vartheta_m} e^{\vartheta_{\text{in}}}}{1 + e^{\vartheta_m} e^{\vartheta_{\text{in}}}} \quad (6.71)$$

which corresponds to a pure kinetic steady state identical to that obtained in Single Pulse Techniques (see Eq. (3.205a)), i.e., the response has no memory of the pulses previous to the m th. Moreover, a constant current is obtained for very negative potentials (for which $e^{\vartheta_m} \cong 0$):

$$\psi_{CV}^{\text{cat, plane, ss}} \Big|_{E \rightarrow -\infty} = \frac{\sqrt{\chi^{\text{CV}}}}{1+K} \quad (6.72)$$

The limiting anodic current under stationary conditions is (see Fig. 6.5b):

$$\psi_{CV}^{\text{cat, plane, ss}} \Big|_{E \rightarrow \infty} = \frac{-K}{1+K} \sqrt{\chi^{\text{CV}}} \quad (6.73)$$

such that the ratio between both limiting currents fulfills

$$\left| \frac{\psi_{CV}^{\text{cat, plane, ss}} \Big|_{E \rightarrow \infty}}{\psi_{CV}^{\text{cat, plane, ss}} \Big|_{E \rightarrow -\infty}} \right| = K \quad (6.74)$$

It is also observed that the location of the CV at the potential axis is not affected by χ^{CV} . Indeed, when a stationary response is reached, the half-wave potential of the I - E curve coincides with the formal potential of the redox couple, as in the case of a reversible charge transfer reaction.

6.3.1.2 Spherical and Disc Electrodes and Microelectrodes

In the case of spherical and disc electrodes, the catalytic CV curve can be written in terms of the planar one (Eq. (6.70) and Table 6.2) as [20, 21]:

$$\psi_{CV}^{\text{cat, spher}} = \psi_{CV}^{\text{cat, radial}} + \frac{\sqrt{A_s}}{(1+K)Q_s} \sum_{m=1}^p \left(Z_m^{\text{cat}} f_{\text{plane}}^{\text{cat}}(\vartheta_m, p) \right) \quad (6.75)$$

$$\psi_{CV}^{\text{cat, disc}} = \psi_{CV}^{\text{cat, radial}} + \frac{\sqrt{A_d}}{(1+K)Q_d} \sum_{m=1}^p \left(Z_m^{\text{cat}} f_{\text{disc}}^{\text{cat}}(Q_d, A_d, \vartheta_m, p) \right) \quad (6.76)$$

with

$$\Lambda_G = \frac{(k_1 + k_2)r_G^2}{D} \quad (6.77)$$

$$Q_G = \sqrt{\frac{\Lambda_G}{\chi^{CV}}} = \sqrt{\frac{a}{D}} r_G \quad (6.78)$$

$$\begin{aligned} f_{\text{disc}}^{\text{cat}}(Q_d, \Lambda_d, \vartheta_{m,p}) &= f_{\text{plane}}^{\text{cat}}(\vartheta_{m,p}) \\ &+ 0.2732\sqrt{\Lambda_d} \int_0^{(\vartheta_{m,p}/Q_d^2)} \exp\left[-\frac{0.39115}{\sqrt{u}} - \Lambda_d u\right] du \\ &+ \frac{0.2732}{\sqrt{\Lambda_d}} \exp\left(-\frac{\Lambda_d}{Q_d^2} \vartheta_{m,p} - \frac{0.39115 Q_d}{\sqrt{\vartheta_{m,p}}}\right) \end{aligned} \quad (6.79)$$

$$\psi_{CV}^{\text{cat,radial}} = \frac{1}{Q_G} \frac{1 - K e^{\vartheta_p} e^{\vartheta_{in}}}{(1 + K)(1 + e^{\vartheta_p} e^{\vartheta_{in}})} \quad (6.80)$$

with u being the integration variable, $f_{\text{plane}}^{\text{cat}}(\vartheta_{m,p})$, given in Table 6.2 and ϑ_m , ϑ_{in} , and Z_m^{cat} given by Eqs. (6.31), (6.32), and (6.65), respectively. The subindex G refers to the geometry considered (G = s for spheres and G = d for discs). Note that

$$\frac{\sqrt{\Lambda_G}}{Q_G} = \sqrt{\chi^{CV}} = \sqrt{\frac{k_1 + k_2}{a}} \quad (6.81)$$

From Eqs. (6.75)–(6.78), it can be seen that parameter Q_G reflects the influence of the electrode size, whereas Λ_G combines the influence of kinetics and electrode size since for nonplanar electrodes both effects are closely related. Thus, the influence of the electrode size on the cyclic voltograms is analyzed in Fig. 6.6 for a given scan rate and two different k_1 values corresponding to transient conditions ($\Lambda_G/Q_G^2 = 0.04$, Fig. 6.6a, c) and stationary conditions ($\Lambda_G/Q_G^2 = 10$, Fig. 6.6b, d).

As observed in Fig. 6.6a, under transient conditions the dimensionless current at disc electrodes is always greater than at spherical ones (of the same radius), the smaller the electrode (i.e., the smaller the Q_G value), the greater the difference. When the stationary response is reached, three different steady states can be defined depending on the value of the rate constants and the electrode radius (see Fig. 6.6b) [21]. Thus, for very small electrodes ($Q_G = 0.01$) the large diffusion transport masks the kinetic contribution and a micro-geometrical steady state is achieved. For these conditions, the response is equivalent to that of a simple charge transfer process, so the ratio between the dimensionless curves at discs and spheres is given by $\psi_{CV}^{\text{cat,disc}}/\psi_{CV}^{\text{cat,sph}} = 4/\pi$ (provided that $r_d = r_s$). On the other hand, for large electrodes ($Q = 5$) or large kinetic constants, a “purely” kinetic steady state is reached and the dimensionless current depends only on the chemical kinetics, and is independent of the electrode size and geometry (i.e., $\psi_{CV}^{\text{cat,disc}}/\psi_{CV}^{\text{cat,sph}} = 1$). In both figures, an intermediate behavior is found for medium-sized electrodes ($Q = 0.5$).

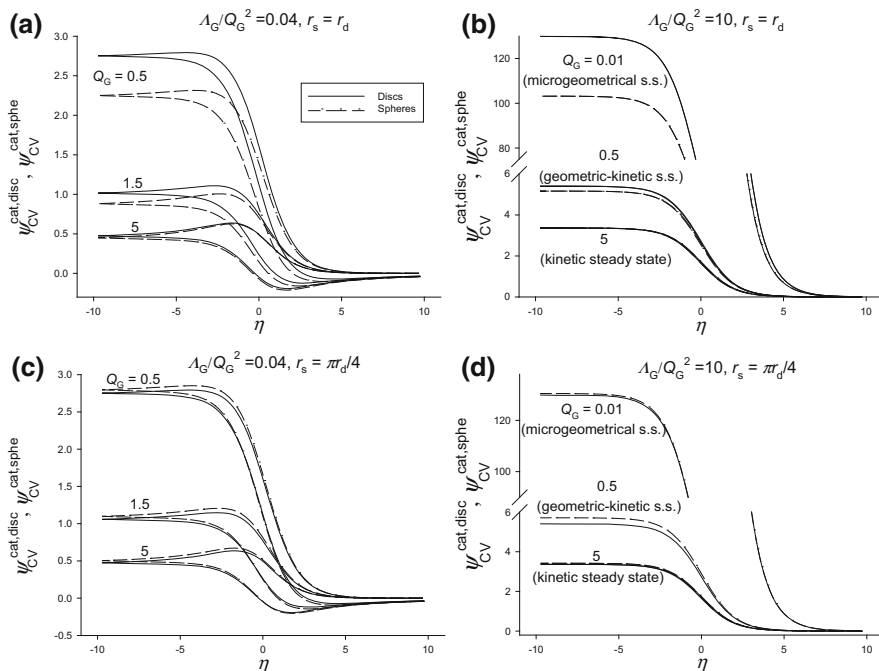
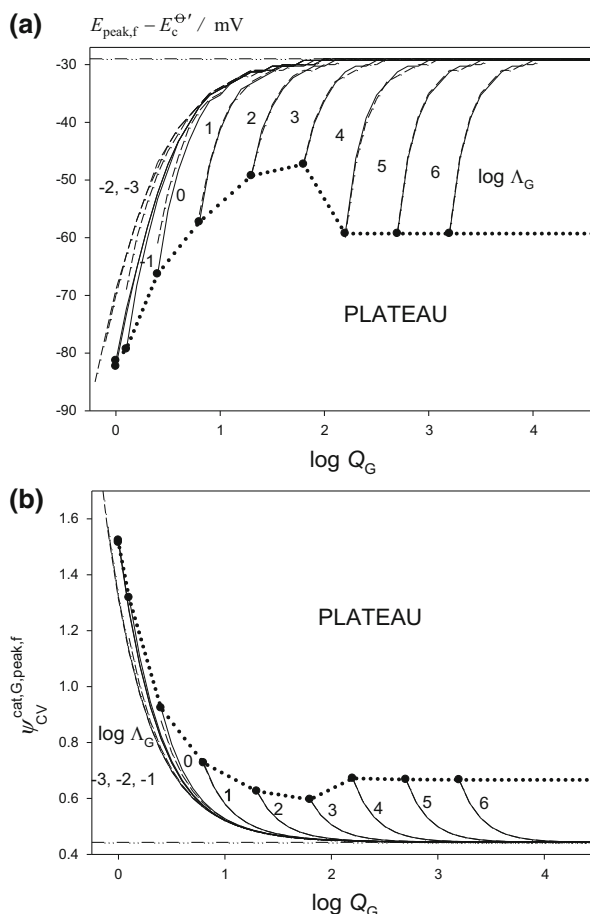


Fig. 6.6 Dimensionless cyclic voltammograms ($\psi_{CV}^{\text{cat},G} - \eta$ curves, with $\eta = F(E - E_c^{\Theta'})/(RT)$) of the first-order catalytic mechanism (with $K=0$) at disc (solid line) and spherical (dashed line) electrodes with slow ($\Lambda_G/Q_G^2 = 0.04$, (a) and (c)) and fast ($\Lambda_G/Q_G^2 = 10$, (b) and (d)) catalytic kinetics. Three different electrode radii are considered in each case (Q_G values marked on the curves). (a) and (b) $r_d = r_s$; (c) and (d) $r_d = 4r_s/\pi$. Reproduced with permission from [21]

The curves in Fig. 6.6c, d are similar to the previous ones, although in this case the values of the electrode radii have been selected so that they fulfill the following equivalence relationship: $r_d/r_s = 4/\pi$ [21]. As a consequence, equivalent cyclic voltammograms are obtained at spherical and disc electrodes under micro-geometrical steady-state conditions (see curves for $Q_G = 0.01$ in Fig. 6.6d). These curves are also coincident in the kinetic steady state (see curves for $Q_G = 5$ in Fig. 6.6d) since, as stated above, the current density under these conditions is independent of the electrode size. In the intermediate geometric-kinetic steady state, some divergence is found, although in this case the dimensionless current corresponding to spherical electrodes is greater. This is also observed under transient conditions (see Fig. 6.6c).

The variation of the voltammetric peak parameters ($E_{\text{peak},f} - E_c^{\Theta'}$, Fig. 6.7a, and $\psi_{CV}^{\text{cat},G,\text{peak},f}$, Fig. 6.7b) versus $\log Q_G$, corresponding to transient CV curves, is plotted in Fig. 6.7. All the cyclic voltammograms have been calculated by fixing the value of parameter Λ_G (Eq. (6.77)) and considering disc (solid lines) and spherical (dashed lines) electrodes of the same radius ($r_d = r_s = 0.01$ cm) for the

Fig. 6.7 Variation of (a) the peak potential and (b) the peak current of the cyclic voltammograms with the scan rate (through the parameter Q_G) at disc (*solid line*) and spherical (*dashed line*) electrodes. The value of the electrode radius is fixed fulfilling that $r_d = r_s = 0.01$ cm. $K = 0$. The values of the peak potential and peak current for a simple fast charge transfer process at planar electrodes are indicated (*dashed-dotted line*). Reproduced with permission from [21]



most common case of $K = 0$ ($K_{\text{eq}} \rightarrow \infty$). From curves in this figure, it can be seen that the cathodic peak potentials become less negative and the dimensionless current decreases as $\log Q_G$ (i.e., the scan rate) increases. For large Q_G values, both the peak potential and the peak current are independent of Q_G and their values coincide with those obtained for a simple charge transfer process at planar electrodes [16, 22]: $E_{\text{peak},f} - E_c^{\Theta'} = -28$ mV and $\psi_{\text{CV}}^{\text{cat},G,\text{peak},f} = 0.446$ (see dotted-dashed lines). The limiting Q_G value to observe this behavior increases with Λ_G . For small values of Λ_G (i.e., $\log \Lambda_G < -2$), no sensitivity of the response to the catalysis kinetics is observed and the differences between disc and spherical electrodes are due to geometrical reasons. On the contrary (i.e., $\log \Lambda_G > 0$), there are no differences in the peak potential and current at discs and spheres, and therefore, although a transient behavior is obtained, it does not depend on the particular electrode geometry but on the kinetics of the chemical step.

The dotted line in Fig. 6.7 marks the maximum values of the ratio (Λ_G/Q_G^2) for which a transient behavior is achieved, i.e., a well-defined peak is obtained in CV (with the relative difference between the peak and plateau currents being greater than 5 %). From the data shown in this figure, it is concluded that values of $(\Lambda_G/Q_G^2) < 0.4$ are required to observe a transient behavior, whatever the electrode radius. For $(\Lambda_G/Q_G^2) > 0.5$, the stationary CV response is obtained (for example, for $k_1 + k_2 = 10 \text{ s}^{-1}$, the stationary voltammogram corresponds to scan rates below 500 mV s^{-1}). Under these conditions, the expression of the voltammogram at disc electrodes is given by

$$\psi_{CV}^{\text{cat, disc, ss}} = \psi_{CV}^{\text{cat, radial}} \left\{ 1 + \sqrt{\Lambda_d} + 0.5465\Lambda_d \int_0^\infty u \exp\left(-\frac{0.39115}{\sqrt{u}} - \Lambda_d u^2\right) du \right\} \quad (6.82)$$

and at spherical electrodes by

$$\psi_{CV}^{\text{cat, sphe, ss}} = \psi_{CV}^{\text{cat, radial}} \left\{ 1 + \sqrt{\Lambda_s} \right\} \quad (6.83)$$

with $\psi_{CV}^{\text{cat, radial}}$ given by Eq. (6.80).

The stationary CV curves given by Eqs. (6.82) and (6.83) have a sigmoidal shape with the plateau currents at very positive (an) or negative (cath) potentials being for disc electrodes

$$\begin{aligned} \psi_{CV}^{\text{cat, disc, ss}})_{E \rightarrow \infty} &= \frac{-K}{1+K} \left(\frac{1}{Q_d}\right) \left\{ 1 + \sqrt{\Lambda_d} + 0.5465\Lambda_d \int_0^\infty u \exp\left(-\frac{0.39115}{\sqrt{u}} - \Lambda_d u^2\right) du \right\} \\ \psi_{CV}^{\text{cat, disc, ss}})_{E \rightarrow -\infty} &= \frac{1}{1+K} \left(\frac{1}{Q_d}\right) \left\{ 1 + \sqrt{\Lambda_d} + 0.5465\Lambda_d \int_0^\infty u \exp\left(-\frac{0.39115}{\sqrt{u}} - \Lambda_d u^2\right) du \right\} \end{aligned} \quad (6.84)$$

For spherical electrodes, these current plateaus take the following expressions:

$$\begin{aligned} \psi_{CV}^{\text{cat, sphe, ss}})_{E \rightarrow \infty} &= \frac{-K}{1+K} \left(\frac{1}{Q_s}\right) \left\{ 1 + \sqrt{\Lambda_s} \right\} \\ \psi_{CV}^{\text{cat, sphe, ss}})_{E \rightarrow -\infty} &= \frac{1}{1+K} \left(\frac{1}{Q_s}\right) \left\{ 1 + \sqrt{\Lambda_s} \right\} \end{aligned} \quad (6.85)$$

such that the ratio between the cathodic and anodic plateau currents is

$$\left| \frac{\psi_{CV}^{\text{cat, G, ss}})_{E \rightarrow \infty}}{\psi_{CV}^{\text{cat, G, ss}})_{E \rightarrow -\infty}} \right| = K, \quad (6.86)$$

independently of the electrode geometry.

Moreover, Eqs. (6.82) and (6.83) lead to two limiting cases, depending on the relationship between $\sqrt{D/(k_1 + k_2)}$ and the characteristic dimension of the electrode, q_G :

- For $\sqrt{D/(k_1 + k_2)} \geq 10q_G$, the kinetics of the chemical step is masked (the catalytic process behaves as a simple charge transfer process), and a microgeometrical steady state is reached:

$$\left. \begin{aligned} \psi_{CV}^{\text{cat, disc, ss}} &= \frac{4}{\pi} \psi_{CV}^{\text{cat, radial}} \\ \psi_{CV}^{\text{cat, sphe, ss}} &= \psi_{CV}^{\text{cat, radial}} \end{aligned} \right\} \quad (6.87)$$

- For $\sqrt{D/(k_1 + k_2)} \leq 10q_G$, the kinetic steady state is attained and the resulting CV curve is independent of the electrode radius and geometry:

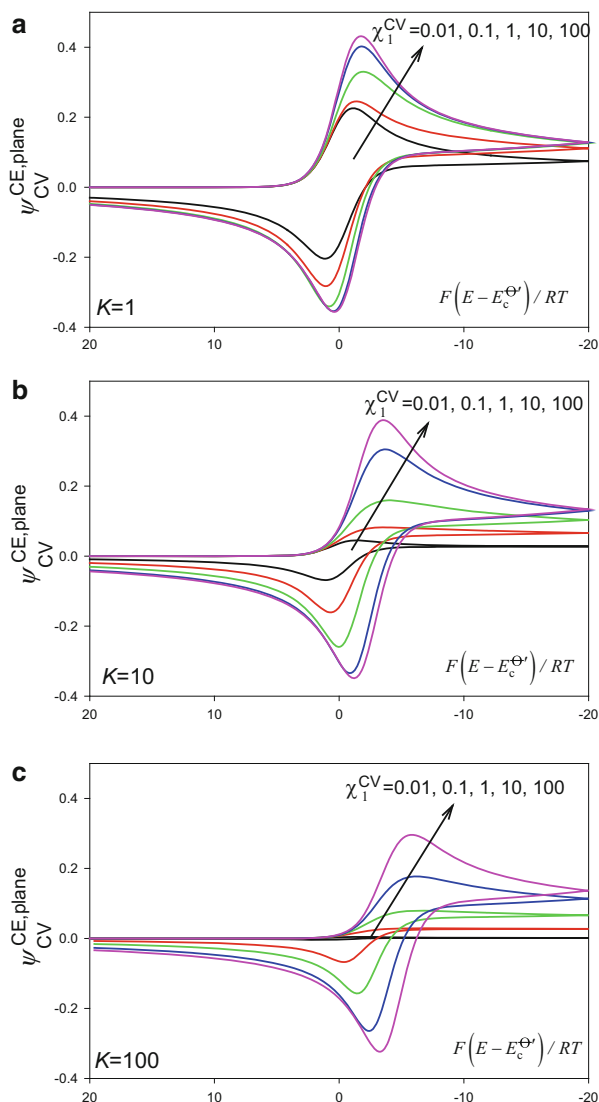
$$\psi_{CV}^{\text{cat, G, ss}} = \frac{1 - Ke^{\theta_p} e^{\theta_{in}}}{(1 + K)(1 + e^{\theta_p} e^{\theta_{in}})} \sqrt{\frac{(k_1 + k_2)}{a}} \quad (6.88)$$

6.3.2 CE and EC Mechanisms

After analyzing the first order catalytic mechanism we now address the CE and EC ones given in reaction scheme (6.IV). These mechanisms are also interesting as examples of simple reaction schemes where a heterogeneous charge transfer reaction is coupled with a homogeneous chemical one. However, as will be shown in this section, the analysis of the cyclic voltammograms corresponding to both reaction schemes by considering linear diffusion is much more complex than that carried out for a catalytic mechanism since the superposition principle cannot be applied because the surface concentrations of the participating species are dependent on time even when approximate treatments as kinetic steady state and diffusive-kinetic steady state (see Sects. 3.4.2–3.4.5 and 4.5.2) are made. As in Sects. 3.4.2 and 3.4.3, for the sake of simplicity, it will be considered that the electrochemical reaction takes place under Nernstian conditions, so that the homogeneous kinetics and the diffusion are the limiting factors.

The general mathematical treatment of CE and EC mechanisms is developed in Appendix H. In Cyclic Voltammetry, these complex expressions are, in general, simplified with great difficulty since, as was shown in Sects. 3.4.2 and 3.4.3, a true stationary current–potential response for these electrode processes (i.e., a time-independent response) cannot be achieved under linear diffusion conditions, as in the case of a catalytic mechanism, because for CE and EC mechanisms the perturbed region adjacent to the electrode surface by the diffusion of participating species (diffusion layer) will never be equal to that region in which the chemical equilibrium is perturbed (reaction layer; see scheme (3.1) in Sect. 3.4.4) except in the extreme case of an inert equilibrium. In other words, the assumption of a kinetic steady state (i.e., $\partial\phi/\partial t = 0$; see Eqs. (3.230)–(3.240)) does not imply the achievement of a stationary response as in the case of a catalytic mechanism, whatever the electrode geometry. In contrast, getting a stationary current–potential response in a CE and EC

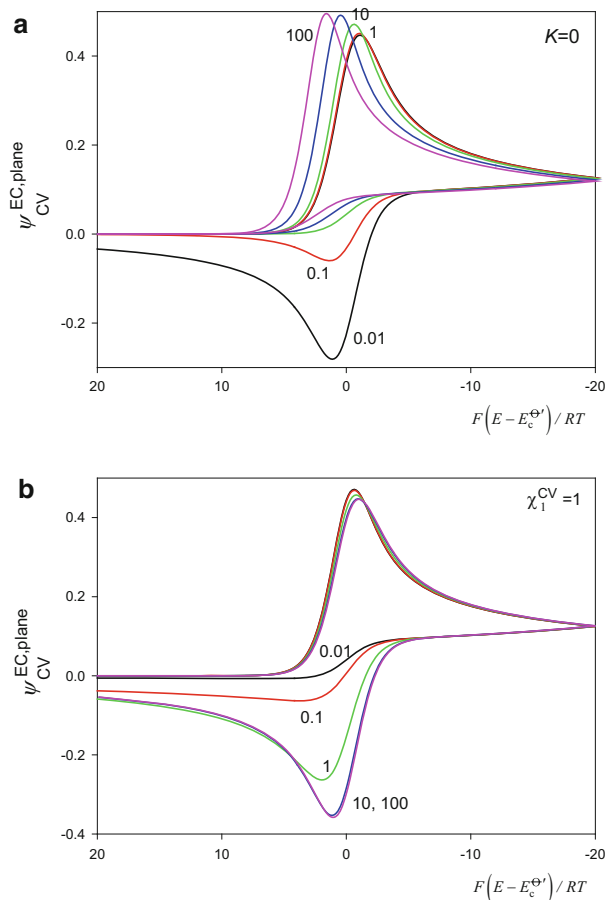
Fig. 6.8 Cyclic voltammograms corresponding to a CE mechanism at a planar electrode calculated by following the numerical procedure given in [23, 24] (see also Appendix I). Effect of the dimensionless rate constant $\chi_1^{\text{CV}} = (k_1 + k_2)/a$ on the current–potential response for three values of $K = 1/K_{\text{eq}}$: (a) 1; (b) 10; (c) 100. The values of $\chi_1^{\text{CV}} = k_1/a$ are: 10^{-2} (black); 0.1 (red); 1 (green); 10 (blue); 100 (pink)



mechanism also implies assuming that $\partial\xi/\partial t = 0$ and $\partial c_i/\partial t = 0$ (with $i = A$ or D for an EC or CE mechanism, respectively), and these conditions cannot be attained at macroelectrodes. In general, a simplification of the current–potential response corresponding to these mechanisms is very difficult since the influence of the chemical kinetics (through $(k_1 + k_2)t$ changes along the voltammogram. So, performing general extrapolations about the behavior of these processes in CV based on their responses in Single Pulse Techniques (like NPV) can be mere vagary.

In Fig. 6.8, normalized cyclic voltammograms corresponding to a CE mechanism for different values of $\chi_1^{\text{CV}} (= k_1/a)$ at three values of K are plotted. It is

Fig. 6.9 Cyclic voltammograms corresponding to an EC mechanism at a planar electrode calculated by following the numerical procedure given in [23, 24] (see also Appendix I). **(a)** Effect of the dimensionless rate constant $\chi_1^{\text{CV}} = k_1/a$ on the current–potential response. $K = 0$. The values of χ_1^{CV} appear in the figure. **(b)** Effect of the equilibrium constant $K_{\text{eq}} = 1/K$ on the current–potential response. $\chi_1^{\text{CV}} = 1$. The values of K appear in the figure



observed how in all the cases the peak height increases with χ_1^{CV} , i.e., when the scan rate decreases or the rate constant increases. This increase is more notable the lower the value of K , i.e., for higher K_{eq} , since the homogeneous chemical equilibrium becomes more labile under these conditions. In fact, for much higher χ_1^{CV} values, this mechanism behaves as a reversible E process with $E_{1/2} = E_c^{\Theta'} + (RT/F)\ln(1 + K)$ (see for example the pink curve in Fig. 6.8a). In contrast, when χ_1^{CV} decreases and K increases, the chemical kinetics has its maximum influence.

From these curves, it can be inferred that the peak potential of the cathodic scan shifts toward more cathodic values as K increases (K_{eq} decreases), since the electrochemical reaction becomes more difficult. Another feature of the voltammograms is that they shift toward more negative potentials when χ_1^{CV} increases, the more so the larger K , since $\chi_2^{\text{CV}} (= k_2/a)$ also increases.

In Fig. 6.9, the influence of χ_1^{CV} and K on the voltammograms of an EC mechanism has been plotted. From Fig. 6.9a (irreversible chemical reaction,

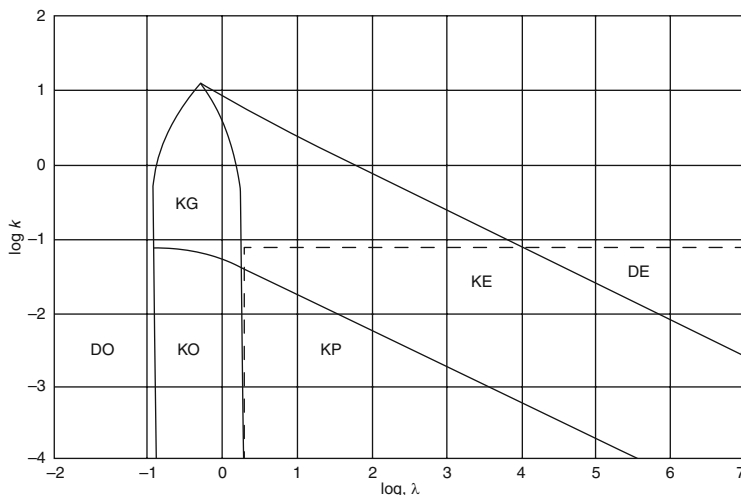


Fig. 6.10 Zone diagram corresponding to a CE mechanism in Cyclic Voltammetry. Reproduced with permission from [25]

$K = 0$), it can be seen how the anodic peak disappears when χ_1^{CV} increases, due to the growing depletion of species B. As can be seen in Fig. 6.9b, $K (= 1/K_{\text{eq}})$ has little influence on the forward scan, whereas the anodic peak decreases when K increases due to the increasing difficulty in the chemical transformation of C into B. For this mechanism, a significant influence of the chemical reaction requires large values of χ_1^{CV} and a very small value of K (large values of K_{eq}). The CV curves become identical to a reversible E process when $K \rightarrow \infty$ ($K_{\text{eq}} \rightarrow 0$). Thus, this mechanism can be easily detected by changing the scan rate since the anodic wave practically disappears when it decreases (species B does not have time to reach the electrode surface to be reoxidized to A before the reverse scan can be completed). Another characteristic of these curves is that for large values of χ_1^{CV} , the cathodic peak shifts toward more positive potentials. This is a consequence of considering that the electrochemical reaction takes place under reversible conditions.

The behavior of these mechanisms has been studied in an approximate way according to “zone diagrams” proposed by Saveant et al. [25] in which different types of responses are located in a 2D plot in terms of the values of the peak potentials calculated for different values of K_{eq} and χ^{CV} . Examples of these types of diagrams corresponding to EC and CE mechanisms appear in Figs. 6.10 and 6.11. Each zone in the diagram corresponds to a response obtained by inserting different simplifying assumptions in the general integral equations for the current that appear in Appendix H (e.g. $\chi^{\text{CV}} \rightarrow \infty$ or $K_{\text{eq}} = 0$). The meanings of the initials KG, DO, KO, etc., is given in detail in Tables 6 and 7 of [25].

As an example, in the case of CE mechanism when $K_{\text{eq}} \gg 1$ and $\chi^{\text{CV}} \ll 1$ (upper left corner of Fig. 6.10), the equilibrium is fully displaced to the right such that the preceding reaction has little effect on the electrochemical response (zone DO and

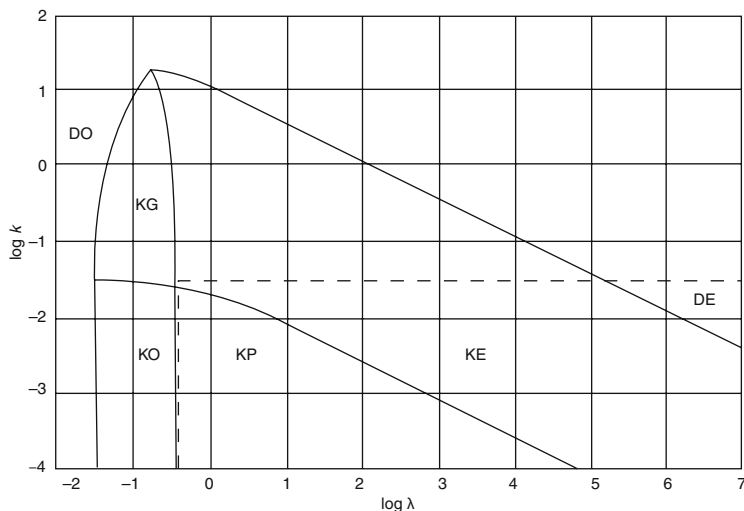


Fig. 6.11 Zone diagram corresponding to an EC mechanism in Cyclic Voltammetry. Reproduced with permission from [25]

curves in Fig. 6.8a). Contrarily, when $K_{\text{eq}} \ll 1$ and $\chi^{\text{CV}} \gg 1$ (lower right corner of Fig. 6.10), the influence of the chemical reaction is maximum (zone KP and curves in Fig. 6.8c) with kinetic steady-state and even diffusive kinetic steady-state approximations being applicable under these conditions. For intermediate values of K_{eq} and χ^{CV} (zones KO, KG, and KE), a rigorous treatment is required. Similar discussions can be carried out for the EC mechanism (see Figs. 6.9 and 6.11).

6.3.2.1 Steady-State Voltammetry and CE and EC Mechanisms

As discussed in Sect. 3.4.7, a stationary current–potential response of these reaction mechanisms can only be obtained when microelectrodes are used. In this case, the expression of the current–potential curves corresponding to CE and EC mechanisms for a microsphere of radius r_s is (see also Eqs. (3.239) and (3.240)):

$$\frac{I^{\text{CE, microsphere}}}{I_{\text{d,c}}^{\text{sph, ss}}(\zeta^*)} = \frac{1}{K(\delta_r^{\text{microsphere}}/r_s) + (1 + (1 + K)e^\eta)} \quad (6.89)$$

$$\frac{I^{\text{EC, microsphere}}}{I_{\text{d,c}}^{\text{sph, ss}}(c_A^*)} = \frac{1 + K}{1 + K + e^\eta(K + \delta_r^{\text{microsphere}}/r_s)} \quad (6.90)$$

with

$$I_{d,c}^{\text{sphc,ss}}(\zeta^*) = 4\pi Fr_s D \zeta^* \quad (6.91)$$

$$I_{d,c}^{\text{sphc,ss}}(c_A^*) = 4\pi Fr_s D c_A^* \quad (6.92)$$

$$\delta_r^{\text{microsphe}} = \frac{1}{\frac{1}{r_s} + \sqrt{\frac{k}{D}}} \quad (6.93)$$

and $k = k_1 + k_2$. The diffusion layer thickness under steady-state conditions coincides with r_s .

Equations (6.89) and (6.90) are only applicable if $\sqrt{Dt}/r_s > 11.3$ with an error of less than 5 %. However, it is interesting to highlight that the detection of the homogeneous kinetics is only possible in a narrow interval of microelectrodes radius ($\sqrt{D/k}/10 \leq r_s \leq \sqrt{\pi Dt}/11.3$) in order for the term $\sqrt{k/D}$ in the reaction layer thickness expression given by Eq. (6.93) not to be negligible with respect to the term $1/r_s$. This range corresponds to $\delta_r^{\text{microsphe}}/r_s < 0.8$ (with $\delta_r^{\text{microsphe}}$ given by Eq. (6.93)). So, for $k = 100 \text{ s}^{-1}$, $D = 10^{-5} \text{ cm}^2 \text{ s}^{-1}$, and $t = 1 \text{ s}$, this condition is equivalent to $(0.6 \leq r_s \leq 3) \text{ }\mu\text{m}$.

Under these conditions, the CV curves are coincident with those obtained in Normal Pulse Voltammetry and the half-wave potentials corresponding to CE and EC mechanisms become independent of time and are given by Eqs. (3.239) and (3.240) by changing δ^{sphc} by r_s .

In the case of a catalytic mechanism, the steady-state voltammetric current-potential curve can be written as (see Eq. (3.243)):

$$\frac{I^{\text{cat, microsphe}}}{FA_s D \zeta^*} = \frac{\delta_r^{\text{microsphe}}}{1 + K} \frac{1 - Ke^\eta}{1 + e^\eta} \quad (6.94)$$

For this reaction scheme, only the condition $\sqrt{D/k} \leq 10r_s$ has to be fulfilled for the kinetic reaction to be detected in a spherical microelectrode, since the catalytic mechanism presents the reaction layer, whose expression is also given by Eq. (6.93). The influence of both reaction and diffusion layers is shown in Fig. 6.12 for a CE and a catalytic mechanism.

The reasons for the different behavior of these mechanisms are explained in Sect. 3.4.4.

A similar discussion can be made, although only in an approximate way, for disc microelectrodes by assuming as valid the analogy between the disc and sphere radius, i.e., by making the change $r_s = \pi r_d/4$ in the expressions of the diffusion and reaction layers (see Sect. 3.4.7).

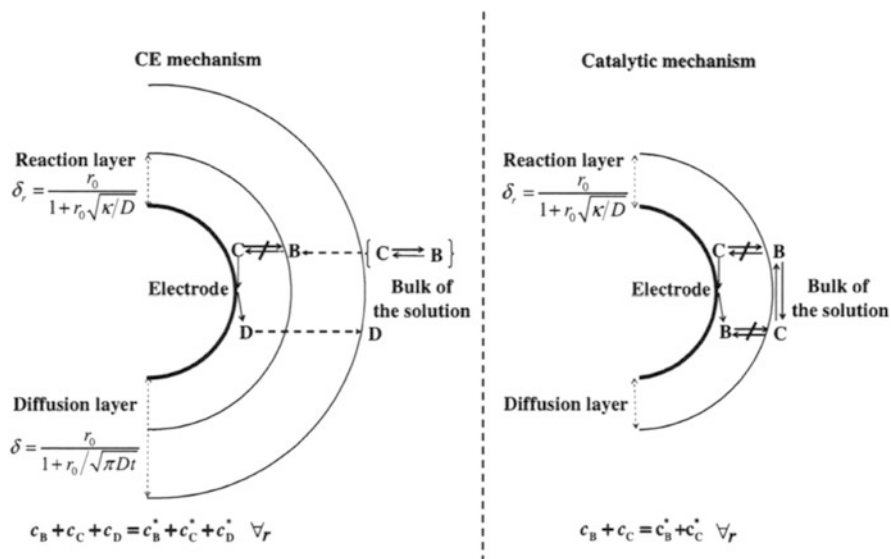
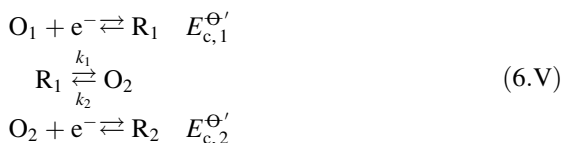


Fig. 6.12 Steady-state spherical diffusion and reaction layers in the case of CE and catalytic mechanisms. Reproduced with permission from [26]

6.3.3 ECE Mechanism

As indicated in Sect. 3.4.8, by considering that the two-electron transfers behave as reversible, the ECE mechanism can be written [27–30]:



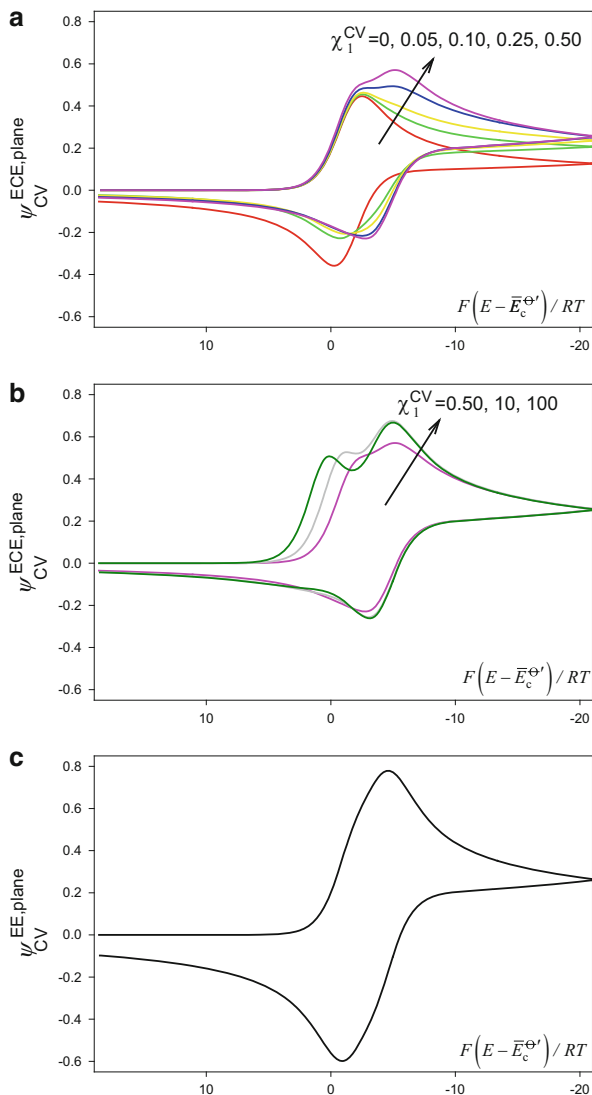
that is, as an EC mechanism in which the reaction product O_2 is capable of being reduced (or oxidized) at the electrode surface. Usually, the chemical reaction is irreversible, i.e., $k_2 \ll k_1$. It can easily be inferred that the voltogram corresponding to this mechanism will depend on the rate constant of the chemical reaction and on the difference between the formal potentials of the two electrochemical steps: $\Delta E_c^{\ominus'} = E_{c,2}^{\ominus'} - E_{c,1}^{\ominus'}$.

As in the case of a two-electron transfer reaction (EE mechanism), there exists the possibility of the following disproportionation reaction at the electrode surface:



with the equilibrium constant

Fig. 6.13 (a, b) Cyclic voltammograms corresponding to an ECE mechanism at planar electrodes calculated by following the numerical procedure given in [23, 24] (see also Appendix I). $\Delta E_c^{\ominus'} = -71.2\text{mV}$. $K = 0$. The values of χ_1^{CV} appear in the figure. (c) CV curves of a reversible two-electron charge transfer process with $\Delta E_c^{\ominus'} = -71.2\text{mV}$ calculated from Eq. (6.33)



$$K_{\text{eq}} = e^{-\frac{F\Delta E_c^{\ominus'}}{RT}} \quad (6.95)$$

So, it can be deduced that the voltammograms corresponding to an ECE mechanism are influenced by reaction (6.VI) in a similar way to those corresponding to an EE process, although in the case of the former the CV curves are affected by reaction (6.VI) even when the diffusion coefficients of the different participating species are assumed to be equal (see also Sect. 3.4.8 for more details). Hereinafter, the intervention of reaction (6.VI) is disregarded for simplicity.

In Figs. 6.13. and 6.14, the current–potential curves corresponding to an ECE mechanism under different kinetic conditions are plotted to show how the

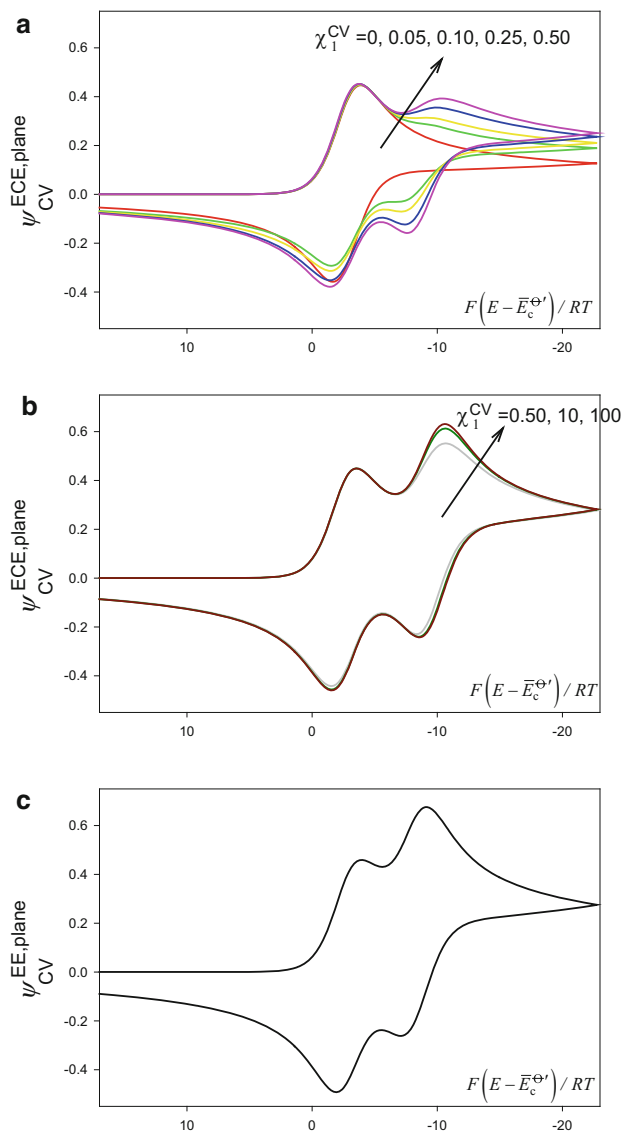


Fig. 6.14 (a, b) Cyclic voltammograms corresponding to an ECE mechanism at planar electrodes calculated by following the numerical procedure given in [23, 24] (see also Appendix I). $\Delta E_c^{\ominus'} = -142.4$ mV. $K = 3$. The values of χ_1^{CV} appear in the figure. (c) CV curves of a reversible two-electron charge transfer process with $\Delta E_c^{\ominus'} = -142.4$ mV calculated from Eq. (6.33)

intermediate chemical reaction can complicate the voltgrams of the two-electron transfer processes. Curve c in Figs. 6.13 and 6.14 corresponds to an EE process with the same value of $\Delta E_c^{\ominus'}$. All the curves are plotted versus $E - \bar{E}_c^{\ominus'}$, with $\bar{E}_c^{\ominus'} = (E_{c,1}^{\ominus'} + E_{c,2}^{\ominus'})/2$.

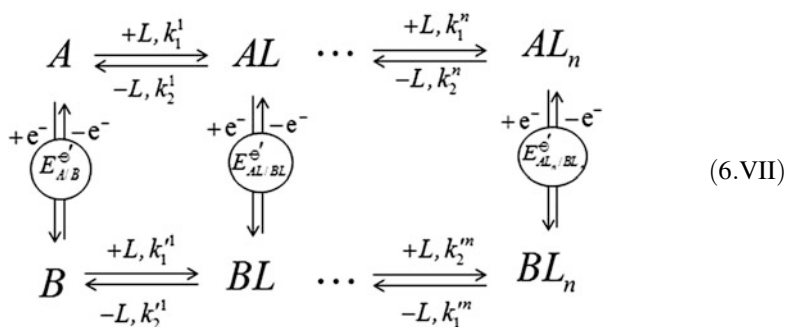
The case corresponding to an irreversible chemical reaction ($k_1 \gg k_2$) is shown in Fig. 6.13. A strong splitting of the voltogram caused by the increase of $\chi_1^{\text{CV}} (= k_1/a)$ due to the facilitation of the first electron transfer can be observed. The second peak in the forward scan increases with χ_1^{CV} (i.e., with a decrease in the scan rate) due to an increasing time for the formation of species O_2 . Indeed, when $\chi_1^{\text{CV}} = 0$, the voltogram only shows one pair of peaks corresponding to the redox couple O_1/R_1 since no further steps take place under these conditions. For the $\Delta E_c^{\ominus'}$ value used (-71.2 mV), the response of EE and ECE mechanisms can be well differentiated because the CV curve presents two peaks in the forward scan and only one in the reverse.

From Fig. 6.14, it can be deduced that for $\Delta E_c^{\ominus'} = -142.4$ mV, the two mechanisms show distinctly different voltammograms for small values of $\chi^{\text{CV}} (= (k_1 + k_2)/a)$, whereas the responses become more similar as the chemical kinetics is faster. Thus, for $\chi^{\text{CV}} > 100$ the voltammetric signal of the ECE mechanism is equivalent to that of an EE mechanism where the half-wave potentials correspond to those of the EC (first electron transfer) and CE (second electron transfer) mechanisms under fully labile conditions (Eqs. (3.201c) and (3.221b) for $\delta_r \rightarrow 0$, respectively).

In any case, the presence of a chemical reaction (ECE mechanism) under these conditions can be detected by changing the scan rate, since the dimensionless cyclic voltammograms will remain insensitive to this change in the case of a reversible EE process unlike what is observed in the presence of kinetic effects.

6.3.4 Reversible Charge Transfers Preceded and Followed by Several Complexation Reactions in Equilibrium at Electrodes of Any Geometry (“Ladder” Mechanism)

In this section, it is considered the general situation where a species A is electro-reduced to B and both species A and B take part in a number of chemical equilibria in solution. These may refer to their complexation with a ligand L [31, 32], protonation [33, 34], or formation of ion pairs [35, 36], the products of which ($AL, BL, \dots, AL_n, BL_n$) are also electro-active in line with the following scheme [37]:



Ligand L is assumed to be present at high concentration ($c_L^* \gg c_A^*, c_{AL}^*, c_{AL_n}^*$) and k_j^i and $k_j^{i'}$ ($j = 1, 2; i = 1, 2, \dots, n$) represent the (pseudo)first-order forward and

backward rate constants of the chemical reactions. Note that this scheme allows different common mechanisms to be studied by adjusting the values of the formation equilibrium constants. Thus, the situation where only the oxidized (A) or the reduced (B) species is involved in the homogeneous chemical equilibria (i.e., only one species reacts in solution) can be studied by setting to zero the equilibrium constant(s) of the other species (C_n^{eq} E^{rev} - or E^{rev} C_n^{eq} -type mechanisms). The E^{rev} C_n^{eq} mechanism is very usual in real systems since the electron transfer generally increases the instability and reactivity of the chemical species, for example, by forming radicals.

In Sect. 3.4.10, it was presented the solution to this reaction scheme when a single potential step is applied. Next the application of any succession of potential steps of the same duration τ , is considered. The general solution corresponding to the p th applied potential can be easily obtained because this is a linear problem, and, therefore, any linear combination of solutions is also a solution of the problem, and also that the interfacial concentrations of all the participating species only depend on the potential and are independent of the “history” of the process regardless of the electrode geometry considered (see Sect. 5.2.1). The two above conditions imply that the superposition principle can be applied [38] in such a way that the solution for the current corresponding to the application of the p th potential can be written as follows:

$$\frac{I_p^{\text{ladder,G}}}{FA_G D} = \sum_{m=1}^p \left(c_T^{\text{A}(m-1)} - c_T^{\text{A}(m)} \right) f_G((p-m+1)\tau, q_G) \quad (6.96)$$

where

$$Z_m^{\text{ladder}} = \frac{c_T^{\text{A}(m-1)} - c_T^{\text{A}(m)}}{c^*} = \left(\frac{1}{1 + \omega e^{\eta_m}} - \frac{1}{1 + \omega e^{\eta_{m-1}}} \right) \quad (6.97)$$

$$\omega = \frac{1 + \sum_{i=1}^n \beta_i}{1 + \sum_{i=1}^n \beta_i} \quad (6.98)$$

with c^* being the total concentration of species A in the bulk of the solution (i.e., $c^* = c_A^* + c_{\text{AL}}^* + \dots + c_{\text{AL}_n}^*$). η_m is given by

$$\eta_m = \left. \frac{F}{RT} \left(E_m - E_{\text{A/B}}^{\ominus'} \right), \quad m \geq 1 \right\} \quad (6.99)$$

In Eq. (6.96), c_T^{A} is the total concentration of species A (for species B an analogous definition can be found in Eq. (3.275)), given by

$$c_T^{\text{A}}(q, t) = c_A(q, t) + \sum_{i=1}^n c_{\text{AL}_i}(q, t) \quad (6.100)$$

and $D = D_{\text{eff}}^{\text{A}} = D_{\text{eff}}^{\text{B}}$, with $D_{\text{eff}}^{\text{A}}$ and $D_{\text{eff}}^{\text{B}}$ being the effective diffusion coefficients of the pseudo-species A_T and B_T , respectively:

$$D_{\text{eff}}^{\text{A}} = \frac{D_{\text{A}} + \sum_{i=1}^n D_{\text{AL}_i} \beta_i}{1 + \sum_{i=1}^n \beta_i} \quad (6.101)$$

$$D_{\text{eff}}^{\text{B}} = \frac{D_{\text{B}} + \sum_{i=1}^n D_{\text{BL}_i} \beta'_i}{1 + \sum_{i=1}^n \beta'_i} \quad (6.102)$$

β_i and β'_i represent the overall formation constant for the different complexes of species A or B, respectively, initially present in solution:

$$\left. \begin{aligned} \beta_i &= \prod_{m=1}^i K_m c_{\text{L}}^* = \frac{c_{\text{AL}_i}(q, t)}{c_{\text{A}}(q, t)} \\ \beta'_i &= \prod_{m=1}^i K'_m c_{\text{L}}^* = \frac{c_{\text{BL}_i}(q, t)}{c_{\text{B}}(q, t)} \end{aligned} \right\} \forall q, t; \quad i \geq 1; \quad (6.103)$$

with K_m and K'_m being

$$\begin{aligned} K_m &= \frac{c_{\text{AL}_m}(q, t)}{c_{\text{AL}_{m-1}}(q, t) c_{\text{L}}^*} \\ K'_m &= \frac{c_{\text{BL}_m}(q, t)}{c_{\text{BL}_{m-1}}(q, t) c_{\text{L}}^*} \end{aligned} \quad (6.104)$$

and $f_{\text{G}}((p-m+1)\tau, q_{\text{G}})$ is defined in Table 2.3 for each electrode geometry.

As Eq. (6.96) is formally identical to that corresponding to a simple reversible electron transfer process, the dependence on the different complexation reactions is contained in the parameter ω (Eq. (6.98)). The I/E responses corresponding to this process shift with ω as a function of the magnitude of the equilibrium constants of the different complexation reactions involved (see Fig. 6.15).

Equation (6.96) can be applied to any sequence of constant potential pulses and so to any voltammetric technique. In the particular case of cyclic voltammetry, the waveform is given by Eq. (5.1) and the current takes the form

$$\begin{aligned} \psi_{\text{CV}}^{\text{ladder, G}} &= \frac{I_{\text{p}}^{\text{ladder, G}}}{F A_{\text{G}} c^* \sqrt{D a}} = \pm \sqrt{\frac{D}{a}} \sum_{m=1}^p Z_m^{\text{ladder}} f_{\text{G}}((p-m+1)\tau, q_{\text{G}}) \\ p &= 1, \dots, N \end{aligned} \quad (6.105)$$

with a given by Eq. (6.25).

When the characteristic dimension of the electrode is such that $q_{\text{G}} \ll \sqrt{\pi D t}$ (with q_{G} being equal to r_{s} , r_{c} w , or r_{d}), stationary or pseudo-stationary conditions are

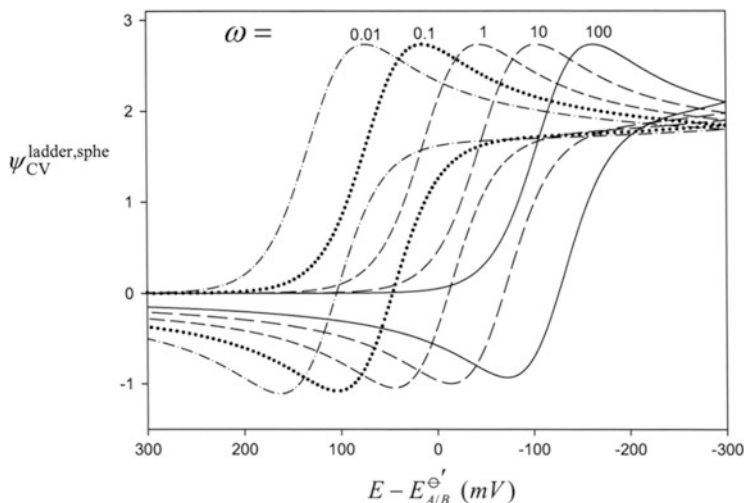


Fig. 6.15 Influence of the parameter ω on the response in CV (Eq. (6.105)) for a spherical electrode of radii $50\ \mu\text{m}$. $|\Delta E| = 0.01\ \text{mV}$, $v = 100\ \text{mV s}^{-1}$. $T = 298\ \text{K}$, $D = 10^{-5}\ \text{cm}^2\ \text{s}^{-1}$

attained and the current in each pulse is dependent only on the applied potential, being independent of the previous pulses. Under these conditions, the expression for the CV signals greatly simplifies. For the case of disc and spheres, a true steady-state current–potential response is obtained under these conditions, while for cylinders and bands only pseudo-stationary currents are achieved.

From the analytical equation (6.105) obtained for CV, the study of the current–potential response in these techniques can be performed along with the analysis of the influence of the key variables. First, the effect of the parameter ω (Eq. (6.98)) is shown in Fig. 6.15 where the curves are plotted for a spherical electrode of $50\ \mu\text{m}$ radius. Note that large ω -values relate to the situation where the complexes of the reactant species A are more stable than those of species B, whereas the opposite situation is found for small ω -values. As can be observed, the only influence of this parameter is the shift of the curves toward more negative potentials when ω increases on account of the hindering of the electro-reduction reaction due to the stabilization of the oxidized species with respect to the reduced ones. According to Eq. (3.289), an “apparent” formal potential can be defined as follows:

$$E_{\text{app}}^{\ominus'} = E_{\text{A/B}}^{\ominus'} + \frac{RT}{F} \ln\left(\frac{1}{\omega}\right) \quad (6.106)$$

The effect of the electrode geometry and size is shown in Fig. 6.16, where the curves are plotted for $\omega = 5$ and different values of the characteristic dimensions of microelectrodes of different geometries (r_s , r_d , and $w/2$ for spheres, discs, and bands respectively with $r_s = r_d = w/2$). For large electrodes (Fig. 6.16a), the curves (i.e., the current density) show small differences because diffusion is almost planar and

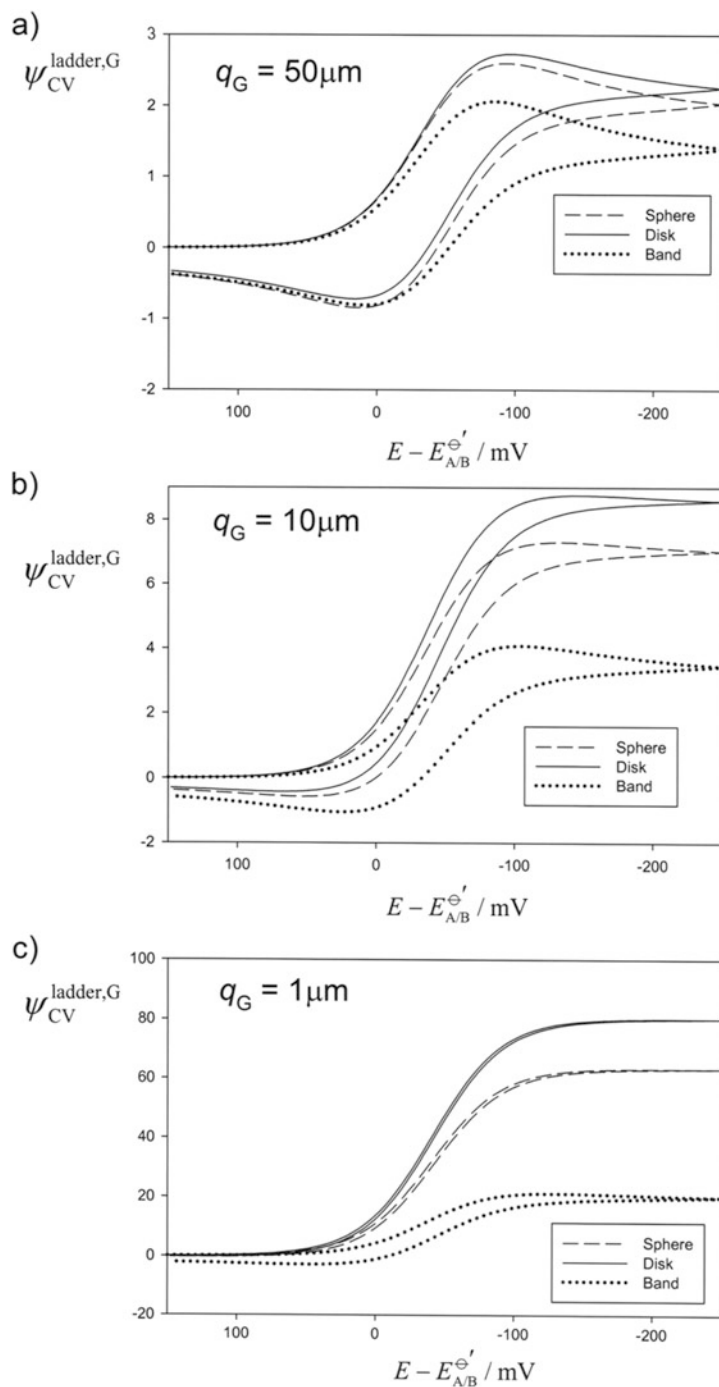


Fig. 6.16 CV [Eq. (6.105)] curves for electrodes of different geometries and characteristic dimensions ($q_G = r_s = r_d = w/2$) and $\omega = 5$. $|\Delta E| = 0.01\text{mV}$, $v = 100\text{mVs}^{-1}$. $T = 298\text{K}$, $D = 10^{-5}\text{cm}^2\text{s}^{-1}$

the electrode geometry plays a less important role. However, these differences are enhanced if the electrode size is decreased toward the steady state (spheres and discs) or pseudo-steady (bands). Thus, the highest current density is observed for discs and the lowest for bands. The position of the voltammograms is not influenced by the electrode geometry and size, so small uncertainties in their determination do not affect the quantitative study of the chemical equilibria.

6.4 Surface-Bound Molecules

The electrochemical behavior of molecules attached to conducting surfaces (i.e., electrode surfaces) forming electro-active monolayers is discussed in the following sections. This situation has frequently been called “modified electrodes” in the literature [39]. The electro-active character of these monolayers arises from the presence of redox molecules on them which are susceptible to transfer to or receive charge from the supporting electrode as well as from species in solution (in this last situation, the attached molecules act as redox mediators between the electrode and the solution and are responsible for the appearance of electrocatalytic processes [39, 40]). Multipulse and Sweep Electrochemical techniques like SCV and CV have proven to be very necessary tools for understanding the behavior of these interfaces and the processes taking place at them.

The preparation and characterization of modified electrodes has been a very active area of Electrochemistry since the 1970s [39, 41, 42]. Among the great variety of molecules that can be immobilized at the electrode surface are viologens, anthraquinones, polyoxometalates, inorganic polymers, biological molecules (enzymes, proteins, . . .), etc. (see Fig. 6.17 for an example of an alkylthiolferrocene monolayer on gold) [43]. Once a particular molecule is attached to the electrode surface, the last one can mimic the chemical, electrochemical, optical, etc., properties of the chemical moiety and thus gain a new functionality. Moreover, these systems enable a molecular-level control of both the nature of the chemical functional groups attached and also their topology [39, 44], which is why they are considered as nanostructured interfaces.

Concerning the substrate, practically any material can be used to form a modified electrode, although the most used are gold, silver, platinum, mercury, and carbon (in its different variants, like glassy carbon, Highly Oriented Pyrolytic Graphite (HOPG), or Boron-Doped Diamond (BDD) electrodes [39]).

From the theoretical point of view, the analysis of the faradaic electrochemical behavior of these systems is simpler than that corresponding to solution soluble species since the mass transport is not present, a fact which greatly simplifies the modellization of these processes (note that, in general, for a redox species in solution, a two- or three-variable problem (coordinates and time) needs to be considered, whereas at the electrode surface only time variable is needed). Thus, it is possible to deduce the electrochemical response of these molecules in a more direct way.

Fig. 6.17 Inferred structure of a monolayer formed by coadsorption of a ferrocene-terminated alkane thiol (highlighted with *black bonds*) and the unsubstituted alkane thiol on Au(111). The conformation around the ester group is chosen to illustrate the closest approach of the ferrocene group to the electrode (~ 20 Å). Reproduced from [43] with permission



The different assumptions needed to make a statement of this problem will be presented in the following section. Then the general solution corresponding to the application of a sequence of potential pulses to attached molecules giving rise to simple charge transfer processes and particular solution corresponding to Multipulse Chronoamperometry and Chronocoulometry and Staircase Voltammetry will be deduced. Cyclic Voltammetry has a special status and will be discussed separately. Finally, some effects that cause deviation from the ideal behavior and more complex reaction schemes like multielectronic processes and chemical reactions in the solution coupled to the surface redox conversion will be discussed.

6.4.1 *One-Electron Electrochemical Reactions: Statement of the Problem*

In the following, the quasi-reversible reduction of electro-active surface-confined species O in line with the following reaction scheme is considered:



In this scheme, O_{ad} and R_{ad} refer to the oxidized and reduced species attached to the electrode surface. The amount of these species is given by the corresponding

surface excesses, Γ_{O} or Γ_{R} (in mol cm^{-2} or mol m^{-2} instead of mol cm^{-3} or mol m^{-3} used for volumetric concentrations). In the theoretical treatment of the electrochemical behavior of this redox couple, the following assumptions are made:

- The total amount of adsorbed species remains constant during the experiment, so, whatever the reversibility degree of the charge transfer process:

$$\Gamma_{\text{O}} + \Gamma_{\text{R}} = \Gamma_{\text{T}} \quad (6.107)$$

is fulfilled for any potential pulse.

- The maximum amount of species O and R at the surface Γ_{M} is independent of the applied potential. This condition implies that no interactions between the surface-confined molecules are considered [45], that is, a low amount of species is at the surface (i.e., $\Gamma_{\text{T}} < \Gamma_{\text{M}}$). In other words, low values of the ratio $\Gamma_i/\Gamma_{\text{M}}$ are considered, with $i = \text{O}$ or R (this situation has been denoted “sub-monolayer,” with the monolayer corresponding to a totally covered electrode surface).
- Charging and faradaic currents are considered as separable.

Under the above conditions, the faradaic current is the result of the redox conversion of the immobilized redox species. When a sequence of potential pulses E_1, E_2, \dots, E_p is considered, the current for the p th potential pulse is given by

$$\frac{I_p}{FA} = -\frac{d\Gamma_{\text{O}}^{(p)}}{dt} = \frac{d\Gamma_{\text{R}}^{(p)}}{dt} \quad (6.108)$$

and the relationship between the current and the kinetics of the electrode reaction can be written as

$$\frac{I_p}{FA} = k_{\text{red},p}\Gamma_{\text{O}}^{(p)} - k_{\text{ox},p}\Gamma_{\text{R}}^{(p)} \quad (6.109)$$

with $k_{\text{red},p}$ and $k_{\text{ox},p}$ being the rate constants for the reduction and oxidation processes, respectively. The form of the potential dependence of these constants is given by the particular kinetic formalist considered (i.e., Butler–Volmer or Marcus–Hush). In any case $k_{\text{ox},p}/k_{\text{red},p} = e^{\eta_p}$ with $\eta_p = F(E_p - E_c^{\Theta'})/RT$. $E_c^{\Theta'}$ is the formal potential of the redox couple. Note that for surface-confined molecules in relation to solution soluble ones the rate constant for the charge transfer process is given in s^{-1} rather than in cm s^{-1} or m s^{-1} .

If the charge transfer reaction is fast, the surface excesses are related by Nernst relationship:

$$\Gamma_{\text{O}}^{(p)} = \Gamma_{\text{R}}^{(p)} e^{\eta_p} \quad (6.110)$$

The current is the most studied variable in the analysis of the electrochemical behavior of these systems. However, another interesting magnitude which provides

valuable information is the converted charge, Q_p , defined as (see Eq. (6.108))¹ [46]:

$$Q_p = \int_0^{t_p} I_p dt_p = -FA \left[\Gamma_O^{(p)} \right]_{t_p=0}^{t_p} \quad (6.111)$$

6.4.1.1 Application of a Potential Pulse

When a constant potential E_1 is applied to the electrode during a time t_1 ($0 \leq t_1 \leq \tau_1$), the rate equation in line with Eqs. (6.108)–(6.109) is given by (see Eq. (6.107)):

$$\frac{I_1}{FA} = -\frac{d\Gamma_O^{(1)}}{dt} = k_{\text{red},1}\Gamma_O^{(1)} - k_{\text{ox},1}(\Gamma_T - \Gamma_O^{(1)}) = k_{T,1}\Gamma_O^{(1)} - k_{\text{ox},1}\Gamma_T \quad (6.112)$$

with

$$k_{T,1} = k_{\text{red},1} + k_{\text{ox},1} \quad (6.113)$$

$\Gamma_O^{(1)}$ is the surface excess of species O (mol cm^{-2}). By assuming that at $t_1 = 0$, the monolayer is totally oxidized ($\Gamma_O^{(1)}(0) = \Gamma_T$), the solution of the differential equation (6.112) leads to the following expression for the surface excess of oxidized species [43, 46]:

$$\Gamma_O^{(1)} = \Gamma_T \frac{k_{\text{red},1} e^{-k_{T,1}t_1} + k_{\text{ox},1}}{k_{T,1}} \quad (6.114)$$

By combining equations (6.111) and (6.114), the transformed charge is easily obtained:

$$Q_1 = FA\Gamma_T \left(\frac{k_{\text{red},1}(1 - e^{-k_{T,1}t_1})}{k_{T,1}} \right) \quad (6.115)$$

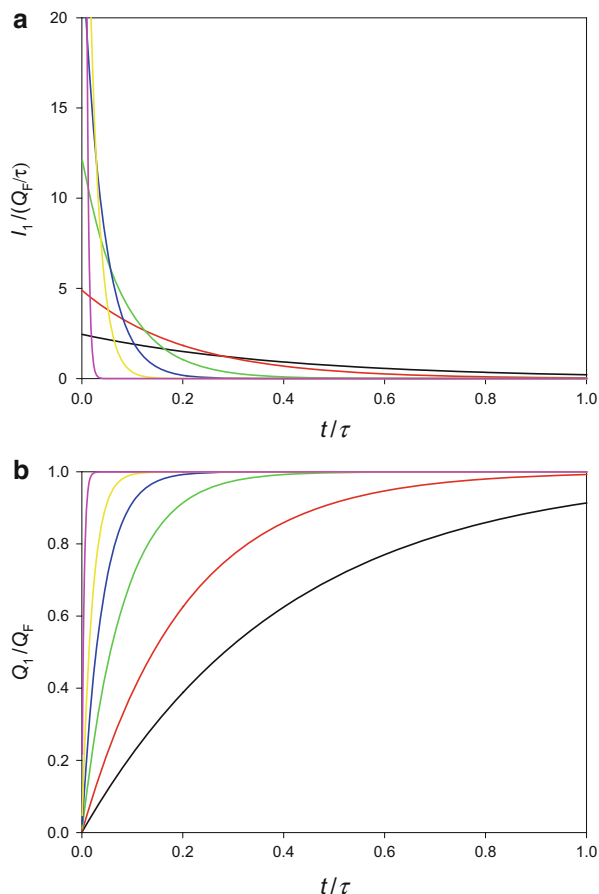
Equations (6.114) or (6.115) enable us to deduce the corresponding expression for the current:

$$I_1 = -FA \left(\frac{d\Gamma_O^{(1)}}{dt} \right) = \left(\frac{dQ_1}{dt} \right) = FA\Gamma_T k_{\text{red},1} e^{-k_{T,1}t_1} \quad (6.116)$$

In the following discussion, it is assumed that the expression of the rate constants for reduction and oxidation processes is given by the Butler–Volmer formalist:

¹ The experimental measurement of the converted charge can be made easily by integrating the recorded current.

Fig. 6.18 Dimensionless current–time (a) and charge–time (b) curves corresponding to the application of a constant potential $E_1 - E_c^{\ominus'} = -0.2$ V to an electro-active monolayer calculated from Eqs. (6.116) and (6.115) assuming a Butler–Volmer kinetics with $\alpha = 0.5$. The values of $(k^0\tau)$ are 0.05 (black), 0.1 (red), 0.25 (green), 0.5 (blue), 1 (yellow), and 5 (pink), $\tau = \tau_1$



$$\left. \begin{aligned} k_{\text{red}} &= k^0 e^{-\alpha\eta} \\ k_{\text{ox}} &= k_{\text{red}} e^{\eta} \end{aligned} \right\} \quad (6.117)$$

with $\eta = F(E - E_c^{\ominus'})/RT$. E is the potential pulse applied and k^0 and α are the standard rate constant and charge transfer coefficient for the electrode reaction in reaction scheme (6.VIII).

The temporal evolution of the current I_1 and the converted charge Q_1 have been plotted in Fig. 6.18 for different values of the dimensionless rate constant $k^0\tau_1$ and $\alpha = 0.5$. Both responses have been written in their dimensionless forms, $I_{N,1} = I_1/(Q_F/\tau_1)$ and $Q_{N,1} = Q_1/Q_F$, with Q_F given by

$$Q_F = FA\Gamma_T \quad (6.118)$$

From the curves in this figure, it can be deduced that the current decreases and the charge increases faster the higher $k^0\tau_1$ is (i.e., the higher the reversibility degree

of the charge transfer process). Indeed, for high enough values of the dimensionless rate constant, the charge takes the following constant value:

$$Q_{N,1} \Big|_{k^0 \tau_1 \gg 1} = Q_{N,1} \Big|_{\text{reversible}} = \frac{1}{1 + e^{\eta_1}} \quad (6.119)$$

and the current becomes zero²:

$$I_{N,1} \Big|_{k^0 \tau_1 \gg 1} = I_{N,1} \Big|_{\text{reversible}} = 0 \quad (6.120)$$

For very small values of $k^0 \tau_1$ (i.e., for irreversible processes), very negative potentials are needed to obtain a measurable response and under these conditions $k_{\text{red},1} \gg k_{\text{ox},1}$. By introducing this condition in Eqs. (6.115) and (6.116), the expressions of the time-dependent converted charge and current become

$$Q_{N,1} \Big|_{k^0 \tau_1 \ll 1} = Q_{N,1} \Big|_{\text{irreversible}} \cong 1 - e^{-k_{\text{red},1} t_1} \quad (6.121)$$

$$I_{N,1} \Big|_{k^0 \tau_1 \ll 1} = I_{N,1} \Big|_{\text{irreversible}} \cong k_{\text{red},1} \tau_1 e^{-k_{\text{red},1} t_1} \quad (6.122)$$

From Eq. (6.122), is clear that a logarithmic plot of the current versus time must be linear and this enables us to determine the values of $k_{\text{red},1}$ from the slope [43, 47].

The expressions for the charge–time and current–time responses for an irreversible anodic process can be obtained from Eqs. (6.115) and (6.116) by inserting the condition $k_{\text{red},1} \ll k_{\text{ox},1}$, and the resulting equations are logically identical to Eqs. (6.121) and (6.122) by changing their sign and $k_{\text{red},1}$ for $k_{\text{ox},1}$.

6.4.1.2 Application of a Sequence of Potential Pulses

The treatment developed in the previous section for a single potential pulse can be generalized for a sequence of potential pulses. Thus, the current I_p corresponding to reduction of O species when the potential pulse E_p of the arbitrary sequence E_1, E_2, \dots, E_p is applied is given by Eq. (6.109). Moreover, the total time elapsed between the application of the first and p th potential steps is given by

$$t = \tau_1 + \tau_2 + \dots + \tau_{p-1} + t_p \quad (6.123)$$

with $0 \leq t_p \leq \tau_p$.

From Eqs. (6.108)–(6.109), the expression of the surface excess of the oxidized species $\Gamma_O^{(p)}$ corresponding to E_p is immediately obtained simply by integrating it with respect to t_p ,

²Note that the current has a paradoxical behavior at times close to zero. When $k^0 \tau_1 \gg 1$ and $t_1 \rightarrow 0$, the current takes the form of a Dirac's delta function, which in practice means that although it could take a very large value, it will be not possible to record it.

$$\int_{\Gamma_{\text{O}}^{(p)}(t_p=0)}^{\Gamma_{\text{O}}^{(p)}(t_p)} \frac{d\Gamma_{\text{O}}^{(p)}}{k_{\text{ox},p}\Gamma_{\text{T}} - (k_{\text{red},p} + k_{\text{ox},p})\Gamma_{\text{O}}^{(p)}} = \int_{t_p=0}^{t_p} dt_p \quad (6.124)$$

with $\Gamma_{\text{O}}^{(p)}(t_p = 0)$ being the value of the surface excess of the oxidized species at the beginning of the application of E_p , i.e., for $t = \tau_1 + \tau_2 + \dots + \tau_{p-1}$.

By solving both integrals in (6.124), the following expression for $\Gamma_{\text{O}}^{(p)}$ is deduced:

$$\Gamma_{\text{O}}^{(p)} = \frac{1}{k_{\text{red},p} + k_{\text{ox},p}} \left(k_{\text{ox},p}\Gamma_{\text{T}} - \left[k_{\text{ox},p}\Gamma_{\text{T}} - (k_{\text{red},p} + k_{\text{ox},p})\Gamma_{\text{O}}^{(p-1)} \right] e^{-(k_{\text{red},p} + k_{\text{ox},p})t_p} \right) \quad (6.125)$$

with

$$\left. \begin{aligned} \Gamma_{\text{O}}^{(p-1)} &= \Gamma_{\text{O}}^{(p)}(t_p = 0) \quad p \geq 1 \\ \Gamma_{\text{O}}^{(0)} &= \Gamma_{\text{T}} \end{aligned} \right\} \quad (6.126)$$

Equation (6.125) is applicable for all the potential pulses of the whole sequence. Thus, from Eqs. (6.125) and (6.126), it is possible to obtain the analytical expression of $\Gamma_{\text{O}}^{(2)}$ by substituting $p = 2$ and inserting the expression of $\Gamma_{\text{O}}^{(1)}$ (Eq. (6.114)) in (6.125). Once $\Gamma_{\text{O}}^{(2)}$ is known, by carrying out this process p times and after a simple rearrangement, the general analytical explicit expression of $\Gamma_{\text{O}}^{(p)}$ is deduced [46]:

$$\frac{\Gamma_{\text{O}}^{(p)}}{\Gamma_{\text{T}}} = \frac{k_{\text{ox},p} + k_{\text{red},p}\theta_p}{k_{\text{T},p}} - \sum_{m=1}^{p-1} \frac{k_{\text{red},m}}{k_{\text{T},m}} (1 - \theta_m) \prod_{h=m+1}^p \theta_h \quad (6.127)$$

with

$$\left. \begin{aligned} \theta_m &= \exp(-k_{\text{T},m}\tau_m) \quad \text{for } 1 \leq m \leq (p-1) \\ \theta_p &= \exp(-k_{\text{T},p}t_p) \end{aligned} \right\} \quad (6.128)$$

and t_p is the variable time of application of the potential p th potential pulse, τ_p the time length of the same ($0 \leq t_p \leq \tau_p$), and $k_{\text{T},i}$ the sum of both heterogeneous rate constants at the potential E_i :

$$k_{\text{T},i} = k_{\text{red},i} + k_{\text{ox},i} \quad 1 \leq i \leq p \quad (6.129)$$

The current corresponding to the p th potential pulse applied, I_p , is [46]:

$$I_p = Q_F \left[k_{\text{red},p} - k_{\text{T},p} \sum_{m=1}^{p-1} \frac{k_{\text{red},m}}{k_{\text{T},m}} (1 - \theta_m) \prod_{h=m+1}^{p-1} \theta_h \right] \theta_p \quad (6.130)$$

The converted charge corresponding to the p th potential pulse applied, Q_p , is (see Eq. (6.111)):

$$\frac{Q_p}{Q_F} = \left(\frac{k_{\text{red},p}}{k_{\text{T},p}} (1 - \theta_p) + \sum_{m=1}^{p-1} \frac{k_{\text{red},m}}{k_{\text{T},m}} (1 - \theta_m) \prod_{h=m+1}^p \theta_h \right) \quad (6.131)$$

with Q_F given by Eq. (6.118).

Equations (6.130) and (6.131) are applicable for any multipulse technique such as Staircase Voltammetry (SCV) and Square Wave Voltammetry (SWV).

Under reversible conditions, the θ_i terms in Eqs. (6.130) and (6.131) become null for any potential pulse considered (see Eq. (6.128)), and

$$\left. \begin{aligned} I_p \Big|_{\text{rev}} &\rightarrow 0 \\ \frac{Q_p}{Q_F} \Big|_{\text{rev}} &= \frac{1}{1 + e^{\eta_p}} \end{aligned} \right\} \quad (6.132)$$

Note that in this case (Q_p/Q_F) is only dependent of E_p , i.e., it has an stationary character being independent of the potential-time waveform applied [48], and has an analogous dependence on the potential to that shown by the normalized voltammetric current ($I/I_{\text{d,c}}$) obtained for a reversible charge transfer reaction under diffusion control (see Eq. (2.36)). Equation (6.132) can be written as

$$E_p = E_c^{\ominus'} + \frac{RT}{F} \ln \left(\frac{Q_F - Q_p}{Q_p} \right) \quad (6.133)$$

Equations (6.132) or (6.133) for the converted charge are valid for any electrochemical technique, i.e., the charge/potential response for a reversible process is universal. The $Q-E$ curves given in these equations present a sigmoidal-type feature which allows us to obtain the Q_F value and, therefore, the total surface excess Γ_T , at sufficiently negative potentials of the cathodic response.

This equivalence between the charge of surface-bound molecules and the current of solution soluble ones is due to two main reasons: first, in an electro-active monolayer the normalized charge is proportional to the difference between the total and reactant surface excesses ($(Q_p/Q_F) \propto (\Gamma_T - \Gamma_O)$), and in electrochemical systems under mass transport control, the voltammetric normalized current is proportional to the difference between the bulk and surface concentrations ($(I/I_{\text{d,c}}) \propto (c_O^* - c_O^s)$) [49]. Second, a reversible diffusionless system fulfills the conditions (6.107) and (6.110) and the same conditions must be fulfilled by the concentrations c_O and c_R when the process takes place under mass transport control (see Eqs. (2.150) and (2.151)) when the diffusion coefficients of both species are equal.

On the contrary, for very small values of ($k^0\tau_i$), a totally irreversible response is attained ($k_{\text{red},i} \gg k_{\text{ox},i}$ with $1 \leq i \leq p$), and Eqs. (6.130) and (6.131) simplify to

$$\left. \begin{aligned} Q_{N,p}|_{\text{irrev}} &= \frac{Q_p}{Q_F}|_{\text{irrev}} = 1 - \exp\left(-\sum_{m=1}^{p-1} k_{\text{red},m}\tau_m - k_{\text{red},p}t_p\right) \\ I_{N,p}|_{\text{irrev}} &= \frac{I_p\tau_p}{Q_F}|_{\text{irrev}} = k_{\text{red},p}\tau_p \exp\left(-\sum_{m=1}^{p-1} k_{\text{red},m}\tau_m - k_{\text{red},p}t_p\right) \end{aligned} \right\} \quad (6.134)$$

6.4.1.3 Multipulse Chronoamperometry and Chronocoulometry

The influence of the reversibility of the surface charge transfer process ($k^0\tau$) on the dimensionless current–time curves is shown in Fig. 6.19, with $\Phi_p = I_p/(Q_F/\tau)$, corresponding to the application of a staircase of 14 potential pulses with a pulse amplitude $|\Delta E| = 25$ mV, $\tau = 1$ s in all the cases and $E_1 - E_c^{\Theta'} = 250$ mV. From these curves, it can be seen that all the currents decrease with time in the way:

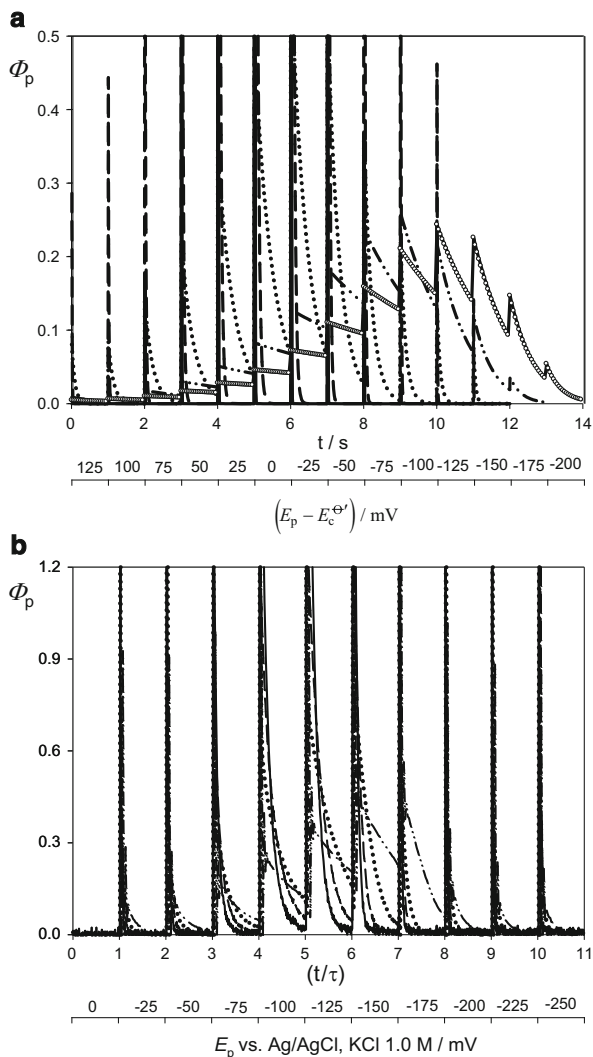
$$\Phi_p = \text{constant} \times e^{-k_{\text{T},p}t_p} \quad (6.135)$$

For high values of $k^0\tau$, very sharp decays of the current–time transients are observed, indicating the almost immediate electrochemical conversion of oxidized species (see solid lines corresponding to $k^0\tau = 100$). Indeed, for $k^0\tau > 100$, the faradaic conversion is so fast that the oxidized species disappears at the very first instants of the experiment and under these conditions $\Phi_p = 0$. When $k^0\tau$ decreases, the observed currents also decrease, since the rate constant modulates the whole faradaic current. For $k^0\tau < 1$, the current transients appear as quasi-linear, with current–time profile being shifted toward more negative potentials. Under these conditions, general equation (6.130) becomes identical to Eq. (6.134), corresponding to irreversible processes.

The experimental verification of the influence of the reversibility of the electrode process corresponding to the system Quinizarin 10 μM + HClO_4 1.0 M in aqueous + 1 % CH_3CN is shown in Fig. 6.19b. These curves have been recorded for different values of τ (10, 5, 2.5, and 1 ms), in order to obtain different ($k^0\tau$) values.

One of the main advantages of the multipulse potential chronoamperograms is the possibility of measuring the sum of both rate constants for each potential pulse applied, $k_{\text{T},p} = k_{\text{red},p} + k_{\text{ox},p}$, with one single experiment and independently of the kinetic model considered. The logarithm of the dimensionless currents of the experimental system Quinizarin 10 μM + HClO_4 1.0 M in aqueous + 1 % EtOH solutions has been plotted in Fig. 6.20a. This curve corresponds to a staircase of 35 potential pulses with a pulse amplitude $|\Delta E| = 15$ mV and $\tau = 3$ ms. The

Fig. 6.19 (a) Theoretical $\Phi_p - t$ curves, with $\Phi_p = I_p / (Q_F / \tau)$ calculated from Eq. (6.130) corresponding to the application of a staircase of 14 potential pulses with a pulse amplitude $|\Delta E| = 25$ mV and $\tau = 1$ s for all the pulses. The values of $(k^0 \tau)$ are: (solid line) 100, (dashed line) 10, (dotted line) 1.0, (dashed-dotted line) 0.1, and (white circles) 0.05. (b) Experimental $\Phi_p - t$ curves corresponding to monolayers of Quinizarin $10 \mu\text{M} + \text{HClO}_4$ 1.0 M in aqueous +1 % CH_3CN on a mercury electrode ($r_s = 0.0315$ cm). The values of the potential pulse time length τ (in ms) are: (solid line) 10, (dashed line) 5, (dotted line) 2.5, and (dashed-dotted line) 1.0. Reproduced with permission from [46]



current–time transients corresponding to the potential window (-5 mV, -185 mV) for which the faradaic process will occur are highlighted.

From the dashed-dotted lines in the inner figure, straight lines with two negative slopes can be observed, with that obtained at smaller times corresponding to the double-layer charging process, and the second one to the faradaic process. For times higher than $5R_u C_{dl}$, at which the non-faradaic processes have a negligible influence (see Sects. 1.9 and 6.4.1.5), the negative slope observed is equal to $k_{T,p}$ (see Eq. (6.135)). The values of the total rate constant $k_{T,p}$ obtained from three experiments with different time lengths τ (3, 5, and 7 ms) are shown in Fig. 6.20b (symbols). These values seem to adjust to a parabolic curve and from the location

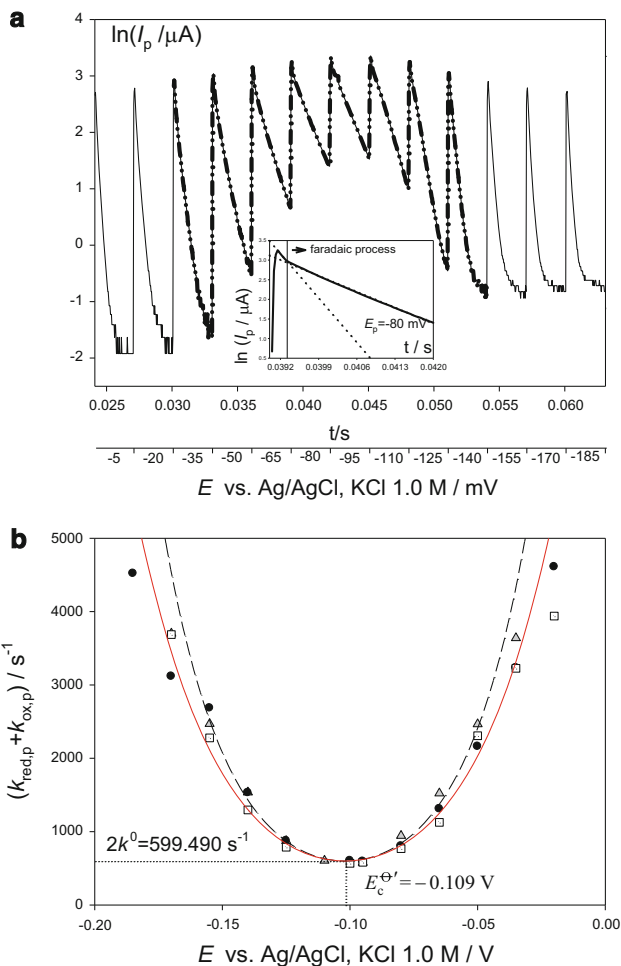


Fig. 6.20 (a) Experimental $\ln(I_p/\mu\text{A}) - t$ curve corresponding to a monolayer of Quinizarin $10 \mu\text{M} + \text{HClO}_4$ 1.0 M in aqueous $+1 \%$ CH_3CN on a mercury electrode ($r_s = 0.0315 \text{ cm}$). $E_j = E_1 - j\Delta E$, $j = 0, 1, \dots, 34$, $\tau = 3 \text{ ms}$, and $\Delta E = 15 \text{ mV}$. $T = 293 \text{ K}$. Bold dashed-dotted lines have been used to highlight those transient currents corresponding to the potential pulses at which the faradaic process takes place. Inset Figure: $\ln(I_p/\mu\text{A}) - t$ curve corresponding to a potential pulse $E_p = -0.08 \text{ V}$. (b) (symbols) $k_{T,p} = k_{\text{red},p} + k_{\text{ox},p}$ (s^{-1}) from logarithmic curves obtained for τ (in ms): 3 (gray triangles), 5 (black circles), and 7 (white squares). (Lines) Theoretical $k_{T,p}$ values calculated for a Butler–Volmer (BV, broken) and Marcus–Hush (MH, red) kinetic schemes with $k^0 = 300 \text{ s}^{-1}$, $E_c^{\ominus'} = -0.102$, $n = 2$, and $T = 293 \text{ K}$. $\alpha = 0.5$ (BV) and $\lambda = 0.75 \text{ eV}$ (MH). Reproduced modified with permission from [46]

and height of the minimum both the surface rate constant k^0 and the formal potential of the surface process $E_c^{\ominus'}$ can be obtained since $E_{\text{minimum}} = E_c^{\ominus'}$ and $(k_{T,p})_{\text{minimum}} = 2k^0$ ($E_c^{\ominus'} = (-0.102 \pm 0.001) \text{ V}$ vs. Ag/AgCl , KCl 1.0 M and $k^0 = (300 \pm 5) \text{ s}^{-1}$). A plot corresponding to the total rate constant expression for a Butler–Volmer

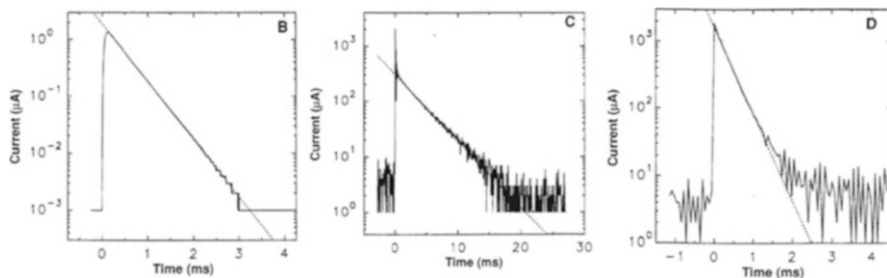


Fig. 6.21 Semi-logarithmic plots of the absolute value of the current following potential steps (*solid*) and linear regression fits to linear portions (*dashed*). Potential versus $E_c^{\ominus'}$, sum of reduction, and oxidation rate constant k_T : (a) 0.0 V, 2.33 s^{-1} ; (b) 0.323 V, 276 s^{-1} ; and (c) -0.577 V , 2980 s^{-1} . Reproduced with permission from [43]

model calculated for $\alpha = 0.5$ (dashed line, Eq. (6.117)) coincides with the data obtained in the potential region around the minimum but deviates from them at higher overpotentials. This suggests the need for a more realistic treatment to explain those deviations based on a Marcus–Hush’s formalist. When this is done (red line, corresponding to $\lambda = 0.75 \text{ eV}$ see Eq. (1.111), the agreement is clearly better.

Chronoamperometric curves have been used as a standard tool to obtain values of the rate constants of surface-bound molecules and they prove as very useful for validating the Marcus–Hush’s formalist, and, indeed, the experimental application of the MH theory to electrode processes has been mainly carried out with surface-bound redox systems. Thus, Chidsey studied the oxidation of ferrocene groups connected to a gold electrode by means of a long alkylthiol chain by using Single Potential Pulse Chronoamperometry (see examples of the experimental responses in Fig. 6.21) [43].

For small values of the reorganization energy, the rate constants found a notable difference with those predicted by the BV approach for large applied overpotentials, reaching a plateau rather than an exponential increase. The Marcus–Hush–Chidsey model (MHC) was able to reproduce this behavior accurately in a wide range of temperatures [50]. The rate constant value obeys an exponential dependence on the distance between the electrode surface and the attached redox species [51]:

$$k^0 = \frac{4\pi^2}{h} \varpi H^2 I(\Lambda, 0) e^{-\beta_r d} \quad (6.136)$$

where h is Planck’s constant, ϖ (eV^{-1}) is the density of states in the electrode, H (eV) is the electronic coupling matrix, $I(\Lambda, 0)$ is an integral given by Eq. (1.112) or (3.110), and β_r is the electronic coupling attenuation coefficient associated with this dependence and $d = r_a - r_0$, with r_a and r_0 being the distance of the attached

redox molecule to the electrode surface and the distance of the closest approach, respectively.

The effect of the reversibility of electrochemical reaction on the theoretical $Q_p - t$ curves calculated from Eq. (6.131) is shown in Fig. 6.22. For reversible processes ($k^0\tau \geq 10$), the charge–time curves present a stepped sigmoid feature and are located around the formal potential of the electro-active couple. Under these conditions, the charge becomes time independent (see Eq. (6.132)). As the process becomes less reversible, both the shape and location of the $Q_p - t$ curves change in such a way that the successive plateaus tend to disappear and a practically continuous quasi-sigmoid, located at more negative potentials as $k^0\tau$ decreases, is obtained. For $k^0\tau \leq 0.1$, general Eq. (6.131) simplifies to Eq. (6.134), valid for irreversible processes and leads to a practically continuous $Q_p - t$ curve.

From the above, it is clear that a simple visual inspection of the charge–time curves allows us to deduce the reversibility degree of the process. This characteristic behavior, in which the discrete nature of the potential is more evident for reversible processes, cannot be obtained when a continuous potential–time perturbation is applied, as in Cyclic Voltammetry, since this kind of perturbation gives rise to continuous charge–potential curves, whatever the reversibility degree of the response (see Sect. 6.4.2).

This behavior can be clearly seen in Fig. 6.22b, in which experimental charge–time curves of quinizarin monolayers on mercury obtained for different values of τ in order to obtain several values of the dimensionless rate constant $k^0\tau$ for this system have been plotted [46]. It can be seen that the charge–time curves are dramatically affected by the time length, so the curve corresponding to $\tau = 10$ ms can be considered as practically reversible (stepped sigmoid), whereas that corresponding to $\tau = 1$ ms presents an almost continuous feature, which is typical of irreversible processes.

6.4.1.4 Staircase Voltammetry and Cyclic Staircase Voltammetry

In this section, the current–potential curves corresponding to the application of a staircase potential of the form given by Eq. (5.2) are analyzed. As in the case of solution soluble species, it is useful to use a dimensionless expression for the SCV current:

$$\psi_{\text{SCV}} = \frac{I_p}{Q_F a} \quad (6.137)$$

with $a = Fv/RT$, I_p being the current corresponding to the potential pulse E_p , Q_F given by Eq. (6.118) and $v = \Delta E/\tau$.

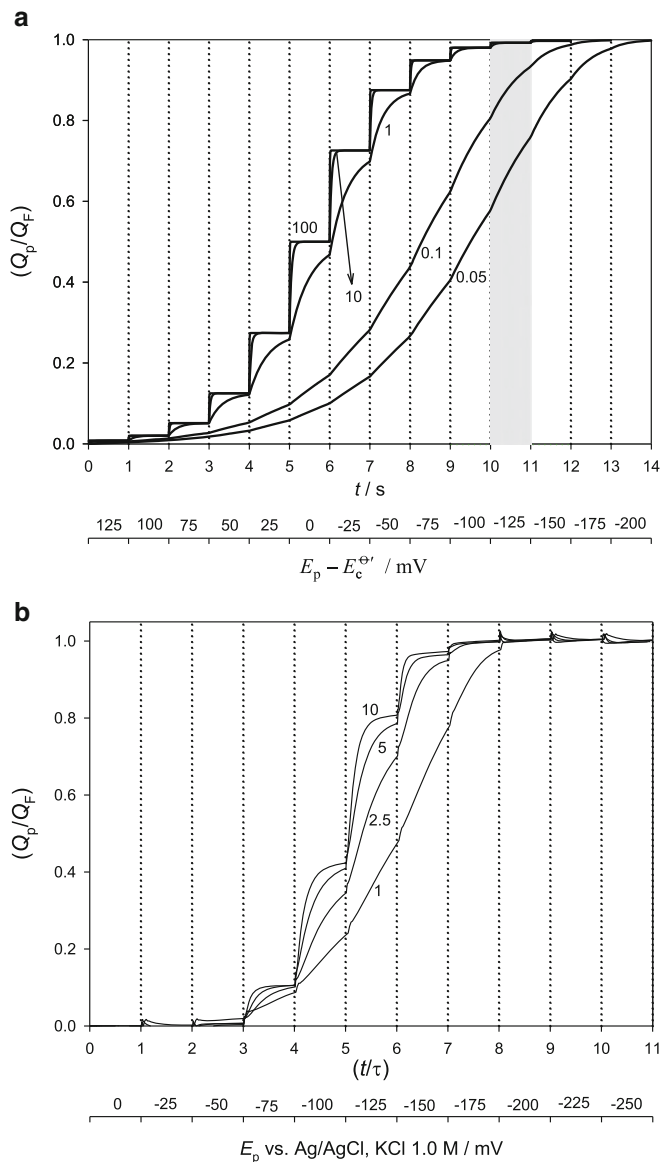


Fig. 6.22 (a) Theoretical $Q_p - t$ curves calculated from Eq. (6.131). $E_1 - E_c^{\ominus'} = 125 \text{ mV}$, $E_j = E_1 - j|\Delta E|$, $j = 0, 1, \dots, 13$, $\tau = 1.0 \text{ s}$, and $|\Delta E| = 25 \text{ mV}$. The values of k^0 (in s^{-1}) appear on the curves. (b) Experimental $Q_p - (t/\tau)$ curves corresponding to monolayers of Quinizarin $10 \mu\text{M} + \text{HClO}_4 \text{ 1.0 M}$ in aqueous + 1% CH_3CN on a mercury electrode of radius $r_s = 0.0315 \text{ cm}$. The values of the time length τ (in ms) appear on the curves. A “potential” axis has been added in both figures which indicate which is the constant potential applied for each of the successive charge–potential–time curves of the whole response. Reproduced with permission [46]

From Eq. (6.130), the following expression for the SCV current is deduced [52]:

$$\psi_{\text{SCV}} = \frac{k^0}{a} \theta_p \left[\frac{k_{\text{red},p}}{k^0} - \frac{k_{\text{T},p}}{k^0} \sum_{m=1}^{p-1} \frac{k_{\text{red},m}}{k_{\text{T},m}} (1 - \theta_m) \prod_{h=m+1}^{p-1} \theta_h \right] \quad (6.138)$$

with θ_i being

$$\left. \begin{aligned} \theta_i &= \exp(-k_{\text{T},i}\tau) \quad \text{for } 1 \leq i < (p-1) \\ \theta_p &= \exp(-k_{\text{T},p}\rho\tau) \end{aligned} \right\} \quad (6.139)$$

and

$$\rho = (t_s/\tau) \quad (6.140)$$

where t_s is the time at which the current is measured ($0 \leq t_s \leq \tau$). For very sluggish electron transfer reactions (i.e., $k_{\text{red},p} \gg k_{\text{ox},p}$, $k^0 \ll 1 \text{ s}^{-1}$), Eq. (6.138) is greatly simplified:

$$\psi_{\text{SCV,irrev}} = \frac{1}{a} k_{\text{red},p} \exp\left(-\frac{\Delta\eta}{a} \left(\sum_{m=1}^p k_{\text{red},m}\right)\right) \quad (6.141)$$

The peak parameters of the irreversible SCV curve can be deduced by making $d\psi_{\text{SCV,irrev}}/dE = 0$. From this condition, and taking into account that for $p > 10$ it holds that

$$\sum_{h=1}^p k_{\text{red},h} = k_{\text{red},p} \sum_{h=1}^{p-1} e^{-ah|\Delta\eta|} = k_{\text{red},p} \frac{e^{-\alpha|\Delta\eta|}}{1 - e^{-\alpha|\Delta\eta|}} \quad (6.142)$$

with

$$\Delta\eta = \frac{F}{RT} \Delta E \quad (6.143)$$

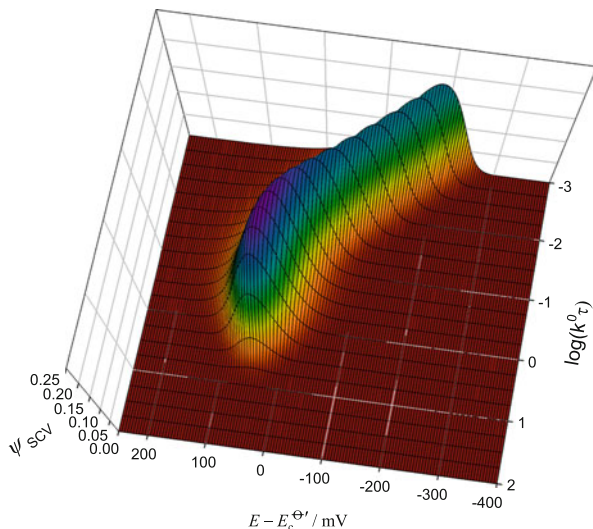
it is possible to obtain the following expressions for the peak potential and height:

$$E_{\text{peak,irrev,f}} = E_c^{\ominus'} + \frac{RT}{\alpha F} \ln(A\alpha|\Delta\eta|) + \frac{RT}{\alpha F} \ln\left(\frac{k^0}{\alpha\alpha}\right) \quad (6.144)$$

$$\psi_{\text{SCV,irrev}}^{\text{peak}} = \frac{1}{eA\alpha|\Delta\eta|} \quad (6.145)$$

with “e” being the base of the natural logarithms and

Fig. 6.23 Influence of the reversibility on the theoretical SCV curves for different values of $(k^0\tau)$ (Eq. (6.138)), when a staircase voltammetry of $|\Delta E| = 5$ mV and $\tau = 1$ s is applied. $t_s = \tau/2$, $T = 298.15$, K and $\alpha = 0.5$. Reproduced with permission [52]



$$A = \frac{e^{-\alpha|\Delta\eta|}}{1 - e^{-\alpha|\Delta\eta|}} \quad (6.146)$$

The influence of the reversibility of the surface electron transfer on the theoretical $\psi_{SCV} - (E - E_c^{\Theta'})$ curves, calculated from Eq. (6.138), is shown in Fig. 6.23, corresponding to the application of a staircase potential sequence of pulse amplitude $\Delta E = 5$ mV and $\tau = 1$ s. In this figure, there are three clearly distinguishable regions. The first corresponds to the reversible behavior and covers the values of $\log(k^0\tau)$ ($2 \rightarrow 1$). In this region, the current is null (see Eq. (6.132)), and therefore, there is no response in SCV. The second region is practically contained between the values of $\log(k^0\tau)$ ($1 \rightarrow -1.5$), for which the electrode process behaves as quasi-reversible. In this zone, it can be observed that the peak height increases until it reaches a maximum value at $\log(k^0\tau) = -1$. When shifted to more negative ($k^0\tau$) values, the peak height slightly decreases until reaching a constant, independent of ($k^0\tau$) value, and the peak potential is shifted linearly with $\log(k^0\tau)$ toward more negative values. This behavior corresponds to a totally irreversible behavior ($\log(k^0\tau) < -1.5$).

Thus, in order to obtain a sensitive response in SCV, it is necessary to decrease the pulse time length, τ , to transform the response to quasi-reversible or irreversible. This behavior contrasts with that observed in Cyclic Voltammetry for which a current-potential response is obtained even for fast charge transfer reactions (see Sect. 6.4.2).

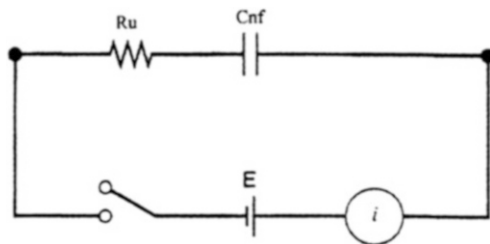


Fig. 6.24 Equivalent circuit corresponding to the non-faradaic contribution of the interface electro-active monolayer solution. R_u is the uncompensated resistance provided by the solution and C_{nf} is the double-layer capacitance

6.4.1.5 Non-faradaic Charge and Current of an Electro-active Monolayer

As stated in Sect. 6.4.1, it has been assumed that the measured experimental currents and converted charges when a potential E_p is applied can be considered as the sum of a pure faradaic contribution, given by Eqs. (6.130) and (6.131), and a non-faradaic one, $I_{p,nf}$ and $Q_{p,nf}$. In order to evaluate the impact of these non-faradaic contributions on the total response, analytical expressions have been obtained. If it is assumed that initially the monolayer is at an open circuit potential, E_{rest} , and then a sequence of potential pulses E_1, E_2, \dots, E_p is applied, the expression for the non-faradaic charge $Q_{p,nf}$ can be deduced from the analogy between the solution–monolayer interface and an RC circuit [53] (shown in Fig. 6.24), so the following differential equation must be solved:

$$\frac{dQ_{p,nf}}{dt} + \frac{Q_{p,nf}}{R_u C_{p,nf}} = \frac{-\Delta E_p}{R_u} \quad (6.147)$$

with R_u being the uncompensated resistance, ΔE_p the potential step applied (which is constant in the case of Staircase Voltammetry), and $C_{p,nf}$ the non-faradaic capacitance of the solution–monolayer interface corresponding to the potential pulse E_p . Different models can be considered for the particular form of $C_{p,nf}$. For the sake of simplicity, the parallel capacitor model introduced by Damaskin is assumed [46], for which $C_{p,nf}$ can be written as

$$C_{p,nf} = C_{nf,O} f_O^{(p)}(\tau) + C_{nf,R} (1 - f_O^{(p)}(\tau)) \quad (6.148)$$

with $C_{nf,O}$ and $C_{nf,R}$ being the limiting values of the non faradaic capacitance corresponding to $f_O^{(p)} = 1$ (totally oxidized monolayer) and $f_O^{(p)} = 0$ (totally reduced monolayer), respectively, which can be considered as practically constant, and $f_O^{(p)}(\tau) (= \Gamma_O^{(p)}(\tau)/\Gamma_T)$ is the surface coverage of oxidized species at time τ . From the relationship between the coverage and the faradaic charge (see Eq. (6.111)), Eq. (6.148) can be rewritten:

$$C_{p,\text{nf}} = C_{\text{nf},\text{O}} + (C_{\text{nf},\text{R}} - C_{\text{nf},\text{O}})(Q_p/Q_F) \quad (6.149)$$

with Q_p being the expression of the faradaic converted charge corresponding to the p th potential pulse given by Eq. (6.131).

By solving Eq. (6.147) and inserting Eq. (6.149), the non-faradaic converted charge at any potential pulse p is deduced:

$$Q_{p,\text{nf}} = \frac{|\Delta E_p|}{R_u} e^{-P(\tau)} \int_0^\tau e^{P(t)} dt + Q_{p-1,\text{nf}} \quad (6.150)$$

with

$$P(t) = \frac{t}{A_p} + \frac{1}{k_{\text{T},p} A_p} \ln \left(\frac{A_p + B_p e^{-k_{\text{T},p} t}}{A_p + B_p} \right) \quad (6.151)$$

$$A_p = R_u C_{\text{nf},\text{O}} + R_u \delta \frac{k_{\text{red},p}}{k_{\text{T},p}} \quad (6.152)$$

$$B_p = R_u \delta \left(\sum_{m=1}^{p-1} \frac{k_{\text{red},m}}{k_{\text{T},m}} (1 - \theta_m) \prod_{h=m+1}^{p-1} \theta_h - \frac{k_{\text{red},p}}{k_{\text{T},p}} \right) \quad (6.153)$$

$$\delta = C_{\text{nf},\text{R}} - C_{\text{nf},\text{O}} \quad (6.154)$$

Under the most simple situation in which it can be assumed that the non-faradaic capacitance of the monolayer is practically constant (i.e., $C_{\text{nf},\text{O}} = C_{\text{nf},\text{R}} = C_{\text{nf}}$, $\delta \cong 0$), Eq. (6.150) simplifies to

$$Q_{p,\text{nf}} = -C_{\text{nf}} \left(E_p - E_{\text{rest}} - \Delta E e^{-t_p/(R_u C_{\text{nf}})} \right) \quad (6.155)$$

with ($R_u C_{\text{nf}}$) being the so-called time constant of the cell and

$$\Delta E = \begin{cases} E_p - E_{p-1} & \text{for } p > 1 \\ E_1 - E_{\text{rest}} & \text{for } p = 1 \end{cases} \quad (6.156)$$

The non-faradaic current can be immediately obtained by differentiating the expression of the non-faradaic charge given by Eqs. (6.150) or (6.155). In this case, the well-known expression (see Sect. 1.9),

$$I_{p,\text{nf}} = \frac{\Delta E}{R_u} e^{-t_p/(R_u C_{\text{nf}})}, \quad (6.157)$$

is obtained. That is, the non-faradaic current has an exponential dependence with time in an analogous way to the faradaic component (Eq. (6.135)) such that its logarithm has a linear dependence with time:

$$\ln(I_{p,\text{nf}}) = \ln\left(\frac{\Delta E}{R_u}\right) - \frac{1}{R_u C_{\text{nf}}} t_p \quad (6.158)$$

with the slope being $1/(R_u C_{\text{nf}})$.

One of the most important advantages of potential pulse techniques in the study of the electrochemical response of surface-bound molecules is that derived from the decoupling of faradaic and non-faradaic contributions. In the case of the current, in agreement with Eq. (6.157), times higher than $5(R_u C_{\text{nf}})$ are needed in order to neglect the non-faradaic component $I_{p,\text{nf}}$ (see inner figure in Fig. 6.20a for a practical example of the different time regimes of faradaic and non-faradaic components of the current. For the converted charges, the non-faradaic contribution cannot be neglected in any case and a subtraction of this contribution to the total response is needed in order to analyze the characteristic parameters of the faradaic charge properly [46, 52].

6.4.2 One-Electron Electrochemical Reactions: Cyclic Voltammetry

The application of Cyclic Voltammetry to the study of electro-active monolayers is of special interest and deserves to be treated separately. The general treatment of these systems was developed by Laviron [45, 54] and the cases of reversible and non-reversible processes will be presented separately.

6.4.2.1 Reversible Reactions

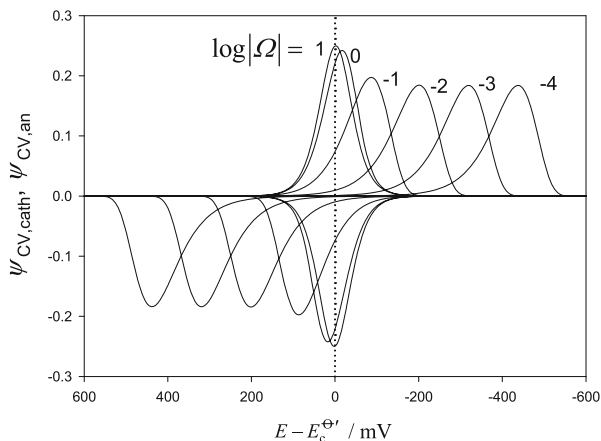
As stated in Sect. 6.4.1, when the charge transfer process is fast, the surface excess of both species O and R is related by Nernst condition (Eq. (6.110)). The combination of this equation with the assumption of constant total excess (Eq. (6.107)) allows us to obtain directly the expressions of Γ_{O} and Γ_{R} :

$$\left. \begin{aligned} \Gamma_{\text{O}} &= \Gamma_{\text{T}} \frac{e^{\eta}}{1 + e^{\eta}} \\ \Gamma_{\text{R}} &= \Gamma_{\text{T}} \frac{1}{1 + e^{\eta}} \end{aligned} \right\} \quad (6.159)$$

In Cyclic Voltammetry, the potential is continuously changing with time as indicated in Eq. (5.1), and, as a consequence, the excesses of both species also change.³ Under these conditions, it is possible to rewrite Eq. (6.108) in terms of the potential:

³ This change is external and directly imposed by the particular form of the potential waveform applied.

Fig. 6.25 CV curves calculated from Eqs. (6.160) and (6.166) for different values of $\log|\Omega|$ (shown in the figure). $\alpha = 0.5$ and $T = 298.15$ K



$$\frac{I}{FA} = -\frac{d\Gamma_O}{dt} = -\frac{d\Gamma_O}{dE} \frac{dE}{dt} = \pm v \frac{d\Gamma_O}{dE} \quad (6.160)$$

with v being the scan rate (the double sign refers to the first and second scans).

By differentiating the expression of Γ_O given by Eq. (6.159) with respect to the potential, it is obtained [54, 55]:

$$\psi_{CV} = \frac{I_{CV}}{aQ_F} = \pm \frac{e^\eta}{(1 + e^\eta)^2} = \pm \operatorname{sech}^2\left(\frac{\eta}{2}\right) \quad (6.161)$$

with $a = Fv/RT$ and $\eta = F(E - E_c^{\Theta'})/RT$.

The reversible CV curve has a symmetrical peak shaped feature for the direct and reverse scans with the following peak parameters (see also Fig. 6.25):

$$\left. \begin{aligned} \psi_{\text{rev}}^{\text{CV,peak}} &= \pm \frac{1}{4} \\ E_{\text{peak,rev}} &= E_c^{\Theta'} \\ W_{1/2} &= 3.53 \frac{RT}{F} \cong 90 \text{ mV} \quad \text{if } T = 298 \text{ K} \end{aligned} \right\} \quad (6.162)$$

As can be expected, the cyclic voltammogram corresponding to a very fast electron transfer of a surface-bound species has identical characteristics to the derivative of the Normal Pulse $I-E$ curve when the redox species are in solution (see Sect. 2.2.2.2).

From Eq. (6.161), it can be concluded that the current corresponding to surface-attached molecules divided by the scan rate is indeed a capacitance since

$$I_{CV} = \frac{dQ_{CV}}{dt} = \frac{dQ_{CV}}{dE} \frac{dE}{dt} = C_{CV}v \quad (6.163)$$

Note that this capacitance is linked to the electron transfer reaction and therefore has a faradaic origin and is not related to the double-layer charging process (this last capacitance corresponds to a pure capacitor; see Sect. 6.4.1.5). In this sense, it has been called “pseudo-capacitance” [56]. The normalized current ψ_{CV} is a ratio of capacitances since, from Eq. (6.161), $\psi_{CV} = (I_{CV}/v)/(Q_F(F/RT)) = C_{CV}/C_F$ [48, 57].

6.4.2.2 Non-reversible Reactions

In this case, the surface excesses are related to the current through Eq. (6.109). If the Butler–Volmer formalist is assumed, the expression of the surface coverage of oxidized species $f_O (= \Gamma_O/\Gamma_T)$ can be obtained by solving the following differential equation which arises from the combination of Eqs. (6.107)–(6.109):

$$\left. \begin{aligned} \frac{df_O}{d\eta} + \Omega f_O (e^{-a\eta} + e^{(1-\alpha)\eta}) &= \Omega e^{(1-\alpha)\eta} \\ \frac{df_R}{d\eta} + \Omega f_R (e^{-a\eta} + e^{(1-\alpha)\eta}) &= \Omega e^{-a\eta} \end{aligned} \right\} \quad (6.164)$$

with

$$\Omega = \frac{k^0}{a} \quad (6.165)$$

and once f_O has been determined, the current can be calculated as $I_{CV} = \pm aQ_F(df_O/d\eta)$, where k^0 and α in Eqs. (6.164) and (6.165) are the rate constant and the charge transfer coefficients of the surface charge transfer process.

From Eqs. (6.160) to (6.164), the following expressions of $\psi_{CV,cath}$ and $\psi_{CV,an}$ are obtained:

$$\left. \begin{aligned} \psi_{CV,cath} &= \Omega e^{-a\eta} \left\{ 1 - \Omega(1 + e^\eta)e^{h(\eta)} \int_\eta^\infty (z^{-(1+\alpha)}e^{-h(z)}) dz \right\} \\ \psi_{CV,an} &= -\Omega e^{-a\eta} \left\{ e^\eta - \Omega(1 + e^\eta)e^{h(\eta)} \int_0^\eta (z^{-\alpha}e^{-h(z)}) dz \right\} \end{aligned} \right\} \quad (6.166)$$

with

$$h(\eta) = \frac{\Omega}{\alpha(1-\alpha)} e^{-a\eta} (1 - \alpha(1 + e^\eta)) \quad (6.167)$$

The integral that appears in Eq. (6.166) needs to be solved numerically except in

the case of totally irreversible processes (i.e., low values of k^0), for which this equation simplifies and the following expressions are found [54]:

$$\left. \begin{aligned} \psi_{\text{CV,cath}} &= \Omega e^{-\alpha\eta} e^{\left(\frac{\Omega e^{-\alpha\eta}}{\alpha}\right)} \\ \psi_{\text{CV,an}} &= -\Omega e^{(1-\alpha)\eta} e^{\left(-\frac{\Omega e^{(1-\alpha)\eta}}{1-\alpha}\right)} \end{aligned} \right\} \quad (6.168)$$

The irreversible cathodic and anodic CV curves given by Eq. (6.168) are shifted toward more negative and positive potentials, respectively, as the rate constant decreases. When $\alpha = 1/2$, they remain symmetrical with respect to the formal potential, although this symmetry is lost for $\alpha \neq 1/2$. The expressions of the peak parameters are:

$$\left. \begin{aligned} \psi_{\text{CV,cath}}^{\text{peak}} &= \frac{\alpha}{e} \\ E_{\text{peak,cath}} &= E_c^{\Theta'} - \frac{RT}{\alpha F} \ln\left(\frac{\alpha}{|\Omega|}\right) \\ W_{1/2,\text{cath}} &= 2.45 \frac{RT}{\alpha F} \end{aligned} \right\} \quad (6.169)$$

for the cathodic (with $\psi_{\text{CV,cath}}^{\text{peak}} = I_{\text{CV,cath}}^{\text{peak}}/|a|Q_F$) and

$$\left. \begin{aligned} \psi_{\text{CV,an}}^{\text{peak}} &= -\frac{(1-\alpha)}{e} \\ E_{\text{peak,an}} &= E_c^{\Theta'} + \frac{RT}{(1-\alpha)F} \ln\left(\frac{(1-\alpha)}{\Omega}\right) \\ W_{1/2,\text{an}} &= 2.45 \frac{RT}{(1-\alpha)F} \end{aligned} \right\} \quad (6.170)$$

for the anodic.

The effect of the reversibility of the charge transfer process on the CV curves of an electro-active monolayer can be seen in Fig. 6.25, while the evolution of the peak current, peak potential, and half-peak width is shown in Fig. 6.26. From these figures, it can be inferred that the decrease of the reversibility of the charge transfer gives rise to similar effects to those observed for solution soluble species (see Fig. 5.12), that is, a decrease of the peak current until a constant value independent of Ω , together with a shift of the cathodic/anodic peak potentials toward more negative/positive values and a broadening of the response. The main feature that defines the response of these processes is the dependence of the peak current on the scan rate (instead of that observed for the square root of the scan rate typical of solution soluble species at macroelectrodes; see Eqs. (5.55) and (5.83), respectively). Moreover, the linearity between the peak potentials and the logarithm of the scan rate shown in Fig. 6.26 can be used to determine the value of k^0 and α , and indeed, this is the most common way to obtain values of these parameters.

In relation to the application of the Marcus–Hush model to immobilized redox groups in LSV and CV, the behavior predicted by MH matches that of the BV

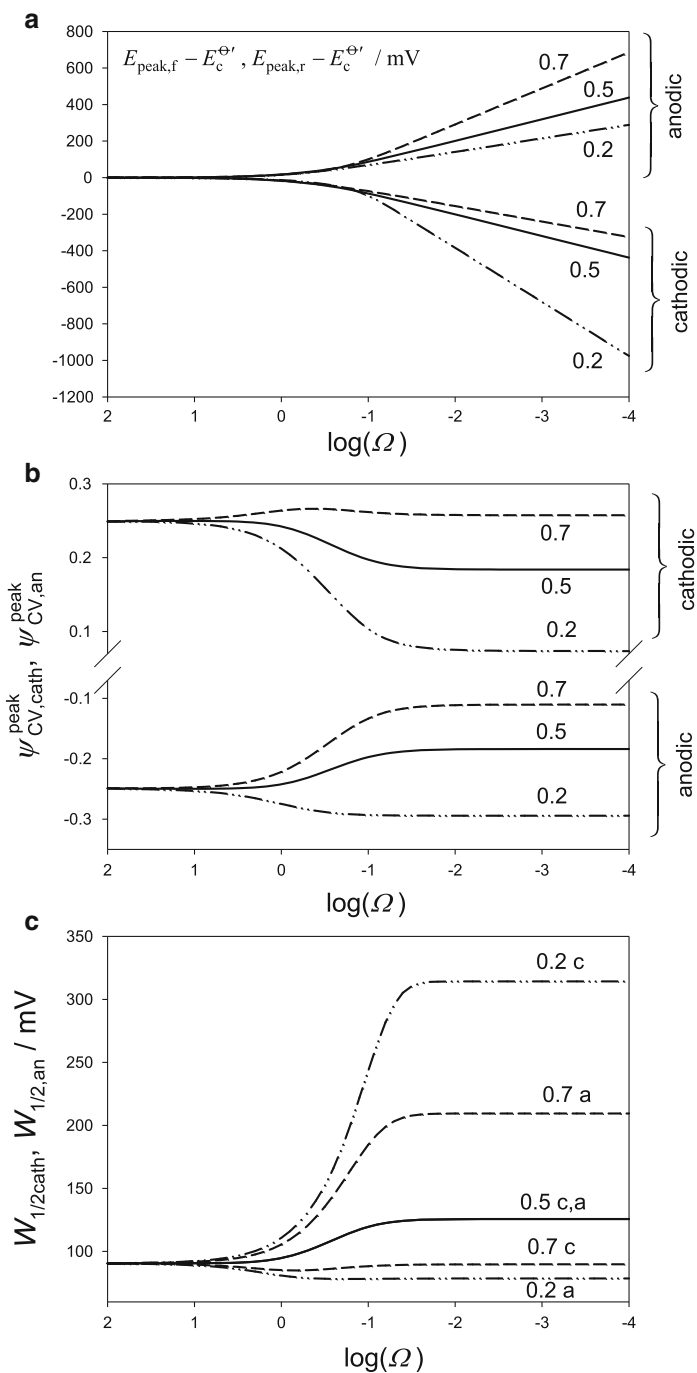
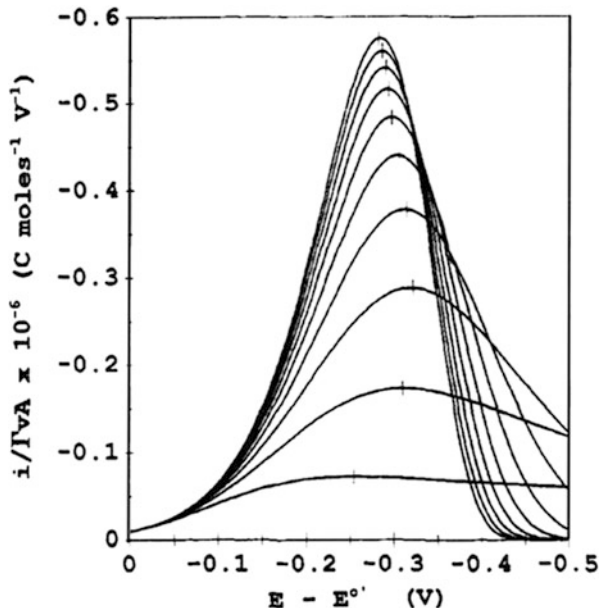


Fig. 6.26 Peak parameters of the CV curves (peak potentials (a); peak heights (b); half-peak widths (c)) calculated by generating voltammograms from Eqs. (6.160) and (6.166) for different values of the dimensionless rate constant Ω . The values of α appear on the curves. Letters “a” and “c” in figure c correspond to anodic and cathodic curves, respectively

Fig. 6.27 Dependence of the normalized CV curves on the reorganization energy λ based on the MH formalism. $T = 273$ K. $\log(v/k^0) = 1.0$. *Top to bottom*, λ (eV) = 1.00, 0.9, 0.8, 0.7, 0.6, 0.5, 0.4, 0.3, 0.2, and 0.1. The *bar* marks the peak potential values. Reproduced with permission from [58]



treatment for very high reorganization energies (λ ; see Sects. 1.7.2 and 3.2.6). However, for $\lambda \leq 2$ eV, the voltgrams are broader and lower than those predicted by the BV model (see Fig. 6.27). Values of the heterogeneous rate constant (k^0) and those of the reorganization energy (λ) obtained from CV for electro-active monolayers with a great variety of redox centers have been reported [50, 51], with these values being in excellent agreement with those obtained in Potential Pulse Chronoamperometry [43].

6.4.2.3 Deviations from the Ideal Behavior

Although very simple, the criteria used to obtain characteristic parameters of surface-confined molecules correspond to an “ideal” behavior in line with the premises presented in Sect. 6.4.1. Unfortunately, it is difficult to meet these criteria and several contributing factors need to be considered in order to explain the non-idealities observed in these redox systems. One of the most common deviations from the ideal criteria is that related to the width of the voltammetric signals, which are typically broader than the values predicted by the ideal model (i.e., $W^{1/2} \cong 90$ mV for reversible systems; see Eq. (6.162)). Some possible reasons for this experimental evidence are:

- Double-layer effects.

The non-faradaic component of the CV curves can be easily obtained as

$$I_{CV,nf} = \frac{dQ_{nf}}{dt} = \frac{dQ_{nf}}{dE} \frac{dE}{dt} = \pm C_{nf}v \quad (6.171)$$

with C_{nf} being the non-faradaic capacitance of the monolayer which is typically a function of the potential. The usual way of dealing with the non-faradaic current is to subtract it from the experimental response as a “baseline correction” (for example, by making an extrapolation of the current at very positive and negative potentials from the faradaic signal at which it can be assumed that the current is only due to the charging process of the double layer). However, when surface-bound redox molecules are considered, this task may not be correct.

For the evaluation of the non-faradaic component of the response in a more realistic way, different proposals have been made. A useful idea is that corresponding to the “interfacial potential distribution” proposed in [59] which assumes that the redox center of the molecules can be considered as being distributed homogeneously in a plane, referred to as the plane of electron transfer (PET), located at a finite distance d from the electrode surface. The diffuse capacitance of the solution is modeled by the Gouy–Chapman theory and the dielectric permittivity of the adsorbed layer is considered as constant. Under these conditions, the CV current corresponding to reversible electron transfer reactions can be written as

$$\psi_{CV} = \left(1 - \frac{\partial \phi_{PET}}{\partial E} \right) \frac{e^\eta}{(1 + e^\eta)^2} \quad (6.172)$$

with ϕ_{PET} being the potential difference between the PET and the bulk solution and $\eta = F(E - \phi_{PET} - E_c^{\ominus})$. The term ϕ_{PET} introduces the correction to the current due to the double layer and gives rise to the appearance of a minimum in the double-layer capacitance at potentials around the formal one [59]. This model has been extended to include slow electrode reactions and the formation of ion pairs [60, 61].

– Surface heterogeneities

It should be borne in mind that it has been assumed that the electro-active monolayer is a homogeneous system, i.e., the environment of a particular molecule cannot be distinguished from any other one present in the monolayer. This is very difficult to achieve in practice since heterogeneity arises very easily. Among the various causes of this heterogeneity are:

- (a) Interactions between adsorbed molecules which cause the surface activity to differ from surface concentration [45, 62].
- (b) Interactions between the local field and the permanent dipoles of uncharged adsorbed molecules [63].
- (c) Different tunneling distance between the redox species and the electrode surface [64].
- (d) A dispersion in the electronic coupling term β caused by conformational changes in the monolayer structure that induce uneven interactions [64].

These effects will give rise to different molecular environments that could lead to surface inhomogeneities, i.e., different formal potentials (thermodynamic dispersion) or different rate constants (kinetic dispersion).

In order to evaluate the influence of a dispersion of formal potentials or redox constants (through different tunneling distances) in the CV peak broadening, a Gaussian distribution of both these parameters can be assumed with a mean μ and standard deviation σ . The current can be obtained as a weighted sum:

$$\psi_{\text{CV}} = \frac{\sum_j (p_j \psi_{\text{CV},j})}{\sum_j (p_j)} \quad (6.173)$$

with $\psi_{\text{CV},j}$ being the CV current calculated for the j th formal potential or rate constant and p_j the weighting of the j th component:

$$p_j = \exp\left(-\frac{(\chi_j - \eta)^2}{2\sigma^2}\right) \quad (6.174)$$

and χ_j is the potential or the rate constant. The values of χ are spread in the range $\chi = \mu \pm x\sigma$ with “ x ” being a number which defines the width of the distribution ($x = 0$ corresponds to no dispersion, i.e., to the ideal case).

6.4.3 Two-Electron Electrochemical Reactions

This section presents the solution corresponding to a surface two-electron charge transfer process (EE mechanism) when a sequence of potential pulses E_1, E_2, \dots, E_p is applied to the reaction scheme (6.II) by assuming that all the species (O_1, O_2 , and O_3) correspond to the oxidation states of a surface-confined molecule O. Under these conditions, Eq. (6.107) has to be replaced by

$$\Gamma_{O_1} + \Gamma_{O_2} + \Gamma_{O_3} = \Gamma_T \quad \text{independently of the applied potential} \quad (6.175)$$

6.4.3.1 Reversible Reactions

For reversible reactions, the surface excesses of species O_1, O_2 and O_2, O_3 are related by the two Nernstian conditions:

$$\left. \begin{aligned} \frac{\Gamma_{O_1}^{(p)}}{\Gamma_{O_2}^{(p)}} &= e^{\frac{F}{RT}(E_p - E_{c,1}^{\Theta'})} \\ \frac{\Gamma_{O_2}^{(p)}}{\Gamma_{O_3}^{(p)}} &= e^{\frac{F}{RT}(E_p - E_{c,2}^{\Theta'})} \end{aligned} \right\} \quad (6.176)$$

By combining Eqs. (6.175) and (6.176), expressions for surface excesses or coverages are obtained, which are obviously identical to those corresponding to the surface concentrations of species O_1 , O_2 , and O_3 for a solution soluble redox process given in Eqs. (3.132) and (3.133).

From this result, the converted charge Q_p^{EE} transferred for a di-electronic transfer process is straightforwardly obtained as the sum of charges $Q_{p,1}$ and $Q_{p,2}$ for steps 1 and 2, respectively

$$Q_p^{EE} = Q_{p,1}^{EE} + Q_{p,2}^{EE} \quad (6.177)$$

with

$$Q_{p,1}^{EE} = -FA\Gamma_T \int_0^\tau \left(\frac{df_{O_1}^{(p)}}{dt} \right) dt = FA\Gamma_T (1 - f_{O_1}^{(p)}) \quad (6.178)$$

$$Q_{p,2}^{EE} = FA\Gamma_T \int_0^\tau \left(\frac{df_{O_3}^{(p)}}{dt} \right) dt = FA\Gamma_T f_{O_3}^{(p)} \quad (6.179)$$

where $f_{O_j}^{(p)} = \Gamma_{O_j}^{(p)}/\Gamma_T$, with $j = 1, 2, 3$, is the surface coverage of species O_j at E_p , A is the area of the electrode, and τ is the duration of the potential pulse applied.

By combining Eq. (6.175) and those corresponding to the surface coverage of the three species, one obtains [65]:

$$Q_{p,N}^{EE} = \frac{1}{Q_F} Q_p^{EE} = \frac{2\sqrt{K} + e^{\bar{\eta}^{(p)}}}{\sqrt{K} + e^{\bar{\eta}^{(p)}} + \sqrt{K} (e^{\bar{\eta}^{(p)}})^2} \quad (6.180)$$

with $\bar{\eta}_p$, K and Q_F given by Eqs. (6.20), (6.22), and (6.118), respectively.

The $Q_p^{EE} - E$ curve for a reversible two-electron transfer taking place in a monolayer is independent of time (i.e., it has a stationary character) and, therefore, is independent of the potential–time waveform applied to the electrode, as in the case of a reversible one-electron transfer reaction. It is also important to highlight that the normalized charge, $Q_{p,N}^{EE}$, has a identical expression to that for the normalized transient current $I_{NPV,N}^{EE}$ obtained for solution soluble species when the NPV technique is applied to an electrode with any geometry (see curves in Fig. 3.16, and Eq. (3.141)), and also to the normalized stationary current obtained for solution soluble species when any potential–time waveform is applied for ultramicroelectrodes with any geometry.

The normalized current–potential curve in CV, ψ_{CV}^{EE} , can be easily obtained from

$$\psi_{CV}^{EE} = \frac{d(Q^{EE}/Q_F)}{d\bar{\eta}} = \frac{K^{3/2}e^{\bar{\eta}} + 4K^2e^{2\bar{\eta}} + K^{3/2}e^{3\bar{\eta}}}{(K + K^{1/2}e^{\bar{\eta}} + Ke^{2\bar{\eta}})^2} \quad (6.181)$$

where $\bar{\eta} = F(E(t) - \bar{E}_c^{\Theta'})/RT$. Equation (6.181) for surface-immobilized molecules has, logically, the same expression as that for the derivative of the NPV response of solution soluble species (see Figs. 6.28 and 3.16).

The evolution of the peak parameters of the $(\psi_{CV}^{EE} - E)$ response with $\Delta E_c^{\Theta'}$ (peak potentials (a), peak heights (b), and half-peak width (c)) for a two-electron transfer can be seen in Fig. 6.29. In Fig. 6.29a, the peak potentials refer to the average formal potential value, $\bar{E}_c^{\Theta'}$. The horizontal black line at $E = \bar{E}_c^{\Theta'}$ and the two symmetrical branches represent, respectively, that only one peak and two peaks are obtained in the corresponding range of $\Delta E_c^{\Theta'}$ values in abscissas, as indicated in the figure.

From Fig. 6.29b, it can be observed that the values of the peak height, $\psi_{CV}^{EE, \text{peak}}$, for an EE process, change with $\Delta E_c^{\Theta'}$ between 1/4 (for $\Delta E_c^{\Theta'} \ll 0$) and 1 (for $\Delta E_c^{\Theta'} \gg 0$), as expected, since the normalized current for an E mechanism with n electrons transferred is $\psi_{CV}^{E, \text{peak}} = n^2/4$; thus, 1/4 for $n = 1$ and 1 for $n = 2$. When only one peak is observed, the peak height is given by:

$$\psi_{CV}^{EE, \text{peak}} = \frac{2\sqrt{K}}{1 + 2\sqrt{K}} \quad \Delta E_c^{\Theta'} \geq -71.2 \text{ mV} \quad (6.182)$$

The values of the peak height calculated with Eq. (6.182) have been included in Fig. 6.29b (black dots).

Figure 6.29c shows that the half-peak width, $W^{1/2}$, changes in the extreme negative and positive values of $\Delta E_c^{\Theta'}$ between 90 mV (E_{1e^-}) and 45 mV (E_{2e^-}) for an EE process, but a sharp jump in the half-peak width, $W^{1/2}$, is observed at $\Delta E_c^{\Theta'} \cong -135 \text{ mV}$, which corresponds to a $\psi - E$ curve with two peaks, whose central trough is situated just at the half-peak height. As in the case of the peak current, a theoretical expression has been reported for the half-peak width when only one peak appears [66, 67]:

$$W_{1/2} = \frac{2RT}{F} \ln\left(B + \sqrt{B^2 - 1}\right) \quad \Delta E_c^{\Theta'} \geq -71.2 \text{ mV} \quad (6.183)$$

where

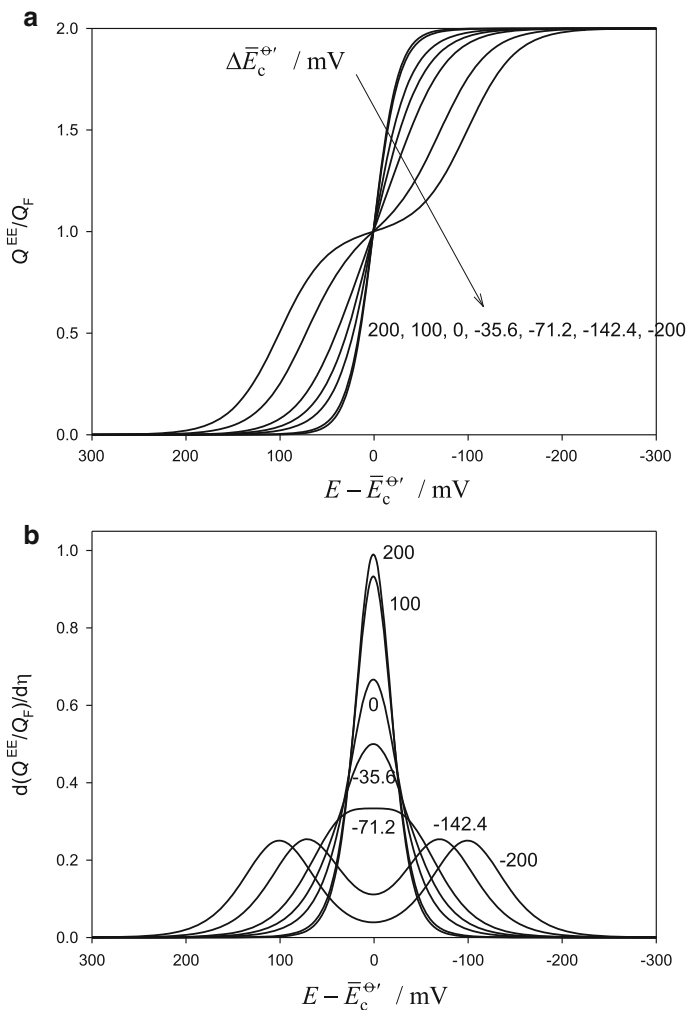


Fig. 6.28 $Q^{EE} - E$ (a) and $\psi_{CV}^{EE} - E$ (b) curves (with $\psi_{CV}^{EE} = d(Q^{EE}/Q_F)/d\eta$) calculated from Eqs. (6.180) and (6.181) for different values of $\Delta E_c^{\Theta'} = E_{c,2}^{\Theta'} - E_{c,1}^{\Theta'}$ (shown in the curves)

$$B = \frac{1 + \sqrt{1 + 4K + 16K\sqrt{K} + 32K^2}}{4K} \quad (6.184)$$

The values of $W^{1/2}$ calculated from Eq. (6.184) have been included in Fig. 6.29c (black dots).

Figure 6.29a–c can be used as working curves to accurately determine the values of $\Delta E_c^{\Theta'}$ and the total surface excess Γ_T for immobilized surface molecules.

The most singular characteristics exhibited by this figure are as follows:

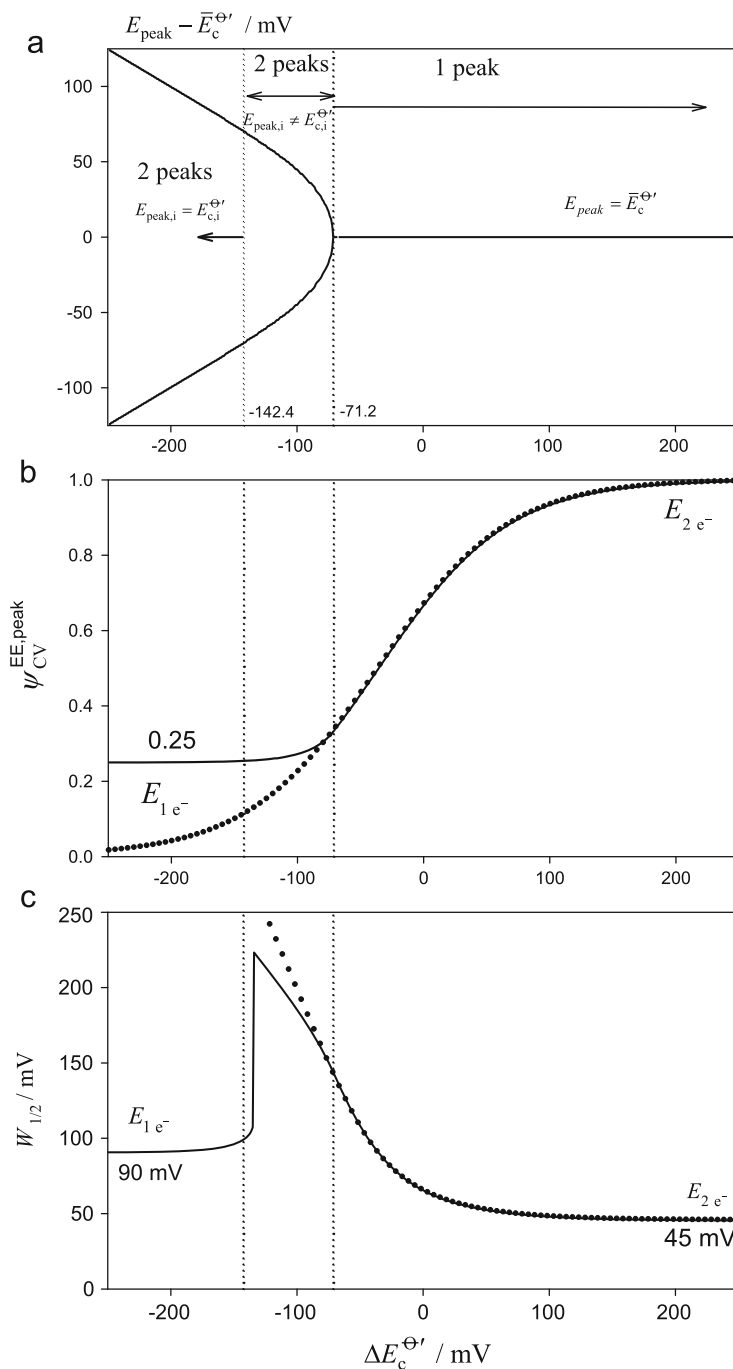


Fig. 6.29 Peak parameters of the $\psi_{CV}^{\text{EE}} - E$ curves with $\Delta E_c^{\Theta'}$ [(a) peak potentials; (b), peak heights; (c) half-peak width], for a two-electron transfer, calculated from Eq. (6.181). The *black dots* in figures (b) and (c) correspond to the values of $\psi_{CV}^{\text{EE,peak}}$ and $W_{1/2}$ calculated from Eqs. (6.182) and (6.183), respectively

1. For $\Delta E_c^{\Theta'} \leq -142.4 \text{ mV}$, the two peak potentials in the voltogram correspond to the individual formal potentials and $\psi_{CV}^{EE, \text{peak}} = 1/4$ (see Fig. 6.29b), with both peak parameters being characteristic of a simple E mechanism.
2. For $\Delta E_c^{\Theta'} = -71.2 \text{ mV}$, a transition 2 peaks–1 peak takes place (see Fig. 6.29a). For more positive values of $\Delta E_c^{\Theta'}$, only one peak appears in the response, whose peak potential corresponds to $\bar{E}_c^{\Theta'}$ (see Fig. 6.29a).
3. For $\Delta E_c^{\Theta'} = -35.6 \text{ mV}$, the response presents a height which is double that for a simple E mechanism, but $W_{1/2} = 90 \text{ mV}$ (Fig. 6.29c).
4. For $\Delta E_c^{\Theta'} > 200 \text{ mV}$, $\psi_{CV}^{EE, \text{peak}} = 1$ and $W^{1/2} = 45 \text{ mV}$ (Fig. 6.29c); therefore, the EE process behaves as an E mechanism of two electrons.

The appearance of one or two peaks in the CV curve is closely related to the roots with physical meaning of the first derivative of Eq. (6.181), which are identical to the second derivative of the normalized NPV signal given in Table 3.1.

6.4.3.2 Non-reversible Reactions

When the electrode processes given in reaction scheme (6.II) are slow, the Nernstian relationship given by Eq. (6.176) is not fulfilled, and the following relationships can be established for the time variation of the surface coverages:

$$\left. \begin{aligned} -\frac{df_{O_1}^{(p)}}{dt_p} &= k_1^p f_{O_1}^{(p)} + k_{\text{ox},1}^p f_{O_3}^{(p)} - k_{\text{ox},1}^p \\ \frac{df_{O_3}^{(p)}}{dt_p} &= -k_2^p f_{O_3}^{(p)} - k_{\text{red},2}^p f_{O_1}^{(p)} + k_{\text{red},2}^p \\ \frac{df_{O_2}^{(p)}}{dt_p} &= -\left(\frac{df_{O_1}^{(p)}}{dt_p} + \frac{df_{O_3}^{(p)}}{dt_p} \right) \end{aligned} \right\} \quad (6.185)$$

with

$$k_i^p = k_{\text{red},i}^p + k_{\text{ox},i}^p \quad i = 1, 2 \quad (6.186)$$

The currents corresponding to first, $I_{p,1}$, and second, $I_{p,2}$, steps, for each potential E_p , are as follows:

$$\left. \begin{aligned} \frac{I_{p,1}^{EE}}{Q_F} &= -\frac{df_{O_1}^{(p)}}{dt_p} \\ \frac{I_{p,2}^{EE}}{Q_F} &= \frac{df_{O_3}^{(p)}}{dt_p} \end{aligned} \right\} \quad (6.187)$$

and the total current, I_p^{EE} , for the two-electron process is given by

$$I_p^{EE} = I_{p,1}^{EE} + I_{p,2}^{EE} \quad (6.188)$$

To solve the differential equation system given by Eqs. (6.185) and (6.187), the following solution is assumed:

$$\left. \begin{aligned} f_{O_1}^{(p)} &= \delta^{(p)} (\theta_1^{(p)} - 1) + f_{O_1}^{(p-1)} \\ f_{O_3}^{(p)} &= \gamma^{(p)} (\theta_2^{(p)} - 1) + f_{O_3}^{(p-1)} \end{aligned} \right\} \quad (6.189)$$

with $\delta^{(p)}$ and $\gamma^{(p)}$ being coefficients to be determined and

$$\theta_i^{(p)} = \exp(-k_i^p t_p) \quad i = 1, 2 \quad (6.190)$$

where t_p is the variable time of the potential E_p (with $0 \leq t_p \leq \tau$). It is assumed that the current of each potential pulse is measured at $t_p = \tau$. In agreement with Eqs. (6.188) and (6.189), the current for any potential can be obtained as

$$\frac{I_p^{EE}}{Q_F} = \delta^{(p)} k_1^p \theta_1^{(p)} - \gamma^{(p)} k_2^p \theta_2^{(p)} \quad (6.191)$$

By inserting the solutions proposed in Eq. (6.189) and condition (6.175) in Eq. (6.185), recurrent expressions for coefficients $\delta^{(p)}$ and $\gamma^{(p)}$ are deduced [68] and by inserting these expressions into (6.191) the current is calculated. These expressions allow us to obtain limiting cases like the reversible and irreversible ones which have a discrete character which makes them applicable to any multipulse technique by simply changing the potential time waveform, including the continuous limit of Cyclic Voltammetry. Moreover, they are independent of the kinetic formalist considered for the process.

For the application of Eq. (6.191) to CV, the Butler–Volmer formalism has been used and the following changes are made:

$$\psi_p^{EE} = \frac{I_p^{EE}}{aQ_F} \quad (6.192)$$

$$\Omega_i = \frac{k_i^0}{a} \quad i = 1, 2 \quad (6.193)$$

with $a = Fv/RT$.

As an example of application, in Fig. 6.30 the CV curves ($\psi_{CV}^{EE} - (E - E_{c,1}^{\Theta'})$) for a two-electron transfer EE mechanism (solid lines), calculated from Eqs. (6.191)–(6.192) for a ratio of the dimensionless heterogeneous rate constants of the two steps (Ω_2/Ω_1) = 0.1, have been plotted. These figures include the curves calculated for three values of the dimensionless rate constant of the first step, Ω_1 : 10, 0.1, and 0.01, in Figures A, B, and C, respectively, and also for three values of $\Delta E_c^{\Theta'} (= E_{c,2}^{\Theta'} - E_{c,1}^{\Theta'})$, in mV: –200, 0, and 200, in Figures I, II, and III, respectively, by assuming $\alpha = 0.5$ for the two-electron transfers in all cases.

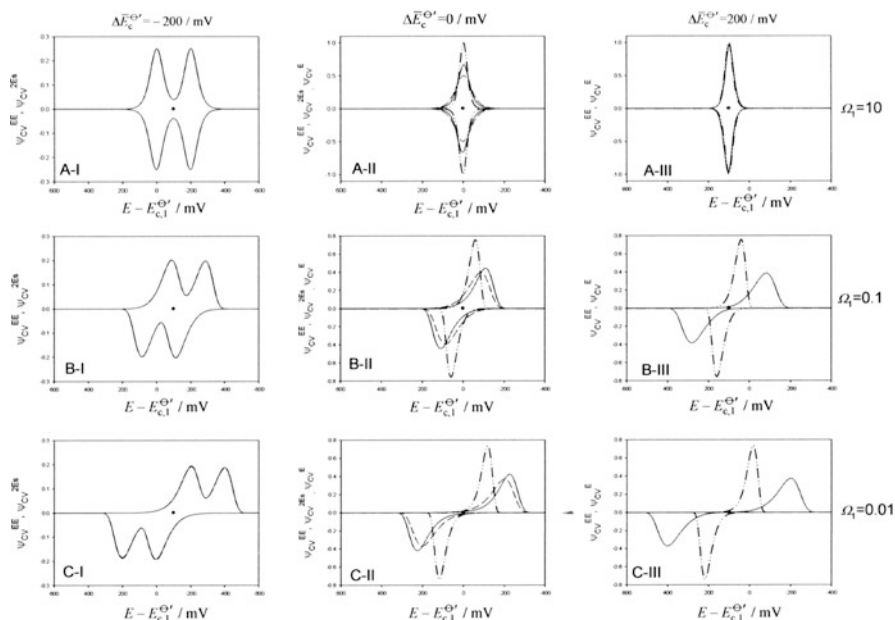


Fig. 6.30 CV curves calculated from Eqs. (6.191) to (6.192) for an EE mechanism ($|\Delta E| = 0.01 \text{ mV}$, *solid lines*) and from (6.166) for two independent electron transfers (*dashed lines*) and an apparent simultaneous two-electron single transfer (*dashed-dotted lines*). These curves have been calculated for three values of the dimensionless rate constant of the first step, Ω_1 , and three values of $\Delta \bar{E}_c^{\Theta'}$ (shown in the *curves*). $\Omega_2/\Omega_1 = 0.1$ for the EE mechanism and the two independent electron transfers. For the two-electron single transfer, it has been assumed that the formal potential coincides with the average potential of the EE mechanism and $\Omega = \Omega_1$. $\alpha = 0.5$. $T = 298 \text{ K}$. Reproduced with permission from [68]

The CV curves for two independent electron transfers (dashed lines) and those corresponding to an apparently simultaneous two-electron transfer (dashed-dotted lines) have also been plotted for comparison with those obtained for an EE mechanism with $\Delta E_c^{\Theta'} = -200$ and 0 mV and $\Delta E_c^{\Theta'} = 0$ and 200 mV , respectively. These figures indicate a great variety of voltammetric responses, showing one or two peaks on the direct and reverse scans, whose heights and relative positions depend on the values of Ω_1 , $\Delta E_c^{\Theta'}$, and the ratio (Ω_2/Ω_1), which is smaller than unity in this set of figures. It is important to highlight that it is not necessary to calculate the CV curves for the inverse case of $\Omega_2 > \Omega_1$, because to obtain the responses for the inverse value of (Ω_2/Ω_1) (i.e., the curves obtained by exchanging the values of Ω_1 and Ω_2), all that is required is a rotation of 180° with respect to the black dot marked in the figures, i.e., the initial direct (cathodic) and reverse (anodic) responses become the reverse (anodic) and direct (cathodic) ones. This singular point is located at

coordinates $(0, E_c^{\Theta'} - E_{c,1}^{\Theta'})$ where $\bar{E}_c^{\Theta'}$ corresponds to the average formal potential, defined in Eq. (6.21).

This general characteristic of the voltammograms allows us to locate the value of the average formal potential $\bar{E}_c^{\Theta'}$ in any response, with symmetrical or asymmetrical voltammograms. In this last case, we have to change the sign of current and invert the sense of the potentials in the experimental response. From comparison of the original and inverted responses, the point $(0, \bar{E}_c^{\Theta'})$ is immediately located. Another important feature of the voltammograms shown in Fig. 6.30 is that for high values of both heterogeneous rate constants, reversible electrochemical reactions are expected. In this case, the CV responses for the direct and the reverse scans are symmetrical with respect to the zero current line. These voltammograms show two peaks centered at the individual formal potentials when $\Delta E_c^{\Theta'}$ is very negative (Fig. 6.30A–I), which evolve to a single peak centered at the average formal potential as $\Delta E_c^{\Theta'}$ increases.

Moreover, for non-reversible charge transfers, the voltammetric curves corresponding to the direct and reverse scans can become very different, and the number of peaks is no longer fixed only by the value of $\Delta E_c^{\Theta'}$ but also by the values of the kinetic constants of steps 1 and 2 in scheme (6.II). Thus, for the CV curves of these figures, the direct response tends to present two peaks as the process becomes more irreversible (an obvious feature for very negative values of $\Delta E_c^{\Theta'}$ but not so obvious for zero or even positive ones), and the reverse voltammogram presents only one.

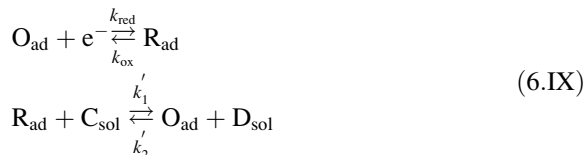
Under these conditions, the determination of the rate constants of both charge transfers becomes very complex. Some general criteria can be found in [68].

6.4.4 *Electrocatalytic Processes at Modified Electrodes*

One of the most fruitful trends in the comprehension and control of electrochemical reaction kinetics and electrocatalysis has been the development of modified electrodes to achieve redox mediators of solution processes. This strategy is based on the electrochemical activation (through the application of an electrical perturbation to the electrode) of different sites at a modified surface. As a result of this activation, the oxidation or the reduction of other species located in the solution adjacent to the electrode surface (which does not occur or occurs very slowly in the absence of the immobilized catalyst) can take place⁴ [40, 69, 70].

⁴The processes analyzed in this section refer to catalytically active molecules attached to the electrode (electron conductor), a case which has been named “molecular electrocatalysis” by Savéant [40].

This section will focus on the study of an electrocatalytic reaction in line with the following reaction scheme:



where O_{ad} and R_{ad} refer to the redox couple bound to the electrode surface and C_{sol} and D_{sol} are species in solution.

6.4.4.1 Pseudo-First-Order Electrocatalytic Processes

We consider first the situation in which the chemical reaction is considered as irreversible. It is assumed that the surface concentration of species C_{sol} remains constant and equal to their bulk value, c_{C}^* (in such a way that the process can be considered as a pseudo-first order process),



with the pseudo-first-order rate constant being

$$k_{\text{c}} = k_1' c_{\text{C}}^* \quad (6.194)$$

When a constant potential E_1 is applied during a time t_1 ($0 \leq t_1 \leq \tau$), the rate equation for the process (6.X) is given by

$$\frac{I_1^{\text{cat}}}{Q_{\text{F}}} = -\frac{df_{\text{O}}^{(1)}}{dt_1} + k_{\text{c}} f_{\text{R}}^{(1)} \quad (6.195)$$

with $f_i^{(1)} = \Gamma_i^{(1)}/\Gamma_T$, $i = \text{O}$ or R , and Q_{F} is given in Eq. (6.118). By combining Eqs. (6.107)–(6.109) and (6.195), one obtains

$$-\frac{df_{\text{O}}^{(1)}}{dt_1} = k_{\text{T},1}^{\text{c}} f_{\text{O}}^{(1)} - (k_{\text{ox},1} + k_{\text{c}}) \quad (6.196)$$

with

$$k_{T,1}^c = k_{T,1} + k_c \quad (6.197)$$

with $k_{T,1}$ given by Eq. (6.113).

Equation (6.196) is formally identical to that corresponding to a simple charge transfer process (given by Eq. (6.112)) by changing $k_{T,1}$ for $k_{T,1}^c$. Therefore, the solution of (6.196), by considering $f_O^{(1)}(t=0) = 1$, leads logically to an expression for the surface coverages of electro-active species O and R which is formally identical to that obtained for a simple charge transfer process with the changes indicated above.

Equations (6.112) and (6.196) also allow us to easily deduce the expression corresponding to the current of the first potential pulse:

$$\frac{I_1^{\text{cat}}}{Q_F} = k_{\text{red},1}\theta_1 + k_c \frac{k_{\text{red},1}}{k_{T,1}^c} (1 - \theta_1) \quad (6.198)$$

with $\theta_1 = \exp(-k_{T,1}^c t_1)$.

This equation shows that the catalytic current is enhanced in relation to that corresponding to a simple surface electrochemical reaction by means of an additive contribution due to the catalytic step (second term in the right-hand side of Eq. (6.198)).

The converted charge can also be obtained by integrating the current:

$$\frac{Q_1^{\text{cat}}}{Q_F} = \frac{k_{\text{red},1}}{k_{T,1}^c} (1 - \theta_1) (1 + k_c t_1) \quad (6.199)$$

When a sequence of p consecutive potential pulses of the same length τ is applied, the analytical expression of the surface excess of species O is, in line with the above discussion, identical to that given for a simple charge transfer reaction in Eq. (6.127) by changing $k_{T,p}$ for $k_{T,p}^c$ with

$$\theta_p = \exp(-k_{T,p}^c \tau) \quad (6.200)$$

$$k_{T,p}^c = k_{T,p} + k_c \quad (6.201)$$

with $k_{T,p}$ given by Eq. (6.129)

The current-potential curve has the expression [69]:

$$\begin{aligned} \frac{I_p^{\text{cat}}}{Q_F} = & - \left(k_{T,p}^c - k_c \right) \sum_{m=1}^{p-1} \left(\frac{k_{\text{red},m}}{k_{T,m}^c} (1 - \theta_m) \prod_{h=m+1}^p \theta_h \right) \\ & + \frac{k_{\text{red},p}}{k_{T,p}^c} \left(k_{T,p}^c - k_c \right) \theta_p + k_c \frac{k_{\text{red},p}}{k_{T,p}^c} \end{aligned} \quad (6.202)$$

For a fast charge transfer process, by introducing the condition $k_{E,p} \gg 1 \text{ s}^{-1}$ in Eq. (6.202), one obtains

$$\frac{I_{p,\text{rev}}^{\text{cat}}}{Q_F} = k_c \frac{1}{1 + e^{\eta_p}} \quad (6.203)$$

with $\eta_p = F(E_p - E_c^{\ominus'})/RT$.

For $E \rightarrow -\infty$ (i.e., $k_{\text{red},p} \rightarrow \infty$) and $E \rightarrow \infty$ (i.e., $k_{\text{ox},p} \rightarrow \infty$) in Eq. (6.202), the limiting currents are

$$\left. \begin{aligned} \frac{I_p^{\text{cat}}}{Q_F} \Big|_{E \rightarrow -\infty} &= k_c \\ \frac{I_p^{\text{cat}}}{Q_F} \Big|_{E \rightarrow \infty} &= 0 \end{aligned} \right\} \quad (6.204)$$

The converted charge corresponding to the p th potential pulse E_p can be obtained by integrating I_p^{cat} given by Eq. (6.202) [70, 71]:

$$\begin{aligned} \frac{Q_p^{\text{cat}}}{Q_F} &= - \sum_{m=2}^p \left(\left(1 - \frac{k_c}{k_{T,m}^c} \right) (1 - \theta_m) f_{R,m-1} \right) \\ &+ \sum_{m=1}^p \left(\frac{k_{\text{red},m}}{k_{T,m}^c} \left(k_c \tau + (1 - \theta_m) \left(1 - \frac{k_c}{k_{T,m}^c} \right) \right) \right) \end{aligned} \quad (6.205)$$

with $f_{R,m-1} = 1 - f_{O,m-1}$ (see Eq. (6.107)).

For fast electron transfers, the expression of the converted charge simplifies to

$$\frac{Q_{p,\text{rev}}^{\text{cat}}}{Q_F} = \frac{1}{1 + e^{\eta_p}} + k_c \tau \sum_{m=1}^p \frac{1}{1 + e^{\eta_m}} \quad (6.206)$$

A stationary behavior is attained when the condition $k_c \gg 1 \text{ s}^{-1}$ holds. Under these conditions, the terms θ_m become null (see Eqs. (6.200) and (6.201)) and Eqs. (6.202) and (6.205) for the current and converted charge take the following simpler form, whatever the reversible degree of the electrode reaction:

$$\frac{I_p^{\text{cat,ss}}}{Q_F} = k_c \frac{k_{\text{red},p}}{k_{T,p}^c} \quad (6.207)$$

$$\frac{Q_p^{\text{cat,ss}}}{Q_F} = \frac{k_{\text{red},p}}{k_{T,p}^c} + k_c \tau \sum_{m=1}^p \frac{k_{\text{red},m}}{k_{T,m}^c} \quad (6.208)$$

Equations (6.207) and (6.208) lead to the following limiting situations depending on the reversibility degree of the electron transfer process:

- For a fast electron transfer reaction, by introducing the condition $k_{T,p} \gg k_c$ in both equations, the reversible limit given by Eqs. (6.203) and (6.206) is recovered.
- For an irreversible charge transfer reaction ($k_{red,p} \ll 1 \text{ s}^{-1}$), two new situations can be analyzed. In the first case, for cathodic potentials $k_{red,p} \gg k_{ox,p}$, Eqs. (6.207)–(6.208) lead to

$$\frac{I_{p,\text{irrev}}^{\text{cat,ss}}}{Q_F} = \frac{k_c k_{red,p}}{k_{red,p} + k_c} = \frac{1}{\frac{1}{k_{red,p}} + \frac{1}{k_c}} \quad (6.209)$$

$$\frac{Q_{p,\text{irrev}}^{\text{cat,ss}}}{Q_F} = \frac{k_{red,p}}{k_{red,p} + k_c} + k_c \tau \sum_{m=1}^p \frac{k_{red,m}}{k_{red,m} + k_c} \quad (6.210)$$

When $k_{red,p} \ll k_c$ at any potential value, Eqs. (6.209)–(6.210) are simplified to

$$\frac{I_{p,\text{irrev}}^{\text{cat,ss}}}{Q_F} = k_{red,p} \quad (6.211)$$

$$\frac{Q_{p,\text{irrev}}^{\text{cat,ss}}}{Q_F} = \tau \sum_{m=1}^p k_{red,m} \quad (6.212)$$

Equation (6.211) coincides with equation (5) of reference [72], deduced by considering that the charge transfer reaction was an oxidation.

6.4.4.1.1 Cyclic Voltammetry and Cyclic Voltcoulometry

The expressions for the current given by Eq. (6.202) can be applied in CV when the pulse amplitude holds $|\Delta E| \leq 0.01 \text{ mV}$, whereas in the case of the converted charge given by Eq. (6.205), it provides a good agreement for $|\Delta E| \leq 1 \text{ mV}$ [69–71]. Under stationary behavior ($k_c \gg 1 \text{ s}^{-1}$), the expression for the current corresponding to a reversible charge transfer (Eq. (6.207)) becomes

$$\psi_{CV}^{\text{cat,ss}} = \frac{I_{CV}^{\text{cat,ss}}}{aQ_F} = \psi_{CV}^E + \chi^{CV} \frac{k_{red}}{k_T^c} \cong \chi^{CV} \frac{k_{red}}{k_T^c} \quad (6.213)$$

which is obtained with

$$\chi^{CV} = \frac{k_c}{a} \quad (6.214)$$

ψ_{CV}^E in Eq. (6.213) refers to the CV current–potential curve of the electron transfer process in the absence of chemical reaction given by Eq. (6.161) and (6.166). Since the assumption of stationary behavior implies that the catalytic component of the

current is much higher than that due to the redox conversion, this contribution can be neglected in the total response. So, under reversible conditions for the electron transfer, Eq. (6.213) becomes [71]:

$$\psi_{CV,rev}^{cat,ss} = \chi^{CV} \frac{1}{1 + e^{\vartheta} e^{\vartheta_{in}}} \quad (6.215)$$

Concerning the expression of the stationary charge potential curves for Cyclic Voltcoulometry, the sum that appears in Eq. (6.208) can be transformed into an integral which for the case of fast and slow charge transfer reactions simplifies to

$$\frac{Q_{CV,rev}^{cat,ss}}{Q_F} = \frac{1}{1 + e^{\vartheta} e^{\vartheta_{in}}} + \chi^{CV} \left\{ \vartheta - \ln \left(\frac{1 + e^{\vartheta} e^{\vartheta_{in}}}{1 + e^{\vartheta_{in}}} \right) \right\} \quad (6.216)$$

$$\frac{Q_{CV,irrev}^{cat,ss}}{Q_F} = \frac{k_{red}}{k_{red} + k_c} + \frac{\chi^{CV}}{\alpha} \ln \left(\frac{k_{red} + k_c}{k_{red,i} + k_c} \right) \quad (6.217)$$

with $\vartheta = F(E(t) - E_{initial})/RT$, $\vartheta_{in} = F(E_{initial} - E_c^{\Theta'})/RT$, and $k_{red,i}$ being the value of k_{red} at $E_{initial}$.

Theoretical $\psi_{SCV}^{cat,ss} - E$ and $Q_{SCVC}/Q_F - E$ curves, calculated from Eqs. (6.202) and (6.205), respectively, for different values of the dimensionless catalytic rate constant χ^{CV} , have been plotted in Fig. 6.31. These curves correspond to a cyclic staircase potential with $\Delta E = 5$ mV and $\tau = 10$ ms ($v = 0.5$ V s⁻¹). Two values of the heterogeneous rate constant k^0 (s⁻¹) = 200 and 2, which refer to reversible (1a and 1b) and totally irreversible (1c and 1d) electrochemical behavior, have been considered.

From Figs. 6.31a, c it can be seen that, when χ^{CV} increases, the current–potential response changes its feature from two peak-shaped curves (with more separated peaks the smaller the reversibility degree of the charge transfer) to a single sigmoidal one (stationary state). The χ^{CV} limit necessary for attaining this stationary behavior increases as the value of the heterogeneous rate constant k^0 decreases (note that in Figure c the steady state has not been reached for $\chi^{CV} = 1$).

From the charge–potential curves in Figures b and d, it is clear that a stationary behavior cannot be reached in any case. From the first scan of these curves, it can be seen that the converted charge is null up to potentials close to $E_c^{\Theta'}$, from which it increases with the potential, with this increase becoming linear for sufficient cathodic values. For the second scan, the charge–potential curves present an opposite behavior, i.e., they increase linearly until they reach a constant value (charge plateau) for enough cathodic potentials.

The above behavior can be characterized when the charge transfer step is fast (b) or slow (d).

Fast Electron Transfer Step Under these conditions, for cathodic potentials, $E \ll E_c^{\Theta'}$, from Eq. (6.216) is obtained [70]:

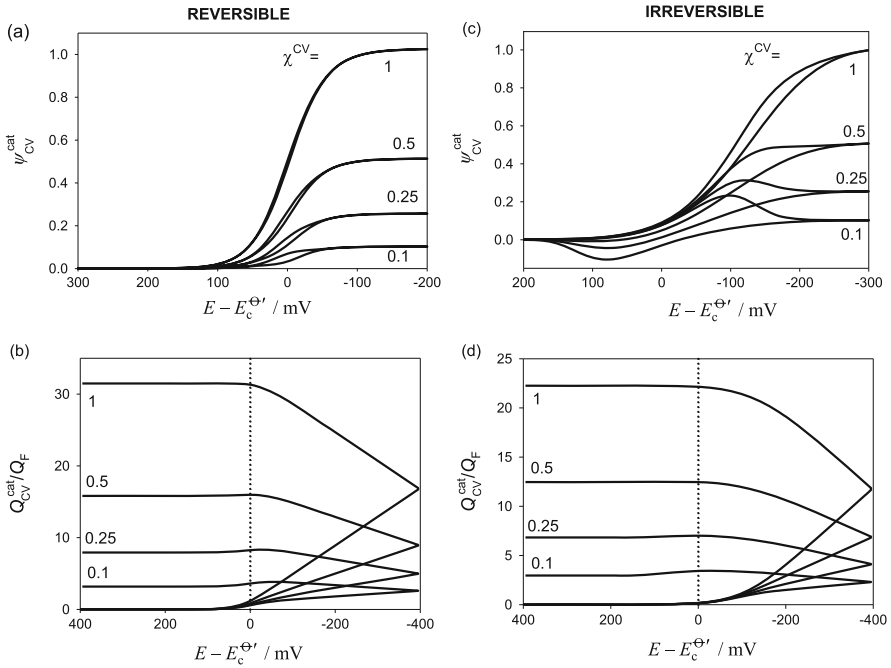


Fig. 6.31 Theoretical $\psi_{CV}^{cat} - E$ ((a) and (c)) and $Q_{CV}^{cat}/Q_F - E$ curves ((b) and (d)) calculated from Eqs. (6.202) and (6.205) in Staircase Voltammetry and Voltcoulometry, respectively, for a catalytic mechanism. The values of χ^{CV} are on the curves. The values of k^0 (in s^{-1}) are: 200 (a, b); 2 (c, d). $\Delta E = 5$ mV, $\tau = 10$ ms, $E_{initial} = -400$ mV, $E_{final} = 400$ mV, $T = 298$ K, $\alpha = 0.5$. $\nu = 0.5$ V s^{-1} . Reproduced with permission from [70]

$$\frac{Q_{CV,rev}^{cat,ss}}{Q_F} = 1 \pm \chi^{CV} \eta \quad (6.218)$$

with the upper sign referring to the first sweep and the lower to the second one.

From this linear relationship between the charge and the potential, k_c is easily deduced from the cathodic slopes of both sweeps. The expression of the reversible cathodic converted charge plateau can also be deduced from Eq. (6.216) by imposing $E \rightarrow -\infty$ in the second cathodic sweep (see Eq. (6.217)):

$$\frac{Q_{CV,rev}^{cat,ss,plateau}}{Q_F} = 1 + 2|\chi^{CV}| \eta_f \quad (6.219)$$

with $\eta_f = F(E_{final} - E_c^{\Theta'})/RT$ and E_{final} being the reversal potential.

Slow Electron Transfer Step In this case, at very cathodic potentials ($E \ll E_c^{\Theta'}$), Eq. (6.217) becomes

$$\frac{Q_{CV}^{cat}}{Q_F} = 1 \pm \frac{\chi^{CV}}{\alpha} \ln\left(\frac{k^0}{k_c}\right) \pm \chi^{CV} \eta \quad (6.220)$$

Concerning the irreversible cathodic charge plateau, it can be obtained by making $E \rightarrow -\infty$ in the expression of the charge for the second sweep (see Eq. (6.217)):

$$\frac{Q_{CV}^{cat, plateau}}{Q_F} = 1 + \frac{2\chi^{CV}}{\alpha} \ln\left(\frac{k^0}{k_c}\right) + 2\chi^{CV} \eta_f \quad (6.221)$$

Note that in agreement with Eqs. (6.218) and (6.220), the absolute value of the slope of these linear regions does not depend on the reversibility degree of the electron transfer step and its measurement will allow us to obtain the catalytic rate constant.

The experimental and theoretical CV (current–potential) and CVC (charge–potential) curves of the system $FcC_6SH - C_6SH$ in a solution 1.0 M $NaClO_4$ and 10 mM in $Fe(CN)_6^{4-}$ obtained for different values of the sweep rate are plotted in Fig. 6.32 (corresponding to an oxidation [70, 71]).

The CV curves in Fig. 6.32a show a sigmoidal feature which is typical of stationary or nearly stationary behavior (see Eq. (6.215)). The increase of the sweep rate does not affect the response as the stationary limit has been reached. Moreover, it can be observed that a well-defined plateau independent of the sweep rate is obtained for $E > 0.200$ V. From the measurement of this plateau, the value $(k_c Q_F) = (11.29 \pm 0.05)$ nA is obtained.

In the case of the CVC curves of Fig. 6.32b, the converted charge increases as the scan rate decreases and they show a clear linear region at potentials above 0.20 V. The slope of these linear zones should be equal to $(k_c Q_F)/v$ (see Eqs. (6.214) and (6.218)). The values of the slopes of the linear regression of these zones for different values of v in the range 0.20–100 $V s^{-1}$ have been plotted vs. the inverse of the sweep rate and from these data $(k_c Q_F) = (11.3 \pm 0.2)$ nA has been obtained. This value is practically coincident with that obtained from the current–potential curves of Fig. 6.32a.

The values of the cathodic charge plateau can also be plotted versus $1/v$ again obtaining a very good linearity. If the ferrocene oxidation can be considered as reversible under these conditions, the linear dependence observed corresponds to that given by Eq. (6.219), with the slope being $2k_c Q_F (E_f - E_c^{\Theta'})$, from which, by taking into account that $E_f = 0.600$ V, the formal potential of the ferrocene/ferrocenium couple: $E_c^{\Theta'} = (0.1000 \pm 0.005)$ V vs. SCE is deduced.

To check the goodness of the data obtained, the theoretical CV and CVC curves calculated from Eqs. (6.215) and (6.218) have been included (symbols). By taking into account that the total charge for the ferrocene monolayer in the 1.0 M $NaClO_4$

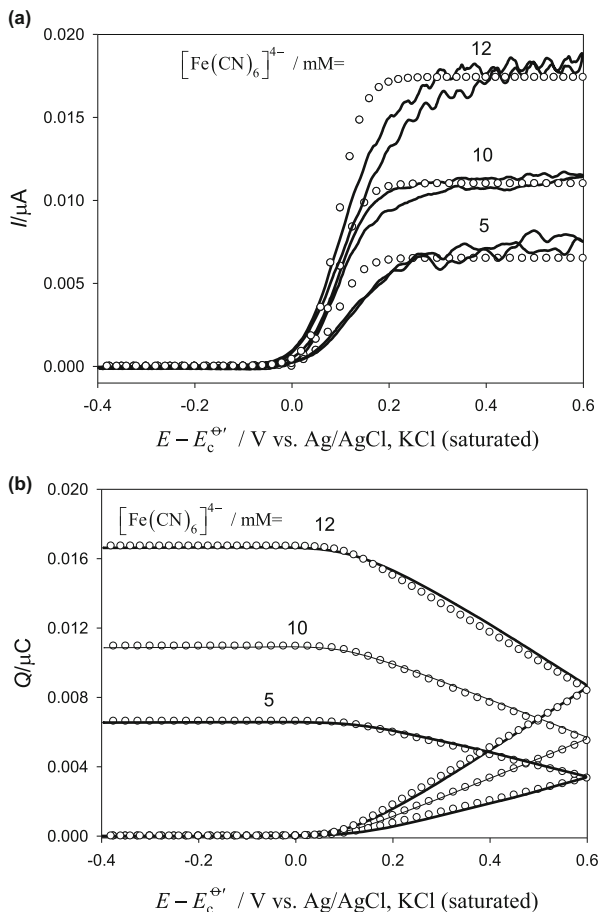


Fig. 6.32 Experimental $I-E$ (a) and $Q-E$ (b) curves obtained in CV and CVC for a mixed ferrocene monolayer ($\text{FcC}_6\text{SH} - \text{C}_6\text{SH}$ 1:20) adsorbed at a disc gold electrode of radius $r_d = 0.001$ cm in an aqueous solution 1 M NaClO_4 with potassium ferrocyanide 10 mM. The values of the scan rate $(E(t) - E_{\text{initial}})/v$ (in V s^{-1}) and for (a) are the following: 0.2 (solid lines), 0.4 (dotted lines), 0.6 (long-dashed lines), 0.8 (short-dashed lines), and 1 (dashed-dot-dot lines). (symbols) $I-E$ (a) and $Q-E$ (b) curves calculated from Eqs. (6.215) to (6.216) by using the following parameters: $E_c^{\Theta'} = 0.095$ V, $k_c = 250 \text{ s}^{-1}$, $Q_F = 0.437$ pC, and $T = 298$ K. Reproduced with permission from [71]

solution is $Q_F = 0.437 \pm 0.050$ pC, the theoretical curves have been calculated using the parameters: $E_c^{\Theta'} = 0.095$ V and $k_c = 250 \text{ s}^{-1}$. From the value of $|\Delta E| = 5$ mV used, we can finally obtain that the true chemical rate constant of the mechanism is $k_1' = 2.5 \times 10^4 \text{ M}^{-1} \text{ s}^{-1}$.

6.4.4.2 Second-Order Electrocatalytic Process

When the surface concentration of species C_{sol} cannot be considered as constant the analysis of the electrochemical response that arises from reaction scheme (6.X) becomes much more complex since the process is of second order and the value of the surface concentration of C_{sol} will be a function of the kinetics of the catalytic reaction and also of the mass transport (and therefore of the electrode geometry). Due to this higher complexity, only the current–potential response in CV will be treated with the additional simplification of fast surface charge transfer.

The analytical resolution of this problem is considerably more difficult. Due to this, only numerical or approximate models were initially available in the literature [73–75].

The rate equation for this process is now given by the following modification of Eq. (6.195):

$$\frac{df_{\text{O}}^{(p)}}{dt} = -\frac{I_p^{\text{cat}}}{Q_F} + k_1' f_{\text{R}}^{(p)} c_{\text{C}}^{(s,p)}(t) \quad (6.222)$$

with $c_{\text{C}}^{(s,p)}(t)$ being the surface concentration of species C, which is a function of time (or potential in the case of CV).

An approximate analytical expression for the CV current of this process when spherical electrodes are used has been given in [74]:

$$\psi_p^{\text{cat}} = \frac{I_p^{\text{cat}}}{FA_s c_{\text{C}}^* \sqrt{aD_C}} = \psi_p^{\text{surf}} + \psi_p^{\text{cat}} \quad (6.223)$$

with:

$$\psi_p^{\text{surf}} = -\frac{\Gamma_{\text{T}}}{c_{\text{C}}^* \sqrt{aD_C}} \frac{df_{\text{R}}^{(p)}}{d\eta_p} = \frac{\Gamma_{\text{T}}}{c_{\text{C}}^* \sqrt{aD_C}} \frac{e^{\eta_p}}{(1 + e^{\eta_p})^2} \quad (6.224)$$

$$\psi_p^{\text{cat}} = \Lambda f_{\text{R}}^{(p)} \frac{\prod_{m=1}^{p-1} [1 + \Lambda f_{\text{R}}^{(m)} \sigma_{m+1,p}]}{\prod_{m=1}^p [1 + \Lambda f_{\text{R}}^{(m)} \sigma_{m,p}]} \quad (6.225)$$

where

$$\Lambda = \frac{k_1' \Gamma_{\text{T}}}{\sqrt{aD_C}} \quad (6.226)$$

$$f_{\text{R}}^{(m)} = \frac{1}{1 + e^{\eta_m}} \quad (6.227)$$

$$\sigma_{m,p} = \frac{1}{\rho + \frac{1}{\sqrt{\pi} \delta_{m,p}}} \quad (6.228)$$

$$\rho = \left(\frac{D_{\text{C}}}{ar_s^2} \right)^{1/2} \quad (6.229)$$

$$\left. \begin{aligned} \delta_{m,p} &= \frac{F}{RT} |E_{p-m+1} - E_{\text{initial}}| & m \leq p/2 \\ \delta_{m,p} &= \frac{F}{RT} |-E_{p-m+1} - E_{\text{initial}} + 2E_{\text{final}}| & m > p/2 \end{aligned} \right\} \quad (6.230)$$

The catalytic term given in Eq. (6.225) is greatly simplified in the case of microelectrodes:

$$\psi_p^{\text{cat, microspher}} = \frac{\Lambda f_{\text{R}}^{(p)}}{1 + \frac{\Lambda}{\rho} f_{\text{R}}^{(p)}} \quad (6.231)$$

so under these conditions the current is only dependent on the applied potential. If the ψ_p^{surf} can be neglected (or removed from the total response, for example, by subtracting the CV curves of the monolayer in absence of species C), the voltammetric current has a sigmoidal shape with a plateau and a half-wave potential given by

$$\psi_p^{\text{cat, microspher, plateau}} = \frac{\Lambda}{1 + \frac{\Lambda}{\rho}} \quad (6.232)$$

$$E_{1/2} = E_c^{\Theta'} + \frac{RT}{F} \ln \left(1 + \frac{\Lambda}{\rho} \right) \quad (6.233)$$

The effects of the catalytic reaction on the CV curve are related to the value of dimensionless parameter Λ in whose expressions appear variables related to the chemical reaction and also to the geometry of the diffusion field. For small values of Λ , the surface concentration of species C is scarcely affected by the catalysis for any value of the electrode radius, such that $c_{\text{C}}^{(s,p)} \rightarrow c_{\text{C}}^*$ and the current becomes identical to that corresponding to a pseudo-first-order catalytic mechanism (see Eq. (6.203)). In contrast, for high values of Λ and $f_{\text{R}}^{(m)} \rightarrow 1$ (cathodic limit), the rate-determining step of the process is the mass transport. In this case, the catalytic limiting current coincides with that obtained for a simple charge transfer process.

Figure 6.33 shows the effects of the electrode size (r_s) and the catalytic rate constant (Λ) on the dimensionless catalytic component of the voltammogram. For a given electrode radius, the increase of Λ (i.e., the increase of the rate constant k_1')

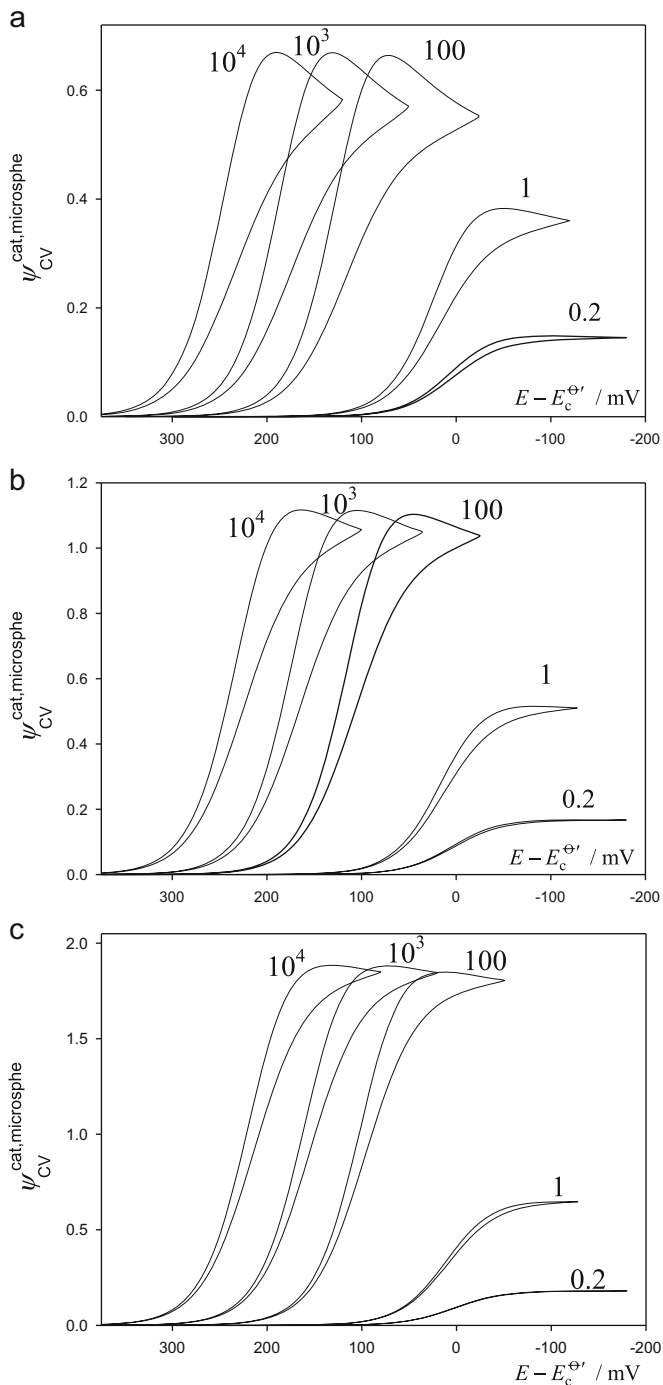


Fig. 6.33 Catalytic CV curves for spherical microelectrodes calculated from Eq. (6.225) for different values of Λ (shown in the curves). These curves have been calculated for $|\Delta E| = 0.01 \text{ mV}$, a scan rate $\nu = 0.1 \text{ V s}^{-1}$, and three electrode radii r_s (in μm): (a) 50, (b) 20, and (c) 10. Reproduced with permission from [76]

enhances ψ_p^{cat} and leads to the shift of the voltammogram toward more anodic potentials. For very fast catalytic reactions ($\Lambda \geq 100$), the peak current becomes independent of Λ in an analogous way to that reported for planar electrodes. On the other hand, the peak potential is also always sensitive to the kinetics.

The shape of the voltammograms is affected by both the electrode radius and Λ . Thus, a transition from a peak-shaped response to a sigmoidal wave is observed as Λ and/or the electrode radius decrease, although this behavior has different causes in each case.

The consideration of chemical equilibrium for this mechanism (scheme (6.IX)), has been treated in detail in references [74, 77], where different methods for obtaining the characteristic parameters of the process are proposed.

References

1. Hale JM (1964) *J Electroanal Chem* 8:181–199
2. Andrieux CP, Saveant J (1970) *J Electroanal Chem* 28:339–348
3. Amatore C, Klymenko O, Svir I (2010) *Electrochem Commun* 12:1170–1173 and 12:1378–1382
4. Lehmann MW, Evans DE (1999) *Anal Chem* 71:1947–1950
5. Molina A, Serna C, Li Q, Laborda E, Batchelor-McAuley C, Compton RG (2012) *J Phys Chem C* 116:11470–11479
6. Molina A, Serna C, Lopez-Tenes M, Chicon R (2000) *Electrochem Commun* 2:267–271
7. Polcyn DS, Shain I (1966) *Anal Chem* 38:370–375
8. Li Q, Batchelor-McAuley C, Lawrence NS, Hartshorne RS, Compton RG (2011) *Chem Commun* 47:11246–11248
9. Gamage RSKA, McQuillan AJ, Peake BM (1991) *J Chem Soc Faraday Trans* 87:3653–3660
10. Flanagan JB, Margel S, Bard AJ, Anson FC (1978) *J Am Chem Soc* 100:4248–4253
11. Hapiot P, Kispert LD, Konovalov VV, Savean JM (2001) *J Am Chem Soc* 123:6669–6677
12. Molina A, Serna C, Lopez-Tenes M, Moreno MM (2005) *J Electroanal Chem* 576:9–19
13. Bard AJ, Faulkner LR (2000) *Electrochemical methods. Fundamental and applications*, 2nd edn. Wiley, Hoboken, Chapters 6 and 12
14. Hilkelmann K, Heinze J (1987) *Ber Bunsenges Phys Chem* 91:243–249
15. Lund H, Hammerich O (eds) (2000) *Organic electrochemistry*, 4th edn. CRC Press, New Jersey
16. Comninellis C, Chen G (2009) *Electrochemistry for the environment*. Springer, New York
17. Bartlett PN (ed) (2008) *Bioelectrochemistry: fundamentals, experimental techniques and applications*. Wiley, New York
18. Weber J (1958) *Chem Listy* 52:1888–1898
19. Molina A (1998) *J Electroanal Chem* 443:163–167
20. Molina A, Serna C, Gonzalez J (1998) *J Electroanal Chem* 545:15–31
21. Molina A, Gonzalez J, Laborda E, Wang Y, Compton RG (2011) *Phys Chem Chem Phys* 13:16694–16704
22. Nicholson RS, Shain I (1964) *Anal Chem* 36:706–723
23. Molina A, Serna C, Martinez-Ortiz F, Laborda E (2008) *J Electroanal Chem* 617:14–26
24. Martinez-Ortiz F, Molina A, Laborda E (2011) *Electrochim Acta* 56:5707–5716
25. Saveant JM, Vianello E (1967) *Electrochim Acta* 12:629–646
26. Molina A, Morales I, Lopez-Tenes M (2006) *Electrochem Commun* 8:1062–1070
27. Sobel H, Smith DE (1970) *J Electroanal Chem* 26:271–284

28. Nadjo L, Saveant JM (1971) *J Electroanal Chem* 30:41–57
29. Banks CE, Compton RG (2011) *Understanding voltammetry*, 2nd edn. Imperial College Press, Singapore
30. Saveant JM (2006) *Elements of molecular electrochemistry: an electrochemical approach to electron transfer chemistry*. Wiley-Interscience, New York
31. Beer PD, Gale PA, Chen GZ (1999) *Coord Chem Rev* 185:3–36
32. Molina A, Torralba E, Serna C, Ortuño JA (2013) *Electrochim Acta* 106:244–257
33. Alligrant TM, Alvarez JC (2011) *J Phys Chem C* 115:10797–10805
34. Weinberg DR, Gagliardi CJ, Hull JF, Murphy CF, Kent CA, Westlake BC, Paul A, Ess DH, McCafferty DG, Meyer TJ (2012) *Chem Rev* 112:4016–4093
35. Atifi A, Ryan MD (2014) *Anal Chem* 86:6617–6625
36. Savéant JM (2008) *J Am Chem Soc* 130:4732–4741
37. Laborda E, Olmos JM, Torralba E, Molina A (2015) *Anal Chem* 87:1676–1684
38. Molina A, Serna C, Camacho L (1995) *J Electroanal Chem* 394:1–6
39. Bard AJ, Stratman M (Eds) (2007) *Encyclopedia of electrochemistry* Vol. 10: Modified electrodes. Wiley-VCH, Weinheim
40. Saveant JM (2008) *Chem Rev* 108:2348–2378
41. Christopher-Love J, Estroff LA, Kriebel JK, Nuzzo RG (2005) *Chem Rev* 105:1103–69
42. Downard AJ (2000) *Electroanalysis* 12:1085–1096
43. Chidsey CED (1991) *Science* 215:919–922
44. Vos JG, Forster RJ, Keyes TE (2003) *Interfacial supramolecular assemblies*. Wiley, New York
45. Laviron E (1982) In: Bard AJ (ed) *Electroanalytical chemistry*, vol. 12. Marcel Dekker, New York, pp 53–177
46. Gonzalez J, Abenza N, Molina A (2006) *J Electroanal Chem* 596:74–86
47. Forster RJ, Faulkner LR (1994) *J Am Chem Soc* 116:5444–5452
48. Gonzalez J, Molina A (2003) *J Electroanal Chem* 557:157–165
49. Molina A, Gonzalez J, Henstridge M, Compton RG (2011) *J Phys Chem C* 115:4054–4062
50. Henstridge M, Laborda E, Rees NV, Compton RG (2012) *Electrochim Acta* 84:12–20
51. Finklea H, Hanshew D (1992) *J Am Chem Soc* 114:3173–3181
52. Abenza N, Gonzalez J, Molina A (2007) *Electroanalysis* 19:936–944
53. Damaskin BB, Petriand OA, Batrakov VV (1971) *Adsorption of organic compounds on electrodes*. Plenum, New York
54. Laviron E (1979) *J Electroanal Chem* 101:19–28
55. Myland JC, Oldham KB (2005) *Electrochem Commun* 7:282–287
56. Gileadi E (2011) *Physical electrochemistry*. Wiley-VCH, Weinheim
57. Molina A, Gonzalez J (2005) *J Electroanal Chem* 583:184–192
58. Tender L, Carter MT, Murray RW (1994) *Anal Chem* 55:3173–3181
59. Smith CP, White HS (1992) *Anal Chem* 64:2396–2405
60. Ohtani M (1999) *Electrochem Commun* 1:488–492
61. Andreu R, Fawcett WR (1994) *J Phys Chem* 98:12753–12758
62. Brown AP, Anson FC (1977) *Anal Chem* 49:1589–1595
63. Gerischer H, Scherson DA (1985) *J Electroanal Chem* 188:33–38
64. Rowe GK, Carter MT, Richardson JN, Murray RW (1995) *Langmuir* 11:1797–1806
65. Lopez-Tenes M, Gonzalez J, Molina A (2014) *J Phys Chem C* 118:12312–12324
66. Gonzalez J, Molina A, Soto CM (2012) *Serna C* 664:53–62
67. Armstrong FA, Camba R, Heering HA, Hirst J, Jeuken LJC, Jones AK, Léger C, McEvoy JP (2000) *Faraday Discuss* 116:191–203
68. Gonzalez J, Lopez-Tenes M, Molina A (2013) *J Phys Chem C* 117:5208–5220
69. Gonzalez J, Soto CM, Molina A (2009) *Electrochim Acta* 26:6154–6160
70. Molina A, Soto CM, Gonzalez J (2009) *Anal Chem* 81:6830–6836
71. Molina A, Soto CM, Gonzalez J (2010) *Electroanalysis* 22:106–112
72. Alleman KS, Weber K, Creager SE (1996) *J Phys Chem* 42:17050–17058
73. Andrieux CP, Saveant JM (1978) *J Electroanal Chem* 93:163–168

74. Aoki K, Tokuda K, Matsuda H (1986) *J Electroanal Chem* 199:69–79
75. Xie Y, Anson FC (1995) *J Electroanal Chem* 384:145–153
76. Molina A, Gonzalez J, Laborda E, Martinez-Ortiz F, Bieniasz LK (2010) *J Phys Chem C* 114:14545–14551
77. Bieniasz LK, Gonzalez J, Molina A, Laborda E (2010) *Electrochim Acta* 56:543–552

Chapter 7

Differential Multipulse and Square Wave Voltammetries

Contents

7.1	Introduction	464
7.2	Reversible Electrochemical Reactions at Electrodes and Microelectrodes of Any Geometry	469
7.2.1	Differential Staircase Voltammetry	469
7.2.2	Differential Multipulse Voltammetry	471
7.2.3	Square Wave Voltammetry	474
7.3	Non-reversible Electrochemical Reactions	485
7.3.1	Differential Multipulse Voltammetry	485
7.3.2	Square Wave Voltammetry	489
7.4	Ion Transport Through Liquid Membranes	499
7.4.1	Differential Multipulse Voltammetry	500
7.4.2	Square Wave Voltammetry	500
7.4.3	Micro-ITIES and Asymmetrical Diffusion	503
7.5	Multi-electron Electrochemical Reactions	507
7.5.1	Reversible Electrochemical Reactions	508
7.5.2	Non-reversible Electrochemical Reactions	520
7.6	First-Order Chemical Reactions Coupled to the Charge Transfer Reaction	522
7.6.1	Catalytic Mechanism	523
7.6.2	CE and EC Mechanisms	528
7.6.3	ECE Mechanism	530
7.6.4	Ladder Mechanism	533
7.7	Surface-Bound Molecules	536
7.7.1	One-Electron Electrochemical Reactions	537
7.7.2	Multi-electron Electrochemical Reactions	557
7.7.3	Electrocatalytic Reactions at Modified Electrodes	563
	References	577

7.1 Introduction

A common feature of the electrochemical techniques considered in this chapter is that the recorded signal is the difference between the current (or converted charge) sampled at the end of consecutive potential pulses of a given sequence E_1, E_2, \dots, E_p without the initial conditions being regained. This difference is plotted versus a potential axis, giving a peak-shaped response in all the cases.

Differential multipulse techniques are, due to their subtractive nature, highly sensitive, and they present high resolution of the peak-shaped voltammogram, and minimization of double-layer and background effects [1–3]. In addition, given that they are pulse techniques and the value of the applied potential remains constant during each pulse, the effect of the charging current is greatly reduced since this sharply decays after the application of the pulse. As a consequence, these techniques are widely used in electroanalysis for determination of trace elements as well as for the study of electrode processes and identification of reaction mechanisms.

This chapter analyzes the subtractive techniques Differential Multipulse Voltammetry (DMPV), Differential Staircase Voltammetry (DSCVC), and Square Wave Voltammetry (SWV). Of these, the most employed SWV will be analyzed in more detail. Interesting alternatives to DSCVC and SWV are Differential Staircase Voltcoulometry (DSCVC) and Square Wave Voltcoulometry (SWVC), which are based on the analysis of the difference of converted faradaic charge signals obtained between two successive potential pulses when a staircase potential or a square wave potential is applied [4, 5], which is very useful for the study of surface-confined redox species. There exists, however, a book in this series devoted entirely to the theory and application of SWV [6], so in some of the reaction mechanisms analyzed, the reader will be directed to this title for a more thorough treatment of the SWV response.

The general features of the potential time perturbations and of the current–potential (or converted charge–potential) responses characteristic of these techniques are:

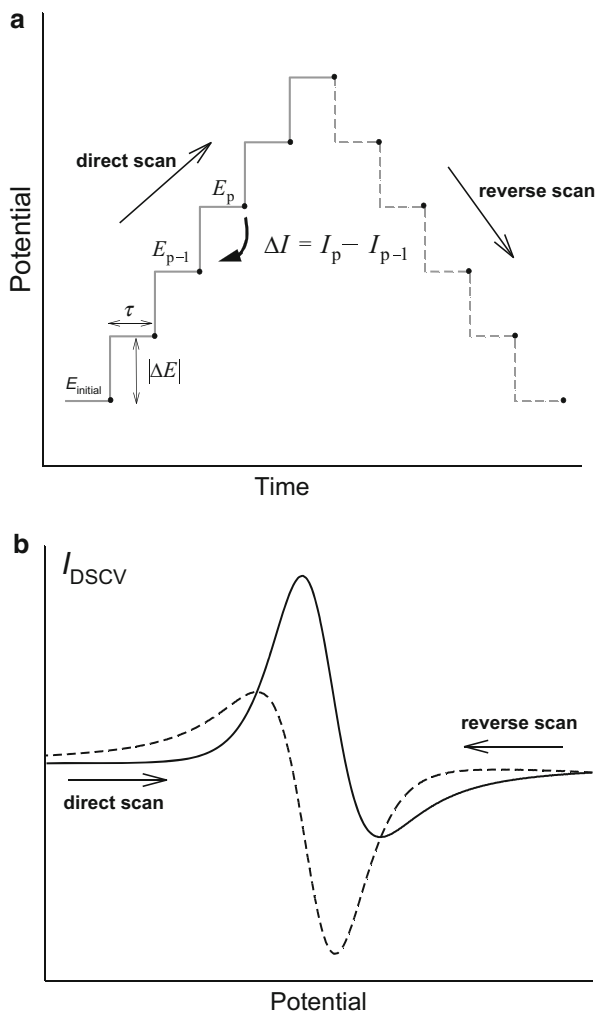
Differential Staircase Voltammetry

This technique was introduced by Scholz et al in [7, 8] in its noncyclic mode as a technique related to DDPV and SCV in which the potential–time wave form is that corresponding to SCV (see Scheme 5.2) and the signal is built through the difference between the currents measured at the end of each pair of consecutive pulses (see Scheme 7.1)

$$I_{\text{DSCV}} = I_p - I_{p-1} \quad (1 < p \leq N) \quad (7.1)$$

with I_p being the voltammetric current corresponding to the p th potential pulse, and N the number of pulses applied. Under these conditions, the current–potential response is obtained in a similar way to that employed for differential double pulse techniques (like DDPV), and I_{DSCV} is plotted versus the potential E_p [9].

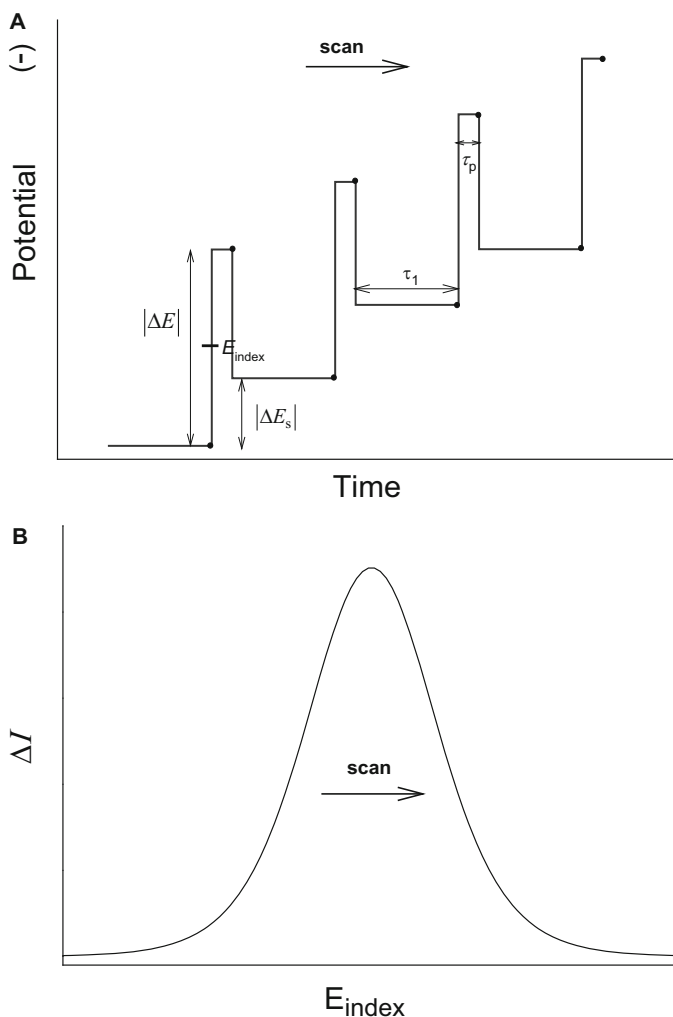
Scheme 7.1 Differential staircase voltammetry and cyclic differential staircase voltammetry. (a) Potential–time waveform. (b) current–potential response with $\Delta I = I_{\text{DSCV}}$. The *black dots* in (a) indicate the time at which the current is measured



A variant of DSCVC is DSCVC, for which the response is built by subtracting the converted charge measured at the end of each pair of consecutive potential pulses applied [4]:

$$Q_{\text{DSCVC}} = Q_p - Q_{p-1} \quad (1 < p \leq N) \quad (7.2)$$

This technique is of special interest in the case of charge transfer processes at surface-bound molecules since it allows a simple and more effective correction of the non-faradaic components of the response than Cyclic Voltammetry. Moreover, this technique presents an intense peak-shaped signal for fast charge transfer, whereas other multipulse techniques give rise to nonmeasurable currents under these conditions and it is necessary to use short potential pulses to transform the response to quasi-reversible, which is much more difficult to analyze [4, 6, 10].



Scheme 7.2 Differential multipulse voltammetry (DMPV). (a) Potential–time waveform. (b) current–potential response. The *black dots* in (a) indicate the time at which the current is measured

Differential Multipulse Voltammetry and Differential Normal Multipulse Voltammetry

The DMPV technique can be viewed as a variant of DDPV (see Scheme 4.3), where the initial conditions are not recovered during the experiment (Scheme 7.2). Thus, the pulse length (τ_p) is much shorter than the period between pulses (τ_1), $\tau_1/\tau_p = 50 - 100$.

The DNMPV is the multipulse variant of the DMPV technique such that the duration of the period between pulses and the duration of the pulses are similar: $\tau_1 \approx \tau_p$.

The response ΔI is the difference between currents corresponding to each pair of consecutive potential pulses, and this is plotted versus E_{index} , which is convenient to define as

$$E_{\text{index}} = E_{\text{initial}} - \left(\text{Int} \left(\frac{p+1}{2} \right) - 1 \right) |\Delta E_s| \quad p \geq 1 \quad (7.3)$$

and

$$E_{\text{initial}} = \frac{E_1 + E_2}{2} \quad (7.4)$$

where $\text{Int}(x)$ is the integer part of the argument x [11].

DMPV is by far the most frequently used in commercial potentiostats referred to Differential Pulse Voltammetry.

Square Wave Voltammetry

SWV is one of the most popular electrochemical techniques, mainly in electroanalysis, due to its great sensitivity, discrimination of background currents, and short experimental times [6, 9, 12]. It was introduced by Baker [13–15] and later developed by the Osteryoungs and coworkers by using a combination of a staircase potential modulation and a periodic square wave potential function [16–19]. In the SWV technique, the potential sequence can be described as (see Scheme 7.3 and [9]):

$$\left. \begin{aligned} E_p &= E_{\text{initial}} \mp \left[\text{Int} \left(\frac{p+1}{2} \right) - 1 \right] \Delta E_s \mp (-1)^{p+1} E_{\text{SW}}; & p = 1, 2, \dots, N/2 \\ E_p &= E_{N-p+1}; & p = (N/2) + 1, \dots, N \end{aligned} \right\} \quad (7.5)$$

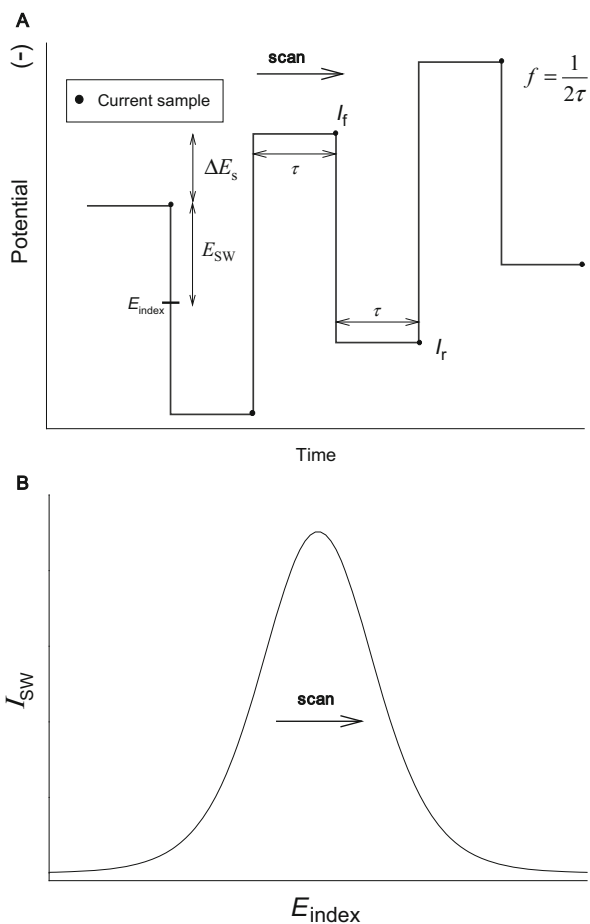
where the upper/lower sign corresponds to a cathodic/anodic scan. N is the total number of potential pulses applied, ΔE_s is the potential step in the staircase, and E_{SW} is the square wave amplitude. According to the SWV waveform shown in Scheme 7.3, three parameters are necessary for its characterization: ΔE_s , E_{SW} , and the frequency or the time pulse length τ .

The current is sampled at the end of each potential pulse and the net response (I_{SW}) is given by the subtraction of the current corresponding to a pulse with odd index (forward current, I_f) and the signal of the following pulse with even index (reverse or backward current, I_r) (see Scheme 7.3):

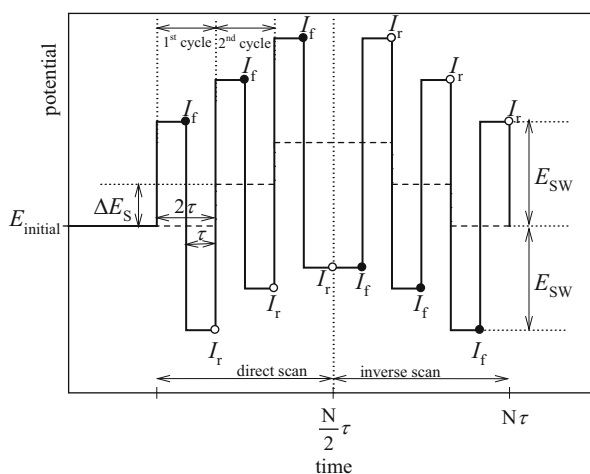
$$I_{\text{SW}} = I_{2p-1} - I_{2p} = I_f - I_r; \quad p = 1, 2, \dots, (N/2) \quad (7.6)$$

where subscripts f and r refer to the forward ($2p-1$) and reverse ($2p$) pulses, respectively, and τ is the semi-period of the square wave and its frequency $f = 1/(2\tau)$. SWV can be applied in cyclic mode as indicated in Scheme 7.4.

Scheme 7.3 Square wave voltammetry. (a) Potential–time waveform. (b) current–potential response. The *black dots* in (a) indicate the time at which the current is measured. f denotes the frequency of SW perturbation



Scheme 7.4 Potential–time waveform of square wave voltammetry in cyclic mode. *Black and white dots* indicate the time at which the forward and reverse currents, respectively, are measured



The SWV current is plotted versus the arithmetic average of the potentials applied in each pair of pulses ($2p - 1, 2p$)

$$E_{\text{index}} = E_p \mp (-1)^p E_{\text{SW}} \quad (7.7)$$

Note that, in agreement with Eq. (7.5), the index potential defined by Eq. (7.7) for a cathodic scan (upper sign) is identical in this case to that given by Eq. (7.3).

In accordance with Scheme 7.4, during the course of a single potential cycle, the electrochemical process is driven in both cathodic and anodic directions, so providing a thorough understanding of the reaction mechanism.

An interesting variant of SWV is SWVC, which is based on the analysis of the difference of converted faradaic charge signals obtained between two successive half-cycles when a square wave potential is applied [5]. The potential perturbation is given by Eq. (7.5) and the response is

$$Q_{\text{SW}} = Q_{2p-1} - Q_{2p} = Q_f - Q_r; \quad p = 1, 2, \dots, (N/2) \quad (7.8)$$

The $Q_{\text{SW}} - E_{\text{index}}$ curves present an intense signal for reversible processes taking place with surface-bound species, so allowing their simple and complete characterization (see Sect. 7.7.1.3).

7.2 Reversible Electrochemical Reactions at Electrodes and Microelectrodes of Any Geometry

In this section, the response corresponding to a fast electrochemical reaction, shown by the following reaction scheme:



when species O and R are soluble in the electrolytic solution, is obtained for differential multipulse techniques by using the general expressions for the current I_p corresponding to any p th potential pulse applied of an arbitrary sequence, deduced in Sect. 5.2.1.

7.2.1 Differential Staircase Voltammetry

According to Scheme 7.1 and Eq. (7.1), by subtracting the currents corresponding to the consecutive potential pulses E_p and E_{p-1} (see Eq. (5.24)), the DSCVC response for any electrode geometry when equal diffusion coefficients for species O and R are assumed is

$$\psi_{\text{DSCVC}}^{\text{G}} = \sqrt{\frac{D}{a}}(1 + c_{\text{R}}^*/c_{\text{O}}^*) \left(Z_p f_{\text{G}}(\tau, q_{\text{G}}) + \sum_{m=1}^{p-1} Z_m (f_{\text{G}}((p-m+1)\tau, q_{\text{G}}) - f_{\text{G}}((p-m)\tau, q_{\text{G}})) \right) \quad (7.9)$$

with

$$\psi_{\text{DSCVC}}^{\text{G}} = \frac{I_{\text{DSCVC}}^{\text{G}}}{FA_{\text{G}}c_{\text{O}}^*\sqrt{aD}} = \frac{I_p^{\text{G}} - I_{p-1}^{\text{G}}}{FA_{\text{G}}c_{\text{O}}^*\sqrt{aD}} \quad (7.10)$$

$$a = \frac{Fv}{RT} \quad (7.11)$$

$$Z_m = \frac{1}{1 + e^{\eta_m}} - \frac{1}{1 + e^{\eta_{m-1}}} \quad 1 \leq m \leq p \quad (7.12)$$

$$\eta_m = \left(\frac{F}{RT} (E_m - E_c^{\ominus}) \right) \quad 1 \leq m \leq p \quad (7.13)$$

and

$$e^{\eta_0} = \exp\left(\frac{F}{RT}(E_{\text{eq}} - E_c^{\ominus})\right) = \frac{c_{\text{O}}^*}{c_{\text{R}}^*} \quad (7.14)$$

Moreover, $f_{\text{G}}(\tau, q_{\text{G}})$ is a function which depends on the electrode geometry (see Table 2.3 for several common situations), c_i^* is the bulk concentration of species i , v is the scan rate ($= \Delta E/\tau$), and E_{eq} is the equilibrium potential given by Nernst equation. The superindex or subindex “G” refers to the electrode geometry considered, and q_{G} to the characteristic dimension of the electrode considered.

7.2.1.1 Planar Electrodes

By making $q_{\text{G}} \rightarrow \infty$ in Eq. (7.9) (see also Table 2.3), the DSCVC curve corresponding to planar electrodes is obtained:

$$\psi_{\text{DSCVC}}^{\text{plane}} = (1 + c_{\text{R}}^*/c_{\text{O}}^*) \frac{1}{\sqrt{\pi a \tau}} \left(Z_p + \sum_{m=1}^{p-1} Z_m \left(\frac{1}{\sqrt{p-m+1}} - \frac{1}{\sqrt{p-m}} \right) \right) \quad (7.15)$$

When different values for the diffusion coefficients of species O and R are assumed, the expression for the current is [9, 20],

$$\begin{aligned}\psi_{\text{DSCVC}}^{\text{plane}} &= \frac{I_p^G - I_{p-1}^G}{FA_G c_O^* \sqrt{aD_O}} \\ &= (1 + c_R^*/\gamma c_O^*) \frac{1}{\sqrt{\pi a \tau}} \left(\sum_{m=1}^p \frac{Z_m}{\sqrt{p-m+1}} - \sum_{m=1}^{p-1} \frac{Z_m}{\sqrt{p-m}} \right)\end{aligned}\quad (7.16)$$

with Z_m being given under these conditions as

$$Z_m = \frac{1}{1 + \gamma e^{\eta_m}} - \frac{1}{1 + \gamma e^{\eta_{m-1}}} \quad 1 \leq m \leq p \quad (7.17)$$

and

$$\gamma = \sqrt{\frac{D_O}{D_R}} \quad (7.18)$$

7.2.1.2 Spherical Electrodes

In this case ($q_G = r_s$), from Eqs. (7.9) to (7.15), we get

$$\psi_{\text{DSCVC}}^{\text{sph}} = \psi_{\text{DSCVC}}^{\text{plane}} + \psi_{\text{DSCVC}}^{\text{sph,ss}} \quad (7.19)$$

with

$$\psi_{\text{DSCVC}}^{\text{sph,ss}} = \sqrt{\frac{D}{a}} (1 + c_R^*/c_O^*) \frac{Z_p}{r_s} \quad (7.20)$$

In Fig. 7.1, the influence of the electrode radius r_s on the dimensionless DSCVC $\psi_{\text{DSCVC}}^G/|\Delta\eta|$ curves (with $|\Delta\eta| = F|\Delta E|/RT$) is shown. Figure 7.1a corresponds to the planar contribution, Fig. 7.1b to the radial or stationary contribution, and the curves corresponding to spherical electrodes obtained from Eq. (7.19) are shown in Fig. 7.1c. From these curves, it can be seen that the peak potential does not coincide with the formal potential in the case of planar electrodes. In the case of spherical electrodes (Fig. 7.1c), the peaks of the first and second scans approach the formal potential as the electrode radius decreases, and $\psi_{\text{DSCVC}}^{\text{sph}}$ responses of both scans become symmetrical.

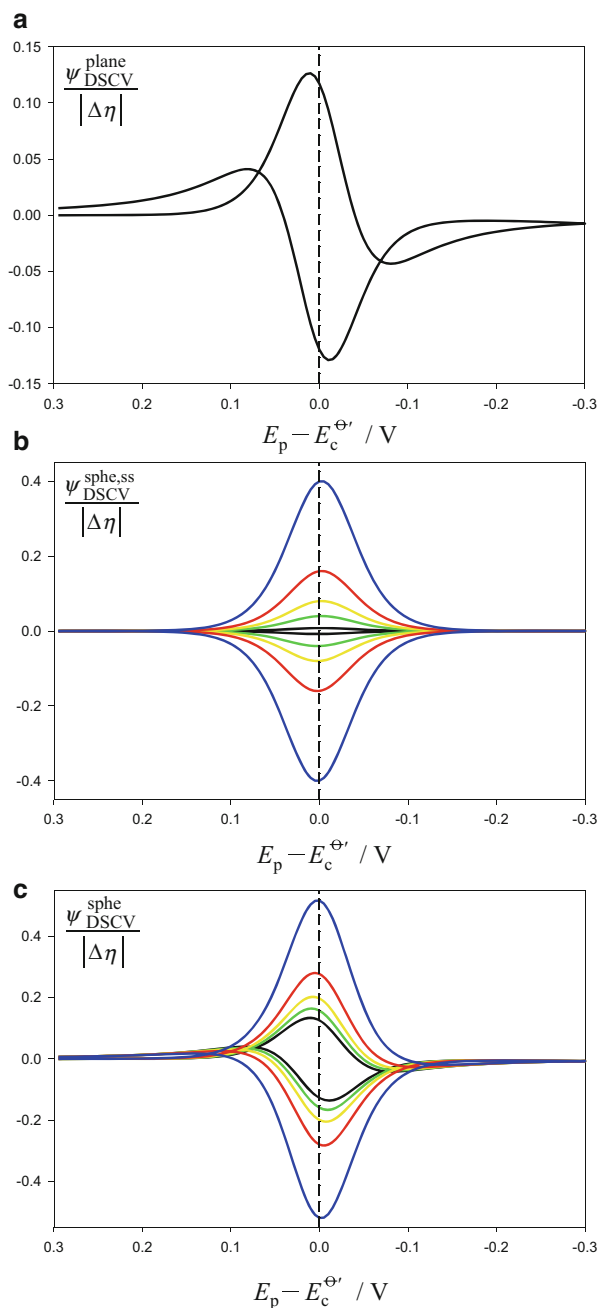
The experimental verification of this behavior can be seen in Fig. 7.2 for the system FeCl_3 1 mM + $\text{K}_2\text{C}_2\text{O}_4$ 0.25 M (pH = 4.70) at mercury electrodes of different radii.

7.2.2 Differential Multipulse Voltammetry

Since in this technique the duration of the pulse (τ_p) is much shorter than the period between pulses (τ_1 , see Scheme 7.2), the response of reversible processes in DMPV is totally coincident with that obtained in the double pulse technique DDPV [9],

Fig. 7.1 Cyclic DSCVC curves $\psi_{\text{DSCV}}^G / |\Delta\eta| - E_p$ corresponding to planar ($G = \text{plane}$, **a**), steady-state ($G = \text{ss}$, **b**), and spherical ($G = \text{sphe}$, **c**) contributions calculated from Eqs. (7.15), (7.19), and (7.20).

$v = 0.1 \text{ V s}^{-1}$, $|\Delta\eta| = F|\Delta E|/RT$ with $|\Delta E| = 5 \text{ mV}$. The values of the spherical electrode r_s (in microns) are 500 (black), 100 (green), 50 (yellow), 25 (red), and 10 (blue). $T = 298 \text{ K}$



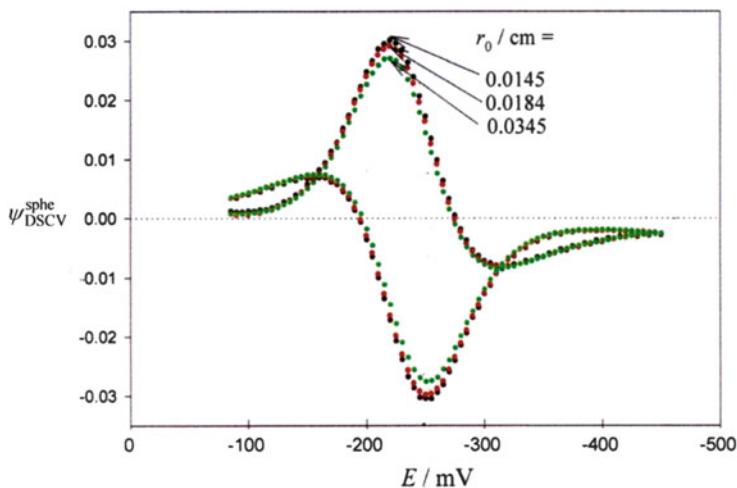


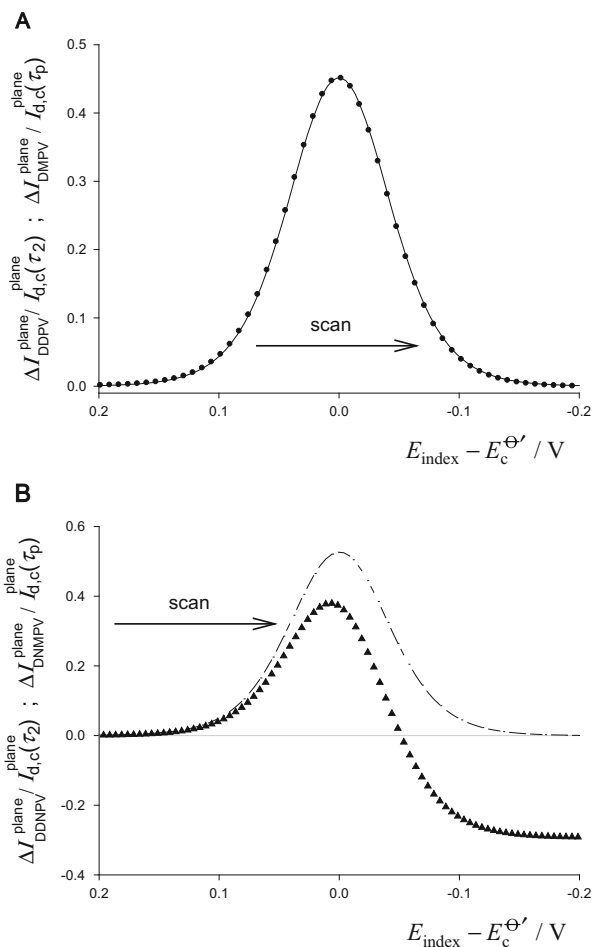
Fig. 7.2 DSCVC curves corresponding the system FeCl_3 1 mM + $\text{K}_2\text{C}_2\text{O}_4$ 0.25 M (pH = 4.70) at mercury electrodes of different radii. The values of the electrode radius ($r_0 = r_s$ in cm) are shown on the curves

because in DMPV the system is able to establish conditions equivalent to DDPV near to the electrode surface during τ_1 , as if previous pulses had not existed. Therefore, under these conditions ($\tau_1 \gg \tau_p$ for any value of p), we can take advantage of simple analytical expressions available for DDPV (see Sect. 4.2.4) together with the faster potential–time program of DMPV. In line with reported results [21, 22], the period between pulses τ_1 must be at least five times longer than τ_p . So, in Fig. 7.3a, it can be seen that the agreement between DDPV and DMPV voltammograms is excellent. However, in Differential Normal Multipulse Voltammetry (DNMPV, $\tau_1 \cong \tau_p$), important differences are found between this technique and the double pulse one (DNDPV) since in DNMPV the period between pulses τ_1 is not sufficient for the equilibrium to be restored.

The clearest difference corresponds to the value of the response at very cathodic potentials which is null for the case of DNMPV, whereas it depends on the ratio (τ_1/τ_2) $\left(\Delta I_{\text{DNDPV}}^{\text{plane}} \propto (1/\sqrt{\tau_1 + \tau_2} - 1/\sqrt{\tau_1})\right)$ for DNDPV, in agreement with Eq. (4.102). Moreover, the peak potential coincides with the formal one in the case of the multipulse technique, whereas it is shifted toward more positive values in the case of the double pulse one.

The location of the response is not affected by the ratio between pulse times in the case of DNMPV. This effect can be seen in Fig. 7.4 in which the current potential curves calculated for different values of (τ_2/τ_1) and planar electrodes have been plotted. This ratio only affects the magnitude of the current and not the peak potential, which coincides with the formal potential in all the cases. For nonplanar electrodes, this behavior also holds when the diffusion coefficients of oxidized and reduced species are equal [9].

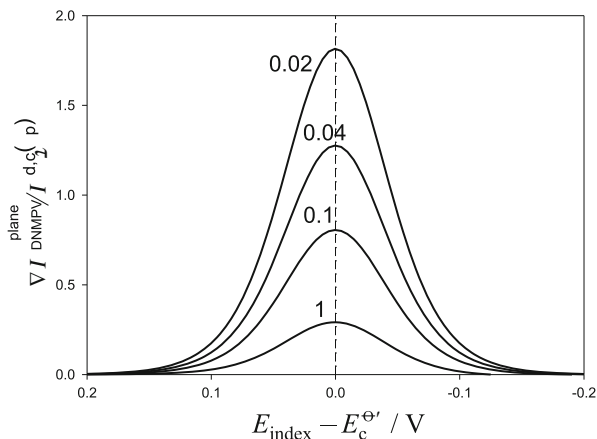
Fig. 7.3 Comparison between DDPV (black circles) and DMPV (solid lines) curves (a), and between DNDPV (black triangles) and DNMPV (dashed lines) curves (b) for reversible electrode processes at planar electrodes. The values of the times are: (a) $\tau_1 = 1$ s, $\tau_1/\tau_2 = \tau_1/\tau_p = 50$; (b) $\tau_1 = 0.02$ s, $\tau_1/\tau_2 = \tau_1/\tau_p = 1$. $\Delta E = -50$ mV, $\Delta E_s = -5$ mV. $I_{d,c}^{\text{plane}}(t) = FAc_O^* \sqrt{D/(\pi t)}$. Reproduced from [9] with permission



7.2.3 Square Wave Voltammetry

As stated in Sect. 7.1, the current in SWV is sampled at the end of each potential pulse and the net response (I_{SW}^G) is given by the subtraction of the current corresponding to a pulse with odd index (forward current, I_f^G) and that of the following pulse with even index (reverse or backward current, I_r^G) (see Eq. (7.6)). By using the expression of the current for any pulse of a given sequence (Eq. (5.23)), the expression for the SWV response of a reversible electrode reaction at electrodes of any geometry is immediately derived [21]:

Fig. 7.4 Influence of the ratio (τ_2/τ_1) on the response of DNMPV for planar electrodes. The values of (τ_2/τ_1) are indicated on the curves. $\Delta E = -50$ mV, $\Delta E_s = -5$ mV.
 $I_{d,c}^{\text{plane}}(\tau) = FAc_O^* \sqrt{D/(\pi\tau)}$



$$\psi_{\text{SW}}^{\text{G}} = \frac{I_{\text{SW}}^{\text{G}} \sqrt{\tau}}{FA_G \sqrt{D} c_O^*} = -(1 + c_R^*/c_O^*) Z_{2p} f_G(1, \xi_G) +$$

$$+ (1 + c_R^*/c_O^*) \sum_{m=1}^{2p-1} (Z_m [f_G((2p-m), \xi_G) - f_G((2p-m+1), \xi_G)]) \quad (7.21)$$

$$p = 1, 2, \dots, (N/2)$$

with

$$\xi_G = \frac{\sqrt{D\tau}}{q_G} \quad (7.22)$$

where q_G is a characteristic dimension of the electrode geometry considered, Z_m is given in Eq. (7.12), and f_G is a dimensionless function given in Table 7.1 for several common electrode geometries.

A C++ code to calculate the response of one-electron reversible electrode processes in SWV at disc, (hemi)spherical, and cylindrical electrodes of any radius can be found in Appendix J.

7.2.3.1 Planar Electrodes

In the particular case of planar electrodes ($q_G \rightarrow \infty$, see Table 7.1), the following simplified expression for Eq. (7.21) is deduced:

Table 7.1 Expressions for functions $f_G(n, \xi_G)$ and $f_{G,\text{micro}}$ for the four electrode geometries considered

Electrode	Function $f_G(n, \xi_G)$	$f_{G,\text{micro}}$
Disc (radius r_d , area $A_d = \pi r_d^2$)	$\frac{4\xi}{\pi^2 d} \left(0.7854 + 0.44315 \frac{1}{\sqrt{n\xi_d}} + 0.2146 \exp\left(-0.39115 \frac{1}{\sqrt{n\xi_d}}\right) \right)$	$\frac{4\xi}{\pi^2 d}$
Sphere (radius r_s , area $4\pi r_s^2$)	$\xi_s + \frac{1}{\sqrt{\pi n}}$	ξ_s
Band (height w , length l , area wl)	$\xi_b + \frac{1}{\sqrt{\pi n}}$ if $n\xi_b^2 < 0.4$ $0.25 \sqrt{\frac{\pi}{n}} e^{-0.4\sqrt{\pi n\xi_b}} + \frac{\pi\xi_b}{\ln(5.2945 + 5.9944\sqrt{n\xi_b})}$ if $n\xi_b^2 \geq 0.4$	$\frac{2\pi\xi_b}{\ln[64n\xi_b^2]}$
Cylinder (radius r_c , length l , area $2\pi r_c l$)	$\frac{1}{\sqrt{\pi n}} e^{-0.1\sqrt{\pi n\xi_c}} + \frac{\xi_c}{\ln(5.2945 + 1.4986\sqrt{n\xi_c})}$	$\frac{2\xi_c}{\ln[4n\xi_c^2]}$

$\xi_G = \sqrt{D\tau}/q_G$ with $q_G = r_d$ for discs; $q_G = r_s$ for spheres or hemispheres; $q_G = r_c$ for cylinders; and $q_G = w$ for bands. Note that functions $f_G(n, \xi_G)$ and $f_{G,\text{micro}}$ are dimensionless

$$\begin{aligned} \psi_{\text{SW}}^{\text{plane}} = & -\left(1 + c_{\text{R}}^*/c_{\text{O}}^*\right) \frac{Z_{2p}}{\sqrt{\pi}} \\ & + \left(1 + c_{\text{R}}^*/c_{\text{O}}^*\right) \frac{1}{\sqrt{\pi}} \sum_{m=1}^{2p-1} \left(Z_m \left[\frac{1}{\sqrt{2p-m}} - \frac{1}{\sqrt{2p-m+1}} \right] \right) \end{aligned} \quad (7.23)$$

When the diffusion coefficients of species O and R are different the current is

$$\begin{aligned} \psi_{\text{SW}}^{\text{plane}} = & \frac{I_{\text{SW}}^{\text{plane}} \sqrt{\tau}}{FA\sqrt{D_{\text{O}}}c_{\text{O}}^*} \\ = & -\left(1 + c_{\text{R}}^*/(\gamma c_{\text{O}}^*)\right) \frac{Z_{2p}}{\sqrt{\pi}} \\ & + \left(1 + c_{\text{R}}^*/(\gamma c_{\text{O}}^*)\right) \frac{1}{\sqrt{\pi}} \sum_{m=1}^{2p-1} \left(Z_m \left[\frac{1}{\sqrt{2p-m}} - \frac{1}{\sqrt{2p-m+1}} \right] \right) \end{aligned} \quad (7.24)$$

with Z_m and γ given by Eqs. (7.17) and (7.18).

The SWV curve (Eqs. (7.23) and (7.24)) presents a peak potential corresponding to the half-wave potential. Moreover, from these equations, an easy expression for the maximum current can be deduced when very large values of E_{SW} are applied ($E_{\text{SW}} \geq 100\text{mV}$), so the potential is completely stepped through the wave. Therefore, near the top of the wave, the forward pulses verify $E_f - E_c^{\Theta} = E_{2p-1} - E_c^{\Theta} \ll 0$, and the reverse pulses fulfill $E_r - E_c^{\Theta} = E_{2p} - E_c^{\Theta} \gg 0$. In these conditions and according to Eq. (7.12), Z_m takes the value

$$Z_m = (-1)^{m+1} \quad (7.25)$$

In these conditions, Eq. (7.23) becomes

$$\psi_{\text{SW}}^{\text{plane}} = (1 + c_{\text{R}}^*/c_{\text{O}}^*) \frac{1}{\sqrt{\pi}} \left\{ 1 + \sum_{m=1}^{2p-1} \left((-1)^{m+1} \left[\frac{1}{\sqrt{2p-m}} - \frac{1}{\sqrt{2p-m+1}} \right] \right) \right\} \quad (7.26)$$

The sum in the brackets of the right-hand side of this equation converges rapidly to 2.144 for $p \geq 10$, so for the maximum value of the current, we obtain [21]

$$\psi_{\text{SW}}^{\text{plane, plateau}} = 1.21(1 + c_{\text{R}}^*/c_{\text{O}}^*) \quad (7.27)$$

7.2.3.2 Spherical Electrodes

In the case of spherical electrodes, by taking into account Table 7.1 and Eq. (7.23), the SW current can be written as

$$\psi_{\text{SW}}^{\text{sph}} = \psi_{\text{SW}}^{\text{plane}} + (1 + c_{\text{R}}^*/c_{\text{O}}^*) \xi_{\text{s}} \left(\frac{1}{1 + e^{\eta_{2p-1}}} - \frac{1}{1 + e^{\eta_{2p}}} \right) \quad (7.28)$$

The above equation indicates that the contribution to the total current due to the electrode radius has a stationary character since it only depends on the last potential cycle considered (i. e., of the $2p$ and $2p - 1$ potential pulses). As in the case of planar electrodes, for very large values of E_{SW} (i.e., $E_{\text{SW}} \geq 100\text{mV}$), a maximum current is obtained which, in agreement with Eqs. (7.27) and (7.28) is given by [21, 23]:

$$\psi_{\text{SW}}^{\text{sph, plateau}} = (1 + c_{\text{R}}^*/c_{\text{O}}^*)(1.21 + \xi_{\text{s}}) \quad (7.29)$$

In the case of spherical microelectrodes under steady-state conditions, Eq. (7.29) becomes

$$\psi_{\text{SW}}^{\text{sph, ss, plateau}} = (1 + c_{\text{R}}^*/c_{\text{O}}^*) \xi_{\text{s}} \quad (7.30)$$

which can be written as (see Eqs. (7.21)–(7.22) and (2.166)):

$$I_{\text{SW}}^{\text{sph, ss, plateau}} = (1 + c_{\text{R}}^*/c_{\text{O}}^*) F A_{\text{s}} D c_{\text{O}}^* \frac{1}{r_{\text{s}}} = (1 + c_{\text{R}}^*/c_{\text{O}}^*) I_{\text{d, c}}^{\text{microsphere, ss}} \quad (7.31)$$

7.2.3.3 Other Electrode Geometries: Microelectrodes and Steady-State Subtractive Voltammetries

Figure 7.5 shows the $\psi_{\text{SW}}^{\text{G}} - (E_{\text{index}} - E_{\text{c}}^{\ominus})$ curves calculated for discs, spheres, bands, and cylinders by considering three values of $q_{\text{G}} (= r_{\text{d}} = r_{\text{s}} = (w/2) = r_{\text{c}})$ (see Eq. (7.21) and Table 7.1). For the largest electrode considered (Fig. 7.5a), all the voltammograms are almost coincident since the prevalent diffusion field is

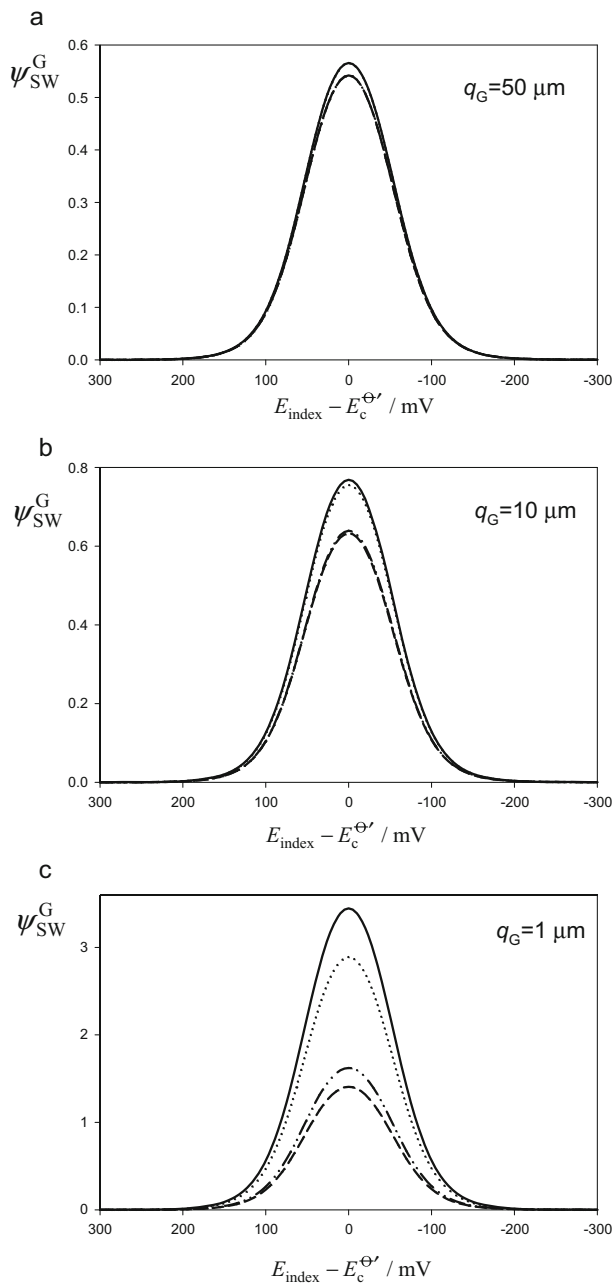


Fig. 7.5 $\psi_{SW}^G - (E_{\text{index}} - E_c^{\Theta'})$ curves at discs (solid lines), spheres (dotted lines), cylinders (dashed lines), and bands (dashed-dotted lines) for different values of q_G ($= r_d = r_s = (w/2) = r_c$) (indicated on the graphs). $E_{SW} = 50 \text{ mV}$, $\Delta E_s = 5 \text{ mV}$, $\tau = 10 \text{ ms}$ ($f = 50 \text{ Hz}$), $T = 298.15 \text{ K}$, $D = 10^{-5} \text{ cm}^2 \text{ s}^{-1}$. Reproduced from [21] with permission

linear such that the electrode geometry is irrelevant. As the electrode size decreases (Fig. 7.5b, c), the different SWV curves separate until they reach the steady-state (disc, sphere) or quasi-steady-state (band, cylinder) behavior (Fig. 7.5c). Under these conditions, the ratio between the SWV currents at spheres and discs is $(\pi/4)$ in agreement with Eqs. (7.35) and (7.36). Note that in all the cases the peak potential does not depend on either the geometry or size of the electrode and it coincides with the formal potential.

The forward and reverse currents ψ_f^G and ψ_r^G of the square wave voltammograms corresponding to Fig. 7.5c are shown in Fig. 7.6a for microelectrodes of the four electrode geometries considered. From these curves, it can be seen that both currents present a sigmoidal shape and they are separated by $2E_{SW}$ in the case of spheres and discs. This behavior clearly shows that the steady state has been attained. On the other hand, in the case of cylinders and bands, ψ_f^G and ψ_r^G show a transient behavior under these conditions. From Fig. 7.6b, c, it can be verified that a decrease in the radius, $((w/2) = r_c = 0.1 \mu\text{m})$ and that of both radius and frequency (Fig. 7.6c, $(w/2) = r_c = 0.1 \mu\text{m}$ and $f = 10 \text{ Hz}$) do not lead to a stationary SWV response at cylinder and band microelectrodes.

In Fig. 7.7, the variation of the dimensionless peak current ($\psi_{SW}^{G,\text{peak}}$) with the parameter $\xi_G = \sqrt{D\tau}/q_G$ (see Eq. (7.22)) is plotted for the four geometries under study with $\Delta E_s = 5 \text{ mV}$ and $E_{SW} = 50 \text{ mV}$.

A linear dependence of $\psi_{SW}^{G,\text{peak}}$ with ξ_G in the case of discs and spheres (equations shown in the graphs) can be seen in this figure which coincides with those previously reported [6, 21]. For cylinders and bands, polynomial dependences are obtained showing a more complex behavior. Note that in the planar-limiting behavior (i.e., $\xi_G \rightarrow 0$), the four geometries logically tend to the constant limit $\psi_{SW}^{\text{plane,peak}} = 0.918/\sqrt{\pi} = 0.518$ [6].

The evolution of the half-peak width ($W_{1/2}$) of the $\psi_{SW}^G - (E_{\text{index}} - E_c^{\Theta'})$ curve with the square wave amplitude E_{SW} for the four geometries considered can be seen in Fig. 7.8. As can be inferred, $W_{1/2}$ increases with E_{SW} from $W_{1/2} = 90 \text{ mV}$ for $E_{SW} \leq 10 \text{ mV}$ to $W_{1/2} = 2E_{SW}$ for $E_{SW} > 100 \text{ mV}$, independently of the electrode geometry and size (i.e., under transient and steady-state conditions). The half-peak width ($W_{1/2}$) is therefore independent of the electrode dimension and its geometry and of the period or the frequency of the square wave, as given by [21]:

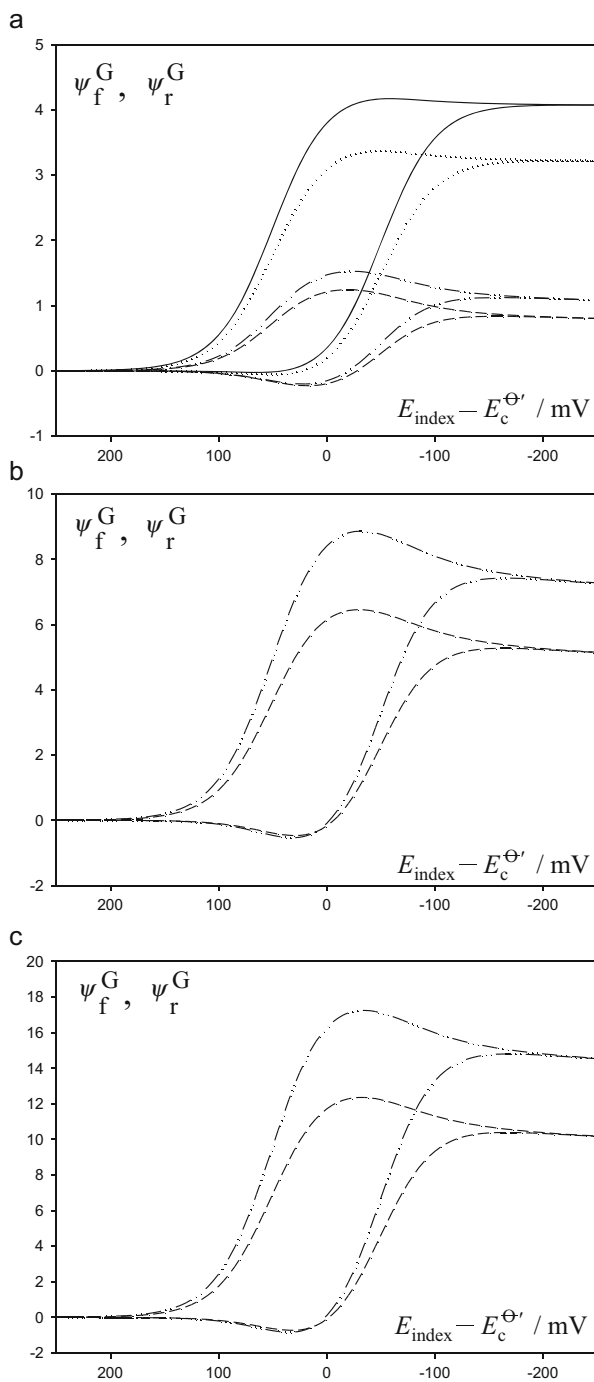
$$W_{1/2} = \frac{RT}{F} \ln \left(\frac{1 + e^{2\eta_{sw}} + 4e^{\eta_{sw}} + \sqrt{(1 + e^{2\eta_{sw}} + 4e^{\eta_{sw}})^2 - 4e^{2\eta_{sw}}}}{1 + e^{2\eta_{sw}} + 4e^{\eta_{sw}} - \sqrt{(1 + e^{2\eta_{sw}} + 4e^{\eta_{sw}})^2 - 4e^{2\eta_{sw}}}} \right) \quad (7.32)$$

with

$$\eta_{sw} = FE_{sw}/RT \quad (7.33)$$

The variation of the logarithm of the peak current ($I_{SW}^{G,\text{peak}}$) with the logarithm of the frequency (f) for the four geometries considered and three values of the

Fig. 7.6 $\psi_f^G - (E_{\text{index}} - E_c^{\ominus'})$ and $\psi_r^G - (E_{\text{index}} - E_c^{\ominus'})$ curves at (a) discs (solid lines), spheres (dotted lines), cylinders (dashed lines), and bands (dashed-dotted lines) for $q_G = 1 \mu\text{m}$ and (b and c) cylinders (dashed lines) and bands (dashed-dotted lines) for $q_G = 0.1 \mu\text{m}$. The frequencies are $f = 50 \text{ Hz}$ (a, b) and 10 Hz (c). $E_{\text{SW}} = 50 \text{ mV}$, $\Delta E_s = 5 \text{ mV}$. Reproduced from [21] with permission



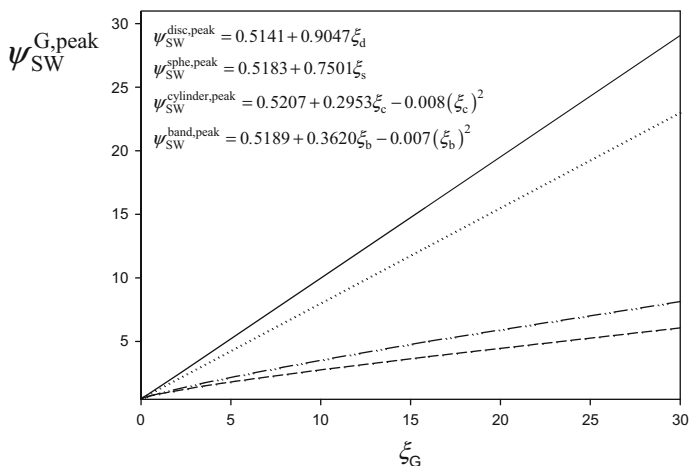


Fig. 7.7 Variation of the dimensionless peak current ($\psi_{SW}^{G,\text{peak}}$) with the parameter $\xi_G = \sqrt{D\tau}/q_G$ at discs (solid lines, $q_G = r_d$), spheres (dotted lines, $q_G = r_s$), cylinders (dashed lines, $q_G = r_c$), and bands (dashed-dotted lines, $q_G = w/2$). $E_{SW} = 50 \text{ mV}$, $\Delta E_s = 5 \text{ mV}$, $T = 298.15 \text{ K}$. Reproduced from [21] with permission

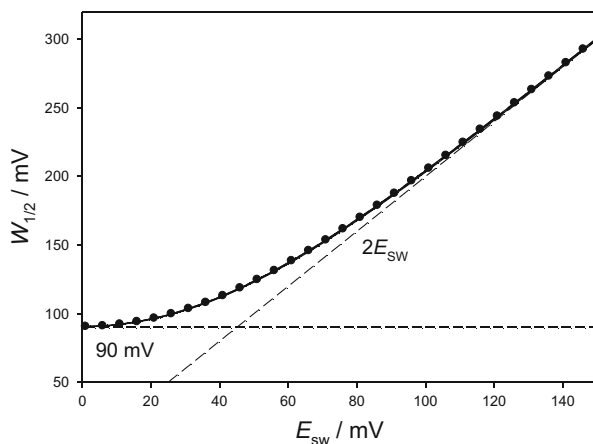


Fig. 7.8 Variation of the half-peak width ($W_{1/2}$, Eq. (7.32)) of the SWV curve with the square wave amplitude (E_{SW}) for the four geometries considered: discs, spheres, cylinders, and bands. $\Delta E_s = 5 \text{ mV}$. $T = 298.15 \text{ K}$

characteristic dimension of the electrode q_G is plotted in Fig. 7.9. For spheres and discs, $I_{SW}^{G,\text{peak}}$ becomes regardless of the frequency f (steady-state behavior) for small frequencies and electrode radii ($f < 10 \text{ Hz}$ in Fig. 7.9a). In the case of bands and cylinders, the peak current always depends on the frequency (i.e., only a pseudo-stationary behavior can be obtained), even for low values of f and q_G (see dashed and dotted-dashed curves in Fig. 7.9a). On the other hand, as f increases, a linear

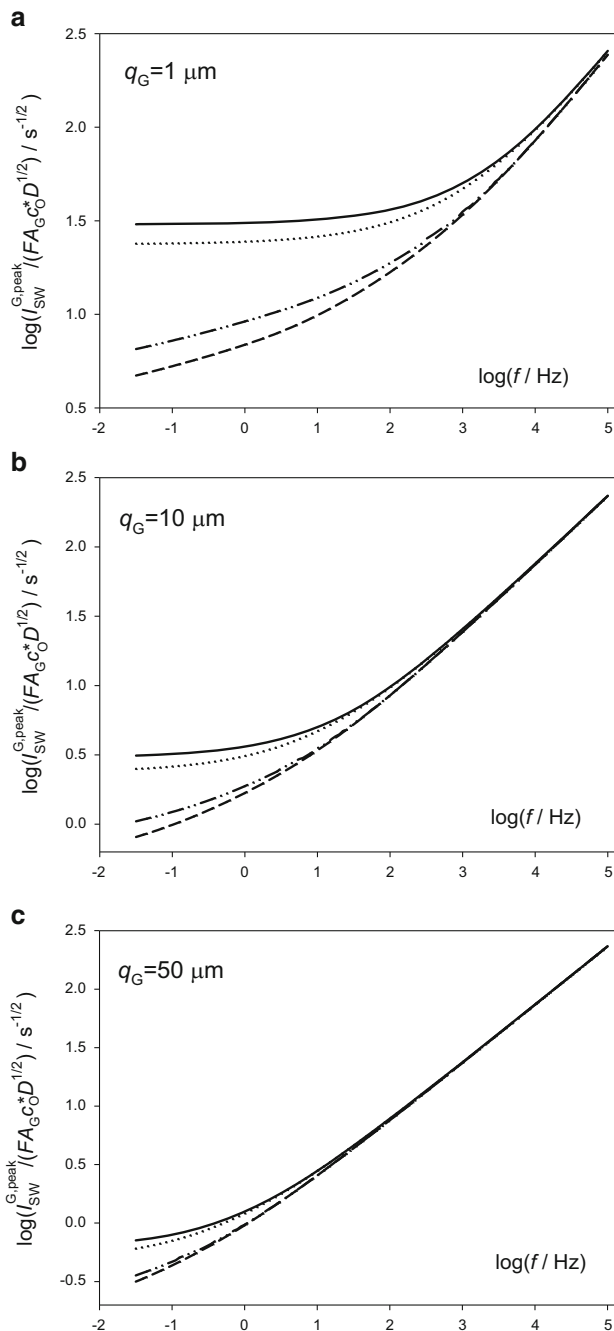


Fig. 7.9 Variation of the logarithm of the peak current ($I_{\text{SW,peak}}^G$) with the logarithm of the frequency (f) at discs (solid lines), spheres (dotted lines), cylinders (dashed lines), and bands (dashed-dotted lines). Three values of the characteristic dimension of the electrode q_G are considered (indicated on the graphs). $E_{\text{SW}} = 50 \text{ mV}$, $\Delta E_s = 5 \text{ mV}$, $T = 298.15 \text{ K}$. Reproduced from [21] with permission

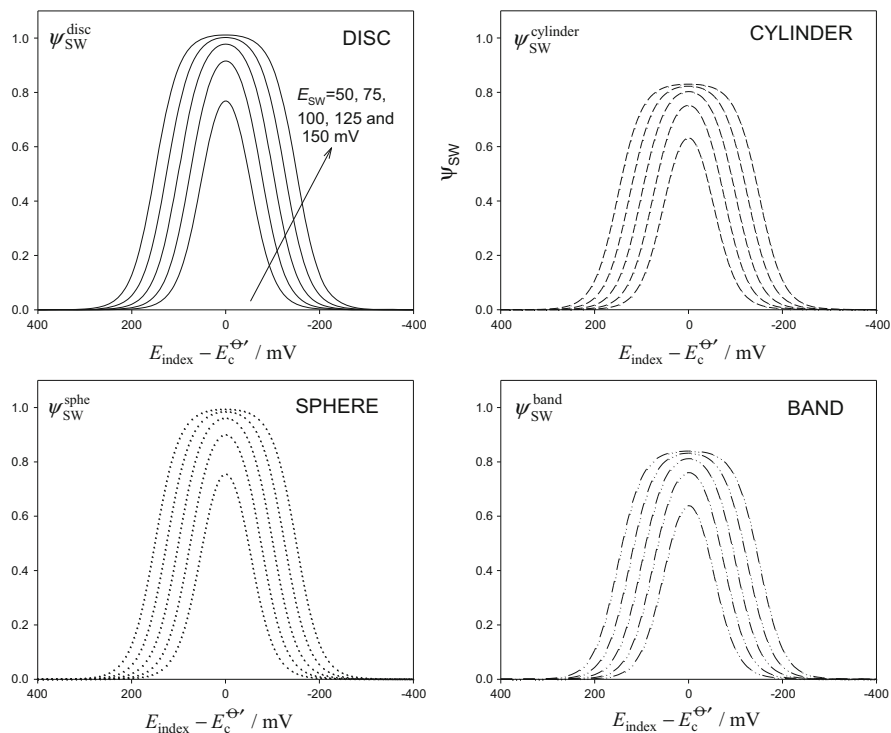


Fig. 7.10 Influence of the square wave amplitude (E_{SW}) on the SWV curves at discs (solid lines), spheres (dotted lines), cylinders (dashed lines), and bands (dashed-dotted lines). Five E_{SW} values are considered: 50, 75, 100, 125, and 150 mV. $\Delta E_s = 5$ mV, $\tau = 10$ ms, $q_G (= r_d = r_s = (w/2) = r_c) = 10 \mu\text{m}$. $T = 298.15$ K. Reproduced from [21] with permission

dependence between the peak current and $\log(f)$ with slope 0.5 arises, and the peak currents of the four geometries are coincident for large f and q_G values. This linearity is typical of a predominant planar diffusion [6, 24].

The influence of E_{SW} on the SWV curves of the four geometries considered is plotted in Fig. 7.10. From these curves, it can be concluded that the peak potential of the $\psi_{SW}^G - (E_{\text{index}} - E_c^{\Theta})$ curves remains unaffected by the variation of E_{SW} and is coincident in any case with the formal potential, and the peak current increases with the square wave potential up to values of $E_{SW} \geq 125$ mV for which a broad plateau is obtained. The value of this current plateau is related to ξ_G , independently of E_{SW} . The current corresponding to this plateau is given by Eq. (7.29) for spheres and for discs

$$\psi_{SW}^{\text{disc, plateau}} = 1.21 + \frac{4}{\pi} \xi_d \quad (7.34)$$

The equation corresponding to spherical electrodes coincides with that previously reported in references [19, 23].

In the case of Cyclic Square Wave Voltammetry (CSWV), the SWV curve obtained in the second scan is a mirror image to that of the first scan whatever the electrode geometry if the diffusion coefficients of species O and R are assumed as equal. In the contrary case, although the peak potentials of both scans are coincident, differences in the peak heights are observed for nonplanar electrodes.

When the characteristic dimension of the electrode fulfills that $q_G \ll \sqrt{\pi D}t$ (with q_G being equal to r_d , r_s , w , or r_c for discs, spheres, bands, or cylinders, respectively), stationary or pseudo-stationary conditions are attained. Under these conditions, the expressions for the signal obtained in SWV as well as those corresponding to differential techniques DSCVC and DMPV previously discussed simplify greatly. In the case of discs or spheres, a true steady-state response can be obtained (see Eqs. (7.20) and Table 7.1):

– *Spherical electrode*

$$\left. \begin{aligned} \psi_{\text{DSCVC}}^{\text{sph},\text{ss}} &= (1 + c_{\text{R}}^*/c_{\text{O}}^*) \xi_{\text{s}} \left(\frac{1}{1 + e^{\eta_p}} - \frac{1}{1 + e^{\eta_{p-1}}} \right) \\ \psi_{\text{DMPV}}^{\text{sph},\text{ss}} &= (1 + c_{\text{R}}^*/c_{\text{O}}^*) \xi_{\text{s}} \left(\frac{1}{1 + e^{\eta_p}} - \frac{1}{1 + e^{\eta_{p-1}}} \right) \\ \psi_{\text{SWV}}^{\text{sph},\text{ss}} &= (1 + c_{\text{R}}^*/c_{\text{O}}^*) \xi_{\text{s}} \left(\frac{1}{1 + e^{\eta_{2p-1}}} - \frac{1}{1 + e^{\eta_{2p}}} \right) \end{aligned} \right\} \quad (7.35)$$

– *Disc electrode*

$$\left. \begin{aligned} \psi_{\text{DSCVC}}^{\text{disc},\text{ss}} &= (1 + c_{\text{R}}^*/c_{\text{O}}^*) \xi_{\text{d}} \frac{4}{\pi} \left(\frac{1}{1 + e^{\eta_p}} - \frac{1}{1 + e^{\eta_{p-1}}} \right) \\ \psi_{\text{DMPV}}^{\text{disc},\text{ss}} &= (1 + c_{\text{R}}^*/c_{\text{O}}^*) \xi_{\text{d}} \frac{4}{\pi} \left(\frac{1}{1 + e^{\eta_p}} - \frac{1}{1 + e^{\eta_{p-1}}} \right) \\ \psi_{\text{SWV}}^{\text{disc},\text{ss}} &= (1 + c_{\text{R}}^*/c_{\text{O}}^*) \xi_{\text{d}} \frac{4}{\pi} \left(\frac{1}{1 + e^{\eta_{2p-1}}} - \frac{1}{1 + e^{\eta_{2p}}} \right) \end{aligned} \right\} \quad (7.36)$$

with ξ_G ($G = s$ for spheres, $q_G = r_s$, and $G = d$ for discs, $q_G = r_d$) given by Eq. (7.22). Note that the current has been written in an identical dimensionless form for the three techniques, $\psi_{\text{SWV}}^G = I_{\text{SWV}}^G \sqrt{\tau} / (FA_G \sqrt{D} c_{\text{O}}^*)$. In agreement with equations (7.35) and (7.36), the response in the three techniques considered is identical if the pulse amplitude is the same in all cases (which in practice means that $\Delta E_{\text{DSCVC}} = \Delta E_{\text{DMPV}} = 2E_{\text{SWV}}$).

The differential curves are peak shaped in all cases even under the stationary state, with a peak potential equal to the formal potential if the current is plotted versus E_{index} (given by equations (7.3) or (7.7)), and the peak current is given by

$$\left. \begin{aligned} I^{\text{sph}, \text{ss}, \text{peak}} &= I^{\text{sph}, \text{ss}} \tanh\left(\frac{F\Delta E}{4RT}\right) \\ I^{\text{disc}, \text{ss}, \text{peak}} &= I^{\text{disc}, \text{ss}} \tanh\left(\frac{F\Delta E}{4RT}\right) \end{aligned} \right\} \quad (7.37)$$

with $I^{\text{disc}, \text{ss}} = 4FDc_{\text{O}}^*r_{\text{d}}$ and $I^{\text{sph}, \text{ss}} = 4\pi FDc_{\text{O}}^*r_{\text{s}}$ being the steady-state diffusion-limiting currents for a disc or spherical electrode, respectively, and $\Delta E = \Delta E_{\text{DSCVC}} = \Delta E_{\text{DMPV}} = 2E_{\text{SW}}$ (see Eqs. (2.166) and (2.168) and [9, 25]).

In the case of cylinders and bands, only pseudo-stationary currents are achieved and no strict equivalence between the three techniques is observed in this case.

7.3 Non-reversible Electrochemical Reactions

For electron transfer processes with finite kinetics, the time dependence of the surface concentrations does not allow the application of the superposition principle, so it has not been possible to deduce explicit analytical solutions for multipulse techniques. In this case, numerical methods for the simulation of the response need to be used. In the case of SWV, a semi-analytical method based on the use of recursive formulae derived with the aid of the step-function method [26] for solving integral equations has been extensively used [6, 17, 27].

As in the case of differential double potential pulse techniques like DDPV, slow electrochemical reactions lead to a decrease in the peak height and a broadening of the response of differential multipulse and square wave voltammeteries as compared with the response obtained for a Nernstian process. Moreover, the peak potential depends on the rate constant and is typically shifted toward more negative potentials (when a reduction is considered) as the rate constant or the pulse length decreases. SWV is the most interesting technique for the analysis of non-reversible electrochemical reactions since it presents unique features which allow us to characterize the process (see below). Hereinafter, unless expressly stated, a Butler–Volmer potential dependence is assumed for the rate constants (see Sect. 1.7.1).

7.3.1 Differential Multipulse Voltammetry

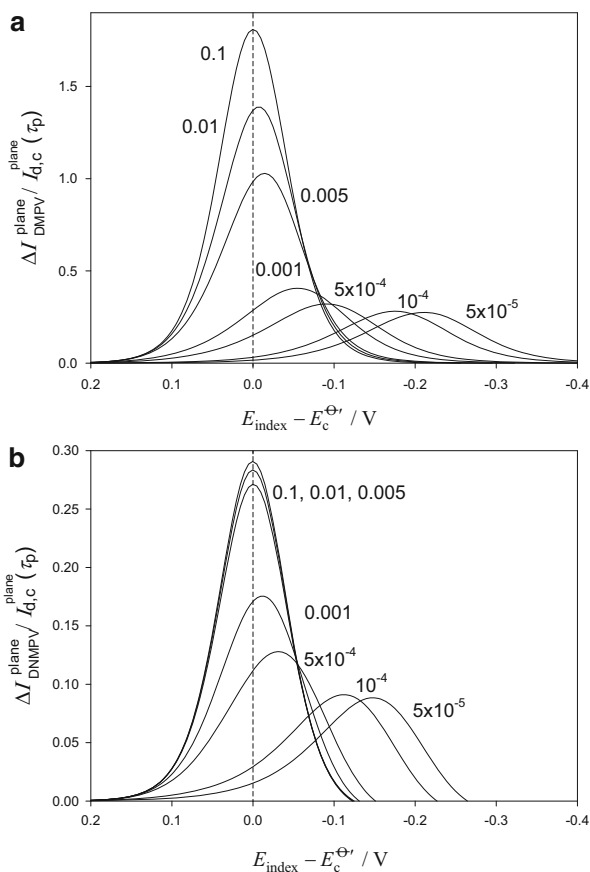
As stated in the previous section, a sluggish electrochemical reaction gives rise to smaller and broader signals than a fast one. This can be seen in Fig. 7.11 in which the influence of the dimensionless rate constant $\kappa_{\text{plane}}^0 = k^0\sqrt{\tau/D}$ on the $\Delta I - (E_{\text{index}} - E_{\text{c}}^{\text{O}^{\ominus}})$ curves obtained in DMPV ($\tau_1/\tau_p = 50$, Fig. 7.11a) and in DNMPV ($\tau_1/\tau_p = 1$, Fig. 7.11b) is plotted. It is interesting to highlight that, although the effect of the decrease of κ_{plane}^0 is qualitatively similar in DMPV and

Fig. 7.11 Influence of the reversibility on the multipulse techniques DMPV and DNMPV curves corresponding to planar electrodes. (a)

$(\tau_1/\tau_p) = 50$. (b)

$(\tau_1/\tau_p) = 1$. The values of $\kappa_{\text{plane}}^0 = k^0 \sqrt{\tau/D}$ appear on the curves. $\Delta E = -50 \text{ mV}$, $\Delta E_s = -5 \text{ mV}$.

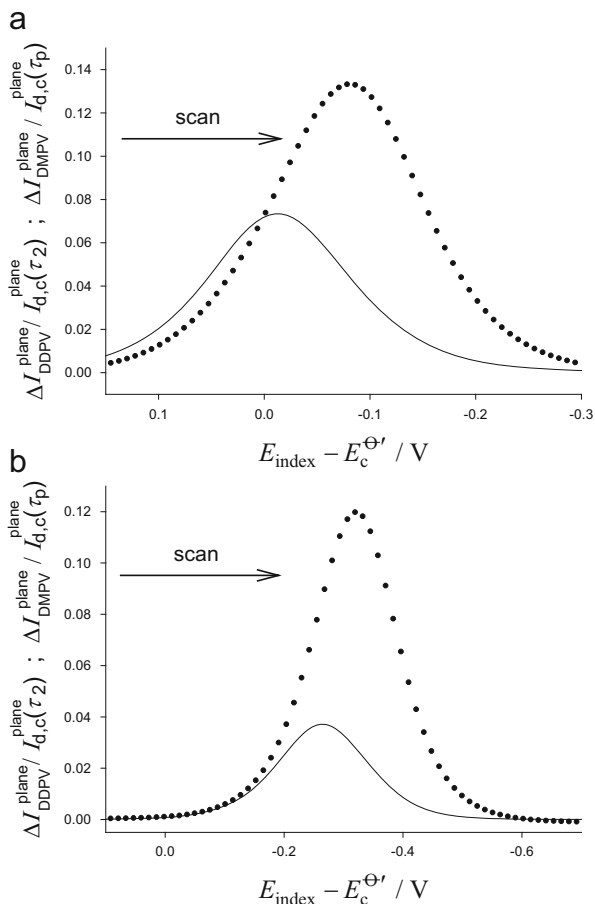
$$I_{d,c}^{\text{plane}}(t) = FAc_O^* \sqrt{D/(\pi t)}$$



DNMPV techniques, there is a smaller influence of the variation of the rate constants in the latter technique (for example, for $\kappa_{\text{plane}}^0 = 10^{-3}$ in DMPV the current has decreased by 78 % compared to the reversible peak height and the peak potential is shifted -55 mV from the formal potential value, whereas in DNMPV the decrease in the peak current is 40 % and the shift of the peak potential is -10 mV).

It is interesting to compare the results obtained in DMPV and DNMPV techniques with those corresponding to DDPV and DNMPV double pulse ones (see Eqs. (4.134) and (4.142)). Thus, in Figs. 7.12 and 7.13, this comparison for quasi-reversible and irreversible processes is made. Unlike reversible processes, for sluggish electrode reactions the disagreement between the curves is apparent whatever the length of the pulses; the slower the charge transfer, the greater the discrepancy of the curves. This affects not only the value of the peak current, but also the position of the peak and the curves corresponding to the multipulse methods (DMPV, DNMPV) appear at less negative potentials.

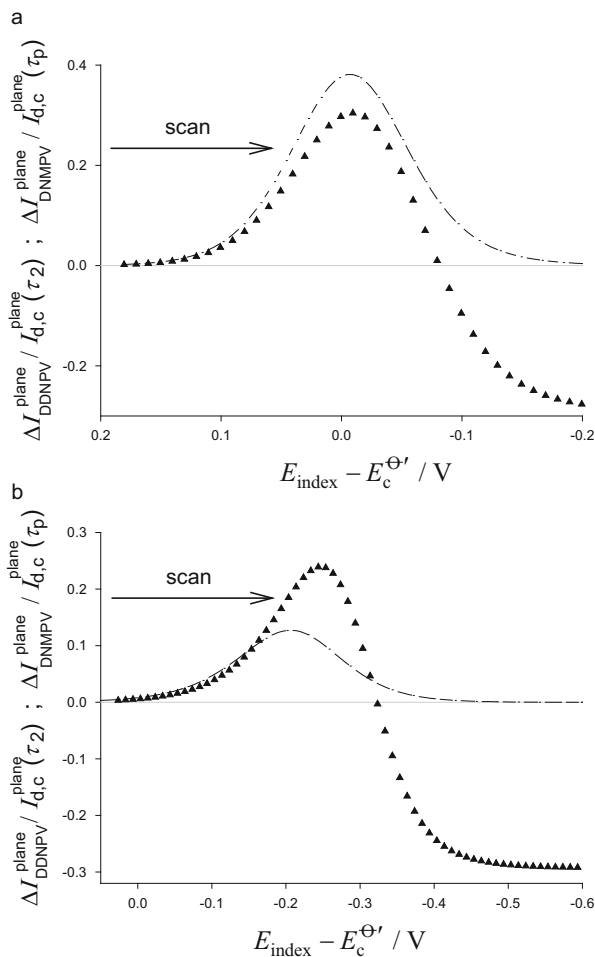
Fig. 7.12 Comparison between double (DDPV, dotted lines) and multipulse (DMPV, solid lines) techniques for different electrode kinetics: (a) quasi-reversible ($k^0 = 10^{-3} \text{ cm s}^{-1}$, $\alpha = 0.5$) and (b) irreversible ($k^0 = 10^{-5} \text{ cm s}^{-1}$, $\alpha = 0.5$) processes. Planar electrode, $\tau_1 = 1 \text{ s}$, $\tau_1/\tau_2 = \tau_1/\tau_p = 50$, $\Delta E = -50 \text{ mV}$, $\Delta E_s = -5 \text{ mV}$. Reproduced from [9] with permission



The discrepancy or similarity between the response in double pulse and multipulse techniques is related to the ability of the system to compensate the accumulative effects taking place in the latter. In the case of irreversible charge transfer processes, these effects are more significant since the electrode reaction does not regenerate the electro-active species and so there is a depletion of the reactant during the scan that gives rise to smaller signals (see Figs. 7.12b and 7.13b). Thus, for example, the comparison of the responses in DDPV and DMPV techniques provides a simple diagnosis test for the reversibility of the electrode process (Fig. 7.12).

According to the above, the electrochemical response in the different differential pulse techniques can be very different, and it is worth analyzing the advantages and disadvantages of each method. Regarding the double pulse methods, in normal mode, DNDPV, this has the inconvenience of presenting asymmetrical peaks that can hinder the experimental determination of the peak current. In addition, the peak

Fig. 7.13 Comparison between double (DNNDPV, *triangle*) and multipulse (DNMPV, *dashed*) techniques for different electrode kinetics: (a) quasi-reversible ($k^0 = 10^{-2} \text{ cm s}^{-1}$, $\alpha = 0.5$) and (b) irreversible ($k^0 = 10^{-4} \text{ cm s}^{-1}$, $\alpha = 0.5$) processes. Planar electrode, $\tau_1 = 0.02 \text{ s}$, $\tau_1/\tau_2 = \tau_1/\tau_p = 1$, $\Delta E = -50 \text{ mV}$, $\Delta E_s = -5 \text{ mV}$. Reproduced from [9] with permission



potential for a reversible process (Fig. 7.3b) is shifted from the half-wave potential. On the other hand, the other techniques (DDPV, DMPV, DNMPV) have well-defined peaks, all of them situated around the half-wave potential in the case of reversible charge transfer processes. As can be observed, the choice of the method will depend on the electrode kinetics of the system under study. Thus, for reversible systems the multipulse DNMPV technique shows greater sensitivity than DDPV and DMPV. For totally irreversible processes, the height of the signal is notably greater in double pulse techniques than in multipulse ones, and therefore we can infer that DDPV is the better method for analyzing slow electrode processes because of its higher sensitivity and well-defined curves. Nevertheless, if the aim is to remove the interference of background irreversible signals when studying a reversible process, multipulse techniques (DNMPV and DMPV) provide greater discriminatory power.

The electrode size is another important factor to be considered since it affects the magnitude of the diffusive transport, as shown in Fig. 7.14 for totally irreversible processes. At planar and spherical electrodes significant differences are found between double pulse and multipulse modes, with the discrepancy diminishing when the electrode radius decreases, since the system loses the “memory” of the previous pulses while approaching the stationary response. Thus, the relative difference in the peak current of a given double pulse technique and the corresponding multipulse variant is always smaller than 2 % when $r_s < 0.1 \sqrt{\pi D \tau_1}$. Note that this implies that attaining equivalent responses requires the use of smaller electrodes when both pulses are short with similar lengths as in DNDPV and DNMPV (see Fig. 7.14f) than when the length of the pulse (τ_2, τ_p) is much shorter than τ_1 as in DDPV and DMPV (see Fig. 7.14c).

7.3.2 Square Wave Voltammetry

In order to use SWV to obtain sufficiently precise kinetic data, it is essential to analyze how complications in a fast electron transfer affect the current–potential response. The usual way to do this for non-reversible electrochemical processes is by changing the frequency and, therefore, the dimensionless rate constant given by

$$\kappa_{\text{plane}}^0 = k^0 \sqrt{\tau/D} \quad (7.38)$$

and to monitor the evolution of the peak parameters, with the response being dependent on both κ_{plane}^0 and on the charge transfer coefficient α . The influence of the dimensionless rate constant on the net current and on the forward and reverse components corresponding to planar electrodes can be seen in Fig. 7.15.

From the curves in this figure, it can be concluded that the effect of the decrease of the electrochemical reversibility is similar to that observed for other differential techniques (compared with the results obtained in DMPV shown in Fig. 7.11). The reverse current is the most affected by the decrease of the reversibility of the charge transfer since it changes from a negative peak-shaped feature for reversible and quasi-reversible processes to a positive pseudo-sigmoidal one for fully irreversible processes (see Fig. 7.15a), which causes a decrease of the net current, compared to that of reversible processes. The following intervals have been proposed for characterizing the SWV response at planar electrodes in terms of reversibility: $\kappa_{\text{plane}}^0 > 10$, reversible process; $0.01 < \kappa_{\text{plane}}^0 < 10$, quasi-reversible process; $\kappa_{\text{plane}}^0 < 0.01$, fully irreversible process [6]. For nonplanar electrodes, the influence of the reversibility on the SWV response is more complex since it depends on the electrode size [9].

The evolution of the peak parameters of the SWV current (peak current, peak potential, and half-peak width) is plotted in Fig. 7.16 for a planar electrode in terms

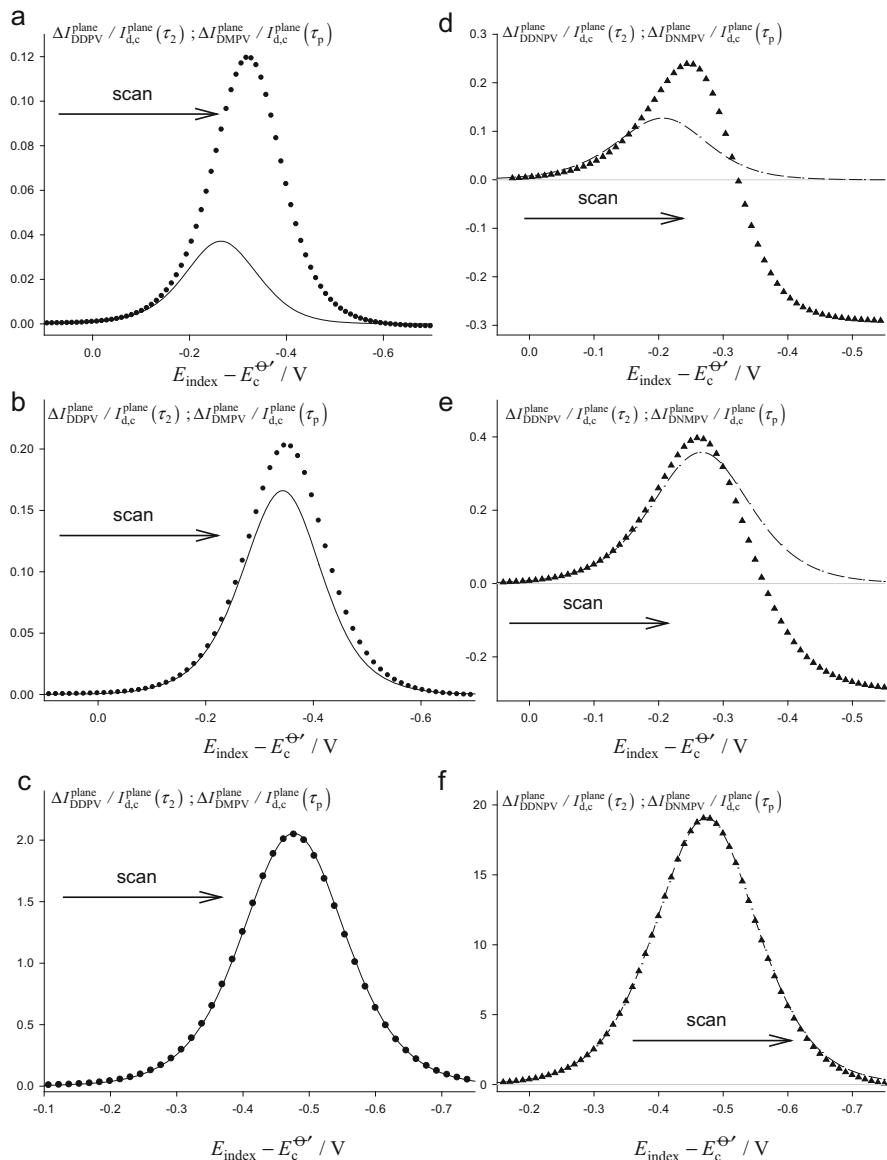


Fig. 7.14 Comparison between DDPV (*dotted*) and DMPV (*solid*) (curves **a**, **b**, and **c**) and of DNDPV (*triangle*) and DNMPV (*dashed*) (curves **d**, **e**, and **f**) for a totally irreversible process ($k^0 = 10^{-5}$ (**a**, **b**, **c**) and $k^0 = 10^{-4}$ (**d**, **e**, **f**) cm s^{-1} , $\alpha = 0.5$) at different electrode sizes: (**a**, **d**) planar electrode; (**b**, **e**) spherical electrode with r_s 30 (**b**) and 10 (**e**) μm ; (**c**, **f**) microelectrode with r_s 1 (**c**) and 0.1 (**f**) μm . In figures **a**, **b**, and **c** $\tau_1 = 1$ s, $\tau_1/\tau_2 = \tau_1/\tau_p = 50$. In figures **d**, **e**, and **f** $\tau_1 = 0.02$ s, $\tau_1/\tau_2 = \tau_1/\tau_p = 1$. $\Delta E = -50$ mV, $\Delta E_s = -5$ mV. Reproduced from [9] with permission

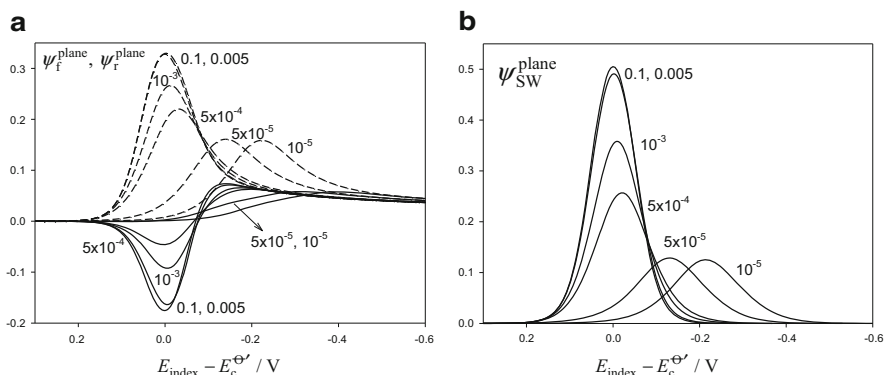


Fig. 7.15 Influence of the dimensionless rate constant $\kappa_{\text{plane}}^0 = k^0 \sqrt{\tau/D}$ on the SWV forward (dashed lines) and reverse (solid lines) currents ψ_f^{plane} and ψ_r^{plane} (a) and on the SWV net current $\psi_{\text{SW}}^{\text{plane}}$ (b), corresponding to a non-reversible electrochemical reaction at a planar electrode. $E_{\text{SW}} = 50 \text{ mV}$, $\Delta E_s = 5 \text{ mV}$, $\alpha = 0.5$. The values of $\kappa_{\text{plane}}^0 = k^0 \sqrt{\tau/D}$ appear on the curves

of κ_{plane}^0 for different values of the charge transfer coefficient α and $E_{\text{SW}} = 50 \text{ mV}$ [27]. From the current–potential curves in these figures, it can be seen that the peak height decreases with κ_{plane}^0 until it reaches a constant value independent of the rate constants for $\kappa_{\text{plane}}^0 < 0.01$. Under these conditions, the value of the peak current depends on α and the following empirical formula has been proposed [28]:

$$\psi_{\text{SW}}^{\text{plane, peak}} = 0.77 \left(\frac{\alpha F \Delta E_s}{RT} \right)^{0.41} \tanh \left(\frac{0.47 \alpha F E_{\text{SW}}}{RT} \right) \quad (7.39)$$

Concerning the peak potential shown in Fig. 7.16b, for slow charge transfers, its value moves away from the formal potential $E_c^{\Theta'}$ (which coincides with the peak potential for fast charge transfers) toward negative values, and the shift is more pronounced the smaller α . The half-peak width of the SWV net current increases as the charge transfer evolves from fast to slow (see Fig. 7.16c) becoming independent of κ_{plane}^0 for values of the rate constant below 0.01 and $\alpha \geq 0.3$. In the case of a reduction process, some anomalies in the general trend are observed for low values of α (see below).

Cyclic Square Wave Voltammetry (CSWV) is very useful in determining the reversibility degree and the charge transfer coefficient of a non-Nernstian electrochemical reaction. In order to prove this, the CSWV curves of a quasi-reversible process with $\kappa_{\text{plane}}^0 = 0.03$ and different values of α have been plotted in Fig. 7.17. In this figure, we have included the net current for the first and second scans (Fig. 7.17b, d, and f) and also the forward, reverse, and net current of a single scan (first or second, Fig. 7.17a, c, e) to help understand the observed response.

From the curves in Fig. 7.17, it can be concluded that if $\alpha = 0.5$, no splitting is observed in the net current in either scan. However, if $\alpha \ll 0.5$, there is a splitting in

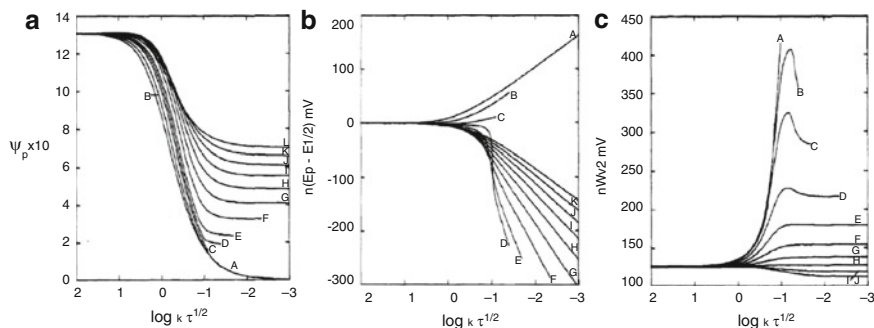


Fig. 7.16 Peak height $\psi_{\text{SW}}^{\text{peak}}$ (a, $\psi_{\text{SW}}^{\text{peak}} = I_{\text{SW}}^{\text{peak}} \sqrt{\pi\tau} / (FA\sqrt{D_{\text{O}}c_{\text{O}}^*})$), peak position $n(E_{\text{peak}} - E_{1/2})$ (b, $E_{1/2} = E_c^{\ominus'} + \frac{RT}{F} \ln(D_{\text{R}}/D_{\text{O}})^{1/2}$), and peak width $nW_{1/2}$ (c) as a function of $\log(k^0 \sqrt{\tau} / (D_{\text{R}}^{\alpha/2} D_{\text{O}}^{(1-\alpha)/2}))$ for a slow electrochemical reaction taking place at planar electrodes. The values of α are (A–L): 0, 0.1, 0.2, 0.25, 0.3, 0.4, 0.5, 0.6, 0.7, 0.8, 0.9, and 1.0. Reproduced from [27] with permission

the net current of the first scan which is not present in the second (see Fig. 7.17b). This splitting is related to the appearance of a minimum in the reverse component of the current at anodic potentials for values of $\alpha < 0.3$ for quasi-reversible processes (Fig. 7.17a). Contrarily, this splitting is only observed in the second scan if $\alpha \gg 0.5$ (Fig. 7.17f). In this case, there is a maximum in the reverse component at cathodic potentials, in agreement with Fig. 7.17e.

The CSWV response of a fully irreversible electrochemical reaction ($\kappa = 0.003$) has been plotted in Fig. 7.18 for the same values of α shown in Fig. 7.17 in order to compare it with the quasi-reversible case discussed above. From these curves, it can be seen that in this case there is no splitting in the first scan, regardless of the value of α , and the dependence of the peak height on the charge transfer coefficient is given by Eq. (7.39) under these conditions. Contrarily, a splitting is always observed in the second scan (with the relative heights of the two peaks being modulated by the value of the charge transfer coefficient).

So, a totally irreversible process could be mistaken for a quasi-reversible one with $\alpha \gg 0.5$ (Fig. 7.17f). In order to discriminate the reversibility degree of the electrochemical reaction, it is necessary to take into account that for a quasi-reversible process the peak corresponding to more cathodic potentials in the second scan (denoted as RC by [29]) is higher than that located at more anodic ones (denoted as RA by [29]) when $\alpha \gg 0.5$, whereas the opposite is observed for a fully irreversible electron transfer for any value of α (see also Table insert, Fig. 7.20).

In order to show this behavior in a clearer way, the CSWV net currents corresponding to the second scan of an electrochemical reaction with $\alpha = 0.8$ are shown in Fig. 7.19 for several values of the dimensionless rate constant. From these curves, it can be inferred that the ratio between RC and RA peak currents corresponding to the second scan for $\kappa_{\text{plane}}^0 = 0.03$ and $\alpha = 0.8$, $\psi_{\text{SW}}^{\text{plane,peak,RC}} / \psi_{\text{SW}}^{\text{plane,peak,RA}}$, is 1.415, whereas

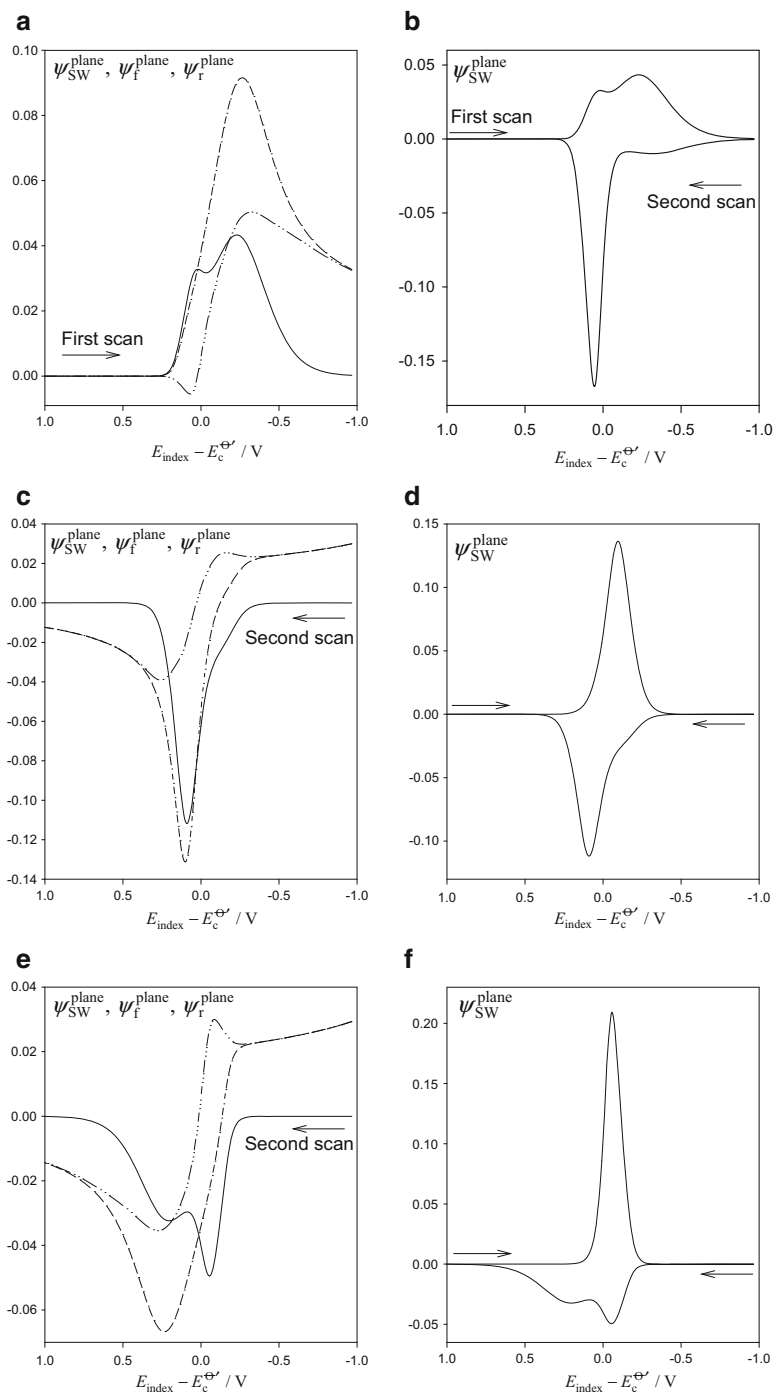


Fig. 7.17 SWV forward (dashed), reverse (dashed-dotted), and net (solid) currents (a, c, e) and CSWV net currents (b, d, f) corresponding to a charge transfer process with $\kappa_{\text{plane}}^0 = 0.03$ at planar electrodes. The values of α are: 0.2 (a, b), 0.5 (c, d) and 0.8 (e, f). $E_{\text{SW}} = 50 \text{ mV}$, $\Delta E_s = 5 \text{ mV}$, $T = 298 \text{ K}$

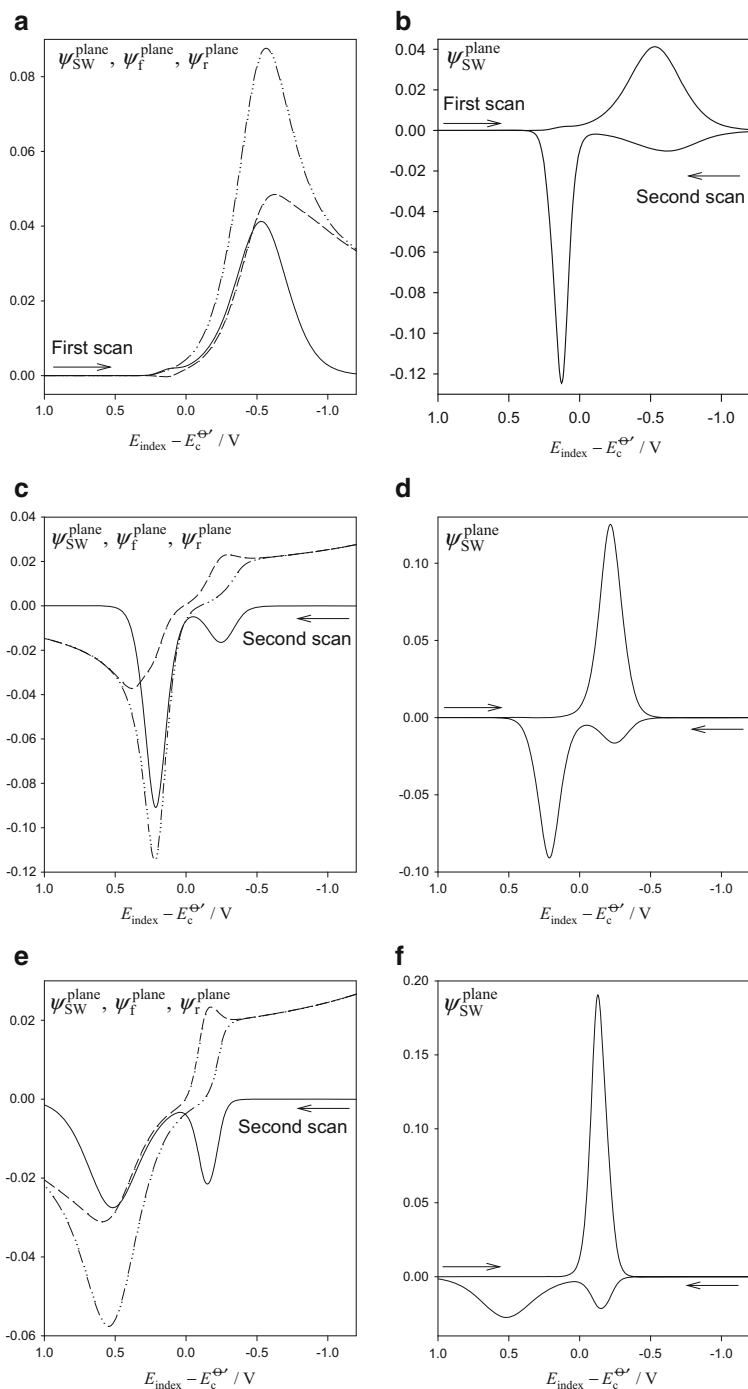


Fig. 7.18 SWV forward (*dashed*), reverse (*dashed-dotted*), and net (*solid*) currents (**a, c, e**) and CSWV net currents (**b, d, f**) corresponding to a charge transfer process with $\kappa_{\text{plane}}^0 = 0.003$ at planar electrodes. The values of α are 0.2 (**a, b**), 0.5 (**c, d**), and 0.8 (**e, f**). $E_{\text{SW}} = 50 \text{ mV}$, $\Delta E_s = 5 \text{ mV}$, $T = 298 \text{ K}$

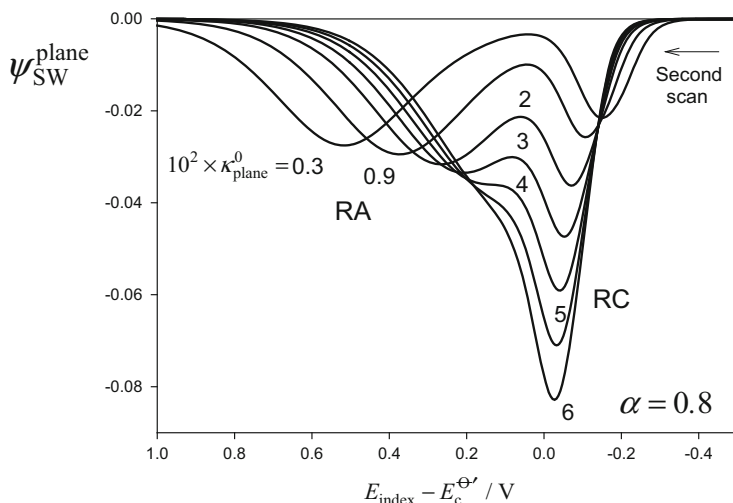


Fig. 7.19 SWV net currents corresponding to a charge transfer process with $\alpha = 0.8$ and different values of κ_{plane}^0 at planar electrodes. The values of $100\kappa_{\text{plane}}^0$ are shown on the curves. $E_{\text{SW}} = 50 \text{ mV}$, $\Delta E_s = 5 \text{ mV}$, $T = 298 \text{ K}$

for $\kappa_{\text{plane}}^0 = 0.003$ (fully irreversible processes) and the same value of α for this ratio is 0.927 (see Fig. 7.20). Moreover, for a fully irreversible process the ratio between peak currents of the second scan is independent of the frequency (or of the pulse time), whereas for quasi-reversible processes this ratio is highly sensitive to it (see Fig. 7.19). Indeed, a strong decrease of the RC peak is observed when the rate constant diminishes, giving rise to an inversion of the ratio $\psi_{\text{SW}}^{\text{plane,peak,RC}} / \psi_{\text{SW}}^{\text{plane,peak,RA}}$. Another feature that should be considered is that the magnitude of the dimensionless current observed for a fully irreversible electrochemical reaction is always smaller than that obtained for a quasi-reversible one.

The appearance of two peaks in the second scan is a feature of the CSWV typical of fully irreversible processes. Since the response of a non-reversible electrochemical reaction can be driven to the fully irreversible limit by using high frequencies (or small pulse time lengths), it is interesting to characterize the response at this limit. The net currents corresponding to the second scan of a totally irreversible process ($\kappa_{\text{plane}}^0 = 0.003$) taking place for different values of α are shown in Fig. 7.20. The displacement of the RC peak corresponding to more cathodic potentials with the dimensionless rate constants obeys the same law as the single peak of the first scan (not shown), whereas the RA peak observed at more anodic potentials reflects the oxidation of species R generated at the electrode surface during the RC peak. It has been reported that the shape and position of both peaks is not dependent on the electrode size (for the case of spherical electrodes [29]). By combining the values of the peak-to-peak separation and the ratio between the peak currents, it is possible to

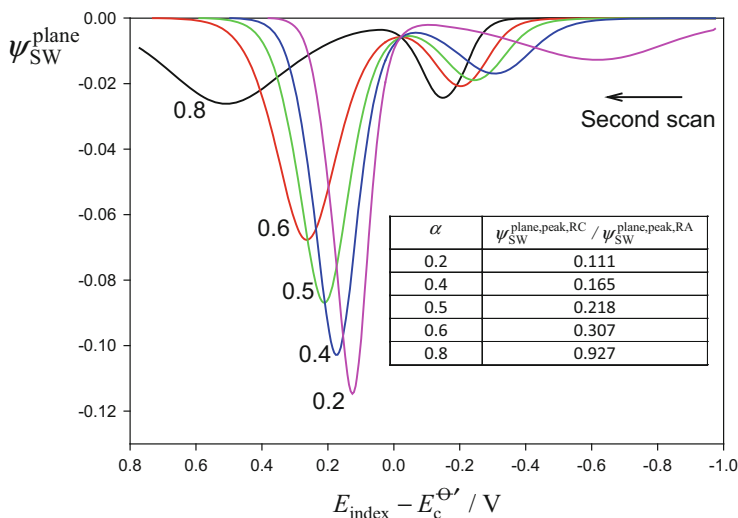


Fig. 7.20 CSWV net currents corresponding to the second scan for an irreversible process ($\kappa_{\text{plane}}^0 = 0.003$) taking place at a planar electrode. The values of α appear on the curves. Inner table: values of the ratio $\psi_{SW}^{\text{plane,peak,RC}} / \psi_{SW}^{\text{plane,peak,RA}}$ for the different charge transfer coefficients considered. $E_{SW} = 50 \text{ mV}$, $\Delta E_s = 5 \text{ mV}$, $T = 298 \text{ K}$

determine the kinetic parameters of the electrochemical reaction. This has been done for the case of the U(V)/U(VI) system in [29].

Due to the great sensitivity of the response of the reverse scan to the kinetic parameters, this has been used to test the accuracy of the Butler–Volmer (BV) and the symmetrical Marcus–Hush (MH) formalisms in the elucidation of the kinetic parameters of different redox couples. As an example, experimental CSWV voltammograms obtained with different frequencies (f) (solid lines) of a 2 mM 2-methyl-2-nitropropane (MeNP), 0.1 M TBAP acetonitrile solution at a mercury hemispherical electrode with $r_s = 25 \mu\text{m}$ are plotted in Fig. 7.21 [30]. As can be observed, a reductive peak is recorded in the first scan at ca. -1.93 V (vs. Ag wire) and in the second scan the peak corresponding to the oxidation of the radical anion MeNP^- is situated at ca. -1.54 V (once the forward and reverse components are analysed, see for example Figs. 7.17e and 7.18c and e). The SWV parameters have been optimized so as to obtain two well-defined peaks in the reverse scan. This requires high frequencies ($f \geq 100 \text{ Hz}$) and a step potential $\Delta E_s = 10 \text{ mV}$, which permits both fast experiments and a sufficient number of points in the voltammograms.

The reductive and oxidative peaks shown in Fig. 7.21 are well resolved and the relative magnitude of the oxidative peak and the peak-to-peak separation increases with frequency. The theoretical reverse SWV voltammograms were fitted to the experimental data assuming both BV and MH models. As can be seen, with the Butler–Volmer formalism (•) excellent fits are obtained between experimental and theoretical SWV curves such that the magnitude and separation of the reduction and

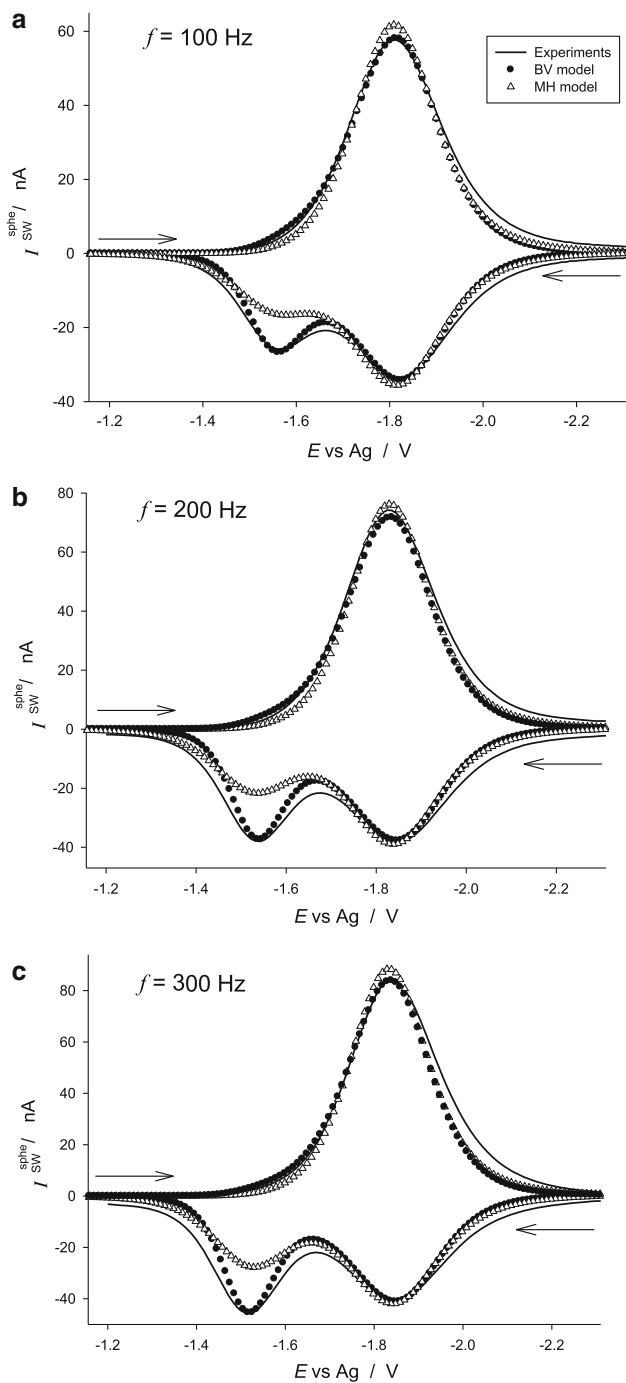


Fig. 7.21 Experimental (solid line) and theoretical (points) SWV voltammograms obtained with Butler–Volmer (dotted) and Marcus–Hush (triangle) models. A positive sign corresponds to

Table 7.2 Values of the standard rate constant (k^0), the transfer coefficient (α), the reorganization energy (λ), and the formal potential ($E_c^{\ominus'}$, vs. Ag) corresponding to the theoretical curves shown in Fig. 7.21. Taken from [30]

f (Hz)	Butler–Volmer	Marcus–Hush
100	$k^0 = 3.1 \times 10^{-3} \text{ cm s}^{-1}$ $\alpha = 0.40$ $E_c^{\ominus'} = -1.652 \text{ V}$	$k^0 = 2.8 \times 10^{-3} \text{ cm s}^{-1}$ $\lambda = 1.8 \text{ eV}$ $E_c^{\ominus'} = -1.678 \text{ V}$
200	$k^0 = 2.9 \times 10^{-3} \text{ cm s}^{-1}$ $\alpha = 0.39$ $E_c^{\ominus'} = -1.647 \text{ V}$	$k^0 = 2.5 \times 10^{-3} \text{ cm s}^{-1}$ $\lambda = 2.6 \text{ eV}$ $E_c^{\ominus'} = -1.679 \text{ V}$
300	$k^0 = 2.8 \times 10^{-3} \text{ cm s}^{-1}$ $\alpha = 0.39$ $E_c^{\ominus'} = -1.638 \text{ V}$	$k^0 = 2.7 \times 10^{-3} \text{ cm s}^{-1}$ $\lambda = 3.1 \text{ eV}$ $E_c^{\ominus'} = -1.673 \text{ V}$
Mean values	$\langle k^0 \rangle = (2.9 \pm 0.1) \times 10^{-3} \text{ cm s}^{-1}$ $\langle \alpha \rangle = 0.393 \pm 0.006$ $\langle E_c^{\ominus'} \rangle = -1.645 \pm 0.007 \text{ V}$	$\langle k^0 \rangle = (2.7 \pm 0.2) \times 10^{-3} \text{ cm s}^{-1}$ $\langle \lambda \rangle = 2.5 \pm 0.7 \text{ eV}$ $\langle E_c^{\ominus'} \rangle = -1.677 \pm 0.003 \text{ V}$

oxidation peaks are well described in all cases. However, when the symmetrical Marcus–Hush relationships (Δ) were employed to describe the electrode kinetics, the simultaneous fit of both peaks was not possible. This limitation of the symmetrical MH formalism has been highlighted with other techniques like CV, but CSWV has proved very suitable for analyzing its degree of validity under different conditions (see [30, 31]). Indeed, when the more flexible asymmetric MH formalist is used for the kinetic analysis of this system, the agreement between theoretical and experimental results is much better [32].

Although the usual way of analyzing the influence of the kinetics of the electron transfer on the SWV response is based on the variation of the frequency at fixed values of the staircase and square wave amplitude, a new approach for carrying out this analysis has been proposed based on the study of the influence of the square wave amplitude E_{SW} on the current potential curves at a fixed value of the frequency (or the time pulse) [19, 33, 34]. The square wave amplitude has been used rarely as a tool in mechanistic and kinetic studies. One of the main reason is that, as stated in Sect. 7.1, in SWV the current is plotted versus an index potential which is an average potential between the forward and reverse potentials (see Eq. (7.7)) and leads to a discrepancy between the plotted and actual potentials at which the current is sampled. Therefore, the role played by E_{SW} in the process is complex.

A novel approach has been reported for the determination of kinetic parameters at a fixed value of the frequency based on a new feature called “amplitude-based quasi-reversible maximum” [33]. This term is related to the “quasi-reversible

Fig. 7.21 (continued) reverse scans. $E_{\text{initial}}^{\text{reverse}} = -2.6 \text{ V}$ (vs. Ag), $E_{\text{SW}} = 25 \text{ mV}$, $\Delta E_S = 10 \text{ mV}$. The values of the kinetic parameters and formal potential extracted in each case are given in Table 7.2. Test solution: 2 mM 2-methyl-2-nitropropane, 0.1 M tetra-*n*-butylammonium perchlorate in acetonitrile. Reproduced from [30] with permission

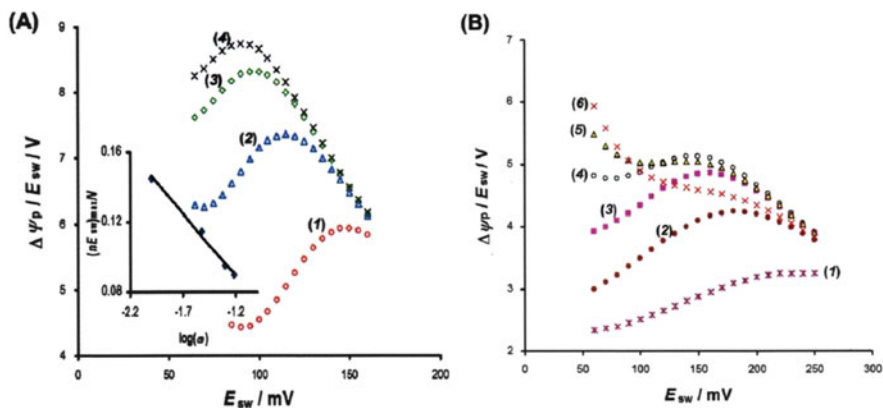


Fig. 7.22 Quasi-reversible electrode reaction of a dissolved redox couple at a planar electrode. Dependence of the amplitude-based quasi-reversible maximum on the rate constant (a) and on the charge transfer coefficient (b). For panel (a), the simulations are conducted for two electrons and the frequencies (in Hz): 0.01 (1), 0.03 (2), 0.05 (3), and 0.06 (4). For panel (b), the simulation conditions are: one electron, frequency 0.1 Hz, and α : 0.2 (1), 0.3 (2), 0.4 (3), 0.5 (4), 0.6 (5), and 0.7 (6). $\Delta E_s = 5$ mV. Reproduced from [33] with permission

maximum” observed for surface-confined molecules introduced by Lovrić [6]. When the square wave pulse amplitude is varied, a maximum appears in the plots of ψ_{SW}^{plane}/E_{SW} versus E_{SW} for quasi-reversible electrochemical reactions which is highly sensitive to the standard rate constants and thus enables its determination (see Fig. 7.22). The position of the amplitude-based maximum, $(E_{SW})_{max}$, depends linearly on the logarithm of the frequency and on the value of the charge transfer coefficient. This procedure has been applied in the determination of the kinetic parameters of the 2-methyl-2-nitropropane system.

Another approach based on the same idea is to analyze the separation between the forward and reverse currents as a function of E_{SW} by using potential-corrected voltammograms, i.e., by plotting the forward and reverse currents ψ_f^{plane} and ψ_r^{plane} versus the real potential at which these currents are obtained, E_{2p-1} and E_{2p} , respectively, in order to avoid artificial separations. These plots provide the basis for the estimation of the rate constant [34].

7.4 Ion Transport Through Liquid Membranes

In this section, the subtractive multipulse techniques DMPV and SWV are applied to reversible ion transfer across different liquid–liquid systems with one or two polarizable interfaces. These electrochemical techniques allow the accurate and easy determination of standard potentials directly from the peak potentials of the current–potential curves since non-faradaic and background currents are minimized [12, 35–40].

7.4.1 Differential Multipulse Voltammetry

In the case of DMPV (see Scheme 7.2), the treatment followed in Sect. 4.2.4.1 for Differential Double Pulse Voltammetry (DDPV) for one and two polarizable interfaces can be used because the equilibrium is quickly reestablished during the longer period τ_1 . Therefore, the peak potential of the DMPV curves when the current is plotted versus the index potential is

$$\left. \begin{aligned} E_{\text{DMPV,peak}} &= E_{1/2} \quad \text{One polarizable interface} \\ E_{\text{DMPV,peak}} &= E_{1/2}^{\text{M}} + 13 \text{ mV} \quad \text{Two polarizable interfaces} \end{aligned} \right\} \quad (7.40)$$

with $E_{1/2}^{\text{M}}$ being the half-wave potential for a two-polarizable interface system

$$E_{1/2}^{\text{M}} = E^{\text{M}, \Theta'} - \frac{RT}{F} \ln \lambda^+ \quad (7.41)$$

$$E^{\text{M}, \Theta'} = \Delta_{\text{M}}^{\text{w}} \phi_{\text{X}^+}^{\Theta'} - \Delta_{\text{w}}^{\text{M}} \phi_{\text{R}^+}^{\Theta'} \quad (7.42)$$

$$\lambda^+ = \frac{2\sqrt{D_{\text{R}^+}^{\text{w}_2} D_{\text{X}^+}^{\text{M}}}}{D_{\text{X}^+}^{\text{w}_1}} \frac{c_{\text{R}^+}^*}{c_{\text{X}^+}^*} \quad (7.43)$$

$\Delta_{\text{M}}^{\text{w}} \phi_{\text{X}^+}^{\Theta'}$ and $\Delta_{\text{w}}^{\text{M}} \phi_{\text{R}^+}^{\Theta'}$ are the formal ion transfer potentials for the target ion X^+ and for the membrane electrolyte cation R^+ , respectively, $c_{\text{R}^+}^*$ is the concentration of the membrane electrolyte cation, R^+ , and $D_{\text{X}^+}^{\text{M}}$ and $D_{\text{R}^+}^{\text{w}_2}$ are the diffusion coefficients of X^+ in the membrane (M phase) and R^+ in the inner aqueous solution (w_2 phase), respectively.

7.4.2 Square Wave Voltammetry

The general expression for the SWV net current applicable to systems with one and two polarizable interfaces is [36–38]:

$$\begin{aligned} I_{\text{SW}} &= I_{2p-1} - I_{2p} \\ &= -I_{\text{d}}(\tau) g_{2p} \\ &\quad + I_{\text{d}}(\tau) \sum_{m=1}^{2p-1} \left((g_{2m-1} - g_{2m}) \left[\frac{1}{\sqrt{2p-m}} - \frac{1}{\sqrt{2p-m+1}} \right] \right) \end{aligned} \quad (7.44)$$

where

$$I_d(\tau) = zFAc_{XZ}^* \sqrt{\frac{D_{XZ}^W}{\pi\tau}} \quad (7.45)$$

$$g_m = \begin{cases} \frac{1}{1 + \gamma e^{\eta_m}} & \text{One polarizable interface} \\ \frac{\sqrt{(\lambda^+ e^{\eta_{M,m}})^2 + 8\lambda^+ e^{\eta_{M,m}} - \lambda^+ e^{\eta_{M,m}}}}{4} & \text{Two polarizable interfaces} \end{cases} \quad (7.46)$$

with

$$\left. \begin{aligned} \eta_m &= \frac{F}{RT} (E_m - \Delta_M^w \phi_{XZ}^{\Theta'}) && \text{One polarizable interface} \\ \eta_{M,m} &= \frac{F}{RT} (E_m - E^{M, \Theta'}) && \text{Two polarizable interfaces} \end{aligned} \right\} \quad (7.47)$$

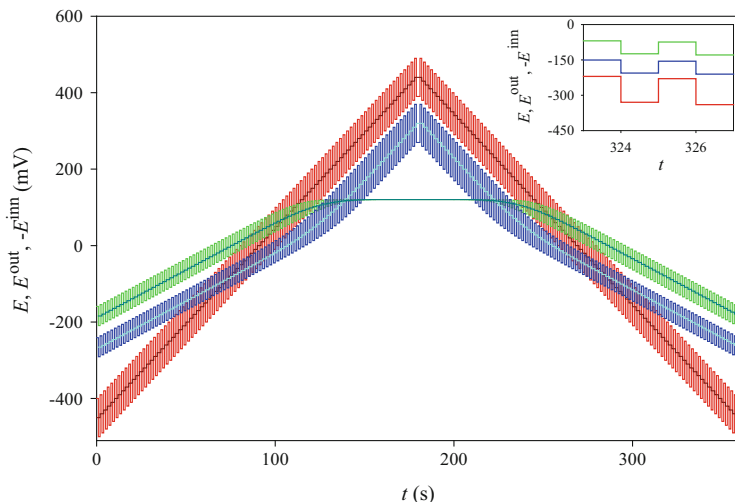
$$\gamma = \sqrt{\frac{D_{XZ}^M}{D_{XZ}^W}} \quad (7.48)$$

and with λ^+ given by Eq. (7.43).

In order to show the distribution of the applied potential between the outer and the inner interface in the case of systems with two polarized interfaces, the potential time waveform used in SWV is depicted in Scheme 7.5. The applied potential, E (red line), and the outer (E^{out} , blue line) and inner potentials (E^{inn} , green line) have been plotted.

It can be seen that in the central part of the cyclic sweep, the outer potential, E^{out} , follows the same trend as the applied potential, E , so in this zone the outer interface presents a behavior similar to that of a system with a single polarizable interface. Concerning the inner interface, E^{inn} is quite sensitive to the external polarization at both extremes of the cyclic sweep, becoming independent of the potential in the central zone of the same. In the inset, it can be seen how the potential pulses are distributed unequally between both outer and inner interfaces [38].

For comparison of the SWV responses provided for systems of one and two polarized interfaces, Fig. 7.23 shows the $I_{\text{SW}} - E$ curves corresponding to the direct and to the reverse scans (solid line and empty circles, respectively) for both kinds of membrane systems, calculated for $E_{\text{SW}} = 50\text{mV}$ by using Eq. (7.44). The peaks obtained when two polarized interfaces are considered are shifted 8 mV with respect to those obtained for a system with a single polarized one, which implies that the half-wave potential for the system with two polarized interfaces can be easily determined from the peak potential by



Scheme 7.5 Potential–time waveform of SWV obtained from Eq. (7.5) (E , red line), and its distribution between the outer interface (E^{out} , dark blue line) and the inner interface (E^{inn} , green line). The three index potentials (the outer index potential, $E^{\text{out, index}}$, the inner index potential, $E^{\text{inn, index}}$, and the membrane index potential, E^{index}) are also included (blue line, dark green line, and black line, respectively). Inset figure: Distribution of the applied potential (red line), between the outer and the inner interfaces (dark blue line and green line, respectively). $E_{\text{initial}} = -450 \text{ mV}$, $E_{\text{final}} = 450 \text{ mV}$, $\Delta E_s = 10 \text{ mV}$, $E_{\text{SW}} = 50 \text{ mV}$, $\tau = 1 \text{ s}$, $A = 0.081$, $\Delta_o^v \phi_{X^+}^{\ominus} = -50 \text{ mV}$, $\Delta_w^o \phi_{R^+}^{\ominus} = -150 \text{ mV}$, $c_{X^+}^* = 0.5 \text{ mM}$, $c_{R^+}^* = 50 \text{ mM}$, $D_{X^+}^{w_1} = D_{R^+}^{w_2} = 10^{-5} \text{ cm}^2 \text{ s}^{-1}$, $D_{X^+}^M = 10^{-8} \text{ cm}^2 \text{ s}^{-1}$. $T = 298.15 \text{ K}$. Reproduced from [38] with permission

$$E_{\text{SW, peak}} = E_{1/2}^M \pm 8 \text{ mV} \quad (7.49)$$

for $E_{\text{SW}} = 50 \text{ mV}$ (with the upper sign for cations and the lower for anions), whereas $E_{\text{SW, peak}} = E_{1/2}$ when only one interface is considered, regardless of the square wave amplitude [38].

In both types of membrane systems, the current–potential curves corresponding to the first and second scans must be mirror images, which indicates that the ion transfer processes taking place at both the outer and inner interfaces are reversible. Thus, CSWV can be used as an excellent tool for analyzing the reversibility of charge transfer processes.

Regarding the influence of the target ion concentration on the SWV curves, the major difference found between systems with one or two polarized interfaces is that this variable causes a shift of the peak potentials toward more anodic values through an increase of $E_{1/2}^M$ in the latter case (see Eqs. (7.41)–(7.43)), whereas only an increase in the peak current is observed for systems with one polarized interface [36]. Therefore, SWV is a very good analytical tool for the determination of ion concentrations in both kinds of membrane systems.

The experimental and theoretical SWV net currents calculated from Eq. (7.44) of several anions and cations can be seen in Fig. 7.24 corresponding to systems of

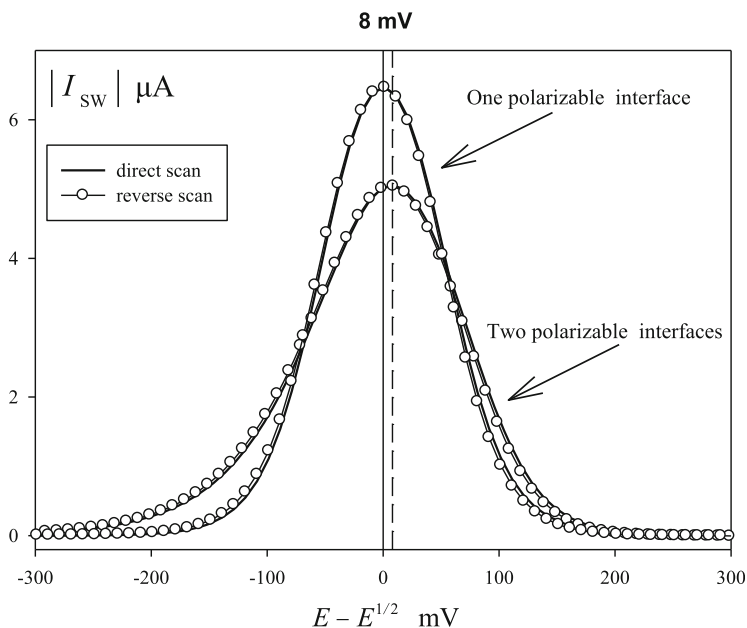


Fig. 7.23 Theoretical $|I_{SW}| - (E - E^{1/2})$ curves corresponding to the direct and reverse scans of the square wave (solid lines and empty circles, respectively) for a system with one and two polarizable interfaces obtained for $E_{SW} = 50$ mV by using Eq. (7.44). $\Delta E_s = 5$ mV. $E^{1/2}$ is the half-wave potential given by Eqs. (2.53) and (2.81) for system with one or two polarizable interfaces, respectively. Others parameters are the same as given in Scheme 7.5. Reproduced from [38] with permission

one polarized interface systems [38]. This series of ions is distributed into a range of potentials of 1200 mV, which constitutes one of the widest potential windows in the literature [36, 41]. As can be seen, the concordance between both sets of data is excellent.

7.4.3 Micro-ITIES and Asymmetrical Diffusion

The advantages derived from the use of microscopic liquid–liquid interfaces have been highlighted in Sect. 5.5.3, and different approaches to support such small liquid–liquid interfaces in pores, pipettes, and capillaries have been addressed. The theoretical treatment of ion transfer through these interfaces needs to consider the asymmetry of the diffusion fields inside and outside the pore or pipette (i.e., diffusion can be approximated as linear in the inner phase, whereas radial diffusion is significant in the outer phase, especially for small sizes) [36, 40, 42–44].

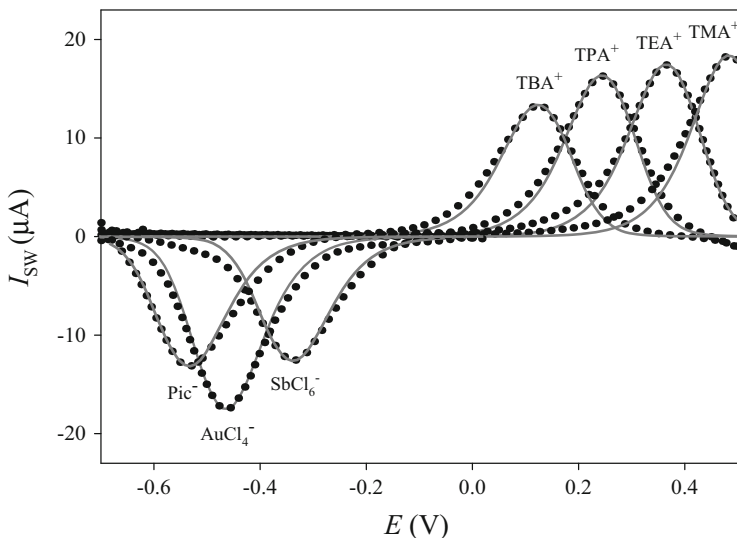


Fig. 7.24 Experimental SWV obtained for 5×10^{-4} M solutions of several ions (shown on the curves). Theoretical curves are given by *solid lines*. $E_{SW} = 50$ mV, $\Delta E_s = 10$ mV, $\tau = 0.3$ s, and $A\sqrt{D_X^{sw}}$ in $\text{cm}^3 \text{s}^{-1/2}$: (a) TMA⁺, 5×10^{-4} ; (b) TEA⁺, 4.9×10^{-4} ; (c) TPA⁺, 4.5×10^{-4} ; (d) TBA⁺, 3.8×10^{-4} ; (f) SbCl₆⁻, 3.3×10^{-4} ; (g) AuCl₄⁻, 4.9×10^{-4} ; (h) Pic⁻, 3.7×10^{-4} . $T = 298.15$ K. Reproduced from [38] with permission

Following the theoretical treatment described in [42], the following expression for the SWV net current corresponding to the transfer of an ion X^Z taking place at a microcapillary of radius a is found:

$$\begin{aligned}
 I_{SW} &= I_{2p-1} - I_{2p} = \\
 &= 4zFD_X^{\text{out}} ac_X^{*, \text{out}} \left\{ \left(\frac{(c_X^{*, \text{in}}/c_X^{*, \text{out}}) + \xi_{SW}\sqrt{2p-1}}{1 + \xi_{SW}\sqrt{2p-1}} e^{\eta_{2p-1}} \right) \times \right. \\
 &\quad \prod_{m=2}^{2p-1} \left(\frac{(c_X^{*, \text{in}}/c_X^{*, \text{out}}) + \xi_{SW}\sqrt{2p-m}}{1 + \xi_{SW}\sqrt{2p-m}} e^{\eta_{m-1}} \right) - \\
 &\quad \left(\frac{(c_X^{*, \text{in}}/c_X^{*, \text{out}}) + \xi_{SW}\sqrt{2p}}{1 + \xi_{SW}\sqrt{2p}} e^{\eta_{2p}} \right) \times \\
 &\quad \left. \prod_{m=2}^{2p} \left(\frac{(c_X^{*, \text{in}}/c_X^{*, \text{out}}) + \xi_{SW}\sqrt{2p-m+1}}{1 + \xi_{SW}\sqrt{2p-m+1}} e^{\eta_{m-1}} \right) \right\} \quad (7.50)
 \end{aligned}$$

with

$$\xi_{SW} = \frac{4}{\pi} \sqrt{\frac{D_X^{\text{out}}}{D_X^{\text{in}}}} \frac{\sqrt{\pi D_X^{\text{out}} \tau}}{a} \quad (7.51)$$

$$\eta_m = \frac{F}{RT} \left(\Delta_{\text{out}}^{\text{in}} \phi_m - \Delta_{\text{out}}^{\text{in}} \phi^{\ominus} \right) \quad (7.52)$$

D_X^{phase} is the diffusion coefficient of the target ion in the different phases and $c_X^{*,\text{in/out}}$ its bulk concentration in the inner/outer solution, $\Delta_{\text{out}}^{\text{in}} \phi_m$ the electric potential difference across the interface corresponding to the m th potential applied, and $\Delta_{\text{out}}^{\text{in}} \phi^{\ominus}$ the formal potential of the ion transfer.

The behavior of the system is defined by the dimensionless parameter ξ_{SW} (Eq. (7.51)) and so by the ratio between the diffusion coefficients ($D_X^{\text{out}}/D_X^{\text{in}}$) and the dimensionless radius of the capillary defined as $\sigma_{\text{SWV}} = a/\sqrt{D_X^{\text{out}}\tau}$.

In cyclic SWV (Fig. 7.25), the typical peak-shaped response is obtained in both the forward and reverse scans for any bulk concentrations of the ion. In contrast to the behavior at macro-interfaces, the forward and backward peaks are not symmetrical with respect to the potential axis, and the peak height of the reverse scan is dependent on the vertex potential. The position of the voltammograms is well described by the analytical solution (7.50) when $\sigma_{\text{SWV}} \leq 0.1$, with a difference between analytical and numerical results for the peak potentials of less than 8 mV at $T = 298$ K for typical SWV conditions: $E_{\text{SW}} = 10 - 50$ mV and $\Delta E_s = 2 - 10$ mV.

The SWV curves cannot be unambiguously related to the ion ingress or egress due to the subtractive nature of the signal. To do this, the analysis of the forward and backward components (Fig. 7.25b) is necessary and this reveals that, when the ion is present in the outer solution, the forward peak in the scan toward negative potentials is associated with the ion ingress and the peak obtained in the reverse scan with the ion egress.

The influences of the pulse amplitude (E_{SW}) and the potential step (ΔE_s) in SWV are shown in Fig. 7.26. Similarly to the case of macro-interfaces, the increase of E_{SW} gives rise to higher and broader peaks. Thus, for very large E_{SW} values (> 100 mV), a plateau rather than a peak is obtained, whereas for smaller pulse amplitudes (≤ 50 mV), the forward and backward peaks are well defined.

With regard to the influence of the potential step (Fig. 7.26c, d), this is not significant for reversible transfers at macro-interfaces (Fig. 7.26d), but this is not the case at micro/nano-interfaces. As can be observed in Fig. 7.26c, the peak potentials shift toward less negative potentials as the step potential is increased. For the conditions considered in the figure, a ca. 15 mV shift is observed between $\Delta E_s = 2$ and 15 mV.

The peak potential varies linearly with $\ln \xi_{\text{SWV}}$ (Eq. (7.53)), where ξ_{SWV} includes the influence of the intrinsic variables of the system (Eq. (7.51)). However, it is difficult to find a general expression for the exact value of the peak potential given that this also depends on the step potential and the pulse amplitude:

$$\Delta \phi_{\text{SW,peak}} = \Delta_{\text{out}}^{\text{in}} \phi^{\ominus} - \frac{RT}{zF} \ln \xi_{\text{SWV}} - \frac{RT}{zF} f(\Delta E_s, E_{\text{SW}}) \quad (7.53)$$

For typical SWV conditions ($\Delta E_s = 2$ mV, $E_{\text{SW}} = 25$ mV, $T = 298$ K), the value $f(\Delta E_s, E_{\text{SW}}) = 1.44$ is obtained from the analytical solution [42].

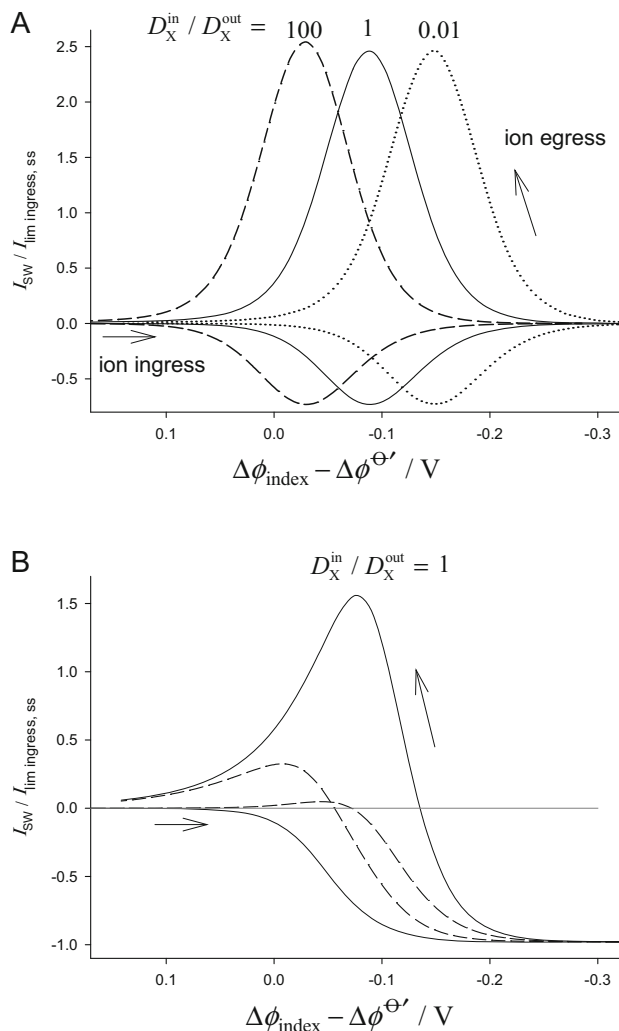


Fig. 7.25 Analytical solution in Cyclic Square Wave Voltammetry (SWV) for different situations with respect to the bulk concentrations of the ion (Eq. (7.50)). (a) net currents; (b) forward (solid lines); and reverse (dashed lines) components. $I_{lim,ingress,ss} = 4zFD_X^{out}ac_X^{*,out}$, $c_X^{*,in} = 0$, $\sigma_{SWV} = 0.1$, $E_{SW} = 25$ mV, $\Delta E_s = 5$ mV, $T = 298$ K. Reproduced modified with permission of [42]

The above expression makes it easy to predict the shift of the voltammograms with the capillary size, experiment timescale, and diffusivities of the ion. Also, provided that the capillary diameter and diffusion coefficients of the ion are known (for example, by means of chronoamperometric experiments), the $\Delta\phi_{SWV,peak}$ value allows the determination of the ion transfer formal potential and the consistency of the value obtained can be easily tested by varying the scan rate or the frequency [42, 44].

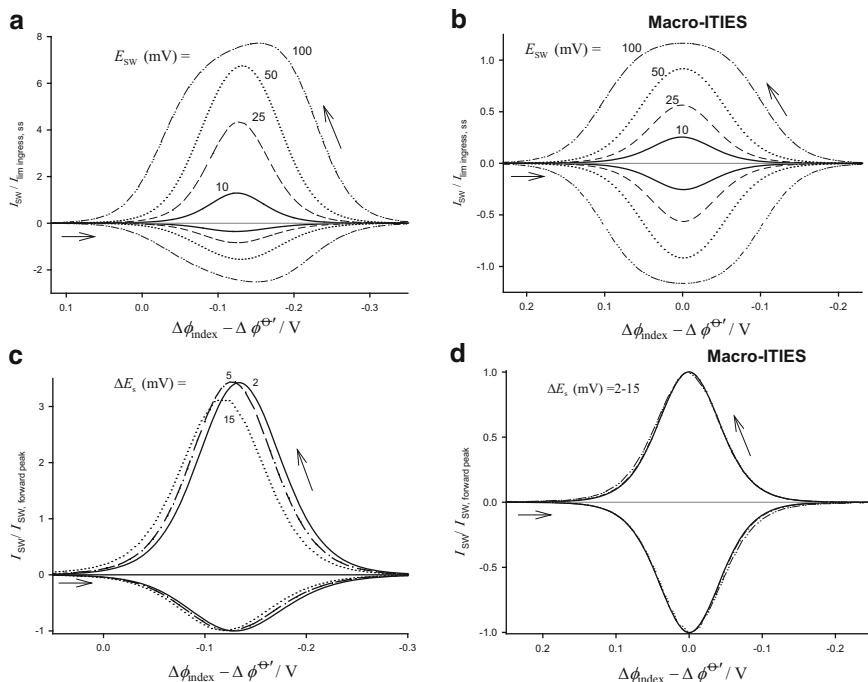


Fig. 7.26 Influence of the pulse amplitude (a, b) and step potential (c, d) in SWV at micro/nano-interfaces ($\sigma_{SWV} = 0.03$; a, c) and at macro-interfaces (b, d). $I_{lim, ingress, ss} = 4zFD_X^{out}ac_X^{*, out}$, $D_X^{in} = D_X^{out}$, $c_X^{*in} = 0$, $E_{SW} = 25$ mV (c, d), $\Delta E_s = 5$ mV (a, b). $T = 298$ K. Reproduced from [42] with permission

7.5 Multi-electron Electrochemical Reactions

The electrochemical characterization of multi-electron electrochemical reactions involves the determination of the formal potentials of the different steps, as these indicate the thermodynamic stability of the different oxidation states. For this purpose, subtractive multipulse techniques are very valuable since they combine the advantages of differential pulse techniques and scanning voltammetric ones [6, 19, 45–52]. All these techniques lead to peak-shaped voltammograms, even under steady-state conditions.

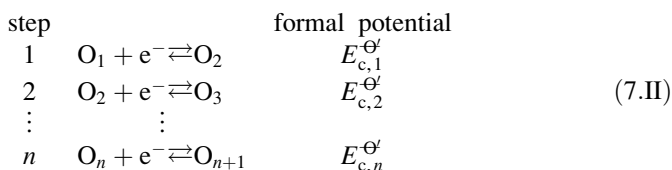
Here, the response of multi-electron electrochemical reactions in subtractive multipulse voltammetries is treated by first considering the situation in which all the electron transfers are reversible. The case corresponding to slow electron transfers with different types of stabilization of the intermediate species is also analyzed.

7.5.1 Reversible Electrochemical Reactions

Equations (6.15) and (6.16) cover an important gap in the electrochemical literature corresponding to multi-electron electrochemical reactions, since they provide the theoretical background for the study of these electrode processes in any electrochemical technique for electrodes of different geometry and size.

7.5.1.1 Differential Staircase Voltammetry

For the reaction scheme



in which the homogeneous comproportionation / disproportionation reactions are not considered (see Sects. 3.3.1 and 3.3.4 for a detailed discussion). $E_{c,i}^{\ominus'}$ ($i = 1, 2, \dots, n$) are the formal potentials of each individual electron transfer, the analytical explicit expression of the DSCVC current according to Eqs. (6.15) and (7.1) is

$$\begin{aligned} \psi_{\text{DSCVC}}^{\text{multiE,G}} &= \frac{I_p^{\text{multiE,G}} - I_{p-1}^{\text{multiE,G}}}{FA_G c_{O_1}^* \sqrt{aD}} \\ &= \sqrt{\frac{D}{a}} \left\{ \sum_{m=1}^{p-1} \left(W^{(m-1,s)} - W^{(m,s)} \right) \left(f_G((p-m+1)\tau, q_G) - f_G((p-m)\tau, q_G) \right) \right. \\ &\quad \left. + \left(W^{(p-1,s)} - W^{(p,s)} \right) f_G(\tau, q_G) \right\} \end{aligned} \quad (7.54)$$

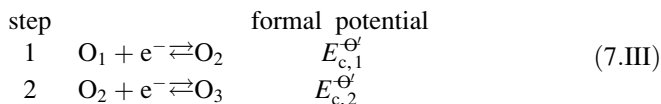
where

$$\left. \begin{aligned} W^{(m,s)} &= c_{O_1}^* \frac{\sum_{i=1}^n \left((n-i+1) \left(\prod_{j=i}^n e^{\eta_{m,j}} \right) \right)}{1 + \sum_{k=1}^n \prod_{h=k}^n e^{\eta_{m,h}}} \quad m = 1, 2, \dots, p \\ W^{(0,s)} &= W^* = n c_{O_1}^* \end{aligned} \right\} \quad (7.55)$$

$$\eta_{p,j} = \frac{F(E_p - E_{c,j}^{\ominus'})}{RT} \quad (7.56)$$

A_G is the electrode area corresponding to G geometry, q_G the characteristic dimension of the electrode, and function $f_G(t_{m,p}, q_G)$ given in Table 2.3 for different

electrode geometries. In the particular case of a two-electron electrochemical reaction ($n = 2$, EE mechanism),



Eq. (7.54) becomes

$$\psi_{\text{DSCVC}}^{\text{EE,G}} = \sqrt{\frac{\bar{D}}{a}} \left\{ \sum_{m=1}^{p-1} Z_m^{\text{EE}} (f_G((p-m+1)\tau, q_G) - f_G((p-m)\tau, q_G)) + Z_p^{\text{EE}} f_G(\tau, q_G) \right\} \quad (7.57)$$

with

$$Z_m^{\text{EE}} = \frac{2\sqrt{K}e^{2\bar{\eta}_{m-1}} + e^{\bar{\eta}_{m-1}}}{\sqrt{K} + e^{\bar{\eta}_{m-1}} + \sqrt{K}e^{2\bar{\eta}_{m-1}}} - \frac{2\sqrt{K}e^{2\bar{\eta}_m} + e^{\bar{\eta}_m}}{\sqrt{K} + e^{\bar{\eta}_m} + \sqrt{K}e^{2\bar{\eta}_m}} \quad (7.58)$$

$$\bar{\eta}_m = \frac{F}{RT} (E_m - \bar{E}_c^{\Theta'}); \quad m = 1, 2, \dots, p \quad (7.59)$$

$$\bar{E}_c^{\Theta'} = \frac{E_{c,1}^{\Theta'} + E_{c,2}^{\Theta'}}{2} \quad (7.60)$$

$$K = \exp\left(\frac{F\Delta E_c^{\Theta'}}{RT}\right) \quad (7.61)$$

$$\Delta E_c^{\Theta'} = E_{c,2}^{\Theta'} - E_{c,1}^{\Theta'} \quad (7.62)$$

DSCVC is much more appropriate and accurate than CV and SCV because it improves the shape and resolution of the peaks. Hence, it is very useful when the peaks in CV or SCV are slightly overlapped. So, in Fig. 7.27 the variation of DSCVC curves with $\Delta E_c^{\Theta'}$ is plotted for an EE mechanism at disc electrodes of different sizes.

When the formal potentials fulfill $\Delta E_c^{\Theta'} < -142.4 \text{ mV}$, the value of the formal potentials can, therefore, be extracted from the average value of the peak potentials of the forward and backward scans

$$\begin{aligned} E_{c,1}^{\Theta'} &= \frac{E_{\text{peak},1}^{\text{forward}} + E_{\text{peak},1}^{\text{backward}}}{2} \\ E_{c,2}^{\Theta'} &= \frac{E_{\text{peak},2}^{\text{forward}} + E_{\text{peak},2}^{\text{backward}}}{2} \end{aligned} \quad (7.63)$$

Evidently, under steady-state conditions, the peak potentials and the formal

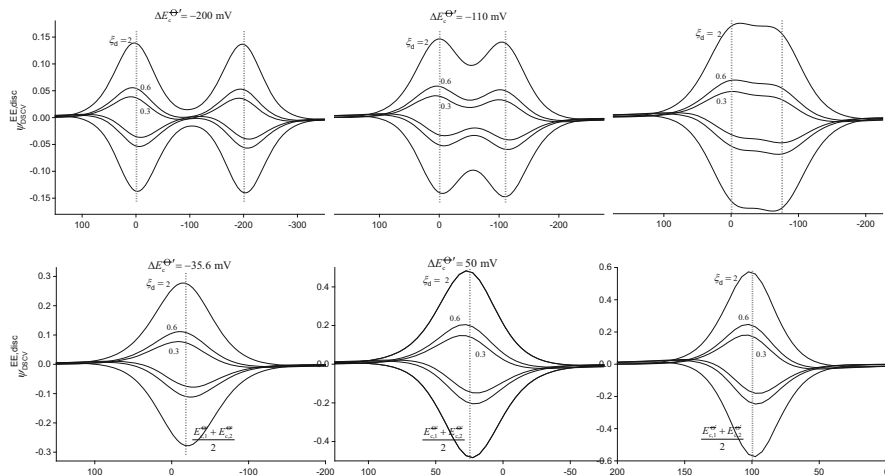


Fig. 7.27 Influence of the difference between the formal potentials ($\Delta E_c^{\Theta'}$ values indicated in the graphs) on the DSCV voltammograms of an EE mechanism at disc microelectrodes of different sizes ($\xi_d (= \sqrt{D/(ar_d^2)})$ values indicated in the graphs). $|\Delta E| = 5$ mV. ψ_{DSCV}^{disc} and a are given by Eqs. (7.10) and (7.11). Reproduced from [48] with permission

potentials coincide, since the DSCVC curve is equivalent to the Differential Double Pulse one [48].

When only one peak is obtained ($\Delta E_c^{\Theta'} > -71.2$ mV), the determination of the formal potentials can be made from the peak current and peak potential. Indeed, the average of the forward and backward peak potentials corresponds to the value of the average formal potential, i.e.,

$$\frac{E_{\text{peak}}^{\text{forward}} + E_{\text{peak}}^{\text{backward}}}{2} = \bar{E}_c^{\Theta'} \quad (7.64)$$

Complementarily, the peak current depends on $\Delta E_c^{\Theta'}$ as can be seen in Fig. 7.28 for the response of the first scan corresponding to discs and spheres.

In Fig. 7.29, explicit Eqs. (6.15), corresponding to Cyclic Staircase Voltammetry (CSCV, Figs. 7.29a, b), and (7.54), corresponding to Differential Cyclic Staircase Voltammetry (DCSCV, Figs. 7.29c, d), have been applied to deduce the response for the four-electron oxidation of bis(1,2-diferrocenyldithiolene)nickel under transient (Fig. 7.29a, c) and stationary (Fig. 7.29b, d) conditions for three different values for the pulse amplitude (ΔE). This complex has four oxidizable ferrocenyl groups and a nickel dithiolene center, so multiple anodic and cathodic processes are possible [53]. In this figure, the four oxidation steps that the neutral species can undergo are considered. As can be observed, the first two steps are well resolved (although they are much better in DCSCV), whereas the third and fourth give rise to overlapped voltammograms.

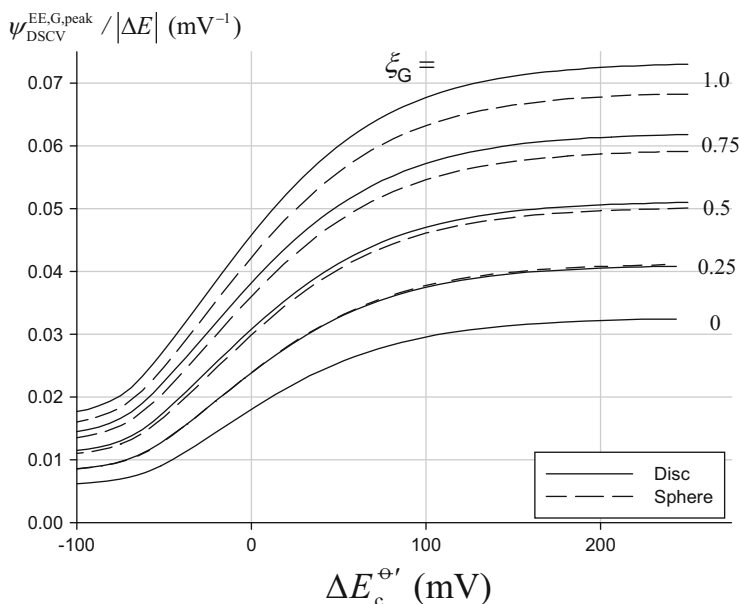


Fig. 7.28 Variation of the current of the forward peak in DSCVC with the $\Delta E_c^{\ominus'}$ value at disc (solid line) and hemispherical (dashed line) microelectrodes of different sizes. The $\xi_G \left(= \sqrt{D/(ar_G^2)} \right)$ values are indicated on the graphs. $|\Delta E| = 0.5 \text{ mV}$. Reproduced from [48] with permission

7.5.1.2 Square Wave Voltammetry

Equation (6.15) is now applied to SWV in order to characterize a two-electron electrochemical reaction. The effects of the difference between the formal potentials, the frequency, the square wave potential, and the staircase potential of the SWV are discussed and procedures for the determination of the formal potentials of both electrochemical reactions are proposed.

When a square wave potential like that depicted in schemes (7.3) and (7.4) is applied to the reaction scheme (7.III) (EE mechanism), the explicit form of the current for any electrode geometry is

$$\begin{aligned} \psi_{SW}^{EE,G} &= \frac{J_{SW}^{EE,G} \sqrt{\tau}}{F A_G c_0^* \sqrt{D}} \\ &= \left\{ \sum_{m=1}^{2p-1} Z_m^{EE} (f_G((2p-m)\tau, \xi_G) - f_G((2p-m+1)\tau, \xi_G)) - Z_{2p}^{EE} f_G(\tau, \xi_G) \right\} \end{aligned} \quad (7.65)$$

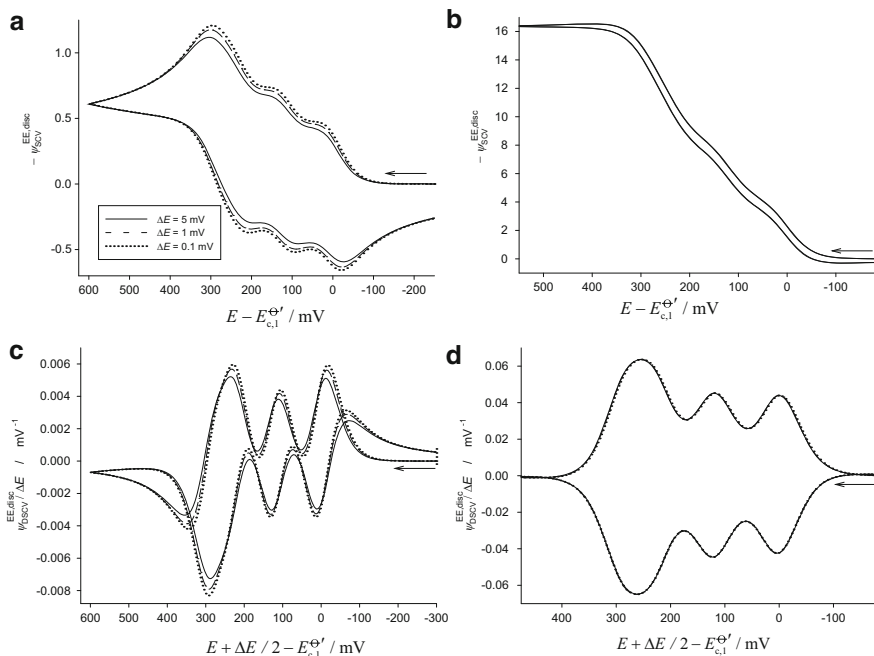


Fig. 7.29 Theoretical voltammograms in staircase cyclic voltammetry (**a** and **b**) and differential staircase voltammetry (**c** and **d**) at disc electrodes for the four-electron oxidation of bis(1,2-diferrocenyldithiolene)nickel in $[\text{NBu}_4][\text{PF}_6]/\text{CH}_2\text{Cl}_2$ solution ($E_{c,2}^{\ominus'} - E_{c,1}^{\ominus'} = 120\text{ mV}$, $E_{c,3}^{\ominus'} - E_{c,1}^{\ominus'} = 230\text{ mV}$, $E_{c,4}^{\ominus'} - E_{c,1}^{\ominus'} = 290\text{ mV}$ [48, 53]). Electrode radius: $r_d = 1\text{ mm}$ (**a** and **c**), and $r_d = 5\text{ }\mu\text{m}$ (**b** and **d**); $\nu = 100\text{ mV s}^{-1}$, $|\Delta E|$ values indicated in the *graphs*

where ξ_G and Z_m^{EE} are given by Eqs. (7.22) and (7.58), respectively, and $f_G(n\tau, \xi_G)$ is given in Table 7.1 for different electrode geometries. In the case of planar electrodes, Eq. (7.65) becomes

$$\psi_{\text{SW}}^{\text{EE, plane}} = \frac{1}{\sqrt{\pi}} \left(\sum_{m=1}^{2p-1} Z_m^{\text{EE}} \left(\frac{1}{\sqrt{2p-m}} - \frac{1}{\sqrt{2p-m+1}} \right) - Z_{2p}^{\text{EE}} \right) \quad (7.66)$$

For spherical electrodes, Eq. (7.65) is transformed into

$$\psi_{\text{SW}}^{\text{EE, sphe}} = \frac{1}{\sqrt{\pi}} \left(\sum_{m=1}^{2p-1} Z_m^{\text{EE}} \left(\frac{1}{\sqrt{2p-m}} - \frac{1}{\sqrt{2p-m+1}} \right) - Z_{2p}^{\text{EE}} (\sqrt{\pi} \xi_s + 1) \right) \quad (7.67)$$

A C++ code to calculate the response of two-electron reversible electrode processes in SWV at disc, (hemi)spherical, and cylindrical electrodes of any radius can be found in Appendix J.

The behavior of the forward, I_f , reverse, I_r , and net, I_{SW} , currents of a two-electron electrochemical reaction with $\Delta E_c^{\Theta'} = -200\text{mV}$ is shown in Fig. 7.30 where a whole square wave cycle with $E_{SW} = 50\text{mV}$ is applied to spherical electrodes of different sizes.

For the reductions, the direct scan is applied in the cathodic direction, so in each square cycle, the forward current is obtained at a more negative potential than the reverse current, and therefore, $I_f^{\text{direct scan}} > I_r^{\text{direct scan}}$. However, for the inverse sweep toward anodic potentials, it is fulfilled that $I_f^{\text{inverse scan}} < I_r^{\text{inverse scan}}$, since the forward currents in each square cycle are now obtained at more positive potentials than with the reverse one (see Scheme 7.4).

As the radius value diminishes, the forward and reverse currents corresponding to different direction sweeps get closer, as can be seen by comparing Fig. 7.30a, b corresponding to electrode radii values of 10^{-3} and 5×10^{-4} cm, respectively. These currents become coincident for small enough radii, i.e., $I_f^{\text{direct scan}} = I_r^{\text{inverse scan}}$ and $I_r^{\text{direct scan}} = I_f^{\text{inverse scan}}$, as occurs in Fig. 7.30c for the minor radius ($r_s = 5 \times 10^{-5}$ cm). This is a proof that the steady state has been reached, something which is impossible to detect at sight if we observe only the $I_{SW}^{\text{EE,G}}$ currents, because they present the same morphology for any radius value, as is shown in the boxes of Fig. 7.30. Thus, $I_{SW}^{\text{EE,G}}$ shows two perfectly defined peaks of the same height for each electronic transfer if $\Delta E_c^{\Theta'} \leq -200\text{mV}$. The positive peaks correspond to the cathodic scan (usually direct scan for reductions), whereas the peaks with negative currents are obtained during the anodic scan.

The currents obtained with the multipulse technique SWV in the steady-state situation, which are shown in the box of Fig. 7.30c, are identical to those obtained with double pulse technique DDPV, whenever $\Delta E_{\text{DDPV}} = 2E_{SW}$ (i.e., when $E_1(\text{DDPV}) = E_f(\text{SW})$ and $E_2(\text{DDPV}) = E_r(\text{SW})$) [46, 49], so the currents obtained with SWV in microelectrodes have the same characteristic as those shown for this double pulse technique.

The effect of frequency on the SWV voltammograms of a two-electron electrochemical reaction is shown in Fig. 7.31 for different $\Delta E_c^{\Theta'}$ values at $T = 298\text{K}$. The responses for disc (solid line) and (hemi)spherical (dashed line) microelectrodes calculated from Eq. (7.65) are considered.

When the formal potential of the first step is much more positive than that of the second, $\Delta E_c^{\Theta'} < -200\text{mV}$ (Fig. 7.31c), the intermediate species O_2 is stable and two well-separated peaks are obtained, centered on the formal potential of each process and with the features of the voltammograms of one-electron electrochemical reaction. When the $\Delta E_c^{\Theta'}$ value increases, the stability of the intermediate decreases and the two peaks are closer, and the transition from two peaks to a single peak is observed ($\Delta E_c^{\Theta'} \approx -71.2\text{mV}$). Eventually, when the formal potential of the second electron transfer is much more positive than that of the first one, $\Delta E_c^{\Theta'} > 200\text{mV}$, the characteristics of the voltammograms are those of an apparently simultaneous two-electron electrochemical reaction (Fig. 7.31a). Note that the

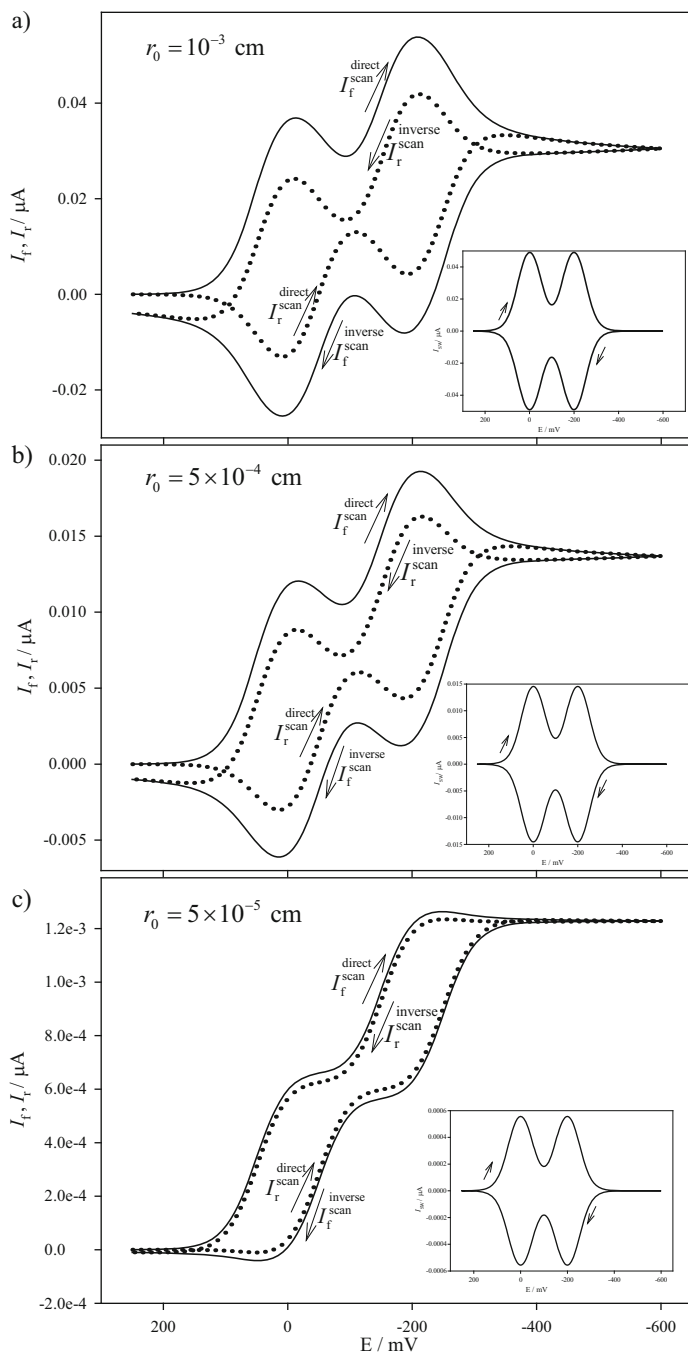


Fig. 7.30 Comparison between $I_f^{\text{EE,G}}$ (solid lines) and $I_r^{\text{EE,G}}$ (dotted lines) currents for a cyclic square wave scan in spherical electrodes of radius (a) $r_s = 10^{-3}$ cm, (b) $r_s = 5 \times 10^{-4}$ cm, and in a

resolution and symmetry of the peaks in SWV (as well as other differential pulse techniques) are better than in linear sweep voltammetry. In addition, SWV offers further reduction of double-layer charging and background currents, which enables more precise quantitative analysis of experimental data.

In any case, the position and width of the peaks are not affected by the value of the frequency or by the geometry of the electrode (see embedded graphs in Fig. 7.31) since the potential and the time-geometrical dependences of the response can be separated. On the other hand, the peak height is affected in the usual way, such that the higher the frequency, the higher the peak.

Regarding the discrepancies between disc and spherical electrodes, these are more evident as the frequency decreases (i.e., longer potential pulses) and so the differences in the diffusion domains are more apparent.

With respect to the peak potentials, their value are independent of all the technique parameters (including the pulse amplitude) and it is corroborated that it coincides with the peak potential in Differential Double Pulse Voltammetry (DDPV) and Differential Multipulse Voltammetry (DMPV). So, by imposing the condition $d\psi_{\text{SWV}}^G/dE = 0$ in Eq. (7.65), the three following roots are obtained in terms of K [49]:

$$\left. \begin{aligned} E_{\text{I}} &= \bar{E}_{\text{c}}^{\Theta'} \quad \text{any value of } K \quad \text{(a)} \\ E_{\text{II}} &= E_{\text{c},1}^{\Theta'} + \frac{RT}{F} \ln \left(-\frac{2K - \sqrt{f_2(K)} - B\sqrt{f_1(K)} + 2B^2K}{2B} \right) \quad \text{(b)} \\ E_{\text{III}} &= E_{\text{c},1}^{\Theta'} + \frac{RT}{F} \ln \left(-\frac{2K + \sqrt{f_2(K)} - B\sqrt{f_1(K)} + 2B^2K}{2B} \right) \quad \text{(c)} \end{aligned} \right\} \begin{aligned} &K < ca. 0.06 \\ &(\Delta E_{\text{c}}^{\Theta'} < ca. -71.2 \text{ mV}) \\ &\text{for } E_{\text{SW}} < 50 \text{ mV} \end{aligned} \quad (7.68)$$

with K given in Eq. (7.61) and

$$f_1(K) = \frac{(4K - 1)(K - B^2 + 2B^2K + B^4K)}{B^2} \quad (7.69)$$

$$\begin{aligned} f_2(K) &= B^2 - K + 8K^2 + 16B^2K^2 + 8B^4K^2 - 10B^2K - B^4K \\ &\quad - 4BK\sqrt{f_1(K)} - 4B^3K\sqrt{f_1(K)} \end{aligned} \quad (7.70)$$



Fig. 7.30 (continued) microelectrode (c) $r_s = 5 \times 10^{-5}$ cm, for $\Delta E_{\text{c}}^{\Theta'} = -200$ mV. The corresponding net currents, $j_{\text{SW}}^{\text{EE,sph}}$, are also shown in boxes. $\Delta E_s = 5$ mV, $E_{\text{SW}} = 50$ mV, $\tau = 0.0025$ s, $c_{\text{O}_1}^* = 1$ mM, $D = 10^{-5}$ cm²s⁻¹, $T = 298$ K. Reproduced from [46] with permission

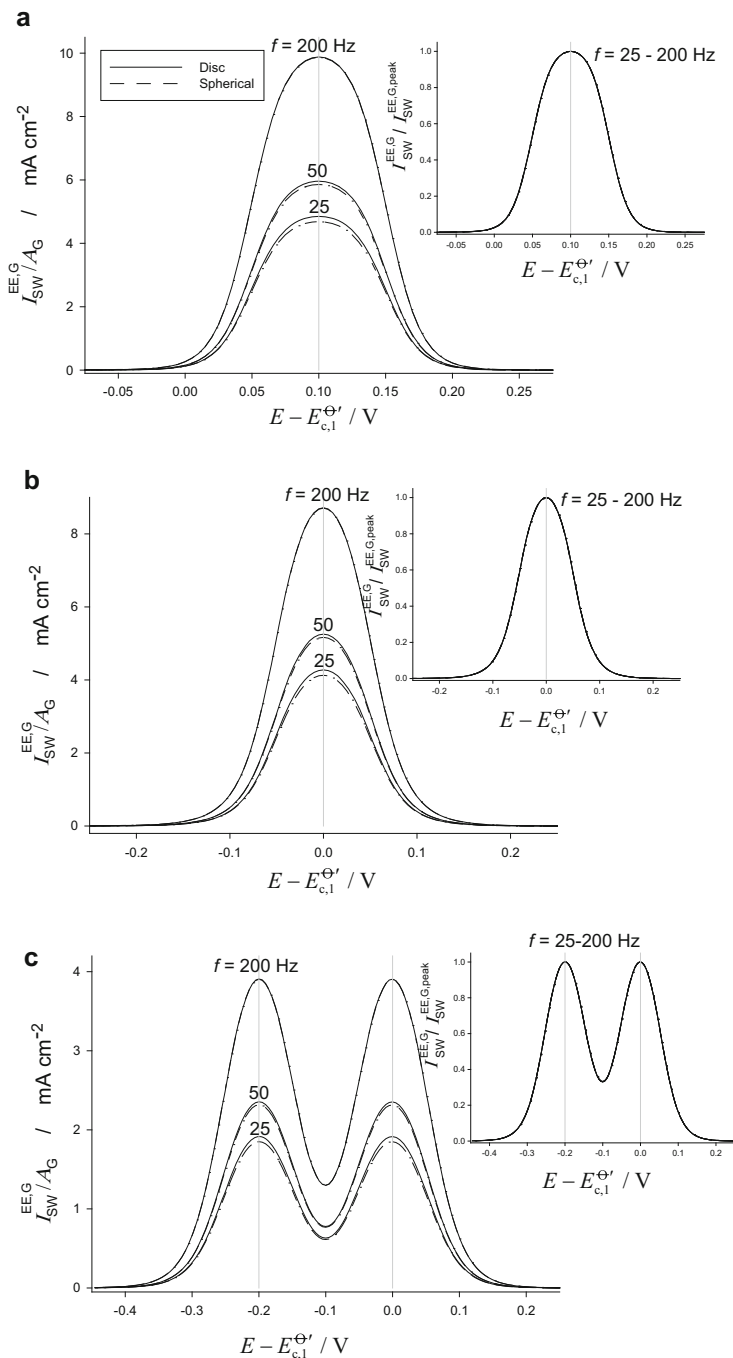


Fig. 7.31 Influence of frequency on the peak height of square wave voltammograms of a two-electron electrochemical reaction at disc (solid line) and (hemispherical) (dashed line)

$$B = \exp\left(\frac{F}{RT}|E_{\text{SW}}|\right) \quad (7.71)$$

The first root (E_I) is valid for any $\Delta E_c^{\Theta'}$ value and corresponds to the average value of the formal potentials:

$$E_I = \bar{E}_c^{\Theta'} = \frac{E_{c,1}^{\Theta'} + E_{c,2}^{\Theta'}}{2} \quad (7.72)$$

Independently of the $\Delta \bar{E}_c^{\Theta'}$ value, the SWV voltammograms are symmetrical with respect to the $\bar{E}_c^{\Theta'}$ value (see Fig. 7.31), which corresponds to the minimum of the valley between peaks for very negative values of $\Delta E_c^{\Theta'}$, and to the peak potential for $\Delta E_c^{\Theta'} \geq -71.2$ mV. This behavior is independent of the electrode size and geometry and of the pulse durations. The roots E_{II} and E_{III} correspond to the peak potentials of separate signals (i.e., to $E_{c,1}^{\Theta'}$ and $E_{c,2}^{\Theta'}$) when $\Delta E_c^{\Theta'} < -142.4$ mV.

As in the case of a reversible one-electron electrochemical reaction, the half-peak width of the SWV does not depend on the electrode geometry. For a two-electron electrochemical reaction, $W_{1/2}$ is only a function of the difference between formal potentials $\Delta E_c^{\Theta'}$ and of the square wave amplitude E_{SW} . The evolution of the half-peak width $W_{1/2}$ with $\Delta E_c^{\Theta'}$ at both disc and (hemi)spherical electrodes has been plotted in Fig. 7.32. These curves give a very general criterion for the characterization of the EE process through $W_{1/2}$.

The half-peak width takes a constant value when two separate peaks are obtained, which corresponds to the width of mono-electronic transfers: $W_{1/2}^{1e^-}(E_{\text{SW}} \rightarrow 0) \rightarrow 90$ mV. For $\Delta E_c^{\Theta'} > -142.4$ mV, two unresolved peaks or a single peak are obtained, and $W_{1/2}$ decreases with $\Delta E_c^{\Theta'}$ until it reaches the value corresponding to two-electron transfer reactions: $W_{1/2}^{2e^-}(E_{\text{SW}} \rightarrow 0) \rightarrow 45$ mV. The sharp change of $W_{1/2}$ corresponds to the $\Delta E_c^{\Theta'}$ value where the height of the central valley between peaks coincides with the half-peak height (≈ -142 mV for $E_{\text{SW}} \rightarrow 0$).

The influence of E_{SW} on the CSWV curves corresponding to quinizarin and pyrazine systems on a static mercury electrode can be seen in Fig. 7.33. The square wave amplitude has been changed in the range 10–450 mV and the voltammograms show that, in general, the net current, $I_{\text{SW}}^{\text{EE,sph}}$, increases with E_{SW} .

The experimental cyclic square wave voltammograms in Fig. 7.33a show two well-defined peaks at small values of E_{SW} ($E_{\text{SW}} < |\Delta E_c^{\Theta'}|/2$) and a broad valley between them, with their positions being independent of E_{SW} (compare curves

Fig. 7.31 (continued) electrodes calculated from Eq. (7.65). Three different $\Delta E_c^{\Theta'} (= E_{c,2}^{\Theta'} - E_{c,1}^{\Theta'})$ values are considered: (a) 200 mV, (b) 0 mV, and (c) -200 mV. The curves normalized with respect to the peak current are also shown in the inserted graphs. $r_G = 10 \mu\text{m}$, $E_{\text{SW}} = 50$ mV, $\Delta E_s = 5$ mV, $T = 298.15$ K, $D = 10^{-5} \text{cm}^2 \text{s}^{-1}$, $c_{O_1}^* = 1 \text{mM}$

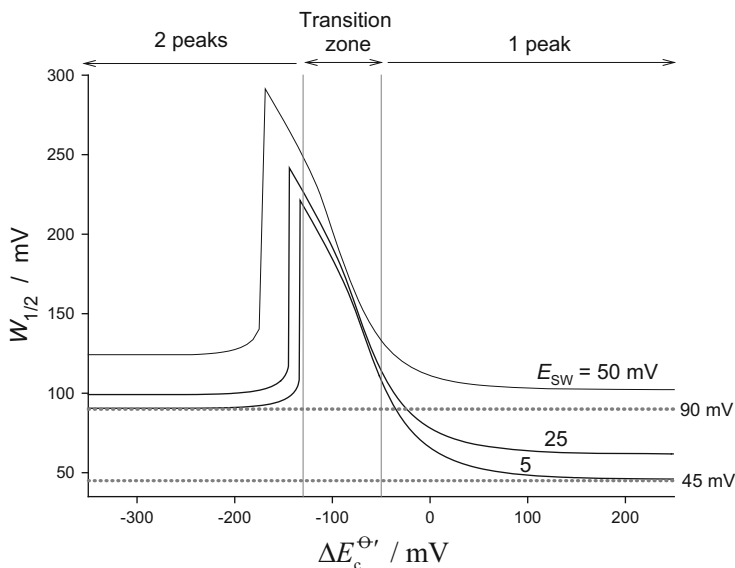


Fig. 7.32 Evolution of the SWV half-peak width, $W_{1/2}$, with $\Delta\bar{E}_c^{\Theta'}$, corresponding to a reversible two-electron electrochemical reaction at disc and (hemi)spherical electrodes for three E_{SW} values (indicated on the curves). $T = 298.15$ K. No significant effect of the value of the step potential on the peak width is found in the range $\Delta E_s = 2 - 10$ mV. Reproduced from [49] with permission

for $E_{SW} = 10, 25, 50$, and 100 mV). Under these experimental conditions, both peaks are located at the formal potential values of each charge transfer reaction obtaining, respectively, $E_{c,1}^{\Theta'} = -825 \pm 1$ mV and $E_{c,2}^{\Theta'} = -1333 \pm 1$ mV, such that $\Delta E_c^{\Theta'} = -505 \pm 2$ mV, whereas according to Eq. (7.68), the valleys are centered at the average of formal potentials, $\bar{E}_c^{\Theta'} = (E_{c,1}^{\Theta'} + E_{c,2}^{\Theta'})/2 = -1079 \pm 1$ mV.

Both peaks in the curve obtained at $E_{SW} = 10$ mV have a half-peak width of $W_{1/2} = 90$ mV, whereas for higher values of E_{SW} the peaks become wider and less defined, reaching the value $W_{1/2} = 2E_{SW}$ for each of the peaks at curves corresponding to $E_{SW} = 100$ and 200 mV. These peaks are already clearly transformed into two plateaus for $E_{SW} = 200$ mV, which merge into a whole plateau for $E_{SW} \approx |\Delta E_c^{\Theta'}|/2$ (see curve with $E_{SW} = 250$ mV in Fig. 7.33a) with height $I_{SW}^{EE, \text{sph}, \text{plateau}}(E_{SW} = 250 \text{ mV}) = 27 \pm 1 \mu\text{A}$.

If E_{SW} increases over $|\Delta E_c^{\Theta'}|/2$ a new and single peak appears which, as in the case of the valley observed at lower E_{SW} , is centered at $\bar{E}_c^{\Theta'}$. The height and width of this peak grow while E_{SW} continues to increase, until for $E_{SW} \approx |\Delta E_c^{\Theta'}|$ a new plateau appears, whose height does not vary now for higher E_{SW} values

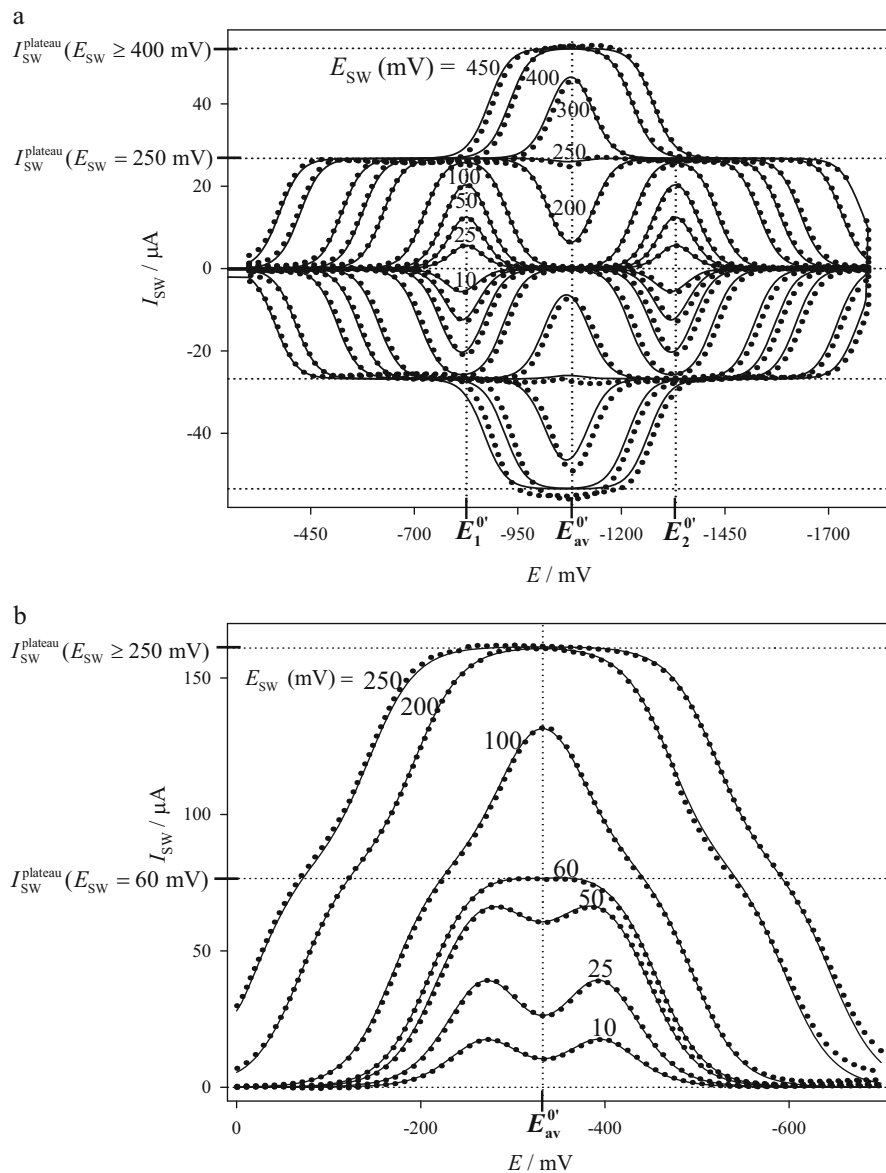


Fig. 7.33 Influence of the square wave amplitude, E_{SW} , on the experimental $J_{SW}^{\text{EE,sphe}} - E$ curves (dotted lines), and comparison with the corresponding theoretical ones (solid lines, Eq. (7.65)), obtained for systems (a) quinizarin 0.75 mM + TBAP 0.1 M in acetonitrile, $E_{c,1}^{\ominus'} = -825 \text{ mV}$, $\Delta E_c^{\ominus'} = -505 \text{ mV}$, $D = 2.5 \times 10^{-5} \text{ cm}^2 \text{ s}^{-1}$, $r_s = 0.029 \text{ cm}$ and (b) pyrazine 2.0 mM at pH = 0.4 in $\text{HClO}_4 + \text{NaClO}_4$ adjusted to ionic strength 1.0 M at a SMDE, $E_{c,1}^{\ominus'} = -269 \text{ mV}$, $\Delta E_c^{\ominus'} = -126 \text{ mV}$, $D = 0.75 \times 10^{-5} \text{ cm}^2 \text{ s}^{-1}$, $r_s = 0.042 \text{ cm}$. $\Delta E_s = 5 \text{ mV}$, $\tau = 0.010 \text{ s}$, $T = 293 \text{ K}$. The values of E_{SW} , in mV, are given on the curves. Reproduced from [46] with permission

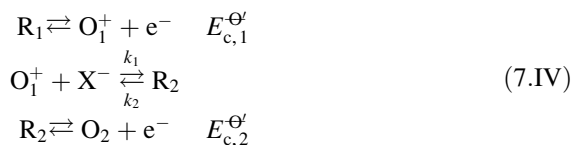
($E_{SW} \geq 400$ mV), and reaches the highest current value of $I_{SW}^{EE, \text{sph}, \text{plateau}}(E_{SW} \geq 400 \text{ mV}) = 54 \pm 1 \mu\text{A}$.

It is possible to calculate the diffusion coefficient from both plateau current values since the current at the higher plateau is in fact twice that of the lower one, according to Eq. (7.29) with two or one electrons, respectively. Hence, the value $D = (2.5 \pm 0.1) \times 10^{-5} \text{ cm}^2 \text{ s}^{-1}$ has been obtained.

For the pyrazine system plotted in Fig. 7.33b, it is possible to get an intermediate plateau, as is shown on the curve at $E_{SW} = 60$ mV with $I_{SW}^{EE, \text{sph}, \text{plateau}}(E_{SW} = 60 \text{ mV}) = 77 \pm 1 \mu\text{A}$, which transforms into a single peak centered at $\bar{E}_c^{\Theta} = -333 \pm 1$ mV (see curve at 100 mV), and turns into a new and higher plateau for $E_{SW} > \Delta E_c^{\Theta}$, reaching a current double that is obtained in the first plateau, $I_{SW}^{EE, \text{sph}, \text{plateau}}(E_{SW} \geq 200 \text{ mV}) = 161 \pm 1 \mu\text{A}$ (see curves with $E_{SW} = 200$ and 250 mV of Fig. 7.33b). From this value and Eq. (7.29) for two electrons, the diffusion coefficient value $D = (0.75 \pm 0.01) \times 10^{-5} \text{ cm}^2 \text{ s}^{-1}$ has been obtained.

The theoretical SWV curves shown in Fig. 7.33b (solid lines) have been calculated with the values obtained for D and \bar{E}_c^{Θ} , and by selecting the value $\Delta E_c^{\Theta} = -126$ mV with which the best adjustment between theoretical and experimental curves is obtained. So, by combining the values of \bar{E}_c^{Θ} and ΔE_c^{Θ} the following individual formal potentials have been deduced: $E_{c,1}^{\Theta} = -269 \pm 1$ mV and $E_{c,2}^{\Theta} = -395 \pm 1$ mV [46].

There is a special case of the EE mechanism in which the reversible electrode reactions are coupled to a very fast chemical reaction such that the chemical equilibrium is quickly reestablished at the electrode surface in line with the following reaction scheme [51]:



Under these conditions, the SWV curves of the EE mechanism depend on ΔE_c^{Θ} and on the chemical equilibrium constant, $K_{\text{eq}} = c_{\text{R}_2}/c_{\text{O}_1^+}$, since the concentration of X^- is in a great excess. Thus, for example, for $\Delta E_c^{\Theta} = 0$ mV, the responses are split if $K_{\text{eq}} > 100$ or $K_{\text{eq}} < 0.01$. This behavior is shown in Fig. 7.34 [51].

7.5.2 Non-reversible Electrochemical Reactions

In this case, the reaction scheme can be written

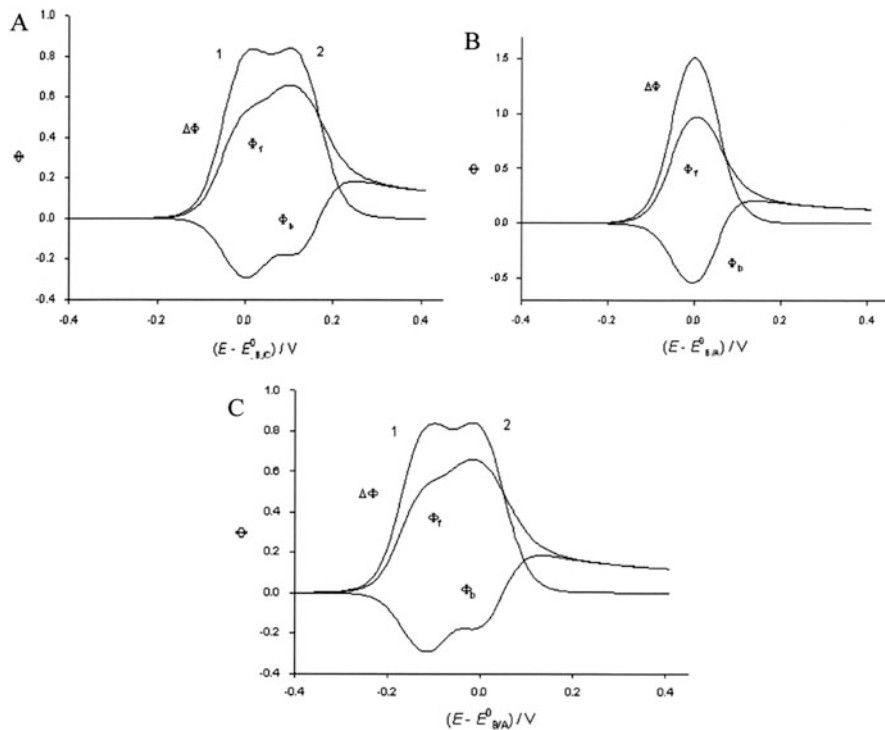
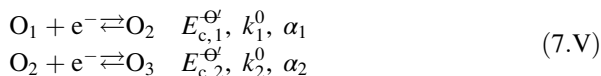


Fig. 7.34 Theoretical SWV curves for a reversible EE mechanism coupled to a very fast chemical reaction. $\Delta E_c^{\Theta} = 0$ mV, $E_{SW} = 50$ mV, $\Delta E_s = 5$ mV. The values of the chemical equilibrium constant K_{ceq} are 0.01 (a), 1 (b), and 100 (c). The dimensionless net current ($\Delta\Phi$) and their forward (Φ_f) and reverse (Φ_b) components are shown. Reproduced from [51] with permission



If linear diffusion is considered and the influence of comproportionation/disproportionation reactions is neglected, the solution for the response of this process in SWV is given as a system of recursive formulae by Lovrić [54] using the numerical integration method proposed by Oldmstead and Nicholson [26].

As stated in Sects. 3.3.3 and 6.2.1.1.4 in this case, the response depends not only on the difference between the formal potentials of the two steps but also on the dimensionless rate constants $\kappa_{plane,i}^0 = k_i^0 \sqrt{\tau/D}$ ($i=1, 2$). As an example, in Fig. 7.35 two SWV responses are shown. In both cases, the value of $\Delta E_c^{\Theta} = 100$ mV means that the intermediate species O_2 is thermodynamically unstable (i.e., $c_{O_2}/(c_{O_1} + c_{O_2} + c_{O_3}) = 0.01$ at the average potential \bar{E}_c^{Θ} , see Sect. 3.3.1). The SWV curve in solid line corresponds to a first reversible step ($\kappa_{plane,1}^0 = 100$) followed by a second quasi-reversible step ($\kappa_{plane,2}^0 = 0.1$). The net current presents a single peak

Fig. 7.35 Theoretical forward (Φ_f), reverse (Φ_r), and net ($-\Delta\Phi$) SWV curves for a quasi-reversible EE mechanism.

$$\Delta E_c^{\Theta'} = 100 \text{ mV},$$

$$\alpha_1 = \alpha_2 = 0.5,$$

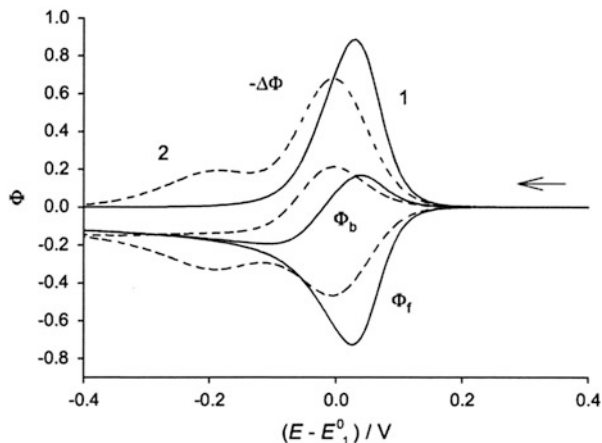
$$\left(\kappa_{\text{plane},2}^0 / \kappa_{\text{plane},1}^0 \right) = 10^{-3},$$

$$E_{\text{SW}} = 50 \text{ mV},$$

$$\Delta E_s = 5 \text{ mV}. \text{ The values of}$$

$\kappa_{\text{plane},2}^0$ are 0.1 (solid line) and 0.001 (dashed line).

Reproduced from [54] with permission



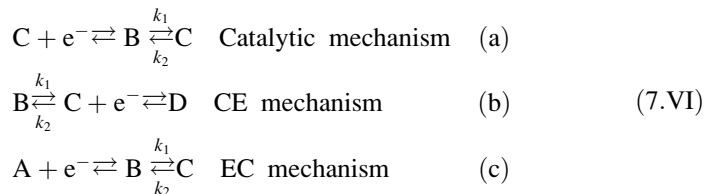
located at 30 mV from $E_{c,1}^{\Theta'}$. The SWV curve in dashed line considers a first quasi-reversible step ($\kappa_{\text{plane},1}^0 = 1$) followed by a fully irreversible one ($\kappa_{\text{plane},2}^0 = 0.001$). In this situation, the net current shows two peaks located at -5 and -185 mV. The appearance of the second peak at more negative potentials is caused by the kinetic stabilization of the intermediate species, i.e., species O_2 needs a significant negative potential to be reduced to species O_3 . So, since the values of the dimensionless rate constants depend on the frequency (or the pulse time length), the response of a quasi-reversible two-electron electrochemical reaction may exhibit one peak at lower frequencies and two peaks at higher frequencies [54].

A detailed study of the different kinetic situations that may arise and of the dependence of the peak parameters on the rate constants of the two steps can be found in [6, 19, 50, 52].

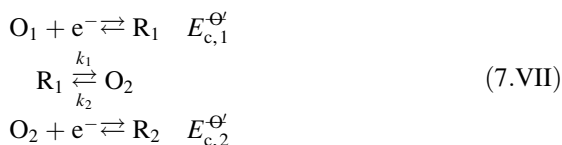
7.6 First-Order Chemical Reactions Coupled to the Charge Transfer Reaction

Electrode processes coupled with homogeneous chemical reactions are very frequent and their study is of interest in many applied fields, such as organic electrosynthesis, ecotoxicity, biosciences, and environmental studies, among others [1–3, 6, 12, 19, 55]. In this section, only the differential multipulse technique SWV is applied to the study of the reaction kinetics and mechanisms of electrogenerated species.

Of the wide range of this type of processes, this study focuses mainly on three first- or pseudo-first-order reaction mechanisms (see reaction scheme (7.VI)): catalytic, CE, and EC processes which are the most analyzed in the Electrochemistry literature.



The ECE mechanism is also analyzed



for which, as in the case of two-electron electrochemical reactions (EE mechanism), the following reaction may occur:



7.6.1 Catalytic Mechanism

As discussed in previous chapters (see Sects. 3.4.1, 4.5.1 and 6.3.1), of the processes with first- or pseudo-first-order homogeneous reactions coupled to the charge transfer, the catalytic mechanism is the simplest to study. The solution corresponding to SWV corresponding to planar, spherical, and disc electrodes will be discussed.

7.6.1.1 Square Wave Voltammetry

From the general expressions for the catalytic current corresponding to any sequence of potential pulses (given by Eq. (6.64)), the following explicit SWV response can be easily deduced for electrodes of different geometry:

$$\begin{aligned}
 \psi_{\text{SW}}^{\text{cat,G}} &= \frac{I_{\text{SW}}^{\text{cat,G}} \sqrt{\tau} (1 + K)}{FA_G \sqrt{D} \zeta^*} \\
 &= -Z_{2p}^{\text{cat}} f_G^{\text{cat}}(\chi^{\text{SW}}, \xi_G) \\
 &\quad + \sum_{m=1}^{2p-1} (Z_m^{\text{cat}} [f_G^{\text{cat}}(\chi_{m,2p-1}, \xi_G) - f_G^{\text{cat}}(\chi_{m,2p}, \xi_G)])
 \end{aligned} \tag{7.73}$$

where

$$\chi_{m,j} = (j - m + 1) \chi^{\text{SW}} \tag{7.74}$$

$$\chi^{\text{SW}} = (k_1 + k_2) \tau \tag{7.75}$$

$$Z_m^{\text{cat}} = \begin{cases} \frac{1 - Ke^{\eta_1}}{1 + e^{\eta_1}} & m = 1 \\ (1 + K) \left(\frac{1}{1 + e^{\eta_m}} - \frac{1}{1 + e^{\eta_{m-1}}} \right) & m > 1 \end{cases} \tag{7.76}$$

$$K = \frac{c_B^*}{c_C^*} = \frac{1}{K_{\text{eq}}} \tag{7.77}$$

ξ_G is given by Eq. (7.22). Functions $f_G^{\text{cat}}(\chi_{m,p}, \xi_G)$ are given in Table 7.3 for planar, spherical, and disc electrodes. Note that these functions are dimensionless. q_G is the characteristic dimension of the electrode of geometry G (i.e., $q_G = r_s$ for spherical electrodes and $q_G = r_d$ for disc ones).

In Fig. 7.36, the SWV curves of a first-order catalytic mechanism for different values of the dimensionless kinetic constant χ^{SW} ($= (k_1 + k_2) \tau$) at disc electrodes are shown. For $\chi^{\text{SW}} > 1.5$, a time-independent current is reached whatever the shape and size of the electrode. In order to determine the transient or stationary nature of the SWV current, the forward (ψ_f) and reverse (ψ_r) components of the response must be analyzed, since the net current is bell shaped in all the cases.

Figure 7.36a–c shows the forward and reverse components of the square wave current. When the chemical kinetics is fast enough to achieve kinetic steady-state conditions ($\chi^{\text{SW}} \geq 1.5$ and $k_1 + k_2 \gg (D/r_d^2)$, see [58, 59]), the forward and reverse responses at discs are sigmoidal in shape and are separated by $2E_{\text{SW}}$. This behavior is independent of the electrode geometry and can also be found for spheres and even for planar electrodes. It is likewise observed for a reversible single charge transfer at microdiscs and microspheres, or for the catalytic mechanism when $r_d \ll \sqrt{D/(k_1 + k_2)}$ (microgeometrical steady state) [59, 60].

Faster attainment of steady-state conditions is also fostered by the use of smaller electrodes, as can be concluded by comparing Fig. 7.36a–c, such that for the smallest radius considered (Fig. 7.36c, $r_d = 1 \mu\text{m}$), both $\psi_f^{\text{cat,disc}} - (E_{\text{index}} - E_c^{\text{O}^{\ominus}})$ and $\psi_r^{\text{cat,disc}} - (E_{\text{index}} - E_c^{\text{O}^{\ominus}})$ curves correspond to the stationary response even for the lowest χ^{SW} value. Moreover, in all the cases the peak potential of the SWV net

Table 7.3 Expressions for function $f_G^{\text{cat}}(\chi_{m,p}, \xi_G)$ for planar, spherical, and disc electrodes [56–60]

Electrode	$f_G^{\text{cat}}(\chi_{m,p}, \xi_G), \xi_G = \sqrt{D\tau}/q_G$
Planar	$\sqrt{\chi^{\text{SW}}} \left[\frac{e^{-\chi_{m,p}}}{\sqrt{\pi\chi_{m,p}}} + \text{erf}(\sqrt{\chi_{m,p}}) \right]$
Sphere	$\xi_s + \sqrt{\chi^{\text{SW}}} \left[\frac{e^{-\chi_{m,p}}}{\sqrt{\pi\chi_{m,p}}} + \text{erf}(\sqrt{\chi_{m,p}}) \right], \xi_s = \frac{\sqrt{D\tau}}{r_s}$
Disc	$\xi_d + \sqrt{\chi^{\text{SW}}} \left[\text{erf}(\sqrt{\chi_{m,p}}) + 0.2732 \frac{\sqrt{\chi_{m,p}}}{\xi_d} \int_0^{(\xi_d)^2} \exp\left[-\frac{0.39115}{\sqrt{u}} - \frac{\chi_{m,p}}{u}\right] du + e^{-\chi_{m,p}} \left[0.2732 \frac{\xi_d}{\sqrt{\chi_{m,p}}} \exp\left(-\frac{0.39115}{\xi_d}\right) + \frac{1}{\sqrt{\pi\chi_{m,p}}} \right] \right], \xi_d = \frac{\sqrt{D\tau}}{r_d}$

$G=d$ for discs and s for spheres or hemispheres. Note that functions $f_G^{\text{cat}}(\chi_{m,p}, \xi_G)$ are dimensionless

curves in Fig. 7.36d–f corresponds to the formal potential of the charge transfer process, $E_{\text{peak}} = E_c^{\Theta'}$, with this behavior being characteristic of the catalytic mechanism and of reversible charge transfer processes.

Concerning the half-peak width ($W_{1/2}$), as can be deduced from Fig. 7.36, its value is independent of the electrode radius and the catalytic rate constants. The dependence of $W_{1/2}$ on the square wave amplitude is identical to that obtained for a simple charge transfer given by Eq. (7.32) (see also Fig. 7.8), i.e., it increases with E_{SW} from $W_{1/2} = 90\text{mV}$ for $E_{\text{SW}} \leq 10\text{mV}$ to $W_{1/2} = 2E_{\text{SW}}$ for $E_{\text{SW}} > 100\text{mV}$.

The peak height of the SWV net current increases in all the cases with the square wave amplitude until it reaches a constant value (plateau) for $E_{\text{SW}} \geq 100\text{mV}$. This value depends on the electrode shape and size and also on the catalytic rate constants. Under steady-state conditions, the plateau current at microspheres and microdiscs is given by

$$I_{\text{SW}}^{\text{cat, sphe, ss, plateau}} = I_{\text{d,c}}^{\text{sphe, ss}} \left(1 + \frac{\sqrt{\chi^{\text{SW}}}}{\xi_s} \right) = I_{\text{d,c}}^{\text{sphe, ss}} \left(1 + r_s \sqrt{\frac{k_1 + k_2}{D}} \right) \quad (7.78)$$

$$I_{\text{SW}}^{\text{cat, disc, ss, plateau}} = I_{\text{d,c}}^{\text{disc, ss}} \left(1 + \frac{\sqrt{\chi^{\text{SW}}}}{\xi_d} \right) f_{\text{disc}}^{\text{cat, ss}}(\chi^{\text{SW}}, \xi_d) \quad (7.79)$$

with [56, 57, 59]

$$f_{\text{disc}}^{\text{cat, ss}}(\chi^{\text{SW}}, \xi_d) = 1 + \frac{\sqrt{\chi^{\text{SW}}}}{\xi_d} + 0.5465 \frac{\sqrt{\chi^{\text{SW}}}}{\xi_d} \int_0^\infty u \exp\left(-\frac{0.39115}{\sqrt{u}} - \frac{\sqrt{\chi^{\text{SW}}}}{\xi_d} u^2\right) du \quad (7.80)$$

and $I_{\text{d,c}}^{\text{sphe, ss}} = 4\pi Fr_s Dc_O^*$ and $I_{\text{d,c}}^{\text{disc, ss}} = 4Fr_d Dc_O^*$.

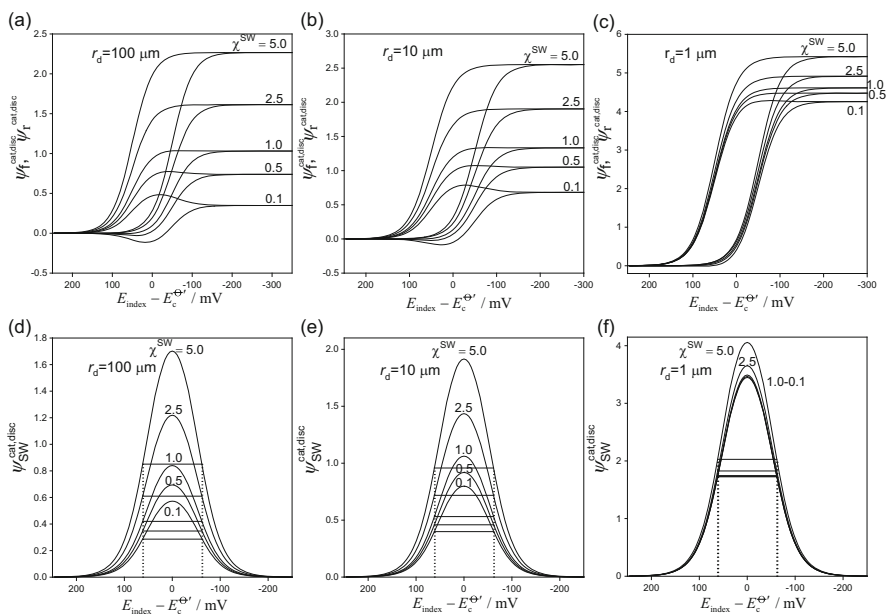
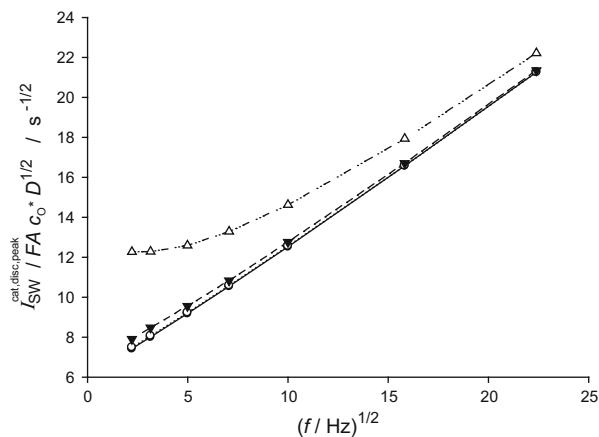


Fig. 7.36 Effect of the electrode radius and the kinetics of the catalytic reaction on the forward (ψ_f), reverse (ψ_r), and net ($\psi_{SW}^{\text{cat,disc}}$) responses in SWV calculated from Eq. (7.73) for a disc electrode. $E_{SW} = 50\text{ mV}$, $\Delta E_s = 5\text{ mV}$, $\tau = 10\text{ ms}$ ($f = 50\text{ Hz}$), $K = 0$, $T = 298.15\text{ K}$, and $D = 10^{-5}\text{ cm}^2\text{ s}^{-1}$. The values of the electrode radius r_d and χ^{SW} are indicated on the graphs. Dotted lines mark the potential values where $\psi_{SWV} = \psi_{SWV,\text{peak}}/2$. Reproduced from [60] with permission

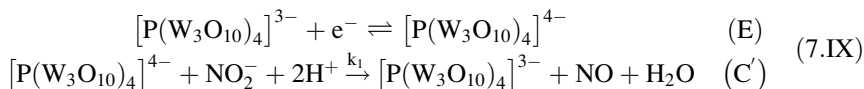
The evolution of the peak current ($I_{SW}^{\text{cat,disc,peak}}$) with frequency (f) is plotted in Fig. 7.37 for the first-order catalytic mechanism with different homogeneous rate constants at microdisc electrodes. For a simple reversible charge transfer process, it is well known that the peak current in SWV scales linearly with the square root of the frequency at a planar electrode [6, 17]. For disc microelectrodes, analogous linear relationships between the peak current and the square root of frequency are found for a reversible electrode reaction (see Fig. 7.37 for the smallest k_1 value).

The variation of the peak current in the presence of a coupled catalytic reaction differs from the above behavior due to the catalytic contribution. Thus, as the chemical rate constant increases and the frequency decreases, that is, as the catalytic component becomes more apparent, there is a deviation from the linear increase of $I_{SW}^{\text{cat,disc,peak}}$ with $f^{1/2}$. This deviation is only significant for $k_1 > 10\text{ s}^{-1}$. When steady-state conditions are achieved (very small frequencies and/or large kinetic constants), the peak current becomes independent of the frequency, as shown in Fig. 7.37 for $k_1 = 100\text{ s}^{-1}$ and $f^{1/2} < 5\text{ s}^{-1/2}$.

Fig. 7.37 Influence of the frequency on the peak current of the SWV curves of a catalytic mechanism at disc electrodes, calculated from Eq. (7.73) with $r_d = 5 \mu\text{m}$. The values of k_1 (in s^{-1}) are 0.1 (black circles), 1 (white circles), 10 (black triangles), and 100 (white triangles). $E_{\text{SW}} = 50 \text{ mV}$, $\Delta E_s = 5 \text{ mV}$, $K = 0$, $T = 298.15 \text{ K}$, and $D = 10^{-5} \text{ cm}^2 \text{ s}^{-1}$. Reproduced from [60] with permission



In Fig. 7.38, the experimental SWV curves are plotted after blank subtraction corresponding to the reduction of the heteropolyanion $[\text{P}(\text{W}_3\text{O}_{10})_4]^{3-}$ in the absence and presence of the nitrite anion NO_2^- at a disc gold microelectrode ($r_d = 15.1 \mu\text{m}$) in sulfuric medium. Under these conditions, the following reaction corresponding to a first-order catalytic mechanism takes place [60, 61]:



The SWV experiments have been carried out with $f = 10 \text{ Hz}$, $E_{\text{SW}} = 25 \text{ mV}$ and $\Delta E_s = 5 \text{ mV}$, with a concentration of nitrite in large excess with respect to the heteropolyanion concentration to ensure pseudo-first-order conditions for the kinetics. The potential region scanned was from 200 to -200 mV (vs. SCE), where the first reduction of $[\text{P}(\text{W}_3\text{O}_{10})_4]^{3-}$ occurs. As can be observed, the peak current increases with $c_{\text{NO}_2^-}^*$, which indicates the incidence of the catalytic reaction that regenerates the oxidized species $[\text{P}(\text{W}_3\text{O}_{10})_4]^{3-}$ and so the signal increases. From the value of the peak potential, the formal potential is immediately extracted: $E_c^{\Theta} = -49 \pm 3 \text{ mV}$ vs. SCE. From the value of the peak currents, the value of the homogeneous rate constant was determined from Eq. (7.73) for the different concentrations of nitrite, obtaining the following mean value after three different experimental measurements: $k_1 = 1860 \pm 60 \text{ M}^{-1} \text{ s}^{-1}$. Using these values, theoretical curves have been generated which lead to a satisfactory fit of experimental and theoretical results [60].

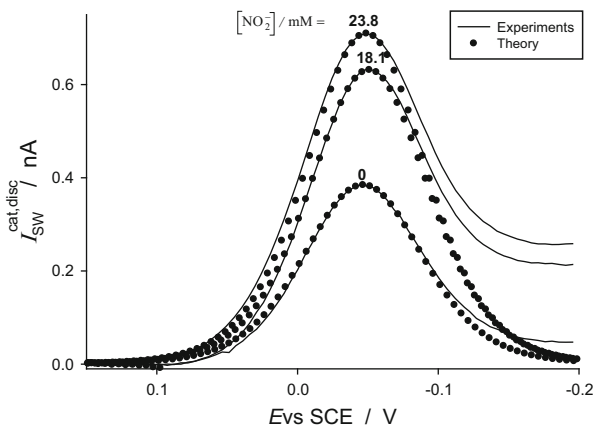


Fig. 7.38 Experimental (solid line) and theoretical (points) square wave voltammograms corresponding to the reduction of $[\text{P}(\text{W}_3\text{O}_{10})_4]^{3-}$ at a gold microelectrode ($r_d = 15.1 \mu\text{m}$) in the presence of different concentrations of the nitrite anion (indicated on the curves). $f = 10 \text{ Hz}$, $E_{\text{SW}} = 25 \text{ mV}$, $\Delta E_s = 5 \text{ mV}$, $T = 293 \text{ K}$. Test solutions: $0.2 \text{ mM } [\text{P}(\text{W}_3\text{O}_{10})_4]^{3-}$, $0.1 \text{ M in } \text{H}_2\text{SO}_4$. Reproduced from [60] with permission

7.6.2 CE and EC Mechanisms

As indicated in Sect. 6.3.2, explicit expressions for the current corresponding to CE and EC mechanisms have not been found in multipulse techniques even when linear diffusion is considered.

7.6.2.1 Square Wave Voltammetry

A treatment for these reaction schemes in SWV based on the mathematical procedure given by Smith [62] considering reversible electrode reactions has been followed in reference [27], and for the case of non-reversible electrode reactions in [6].

For a first-order or pseudo-first-order CE mechanism with a reversible electrode reaction, the SWV response is determined by the thermodynamic and kinetic parameters of the chemical reaction. So, the peak current $\psi_{\text{SWV}}^{\text{G,peak}}$ and the peak potential are notably dependent on them.

In Fig. 7.39, the dependence of the peak current with $\log \chi^{\text{SW}}$ ($= \log((k_1 + k_2)\tau)$) is shown for a CE mechanism for different values of the equilibrium constant K_{eq} . As can be observed, $\psi_{\text{SWV}}^{\text{CE,plane,peak}}$ (ψ_p in the figure), increases with χ^{SW} for any value of K_{eq} , until it reaches a maximum value (highest plateau) corresponding to the labile equilibrium where it is controlled by the reversible reduction of both species B and C (see reaction scheme (7.VIb)). This

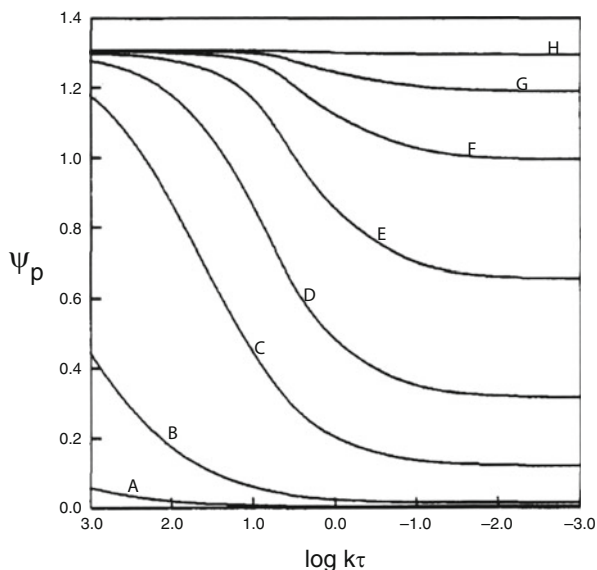


Fig. 7.39 SWV Peak current for a CE mechanism at a planar electrode as a function of $\log \chi^{\text{SW}}$ ($= \log((k_1 + k_2)\tau)$) for several values of $\log(K_{\text{eq}})$: (A–H) 2, 1, 0.5, 0, -0.5 , -1 , -2 , and -3 . $\psi_p = \psi_{\text{SW}}^{\text{CE,plane,peak}} = I_{\text{SW}}^{\text{CE,plane,peak}} \sqrt{\pi\tau} / (FA\sqrt{D}c_0^*)$. Reproduced from [27] with permission

maximum value is reached more easily (i.e., at lower values of χ^{SW}) the smaller K_{eq} (for $\log \chi^{\text{SW}} \geq 0.2$ if $\log(K_{\text{eq}}) \leq -2$). Contrarily, when the chemical reaction is slow enough or for small enough pulse times (i.e., $\log \chi^{\text{SW}} < -1$), the chemical equilibrium becomes less labile and $\psi_{\text{SWV}}^{\text{CE,plane,peak}}$ is controlled only by the reduction of C species, and its production from species B is negligible during the timescale of the square wave experiment. This situation corresponds to the lower plateaus of the curves in Fig. 7.39. In the rising zone of these sigmoidal shaped curves, $\psi_{\text{SWV}}^{\text{CE,plane,peak}}$ is controlled by the kinetics of the preceding chemical reaction and the chemical rate constants k_1 and k_2 can be easily determined from $\psi_{\text{SWV}}^{\text{CE,plane,peak}}$ measurements [27].

The peak potential is generally shifted toward more negative values as χ^{SW} increases for a given value of the equilibrium constant K_{eq} , and more noticeably the smaller the K_{eq} value. The half-peak width is slightly affected by the kinetics parameter of the chemical reaction.

When the electrode reaction is quasi-reversible, the analysis of the SWV response of a CE mechanism by varying the frequency becomes cumbersome, since it simultaneously affects both the electrode and chemical reactions. A brief discussion of this situation can be found in reference [6].

For an EC mechanism (see reaction scheme (7.VIc)), the variation of $\psi_{\text{SWV}}^{\text{EC,plane,peak}}$ with the equilibrium and rate constants is shown in Fig. 7.40. As can be clearly observed, these curves present a minimum whose position depends on

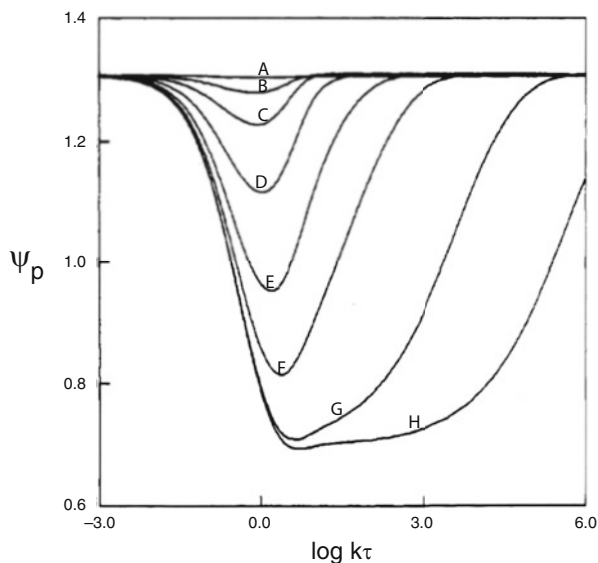


Fig. 7.40 SWV Peak current for a EC mechanism at a planar electrode as a function of $\log \chi^{\text{SW}}$ ($= \log((k_1 + k_2)\tau)$) for several values of $\log(K_{\text{eq}})$: (A–H) -2 , -1 , -0.5 , 0 , 0.5 , 1 , 2 , and 3 . $\psi_p = \psi_{\text{SWV}}^{\text{EC, plane, peak}} = I_{\text{SWV}}^{\text{EC, plane, peak}} \sqrt{\pi\tau} / (FA\sqrt{D}c_0^*)$. Reproduced from [27] with permission

K_{eq} and is shifted to larger χ^{SW} values the larger K_{eq} . This behavior has been explained by considering that the decreasing branch of these curves is predominantly controlled by the rate of the forward chemical reaction, whereas in the rising branch, it is the reverse reaction which becomes dominant. The dependence of these curves with K_{eq} is because an enhancing of K_{eq} increases the concentration of electro-inactive product C and higher values of χ^{SW} are necessary to produce the electro-active species B on the timescale of the reverse potential pulses. The peak potential is generally shifted toward more positive potentials when χ^{SW} increases, whereas the half-peak width is scarcely affected by the kinetic parameters of the chemical reaction.

A discussion of the behavior of an EC mechanism with reversible and non-reversible electrochemical reaction is given in [6]

7.6.3 ECE Mechanism

This electrode process (scheme (7.VII)), has been studied in SWV by considering that the homogeneous chemical reaction is fully irreversible and without consideration of the reaction (7.VIII) (see also Sect. 3.4.8 for more details) [63–65].

7.6.3.1 Square Wave Voltammetry

In order to analyze the influence of the chemical kinetics on the SWV response of this mechanism when the chemical reaction behaves as irreversible ($K_{\text{eq}} \rightarrow \infty$), it can be compared with that obtained for a reversible two-electron electrochemical reaction (EE mechanism) at the same values of the difference between the formal potentials of the electrochemical steps, $\Delta E_c^{\Theta'} = E_{c,2}^{\Theta'} - E_{c,1}^{\Theta'}$ (which is always centered at $E_{\text{index}} = (E_{c,1}^{\Theta'} + E_{c,2}^{\Theta'})/2$).

The behavior of an ECE mechanism with an irreversible chemical reaction for $\Delta E_c^{\Theta'}$ values between -200 and 200 mV can be seen in Fig. 7.41. In all these curves, it can be observed that the peak currents corresponding to an ECE mechanism are lower than those corresponding to an EE one. If $\Delta E_c^{\Theta'} < -71.2$ mV (Fig. 7.41a, b), two peaks centered in $E_{c,1}^{\Theta'}$ and $E_{c,2}^{\Theta'}$ appear in the SWV curves

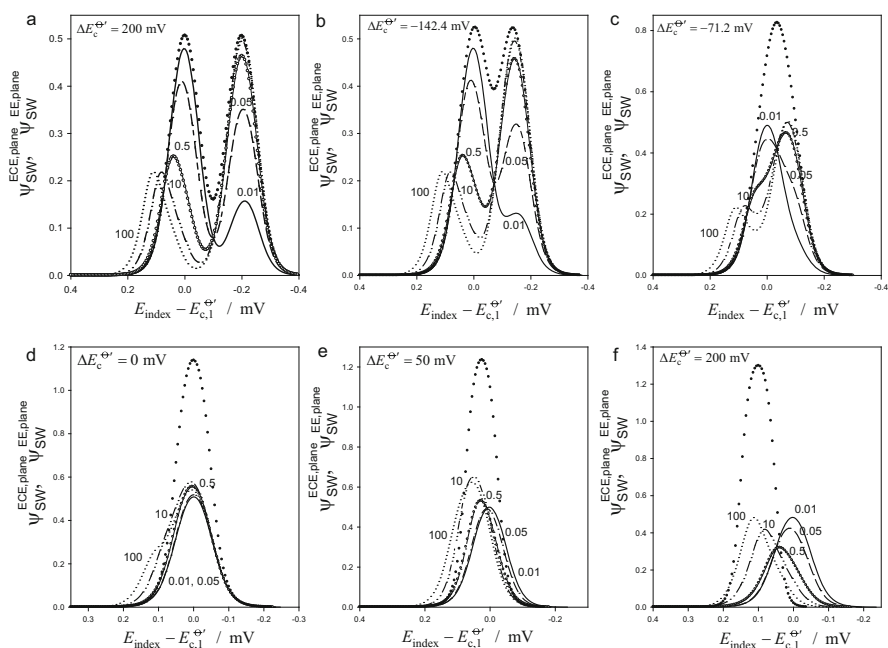


Fig. 7.41 Square Wave Voltammetry. Net currents corresponding to ECE and EE mechanisms at planar electrodes calculated by using the numerical procedure described in [66, 67] (ECE) and Eq. (7.65) (EE). The values of χ_1^{SW} for the ECE mechanism are 0.01 (solid lines), 0.05 (dashed lines), 0.5 (white circles), 10 (dashed-dotted lines), and 100 (dotted lines). The curves corresponding to the EE mechanism appear with black circles. The values of $\Delta E_c^{\Theta'}$ in mV appear in the figures. $E_{\text{SW}} = 50$ mV, $\Delta E_s = 5$ mV, $T = 298$ K

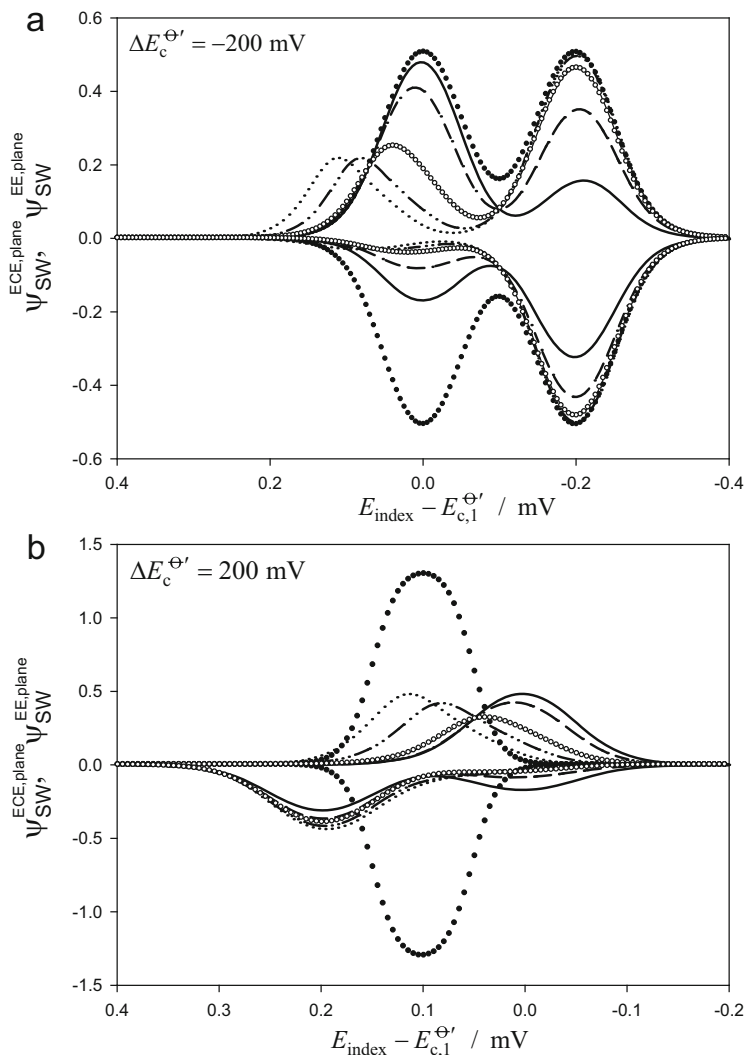


Fig. 7.42 Cyclic Square Wave Voltammetry. Net currents corresponding to ECE and EE mechanisms at planar electrodes calculated by using the numerical procedure described in [66, 67] (ECE) and Eq. (7.65) (EE). The values of χ_1^{SW} for the ECE mechanism are 0.01 (solid lines), 0.05 (dashed lines), 0.5 (white circles), 10 (dashed-dotted lines), and 100 (dotted lines). The curves corresponding to the EE mechanism appear with black circles. The values of $\Delta E_c^{\Theta'}$ in mV appear in the figures. $E_{SW} = 50 \text{ mV}$, $\Delta E_s = 5 \text{ mV}$, $T = 298 \text{ K}$

corresponding to an EE mechanism. In the case of an ECE process, the peak located at more positive potentials diminishes its height until it reaches a constant value for $\chi_1^{SW} = k_1 \tau > 5 \text{ s}^{-1}$, with the peak potentials being shifted toward more positive potentials as χ_1^{SW} increases because of the facilitated conversion of

species O_1 into R_1 . Contrarily, the height of the peak located at more negative potentials increases with χ_1^{SW} and its position is slightly shifted toward potentials less than $E_{c,2}^{\Theta}$. The height of this last peak tends to that corresponding to the more cathodic peak of an EE process faster, the lesser the value of ΔE_c^{Θ} and the greater χ_1^{SW} .

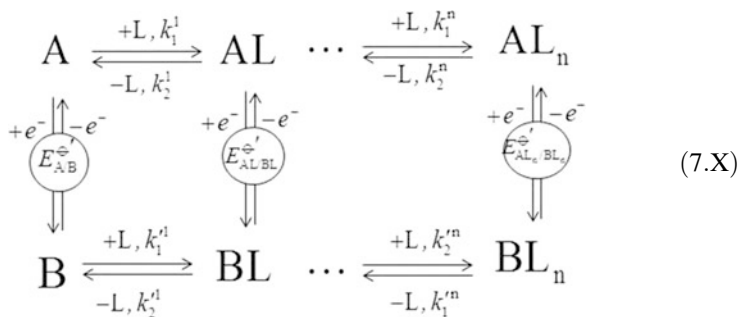
For $-71.2 \leq \Delta E_c^{\Theta} \leq 0$ mV (Fig. 7.41c, d), only one peak is observed for small values of χ_1^{SW} whose peak height is much lower than that corresponding to an EE process (dotted curves). An increase of χ_1^{SW} causes a splitting of this response, which is less pronounced when ΔE_c^{Θ} increases (compare curves corresponding to $\chi_1^{SW} \leq 0.5$ in Fig. 7.41c, d).

For $\Delta E_c^{\Theta} \gg 0$ (Fig. 7.41e, f), only one peak is observed and its position is shifted toward more anodic potentials as χ_1^{SW} increases, whereas its height shows a complex dependence on χ_1^{SW} .

In Fig. 7.42a, b, the cyclic SWV curves obtained for $\Delta E_c^{\Theta} = -200$ and 200 mV have also been plotted. As can be observed, the characterization of an ECE is very complex from these curves. So, from the CSWV response obtained for $\Delta E_c^{\Theta} = -200$ mV, the most cathodic peak corresponding to the second (anodic) scan loses symmetry with respect to that obtained in the first scan when χ_1^{SW} increases, whereas for the peak corresponding to more anodic potentials this symmetry is never observed, and the peak height is always lower, with the peak potential being shifted toward more positive values than the corresponding to the peak in the first scan. For $\Delta E_c^{\Theta} = 200$ mV, no symmetry with the curves obtained for the first scan is observed and the very complex influence of χ_1^{SW} makes it advisable to vary the pseudo-first-order rate constant k_1 (through the variation of the concentration of the corresponding species or the SW frequency) and compare experimental and theoretical data under different experimental conditions.

7.6.4 Ladder Mechanism

In this section, we consider the application of SWV to the characterization of the electroreduction of a species A into species B with both species A and B taking part in a number of chemical equilibria in solution in line with the following reaction scheme [68–70]:



As stated in Sect. 6.3.4, ligand L is assumed to be present at high concentration ($c_L^* \gg c_A^*, c_B^*, c_{\text{AL}_i}^*, c_{\text{BL}_i}^*$) and k_j^i and k_j^i ($j = 1, 2; i = 1, 2, \dots, n$) represent the (pseudo)first-order forward and backward rate constants of the chemical reactions.

7.6.4.1 Square Wave Voltammetry

Section 6.3.4 presented the solution to this reaction scheme when any succession of potential steps of the same duration τ is applied. For SWV, by taking into account Eqs. (6.96)–(6.98) and (7.6), the following expression for the current is obtained:

$$\begin{aligned}
 \psi_{\text{SW}}^{\text{ladder, G}} &= \frac{I_{\text{SW}}^{\text{ladder, G}} \sqrt{\tau}}{F A_G \sqrt{D} c^*} = -Z_{2p}^{\text{ladder}} f_G(\tau, \xi_G) \\
 &+ \sum_{m=1}^{2p-1} (Z_m^{\text{ladder}} [f_G((2p-m)\tau, \xi_G) - f_G((2p-m+1)\tau, \xi_G)])
 \end{aligned} \quad (7.81)$$

where

$$Z_m^{\text{ladder}} = \left(\frac{1}{1 + \omega e^{\eta_m}} - \frac{1}{1 + \omega e^{\eta_{m-1}}} \right) \quad (7.82)$$

$$\omega = \frac{1 + \sum_{i=1}^n \beta_i}{1 + \sum_{i=1}^n \beta_i'} \quad (7.83)$$

$$\eta_m = \frac{F}{RT} (E_m - E_{A/B}^{\ominus}), \quad m \geq 1 \quad (7.84)$$

ξ_G is given by Eq. (7.22) and $D = D_{\text{eff}}^A = D_{\text{eff}}^B$, with D_{eff}^A and D_{eff}^B being the effective diffusion coefficients of the pseudo-species A_T and B_T , respectively (see Eqs. (3.274)–(3.275)):

$$D_{\text{eff}}^A = \frac{D_A + \sum_{i=1}^n D_{AL_i} \beta_i}{1 + \sum_{i=1}^n \beta_i} \quad (7.85)$$

$$D_{\text{eff}}^B = \frac{D_B + \sum_{i=1}^n D_{BL_i} \beta'_i}{1 + \sum_{i=1}^n \beta'_i} \quad (7.86)$$

β_i and β'_i represent the overall formation constant for the different complexes of species A or B, respectively, initially present in solution:

$$\left. \begin{aligned} \beta_i &= \prod_{m=1}^i K_m c_L^* = \frac{c_{AL_i}(q, t)}{c_A(q, t)} \\ \beta'_i &= \prod_{m=1}^i K'_m c_L^* = \frac{c_{BL_i}(q, t)}{c_B(q, t)} \end{aligned} \right\} \forall q, t; i \geq 1; \quad (7.87)$$

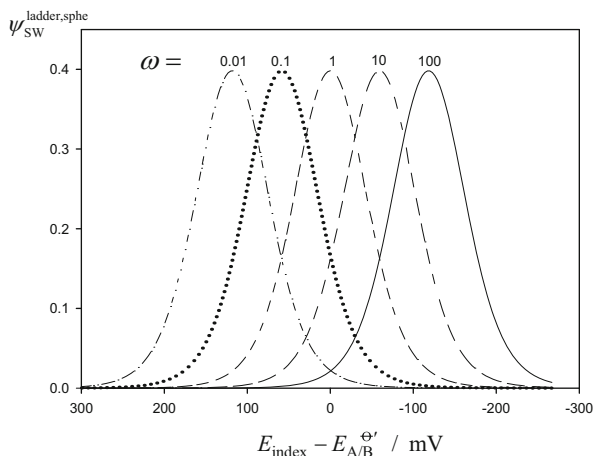
with K_m and K'_m being

$$\begin{aligned} K_m &= \frac{c_{AL_m}(q, t)}{c_{AL_{m-1}}(q, t) c_L^*} \\ K'_m &= \frac{c_{BL_m}(q, t)}{c_{BL_{m-1}}(q, t) c_L^*} \end{aligned} \quad (7.88)$$

and $f_G((p - m + 1)\tau, \xi_G)$ is defined in Table 7.1 for different electrode geometries.

The effect of the parameter ω (given by Eq. (7.83)) on the SWV curves is shown in Fig. 7.43 for a spherical electrode of 50- μm radius. Large ω -values relate to the situation where the complexes of the reactant species A are more stable than those of species B, whereas the opposite situation is found for small ω -values. As can be observed, the only influence of this parameter is the shift of the curves toward more negative potentials when ω increases on account of the hindering of the electro-reduction reaction caused by the stabilization of the oxidized species with respect to the reduced ones. The peak potential in SWV coincides with the half-wave potential such that

Fig. 7.43 Influence of the parameter ω on the response in SWV (Eq. (7.81)) for a spherical electrode of radii $50 \mu\text{m}$. $E_{\text{SW}} = 30 \text{ mV}$, $\Delta E_s = 3 \text{ mV}$, $\tau = 10 \text{ ms}$ ($f = 50 \text{ Hz}$). $T = 298 \text{ K}$, $D = 10^{-5} \text{ cm}^2 \text{ s}^{-1}$. Reproduced from [70] with permission



$$E_{\text{peak}} = E_{\text{A/B}}^{\Theta'} + \frac{RT}{F} \ln\left(\frac{1}{\omega}\right) \quad (7.89)$$

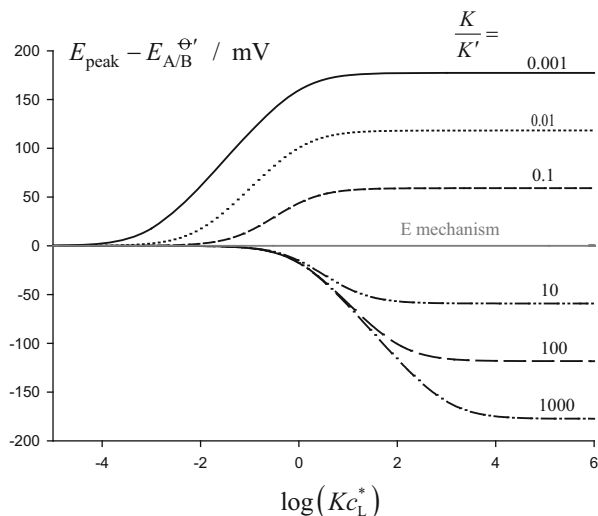
In practice, the influence of the ω -value on the voltammograms can be revealed experimentally by changing the bulk concentration of species L, c_L^* , that is, of the complexing agent, protons, counterions... In this respect, Fig. 7.44 shows the variation of the peak potential in SWV (E_{peak}) with c_L^* for the $\text{C}^{\text{eq}}\text{E}^{\text{rev}}\text{C}^{\text{eq}}$ mechanism (i.e., a coupled chemical reaction takes place “before” and “after” the electron transfer). As can be observed, the variation of the signal position informs about the relative stability of the oxidized and reduced species. When $K/K' > 1$, the stabilization of the oxidized species by the chemical equilibrium is greater and the voltammograms move toward more negative overpotentials, whereas the opposite is true for $K/K' < 1$. Note that these situations include as extreme cases the $\text{C}^{\text{eq}}\text{E}^{\text{rev}}$ and $\text{E}^{\text{rev}}\text{C}^{\text{eq}}$ mechanisms, where $K' = 0$ and $K = 0$, respectively.

As shown in Fig. 7.44, in the absence of coupled reactions (the so-called E mechanism), the voltammetry is insensitive to changes in the concentration of species L provided that this does not lead to significant changes in the ionic strength. Therefore, the study of the position of the voltammograms in the presence of different concentrations of species L offers a simple criterion to discriminate between simple electron transfer processes and those complicated by coupled chemical equilibria.

7.7 Surface-Bound Molecules

In this section, the application of differential multipulse and Square Wave Voltammetric techniques to strongly adsorbed species is treated. Special detail is paid to SWV, since it is the most important technique. Differential Staircase

Fig. 7.44 Variation of the SWV peak potential (Eq. (7.89)) with the concentration of the ligand (c_L^*) for a $C^{eq}E^{rev}C^{eq}$ mechanism with different K/K' values (given in the graph). It is assumed that the change of c_L^* does not lead to a significant variation of the ionic strength. Reproduced from [70] with permission



Voltcoulometry (DSCVC) and Square Wave Voltcoulometry (SWVC) are also considered, since they are very valuable tools for the analysis of fast electrochemical reactions between surface-confined molecules. First, a simple mono-electronic electrochemical reaction is analyzed and, after that, the cases corresponding to multi-electron electrochemical reactions and chemical reactions coupled to the surface charge transfer, including electrocatalytic processes, are discussed.

7.7.1 One-Electron Electrochemical Reactions

The expressions corresponding to the current and charge obtained for a surface one-electron electrochemical reaction under the conditions described in Sect. 6.4.1.2 when an arbitrary sequence of potential pulses is applied are given in Eqs. (6.130) and (6.131), respectively.

7.7.1.1 Differential Staircase Voltcoulometry

As stated in Sect. 7.1, DSCVC is of special interest in the case of surface-bound molecules, because its response makes it possible to characterize electrode processes of any reversibility. Thus, from the expression of the converted charge Q_p corresponding to the p th potential pulse applied of an arbitrary sequence given by Eq. (6.131), and inserting it into that corresponding to the response in DSCVC given by Eq. (7.2) we obtain [4]:

$$Q_{\text{DSCVC}} = Q_{\text{F}} \left[\frac{1}{1 + e^{\eta_p}} (1 - \theta_p) - \frac{1}{1 + e^{\eta_{p-1}}} (1 - \theta_{p-1}) + \sum_{j=1}^{p-1} \frac{(1 - \theta_j)}{1 + e^{\eta_j}} \right. \\ \left. \times \prod_{h=j+1}^p \theta_h - \sum_{j=1}^{p-2} \frac{(1 - \theta_j)}{1 + e^{\eta_j}} \prod_{h=j+1}^{p-1} \theta_h \right] \quad (7.90)$$

where

$$\theta_h = \exp(-k_{\text{T},h}\tau) \quad h = 1, 2, \dots, p \quad (7.91)$$

$$k_{\text{T},h} = k_{\text{red},h} + k_{\text{ox},h} \quad h = 1, 2, \dots, p \quad (7.92)$$

$$Q_{\text{F}} = FA\Gamma_{\text{T}} \quad (7.93)$$

In the above equations, $k_{\text{red},h}$ and $k_{\text{ox},h}$ are the first-order heterogeneous rate constants (in s^{-1}) at potential E_h of a pulse sequence, for the electro-reduction and electro-oxidation reactions, respectively. It will be assumed that the potential dependence of the rate constants is in agreement with the Butler–Volmer formalism (see Eq. (1.101)), i.e.,

$$\left. \begin{aligned} k_{\text{red},h} &= k^0 e^{-\alpha\eta_h} \\ k_{\text{ox},h} &= k_{\text{red},h} e^{\eta_h} \end{aligned} \right\} \quad (7.94)$$

with

$$\eta_h = \frac{F}{RT} (E_h - E_c^{\Theta'}) \quad (7.95)$$

and k^0 and α are the heterogeneous rate constant and the charge transfer coefficient, respectively [1, 2].

The DSCVC response has a peak-shaped feature similar to that obtained in Cyclic Voltammetry. Indeed, the most appropriate way of analyzing the DSCVC response is to divide Q_{DSCVC} by the pulse amplitude ΔE in order to obtain the $(Q_{\text{DSCVC}}/\Delta E) - E$ response, since the following relationship between the continuous current–potential curve corresponding to CV and the $(Q_{\text{DSCVC}}/\Delta E) - E$ curve obtained from a discrete staircase potential sequence can be established for $\Delta E \ll RT/F$:

$$I_{\text{CV}} = \frac{dQ_{\text{CV}}}{dt} = v \frac{dQ_{\text{CV}}}{dE} \simeq v \left(\frac{Q_{\text{DSCVC}}}{\Delta E} \right) \quad (7.96)$$

with v being the CV scan rate. In practice, CV and DSCVC responses present differences of less than 5 % for values of $|\Delta E| < 10 \text{ mV}$ [4]. The above relationship means that the $(I_{\text{CV}}/v) - E$ response, which corresponds to the faradaic capacitance

obtained by using CV, should be coincident with the $(Q_{\text{DSCVC}}/\Delta E) - E$ one. Equation (7.96) can be simplified in the following situations:

Fast Charge Transfer

Under reversible conditions, only the first two terms of Eq. (7.90) remain, since $\theta_p \rightarrow 0$ (see Eq. (7.91)), so the Q_{DSCVC} curve is simplified to

$$Q_{\text{DSCVC}} = Q_{\text{F}} \left(\frac{1}{1 + e^{\eta_p}} - \frac{1}{1 + e^{\eta_{p-1}}} \right) \quad (7.97)$$

By making $dQ_{\text{DSCVC}}/d\bar{E}_p = 0$ (with $\bar{E}_p = (E_p + E_{p+1})/2$) in this expression, the peak potential and height are obtained

$$E_{\text{DSCVC,peak}} = E_c^{\Theta'} \quad (7.98)$$

$$Q_{\text{DSCVC,rev}}^{\text{peak}} = Q_{\text{F}} \tanh \left(\frac{F|\Delta E|}{4RT} \right) \quad (7.99)$$

Fully Irreversible Cathodic Charge Transfer

In this case, Eq. (7.90) becomes

$$Q_{\text{DSCVC,irrev}} \cong Q_{\text{F}} e^{-\left(\sum_{h=1}^{p-1} k_{\text{red},h} \right) \tau} k_{\text{red},p} \tau \quad (7.100)$$

By equating to zero, its derivative the following expressions for the peak coordinates (potential and height) are obtained:

$$E_{\text{DSCVC,peak}} = E_c^{\Theta'} + \frac{RT}{\alpha F} \ln(\alpha |\Delta \eta| B) + \frac{RT}{\alpha F} \ln \left(\frac{k^0}{\alpha \alpha} \right) \quad (7.101)$$

$$Q_{\text{DSCVC,irrev}}^{\text{peak}} = \frac{1}{|\Delta E| e B} Q_{\text{F}} \quad (7.102)$$

with “e” being the base of the natural logarithms and $|\Delta \eta|$ and B given by Eqs. (7.104) and (7.108), respectively. In both limiting reversible and fully irreversible behavior, on imposing $\Delta E \ll RT/F$ in the expressions for the DSCVC response, the $(Q_{\text{DSCVC}}/\Delta E) - E$ curves transform into those obtained for the voltammetric $(I_{\text{CV}}/v) - E$ ones (see Eqs. (6.161) and (6.168), respectively). Thus, the peak parameters obtained in DSCVC become identical to those given in CV by Eqs. (6.162) and (6.169)–(6.170). In the case of the peak potential, the differences between DSCVC and CV are of lower than 2 mV and the error in the peak height is less than 5 % for values of $|\Delta E| < 10 \text{ mV}$ [4].

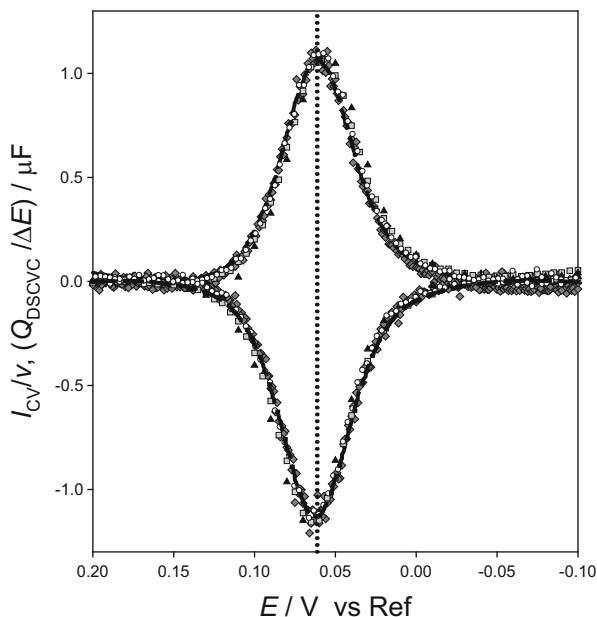
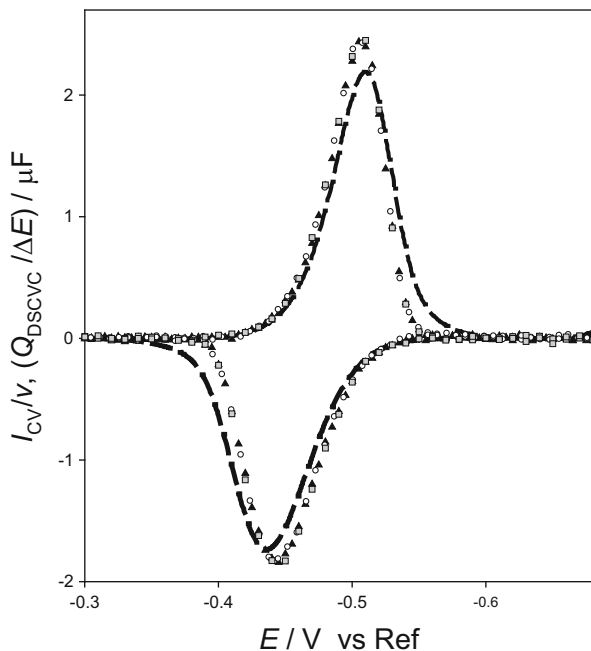


Fig. 7.45 Experimental corrected $(Q_{\text{DSCVC}}/\Delta E) - E$ curves (symbols) and $(I_{\text{CV}}/\nu) - E$ ones (dashed lines) corresponding to the disodium salt of the 2,6-Anthraquinonedisulfonic acid (AQDS) $1.0 \mu\text{M} + \text{HClO}_4$ 0.5 M adsorbed on a mercury electrode. The sweep rate in both techniques is $\nu = 1.0 \text{ V s}^{-1}$. The values of ΔE (in mV) of the DSCVC curves are 1 (dark gray diamonds), 3 (white circles), 5 (gray squares), and 10 (black triangles). The initial potential in both DSCVC and CV technique was $E_{\text{initial}} = -150 \text{ mV}$. $r_s = 0.0316 \text{ cm}$, and $T = 296 \text{ K}$. A vertical dotted line indicates the value of the formal potential $E_c^{0f} = 0.062 \text{ V}$ vs. Reference. Reproduced from [4] with permission

The experimental verification of the theoretical behavior of DSCVC responses is presented in [4] for two systems which have been adsorbed on a mercury electrode forming stable sub-monolayers: the disodium salt of the 2,6-Anthraquinonedisulfonic acid (AQDS) $1.0 \mu\text{M} + \text{HClO}_4$ 0.5 M , which behaves as reversible (Fig. 7.45), and the 4-PhenylazoPhenol $5 \mu\text{M} + 0.5 \text{ M KNO}_3$ ($\text{pH} = 8.0$), which behaves as quasi-reversible (Fig. 7.46).

The corrected cathodic and anodic $(I_{\text{CV}}/\nu) - E$ curves (dashed lines) and the $(Q_{\text{DSCVC}}/\Delta E) - E$ ones (symbols) corresponding to an AQDS sub-monolayer, for different values of the pulse amplitude ΔE (1, 3, 5, and 10 mV) in the DSCVC curves, are plotted in Fig. 7.45. The correction mentioned above refers to the non-faradaic component of the response and has been carried out as discussed in [4]. On comparing the cathodic and anodic CV and DSCVC curves in Fig. 7.45, an excellent concordance between both techniques is observed. From the values of the peak heights the faradaic charge Q_{F} and the surface excess Γ_{T} of the anthraquinone system have been obtained by using Eq. (7.98). For small values of ΔE , the peak potentials of the CV and DSCVC curves coincide ($\Delta E = 1 \text{ mV}$, $E_{\text{CV,peak}}$

Fig. 7.46 Experimental corrected $(I_{CV}/v) - E$ curves (dashed lines) and $(Q_{DSCVC}/\Delta E) - E$ ones (symbols) corresponding to the 4-PhenylazoPhenol $5 \mu\text{M} + 0.5 \text{ M KNO}_3$ ($\text{pH} = 8.0$) adsorbed on a mercury electrode. $v = 1.0 \text{ V s}^{-1}$. The values of ΔE (in mV) of the DSCVC curves are 5 (black triangles), 7 (white circles), and 10 (gray squares). $E_{\text{initial}} = -150 \text{ mV}$. $r_s = 0.0316 \text{ cm}$, and $T = 296 \text{ K}$. Reproduced from [4] with permission



$\approx E_{\text{DSCVC,peak}} = E_c^\ominus = 62 \text{ mV}$ vs. Reference, with both cathodic and anodic responses being mirror images). From the analysis of the peak parameters, it can be seen that the experimental DSCVC curves show a better agreement with the ideal theoretical predictions than the corresponding CV ones. Thus, the ratio between peak heights in CV differs from the unity by 4 %, whereas in DSCVC, this ratio is equal to the unity with negligible error. Moreover, the half-peak widths of the CV curves are 16 % broader than the ideal value and in the DSCVC curves these differences are of the order of 10 %.

The non-reversible behavior is plotted in Fig. 7.46, which corresponds to the corrected $(I_{CV}/v) - E$ curves (dashed lines) and the $(Q_{\text{DSCVC}}/\Delta E) - E$ ones (symbols) of the system 4-PhenylazoPhenol. From these curves, it can be seen that although the DSCVC curves are perfectly superimposable, the CV ones clearly show smaller peak heights in both scans. This systematic decrease of the CV signals, which cannot be theoretically predicted, is 5–10 %, and it has been reported when the response of electro-active monolayers in CV has been compared with other voltammetric and chronopotentiometric electrochemical techniques [71, 72]. Due to the quasi-reversible nature of the charge transfer reduction of the 4-PhenylazoPhenol, no simple equations for the peak parameters are available. So, a numerical comparison between theoretical and experimental curves for different sets of parameters should be made in order to obtain the kinetic and thermodynamic parameters of the system.

7.7.1.2 Differential Staircase Voltammetry

In the case of surface-bound molecules, due to the characteristics of the current obtained when a sequence of potential pulses is applied (see Sect. 6.4.1.2), the use of DSCVC is only recommended for the analysis of non-reversible electrochemical reactions, since for very fast electrochemical reactions (i.e., for values of the dimensionless rate constant which fulfill $\log(k^0\tau) \geq 0.5$), the current becomes negligible, in accordance with Eq. (6.132). The response obtained in DSCVC when non-reversible electrochemical reactions are considered presents two peaks, one maximum positive ($\psi_{\text{DSCVC}}^{\text{Max}}$) and one minimum negative ($\psi_{\text{DSCVC}}^{\text{min}}$) which appear for values of the applied potentials E_{Max} and E_{min} , respectively (with $\psi_{\text{DSCVC}} = I_{\text{DSCVC}}/(aQ_F)$). The cross potential value, at which $\psi_{\text{DSCVC}} = 0$, is E_{cross} .

When the electrochemical reaction can be considered as fully irreversible, it is possible to deduce analytical expressions for the maximum, minimum, and cross potentials. By taking into account equation (6.134) for the dimensionless current under these conditions, we obtain [73]:

$$\begin{aligned} \psi_{\text{DSCVC,irrev}} &= \frac{I_{\text{DSCVC,irrev}}}{aQ_F} \\ &= \frac{1}{a} k_{\text{red},p} \exp\left(-k_{\text{red},p}\tau \frac{e^{-\alpha|\Delta\eta|}}{1 - e^{-\alpha|\Delta\eta|}}\right) (e^{-k_{\text{red},p}\tau} - e^{-\alpha|\Delta\eta|}) \end{aligned} \quad (7.103)$$

with

$$|\Delta\eta| = \frac{F|\Delta E|}{RT} \quad (7.104)$$

and a given by Eq. (7.11).

In this case, the cross potential or null current potential is

$$E_{\text{cross}} = E_c^{\ominus} + \frac{RT}{\alpha F} \ln\left(\frac{k^0\tau}{\alpha|\Delta\eta|}\right) \quad (7.105)$$

whereas the potentials of the maximum and the minimum, E_{Max} and E_{min} , respectively, can be obtained by imposing $d\Delta\psi_{\text{DSCVC,irrev}}/dE = 0$ in Eq. (7.103):

$$\left. \begin{aligned} E_{\text{Max}} &= E_c^{\ominus} + \frac{RT}{\alpha F} \ln\left(\frac{k^0}{\alpha\alpha}\right) - \frac{RT}{\alpha F} \ln\left(\frac{Y_{\text{Max}}}{\alpha|\Delta\eta|}\right) \\ E_{\text{min}} &= E_c^{\ominus} + \frac{RT}{\alpha F} \ln\left(\frac{k^0}{\alpha\alpha}\right) - \frac{RT}{\alpha F} \ln\left(\frac{Y_{\text{min}}}{\alpha|\Delta\eta|}\right) \end{aligned} \right\} \quad (7.106)$$

with

$$Y_{\text{Max}}^{\text{min}} = \frac{(2 + B(1 - e^{\alpha|\Delta\eta|})) \mp \sqrt{(2 + B(1 - e^{\alpha|\Delta\eta|}))^2 - 4(B + 1)(1 - e^{\alpha|\Delta\eta|})}}{2(B + 1)} \quad (7.107)$$

$$B = \frac{e^{-\alpha|\Delta\eta|}}{1 - e^{-\alpha|\Delta\eta|}} \quad (7.108)$$

Y_{Max} and Y_{min} are the values of Y corresponding to the upper and lower sign in Eq. (7.107), respectively.

In agreement with Eq. (7.106), the distance between both maximum and minimum potentials is only dependent on α and $\alpha|\Delta\eta|$,

$$E_{\text{Max}} - E_{\text{min}} = \frac{RT}{\alpha F} \ln \left(\frac{Y_{\text{min}}}{Y_{\text{Max}}} \right) \quad (7.109)$$

and the same behavior is observed for the ratio between the maximum and minimum peak heights given by

$$R_{\psi} = \left| \frac{\psi_{\text{DSCVC}}^{\text{Max}}}{\psi_{\text{DSCVC}}^{\text{min}}} \right| = \left| \frac{Y_{\text{Max}} e^{-Y_{\text{Max}} B} (e^{-Y_{\text{Max}}} - e^{-\alpha|\Delta\eta|})}{Y_{\text{min}} e^{-Y_{\text{min}} B} (e^{-Y_{\text{min}}} - e^{-\alpha|\Delta\eta|})} \right| \quad (7.110)$$

For $|\Delta\eta| \ll 1$, the DSCVC current–potential curves given by Eq. (7.103) can be written in a simpler way as the derivative ($d\psi/dE$). Under these conditions, it is obtained

$$\left(\frac{d\psi_{\text{DSCVC}}}{dE} \right)_{\text{irrev}} = \frac{-\alpha k_{\text{red}}}{|v|} e^{-\frac{k_{\text{red}}}{\alpha a}} \left(1 - \frac{k_{\text{red}}}{\alpha a} \right) \quad (7.111)$$

whereas Eqs. (7.107)–(7.110) become

$$Y_{\text{Max}}^{\text{min}} = \frac{3 \pm \sqrt{5}}{2} \quad (7.112)$$

$$E_{\text{Max}} - E_{\text{min}} = \frac{RT}{\alpha F} \ln \left(\frac{3 + \sqrt{5}}{3 - \sqrt{5}} \right) \quad (7.113)$$

$$R_{\psi} = 0.521 \quad (7.114)$$

$\psi_{\text{DSCVC}} - (E - E_c^{\Theta'})$ curves calculated from Eqs. (6.130) and (7.1) for a staircase potential with $\Delta E = 5 \text{ mV}$, $\alpha = 0.5$, and different values of the dimensionless surface rate constant ($k^0\tau$) are shown in Fig. 7.47. As can be seen, the shape of

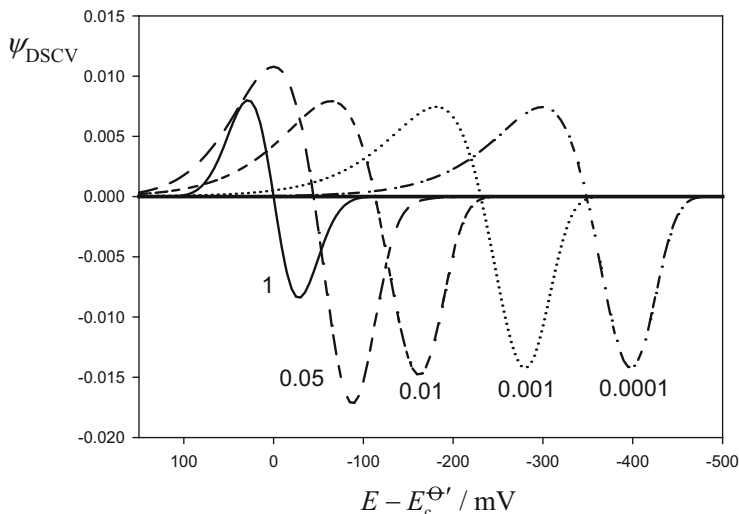


Fig. 7.47 Influence of the reversibility on the theoretical $\psi_{\text{DSCV}} - (E - E_c^{\Theta'})$ curves calculated from Eqs. (6.130) and (7.1). The values of the dimensionless surface rate constant $k^0\tau$ are shown on the curves. $\Delta E = 5 \text{ mV}$, $\tau = 1 \text{ s}$, $\alpha = 0.5$, $T = 298 \text{ K}$. Reproduced from [73] with permission

the curves changes gradually with $k^0\tau$. Thus, for $k^0\tau = 1$, the $|I_{\text{DSCVC}}^{\text{Max}}/I_{\text{DSCVC}}^{\text{min}}|$ ratio is practically equal to the unity and the potential at which $\psi_{\text{DSCVC}} = 0$ coincides with $E_c^{\Theta'}$, due to the reversible behavior of the system (solid line in Fig. 7.47). Note that, under these conditions, the reversible limit can be established, and this can be observed from the symmetrical shape of the $\psi_{\text{DSCVC}} - (E - E_c^{\Theta'})$ curve. For smaller values of ($k^0\tau$), the electron transfer process behaves as non-reversible and, then, the response is shifted toward more negative potentials. Moreover, the positive peaks tend to be broader and lower, whereas the negative ones become sharper and higher, so for a totally irreversible behavior, the $|I_{\text{DSCVC}}^{\text{Max}}/I_{\text{DSCVC}}^{\text{min}}|$ ratio takes the constant value of 0.523, in line with Eq. (7.110) (see curves with ($k^0\tau$) < 0.1).

7.7.1.3 Square Wave Voltcoulometry

In general, Cyclic Voltammetry (CV) is the most used technique in the study of mono-electron or multi-electron electrochemical reactions for surface-bound molecules, although it may be more advantageous to use discrete potential perturbations like those based on square wave and staircase waveforms, for which signals are recorded with improved faradaic-to-background ratio which are much less affected by double layer influence. When the electron transfers behave as reversible, techniques based on charge measurements, such as SWVC or DSCVC, provide an easily characterizable peak-shaped charge-potential response. On the other

hand, more usual techniques based on the recording of currents such as SWV, Staircase Voltammetry (SCV), and DSCVC provide negligible measured currents for adsorbed molecules with reversible behavior and, therefore, cannot be used in these conditions. In order to apply these last techniques, high values of the square wave frequency or small time pulses must be used, for which a quasi-reversible behavior is exhibited by the system under study.

SWVC technique presents the following additional advantages which makes it particularly suitable for the study of multi-electron reversible systems: (a) The charge–potential curves present a practically constant baseline; (b) The peak parameters of the SWVC curves show great sensitivity in determining the characteristic parameters of the process; (c) SWVC shows an enhanced resolution for experimental responses. Note also that recording the charge can be easily implemented in traditional electrochemical instrumentation [5].

In SWVC, the square wave potential sequence given by Eq. (7.5) is applied to the analysis of the converted charge in an electrochemical reaction between surface-bound molecules in order to obtain the $Q_{\text{SW}} - E$ curves, in line with Eq. (7.8), instead of the usual $I_{\text{SW}} - E$ curves corresponding to SWV. The $Q_{\text{SW}} - E$ curves present an intense signal for reversible processes from which they can be completely characterized [5]. The analytical expression of the SWVC charge–potential is (see Eqs. (6.131) and (7.8)):

$$Q_{\text{SW}} = Q_{\text{F}} \left[\frac{1}{1 + e^{\eta_{2p-1}}} (1 - \theta_{2p-1}) - \frac{1}{1 + e^{\eta_{2p}}} (1 - \theta_{2p}) + \sum_{j=1}^{2p-2} \frac{(1 - \theta_j)}{1 + e^{\eta_j}} \right. \\ \left. \times \prod_{h=j+1}^{2p-1} \theta_h - \sum_{j=1}^{2p-1} \frac{(1 - \theta_j)}{1 + e^{\eta_j}} \prod_{h=j+1}^{2p} \theta_h \right] \quad p = 1, 2, \dots, N \quad (7.115)$$

with θ_j and η_j given by Eqs. (7.91) and (7.95), respectively.

Under reversible conditions, $\theta_j \rightarrow 0$, and Eq. (7.115) takes the following simpler form:

$$Q_{\text{SW}} = Q_{\text{F}} \left(\frac{1}{1 + e^{\eta_{2p-1}}} - \frac{1}{1 + e^{\eta_{2p}}} \right) \quad (7.116)$$

with $\eta_{2p-1} = \eta_{2p} + (2F/(RT))|E_{\text{SW}}|$.

Equation (7.116) for the SW charge–potential response of surface-bound molecules presents a potential dependence identical to that obtained for the stationary SW current of a one-electron electrochemical reaction between solution soluble molecules at electrodes of any geometry (see for example Eqs. (7.35) and (7.36) for spherical and disc electrodes, respectively). Therefore, the expression of the peak parameters will be analogous to those obtained in the case of solution soluble molecules (see Eq. (7.37)):

$$E_{\text{index, peak}} = E_c^{-\Theta'} \quad (7.117)$$

$$Q_{\text{SW}}^{\text{peak}} = Q_F \tanh\left(\frac{F|E_{\text{SW}}|}{2RT}\right) \quad (7.118)$$

and the half-peak width is given by Eq. (7.32) (see also Fig. 7.8).

The peak charge and the half-peak width, $W_{1/2}$, depend on the square wave amplitude and present the following limiting values:

$$\begin{aligned} W_{1/2} = 90 \text{ mV} \quad Q_{\text{SW}}^{\text{peak}} &= \frac{F|E_{\text{SW}}|}{2RT} Q_F \quad \text{for } |E_{\text{SW}}| < 10 \text{ mV and } T = 298 \text{ K} \\ W_{1/2} = 2|E_{\text{SW}}| \quad Q_{\text{SW}}^{\text{peak}} &= Q_F \quad \text{for } |E_{\text{SW}}| > 120 \text{ mV} \end{aligned} \quad (7.119)$$

It is evident that the square wave charge–potential curves corresponding to surface-bound molecules behave in a similar way to the normalized current–potential ones observed for a soluble solution reversible redox process in SWV when an ultramicroelectrode is used (i.e., when steady-state conditions are attained), providing the analogous role played by Q_{SW} (surface-bound species) and I_{SW}^{G} (soluble solution species), and also Q_F (Eq. (7.93)) and the steady-state diffusion-limited current ($I_{\text{d,c}}^{\text{G,ss}}$), see Sect. 2.7. This analogy can be made because the normalized converted charge in a surface reversible electrode process is proportional to the difference between the initial surface concentration (Γ_{T}) and that corresponding to potential E_p , $(Q_p/Q_F) \propto (\Gamma_{\text{T}} - \Gamma_{\text{O}}^{(p)})$, and in electrochemical systems under mass transfer control, the voltammetric normalized current is proportional to the difference between the bulk (c_{O}^*) and surface concentration ($c_{\text{O}}^{(p,s)}$) at potential E_p , $(I_p^{\text{G}}/I_{\text{d,c}}^{\text{G,ss}}) \propto (c_{\text{O}}^* - c_{\text{O}}^s)$. Moreover, both types of systems fulfill

$$\frac{\Gamma_{\text{T}} - \Gamma_{\text{O}}^{(p)}}{\Gamma_{\text{T}}} = \frac{c_{\text{O}}^* - c_{\text{O}}^{(p,s)}}{c_{\text{O}}^*} = \frac{1}{1 + e^{\eta_p}} \quad (7.120)$$

Equation (7.116) indicates that the charge–potential curves for reversible processes are only dependent on the square wave amplitude E_{SW} and are independent of the frequency $f = 1/2\tau$ and the staircase amplitude ΔE_s . As a consequence, they are superimposable on those obtained at any differential electrochemical technique, such as DSCVC, provided that the differences between the successive potential pulses coincide ($\Delta E = 2E_{\text{SW}}$). Moreover, when this difference is much less than RT/F (i.e., less than 25 mV at $T = 198 \text{ K}$), the responses obtained in Cyclic Voltammetry (CV), Alternating Current Voltammetry, Potentiometric Stripping Analysis (PSA) and also in any Reciprocal Derivative Chronopotentiometry (RDCP) fulfill [5, 74, 75]:

$$\begin{aligned} \left(\frac{Q_{\text{SWVC}}}{|E_{\text{SW}}|} \right)_{|E_{\text{SW}}| \ll RT/F} &= \left(\frac{Q_{\text{DSCVC}}}{|\Delta E_s|} \right)_{|\Delta E_s| \ll RT/F} \simeq \frac{dQ}{dE} = \frac{I_{\text{CV}}}{v_{\text{CV}}} = \frac{I_{\text{ACV}}}{v_{\text{ACV}}} \\ &= I(t)_{\text{applied}} \frac{dt}{dE} \end{aligned} \quad (7.121)$$

The influence of the reversibility of the electrochemical reaction on the SW net charge–potential curves ($(Q_{\text{SW}}/Q_{\text{F}}) - (E_{\text{index}} - E_{\text{c}}^{\ominus})$) is plotted in Fig. 7.48 for different values of the square wave amplitude ($E_{\text{SW}} = 25, 50, 100,$ and 150 mV) and three values of the dimensionless surface rate constant ($\bar{k}^0 (= k^0 \tau) = 10, 0.25,$ and 0.01), which correspond to reversible, quasi-reversible, and fully irreversible behaviors. Thus, it can be seen that for a reversible process (Fig. 7.48a), the $(Q_{\text{SW}}/Q_{\text{F}}) - (E_{\text{index}} - E_{\text{c}}^{\ominus})$ curves present a well-defined peak centered at the formal potential (dotted line), whose height and half-peak width increase with E_{SW} (in line with Eqs. (7.118) and (7.119)), until, for $E_{\text{SW}} > 100$ mV, the peak becomes a broad plateau whose height coincides with Q_{F} . This behavior can also be observed for the quasi-reversible case shown in Fig. 7.48b, although in this case, there is a smaller increase of the net charge curves with E_{SW} , and the plateau is not obtained for the values of E_{SW} used, with a higher square wave amplitude needed to obtain it. Nevertheless, even for this low value of the dimensionless rate constant, the peak potential of the SWVC curves coincides with the formal potential. This coincidence can be observed for values of $E_{\text{SW}} > 10$ mV.

The fully irreversible behavior is shown in Fig. 7.48c. In this case, a negative net charge appears (see the curve with $E_{\text{SW}} = 25$ mV). An increase of the square wave pulse leads to a growing peak in the SWVC curve, with its peak potential being shifted up to values close to that corresponding to formal potential. From these results, the following reversibility criteria as a function of the dimensionless rate constant

$$\bar{k}^0 = k^0 \tau \quad (7.122)$$

can be established:

Reversible Conditions ($\bar{k}^0 > 5$) The SWVC curve will reach a plateau for $E_{\text{SW}} > 100$ mV (with a deviation of less than 5 %). In contrast, the SWV curve is null.

Quasi-Reversible Conditions ($5 > \bar{k}^0 > 0.05$) The SWVC signal will reach the plateau for higher E_{SW} values than in the reversible case. Under these conditions, the SWV response is not null and shows a clear splitting for high enough E_{SW} values [6]. For example, for $\bar{k}^0 = 0.25$, values of $E_{\text{SW}} \geq 180$ mV and $E_{\text{SW}} \geq 140$ mV must be used to reach a well-defined charge plateau and a splitting of the current response, respectively.

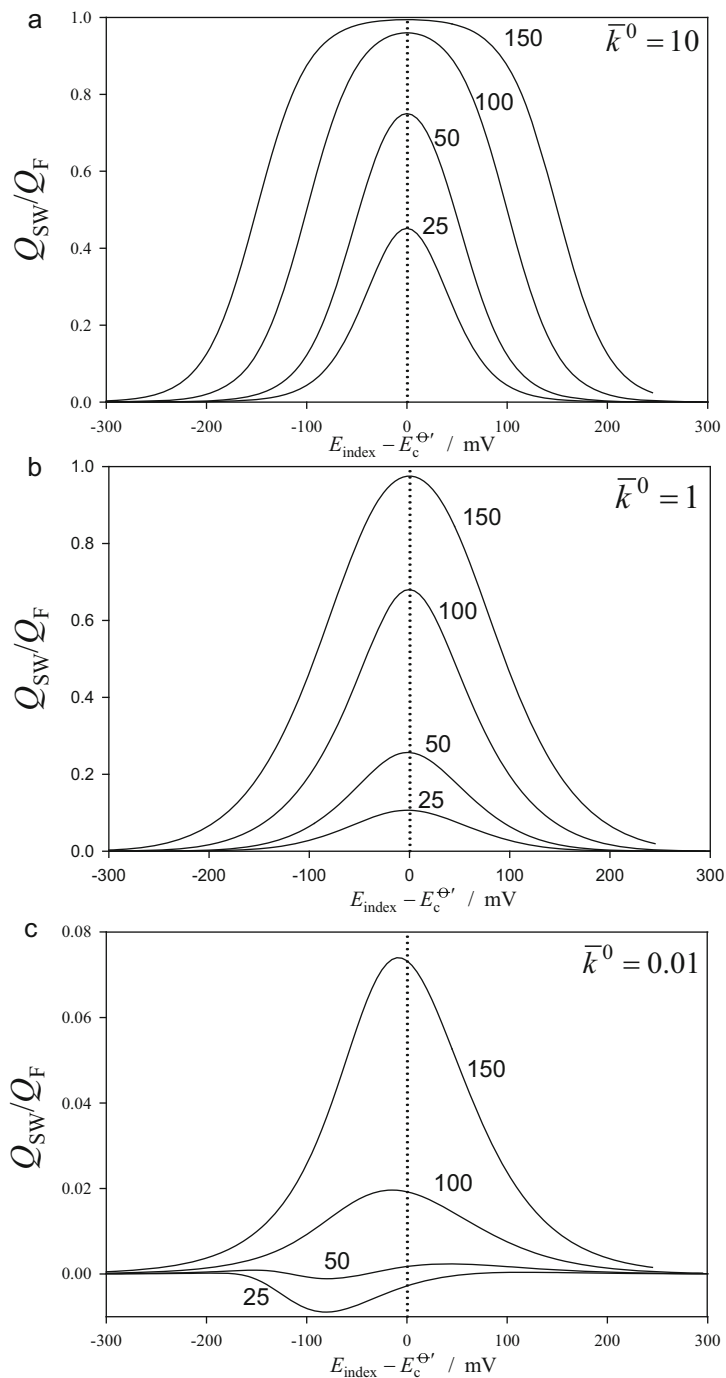


Fig. 7.48 Theoretical SWVC (Q_{SW}/Q_F) - ($E_{index} - E_c^{\Theta'}$) curves calculated from Eq. (7.115). The values of E_{SW} (in mV) and of the dimensionless rate constant \bar{k}^0 are shown in the figure. $|\Delta E_s| = 5$ mV, $T = 298.15$ K. Dotted lines mark the formal potential position. Reproduced from [5] with permission

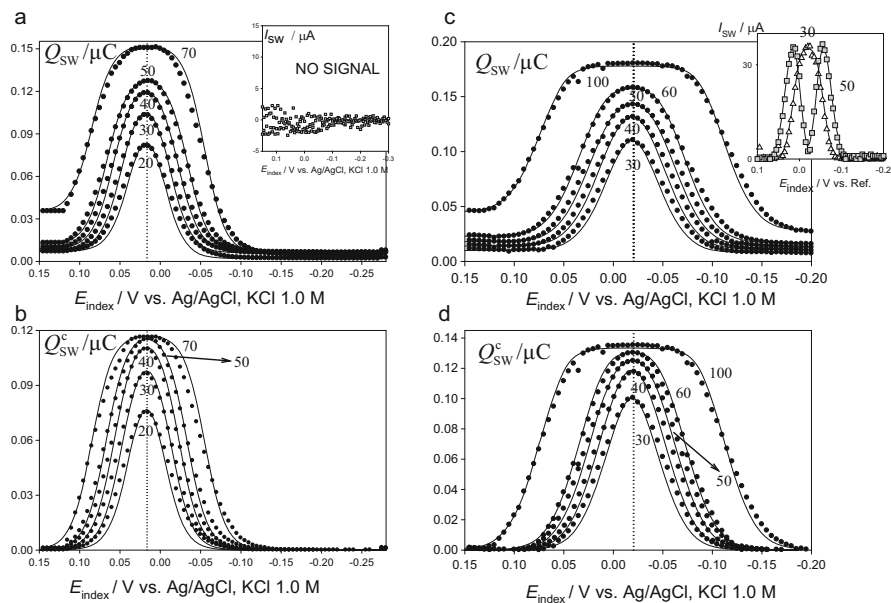


Fig. 7.49 Black dots: experimental cathodic SWVC $Q_{\text{SW}} - E$ curves (a and c) and corrected faradaic SWVC cathodic $Q_{\text{SW}}^c - E$ curves (b and d) of the 2-AQCA $10 \mu\text{M} + \text{HClO}_4$ 1 M adsorpted on a mercury electrode, $\tau = 5 \text{ ms}$ (a, b) and 0.5 ms (c, d). The values of the square wave pulse amplitudes (in mV) are shown in the figures. Solid lines: theoretical $Q_{\text{SW}} - E$ (a) and $Q_{\text{SW}}^c - E$ (b) curves for the above system calculated from Eqs. (7.116) and (7.138) corresponding to reversible processes with $E_c^{\Theta} = 0.017 \text{ V}$, $Q_F = 119 \text{ nC}$, $E_{\text{initial}} = 0.1$ (a, b) and 0.1500 V (c, d), $\Delta E_s = 5 \text{ mV}$, $R_u = 150 \Omega$, $r_s = 0.03445 \text{ cm}$, $n = 2$, and $T = 298 \text{ K}$. Inset figures in a and c: Experimental $I_{\text{SW}} - E$ curves for the 2-AQCA system corresponding to $\tau = 5 \text{ ms}$ (a) and 0.5 ms (c), $\Delta E_s = 5 \text{ mV}$ and $E_{\text{SW}} = 40 \text{ mV}$ (a) and $30, 50 \text{ mV}$ (b). Dotted line marks the formal potential position. Reproduced from [5] with permission

An increase in the pulse time τ allows the measurement of both E_c^{Θ} and Q_F from the SWVC curves, since the charge transfer process can be considered as reversible. Once these values are known, the kinetic parameters α and \bar{k}^0 can be obtained from the comparison between theoretical and experimental curves.

The experimental verification of the theoretical predictions for reversible and quasi-reversible behavior can be seen in Fig. 7.49, where the $Q_{\text{SW}} - E_{\text{index}}$ curves (symbols) are plotted corresponding to the di-electronic reduction of the system Anthraquinone-2-carboxylic acid (2-AQCA) $10 \mu\text{M}$ in HClO_4 1.0 M . These curves have been obtained for different values of the square wave pulse amplitude and for two values of the pulse time length $\tau = 5$ (reversible, Fig. 7.49a, b) and 0.5 ms (quasi-reversible, Fig. 7.49c, d).

Under reversible conditions, this process leads to a null square wave faradaic current, i.e., the current corresponding to this system cannot be distinguished from the background values (see inner figure in 7.49a). According to this, a broad plateau, independent of the value of the square wave pulse amplitude, should be

seen in the experimental charge–potential curves at values of $|E_{SW}| \geq 100\text{mV}$, in agreement with Eq. (7.119). However, although the curves corresponding to the highest E_{SW} values in Fig. 7.49a present this plateau, it increases with E_{SW} due to the contribution of the non-faradaic charge to the whole response (also responsible for the asymmetric non-faradaic baseline). This non-faradaic contribution can be easily quantified and eliminated (see Sect. 7.7.1.5) and the corrected charge–potential curves can be easily obtained by subtracting the non-faradaic component of the response, so obtaining the curves shown in Fig. 7.49b, which now show that the charge plateau is independent of the square wave pulse amplitude. The Q_F value obtained gives rise to a surface excess of $\Gamma_T = (4.1 \pm 0.1) \times 10^{-11} \text{ mol cm}^{-2}$ [5]. In Fig. 7.49a, b, the theoretical total $((Q_{SW} + Q_{SW,nf}) - E_{\text{index}})$ and corrected $(Q_{SW} - E_{\text{index}})$ faradaic curves have also been plotted, calculated from Eqs. (7.116) and (7.138) (solid lines), showing a very good agreement with the experimental ones.

The quasi-reversible behavior of the system 2-AQCA is plotted in Fig. 7.49c, d. The increase of the pH and the subsequent smaller availability of protons in solution cause a decrease of the surface rate constant and a shift of the formal surface potential of this system toward more negative values. The quasi-reversibility is confirmed from the current–potential curves shown in the inset figure of Fig. 7.49c, which shows a splitting of the $I_{SW} - E_{\text{index}}$ response for $E_{SW} = 50\text{mV}$ (see Sect. 7.7.1.4). The experimental $Q_{SW} - E_{\text{index}}$ curves of 2-AQCA under these conditions also increase with E_{SW} and present a well-defined charge plateau, but the square wave amplitude necessary for reaching it is higher than that corresponding to the reversible case. In order to obtain the values of the kinetic parameters of this system, theoretical $Q_{SW} - E_{\text{index}}$ curves have been calculated for different sets of values of \bar{k}^0 , α , and Q_F and compared with the experimental ones. The best fittings correspond to the following parameters: $\bar{k}^0 = 0.9$, $\alpha = 0.5$, and $Q_F = 0.135 \mu\text{C}$. In Fig. 7.49d, the experimental corrected charge–potential curves for this system have been plotted, along with the theoretical faradaic ones, calculated using Eqs. (7.116) and (7.138) and showing excellent agreement.

7.7.1.4 Square Wave Voltammetry

As in the case of DSCVC, the analysis of the SWV response of electrochemical reactions of surface-bound molecules has been carried out for non-reversible processes only, since in the case of fast charge transfers, negligible currents are obtained for the applications of potential pulses.

The expression for the SWV net current can be obtained from Eq. (6.130) and (7.6):

$$\psi_{\text{SW}} = \frac{I_{\text{SW}}}{(Q_{\text{F}}/\tau)} = \left[\bar{k}_{\text{red},2p-1}\theta_{2p-1} - \bar{k}_{\text{red},2p}\theta_{2p} - \bar{k}_{\text{T},2p-1} \sum_{j=1}^{2p-2} \frac{(1-\theta_j)}{1+e^{\eta_j}} \prod_{h=j+1}^{2p-1} \theta_h \right. \\ \left. + \bar{k}_{\text{T},2p} \sum_{j=1}^{2p-1} \frac{(1-\theta_j)}{1+e^{\eta_j}} \prod_{h=j+1}^{2p} \theta_h \right] \quad (7.123)$$

with θ_j given by Eq. (7.91) and

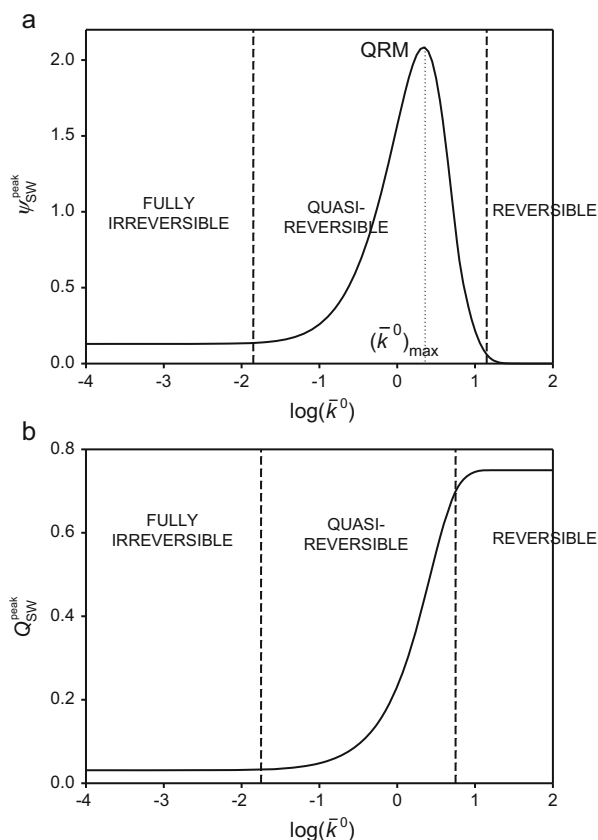
$$\left. \begin{aligned} \bar{k}_{\text{T},p} &= \bar{k}_{\text{red},p} + \bar{k}_{\text{ox},p} \\ \bar{k}_{\text{red},p} &= k_{\text{red},p}\tau \\ \bar{k}_{\text{ox},p} &= k_{\text{ox},p}\tau \end{aligned} \right\} \quad (7.124)$$

The SWV current of non-reversible electrochemical reactions depends on the dimensionless rate constant \bar{k}^0 (see Eq. (7.122)), on the charge transfer coefficient, and on the square wave amplitude E_{SW} . The main characteristics of the currents are the appearance of a “quasi-reversible maximum (QRM)” when the peak current is monitored in terms of the frequency (or the pulse length) [6] and the splitting of the net current. Thus, as can be observed in Staircase Voltammetry (see Fig. 6.23), the SWV current increases with \bar{k}^0 (or $\omega = k^0/f$) until reaching a maximum and then it falls sharply (see Fig. 7.50a). By determining \bar{k}_{max}^0 (or $\omega_{\text{max}} = k^0/f_{\text{max}}$) the value of k^0 can be obtained [6]. \bar{k}_{max}^0 (or ω_{max}) depends on the charge transfer coefficient and on the square wave amplitude E_{SW} , although average values of \bar{k}_{max}^0 (or ω_{max}) can be used if the charge transfer coefficient is not known. As indicated in Sect. 7.7.1.3, the charge increases with \bar{k}^0 until it reaches a plateau for fast charge transfers (see Fig. 7.50b).

The splitting of the SWV net current appears on increasing the square wave amplitude and the ratio ω . For example, for $E_{\text{SW}} = 50\text{mV}$, the splitting appears for surface electrode reactions with $\omega > 3$. Therefore, the values of the peak current shown in Fig. 7.50 for $\log(\bar{k}^0) \geq 0.17$ correspond to the appearance of two symmetrical peaks. The causes of the splitting are complex and are discussed in detail in [6]. The separation between the peak potentials is a linear function of E_{SW} and can also be used to estimate the rate constant of the process [33, 76, 77].

Various methods for the measure of k^0 based on the effect of the square wave amplitude on the SWV response have been proposed [33, 34]. The first relies on the so-called amplitude-based quasi-reversible maximum, i.e., a maximum value of the peak height which appears as a function of E_{SW} in the interval $0.01 \leq \omega \leq 0.5$ and

Fig. 7.50 Evolution of the SWV peak current ((a), Eq. (7.123)) and of the SWVC peak charge ((b), Eq. (7.115)) of a electrochemical reactions in terms of \bar{k}^0 . $E_{SW} = 50\text{ mV}$, $\Delta E_s = 5\text{ mV}$, $\alpha = 0.5$, $T = 298\text{ K}$



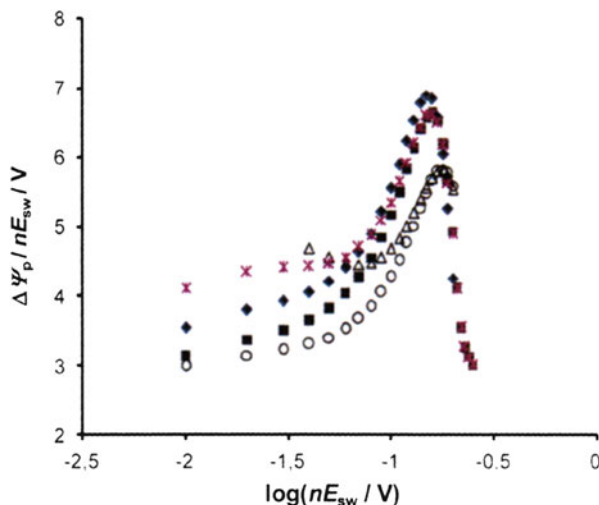
is independent of the charge transfer coefficient in the range $0.3 \leq \alpha \leq 0.7$ (see Fig. 7.51). The location of this maximum shifts linearly with ω , obeying the expression:

$$E_{SW,max}(\text{mV}) = -148.08 \log \omega + 0.80 \quad (7.125)$$

This relationship can be used to estimate k^0 .

The second procedure is based on the effect of the square wave amplitude on the peak potential separation between the anodic and cathodic components of the SWV response. This separation depends on both the reversibility of the surface charge transfer (through ω and E_{SW}). Thus, by plotting the differences $\Delta E_p = E_{p,c} - E_{p,a}$, with $E_{p,c}$ and $E_{p,a}$ being the peak potentials of the forward and reverse currents measured versus the index potential, or $\Delta E'_p = E'_{p,c} - E'_{p,a}$ with $E'_{p,c}$ and $E'_{p,a}$ being the peak potentials of the forward and reverse currents measured versus the real potential that is applied in each case (potential-corrected voltammograms), it is possible to obtain linear dependences between the peak potentials separation and

Fig. 7.51 Quasi-reversible surface-confined electrode mechanism. Amplitude-based quasi-reversible maxima for different values of the charge transfer coefficient. $(k^0/f) = 0.1$, $\Delta E_s = 5 \text{ mV}$, $n = 1$, $\alpha = 0.3$ (white circles); 0.4 (black squares); 0.5 (black diamonds); 0.6 (red asterisks); and 0.7 (white triangles). $T = 298 \text{ K}$. Reproduced from [33] with permission



E_{SW} which allows us to estimate the rate constant in the range $1 \leq (k^0 / \text{s}^{-1}) \leq 2000$ [34]. As an example, the SWV response and the plots of ΔE_p and $\Delta E'_p$ versus E_{SW} corresponding to a monolayer of azobenzene at a mercury electrode obtained for different frequencies are plotted in Fig. 7.52. By assuming a charge transfer coefficient of $\alpha = 0.5$, the value $k^0 = (23 \pm 2) \text{ s}^{-1}$ is found.

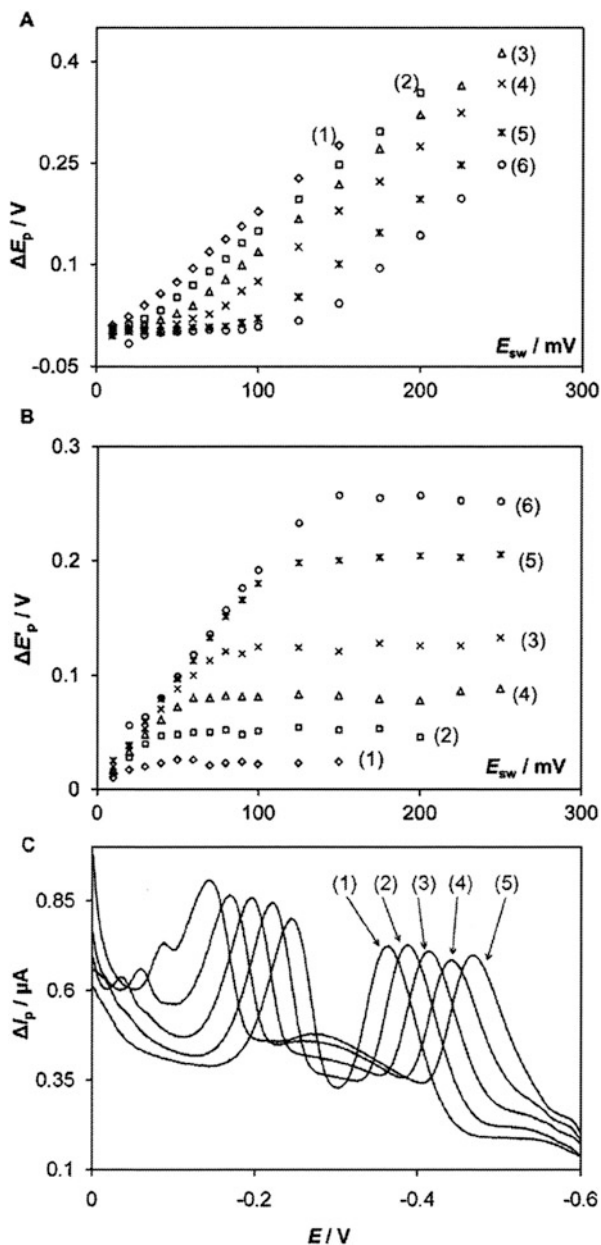
7.7.1.5 Non-faradaic Charge and Current Correction

As stated in Sect. 6.4.1, in the theoretical treatment of the electrochemical responses of surface-bound molecules, it has been assumed that the measured experimental currents and converted charges when a potential E_p is applied can be considered as the sum of a pure faradaic contribution, given by Eqs. (6.130) and (6.131), and a non-faradaic one, $Q_{p,nf}$ and $I_{p,nf}$ (given by Eqs. (6.150) and (6.157)). The correction of this non-faradaic component of the response can be done simply when subtractive electrochemical techniques are used). We assume the parallel capacitors model introduced by Damaskin [78], for which $C_{p,nf}$ can be written as

$$C_{p,nf} = C_{nf,O} f_O^{(p)}(\tau) + C_{nf,R} (1 - f_O^{(p)}(\tau)) \quad (7.126)$$

with $C_{nf,O}$ and $C_{nf,R}$ being the limiting values of the non-faradaic capacitance corresponding to $f_O^{(p)} = 1$ (totally oxidized monolayer) and $f_O^{(p)} = 0$ (totally reduced monolayer), respectively, which can be considered as practically constant, and $f_O^{(p)}(\tau) (= \Gamma_O^{(p)}(\tau) / \Gamma_T)$ is the surface coverage of oxidized species at time τ .

Fig. 7.52 Electrode reaction of azobenzene at HMDE. The dependence of the peak potential of conventional voltammograms (a) and potential-corrected voltammograms (b) on the amplitude, measured at different frequencies: f (in Hz) = 8 (1); 25 (2); 50 (3); 100 (4); 251 (5); and 398 (6). (c) Net SWV curves of azobenzene recorded at $f = 50$ Hz and E_{sw} (mV) = 100 (1); 125 (2); 150 (3); 175 (4); and 200 (5). The concentration of azobenzene is $0.1 \mu\text{M}$ in a phosphate buffer (pH = 6.75). The accumulation is carried out for 30 s at 0 V, $\Delta E_s = 1$ mV. Reproduced from [34] with permission



The analysis of the influence of the non-faradaic component corresponding to the converted charge-potential (Q - E) and current-potential (I - E) curves, is very different. A short discussion of this influence in some of the subtractive techniques analyzed follows.

Differential Staircase Voltcoulometry and Cyclic Voltammetry

In the case of Differential Staircase Voltcoulometry (DSCVC), the response $(Q_{\text{DSCVC}}/\Delta E) - \bar{E}$, with $\bar{E} = (E_j + E_{j+1})/2$ is, indeed, a capacitance which can be written as the sum of the faradaic contribution, given by Eq. (7.97) for reversible processes (and by Eq. (6.161) in CV, $(I_{\text{CV}}/v) - E$ response), and of the non-faradaic contribution (Eq. (7.126)). Thus, for a potential pulse E_p ,

$$C_T = C_f + C_{\text{nf}} = \frac{Q_F}{\Delta E} \left(\frac{1}{1 + e^{\eta_p}} - \frac{1}{1 + e^{\eta_{p-1}}} \right) + C_{\text{nf},\text{O}} + (C_{\text{nf},\text{R}} - C_{\text{nf},\text{O}}) (Q_p/Q_F) \quad (7.127)$$

for DSCVC, whereas for CV the total capacitance is

$$C_T = C_f + C_{\text{nf}} = \frac{F}{RT} Q_F \frac{e^{\eta}}{(1 + e^{\eta})^2} + C_{\text{nf},\text{O}} + (C_{\text{nf},\text{R}} - C_{\text{nf},\text{O}}) (Q/Q_F) \quad (7.128)$$

From Eq. (7.127) the following expression for the peak parameters of the capacitance–potential response $((Q_{\text{DSCVC}}/\Delta E) - \bar{E})$ are obtained [73]:

$$E_{\text{DSCVC,peak}} = E_c^{\Theta} + \frac{RT}{F} \ln \rho \quad (7.129)$$

$$\frac{Q_{\text{DSCVC}}^{\text{peak}}}{\Delta E} = \frac{Q_F}{\Delta E} \rho \frac{(e^{-\Delta\eta/2} - e^{\Delta\eta/2})}{1 - \rho^2 e^{\Delta\eta}} + C_{\text{nf},\text{O}} + (C_{\text{nf},\text{R}} - C_{\text{nf},\text{O}}) \frac{1}{1 + \rho e^{\Delta\eta/2}} \quad (7.130)$$

with

$$\rho = \frac{-(\delta/C_F)\Delta\eta e^{-\Delta\eta/2} + (e^{-\Delta\eta} - 1)\sqrt{1 + (\delta/C_F)\Delta\eta}}{e^{-\Delta\eta} - 1 + (\delta/C_F)\Delta\eta e^{-\Delta\eta/2}} \quad (7.131)$$

$$\delta = (C_{\text{nf},\text{R}} - C_{\text{nf},\text{O}}) \quad (7.132)$$

$$C_F = \frac{FQ_F}{RT} \quad (7.133)$$

$$\Delta\eta = \frac{F}{RT} \Delta E \quad (7.134)$$

Equations (7.129) and (7.130) take the following, simpler, expressions when $\Delta E \rightarrow 0$ (CV limit):

$$E_{\text{CV,peak}} = E_c^{\Theta} + \frac{RT}{F} \ln \left(\frac{1 + \delta}{1 - \delta} \right) \quad (7.135)$$

$$I_{\text{CV}}^{\text{peak}}/v = \frac{F}{4RT} Q_F (1 - \delta^2) + C_{\text{nf},\text{O}} + \frac{(C_{\text{nf},\text{R}} - C_{\text{nf},\text{O}})}{2} (1 + \delta) \quad (7.136)$$

Note that when there are no differences between the structure of an oxidized or reduced monolayer, it is fulfilled that $C_{\text{nf},\text{R}} \cong C_{\text{nf},\text{O}}$ (i.e., $\delta \cong 0$). Under these

conditions, the expression of the peak potential (divided by ΔE) would coincide with Eq. (7.98), i.e., it is not affected by double-layer effects, whereas the peak height given by Eq. (7.130) would be equivalent to that of Eq. (7.99) plus a constant value $C_{\text{nf},\text{O}}$.

Square Wave Voltcoulometry

In the case of SWVC, the net non-faradaic charge, which corresponds to the difference $Q_{\text{SW},\text{nf}} = Q_{2p-1,\text{nf}} - Q_{2p,\text{nf}} = Q_{\text{f},\text{nf}} - Q_{\text{r},\text{nf}}$, is (see Eq. (6.150)),

$$Q_{\text{SW},\text{nf}} = \frac{2|E_{\text{SW}}|}{R_{\text{u}}} e^{-P(\tau)} \int_0^{\tau} e^{P(t)} dt \quad (7.137)$$

with R_{u} being the uncompensated resistance and $P(t)$ given by Eq. (6.151). Equation (7.137) has been obtained by considering that the pulse time length τ is much greater than the time constants ($R_{\text{u}}C_{\text{nf},\text{O}}$) and/or ($R_{\text{u}}C_{\text{nf},\text{R}}$) [5].

Note that, in agreement with Eq. (7.137), the non-faradaic contribution to the $Q_{\text{SW}} - E$ curve is due only to the potential jump (equal to $2E_{\text{SW}}$). This behavior is due to the differential character of the $Q_{\text{SW},\text{nf}} - E$ response.

Under reversible conditions, the following simplified expression for the net non-faradaic charge is obtained:

$$Q_{\text{SW},\text{nf}} = 2E_{\text{SW}} \left(C_{\text{nf},\text{O}} + \frac{\delta}{1 + e^{\eta_{2p}}} \right) \quad (7.138)$$

This equation indicates that $Q_{\text{SW},\text{nf}}$ gives rise to a baseline equal to $2E_{\text{SW}}C_{\text{nf},\text{R}}$ for $E_p \ll E_c^{\ominus}$, and equal to $2E_{\text{SW}}C_{\text{nf},\text{O}}$ for $E_p \gg E_c^{\ominus}$.

Equation (7.138) can be considered as valid for dimensionless rate constants of the order of $(k^0\tau) \geq 1$. For smaller $(k^0\tau)$ values, the general expression of $Q_{\text{SW},\text{nf}}$, given by Eq. (7.137), must be used.

Finally, note that when $C_{\text{nf},\text{O}} \simeq C_{\text{nf},\text{R}} = C_{\text{nf}}$, the non-faradaic charge logically takes the constant value $2E_{\text{SW}}C_{\text{nf}}$, whatever the value of k^0 was.

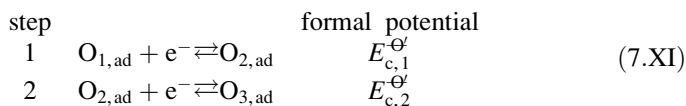
Square Wave Voltammetry

The correction of the non-faradaic component of the current curve is of special relevance in the case of surface-bound molecules, especially in the case of biological molecules such as proteins or enzymes, since for these species the coverages are very low and the faradaic response can be much smaller than the non-faradaic one [79–81]. In this sense, SWV has the advantage of giving rise to practically constant non-faradaic currents due to the subtractive nature of the signal which are typically removed from the total response as a baseline correction. In the case of the non-faradaic current taking different values at very positive and negative potentials, the usual strategy is to carry out a polynomial interpolation of these values in order to generate a complete non-faradaic response which will be subtracted from the total response [79–83].

Another more sophisticated approach is to make a Fourier Transform analysis of the response in the way proposed by Bond et al. [84, 85]. In this case, the perturbation is a continuous function of time (a ramped square wave waveform) which combines a dc potential ramp with a square wave of potential that can be described as a combination of sinusoidal functions. Under these conditions, the faradaic contribution to the response generates even harmonics only (i.e., the non-faradaic current goes exclusively through odd harmonics). Thus, the analysis of the even harmonics will provide excellent faradaic-to-non-faradaic current ratios.

7.7.2 Multi-electron Electrochemical Reactions

In this section, surface two-electron transfer reactions in line with the following reaction scheme:



are analyzed using some subtractive techniques.

7.7.2.1 Reversible Electrochemical Reactions

When both electron transfers are very fast, only Differential Staircase Voltcoulometry (DSCVC) and SWVC are employed, since the corresponding DSCVC and SWV are not adequate under these conditions.

The converted charge in DSCVC for a reversible EE mechanism is given by [86] (see Eq. (6.180) and Eq. (7.2))

$$\frac{1}{Q_F} Q_{DSCVC}^{EE} = Z_p^{EE} \quad (7.139)$$

with Z_p^{EE} given by Eq. (7.58).

When $\Delta E \leq 10 \text{ mV}$

$$\frac{Q_{DSCVC}^{EE}}{\Delta E} \cong \frac{dQ^{EE}}{dE} = \frac{I_{CV}^{EE}}{\nu} \quad (7.140)$$

So, the DSCVC curves have similar behavior to the CV ones (see Sect. 6.4.3.1). Nevertheless, DSCVC has the advantage of presenting a time-independent, easily characterizable peak-shaped response for any value of the pulse amplitude.

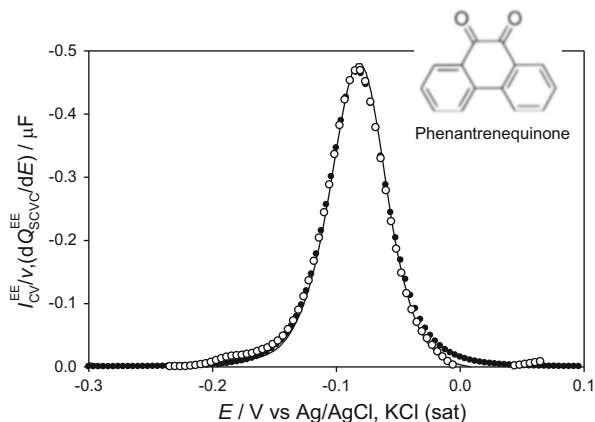


Fig. 7.53 Experimental DSCVC $dQ_{\text{SCVC}}^{\text{EE}}/dE - E$ curves (white dots) and LSV $I_{\text{CV}}^{\text{EE}}/v - E$ ones (solid lines) corresponding to PQ $1 \mu\text{M}$ + PBS 0.1 M ($\text{pH} = 7.2$) adsorbed on a mercury electrode ($r_s = 0.02 \text{ cm}$). The scan rate is in both cases $v = 150 \text{ mV s}^{-1}$. The pulse amplitude in DSCVC is $E_s = 5 \text{ mV}$. Theoretical DSCVC curves (black dots) were calculated from Eq. (7.139) using the following parameters: $E_{c,1}^{\text{Ox}} = -99 \text{ mV}$, $E_{c,2}^{\text{Ox}} = -65 \text{ mV}$, $Q_F = 15.1 \text{ nC}$. $T = 298 \text{ K}$. Reproduced from [86] with permission

An experimental example can be seen in Fig. 7.53 in which the DSCVC curves obtained for a staircase potential ($dQ^{\text{EE}}/dE - E$ curves, white dots) are plotted together with the LSV ones corresponding to the application of a linear potential sweep ($I_{\text{CV}}^{\text{EE}}/v - E$ curves, solid lines) to a solution of Phenantrenequinone (PQ) in an aqueous-buffered media adsorbed at a mercury electrode. These curves have been obtained for a scan rate $v = 150 \text{ mV s}^{-1}$ in both techniques. PQ has two carbonyl groups, which can be reduced in a two-electron two-proton reversible conversion, where these last transfers not being rate limiting [86]. Both DSCVC and CV responses in this figure are superimposed, which points to a reversible electrochemical conversion (i.e., responses independent of the electrochemical technique from which they have been obtained [75, 86]). The half-peak width of the curves in Fig. 7.53 is $W_{1/2} = 51 \text{ mV}$, a higher value than the 45 mV expected for an E process of two electrons. Therefore, it can be considered that it behaves as a two-electron electrochemical reaction with superimposed signals. Thus, from the expression of $W_{1/2}$ given by Eq. (6.183), we get the following value of $\Delta E_c^{\text{Ox}} = 34 \text{ mV}$ ($K = 3.76$; see Eq. (7.61)). By combining this value with the peak potential which coincides with the average formal potential \bar{E}_c^{Ox} , the following values of the formal potentials are obtained: $E_{c,1}^{\text{Ox}} = -99 \text{ mV}$ and $E_{c,2}^{\text{Ox}} = -65 \text{ mV}$ vs. Reference. The surface concentration of PQ can be determined from the peak height leading to $Q_F = 15.1 \text{ nC}$ (i.e., $\Gamma_T = 3.11 \times 10^{-11} \text{ mol cm}^{-2}$). An additional verification of the reversibility of the responses arises from the excellent agreement between the

experimental DSCVC and CV curves and the theoretical response calculated from Eq. (7.139), by using the experimental values obtained from this figure.

With respect to SWVC, as indicated in Sect. 7.7.1.3, this technique has important advantages since, in addition to the benefits derived from the application of a square waveform, the $Q_{\text{SW}} - E$ curves present a stationary character when the electrode processes are fast given by

$$\frac{Q_{\text{SW}}}{Q_{\text{F}}} = \frac{Q_{2p-1} - Q_{2p}}{Q_{\text{F}}} = -Z_{2p}^{\text{EE}} \quad (7.141)$$

with Z_p^{EE} given by Eq. (7.58).

This technique has been applied to the study of the reduction of the Keggin heteropolyanion $[\text{PMo}_{12}\text{O}_{40}]^{3-}$ immobilized at the surface of a BDD electrode in aqueous media with two electrolytes: HClO_4 1.0 M and LiClO_4 0.1 M. In the case of carbon electrodes like Glassy Carbon or Pyrolytic Graphite electrodes, in aqueous acidic media, three reversible waves are observed in the potential range (0.6, -0.2) V, for each of which a two-electron transfer has been assigned [61, 74].

Square Wave charge-potential curves corresponding to $[\text{PMo}_{12}\text{O}_{40}]^{3-}$ monolayers in both electrolytes for $E_{\text{SW}} = 25$ mV and $\tau = 100$ ms (lines) are shown in Fig. 7.54. These curves show three very well-defined peaks with a nearly constant baseline. Actually, the resolution achieved in the three peaks is a great improvement on that obtained with Cyclic Voltammetry.

It has been assumed that each peak corresponds to an isolated EE process with a not very negative or even a positive value of ΔE_c^{\ominus} such that each one (denoted as processes I, II, and III) can be treated separately from the others. From the values of the peak parameters of these responses, it is possible to obtain the formal potentials of the different steps. From these values, theoretical $Q_{\text{SW}}^{\text{EE}} - E_{\text{index}}$ curves have been calculated using Eq. (7.141) for each of the three processes, concluding that the overall response is the sum of the three individual ones. From the results, it can be concluded that the above assumption of three isolated EE processes is justified, since no significant difference between the three different individual processes and the overall response is obtained (relative error between individual and overall lesser than 3 %) [74].

An excellent agreement is obtained from the comparison between experimental and theoretical data. The results obtained for the formal potentials are shown in Table 7.4. From these values it can be concluded that an aprotic electrolyte leads to a shift in the formal potential of the different steps which is more noticeable in process III (shift of 240 mV in ΔE_c^{\ominus}). This may be due to the increasing formal charge in the immobilized molecules, which cannot be compensated for the addition of protons [87].

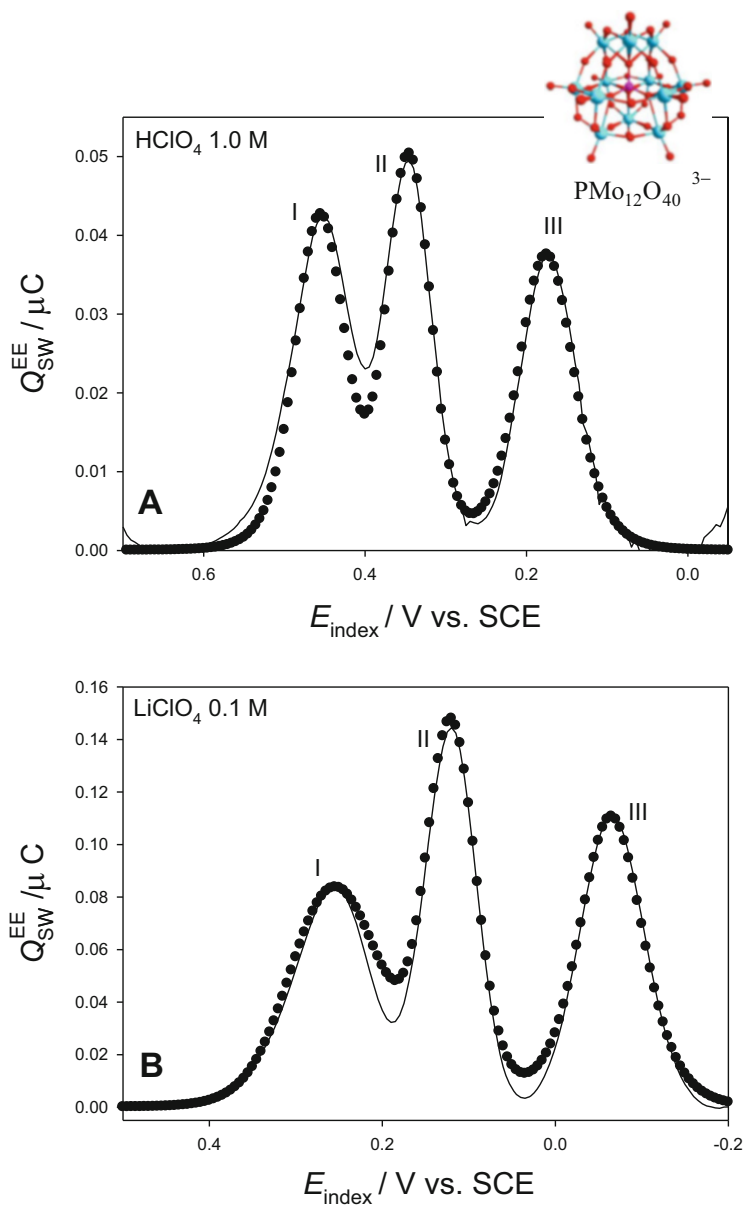


Fig. 7.54 (Lines) Experimental $Q_{SW}^{EE} - E_{index}$ curves of a $[PMo_{12}O_{40}]^{3-}$ monolayer at a BDD electrode for aqueous $HClO_4$ 1.0 M (a) and $LiClO_4$ 0.1 M (b) media. $\tau = 100$ ms ($f = 5$ Hz). (Black dots) Theoretical $Q_{SW}^{EE} - E_{index}$ curves calculated from Eq. (7.141) by using the data shown in Table 7.4 for the two media above. Reproduced from [74] with permission

Table 7.4 Average potentials $\bar{E}_{c,i}^{\Theta'}$ and $\Delta E_{c,i}^{\Theta'} = E_{c,2,i}^{\Theta'} - E_{c,1,i}^{\Theta'}$, for the three peaks ($i = \text{I, II, and III}$), corresponding to the direct response of $[\text{PMo}_{12}\text{O}_{40}]^{3-}$ monolayer shown in Fig. 7.54 [74]. $\tau = 100\text{ms}$

HClO ₄ 1.0 M				
Process	$\bar{E}_{c,i}^{\Theta'}$ (mV) vs. SCE	$Q_{\text{SW}}^{\text{peak},i}/Q_{\text{F}}$	$\Delta E_{c,i}^{\Theta'}$ (mV) vs. SCE	$E_{c,1,i}^{\Theta'}, E_{c,2,i}^{\Theta'}$ (mV) vs. SCE
I	451	1.21	17	447, 463
II	348	1.41	85	305, 385
III	173	1.07	-10	180, 170
LiClO ₄ 0.1 M				
Process	$\bar{E}_{c,i}^{\Theta'}$ (mV) vs. SCE	$Q_{\text{peak},i}/Q_{\text{F}}$	$\Delta E_{c,i}^{\Theta'}$ (mV) vs. SCE	$E_{c,1,i}^{\Theta'}, E_{c,2,i}^{\Theta'}$ (mV) vs. SCE
I	255	0.77	-55	282, 227
II	120	1.32	46	97, 143
III	-65	1.01	-19	-55, -74

7.7.2.2 Non-reversible Electrochemical Reactions

When both redox reactions are sluggish, both SWV and SWVC responses become very complex because they are influenced by both the kinetic and thermodynamic parameters of the electrode reactions and those associated with the square wave waveform (i.e., E_{SW}, f , and ΔE_{s}). Basically, when two peaks are observed, their peak heights are determined mainly by the magnitude of the dimensionless kinetic constants $\bar{k}_1^0 = k_1^0\tau$ and $\bar{k}_2^0 = k_2^0\tau$, and the charge transfer coefficients α_1 and α_2 , whereas their position depends on the difference between formal potentials $\Delta E_{\text{c}}^{\Theta'}$ and the ratio \bar{k}_1^0/\bar{k}_2^0 [6, 88].

In order to obtain some examples of the SWV and SWVC curves for several characteristic values of $\Delta E_{\text{c}}^{\Theta'}$ and \bar{k}_1^0/\bar{k}_2^0 , the recurrent expressions for the current given by Eqs. (6.185)–(6.191) have been applied to the square wave potential sequence (the charge have been calculated by integrating the corresponding currents).

In Fig. 7.55, the SWV and SWVC curves for an EE mechanism with identical values of the surface rate constants $\bar{k}_1^0/\bar{k}_2^0 = 1$ are plotted. As can be inferred, the Square Wave Voltammograms (curves a and b) present a maximum value for the peak currents (quasi-reversible maximum, QRM, see Sect. 7.7.1.4) for $\bar{k}_1^0 = \bar{k}_2^0 = 1$, and a splitting is observed for $\bar{k}_1^0 = \bar{k}_2^0 = 1.5$ with much lower peak height. For $\bar{k}_i^0 \ll 1$ ($i = 1, 2$), the current decreases with \bar{k}_i^0 .

From Fig. 7.55c, d, it is clear that the converted charge–potential curves obtained with SWVC are much more sensitive than the SWV ones for quasi-reversible electrode reactions, although the response charge–potential (SWVC curves) is very weak for \bar{k}_i^0 values below 0.05 (compare curves 7.55a, b with 7.55c and d for these \bar{k}_i^0 values). This can also be observed from these curves as both SWV and

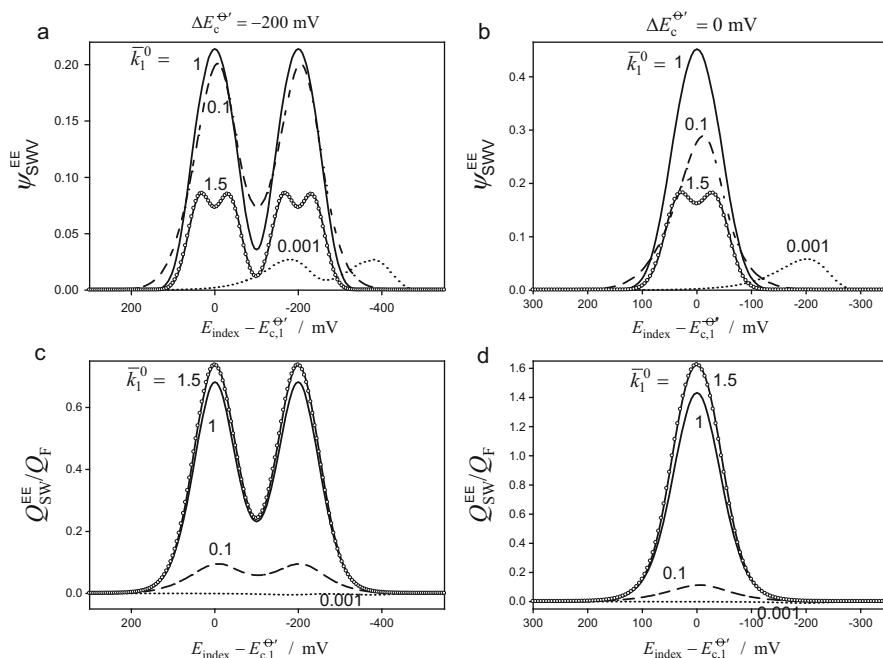


Fig. 7.55 SWV and SWVC curves for a non-reversible surface EE process calculated from Eqs. (6.185) to (6.191) and Eq. (7.5). The values of the dimensionless rate constant \bar{k}_1^0 and of the difference between formal potentials $\Delta E_c^{\Theta'}$ appear on the figures. $\bar{k}_1^0/\bar{k}_2^0 = 1$, $\alpha_1 = \alpha_2 = 0.5$, $E_{\text{SW}} = 50$ mV, $\Delta E_s = 5$ mV, $T = 298$ K

SWVC signals are not centered with respect to the average formal potential $E_c^{\Theta'}$ and shift toward more negative potentials as \bar{k}_i^0 decreases.

In Fig. 7.56, SWV and SWVC curves for $\bar{k}_1^0/\bar{k}_2^0 = 10^2$ under the same conditions of Fig. 7.55 are plotted. As can be seen, for $\Delta E_c^{\Theta'} = -200$ mV, the behavior of these curves (see Fig. 7.56a, c) is markedly different to that shown in Fig. 7.55a, c, since the first peak in Fig. 7.56a (which is itself split for $\bar{k}_1^0 = 1.5$) is higher than the second. Moreover, for $\bar{k}_1^0 \leq 1.5$ the second peak is shifted toward much more negative potentials than in Fig. 7.55a. Contrary to what is observed in Fig. 7.55c, SWCV curves in Fig. 7.56c do not present splitting. Figure 7.56b, d corresponding to $\Delta E_c^{\Theta'} = 0$ mV present a slightly different morphology to that corresponding to Fig. 7.55b, d, although their peak heights are halved.

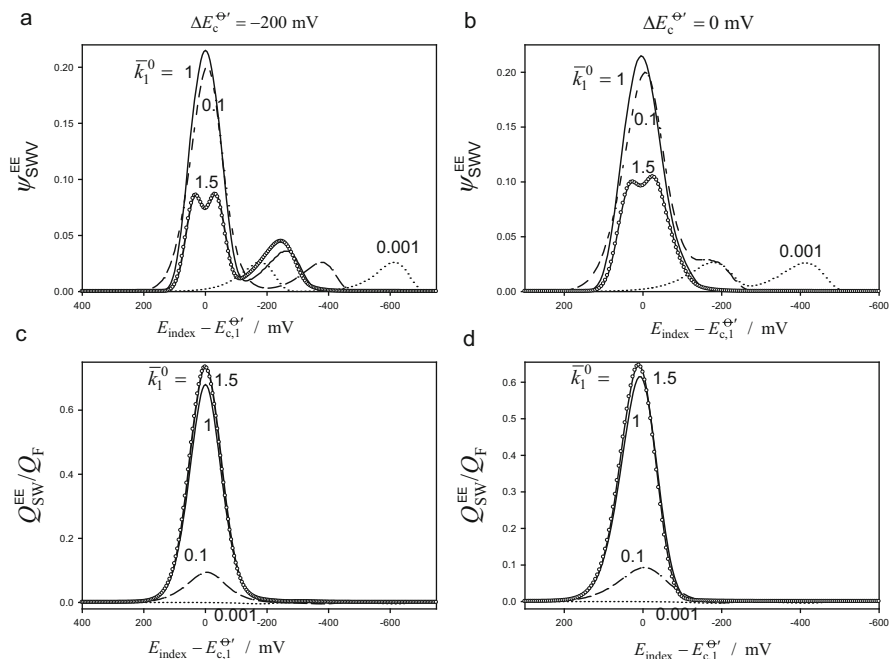


Fig. 7.56 SWV and SWVC curves for a non-reversible surface EE process calculated from Eqs. (6.185) to (6.191) and Eq. (7.5). The values of the dimensionless rate constant \bar{k}_1^0 and of the difference between formal potentials $\Delta E_c^{\Theta'}$ appear on the figures. $\bar{k}_1^0/\bar{k}_2^0 = 10^2$, $\alpha_1 = \alpha_2 = 0.5$, $E_{SW} = 50\text{ mV}$, $\Delta E_s = 5\text{ mV}$, $T = 298\text{ K}$

7.7.3 Electrocatalytic Reactions at Modified Electrodes

In the last 20 years, a big effort has been made to characterize different reaction schemes taking place at modified electrodes, with special focus on the case of biomolecules in what has been called “Protein Film Voltammetry” [79–83]. Among the different situations analyzed with multipulse techniques (including Cyclic Voltammetry), it can be cited the surface ECE process [89, 90] and surface reactions preceded by homogeneous chemical reactions [91]. For a more detailed revision of the different mechanisms analyzed in the case of SWV, see [19].

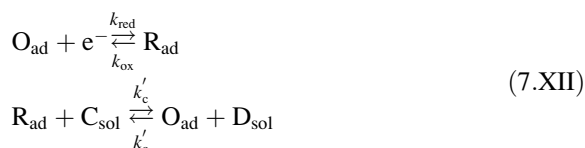
The most interesting reaction scheme is the electrocatalytic one. Electrocatalysis at modified electrodes is accomplished by an immobilized redox mediator, which is activated electrochemically by applying an electrical perturbation (potential or current) to the supporting electrode. As a result, the chemical or electrochemical conversion of other species located in the solution adjacent to the electrode surface (which does not occur, or occurs very slowly in the absence of the immobilized catalyst) takes place [1, 92–94]. The main advantage of this kind of electrocatalyzed reactions lies in the large number of synthetic procedures for

modifying different electrode surfaces with electrochemically active molecules or biomolecules (e.g., proteins, enzymes).

Two different variants of the electrocatalytic process are analyzed here. The first one corresponds to first-order conditions and in this case one-electron and two-electron charge transfers coupled to the chemical reaction are discussed under SWV and Voltcoulometry conditions [19, 83, 95–97]. After that, a second-order catalytic scheme is presented in which the mass transport of the substrate of the chemical reaction is considered [98, 99].

7.7.3.1 Pseudo-First-Order Electrocatalytic Processes: EC' Process

The following reaction scheme is considered:



where O_{ad} and R_{ad} refer to the redox couple bound to the electrode surface and C_{sol} and D_{sol} are species in solution. In this case, the redox mediator O suffers a single reduction. It is assumed that the surface concentration of species C_{sol} remains constant and equal to its bulk value, c_{C}^* (such that the chemical reaction can be considered to be of pseudo-first order) and the chemical reaction behaves as irreversible,



with the pseudo-first-order rate constant given by

$$k_c = k_c' c_{\text{C}}^* \quad (7.142)$$

The expressions for the SWV and SWVC curves obtained for the application of an arbitrary sequence of potential pulses are given by Eqs. (6.202) and (6.205), respectively. For the usual particular case of a fast catalytic reaction, i.e., $k_c \gg 1$, the following limiting expressions for the SWV current and SWVC charge can be obtained:

SWV (Current–Potential Curves)

For fast catalyzed reactions, the stationary (independent of time) $I_{\text{SWV}} - E$ response is given by (see Eqs. (6.207) and (7.6)),

$$\psi_{\text{SW}}^{\text{cat}} = \frac{I_{\text{SW}}^{\text{cat}}}{(Q_{\text{F}}/\tau)} = \bar{k}_{\text{c}} \left(\frac{k_{\text{red},\text{f}}}{k_{\text{T},\text{f}}^{\text{c}}} - \frac{k_{\text{red},\text{r}}}{k_{\text{T},\text{r}}^{\text{c}}} \right) \quad (7.143)$$

where

$$k_{\text{T},\text{i}}^{\text{c}} = k_{\text{red},\text{i}} + k_{\text{ox},\text{i}} + k_{\text{c}} \text{ i} = \text{f, r} \quad (7.144)$$

$$\bar{k}_{\text{c}} = k_{\text{c}} \tau \quad (7.145)$$

and Q_{F} given by Eq. (7.93). Subindexes “f” and “r” refer to the forward and reverse pulses (i.e., $2p - 1$ and $2p$, respectively).

For a reversible charge transfer, Eq. (7.143) becomes

$$\psi_{\text{SW,rev}}^{\text{cat}} = \bar{k}_{\text{c}} \left(\frac{1}{1 + e^{\eta_{\text{f}}}} - \frac{1}{1 + e^{\eta_{\text{r}}}} \right) \quad (7.146)$$

with $\eta_{\text{f}} = \eta_{\text{r}} + (2F/(RT))E_{\text{SW}}$.

The dimensionless SWV curve is identical to the stationary SWV curve obtained for a fast electrochemical reaction with solution soluble molecules given by Eqs. (7.35) or (7.36) for spherical or disc electrodes, respectively, and also to that obtained for a reversible surface electrode process (Eq. (7.116)). Therefore, the peak potential coincides with the formal potential and the half-peak width is given by Eq. (7.32). The peak height is amplified by \bar{k}_{c} :

$$\psi_{\text{SW,rev}}^{\text{cat,peak}} = \bar{k}_{\text{c}} \tan h \left(\frac{FE_{\text{SW}}}{2RT} \right) \quad (7.147)$$

SWVC (Charge–Potential Curves)

Under these conditions ($\bar{k}_{\text{c}} \gg 1$), the following $Q_{\text{SW}} - E$ relation is obtained (see Eqs. (6.208) and (7.8)):

$$\frac{Q_{\text{SW}}^{\text{cat}}}{Q_{\text{F}}} = \frac{k_{\text{red},\text{f}}}{k_{\text{T},\text{r}}^{\text{c}}} - \frac{k_{\text{red},\text{r}}(1 + k_{\text{c}}\tau)}{k_{\text{T},\text{r}}^{\text{c}}} - \frac{k_{\text{c}}}{k_{\text{T},\text{r}}^{\text{c}}} \left(\frac{k_{\text{red},\text{f}}}{k_{\text{T},\text{r}}^{\text{c}}} - \frac{k_{\text{red},\text{r}}}{k_{\text{T},\text{r}}^{\text{c}}} \right) \quad (7.148)$$

This equation shows that a steady state (i.e., an independent of time behavior) cannot be obtained for the $Q_{\text{SW}}^{\text{cat}} - E$ curves.

For a reversible charge transfer, Eq. (7.148) simplifies to

$$\frac{Q_{\text{SW,rev}}^{\text{cat}}}{Q_{\text{F}}} = \frac{1}{1 + e^{\eta_{\text{f}}}} - \frac{1 + \bar{k}_{\text{c}}}{1 + e^{\eta_{\text{r}}}} \quad (7.149)$$

These curves also present a peak-shaped response, but it is distorted by the catalytic contribution $(1 + \bar{k}_{\text{c}})$ which appears in the backward term. In

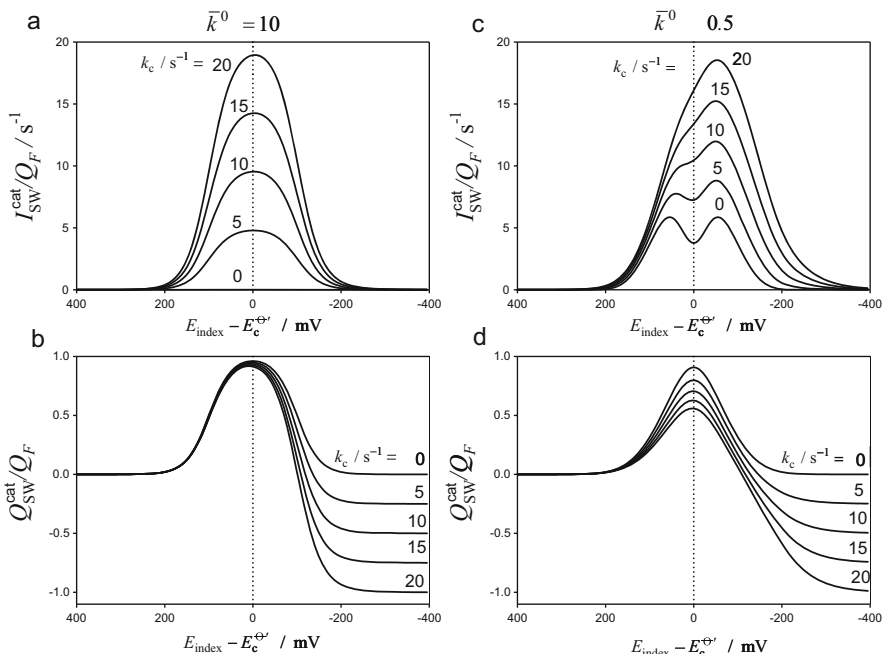


Fig. 7.57 Theoretical $I_{SW}^{cat}/Q_F - (E - E_c^{\Theta'})$ (a, c) and $Q_{SW}^{cat}/Q_F - (E - E_c^{\Theta'})$ (b, d) calculated from Eqs. (7.143) to (7.149) in Square Wave Voltammetry and Voltcoulometry, respectively, for a catalytic mechanism. $k_c = 10 \text{ s}^{-1}$. The values of k_c (in s^{-1}) and of the dimensionless heterogeneous rate constant \bar{k}^0 are on the curves. $\Delta E_s = 5 \text{ mV}$, $E_{SW} = 100 \text{ mV}$, $\tau = 50 \text{ ms}$, $T = 298 \text{ K}$, $\alpha = 0.5$. Reproduced from [95] with permission

agreement with Eqs. (7.148) and (7.149), the following charge limits are obtained for $E \rightarrow \pm\infty$:

$$\left. \begin{aligned} \frac{Q_{SW}^{cat}}{Q_F} \Big|_{E \rightarrow \infty} &= 0 \\ \frac{Q_{SW}^{cat}}{Q_F} \Big|_{E \rightarrow -\infty} &= -\bar{k}_c \end{aligned} \right\} \quad (7.150)$$

When the charge transfer step is an oxidation instead of a reduction, Eqs. (7.143) and (7.148) remain valid by changing k_{red} for k_{ox} .

Theoretical $I_{SW}^{cat}/Q_F - (E - E_c^{\Theta'})$ and $Q_{SW}^{cat} - (E - E_c^{\Theta'})$ curves, calculated from Eqs. (7.143) and (7.148), for different values of the catalytic rate constant k_c and a fixed square wave pulse amplitude $E_{SW} = 100 \text{ mV}$ are plotted in Fig. 7.57. Two values of the dimensionless heterogeneous rate constant have been considered $\bar{k}^0 = 10$ and 0.5 , which refer to reversible (Fig. 7.57a, b) and quasi-reversible (Fig. 7.57c, d) electrochemical behavior. The case corresponding to a simple

charge transfer process ($\bar{k}_c = 0$) has been included for comparison. Note that this process gives rise to null current under Nernstian conditions (see Fig. 7.57a) [5].

From the $I_{\text{SW}}^{\text{cat}}/Q_{\text{F}} - (E - E_{\text{c}}^{\Theta'})$ curves in Fig. 7.57a, c, it can be seen that the current increases with \bar{k}_c , whatever the reversibility degree of the electrochemical step. Under reversible conditions (Fig. 7.57a), these curves present a peak-shaped feature centered at the formal potential of the immobilized electro-active species (dotted line). When the charge transfer step is quasi-reversible, the current curves show one or two peaks depending on the values of \bar{k}_c and E_{SW} . Typically, an increase of \bar{k}_c gives rise to a single peak located at more negative potentials than $E_{\text{c}}^{\Theta'}$ (see Fig. 7.57c). No simple expressions for the peak parameters can be obtained in these conditions.

The $Q_{\text{SW}}^{\text{cat}} - (E - E_{\text{c}}^{\Theta'})$ curves in Fig. 7.57b, d show a peak-shaped response whose cathodic limit is determined by the catalytic rate constant value (see Eq. (7.150)), independently of the heterogeneous rate constant \bar{k}^0 . The peak height of the charge–potential curves increases with E_{SW} until a charge plateau equal to Q_{F} is obtained for $E_{\text{SW}} \geq 120\text{mV}$ in the reversible case (see Fig. 7.57b). For processes with non-reversible charge transfer step a higher $|E_{\text{SW}}|$ is necessary to reach a plateau, independently of the square wave pulse amplitude.

The peak potential expression of the $Q_{\text{SW}}^{\text{cat}} - E$ curves can be obtained for reversible conditions by imposing $dQ_{\text{SW}}^{\text{cat}}/dE = 0$ in Eq. (7.149):

$$E_{\text{peak}} = E_{\text{c}}^{\Theta'} - \frac{RT}{F} \ln \left(\frac{\bar{k}_c - (e^{\eta_{\text{SW}}} - e^{-\eta_{\text{SW}}})\sqrt{1 + \bar{k}_c}}{e^{-\eta_{\text{SW}}} - (1 + \bar{k}_c)e^{\eta_{\text{SW}}}} \right) \quad (7.151)$$

with η_{SW} given by Eq. (7.33).

This equation indicates that the peak potential is located at more negative values than $E_{\text{c}}^{\Theta'}$ and it moves toward the formal potential as E_{SW} increases. When high values of the square wave pulse amplitude are used, the $Q_{\text{SW}}^{\text{cat}} - E$ curves show a broad plateau which is centered at a potential $E = E_{\text{c}}^{\Theta'} - (RT/(2F))\ln(1 + \bar{k}_c)$. Another interesting characteristic of the $Q_{\text{SW}}^{\text{cat}} - E$ curve is the cross potential for which the converted charge is null. For reversible conditions, it is given by (see Eq. (7.149) for $Q_{\text{SW}}^{\text{cat}} = 0$),

$$E_{Q_{\text{SW}}^{\text{cat}}=0} = E_{\text{c}}^{\Theta'} + \frac{RT}{F} \ln \left(\frac{e^{\eta_{\text{SW}}} - e^{-\eta_{\text{SW}}}(1 + \bar{k}_c)}{\bar{k}_c} \right) \quad (7.152)$$

This expression simplifies for high values of the square wave pulse amplitude:

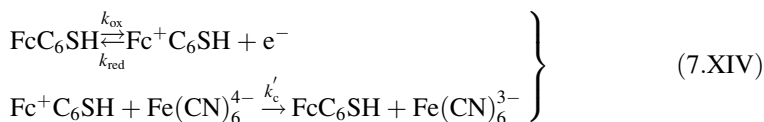
$$E_{Q_{\text{SW}}^{\text{cat}}=0} = E_{\text{c}}^{\Theta'} - \frac{RT}{F} \ln(\bar{k}_c) + E_{\text{SW}} \quad (7.153)$$

so this potential moves linearly toward positive values with E_{SW} .

For quasi-reversible conditions (Fig. 7.57d), the shape of the $Q_{\text{SW}}^{\text{cat}} - E$ curves is similar to that of the reversible ones, although the peak heights are smaller.

The applicability of the theoretical expressions discussed above has been tested with different systems such as the oxidation of protein myoglobin in the presence of sodium ascorbate [96] or the oxidation of ferrocene in the presence of potassium ferrocyanide [95]. The case corresponding to ferrocene-containing monolayers on a gold electrode in the presence of potassium ferrocyanide will be addressed here.

The redox reaction of the ferrocene moiety in a 6-(ferrocenyl)hexanethiol-hexanethiol ($\text{FcC}_6\text{SH} - \text{C}_6\text{SH}$, 1:20) mixed monolayer has been studied in the presence of potassium ferrocyanide as reducing agent. Thus, the ferrocenium formed at anodic potentials is reduced to ferrocene by the ferrocyanide in solution and the whole process becomes a surface catalytic reaction, in agreement with the following reaction scheme:



The process implies a first electrochemical step with a very fast conversion of the ferrocene/ferrocenium couple, due to the short length of the alkyl chain, and a second chemical step with a simple electron transfer between the iron complex in solution and that of the monolayer. Moreover, the thiols block the gold surface in such a way that the $\text{Fe}(\text{CN})_6^{4-}$ oxidation will take place due solely to the ferrocene mediation at the monolayer, and with a very high efficiency (i.e., the catalytic way is observed at potentials 500 mV lower than those corresponding to a gold electrode with a C_6SH monolayer).

The experimental $I_{\text{SW}}^{\text{cat}}/Q_{\text{F}} - (E - E_c^{\Theta'})$ and $Q_{\text{SW}}^{\text{cat}} - (E - E_c^{\Theta'})$ curves of the $\text{FcC}_6\text{SH} - \text{C}_4\text{SH}$ mixed monolayer at a disc gold electrode of 100 μm diameter in a solution 1.0 M NaClO_4 , obtained for different values of the square wave pulse amplitude and a fixed ferricyanide concentration 10 mM, are plotted in Fig. 7.58. It can be seen that whereas the peak height of the charge-potential curves increases with E_{SW} until charge plateau for $|E_{\text{SW}}| > 110\text{mV}$ is obtained, the anodic limit region remains unaffected, in line with Fig. 7.57b and Eq. (7.150). From the measurement of the charge plateau for $E_{\text{SW}} = 130\text{mV}$, the value $Q_{\text{F}} = (2.0 \pm 0.1)\text{nC}$.

Moreover, the anodic limit should be equal to $-\bar{k}_c$, in agreement with Eq. (7.150). From the curves for $E_{\text{SW}} \geq 110\text{mV}$ the value $\bar{k}_c = 0.75$ has been obtained ($k'_c = 2.5 \times 10^4 \text{M}^{-1} \text{s}^{-1}$). The theoretical $I_{\text{SW}}^{\text{cat}}/Q_{\text{F}} - (E - E_c^{\Theta'})$ and $Q_{\text{SW}}^{\text{cat}} - (E - E_c^{\Theta'})$ curves have been included for comparison (symbols) showing an excellent agreement in all the cases.

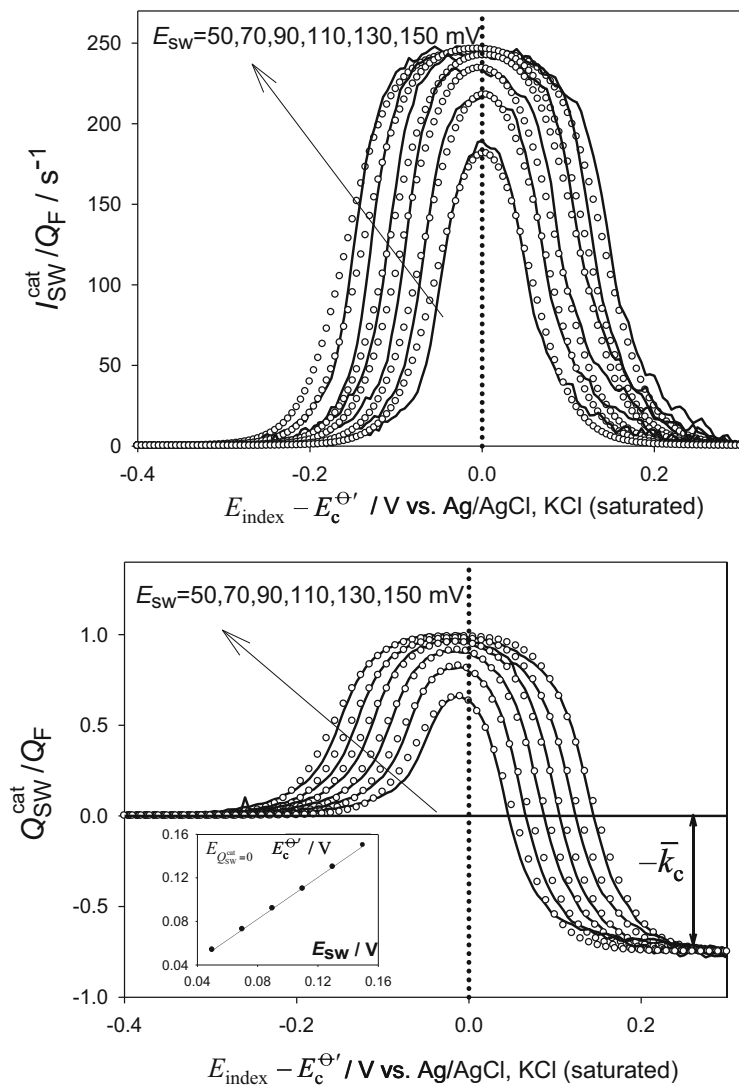


Fig. 7.58 (solid lines) Experimental $I_{\text{SW}}^{\text{cat}}/Q_F - (E - E_c^{\Theta'})$ (a) and $Q_{\text{SW}}^{\text{cat}}/Q_F - (E - E_c^{\Theta'})$ (b) curves obtained in SWV and SWVC for a mixed FcC₆SH - C₆SH monolayer in 1 M NaClO₄ solution with 10 mM in potassium ferrocyanide. Electrode radius $r_d = 50 \mu\text{m}$. $\Delta E_s = 5 \text{ mV}$. The values of E_{SW} (in mV) appear on the curves. (symbols) Theoretical current-potential (a) and charge-potential (b) curves calculated from Eqs. (7.146) to (7.149) by using the following parameters: $E_c^{\Theta'} = 0.100 \text{ V}$, $\bar{k}_c = 0.75$, $Q_F = 1950 \text{ pC}$, and $T = 298 \text{ K}$. Reproduced from [95] with permission

$$Q_{\text{SW}}^{\text{EEcat, route } i(i=1,2,3)} = Q_{\text{SW}}^{\text{EE}} - \begin{cases} \bar{k}_c f_{\text{O}_2}^{(2p)} & \text{Route 1} \\ \bar{k}_c f_{\text{O}_3}^{(2p)} & \text{Route 2} \\ 2\bar{k}_c f_{\text{O}_3}^{(2p)} & \text{Route 3} \end{cases} \quad (7.157)$$

where

$$Q_{\text{SW}}^{\text{EE}} = \frac{2\sqrt{K} + e^{\bar{\eta}_{2j-1}}}{\sqrt{K} + e^{\bar{\eta}_{2j-1}} + \sqrt{K}e^{2\bar{\eta}_{2j-1}}} - \frac{2\sqrt{K} + e^{\bar{\eta}_{2j}}}{\sqrt{K} + e^{\bar{\eta}_{2j}} + \sqrt{K}e^{2\bar{\eta}_{2j}}} \quad (7.158)$$

The SWV and SWVC curves for the EEC' reaction schemes, calculated from Eqs. (7.154) and (7.157), can be seen in Figs. 7.59 and 7.60, respectively. These curves have been obtained for different values of the dimensionless chemical rate constant \bar{k}_c and $\Delta E_c^{\Theta'}$ (i.e., the difference between the formal potentials of the electron transfer reactions). SWV proves highly sensitive for detecting the presence of the catalysis, since no measurable response is obtained in the absence of the same. From Fig. 7.59, it can be deduced that when catalysis takes place, route

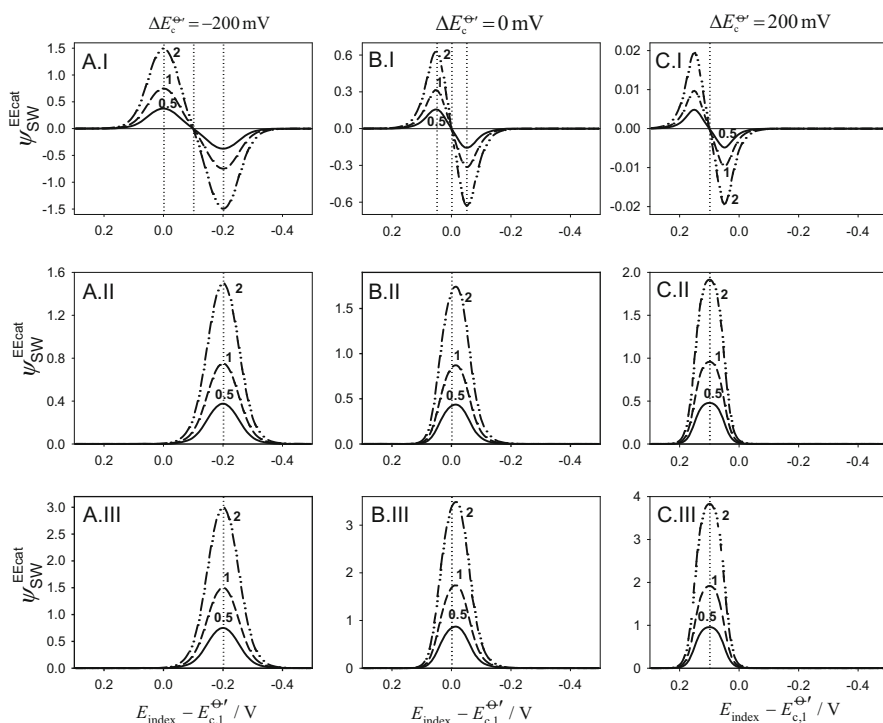


Fig. 7.59 SWV curves corresponding to an EEC' mechanism for its three possible routes calculated from Eq. (7.154). The values of the dimensionless chemical rate constant \bar{k}_c appear on the curves. $\Delta E_s = 5 \text{ mV}$, $E_{\text{SW}} = 50 \text{ mV}$, $T = 298 \text{ K}$

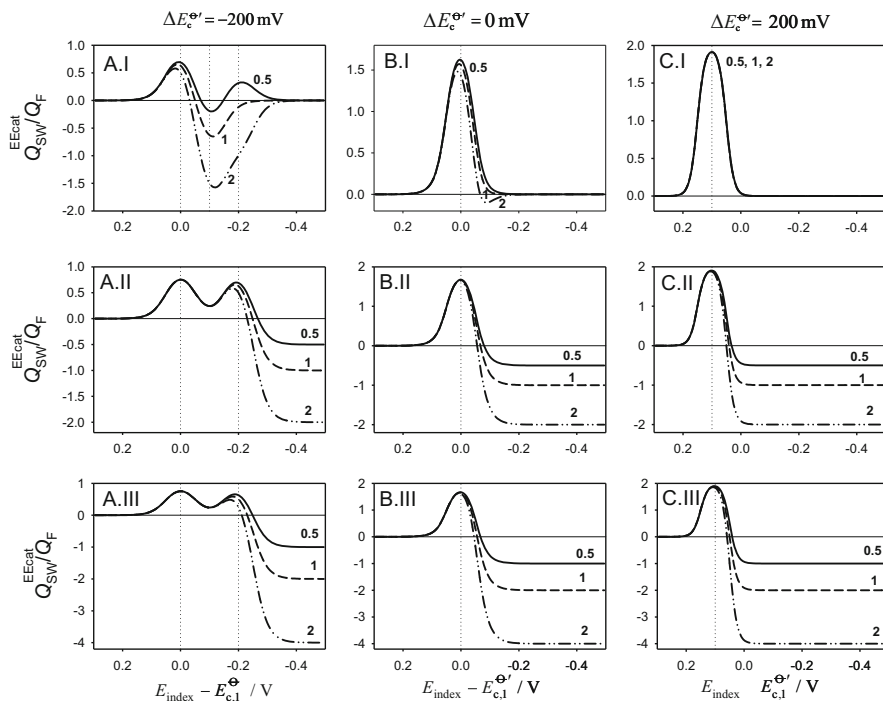


Fig. 7.60 SWVC curves corresponding to an EEC' mechanism for its three possible routes calculated from Eq. (7.157). The values of the dimensionless chemical rate constant \bar{k}_c appear on the curves. $\Delta E_s = 5 \text{ mV}$, $E_{SW} = 50 \text{ mV}$, $T = 298 \text{ K}$

1 always gives rise to two well-defined symmetric peaks with respect to the null current point corresponding to positive and negative values of ψ_{SW} , whose heights increase with \bar{k}_c (see Figs. A.I–A.III in 7.59). The null current potential or cross potential coincides with the average formal potential $\bar{E}_c^{\Theta'}$ independently of the value of $\Delta E_c^{\Theta'}$. Moreover, both peak potentials coincide with $E_{c,1}^{\Theta'}$ and $E_{c,2}^{\Theta'}$ for $\Delta E_c^{\Theta'} \ll 0$ (see Fig. A.I in 7.59). The peak potential separation fulfill that $\Delta E_{\text{peak}} = |\Delta E_c^{\Theta'}|$ for $\Delta E_c^{\Theta'} \leq -142.4 \text{ mV}$.

The SWV curves corresponding to the routes 2 and 3 cannot be distinguished since they lead to similar expressions which only differ by a factor of 2 (see Eq. (7.154)). Under these conditions (curves A.II–C.II and A.III–C.III in Fig. 7.59), the SWV curves present only one peak and lose their symmetry. So, it can be inferred that SWV technique is highly suitable for distinguishing route 1 from routes 2 and 3. However, the determination of $E_{c,1}^{\Theta'}$ and $E_{c,2}^{\Theta'}$ becomes complex in general in route 1 for $\Delta E_c^{\Theta'} \gg 0$.

SWVC charge–potential curves show a constant negative value at cathodic potentials from which it is possible to make an estimation of the catalytic rate

constant for routes 2 and 3. In the case of route 1, for very positive values of ΔE_c^{Θ} , there is no influence of the catalytic step.

7.7.3.3 Second-Order Electrocatalytic Processes

When the surface concentration of species C_{sol} cannot be considered as constant, the analysis of the electrochemical response that arises from reaction scheme (7.XII) becomes much more complex, since the process is of second order and the values of the surface concentrations of C_{sol} are a function of the kinetics of the catalytic reaction and also of the mass transport (and, therefore, of the electrode geometry). Due to this higher complexity, only the current–potential response in SWV will be treated, with the additional simplification of fast surface charge transfer. In this case, when discrete constant potentials are applied, the surface coverages of both species are constant (i.e., $df_O^{(p)}/dt = -df_R^{(p)}/dt = 0$ for any potential E_p), such that the current corresponding to the p th applied potential applied to a spherical electrode is given by

$$\frac{I_p^{\text{cat, sphe}}}{FA\Gamma_T} = k_c f_R^{(p)} c_C^{(p)}(r_s, t) \quad (7.159)$$

with r_s being the electrode radius. The following approximate expression for the SWV net current has been obtained [99]:

$$I_{\text{SW}}^{\text{cat, sphe}} = FAC_C^* \sqrt{\frac{D_C}{\tau}} \Lambda \left\{ f_R^{(2p-1)} \frac{\prod_{h=1}^{2p-2} [1 + \Lambda f_R^{(h)} \sigma_{h+1, 2p-1}]}{\prod_{h=1}^{2p-1} [1 + \Lambda f_R^{(h)} \sigma_{h, 2p-1}]} - f_R^{(2p)} \frac{\prod_{h=1}^{2p-1} [1 + \Lambda f_R^{(h)} \sigma_{h+1, 2p}]}{\prod_{h=1}^{2p} [1 + \Lambda f_R^{(h)} \sigma_{h, 2p}]} \right\} \quad p = 1, 2, \dots, NP/2 \quad (7.160)$$

where

$$f_R^{(h)} = \frac{\Gamma_R^{(h)}}{\Gamma_T} = \frac{1}{1 + e^{\eta_h}} \quad (7.161)$$

$$\Lambda = k_c \Gamma_T \sqrt{\frac{\tau}{D_C}} \quad (7.162)$$

$$\sigma_{h, m} = \frac{1}{\xi_s + \frac{1}{\sqrt{\pi(m-h+1)}}} \quad (7.163)$$

$$\xi_s = \frac{\sqrt{D_C \tau}}{r_s} \quad (7.164)$$

The response obtained in SWV is peak shaped, and, due to the complexity of Eq. (7.160), the peak coordinates cannot be analytically deduced, with the exception of simpler situations like stationary conditions.

First-Order Behavior

By considering the limit $\Lambda \rightarrow 0$ (i.e., very low demand from the chemical process at the monolayer/solution interface), the square wave response is given by

$$\begin{aligned} I_{\text{SW}}^{\text{cat, sphe}} \Big|_{\Lambda \rightarrow 0} &\cong FAc_C^* \sqrt{\frac{D_C}{\tau}} \Lambda \left\{ f_{\text{R}}^{(2p-1)} - f_{\text{R}}^{(2p)} \right\} \\ &= Q_{\text{F}} k_{\text{c}} \left(\frac{1}{1 + e^{\eta_{\text{r}}}} - \frac{1}{1 + e^{\eta_{\text{r}}}} \right) \end{aligned} \quad (7.165)$$

which is logically coincident with Eq. (7.146), deduced by assuming first-order conditions. Therefore, Eq. (7.165) leads to the same peak parameters as those obtained with Eq. (7.146).

Small Electrodes

Considering the limiting condition $\xi_s \gg 1$ (i.e., small values of the radius) in Eq. (7.160) (i.e., $\sigma_{h,m} \rightarrow (1/\xi_s)$), the following simplified expression is obtained

$$I_{\text{SW}}^{\text{cat, sphe}} = FAc_C^* \sqrt{\frac{D_C}{\tau}} \Lambda \left(\frac{f_{\text{R}}^{(2p-1)}}{1 + \Theta f_{\text{R}}^{(2p-1)}} - \frac{f_{\text{R}}^{(2p)}}{1 + \Theta f_{\text{R}}^{(2p)}} \right) \quad (7.166)$$

with

$$\Theta = \frac{\Lambda}{\xi_s} = \frac{k_{\text{c}} \Gamma_{\text{T}} r_s}{D_C} \quad (7.167)$$

By taking into account that $E_{2p-1} = E_{2p} \mp 2E_{\text{SW}}$, with the upper sign being applied in the first (cathodic) sweep and the lower corresponding to the second (anodic) one, Eq. (7.166) can be rewritten as

$$I_{\text{SW}}^{\text{cat, sphe}} = FAc_C^* \sqrt{\frac{D_C}{\tau}} \Lambda \left(\frac{1}{1 + \Theta + e^{\eta_{2p-1}}} - \frac{1}{1 + \Theta + e^{\eta_{2p-1} \pm 2\eta_{\text{SW}}}} \right) \quad (7.168)$$

In this case, it is possible to obtain the following simple expressions for the peak parameters:

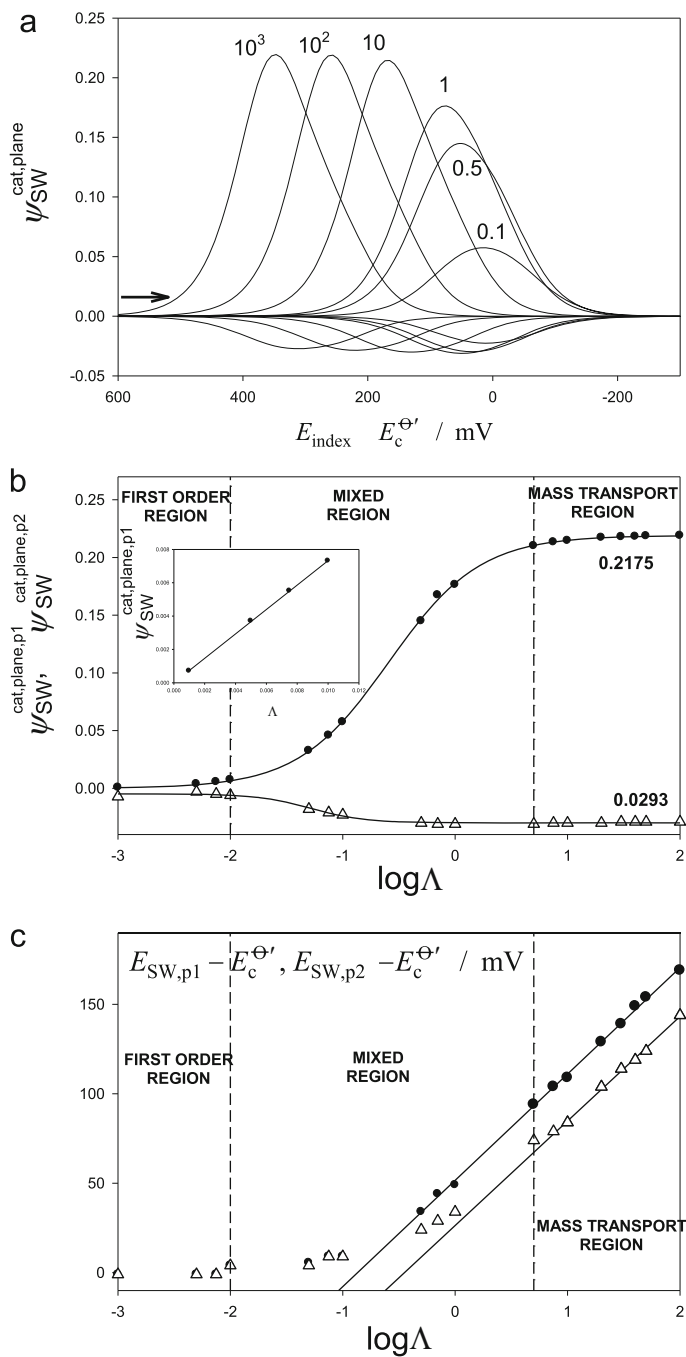


Fig. 7.61 (a) $i_{SW}^{cat,plane} - (E_{index} - E_c^{\Theta'})$ (solid lines) at a planar electrode for different values of Λ (indicated on the graphs). Peak currents (b) and potentials (c) of the first (black circles) and second

$$E_{\text{SW,peak}}^{\text{ss}} = E_c^{\Theta'} + \frac{RT}{F} \ln(1 + \Theta) \quad (7.169)$$

$$\begin{aligned} I_{\text{SW}}^{\text{cat, sphe, peak}} &= \pm F A C_C^* \sqrt{\frac{D_C}{\tau}} \frac{\Lambda}{1 + \Theta} \tanh\left(\frac{\eta_{\text{SW}}}{2}\right) \\ &= \pm F A C_C^* k_c \Gamma_T \frac{1}{1 + \Theta} \tanh\left(\frac{\eta_{\text{SW}}}{2}\right) \end{aligned} \quad (7.170)$$

In the cyclic mode of SWV, two scans can be analyzed in an analogous way to Cyclic Voltammetry. In Fig. 7.61, the Cyclic SWV curves (7.61a) of the catalytic process given in (7.XI) for different values of Λ at planar electrodes have been plotted, together with the evolution of the peak currents (7.61b) and peak potentials (7.61c) of the first (1) and second (2) scans toward cathodic and anodic potentials, respectively, as a function of $\log\Lambda$.

From these curves, we can see that the increase of Λ gives rise to the increase of both responses up to a value of $\Lambda \geq 5$, as of which no influence is observed on the peak currents (see also Fig. 7.61b). For low Λ values, identical peak heights proportional to Λ are obtained in both sweeps. This feature is typical of first-order catalytic behavior (see figure embedded in Fig. 7.61b). As Λ increases, a strong asymmetry appears between the responses of the first and second sweeps, with the former being higher than the latter. For $\log\Lambda > 1$ the ratio between both peaks takes the constant value 7.42. A numerical expression for the dependence of the both peak currents with $\log\Lambda$ which covers the whole range of values shown in Fig. 7.61b is obtained:

$$\left. \begin{aligned} \psi_{\text{SW}}^{\text{cat, plane, p1}} &\cong \frac{0.2191}{1 + e^{-\frac{(\log\Lambda + 0.5891)}{0.4037}}} \\ \psi_{\text{SW}}^{\text{cat, plane, p2}} &\cong \frac{-0.0301}{1 + e^{-\frac{(\log\Lambda + 1.4655)}{0.3715}}} \end{aligned} \right\} \quad (7.171)$$

from which obtaining Λ is immediate. In the case of the anodic peaks, the errors are higher due to the small values of $\psi_{\text{SW}}^{\text{cat, plane, p2}}$ (the relative error is higher than 5 % for $\log\Lambda \leq -1$), so the use of the expression for the peak heights of the first sweep is more appropriate.

Concerning the peak potentials, both values coincide with $E_c^{\Theta'}$ for $\log\Lambda < -2$ (first-order behavior) and both responses shift toward more positive potentials as Λ increases. Moreover, the peak potentials of both responses depend linearly on $\log\Lambda$

Fig. 7.61 (continued) (*white triangles*) scans as a function of $\log\Lambda$. $E_{\text{SW}} = \mp 50 \text{ mV}$, $\Delta E_s = \mp 5 \text{ mV}$, with the upper sign corresponding to the first scan (cathodic) and the lower to the second (anodic), respectively. Inner figure in 7.61b: peak currents of the first sweep as a function of Λ . $\tau = 10 \text{ ms}$, $T = 298.15 \text{ K}$, $D = 10^{-5} \text{ cm}^2 \text{ s}^{-1}$. Reproduced from [99] with permission

for $\Lambda > 1$ with a slope that is approximately equal to 59 mV, in agreement with the following expressions ($T = 298$ K):

$$\left. \begin{aligned} E_{SW, p1} - E_c^{\Theta} (\text{mV}) &\cong 51.6 + 59.4 \log(\Lambda) \\ E_{SW, p2} - E_c^{\Theta} (\text{mV}) &\cong 26.4 + 58.4 \log(\Lambda) \end{aligned} \right\} \Lambda > 1 \quad (7.172)$$

The difference between peak potentials of the two sweeps becomes constant and equal to $\Delta E_{SW, p} \cong 25$ mV for $\log \Lambda > 1$.

On the basis of these results, three different behaviors can be distinguished in the SWV response:

- First-order region ($\Lambda < 0.01$). In this region, the chemical rate constant k_c is low and therefore the surface concentration is approximately equal to the bulk value. The peak current is proportional to Λ (see figure embedded in 7.61b), and the peak potential coincides with the formal potential of the surface-attached redox catalyst, E_c^{Θ} .
- Mixed region ($0.01 < \Lambda < 10$). For intermediate values of Λ , the surface concentration of species C decreases more rapidly and at more positive potentials as Λ increases. Under these conditions, the current increases and the SWV peak potentials of both sweeps shift toward more anodic values when Λ increases.
- Mass transport control region ($\Lambda > 10$). This zone corresponds to high values of the chemical rate constant (i.e., very fast conversion of species C by the immobilized redox catalyst). The chemical conversion of C_{sol} through the assistance of the attached mediator R is very fast, so the diffusive mass transport is the limiting step. In this case, the peak currents become independent of Λ and the peak potentials show a logarithmic dependence on the chemical rate constant (i.e., Λ). The behavior of the peak potential is similar to the variation of the peak potential of a totally irreversible charge transfer reaction with the logarithm of the heterogeneous rate constant.

An in-depth analysis of the response at spherical electrodes and microelectrodes can be found in [99].

References

- Bard AJ, Faulkner LR (2000) *Electrochemical methods: fundamental and applications*, 2nd edn. Wiley, New York
- Compton RG, Banks CE (2011) *Understanding voltammetry*, 2nd edn. ICP, London
- Galus Z (1993) *Fundamentals of electrochemical analysis* (2nd/Rev edition) (Ellis horwood series in analytical chemistry). Ellis Horwood, Chichester
- Molina A, Gonzalez J, Abenza N (2007) *Electrochim Acta* 52:4351–4362
- Gonzalez J, Molina A, Abenza N, Serna C, Moreno MM (2007) *Anal Chem* 79:7580–7589
- Mirčeski V, Komorsky-Lovrić S, Lovrić M (2007) *Square-wave voltammetry, theory and application*. Springer, Berlin

7. Scholz F, Nitschke L, Henrion G (1988) *Fresenius Z Anal Chem* 332:805–808
8. Scholz F, Draheim M, Henrion G (1990) *Fresenius Z Anal Chem* 336:136–138
9. Molina A, Laborda E, Martinez-Ortiz F, Bradley DF, Schiffrin DJ, Compton RG (2011) *J Electroanal Chem* 659:12–24
10. Gonzalez J, Abenza N, Molina A (2006) *J Electroanal Chem* 596:74–86
11. Oldham KB, Myland J, Spanier J (2009) *An atlas of functions*, 2nd edn. Springer, New York
12. Chen A, Badal S (2013) *Anal Methods* 5:2158–2173
13. Barker GC, Jenkins JL (1952) *Analyst* 77:685–696
14. Barker GC (1958) *Anal Chim Acta* 18:118–131
15. Barker GC, Gardner AW (1992) *Analyst* 117:1811–1828
16. Ruzič I (1972) *J Electroanal Chem* 39:111–122
17. Osteryoung J, O’Dea JJ (1986) In: Bard AJ (ed) *Electroanalytical chemistry*, vol 14. New York, Marcel Dekker
18. Osteryoung JG, Schreiner MM (1988) *CRC Crit Rev Anal Chem* 19:S1–S26
19. Mirčeski V, Gulaboski R, Lovrić M, Bogeski I, Kappl R, Hoth M (2013) *Electroanalysis* 11: 2411–2422
20. Laborda E, Rogers EI, Martinez-Ortiz F, Molina A, Compton RG (2010) *Electroanalysis* 22: 2784–2793
21. Molina A, Gonzalez J, Laborda E, Compton RG (2012) *Russ J Electrochem* 48:600–609
22. Lovrić M (1999) *Electroanalysis* 11:1089–1093
23. Krulic D, Fatouros N, El Belamachi MM (1995) *J Electroanal Chem* 385:33–38
24. Whelan DP, O’Dea JJ, Osteryoung JG, Aoki K (1986) *J Electroanal Chem* 202:23–36
25. Molina A, Gonzalez J (2012) *Microelectrodes*. In: Kaufmann P (ed) *Characterization of materials*. Wiley, New York
26. Olmstead ML, Nicholson RS (1968) *J Electroanal Chem* 16:145–151
27. O’Dea JJ, Osteryoung JG, Osteryoung RA (1981) *Anal Chem* 53:695–701
28. Fatouros N, Krulic D (1998) *J Electroanal Chem* 443:262–265
29. Fatouros N, Krulic D (2002) *J Electroanal Chem* 520:1–5
30. Laborda E, Wang Y, Henstridge MC, Martinez-Ortiz F, Molina A, Compton RG (2011) *Chem Phys Lett* 512:133–137
31. Henstridge MC, Laborda E, Rees N, Compton RG (2012) *Electrochim Acta* 84:12–20
32. Henstridge MC, Laborda E, Wang Y, Suwatchara D, Rees N, Molina A, Martinez-Ortiz F, Compton RG (2012) *J Electroanal Chem* 672:45–52
33. Mirčeski V, Laborda E, Guziejewski D, Compton RG (2013) *Anal Chem* 85:5586–5594
34. Mirčeski V, Guziejewski D, Lisichkov K (2013) *Electrochim Acta* 114:667–673
35. Beni V, Ghita M, Arrigan DWM (2005) *Biosen Bioelectro* 20:2097–2103
36. Molina A, Serna C, Ortuño JA, Torralba E (2012) *Ann Rep Chem Sect C RSC* 108:126–176
37. Ortuño JA, Serna C, Molina A, Torralba E (2009) *Electroanalysis* 21:2297–2302
38. Molina A, Ortuño JA, Serna C, Torralba E, Gonzalez J (2010) *Electroanalysis* 22:1634–1642
39. Molina A, Ortuño JA, Serna C, Torralba E (2010) *Phys Chem Chem Phys* 12:13296–13303
40. Girault HH (2010) In: Bard AJ, Zoski CG (eds) *Electroanalytical chemistry: a series of advances*, vol 23. CRC Press, Boca Raton
41. Cousens NEA, Kucernak AR (2011) *Electrochem Commun* 13:1539–1541
42. Molina A, Laborda E, Compton RG (2014) *J Phys Chem C* 118:18249–18256
43. Molina A, Laborda E, Compton RG (2014) *Chem Phys Lett* 597:126–133
44. Molina A, Laborda E, Gonzalez J, Compton RG (2015) *Electroanalysis* 27:93–100
45. Lopez-Tenes M, Serna C, Moreno MM, Molina A (2007) *Port Electrochim Acta* 25:103–118
46. Molina A, Moreno MM, Serna C, Lopez-Tenes M, Gonzalez J, Abenza N (2007) *J Phys Chem C* 111:12446–12453
47. Helfrick JC, Bottomley LA (2009) *Anal Chem* 81:9041–9047
48. Molina A, Serna C, Li Q, Laborda E, Batchelor-McAuley C, Compton RG (2012) *J Phys Chem C* 116:11470–11479

49. Laborda E, Molina A, Li Q, Batchelor-McAuley C, Compton RG (2012) *Phys Chem Chem Phys* 14:8319–8327
50. Lovrić M, Komorsky-Lovrić S (2012) *Croat Chim Acta* 85:569–575
51. Komorsky-Lovrić S, Lovrić M (2013) *Anal Bioanal Electrochem* 5:291–304
52. Komorsky-Lovrić S, Lovrić M (2014) *Int J Electrochem Sci* 9:435–444
53. Barrière F, Geiger WE (2006) *J Am Chem Soc* 128:3980–3989
54. Komorsky-Lovrić S, Lovrić M (2011) *J Electroanal Chem* 660:22–25
55. Berek J, Mesjtrik V, Muck A, Zima J (2000) *Crit Rev Anal Chem* 30:37–57
56. Galceran J, Taylor SL, Bartlett PN (1999) *J Electroanal Chem* 466:15–25
57. Galceran J, Taylor SL, Bartlett PN (1999) *J Electroanal Chem* 476:132–147
58. Molina A, Serna C, Martinez-Ortiz F (2000) *J Electroanal Chem* 486:9–15
59. Molina A, Gonzalez J, Laborda E, Henstridge MC, Compton RG (2011) *Electrochim Acta* 56:7404–7410
60. Molina A, Gonzalez J, Laborda E, Wang Y, Compton RG (2011) *Phys Chem Chem Phys* 13:16748–16755
61. Sadakane M, Steckhan E (1998) *Chem Rev* 98:219–237
62. Smith DE (1963) *Anal Chem* 35:602–609
63. O’Dea JJ, Wikiel K, Osteryoung J (1990) *Anal Chem* 62:3628–3636
64. Amatore C, Savéant JM (1978) *J Electroanal Chem* 227–232
65. Amatore C, Gareil M, Savéant JM (1983) *J Electroanal Chem* 147:1–38
66. Molina A, Serna C, Martinez-Ortiz F, Laborda E (2008) *J Electroanal Chem* 617:14–26
67. Martinez-Ortiz F, Molina A, Laborda E (2011) *Electrochim Acta* 56:5707–5716
68. Torralba E, Ortuño JA, Serna C, Molina A, Karimian F (2014) *Anal Chim Acta* 826:12–20
69. Laborda E, Olmos JM, Martinez-Ortiz F, Molina A (2015) *J Solid State Electrochem* 19:549–561
70. Laborda E, Olmos JM, Torralba E, Molina A (2015) *Anal Chem* 87:1676–1684
71. Forster RJ (1995) *Langmuir* 11:2247–2255
72. Gonzalez J, Molina A (2003) *Langmuir* 19:406–415
73. Abenza N, Gonzalez J, Molina A (2007) *Electroanalysis* 19:936–944
74. Gonzalez J, Molina A, Lopez-Tenes M, Karimian F (2013) *Anal Chem* 85:8764–8772
75. Gonzalez J, Molina A (2003) *J Electroanal Chem* 557:157–165
76. Reeves JH, Song S, Bowden EF (1993) *Anal Chem* 65:683–688
77. O’Dea JJ, Osteryoung JG (1993) *Anal Chem* 65:3090–3097
78. Damaskin BB, Petriiand OA, Batrakov VV (1971) *Adsorption of organic compounds on electrodes*. Plenum, New York
79. Armstrong FA, Heering HA, Hirst J (1997) *Chem Soc Rev* 26:169–179
80. Bartlett PN (2008) *Bioelectrochemistry: fundamentals, experimental techniques and applications*. Wiley, Chichester
81. Leger C, Bertrand P (2008) *Chem Rev* 108:2379–2438
82. Honeychurch MJ, Rechnitz GA (1998) *Electroanalysis* 10:285–293
83. Hirst J (2006) *Biochim Biophys Acta (BBA) – Bioenergetics* 1757:225–239
84. Zhang J, Guo S-X, Bond AM, Honeychurch MJ, Oldham KB (2005) *J Phys Chem B* 109:8935–8947
85. Fleming BD, Barlow NL, Zhang J, Bond AM, Armstrong FA (2006) *Anal Chem* 78:2948–2956
86. Gonzalez J, Molina A, Soto CM, Serna C (2012) *J Electroanal Chem* 664:53–62
87. Maeda K, Himeno S, Osakai T, Saito A, Hori T (1994) *J Electroanal Chem* 364:149–154
88. O’Dea JJ, Osteryoung JG (1997) *Anal Chem* 69:650–658
89. Xie Y, Kang C, Anson FC (1996) *J Chem Soc Faraday Trans* 92:3917–3923
90. Gulaboski R (2009) *J Solid State Electrochem* 13:1015–1024
91. Gulaboski R, Mirčeski V, Lovrić M, Bogeski I (2005) *Electrochem Commun* 7:515–522

92. Bard AJ, Stratmann M, Fujihira M, Rusling JF, Rubinstein I (eds) (2007) Encyclopedia of electrochemistry, vol 10. Willey-VCH, Weinheim
93. Savéant JM (2008) Chem Rev 108:2348–2378
94. Murray RW (1981) Philos Trans R Soc Lond 302:253–265
95. Gonzalez J, Soto CM, Molina A (2009) J Electroanal Chem 634:90–97
96. Gonzalez J, Molina A (2013) J Solid State Electrochem 17:537–546
97. Gulaboski R, Mihajlov L (2011) Biophys Chem 155:1–9
98. Polcyn DS, Shain I (1966) Anal Chem 38:376–382
99. Gonzalez J, Molina A, Martinez-Ortiz F, Laborda E (2012) J Phys Chem C 116:11206–11215

Appendix A. Dimensionless Parameter Method: Solution for the Application of a Constant Potential to a Simple Charge Transfer Process at Spherical Electrodes When the Diffusion Coefficients of Both Species are Different

The Dimensionless Parameter is a mathematical method to solve linear differential equations. It has been used in Electrochemistry in the resolution of Fick's second law differential equation. This method is based on the use of functional series in dimensionless variables—which are related both to the form of the differential equation and to its boundary conditions—to transform a partial differential equation into a series of total differential equations in terms of only one independent dimensionless variable. This method was extensively used by Koutecký and later by other authors [1–9], and has proven to be the most powerful to obtain explicit analytical solutions. In this appendix, this method will be applied to the study of a charge transfer reaction at spherical electrodes when the diffusion coefficients of both species are not equal. In this situation, the use of this procedure will lead us to a series of homogeneous total differential equations depending on the variable s given in Eq. (A.1). In other more complex cases, this method leads to nonhomogeneous total differential equations (for example, the case of a reversible process in Normal Pulse Polarography at the DME or the solutions of several electrochemical processes in double pulse techniques). In these last situations, explicit analytical solutions have also been obtained, although they will not be treated here for the sake of simplicity.

The homogeneous differential equation,

$$\rho_j''(s) + 2s\rho_j'(s) - 2j\rho_j(s) = 0, \quad (\text{A.1})$$

has two linearly independent solutions given by the following series:

$$\left. \begin{aligned} K_j(s) &= \sum_{i=0}^{\infty} a_i^{(j)} s^i \\ L_j(s) &= \sum_{i=0}^{\infty} c_i^{(j)} s^{i+1} \end{aligned} \right\} \tag{A.2}$$

where the coefficients $a_i^{(j)}$ and $c_i^{(j)}$ are given by the following recurrence relationships:

$$\left. \begin{aligned} \frac{a_{i+2}^{(j)}}{a_i^{(j)}} &= \frac{2(j-i)}{(i+1)(i+2)} \\ \frac{c_{i+2}^{(j)}}{c_i^{(j)}} &= \frac{2(j-i-1)}{(i+2)(i+3)} \end{aligned} \right\} \tag{A.3}$$

with

$$a_0^{(j)} = c_0^{(j)} = 1 \tag{A.4}$$

such that the coefficients not included in Eqs. (A.3) and (A.4) are null. A new solution for Eq. (A.1) can be written as a linear combination of the series $K_j(s)$ and $L_j(s)$,

$$\rho_j(s) = b_{1j}K_j(s) + b_{2j}L_j(s) \tag{A.5}$$

where b_{1j} and b_{2j} are constants. The following function:

$$\psi_j(s) = K_j(s) - p_j L_j(s) \tag{A.6}$$

with [1, 6],

$$p_j = \lim_{s \rightarrow \infty} \frac{K_j(s)}{L_j(s)} = \frac{2\Gamma(1+j/2)}{\Gamma((1+j)/2)}, \tag{A.7}$$

is also a solution of Eq. (A.1) as can be easily demonstrated by direct substitution. $\Gamma(x)$ in Eq. (A.7) is the Euler's Gamma function [10]:

$$\Gamma(x) = \int_0^{\infty} t^{x-1} e^{-t} dt \tag{A.8}$$

Moreover,

$$p_0 = \frac{2}{\sqrt{\pi}} \quad (\text{A.9})$$

$$p_j p_{j+1} = 2(j+1) \quad (\text{A.10})$$

The so-called Koutecký Functions [1], $\psi_j(s)$, have the following properties:

$$\psi_j^{(\pm)}(0) = 1 \quad (\text{A.11})$$

$$\psi_j^{(\pm)}(\pm\infty) = 0 \quad (\text{A.12})$$

$$\psi_j^{(\pm)'}(s) = \pm p_j \psi_{j-1}^{(\pm)}(s) \quad (\text{A.13})$$

$$\psi_0^{(\pm)}(s) = 1 \pm \operatorname{erf}(s) \quad (\text{A.14})$$

with

$$\operatorname{erf}(s) = (2/\sqrt{\pi}) \int_0^s e^{-t^2} dt \quad (\text{A.15})$$

being the Gauss error function [10].

The lower sign in the above functions applies where the variable s takes positive values (for example, solution soluble species), and the upper sign where $s < 0$ (for example, when the species amalgamates and diffuses into the electrode; see Sect. 2.5). Similarly, in the case of ITIES (Sect. 2.3), the organic phase is considered to correspond to $s > 0$ and then the lower sign applies, whereas the aqueous phase corresponds to $s < 0$ and the upper sign is taken.

If the boundary conditions for Eq. (A.1) are

$$\rho_j(s=0) = h_j \quad (\text{A.16})$$

and

$$\rho_j(s \rightarrow \infty) = \rho_j^* \quad (\text{A.17})$$

from Eqs. (A.2)–(A.5), (A.7), and (A.16)–(A.17), the constants b_{1j} and b_{2j} can be determined:

$$b_{1j} = h_j \quad (\text{A.18})$$

$$b_{2j} = \frac{\rho_j^*}{\lim_{s \rightarrow \infty} L_j(s)} - b_{1j} p_j \quad (\text{A.19})$$

and by introducing Eqs. (A.18)–(A.19) into Eq. (A.5), one obtains

$$\rho_j(s) = h_j \psi_j(s) + \left(\frac{\rho_j^*}{\lim_{s \rightarrow \infty} L_j(s)} \right) L_j(s) \quad (\text{A.20})$$

Thus, for $j=0$, from Eqs. (A.2) and (A.3), the function $\rho_0(s)$ is given by

$$\rho_0(s) = h_0 \psi_0(s) + \left(\frac{\rho_0^*}{\lim_{s \rightarrow \infty} L_0(s)} \right) L_0(s) \quad (\text{A.21})$$

with

$$L_0(s) = \int_0^s e^{-t^2} dt \quad (\text{A.22})$$

$$L_0(0) = 0 \quad (\text{A.23})$$

$$L_0(s \rightarrow \infty) = \int_0^\infty e^{-t^2} dt = \frac{\sqrt{\pi}}{2} = \frac{1}{p_0} \quad (\text{A.24})$$

So, Eq. (A.20) for $j=0$ can be written as

$$\rho_0(s) = h_0 \psi_0(s) + \rho_0^* \operatorname{erf}(s) = \rho_0^* + (h_0 - \rho_0^*) \operatorname{erfc}(s) \quad (\text{A.25})$$

Regarding $L_1(s)$, from Eqs. (A.2) and (A.3) one can deduce that $L_1(s) = s$, since $c_2^{(1)} = c_4^{(1)} = \dots = 0$. Note that if $\rho_j^* = 0$ for $j > 0$,

$$\rho_j(s) = h_j \psi_j(s), \quad j > 0 \quad (\text{A.26})$$

The dimensionless parameter method has been successfully applied to the resolution of electrochemical problems [1–9]. Next, as an example, this method will be applied to the resolution of the problems described in Sect. 2.5.1.

First, the following change of variable is made:

$$\left. \begin{aligned} u_{\text{O}}(r, t) &= \frac{c_{\text{O}}(r, t)r}{c_{\text{O}}^* r_s} \\ u_{\text{R}}(r, t) &= \frac{c_{\text{R}}(r, t)r}{c_{\text{O}}^* r_s} \end{aligned} \right\} \quad (\text{A.27})$$

where r is the distance to the electrode center, t is the electrolysis time, $c_i(r, t)$ is the concentration of species i ($i = \text{O}, \text{R}$), c_{O}^* is the initial concentration of species O, and r_s is the electrode radius.

Considering the new variable, the differential equation system that describes mass transport [given by Eq. (2.131)] changes into

$$\left. \begin{aligned} \frac{\partial u_O(r,t)}{\partial t} &= D_O \frac{\partial^2 u_O(r,t)}{\partial r^2} \\ \frac{\partial u_R(r,t)}{\partial t} &= D_R \frac{\partial^2 u_R(r,t)}{\partial r^2} \end{aligned} \right\} \tag{A.28}$$

where D_O and D_R are the diffusion coefficients of the electro-active species O and R, respectively. The boundary value problem (bvp) takes the form:

$$\left. \begin{aligned} t = 0; r \geq r_s \\ t \geq 0; r \rightarrow \mp\infty \end{aligned} \right\} u_O(r,t) = \frac{r}{r_s}; \quad u_R(r,t) = \mu \frac{r}{r_s} \tag{A.29}$$

with

$$\mu = \frac{c_R^*}{c_O^*} \tag{A.30}$$

$t > 0; r = r_s$

$$D_O \left(\left(\frac{\partial u_O(r,t)}{\partial r} \right)_{r=r_s} - \frac{u_O(r_s,t)}{r_s} \right) = \pm D_R \left(\left(\frac{\partial u_R(r,t)}{\partial r} \right)_{r=r_s} - \frac{u_R(r_s,t)}{r_s} \right) \tag{A.31}$$

$$u_O(r_s,t) = e^\eta u_R(r_s,t) \tag{A.32}$$

with $\eta = (F/RT)(E - E_c^{\Theta})$.

Again, when two signs appear in Eq. (A.31) and in the following, the lower one refers to the case where both species diffuse in the same phase whereas the upper sign to the situation where the electro-active species are diffusive in different phases, such as in amalgamation and uptake processes.

The variable s_i given by

$$s_i = \frac{r - r_s}{2\sqrt{D_i t}} \quad (i = O, R) \tag{A.33}$$

is introduced in the bvp, such that this reveals that the bvp depends on the new dimensionless variable:

$$\xi = \frac{2\sqrt{D_R t}}{r_s J(\eta)} \tag{A.34}$$

where

$$J(\eta) = \frac{(1 + \gamma e^\eta)}{(\gamma^2 e^\eta \mp 1)} \tag{A.35}$$

and $\gamma = \sqrt{D_O/D_R}$.

In order to apply this method, the solutions are written as the series:

$$\begin{aligned} u_O(r, t) &= u_O(s_O, \xi) = \sum_{j=0}^{\infty} \sigma_j^{(-)}(s_O) \xi^j \\ u_R(r, t) &= u_R(s_R, \xi) = \sum_{j=0}^{\infty} \phi_j^{(\pm)}(s_R) \xi^j \end{aligned} \tag{A.36}$$

Taking into account the dimensionless variables s_i and ξ , the differential equation system (A.28) becomes

$$\left. \begin{aligned} \frac{\partial^2 u_O(s_O, \xi)}{\partial s_O^2} + 2s_O \frac{\partial u_O(s_O, \xi)}{\partial s_O} - 2\xi \frac{\partial u_O(s_O, \xi)}{\partial \xi} &= 0 \\ \frac{\partial^2 u_R(s_R, \xi)}{\partial s_R^2} + 2s_R \frac{\partial u_R(s_R, \xi)}{\partial s_R} - 2\xi \frac{\partial u_R(s_R, \xi)}{\partial \xi} &= 0 \end{aligned} \right\} \tag{A.37}$$

with the boundary value problem given by

Soluble solution product

$$\left. \begin{aligned} t = 0 \\ r \geq r_s \end{aligned} \right\} \left. \begin{aligned} s_i \rightarrow \infty; \xi = 0 \\ t \geq 0 \\ r \rightarrow \infty \end{aligned} \right\} \left. \begin{aligned} u_O(\infty) &= \frac{r}{r_s} = 1 + \gamma J(\eta) s_O \xi \\ u_R(\infty) &= \mu \frac{r}{r_s} = \mu (1 + J(\eta) s_R \xi) \end{aligned} \right\} \tag{A.38}$$

Amalgam formation

$$\left. \begin{aligned} t = 0 \\ r \geq r_s \end{aligned} \right\} \left. \begin{aligned} s_O \rightarrow \infty; \xi = 0 \\ t \geq 0 \\ r \rightarrow \infty \end{aligned} \right\} \left. \begin{aligned} u_O(\infty) &= \frac{r}{r_s} = 1 + \gamma J(\eta) s_O \xi \end{aligned} \right\} \tag{A.39}$$

$$\left. \begin{aligned} t = 0 \\ r \leq r_s \end{aligned} \right\} \left. \begin{aligned} s_R \rightarrow -\infty; \xi = 0 \\ t \geq 0 \\ r \rightarrow -\infty \end{aligned} \right\} \left. \begin{aligned} u_R(-\infty) &= \mu \frac{r}{r_s} = \mu (1 + J(\eta) s_R \xi) \end{aligned} \right\} \tag{A.40}$$

$$\left. \begin{array}{l} t > 0 \\ r = r_s \end{array} \right\} \quad s_i = 0 \quad (i = O, R)$$

$$\gamma \left[\left(\frac{\partial u_O(s_O, \xi)}{\partial s_O} \right)_{s_O=0} - \gamma J(\eta) \xi u_O(0, \xi) \right] \quad (A.41)$$

$$= \pm \left[\left(\frac{\partial u_R(s_R, \xi)}{\partial s_R} \right)_{s_R=0} - J(\eta) \xi u_R(0, \xi) \right]$$

$$u_O(0, \xi) = e^\eta u_R(0, \xi) \quad (A.42)$$

By introducing expressions (A.36) into Eq. (A.37), the equations system becomes

$$\left. \begin{array}{l} \sigma_j^{(-)''}(s_O) + 2s_O \sigma_j^{(-)'}(s_O) - 2j \sigma_j^{(-)}(s_O) = 0 \\ \phi_j^{(\pm)''}(s_R) + 2s_R \phi_j^{(\pm)'}(s_R) - 2j \phi_j^{(\pm)}(s_R) = 0 \end{array} \right\} \quad (A.43)$$

Note that Eq. (A.43) is identical to Eq. (A.1); therefore, the solutions of this homogeneous differential equation system have the following form (see Eq. (A.20)):

$$\left. \begin{array}{l} \sigma_j^{(-)}(s_O) = \frac{\sigma_j^{(-)}(+\infty)}{\lim_{s_O \rightarrow \infty} L_j} L_j + a_j \Psi_j^{(-)}(s_O) \\ \phi_j^{(\pm)}(s_R) = \frac{\phi_j^{(\pm)}(\mp\infty)}{\lim_{s_R \rightarrow \mp\infty} L_j} L_j + b_j \Psi_j^{(\pm)}(s_R) \end{array} \right\} \quad \forall j \quad (A.44)$$

where $\Psi_j^{(\pm)}(s_i)$, ($i = O, R$), are the Koutecký functions [1, 6], a_j and b_j are constants that will be determined by applying the boundary value problem, and L_j is given by Eq. (A.2).

By considering expression (A.36) and Koutecký functions properties, the boundary value problem is given by

Soluble solution product

$$\left. \begin{array}{l} t = 0 \\ r \geq r_s \\ t \geq 0 \\ r \rightarrow \infty \end{array} \right\} \quad \left. \begin{array}{l} s_i \rightarrow \infty; \xi = 0 \\ s_i \rightarrow \infty \end{array} \right\} \quad \left. \begin{array}{l} \sigma_0(\infty) = 1; \\ \sigma_1(\infty) = \gamma J(\eta) s_O; \\ \sigma_j(\infty) = 0; \end{array} \right\} \quad \left. \begin{array}{l} \phi_0(\infty) = \mu \\ \phi_1(\infty) = \mu J(\eta) s_R \\ \phi_j(\infty) = 0 \quad j > 1 \end{array} \right\} \quad (A.45)$$

Amalgam formation

$$\left. \begin{array}{l} t = 0 \\ r \geq r_s \end{array} \right\} \left. \begin{array}{l} s_O \rightarrow \infty; \xi = 0 \\ s_O \rightarrow \infty \end{array} \right\} \left. \begin{array}{l} \sigma_0(\infty) = 1 \\ \sigma_1(\infty) = \gamma J(\eta) s_O \\ \sigma_j(\infty) = 0 \end{array} \right\} \quad (\text{A.46})$$

$$\left. \begin{array}{l} t = 0 \\ r \leq r_s \end{array} \right\} \left. \begin{array}{l} s_R \rightarrow -\infty; \xi = 0 \\ s_R \rightarrow -\infty \end{array} \right\} \left. \begin{array}{l} \phi_0(-\infty) = \mu \\ \phi_1(\infty) = \mu J(\eta) s_R \\ \phi_j(\infty) = 0 \quad j > 1 \end{array} \right\} \quad (\text{A.47})$$

$$\left. \begin{array}{l} t > 0 \\ r = r_s \end{array} \right\} \quad s_i = 0 \quad (i = O, R),$$

$$\gamma \left[\sigma_j^{(-)'}(0) - \gamma J(\eta) \sigma_{j-1}^{(-)}(0) \right] = \pm \left[\phi_j^{(\pm)'}(0) - J(\eta) \phi_{j-1}^{(\pm)}(0) \right] \quad \forall j \quad (\text{A.48})$$

$$\sigma_j^{(-)}(0) = e^\eta \phi_j^{(\pm)}(0) \quad \forall j \quad (\text{A.49})$$

with $\sigma_{-1}^{(-)}(0) = \phi_{-1}^{(\pm)} = 0$.

For the solutions of the homogeneous differential equation system (A.43) with conditions (A.45)–(A.49), it is obtained

$$\left. \begin{array}{l} \sigma_0^{(-)}(s_O) = 1 - \frac{(c_O^* - c_O^{s,r})}{c_O^*} \Psi_0^{(-)}(s_O) \\ \sigma_1^{(-)}(s_O) = \gamma J(\eta) s_O + \frac{(c_O^* - c_O^{s,r})}{c_O^*} \frac{e^\eta (\gamma \pm 1) \gamma}{p_1 (\gamma^2 e^\eta \mp 1)} \Psi_1^{(-)}(s_O) \\ \sigma_j^{(-)}(s_O) = \frac{(c_O^* - c_O^{s,r})}{c_O^*} \frac{e^\eta (\gamma \pm 1) \gamma (-1)^{j-1}}{(\gamma^2 e^\eta \mp 1) \prod_{l=1}^j p_l} \Psi_j^{(-)}(s_O) \quad j > 1 \end{array} \right\} \quad (\text{A.50})$$

$$\left. \begin{array}{l} \phi_0^{(\pm)}(s_R) = \mu - \frac{(c_R^* - c_R^{s,r})}{c_O^*} \Psi_0^{(\pm)}(s_R) \\ \phi_1^{(\pm)}(s_R) = \mu J(\eta) s_R - \frac{(c_R^* - c_R^{s,r})}{c_O^*} \frac{(\gamma \pm 1)}{p_1 (\gamma^2 e^\eta \mp 1)} \Psi_1^{(\pm)}(s_R) \\ \phi_j^{(\pm)}(s_R) = \frac{(c_R^* - c_R^{s,r})}{c_O^*} \frac{(-1)^j (\gamma \pm 1)}{(\gamma^2 e^\eta \mp 1) \prod_{l=1}^j p_l} \Psi_j^{(\pm)}(s_R) \quad j > 1 \end{array} \right\} \quad (\text{A.51})$$

with $c_O^{s,r}$ and $c_R^{s,r}$ given by Eq. (2.20).

From Eqs. (A.36), (A.50), and (A.51), and taking into account the definition of variable u_i ($i = O, R$) given by Eq. (A.27), we deduce the following expressions for the concentration profiles of species O and R:

$$c_O(s_O, \xi) = c_O^* - \frac{(c_O^* - c_O^{s,r})}{1 + \gamma J(\eta) s_O \xi} \left[\operatorname{erfc}(s_O) + \frac{e^\eta \gamma (\gamma \pm 1)}{(\gamma^2 e^\eta \mp 1)} \sum_{j=1}^{\infty} \frac{(-1)^j}{j} \xi^j \Psi_j^{(-)}(s_O) \prod_{l=1}^j p_l \right] \quad (\text{A.52})$$

$$c_R(s_R, \xi) = c_R^* - \frac{(c_R^* - c_R^{s,r})}{1 + J(\eta) s_R \xi} \left[\operatorname{erfc}(|s_R|) - \frac{(\gamma \pm 1)}{(\gamma^2 e^\eta \mp 1)} \sum_{j=1}^{\infty} \frac{(-1)^j}{j} \xi^j \Psi_j^{(\pm)}(s_R) \prod_{l=1}^j p_l \right] \quad (\text{A.53})$$

From these expressions and taking into account the properties of Koutecký functions, the expressions for the current and surface concentrations shown in Sect. 2.5.1 are obtained [Eqs. (2.137) and (2.140), respectively].

References

1. Koutecký J (1953) Czech J Phys 2:50–55
2. Weber J, Koutecký J, Koryta J (1959) Z Electrochem 63:583
3. Koutecký J (1953) J Phys 2:50
4. Čížek J, Koryta J, Koutecký J (1959) Collect Czech Chem Commun 24:663
5. Koutecký J, Čížek J (1957) Collect Czech Chem Commun 22:914–928
6. Brikmann AAAM, Loss JM (1964) J Electroanal Chem 7:171–183
7. Galvez J, Serna A (1976) J Electroanal Chem 69:133–143
8. Galvez J, Molina A, Fuente T (1980) 107:217–231
9. Molina A, Laborda E, Gonzalez J, Compton RG (2013) Phys Chem Chem Phys 15:2381–2388
10. Oldham KB, Myland J, Spanier J (2009) An atlas of functions, 2nd edn. Springer Science + Business Media LLC, New York

Appendix B. Laplace Transform Method: Solution for the Application of a Constant Potential to a Simple Charge Transfer Process at Spherical Electrodes When the Diffusion Coefficients of Both Species are Equal

Transform methods are used to solve two-variable linear differential equations essentially by means of the transformation of a partial differential equation into a total differential equation of one independent variable (in general, the number of variables is reduced by one) [1]. The major inconvenience of these methods to find analytical solutions is that the inverse transformation is frequently very difficult or cannot be done at all even for not too complex electrochemical processes. In these cases, the solutions have an integral non-explicit form, from which it is not possible to deduce limit behaviors and the influence of the different variables cannot be inferred for a glance. In Electrochemistry, this method has been extensively used to solve the diffusion equation, which is a two-variable partial differential equation.

In general, any integral transform T of a function $f(t)$ is given by

$$T(f(t)) = \int_a^b f(t)K(t,p)dt = \tilde{f}(p) \quad (\text{B.1})$$

This operation may also be described as mapping a function $f(t)$ in t -space into another function $\tilde{f}(p)$ in p -space.

There are numerous useful integral transforms, each of which is specified by a two-variable function $K(t, p)$ called the Kernel function or nucleus of the transform.

The Laplace transform or the Laplace integral of a function $f(t)$, defined for $0 \leq t \leq \infty$, is

$$L(f(t)) = \int_0^{\infty} f(t) e^{-pt} dt = \bar{f}(p), \quad (\text{B.2})$$

i.e., the Laplace Kernel is e^{-pt} .

The formal properties of calculus integrals and the integration by parts formula lead, among others, to the following rules of the Laplace transform:

– *Linearity*

The Laplace transform, as any integral, has the following properties:

$$(a) \quad L(f(t) + g(t)) = L(f(t)) + L(g(t)) \tag{B.3}$$

$$(b) \quad L(cf(t)) = cL(f(t)) \tag{B.4}$$

– *The t-Derivative Rule*

Let $f(t)$ be continuous, of exponential order, and let $f'(t)$ piecewise continuous on $t \geq 0$. Then $L(f'(t))$ exists and

$$L(f'(t)) = pL(f(t)) - f(0) \tag{B.5}$$

This rule can be extended to the n th derivative in the way,

$$L(f^n(t)) = p^n L(f(t)) - \sum_{k=0}^{n-1} (p^{n-k-1}) f^k(0) \tag{B.6}$$

– *The t-Integral Rule*

Let $f(t)$ be of exponential order and continuous for $t \geq 0$. Then

$$L\left(\int_0^t f(x) dx\right) = \frac{1}{p}L(f(t)) \tag{B.7}$$

– *First Shifting Rule*

Let $f(t)$ be of exponential order and $-\infty < a < \infty$. Then,

$$L(e^{at} f(t)) = L(f(t))|_{p=p-a} \tag{B.8}$$

Table B.1 Laplace transforms of some common functions [2]

$f(t)$	$L(f(t)) = \bar{f}(p)$
t^n	$n! / p^{1+n}$
t^α	$\Gamma(1 + \alpha) / p^{1+\alpha}$ ($\Gamma(1 + \alpha) = \int_0^\infty e^{-x} x^\alpha dx$)
$t^{-1/2}$	$\sqrt{\pi/p}$
e^{at}	$1/(p - a)$
$\cos(at)$	$p/(p^2 + a^2)$
$\sin(at)$	$a/(p^2 + a^2)$
$(a/\pi t)^{1/2} e^{-x^2/4at}$	$e^{-(p/a)^{1/2}x} / (p/a)^{1/2}$
$\operatorname{erfc}(x/\sqrt{4at})$	$e^{-(p/a)^{1/2}x} / p$
$e^{a^2 t} \operatorname{erfc}(at^{1/2})$	$1/p^{1/2} (p^{1/2} + a)$

– *Second Shifting Rule*

Let $f(t)$ and $g(t)$ be of exponential order and continuous and assume $a \geq 0$. Then

$$(a) \quad L(f(t - a)H(t - a)) = e^{-ap}L(f(t)), \tag{B.9}$$

$$(b) \quad L(g(t)H(t - a)) = e^{-ap}L(g(t + a)) \tag{B.10}$$

where $H(x)$ is the Heaviside (step) function:

$$H(x) = \begin{cases} 1 & \text{for } x \geq 0 \\ 0 & \text{otherwise} \end{cases} \tag{B.11}$$

– *Convolution Rule*

Let $f(t)$ and $g(t)$ be of exponential order. Then,

$$L(f(t))L(g(t)) = L(f * g) = L\left(\int_0^t f(x)g(t - x)dx\right) \tag{B.12}$$

Some examples of application of the Laplace Transform are as follows:

$$L(e^{at}) = \int_0^\infty e^{at}e^{-pt}dt = \frac{1}{p - a} \tag{B.13}$$

$$L(t) = \int_0^\infty te^{-pt}dt = \lim_{x \rightarrow \infty} \left[\frac{xe^{-xp}}{p} + \frac{1 - e^{-xp}}{p^2} \right] = \frac{1}{p^2} \tag{B.14}$$

$$L(\sinh(\omega t)) = \int_0^\infty \frac{1}{2}(e^{\omega t} - e^{-\omega t})e^{-pt}dt = \frac{1}{2}\left(\frac{1}{p - \omega} - \frac{1}{p + \omega}\right) \tag{B.15}$$

Next, this method will be applied to find the concentration profiles of species O and R when a potential step is applied to a spherical electrode of radius r_s by assuming that diffusion coefficients of both species are equal (i.e., $D_O = D_R = D$). The differential equation system to solve is given by Eq. (2.131). The following variable change will be done:

$$\left. \begin{aligned} u_O &= \frac{c_O r}{c_O^* r_s} \\ u_R &= \frac{c_R r}{c_O^* r_s} \end{aligned} \right\} \tag{B.16}$$

By introducing the new variables u_O and u_R into Eqs. (2.131)–(2.136), they become

$$\left. \begin{aligned} \frac{\partial u_O}{\partial t} &= D \frac{\partial^2 u_O}{\partial r^2} \\ \frac{\partial u_R}{\partial t} &= D \frac{\partial^2 u_R}{\partial r^2} \end{aligned} \right\} \quad (\text{B.17})$$

$$\left. \begin{aligned} t &\geq 0, & r &\rightarrow \infty \\ t &= 0, & r &\geq r_s \end{aligned} \right\} \quad u_O = \frac{r}{r_s}, \quad u_R = \mu \frac{r}{r_s} \quad (\text{B.18})$$

with $\mu = c_R^*/c_O^*$.

$$\left. \begin{aligned} t &> 0, & r &= r_s \\ u_O(r_s, t) &= e^\eta u_R(r_s, t) \end{aligned} \right\} \quad (\text{B.19})$$

$$\left(\frac{\partial u_O}{\partial r} \right)_{r=r_s} - \frac{u_O(r_s, t)}{r_s} = - \left[\left(\frac{\partial u_R}{\partial r} \right)_{r=r_s} - \frac{u_R(r_s, t)}{r_s} \right] \quad (\text{B.20})$$

If Laplace Transform is applied to Eq. (B.17),

$$L\left(\frac{\partial u_i}{\partial t}\right) = L\left(D\left(\frac{\partial^2 u_i}{\partial r^2}\right)\right) \quad i = O, R \quad (\text{B.21})$$

By taking into account Eqs. (B.4)–(B.5) and writing hereafter for the sake of simplicity $L(u_i) = \bar{u}_i$, it is obtained:

$$\left. \begin{aligned} \frac{d^2 \bar{u}_O}{dr^2} - \frac{p}{D} \bar{u}_O &= -\frac{r}{r_s D} \\ \frac{d^2 \bar{u}_R}{dr^2} - \frac{p}{D} \bar{u}_R &= -\frac{r\mu}{r_s D} \end{aligned} \right\} \quad (\text{B.22})$$

If the following variable change is made:

$$\left. \begin{aligned} \bar{u}_O' &= \frac{r}{r_s p} - \bar{u}_O \\ \bar{u}_R' &= \frac{r\mu}{r_s p} - \bar{u}_R \end{aligned} \right\} \quad (\text{B.23})$$

Eq. (B.22) is transformed as follows

$$\left. \begin{aligned} \frac{d^2 \bar{u}_O'}{dr^2} - \frac{p}{D} \bar{u}_O' &= 0 \\ \frac{d^2 \bar{u}_R'}{dr^2} - \frac{p}{D} \bar{u}_R' &= 0 \end{aligned} \right\} \quad (\text{B.24})$$

The solutions of this differential equation system (B.24) are the following:

$$\left. \begin{aligned} \bar{u}_O'(r) &= a_1 e^{\sqrt{\frac{p}{b}}(r-r_s)} + a_2 e^{-\sqrt{\frac{p}{b}}(r-r_s)} \\ \bar{u}_R'(r) &= b_1 e^{\sqrt{\frac{p}{b}}(r-r_s)} + b_2 e^{-\sqrt{\frac{p}{b}}(r-r_s)} \end{aligned} \right\} \quad (\text{B.25})$$

with $a_1, a_2, b_1,$ and b_2 being constants to be determined. Thus, from Eq. (B.25), it is deduced that to ensure that solutions \bar{u}_i remain finite as $r \rightarrow \infty$, it must be fulfilled that

$$a_1 = b_1 = 0 \quad (\text{B.26})$$

For $r = r_s$ solutions (B.25) become

$$\left. \begin{aligned} \bar{u}_O'(r_s) &= a_2 \\ \bar{u}_R'(r_s) &= b_2 \end{aligned} \right\} \quad (\text{B.27})$$

in such a way that Eq. (B.25) become

$$\left. \begin{aligned} \bar{u}_O'(r) &= \bar{u}_O'(r_s) e^{-\sqrt{\frac{p}{b}}(r-r_s)} \\ \bar{u}_R'(r) &= \bar{u}_R'(r_s) e^{-\sqrt{\frac{p}{b}}(r-r_s)} \end{aligned} \right\} \quad (\text{B.28})$$

which, by taking into account Eqs. (B.16) and (B.23), can be rewritten as

$$\left. \begin{aligned} r \left[\frac{1}{r_s p} - \frac{\bar{c}_O(r, p)}{c_O^* r_s} \right] &= \left[\frac{1}{p} - \frac{\bar{c}_O(r_s, p)}{c_O^*} \right] e^{-\sqrt{\frac{p}{b}}(r-r_s)} \\ r \left[\frac{\mu}{r_s p} - \frac{\bar{c}_R(r, p)}{c_O^* r_s} \right] &= \left[\frac{\mu}{p} - \frac{\bar{c}_R(r_s, p)}{c_O^*} \right] e^{-\sqrt{\frac{p}{b}}(r-r_s)} \end{aligned} \right\} \quad (\text{B.29})$$

By working out $\bar{c}_O(r, p)$ and $\bar{c}_R(r, p)$ in the above equations, one obtains

$$\left. \begin{aligned} \bar{c}_O(r, p) &= \frac{c_O^*}{p} - \left[\frac{c_O^*}{p} - \bar{c}_O(r_s, p) \right] \frac{r_s}{r} e^{-\sqrt{\frac{p}{b}}(r-r_s)} \\ \bar{c}_R(r, p) &= \frac{c_R^*}{p} - \left[\frac{c_R^*}{p} - \bar{c}_R(r_s, p) \right] \frac{r_s}{r} e^{-\sqrt{\frac{p}{b}}(r-r_s)} \end{aligned} \right\} \quad (\text{B.30})$$

Both $\bar{c}_O(r, p)$ and $\bar{c}_R(r, p)$ fulfill

$$\left(\frac{d\bar{c}_i(r, p)}{dr} \right)_{r=r_s} = \left[\frac{c_i^*}{p} - \bar{c}_i(r_s, p) \right] \left[\sqrt{\frac{p}{b}} + \frac{1}{r_s} \right] \quad i = O, R \quad (\text{B.31})$$

From the mass conservation condition, it is obtained that

$$\bar{c}_O(r_s, p) + \bar{c}_R(r_s, p) = \frac{c_O^* + c_R^*}{p} \quad (\text{B.32})$$

Combining Eq. (B.32) with the Nernstian condition [$\bar{c}_O(r_s, p) = e^\eta \bar{c}_R(r_s, p)$], see Eq. (B.19)], the next expressions for the surface concentrations are obtained:

$$\left. \begin{aligned} \bar{c}_O(r_s, p) &= \frac{(c_O^* + c_R^*)e^\eta}{p(1 + e^\eta)} \\ \bar{c}_R(r_s, p) &= \frac{c_O^* + c_R^*}{p(1 + e^\eta)} \end{aligned} \right\} \quad (\text{B.33})$$

Equation (B.33) lead to the following anti-transforms:

$$\left. \begin{aligned} c_O(r_s) &= \frac{(c_O^* + c_R^*)e^\eta}{1 + e^\eta} \\ c_R(r_s) &= \frac{c_O^* + c_R^*}{1 + e^\eta} \end{aligned} \right\} \quad (\text{B.34})$$

Regarding the concentration profile, by introducing Eq. (B.33) into Eq. (B.30),

$$\left. \begin{aligned} \bar{c}_O(r, p) &= \frac{c_O^*}{p} - \left[\frac{c_O^*}{p} - \frac{(c_O^* + c_R^*)e^\eta}{p(1 + e^\eta)} \right] \frac{r_s}{r} e^{-\sqrt{\frac{p}{D}}(r-r_s)} \\ \bar{c}_R(r, p) &= \frac{c_R^*}{p} - \left[\frac{c_R^*}{p} - \frac{c_O^* + c_R^*}{p(1 + e^\eta)} \right] \frac{r_s}{r} e^{-\sqrt{\frac{p}{D}}(r-r_s)} \end{aligned} \right\} \quad (\text{B.35})$$

and by carrying out the anti-transform of the above equations (see Table B.1),

$$\left. \begin{aligned} c_O(r, t) &= c_O^* - \frac{r_s}{r} \left(\frac{c_O^* - c_R^* e^\eta}{1 + e^\eta} \right) \operatorname{erfc} \left(\frac{r - r_s}{2\sqrt{Dt}} \right) \\ c_R(r, t) &= c_R^* + \frac{r_s}{r} \left(\frac{c_O^* - c_R^* e^\eta}{1 + e^\eta} \right) \operatorname{erfc} \left(\frac{r - r_s}{2\sqrt{Dt}} \right) \end{aligned} \right\} \quad (\text{B.36})$$

The expression for the current can be obtained by differentiating Eq. (B.36) with respect to r , and thus Eq. (2.142) is deduced.

References

1. Arfken G (1985) *Mathematical methods for physicists*, 3rd edn. Academic Press, San Diego
2. Spiegel MR, Lipshutz S, Liu J (2006) *Mathematical handbook of formulas and tables*, 4th edn. McGraw Hill, New York

Appendix C. Solutions for Reversible Electrode Reactions at Microspheres and Microdiscs under Steady State Conditions

Stationary Diffusion to Spherical Microelectrodes

The differential equation system to solve is (see Scheme C.1):

$$\frac{d^2c_i}{dr^2} + \frac{2}{r} \frac{dc_i}{dr} = 0 \quad i = O, R \quad (\text{C.1})$$

with the following initial and limiting conditions,

$r \rightarrow \infty$

$$c_O = c_O^*, \quad c_R = c_R^* \quad (\text{C.2})$$

$r = r_s$

$$D_O \left(\frac{\partial c_O}{\partial r} \right)_{r=r_s} = -D_R \left(\frac{\partial c_R}{\partial r} \right)_{r=r_s} \quad (\text{C.3})$$

$$c_O(r_s) = e^\eta c_R(r_s) \quad (\text{C.4})$$

with $\eta = (F/RT)(E - E_c^{\ominus'})$.

By introducing the change $y_i = dc_i/dr$ in Eq. (C.1), this is transformed into

$$\frac{dy_i}{dr} + \frac{2}{r} y_i = 0 \quad i = O, R \quad (\text{C.5})$$

which can be directly integrate to yield to

$$y_i(r) = y_i(r_s) \left(\frac{r_s}{r} \right)^2 \quad (\text{C.6})$$

or

$$\frac{dc_i}{dr} = \left(\frac{dc_i}{dr} \right)_{r=r_s} \left(\frac{r_s}{r} \right)^2 \quad (\text{C.7})$$

By integrating Eq. (C.7), one obtains

$$c_i(r) - c_i(r_s) = \left(\frac{dc_i}{dr} \right)_{r=r_s} r_s \left(1 - \frac{r_s}{r} \right) \quad (\text{C.8})$$

and, by introducing condition Eq. (C.2) in Eq. (C.8),

$$\left(\frac{dc_i}{dr} \right)_{r=r_s} = \frac{c_i^* - c_i(r_s)}{r_s} \quad (\text{C.9})$$

and,

$$c_i(r_s) = c_i^* + (c_i(r_s) - c_i^*) \frac{r_s}{r} \quad (\text{C.10})$$

From Eqs. (C.3)–(C.4), and (C.10), the surface concentrations expressions are as follows:

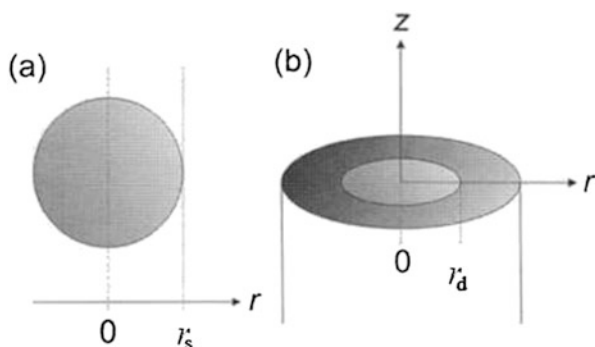
$$\left. \begin{aligned} c_{\text{O}}(r_s) &= e^{\eta} \left(\frac{\gamma^2 c_{\text{O}}^* + c_{\text{R}}^*}{1 + \gamma^2 e^{\eta}} \right) \\ c_{\text{R}}(r_s) &= \frac{\gamma^2 c_{\text{O}}^* + c_{\text{R}}^*}{1 + \gamma^2 e^{\eta}} \end{aligned} \right\} \quad (\text{C.11})$$

with $\gamma^2 = D_{\text{O}}/D_{\text{R}}$ [see Eq. (2.21)].

The current is given by

$$I^{\text{microsphere, ss}} = FA_s D_{\text{O}} \left(\frac{dc_{\text{O}}}{dr} \right)_{r=r_s} \quad (\text{C.12})$$

By introducing Eqs. (C.10)–(C.11) into Eq. (C.12), the expression for the current given in Eq. (2.164) is obtained.



Scheme C.1 Geometries and coordinate systems of (a) a microspherical electrode, (b) a microdisc embedded in an insulating surface

Stationary Diffusion to Disc Microelectrodes

The diffusion equations in this case depend on two spatial coordinates, z and r , in the way (see Scheme C.1):

$$\frac{\partial^2 c_i}{\partial r^2} + \frac{1}{r} \frac{\partial c_i}{\partial r} + \frac{\partial^2 c_i}{\partial z^2} = 0 \quad i = O, R \quad (\text{C.13})$$

with the following boundary conditions:

$$\left. \begin{array}{l} r \geq 0, \quad z \rightarrow \infty \\ z \geq 0, \quad r \rightarrow \infty \end{array} \right\} c_O = c_O^*, \quad c_R = c_R^* \quad (\text{C.14})$$

$$z = 0, \quad r \leq r_d$$

$$c_O(z = 0) = e^\eta c_R(z = 0) \quad (\text{C.15})$$

$$D_O \left(\frac{\partial c_O}{\partial z} \right)_{z=0} = -D_R \left(\frac{\partial c_R}{\partial z} \right)_{z=0} \quad (\text{C.16})$$

A solution for Eq. (C.13), if it is assumed that the surface concentrations are constant in the complete disc surface, i.e., that they are independent of r for $r \leq r_d$, is the following [1]:

$$c_i(r, z) = c_i^* + (c_i(z = 0) - c_i^*) \frac{2}{\pi} \int_0^\infty \frac{\sin(mr)}{m} J_0(mr) e^{-mz} dm \quad (\text{C.17})$$

with $J_0(x)$ being the zeroth order Bessel function [2].

Therefore,

$$\begin{aligned} \left(\frac{\partial c_i}{\partial z}\right)_{z=0} &= \frac{2}{\pi}(c_i^* - c_i(z=0)) \int_0^{\infty} \sin(mr)J_0(mr)dm \\ &= \frac{2}{\pi}(c_i^* - c_i(z=0)) \frac{1}{\sqrt{r_d^2 - r^2}} \end{aligned} \quad (\text{C.18})$$

By introducing Eq. (C.18) into Eq. (C.16), it can be easily deduced:

$$D_O(c_O^* - c_O(z=0)) = -D_R(c_R^* - c_R(z=0)) \quad (\text{C.19})$$

By combining Eqs. (C.15) and (C.19), it is obtained

$$\left. \begin{aligned} c_O(z=0) &= e^{\eta} \left(\frac{\gamma^2 c_O^* + c_R^*}{1 + \gamma^2 e^{\eta}} \right) \\ c_R(z=0) &= \frac{\gamma^2 c_O^* + c_R^*}{1 + \gamma^2 e^{\eta}} \end{aligned} \right\} \quad (\text{C.20})$$

The quantity of species electrolyzed at the total electrode surface per unit of time, C , is

$$C = 4D_O(c_O^* - c_O(z=0)) \int_0^{r_d} \frac{r}{\sqrt{r_d^2 - r^2}} dr = 4r_d D_O(c_O^* - c_O(z=0)) \quad (\text{C.21})$$

The disc current is obtained by multiplying C by the factor “ F ” as follows [1]:

$$I = 4r_d F D_O(c_O^* - c_O(z=0)) \quad (\text{C.22})$$

By introducing Eq. (C.20) into Eq. (C.22), the final expression for the current given in Eq. (2.169) is deduced.

References

1. Saito Y (1968) Rev Polarograph 15:177–187
2. Oldham KB, Myland J, Spanier J (2009) An atlas of functions, 2nd edn. Springer Science + Business Media LLC, New York

Appendix D. Solutions for the Application of a Constant Potential to for Different Electrode Processes with Presence of Homogeneous and Heterogeneous Kinetic Effects at Macroelectrodes

Solution for a Non-reversible Electrode Process at a Planar Electrode

The differential equation given by Eq. (3.1), with the change of variables proposed in Eqs. (3.6) and (3.11) of Sect. 3.2.1, becomes

$$\left. \begin{aligned} \frac{\partial^2 c_O}{\partial (s_O^p)^2} + 2s_O^p \frac{\partial c_O}{\partial s_O^p} - 2\chi \frac{\partial c_O}{\partial \chi} &= 0 \\ \frac{\partial^2 c_R}{\partial (s_R^p)^2} + 2s_R^p \frac{\partial c_R}{\partial s_R^p} - 2\chi \frac{\partial c_R}{\partial \chi} &= 0 \end{aligned} \right\} \quad (\text{D.1})$$

with

$$s_i^p = \frac{x}{2\sqrt{D_i t}} \quad i = O, R \quad (\text{D.2})$$

$$\chi = 2k_{\text{red}} \sqrt{\frac{t}{D_O}} (1 + \gamma e^\eta) \quad (\text{D.3})$$

with $\gamma = \sqrt{D_O/D_R}$.

Differential equations (D.1) have the following boundary conditions:

$$\left. \begin{aligned} s_i^p &\rightarrow \infty & c_i &= c_i^* \\ s_i^p &= 0 & \left(\frac{\partial c_O}{\partial s_O^p} \right)_{s_O^p=0} &= -\frac{1}{\gamma} \left(\frac{\partial c_R}{\partial s_R^p} \right)_{s_R^p=0} \end{aligned} \right\} \quad (\text{D.4})$$

$$\left(\frac{\partial c_O}{\partial s_O^P}\right)_{s_O^P=0} = \chi \frac{[c_O(0) - e^\eta c_R(0)]}{1 + \gamma e^\eta} \tag{D.5}$$

The solutions of differential equations system (D.1) with the boundary value problem given by Eqs. (D.4)–(D.5) can be written as the following functional series of the variable χ with their coefficients being dependent on the variable s_i^P ($i = O, R$):

$$\begin{aligned} c_O(x, t) &= c_O(s_O^P, \chi) = \sum_{j=0}^{\infty} \sigma_j(s_O^P) \chi^j \\ c_R(x, t) &= c_R(s_R^P, \chi) = \sum_{j=0}^{\infty} \rho_j(s_R^P) \chi^j \end{aligned} \tag{D.6}$$

By introducing Eq. (D.6) in Eq. (D.1) the following differential equation system only dependent on s_O^P or s_R^P parameters is obtained:

$$\left. \begin{aligned} \sigma_j''(s_O^P) + 2s_O^P \sigma_j'(s_O^P) - 2j\sigma_j(s_O^P) &= 0 \\ \rho_j''(s_R^P) + 2s_R^P \rho_j'(s_R^P) - 2j\rho_j(s_R^P) &= 0 \end{aligned} \right\} \tag{D.7}$$

and the boundary conditions are as follows:

$$s_i^P \rightarrow \infty$$

$$\begin{aligned} \sigma_0(s_O^P \rightarrow \infty) &= c_O^*; & \rho_0(s_R^P \rightarrow \infty) &= c_R^* \\ \sigma_j(s_O^P \rightarrow \infty) &= 0; & \rho_j(s_R^P \rightarrow \infty) &= 0 \quad j \geq 1 \end{aligned} \tag{D.8}$$

$$s_i^P = 0$$

$$\sigma_j'(0) = -\frac{1}{\gamma} \rho_j'(0) \tag{D.9}$$

$$\sigma_j'(0) = \frac{\sigma_{j-1}(0) - e^\eta \rho_{j-1}(0)}{1 + \gamma e^\eta} \tag{D.10}$$

with [see Eqs. (A.25)–(A.26)]:

$$\left. \begin{aligned} \sigma_0(s_O^P) &= h_0 \psi_0 + c_O^* \operatorname{erf}(s_O) \\ \sigma_j(s_O^P) &= h_j \psi_j \quad j \geq 1 \end{aligned} \right\} \tag{D.11}$$

$$\left. \begin{aligned} \rho_0(s_R^P) &= g_0 \psi_0 + c_R^* \operatorname{erf}(s_R) \\ \rho_j(s_R^P) &= g_j \psi_j \quad j \geq 1 \end{aligned} \right\} \tag{D.12}$$

and $\sigma_{-1}(0) = \rho_{-1}(0) = 0$

Introducing Eqs. (D.11)–(D.12) into Eqs. (D.8)–(D.10), it is obtained

$$h_0 = c_O^* \tag{D.13}$$

$$g_0 = c_R^* \tag{D.14}$$

$$h_j = (-1)^j \frac{(c_O^* - \gamma e^\eta c_R^*)}{(1 + \gamma e^\eta) \prod_{h=1}^j p_h} \quad j \geq 1 \tag{D.15}$$

$$g_j = -\gamma h_j \quad j \geq 1 \tag{D.16}$$

where p_h is given by Eq. (A.7).

From Eqs. (D.11)–(D.16), it is obtained

$$\left. \begin{aligned} \sigma_0(s_O^P) &= c_O^* \\ \sigma_j(s_O^P) &= \left(\frac{c_O^* - c_R^* e^\eta}{1 + \gamma e^\eta} \right) \frac{(-1)^j}{\prod_{h=1}^j p_h} \Psi_j^{(-)}(s_O^P) \quad \text{for } j \geq 1 \end{aligned} \right\} \tag{D.17}$$

$$\left. \begin{aligned} \rho_0(s_R^P) &= c_R^* \\ \rho_j(s_R^P) &= \gamma \left(\frac{c_O^* - c_R^* e^\eta}{1 + \gamma e^\eta} \right) \frac{(-1)^{j+1}}{\prod_{h=1}^j p_h} \Psi_j^{(-)}(s_R^P) \quad \text{for } j \geq 1 \end{aligned} \right\} \tag{D.18}$$

such that the concentration profiles of the electroactive species are given by:

$$c_O(s_O^P, \chi) = c_O^* \left[1 + \left(\frac{1 - \mu e^\eta}{1 + \gamma e^\eta} \right) \sum_{j=1}^{\infty} \frac{(-1)^j}{\prod_{h=1}^j p_h} \Psi_j^{(-)}(s_O^P) \chi^j \right] \tag{D.19}$$

$$c_R(s_R^P, \chi) = c_R^* \left[1 - \frac{\gamma}{\mu} \left(\frac{1 - \mu e^\eta}{1 + \gamma e^\eta} \right) \sum_{j=1}^{\infty} \frac{(-1)^j}{\prod_{h=1}^j p_h} \Psi_j^{(-)}(s_R^P) \chi^j \right] \tag{D.20}$$

Solution for a First-Order Catalytic Mechanism at a Planar Electrode

The differential equation (3.183) can be written as

$$\frac{\partial \phi}{\partial t} = D \frac{\partial^2 \phi}{\partial x^2} \quad (\text{D.21})$$

with the boundary conditions (3.191.a)–(3.192.a) which can be solved by introducing the dimensionless parameters:

$$s^{\text{P}} = \frac{x}{2\sqrt{Dt}} \quad (\text{D.22})$$

$$\chi = (k_1 + k_2)t \quad (\text{D.23})$$

in Eq. (D.21), obtaining

$$\frac{\partial^2 \phi}{\partial (s^{\text{P}})^2} + 2s^{\text{P}} \frac{\partial \phi}{\partial s^{\text{P}}} - 4\chi \frac{\partial \phi}{\partial \chi} = 0 \quad (\text{D.24})$$

for the differential equation and

$$s^{\text{P}} \rightarrow \infty,$$

$$\phi = 0 \quad (\text{D.25})$$

$$s^{\text{P}} = 0,$$

$$e^{-\chi} \phi^s = \frac{1 - Ke^{\eta}}{1 + e^{\eta}} \zeta^* \quad (\text{D.26})$$

This problem can be solved by supposing that

$$\phi(x, t) = \phi(s^{\text{P}}, \chi) = \sum_{j=0}^{\infty} \sigma_j(s^{\text{P}}) \chi^j \quad (\text{D.27})$$

By introducing Eq. (D.27) into Eq. (D.24), we obtain a differential equation only dependent on the variable s^{P} , from which the functions $\sigma_j(s^{\text{P}})$ can be determined:

$$\sigma_j''(s^{\text{P}}) + 2s^{\text{P}} \sigma_j'(s^{\text{P}}) - 4j \sigma_j(s^{\text{P}}) = 0 \quad (\text{D.28})$$

$$s^{\text{P}} \rightarrow \infty,$$

$$\sigma_j(s^{\text{P}} \rightarrow \infty) = 0 \quad \forall j \geq 0 \quad (\text{D.29})$$

$$s^{\text{P}} = 0,$$

$$\left. \begin{aligned} \sigma_j(s^p = 0) &= \frac{h_0}{j!} \\ h_0 &= \frac{1 - Ke^\eta}{1 + e^\eta} \zeta^* \end{aligned} \right\} j \geq 0 \quad (\text{D.30})$$

Therefore,

$$\phi(s^p, \chi) = h_0 \sum_{j=0}^{\infty} \left(\frac{\psi_{2j} \chi^j}{j!} \right) \quad (\text{D.31})$$

with ψ_i being the Koutecký functions (see Eqs. (A.6)–(A.15)) and

$$\left(\frac{\partial \phi}{\partial s^p} \right)_{s^p=0} = -h_0 \sum_{j=0}^{\infty} \left(\frac{p_{2j} \chi^j}{j!} \right) \quad (\text{D.32})$$

and p_i is given by Eq. (A.7).

The current can be written as

$$\frac{I^{\text{cat}}}{FAD\zeta^*} = \frac{1 - Ke^\eta}{(1 + K)(1 + e^\eta)} \sqrt{\frac{k_1 + k_2}{D}} \left[\left(\frac{e^{-\chi}}{\sqrt{\pi\chi}} + \frac{e^{-\chi}}{2\sqrt{\chi}} \sum_{j=1}^{\infty} \left(\frac{p_{2j} \chi^j}{j!} \right) \right) \right] \quad (\text{D.33})$$

with

$$\frac{e^{-\chi}}{2\sqrt{\chi}} \sum_{j=1}^{\infty} \left(\frac{p_{2j} \chi^j}{j!} \right) = \text{erf}(\sqrt{\chi}) \quad (\text{D.34})$$

To obtain Eq. (D.34), it has been taken into account that

$$p_{2i} = \frac{(2i)!!}{(2i-1)!!} \frac{2}{\sqrt{\pi}} \quad (\text{D.35})$$

Rigorous Solution for a CE Process at a Planar Electrode

The differential equation system (3.186.b)–(3.188.b) with the change of variables proposed in Eqs. (D.22)–(D.23) transforms into

$$\left. \begin{aligned} \frac{\partial^2 \zeta}{\partial (s^p)^2} + 2s^p \frac{\partial \zeta}{\partial s^p} - 4\chi \frac{\partial \zeta}{\partial \chi} &= 0 \\ \frac{\partial^2 \phi}{\partial (s^p)^2} + 2s^p \frac{\partial \phi}{\partial s^p} - 4\chi \frac{\partial \phi}{\partial \chi} &= 0 \\ \frac{\partial^2 c_D}{\partial (s^p)^2} + 2s^p \frac{\partial c_D}{\partial s^p} - 4\chi \frac{\partial c_D}{\partial \chi} &= 0 \end{aligned} \right\} \quad (\text{D.36})$$

It will be assumed that the solutions for $\zeta(x, t)$, $\phi(x, t)$, and $c_D(x, t)$ are given by the following functional series:

$$\zeta(x, t) = \zeta(s^P, \chi) = \sum_{j=0}^{\infty} \sigma_j(s^P) \chi^j \tag{D.37}$$

$$\phi(x, t) = \phi(s^P, \chi) = \sum_{j=0}^{\infty} \delta_j(s^P) \chi^j \tag{D.38}$$

$$c_D(x, t) = c_D(s^P, \chi) = \sum_{j=0}^{\infty} \rho_j(s^P) \chi^j \tag{D.39}$$

By introducing Eqs. (D.37)–(D.39) into the differential equation system (D.36), it is obtained

$$\left. \begin{aligned} \sigma_j''(s^P) + 2s^P \sigma_j'(s^P) - 4j\sigma_j(s^P) &= 0 \\ \delta_j''(s^P) + 2s^P \delta_j'(s^P) - 4j\delta_j(s^P) &= 0 \\ \rho_j''(s^P) + 2s^P \rho_j'(s^P) - 4j\rho_j(s^P) &= 0 \end{aligned} \right\} \tag{D.40}$$

and the boundary conditions given by Eqs. (3.189.b)–(3.192.b) become $s^P \rightarrow \infty$,

$$\left. \begin{aligned} \sigma_0(s^P \rightarrow \infty) &= \zeta^* \\ \sigma_j(s^P \rightarrow \infty) &= 0 \quad \forall j \geq 1 \\ \delta_j(s^P \rightarrow \infty) &= 0 \quad \forall j \\ \rho_j(s^P \rightarrow \infty) &= 0 \quad \forall j \end{aligned} \right\} \tag{D.41}$$

$s^P = 0$,

$$\sigma_j'(0) = -\rho_j'(0) \tag{D.42}$$

$$-K \sum_{n=0}^j \frac{\sigma_n'(0)}{(j-n)!} = \delta_j'(0) \tag{D.43}$$

$$\sum_{n=0}^j \frac{\sigma_n(0)}{(j-n)!} - \delta_j(0) = (1+K)e^{\eta} \sum_{n=0}^j \frac{\rho_n(0)}{(j-n)!} \tag{D.44}$$

The solutions for the differential equation system (D.40) take the form:

$$\left. \begin{aligned} \sigma_j(s^P) &= h_j \Psi_{2j}(s^P) + \frac{\sigma_j(\infty)}{\lim_{s^P \rightarrow \infty} L_j} L_j \\ \delta_j(s^P) &= g_j \Psi_{2j}(s^P) + \frac{\delta_j(\infty)}{\lim_{s^P \rightarrow \infty} L_j} L_j \\ \rho_j(s^P) &= k_j \Psi_{2j}(s^P) + \frac{\rho_j(\infty)}{\lim_{s^P \rightarrow \infty} L_j} L_j \end{aligned} \right\} \forall j \quad (D.45)$$

being

$$\left. \begin{aligned} \sigma_0(s^P) &= h_0 \Psi_0(s^P) + \zeta^* \operatorname{erf}(s^P) \\ \sigma_j(s^P) &= h_j \Psi_{2j}(s^P) \quad \forall j \neq 0 \\ \delta_j(s^P) &= g_j \Psi_{2j}(s^P) \quad \forall j \\ \rho_j(s^P) &= k_j \Psi_{2j}(s^P) \quad \forall j \end{aligned} \right\} \quad (D.46)$$

in such a way that

$$\left. \begin{aligned} \sigma'_0(s^P) &= -p_0(h_0 - \zeta^*) \Psi_{-1}(s^P) \\ \sigma'_j(s^P) &= -h_j p_{2j} \Psi_{2j-1}(s^P) \quad \forall j \neq 0 \\ \delta'_j(s^P) &= -g_j p_{2j} \Psi_{2j-1}(s^P) \quad \forall j \\ \rho'_j(s^P) &= -k_j p_{2j} \Psi_{2j-1}(s^P) \quad \forall j \end{aligned} \right\} \quad (D.47)$$

and at the electrode surface ($s^P = 0$), it is fulfilled that

$$\left. \begin{aligned} \sigma_j(0) &= h_j \\ \delta_j(0) &= g_j \\ \rho_j(0) &= k_j \end{aligned} \right\} \quad \forall j \quad (D.48)$$

$$\left. \begin{aligned} \sigma'_0(0) &= -p_0(h_0 - \zeta^*) \\ \sigma'_j(0) &= -h_j p_{2j} \quad \forall j \neq 0 \\ \delta'_j(0) &= -g_j p_{2j} \quad \forall j \\ \rho'_j(0) &= -k_j p_{2j} \quad \forall j \end{aligned} \right\} \quad (D.49)$$

where (see also Appendix A):

$$p_j = \frac{2\Gamma(1 + \frac{j}{2})}{\Gamma(\frac{1+j}{2})} \quad (D.50)$$

By applying the surface conditions (D.42)–(D.43), and taking into account Eq. (D.49), the following is obtained for $j = 0$:

$$k_0 = \zeta^* - h_0 \quad (\text{D.51})$$

$$g_0 = K(\zeta^* - h_0) \quad (\text{D.52})$$

and from the Nernstian condition (D.44), by considering the two above equations and Eq. (D.48):

$$h_0 = \frac{K + (1 + K)e^\eta}{(1 + K)(1 + e^\eta)} \zeta^* \quad (\text{D.53})$$

Therefore,

$$g_0 = \frac{K}{(1 + K)(1 + e^\eta)} \zeta^* \quad (\text{D.54})$$

$$k_0 = \frac{1}{(1 + K)(1 + e^\eta)} \zeta^* \quad (\text{D.55})$$

For $j \neq 0$, it is obtained

$$k_j = -h_j \quad (\text{D.56})$$

$$g_j = -K \sum_{n=0}^j \frac{h_n}{(j-n)!} p_{2n} \quad (\text{D.57})$$

$$g_j = \sum_{n=0}^j \frac{h_n - (1 + K)e^\eta k_n}{(j-n)!} \quad (\text{D.58})$$

By combining Eqs. (D.56)–(D.58), it can be deduced

$$h_j(1 + K)(1 + e^\eta) = \frac{g_0}{j!} \left(\frac{p_0}{p_{2j}} - 1 \right) - \sum_{i=1}^{j-1} \frac{h_i}{(j-i)!} \left(K \frac{p_{2i}}{p_{2j}} + 1 + (1 + K)e^\eta \right) \quad j \neq 0 \quad (\text{D.59})$$

The coefficients h_j can be rewritten as

$$h_j = - \frac{g_0 p_0 \varepsilon_j^{\text{CE}}}{(1 + K)(1 + e^\eta) p_{2j}} \quad j \neq 0 \quad (\text{D.60})$$

in such a way that

$$\varepsilon_j^{\text{CE}} = \frac{1}{j!} \left(\frac{p_{2j}}{p_0} - 1 \right) - \frac{1}{(1+K)(1+e^\eta)} \sum_{i=1}^{j-1} \frac{\varepsilon_i^{\text{CE}}}{(j-i)!} \left[K + (1 + (1+K)e^\eta) \frac{p_{2j}}{p_{2i}} \right] \quad j \neq 0 \quad (\text{D.61})$$

with

$$\varepsilon_1^{\text{CE}} = \frac{p_2}{p_0} - 1 \quad (\text{D.62})$$

Taking into account Eqs. (3.193b), (D.37), (D.46), (D.53) and (D.60), the expression (3.149b) is obtained for the current corresponding to the CE mechanism.

For an EC mechanism, the solution for the differential equation system given by Eqs. (3.186.c)–(3.188.c) with the boundary conditions (3.189.c)–(3.192.c) can be deduced by following a similar procedure to that described for a CE mechanism. The expression of the coefficients of the series S^{EC} which appears in the expression of the current [Eq. (3.194.c)] is

$$\varepsilon_j^{\text{EC}} = \frac{1}{j!} \left[\frac{p_{2j}}{p_0} - 1 \right] - \sum_{i=1}^{j-1} \left(\frac{\varepsilon_i^{\text{EC}}}{(j-i)!} \left[1 + \frac{1+K(1+e^\eta)}{(1+K)(1+e^\eta)} \right] \left[\frac{p_{2j}}{p_{2i}} - 1 \right] \right) \quad j \geq 1 \quad (\text{D.63})$$

Appendix E. The $F(x)$ Function

The $F(x)$ function is defined in general for any electrode whose area increases with an arbitrary power of time z ($z = 0$ for a Planar Electrode and $z = 2/3$ for a Dropping Mercury Electrode) as [1]:

$$F(x) = \sum_{j=0}^{\infty} \frac{(-1)^j (x)^{j+1}}{\prod_{h=0}^j p_h(z)} \quad (\text{E.1})$$

with

$$p_j(z) = \frac{2\Gamma\left(1 + \frac{j}{4z+2}\right)}{\Gamma\left(\frac{1}{2} + \frac{j}{4z+2}\right)} \quad (\text{E.2})$$

$$p_0(0) = \frac{2}{\sqrt{\pi}} \quad (\text{E.3})$$

$$p_i(z) p_{i+1}(z) = 2(i+1) \quad (\text{E.4})$$

with i being

$$i = 2\left(\frac{j}{2z+2}\right) \quad (\text{E.5})$$

Planar Electrodes

F function takes the following compact form in the particular case of planar electrodes ($z = 0$):

$$F(x)|_{\text{plane}} = \sum_{j=0}^{\infty} \frac{(-1)^j (x)^{j+1}}{\prod_{h=0}^j p_h(0)} = \frac{\sqrt{\pi}x}{2} - \frac{x^2}{2} + \frac{8x^3}{\sqrt{\pi}} - \dots \tag{E.6}$$

$$= \sqrt{\pi}(x/2)\exp(x/2)^2\text{erfc}(x/2)$$

$$p_j(0) = \frac{2\Gamma(1 + \frac{j}{2})}{\Gamma(\frac{1}{2} + \frac{j}{2})} \tag{E.7}$$

being in this case $i = j$ in Eq. (E.5) and [2]:

$$\text{erfc}(x) = 1 - \text{erf}(x) = 1 - \frac{2}{\sqrt{\pi}} \int_0^x e^{-u^2} du \tag{E.8}$$

In Fig. E.1, it has been plotted the behavior of function $F(x)|_{\text{plane}}$ for positive values of the variable x .

For high values of the argument x , function $F(x)|_{\text{plane}}$ admits an asymptotic expansion:

$$F(x)|_{x \gg 1} = 1 + 2 \sum_{j=1}^{\infty} \frac{(-1)^j (2j-1)!}{(j-1)! x^{2j}} = 1 - \frac{2}{x^2} + \frac{12}{x^4} - \frac{120}{x^6} + \dots \tag{E.9}$$

An usual approximation to F function is the following:

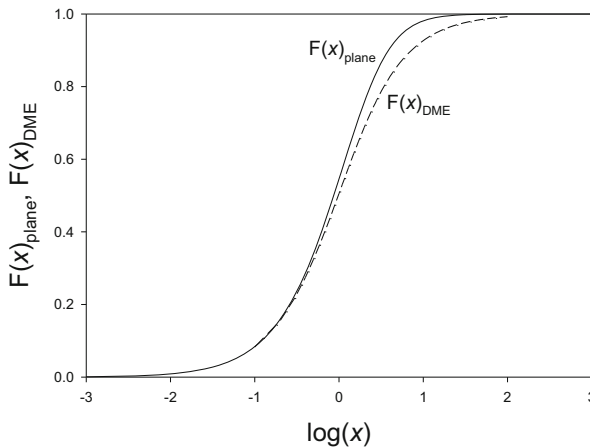


Fig. E.1 Dependence of $F(x)|_{\text{DME}}$ and $F(x)|_{\text{plane}}$ with x calculated from Eqs. (E.1) and (E.6)

$$F_{\text{approx}}(x)|_{\text{plane}} \approx \frac{(\sqrt{\pi}/2)x}{1 + (\sqrt{\pi}/2)x} \tag{E.10}$$

In Fig. E.2, a comparison between F function and approximation given by Eq. (E.10) can be seen. This approximation leads to errors below 5 % for $x \leq 0.185$ and $x \geq 19.7$, although the maximum error is below 16 %.

A function related to $F(x)|_{\text{plane}}$ is $H(x)$, defined as

$$H(x)|_{\text{plane}} = \frac{F(x)|_{\text{plane}}}{\sqrt{\pi}(x/2)} = \exp(x/2)^2 \text{erfc}(x/2) \tag{E.11}$$

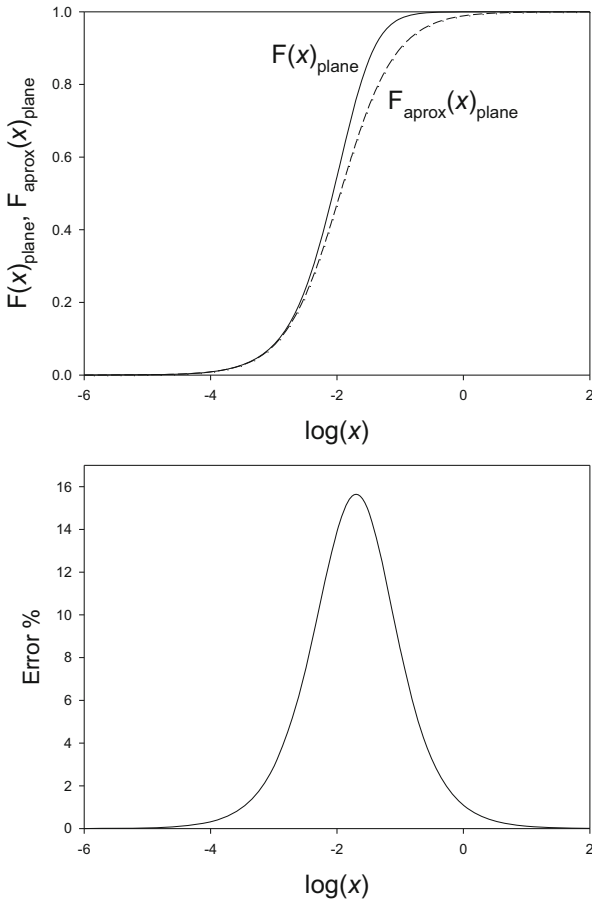


Fig. E.2 Comparison between $F(x)|_{\text{plane}}$ (solid line) and $F_{\text{approx}}(x)|_{\text{plane}}$ (dashed line) calculated from Eqs. (E.6) and (E.10), respectively

Dropping Mercury Electrode

For a Dropping Mercury Electrode, the value $z=2/3$ must be introduced in Eqs. (E.1)–(E.2), and no compact form has been found. Note that in this case

$$p_j(2/3) = \frac{2\Gamma(1 + \frac{3j}{14})}{\Gamma(\frac{1}{2} + \frac{3j}{14})} \quad (\text{E.12})$$

The behavior of this function is similar to that obtained for a plane electrode (see Fig. E.1). For high values of the argument x , function $F(x)|_{\text{DME}}$ admits an asymptotic expansion:

$$F(x)|_{\text{DME}, x \gg 1} \cong 1 - \frac{0.7498}{x} + \frac{0.1733}{x^2} - \frac{0.1116}{x^3} + \frac{0.3733}{x^4} - \dots \quad x \geq 7.1 \quad (\text{E.13})$$

Different approximations have been proposed for $F(x)|_{\text{DME}}$. The most usual are as follows:

- Approximation by Smith et al. [3]

$$F(x)|_{\text{DME}} \cong \frac{(1.030x)^{1.091}}{1 + (1.030x)^{1.091}} \quad (\text{E.14})$$

- Approximation by Oldham and Parry [4]

$$F(x)|_{\text{DME}} \cong \frac{3}{2} \left[1 + b - \sqrt{b^2 + \frac{2b}{3} + 1} \right] \quad (\text{E.15})$$

With $b = 0.85923x$

- Approximation by Nishihara and Matsuda [5]

$$\frac{F(x)|_{\text{DME}}}{1 - F(x)|_{\text{DME}}} \cong 0.224x[\tanh(1.3\log(0.474x)) + 4.96] \quad (\text{E.16})$$

References

1. Koutecký J (1953) Czech J Phys 2:50
2. Oldham KB, Myland J, Spanier J (2009) An atlas of functions, 2nd edn. Springer Science + Business Media LLC, New York
3. Smith DE, McCord TG, Hung HL (1967) Anal Chem 39: 1149
4. Oldham KB, Parry EP (1968) Anal Chem 40:65
5. Nishihara C, Matsuda H (1976) J Electroanal Chem 73:261

Appendix F. Application of a Second Potential Pulse to a Reversible Electrode Reaction Taking Place at Spherical Electrodes When the Diffusion Coefficients of Both Species Are Assumed as Different

Let us consider a reversible charge transfer reaction:



when a double potential pulse is applied at a stationary spherical electrode of radius r_s , taking into account that the reduced species is soluble in the electrolytic solution or in the electrode (electrolyte drop electrodes, amalgamation) and that the diffusion coefficients of the electroactive species may be different.

The applied potential is set at a value E_1 in the interval $0 \leq t \leq \tau_1$ and stepped from E_1 to E_2 at the time $t > \tau_1$ ($t = \tau_1 + t_2$; $0 \leq t_2 \leq \tau_2$). During this second period ($0 \leq t_2 \leq \tau_2$), the mass transport of the species O and R is described by the following differential equation system:

$$\hat{\delta}_{\text{O}} c_{\text{O}}^{(2)}(r, t) = \hat{\delta}_{\text{R}} c_{\text{R}}^{(2)}(r, t) = 0 \quad (\text{F.2})$$

with

$$\hat{\delta}_{\text{k}} = \frac{\partial}{\partial t_2} - D_{\text{k}} \left(\frac{\partial^2}{\partial r^2} + \frac{2}{r} \frac{\partial}{\partial r} \right), \quad \text{k} \equiv \text{O, R} \quad (\text{F.3})$$

The boundary value problem is given by the following:

Solution soluble product:

$$\left. \begin{array}{l} t_2 \geq 0, \quad r \rightarrow \infty \\ t_2 = 0, \quad r \geq r_s \end{array} \right\} c_{\text{O}}^{(2)} = c_{\text{O}}^{(1)}, \quad c_{\text{R}}^{(2)} = c_{\text{R}}^{(1)} \quad (\text{F.4})$$

Electrode soluble product:

$$\left. \begin{matrix} t_2 \geq 0, & r \rightarrow \infty \\ t_2 = 0, & r \geq r_s \end{matrix} \right\} c_O^{(2)} = c_O^{(1)}, c_R^{(2)} = 0 \tag{F.5}$$

$$\left. \begin{matrix} t_2 \geq 0, & r \rightarrow -\infty \\ t_2 = 0, & r \leq r_s \end{matrix} \right\} c_O^{(2)} = 0, c_R^{(2)} = c_R^{(1)} \tag{F.6}$$

$t_2 > 0, \quad r = r_s :$

$$c_O^{(2)}(r_s, t) = e^{\eta_2} c_R^{(2)}(r_s, t) \tag{F.7}$$

$$D_O \left(\frac{\partial c_O^{(2)}(r, t)}{\partial r} \right)_{r=r_s} = \mp D_R \left(\frac{\partial c_R^{(2)}(r, t)}{\partial r} \right)_{r=r_s} \tag{F.8}$$

with

$$\eta_2 = \frac{F}{RT} (E_2 - E_c^{\Theta'}) \tag{F.9}$$

Hereafter, the upper sign in any equation refers to solution soluble product while the lower sign refers to electrode soluble product.

In order to solve the differential equation system [Eq. (F.2)], it is convenient to introduce the following variable change:

$$u_k(r, t) = \frac{c_k(r, t) \times r}{c_O^* \times r_s} \quad (k \equiv O, R) \tag{F.10}$$

Taking into account the new variable $u_k(r, t)$ and that the operator $\hat{\delta}_k$ given by Eq. (F.3) is linear, solutions corresponding to the second potential step can be written as

$$u_k^{(2)}(r, t) = u_k^{(1)}(r, t) + \tilde{u}_k^{(2)}(r, t_2) \quad (k \equiv O, R) \tag{F.11}$$

being $u_k^{(1)}(r, t)$ the solutions of the first potential pulse [1], and $\tilde{u}_k^{(2)}(r, t_2)$ the new unknown partial solutions with null initial conditions ($t_2 = 0$).

The differential equation system becomes

$$\left. \begin{matrix} \frac{\partial \tilde{u}_O^{(2)}(r, t_2)}{\partial t_2} = D_O \frac{\partial^2 \tilde{u}_O^{(2)}(r, t_2)}{\partial r^2} \\ \frac{\partial \tilde{u}_R^{(2)}(r, t_2)}{\partial t_2} = D_R \frac{\partial^2 \tilde{u}_R^{(2)}(r, t_2)}{\partial r^2} \end{matrix} \right\} \tag{F.12}$$

and the boundary value problem is given by

Solution soluble product

$$\left. \begin{matrix} t_2 \geq 0, & r \rightarrow \infty \\ t_2 = 0, & r \geq r_s \end{matrix} \right\} \tilde{u}_O^{(2)} = \tilde{u}_R^{(2)} = 0 \tag{F.13}$$

Electrode soluble product

$$\left. \begin{matrix} t_2 \geq 0, & r \rightarrow \infty \\ t_2 = 0, & r \geq r_s \end{matrix} \right\} \tilde{u}_O^{(2)} = 0; \quad \left. \begin{matrix} t_2 \geq 0, & r \rightarrow -\infty \\ t_2 = 0, & r \leq r_s \end{matrix} \right\} \tilde{u}_R^{(2)} = 0 \tag{F.14}$$

$$\left. \begin{matrix} t_2 > 0 \\ r = r_s \end{matrix} \right\} \gamma^2 \left[\left(\frac{\partial \tilde{u}_O^{(2)}(r, t_2)}{\partial r} \right)_{r=r_s} - \frac{\tilde{u}_O^{(2)}(r_s, t_2)}{r_s} \right] = \mp \left[\left(\frac{\partial \tilde{u}_R^{(2)}(r, t_2)}{\partial r} \right)_{r=r_s} - \frac{\tilde{u}_R^{(2)}(r_s, t_2)}{r_s} \right] \tag{F.15}$$

$$\tilde{u}_O^{(2)}(r_s, t_2) - e^{\eta_2} \tilde{u}_R^{(2)}(r_s, t_2) = e^{\eta_2} u_R^{(1)}(r_s, t) - u_O^{(1)}(r_s, t) \tag{F.16}$$

with

$$\gamma = \sqrt{\frac{D_O}{D_R}} \tag{F.17}$$

As can be seen, the differential equation system (F.12) only depends on the new functions $\tilde{u}_O^{(2)}(r, t_2)$, while the surface condition (F.16) introduces dependence with the first potential pulse.

This problem has been solved by means of Koutecký's dimensionless parameters method [2]. In order to apply it, it has been supposed that solutions have the form:

$$\begin{aligned} \tilde{u}_O^{(2)}(r, t_2) &= \tilde{u}_O^{(2)}(s_{O,2}, \xi_1, \alpha) = \sum_{i,j=0}^{\infty} \sigma_{i,j}^{(-)}(s_{O,2}) \xi_1^i \alpha^j \\ \tilde{u}_R^{(2)}(r, t_2) &= \tilde{u}_R^{(2)}(s_{R,2}, \xi_1, \alpha) = \sum_{i,j=0}^{\infty} \phi_{i,j}^{(\mp)}(s_{R,2}) \xi_1^i \alpha^j \end{aligned} \tag{F.18}$$

with

$$s_{k,2} = \frac{r - r_s}{2\sqrt{D_k t_2}} \quad (k \equiv O, R) \tag{F.19}$$

$$\xi_1 = \frac{2\sqrt{D_R(\tau_1 + t_2)}}{r_s J_1} \tag{F.20}$$

$$J_1 = \frac{1 + \gamma e^{\eta_1}}{\gamma^2 e^{\eta_1} \pm 1} \quad (\text{F.21})$$

$$\alpha = \sqrt{\frac{t_2}{\tau_1 + t_2}} \quad (\text{F.22})$$

$$\eta_1 = \frac{F}{RT} (E_1 - E_c^{\theta'}) \quad (\text{F.23})$$

Taking into account the dimensionless variables, the differential equation system (F.12) becomes

$$\left. \begin{aligned} \frac{\partial^2 \tilde{u}_O^{(2)}(s_{O,2}, \xi_1, \alpha)}{\partial s_{O,2}^2} + 2s_{O,2} \frac{\partial \tilde{u}_O^{(2)}(s_{O,2}, \xi_1, \alpha)}{\partial s_{O,2}} - 2\alpha^2 \xi_1 \frac{\partial \tilde{u}_O^{(2)}(s_{O,2}, \xi_1, \alpha)}{\partial \xi_1} - 2\alpha(1 - \alpha^2) \frac{\partial \tilde{u}_O^{(2)}(s_{O,2}, \xi_1, \alpha)}{\partial \alpha} &= 0 \\ \frac{\partial^2 \tilde{u}_R^{(2)}(s_{R,2}, \xi_1, \alpha)}{\partial s_{R,2}^2} + 2s_{R,2} \frac{\partial \tilde{u}_R^{(2)}(s_{R,2}, \xi_1, \alpha)}{\partial s_{R,2}} - 2\alpha^2 \xi_1 \frac{\partial \tilde{u}_R^{(2)}(s_{R,2}, \xi_1, \alpha)}{\partial \xi_1} - 2\alpha(1 - \alpha^2) \frac{\partial \tilde{u}_R^{(2)}(s_{R,2}, \xi_1, \alpha)}{\partial \alpha} &= 0 \end{aligned} \right\} \quad (\text{F.24})$$

with the boundary value problem given by

Solution soluble product

$$\left. \begin{aligned} t_2 \geq 0, \quad r \rightarrow \infty \\ t_2 = 0, \quad r \geq r_s \end{aligned} \right\} s_{k,2} \rightarrow \infty \quad (k \equiv O, R) : \quad \tilde{u}_O^{(2)}(\infty) = \tilde{u}_R^{(2)}(\infty) = 0 \quad (\text{F.25})$$

Electrode soluble product

$$\left. \begin{aligned} t_2 \geq 0, \quad r \rightarrow \infty \\ t_2 = 0, \quad r \geq r_s \end{aligned} \right\} s_{O,2} \rightarrow \infty, \quad \tilde{u}_O^{(2)}(\infty) = 0 \quad (\text{F.26})$$

$$\left. \begin{aligned} t_2 \geq 0, \quad r \rightarrow -\infty \\ t_2 = 0, \quad r \leq r_s \end{aligned} \right\} s_{R,2} \rightarrow -\infty, \quad \tilde{u}_R^{(2)}(-\infty) = 0 \quad (\text{F.27})$$

$$\left. \begin{aligned} t_2 > 0 \\ r = r_s \end{aligned} \right\} s_{k,2} = 0 \quad (k \equiv O, R)$$

$$\gamma \left[\left(\frac{\partial \tilde{u}_O^{(2)}(s_{O,2}, \xi_1, \alpha)}{\partial s_{O,2}} \right)_{s_{O,2}=0} - \xi_1 \gamma \alpha J_1 \tilde{u}_O^{(2)}(0, \xi_1, \alpha) \right] \quad (\text{F.28})$$

$$= \mp \left[\left(\frac{\partial \tilde{u}_R^{(2)}(s_{R,2}, \xi_1, \alpha)}{\partial s_{R,2}} \right)_{s_{R,2}=0} - \xi_1 \alpha J_1 \tilde{u}_R^{(2)}(0, \xi_1, \alpha) \right]$$

$$\tilde{u}_O^{(2)}(0, \xi_1, \alpha) - e^{\eta_2} \tilde{u}_R^{(2)}(0, \xi_1, \alpha) = e^{\eta_2} u_R^{(1)}(0, \xi_1) - u_O^{(1)}(0, \xi_1) \quad (\text{F.29})$$

By introducing expressions (F.18) into Eq. (F.24), the equation system becomes

$$\left. \begin{aligned} \sigma''_{i,j}(-)(s_{O,2}) + 2s_{O,2}\sigma'_{i,j}(-)(s_{O,2}) - 2j\sigma_{i,j}(-)(s_{O,2}) &= -2(j-i-2)\sigma_{i,j-2}(-)(s_{O,2}) \\ \phi''_{i,j}(\mp)(s_{R,2}) + 2s_{R,2}\phi'_{i,j}(\mp)(s_{R,2}) - 2j\phi_{i,j}(\mp)(s_{R,2}) &= -2(j-i-2)\phi_{i,j-2}(\mp)(s_{R,2}) \end{aligned} \right\} \quad (F.30)$$

By considering expressions (F.18), the boundary value problem is given by *Solution soluble product*

$$\left. \begin{aligned} t_2 \geq 0, \quad r \rightarrow \infty \\ t_2 = 0, \quad r \geq r_s \end{aligned} \right\} s_{k,2} \rightarrow \infty \quad (k \equiv O, R) : \quad \sigma_{i,j}(-)(\infty) = 0; \quad \phi_{i,j}(-)(\infty) = 0 \quad \forall i, j \quad (F.31)$$

Electrode soluble product

$$\left. \begin{aligned} t_2 \geq 0, \quad r \rightarrow \infty \\ t_2 = 0, \quad r \geq r_s \end{aligned} \right\} s_{O,2} \rightarrow \infty, \quad \sigma_{i,j}(-)(\infty) = 0 \quad \forall i, j$$

$$\left. \begin{aligned} t_2 \geq 0, \quad r \rightarrow -\infty \\ t_2 = 0, \quad r \leq r_s \end{aligned} \right\} s_{R,2} \rightarrow -\infty, \quad \phi_{i,j}^{(+)}(-\infty) = 0 \quad \forall i, j \quad (F.32)$$

$$\left. \begin{aligned} t_2 > 0 \\ r = r_s \end{aligned} \right\} s_{k,2} = 0 \quad (k \equiv O, R)$$

$$\gamma \left[\sigma_{i,j}^{(-)'}(0) - \gamma J_1 \sigma_{i-1,j-1}^{(-)}(0) \right] = \mp \left[\phi_{i,j}^{(\mp)'}(0) - J_1 \phi_{i-1,j-1}^{(\mp)}(0) \right] \quad \forall j \quad (F.33)$$

$$\left. \begin{aligned} \sigma_{i,0}^{(-)}(0) - e^{\eta_2} \phi_{i,0}^{(\mp)}(0) &= e^{\eta_2} \phi_{i,0}^{(\mp)}(0) - \sigma_{i,0}^{(-)}(0) \quad j = 0 \\ \sigma_{i,j}^{(-)}(0) &= e^{\eta_2} \phi_{i,j}^{(\mp)}(0) \quad j > 0 \end{aligned} \right\} \quad (F.34)$$

where $\phi_i^{(\mp)}(0)$ and $\sigma_i^{(-)}(0)$ correspond to the first potential pulse solutions [2].

Solutions of the differential equation system have the following form:

When $j - i - 2 = 0$ or $j < 2$ (*homogeneous differential equations*)

$$\left. \begin{aligned} \sigma_{i,j}^{(-)}(s_{O,2}) &= \frac{\sigma_{i,j}^{(-)}(+\infty)}{\lim_{s_{O,2} \rightarrow \infty} L_j} L_j + a_{i,j} \Psi_j^{(-)}(s_{O,2}) \\ \phi_{i,j}^{(\mp)}(s_{R,2}) &= \frac{\phi_{i,j}^{(\mp)}(\pm\infty)}{\lim_{s_{R,2} \rightarrow \pm\infty} L_j} L_j + b_{i,j} \Psi_j^{(\mp)}(s_{R,2}) \end{aligned} \right\} \quad \forall i, j \quad (F.35)$$

When $j - i - 2 \neq 0$ (nonhomogeneous differential equations)

$$\left. \begin{aligned} \sigma_{i,2j}^{(-)}(s_{O,2}) &= \frac{\sigma_{i,2j}^{(-)}(+\infty)}{\lim_{s_{O,2} \rightarrow \infty} L_j} L_j + \sum_{m=0}^j a_{i,2j,m} \Psi_{2m}^{(-)}(s_{O,2}) \\ \phi_{i,2j}^{(\mp)}(s_{R,2}) &= \frac{\phi_{i,2j}^{(\mp)}(\pm\infty)}{\lim_{s_{R,2} \rightarrow \pm\infty} L_j} L_j + \sum_{m=0}^j b_{i,2j,m} \Psi_{2m}^{(\mp)}(s_{R,2}) \end{aligned} \right\} \forall i, j \quad (\text{F.36})$$

$$\left. \begin{aligned} \sigma_{i,2j+1}^{(-)}(s_{O,2}) &= \frac{\sigma_{i,2j+1}^{(-)}(+\infty)}{\lim_{s_{O,2} \rightarrow \infty} L_j} L_j + \sum_{m=0}^j a_{i,2j+1,m} \Psi_{2m+1}^{(-)}(s_{O,2}) \\ \phi_{i,2j+1}^{(\mp)}(s_{R,2}) &= \frac{\phi_{i,2j+1}^{(\mp)}(\pm\infty)}{\lim_{s_{R,2} \rightarrow \pm\infty} L_j} L_j + \sum_{m=0}^j b_{i,2j+1,m} \Psi_{2m+1}^{(\mp)}(s_{R,2}) \end{aligned} \right\} \forall i, j \quad (\text{F.37})$$

where $a_{i, j, m}$ and $b_{i, j, m}$ are constants that we will determine by applying the boundary value problem, L_j are s_k -powers numeric series, and $\Psi_m^{(\pm)}(s_k)$ ($k \equiv O, R$) are Koutecký's functions [3], which have the following properties (see also Appendix A):

$$\Psi_m^{(\pm)}(0) = 1 \quad (\text{F.38})$$

$$\Psi_m^{(\mp)}(\pm\infty) = 0 \quad (\text{F.39})$$

$$\Psi_m^{(\pm)'}(s_k) = \mp p_m \Psi_{m-1}^{(\pm)}(s_k) \quad (\text{F.40})$$

$$\Psi_0^{(\pm)}(s_k) = 1 \mp \operatorname{erf}(s_k) \quad (\text{F.41})$$

Finally, considering that

$$\frac{I_2^{\text{sph}}}{FA_s} = D_O \left(\frac{\partial c_O^{(2)}(r, t)}{\partial r} \right)_{r=r_s} = \mp D_R \left(\frac{\partial c_R^{(2)}(r, t)}{\partial r} \right)_{r=r_s} \quad (\text{F.42})$$

the following expression for the response corresponding to the second potential pulse is obtained:

$$\begin{aligned} I_2^{\text{sph}} &= I_1^{\text{sph}}(\tau_1 + t_2) + I_{d,2}^{\text{plane}}(t_2) Z_{1,2} [1 + (c_R^*/\gamma c_O^*)] (1 + \gamma \Omega_2 \xi_2) \\ &+ I_{d,2}^{\text{plane}}(t_2) Z_{1,2} P_1 \{ (1 + \gamma \Omega_2 \xi_2) [1 - H(\xi_1)] + \frac{\xi_1}{\sqrt{\pi}} [G(\alpha) - 1] \\ &+ \gamma \xi_2 Y_{1,2} S^{\text{even}}(\alpha, \xi_1) + \frac{\gamma \xi_2}{\sqrt{\pi}} S^{\text{odd}}(\alpha, \xi_1) \} \end{aligned} \quad (\text{F.43})$$

with $I_1^{\text{sph}}(\tau_1 + t_2)$ and $H(\xi_1)$ given by Eqs. (2.137) and (2.138), respectively, and

$$\xi_2 = \frac{\sqrt{\pi D_R \tau_2}}{r_s} \tag{F.44}$$

$$I_{d,2}^{\text{plane}}(\tau_2) = \frac{FA_s c_O^* \sqrt{D_O}}{\sqrt{\pi \tau_2}} \tag{F.45}$$

$$\Omega_m = \frac{1 \pm e^{\eta_m}}{1 + \gamma e^{\eta_m}} \quad m \equiv 1, 2 \tag{F.46}$$

$$Z_{1,2} = \frac{\gamma(e^{\eta_1} - e^{\eta_2})}{(1 + \gamma e^{\eta_1})(1 + \gamma e^{\eta_2})} \tag{F.47}$$

$$Y_{1,2} = \frac{e^{\eta_2}(\gamma \mp 1)(\gamma J_2 - 1)J_1^2}{(1 + \gamma e^{\eta_2})J_2^2} \tag{F.48}$$

$$P_1 = \frac{(\gamma - 1)(1 - (c_R^*/c_O^*)e^{\eta_1})}{(\gamma^2 e^{\eta_1} \pm 1)} \tag{F.49}$$

$$J_2 = \frac{1 + \gamma e^{\eta_2}}{\gamma^2 e^{\eta_2} \pm 1} \tag{F.50}$$

$$S^{\text{even}}(\alpha, \xi_1) = \sum_{\substack{i=2 \\ j=1}}^{\infty} \left\{ \frac{(-1)^{j+i} (\xi_1)^i \alpha^{2j} A}{\prod_{l=1}^i p_l} \right\} \tag{F.51}$$

$$S^{\text{odd}}(\alpha, \xi_1) = \sum_{\substack{i=1 \\ j=0}}^{\infty} \left\{ \frac{(-1)^{j+i} (\xi_1)^i \alpha^{2j+1} p_i B}{(i+1) \prod_{l=1}^i p_l} \right\} \tag{F.52}$$

where function $G(x)$ is given by equation (4.43) and

$$p_h = \frac{2\Gamma(1 + \frac{h}{2})}{\Gamma(\frac{1+h}{2})} \tag{F.53}$$

being $\Gamma(x)$ the Euler Gamma Function [4], and

$$\text{if } 2j < i: \quad A = \frac{\prod_{l=0}^{j-1} (i - 2l)}{2^j j!} \left[1 - \left(\frac{J_1}{J_2} \right)^2 \right]^{j-1} \tag{F.54}$$

if $2j = i$:

$$A = \sum_{h=0}^{j-2} \left[(-1)^h \left(\frac{J_1}{J_2} \right)^{2h} \frac{(j-1)!}{h!(j-h-1)!} \right] + \frac{1 + (c_R^*/\gamma c_O^*)}{P_1} \frac{(-1)^j \prod_{h=1}^j p_h}{2^j j!} \left(\frac{J_1}{J_2} \right)^{2(j-1)} \quad (\text{F.55})$$

where the sum is only effective for $j \geq 2$.

$$\text{if } 2j > i \begin{cases} i \text{ odd:} & A = \frac{\prod_{h=0}^{j-1} (i-2h)}{2^j j!} \sum_{h=0}^{i/2-1} \left[(-1)^h \left(\frac{J_1}{J_2} \right)^{2h} \frac{(j-1)!}{h!(j-h-1)!} \right] \\ i \text{ even:} & A = 0 \end{cases} \quad (\text{F.56})$$

and

$$\begin{aligned} \text{if } 2j+1 < i: B &= \frac{\prod_{h=0}^j (i-2h+1)}{(2j+1)2^j(j+1)!} \left[\frac{1}{2\gamma J_1} + Y_{1,2} \sum_{m=0}^j \left\{ (-1)^m 2^m \left[\frac{J_1}{J_2} \right]^{2m-1} \prod_{k=0}^m \left(\frac{j-k+1}{2k-1} \right) \right\} \right] \quad (\text{F.57}) \\ \text{if } 2j+1 = i: B &= \frac{1}{(2j+1)\gamma J_1} + \frac{2Y_{1,2}}{(2j+1)} \sum_{m=0}^{j-1} \left\{ (-1)^m 2^m \left[\frac{J_1}{J_2} \right]^{2m-1} \prod_{k=0}^m \left(\frac{j-k+1}{2k-1} \right) \right\} \\ &+ \frac{Y_{1,2} [1 + (c_R^*/\gamma c_O^*)]}{P_1} \frac{(-1)^j (i+1)j! \prod_{h=1}^i p_h}{p_i (2j+1)!} \left(\frac{J_1}{J_2} \right)^{2j-1} \end{aligned} \quad (\text{F.58})$$

where the sum is only effective for $j \geq 1$.

if $2j+1 > i$

$$\begin{aligned} i \text{ even: } B &= \frac{\prod_{h=0}^j (i-2h+1)}{(2j+1)2^j(j+1)!} \left[\frac{1}{2\gamma J_1} + Y_{1,2} \sum_{m=0}^{i/2-1} \left\{ (-1)^m 2^m \left[\frac{J_1}{J_2} \right]^{2m-1} \prod_{k=0}^m \left(\frac{j-k+1}{2k-1} \right) \right\} \right] \\ i \text{ odd: } B &= 0 \end{aligned} \quad (\text{F.59})$$

The number of terms to be considered in series $S^{\text{even}}(\alpha, \xi_1)$ and $S^{\text{odd}}(\alpha, \xi_1)$ obviously depends on the electrode sphericity (through ξ_1) and on the duration of the potential pulses (through α), so that the higher sphericity and the greater α value, the higher order of i -powers and j -powers, respectively, must be considered. In reference [5], a discussion about this point is presented, showing that to obtain a relative error less than 1 % when $\gamma = 0.7$, $E_1 \rightarrow -\infty$, $E_2 \rightarrow +\infty$, $t_1 = 1$ s, and

$t_2 = 0.5$ s, we need to consider up to the 11th order (ξ_1^{11}) for $r_s = 5 \times 10^{-3}$ cm, up to the 175th order (ξ_1^{175}) for $r_s = 10^{-3}$ cm, and up to the 275th order (ξ_1^{275}) for $r_s = 8 \times 10^{-4}$ cm, being in all cases up to α^{75} -term considered [2].

References

1. Molina A, Serna C, Martinez-Ortiz F, Laborda E (2008) *J Electroanal Chem* 617:14–26
2. Molina A, Compton RG, Serna C, Martinez-Ortiz F, Laborda E (2009) *Electrochim Acta* 54:2320–2328
3. Koutecký J (1953) *Czech J Phys* 2:50–55
4. Oldham KB, Myland J, Spanier J (2009) *An atlas of functions*, 2nd edn. Springer Science + Business Media LLC, New York
5. Molina A, Serna C, Martinez-Ortiz F, Laborda E (2008) *Electrochem Commun* 10:376–381

Appendix G. Application of Two Potential Pulses to a Non-reversible Charge Transfer: Differential Double Pulse Voltammetry and Reverse Pulse Voltammetry

Solution for Spherical Electrodes in Differential Double Pulse Voltammetry

The following charge transfer reaction taking place at a spherical electrode of radius r_s will be considered:



with k_{red} and k_{ox} being the rate constants for the electro-reduction and electro-oxidation processes which, for the Butler–Volmer formalist, are given by

$$\left. \begin{aligned} k_{\text{red},j} &= k^0 e^{-\alpha \eta_j} \\ k_{\text{ox},j} &= e^{\eta_j} k_{\text{red},j} \end{aligned} \right\} \quad (G.1)$$

with

$$\eta_j = \frac{F}{RT} (E_j - E_c^{\Theta}) \quad j = 1, 2 \quad (G.2)$$

k^0 and α are the heterogeneous rate constant and the charge transfer coefficient, respectively.

In order to solve the problem, we introduce the following variable change [1]:

$$u_i^{(j)}(r, t) = \frac{c_i^{(j)}(r, t)r}{c_O^* r_s} \quad \begin{array}{l} i \equiv O, R \\ j \equiv 1, 2 \end{array} \quad (G.3)$$

Considering the new variable, $u_i^{(j)}(r, t)$, the differential equation system and the corresponding boundary value problem for the first potential pulse E_1 ($t = t_1$; $0 \leq t_1 \leq \tau_1$) become [see Eqs. (4.111)–(4.115)]:

$$\left. \begin{aligned} \frac{\partial u_O^{(1)}(r,t)}{\partial t} &= D \frac{\partial^2 u_O^{(1)}(r,t)}{\partial r^2} \\ \frac{\partial u_R^{(1)}(r,t)}{\partial t} &= D \frac{\partial^2 u_R^{(1)}(r,t)}{\partial r^2} \end{aligned} \right\} \tag{G.4}$$

$$\left. \begin{aligned} t \geq 0, & \quad r \rightarrow \infty \\ t = 0, & \quad r \geq r_s \end{aligned} \right\} u_O^{(1)} = \frac{r}{r_s}; \quad u_R^{(1)} = (c_R^*/c_O^*) \frac{r}{r_s} \tag{G.5}$$

$$\left. \begin{aligned} t > 0 \\ r = r_s \end{aligned} \right\} \left(\frac{\partial u_O^{(1)}}{\partial r} \right)_{r=r_s} - \frac{u_O^{(1)}(r_s)}{r_s} = - \left[\left(\frac{\partial u_R^{(1)}}{\partial r} \right)_{r=r_s} - \frac{u_R^{(1)}(r_s)}{r_s} \right] \tag{G.6}$$

$$D \left[\left(\frac{\partial u_O^{(1)}}{\partial r} \right)_{r=r_s} - \frac{u_O^{(1)}(r_s)}{r_s} \right] = k^0 e^{-\alpha \eta_1} u_O^{(1)}(r_s) - k^0 e^{(1-\alpha)\eta_1} u_R^{(1)}(r_s) \tag{G.7}$$

with η_1 given by Eq. (G.2).

By applying Koutecký's dimensionless parameter method [1], we suppose that solutions are functional series of the dimensionless variable ξ :

$$u_O^{(1)}(r,t) = u_O^{(1)}(s,\xi) = \sum_k \sigma_k^{(1)}(s) \xi^k \tag{G.8}$$

$$u_R^{(1)}(r,t) = u_R^{(1)}(s,\xi) = \sum_k \rho_k^{(1)}(s) \xi^k \tag{G.9}$$

with

$$\xi = \frac{2\sqrt{Dt}}{r_s} \tag{G.10}$$

$$s = \frac{r - r_s}{2\sqrt{Dt}} \tag{G.11}$$

Taking into account the dimensionless variables s and ξ , the differential equation system and the boundary value problem turn into

$$\left. \begin{aligned} \frac{\partial^2 u_O^{(1)}}{\partial s^2} + 2s \frac{\partial u_O^{(1)}}{\partial s} - 2\xi \frac{\partial u_O^{(1)}}{\partial \xi} &= 0 \\ \frac{\partial^2 u_R^{(1)}}{\partial s^2} + 2s \frac{\partial u_R^{(1)}}{\partial s} - 2\xi \frac{\partial u_R^{(1)}}{\partial \xi} &= 0 \end{aligned} \right\} \tag{G.12}$$

$s \rightarrow \infty$

$$u_{\text{O}}^{(1)}(\infty) = 1 + s\xi; \quad u_{\text{R}}^{(1)}(\infty) = (c_{\text{R}}^*/c_{\text{O}}^*)(1 + s\xi) \quad (\text{G.13})$$

$s = 0$

$$\left(\frac{\partial u_{\text{O}}^{(1)}}{\partial s} \right)_{s=0} - \xi u_{\text{O}}^{(1)}(0) = - \left[\left(\frac{\partial u_{\text{R}}^{(1)}}{\partial s} \right)_{s=0} - \xi u_{\text{R}}^{(1)}(0) \right] \quad (\text{G.14})$$

$$\left(\frac{\partial u_{\text{O}}^{(1)}}{\partial s} \right)_{s=0} - \xi u_{\text{O}}^{(1)}(0) = \frac{r_s k^0 e^{-\alpha \eta_1}}{D} [u_{\text{O}}^{(1)}(0) - e^{\eta_1} u_{\text{R}}^{(1)}(0)] \xi \quad (\text{G.15})$$

By introducing the expressions (G.8) and (G.9) into Eq. (G.12), the differential equation system becomes

$$\left. \begin{aligned} \sigma_k^{(1)''}(s) + 2s\sigma_k^{(1)'}(s) - 2k\sigma_k^{(1)}(s) &= 0 \\ \rho_k^{(1)''}(s) + 2s\rho_k^{(1)'}(s) - 2k\rho_k^{(1)}(s) &= 0 \end{aligned} \right\} \quad (\text{G.16})$$

the solutions of which have the following form:

$$\left. \begin{aligned} \sigma_k^{(1)}(s) &= \frac{\sigma_k^{(1)}(\infty)}{\lim_{s \rightarrow \infty} L_k} L_k + a_k^{(1)} \Psi_k(s) \\ \rho_k^{(1)}(s) &= \frac{\rho_k^{(1)}(\infty)}{\lim_{s \rightarrow \infty} L_k} L_k + b_k^{(1)} \Psi_k(s) \end{aligned} \right\} \quad (\text{G.17})$$

where $a_k^{(1)}$ and $b_k^{(1)}$ are constants that will be determined from the boundary value problem, L_j are s -powers numeric series, and $\Psi_k(s)$ are Koutecký functions which have different properties indicated in Eqs. (A.11)–(A.14) (see also [2]). Taking into account the form of the solutions [Eq. (G.17)] along with the properties of Koutecký functions, the boundary value problem is given by

$s \rightarrow \infty$

$$\begin{aligned} \sigma_0^{(1)}(\infty) &= 1 & \rho_0^{(1)}(\infty) &= (c_{\text{R}}^*/c_{\text{O}}^*) \\ \sigma_1^{(1)}(\infty) &= s & \rho_1^{(1)}(\infty) &= (c_{\text{R}}^*/c_{\text{O}}^*)s \\ \sigma_k^{(1)}(\infty) &= 0 & \rho_k^{(1)}(\infty) &= 0; \quad k > 1 \end{aligned} \quad (\text{G.18})$$

$s = 0$

$$\sigma_k^{(1)'}(0) - \sigma_{k-1}^{(1)}(0) = -\rho_k^{(1)'}(0) + \rho_{k-1}^{(1)}(0) \quad (\text{G.19})$$

$$\sigma_k^{(1)'}(0) - \sigma_{k-1}^{(1)}(0) = \frac{r_s k_0}{D} e^{-\alpha \eta_1} \left[\sigma_{k-1}^{(1)}(0) - e^{\eta_1} \rho_{k-1}^{(1)}(0) \right] \quad (\text{G.20})$$

and $\sigma_{-1}^{(1)}(0) = \rho_{-1}^{(1)}(0) = 0$

By applying Eqs. (G.18)–(G.20), we obtain the expressions for $\sigma_k^{(1)}(s)$ and $\rho_k^{(1)}(s)$, and by introducing them in Eqs. (G.8) and (G.9), we find the solutions of the problem ($u_O^{(1)}(r, t)$ and $u_R^{(1)}(r, t)$). From these, the I – E expression for the application of the first potential pulse at spherical electrodes is obtained:

$$\frac{I_1^{\text{sph}}}{I_{d,c}^{\text{sph}}} = \frac{\kappa_{\text{sph}} (1 - (c_R^*/c_O^*) e^{\eta_1})}{\vartheta_1 (1 + e^{\eta_1})} \left[1 + \kappa_{\text{sph}} \left(1 + \frac{2}{\sqrt{\pi}} \frac{\vartheta_1}{\chi_{s,1}} \right) H(\chi_{s,1}) \right] \quad (\text{G.21})$$

with

$$H(\chi_s) = 2F(\chi_s) / (\sqrt{\pi} \chi_s) = e^{\chi_s^2/4} \text{erfc}(\chi_s/2) \quad (\text{G.22})$$

$$\vartheta_1 = 1 + \frac{k^0 r_s}{D} \frac{1 + e^{\eta_1}}{e^{\alpha \eta_1}} \quad (\text{G.23})$$

$$\chi_{s,1} = \frac{2\sqrt{Dt}}{r_s} \vartheta_1 \quad (\text{G.24})$$

$$\kappa_{\text{sph}} = \kappa_{\text{sph}}^0 e^{-\alpha \eta_1} (1 + e^{\eta_1}) \quad (\text{G.25})$$

$$\kappa_{\text{sph}}^0 = \frac{\frac{k^0 r_s}{D}}{1 + \frac{r_s}{\sqrt{\pi Dt}}} \quad (\text{G.26})$$

$$I_{d,c}^{\text{sph}} = FADc_O^* \left(\frac{1}{r_s} + \frac{1}{\sqrt{\pi Dt}} \right) \quad (\text{G.27})$$

Regarding the application of the second potential step ($t = \tau_1 + t_2$; $0 \leq t_2 \leq \tau_2$), due to that the diffusion operator for spherical diffusion is linear, the solutions of the differential equation system can be written as

$$u_i^{(2)}(r, t) = u_i^{(1)}(r, t) + \tilde{u}_i^{(2)}(r, t_2) \quad i \equiv \text{O, R} \quad (\text{G.28})$$

being $\tilde{u}_i^{(2)}(r, t_2)$ the new unknown partial solutions with null initial conditions:

$$\left. \begin{aligned} \frac{\partial \tilde{u}_O^{(2)}(r, t_2)}{\partial t_2} &= D \frac{\partial^2 \tilde{u}_O^{(2)}(r, t_2)}{\partial r^2} \\ \frac{\partial \tilde{u}_R^{(2)}(r, t_2)}{\partial t_2} &= D \frac{\partial^2 \tilde{u}_R^{(2)}(r, t_2)}{\partial r^2} \end{aligned} \right\} \quad (\text{G.29})$$

$$\left. \begin{array}{l} t_2 \geq 0, \quad r \rightarrow \infty \\ t_2 = 0, \quad r \geq r_s \end{array} \right\} \quad \tilde{u}_O^{(2)} = 0; \tilde{u}_R^{(2)} = 0 \quad (\text{G.30})$$

$$\left. \begin{array}{l} t_2 > 0 \\ r = r_s \end{array} \right\}$$

$$\left(\frac{\partial \tilde{u}_O^{(2)}}{\partial r} \right)_{r=r_s} - \frac{\tilde{u}_O^{(2)}(r_s)}{r_s} = - \left[\left(\frac{\partial \tilde{u}_R^{(2)}}{\partial r} \right)_{r=r_s} - \frac{\tilde{u}_R^{(2)}(r_s)}{r_s} \right] \quad (\text{G.31})$$

$$\begin{aligned} D \left[\left(\frac{\partial \tilde{u}_O^{(2)}}{\partial r} \right)_{r=r_s} - \frac{\tilde{u}_O^{(2)}(r_s)}{r_s} \right] - k^0 e^{-\alpha \eta_2} \tilde{u}_O^{(2)}(r_s) + k^0 e^{(1-\alpha)\eta_2} \tilde{u}_R^{(2)}(r_s) = \\ - \left\{ D \left[\left(\frac{\partial u_O^{(1)}}{\partial r} \right)_{r=r_s} - \frac{u_O^{(1)}(r_s)}{r_s} \right] - k^0 e^{-\alpha \eta_2} u_O^{(1)}(r_s) + k^0 e^{(1-\alpha)\eta_2} u_R^{(1)}(r_s) \right\} \end{aligned} \quad (\text{G.32})$$

Again this problem can be solved by means of Koutecký's dimensionless parameter method. Thus, we introduce the dimensionless variables:

$$s_2 = \frac{r - r_s}{2\sqrt{Dt_2}} \quad (\text{G.33})$$

$$\xi_2 = \frac{2\sqrt{Dt_2}}{r_s} \quad (\text{G.34})$$

so that the solutions are given by

$$\tilde{u}_O^{(2)}(r, t_2) = \tilde{u}_O^{(2)}(s_2, \xi_2) = \sum_k \sigma_k^{(2)}(s_2) \xi_2^k \quad (\text{G.35})$$

$$\tilde{u}_R^{(2)}(r, t_2) = \tilde{u}_R^{(2)}(s_2, \xi_2) = \sum_k \rho_k^{(2)}(s_2) \xi_2^k \quad (\text{G.36})$$

and the differential equation system and the boundary value problem turn into

$$\left. \begin{array}{l} \frac{\partial^2 \tilde{u}_O^{(2)}}{\partial s_2^2} + 2s_2 \frac{\partial \tilde{u}_O^{(2)}}{\partial s_2} - 2\xi_2 \frac{\partial \tilde{u}_O^{(2)}}{\partial \xi_2} = 0 \\ \frac{\partial^2 \tilde{u}_R^{(2)}}{\partial s_2^2} + 2s_2 \frac{\partial \tilde{u}_R^{(2)}}{\partial s_2} - 2\xi_2 \frac{\partial \tilde{u}_R^{(2)}}{\partial \xi_2} = 0 \end{array} \right\} \quad (\text{G.37})$$

$s_2 \rightarrow \infty$

$$\tilde{u}_O^{(2)}(\infty) = 0; \quad \tilde{u}_R^{(2)}(\infty) = 0 \tag{G.38}$$

$s_2 = 0$

$$\left(\frac{\partial \tilde{u}_O^{(2)}}{\partial s_2} \right)_{s_2=0} - \xi_2 \tilde{u}_O^{(2)}(0) = - \left[\left(\frac{\partial \tilde{u}_R^{(2)}}{\partial s_2} \right)_{s_2=0} - \xi_2 \tilde{u}_R^{(2)}(0) \right] \tag{G.39}$$

$$\left(\frac{\partial \tilde{u}_O^{(2)}}{\partial s_2} \right)_{s_2=0} - \xi_2 \tilde{u}_O^{(2)}(0) - \frac{r_s k^0 e^{-\alpha \eta_2}}{D} \left[\tilde{u}_O^{(2)}(0) - e^{\eta_2} \tilde{u}_R^{(2)}(0) \right] \xi_2 = - \left\{ \left(\frac{\partial u_O^{(1)}}{\partial s_1} \right)_{s_1=0} \frac{1}{\xi_1} - u_O^{(1)}(0) - \frac{r_0 k^0 e^{-\alpha \eta_2}}{D} \left[u_O^{(1)}(0) - e^{\eta_2} u_R^{(1)}(0) \right] \right\} \xi_2 \tag{G.40}$$

The solutions of the system (G.37) have the following form:

$$\left. \begin{aligned} \sigma_k^{(2)}(s_2) &= \frac{\sigma_k^{(2)}(\infty)}{\lim_{s_2 \rightarrow \infty} L_k} L_k + a_k^{(2)} \Psi_k(s_2) \\ \rho_k^{(2)}(s_2) &= \frac{\rho_k^{(2)}(\infty)}{\lim_{s_2 \rightarrow \infty} L_k} L_k + b_k^{(2)} \Psi_k(s_2) \end{aligned} \right\} \tag{G.41}$$

which must fulfill the following limit and surface conditions:

$s_2 \rightarrow \infty$

$$\sigma_k^{(2)}(\infty) = 0; \quad \rho_k^{(2)}(\infty) = 0 \quad \forall k \tag{G.42}$$

$s_2 = 0$

$$\sigma_k^{(2)'}(0) - \sigma_{k-1}^{(2)}(0) = -\rho_k^{(2)'}(0) + \rho_{k-1}^{(2)}(0) \tag{G.43}$$

$$\left. \begin{aligned} \bullet \quad \sigma_k^{(2)'}(0) - \sigma_{k-1}^{(2)}(0) - \frac{r_s k_0 e^{-\alpha \eta_2}}{D} \left[\sigma_{k-1}^{(2)}(0) - e^{\eta_2} \rho_{k-1}^{(2)}(0) \right] &= 0 \quad k \neq 1 \\ \bullet \quad \sigma_1^{(2)'}(0) - \sigma_0^{(2)}(0) - \frac{r_s k_0 e^{-\alpha \eta_2}}{D} \left[\sigma_0^{(2)}(0) - e^{\eta_2} \rho_0^{(2)}(0) \right] &= \\ - \left\{ \left(\frac{\partial u_O^{(1)}}{\partial s_1} \right)_{s_1=0} \frac{1}{\xi_1} - u_O^{(1)}(0) - \frac{r_0 k_0 e^{-\alpha \eta_2}}{D} \left[u_O^{(1)}(0) - e^{\eta_2} u_R^{(1)}(0) \right] \right\} & \quad k = 1 \end{aligned} \right\} \tag{G.44}$$

As can be seen, the surface condition (G.44) introduces dependence with the first potential pulse. Given that in DDPV technique we have that $t_1 \gg t_2$, it can be

assumed that the mathematical form of the solutions corresponding to the first pulse ($u_{\text{O}}^{(1)}(r, t)$ and $u_{\text{R}}^{(1)}(r, t)$) is not disturbed by the application of the second one.

By applying the conditions given by Eqs. (G.42)–(G.44), we deduce the expressions for $\sigma_k^{(2)}(s_2)$ and $\rho_k^{(2)}(s_2)$, and taking into account Eqs. (G.28), (G.35), and (G.36), the solutions $u_i^{(2)}(r, t)$ are obtained. From these, the equation for the current corresponding to the second potential pulse [Eq. (4.134)] is derived.

Solution for the Second Current in Reverse Pulse Voltammetry

To solve the problem corresponding to the second potential step, the Koutecký's dimensionless parameter method [3] has been applied by assuming that the solutions of the differential equation system (G.29) are functional series of the dimensionless variables χ_2 and β :

$$\tilde{u}_{\text{O}}^{(2)}(r, t) = \tilde{u}_{\text{O}}^{(2)}(s_2, \chi_2, \beta) = \sum_{i,j} \sigma_{i,j}(s_2) \chi_2^i \beta^{j/2} \quad (\text{G.45})$$

$$\tilde{u}_{\text{R}}^{(2)}(r, t) = \tilde{u}_{\text{R}}^{(2)}(s_2, \chi_2, \beta) = \sum_{i,j} \delta_{i,j}(s_2) \chi_2^i \beta^{j/2} \quad (\text{G.46})$$

with

$$\chi_2 = \frac{2\sqrt{Dt_2}}{r_s} + 2\sqrt{\frac{t_2}{D}} k^0 e^{-\alpha\eta_2} (1 + e^{\eta_2}) \quad (\text{G.47})$$

$$\beta = \frac{t_2}{\tau_1 + t_2} \quad (\text{G.48})$$

Taking into account the definition of s_2 (Eq. (G.33)), χ_2 , and β , the differential equation system and the boundary value problem turn into

$$\left. \begin{aligned} \frac{\partial^2 \tilde{u}_{\text{O}}^{(2)}}{\partial s_2^2} + 2s_2 \frac{\partial \tilde{u}_{\text{O}}^{(2)}}{\partial s_2} - 2\chi_2 \frac{\partial \tilde{u}_{\text{O}}^{(2)}}{\partial \chi_2} - 4\beta(1-\beta) \frac{\partial \tilde{u}_{\text{O}}^{(2)}}{\partial \beta} &= 0 \\ \frac{\partial^2 \tilde{u}_{\text{R}}^{(2)}}{\partial s_2^2} + 2s_2 \frac{\partial \tilde{u}_{\text{R}}^{(2)}}{\partial s_2} - 2\chi_2 \frac{\partial \tilde{u}_{\text{R}}^{(2)}}{\partial \chi_2} - 4\beta(1-\beta) \frac{\partial \tilde{u}_{\text{R}}^{(2)}}{\partial \beta} &= 0 \end{aligned} \right\} \quad (\text{G.49})$$

$s_2 \rightarrow \infty$

$$\tilde{u}_O^{(2)}(\infty) = 0; \quad \tilde{u}_R^{(2)}(\infty) = 0 \quad (\text{G.50})$$

$s_2 = 0$

$$\left(\frac{\partial \tilde{u}_O^{(2)}}{\partial s_2} \right)_{s_2=0} - \frac{\chi_2 \tilde{u}_O^{(2)}(0)}{\theta_2} = - \left[\left(\frac{\partial \tilde{u}_R^{(2)}}{\partial s_2} \right)_{s_2=0} - \frac{\chi_2 \tilde{u}_R^{(2)}(0)}{\theta_2} \right] \quad (\text{G.51})$$

$$\begin{aligned} & \left(\frac{\partial \tilde{u}_O^{(2)}}{\partial s_2} \right)_{s_2=0} - \frac{\chi_2 \tilde{u}_O^{(2)}(0)}{\theta_2} - \frac{\chi_2 \kappa_{\text{sphe,ss}}^0}{\theta_2} e^{-\alpha \eta_2} \left(\tilde{u}_O^{(2)}(0) - e^{\eta_2} \tilde{u}_R^{(2)}(0) \right) \\ &= -\frac{2}{\sqrt{\pi}} \beta^{1/2} + Z \chi_2 \end{aligned} \quad (\text{G.52})$$

with

$$\kappa_{\text{sphe,ss}}^0 = \frac{k^0 r_s}{D} \quad (\text{G.53})$$

$$Z = -\frac{1 + \kappa_{\text{sphe,ss}}^0 e^{(1-\alpha)\eta_2} \left(1 + \frac{c_R^*}{c_O^*} \right)}{1 + \kappa_{\text{sphe,ss}}^0 e^{-\alpha \eta_2} (1 + e^{\eta_2})} \quad (\text{G.54})$$

$$\theta_2 = 1 + \kappa_{\text{sphe,ss}}^0 e^{-\alpha \eta_2} (1 + e^{\eta_2}) \quad (\text{G.55})$$

and the expression for the current is given by

$$\begin{aligned} \frac{I_2^{\text{sphe}}}{FADc_O^*} &= I_{\text{d,c}}^{\text{sphe}} (\tau_1 + t_2) + \frac{1}{2\sqrt{Dt_2}} \left[\left(\frac{\partial \tilde{u}_O^{(2)}}{\partial s_2} \right)_{s_2=0} - \frac{\chi_2 \tilde{u}_O^{(2)}(0)}{\theta_2} \right] \\ &= I_{\text{d,c}}^{\text{sphe}} (\tau_1 + t_2) + \frac{1}{2\sqrt{Dt_2}} \left[\sum_{i,j} \sigma'_{i,j}(0) \chi_2^i \beta^{j/2} - \frac{1}{\theta_2} \sum_{i,j} \sigma_{i,j}(0) \chi_2^{i+1} \beta^{j/2} \right] \end{aligned} \quad (\text{G.56})$$

By introducing the expressions (G.45)–(G.46) into Eqs. (G.49)–(G.52), the differential equation system and the boundary value problem become

$$\left. \begin{aligned} \sigma''_{i,j}(s_2) + 2s_2 \sigma'_{i,j}(s_2) - 2(i+j) \sigma_{i,j}(s_2) &= -2(j-2) \sigma_{i,j-2}(s_2) \\ \delta''_{i,j}(s_2) + 2s_2 \delta'_{i,j}(s_2) - 2(i+j) \delta_{i,j}(s_2) &= -2(j-2) \delta_{i,j-2}(s_2) \end{aligned} \right\} \quad (\text{G.57})$$

$s_2 \rightarrow \infty$

$$\sigma_{i,j}(\infty) = 0; \delta_{i,j}(\infty) = 0 \quad i, j \geq 0 \quad (\text{G.58})$$

$$s_2 = 0$$

$$\sigma'_{i,j}(0) - \frac{\sigma_{i-1,j}(0)}{\theta_2} = -\delta'_{i,j}(0) + \frac{\delta_{i-1,j}(0)}{\theta_2} \quad (\text{G.59})$$

$$\begin{aligned} & \sigma'_{i,j}(0) - \frac{\sigma_{i-1,j}(0)}{\theta_2} - \frac{\kappa_{\text{sph},\text{ss}}^0 e^{-\alpha\eta_2}}{\theta_2} (\sigma_{i-1,j}(0) - e^{\eta_2} \delta_{i-1,j}(0)) \\ &= \begin{cases} -\frac{2}{\sqrt{\pi}} & \text{for } i = 0, j = 1 \\ Z & \text{for } i = 1, j = 0 \\ 0 & \text{otherwise} \end{cases} \quad (\text{G.60}) \end{aligned}$$

By applying Eqs. (G.58)–(G.60), the following relationships are obtained:

$$\sigma'_{0,1}(0) = -\frac{2}{\sqrt{\pi}} \quad (\text{G.61})$$

$$\sigma'_{0,j}(0) = 0 \quad \text{for } j \neq 1 \quad (\text{G.62})$$

$$\sigma'_{1,0}(0) = Z \quad (\text{G.63})$$

$$\sigma'_{i,j}(0) = \sigma_{i-1,j}(0) \quad \text{for } i \geq 1, j \text{ odd} \quad (\text{G.64})$$

$$\sigma'_{i,j}(0) = \sigma_{i,j}(0) = 0 \quad \text{for } i \geq 1, j \text{ even} \quad (\text{G.65})$$

From these results, and taking into account Eq. (G.56), the expression for the RPV current is deduced [Eq. (4.120)].

References

1. Molina A, Martinez-Ortiz F, Laborda E, Compton RG (2010) *Electrochim Acta* 55:5163–5172
2. Koutecký J (1953) *Czech J Phys* 2:50–55
3. Molina A, Martinez-Ortiz F, Laborda E, Compton RG (2010) *J Electroanal Chem* 648:67–77

Appendix H. Solution for the Application of a Cyclic Linear Sweep Potential to Different Charge Transfer Processes. Planar Electrodes

In this section, a brief discussion will be presented about the solution for the current–potential response of different charge transfer processes taking place at a planar electrode when a cyclic linear sweep potential is applied. This procedure has been discussed in detail in references [1–3] and only a short deduction will be provided here. The potential waveform can be written as

$$\left. \begin{aligned} E(t) &= E_{\text{initial}} - vt && \text{for } t \leq t_{\text{inv}} && \text{a} \\ E(t) &= E_{\text{final}} + vt && \text{for } t > t_{\text{inv}} && \text{b} \end{aligned} \right\} \quad (\text{H.1})$$

a) Nernstian Charge Transfer

We will consider first the application of the linear sweep potential until $t = t_{\text{inv}}$. The boundary value problem to solve is given by

$$\left. \begin{aligned} \frac{\partial c_{\text{O}}}{\partial t} &= D \frac{\partial^2 c_{\text{O}}}{\partial x^2} \\ \frac{\partial c_{\text{R}}}{\partial t} &= D \frac{\partial^2 c_{\text{R}}}{\partial x^2} \end{aligned} \right\} \quad (\text{H.2})$$

$$\left. \begin{aligned} t &\geq 0, \quad x \rightarrow \infty \\ t &= 0, \quad x \geq 0 \end{aligned} \right\} \quad c_{\text{O}} = c_{\text{O}}^*, \quad c_{\text{R}} = 0 \quad (\text{H.3})$$

$$t > 0, \quad x = 0,$$

$$D_{\text{O}} \left(\frac{\partial c_{\text{O}}}{\partial x} \right)_{x=0} = -D_{\text{R}} \left(\frac{\partial c_{\text{R}}}{\partial x} \right)_{x=0} \quad (\text{H.4})$$

$$c_{\text{O}}^{\text{s}} = e^{\eta(t)} c_{\text{R}}^{\text{s}} \quad (\text{H.5})$$

with

$$\eta(t) = \frac{F}{RT} (E(t) - E_{\text{c}}^{\Theta t}) = \frac{F}{RT} (E_{\text{initial}} - vt - E_{\text{c}}^{\Theta t}) \quad (\text{H.6})$$

The time dependence of Eq. (H.5) is significant and it greatly complicates the resolution of the problem. This equation can be rewritten as

$$\frac{c_{\text{O}}^{\text{s}}}{c_{\text{R}}^{\text{s}}} = \theta e^{-at} = \theta S(t) \quad (\text{H.7})$$

with

$$\theta = \exp\left(\frac{F}{RT} (E_{\text{initial}} - E_{\text{c}}^{\Theta t})\right) \quad (\text{H.8})$$

$$a = \frac{Fv}{RT} \quad (\text{H.9})$$

$$S(t) = e^{-at} \quad (\text{H.10})$$

Note that $\theta S(t) = e^{\eta(t)}$ because $v = (E_{\text{initial}} - E(t))/t$.

The expression for the concentrations of species O and R can be found by applying the Laplace Transform method in the way discussed in Appendix B. Thus, the following expression is found for $\bar{c}_{\text{O}}(x, p)$ [see Eqs. (B.17)–(B.28)]:

$$\bar{c}_{\text{O}}(x, p) = \frac{c_{\text{O}}^*}{p} + a_2 e^{-\sqrt{\frac{p}{D_{\text{O}}}} x} \quad (\text{H.11})$$

By taking into account that the current is

$$\bar{I} = FAD_{\text{O}} \left(\frac{\partial \bar{c}_{\text{O}}(x, p)}{\partial x} \right)_{x=0} = -FA\sqrt{D_{\text{O}} p} a_2 \quad (\text{H.12})$$

it is possible to rewrite the expression of the surface concentration of species O:

$$\bar{c}_{\text{O}}^{\text{s}} = \frac{c_{\text{O}}^*}{p} - \frac{\bar{I}}{FA\sqrt{D_{\text{O}} p}} \quad (\text{H.13})$$

and by carrying out the inverse of the transform and taking into account the Convolution theorem [see Eq. (B.12)], it is deduced:

$$c_{\text{O}}^{\text{s}} = c_{\text{O}}^* - \frac{1}{FA\sqrt{\pi D_{\text{O}}}} \int_0^t I(\tau) \frac{1}{\sqrt{t-\tau}} d\tau \quad (\text{H.14})$$

In an analogous way, for species R is obtained

$$c_{\text{R}}^{\text{s}} = \frac{1}{FA\sqrt{\pi D_{\text{R}}}} \int_0^t I(\tau) \frac{1}{\sqrt{t-\tau}} d\tau \quad (\text{H.15})$$

From Eqs. (H.14)–(H.15), it is found

$$\gamma c_{\text{O}}^{\text{s}} + c_{\text{R}}^{\text{s}} = \gamma c_{\text{O}}^* \quad (\text{H.16})$$

with

$$\gamma = \sqrt{\frac{D_{\text{O}}}{D_{\text{R}}}} \quad (\text{H.17})$$

By combining Eqs. (H.7) and (H.16), it is possible to write c_{O}^{s} in the way:

$$c_{\text{O}}^{\text{s}} = c_{\text{O}}^* \frac{\gamma \theta S(t)}{1 + \gamma \theta S(t)} \quad (\text{H.18})$$

and inserting Eq. (H.18) into Eq. (H.14),

$$\int_0^t I(\tau) \frac{1}{\sqrt{t-\tau}} d\tau = \frac{FAc_{\text{O}}^* \sqrt{\pi D_{\text{O}}}}{1 + \gamma \theta S(t)} \quad (\text{H.19})$$

Equation (H.19) allows us to calculate the current in terms of time. In order to work with potential values instead of time values, a change of variable can be carried out. Let's define

$$\chi(z) = \frac{I(at)}{FAc_{\text{O}}^* \sqrt{\pi D_{\text{O}} a}} \quad (\text{H.20})$$

It is possible to rewrite Eq. (H.19) in terms of $\chi(z)$:

$$\int_0^{at} \frac{\chi(z)}{\sqrt{at-z}} dz = \frac{1}{1 + \gamma\theta S(t)} \quad (\text{H.21})$$

From the above equation, it is possible to calculate $\chi(z)$ for each value of the potential and the current can be obtained from Eq. (H.20):

$$I(at) = FAc_0^* \sqrt{\pi D_0 a} \chi(at) \quad (\text{H.22})$$

with

$$at = \frac{F}{RT} (E_{\text{initial}} - E(t)) \quad (\text{H.23})$$

For the reverse sweep with the potential perturbation given by (b) in Eq. (H.1), the procedure is the same with function $S(t)$ given now as

$$S(t) = e^{-at-2at_{\text{inv}}} \quad (\text{H.24})$$

Logically, the shape of the reverse peak will depend on the inversion of final potential of the first sweep.

Values for function $\chi(at)$ have been calculated by numerical integration [3], by a series solution [2, 4], and other methods [5–8].

The evolution of function $\sqrt{\pi}\chi(at)$ can be seen in Fig. H.1. The maximum value of $\chi(at)$ is 0.4463, corresponding to $E - E_c^{\Theta'} = -0.0285$ V ($\gamma = 1$). This value leads to the peak current given by Eq. (5.55).

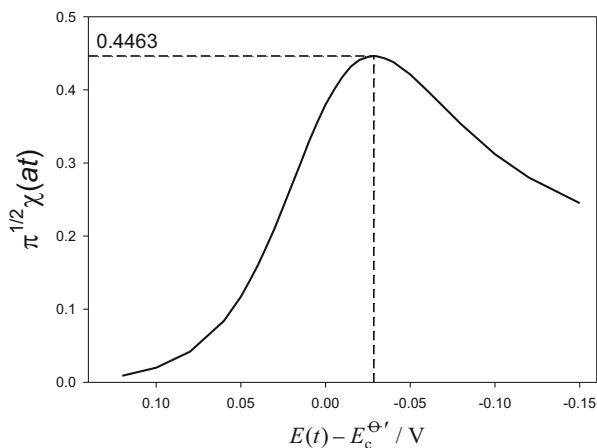


Fig. H.1 Evolution of $\sqrt{\pi}\chi(at)$ given by Eqs. (H.20)–(H.21) in terms of $E - E_c^{\Theta'}$ ($D_0 = D_R$). $T = 298$ K

b) Quasi-reversible Charge Transfer Processes

In this case, the Nernstian condition given in Eq. (H.5) must be replaced by the following relationship [in which a Butler–Volmer kinetics formalism has been assumed; see Eq. (1.101)]:

$$\frac{I}{FAk^0} = \left(c_{\text{O}}^{(\text{s})} e^{-\alpha\eta(t)} - c_{\text{R}}^{(\text{s})} e^{(1-\alpha)\eta(t)} \right) \quad (\text{H.25})$$

with $\eta(t)$ given in Eq. (H.6). k^0 and α are the heterogeneous rate constant and the charge transfer coefficient, respectively. By taking into account the time dependence of the perturbation [Eq. (H.1)], the above expression can be written as

$$\frac{I}{FAk^0} = (\vartheta S(t))^{-\alpha} \left(c_{\text{O}}^{(\text{s})} - c_{\text{R}}^{(\text{s})} \vartheta S(t) \right) \quad (\text{H.26})$$

and by inserting the expressions of $c_{\text{O}}^{(\text{s})}$ and $c_{\text{R}}^{(\text{s})}$ given by Eqs. (H.14)–(H.15) into Eq. (H.26), it is obtained

$$\frac{I}{FAk^0(\vartheta S(t))^{-\alpha}} = \left(c_{\text{O}}^* - \frac{1}{FA\sqrt{\pi D_{\text{O}}}} \int_0^t I(\tau) \frac{1}{\sqrt{t-\tau}} d\tau - \frac{\vartheta S(t)}{FA\sqrt{\pi D_{\text{R}}}} \int_0^t I(\tau) \frac{1}{\sqrt{t-\tau}} d\tau \right) \quad (\text{H.27})$$

By assuming $D_{\text{O}} = D_{\text{R}} = D$, Eq. (H.27) simplifies to

$$\frac{I}{FAk^0 c_{\text{O}}^* (\vartheta S(t))^{-\alpha}} = 1 - S(t) - \frac{(1 + \vartheta S(t))}{FAc_{\text{O}}^* \sqrt{\pi D}} \int_0^t I(\tau) \frac{1}{\sqrt{t-\tau}} d\tau \quad (\text{H.28})$$

and rewriting Eq. (H.28) in terms of $\chi(z)$, it is found

$$\frac{\chi(at)}{\Lambda(\vartheta S(t))^{-\alpha}} = 1 - S(t) - (1 + \vartheta S(t)) \int_0^{at} \frac{\chi(z)}{\sqrt{at-z}} dz \quad (\text{H.29})$$

with

$$\Lambda = \frac{k^0}{\sqrt{\pi Da}} \quad (\text{H.30})$$

The current can be obtained by solving the integral equation (H.29) for a given value of Λ and α [see also Eq. (H.20)]. If the electrode process can be considered as totally irreversible, condition (H.25) becomes

$$\frac{I}{FAk^0} = c_O^{(s)} e^{-\alpha\eta(t)} \quad (\text{H.31})$$

and by following an analogous procedure to that described in section a, it is found

$$\frac{\chi(at)}{\Lambda(\partial S(t))^{-\alpha}} = 1 - \int_0^{at} \frac{\chi(z)}{\sqrt{at-z}} dz \quad (\text{H.32})$$

The values of the function $\chi(at)$ for this last situation have been calculated in [3] and it has been found that $\chi(at)$ and therefore the current presents a maximum value equal to 0.4958 for a value of the dimensionless potential $\alpha F(E - E_c^{\Theta})/RT + \ln(\sqrt{\pi D_O a}/k^0) = -0.21$. These values lead to the expressions of the peak current and potential given by Eqs. (5.83) and (5.84), respectively.

Reaction Mechanisms

CE Mechanism

The reaction scheme in this case is the following:



and in this case the differential equations and the boundary value problem are

$$\left. \begin{aligned} \hat{\delta}_p c_B &= -k_1 c_B + k_2 c_C \\ \hat{\delta}_p c_C &= k_1 c_B - k_2 c_C \\ \hat{\delta}_p c_D &= 0 \end{aligned} \right\} \quad (\text{H.33})$$

$$\left. \begin{aligned} t &= 0, x \geq 0 \\ t &\geq 0, x \rightarrow \infty \end{aligned} \right\}$$

$$\left. \begin{aligned} c_C &= c_C^* \\ c_B &= c_B^*; K = \frac{c_B^*}{c_C^*} = \frac{k_2}{k_1} \\ c_D &= 0 \end{aligned} \right\} \quad (\text{H.34})$$

$t > 0, x = 0$

$$D_C \left(\frac{\partial c_C}{\partial x} \right)_{x=0} = -D_D \left(\frac{\partial c_D}{\partial x} \right)_{x=0} \quad (\text{H.35})$$

$$D_B \left(\frac{\partial c_B}{\partial x} \right)_{x=0} = 0 \quad (\text{H.36})$$

$$c_C^s = e^{\eta(t)} c_D^s \quad (\text{H.37})$$

with $\eta(t)$ given by Eq. (H.6) and $\hat{\delta}_p = \frac{\partial}{\partial t} - D_i \frac{\partial^2}{\partial x^2}$.

The current is related to the fluxes of species C and D and is given by

$$\frac{I^{\text{CE}}}{FA} = D_C \left(\frac{\partial c_C}{\partial x} \right)_{x=0} = -D_D \left(\frac{\partial c_D}{\partial x} \right)_{x=0} \quad (\text{H.38})$$

Considering $D_B = D_C = D$ and using the following variable changes:

$$\zeta = c_B + c_C \quad (\text{H.39})$$

$$\phi = c_B - K c_C \quad (\text{H.40})$$

with K being the inverse of the equilibrium constant, it is fulfilled that [9]:

$$\frac{\partial \zeta}{\partial T} = D \frac{\partial^2 \zeta}{\partial X^2} \quad (\text{H.41})$$

$$\frac{\partial \phi}{\partial T} = D \frac{\partial^2 \phi}{\partial X^2} - \lambda \phi \quad (\text{H.42})$$

$$\frac{\partial c_D}{\partial T} = D_D \frac{\partial^2 c_D}{\partial X^2} \quad (\text{H.43})$$

with

$$\lambda = \lambda_1 + \lambda_2 \quad (\text{H.44})$$

$$\lambda_j = \frac{k_j}{a} \quad j = 1, 2 \quad (\text{H.45})$$

$$X = \sqrt{\frac{a}{D}} x \quad (\text{H.46})$$

$$T = at \quad (\text{H.47})$$

Equations (H.41) and (H.43) are analogous to Eq. (H.2). Thus, their integration leads to [see Eqs. (H.14)–(H.15)]:

$$\zeta^s = 1 - \frac{1}{\sqrt{\pi}} \int_0^{at} \frac{\chi(z)}{\sqrt{at-z}} dz \quad (\text{H.48})$$

$$c_D^s = \frac{1}{\sqrt{\pi}} \int_0^{at} \frac{\chi(z)}{\sqrt{at-z}} dz \quad (\text{H.49})$$

By solving the Laplace transform of differential equation (H.42) and taking into account that ϕ remains finite ($\bar{\phi} = 0$) for $X \rightarrow \infty$, it follows that

$$\bar{\phi} = \left(\bar{\phi}^s - \frac{1}{\sqrt{p+\lambda}} \left(\frac{\partial \phi}{\partial X} \right)_{X=0} \right) \frac{e^{-\sqrt{p+\lambda}X}}{2} \quad (\text{H.50})$$

Therefore,

$$\bar{\phi}^s = \frac{\bar{\psi}}{\sqrt{p+\lambda}} \quad (\text{H.51})$$

with

$$\bar{\psi} = \frac{I^{\text{CE}}}{FA\sqrt{D}\zeta^{*s}a} \quad (\text{H.52})$$

and

$$\zeta^{*s} = c_B^* + c_C^* \quad (\text{H.53})$$

Returning Eq. (H.51) to the initial space, one obtains

$$\phi^s = \frac{1}{\sqrt{\pi}} \int_0^{at} e^{-\lambda(at-z)} \frac{\chi(z)}{\sqrt{at-z}} dz \quad (\text{H.54})$$

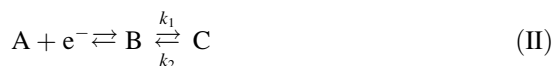
and combining Eqs. (H.48)–(H.54), the surface concentration of species C is obtained:

$$c_C^s = \frac{K}{1+K} \left(1 - \frac{1}{\sqrt{\pi}} \int_0^{at} \left(1 + \frac{e^{-\lambda(at-z)}}{K} \right) \frac{\chi(z)}{\sqrt{at-z}} dz \right) \quad (\text{H.55})$$

Finally, by introducing the expressions for c_D^s and c_C^s in the Nernst condition (H.37), a non-explicit integral expression for the CV current can be deduced.

EC Mechanism

The reaction scheme is



For this reaction, the differential equations and boundary value problem are

$$\left. \begin{aligned} \hat{\delta}_p c_A &= 0 \\ \hat{\delta}_p c_B &= -k_1 c_B + k_2 c_C \\ \hat{\delta}_p c_C &= k_1 c_B - k_2 c_C \end{aligned} \right\} \quad (\text{H.56})$$

$$\left. \begin{aligned} t = 0, x \geq 0 \\ t \geq 0, x \rightarrow \infty \end{aligned} \right\} \left. \begin{aligned} c_A &= c_A^* \\ c_B &= c_C = 0 \end{aligned} \right\} \quad (\text{H.57})$$

$$t > 0, x = 0$$

$$D_A \left(\frac{\partial c_A}{\partial x} \right)_{x=0} = -D_B \left(\frac{\partial c_B}{\partial x} \right)_{x=0} \quad (\text{H.58})$$

$$D_C \left(\frac{\partial c_C}{\partial x} \right)_{x=0} = 0 \quad (\text{H.59})$$

$$c_A^s = e^{\eta(t)} c_B^s \quad (\text{H.60})$$

with $\hat{\delta}_p = \frac{\partial}{\partial t} - D_i \frac{\partial^2}{\partial x^2}$.

The current is related to the fluxes of species A and B in the way

$$\frac{J^{\text{EC}}}{FA} = D_A \left(\frac{\partial c_A}{\partial x} \right)_{x=0} = -D \left(\frac{\partial c_B}{\partial x} \right)_{x=0} \quad (\text{H.61})$$

By assuming $D_B = D_C = D$ and using the variables defined in Eqs. (H.39)–(H.40), it is fulfilled that [9]:

$$\frac{\partial c_A}{\partial T} = D_A \frac{\partial^2 c_A}{\partial X^2} \tag{H.62}$$

$$\frac{\partial \zeta}{\partial T} = D \frac{\partial^2 \zeta}{\partial X^2} \tag{H.63}$$

$$\frac{\partial \phi}{\partial T} = D \frac{\partial^2 \phi}{\partial X^2} - \lambda \phi \tag{H.64}$$

where λ , X and T are given by Eqs. (H.44), (H.46) and (H.47), respectively.

Since Eqs. (H.62) and (H.63) are analogous to Eq. (H.2), their integration leads to

$$c_A^s = 1 - \frac{1}{\sqrt{\pi}} \int_0^{at} \frac{\chi(z)}{\sqrt{at-z}} dz \tag{H.65}$$

$$\zeta^s = \frac{1}{\sqrt{\pi}} \int_0^{at} \frac{\chi(z)}{\sqrt{at-z}} dz \tag{H.66}$$

And solving the Laplace transform for Eq. (H.64), it is obtained

$$\bar{\phi} = \left(\bar{\phi}^s - \frac{1}{\sqrt{p+\lambda}} \left(\frac{\partial \phi}{\partial X} \right)_{X=0} \right) \frac{e^{-\sqrt{p+\lambda}X}}{2} \tag{H.67}$$

and hence

$$\bar{\phi}^s = \frac{K\bar{\psi}}{\sqrt{p+\lambda}} \tag{H.68}$$

with

$$\bar{\psi} = \frac{I^{EC}}{FA\sqrt{D}c_A^*a} \tag{H.69}$$

Therefore,

$$\phi^s = \frac{K}{\sqrt{\pi}} \int_0^{at} e^{-\lambda(at-z)} \frac{\chi(z)}{\sqrt{at-z}} dz \tag{H.70}$$

By combining Eqs. (H.66) and (H.70), one obtains

$$c_B^s = \frac{1}{\sqrt{\pi}} \int_0^{at} \left(\frac{1}{1+K} + \frac{K}{1+K} e^{-\lambda(at-z)} \right) \frac{\chi(z)}{\sqrt{at-z}} dz \quad (\text{H.71})$$

and inserting Eqs. (H.65) and (H.71) in Nernst's condition (H.60), an integral non-explicit expression of the cyclic voltogram corresponding to the EC mechanism is obtained.

References

1. Randles SEB (1948) *Trans Faraday Soc* 44:327
2. Sevcik A (1948) *Coll Czech Chem Commun* 13:349
3. Nicholson RS, Shain I (1964) *Anal Chem* 36:706
4. Reinmuth WH (1957) *J Am Chem Soc* 79:6358
5. Matsuda H, Ayabe Y (1959) *Z Elektrochem* 59:594
6. Gokhshtein YP (1959) *Dokl Akad Nauk SSSR* 126:598
7. Myland JC, Oldham KB (1983) *J Electroanal Chem* 153:43
8. Ramamurthy AC, Rangarajan SK (1981) *Electrochim Acta* 26:111
9. Saveánt JM, Vianello E (1967) *Electrochim Acta* 12:629–646

Appendix I. Numerical Simulation

The electrochemical responses presented in this book typically consider quiescent solutions where mass transport takes place only by diffusion. As stated in Sect. 1.8, the flux of a species i by diffusion is described by Fick's first law:

$$J_{\text{diffusion},i} = -D_i \nabla c_i \quad (\text{I.1})$$

where $J_{\text{diffusion},i}$ is the flux, D_i the diffusion coefficient, and ∇ represents the gradient operator which typically has a vectorial character. For the simpler case of transport through one single direction x , Eq. (I.1) becomes

$$J_{\text{diffusion},i} = -D_i \frac{\partial c_i}{\partial x} \quad (\text{I.2})$$

The concentration of an electroactive species is changing with time and distance in such a way that a temporal evolution equation is needed for analyzing the current–potential behavior. This evolution is typically given by Eq. (1.173):

$$\frac{\partial c_i}{\partial t} = D_i \nabla^2 c_i \quad (\text{I.3})$$

which for a single x direction becomes

$$\frac{\partial c_i}{\partial t} = D_i \frac{\partial^2 c_i}{\partial x^2} \quad (\text{I.4})$$

Equation (I.4) is a second-order differential equation in partial derivatives. In order to solve it, it is necessary to specify some boundary conditions relative to the value of the concentration at some points/times (Dirichlet boundaries) or its derivative at some points/times (Neumann boundaries). The solution of Eq. (I.4) is called a concentration profile, $c_i(x, t)$, which is a function of coordinates and time.

For these situations in which it is not possible to find an analytical expression for $c_i(x, t)$, the usual alternatives are to consider simpler situations (e.g., steady-state conditions for avoiding the temporal dependence) or to solve Eq. (I.3) numerically. Here it will be considered the case of a single dimension x although the procedure can be extended to a higher number of coordinates.

There are different approaches for carrying out the numerical solution of the differential equations involved in electrochemical problems, with the most popular being the Finite Difference Method (FDM) and the Finite Element Method (FEM) [1–3]. This appendix will be focused on the first one.

FDM was applied to electrochemical problems very early [4], but it was in the 1960s when Feldberg developed the basis of digital simulation of electrochemical processes by means of the “box method,” which at present is considered as a FEM-like method (see [5]).

For solving Eq. (I.4), the first step is to change the conventional variables (concentrations, distance, times), into dimensionless ones in order to get a more general approach and to avoid problems relative to particular units. An adequate set of dimensionless variables used in this problem is

$$T = \frac{t}{t_R} \quad (\text{I.5})$$

$$C_i = \frac{c_i}{c_O^*} \quad i = O, R \quad (\text{I.6})$$

$$X = \frac{x}{\sqrt{D_O t_R}} \quad (\text{I.7})$$

$$g = \frac{D_O}{D_R} \quad (\text{I.8})$$

with t_R being an arbitrary reference time. By inserting the above dimensionless variables into Eq. (I.4), the differential equation system becomes

$$\left. \begin{aligned} \frac{\partial C_O}{\partial T} &= \frac{\partial^2 C_O}{\partial X^2} \\ \frac{\partial C_R}{\partial T} &= g \frac{\partial^2 C_R}{\partial X^2} \end{aligned} \right\} \quad (\text{I.9})$$

Subsequently, both the differential equation and the boundary conditions are discretized. “Discretization” consists in that the time and spatial coordinates, which are continuous, are approximated as a set of values—discrete “points”—in time and space [1–3]. Thus, time and space can be divided into equally spaced small intervals:

$$\begin{aligned} X &= iH & i &= 0, 1, \dots, n \\ T &= j\delta T & j &= 0, 1, \dots, m \end{aligned} \quad (\text{I.10})$$

where the value of m is determined by the overall duration of the experiment:

$$m = \frac{T_{\max}}{\delta T} \quad (\text{I.11})$$

with T_{\max} being the duration of the experiment, whereas the value of n is such that the concentration at this point is not altered throughout the experiment. Typically a value $X_{\max} = nH = 6\sqrt{T_{\max}}$ is chosen.

The key point in FDM is the approximation of a function and its derivatives through the use of series expansion of a function (i.e., by means of a Taylor expansion), in order to rewrite the expressions of the derivatives in an algebraic way. If we consider a generic function $f(x)$ and we want to approximate it at the points $(x+h)$ and $(x-h)$,

$$\begin{aligned} f(x+h) &= f(x) + hf'(x) + \frac{h^2}{2!}f''(x) + \frac{h^3}{3!}f'''(x) + \dots \\ &= f(x) - hf'(x) + \frac{h^2}{2!}f''(x) - \frac{h^3}{3!}f'''(x) + \dots \end{aligned} \quad (\text{I.12})$$

By making

$$y_{i+k} = f(x+kh) \quad (\text{I.13})$$

Equation (I.12) can be written as

$$\begin{aligned} y_{i+1} &= y_i + hy'_i + \frac{h^2}{2!}y''_i + \frac{h^3}{3!}y'''_i + \dots \\ y_{i-1} &= y_i - hy'_i + \frac{h^2}{2!}y''_i - \frac{h^3}{3!}y'''_i + \dots \end{aligned} \quad (\text{I.14})$$

From Eq. (I.14), it is possible to obtain different approximations for the first and second derivatives of a given function. For example, it is possible to approximate the first derivative with a two-point expression:

$$y'_i \approx \frac{y_{i+1} - y_i}{h} \quad (\text{I.15})$$

and the second derivative can be written as an approximation of three points:

$$y''_i \approx \frac{y_{i+1} - 2y_i + y_{i-1}}{h^2} \quad (\text{I.16})$$

By taking into account the above approximate expressions for the first and second derivatives, the finite-difference method proceeds as follows. First, the

concentration profile of both species is transformed into a set of discrete values that will be denoted as

$$C(X, T) = C(iH, j\delta T) = C_{i,j} \quad (\text{I.17})$$

The first derivative of the concentrations with time will be approximated by using Eq. (I.15):

$$\frac{\partial C_{i,j}^O}{\partial T} \approx \frac{C_{i,j+1}^O - C_{i,j}^O}{\delta T} \quad (\text{I.18})$$

and the second derivative with respect to X will be approximated by using Eq. (I.16):

$$\frac{\partial^2 C_{i,j}^O}{\partial X^2} \approx \frac{C_{i+1,j}^O - 2C_{i,j}^O + C_{i-1,j}^O}{H^2} \quad i = 1, 2, \dots \quad (\text{I.19})$$

– *The Explicit Finite-Difference Method (EFDM)*

In this case, by inserting Eqs. (I.18) and (I.19) into Eq. (I.9), it is possible to obtain an explicit expressions for $C_{i,j+1}^O$ and $C_{i,j+1}^R$ in terms of the concentrations of O and R at the previous time,

$$\begin{aligned} C_{i,j+1}^O &= C_{i,j}^O + \lambda \left(C_{i+1,j}^O - 2C_{i,j}^O + C_{i-1,j}^O \right) \\ C_{i,j+1}^R &= C_{i,j}^R + g\lambda \left(C_{i+1,j}^R - 2C_{i,j}^R + C_{i-1,j}^R \right) \end{aligned} \quad (\text{I.20})$$

with

$$\lambda = \frac{\delta T}{H^2} \quad (\text{I.21})$$

The boundary conditions for this problem, by assuming the application of a constant potential with $E \ll E_c^{\theta'}$ (cathodic limiting current; see Sect. 2.2.2.1), are $t = 0, \forall x$

$$C_{i,0}^O = 1, C_{i,0}^R = 0 \quad (\text{I.22})$$

$t > 0$

$$C_{nH,j}^O = 1 \quad (\text{I.23})$$

$$C_{0,j}^O = 0 \tag{I.24}$$

From Eq. (I.20) and the values of concentrations given by the initial and limiting conditions [Eqs. (I.22)–(I.24)], it is possible to obtain the values at the successive times in a direct way. The restriction $\lambda < 0.5$ is required for the procedure to be convergent (i.e., the spatial and temporal intervals are related). For example, by taking $m = 1/\lambda H^2$, if $H = 0.1$ then $m = 200$ but if $H = 0.001$ then $m = 2 \times 10^6$.

Moreover, the convergence of the approximate solutions is proportional to δT .
 – *The Fully implicit method (FIM)*

An improvement over the explicit method is done by the fully implicit method in which the concentration corresponding to time $(j + 1)$ is calculated as

$$C_{i,j+1}^O = C_{i,j}^O + \lambda \left(C_{i+1,j+1}^O - 2C_{i,j+1}^O + C_{i-1,j+1}^O \right) \tag{I.25}$$

In this case, in order to solve Eq. (I.25), it is necessary to take into account the boundary conditions. Thus, by taking into account conditions (I.22)–(I.24), it is possible to make an arrangement of the set of linear equations for the concentrations into a matrix equation:

$$\begin{pmatrix} C_{0,j}^O \\ C_{1,j}^O \\ C_{2,j}^O \\ \dots \\ C_{i_{\max}-1,j}^O \\ C_{i_{\max},j}^O + \lambda \end{pmatrix} = \begin{pmatrix} 1 & 0 & 0 & & & & & & & \\ & 0 & -\lambda & 1+2\lambda & -\lambda & 0 & & & & \\ & & 0 & -\lambda & 1+2\lambda & -\lambda & 0 & & & \\ & & & & & \dots & & & & \\ & & & & & 0 & -\lambda & 1+2\lambda & -\lambda & 0 \\ & & & & & & & 0 & 0 & 1 \end{pmatrix} \begin{pmatrix} 0 \\ C_{1,j+1}^O \\ C_{2,j}^O \\ \dots \\ C_{i_{\max}-1,j+1}^O \\ 1 \end{pmatrix} \tag{I.26}$$

When the solution of a given problem depends on a single species or on different species which are only related by the surface conditions, the matrix equation given by (I.26) can be solved sequentially to give a concentration vector for each value of time j by using the Thomas’ algorithm [6, 7]. There is no restriction in the value of λ in order to obtain a convergent solution unlike in the case of the EFDM, but the resolution is obviously more complex whereas the convergence of the method is still proportional to δT .

– *The Crank–Nicholson method (CNM)*

This method is similar to the FIM discussed above, although the right-hand member of Eq. (I.25) is now taken as an average between times j and $j + 1$, i.e.,

$$C_{i,j+1}^O = C_{i,j}^O + \frac{\lambda}{2} \left(C_{i+1,j}^O - 2C_{i,j}^O + C_{i-1,j}^O + C_{i+1,j+1}^O - 2C_{i,j+1}^O + C_{i-1,j+1}^O \right) \tag{I.27}$$

Again, Thomas’ algorithm can be used, but in this case the convergence is proportional to δT^2 .

There are different improvements that can be included in the different methods presented here. Thus, multi-point approximations to the derivatives [1], the use of unequally spaced spatial and time intervals [1, 8, 9], and the use of more sophisticated methods of time integration [1], among others, have been developed.

For a more detailed review on these methods and for obtaining sample codes of them, the reader may refer [1, 10].

References

1. Britz D (2005) *Digital simulation in electrochemistry*, 3rd edn. Springer, Berlin
2. Feldberg SW (1969) In: Bard AJ (ed) *Electroanalytical chemistry*. Dekker, New York
3. Gooch KA, Qiu FL, Fischer AC (2003) In: Bard AJ, Stratmann M, Calvo EJ (eds) *Encyclopedia of electrochemistry*, vol 2. Wiley-VCH, Weinheim
4. Randles JEB (1948) *Trans Faraday Soc* 44:327–338
5. Rudolph M (1995) In: Rubinstein I (ed) *Physical electrochemistry*. Dekker, New York
6. Thomas LH (1949) *Elliptical problems in linear difference equations over a network*. Watson Scientific Computing Laboratory Report, Columbia University, New York
7. Bruce GH, Peaceman DW, Rachford HH, Rice JD (1953) *Trans Am Inst Min Engrs* 198:79
8. Molina A, Serna C, Martinez-Ortiz F, Laborda E (2008) *J Electroanal Chem* 617:14–26
9. Martinez-Ortiz F, Molina A, Laborda E (2011) *Electrochim Acta* 56:5707–5716
10. Compton RG, Laborda E, Ward KR (2013) *Understanding voltammetry: simulation of electrode processes*. Imperial College Press, Singapore

Appendix J. C++ Programs to Calculate the Response of Two-Electron Reversible Electrode Processes in Cyclic Staircase Voltammetry and Square Wave Voltammetry at Disc, (Hemi)Spherical, and Cylindrical Electrodes of Any Radius

```
/* C++ PROGRAM TO CALCULATE THE RESPONSE OF A TWO-ELECTRON REVERSIBLE
ELECTRODE PROCESS IN CYCLIC STAIRCASE VOLTAMMETRY AT DISC, (HEMI)
SPHERICAL AND CYLINDRICAL ELECTRODES OF ANY RADIUS 'R0' */

//By making 'E02' negative enough with respect to the vertex potential,
the case of a 1-electron process can be simulated
//By making 'Step' small enough (<0.01 mV), the response in staircase
voltammetry is equivalent to that in cyclic voltammetry

#include <fstream>
#include <iostream>
#include <vector>
#include <cmath>
#include <omp.h>

using namespace std;

int main (void) {
    //Constants
    double pi = 4.0*atan(1.0);
    double Far = 96485.3365; //Faraday constant (C mol-1)
    double R = 8.314462; //Gas constant (J K-1 mol-1)

    //***** INPUT *****
    //Experimental conditions
    double Temp = 298.15; //Absolute temperature (K)
    double Cbulk = 1.e-6; //Bulk concentration of the oxidized
    species (mol cm-3)
    double Dif = 1.e-5; //Diffusion coefficient of all the species
    (cm2 s-1)
    double R0 = 1.e-1; //Electrode radius (cm)
    double LL = 1.e0; //Length of the cylindrical electrode (cm)
```

```

double E01=0.000; //Formal potential of the first electron
transfer (V)
double E02=-1.000; //Formal potential of the second electron
transfer (V)

//Technique parameters
double Eini=0.200; //Initial (and final) potential (V)
double Evtx=-0.200; //Vertex potential (V)
double Step=1.e-5; //Step potential (V)
double Rate=1.0; //Scan rate (V s-1)

//Saving the data
int PointsToSave=500; //Maximum number of points to save
ofstream Disc("CSV_disc.txt"); //Name of the file for the data
of the disc electrode
ofstream Sph("CSV_spherical.txt"); //Name of the file for the
data of the spherical electrode
ofstream Hemi("CSV_hemispherical.txt"); //Name of the file
for the data of the hemispherical electrode
ofstream Cyl("CSV_cylindrical.txt"); //Name of the file for
the data of the cylindrical electrode

//*****
//CALCULATIONS
//Potential-time perturbation
double ff=Far/(R*Temp);
double tau=Step/Rate;
int points=2*abs(Evtx - Eini)/Step+1;
int pm=(Evtx - Eini)/abs(Evtx - Eini);
double Jnu1, Jnu2;
vector<double> Nu1(points+1,0.0);
vector<double> Nu2(points+1,0.0);
vector<double> WW(points+1,0.0);
WW[0]=2.0*Cbulk;

for(int j=1; j<=points; j++)
{
    if(j<=(points/2)) //forward scan
    {
        Nu1[j]=ff*(Eini+pm*Step*(j-1)-E01);
        Nu2[j]=ff*(Eini+pm*Step*(j-1)-E02);
    }
    else //reverse scan
    {
        Nu1[j]=ff*(Evtx-pm*Step*
(j-points/2)-E01);
        Nu2[j]=ff*(Evtx-pm*Step*
(j-points/2)-E02);
    }
}

```

```

        Jnu1 = exp (Nu1 [j] );
        Jnu2 = exp (Nu2 [j] );
        WW[j] = Cbulk*(2.0*Jnu1*Jnu2 + Jnu2) / (1.0 + Jnu1*Jnu2 + Jnu2);
    }

    //fG-functions (included the cases of disc, spherical and
    cylindrical electrodes)
    double time;
    vector<double> fdisc(points+1,0.0);
    vector<double> fsph(points+1,0.0);
    vector<double> fcyl(points+1,0.0);

    for(int j=1; j<=points; j++)
    {
        time = tau*j;

        fdisc[j] = (4.0/(pi*R0)) * (0.7854 + 0.44315*R0/sqrt
            (Dif*time) + 0.2146*exp(-0.39115*R0/sqrt(Dif*time)));
        fsph[j] = 1.0/R0 + 1.0/sqrt(pi*Dif*time);
        fcyl[j] = exp(-0.1*sqrt(pi*Dif*time)/R0) /sqrt
            (pi*Dif*time) + 1.0/(R0*log(5.2945 + 1.4986*sqrt
            (Dif*time)/R0));
    }

    //current response (in Amp)
    PointsToSave = fmin(PointsToSave, points);

    vector<double> disc(PointsToSave+1,0.0);
    vector<double> sph(PointsToSave+1,0.0);
    vector<double> hemi(PointsToSave+1,0.0);
    vector<double> cyl(PointsToSave+1,0.0);
    vector<double> Potential(PointsToSave+1,0.0);

    double Ad = pi*R0*R0; //area disc electrode
    double As = 4.0*pi*R0*R0; //area spherical electrode
    double Ah = 2.0*pi*R0*R0; //area hemispherical electrode
    double Ac = 2.0*pi*R0*LL; //area cylindrical electrode

    for(int m=1; m<=PointsToSave; m++)
    {
        int pulse = m*points/PointsToSave;

        for(int k=1; k<=pulse; k++)
        {
            disc[m] = disc[m] + Far*Ad*Dif * (WW[k-1]-WW[k])
                *fdisc[pulse-k+1];
            sph[m] = sph[m] + Far*As*Dif * (WW[k-1]-WW[k])
                *fsph[pulse-k+1];
        }
    }

```



```

        hemi [m] = hemi [m] + Far*Ah*Dif * (WW[k-1]-WW[k])
        * fsph[pulse-k+1];
        cyl [m] = cyl [m] + Far*Ac*Dif * (WW[k-1]-WW[k])
        * fcyl [pulse-k+1];
    }
    Potential [m] = Nul [pulse] / ff + E01;

    Disc << Potential [m] << "\t" << disc [m] << "\n";
    Sph << Potential [m] << "\t" << sph [m] << "\n";
    Hemi << Potential [m] << "\t" << hemi [m] << "\n";
    Cyl << Potential [m] << "\t" << cyl [m] << "\n";
}
return 0;}
/* C++ PROGRAM TO CALCULATE THE RESPONSE OF A TWO-ELECTRON REVERSIBLE
ELECTRODE PROCESS IN SQUARE WAVE VOLTAMMETRY AT DISC, (HEMI) SPHERICAL
AND CYLINDRICAL ELECTRODES OF ANY RADIUS 'R0'*/

//By making 'E02' negative enough with respect to the vertex potential,
the case of a 1-electron process can be simulated

#include <fstream>
#include <iostream>
#include <vector>
#include <cmath>
#include <omp.h>

using namespace std;

int main (void) {
    //Constants
    double pi = 4.0*atan(1.0);
    double Far = 96485.3365; //Faraday constant (C mol-1)
    double R = 8.314462; //Gas constant (J K-1 mol-1)

    //***** INPUT *****
    //Experimental conditions
    double Temp = 298.15; //Absolute temperature (K)
    double Cbulk = 1.e-6; //Bulk concentration of the oxidized
    species (mol cm-3)
    double Dif = 1.e-5; //Diffusion coefficient of all the species
    (cm2 s-1)
    double R0 = 0.1; //Electrode radius (cm)
    double LL = 1.e0; //Length of the cylindrical electrode (cm)
    double E01 = 0.000; //Formal potential of the first electron
    transfer (V)
    double E02 = -1.000; //Formal potential of the second electron
    transfer (V)

```

```

//Technique parameters
double Eini = 0.2; //Initial (and final) potential (V)
double Evtx = -0.2; //Vertex potential (V)
double Step = 5.e-3; //Step potential (V)
double Esw = 25.e-3; //Square wave potential (V)
double Freq = 50.0; //Frequency (Hz)

//Saving the data
ofstream Disc("SWV_disc.txt"); //Name of the file for the data
of the disc electrode
ofstream Sph("SWV_spherical.txt"); //Name of the file for the
data of the spherical electrode
ofstream Hemi("SWV_hemispherical.txt"); //Name of the file
for the data of the hemispherical electrode
ofstream Cyl("SWV_cylindrical.txt"); //Name of the file for
the data of the cylindrical electrode

//*****

//CALCULATIONS

//Potential-time perturbation
double ff = Far / (R * Temp);
double tau = 1.0 / (2.0 * Freq);
int points = 2 * abs(Evtx - Eini) / Step;
int cycles = points / 2;
int pm = (Evtx - Eini) / abs(Evtx - Eini);

double Jnu1, Jnu2;
vector<double> Nu1(points + 1, 0.0);
vector<double> Nu2(points + 1, 0.0);
vector<double> WW(points + 1, 0.0);
WW[0] = 2.0 * Cbulk;
for(int j = 1; j <= points; j++)
{
    int cycle;
    if(j%2==0) //even pulses
    {
        cycle = j/2;
        Nu1[j] = ff * (Eini + pm * Step * (cycle - 1) - pm * Esw - E01);
        Nu2[j] = ff * (Eini + pm * Step * (cycle - 1) - pm * Esw - E02);
    }
    else //odd pulses
    {
        cycle = j/2 + 1;
        Nu1[j] = ff * (Eini + pm * Step * (cycle - 1) + pm * Esw - E01);
        Nu2[j] = ff * (Eini + pm * Step * (cycle - 1) + pm * Esw - E02);
    }
}

```

```

        Jnu1 = exp(Nu1[j]);
        Jnu2 = exp(Nu2[j]);

    WW[j] = Cbulk*(2.0*Jnu1*Jnu2 + Jnu2)/(1.0 + Jnu1*Jnu2 + Jnu2);
}
//fG-functions (included the cases of disc, spherical and
cylindrical electrodes)
double time;
vector<double> fdisc(points+1,0.0);
vector<double> fsph(points+1,0.0);
vector<double> fcyl(points+1,0.0);

for(int j=1; j<=points; j++)
{
    time = tau*j;

    fdisc[j] = (4.0/(pi*R0))*(0.7854+0.44315*R0/sqrt
(Dif*time)+0.2146*exp(-0.39115*R0/sqrt(Dif*time)));
    fsph[j] = 1.0/R0+1.0/sqrt(pi*Dif*time);
    fcyl[j] = exp(-0.1*sqrt(pi*Dif*time)/R0)/sqrt
(pi*Dif*time)+1.0/(R0*log(5.2945+1.4986*sqrt
(Dif*time)/R0));
}
//SWV response (in Amp)
vector<double> disc(points+1,0.0);
vector<double> sph(points+1,0.0);
vector<double> hemi(points+1,0.0);
vector<double> cyl(points+1,0.0);
vector<double> Potential(points+1,0.0);

double Ad=pi*R0*R0;//area disc electrode
double As=4.0*pi*R0*R0;//area spherical electrode
double Ah=2.0*pi*R0*R0;//area hemispherical electrode
double Ac=2.0*pi*R0*LL;//area cylindrical electrode

for(int m=1; m<=points; m++)
{
    for(int k=1; k<=m; k++)
    {
        disc[m] = disc[m] + Far*Ad*Dif *(WW[k-1]-WW[k]) *fdisc
[m-k+1];
        sph[m] = sph[m] + Far*As*Dif *(WW[k-1]-WW[k]) *fsph
[m-k+1];
        hemi[m] = hemi[m] + Far*Ah*Dif *(WW[k-1]-WW[k]) *fsph
[m-k+1];
        cyl[m] = cyl[m] + Far*Ac*Dif *(WW[k-1]-WW[k]) *fcyl
[m-k+1];
    }
}

```

```
    if(m%2 == 0)
    {
        Potential[m] = (Nu1[m] + Nu1[m-1]) / 2.0 / ff + E01;

        Disc << Potential[m] << "\t" << (disc[m-1] - disc[m]) <<
            "\n";
        Sph << Potential[m] << "\t" << (sph[m-1] - sph[m]) <<
            "\n";
        Hemi << Potential[m] << "\t" << (hemi[m-1] - hemi
            [m]) << "\n";
        Cyl << Potential[m] << "\t" << (cyl[m-1] - cyl[m]) <<
            "\n";
    }
}
return 0;}
```

About the Authors



Ángela Molina is a Professor of Physical Chemistry since 1994 at the University of Murcia (Spain) where she obtained her Ph.D. in Chemistry. She has taught in undergraduate and specialist postgraduate courses, and has supervised 12 Ph.D. theses. She is the Head of the Research Group *Theoretical and Applied Electrochemistry*, where she has lead more than 20 research projects. Her scientific contributions include the design and implementation of electrochemical techniques with both controlled potential and controlled current. For this purpose, she has carried out the mathematical treatment with the aim of obtaining closed-form analytical solutions for very different situations. These include charge transfer processes at macrointerfaces and micro- and nano-interfaces of very different geometries, namely, electron transfer reactions complicated by

coupled chemical processes, molecular electrocatalysis at modified electrodes, and simple and assisted ion transfers across liquidliquid interfaces. As a result of her scientific activity, Prof. Molina has published more than 220 papers and six book chapters, and she has been invited as a speaker in several international meetings. She is a regular reviewer for the Spanish *National Evaluation and Foresight Agency* and for scientific journals in the areas of Physical Chemistry, Electrochemistry, and Analytical Chemistry. Also, Prof. Molina is a fellow of the Academy of Science of the Region of Murcia (Spain) and a member of several editorial boards of scientific journals.



Joaquin Gonzalez is a Lecturer at the University of Murcia, Spain. He follows studies of Chemistry at this University and got his Ph.D. in 1997. He has been part of the Theoretical and Applied Electrochemistry group directed by Professor Molina since 1994. He is author of more than 80 research papers. Between 1997 and 1999, he also collaborated with Prof. M^a Luisa Abrantes of the University of Lisboa. He is the coauthor of four chapters, including "Ultramicroelectrodes" in *Characterization of Materials* second Ed (Kaufmann, Ed). He has taught in undergraduate and specialist postgraduate courses and has supervised three Ph.D. theses. His working areas are physical electrochemistry, the development of new electrochemical techniques, and the modelization, analytical treatment, and study of electrode processes at the solution and at the electrode surface (especially those related to electrocatalysis).

About the Editor



Fritz Scholz is a Professor at the University of Greifswald, Germany. Following studies of chemistry at Humboldt University, Berlin, he obtained a Dr. rer. nat. and a Dr. sc. nat. (habilitation) from that University. In 1987 and 1989, he worked with Alan Bond in Australia. His main interest is in electrochemistry and electroanalysis. He has published more than 300 scientific papers, and he is editor and coauthor of the book “Electroanalytical Methods” (Springer, 2002, 2005, 2010, and Russian Edition: BINOM, 2006), coauthor of the book “Electrochemistry of Immobilized Particles and Droplets” (Springer 2005), coeditor of the “Electrochemical Dictionary” (Springer, 2008; second ed., 2012), and coeditor of volumes 7a and 7b of the “Encyclopedia of Electrochemistry” (Wiley-VCH 2006).

In 1997, he has founded the *Journal of Solid State Electrochemistry* (Springer) and serves as Editor-in-Chief since that time. In 2014, he has founded the journal *ChemTexts—The Textbook Journal* (Springer). He is the editor of the series “Monographs in Electrochemistry” (Springer) in which modern topics of electrochemistry are presented. Scholz introduced the technique “Voltammetry of Immobilized Microparticles” for studying the electrochemistry of solid compounds and materials, he introduced three-phase electrodes to determine the Gibbs energies of ion transfer between immiscible liquids, and currently he is studying the interaction of free oxygen radicals with metal surfaces, as well as the interaction of liposomes with the surface of mercury electrodes in order to assess membrane properties. In the last years, his research also comprises the interaction of electrode surfaces with free oxygen radicals.

Index

- A**
Absolute mobility, 44
Accessibility, 111
Activation control, 58
Activity coefficient, 14, 44, 48, 49, 83
Additive differential double pulse voltammetry (ADDPV), 230–233, 260–264, 274, 276, 278, 287–291, 308–311, 314
Adiabaticity, 2, 34, 38–42
Adsorption, 22, 24–26, 246, 247, 416
Alternating Current Voltammetry, 546
Anthraquinone, 415
Anti-cooperativity, 171
Asymmetrical diffusion, 369–372, 503–506
Azobenzene, 553, 554
391, 401–407, 523, 528–530, 609, 643–645
CE mechanism, 134, 189, 190, 196–207, 209–215, 218, 291, 301–311, 376, 390, 401–406, 523, 528–530, 609, 640–643
Charge mobility, 44–46
Charge transfer coefficient, 57, 137, 149, 183, 350, 352, 356, 419, 435, 489, 491, 492, 496, 499, 538, 551–553, 561, 625, 639
Chemical potential, 4–7, 17, 18
Chronoamperometry, 74–79, 138–145, 168, 170, 194
Chronocoulometry, 239–247
Complexation, 220–225, 410–415
Comproportionation, 134, 171, 172, 175, 184, 376, 377, 521
Concentration profile, 50–53, 70, 72–74, 80, 85, 92, 104, 108, 109, 115, 116, 124, 125, 137–139, 212, 273, 279, 323, 325, 327, 363, 364, 370, 377, 589, 593, 596, 603, 647, 650
Conductivity, 47–49, 60, 359
Convection, 42, 44, 50–53, 58, 75, 76, 96, 97, 123, 124, 126, 361
Converted charge, 245, 246, 418–420, 422, 431–433, 441, 450–455, 465, 537, 545, 546, 553, 557, 567, 570
Cooperativity, 171
Cottrell equation, 75, 76
Counter and secondary electrode, 59, 60
Cross potential, 249, 262, 263, 290, 308, 542, 567
Current density, 61, 104, 105, 122, 182, 242, 243, 255, 360, 386, 398, 413, 415
- B**
Band electrode, 113, 114, 345
Born theory of solvation, 36
Butler–Volmer formalism, 56, 137, 168, 419, 434, 446, 496, 553
- C**
Capacitance, 15, 21–26, 49, 62, 75, 346, 347, 360, 361, 431, 432, 434, 435, 439, 535, 553, 555
Catalytic mechanism, 191, 193–197, 199, 204, 205, 207, 209–211, 213, 218–220, 291–301, 306, 310, 390–401, 406, 407, 454, 458, 523–527, 566, 603–605
Catalytic (EC') mechanism, 134, 190–193, 201–214, 216, 291, 301–311, 376, 390,

- Cyclic Voltammetry, 68, 121, 282, 312, 318, 320, 328–348, 356, 361, 366–369, 375, 380–390, 401, 404, 405, 412, 416, 427, 430, 433, 446, 452–456, 465, 512, 538, 544, 546, 555–556, 559, 563, 576
- Cyclic Voltcoulometry, 376, 452–456
- Cylindrical electrode, 61, 111, 329, 475, 512
- D**
- dc Polarography (dcP), 96–99, 101, 152–153
- DDPV. *See* Differential double pulse voltammetry (DDPV)
- DDTPV. *See* Double Differential Triple Pulse Voltammetry (DDTPV)
- Derivative Chronopotentiometry, 546
- Derivative Voltammetry, 262
- Differential double pulse voltammetry (DDPV), 230–233, 253, 254, 256–260, 262, 264, 266, 270–275, 278, 282–287, 297–301, 305–308, 464, 466, 471, 473, 474, 485–490, 500, 513, 515
- Differential multipulse voltammetry (DMPV), 232, 233, 464, 466–467, 471–474, 484–490, 499–503, 515
- Differential Normal Double Pulse Voltammetry (DNNDPV), 230, 260, 261
- Differential Normal Multipulse Voltammetry (DNMPV), 466–467, 473–475, 485, 486, 488–490
- Differential Staircase Voltammetry (DSCV), 464–466, 469–473, 484, 508–512, 542–546, 550, 557
- Differential Staircase Voltcoulometry (DSCVC), 464, 465, 536–541, 555, 557–559
- Diffusion
- coefficient, 45, 54, 55, 69–71, 75–77, 92, 98, 102–111, 118, 122, 135, 143, 155, 159, 160, 163, 164, 167, 168, 172, 177, 181, 184, 186, 192, 196, 205, 213, 223, 238–244, 248, 249, 252–255, 257, 258, 262–265, 279, 280, 288, 291, 301, 322, 325, 327, 332–340, 358, 361, 365, 377, 389, 391, 408, 412, 423, 469, 470, 473, 476, 484, 500, 505, 520, 535, 581, 585, 593, 647
- layer, 52–54, 58, 69, 73, 74, 99, 108, 109, 115, 118, 126, 137, 138, 140, 141, 146, 148, 159–161, 171, 199, 204, 212, 344–346, 353, 361, 363, 364, 391, 401, 406
- Diffusion controlled limiting current, 74, 128, 142, 176, 181, 213, 239
- Diffusive-kinetic steady state, 199, 202, 203, 216, 308, 401, 405
- Disc electrode, 245–247, 249, 250, 255, 260, 261, 282, 288, 289, 294–297, 299, 301
- Disproportionation, 134, 171, 172, 175, 184, 185, 216, 279, 376, 380, 407
- DME. *See* Dropping mercury electrode (DME)
- DMPV. *See* Differential multipulse voltammetry (DMPV)
- DNNDPV. *See* Differential Normal Double Pulse Voltammetry (DNNDPV)
- DNMPV. *See* Differential Normal Multipulse Voltammetry (DNMPV)
- Double Differential Triple Pulse Voltammetry (DDTPV), 230, 311, 313–314
- Double layer, 2, 15–26, 49, 62, 75, 99, 120, 230, 347, 359, 360, 364, 431, 438, 439, 464, 544, 556
- Double layer charging, 246, 346, 424, 435, 515
- Double Pulse Chronoamperometry (DPC), 230, 231, 239–248
- Driving force, 43–45
- Dropping mercury electrode (DME), 51, 52, 55, 60, 68, 94–102, 111, 123, 152–154, 229, 230, 232, 581, 614
- DSCV. *See* Differential Staircase Voltammetry (DSCV)
- DSCVC. *See* Differential Staircase Voltcoulometry (DSCVC)
- E**
- ECE mechanism, 134, 191, 216–218, 376, 407–410, 523, 530–533
- EC mechanism, 134, 190–193, 201–214, 216, 291, 301–311, 376, 390, 391, 401–407, 523, 528–530, 609, 643–645
- EEC' mechanism, 570–573
- EE mechanism, 171, 175–179, 182–184, 192, 216, 218, 279, 288–290, 376, 379, 381, 383, 385, 407, 441, 446, 447, 509–511, 520–523, 531, 532, 557, 561
- Electrocapillary equation, 19
- Electrocatalysis, 26, 448, 449, 563
- Electrochemical cell, 10, 11, 17, 53, 58, 359
- Electrochemical potential, 1, 5–8, 11, 12, 17, 29, 44
- Electrode geometry, 50, 53–55, 57, 60, 61, 76, 106, 111–115, 118, 123, 154, 163, 166, 174, 180–183, 186, 188, 214, 216, 221, 225, 237, 248, 249, 252, 254, 262, 264, 279, 281, 282, 287, 297, 299, 323, 324, 327, 330–332, 337, 340–346, 353–356, 375, 377, 384, 389, 391, 393, 400, 401,

- 412, 413, 415, 469, 470, 475–485, 509, 511, 512, 517, 524
- Electron work function, 7
- Equilibrium constant, 172, 185, 192, 199, 202, 205, 210, 213, 221, 292, 293, 303, 307, 308, 310, 311, 380, 392, 395, 403, 407, 411, 412, 520, 521, 528, 529, 641
- F**
- Fermi energy, 7
- Fermi level, 36
- Fick's law, 97
- First order, 17, 29, 189–225, 291–311, 390–415, 418, 522–536, 538, 574–577
- First-order catalytic process, 191, 193, 205, 209, 299, 310, 376, 391, 398, 401, 524, 526, 527, 564, 603–605
- Flux, 42–46, 49–52, 54, 61, 70, 71, 80, 84, 86, 104, 111, 112, 114, 115, 120, 123, 147, 153, 163, 235, 238, 352, 361, 641, 643, 647
- Formal electrode potential, 2, 14
- Formal potential, 13, 28, 30–32, 37, 49, 70, 76, 79, 110, 134, 137, 147–149, 151, 159, 161, 167, 171–172, 175–177, 179, 180, 182, 185, 192, 217, 256, 257, 262, 271, 278, 279, 282, 283, 287–290, 296, 304, 305, 310, 312, 337, 351, 352, 356, 375, 376, 379, 380, 382, 383, 387–389, 396, 407, 413, 417, 425, 427, 436, 440, 442, 445, 447, 448, 455, 471, 473, 479, 483, 484, 486, 491, 498, 505–511, 513, 517, 518, 520, 521, 527, 540, 547–549, 557–559, 561–563, 565, 567, 571, 572, 577
- Forward component, 489, 505, 521, 524
- Franck–Condon principle, 33
- Frequency, 38, 40–42, 358, 467, 468, 479, 481, 482, 489, 495, 496, 498, 499, 506, 511, 513, 515, 516, 522, 526, 527, 529, 533, 545, 546, 551
- G**
- Galvani potential difference, 3, 6, 9, 18
- Gibbs energy, 5, 17, 28, 30, 33–35, 38, 39, 83, 356
- H**
- Half-peak potential, 335, 350
- Half peak width, 252, 259, 286, 287, 299, 436, 437, 442, 444, 479, 481, 489, 491, 517, 518, 525, 529, 530, 541, 546, 547, 558, 565
- Half wave potential, 68, 76, 79, 81, 85, 106, 110, 118, 120, 122, 123, 126, 134, 141, 149, 150, 153, 158, 162, 177, 179, 191, 205, 210, 213, 225, 249, 250, 253–256, 258, 259, 262–264, 303–305, 336, 337, 406, 476, 488, 500, 501, 503, 535
- Heterogeneous rate constant, 31, 32, 37, 41, 56, 137, 138, 140, 142, 143, 147, 149, 159, 161, 167, 169, 268, 270, 271, 273, 274, 276, 277, 350–353, 418, 421, 438, 446, 448, 453, 538, 566, 567, 577, 625, 639
- Heteropolyanion, 527, 559
- Homogeneous chemical reaction, 134, 172, 189, 309, 522, 563
- I**
- IHP. *See* Inner Helmholtz plane (IHP)
- Index potential, 469, 498, 500, 502, 552
- Inner Helmholtz plane (IHP), 23, 25–27
- Inner potential, 2–5, 28, 83, 89
- Interaction(s), 2, 7, 25, 27, 38, 39, 41, 102, 171, 183, 190, 287, 417, 439, 440
- Interface, 2, 3, 5, 6, 8, 10, 15–19, 21–26, 29, 36, 38, 40, 50, 58, 59, 81–94, 258, 259, 263, 365–372, 415, 431, 499–503, 505, 574
- Interfacial potential distribution, 439
- Inverted potential difference, 171
- Ion pairing, 171, 387
- Irreversible process, 89, 142, 143, 147–149, 153, 154, 161, 162, 169, 277, 349, 351, 353, 420, 423, 427, 436, 486, 488–490, 492, 495, 496
- ITIES, 81, 82, 84, 367, 583
- K**
- Kinetic parameter(s), 149–152, 159, 205, 207–210, 274, 276, 299, 304, 357, 358, 364, 376, 496, 498, 530, 549
- Kinetic steady state, 195–203, 211, 213, 216, 295, 296, 298, 299, 302, 308, 396–398, 401, 405, 524
- L**
- Ladder mechanism, 220–225, 410–415, 533–536
- Limiting current, 54, 55, 57, 58, 62, 63, 74–76, 80, 98, 99, 104, 105, 110, 113, 115, 123, 125, 128, 141, 142, 152, 166, 168, 169, 181, 191, 194, 196, 199, 200, 205, 207–211, 213–215, 217, 218, 224, 225, 230, 232, 239, 242–244, 249, 250, 252, 268, 296, 297, 303–305, 312, 387, 396, 451, 458, 485, 650

Linear diffusion layer, 53, 54, 115, 138, 140, 148, 159–161
 Linear sweep voltammetry (LSV), 64, 318, 320–321, 515

M

Macroelectrode, 52, 53, 55, 62, 63, 69, 76, 78, 160, 232, 246, 278, 322, 337, 346, 347, 354, 359, 360, 386, 387, 391, 402, 436
 Marcus–Hush–Chidsey formalism, 36–38
 Marcus–Hush formalism, 2
 Mass transport coefficient, 52–58, 147, 149, 161, 352, 353
 Mass transport control, 54, 57, 423, 577
 Membrane potential, 81, 89, 369
 Membrane system(s), 81–84, 89, 258, 259, 367, 501, 502
 Microdisc, 255
 Microdisc electrodes, 255
 Microelectrode arrays, 362–364
 Microelectrodes, 55, 59, 102, 112, 116, 117, 120–123, 134, 135, 154–164, 166–168, 182–183, 213, 214, 218, 219, 234–239, 252, 255, 273, 276, 278, 282, 322–325, 327–332, 340–347, 354–356, 358–364, 369, 372, 376–391, 396–401, 405, 406, 413, 458, 459, 469–485, 490, 510, 511, 513, 515, 526–528, 577, 597–600
 Micro-ITIES, 369–372, 503–507
 Microsphere, 122, 123, 156, 162, 166, 167, 182, 213, 241, 255, 355, 405, 524, 525, 597–600
 Migration, 46, 49–50, 52, 87, 172
 Modified electrodes, 376, 415, 448–460, 563–577
 Molar conductivity, 47, 48
 Monolayer, 415–419, 422, 424, 425, 427, 428, 431–433, 436, 439–441, 455, 456, 458, 541, 553, 555, 560, 561, 568, 569, 574
 Multicenter molecules, 387–389
 Multi-electron electrochemical reaction, 171–189, 278–291, 376–390, 507–522, 537, 544, 557–563
 Multipulse, 63–65, 68, 230, 232, 233, 317–372, 375–460, 463–577
 Multipulse chronoamperometry, 318–319, 325–328, 376, 416, 423–427
 Multipulse chronocoulometry, 318–319, 376, 416, 423–427

N

Nanoelectrode, 120, 364
 Nernst diffusion layer, 73, 74, 79, 109, 118, 137, 344, 345
 Nernst–Einstein relationship, 45
 Nernst equation, 2, 8–14, 16, 28, 69, 83, 93, 134–136, 325, 349
 Nernstian behavior, 69, 70, 219
 Non-faradaic charge, 431, 433, 550, 553–557
 Non-faradaic current, 432, 439, 556, 557
 Non-polarizable interface, 16–18, 83, 369
 Non-reversible electrochemical reaction, 133–225, 349–358, 389–390, 485–499, 542, 551, 561–563
 Normal potential difference, 171
 Normal Pulse Polarography (NPP), 68, 96, 99–101, 153
 Normal Pulse Voltammetry (NPV), 68, 83, 84, 94, 157, 230, 252, 268, 278, 286, 306, 314, 318, 344, 354, 402, 406, 441, 442, 445
 NPP. *See* Normal Pulse Polarography (NPP)
 NPV. *See* Normal Pulse Voltammetry (NPV)

O

Ohmic drop, 2, 49, 58–63, 81, 120, 282, 346, 347, 359–361, 369
 Outer Helmholtz plane (OHP), 23, 24, 26, 27, 29
 Outer potential, 3

P

Peak current, 233, 252, 254, 255, 260, 262, 273, 274, 276, 277, 284, 299, 301, 307, 309, 310, 334, 335, 338, 340, 347, 350–352, 356, 386, 399, 436, 460, 479, 481–484, 486, 487, 489, 491, 492, 495, 502, 510, 517, 526–531, 551, 552, 561, 575–577, 638, 640
 Peak height, 286, 287, 297, 299–301, 403, 430, 437, 442, 444, 484–486, 491, 492, 505, 515–517, 525, 533, 539–541, 543, 551, 556, 558, 561, 562, 565, 567, 568, 576
 Peak potential, 233, 252, 254–257, 260, 273, 274, 276, 282, 285, 287, 297, 299, 307, 309, 310, 335, 336, 340–342, 347, 350–352, 368, 382, 383, 399, 403, 429, 430, 436–438, 442, 444, 445, 460, 471, 473, 476, 479, 483, 484, 486, 491,

- 499–502, 505, 509, 510, 515, 517, 524,
527, 529, 530, 532, 535–537, 539, 540,
547, 551, 552, 554, 556, 558, 565, 567,
572, 576, 577
- Peak splitting, 273
- Phase, 2–6, 9, 12, 15–18, 21, 82, 83, 85–87, 90,
91, 94, 102, 172, 258, 279, 359,
365–367, 370, 372, 500, 503, 505, 583,
585, 663
- Planar electrode, 69–81, 97, 99, 101, 104, 107,
110, 111, 118, 120, 126, 135–153,
158–160, 169, 170, 182, 183, 192, 195,
200, 210, 211, 213, 238–239, 241–243,
245, 246, 249, 251, 252, 254, 256,
257, 260, 262, 264, 267–269, 272,
273, 276, 291, 296, 301–311, 325–327,
332–338, 340, 341, 344, 347–352,
354, 366, 381–384, 391, 393–397,
399, 402, 403, 408, 409, 460, 470, 471,
473–477, 484, 487–496, 499, 524, 526,
529–532, 575, 576, 605–609, 611–613,
635–645
- Plateau, 37, 38, 42, 217, 268, 400, 426,
427, 453–456, 458, 483, 485, 518,
520, 525, 528, 529, 547, 549, 550,
567, 568
- Polarizable interface, 15, 16, 90, 258, 259, 367,
368, 499–501, 503
- Polarized interface, 82–90, 365–367, 501–503
- Potential of Zero Charge, 101, 364
- Potential pulse, 63, 64, 68, 73, 96, 99–101, 109,
134, 224, 229, 230, 234–249, 252, 262,
264–266, 268–270, 272, 273, 278–281,
286, 288, 292–295, 297, 301, 302, 311,
314, 318, 320, 322–325, 328, 329, 344,
347, 349, 365, 366, 377–379, 391, 412,
416–427, 431–433, 438, 440, 441, 446,
450, 464–467, 469, 485, 501, 515, 523,
530, 537, 542, 550, 555, 564, 615–617,
619, 622, 625–633
- Pseudo first order, 189–192, 205, 213, 220,
291, 390, 410, 449–456, 458, 522, 523,
527, 528, 533, 534, 564–573
- Pulse length, 466, 467, 485, 551
- PZC. *See* Zero charge potential (PZC)
- Q**
- Quasi-reversible process, 138, 149, 150, 353,
489, 492, 495
- R**
- RA peak, 492, 495
- Rate constant, 29–33, 35–38, 40–42, 49, 56, 57,
84, 134, 137, 138, 140, 142–145, 147,
149–151, 157–159, 161, 163, 165–170,
183, 186, 191, 199, 205, 214, 218, 220,
264, 268, 270, 271, 273, 274, 276, 277,
297, 299, 301, 303, 306–310, 312,
349–354, 356, 389, 391, 395, 397, 402,
403, 407, 411, 417–421, 423, 425–427,
434–438, 440, 446–449, 453, 456, 458,
460, 485, 489, 491, 492, 495, 498, 499,
521, 522, 525–527, 529, 533, 534,
542–544, 547, 548, 550, 551, 553, 556,
561–564, 566, 567, 571, 572, 577, 625,
639
- RC peak, 495
- RC time-constant, 2, 58–63
- RDPV. *See* Reverse differential pulse
voltammetry (RDPV)
- Reaction layer, 53, 195, 204, 205, 211, 213,
216, 295, 303, 391, 401, 406, 407
- Real potential, 7, 499, 552
- Reference electrode, 10, 12, 14, 19, 28, 58, 59,
61, 62, 81, 271
- Relative surface excess, 19
- Resistance, 15, 16, 49, 54, 57–63, 75, 81, 120,
145, 346–348, 359, 361, 431, 556
- Reverse component, 492, 524
- Reverse differential pulse voltammetry
(RDPV), 230, 311–313
- Reverse pulse voltammetry (RPV), 230, 232,
247–252, 264, 266–271, 295–298,
302–305, 311, 312, 633
- Reversibility criteria, 56, 79, 147–149,
352–353, 547
- Reversibility degree, 56, 147, 148, 150, 160,
161, 183, 267, 304, 351, 353, 354, 417,
427, 451, 453, 455, 491, 492, 567
- Reversible behavior, 69, 140, 147, 351, 352,
430, 544, 545
- Reversible process, 68, 135, 138, 140,
142–145, 147, 150, 153, 154, 160–162,
169, 252, 276, 290, 318, 335, 344, 351,
353, 422, 427, 469, 471, 486, 488, 489,
492, 545, 547, 549, 555
- Room temperature ionic liquid, 189, 242
- Room temperature ionic liquids (RTIL), 102,
189, 242
- Rotating disc electrode, 51, 52, 55, 123–126

- RPV. *See* Reverse pulse voltammetry (RPV)
- RTIL. *See* Room temperature ionic liquids (RTIL)
- S**
- Saturated calomel electrode (SCE), 14, 271, 387, 455, 527, 561
- SCE. *See* Saturated calomel electrode (SCE)
- Second order, 376, 457, 573, 647
- Second order catalytic process, 218, 220
- Single polarizable interface, 259
- Specific adsorption, 22, 24–27
- Spherical electrode, 55, 61, 101–111, 118, 120–122, 154–163, 168, 210–216, 238–243, 245, 248, 249, 251, 253, 255, 257, 264–266, 268–270, 272, 274, 286, 290, 291, 296, 300, 327–329, 336–340, 344, 345, 355, 364, 384, 386, 399, 400, 413, 457, 471, 472, 477, 484, 485, 489, 490, 496, 512–515, 518, 535, 536, 573, 577, 581, 593, 615–623, 625–631, 654, 655, 657, 658
- Spherical geometry, 101, 102, 121, 327
- Spherical nanoparticle, 123, 355
- Square wave amplitude, 467, 479, 481, 483, 498, 517, 519, 525, 546, 547, 550–552
- Square wave voltammetry (SWV), 422, 464, 467, 469, 474–476, 479, 481, 483–485, 489, 491, 493–497, 499–502, 504–507, 513, 515, 517, 518, 520–531, 533–537, 544–547, 550–554, 556, 557, 561–565, 569–574, 576, 577
- Square wave voltammetry (SWVC), 464, 469, 537, 544–550, 552, 556, 557, 559, 561, 562, 564–569, 571, 572
- Staircase voltammetry, 121, 134, 318, 320–321, 365, 381, 416, 430, 431, 454
- Standard electrode potential, 8–14
- Standard Gibbs energy of ion transfer, 83
- Standard hydrogen electrode (SHE), 10–12, 14, 16
- Standard partition coefficient, 83
- Static mercury drop electrode (SMDE), 67, 101, 241, 263, 291, 297, 298
- Stationary response, 120–123, 163, 196, 346, 354, 372, 384, 391, 396, 397, 401, 489, 524
- Steady state, 52, 53, 55, 110, 118, 120–122, 124, 154, 156, 159, 163–166, 169, 182–183, 191, 195–199, 202–204, 211, 213, 214, 216, 217, 219–220, 241, 255, 273, 283, 295, 296, 298, 299, 302, 308, 310, 344, 354, 358–361, 372, 386, 387, 391, 396–398, 401, 405–107, 415, 453, 472, 477–485, 507, 509, 513, 524–526, 546, 565, 597–600, 648
- Steps, 63, 64, 67, 68, 76, 89, 96, 99, 114–116, 121, 134, 138, 139, 154, 169–172, 183–187, 189, 191, 199, 205, 210, 211, 216, 217, 234, 244, 246, 253, 258, 265, 282, 287–290, 293, 297, 299, 304, 307, 313, 317, 326, 345, 358, 375, 376, 379, 386, 387, 389, 399, 401, 407, 410, 411, 420, 426, 427, 431, 441, 445–448, 450, 453–455, 458, 467, 476, 485, 496, 505, 507–510, 513, 518, 521, 522, 531, 534, 557, 559, 566–568, 573, 577, 593, 615, 616, 628, 631, 648
- Stepwise process, 171, 186
- Stokes–Einstein relationship, 46
- Stripping Analysis, 102
- Superposition principle, 241, 324, 350, 391, 401, 411, 485
- Surface bound molecules, 376, 415–460, 465, 536–577
- Surface coverage, 362, 431, 435, 441, 445, 450, 553
- Surface excess, 17, 19, 20, 417, 418, 421, 422, 433, 435, 440, 441, 443, 450, 540, 550
- Surface heterogeneity, 439
- Surface potential, 3, 7, 25
- Surface tension, 16, 17, 19–22
- SWVC. *See* Square wave voltammetry (SWVC)
- T**
- Thin layer, 53, 126–129
- Total steady state, 213–216
- Transfer coefficient, 31, 32, 37, 38, 54, 57, 137, 147, 149, 167, 183, 270, 271, 273, 275, 277, 312, 350, 352, 354, 356, 419, 435, 489, 491, 492, 496, 498, 499, 538, 551–553, 561, 625, 639
- Transport number, 46, 49
- Two-electron electrochemical reaction, 172–184, 389–390, 440–448, 509, 513, 516–518, 522, 523, 531, 558
- Two independent E process, 176, 178
- Two polarizable interfaces, 258, 268, 500, 501, 503
- U**
- Ultrafast voltammetry, 361–362
- Ultramicroelectrodes, 241–243, 249, 251–253, 255, 257, 267, 273, 276, 283, 441, 546

Uncompensated resistance, 75, 346–348, 359,
431, 556

V

Viscosity, 46, 48, 51, 55, 124

Volta potential difference, 3

W

Working electrodes, 10, 12, 28, 58–61,
126–128, 134, 238, 346, 360

Z

Zero charge potential (PZC), 19, 24–26

Zone diagram, 404, 405